Springer Proceedings in Materials

A. Praveen Kumar
Tatacipta Dirgantara
P. Vamsi Krishna *Editors*

Advances in Lightweight Materials and Structures

Select Proceedings of ICALMS 2020

Springer

Springer Proceedings in Materials

Volume 8

Series Editors

Arindam Ghosh, Department of Physics, Indian Institute of Science, Bangalore, India

Daniel Chua, Department of Materials Science and Engineering, National University of Singapore, Singapore, Singapore

Flavio Leandro de Souza, Universidade Federal do ABC, Sao Paulo, São Paulo, Brazil

Oral Cenk Aktas, Institute of Material Science, Christian-Albrechts-Universität zu Kiel, Kiel, Schleswig-Holstein, Germany

Yafang Han, Beijing Institute of Aeronautical Materials, Beijing, Beijing, China

Jianghong Gong, School of Materials Science and Engineering, Tsinghua University, Beijing, Beijing, China

Mohammad Jawaid, Laboratory of Biocomposite Tech., INTROP, Universiti Putra Malaysia, Serdang, Selangor, Malaysia

Springer Proceedings in Materials publishes the latest research in Materials Science and Engineering presented at high standard academic conferences and scientific meetings. It provides a platform for researchers, professionals and students to present their scientific findings and stay up-to-date with the development in Materials Science and Engineering. The scope is multidisciplinary and ranges from fundamental to applied research, including, but not limited to:

- Structural Materials
- Metallic Materials
- Magnetic, Optical and Electronic Materials
- Ceramics, Glass, Composites, Natural Materials
- Biomaterials
- Nanotechnology
- Characterization and Evaluation of Materials
- Energy Materials
- Materials Processing

To submit a proposal or request further information, please contact one of our Springer Publishing Editors according to your affiliation:

European countries: **Mayra Castro** (mayra.castro@springer.com)
India, South Asia and Middle East: **Priya Vyas** (priya.vyas@springer.com)
South Korea: **Smith Chae** (smith.chae@springer.com)
Southeast Asia, Australia and New Zealand: **Ramesh Nath Premnath** (ramesh.premnath@springernature.com)
The Americas: **Michael Luby** (michael.luby@springer.com)
China and all the other countries or regions: **Mengchu Huang** (mengchu.huang@springer.com)

More information about this series at http://www.springer.com/series/16157

A. Praveen Kumar · Tatacipta Dirgantara ·
P. Vamsi Krishna
Editors

Advances in Lightweight Materials and Structures

Select Proceedings of ICALMS 2020

Springer

Editors
A. Praveen Kumar
Department of Mechanical Engineering
CMR Technical Campus
Kandlakoya, Telangana, India

P. Vamsi Krishna
Department of Mechanical Engineering
National Institute of Technology Warangal
Warangal, Telangana, India

Tatacipta Dirgantara
Faculty of Mechanical and Aerospace Engineering
Institut Teknologi Bandung
Bandung, Indonesia

ISSN 2662-3161 ISSN 2662-317X (electronic)
Springer Proceedings in Materials
ISBN 978-981-15-7826-7 ISBN 978-981-15-7827-4 (eBook)
https://doi.org/10.1007/978-981-15-7827-4

© Springer Nature Singapore Pte Ltd. 2020
This work is subject to copyright. All rights are reserved by the Publisher, whether the whole or part of the material is concerned, specifically the rights of translation, reprinting, reuse of illustrations, recitation, broadcasting, reproduction on microfilms or in any other physical way, and transmission or information storage and retrieval, electronic adaptation, computer software, or by similar or dissimilar methodology now known or hereafter developed.
The use of general descriptive names, registered names, trademarks, service marks, etc. in this publication does not imply, even in the absence of a specific statement, that such names are exempt from the relevant protective laws and regulations and therefore free for general use.
The publisher, the authors and the editors are safe to assume that the advice and information in this book are believed to be true and accurate at the date of publication. Neither the publisher nor the authors or the editors give a warranty, expressed or implied, with respect to the material contained herein or for any errors or omissions that may have been made. The publisher remains neutral with regard to jurisdictional claims in published maps and institutional affiliations.

This Springer imprint is published by the registered company Springer Nature Singapore Pte Ltd.
The registered company address is: 152 Beach Road, #21-01/04 Gateway East, Singapore 189721, Singapore

Preface

The International Conference on Advanced Lightweight Materials and Structures (ICALMS 2020), the first-of-its-kind conference in India, is dealing solely with recent advances in lightweight materials and its structures. This conference was focused on basic academic research related to innovations and future trends in the era of advanced composites, as well as associated industry challenges. Experts from different parts of the globe dealing in Mechanical and Materials Science Engineering attended ICALMS 2020. This conference provided an international forum to present, discuss and exchange innovative ideas and recent developments in the field of Materials Science and Structural Engineering.

ICALMS 2020 received an overwhelming response with more than 200 full-paper submissions. The papers submitted have been reviewed by experts from renowned institutions, and subsequently, the authors have revised the papers, duly incorporating the suggestions of the reviewers. This has led to significant improvement in the quality of the contributions. Springer Nature have agreed to publish the selected papers of the conference in their book series of Springer Proceedings in Materials. This enables fast dissemination of the papers worldwide and increases the scope of visibility for the research contributions of the authors.

This book comprises five parts, viz. design of automotive lightweight structures, mechanical behaviour of composite materials, advanced manufacturing processes of lightweight materials, lightweight material joining techniques and numerical analysis of smart materials. Each part consists of relevant full papers in the form of chapters. The design of automotive lightweight structures part consists of chapters on research related to crashworthiness, thin-walled structures, impact simulation, metal forming, etc. The mechanical behaviour of composite materials part consists of chapters on composites, hybrid composites, nanocomposites and green composites. The advanced manufacturing processes of lightweight materials part consist of chapters on machining, unconventional machining and industrial engineering areas. Lightweight material joining techniques part contains chapters from various welding techniques, additive manufacturing processes etc. The numerical analysis of smart materials part consists of chapters on heat transfer, computational fluid dynamics

biomechanics, etc. This book provides a snapshot of the current research in the field of materials and structural engineering and hence will serve as valuable reference material for the students and research community.

Editors

Kandlakoya, India — Dr. A. Praveen Kumar
Bandung, Indonesia — Dr. Tatacipta Dirgantara
Warangal, India — Dr. P. Vamsi Krishna

Acknowledgements

We are extremely grateful to the chief patrons **Shri. C. Gopal Reddy**, Chairman, and **Smt. C. Vasantha Latha**, Secretary, CMR Technical Campus, for their motivation and valuable guidance that have enabled to complete this conference successfully. We register our deep sense of gratitude to the patrons **Dr. A. Raji Reddy**, Director, and **Dr. M. Ahmed Ali Baig**, Dean (Academics), for their meticulous guidance, encouragement and continuous support towards ICALMS 2020. We also sincerely thank the conference chair **Dr. D. Maneiah**, Professor and Head, Department of Mechanical Engineering, for his keen interest, inspiring guidance during all stages of the event.

We are very grateful to the international/national advisory committee, session chairs, student volunteers and administrative assistants who selflessly contributed to the success of this conference. Efforts taken by peer reviewers to improve the quality of papers provided constructive critical comments; improvements and corrections to the authors are gratefully appreciated. Also, we are thankful to all the massive knowledge treasure trove, the participants, without whom there would have not been any ICALMS 2020. We are grateful for their immense contributions to the conference in the form of potential research works. Our sincere thanks to **Dr. Akash Chakraborty** and **Priya Vyas**, Associate Editors, Applied Sciences and Engineering, Springer, for their support and guidance during the publication process.

Last but not least, we are thankful for the enormous support of DST-SERB for helping us financially. Their support was not only the strength but also an inspiration for organizers. It is our pleasure to acknowledge the efforts of all the persons who have worked conjointly, relentlessly and spilled their sweat to make this conference a great success

Editors
Dr. A. Praveen Kumar
Dr. Tatacipta Dirgantara
Dr. P. Vamsi Krishna

Contents

Design of Automotive Lightweight Structures

Meso-modeling of Closed-Cell Aluminum Foam Under Compression Loading 3
Eka Oktavia Kurniati, Tatacipta Dirgantara, Leonardo Gunawan, and Annisa Jusuf

Design of Active Noise Reduction Equipment Using Multipole Secondary Source 19
Muhammad Kusni, Purnomo, Leonardo Gunawan, and Husein Avicenna Akil

Numerical Analysis of Double-Hat Multi-Corner Column Under Axial Loading 31
Annisa Jusuf, Leonardo Gunawan, Tatacipta Dirgantara, and Fadhil Mubarhak

Influence of Triggers on the Damage Characteristics and Initial Peak Load of Composite Tubular Energy Absorbers for Low-Velocity Impact Applications 43
Venkateswarlu Gattineni and Venukumar Nathi

Finite Element Investigations on the Fatigue Behaviour and Life Calculation for Axle of Aircraft 55
Rishabh Chaudhary and Srishti Singh

Identification of Rattan Cane in Structural Applications 65
N. Srujana, G. Monesh, and T. Bhavani

A Review on Crashworthiness and Cooling Models for Lithium-Ion Batteries in Electric Vehicles 75
Mohammed Mushtaq and S. V. Satish

Correlation Involving Compressive Strength and Flexural Strength of Polyester Fiber-Reinforced Binary Blended Concrete 85
N. K. Amudhavalli, S. Sivasankar, M. Shunmugasundaram, and A. Praveen Kumar

Optimization of Rectangular Plate with Circular Opening to Improve Buckling Characteristics 97
A. Agarwal, O. M. Seretse, M. T. Letsatsi, and J. Pumwa

Modelling and Structural Analysis of Stiffened Plate in Vertical Configuration Using ANSYS 107
M. T. Letsatsi, O. M. Seretse, and A. Agarwal

Review on Behavior of Hybrid Fiber-Reinforced Concrete 117
Banka Hadassa Joice, A. Aravindan, and Satish Brahmalla

Design and Analysis of Hybrid Composite Leaf Spring for Automotive Applications: An Extensive Study 127
Smaranika Nayak, Isham Panigrahi, and Ramesh Kumar Nayak

Effect of Carbon Fiber-Reinforced Polymer Strips on Square Steel Tubular Sections Under Compression 133
S. Sivasankar, N. K. Amudhavalli, A. Praveen Kumar, and M. Shunmugasundaram

Design and Analysis of Cap Forward Armrest Component 145
Kishore Kumar Kandi, Nagaveni Thallapalli, Mayank Sunder, and Rahul Vuda

Design Optimization of Knuckle Stub Using Response Surface Optimization 155
A. Agarwal, O. B. Molwane, and R. Marumo

Numerical Analysis of Rear Spoilers in Improving Vehicle Traction 165
R. Marumo, O. B. Molwane, and A. Agarwal

Automated Vision System to Measure Weld Length of Hand Brake . . . 175
M. Palaninatharaja, S. Julius Fusic, S. Karthikeyan, and H. Ramesh

Behaviour of Multi-layered Hybrid Fibrous Ferrocement Panels 187
Srujan Varma Kaithoju, D. Vijay Venu Gopal, V. Aastritha Vatchala, and Uzair Ahmed

Mechanical Behaviour of Composite Materials

Micromechanical Finite Element Elastic Properties Modeling of Plain Woven Composite 199
Agnes Listyo Rini, Tatacipta Dirgantara, Satrio Wicaksono, Khodijah Kholish Rumayshah, and Hermawan Judawisastra

Effect of Nano Fillers on the Mechanical Behavior of Mercerized Plain Weaved Flax Fabric Reinforced Polymer Composites 209
A. Praveen Kumar, M. Shunmugasundaram, S. Sivasankar, and N. K. Amudhavalli

Tensile and Bending Characteristics of Hybrid Basalt Fabric–Aluminium Laminates Reinforced with MW-CNT Fillers 217
A. Praveen Kumar, S. Lohith Reddy, D. Nageswararao, and L. Ponraj Sankar

Effect of Silicon Carbide Particle Size on the Physical and Mechanical Properties of Hierarchical Layered Composite Material 225
Mulugundam Siva Surya and G. Prasanthi

Mechanical Properties of Aluminum Wire-Reinforced GFRP Laminates 233
J. Jayapriya, D. Muruganandam, and C. Balasubramaniyan

Investigations on the Tensile and Flexural Properties of Vacuum-Infused Areca Polymer Nanocomposites 243
M. Shunmugasundaram, A. Praveen Kumar, N. K. Amudhavalli, and S. Sivasankar

Theoretical Research and Performance of Engineered Cementitious Composite 253
Lakshmi Meghana Srikakulam and Veerendrakumar C. Khed

Experimental Investigation on Tensile Property of Vacuum Infused Kenaf-Based Polymer Composite with the Presence of Nanofillers 265
M. Shunmugasundaram, P. Anand, Maughal Ahmed Ali Baig, and Yamini Kasu

Investigation on Mechanical Properties of Chemically Treated Banana and Areca Fiber Reinforced Polypropylene Composites 273
G. Sai Krishnan, Shanmugasundar, Raghuram Pradhan, and Ganesh Babu Loganathan

Tensile Loading Rate Effect on Open-Hole Tensile Strength and Failure Mechanism of Polymer Composites 281
Sunny, K. K. Singh, and Ruchir Shrivastava

Soil Stabilization with Nanomaterials and Extraction of Nanosilica: A Review 293
Karumanchi Meeravali, Nerella Ruben, and Mikkili Indira

Mechanical Properties of AA7050/Coconut Shell Ash Composites Manufactured via Stir Casting Technique 301
V. Mohanavel, M. Ravichandran, K. S. Ashraff Ali, and A. Praveen Kumar

Improvement of Compressibility, Shear Strength Characteristics of Soft Soil with Quarry Dust and Vitrified Polish Waste 309
Satish Brahmalla, Habibunnisa Syed, and Banka Hadassa Joice

Tensile and Fatigue Behavior of Glass Fiber Laminated Aluminum-Reinforced Epoxy Composite 319
Tripti Sonker, Ajaya Bharti, and Pranshu Malviya

Comparative Study of Aluminium—Alumina Composite Prepared by Mechanical Mixing and Oxidation 329
Jayanta Kumar Mahato

Microstructure and Mechanical Characterization of AA7150/ZrO_2 Composites Manufactured by Stir Casting Route 341
V. Mohanavel, M. Ravichandran, S. Suresh Kumar, and A. Praveen Kumar

Tribological Characterization of Lightweight Hybrid Aluminium Composite Under Lubricated Sliding Condition 349
Pranav Dev Srivyas and M. S. Charoo

Electrical Study of Lead Calcium Titanate Borosilicate Glass Ceramics 361
Sangeeta Das, S. S. Gautam, and C. R. Gautam

Usage of Poly-Ether-Ether-Ketone Polymer for the Biomedical Application—A Critical Review 371
M. Ajay Kumar, M. S. Khan, and S. B. Mishra

Effect of Silicon Carbide on Properties of Styrene-Butadiene Rubber 381
T. P. Anirudh Mohan, R. Harikrishnan, N. Rahulan, and Sundararaman Gopalan

Experimental Investigation of a Single Molecule Detection in Thermoplastics 391
V. V. Prathibha Bharathi

Fabrication and Characterization of E-glass Fabric Composites Using Amine-Terminated Butadiene Acrylonitrile 399
Balu Maloth, N. V. Srinivasulu, and R. Rajendra

Effect of Directional Grain Structure on Microstructure, Mechanical and Ballistic Properties of an AA-7017 Aluminium Alloy Plate 409
Pradipta Kumar Jena, K. Siva Kumar, R. K. Mandal, and A. K. Singh

Investigations on the Cutting Quality of Interleaved Flax Fiber with Fly Ash-Reinforced Hybrid Polymer Composite 419
K. Ramraji, K. Rajkumar, M. Rajesh, and K. M. Nambiraj

Advanced Manufacturing Processes of Lightweight Materials

Impact Strength of Ramie/HDPE Composites Manufactured Using Hot Compression Molding 433
Andi Kuswoyo, Lies Banowati, Khodijah Kholish Rumayshah, and Bambang Kismono Hadi

A Review on Coolant Feeding System of CNC Machining Process 441
Araveeti C. Sekhara Reddy, D. V. Paleshwar, K. L. N. Murthy, and B. Sandeep

Experimental Execution Analysis of Wire Electric Discharge Machining 451
Manikyam Sandeep and P. Jamaleswara Kumar

An Approach to Form Manual Power Generalized Experimental Model for Wood Chipping Process 461
V. M. Sonde, P. N. Warnekar, P. P. Ashtankar, and V. S. Ghutke

Calculation of Reliability Approximation of Mathematical Model Formed for Manually Operated Wood Chipper 469
V. M. Sonde, P. N. Warnekar, P. P. Ashtankar, and V. S. Ghutke

Analysis of Machining Parameters on D2Tool Steel in Wire Cut EDM 479
Manikyam Sandeep and P. Jamaleswara Kumar

Dry Sliding Wear Performance Studies of WC–12Co Deposited on AISI 420 Steel Through Microwave Energy 489
Ajit M. Hebbale, J. S. Vishwanatha, M. S. Srinath, and Ravindra I. Badiger

A Review on Influence of Cutting Fluid on Improving the Machinability of Inconel 718 497
Prajith Sivadasan, Gotimayum Sachidev Sharma, Ivan Sunit Rout, and P. Pal Pandian

Condition Monitoring of a Worm Gearbox Under Dynamic Loading Condition 505
Anupkumar Dube and M. D. Jaybhaye

A Review on Optimization of Process Parameters of EDM on Aluminum Metal Matrix Composites Using Various Optimization Techniques 513
S. Prashanth, M. Kannan, R. Karthikeyan, and K. Sunil Kumar Reddy

Reliability Design for Bending Fatigue Strength of Carburized Gears of Low-Carbon Case Hardenable Steels 20CrMo, 20MnCr5, and SAE 8620 521
Rajeshkumar Ramasamy, Senthil Ram Nagapillai Durairaj, Thulasirajan Ganesan, and Praveen Chakrapani Rao

Finish Hard Turning: A Review of Minimum Quantity Lubrication Using Paraffin-Based Nanofluids 531
Faraj Saeid Adrees Majeed, Nordin Bin Mohd Yusof, and Mohd Azlan Suhaimi

Neuro-Fuzzy Modeling and Wear Rate Predictions of Microwave Clads 541
Keerthana Chigateri, Ajit M. Hebbale, Baswanta S. Patil, and M. Anjani Prasad

Microstructural Evaluation of Tungsten Carbide GT30 Machined by Abrasive Jet Machining 551
D. V. Sreekanth, P. Santosh Kumar Patra, and M. Sreenivasa Rao

A X-Ray Diffraction Study of Residual Stresses Due to Multipass Welding of INCONEL600 561
Harinadh Vemanaboina, R. Gopi Chandh, P. Sivakrishna, A. Kishore Kumar, K. Malli Karjuna, and Y. Sailinga Reddy

Evaluation of Surface Integrity of Multi-stacked Glass Interplyed with Flax Laminate by Abrasive Waterjet Machining 569
M. Rajesh, K. Rajkumar, K. M. Nambiraj, and K. Ramraji

Experimental Study on Machining of Aluminium Silicon Alloy (LM6) in Wire Electrical Discharge Machining 579
S. Ram Prakash, G. Selvakumar, and S. Vijayan

Effect of Solid Lubricant in Dry Machining on Al-B_4C Composite 587
K. M. Nambiraj, K. Rajkumar, M. Rajesh, and A. Gnanavelbabu

Lightweight Material Joining Techniques

Analysis of Synthetic Fiber-Reinforced LLDPE Based on Melt Flow Index for Rotational Molding 599
Nikita Gupta and PL. Ramkumar

Experimental Investigation of Weld Charcteristics in Friction Stir Welded Joints Aa 6082-T6 Aluminum Alloy by X-Ray Radiography 607
K. Vijaya Krishna Varma, B. V. R. Ravi Kumar, and M. Venkata Ramana

Investigation on the 3D-Printed Vortex Tube as a Lightweight Cooling Device 617
Pushkar Kamble, Subodh Chavan, Gopal Gote, and K. P. Karunakaran

Strength and Hardness of 3D Printed Poly Lactic Acid and Carbon Fiber Poly Lactic Acid Thermoplastics 625
J. Durga Prasad Reddy, Debashis Mishra, and Nagaraj Chetty

Open-Source Designing for Additive Manufacturing of Metallic Triply Periodic Minimal Surfaces 635
Hrushikesh Chavan, Ashish Kumar Mishra, and Arvind Kumar

Production of Multi-functional and Lightweight Parts with the Use of Topology Optimization and Additive Manufacturing Technique—A Review 645
J. Durga Prasad Reddy, Debashis Mishra, and M. Ajay Kumar

Design and Development of Digital Light Processing (DLP) 3D Printer 653
Yogesh Patil, Richa Patil, N. S. Chandrashekhar, and K. P. Karunakaran

A Review on the Challenges in Welding of Aluminium AA2219 Alloy 663
M. A. Trishul and Bijayani Panda

Powder Feeding Mechanisms in Additive Manufacturing: A Review 673
Yogesh Patil, Ashik Kumar Patel, Amisha Goutam, Subodh Chavan, Milan Pandya, Mitesh Malaiya, and K. P. Karunakaran

Influence of Friction Stir Welding Process Parameters on Mechanical Properties of AA6061-9 wt.% SiC Composites 683
B. N. Venkatesha and M. S. Bhagyashekar

Process Optimization of Segmented Object Manufacturing for Expendable Polystyrene Foam 695
Gopal Gote, Pushkar Kamble, Shishir Kori, and K. P. Karunakaran

Effect of Squeeze Casting on Microstructure and Wear Properties of Aluminium Al–Si Alloy 705
Reeturaj Tamuly, Amit Behl, and Hemant Borkar

Numerical Analysis of Smart Materials

Double Diffusion Due to Centrally Heated Strip in Porous Material . . . 717
N. Ameer Ahamad, Azeem, Maughal Ahmed Ali Baig, and A. Praveen Kumar

Conjugate Heat and Mass Transfer Due to Solid Block in Porous Material 727
N. Ameer Ahamad, Azeem, Maughal Ahmed Ali Baig, and M. Shunmugasundaram

Double Diffusion Caused by Hot Strip in Porous Material 739
N. Ameer Ahamad, Azeem, Maughal Ahmed Ali Baig, and D. Maneiah

Dynamic Characteristics of a Single Orifice Aerostatic Thrust Bearing with Nonlinear Spring Model of Air Film 751
K. S. Srinivasa Prasad, Sushil S. Athreya, Vaibhav Kamath, and Shyam Rajgopal

Industrial Computational Analysis of Aerodynamic Characteristics of Delta-Shaped Aircraft 761
O. B. Molwane, A. Agarwal, and R. Marumo

Transient Thermal Analysis of Vehicle Air Conditioning System by Varying Air Vent Location 771
A. Agarwal, R. Marumo, O. B. Molwane, and I. Pitso

Energy Release Rate Evaluation of Bi-material Interface Cracks 781
M. Prajwal, K. B. Yogesha, Kalmeshwar Ullegaddi, and K. G. Basava Kumar

Vibration Analysis of Femur with Different Hyperelastic Materials 793
Sridhar Adibhatla, A. Satyadevi, and N. V. Swamy Naidu

Analysis of Anterior Cruciate Ligament of the Human Knee Using a Mathematical Model 801
Ahmed Imran

MATLAB-Based Educational Tool for Failure Analysis of Composite Laminates 807
J. S. Mohamed Ali and Iqtidar Mizuar

A Discrete Artificial Immune System Algorithm for the Lot Streaming Flow Shop Scheduling Problem 817
R. Kamalakannan, M. Shunmugasundaram, R. Nagaraj, D. Aravindhan, and S. Mohammed Thouffic

About the Editors

Dr. A. Praveen Kumar is presently working as an Associate Professor in the Department of Mechanical Engineering, CMR Technical Campus, Hyderabad, Telangana. He acquired distinction in bachelor's degree (mechanical engineering) and university first rank in master's degree (engineering design) from Anna University, Chennai. He completed his Ph.D. degree in the area of crashworthiness of thin-walled structures from Anna University, Chennai. His major areas of research interests include metal forming simulation, composite materials and structures, impact loading of hybrid tubes, and use of light-weight materials in automotive applications. He has authored a book titled "Mechanical behaviour of hybrid jute/glass polymer composites" and co-authored a book titled "Development of Labyrinth Type Solar Thermal Energy Storage System" in Lambert Academic Publishing, Germany. He has published 49 research papers in reputed international journals and presented 10 papers in international/national conferences. He is currently an editorial board member in Journal of Transactions on Advancements in Science and Technology and reviewer in reputed journals like Journal of Industrial Textiles, International Journal of Crashworthiness, International Journal of Mechanical Sciences, The Journal of the Brazilian Society of Mechanical Sciences and Engineering. He is also a life member of various professional bodies including Indian Society of Technical Education (ISTE), Association of Machines and Mechanisms (AMM), International Association of Engineers (IAE) and Indian Society of Mechanical Engineers (ISME).

Dr. Tatacipta Dirgantara is presently a Professor of Computational Mechanics in the Faculty of Mechanical and Aerospace Engineering, Institut Teknologi Bandung (FMAE - ITB), Indonesia. Since June 2020, he has been appointed as the Dean of FMAE - ITB. He obtained both his bachelor's and post graduate degree in Mechanical Engineering from Institut Teknologi Bandung, and completed his Ph.D. degree from Queen Mary, University of London, United Kingdom. He is also registered as a professional engineer from the Institution of Engineers Indonesia and ASEAN Federation of Engineering Organisations. He has more than 20 years' experiences in research, teaching, consultancy, and training assignment at national

as well as international level in the area of solid and structural mechanics, computational and experimental mechanics, fracture mechanics and bio mechanics. He has contributed towards more than 80 research papers in international and national journals and conferences, and owns several patents. He has authored a book titled "Boundary Element Analysis of Crack in Shear Deformable Plates and Shells", and co-authored a book titled, "Boundary Element Methods in Engineering and Sciences, Computational and Experimental Methods in Structures". He is currently an editorial board member of the Journal of Engineering and Technological Sciences. He has also supervised more than 100 undergraduate, master and doctoral students.

Dr. P. Vamsi Krishna is currently working as an Associate Professor in the Department of Mechanical Engineering, National Institute of Technology, Warangal, Telangana. He obtained his B.Tech. degree in mechanical engineering and M.Tech degree in production engineering from S V University. He obtained his Ph.D degree with specialization in manufacturing engineering from Andhra University. He has more than 17 years' of teaching experience in reputed engineering colleges and his areas of research interests include machining processes, application of solid lubricants in machining, application of nano materials in machining, sustainable manufacturing and composite materials. He has published 65 research papers in the reputed international journals, 38 papers in national/international conferences and owns a patent. He has co-authored a text book "Production Technology", and authored a book chapter "Nano Cutting Fluids" in Metal working fluids book by Jerry P. Byers. He is currently an editorial board member of journals like American Journal of Mechanical Engineering (AJME), Nanoscience and Nanotechnology Research (NNR), American Journal of Nanomaterials (AJN), Journal of Production Research and Management (JoPRM), Journal of Manufacturing Science and Technology, Horizon Research Publishing Corporation, and is also acting as a reviewer for various reputed international journals.

Design of Automotive Lightweight Structures

Meso-modeling of Closed-Cell Aluminum Foam Under Compression Loading



Eka Oktavia Kurniati, Tatacipta Dirgantara, Leonardo Gunawan, and Annisa Jusuf

Abstract In this study, aluminum foam modeling in the mesoscale has been done under compression loading to consider the closed-cell aluminum foam deformation behavior. The detailed geometry of aluminum foam in mesoscale was developed using a micro-CT scan. The shape of aluminum foam cells was modeled as a circle with various radius. The data of the radius was calculated using ImageJ software. It was known that the distribution of the cell radius is normal. The cells were constructed randomly using MATLAB following a normal distribution. The finite element software LS-DYNA was used for compression loading on closed-cell aluminum foam 2D simulation. It was revealed that cell walls were collapsed during compression until dense, which caused densification. The compressive stress–strain curve was generated from compression simulation for relative density 0.15 and various strain rates. The numerical result for compression was in good agreement with the experimental result.

Keywords Meso-modeling · Micro-CT scan · Closed-cell · Aluminum foam

1 Introduction

Many types of cellular material are used as a lightweight material. Metal foams are widely applied in an automotive, high-speed train, aerospace, military tank, and so on. Aluminum foam is one type of metal foam that is commonly used. The greatness of energy absorption of aluminum foam under compression loading is indicated by high plateau stress. Aluminum foam is potentially suitable for high compressive strength to weight.

The collapse mechanism of different relative densities ALPORAS foams was investigated by Kadar [1] with the X-ray tomography and finite element method. Based on both modes, cell collapse and buckling of the cell wall are the primary deformations of the densified region. The material properties of the foam are not

E. O. Kurniati · T. Dirgantara (✉) · L. Gunawan · A. Jusuf
Lightweight Structures Research Group, Faculty of Mechanical and Aerospace Engineering, Institut Teknologi Bandung, Jl. Ganesha 10, Bandung 40132, Indonesia
e-mail: tdirgantara@ftmd.itb.ac.id

© Springer Nature Singapore Pte Ltd. 2020

A. Praveen Kumar et al. (eds.), *Advances in Lightweight Materials and Structures*, Springer Proceedings in Materials 8, https://doi.org/10.1007/978-981-15-7827-4_1

determined. The mechanical properties of the closed-cell aluminum foam cell wall which are the elastic modulus, yield stress, and power-law hardening coefficient have been obtained by Jeon [2]. The deformation mechanisms of closed-cell aluminum foams subjected to uniaxial compression are compared using finite elements and experimental methods in [3]. The plastic deformation of the foam is caused by localized plastic strain in the cell walls. The strain rate and density of the aluminum foam effect are not included in the previous study. Shen [4] investigated the strain rate effect experimentally. The dissipated energy per unit volume of ALPORAS aluminum foam increases as increasing the strain rate. In [5] and [6], Dou examined the strain rate sensitivity and effect of micro-inertia of aluminum foam sandwich panels. It was found that aluminum foam sandwich panels with high porosity had a low strain rate effect. The research about the compression behavior of aluminum foam sandwich panels gives adequate results using a numerical simulation method. A comparison between numerical and experimental results has not been carried out in aluminum foam sandwich panels previously.

In the present study, a current method to obtain mechanical properties of closed-cell aluminum foam is explained. The aluminum foam is modeled as a 2D sample in mesoscale using micro-CT scan to describe the interior of closed-cell aluminum foam. The aluminum foam cell is modeled using MATLAB and Solidworks. Aluminum foam cell wall behaviors are investigated in various strain rates and density using finite element analysis. The one direction compressive stress–strain from simulation result is compared to the experimental result.

2 Meso-modeling Methods

2.1 Scanning Aluminum Foam Sample

The aluminum foam sample, which was scanned, is ALPORAS. The density ratio between foam and base material is 0.15, and the dimension is 53 × 53 × 53 mm. Figure 1a shows the typical aluminum foam for sampling. The scanner for sample scanning is micro-CT scan Skyscan 1173. The micro-CT scan Skyscan 1173 could scan in 2D and 3D. The maximum diameter and height of the object which can be scanned are 140 mm and 200 mm, respectively. The applied resolution and rotation steps were 50 μm dan 0.2 degrees. The results of scanning aluminum foam in 2D are shown in Fig. 1b.

2.2 Image Analysis

2D scanned images were analyzed to obtain cell size distribution using ImageJ software. ImageJ can detect area, perimeter, major radius, minor radius, and others.

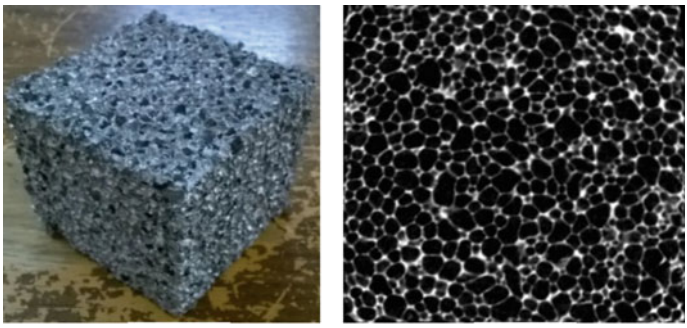


Fig. 1 Closed-cell aluminum foam: **a** sample, **b** scanning result

Besides, the mean and standard deviation of cell size can be calculated directly. The cells in aluminum foam that can be detected are shown in Fig. 2. The number of cells in the aluminum foam that was detected was 493 cells. Data that can be generated from image analysis in ImageJ is shown in Table 1.

The size parameter to be detected was the perimeter because the cells in aluminum foam are not perfectly circular so that the cell radius would be easily calculated by the circle perimeter equation ($p = 2\pi r$) where p is the perimeter and r is the radius. The shape of the aluminum foam cell that was modeled is circular. Perimeter data

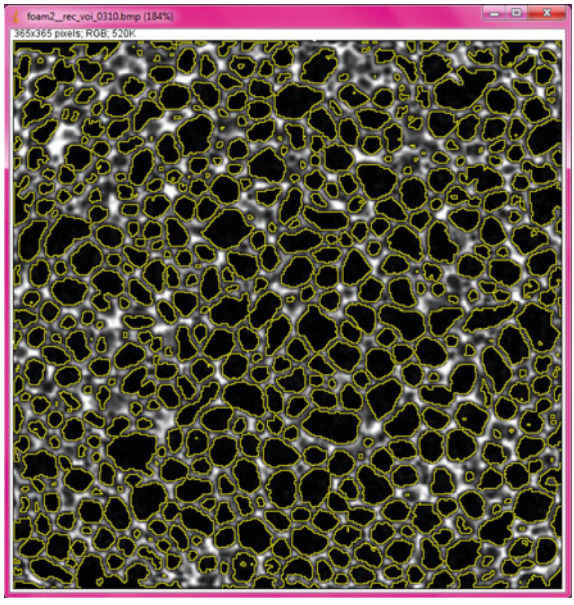


Fig. 2 Detected cells in aluminum foam

Table 1 Data from image analysis in ImageJ

No.	Area	Perimeter
1	9.48	27.57
2	0.06	0.89
3	1.48	8.84
⋮	⋮	⋮
493	0.04	0.60
Mean	2.76	6.09
SD	2.92	4.35
Min	0.02	0.4
Max	18.77	31.44

that has been obtained was converted into a radius. The mean radius and standard deviation obtained were 1.39 mm and 0.37 mm, respectively.

2.3 Cell Size Distribution

Cell size distribution was determined after radius, average, and standard deviation data was obtained. The distribution was normal because the size distribution of cells in aluminum foam approaches the normal distribution. Normal distribution curves could be formed using Microsoft Excel software. The normal distribution curve for the scanned aluminum foam cell radius is shown in Fig. 3.

A calculation using interval prediction according to Eq. (1) is required to determine the minimum and maximum radius based on the normal distribution curve because the results of image analysis using ImageJ were samples, not population.

$$\bar{x} - t_{\alpha/2} s \sqrt{1 + \frac{1}{n}} < x_0 < \bar{x} + t_{\alpha/2} s \sqrt{1 + \frac{1}{n}} \tag{1}$$

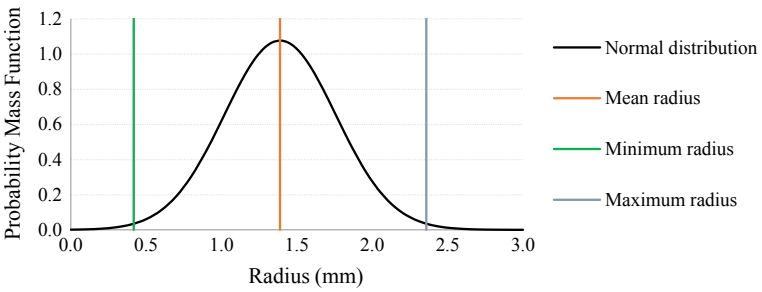


Fig. 3 Normal distribution curve for the radius of the scanned aluminum foam cell

By using Eq. (1) for a sample of more than 200 data and a confidence level of 0.99, the uncertainty value is obtained at 0.97 mm so that the minimum and maximum radius are 0.42 mm and 2.36 mm, respectively.

2.4 2D Image Visualization

Meso-modeling 2D aluminum foam visualization was carried out using MATLAB software. The desired image is a picture of the pattern of spread of random aluminum foam cells that follows the form of a normal distribution with a minimum and maximum radius limit value and relative density/porosity values that can be changed. Input variables needed are 2D aluminum foam model size (length and width), maximum radius, minimum radius, mean radius, standard deviation, and porosity. The algorithm of the visualization of 2D aluminum foam images is shown in Fig. 4. Examples of 2D image visualization results for image sizes of 200 × 200 mm, and porosity 0.5 are shown in Fig. 5.

2.5 Image Converting to Point Cloud

The image produced by the visualization in the previous step is an image in *.jpg format. It could not be directly processed using CAD software. The image consists of pixels containing binary numbers (0 and 1). 0 indicates the black part, and 1 shows the white part. The collection of pixels could be converted into a group of points (point cloud). It could be processed in CAD software. An algorithm for converting pixels into dots is shown in Fig. 6. The point clouds formed from the results of 2D image visualization for image sizes of 200 × 200 mm and porosity of 0.15 are shown in Fig. 7.

2.6 Surface Construction

The surface was constructed from the point cloud using Solidworks. The point cloud was imported in the form of *.xyz file and then created a surface using the planar surface. The formed surface from point clouds for image sizes of 200 × 200 mm and porosity of 0.15 is shown in Fig. 8.

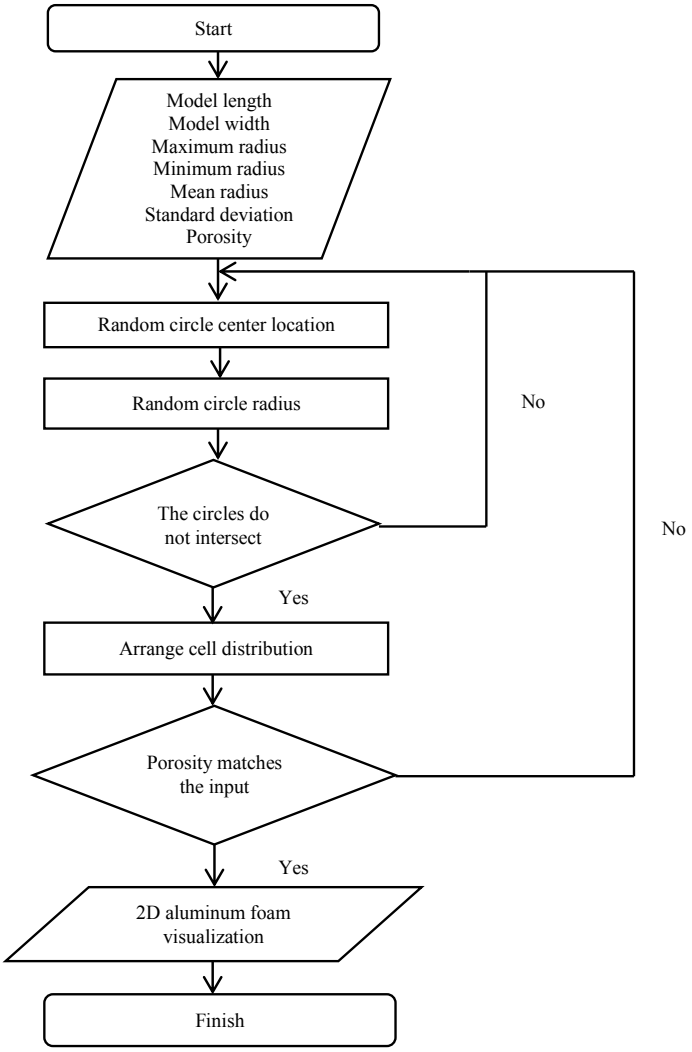


Fig. 4 Algorithm of 2D aluminum foam image visualization

2.7 Compression Simulation

A compression test simulation on the 2D aluminum foam model was performed using LS-DYNA software [7–9]. The simulated aluminum foam model was adjusted to the aluminum foam tested experimentally: aluminum foam which has ratio as 0.15 between aluminum foam density and aluminum solid density (relative density 0.15). Also, simulations were carried out on aluminum foam with a relative density 0.4. Finite element modeling in the simulation of aluminum foam compression test is

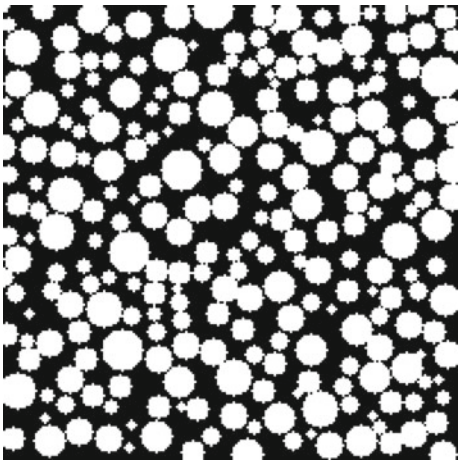


Fig. 5. 2D image visualization results for image size 200 × 200 mm and porosity 0.5

shown in Fig. 9. The size of the aluminum foam model was 50 × 50 mm. The size of the aluminum foam model is at least seven times the cell size to avoid the effect of cell size on the foam [10]. According to ASTM E9-89A, the surface of the plate is made slippery to make frictionless between the specimen foam and the plate so that the coefficient of friction used is zero. Figure 9a shows that cells in aluminum foam have a lot of overlapping, by following the actual condition of the aluminum foam cells, as shown in Fig. 10.

The 2D aluminum foam model was modeled using a shell element with three nodal points. The size of the element was 0.9 mm. The formulation element was element formulation 2, namely Belytschko-Tsay. The thickness of the shell was 0.1 mm. The direction of thickness was constrained to prevent buckling. The velocity of compression was 100, 300, 500, and 700/s.

The material model was piecewise linear plasticity. The base material was aluminum alloy (Al–Ca–Ti). Material properties of the base material are given in Table 2. The true stress–strain compression curve of the base material is presented in Fig. 11.

2.8 Results and Discussion

The compression test simulation on the 2D aluminum foam model was carried out for aluminum foam with a relative density of 0.15 and 0.4. For aluminum foam with a relative density of 0.15, the velocities of the compression test were 100, 300, 500, and 700/s to recognize the strain rate sensitivity. For aluminum foam with a relative density 0.4, the velocity of a compression test is the only 100/s, and the results were compared with relative density 0.15 of aluminum foam.

Figures 12, 13, 14, and 15 show the results of the compression test simulation on

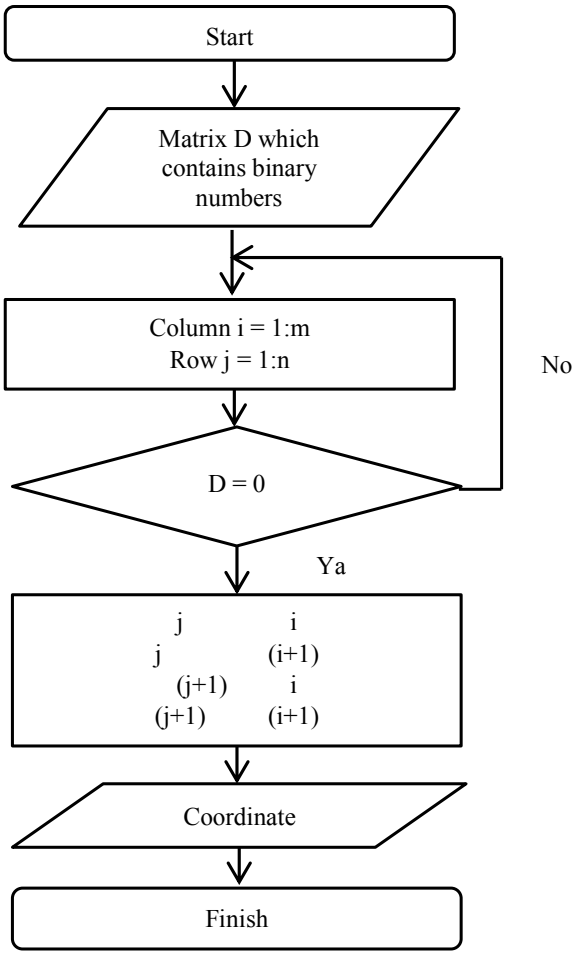


Fig. 6 Algorithm for converting pixels into dots

aluminum foam which has a relative density of 0.15 with various compression velocities. The aluminum foam cells have buckling until the aluminum foam cells become dense. Aluminum foam strength increases as increasing compression velocity. The earlier densification on the aluminum foam cells and the inertia effect cause the increasing of aluminum foam strength.

Figure 16 shows the curve of compression test simulation results on aluminum foam. The comparison between simulation and modified experimental [11, 12] result curves at strain rate 700/s is in a good agreement. The difference between simulation with experiment result occurs because the mesh in the aluminum foam model is still less than perfect when using a mesh size of 0.9 for the relative density 0.15 of the aluminum foam model.

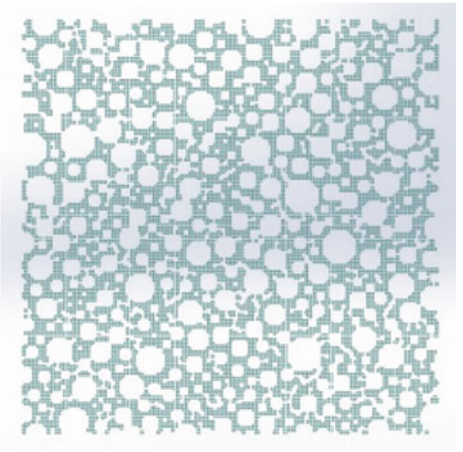


Fig. 7 Point cloud from the results of 2D image visualization for image sizes of 200 × 200 mm and porosity of 0.15

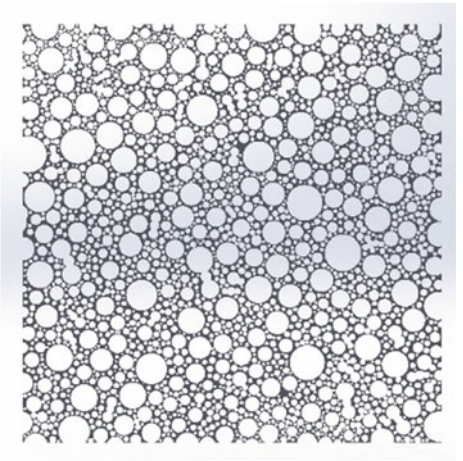


Fig. 8 The surface from point clouds for image sizes of 200 × 200 mm and porosity of 0.15

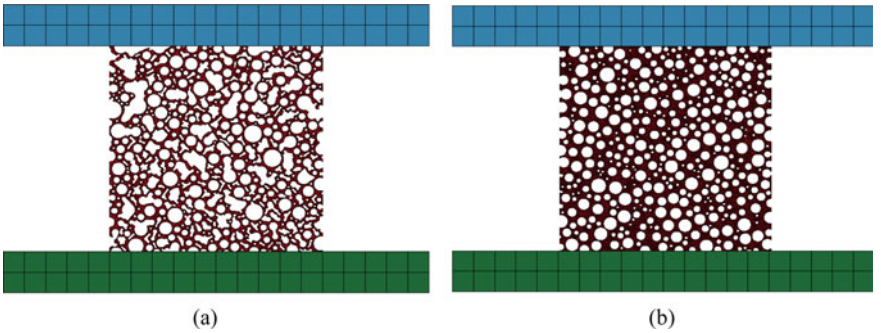


Fig. 9 Finite element modeling in simulation of aluminum foam **a** relative density 0.15, **b** relative density 0.4

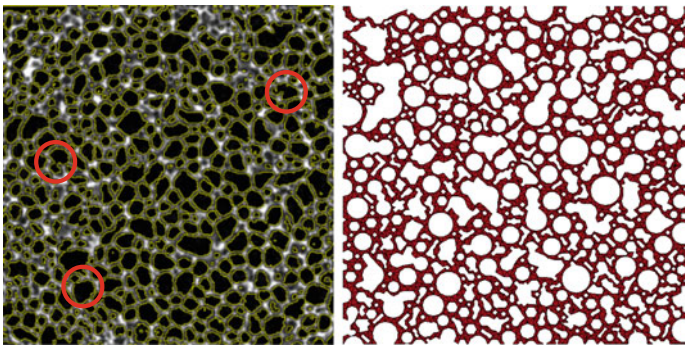
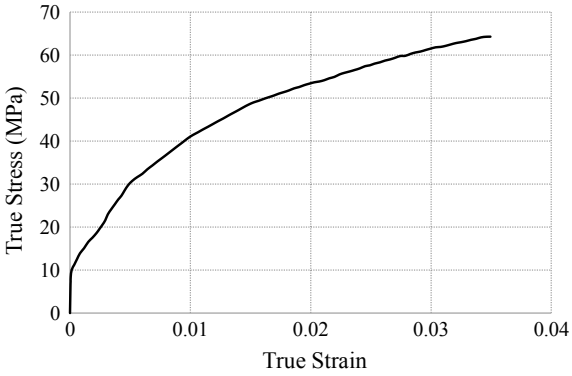


Fig. 10 Comparison of 2D pieces of aluminum foam **a** original, **b** modeling

Table 2 Material properties of base material [2]

Density, ρ_s (kg/m^3)	2700
Modulus Young, E_s (GPa)	61.7
Yield strength, σ (MPa)	11.16
Poisson's ratio, ν	0.3

Fig. 11 True stress–strain curve for base material [2]



The strain rate sensitivity on the stress–strain curve resulting from the meso-modeling is noticeable. The gas trapped in aluminum foam cells is not the main cause of the strain rate sensitivity, so it does not need to be modeled.

Figure 17 shows the compression test simulation results on the aluminum foam which has relative density of 0.4 with strain rate of 100/s. The aluminum foam is more difficult to buckle because it has more solid foam parts.

Figure 18 shows the comparison curve of compression test simulation results on aluminum foam with different relative density and same strain rate 100/s. Aluminum foam with higher relative density has higher compression strength because a solid

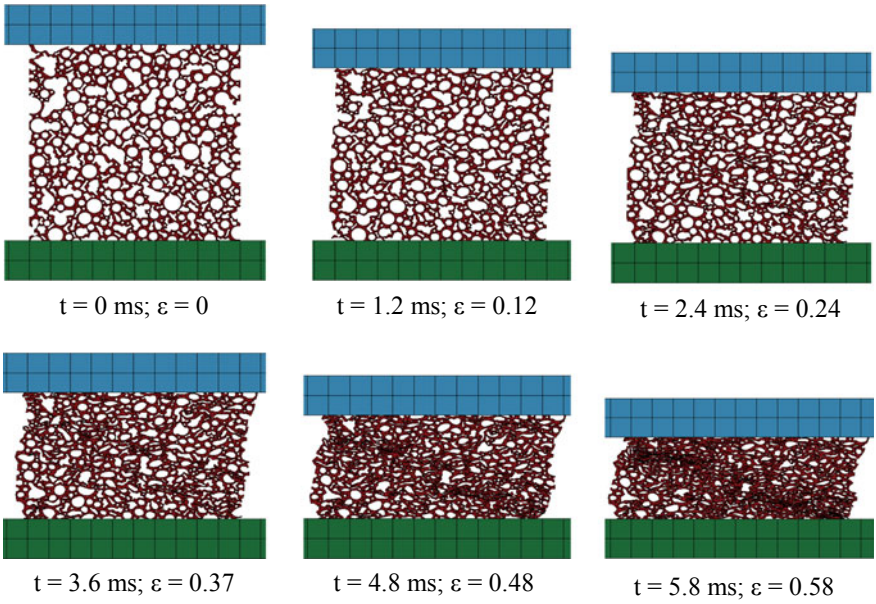


Fig. 12 Compression test on aluminum foam (relative density 0.15) with strain rate 100/s

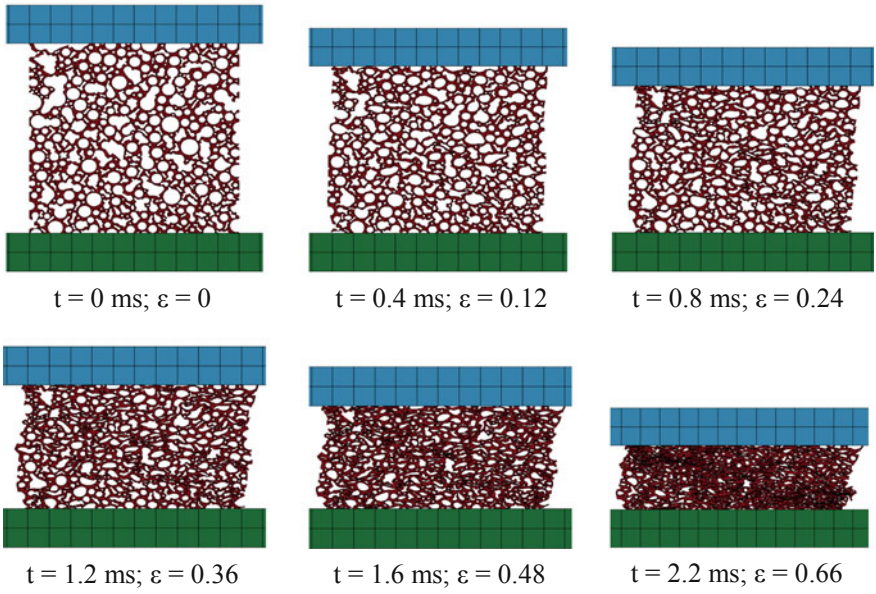


Fig. 13 Compression test on aluminum foam (relative density 0.15) with strain rate 300/s

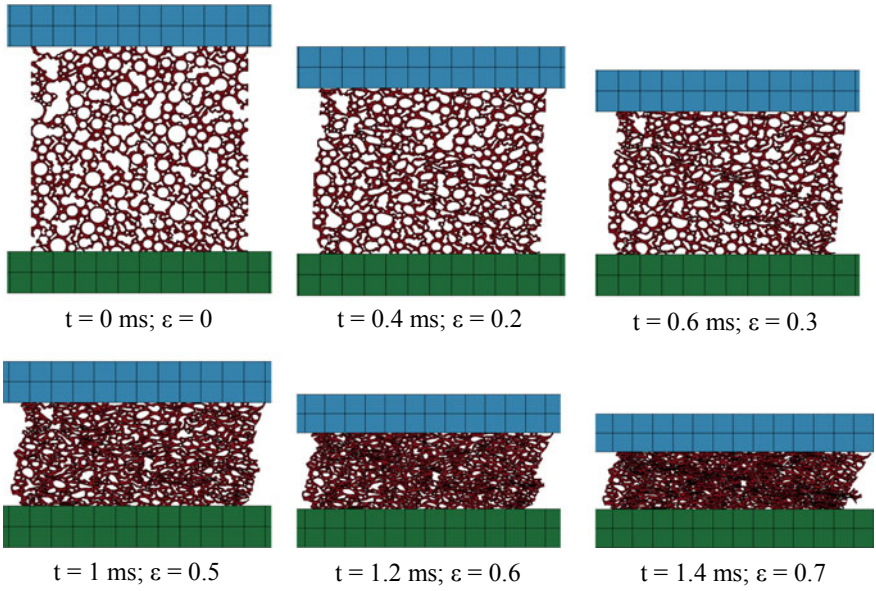


Fig. 14 Compression test on aluminum foam (relative density 0.15) with strain rate 500/s

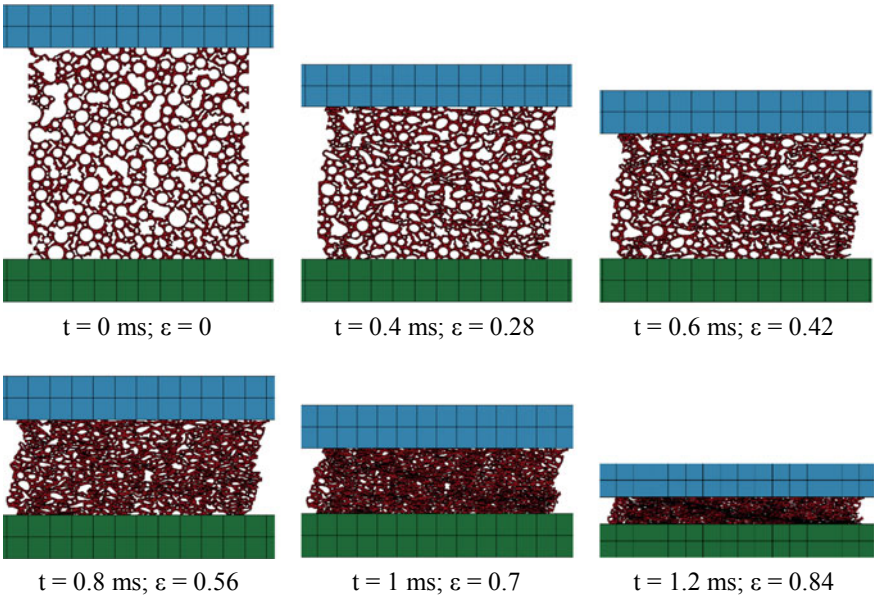


Fig. 15 Compression test on aluminum foam (relative density 0.15) with strain rate 700/s

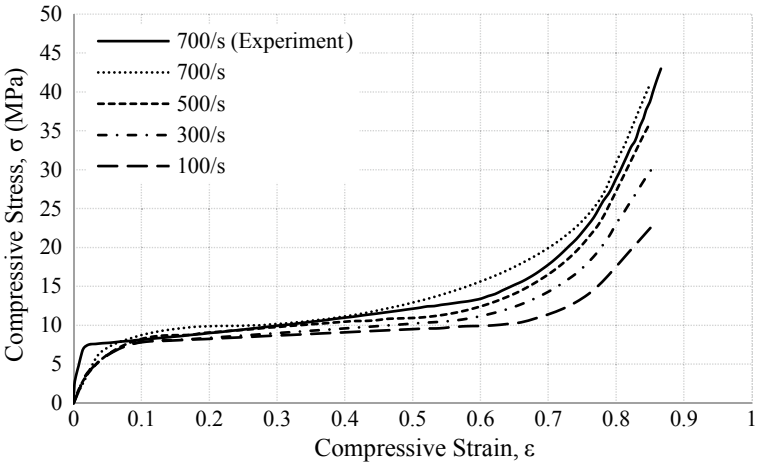


Fig. 16 Stress–strain curve in aluminum foam model (relative density 0.15)

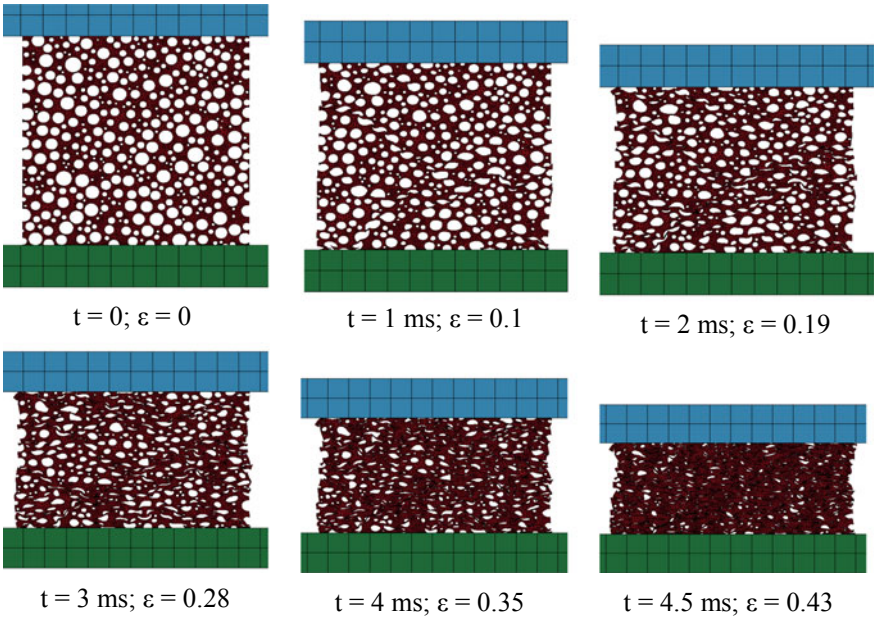


Fig. 17 Compression test on aluminum foam (relative density 0.4) with strain rate 100/s

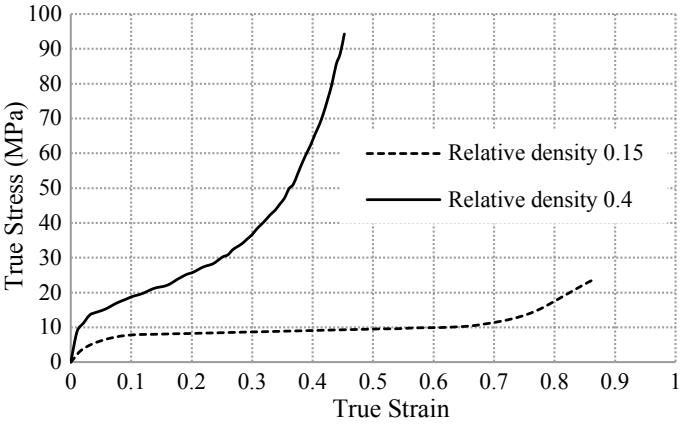


Fig. 18 True stress–strain in aluminum foam model (relative density 0.15 and 0.4)

section of the aluminum foam requires more strength to be able to buckle. The densification strains occur early because of an earlier cell wall touching each other.

3 Conclusion

Meso-modeling of closed-cell aluminum foam subjected to compression loading has been carried out. Based on meso-modeling aluminum foam modeling results and compression test simulation, the simulation results are in good approach to the experimental results at the strain rate 700/s. The strain rate sensitivity occurs in the results of simulations with different compression velocities. Aluminum foam with a greater relative density has more significant impact strength.

Acknowledgement The authors would like to acknowledge the Basic Research of Higher Education (PDUPT) Grant 2019-2020, Ministry of Research, Technology and Higher Education, Republic of Indonesia for the funding for this research. The authors also would like to thank Livermore Software Technology Corporation (LSTC) for providing an academic license of LS-DYNA software.

References

1. Cs K et al (2004) X-ray tomography and finite element simulation of the indentation behavior of metal foams. Mater Sci Eng A 387–389:321–325
2. Jeon I et al (2009) Cell wall mechanical properties of closed-cell Al foam. Mech Mater 41:60–73
3. Jeon I et al (2010) Finite element simulation of the plastic collapse of closed-cell aluminum foams with X-ray computed tomography. Mech Mater 42:227–236
4. Shen J, Lu G, Ruan G (2010) Compressive behaviour of closed-cell aluminium foams at high strain rates. Compos B 41:678–685

5. Dou R et al (2016) Simulation of compression behavior and strain-rate effect for aluminum foam sandwich panels. Comput Mater Sci 112:205–209
6. Dou R, Qiu S, Ju Y (2016) Simulation of effect of loading rate on compression properties in the two-dimensional model of aluminum foam sandwich panels. Mater Trans 57(10):1857
7. Praveen Kumar A, Akbar A, Jusuf A, Gunawan L (2019) Significance of material constitutive model and forming parameters on the crashworthiness performance of capped cylindrical tubular structures. Proc Inst Mech Eng Part L J Mater Des Appl 234(2):320–334
8. Praveen Kumar A, Sivasankar S (2019) Importance of anisotropic coefficients for material constitutive models in forming and crushing simulations. Int J Mecha Prod Eng Res Dev 9(6):765–778
9. Praveen Kumar A, Shrivaathsav S (2019) Influence of forming parameters on the crash performance of capped cylindrical tubes using LS-DYNA follow-on simulations. Int J Interact Des Manuf 13(3):1215–1232
10. Ashby MF et al (2000) Metal foams: a design guide. Butterworth-Heinemann, MA
11. Lankford J, Nicholls A, Danemann. Dynamic compressive behavior of closed-cell aluminum foams. Mechanical and Materials Engineering Division, Southwest Research Institute. USA
12. Dirgantara T (2018) Crashworthiness analysis of foam–filled square column considering strain rate effect of the foam. Thin-Walled Struct 129:365–380

Design of Active Noise Reduction Equipment Using Multipole Secondary Source

Muhammad Kusni, Purnomo, Leonardo Gunawan, and Husein Avicenna Akil

Abstract The development of the active noise reduction method is quite interesting because it is more economical and effective in reducing noise than passive noise reduction. However, active noise reduction using a conventional secondary source can become complicated if required significant noise reduction. It will need a large number of secondary sources. The active noise reduction is also ineffective to reduce high-frequency noise. Multipole secondary source is developed to solve those problems. Multipole secondary source is a combination of monopoles, dipoles, and quadrupoles secondary sources which are arranged in a certain way. The dodecahedron speaker model is chosen to be able to produce a multipole secondary source. The optimal secondary source strength can be obtained through the direct approach and the optimization approach. The optimization approach method is chosen because it depends on the frequency variable for determining the strength of multipole secondary sources. The design of active noise reduction equipment can be applied to reduce noise from industrial machinery.

Keywords Active noise control · Multipole source · Dodecahedron speaker

1 Introduction

Noise control is required to create a comfortable environment for humans. Research about noise control has been carried out by many researchers [1–5]. Noise reduction can be performed in two methods: passive and active. Passive noise reduction works by blocking noise propagation, while active noise reduction works on the principle of wave superposition. On the principle of wave superposition, noise (as primary sound) is opposed by anti-noise (as secondary sound). Amplitude and frequency

M. Kusni (✉) · Purnomo · L. Gunawan
Lightweight Structure Research Group, Faculty of Mechanical and Aerospace Engineering, Institut Teknologi Bandung, Jl. Ganesha 10, Bandung 40132, Indonesia
e-mail: muhammad_kusni@yahoo.com

H. A. Akil
Research Center for Metrology, Indonesia Institute of Science, Kompleks Puspiptek, Serpong, Tangerang, Selatan 15314, Indonesia

© Springer Nature Singapore Pte Ltd. 2020

A. Praveen Kumar et al. (eds.), *Advances in Lightweight Materials and Structures*, Springer Proceedings in Materials 8, https://doi.org/10.1007/978-981-15-7827-4_2

of anti-noise and noise are the same, but the phase difference is 180°, then those two sound sources would weaken each other. Active noise reduction, which uses conventional anti-noise source, is ineffective for noise reduction, especially for three-dimensional sound fields. Producing three-dimensional sound fields could be reached if the placement of secondary sound source is on the exact primary sound source location. Furthermore, conventional anti-noise source is not suitable to reduce high-frequency noise. Multipole secondary source is used to solve the problem of the conventional secondary source.

The advantages of using a multipole secondary source can reduce high-frequency noise and the number of the secondary source, so that make the active noise reduction system more compact. The multipole secondary source could not be used in infinite order due to its limitation. Optimization has carried out to obtain a specific power of secondary sound source in finite order and allow efficient sound reduction by Kusni and Soenarko [8]. Noise reduction in several cases occurred in engineering problems has been presented in [6–8], and the results show that multipole secondary source could reduce noise effectively. The concept of sound reduction with a multipole source has been developed in sound radiation problems in [9]. For aerodynamics, multipoles have been utilized [10, 11] and comprehensively described in the other research [12]. The utilization of monopole and multipole acoustic sources has already researched [13–15]. Utilization techniques of multipole sources for sound field description and cancellation have been explained [16–21]. Those studies are used as references to develop the present method.

In this paper, the design of active noise reduction equipment using multipole secondary source is presented. The pattern of secondary sound in this equipment has been calculated to get better noise reduction. Method and design in this research can be used to reduce noise in industrial machines or other noise, without noise increasing in other machines.

2 Active Noise Reduction Method

The initial process of noise reduction using a multipole secondary source is the identification of unwanted noise. There are two methods of noise identification, i.e., offline and online noise identification. Offline noise identification is applied if noise is constant. If noise is fluctuating, online noise identification is applied. The microphone is used for the noise identification process. The generated analog signal is converted to a digital signal using the analog to the digital card. Digital signal from the noise is processed using fast Fourier transform to produce a supporting sound signal of noise. Multipole principle is applied to every supporting signal of noise then added. Anti-noise is generated by some calculations and using the software. Anti-noise is formed in the digital signal, which is converted into an analog signal using digital to the analog card. The output power is calculated and strengthened using the amplifier. The output analog signal is then changed to a sound field with a specific pattern speaker.

3 Multipole Secondary Sources Design

Active noise reduction equipment design is illustrated in Fig. 1. The main components are microphones (1.a, 1.b until 1.n) as noise sensor, pre-amplifiers (2.a, 2.b until 2.n), analog-to-digital converters/ADC (3.a, 3.b until 3.n), computers (4) as signal processor, digital-to-analog converters/DAC (5.a, 5.b until 5.n), power amplifier (6.a, 6.b until 6.n), multipole speaker (7). Some DAC and power amplifiers are required to form multipole secondary sound waves (the number of n depends on the complexity of noise pattern).

Microphones are used as a noise sensor, which will detect the noise that needs to be reduced. The type of this microphone is a condenser microphone. The microphones work by converting sound pressure to an electric signal and could be integrated with computer easily. The strength of noise source (primary source), noise source pattern, and supporting frequencies that compile noise will be known through the identification process. Inversion software and fast Fourier transform are required for this identification process.

The generated sound signal from the microphone needs to be amplified because it is a weak analog signal output. The number of pre-amplifiers shall be the same as the number of microphones. The output signal from pre-amplifiers is then converted to a digital signal using ADC. The digital signal output from ADC will be identified using

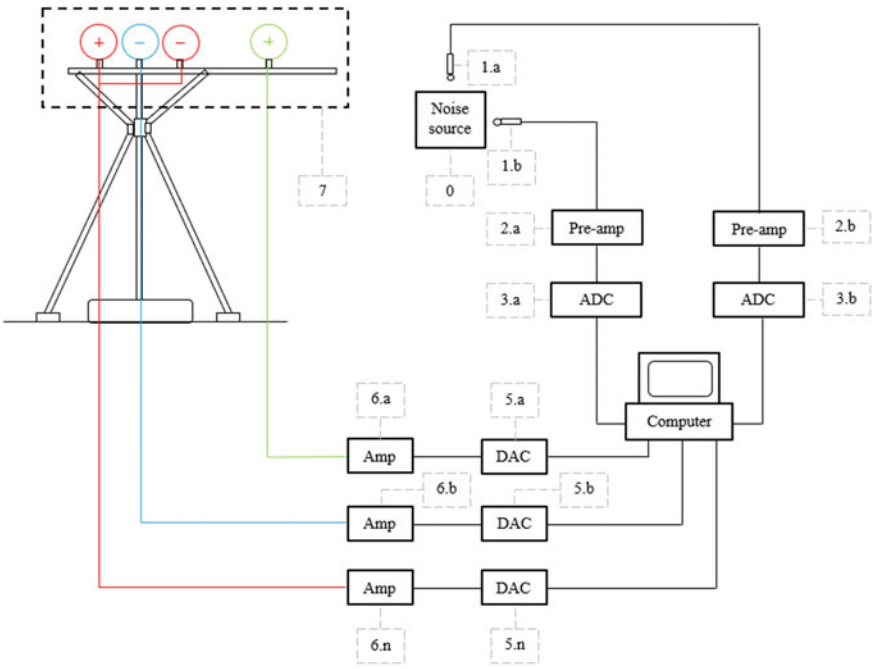


Fig. 1 Active noise reduction equipment design

inversion software and fast Fourier transform, which are installed on the computer. The identification of the signal produces the noise (primary source) strength, noise pattern, and supporting frequencies that compile noise.

The noise (primary source) strength, pattern, and supporting frequencies that compile noise are used as input to produce a particular electric signal which is used to form multipole secondary sound field. Speakers arrangement is also required to form a multipole secondary sound field. In general, the function of the speaker is converting the electric signal to the sound field. Dodecahedron speaker, which is illustrated in Fig. 2, is used to produce multipole secondary sound.

The dodecahedron speaker system consists of 12 speakers which are arranged in parallel and series and placed on the twelve sides of the dodecahedron structure, as shown in Fig. 3. The advantages of parallel and series arrangement in the dodecahedron speaker system are:

1. The total impedance does not change much from the compiler speaker impedance, so that the dodecahedron speaker system characteristic does not change much from the compiler speaker characteristic.
2. The total impedance corresponds to the output impedance of the power amplifier.
3. The output power of the dodecahedron speaker system can reach a maximum value.
4. Able to receive high output voltage from the amplifier.

The multipole secondary sound field is composed of monopole, dipole, and quadrupole sound field. The monopole sound filed is formed by one unit of dodecahedron speaker. Two adjacent monopoles with opposing phase form the dipole sound field. Two units of dodecahedron speakers are used to make the dipole source model. The two speakers are arranged in parallel with the voltage input polarization of one of the speakers arranged upside down. There are two simple conventions used to help the installation procedure. If the output pole of power amplifier is same with

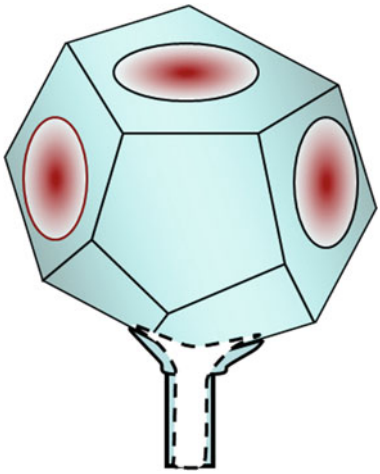


Fig. 2 Design of monopole dodecahedron speaker

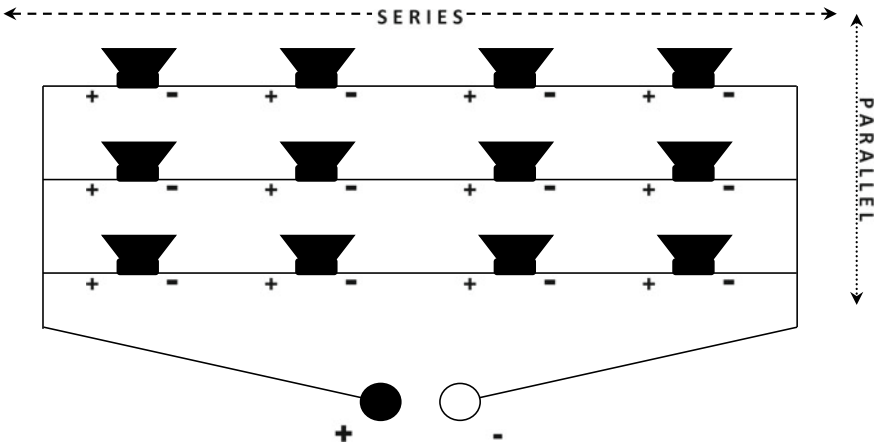


Fig. 3 Speaker arrangement in the dodecahedron system

the input pole of the speaker, a monopole is marked by sign (+), and if the output pole of power amplifier is not the same with input pole of the speaker, monopole is marked by sign (−). The sketch of the arrangement of two dodecahedron speakers to produce a dipole source is given in Fig. 4. Sound patterns which are produced by one, two, and four dodecahedron speaker arrangement are shown in Fig. 5, respectively. A multipole source consists of a monopole, dipole, quadruple source configuration, which is activated simultaneously.

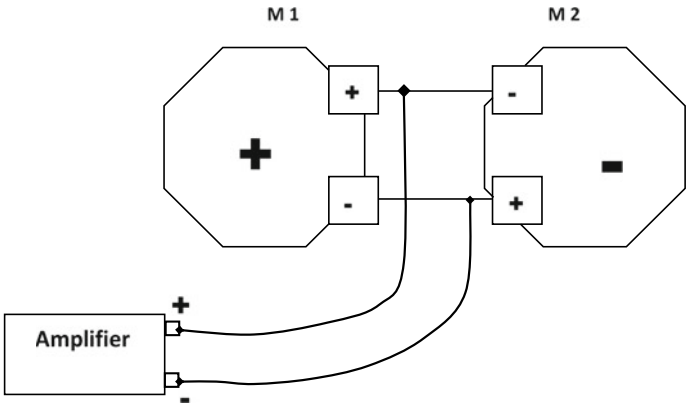


Fig. 4 Arrangement of two dodecahedron speakers to produce a dipole source

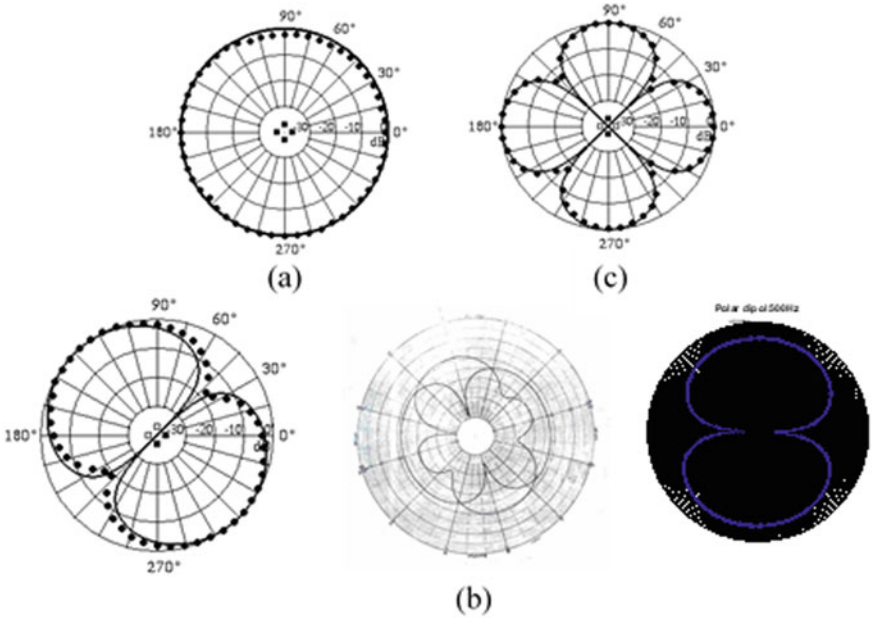


Fig. 5 Output sound pattern by **a** monopole speaker, **b** dipole speaker, **c** quadruple speaker which is a basis to form multipole secondary source

4 Secondary Source Strength Determination

Secondary source strength could be obtained by two methods: direct approach and optimization [6–8]. Multipole source strength determination by using the direct approach method is stated in equation:

$$Q_{\mathrm{sn}} = \frac{h^n Q_{\mathrm{pm}}}{n!} \tag{1}$$

As seen in Eq. (1), the power ratio is not a frequency function. Monopole source strength and dipole source strength are given in Eqs. (2) and (3), respectively:

$$Q_{\mathrm{sm}} = \frac{h^0 Q_{\mathrm{pm}}}{0!} = Q_{\mathrm{pm}} \tag{2}$$

$$Q_{\mathrm{sd}} = \frac{h^1 Q_{\mathrm{pm}}}{1!} = 0.5 Q_{\mathrm{pm}} \tag{3}$$

The power ratio is converted to input voltage in each speaker to simplify the implementation process. The conversion must fulfill the requirements:

1. Sound power is a function of electrical power in each speaker

$$P_e = C P_{\text{acoustic}} \tag{4}$$

2. The acoustic and electric characteristics of each dodecahedron speaker are identical. Each speaker has an equal total impedance, which is 16 Ω. The ratio of the electric power absorbed by each speaker can be considered proportional to the ratio of the square of the voltage applied to each speaker.

In this method, the sound power ration is not frequency function. The sound power ratio (converted to voltage) given to each sound source is the same for all frequencies.

The second method to obtain multipole secondary source power is optimization. Power optimization in active noise reduction systems aims to get minimal total power (resulting from noise and anti-noise). The ratio of the strengths of multipole source compilers (monopole and dipole) is given in equation, respectively:

$$Q_{\text{sm}} = -\frac{\sin(\text{kh})}{\text{kh}} Q_{\text{pm}} \tag{5}$$

$$Q_{\text{sd}} = -\frac{3}{k}\left(\frac{\sin(\text{kh})}{(\text{kh})^2} - \frac{\cos(\text{kh})}{\text{kh}}\right) Q_{\text{pm}} \tag{6}$$

when $k = \frac{\omega}{c}$ and $\omega = 2\pi f$. c is the speed of sound, and f is frequency.

In this method, frequency has a significant influence on the strength ratio. Each frequency has a different strength ratio. The ratio of monopole and dipole source strength in optimization method for different frequency are given in Table 1. The ratio of multipole sound power to the primary source at frequencies above 300 Hz is minimal.

Table 1 Noise and anti-noise source strength ratio

Frequency (Hz)	Q_{pm}	Q_{sm}	Q_{sd}
100	10	8.659317716	4.592922448
150	10	7.138014106	4.117678773
200	10	5.274080015	3.51123798
250	10	3.286189337	2.824396197
300	10	1.396564867	2.112079454
350	10	-0.199863007	1.427461336
400	10	-1.361143609	0.816550421
450	10	-2.015017577	0.313898271

5 Results and Discussions

5.1 Active Noise Reduction Using Direct Approach

Figure 6 shows the sound pressure level for each phase angle. It shows that anti-noise using multipole secondary source with the direct approach is better than conventional anti-noise for various frequencies to reduce the noise.

5.2 Active Noise Reduction Using Optimization

Figure 7 shows the sound pressure level for each phase angle. It could be seen that anti-noise using multipole secondary source with an optimization approach is better than conventional anti-noise for various frequencies to reduce the noise.

Figure 8 shows the comparison between direct and optimization methods to determine the suitable method to generate anti-noise.

6 Conclusion

The design of active noise reduction equipment using multipole secondary source that consists of monopole, dipole, and quadrupole source has been presented. Dodecahedron speaker is chosen to generate multipole anti-noise signal because of several advantages. The technique and results show that the method is practical as a noise reduction system.

Based on the comparison of the noise reduction method, which is direct and optimization, it can be concluded that:

1. Noise reduction using optimization generates a more significant sound reduction
2. There is a similarity of sound reduction patterns produced in the two methods in each test frequency.
3. The best reduction pattern occurs at a frequency of 200 Hz.

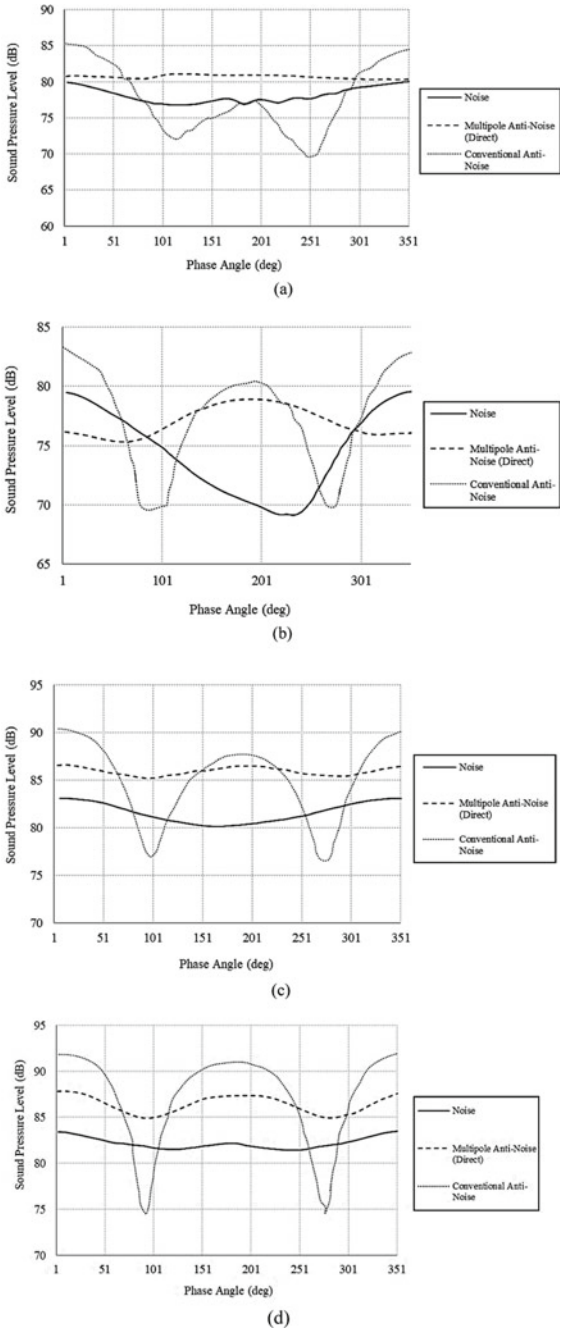
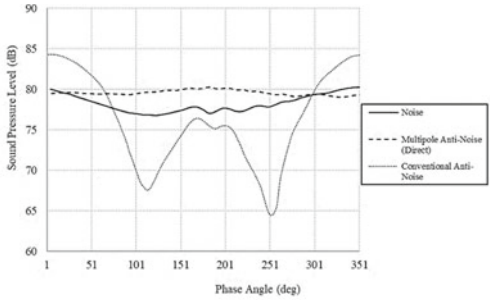
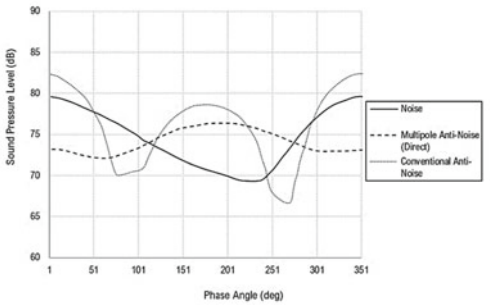


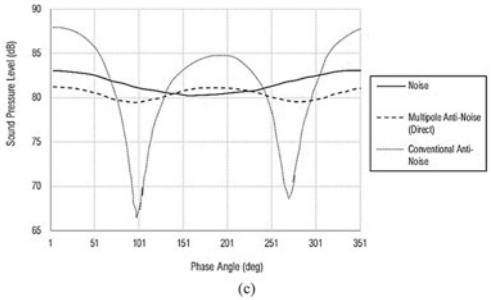
Fig. 6 Comparison between multipole (using direct method) and conventional anti-noise in: **a** 100 Hz, **b** 150 Hz, **c** 200 Hz, **d** 250 Hz



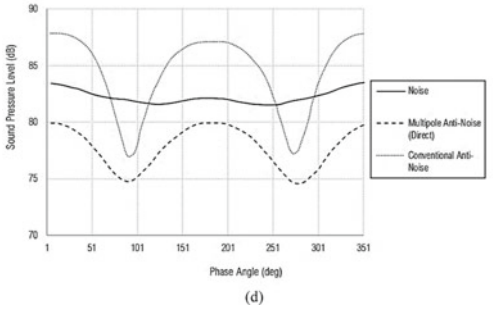
(a)



(b)



(c)



(d)

Fig. 7 Comparison between multipole (using optimization method) and conventional anti-noise in: **a** 100 Hz, **b** 150 Hz, **c** 200 Hz, **d** 250 Hz

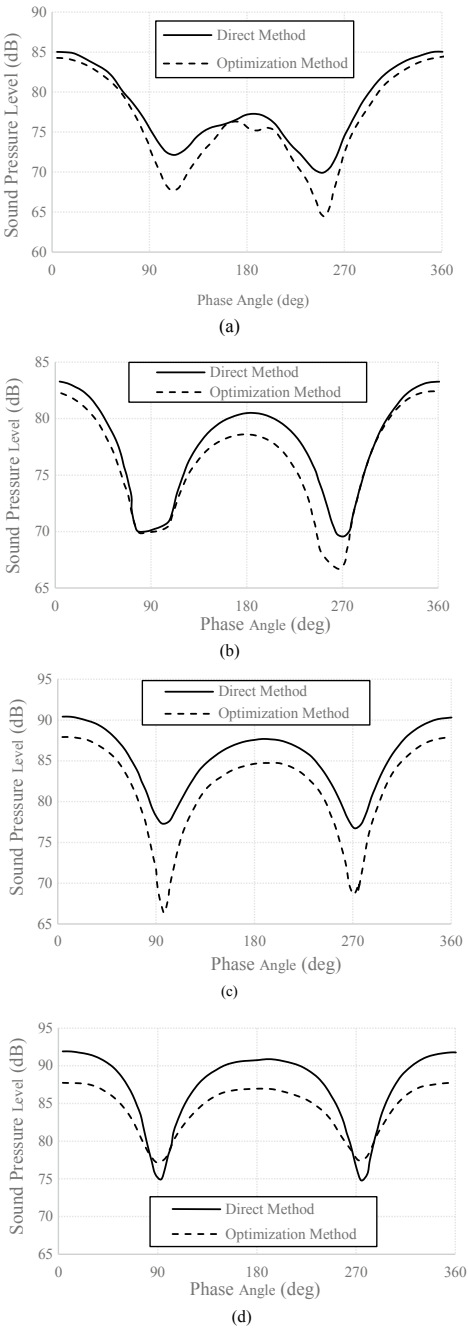


Fig. 8 Comparison between direct and optimization method in: **a** 100 Hz, **b** 150 Hz, **c** 200 Hz, **d** 250 Hz

Acknowledgements The authors gratefully acknowledge the grant from Research, Community Service, and Innovation Program (P3MI) 2018, Institut Teknologi Bandung, Indonesia, for the support for this research.

References

1. Kempton AJ (1976) The ambiguity of acoustic sources-A possibility for active control. J Sound Vib 48:475–483
2. Germain P. (2000) Active control of run-up noise from propeller aircraft. Master of Applied Science Thesis, Uni. British Columbia, May 2000
3. Johansson S (2000) Active control of propeller-induced noise in aircraft: algorithms and methods. Doctoral thesis, Department of Telecommunications and Signal Processing, Blekinge Institute of Technology, Sweden, December 2000
4. Pabst O, Kletschkowski T, Sachau D (2009) Combined active noise control and audio in a light jet. In: The 16th international congress on sound and vibration, Krakow, 5–9 July 2009
5. Griffin (2009) The control of interior cabin noise due to a turbulent. MSc Thesis, VPISU, 2009
6. Kusni M, Soenarko B (2001) Dipole wave cancellation using a multipole secondary source. In: Symposium on wave propagation, Sept 2001
7. Kusni M (2002) The active noise control of propeller noise using a multipole secondary source, paper ICAS 2002, 852
8. Kusni M, Soenarko B, Djojodihardjo H (2014) Application of multipole secondary source for propeller active noise control. Appl Mech Mater 564:135–142
9. Seybert AF, Soenarko B, Rizzo FJ, Shippy DJ (1984) Application of the BIE method to sound radiation problem using an isoparametric element. ASME Trans J Vib Acoust Stress Rel Des 106: 414–420
10. Hess JL, Smith AMO (1967) Calculation of potential flow about arbitrary bodies. Progr Aeronaut Sci 8:1–138
11. Djojodihardjo H, Widnall SE (1969) AIAA J 7(10)
12. Ashley H, Rodden WP (1972) Wing-body aerodynamic interaction. Annu Rev Fluid Mech 4:431–472
13. Djojodihardjo H (2009) Application of fast multipole boundary element method for unified FMBEM-FEM acoustic-structural coupling. In: Proceedings international astronautical congress 2009, paper number IAC-09.C2.3.5
14. Yu KH, Kadarman H, Djojodihardjo H (2010) Development and implementation of some BEM variants-a critical review. Eng Anal Bound Elements
15. Djojodihardjo H (2013) J Mech Eng Autom 3: 209–220
16. Nelson PA, Curtis ARD, Elliott SJ (1986) Optimal multipole source distribution for the active suppression and absorption of acoustic radiation. In: Proc Euromech Colloc 213
17. Rujigrok GJJ (1993) Element of aviation acoustics. Delft University Press
18. Koopman GH, Song L, Fahnline JB (1992) J Acoust Soc Am 91: 2349 (A)
19. Bolton JS, Beauvilain TA (1992) J Acoust Soc Am 9l: 2349 (A)
20. Beauvilain TA, Bolton JS (1993) Cancellation of radiated sound fields by the use of multipole secondary sources. In: Proceedings of the second conference on recent advances in active control of sound and vibration. Technomic, Lancaster, PA, pp 957–968
21. Bolton JS, Gardner BK, Beauvilain TA (1995) J Acoust Soc Am 98(A)

Numerical Analysis of Double-Hat Multi-Corner Column Under Axial Loading

Annisa Jusuf, Leonardo Gunawan, Tatacipta Dirgantara, and Fadhil Mubarhak

Abstract Vehicle safety is an essential parameter in vehicle manufacturing. System absorber is required to absorb kinetic energy during the crash to avoid excessive structure damage and injury to passengers. Energy absorber technology was developed in various designs. The crash box is one of the energy absorber components. In the past, the ability to absorb impact energy was increased by thickening wall thickness and increasing wall density. Nowadays, the energy absorbing capacity could be gained by increasing the number of corners in a crash box. In this paper, the numerical analysis of the double-hat multi-corner column was conducted by using LS-DYNA software. Several different spot-weld pitch variations in the double-hat multi-corner column have been studied to obtain sufficient distance between spot-weld. Further, the crushing response of the double-hat multi-corner column then compared with a square column, a square double-hat column, a multi-corner column with 12 corners, and a multi-corner column with 20 corners. The result shows that the double-hat multi-corner column with a narrow spot-weld pitch has better energy absorption capacity. It is also observed that the column with a larger number of corners has more capability to absorb energy.

Keywords Double-hat multi-corner column · Impact · Dynamic axial crushing

1 Introduction

Vehicle crashworthiness is a critical aspect of designing the automotive product. The crash box is usually used to improve crashworthiness by plastic deformation mechanism. It is located on the front of the vehicle commonly to absorb energy during a frontal collision. Crash box design improvement was carried out continuously to get the most effective energy absorption capacity. The thin-walled column is commonly used as an energy absorber. The simplest way to improve crushing resistance is by thickening the column wall. However, it could increase the column mass. Several

A. Jusuf (✉) · L. Gunawan · T. Dirgantara · F. Mubarhak
Lightweight Structures Research Group, Faculty of Mechanical and Aerospace Engineering, Institut Teknologi Bandung, Jl. Ganesha 10, Bandung 40132, Indonesia
e-mail: annisajusuf@ftmd.itb.ac.id

© Springer Nature Singapore Pte Ltd. 2020

A. Praveen Kumar et al. (eds.), *Advances in Lightweight Materials and Structures*, Springer Proceedings in Materials 8, https://doi.org/10.1007/978-981-15-7827-4_3

kinds of researches have been carried out to find other crash box designs. Alternatively, multi-corner, top-hat, and double-hat column could be considered to improve crashworthiness performance.

Abramowicz and Wierzbicki [1] firstly predicted an analytical solution for the collapse behavior of the multi-corner column. Theoretical predictions are made only for even the number of corners in some columns cross sections such as square, hexagonal, and rhomboidal. Other researchers had conducted a study about the effect of the additional number of corners on crashworthiness parameters. Jusuf [2] had investigated some columns with several cross sections. It was found that the circular column was absorbing energy more efficiently. The mean crushing force is increased by thickening column wall and increasing perimeter of the column. Abassi [3] and Reddy [4] had surveyed about multi-corner column optimization. Rectangular, hexagonal, octagonal, and 12-edge cross-sectional profiles were analyzed. It was found that 12-edge cross-sectional configuration has 2.72 times higher than square configuration. The other technique to improve crash energy absorption capacity is introducing ribs between the inner and outer walls as corner addition, which had explained in [5].

The tubular-hat section is another configuration to raise higher energy absorption capability because of production simplicity. White and Jones [6–8], and Abramowicz [8] had carried out researches about top-hat and double-hat columns in 1999. In [6], experimental quasi-static axial loading of top-hat and double-hat columns has been achieved. The double-hat columns had a higher peak and mean loads compared to the top-hat columns. The double-hat structures had a potentially more significant ability to absorb energy due to regular progressive collapse. Theoretical prediction for the dynamic and quasi-static loading of the top-hat and double-hat column has been presented in [7] and [8]. The theoretical prediction shows that the double-hat column is better to absorb energy. The comparison between theoretical and experimental results has been in good agreement.

The effect of spot-weld pitch on the top-hat crash box has been analyzed numerically by Dimas [9]. It shows that the spot-weld pitch does not give a significant effect to the crushing behavior of the top-hat column if the spot-weld modeled by beam element. Meanwhile, the solid element spot-weld model shows the opposite trend.

Wang [10] studied about crushing behavior of the top-hat and double-hat column by using the experiment and theoretical method. Specific energy absorption (SEA) of the double-hat column is greater than the top-hat column. A parametric study about the thickness column was also carried out. SEA of double-hat and top-hat column increased as increasing wall thickness. Experimental and numerical analysis of the top-hat and double-hat column has been performed by Song [11]. Based on the numerical result, the mean crushing force of the top-hat column was 41.04 kN, while the double-hat column was 65.95 kN. Wang [12] has studied dynamic axial crushing resistance and parametric study about increasing column thickness in the double-hat column. Based on the test result and theoretical prediction, the double-hat column has a better crushing response. Dynamic mean crushing force of thin-walled structures such as square, top-hat, and double-hat cross-section has also been analyzed in [13]. The mean crushing force of the double-hat column is about 90% higher than the square column, while top-hat is only about 16.3%.

The joining method to combine top-hat into a double-hat column has been carried out by Lee in [14]. It was found that using spot-weld is better than self-piercing riveting joining and adhesive bonding because of the high energy absorption capacity.

In some previous studies, the effect of the welding method and spot-weld pitch on the double-hat column has not been carried out. Furthermore, the different types of cross sections such as (1) square column, (2) square double-hat column, (3) multi-corner column with 12 corners, (4) double-hat multi-corner column, and (5) multi-corner column with 20 corners column has not been compared to each other to determine the most proper column while absorbing energy. In this paper, the study of the welding method (spot-weld and continuous weld), which is applied to the double-hat multi-corner column, is presented. A parametric study about spot-weld pitch is also explained to complete the review of the welding method. The result from the parametric study about spot-weld distance is used to analyze and compare the axial crushing behavior of square column, square double-hat column, multi-corner column with 12 corners, double-hat multi-corner column, and multi-corner column with 20 corners column. The numerical analysis was performed using LS-DYNA software.

2 The Geometry of the Columns

Five types of column cross sections were modeled in this study, i.e., square (SQ), square double-hat (SQDH), multi-corner with 12 corners (MC12), double-hat multi-corner (MCDH16), and multi-corner with 20 corners (MC20). The detailed geometry of each column cross section is shown in Fig. 1. The mass, length, thickness, and perimeter of the columns were set to be constant, i.e., 0.26 kg, 180 mm, 0.7 mm, and 320 mm, respectively.

The SQDH and MCDH16 columns were created from two separate bent plates, which were joined together by spot-welding, as shown in Fig. 1b, d, while other columns were considered perfect columns. The radius of the spot-weld was 2.5 mm, and later, the spot-weld pitch will be varied into 15, 20, and 25 mm to study its effect on crashworthiness parameters.

3 Finite Element Model Description

Crushing simulation on five types of the column was simulated using LS-DYNA explicit finite element software. The column was modeled using 1 × 1 mm four nodes quadrilateral shell element with Belytschko–Tsay formulation. The size of the element was determined based on the convergence test on the square column, as shown in Fig. 2. The rigid impactor, with 130 kg mass, was modeled using eight-node hexahedron solid elements and located above the column model. Figure 3

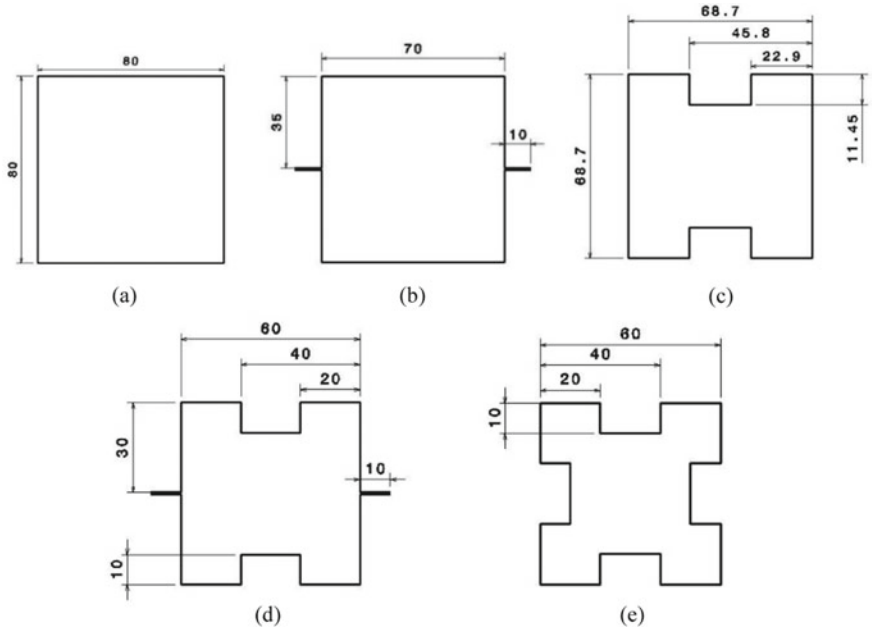


Fig. 1 Detail geometry of each column cross section: **a** SQ, **b** SQDH, **c** MC12, **d** MCDH16, **e** MC20

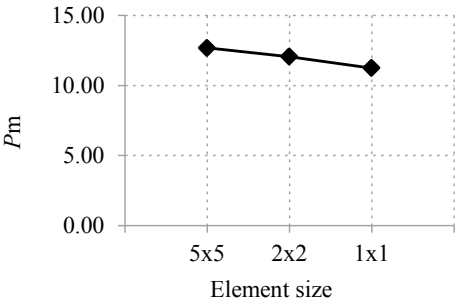


Fig. 2 Results of the convergence test on the square column

shows the example of the MCDH16 column finite element model, which consists of the impactor, column, and spot-weld.

In this case, there were two boundary conditions applied, as shown in Fig. 3. The impactor was set to move freely in the vertical direction. Meanwhile, the column was constrained in all directions at the bottom part. Those boundary conditions made the column crashed in a perfect axial direction. Two different velocities of the impactor will be analyzed to study the effect spot-weld pitch to the crushing behavior of the column, i.e., 4 and 6 m/s.

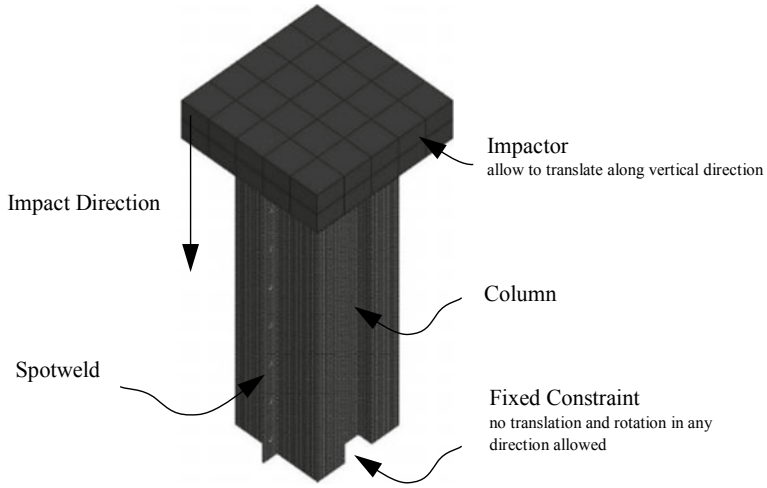


Fig. 3 Typical finite element model for double-hat multi-corner column (MCDH16)

Two types of contact algorithms were used for SQ, MC12, and MC20 column simulation, which are automatic nodes to surface and automatic single surface. Meanwhile, for SQDH and MCDH12 columns that were introduced spot-weld at their connections, three different types of contact algorithms were established for the simulation, i.e., automatic nodes to surface, automatic single surface, and spot-weld. The static and dynamic friction coefficient was set 0.4 and 0.3, respectively.

To simulate elastic–plastic and strain rate sensitive material behavior of the column during impact, the piecewise linear plasticity material model was applied to the column. The material of the column is mild steel St 37, which has density (ρ) = 7.83 × 10–6 kg/mm^3, Young's modulus (E) = 200 GPa, Poisson's ratio (ν) = 0.3, and the Cowper-Symonds variables are $D = 6884\ s^{-1}$ and $q = 3.91$. Figure 4 shows the true stress–effective plastic strain for the material. The spot-weld was modeled using AISI steel as beam element, which has a density (ρ) = 7.80 × 10–6 kg/mm^3, Young's modulus (E) = 210 GPa, and Poisson's ratio (ν) = 0.3.

4 Result and Analysis

4.1 Effect of Spot-Weld Pitch

In this study, the axial impact on the double-hat multi-corner column (MCDH16) was simulated with two different velocities, i.e., 4 and 6 m/s. In the first step of the simulation, the joint of the column was modeled as spot-weld. The spot-weld pitch was 15 mm (D15), 20 mm (D20), 25 mm (D25). For the next step, the simulation

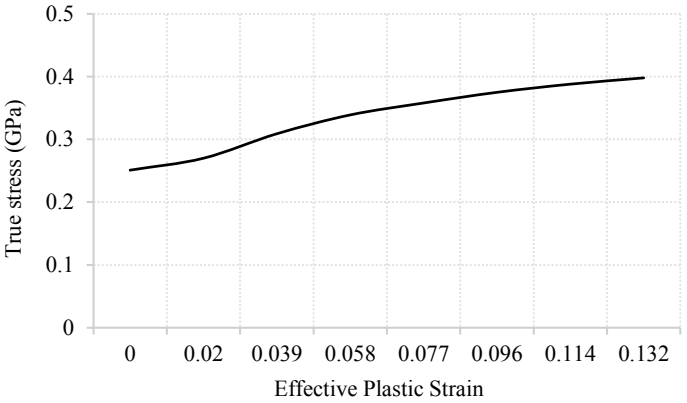


Fig. 4 True stress–effective plastic strain of mild steel St. 37 [15]

will be continued with the column that was connected by continuous welding to see the effect on the crushing behavior of the column.

Figure 5 shows the crushing response in terms of instantaneous crushing force (P) and mean crushing force (Pm) versus crushing length curve of D15, D20, and D25 columns with 4 m/s impact velocity. From Fig. 5a, two peaks are identified for each curve, which means there is only one folding that occurs on every column configuration after crushing. This phenomenon happens due to a large number of column corners (16 corners), which makes the column very stiff, and low impact velocity. Based on Fig. 5b and Table 1, the mean crushing force increases when narrowing the spot-weld pitch. The result shows that the mean crushing force of D15 column is 3% higher than D20, and 23% higher compare to D25.

Figure 6 shows the plastic deformation modes of D15, D20, and D25 column. It can be seen from the figure that the most regular and stable deformation is found on the MCDH16 column with a 20 mm spot-weld pitch (D20). The stable deformation

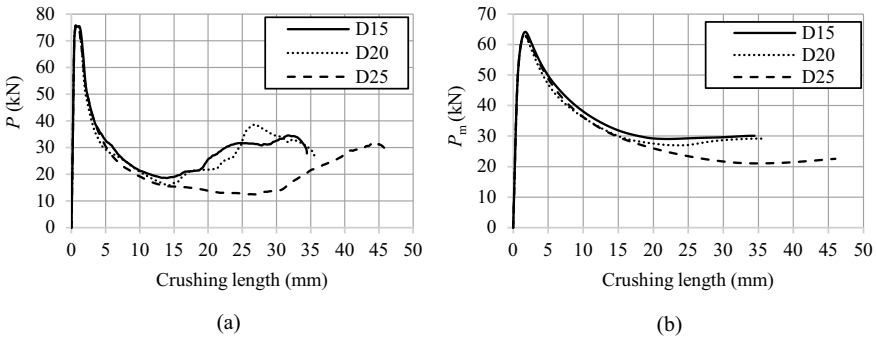


Fig. 5 Crushing force response of MCDH16 column for D15, D20, and D25; **a** instantaneous crushing force vs crushing length, **b** mean crushing force vs crushing length

Table 1 Crashworthiness parameters of the MCDH16 column under axial crushing velocity 4 m/s

Weld distance	EA (J)	P_{max} (kN)	P_m (kN)	δ_{max} (mm)	SEA (J/kg)	CFE (%)
Cont.	1035	77	53	20	30,552	69
D15	1037	76	30	34	20,834	40
D20	1037	76	29	36	20,194	39
D25	1037	76	23	46	15,613	30



Fig. 6 Deformation of double-hat multi-corner column: **a** D15, **b** D20, **c** D25

has become the reason why the mean crushing force results obtained from the simulation are slightly different from D15. It can be concluded that the energy absorption capacity of the column will be increased when the deformation pattern is regular.

After observing the behavior of the MCDH16 column with the spot-weld joining method, the next step is to include the continuous welding method to the finite element model to prove that by reducing the weld distance, the energy absorption capacity will be increased. The crashworthiness parameters [16–20] such as energy absorption (EA), maximum or peak force (P_{max}), mean crushing force (P_m), crushing length (δ_{max}), specific energy absorption (SEA), and crushing force efficiency (CFE) are given in Table 1. The results in Table 1 show that the column with continuous welding has the higher P_m, SEA, and CFE than column joined by spot-welding, while the δ_{max} is the shortest. This result is to confirm the previous analysis that mentioned the energy absorption capacity would increase by narrowing the spot-weld pitch.

Furthermore, the axial impact velocity was increased to 6 m/s to determine the most proper design of the double-hat multi-corner column. Table 2 presents the crashworthiness parameter of the columns under 6 m/s axial impact velocity. The result also showed that the column with spot-weld pitch 20 mm (D20) has a higher P_m, SEA, and CFE. The most proper design of the double-hat multi-corner column is D20 because of the higher energy absorption capacity and the most regular deformation modes.

Table 2 Crashworthiness parameters of the MCDH16 column under axial crushing velocity 6 m/s

Weld distance	EA (J)	P_{max} (kN)	P_m (kN)	δ_{max} (mm)	SEA (J/kg)	CFE (%)
Cont	2333	102	46	51	26,618	45
D15	2334	102	44	53	25,372	36
D20	2334	102	49	50	26,928	48
D25	2334	102	45	52	25,699	44

4.2 Effect of Cross Section and Number of Corners of Column

From previous results, the double-hat multi-corner column with spot-weld distance 20 mm (MCDH16 D20) was determined as the most proper configuration to absorb crushing energy. Further, in this work, the MCDH16 D20 column will be used to investigate the effect of the cross section and number of corners on the crushing behavior of a column. The MCDH16 D20 is compared to other cross sections such as square (SQ), square double-hat (SQDH), multi-corner with 12 corners (MC12), and multi-corner with 20 corners (MC20) with the same thickness, mass, and perimeter. The axial crushing velocity was set to be constant 4 m/s for all impact simulation.

Figure 7 shows the instantaneous crushing force and mean crushing force versus the crushing length curve for five types of cross sections. The results show that the mean crushing force of MC20 is higher than SQ, SQDH, MC12, and MCDH16 D20, while SQ has the lowest mean crushing force. These results occur due to MC20 has the highest number of corners, and SQ has the lowest number of corners. It can be concluded that the number of corners has a significant effect on increasing the mean crushing force.

Figure 8 shows the deformation mode of each column. From the figure, it can be observed that the largest folding length and highest crushing length occurs in SQ and

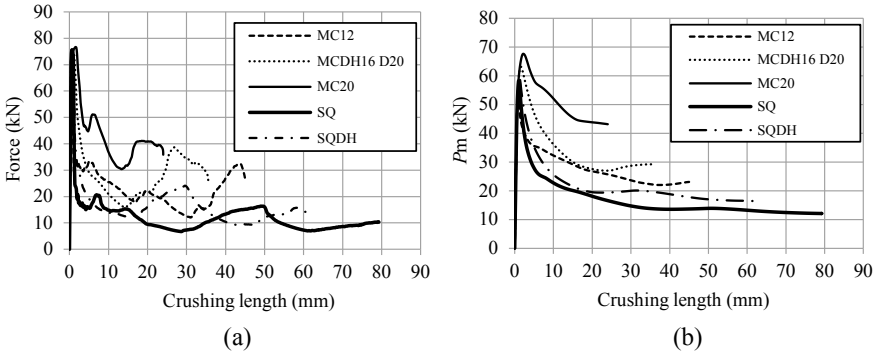


Fig. 7 Crushing force response on each column cross section: **a** instantaneous crushing force versus crushing length, **b** mean crushing force versus crushing length

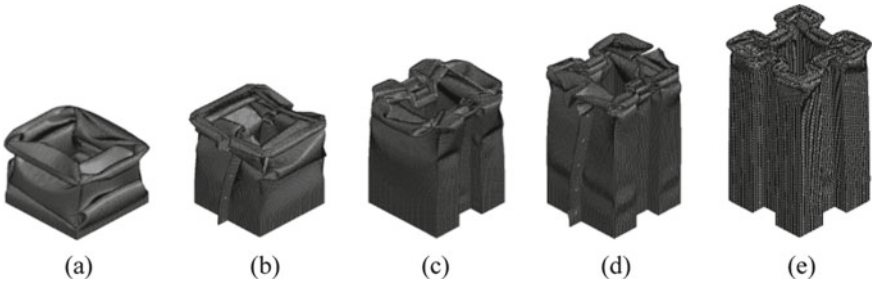


Fig. 8 Deformation mode: **a** SQ, **b** SQDH, **c** MC12, **d** MCDHD16 D20, **e** MC20

Table 3 Crashworthiness parameters for each column cross-section

Cross section	EA (J)	P_{max} (kN)	P_m (kN)	δ_{max} (mm)	SEA (J/kg)	CFE (%)
SQ	1039	76	32	77	7765	43
SQDH	1038	76	35	64	9402	46
MC12	1037	75	42	45	13,299	56
MCDH16—D20	1037	76	48	36	16,828	63
MC20	1036	77	62	24	24,878	81

SQDH columns. Meanwhile, in MC20, MCDH16 D20, and MC12 columns have shorter folding length and crushing length.

The detailed crashworthiness parameter results from the simulations are given in Table 3. The values of P_m, SEA, and CFE MCDH16 D20 column are 50.00%, 116.72%, 46.51% higher than the SQ column, respectively. Meanwhile, for MC20 column are 93.75%, 220.38%, 88.37% higher than SQ column, respectively.

SEA and CFE are significant crashworthiness parameters to represent energy absorption efficiency. Figure 9 shows the normalized SEA and CFE for each column cross section. Based on Fig. 9, the enhancement of SEA and CFE is followed by the number of corners addition. As can be seen from the figure that the MC20 has the highest SEA and CFE, followed by MCDH16 D20, MC12, SQDH, SQ, respectively. It also can be observed that the value of SEA and CFE for the MCDH16 D20 column are 2.17 and 1.50 times than the SQ column. Meanwhile, for MC20 column is 3.20 and 1.93 times than the SQ column, respectively.

5 Conclusion

In this work, a numerical analysis of the double-hat multi-corner column has been carried out. The result shows that the double-hat multi-corner column with narrow spot-weld pitch has better energy absorption capacity, which is indicated by a higher mean crushing force. The result also showed that the double-hat multi-corner column

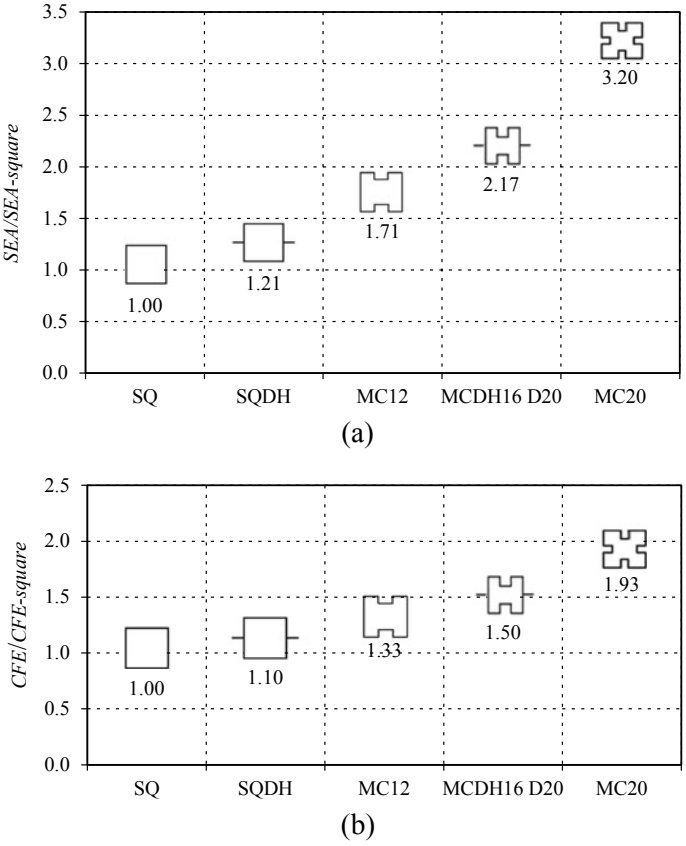


Fig. 9 Comparison of crashworthiness parameters between five types of column normalized to the square column: **a** Specific energy absorption, **b** crushing force efficiency

with spot-weld pitch 20 mm has a more regular and stable deformation mode. This type of deformation will affect the value of the mean crushing force of the column. From this work, it also can be concluded that the column with a larger number of corners has more capability to absorb energy, where MC20 has the highest P_m, SEA, and CFE, followed by MCDH16 D20, MC12, SQDH, SQ, respectively. The P_m for MC20 is 93.75% higher than the SQ column, while MCDH16 D20 is 50.00% higher than the SQ column. The SEA and CFE for the MCDH16 D20 column are 2.17 and 1.50 times than the SQ column, respectively, while for MC20 column is 3.20 and 1.93 times compare to the SQ column.

Acknowledgements The authors would like to acknowledge the Basic Research of Higher Education (PDUPT) Grant 2019-2020, Ministry of Research, Technology and Higher Education, Republic of Indonesia, for the funding for this research. The authors also would like to thank to Livermore Software Technology Corporation (LSTC) for providing an academic license of LS-DYNA software.

References

1. Abramowicz W, Wierzbicki T (1989) Axial crushing of multicorner sheet metal columns. J Appl Mech 56:113–120
2. Jusuf A, Allam FS, Dirgantara T, Gunawan L, Putra IS (2011) Low velocity impact analyses of prismatic columns using finite element method. Key Eng Mater 462–463:1308–1313
3. Abbasi M, Reddy S, Nazari AG, Fard M (2015) Multiobjective crashworthiness optimization of multi-cornered thin-walled sheet metal members. Thin-Walled Struct 89:31–41
4. Reddy S, Abbasi M, Fard M (2015) Multi-cornered thin-walled sheet metal members for enhanced crashworthiness and occupant protection. Thin-Walled Struct 94:56–66
5. Jusuf A, Dirgantara T, Gunawan L, Putra IS (2015) Crashworthiness analysis of multi-cell prismatic structures. Int J Impact Eng 78:34–50
6. White MD, Jones N (1999) Experimental quasi-static axial crushing of top-hat and double-hat thin-walled sections. Int J Mech Sci 41:179–208
7. White MD, Jones N (1999) A theoretical analysis for the dynamic axial crushing of top-hat and double-hat thin-walled sections. Proc Inst Mech Eng Part D J Autom Eng
8. White MD, Jones N, Abramowicz W (1999) A theoretical analysis for the quasi-static axial crushing of top-hat and double-hat thin-walled sections. Int J Mech Sci 41:209–233
9. Dimas A, Dirgantara T, Gunawan L, Jusuf A, Putra IS (2014) The effects of spotweld pitch to the axial crushing characteristics of top-hat crash box. Appl Mech Mater 660:578–582
10. Wang Q, Fan Z, Gui L (2007) Theoretical analysis for axial crushing behaviour of aluminium foam-filled hat sections. Int J Mech Sci 49:515–521
11. Song HW, Fan Z, Yu G, Wang Q, Tobota A (2005) Partition energy absorption of axially crushed aluminum foam-filled hat sections. Int J Solids Struct 42:2575–2600
12. Wang QA, Fan Z, Gui L (2006) A theoretical analysis for the dynamic axial crushing behaviour of aluminium foam-filled hat sections. Int J Solids Struct 43:2064–2075
13. Putra IS, Dirgantara T, Anh LH, Homma H, Kishimoto K (2008) Behavior of thin walled square tube and tubular hat sections subjected to low velocity impact loading. Adv Mater Res 33–37:387–394
14. Lee MH, Kim HY, Oh SI (2006) Crushing test of double hat-shaped members of dissimilar materials with adhesively bonded and self-piercing riveted joining methods. Thin-Walled Struct 44:381–386
15. Jusuf A, Dirgantara T, Gunawan L, Putra IS (2012) Numerical and experimental study of single-walled and double-walled columns under dynamic axial crushing. J Mech Eng 9
16. Praveen Kumar A, Manieah D (2019) Deformation studies on the significance of combined geometry tubes as energy absorbing structures. Int J Civil Eng Technol 10(1): 2812–2820
17. Praveen Kumar A (2019). Influence of plain end-cap on the energy absorption characteristics of cylindrical tubular structures for lateral impact vehicle collisions. Thin-Walled Struct 138(C): 32–45
18. Praveen Kumar A, Manieah D (2019) Crashworthiness behaviour of capped cylindrical aluminium tubular structures subjected to lateral compression. Int J Mech Prod Eng Res Dev 9(4):1167–1172
19. Praveen Kumar A, Shrivaathsav S (2019) Influence of forming parameters on the crash performance of capped cylindrical tubes using LS-DYNA follow-on simulations. Int J Interact Des Manuf 13(3):1215–1232
20. Praveen Kumar A, Jusuf A, Santosa SP, Dirgantara T (2019) Investigations on the influence of spherical caps in the axial impact characteristics of press-formed cylindrical tubular structures. Adv Struct Eng: 1–14. https://doi.org/10.1177/1369433218819576

Influence of Triggers on the Damage Characteristics and Initial Peak Load of Composite Tubular Energy Absorbers for Low-Velocity Impact Applications



Venkateswarlu Gattineni and Venukumar Nathi

Abstract Carbon fiber reinforced polymer (CFRP)-based thin-walled composite tubes used as sacrificial energy absorbers in the transportation sector are provided with triggers in design which are stress concentration zones. These triggers serve to reduce the initial peak impact load value that shall be experienced during the energy absorption process. Detailed finite element-based computations are done to study the influence of configuration and angle for the trigger designs with which the thin-walled quasi-isotropic composite tubes are proposed to be made, for slow speed impact. A trigger angle that could result in the lowest possible initial peak load can act as a stress concentration zone and cause partial damage even during slow speed impacts which might not be fatal. Hence, an optimal combination of trigger configuration and angle is suggested based on sensitivity studies.

Keywords Trigger · Bevel · Damage · Quasi-isotropy · Quasi-static · CFRP · Energy absorption

1 Introduction

Millions of lives are lost [1] each year due to road accidents, globally. Most of the causalities are seen to occur in developing countries, where the quality of road infrastructure may not be up to the international benchmark. Due to rapid urbanization, traffic jams and slow-moving traffic have become common in towns and cities of low- and middle-income group countries. These traffic conditions could cause low-speed impacts.

In the transportation sector, composites are being considered for the body design to make the vehicles weigh less and safe, besides being fuel-efficient. Fiber-reinforced polymer (FRP) composites as structural materials exhibit improved strength and structural properties compared to metals. CFRP structures weigh about one-fifth as much as steel and half as much as aluminum. These are better compared to steel

V. Gattineni (✉) · V. Nathi
GITAM School of Technology, Hyderabad, India
e-mail: ammu.abhi.sammi@gmail.com

© Springer Nature Singapore Pte Ltd. 2020

A. Praveen Kumar et al. (eds.), *Advances in Lightweight Materials and Structures*,
Springer Proceedings in Materials 8, https://doi.org/10.1007/978-981-15-7827-4_4

or aluminum in terms of strength, stiffness and specific energy absorption. CFRP material also does not rust or corrode or degrade due to environmental factors like metals. Vehicles with bodies made of CFRP material exhibit marked increase with regards to specific fuel consumption, due to reduced vehicle weight. Extensive studies have been done on the behavior of CFRP materials as energy absorbers. But the focus of such studies has been mostly confined to the study of energy absorption rates sacrificially due to high-speed impacts. Hence the influence of a few key design parameters must be studied in detail, to avoid possible premature and/or partial failure due to slow speed impacts.

Tubular structures referred to as "Crush Can (CC)" hereafter referred to as CC is (Illustrated in Fig. 1) attached to the bumpers on one side and the car body on the other side. During an accident, the CC gets crushed and absorbs energy to save occupants. Due to lightweight requirements, metallic tubes are being replaced by composite (CFRP) tubes. When composites are used as CC materials, due to their high directional stiffness, the initial peak impact force/load would be high [2 and 3] which might cause a big jolt to the passengers, during an accident. Hence, toward the end of the tube which gets attached to the bumper, chamfer-based cuts (called as a trigger) are provided in the design. These chamfers act as stress concentration zones and reduce the initial peak impact force, by promoting progressive crushing. Most of the research undertaken seems to have focused on the effect of chamfer/trigger designs for high-speed impacts only. During parking or bumper-to-bumper kind of driving scenarios, low-speed impacts are possible [4]. Even low-speed impact on to a bumper can cause the brittle composite material of CC to get damaged at the trigger location. A quick survey of the literature suggests that studies need to be performed to check for possible damage due to low-speed impacts, at trigger locations.

Hence, the trigger designs that are proposed to be used for the CC need to be evaluated considering the possibility of damage due to slow speed impacts [5]. Based on the study findings, a trigger design that not only can reduce the initial peak impact load but which also does not get damaged during slow-speed impact should be

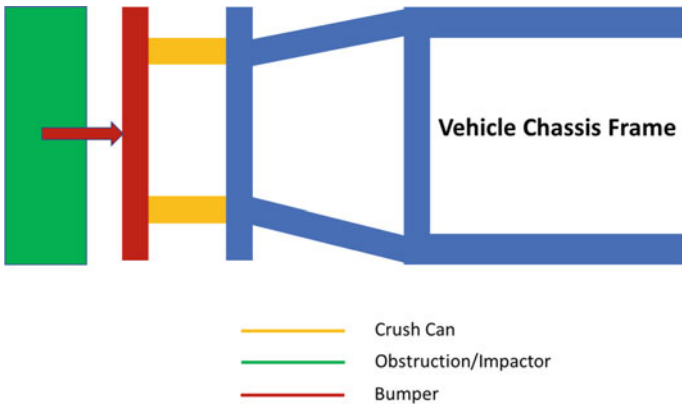


Fig. 1 Illustration of CC in a vehicle

selected. If the design is not improved to eliminate damage at low-speed impacts, the vehicle is possibly left with a partially damaged CC which might be impaired to absorb the intended energy, when the actual fatal impact occurs [6]. Performed to check for possible damage due to low-speed impacts, at trigger locations.

The current study focuses on the following:

1. Exploration of popular trigger designs available in the literature for CC designs made of CFRP
2. Choose the trigger designs that could be implemented with the least possible manufacturing costs/constraints, for study
3. Compare the effect of the trigger angle as a parameter for initial peak load reduction and damage progression, due to slow impact.

2 Methodology—Study Parameter Selection

A trigger is a stress concentration zone that is intentionally introduced, for the fracture to get initiated at a specific area within the structure, for a thin-walled composite tube. Previous studies [7 and 8] indicated that triggers need to be incorporated at appropriate locations in the components to initiate stable progressive crushing failure for composite tubes. End modifications for composite tubes which have been proved to work well include chamfers [7] and slots [8]. Trigger designs ensure stable progressive crushing behavior and serve to reduce the initial peak load experienced by CC, during an accident.

2.1 Different Kinds of Trigger Designs

Studies have been performed [7 and 8] using different configurations of trigger geometries which are as shown in Fig. 2a–d. As can be seen, the simplest form of the trigger is a chamfer provided at an angle on the end of the tube across the thickness. This is referred to as a single-bevel trigger. When the chamfer is provided on either side, using the mid of the tube thickness as the center, it is referred to as a double-bevel trigger. As shown in Fig. 2c, sometimes in addition to chamfer, a cap is used to cover the bevel/chamfer end of the tube, which further can reduce the initial peak impact force, without losing the energy absorption capacity. As shown in Fig. 2d, few studies have also been performed making rectangular slots along the circumference and along the axis of the tube, which are referred to as a slot type of trigger.

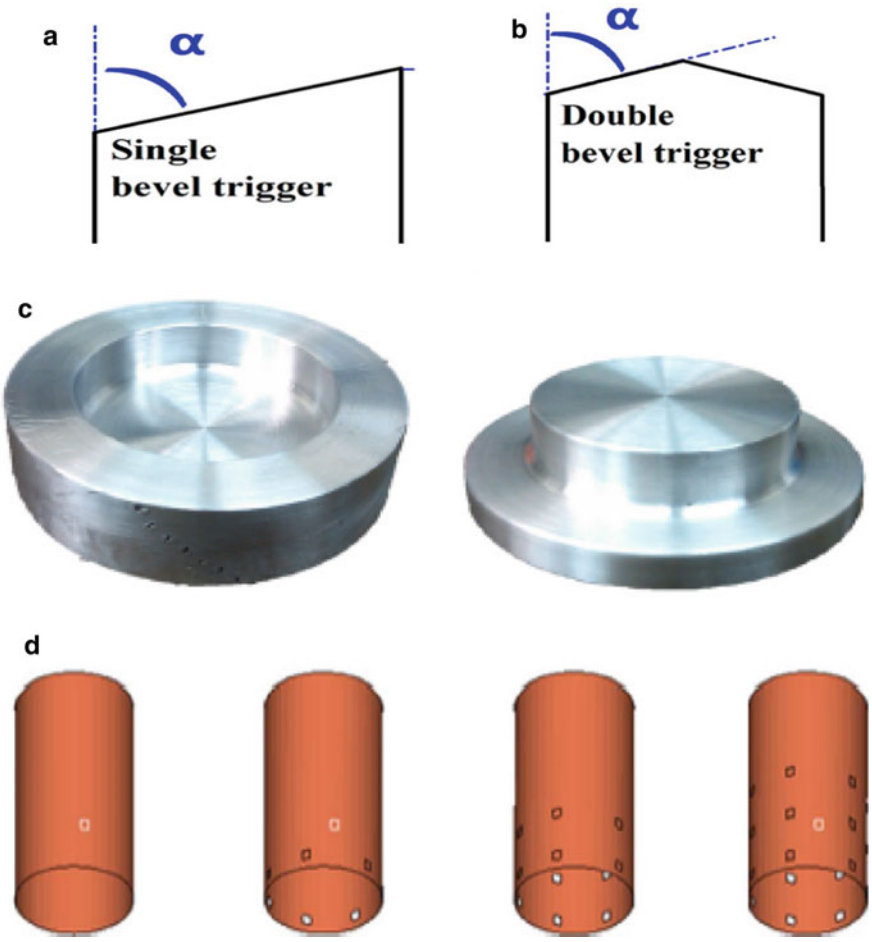


Fig. 2 **a** Single bevel, **b** double bevel, **c** triger cap (2 views), **d** slots along the tube

2.2 The Design Intent of Trigger

For CFRP-based CC designs, the value of initial peak impact load shall be usually very high compared [9] to the mean value, due to high material stiffness. Hence, to reduce the same and make it closer to the mean value, triggers are provided at the end of the CC. Energy absorbed by the CC is given by region under force-displacement curve, up to stroke length. An efficient CC design needs to ensure that the value of peak be reduced/moderated to be close to mean impact force (Fig. 3).

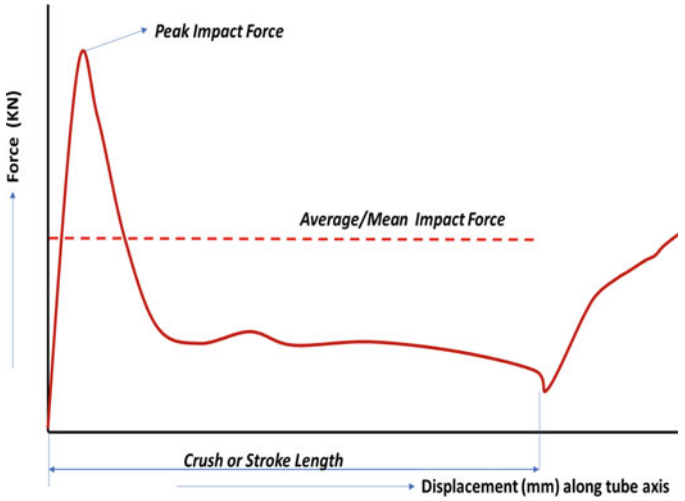


Fig. 3 Typical force–displacement curve during an accident/impact for CC

2.3 Choice of Trigger Configurations for the Current Study

As can be seen, the bevel and double-bevel configurations are easy to implement for the tubes, from manufacturing cost/ease wise. The cap configuration shown in Fig. 2c consumes some length/space besides being an extra part. The slotted configuration shown in Fig. 1d requires machining or slotting to be performed on the tube. Hence, the study has been limited to bevel and double-bevel configurations [8] which are simple to be implemented (ease of manufacturing and associated costs).

3 Finite Element Simulation

For the sake of study, CFRP material [4] whose properties as listed in Table 1, have been used. To achieve quasi-isotropy in the CC structural behavior, the same tube configuration (ply angle, thickness, length, number of layers) as available in the literature [4] has been adopted. Only circular tubular configuration has been considered as studies have shown that tubes with circular cross section [9] are optimal for energy absorption compared to others. For the current study, three different bevel angle configurations of 20°, 30°, and 45° have been considered. Values beyond 45° were not considered as they were not found [7] to be in-effective in reducing the initial peak impact forces.

Table 1 Material properties used for the study [6]

Anisotropic linear material properties		
Directional moduli (MPa)	$E_{xx}/E_{yy}/E_{zz}$	58093/58093/9759
Shear moduli (MPa)	$G_{xy}/G_{yz}/G_{zx}$	3545/2564/2564(MPa)
Poisson' ratio	$V_{xy}/V_{yz}/V_{zx}$	0.0154/0.5356/0.1575
Failure material properties *(Anisotropic)*	Symbol	Value (MPa)
Allowable tensile strength in *X*/*Y*/*Z* direction(s)	$X_T/Y_T/Z_T$	650/650/10
Allowable compressive strength in *X*/*Y*/*Z* direction(s)	$X_C/Y_C/Z_C$	555/555/500
Allowable strength in *XY*/*YZ*/*ZX* direction(s)	$T_{xy}/T_{yz}/T_{zx}$	181/132/132
Individual layer thickness: 0.1 mm, number of layers = 30, ply angle 45°/−45°		

3.1 Material Properties

The material properties [7] used for the study are as given in Table 1.

3.2 The Geometric Configuration of Trigger Used for the Study

The geometric configurations of the trigger used for the study are as shown in Fig. 4a, b. Here, Di is the inner radius of tube = 50 mm, t is the thickness of tube = 3 mm, and L is the length of the tube = 125 mm. θ Values of 20°, 30°, and 45° are used.

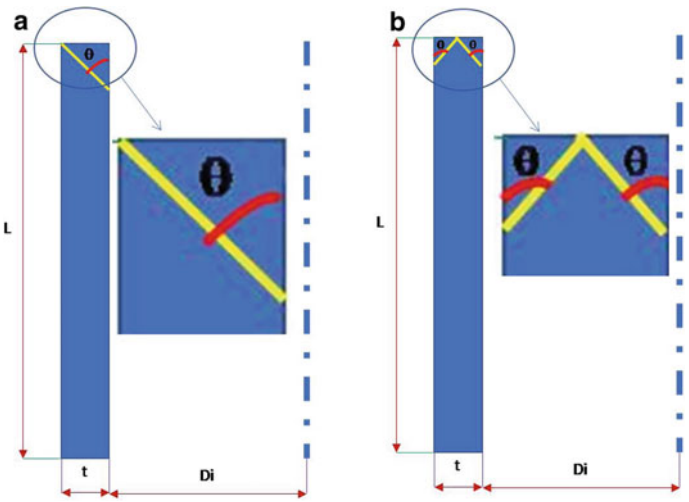


Fig. 4 **a** Bevel trigger, **b** double-bevel trigger

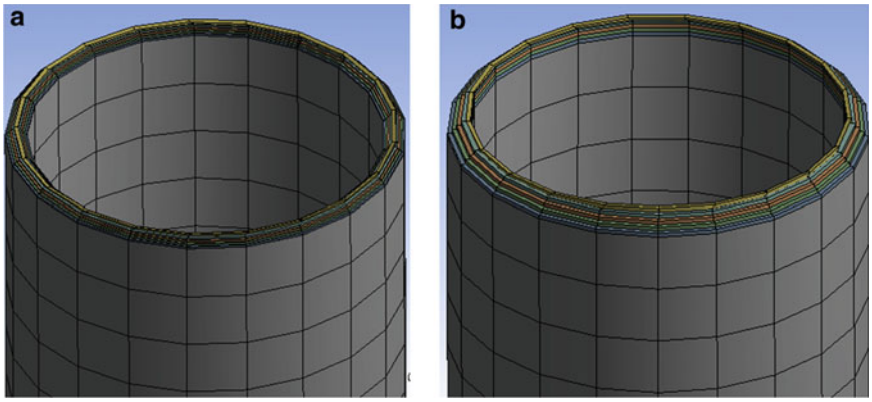


Fig. 5 **a** Bevel trigger mesh, **b** double-bevel trigger mesh

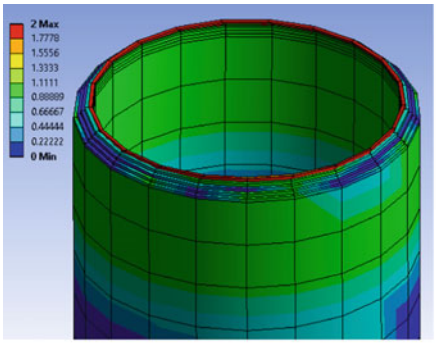
3.3 Conditions Used for the Study

Layered shell elements have been used for finite element mesh generation. The trigger configurations in the elements at the end of the CC have been achieved using thickness offset and mean thickness options. The trigger mesh configuration as generated for single and double bevel are as shown in Fig. 5a, b.

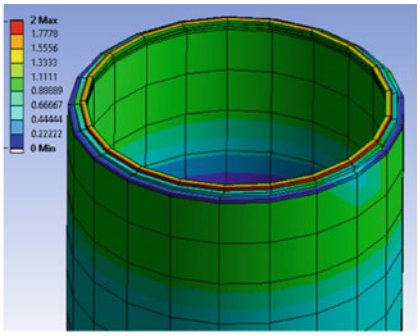
The nodes of the CC tube have been fixed on one end (non-trigger side). Steady-state compressive displacement has been applied on the edge nodes which lie on the trigger end of the tube to act along the axis of the tube (compressing it). This displacement generates reaction force which is equivalent to an impact at slow speed (less than 5 km/h, quasi-static condition). Interactive failure criteria [10 and 11] have been used for the evaluation of equivalent/effective stress. Failure criteria based on the Hashin model [4] have been used for assessing damage initiation and evolution. The simulation is performed as in quasi-static conditions [12, 13]

3.4 Results of the Study

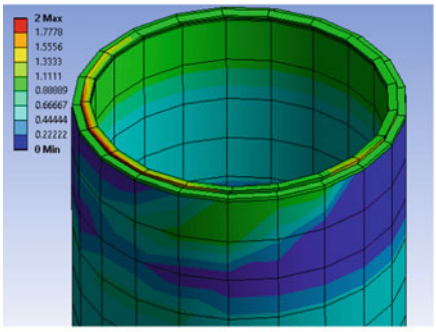
Figure 6a–c depicts the damage contours for the trigger configuration with bevel shape and respective associated angles. Figure 6d–f depicts the damage contours for the trigger configuration with double-bevel shape. As per the notation [10 and 11] shown in the contours, damage range between 1 and 2 indicates the crush of the tube in fracture mode (damage evolution). Damage contour value of 1 indicates just failure (damage initiation). Damage value between 0 and 1 indicates no failure.



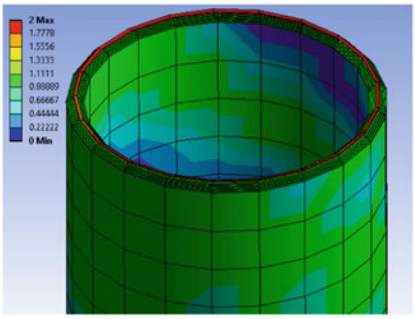
(a), θ = 45°



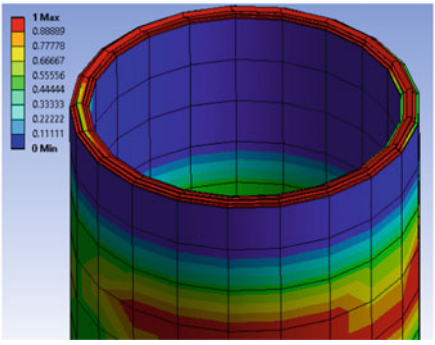
(b), θ = 30°



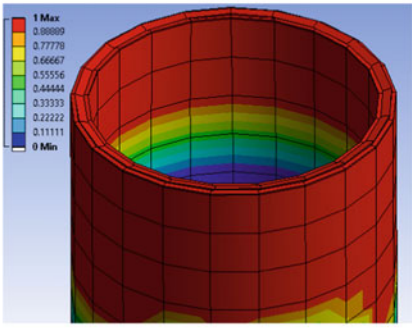
(c), θ = 20°



(d), θ = 45°



(e), θ = 30°



(f), θ = 20°

Fig. 6 **a** $\theta = 45°$, **b** $\theta = 30°$, **c** $\theta = 20°$, **d** $\theta = 45°$, **e** $\theta = 30°$, **f** $\theta = 20°$

Table 2 Impact force and damage status

Tube configuration	The peak value of impact force in KN	Tube end damage status
Normal tube	120.23	No
Tube with bevel (45°)	24.67	Yes
Tube with bevel (30°)	28.87	Yes
Tube with bevel (20°)	26.54	Yes
Tube with double bevel (45°)	30.20	Yes
Tube with double bevel (30°)	31.03	No
Tube with double bevel (20°)	27.69	No

3.5 Peak Impact Force and Damage Status

The peak impact force and the associated damage status for the slow speed (quasi-static) impact is tabulated and presented in Table 2.

4 Discussion on Results

The study has been mainly focused on the damage pattern of the material in the trigger zones. A simple quasi-isotropic lamination sequence of ±45° has been used for the alternate layers along with varying trigger configurations to avoid unwanted high stiffness of the tube. The results contours indicate that the trigger locations serve as stress concentration zones, promoting progressive damage at their respective locations. The CFRP thickness variation (due to the trigger) along the axis of the tube is achieved using thickness offset options for the individual layer of shell elements. Tubular designs without trigger not only result in very high value of initial peak force, but also result in low stroke length. As can be seen from Table 2, triggers can reduce the peak value of impact force drastically, which is a desired condition for the energy absorber. A review of damage contours from Fig. 6a–f suggests that a chamfer/cut with single or double bevel with 45° angle introduces stress concentration as it results in minimum material condition at the end of the tube. With a 45° trigger (either single- or double-bevel configuration), tube end is prone to damage even for low-speed impact. At an angle of 30°, the impact force increases slightly for both (single- and double-bevel) configurations of the trigger. However, there is some damage at the end of the tube for the single-bevel configuration, and the same is not present for the double-bevel configuration. A further reduction in the bevel angle (from 30° to

20°) is expected to increase the impact force further. But the same does not happen, as the failure mode shifts from major compression to shear, due to the lamination angle effect. However, there is no damage seen for both configurations of trigger (single-bevel and double-bevel) at this angle of the chamfer.

5 Conclusions

- Even the best trigger designs which can reduce the peak impact forces significantly can cause damage to the tube end, even at low-impact or parking speeds, as observed through the study.
- All CC designs optimized with trigger configurations for energy absorption and peak impact force must be mandatorily checked for the possibility of damage at low speeds. This is to ensure that there is no damage accumulation due to low-speed impact.
- Double-bevel trigger designs with low chamfer angles serve as an optimal configuration in terms of initial peak impact forces and damage accumulation.
- The damage potential of the energy absorbers at low or static impacts should not be neglected.

6 Future Scope

Explore the possibility of using approximate or pseudo-elastic methods [6] to estimate the possible damage at the trigger locations. The current tube material has simple quasi-isotropic configuration (lamination angle). The design can be subjected to optimization using the lamination angle as a parameter to result in smooth force deflection curve, which could be close to the ideal condition.

References

1. https://www.asirt.org/safe-travel/road-safety-facts/
2. Ma Y, Jin S, Zhang S (2018) Effect of trigger on crashworthiness of unidirectional carbon fiber reinforced polyamide 6 composites. Plast, Rubber Compos. https://doi.org/10.1080/14658011.2018.1466502
3. Siromani D, Henderson G, Mikita D, Mirarchi K, Park R, Smolko J, Awerbuch J, Tan TM (2014) An experimental study on the effect of failure trigger mechanisms on the energy absorption capability of CFRP tubes under axial compression. Compos A 64:25–35. https://doi.org/10.1016/j.compositesa.2014.04.019
4. Hashin Z (1980) Failure criteria for unidirectional fiber composites. ASME J Appl Mech 47(2): 329–334

5. Sonawane CR, Shelar AL (2018) Strength enhancement of car front bumper for slow speed impact by FEA method as per IIHS regulation. J Inst Eng India Ser C 99(5): 599–606. https://doi.org/10.1007/s40032-017-0365-y
6. Gattineni V, Nathi V (2019) Pseudo elastic methods for damage assessment of composite tubes. J Mech Eng Res Dev JMERD 42(3): 94–101. https://doi.org/10.26480/jmerd.03.2019.94.101
7. Luo H, Yan Y, Meng X, Jin C (2016) Progressive failure analysis and energy-absorbing experiment of composite tubes under axial dynamic impact. Composites Part B 87: 1–11
8. Nasir Hussain N, Regalla SP, RaoYendluri VD (2017) Numerical investigation into the effect of various trigger configurations on crash worthiness of GFRP crash boxes made of different types of cross sections. Int J Cash Worthiness. https://doi.org/10.1080/13588265.2017.1286964
9. Reddy TJ, Rao YVD, Narayanamurthy V (2017) Thin-walled structural configurations for enhanced crashworthiness. Int J Crashworth
10. Ansys theory manual, version 19.0
11. Abaqus theory manual version 2019
12. Praveen Kumar A (2019) Influence of plain end-cap on the energy absorption characteristics of cylindrical tubular structures for lateral impact vehicle collisions. Thin-Walled Struct 138(C): 32–45
13. Praveen Kumar A, Shrivaathsav S (2019) Influence of forming parameters on the crash performance of capped cylindrical tubes using LS-DYNA follow-on simulations. Int J Interact Des Manuf 13(3):1215–1232

Finite Element Investigations on the Fatigue Behaviour and Life Calculation for Axle of Aircraft



Rishabh Chaudhary and Srishti Singh

Abstract The data collected over the years illustrate that more than 50% of the failure in aircraft components are due to fatigue. This raises the need for fatigue resistant materials for the components of aircraft. The axle of the aircraft supports the whole weight of the aircraft and hence is subjected to fatigue loading during its entire service life. Titanium alloys are commonly used material in aviation sector since decades. In this paper, the behaviour of two titanium alloys, namely TIMETAL 834 and Ti–6Al–4V has been compared under fatigue loading which are used for axle of the aircraft. The fatigue life of the axle is increased by 81,230 cycles for TIMETAL 834 which is 17.77% of life for component if Ti–6Al–4V is used. The 3D model of axle is built in Creo 3.0 and exported to ANSYS. The fatigue analysis is carried out using fatigue tool in ANSYS Workbench 2019 R2.

Keywords Axle · Fatigue life · Fatigue loading · Landing gear · Titanium alloys

1 Introduction

The landing gear is the principle support to an aircraft for landing and taxiing purpose. It includes combination of brake, wheels, retract mechanism, controls and shock mechanism. The entire weight of aircraft is supported by the axle [1]. The suspension system consists of telescoping cylinders that are connected to wheels by a shock strut and the axle assembly. A shock strut is a sub-assembly of landing gear which absorbs and releases impact loads during taxi, roll-out and compression by using hydraulic fluid, generally skydrol, along with nitrogen. Axle assembly is integrated with lower cylinder of shock strut in most cases to support wheels while the upper cylinder is connected to fuselage. The material of the axle is same as that of lower cylinder of the strut. Axle is subjected to fatigue loads which are non-proportional during harsh landing while constant and proportional during smooth landing. These forces are transmitted to the axle and must be resisted to ensure proper working because

R. Chaudhary (✉) · S. Singh
Department of Mechanical Engineering, JSSATE, Noida, India
e-mail: rishabh980873@gmail.com

© Springer Nature Singapore Pte Ltd. 2020

A. Praveen Kumar et al. (eds.), *Advances in Lightweight Materials and Structures*,
Springer Proceedings in Materials 8, https://doi.org/10.1007/978-981-15-7827-4_5

they develop cracks which suddenly propagates after reaching the critical size and the axle can fail [2]. Antiskid sub-assembly is also mounted on the axle to detect skidding of the wheel and automatically release the pressure when needed.

About 40% of damage in landing gear is due to landing stroke. The damage caused due to fatigue loading has been a complex phenomenon. In stress-based fatigue, the localized stress concentration in a component leads to formation of crack which is followed up by the propagation and finally reaches to fracture point and this impairs the component [3, 4]. The failure due to fluctuating load occurs at comparatively lesser magnitude of load, than for static load, so the material fails before the expected strength (ultimate strength) for the material. Materials behave differently towards the type of loading. The load may attain a maximum value in both directions, that is, forward and reverse which is often called as fully reverse loading. While in many cases, the applied load may fluctuate only in one direction, known as alternate loading. Alloys of titanium possess excellent fatigue properties and common applications include naval ships, armor plating and spacecraft.

For reliable modelling, fatigue analysis provides essential information and fatigue tests are used to derive stress-life (S-N) curves. Fatigue curves describe fatigue properties of the material. For materials like titanium and steel, there is minimum stress value below which material never fails, which is known as fatigue limit or endurance limit. Its value depends on factors including surface conditions, residual stresses, temperature and geometry.

Franco et al. [5] studied the causes for formation of crack in landing gear for a military aircraft and found fatigue as the major cause for the crack growth. Ossa [6] investigated causes of failure of a civil aircraft's main landing gear by analyzing failed element using optical analysis and found that shear load due to sudden impact is the cause of initiated failure. Jarkko and Patria [7] analysed the fatigue-based life calculations for the critical location in the structure of aircraft by virtual fatigue test. Turan et al. [8] examined the cracks in five strut bearings of training aircrafts by using the light microscope. TIMETAL 834 used in this analysis is having superior tensile and fatigue properties than Grade 5 titanium (Ti–6Al–4V).

2 Methodology

2.1 Finite Element Method

The finite element method is utilized for the fatigue analysis of the axle of an aircraft. The finite element analysis gives an easy way to study the behaviour of system by applying input parameters (load, boundary conditions) with design conditions [9]. The minimum edge length of 20 mm with element size of 4 mm and the patch conforming algorithm is utilized for meshing the model. In this fatigue analysis, finite element tool ANSYS is used.

Properties of Ti–6Al–4V and TIMETAL 834 [9]

Properties	Ti–6Al–4V	TIMETAL 834
Young's modulus (GPa)	113.8	120
Poisson's ratio	0.342	0.32
Tensile yield strength (MPa)	880	930
Tensile ultimate strength (MPa)	950	1050

2.2 Mean Stress Correction

Goodman criteria which is also called Haigh's criteria is the criteria in the form of equations which shows relation between alternating and mean stresses and its effect in life of component. Goodman equation is used for brittle material. Also, it is not excessive conservative as Soderberg's equation.

$$\frac{\sigma_{\text{alternating}}}{S_{\text{endurance\_ limit}}} + \frac{\sigma_{\text{mean}}}{S_{\text{ultimate\_ strength}}} = 1 \tag{1}$$

2.3 Geometry Specifications and Material Properties

The axle geometry is created in PTC Creo 3.0. The created finite element model was subjected to fatigue analysis after the assignment of material and boundary condition. The axle of a commercial aircraft is selected having effective diameter of 100 mm and length of 420 mm.

Ti-6Al-4 V and TIMETAL 834 are used in this analysis and their properties are shown in Table 1.

The S-N curve is important to predict the fatigue behaviour of the material. The S-N curve for these two alloys are shown in Figs. 1, 2.

3 Analysis of Axle in ANSYS

3.1 Importing Model to ANSYS and Meshing

A simplified model of the axle of aircraft in fatigue analysis is required for the optimum use of computer resources. As the structure of axle of aircraft is same for nose and main landing gear, the axle of nose landing gear is taken for analysis. The model was generated in PTC Creo 3.0 and then it is imported into ANSYS as IGES file.

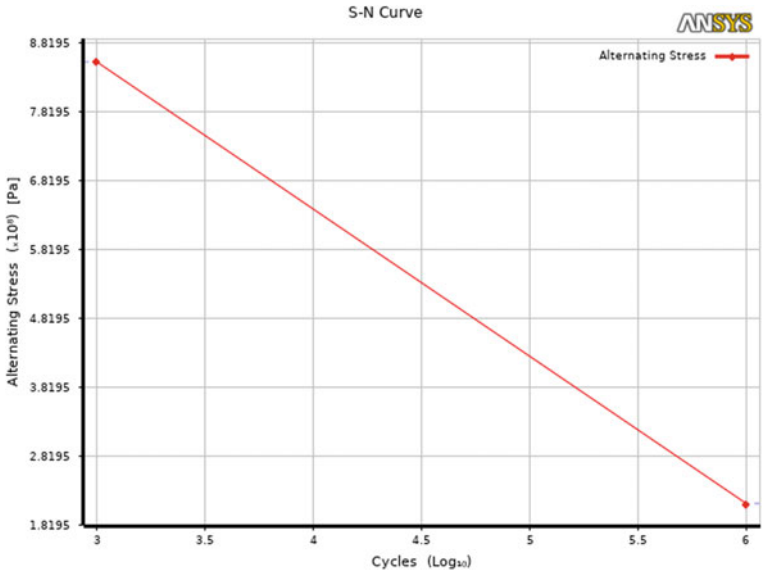


Fig. 1 S-N curve for Ti–6Al–4V

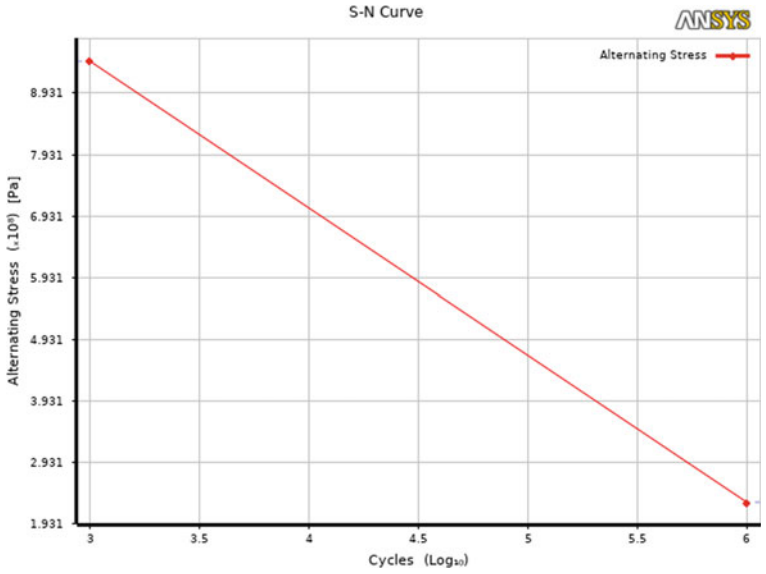


Fig. 2 S-N curve for TIMETAL 834

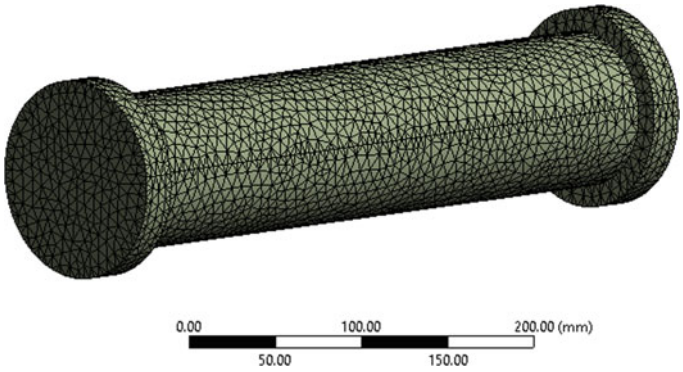


Fig. 3 Meshing of axle geometry

The method of discretizing a model into large number of small size blocks is done before analyzing in finite element analysis this is known as meshing. The solid geometry of axle is discretized by using a mesh size of 4 mm. The tetrahedron mesh is created with 31,503 nodes and 18,149 elements. The meshed axle geometry is shown in Fig. 3.

3.2 Load and Boundary Condition

The axle of aircraft is supported by bearings with heavy load capabilities and good wear and frictional properties. The model is provided a fixed support as shown in Fig. 4.

As the axle bears the load of aircraft, a load of 130 kN is applied, according to weight of the aircraft, on the axle as shown in Fig. 5.

4 Result and Discussion

4.1 Fatigue Life

Fatigue life refers to the number of cycles of stress or loading that the specimen can sustain before its failure. Fatigue life depends on the magnitude of cyclic stress, properties of the material, residual stresses, design geometry, internal defects, temperature, etc. The fatigue life for Ti–6Al–4V is 456,870 cycles for mentioned loading conditions as shown in Fig. 6. Fatigue life for TIMETAL834 is 538,100 cycles for the same boundary conditions which is more than life for Ti–6Al–4V as shown in Fig. 7.

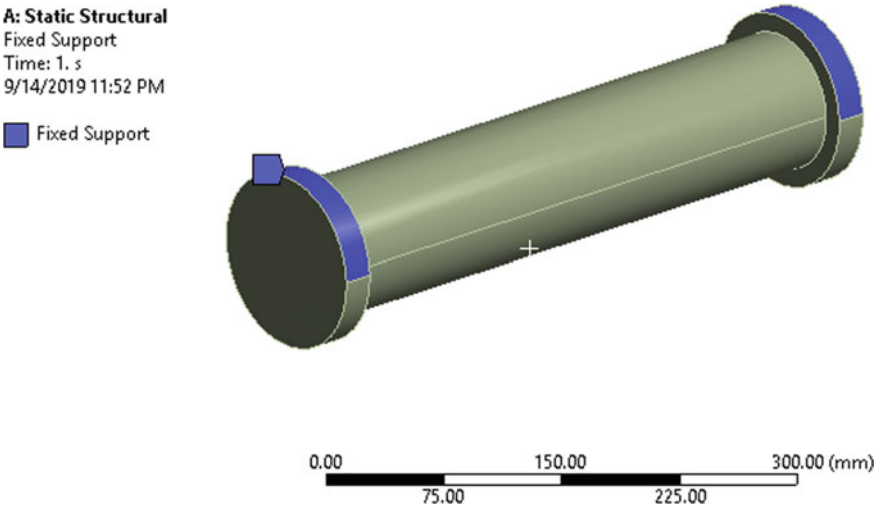


Fig. 4 Fixed support on axle

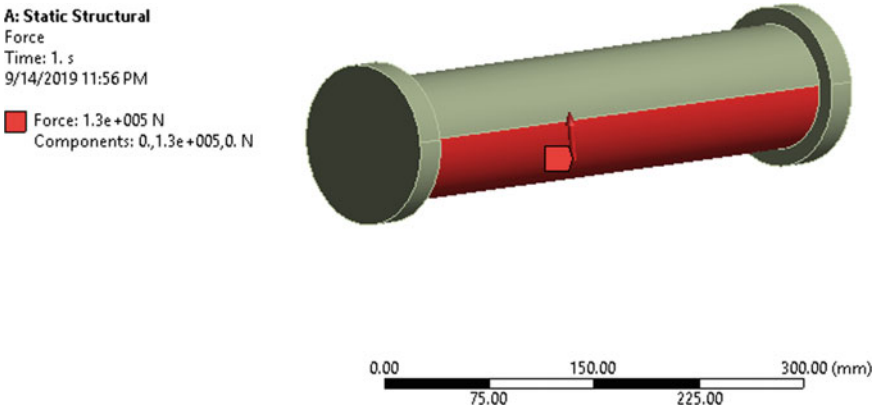


Fig. 5 Load on axle

4.2 Damage

Fatigue damage is the ratio of design life and the service life. Service life is also called available life. The default value of design life is 10E6 cycles. The component fails before the design life if the value of fatigue damage is greater than one. The value of fatigue damage is 2.18 for Ti–6Al–4V and 1.85 for TIMETAL 834 which is lesser than Ti–6Al–4V as shown in Figs. 8 and 9.

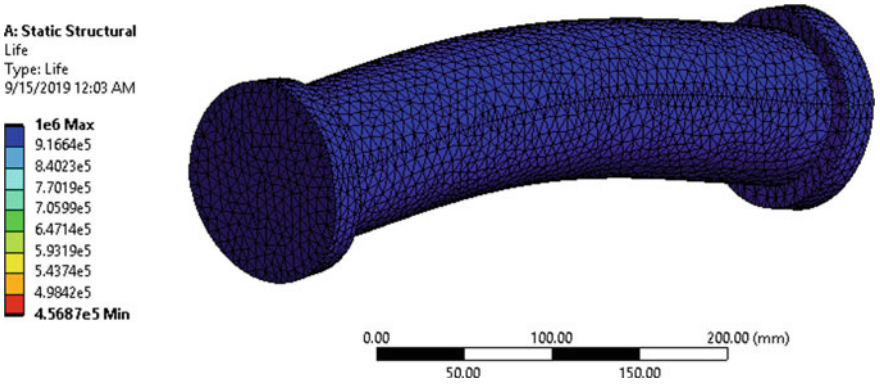


Fig. 6 Cycles for Ti–6Al–4V

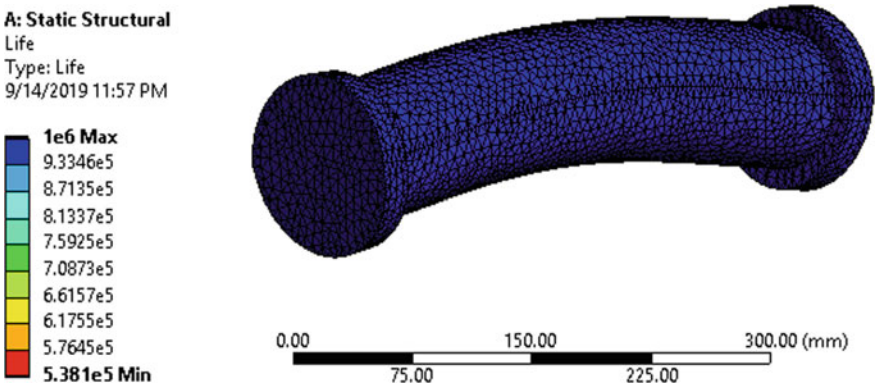


Fig. 7 Cycles for TIMETAL 834

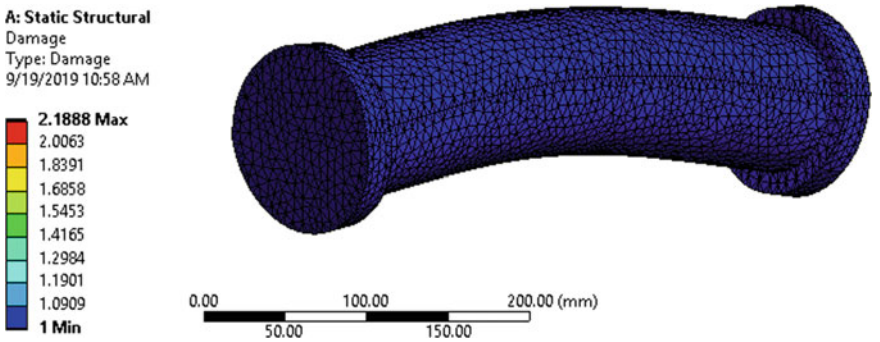


Fig. 8 Damage for Ti–6Al–4V

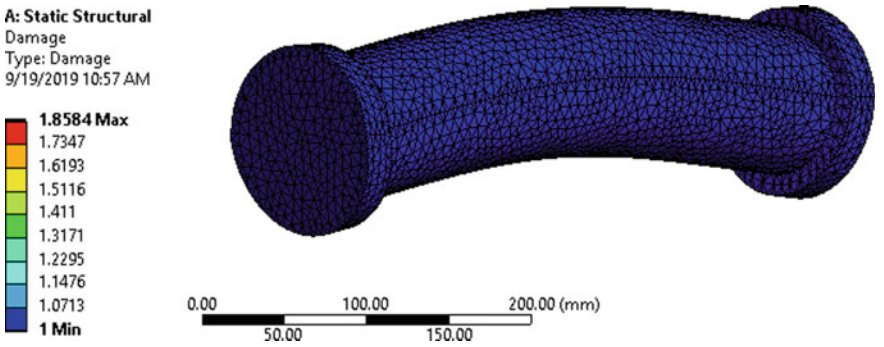


Fig. 9 Damage for TIMETAL 834

4.3 Fatigue Safety Factor

Fatigue safety factor for given design life is the factor of safety to describe fatigue failure. It is the ratio of strength-to-maximum load value. If the value of factor of safety is less than one, it indicates failure of component before design life. This is because in that case, the stress in the particular position exceeds the strength of the material. Also, a safety factor much greater than one everywhere in the model indicates that the part is over-engineered. Larger the magnitude of fatigue safety factor, higher will be the load-bearing capacity. The maximum value of fatigue safety factor is 15. For given loading condition, the minimum safety factor is 0.746 for Ti–6Al–4V as shown in Fig. 10 and 0.780 for TIMETAL 834 as shown in Fig. 11.

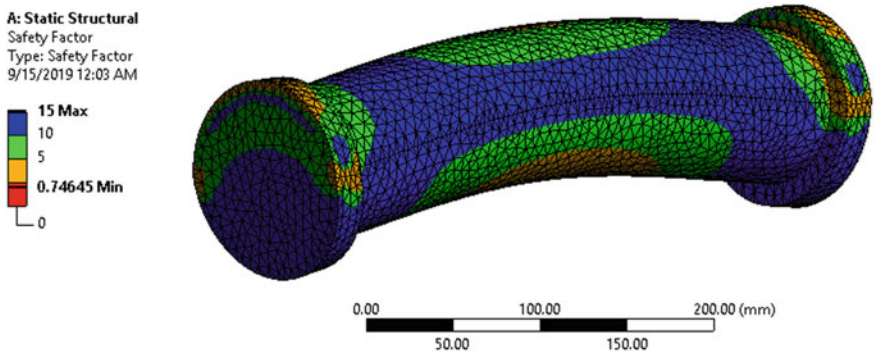


Fig. 10 Safety factor for Ti–6Al–4V

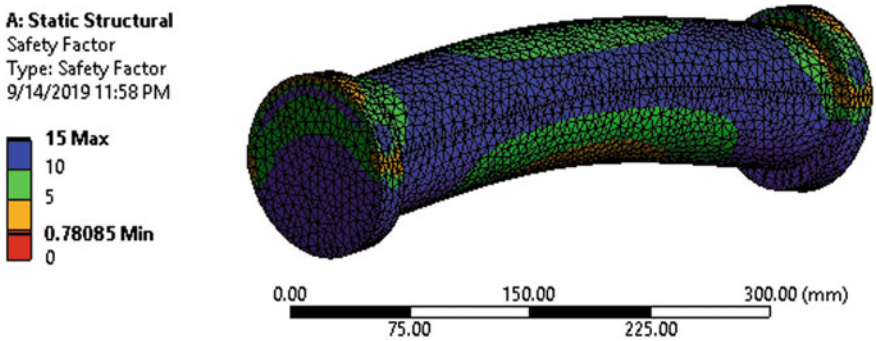


Fig. 11 Safety factor for TIMETAL 834

5 Conclusion

Fatigue analysis of axle in aircraft landing gear is carried out for Ti–6Al–4V and TIMETAL 834 under same loading conditions. The results for three parameters which include life, damage and safety factor are produced in ANSYS. The life for TIMETAL 834 which is 538,100 has improved by 17.77% compared to Ti–6Al–4V. The improved fatigue life will reduce overall cost of axle for TIMETAL 834. Damage is decreased by 15.13% for TIMETAL 834 that in turn lowers the risk of failure. TIMETAL 834 is better under fatigue loading as the fatigue minimum safety factor which is 0.780 has increased by 4.55% than Ti–6Al–4V. In future, the TIMETAL 834 can be used for other components of landing gear like oleo strut.

References

1. Gowda AC, Basha N (2014) Linear static and fatigue analysis of nose landing gear for trainer aircraft. Measurement 2: 5
2. Bagnoli F, Dolce F, Colavita M, Bernabei M (2008) Fatigue fracture of a main landing gear swinging lever in a civil aircraft. Eng Fail Anal 15(6):755–765
3. Kim JH, Lee SB, Hong SG (2003) Fatigue crack growth behavior of Al7050-T7451 attachment lugs under flight spectrum variation. Theoret Appl Fract Mech 40(2):135–144
4. Freitas M, Infante V, Baptista R (2019) Failure analysis of the nose landing gear axle of an aircraft. Eng Fail Anal 101:113–120
5. Franco LAL, Lourenco NJ, Graca MLA, Silva OMM, De Campos PP, Von Dollinger CFA (2006) Fatigue fracture of a nose landing gear in a military transport aircraft. Eng Fail Anal 13(3):474–479
6. Ossa EA (2006) Failure analysis of a civil aircraft landing gear. Eng Failure Anal 13(7): 1177–1183
7. Tikka J (2002) Fatigue life evaluation of critical locations in aircraft structures using virtual fatigue test. In: Proceedings of the 23rd international congress of aeronautical sciences (ICAS)
8. Turan D, Karabayrak B, Baskut S, Dalkilic S (2017) Failure analysis of landing gears strut bearings. Eng Fail Anal 82:525–532
9. Matweb. https://www.matweb.com/. Last accessed 15 Sep 2019

Identification of Rattan Cane in Structural Applications



N. Srujana, G. Monesh, and T. Bhavani

Abstract In the context of producing environment-friendly materials while opposing global warming, developing and utilization of natural material such as bamboo and rattan cane for engineering applications have become the prime need of the study. In comparison to bamboo, cane wood is ductile in nature. This property carried the attention in the preparation of green material for the development of mechanical components used in dynamic loading conditions. Although limited literature is available on cane material, a comprehensive study on strength properties is required. Initiation has been done in attempting cane as load-bearing member. A comparative study on the strength properties of bamboo and cane wood is presented in the paper. It is identified that treated cane wood shows the high bending strength properties than bamboo. The results encouraged the authors to identify stiffness parameters under lateral loading conditions generally observed in the case of leaf springs. At the loads of dynamically varying, fundamental frequencies of leaf springs play a critical role in the performance of a system. Hence, the fundamental frequency of the cane sample is calculated for various support conditions using analytical expressions of transverse vibrations. These critical frequencies are validated using gyro sensors arranged at the end of the cane bar. Conclusions are drawn from the study that the cane material is suitable for light-weight dynamic load applications. Further, the practice can be extended to heavy components introducing cane fiber composites.

Keywords Mechanical properties · Cane leaf springs · Gyro sensors · Natural frequencies

N. Srujana (✉) · G. Monesh · T. Bhavani
Vardhaman College of Engineering, Hyderabad 501218, India
e-mail: n.srujana@gmail.com

G. Monesh
e-mail: moneshyadav131@gmail.com

T. Bhavani
e-mail: bhavanitalasila971@gmail.com

© Springer Nature Singapore Pte Ltd. 2020

A. Praveen Kumar et al. (eds.), *Advances in Lightweight Materials and Structures*,
Springer Proceedings in Materials 8, https://doi.org/10.1007/978-981-15-7827-4_6

1 Introduction

Employing eco-friendly material in multiple applications, naturally grown green materials such as bamboo and cane gathering the attention of many. Partial research is available on bamboo housing construction and other secondary applications. Leake [1] presented work on house construction using bamboo in the context of low affordable houses. The solution is given by supplying a multi-purpose kit that includes prefabricated connections, tools, and instructions to empower the population in becoming independent providers of housing and storage spaces for their families from the readily available resources like bamboo. Medhi et al. [2] conducted a survey in the region for bamboo and rattan to quantify the species available and its local consumption. It is identified the majority of bamboo is used in construction and the other species are used in miscellaneous items, but the consumption of rattan is limited to ritual rites and food items. Nevertheless, the cane is not yet been used in engineering applications other than household applications.

Mechanical properties and fiber arrangement of rattan cane are comparable to bamboo. The rattan cane plantation is seen in most of the East Asian tropical regions. There are more than 51 variety species of cane grown in Assam, India. The cane material is stronger than Oakwood and less water infectant. Because of the material qualities like suppleness, durability, and resilience, the rattan cane has become part of making umbrella handles, walking sticks, tool handles, fishing rods, tent poles, ladders, and hand fans.

Abasolo [3] investigated rattan cane *Calamus merrillii* for assessing longitudinal compressive stress and the study led to the compressive stress existed at the periphery while longitudinal tensile stress existed at the core and the compressive stress varied from base to top. Such stress patterns are due to the variation in the proportion of the fibers. Bhat et al. [4] classified cane wood based on the strength parameter, i.e., strong to very strong, taken from ten South Indian cane rattan species representing large, medium, and small diameter based on static bending, tensile, compression strengths, and the position of the stem. It is observed the majority of the species from the region categorized under medium-strong. Indian rattan canes are comparable to rattan canes available in East Asia. Obilade [5] carried out flexural tests on plane concrete beam and singly rattan cane reinforced beam. The load-carrying capacity of the rattan cane reinforced concrete beam has been increased to 20% of the plain concrete beam. Rachchh et al. [6] proposed lightweight and cost-effective composite material developed from rattan fiber and unsaturated polyester resin using hand layup method. Tests are conducted on six types of laminates and fiber composite material leads to 12.5% of increment in mechanical properties.

Ratna Prasad et al. [7] introduced natural fiber from golden cane (Chrysalido carpuslutescens) as reinforcement in polymers in the application of lightweight structures. The composites were formulated upto a maximum volume fraction of 0.43 with tensile strength and flexural strength. The study exposed golden cane has the potential as reinforcing fillers in plastics with high toughness. Cerqueira [8] developed an alternative material to conventional sugarcane bagasse fiber. The sugar cane

fiber is pretreated with sulfuric acid, sodium hydroxide solution, and mixed with polypropylene in thermo kinetic mixer. The mechanical properties of the composite are evaluated from three-point bending and impact tests. The composite is exposed to secondary electron mode analysis to enhance fiber strength.

In the past, cane-related research is restrained at the level of assessing strength parameters. The study is focused on evolving cane as a structural member rather than non-engineering applications. This paper is about the quantification of the mechanical properties of cane wood or cane bars. The results encouraged the authors to prepare cane spring samples which can be alternative to steel springs used in lightweight structures (go-kart vehicles, drones, and marine applications). Such structures encounter time-varying loads as per the working application, critical/resonance frequencies are dominant when it is considered for structural safety. Fundamental frequencies of cane bar with support conditions of both ends fixed and one end fixed are calculated using analytical expressions of axial vibrations. The critical frequencies for cane samples with cantilever support conditions are validated using gyro sensors arranged at the end of the sample. The results are in good harmony among analytical and experimental methodologies. The work comprises of two phases; the first phase is on the preliminary investigation on strength properties of cane and the second phase is on identifying cane as load-bearing member.

2 Mechanical Properties of Bamboo and Cane

To characterize the naturally grown material for engineering applications, preliminary tests have been carried out on bamboo and cane wood samples. The samples are well treated with borax liquid and dried in the shade for the duration of the week to ten days to remove the leftover sap content.

Testing samples are prepared for both materials according to IS 6874(2008): Method of tests for bamboo [9] since testing standards are not available for the cane bars. Mechanical strength tests are conducted on bamboo and cane samples using the universal testing machine available at strength of material laboratory located in Vardhaman college of engineering. The samples are taken from the mid culm of the whole stem. Based on the stress–strain graphs of the tested bamboo and cane samples, larger deformations at ultimate strength are observed for all the strength properties. It is noticed cane samples displayed high bending strength than bamboo samples. Hence, the unique nature of cane can be effectively used to develop simple components where weight is the constraint and it satisfies the ecological aspects as well. The results evolved from the experimental setups of compression, tension, and bending strengths on bamboo and cane material are presented in Table 1.

A sample of 1.5 m length bamboo with 6 cm outer diameter and 1.1 cm thickness subjected four-point load bending. A sample of 0.9 m length of cane sample with solid diameter 2.5 cm is tested under three-point bending with grips provided at both sides since placing and holding the cane bar under the bending load were critical due to the smoothness of outer layer (see Fig. 1a, b). It is observed typical failure patterns

Table 1 Mechanical properties of bamboo and cane

	Bending strength kN/mm^2	Tension strength kN/mm^2	Compressive strength kN/mm^2	Modulus of elasticity (Mpa)
Bamboo	0.0029 (length of 1.5 m with c/s area 2725 mm^2)	257.18 (c/s area 14 mm^2)	7.24 (c/s area 18.212 mm^2)	15
Cane	0.1 (length of 0.9 m with c/s area 78.4 mm^2)	0.84 (c/s area 5.00 mm^2)	0.089 (c/s area 95.03 mm^2)	3000



Fig. 1 **a** Cane sample at three-point bending test, **b** cane samples after bending

Table 2 Stiffness of cane of different lengths

Support positions	Length of the cane (mm)	Stiffness (N/mm)
One end fixed	180	2.27
	220	1.47
	300	1.12
	350	1.03
	400	0.8
Both ends fixed	952	380
	870	320
	820	330
	800	320

of cane bars under compression and tension are like bamboo due to the longitudinal arrangement of fibers.

Based on bending strength tests carried out on the cane samples, rattan cane exhibited the resistance of 0.1 kN/mm^2 opposing lateral load of 7.85 kN. The result necessitates the study on the stiffness of cane bars of various dimensions when exposed to lateral loads.

The cane rods of lengths 18, 22, 30, 35, and 40 cm with one end fixed support condition are considered and load applied at 5 cm from the free end. Another set of samples 95.2, 87, 820, and 800 cm with both ends fixed support conditions are considered. Stiffness identification tests are carried out on the samples. Deflections are measured using strain gauge linked at the free end. Lateral stiffness of varying cane lengths is tabulated in Table 2.

3 Identification of Fundamental Frequencies of Cane

The member axis of the cane sample remains unchanged even after the removal of load in the elastic region. All the samples attained a larger elastic region before the ultimate strength and reached larger deformation before the fracture point. Such materials are best suited for energy absorbers used as vibration mitigating devices. In general, springs are used to sustain static and dynamic loads in most of the equipment depend upon the type of application. The objective is to prepare the improvised samples that can be used efficiently under time-varying loads. Therefore, it is required to estimate the fundamental frequency of the cane spring sample to understand the behavior under dynamic loads. The critical frequencies are estimated using two methodologies: analytical and experimental approaches.

(a) **Analytical approach**. Using Euler Bernoulli's expression, the internal forces are represented as below.

Hence, the equation of motion is

$$\widetilde{m}\frac{\partial^2 y(x,t)}{\partial t^2} + \mathrm{EI}\frac{\partial^4 y(x)}{\partial x^4} + ky = 0 \tag{1}$$

On solving the equation of motion for the fundamental frequencies of beams with distributed mass and stiffness properties (continuous systems),

$$C_n\sqrt{\frac{EI+k}{\widetilde{m}L^4}} = \omega_i^2 \tag{2}$$

The constant $C_n = (a_n L)^2$, where n is the number of modes.

The constant C_n varies at each mode for different support conditions when both ends fixed and cantilever beams. The fundamental frequencies are estimated, and the results are presented in Table 3.

(a) **Experimental approach**. A small experimental setup is implemented using a cantilever test setup and Arduino gyro sensor. Minimal vibration is initiated in the cane samples using a tuning fork. By making use of a gyro sensor with the esp8266controller, the free vibration signals are logged into a Web portal (see Fig. 2).

(b) The gyro sensor records the readings in acceleration vs. time in the direction of excitation. The data is logged in to the external device such as a computer or portable device. An open-source Seismosoft tool is used in extracting the time domain data to the frequency domain using DFFT analysis. For the samples of shorter lengths 180 and 220 mm, the first frequencies are noticed at 9 and

Table 3 Fundamental frequencies from analytical method

	C_n	Natural frequencies (rad/sec)
Both ends fixed (952 mm)	22.7	0.086
	61.67	0.238
	122.37	0.472
	199.85	0.770
	298.55	1.151
One end fixed and another end free (180 mm)	3.5	5.448
	22.03	10.627
	61.69	27.742
	120.09	57.920
	199.87	96.393
One end fixed and another end free (220 mm)	3.5	1.135
	22.03	7.912
	61.69	19.916
	120.09	38.771
	199.87	64.521

23.24 Hz (see Figs. 3 and 4). For 952 mm sample with fixed support condition, the first mode is identified at 5.62 Hz (see Fig. 5). The response accelerations corresponding attained fundamental frequencies for the samples are mentioned in Table 4.



Fig. 2 Cane sample with gyro sensor attached at the free end

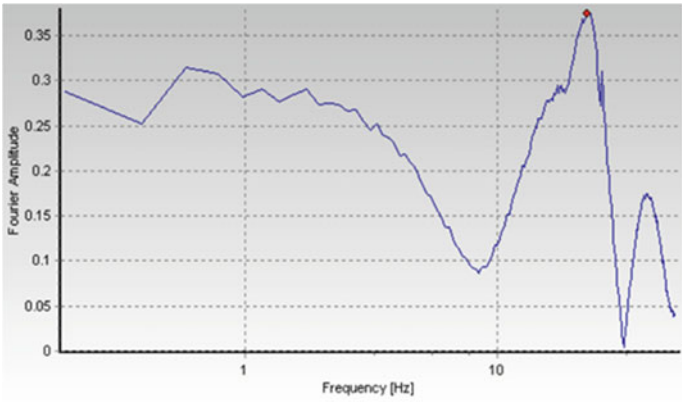


Fig. 3 Fundamental frequency of the sample of length 180 mm

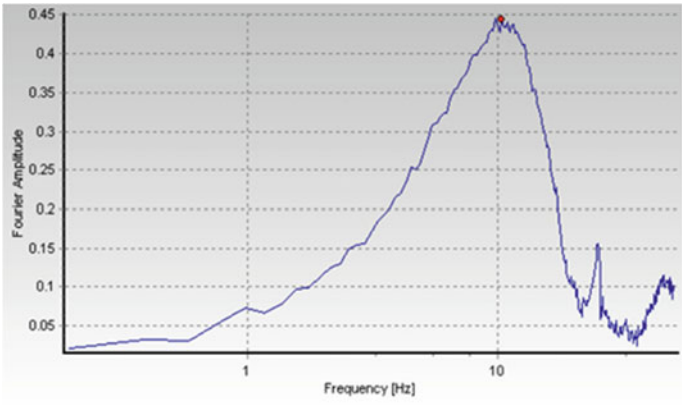


Fig. 4 Fundamental frequency of the sample of length 220 mm

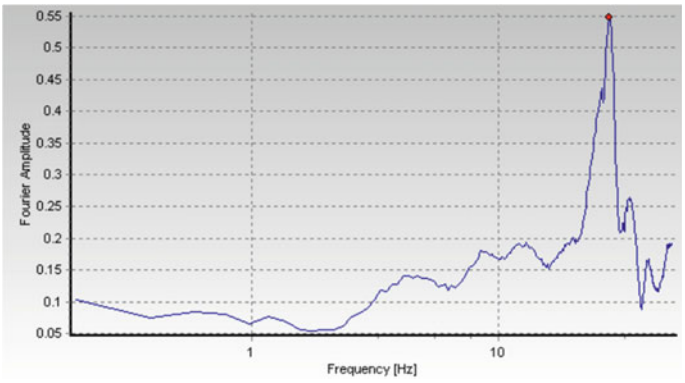


Fig. 5 Fundamental frequency of the sample of length 952 mm

Table 4 Fundamental frequencies of cane of different lengths from experimental setups

Length of the sample (mm)	Fundamental frequency (Hz)	Amplitude (m/s^2)
952	5.62	0.55
180	23.24	0.35

4 Results and Discussions

The below results are from simple experiments on cane samples of different lengths.

(a) Bending strengths of bamboo and cane samples are compared. Cane exhibited higher strength of 100 Mpa to the bamboo of 0.29 Mpa. Compression and tensile

properties are quantified as per the standard recommendations and measured as 89 Mpa and 840 Mpa, respectively. Details are presented in Table 2.

(b) Lateral stiffness properties are assessed for the samples of lengths 180, 220, 300, 350, and 400 mm as 2.27, 1.47, 1.123, 1.03, and 0.8 N/mm at the support condition of one end fixed and other end is left free. The stiffness properties for the long lengths of 952, 870, 820, and 800 mm are evaluated as 380, 320, 330, and 320 N/mm at the support condition of both ends fixed.

(c) Using the conventional analytical approach, the fundamental frequencies are estimated with the assumption of continuous systems with distributed mass and stiffness properties. It is observed fundamental frequency as 1.151 rad/s at fifth mode for the sample of length 952 mm at both ends fixed condition. For the length of samples 180 and 220 mm at cantilever condition, the fundamental frequency is noticed as 5.448 and 1.135 rad/s.

(d) Using experimental setup, the samples have shown 35.3, 146.02, and 61.32 rad/s in the case of samples 952, 180, and 220 mm. The response accelerations are 0.55 m/s^2, 0.35 m/s^2, and 0.44 m/s^2, respectively.

(e) The frequencies determined for the samples of length 952 and 220 mm from the experimental setup are not meeting with the frequencies of the analytical approach. In the case of 220 mm sample, the experimental frequency is matched with the fourth mode of analytical approach.

5 Conclusions

The study on characterization of cane for structural application is concluded as

(a) Due to the capacity of high bending strength in cane, larger deformation results ductility in the material, the property of which is highly required in the designing of structural/mechanical components subjected to severe dynamic loads.

(b) The results from experimental spring setups for the short span sample of length 220 mm are partially validated with the analytical models. But there is a severe discrepancy observed between the experimental model to the analytical model in the case of samples 952 and 180 mm. The gap can be justified by conducting more experimentation on multiple samples of different lengths. However, higher length samples showed high stiffness, but response acceleration is similar to the samples with low stiffness.

(c) Upon successful validation of cane spring samples, the critical frequency data can be used in designing the support mounts which perform the role of dissipating unwanted shocks. Moreover, the frequency data is essential in the analysis of superstructures subjected to dynamic loads.

(d) Bending strength of the material will be improved provided cane fibers are composite with resins.

(e) The outcome of the research is to develop green engineering material from ingenious naturally available material-cane wood, that can be used in multi-level applications such as lightweight drones, marine applications and so on.

References

1. Leake G, Toole K, Divis P, Torres-Sánchez C (2010) Bamboo as a solution for low-cost housing and storage in Pabal (India). In: EWB-UK national research conference 2010 'from small steps to giant leaps...putting research into practice
2. Medhi P, Borthakur SK, Hore DK (2010) Phyto resources from North Cachar Hills of Assam, India-IV: Bamboos and Rattans. J Bamboo Rattan 9(3 & 4):115–125
3. Willie A, Masato Y, Hiroyuki Y, Takashi O (1999) Internal stress generation in rattan canes. IAWA J 20(1): 45–58
4. Bhat KM, Thulasidas PM (1992) J Tropical Forest Sci 5(1): 26–34
5. Obilade IO, Olutoge FA (2014) Flexural characteristics of rattan cane reinforced concrete beams. Int J Eng Sci 3:38–42
6. Rachchha NV, Ujeniyab PS, Misrac RK (2014) Mechanical characterisation of rattan fiber polyester composite. In: 3rd international conference on materials processing and characterisation. Elsevier, India
7. Ratna Prasad VK, Mohana Rao K, Gupta AVSSKS (2013) Experimental investigation of mechanical properties of golden cane fiber–reinforced polyester composites. Int J Polymer Anal Char 18(1): 30–39
8. Cerqueiraa EF, Baptistab CARP, Mulinaria DR (2011) Mechanical behaviour of polypropylene reinforced sugarcane bagasse fibers composites. In: 11th international conference on mechanical behaviour of composites. Elsevier, Italy
9. Indian Standard: Method of tests for bamboo 6874 (2008)

A Review on Crashworthiness and Cooling Models for Lithium-Ion Batteries in Electric Vehicles



Mohammed Mushtaq and S. V. Satish

Abstract The mobility of electric vehicles is to spread completely by the end of the twenty-first century. The only source of power for a pure electric vehicle is a battery pack; Research has been carried out to design an efficient battery pack to resolve the problems related to mechanical, electrical, and thermal domains. Critical issues apprehended in designing a vehicle are the parameters such as noise, vibrations, structural failure, and deformations. The operating conditions of EV batteries are severe; neglecting such conditions adversely affects the body temperature of an individual cell or a complete battery pack, also during events like crash the chances of internal short-circuiting of a Li-ion cell becomes a criterion for destruction when protection is not employed to the battery module. Such technical issues stimulated to develop lithium as an energy source with complete protection to batteries. A generalized review on the design of an energy storage system employing various protection devices, crashworthiness of the designed model, battery management system, failures of battery cells, and battery pack cooling models are proposed. The current challenges and issues to develop an efficient battery pack; an initiative to "Electric Mobility" by governing bodies are discussed in brief.

Keywords Li-ion battery protection · Crashworthiness · Cooling models

1 Introduction

Lithium-ion batteries-driven electric vehicles are been incorporated mainly to reduce gaseous emissions from petrol/diesel-driven IC engine vehicles. The introduction of Chevrolet's Bolt and Tesla's Model 3 marked a new era for the automotive industry. Due to its most advantageous properties such as long cycle life, higher energy density, low self-discharge rate, and high-efficiency lithium-ion battery (LIB) packs are most popularly employed for such electric vehicle (EV) applications. However, as mentioned in [1–4], health and performance of the batteries are correlated strongly

M. Mushtaq (✉) · S. V. Satish
Mechanical Engineering, PES University, Bangalore 560085, India
e-mail: mushtaqme.rymec@gmail.com

© Springer Nature Singapore Pte Ltd. 2020

A. Praveen Kumar et al. (eds.), *Advances in Lightweight Materials and Structures*,
Springer Proceedings in Materials 8, https://doi.org/10.1007/978-981-15-7827-4_7

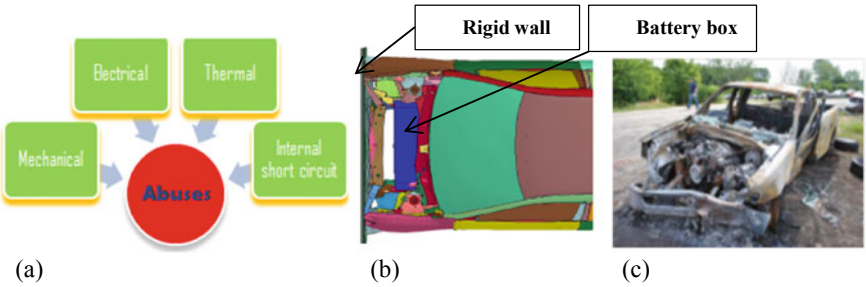


Fig. 1 Lithium-ion battery failure during accidents **a** abuses, **b** mechanical failure during accident/crash [6], **c** internal short circuiting owing to battery damages

on working conditions as well as its temperatures. The most important component in an EV is a power train [5] especially, battery modules. A damage tolerant battery pack as a multifunctional system [6] is developed by Kukreja et al. by the combination of energetic materials and mechanically sacrificing elements to overcome the damages caused by mechanical stresses and to dissipate energy. Zhu [7] carried out various experiments on 18,650 cells by Normalized Critical Displacement (NCD) to short circuit method with and without protection using a hemispherical punch, lateral compression, cylindrical punch, and 3-point bending to verify the mechanical abusing factors leading explosions and damages. Yann leost and Matthias boljen carried out mechanical abuse testing by creating a scenario of "crash," performing knife tests and penetration tests on Li-ion-pouched cells used for Toyota's first-generation electric vehicle model "Yaris." Various abuse causing factors [8] are represented pictorially in Fig. 1a.

Design, fabrication, and performance of a Li-ion battery as a multifunctional energy storage composite structure (MECS) as the load-bearing energy storage unit have been determined in [9]. A model was proposed by Moyer et al. [10] stating the production of high-performance structural battery by direct integration of pouched Li-ion battery materials into a carbon fiber-containing composite matrix using traditional composite layup process. The proposed concept of structural batteries relates the materials' ability to store energy and carry mechanical loads. The potential of storing energy into a carbon fiber-reinforced plastic is analogous to lithium-ion batteries (LIBs) depending on their material compositions and structural design [11].

Vibrational properties of the lithium batteries are determined numerically and experimentally [12, 13] to determine their natural frequencies. Even failure of a single battery can lead to disaster and the public's positive view towards electric mobility may turn down affecting the manufacturer of the product and economy of the industry. An overcharged battery, too-high discharge rates, or a short circuit (internal or external) can cause thermal runaway, these events particularly depend on the chemistry of a Li-ion cell, therefore, it is the responsibility of battery management system to ensure that the cells of a battery operate within their rated specifications. Temperature uniformity for any battery pack is an essential need for long-term usage; therefore, its maintenance can lead to a healthier battery pack [14–16]. Battery

cooling models by active, passive, or integration of active and passive models are proposed stating their own advantages and disadvantages in [17–20].

Consequently, in this paper, a generalized review is carried out to entertain the events affecting the structure of an electric vehicle, heating/cooling models, placement, and protection of battery packs.

2 Materials Composition

A 24 kWh battery pack with each cell having a voltage of 3.85 V 32 ah capacity consisting of 192 lithium-ion batteries is used to configure a battery pack [21]. Kukreja et al. proposed a granule-based assembly (GBA) configuration [6] with dimensions of 9.53 mm tube diameter, tube wall thickness of 1.0 mm and 18,650 cells were used, four configurations were examined in their study (a) batteries only (EV1), (b) batteries with Gba with reduced storage capacity (EV2), (c) batteries protected using external foam (EV3), (d) batteries having the same configuration as EV1 with GBA (EV4). In another study made by Bouvy et al., a 18,650 cell with geometrically varying small battery cells was selected; these cells in a certain specified configuration are combined as mechanical units to determine the factors affecting mechanical properties of the battery pack [22]. The material composition by Ladpli et al. [12] is a battery core with required geometrical specifications constructed by stacking Li-ion cells with cathode and anode layers arranged alternatively and separated by "polyolefin separator layers."

Wei and Agelin-Chaab [18] used an Efest made IMR 26,650 5200 mAh battery cells arranged in eight rows each having a nominal voltage of 3.7 V and weighing 92 g in combination with cooling devices such as air cooling fiber strips, water coolant reservoir, and a fan for analysis of a hybrid cooling concepts for a battery pack. Different configurations of design such as inlet plenums, jet inlets, and multiple delta winglet vortex generators were used as cooling models in [23]. Whereas in [14], a simple battery pack with a total of 32 cells was developed by 18,650 commercial Li-ion cells made of Samsung model no. INR18650-25R, as mentioned, was used in the study for determining heat flow and non-uniform temperature distribution. S. Al Hallaj and J. R. Selman first proposed a passive cooling model in the year 2000 by using "phase change materials," and different design was proposed as cooling models using PCM's considering Hallaj's model as a base [17, 18 and 24].

3 Experimental, Simulations, and Their Outcomes

3.1 Impact Tests

The electric vehicle concept is generalized by the removal of the internal combustion (IC) components from the vehicle model to obtain a basic vehicle frame. Four different EV configurations were investigated by J. Kukreja et al.; the secondary safe zone and the frontal section of a vehicle are utilized for placing battery packs, away from interior space adjacent to a firewall shown in Fig. 2a. Performance of battery packs located at secondary safe zone of a conceptual EV undergoing a frontal crash test has proven to be more efficient than located at primary safe zone considering a "damage tolerant battery pack," and granular based assembly (GBA) battery pack is multifunctional and more effective in alleviating battery failure in a crash. Similarly, in [25], an efficient layout for electric vehicles with certain corrections was developed similar to an IC engine vehicle for determination of cabin deformations during a frontal crash placing a battery pack outside the passenger's compartment is shown in (b). However, the definition of vehicle structure remains unchanged and defines battery pack placement at safe zones in the above cases. The characteristics relating deformation of a vehicle depend strongly on the parts that are stiffer. Deformation matrixes, cell frequency, and deformation zones are expressed as the interpolation of a maximum number of linear points on a vehicle.

Computer-aided design (CAD) tools are used to obtain the construction data of any model; Claude Bouvy et.al proposed a holistic and model-based design approach which resulted in an excellent design for the protection of batteries due to increasing energy absorption structures [8]. A one-dimensional energetic simulation platform is used to integrate the overall system to influence the functionality and efficiency of the model. The mechanical, electrochemical properties, and chemistry of a chosen battery for the structural composite panels are examined at various points throughout the tensile test by the use of galvanostatic measurements [10]. Carbon fibers are important for the development of a structural battery by considering it as an electrode member to obtain dimensional stability during charging and discharging and also it is

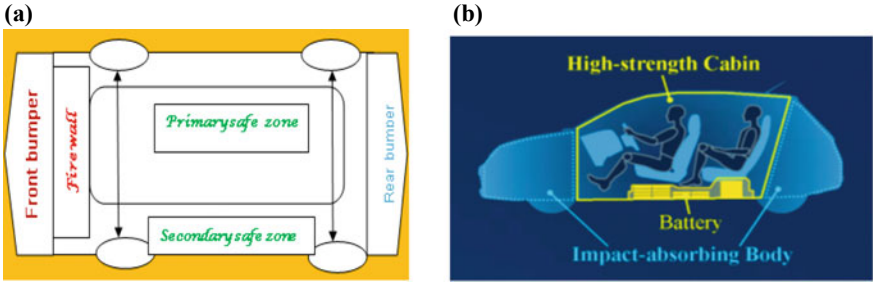


Fig. 2 Battery placement zones **a** GBA configuration, **b** Cabin deformation [23]

capable withstanding higher mechanical loads [26]. By the use of interlocking rivets for joining the two split composite plates or beams with batteries between their layers was able to carry the transverse shear load. Hence by [6, 10], it has resulted that deformation of multifunctional energy storage composites requires higher quasi-static forces due to their increase in bending resistance.

The crash simulations [6] are performed using the Ls Dyna tool. The "New Car Assessment Program" (NCAP) was used to validate the model with the stated Frontal Impact Test number 7520 (35 mph, 56 km/h). Specific absorption energy during a crash is always an idealized principle for any mechanically designed battery pack [8]. Front pole impact, undercarriage impact, moving side pole barrier, and car-to-car crash tests [20] were performed by "Ever safe" to determine the deformations due to loading and ability to withstand abuses where all the above models proposed resulted in safety features of any battery pack due to increase in their capabilities to withstand higher loads during crash also can be investigated by computing the values of the maximum principal compressive stress ($\sigma_{\text{comp}).}$ The allowable stress level (σ_{allow}) is determined using Eq. 1 and elements failed in a battery pack is given by Eq. 2 where σ_{allow} is the Allowable stress; σ_{f} = Failure stress and F_{s} = Factor of safety also.

$$\sigma_{\text{allow}} = \sigma_{\text{f}}/F_{\text{s}} \tag{1}$$

$$\sigma_{\text{comp}} \geq \sigma_{\text{allow}} \tag{2}$$

If maximum principal stress is greater than or equal to allowable stress, the elements will failed.

4 Heat Flow, Cooling Models for Battery Pack

The heat produced while discharging a battery in electric vehicles creating a nuisance led to the development of thermal storage systems. The cooling and heating concept for the proposed geometrical designs are simulated by computational fluid dynamics (CFD) [8, 14, 15, 16]. In [10], a state of charge (SOC)-controlled range extender without the heat pump, thermally controlled range extender with heat pump are used as an experimental setup for determination of heat accumulated, depicting the European winter scenario. Seonggi Park et al. proposed an improvised cooling system with the combination of refrigerant-cooling and forced air-cooling [17] also in [16], it has been proved that temperature of the battery can be maintained by optimal arrangement of battery cells and controlled coolant flow rate. The problem relating non-uniform cooling of cylindrical cells is addressed by Shahid and Agelin-Chaab [14] for a simple battery pack configurations they proposed a passive approach model to improve uniformity in temperature, as a solution an inlet plenums (This plenum acts as a nozzle to accelerates air flow rate and changing the flow direction and eliminating the dead heat accumulation zones inside a pack) with three different

configurations are added to the battery pack whereas Wei and Agelin-Chaab [15] proposed a model (hybrid) using a series of "hydrophilic fiber channels" which acts as a simple air cooling duct placed between the spaces of each cells and a water coolant placed beneath the battery and fiber channels is driven purely by capillary forces and extraction of heat (latent) by evaporation of water from the battery. A new conjugated cooling model using liquid cooling technique and phase change material as an arrangement of the cold plate at the bottom and PCM filled between the Li-ion cell gaps was detailed in [24].

5 Discussion and Challenges

Globally developing automotive companies are looking forward to develop their own passenger cars for electric mobility (Table 1); the graphical representation for different models of car is shown in Fig. 3a and its trend in future (Fig. 3b) depicts how far a car can propel when it is 100% charged. Figure 4a, b shows various parameters related.

Battery and vehicle safety of a developed multifunctional models [9–11] have been explored very little. More research work is yet to be carried out in this area. Manufacturing methods, validation, and refinement of the battery packs for cooling and electrical connection are yet to be explored for higher energy absorption during accidents/crash, penetration by sharp objects, or by any other forms of mechanical failure. Parameters' affecting the vibrational properties of an EV have been less explored, and also cooling of Li-ion cells by passive cooling models [27] has been less explored.

Another challenge is the disposal of batteries as it is a main energy storage device that contains certain hazardous chemicals such as lead, lithium, cobalt, nickel, which lead to the environmental issues and can affect the health of an individual.

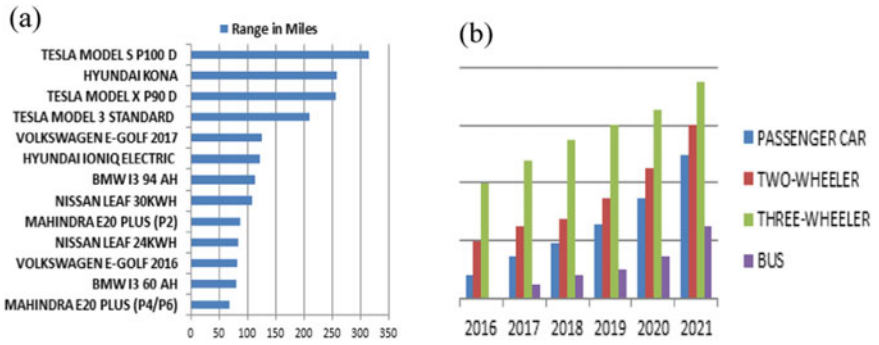


Fig. 3 **a** Electric cars range per full charge, **b** trend of electric vehicles in period

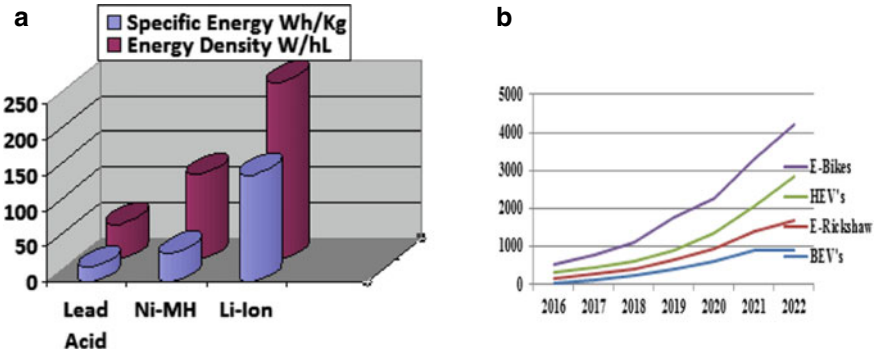


Fig. 4 Graphical representations. **a** Specific energy and energy density, **b** electric vehicle storage opportunities (GW) till 2022 and the anticipated growth

The electric vehicles initiative (EVI) is a multi-government policy forum for the introduction and adoption of electric vehicles thereby thirteen countries such as Canada, France, Japan, Norway, Chile, Germany, Netherlands, Sweden, China, India, New-Zealand, United Kingdom, and USA being the members. The development of EV's in India is largely supported and driven by the country's government and policies. In 2015, an initiative named "FAME" (Faster Adoption and Manufacture of Electric vehicles), a part of the National Electric Mobility Mission Plan, has been undertaken for production and promotion of eco-friendly vehicles including hybrid and electric vehicles. Global Environment Facility project on EV is elaborated by United Nations Environment Programme (UNEP) and International Energy Agency (IEA) to widen the EVI by reaching Latin America, South-East Asia, Central, and Eastern Europe.

6 Conclusions

To summarize, this paper has reviewed the development of electric vehicles powered by lithium-ion cells. The materials and components of a battery, design, and crashworthiness of the proposed models have been well studied. Designing a fully protective battery pack is solemnly a critical process, poor design leads to mechanical, electrical, and thermal abusing conditions, and this can be improved by the use of various origami structures that can resist the higher impacts. Also, various battery cooling models using the active cooling methods have been studied which is agreeable with the proposed design but has the number of working parts, the use of efficiently designed passive cooling models by paraffin wax as a medium can improve the performance of the module.

Table 1 Some electric vehicles, price, power, toque, range

Class Sedan	Price $	Power Hp	Torque Nm	Range mile/fullcharge	Class hatchback	Price $	Power Hp	Torque Nm	Range mile/fullcharge	Class SUV	Price $	Range mile/fullcharge
Tata tigor ev	14,031	41.5	105	82	Mahindra e20 plus	11376	25.8	70	70	Hyundai kona electric	33,287	270
Mahindra e verito	17,273	41	91	68	BMW i3	45,450	168	250	153	Tesla model X	132,000	238
Volkswagen e-golf	31,895	134	290	126	Nissan leaf	29,990	148	320	170	Audie-tron	74,800	150
Chevrolet Bolt	37,495	200	340	240	Ford Focus Electric	14500	143	160	115	JaguarI-Pace	70,000	234

Reference

1. Yang N (2015) Assessment of the forced air-cooling performance for cylindrical lithium-ion battery packs: a comparative analysis between aligned and staggered cell arrangements. Appl Therm Eng 80: 55–65
2. Rao Z (2011) A review of power battery thermal energy management. Renew Sustain Energy Rev 15(9): 4554–4571
3. Xu J (2017) Prevent thermal runaway of lithium-ion batteries with mini-channel cooling. Appl Therm Eng 110: 883–890
4. Gu W (2000) Thermal-electrochemical modeling of battery systems. J Electrochem Soc 147(8):2910
5. Warner M (2011) The electric vehicle conversion handbook. Penguin
6. Kukreja J (2016) Crash analysis of a conceptual electric vehicle with a damage-tolerant battery pack
7. Zhu J (2019) Mechanical failure of lithium-ion batteries. June 2019
8. Moyer K (2012) Carbon fiber reinforced structural lithium-ion battery composite: multifunctional power integration for CubeSats. In: Proc. 21st Aachen colloquium automobile and engine technology, 2 Aug 2019. Holistic battery packs design, Bouvy, pp 367–380
9. Ladpli P (2019) Multifunctional energy storage composite structure with embedded lithium-ion batteries. J Power Sour 414: 517–529
10. Yu Y (2017) Multifunctional structural lithium ion batteries based on carbon fiber reinforced plastic composites. 22 Apr 2017
11. Thomas JP (2004) Mechanical design and performance of composite multifunctional materials. Acta Mater 52(8):2155–2164
12. Galos J (2019) Vibration and acoustic properties of composites with embedded lithium-ion polymer batteries. Compos Struct 220: 677–686
13. Zhang L (2017) Effects of vibrations on the electrical performance of lithium-ion cells based on mathematical statistics. Appl Sci 7: 802
14. Wei Y (2019) Development and experimental analysis of a hybrid Cooling concept for electric vehicle battery packs. J Energy Storage 25: 100906
15. Ji B, Song XG Active temperature control of li-ion batteries in electric vehicles
16. Huang Y (2018) Experimental and optimization of material synthesis process parameters for improving capacity of lithium-ion battery. Int J Energy Res: 1–10
17. Al Hallaj S (2000) A novel thermal management system for electric vehicle batteries using phase-change material. J Electro Chem Soc 147(9): 3231–3236
18. Yan J (2016) Experimental study on the application of phase change material in the dynamic cycling of battery pack system. Energy Convers Manage 128: 12–19
19. Song L (2019) Thermal analysis of conjugated cooling configurations using phase change material and liquid cooling techniques for a battery module. Int J Heat Mass Transf 133: 827–841
20. Zhang R (2018) A study on the open circuit voltage and state of charge characterization of high capacity lithium-ion battery under different temperature. Energies 11: 2408. https://doi.org/10.3390/en11092408
21. Yuan C (2017) Manufacturing energy analysis of lithium-ion battery pack for electric vehicles
22. Bouvy C (2012) Holistic battery packs design. In: Proceedings of 21st Aachen Colloquium Automobile and Engine Technology, pp 367–380
23. Uwai H Development of body structures for crash safety of the newly developed electric vehicle. Nissan motor co., Ltd., 11-0199
24. Bakker J (2011) Analysis of fuel cell vehicles equipped with compressed hydrogen storage systems from a road accident safety perspective. 2011-01-0545
25. Léost Y Crash simulations of electric cars in the ever safe project. In: XIII international conference on computational plasticity. Fundamentals and applications
26. Miao Y (2019) Current li-ion battery technologies in electric vehicles and opportunities for advancements. Energies 12: 1074

27. Shahid S (2018) Development and analysis of a technique to improve air-cooling and temperature uniformity in a battery pack for cylindrical batteries. Therm Sci Eng Progr 5: 351–363

Correlation Involving Compressive Strength and Flexural Strength of Polyester Fiber-Reinforced Binary Blended Concrete



N. K. Amudhavalli, S. Sivasankar, M. Shunmugasundaram, and A. Praveen Kumar

Abstract Fibers were in increasing demand by the desirable quality of elongation and ductility, enhance the show of normal concrete. The recent venture was a relative study to resolve the correlation involving the strength parameters of fiber-reinforced binary blended concrete composites. Polyester fibers are exploited in trial exploration in various parts by addition to the weight of cement with an optimum dose of silica fume and rice husk ash as fractional substitution of ordinary portland cement. In this research, the flexural and compressive strength of polyester fiber-reinforced blended concrete were studied and begin that in present, there was major progress in the strength properties, by utilization of fiber with mineral admixtures in concrete. It was seen that the correlation between flexural and compressive strength played a crucial role and the empirical expression for calculating the strength features of polyester fiber-reinforced blended concrete was featured based on the regression analysis. The properties of concrete were found to be significantly developed by the addition of fiber reinforcement.

Keywords Polyester fiber-reinforced blended concrete · Silica fume · Rice husk ash · Compressive strength · Flexural strength · Regression equation

1 Introduction

The economic advantages and performance properties of concrete with fiber were far more considerable when compared to conventional concrete. The characteristics

N. K. Amudhavalli (✉)
Department of Civil Engineering, CMR College of Engineering & Technology, Hyderabad 501401, India
e-mail: drnkamudhavalli@cmrcet.org

S. Sivasankar
Department of Civil Engineering, CMR Technical Campus, Hyderabad, Telangana 501401, India

M. Shunmugasundaram · A. Praveen Kumar
Department of Mechanical Engineering, CMR Technical Campus, Hyderabad, Telangana 501401, India

© Springer Nature Singapore Pte Ltd. 2020

A. Praveen Kumar et al. (eds.), *Advances in Lightweight Materials and Structures*, Springer Proceedings in Materials 8, https://doi.org/10.1007/978-981-15-7827-4_8

of fiber-reinforced concrete led to its large-scale recognition by the construction industry. The extent of the change depends on the quantity and quality of fibers used [1]. In present days, fibers such as polyester, polypropylene, and polyethylene were used in the market and became acceptable in the construction industry due to their exclusive properties. Exceptionally, a less number of literature were existing for understanding the behaviors of polyester fiber-reinforced blended concrete. Polyester strands were to some degree hydrophobic and the fibers have been utilized at a low amount to control plastic-shrinkage splitting in concrete [2]. In a hardened state, polyester fibers reduce micro-cracks and crack propagations [3]. An increase of about 15% in compressive strength and a significant improvement in flexural toughness were observed in the case of concrete containing polyester fiber (PE) [4].

The utilization of silica fume (SF) helps in accomplishing high starting age quality. The expansion in quality seen between 3 and 7 days, both in compressive and split tensile strength [5], was best to improve the property of the concrete composites due to the lessening of water ingestion in the composites [6, 7]. But there was no reasonable conclusion on SF substitution level, although some of the researchers had detailed different substitution levels [6, 8, 9]. Many researchers have undergone an investigation on the utilization of agricultural residue and extended in the construction industry. India produces a major quantum of rice husk ash (RHA) from the agricultural residue [10, 11]. In ultra-high performance, concrete with compressive strength of 120 MPa or more can be achieved by using an advantageous material RHA [10].

It was reviewed that in India, one-third of the accessible husk can be gathered and converted to ash about 20 million tonnes and can be used for substitution of cement. Along these lines, around one-million ton of RHA was conceivably accessible as mineral admixture as per the records [12, 13]. Cost reduction, performance, durability, and environmental factors are the essential attributes that can make RHA a substantial exchange for portland cement.

By and large, it was inferred that the incorporation of fiber improves compressive strength in the early days [14]. Fibers were known for the significant effect on the workability of the material. The rise in fiber capacity and aspect ratio impacts its workability in concrete [15, 16] The addition of superplasticizer increases the workability (120–150 mm slump). Tensile cracking in the combination of the material was reduced by adding fiber to concrete [17]. Enhancement of the concrete was attained depending upon the measurement rate and kind of fiber [18]. The essential target of this examination was to decide the advantages of utilizing PE in fiber-reinforced concrete. Simple regression analysis also additionally achieved to get expression and to build up the correlation between different strength given polyester fiber-reinforced blended concrete (PEFRBC) test outcomes.

2 Material Selection

2.1 Materials and Methods

Cement and supplementary materials such as SF and RHA were used in this investigation. 53 Grade cement affirming to IS: 12,269-1987(9), SF (Grade 920 D) affirming to ASTM-C (1240-2000) was utilized in the present study. 3.15, 2.2, and 2.67 were specific gravity of cement, SF, and RHA, respectively. The fineness of SF, RHA, and cement was found as 20000cm2/g, 2170 cm2/g, and 2950cm2/g independently. COLOPLAST-SP 430 affirming to IS: 9103-1999 and ASTM 494 was used as a superplasticizer. River sand and crushed aggregates of size 20 mm were utilized as fine aggregates and coarse aggregates affirming to IS: 383-1987.

2.2 Mix Proportions and Mix Details

The concrete mix proportions (m^3 of concrete) adopted in this investigation were given in Table 1. Mix design was followed as per IS 10,262-1982. Water binder ratio considered for this mixes was 0.5, 0.43, 0.38, and 0.35 for M20,M25,M30 and M35 grades of concrete. Fibers were reinforced in concrete during mixing in weight fractions of 0.2, 0.4, 0.6, 0.8 percentages and details were given in Table 2. Samples without fibers were cast as reference concrete. The quantities of cementitious

Table 1 Mix fraction for control concrete

Materials required per m^3 of concrete				
Concrete grade	Cement (kg)	Fine aggregate (kg)	Coarse aggregate (kg)	Water (litre)
M20	383	578	1281.6	191.58
M25	445.53	537.64	1268.10	191.58
M30	487.83	431.65	1367.38	185.4
M35	515	463.5	1501.33	185.15

Table 2 Percentage of polyester fiber required for blended concrete

Polyester fiber (%)	Fibers required per m^3 of concrete (kg)			
	M20	M25	M30	M35
0.2	0.77	0.89	0.97	1.03
0.4	1.53	1.78	1.95	2.06
0.6	2.3	2.67	2.92	3.09
0.8	3.06	3.56	3.89	4.12

constituents in various mix combinations of blended concrete were shown in Table 3.

3 Experimental Program

Mixes with four different grades of concrete with different percentages of polyester fibers were cast. For all mixes, the time for mixing was kept consistent throughout the research. Compressive strength at 28 and 90 days was found with standard size cube specimens with the optimal proportion of SF and RHA. Prism and cubes were used to find the strength parameters such as flexural and compressive strength of PEFRBC as shown in Figs. 1 and 2. Curing was done for 28 days. The average strength of three specimens was taken for each strength value. A correlation involving the compressive and flexural strength of PEFRBC in the form of a simple regression equation had been proposed to examine the performance of PEFRBC. An experimental study in this research was mainly focused to develop a correlation between the compressive and flexural strength of SF- and RHA-based PEFRBC.

4 Results and Discussions

4.1 Compressive Strength Development of Silica Fume and RHA-Based Concrete

The strength at 28 and 90 days of various mixes was taken as the average test results of the three specimens each for obtaining the optimum percentage of SF and RHA in PEFRBC. Figure 3 shows the plot of compressive strength for various grades of concrete, against different percentages of SF content. It was practically observed that SF incorporation increases the strength in all grades of concrete. The voids filled by SF altogether improved the compressive strength; however, at more elevated levels, the improvement diminished. From the test outcomes, it was found that the compressive strength concrete with 7.5% replacement of cement by SF was higher than control concrete by 34.50, 20.47, 23.69, and 26.91% at 28 days and 33.31, 21.53, 22.63, and 26.92% at 90 days curing. Figure 4 shows the variation of compressive strength on the replacement of cement with RHA at 28 and 90 days. RHA diminished the porosity and subsequently increases the strength of the concrete composites at 28 and 90 days. From this examination result, it could be seen that the strength of 15% supplanting of concrete composite with RHA was elevated than the conventional concrete by 18.99%, 16.06%, 14.28%, 18.34%, and 18.98%, 18.12%, 13.30%, 18.34% at 28 days and 90 days, respectively. The results inferred, optimum percentage of SF and RHA in concrete was 7.5 and 15%.

Table 3 Cementitious material combinations for binary blended concrete

Mix	Cement content (kg/m^3)				Mineral admixture content (kg/m^3)							
					Silica fume (7.5%)				Rice husk ash (15%)			
	M 20	M 25	M 30	M 35	M 20	M 25	M30	M35	M20	M25	M30	M35
OPC	383	446	488	515	–	–	–	–	–	–	–	–
OPC + SF	354	412	451	476	29	33	37	39	–	–	–	–
OPC + RHA	326	379	415	438	–	–	–	–	57	67	73	77



Fig.1 Cube under compression test



Fig. 2 Prism under flexural test

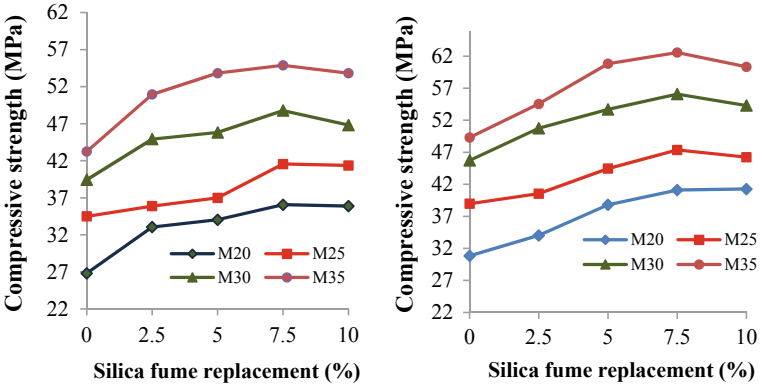


Fig. 3 Compressive strength development of silica-fume-based concrete at 28 and 90 days curing

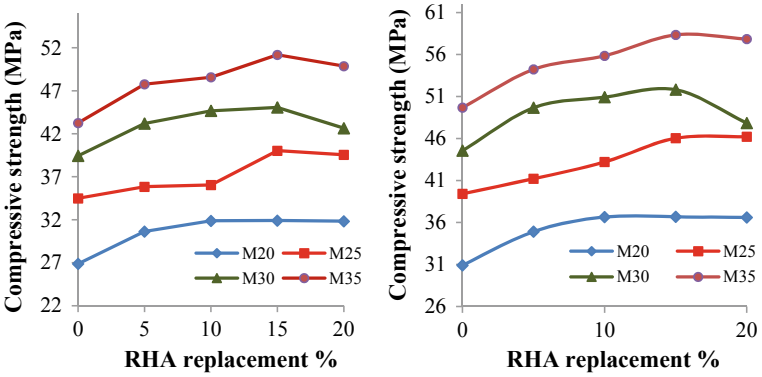


Fig. 4 Compressive strength development of RHA-based concrete at 28 and 90 days curing

4.2 Compressive Strength of Polyester Fiber-Reinforced Concrete

The strength of concrete composite blends made with admixtures SF and RHA with changing the level of polyester fiber was estimated at 28 days curing. The outcome for various grades of concrete in Figs. 5a, 6a, 7a and 8a was plotted. From the figure, it could be seen that development in strength proportionates an increase of fiber. However, the maximum strength at various percentages of fibers to 7.5% replacement of SF admixtures was more predominant. This trend was more obvious between 0.4 and 0.6% percentages for the addition of polyester fibers into the concrete. However, maximum compressive strength was found at 0.5% of polyester fiber in all mixes. This may be of pozzolanic effect and a toughened bond of the mortar and the aggregate. The compressive strength was 34.06 MPa and when fiber 0.5% was incorporated with SF-based concrete, there was a marginal increase in strength about 34.23 MPa in M20 grade of SF-based concrete composites at optimum % of SF (7.5%). For the same grade of concrete at optimum % of RHA (15%), the compressive strength was 31.9 MPa and with fiber (0.5%) incorporation with RHA-based concrete, the strength found was 33.56 MPa. The same increase was found in all grades of concrete. Fiber addition improves the strength; furthermore, it was observed that the strength marginally increased while fiber was added to the concrete, and this could be due to the bond between the mortar and the aggregate.

4.3 Flexural Strength of Polyester Fiber-Reinforced Concrete

The results for the strength of various grades of blended concrete composites (M20, M25, M30, and M35) were plotted against different percentages of fiber volumes. From Figs. 5b, 6b, 7b and 8b, it can be seen that when OPC was mixed with PE, a

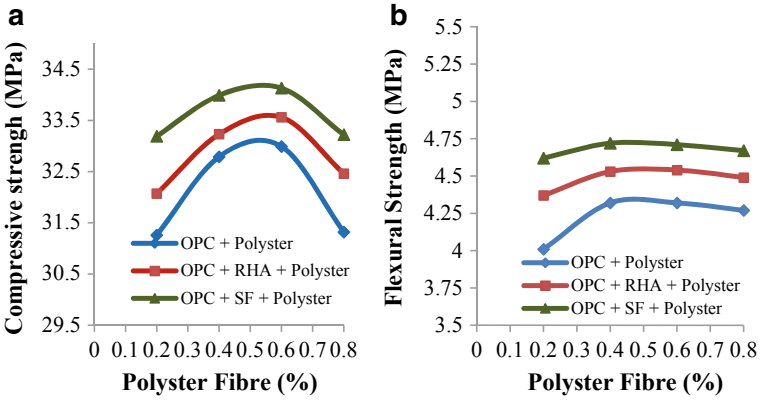


Fig. 5 **a** Compressive strength versus percentage, **b** flexural strength versus percentage of the polyester fiber of M20 grade of concrete polyester fiber of m20 grade of concrete

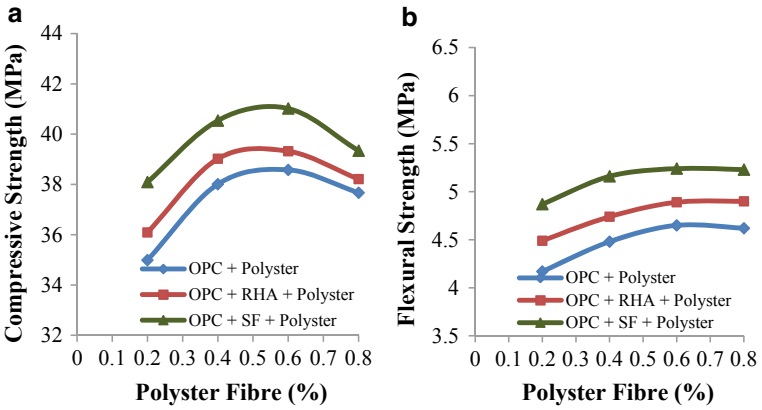


Fig. 6 **a** Compressive strength versus percentage, **b** flexural strength versus percentage of polyester fiber of M25 grade of concrete polyester fiber of m25 grade of concrete

noteworthy rise in strength was obtained. Flexural strength increased tremendously when fiber was combined with SF and it was computed as 70.04, 54.03, 91.14, and 68.60%. There was a decrease in strength in RHA-based PEFRBC. This may be of delayed pozzolanic effect forming pozzolanic C–S–H gel in RHA-based PFRBC.

For all grades of concrete, the optimum percentage of polyester fiber was 0.4–0.6%. Polyester fiber addition results in an increase of compressive strength related to plain concrete for grades M20, M25, M30, and M35. The highest compressive strength was examined in concrete containing 0.5% of polyester fiber to the weight of cement and at 7.5% of silica fume. The level of increment in compressive strength of binary blended mixes to that of binary blended concrete with PE, the strength improvement was negligible. The consequences of the present examination were to

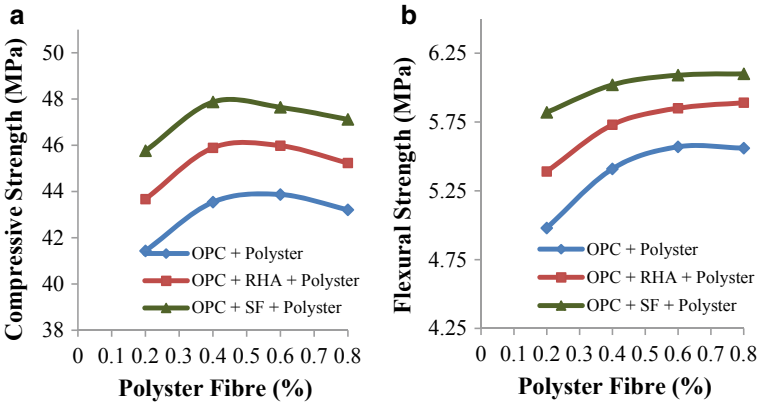


Fig. 7 **a** Compressive strength versus percentage, **b** flexural strength versus percentage of polyester fiber of M30 grade of concrete polyester fiber of m30 grade of concrete

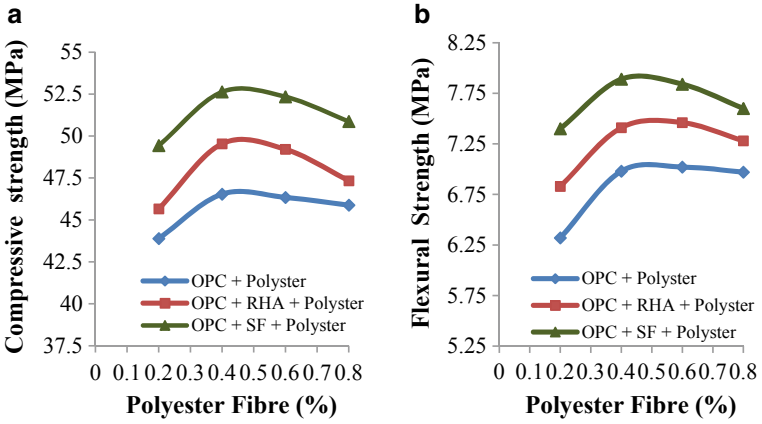


Fig. 8 a Compressive strength versus percentage, **b** flexural strength versus percentage of polyester fiber of M35 grade of concrete polyester fiber of m35 grade of concrete

specify that the incorporation of fiber in binary blended concrete was not constant but it was a component of C–S–H gel.

Once fibers were added toward the blended concrete and plain concrete, there were significant improvements in flexural toughness. The increase in flexural strength was as high as 70.40, 57.01, 62.33, and 70.11% in SF-blended concrete with polyester fiber to that of OPC. But in RHA-blended concrete with polyester fiber, flexural strength decreases. SF-blended concrete with fiber showed greater improvement in tensile strength when compared to RHA-blended concrete with fiber. These results might be due to the greater surface area of SF when compared to RHA and due to the incorporation of fibers which increased the flexibility of concrete composites. The

role of fibers in the flexural strength of concrete was noteworthy as compared to the compression strength of concrete. Despite the fiber content that does not assume a significant role in the compressive strength of concrete could enormously raise the tensile strength of concrete composites.

Figure 9 shows the correlation graph of compressive vs flexural strength of polyester fiber-reinforced concrete with the value of $R^2 = 0.9214$. The correlation involving the investigational and calculated flexural strength results for all grades of polyester fiber-reinforced concrete was revealed in Fig. 10. It was seen that the regression line passes through the origin with an angle of 45° which indicates that

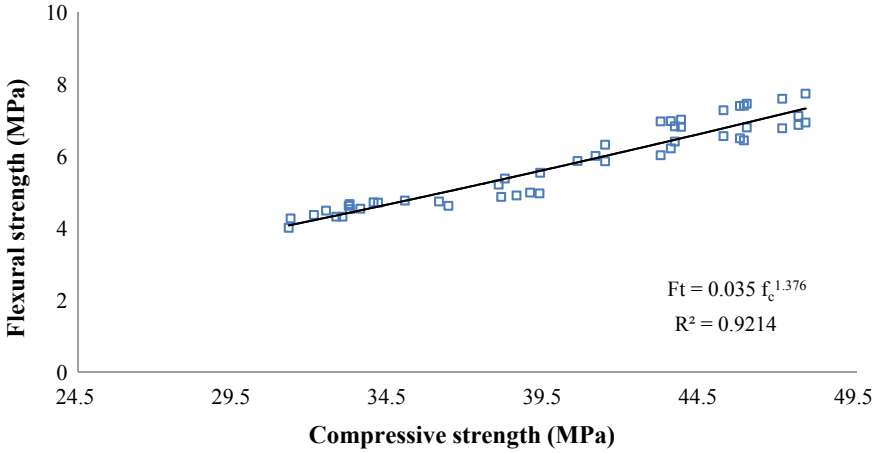


Fig. 9 Correlation graph of compressive versus flexural strength of polyester fiber-reinforced concrete

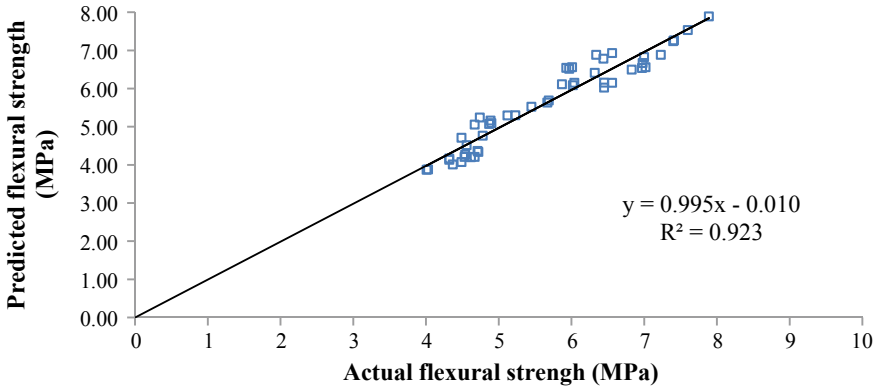


Fig. 10 Experimental and predicted flexural strength results for all grades of concrete of polyester fiber -reinforced concrete

the predicted value expressed in the *Y*-axis was equal to the actual value of flexural strength in the *X*-axis.

5 Conclusions

The important conclusions of the investigation with polyester fiber-reinforced SF- and RHA-based-blended concrete were summarized as below:

- The optimal gain of SF and RHA found was 7.5 and 15%. For different strength characteristics of fibers under the study, the optimum weight fraction of fiber ranged from 0.4 to 0.6%
- Compressive strength of concrete enhanced as the proportion of fiber raises. Adding polyester fiber along with SF results in enhance compression strength over polyester fiber with or without RHA.
- Owing to the addition of fibers in blended concrete and plain concrete, noteworthy improvements in flexural toughness were observed.
- The contribution of fibers toward the flexure strength of concrete was noteworthy as estimated to the compression strength of concrete. Though the fiber content does not play a major role in the compressive strength, it could greatly enhance the tensile strength of concrete composites.

References

1. Saraswathy V, Kwon SJ, Karthick S (2014) Studies on the performance of self healing of plastic cracks using natural fibers inconcrete. J Rec Const Res 2(2): 115–127
2. ACI 544.1R-96 (2002) State-of-the-art report on fiber reinforced concrete, ACI manual of concrete practice, Part 1. American Concrete Institute, Farmington Hills, Michigan, US
3. Shah DL, Modhere CD (2009) Parameter-study on the influence of steel and polyester fibers in the self-compacting concrete. Pacific J Sci Technol 10: 178–186
4. Baruah P, Talukdar S (2007) A comparative study of compressive, flexural, tensile and shear strength of concrete with fibers of different origins. Indian Concr J 81(7):17–24
5. Jones MR, Dhir RK, Magee B (1997) Concrete containing ternary blended binders: resistance to chloride ingress and carbonation. Cement Concr Res 27(6): 825–831
6. Hou J, Chung DDL (2000) Effect of admixtures in concrete on the corrosion resistance of steel reinforced concrete. Corros Sci 42(9):1489–1507
7. Xu W, Lo TY, Wang W, Ouyang D, Wang P, Xing F (2016) Pozzolanic reactivity of silica fume and ground rice husk ash as reactive silica in a cementitious system: a comparative study. Materials 9(3):146
8. Bhaskar S, Gettu R, Bharatkumar BH, Neelamegam M (2012) Strength, bond and durability related properties of concretes with mineral admixtures. Indian Concr J 86(2): 9–16
9. Luo X, Si Y, Wanqing Gu (2019) Effect of silica fume on mechanical properties of concrete incorporating steel slag powder. Wuhan Univ J Nat Sci 24(1):86–92
10. Al-Khalaf MN, Yousif H (1984) A: Use of rice husk ash in concrete. Int J Cem Compos Lightweight Concrete 6(4):241–248

11. Fapohunda C, Akinbile B, Shittu A (2017) Structure and properties of mortar and concrete with rice husk ash as partial replacement of ordinary Portland cement–a review. Int J Sustain Built Environ 6(2):675–692
12. Van Tuan N, Ye G, Van Breugel K, Fraaij AL, Dai Bui D (2011) The study of using rice husk ash to produce ultra high performance concrete. Constr Build Mater 25(4): 2030–2035
13. Sharma RK (2014) Effect of substitution of cement with rice husk ash on compressive strength of concrete using plastic fibers and super plasticizer. KSCE J Civil Eng 18(7):2138–2142
14. Rohit M, Patel I, Modhera C (2012) Comparative study on flexural strength of plain and fiber reinforced HVFA concrete by destructive and non destructive techniques. Int J Eng Sci 1(2): 42–48
15. DJ H (1978) Fiber cements and fiber concretes
16. Swamy RN (1974) The technology of steel fiber reinforced concrete for practical applications. Proc Inst Civ Eng 56(2):143–159
17. Labib W, Eden N (2006) An investigation into the use of fibers in concrete industrial ground-floor slabs. Liverpool John Moores University, Liverpool
18. ACI Committee 544 (1990).State-of-art report on fiber reinforced concrete. In: ACI manual of concrete practice, part 5-1990. American Concrete Institute, Michigan, USA

Optimization of Rectangular Plate with Circular Opening to Improve Buckling Characteristics

A. Agarwal, O. M. Seretse, M. T. Letsatsi, and J. Pumwa

Abstract The use of stiffeners in improving structural integrity and buckling resistance of plates has been under investigation from last few decades. The current research investigates the use of I shaped stiffener in improving strength and buckling characteristics of rectangular plate with circular opening. The rectangular plate is applied with vertical loading conditions to determine stresses, deformation and buckling characteristics. The FEA analysis is conducted using ANSYS 18.1 software and dimensions of stiffener is optimized using Taguchi response surface method. The responses of optimization parameters are generated, and sensitivities are plotted along with goodness of fit curve. The significant improvement of strength is observed with optimized dimensions of stiffener. The sensitivity plot generated through response surface optimization method enabled to analyze individual effect of optimization parameters, i.e., beam lower width (x_1) and beam upper width (x_2) in improving load-bearing capability of flat plates subjected to vertical loads. The method also enabled to determine optimized value of both variables, i.e., beam lower width (x_1) and beam upper width (x_2) which would enable engineers to design best possible flat plates for various industrial applications.

Keywords Buckling resistance · Stiffener · Taguchi optimization · Deformation · Stress

A. Agarwal (✉) · O. M. Seretse
Department of Mechanical Engineering, FET, University of Botswana, Gaborone, Botswana
e-mail: agarwala@ub.ac.bw

M. T. Letsatsi
Department of Industrial Design and Technology, FET, University of Botswana, Gaborone, Botswana

J. Pumwa
Department of Mechanical Engineering (Unitech PNG), PNG University of Technology, Lae, Papua New Guinea

© Springer Nature Singapore Pte Ltd. 2020

A. Praveen Kumar et al. (eds.), *Advances in Lightweight Materials and Structures*,
Springer Proceedings in Materials 8, https://doi.org/10.1007/978-981-15-7827-4_9

1 Introduction

The buckling resistance of structural member can be considerably increased with the use of stiffeners. The use of stiffeners in structures commenced from early 70's. Various experimentations are conducted to determine the feasibility of stiffeners in improving structural integrity of load-resisting members. The buckling process of stiffened plates show nonlinear behavior. The stiffened structures are more efficient in load-bearing capability as compared to structures without stiffeners. The proper design and appropriate location of stiffener is imperative in improving load resistance characteristics of structure, otherwise it would reduce the overall load-bearing capability.

Rhodes [1] has investigated thin plates subjected to vertical loads. The buckling and post-buckling characteristics of thin plates are studied. The author has developed compatibility equations describing in-plane and out-of-plane displacements. Rhodes [2] investigated buckling and post-buckling behavior of tubular structure with Z, C, and H sections. The elastic analysis was conducted with simply supported unloaded end to determine load deformation curve. Plastic mechanism analysis was also conducted to determine empirical correlations. Raghu Prasad and Singh [3] have numerically investigated buckling of plates with opening using finite element method. The ends of plates were simply supported, and meshing was varied to get optimized results. Further analysis was conducted on plate with partial edge comparison. The findings have shown that the stress distribution had minor variations for plate without opening and plate with opening. Pouladkhan et al. [4] has conducted numerical studies on simply supported rectangular plates using FEA software ABAQUS. The buckling load equations was derived using equilibrium equations. The meshing was varied using shell elements to get optimized results.

The analytical results and FEA results were in close agreements with each other. Cho and Lee [5] has investigated effect of lateral collision of stiffened plates used for ships. The experimental testing was conducted on 33 specimens. The collision was done using striker on localized area to get buckling pattern of plate. The kinetic and potential energy stored is then determined from analytical method. Houlston et al. [6–8] studied the dynamic plastic response of stiffened panels under air blast loading by a series of experiments, ADINA, and the finite strip method, and the numerical results approximately agreed with the experimental data. Nurick et al. [9] and Rudrapatna et al. [10] conducted experimental and numerical works on stiffened square plates subjected to blast pressure loading, respectively. Louca and Pan [11, 12] considered the effects of boundary conditions, initial imperfections, and local stiffener buckling on the response of stiffened plates subjected to gas explosions.

The objective of this research is to optimize design of dimensions of I-shaped stiffeners used in rectangular plate subjected to vertical loading conditions. The material used for shear plates is structural steel, and optimization parameters are beam lower with and beam upper width of I-shaped stiffeners. The optimization is done using Taguchi response surface method, and structural analysis is conducted using finite element method.

2 Structural Analysis of I-Shaped Stiffener

The structural analysis of rectangular plate is done using finite element method (FEM) which is based on discretization of domain. The analysis has three stages, i.e., preprocessing, solution, and post-processing.

The first stage is CAD modeling using ANSYS software. ANSYS design modeler is specific tool used for designing and editing operation. The CAD model of rectangular plate is modeled in ANSYS design modeler as shown in Fig. 1. The two-dimensional CAD model is developed. The model is meshed using tetra elements of appropriate size and shape. After meshing, appropriate loads and boundary conditions are assigned.

The CAD model is meshed using beam element, shell element with fine sizing with curvature effects on. The number of elements generated is 18,895 and number of nodes generated is 10,432 as shown in Fig. 2. The CAD model of rectangular plate after being meshed is applied with appropriate loads and boundary conditions. The bottom face of plate is kept fixed, and top face is applied with force of 900000 N in downward direction. The next step is solution stage in which software formulates element stiffness matrix which are assembled to form global stiffness matrix. The

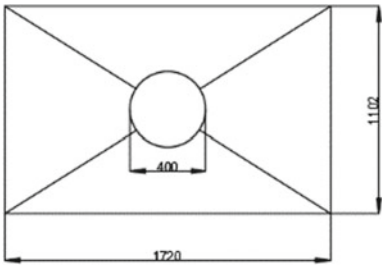


Fig. 1 Schematic of rectangular plate with hole

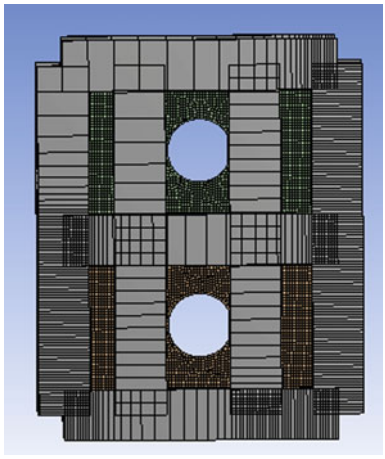


Fig. 2 Meshed model of rectangular plate

further process involves matrix inversions and multiplications to determine deformation and stresses at nodes, and these results are interpolated for entire element edge length.

3 Results and Discussion

The FEA analysis is conducted to determine stresses, deformation, and buckling load which are discussed in this section. The maximum deformation is observed at upper left portion of SPSW with magnitude of 0.429 mm. As we move away from top edge, the deformation decreased and remaining portion of SPSW especially bottom portion has negligible deformation. The maximum principal stress is obtained on lower circular opening with maximum magnitude of 113.98 MPa and reduces on nearby regions. The upper portion experiences negligible stresses. The maximum principal strain is obtained on lower circular opening with maximum magnitude of 0.000533 and reduces on nearby regions. The upper portion experiences negligible strain.

The total deformation load multiplier determined from safety factor is obtained by multiplying load multiplier to applied load which gives 3554.1 N as shown in Fig. 3. The responses which are output variable are optimized on the basis of input variable which are independent. The independent variables are denoted by $x_1, x_2, x_3 \ldots x_n$. These variables are independent and controlled by experimenter with negligible error. The relationship between independent variable and dependent variable can be expressed as

$$Y = f(x_1, x_2, x_3 \ldots x_n) + \in \tag{1}$$

where ϵ is error observed in the response y.

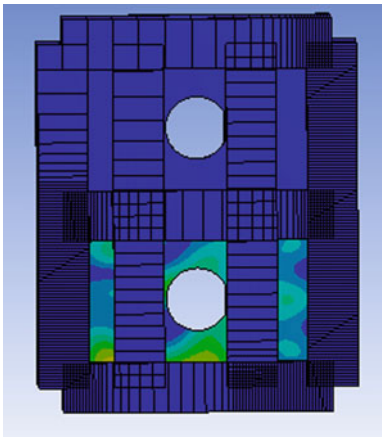


Fig. 3 Total deformation load multiplier for circular opening with I beams

The response of design is function of multiple design variables (x_i), and the response surface behavior can be expressed by the approximation as a polynomial $y = f(x)$ on the basis of observation data. The two variable regression model of quadratic response is given by

$$y = \beta_0 + \beta_1 x_1 + \beta_2 x_2 + \beta_3 x_1^2 + \beta_4 x_2^2 + \beta_5 x_1 x_2 \tag{2}$$

where β_0, β_1, β_2, β_3, β_4 and β_5 are the regression coefficients. The response surface optimization of the current research deals with two design parameters which are beam lower width (x_1) and beam upper width (x_2). To establish the cause and effect relationship, design of experiments (DOE) is performed using ANSYS software. These experiments are conducted using central composite design method or CCD.

The goodness of fit curve of linear regression model shows the difference between the observed values and expected values of output quantities. It also describes the accuracy of prediction for future set of observations. The plot type is of X–Y scatter showing the difference between data points and linear fit as shown in Fig. 4

From the response surface plot shown in Fig. 5, the maximum total deformation load multiplier value is obtained for beam lower width ranging from 145 to 148 mm and for beam upper width ranging from 145 to 165 mm. The lowest value of total deformation is obtained for different ranges of beam upper with and beam lower width shown by dark blue contours. Maximum principal stress is maximum for beam lower width dimension of 144 mm and decreases linearly upto 160 mm beam lower width. For further increase in beam lower width, the maximum principal stress increases upto 176 mm. The maximum principal stress value is obtained for beam lower width ranging from 145 to 150 mm and also from 155 to 165 mm and for beam upper width ranging from 145 to 150 mm and also from 155 to 165 mm.

From the response surface plot shown in Fig. 6, the maximum principal elastic

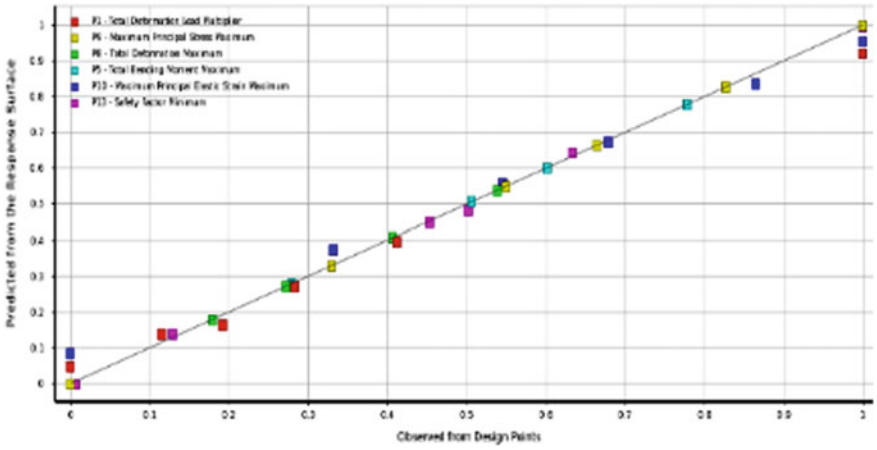


Fig. 4 Goodness of fit curve for circular opening with I beams

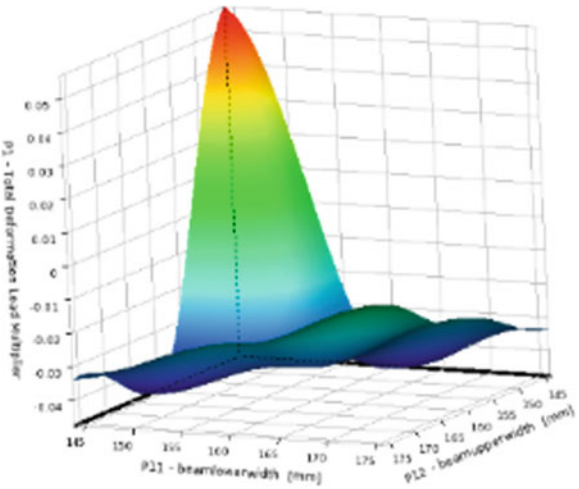


Fig. 5 Response surface plot of deformation multiplier for circular opening with I beams

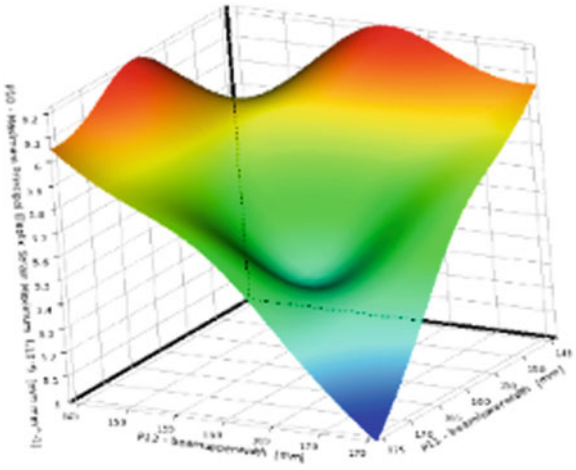


Fig. 6 Response surface plot of maximum principal elastic strain for circular opening with I beams

strain is obtained for beam lower width less than 150 mm and for beam upper width less than 150 mm. The lowest value principal elastic strain is obtained for different ranges of beam upper with and beam lower width shown by dark blue contours for both variable ranging from 165 to 175 mm.

Safety factor variation with respect to beam lower width shows increase in safety factor with increase in beam lower width. The lowest safety factor is observed for beam lower width of 144 mm, and maximum safety factor is obtained for beam lower width if 176 mm. The lowest safety factor is observed for beam upper width of 144 mm, and maximum safety factor is obtained for beam upper width if 176 mm.

From the response surface plot shown in Fig. 7, safety factor minimum is for beam lower width range from 145 to 152 mm and for beam upper width range from

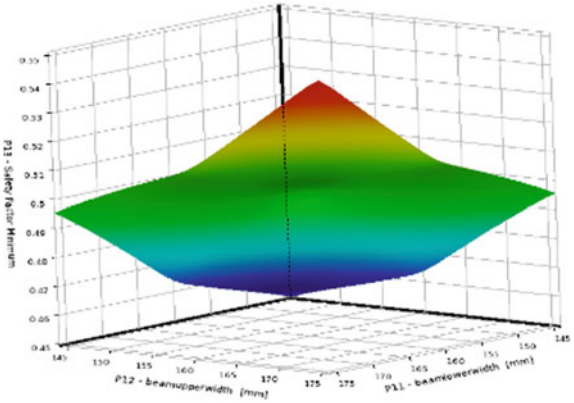


Fig. 7 Response surface plot of safety factor for circular opening with I beams



Fig. 8 Sensitivity plot of various parameters for circular opening with I beams

145 to 152 mm. The highest value of safety factor is obtained for beam lower width range from 165 to 175 mm and for beam upper width range from 165 to 175 mm as shown in Fig. 8.

4 Conclusion

As experimental testing of components has become costly and requires manpower and support, therefore, numerical method of analysis involving use of computer programmes has become viable option. From the structural analysis of rectangular plate conducted using ANSYS software, stresses and strain energy are determined. The model is optimized using central composite design (CCD) scheme. For total deformation load multiplier variable, both beam lower width and beam upper width

show positive sensitivities. Beam lower width sensitivity percentage is 22.352 (positive), and beam upper width sensitivity percentage is 22.353 (positive). Therefore, beam upper width dimensions has larger effect on total deformation load multiplier as compared to beam lower width observed for SPSW.

For maximum principal stress, both beam lower width and beam upper width show negative sensitivities. Beam lower width sensitivity percentage is 66.828 (negative), and beam upper width sensitivity percentage is 65.224 (negative). Therefore, beam upper width dimensions has larger effect on maximum principal stress as compared to beam lower width observed for SPSW. For total deformation, both beam lower width and beam upper width shows negative sensitivities. Beam lower width sensitivity percentage is 36.904 (negative), and beam upper width sensitivity percentage is also 36.904 (negative). Therefore, both beam upper width dimensions and beam lower width has same effect on total deformation observed for SPSW. For maximum principal elastic strain, both beam lower width and beam upper width shows negative sensitivities. Beam lower width sensitivity percentage is 58.6 (negative), and beam upper width sensitivity percentage is also 58.6 (negative). Therefore, both beam upper width dimensions and beam lower width have same effect on maximum principal elastic strain observed for SPSW. For minimum safety factor, both beam lower width and beam upper width show positive sensitivities. Beam lower width sensitivity percentage is 50.263 (positive) and beam upper width sensitivity percentage is also 50.261 (positive). Therefore, both beam upper width dimensions has slightly higher effect on safety factor observed for SPSW.

A vast scope of work lies in investigating other type of openings like rectangular or square for rectangular plates subjected to vertical loading conditions. These opening types, i.e., square or rectangular type, can be investigated by selecting optimization variables of rectangular dimensions and square dimensions using the same methodology.

References

1. Rhodes J (2003) Some observation of the post-buckling behavior of thin plates and thin walled members. Thin-Walled Struct 41(2–3):207–226
2. Rhodes J (2002) Buckling of thin plate members-and early work on rectangular tubes. Thin-Walled Struct 40(2):87–108
3. Raghu Prasad N, Singh J (2015) Buckling analysis of Rectangular plates with cutout and partial edge compression. Int Adv Res J Sci Eng Technol 2(5): 126–129
4. Pouladkhan AR, Emadi J, Safemehr M (2011) Numerical study of buckling of thin plates. World Acad Sci Eng Technol
5. Cho S-R, Lee H-S (2009) Exprimental and analytical investigations on the response of stiffened plates subjected to lateral collision. Marine Struct 22(1):84–95
6. Houlston R, Slater JE (1987) A summary of experimental results on square plates and stiffened panels subjected to air-blast loading. In: 57th shock and vibration symposium. New Orleans, Louisiana
7. Houlston R, Desrochers CG (1987) Nonlinear structural response of ship panels subjected to air blast loading. Comput Struct 26(1/2):1–15

8. Houlston R (1989) Finite strip analysis of plates and stiffened panels subjected to air-blast loads. Comput Struct 32(3/4):647–659
9. Nurick GN, Olson MD, Fagnan JR, Levin A (1995) Deformation and tearing of blast-loaded stiffened square plates. Int J Impact Eng 16:273–291
10. Rudrapatna NS, Vaziri R, Olson MD (2000) Deformation and failure of blast-loaded stiffened plates. Int J Impact Eng 24:457–474
11. Louca LA, Pan YG, Harding JE (1998) Response of stiffened and unstiffened plates subjected to blast loading. Eng Struct 20(12):1079–1086
12. Pan Y, Louca LA (1999) Experimental and numerical studies on the response of stiffened plates subjected to gas explosions. J Constr Steel Res 52(2):171–193

Modelling and Structural Analysis of Stiffened Plate in Vertical Configuration Using ANSYS



M. T. Letsatsi, O. M. Seretse, and A. Agarwal

Abstract Stiffeners are generally used in plated structures to enhance its buckling and post-buckling characteristics. The strength of plated structures can be significantly increased by optimizing the dimensions of stiffeners. The current research investigates the use of I-shaped stiffener in vertical configuration in rectangular plate with rectangular opening for improving strength and buckling characteristics. Structural analysis of rectangular plate is done using ANSYS FEA software to determine stresses, strain, deformation, and buckling load. Dimensions of stiffeners are optimized using Taguchi design of experiments (DOE). The responses of different variables are generated along sensitivity plots. Beam lower-width sensitivity percentage is 49.956 (positive) and beam upper-width sensitivity percentage is also 49.956 (positive). Therefore, both beam upper-width dimensions and beam lower-width dimensions have same effect on safety factor observed for SPSW. Therefore, significant improvement of buckling strength is observed with optimized dimensions of stiffener.

Keywords Strength · ANSYS · Response surface optimization · Compressive loading

1 Introduction

The application of plates can be found in various engineering structures like ships, cranes, and wings of aircraft. The tensile loading characteristics of plates are quite good against compressive loading characteristics. The plates buckle suddenly, during compression, causes failure; thereby, it becomes imperative to understand buckling capacities of the plates in order to avoid premature failure. The buckling resistance of

M. T. Letsatsi (✉)
Department of Industrial Design and Technology, FET, University of Botswana, Gaborone, Botswana
e-mail: Matlhogonolo.Letsatsi@mopipi.ub.bw

O. M. Seretse · A. Agarwal
Department of Mechanical Engineering, FET, University of Botswana, Gaborone, Botswana

© Springer Nature Singapore Pte Ltd. 2020

A. Praveen Kumar et al. (eds.), *Advances in Lightweight Materials and Structures*,
Springer Proceedings in Materials 8, https://doi.org/10.1007/978-981-15-7827-4_10

structural member can be considerably increased with the use of stiffeners. The use of stiffeners in structures commenced from early 70's. Various experimentation are conducted to determine the feasibility of stiffeners in improving structural integrity of load resisting members. The buckling process of stiffened plates shows nonlinear behavior. The type of opening and stiffener used in flat plates effects its load resistance characteristics. The optimized dimension of stiffener would strengthen the structure and improve its buckling characteristics.

Mimura and Akiyama [1] studied the cyclic behavior of rectangular steel plate cutting panels using analytical methods. The structural behavior of the filler plates is superimposed with the structural behavior of the wall panel. The instability capacity of the filling plates is foreseen using the classic plate theory. Thorburn et al. [2] studied the shear behavior of thin rectangular shear wall using the diagonal stress field theory. Its model was known as the multiple stripe pattern, the orientation of the strips was parallel to the voltage range, and the area assigned to each strip was equal to the strip for the plate thickness. The edge radii were rigid and connected to the columns and the limit columns were assigned to the actual rigidity.

Elgaaly et al. [3] analyzed the effect of the lattice and the angle of inclination used in the model of several strips. The amount of strip that will be used will depend on the slenderness of the cutting panels and the rigidity of the profile elements. The results showed that small variations in the angle of inclination have a very low effect on the stiffness.

Pouladkhan et al. [4] have conducted numerical studies on simply supported rectangular plates using FEA software ABAQUS. The buckling load equations were derived using equilibrium equations. The meshing was varied using shell elements to get optimized results. The analytical results and FEA results were in close agreements with each other. Cho and Lee [5] have investigated effect of lateral collision of stiffened plates used for ships. The experimental testing was conducted on 33 specimens. The collision was done using striker on localized area to get buckling pattern of plate. The kinetic energy and potential energy stored are then determined from analytical method. Houlston et al. [6–8] studied the dynamic plastic response of stiffened panels under air blast loading by a series of experiments, ADINA and the finite strip method, and the numerical results approximately agreed with the experimental data. Nurick et al. [9] and Rudrapatna et al. [10] conducted experimental and numerical works on stiffened square plates subjected to blast pressure loading, respectively. Louca and Pan [11, 12] considered the effects of boundary conditions, initial imperfections, and local stiffener buckling on the response of stiffened plates subjected to gas explosions. The objective of this research is to optimize design of dimensions of I-shaped stiffeners used in rectangular plate with rectangular opening subjected to vertical loading conditions. The material used for shear plates is structural steel and optimization parameters are beam lower with and beam upper width of I-shaped stiffeners. The optimization is done using Taguchi response surface method and structural analysis is conducted using finite element method.

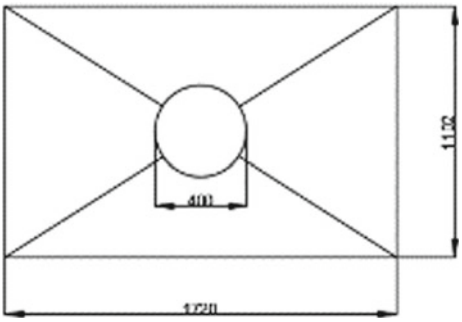


Fig. 1 Schematic of rectangular plate with hole

1.1 I-Shaped Stiffeners in Rectangular Plate

The structural analysis of rectangular plate is done using finite element method (FEM) which is based on discretization of domain. The analysis has three stages, i.e., preprocessing, solution, and post-processing.

The first stage is CAD modeling using ANSYS software. ANSYS design modeler is specific tool used for designing and editing operation. The CAD model of rectangular plate is modelled in ANSYS design modeler with schematic as shown in Fig. 1. The two-dimensional CAD model is developed and the opening is changed from circular to rectangular. The model is meshed using tetra elements of appropriate size and shape. After meshing, appropriate loads and boundary conditions are assigned.

The CAD model is meshed using beam element, shell element with fine sizing with curvature effects on. The number of elements generated is 18,895 and number of nodes generated is 10,432 as shown in Fig. 2. The CAD model of rectangular plate after being meshed is applied with appropriate loads and boundary conditions. The bottom face of plate is kept fixed and top face is applied with force of 900000 N in downward direction as shown in Fig. 3.

The next step is solution stage in which software formulates element stiffness matrix which is assembled to form global stiffness matrix. The further process involves matrix inversions and multiplications to determine deformation and stresses at nodes and these results are interpolated for entire element edge length.

2 Results and Discussion

The FEA analysis is conducted to determine stresses, deformation, and buckling load which are discussed in this section.

The maximum deformation is observed at upper left portion of SPSW with magnitude of 0.425 mm as shown in Fig. 4. As we move away from top edge, the deformation decreased and remaining portion of SPSW especially bottom portion has

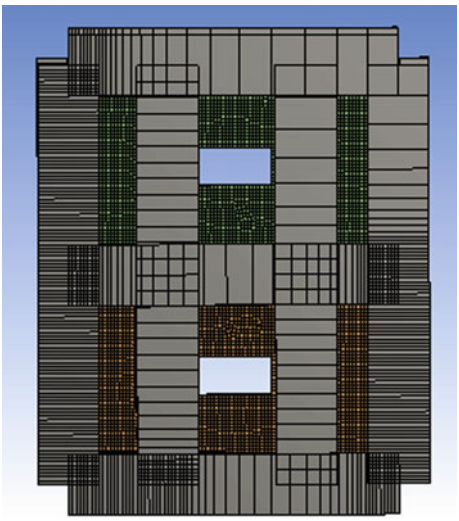


Fig. 2 Meshed model of rectangular plate

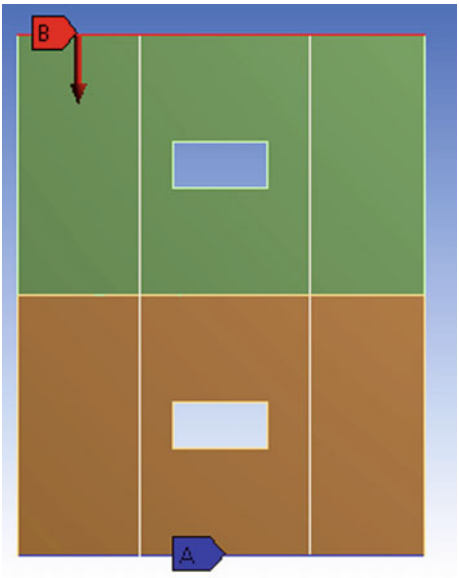


Fig. 3 Loads and boundary conditions

negligible deformation. The maximum principal stress is obtained on lower rectangular opening with maximum magnitude of 160.74 MPa and reduces on nearby regions. The maximum principal strain is obtained on lower rectangular opening with maximum magnitude of 0.000832 and reduces on nearby regions.



Fig. 4 Deformation plot for rectangular opening with I beams

The maximum principal strain is obtained on top beam mid portion with maximum magnitude of 10,429 N mm and reduces on nearby regions. The middle and lower portions experience negligible bending moment as can be seen from Fig. 5.

The minimum safety factor after conducting buckling analysis is found to be 0.4529 as can be seen from Fig. 6. The regions of higher safety factors are stiffeners and top left regions and in vicinity of top opening.

The total deformation load multiplier determined from safety factor is obtained by multiplying load multiplier to applied load which gives 8,640,000 N as can be seen from Fig. 7. The responses which are output variable are optimized on the basis

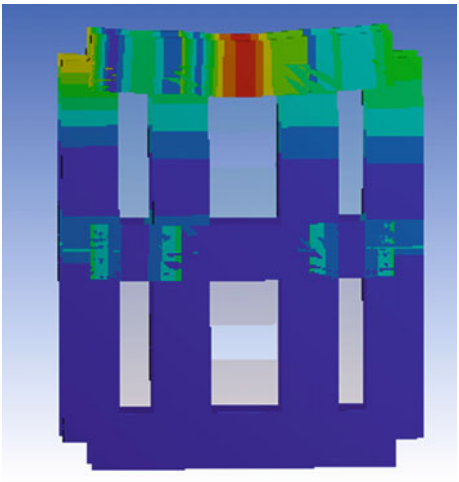


Fig. 5 Total bending moment for rectangular opening with I-beams

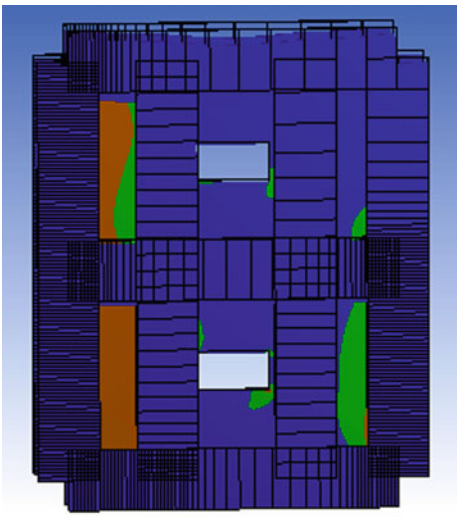


Fig. 6 Safety factor for rectangular opening with I beams

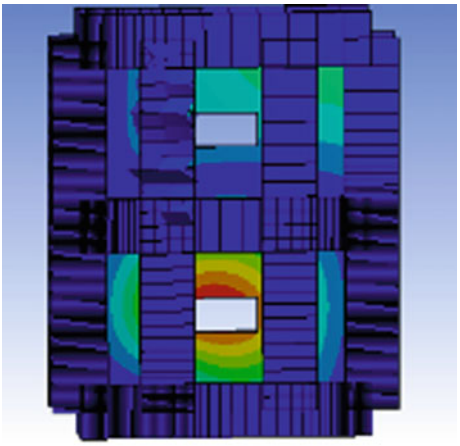


Fig. 7 Total deformation load multiplier for rectangular opening with I beams

of input variable which are independent. The independent variables are denoted by x_1, x_2, x_3 … x_n. These variables are independent and controlled by experimenter with negligible error. The relationship between independent variable and dependent variable can be expressed as

$$Y = f(x_1, x_2, x_3 \ldots x_n) + \in \tag{1}$$

where $\in$ is error observed in the response y.

The response of design which is function of multiple design variables (x_i), the response surface behavior can be expressed by the approximation as a polynomial $y = f(x)$ on the basis of observation data. The two-variable regression model of

quadratic response is given by

$$y = \beta_0 + \beta_1 x_1 + \beta_2 x_2 + \beta_3 x_1^2 + \beta_4 x_2^2 + \beta_5 x_1 x_2 \quad (2)$$

where β_0, β_1, β_2, β_3, β_4, and β_5 are the regression coefficients. The response surface optimization of the current research deals with two-design parameters which are beam lower width (x_1) and beam upper width (x_2). To establish the cause and effect relationship, design of experiments (DOE) is performed using ANSYS software. These experiments are conducted using central composite design method or CCD. The design points are generated from DOE. The goodness of fit curve of linear regression model observes the difference between the observed values and expected values of output quantities. It also describes the accuracy of prediction for future set of observations.

From the response surface plot shown in Fig. 8, the maximum total deformation load multiplier value is obtained for beam lower width ranging from 162 to 165 mm and for beam upper width ranging from 163 to 165 mm. The lowest value of total deformation is obtained for different ranges of beam upper with and beam lower width shown by dark blue contours. The maximum principal stress value is obtained for beam lower width ranging from 155 to 157 mm and for beam upper width ranging from 155 to 157 mm.The lowest value of total deformation is obtained for different ranges of beam upper with and beam lower width shown by dark blue contours for both variable ranging from 162 to 165 mm.

From the response surface plot shown in Fig. 9, the maximum deformation value is obtained for beam lower width less than 157 mm and for beam upper width less than 157 mm. The lowest value of total deformation is obtained for different ranges

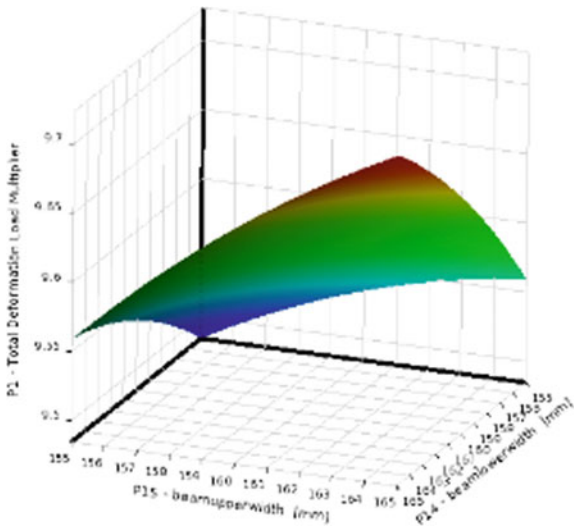


Fig. 8 Response surface plot of deformation multiplier for rectangular opening with I beams

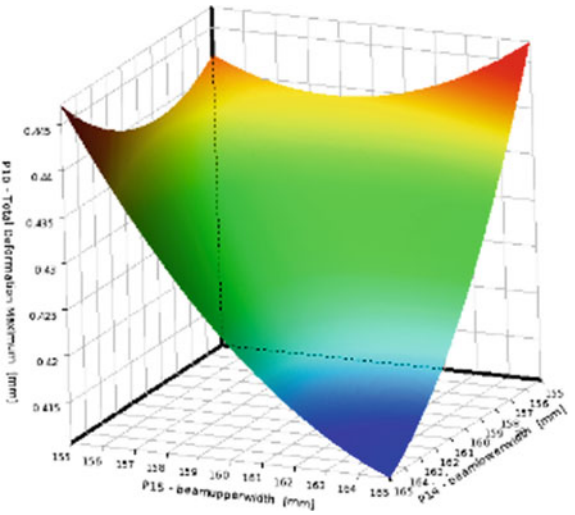


Fig. 9 Response surface plot of total deformation for rectangular opening with I beams

of beam upper with and beam lower width shown by dark blue contours for both variable ranging from 165 to 165 mm.

From the response surface plot shown in Fig. 10, safety factor minimum is for beam lower width range from 155 to 159 mm and for beam upper width range from 155 to 159 mm. The highest value of safety factor is obtained for beam lower width range from 162 to 165 mm.The highest value of safety factor is obtained for beam upper width range from 162 to 175 mm. Bending moment is minimum for beam lower width range from 155 to 159 mm and for beam upper width range from

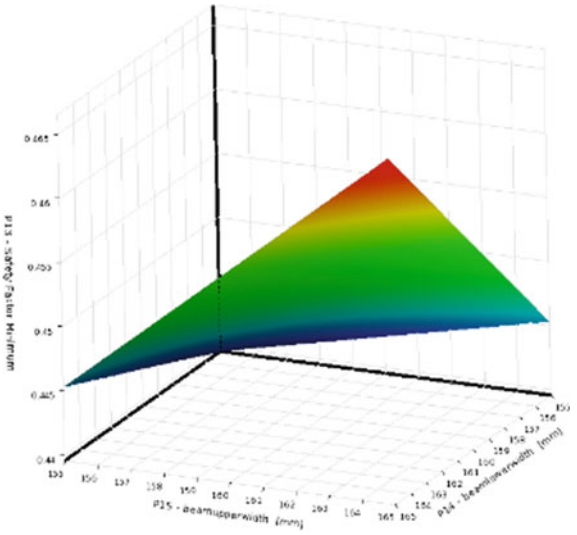


Fig. 10 Response surface plot of safety factor for rectangular opening with I beams

155 to 159 mm. The bending moment is maximum for beam lower width range from 162 to 165 mm and for beam upper width range from 162 to 165 mm. The sensitivities of different optimization variables are studied to determine its effect on output variables. This would enable designer/engineer to identify the optimization variable which could cause maximum variation in output variable (the one having higher sensitivity percentage).

From sensitivity plot, total deformation load multiplier variable for both beam lower width and beam upper width shows positive sensitivities as shown in Fig. 11. Beam lower-width sensitivity percentage is 50.34 (positive) and beam upper-width sensitivity percentage is 50.34 (positive). Therefore, beam upper width and beam lower width have same effect on total deformation load multiplier. Maximum principal stress of both beam lower width and beam upper width shows positive sensitivities. Beam lower-width sensitivity percentage is 49.97 (positive) and beam upper-width sensitivity percentage is 49.97 (positive). Therefore, beam upper width and beam lower width have same effect on maximum principal stress. Total deformation of both beam lower width and beam upper width shows negative sensitivities. Beam lower-width sensitivity percentage is 45.206 (negative) and beam upper-width sensitivity percentage is also 45.206 (negative). Therefore, both beam upper-width dimensions and beam lower-width dimensions have same effect on total deformation observed for SPSW. Maximum principal elastic strain of both beam lower width and beam upper width show negative sensitivities. Beam lower-width sensitivity percentage is 50.618 (negative) and beam upper-width sensitivity percentage is also 50.618 (negative). Therefore, both beam upper width dimensions and beam lower width dimensions have same effect on maximum principal elastic strain observed for SPSW. Safety factor minimum of both beam lower width and beam upper width shows positive sensitivities. Beam lower-width sensitivity percentage is 49.956 (positive) and beam upper-width sensitivity percentage is also 49.956 (positive). Therefore, both beam upper width dimensions and beam lower width dimensions have same effect on safety factor observed for SPSW.

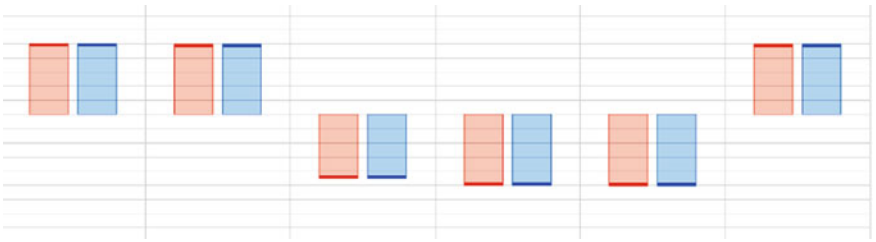


Fig. 11 Sensitivity plot of various parameters for rectangular opening with I-beams

3 Conclusion

The static structural analysis of rectangular plate subjected to compressive loading is conducted using ANSYS FEA software. The type of opening used in flat plate has significant effect on stress distribution across rectangular plate. I-shaped stiffener is optimized using central composite design (CCD) scheme of response surface method to get necessary design points. The responses of different optimization parameters with respect to output variables are captured. These responses enabled to determine optimum values of parameters, i.e., beam lower width and beam upper width for which best design of flat plate could be proposed. These optimum dimensions are 162–165 mm for beam lower width and 162–175 mm for beam upper width. The sensitivity plot generated enabled to study the effect of each optimization parameter with respect to deformation, buckling load, bending moment, principal stress, principal elastic strain, and safety factor. A huge scope of investigation is required in optimizing dimensions of opening (rectangular or square) which could improve buckling characteristics of flat plates subjected to vertical loads. Other design of experiments (DOE) schemes like optimal space filling design, sparse grid initialization requires could be employed in optimization.

References

1. Mimura H, Akiyama H (1977) Load-deflection relationship of earthquake-resistant steel shear walls with a developed diagonal tension field. Trans Arch Inst Jpn 260: 109–114
2. Thorburn LJ, Kulak GL (1983) Montgomery CJ: analysis of steel plate shear walls. structural engineering report no. 107. Department of Civil Engineering, University of Alberta, Edmonton
3. Elgaaly M (1998) Thin steel plate shear walls behavior and analysis. Thin-Walled Struct 32:151–180
4. Pouladkhan AR, Emadi J, Safemehr M (2011) Numerical study of buckling of thin plates. World Acad Sci Eng Technol
5. Cho SR, Lee HS (2009) Experimental and analytical investigations on the response of stiffened plates subjected to lateral collisions. Marine Struct 22(1):84–95
6. Houlston R, Slater JE (1987) A summary of experimental results on square plates and stiffened panels subjected to air-blast loading. In: 57th shock and vibration symposium. New Orleans, Louisiana
7. Houlston R, Desrochers CG (1987) Nonlinear structural response of ship panels subjected to air blast loading. Comput Struct 26(1/2):1–15
8. Houlston R (1989) Finite strip analysis of plates and stiffened panels subjected to air-blast loads. Comput Struct 32(3/4):647–659
9. Nurick GN, Olson MD, Fagnan JR, Levin A (1995) Deformation and tearing of blast-loaded stiffened square plates. Int J Impact Eng 16:273–291
10. Rudrapatna NS, Vaziri R, Olson MD (2000) Deformation and failure of blast-loaded stiffened plates. Int J Impact Eng 24:457–474
11. Louca LA, Pan YG, Harding JE (1998) Response of stiffened and unstiffened plates subjected to blast loading. Eng Struct 20(12):1079–1086
12. Pan Y, Louca LA (1999) Experimental and numerical studies on the response of stiffened plates subjected to gas explosions. J Constr Steel Res 52(2):171–193

Review on Behavior of Hybrid Fiber-Reinforced Concrete



Banka Hadassa Joice, A. Aravindan, and Satish Brahmalla

Abstract A review about attainment for hybrid fiber-reinforced concrete (HFRC) by adding small fibers, it gives more efficient and here the combination of fibers with firm spacing and evenly dispersed fibers which will resist the fractures that extensively develops its properties. It is a study of the effect of hybrid fibers on the behavior of concrete and strength in a structural element by addition of glass fibers and steel in concrete to analyze structural integrity with hybrid FRC and convention concrete and structural behavior beam in tension and compression zone. Plotting typical load-deflection curve for different volume fractions of fibers gives a scope for the future studies and practices.

Keywords Hybrid fiber-reinforced concrete (HFRC) · Steel and glass fibers · Ultimate strength · Strain capacity · Toughness

1 Introduction

The approach of high-performance concrete (HPC) was observed in the initial 80s. It is estimated that the use of HPC can be used for 500 years based on data given by Japanese scientists. It has given a tremendous gain in the strength, chemical resistance, volume stability, attrition resistance, durability, good workability and low absorption [1]. On increasing the strain rates, the HPC is more conscious to loading rate compared to conventional-type concrete, so adding of fibers can resolve this aspect. The HPC with the combination of fly ash gives improved mechanical properties with steel fibers [2] when the steel fibers are added to concrete breakdown gradually varies from bristle to ductile. Fiber-reinforced concrete is combination of material which consists of the amounts of mortar or concrete and alternate various

B. Hadassa Joice (✉) · A. Aravindan
Department of Civil Engineering, Koneru Lakshmaiah Education Foundation Guntur, Andhra Pradesh, India
e-mail: sagar.sampoorna@gmail.com

S. Brahmalla
Department of Civil Engineering, Jayamukhi Institute of Technological Sciences, Warangal, Telangana, India

© Springer Nature Singapore Pte Ltd. 2020

A. Praveen Kumar et al. (eds.), *Advances in Lightweight Materials and Structures*,
Springer Proceedings in Materials 8, https://doi.org/10.1007/978-981-15-7827-4_11

firmly spread suitable fibers. They are different fiber types and have many advantageous properties, but the materials are not considered as such as woven fabrics, stable screen, long wires or rods [3].

The fiber-reinforced concrete (FRC) is characterized on the point of compound material along with concrete, cement or mortar and incohessive, distinct, consistently spread suitable fibers. FRC is present in differentials they possess most advantageous [4]. Regular meshes are interlaced fibers and also treated as distinct fibers. Fiber is a limited fragment of strengthening material carrying certain properties. They can be present in annular or even shape. The fibers are generally expressed by proper criterions called "Ratio of Aspect" that its division of length with diameter. Range of the aspect ratio is 35–155. FRC is concrete consisting fibroid component that improves skeletal probity. It consists of precise distinct fibers regularly divided and inconstantly conformed. A fiber consists such as steel, glass, synthetic and natural. Among these fibers, the characters of these fibers differentiate depending on the concrete, materials, geometrics orientation, dispersion and densities. Fiber reinforcement is prominently used in concrete and normal concrete. The traditional concrete with fiber is pre-owned in sidewalk pavements and bottom floors, and it is suggested in other construction for structural elements. The concept of choosing the combination of fibers and suitability matters depending upon the improved properties.

2 Materials and Experimentation

The fibrous material is utilized to reduce the shrinkage fracture in dry condition as well as plastic condition of the concrete. Its capability have decreased the permissibility of the concrete and decreasing the draining of water. Few fibrous show more property in impact, abrasion and scrape resistivity in the concrete. As fibers will no more improve flexural stability of concrete, therefore changing of moment resistance and structural steel reinforcement is not applicable. So, some of the fibers can decrease its strength. Therefore, extent of fibrous material is added by calculating its total volume of composition material in percentage (concrete and fibers) which is described as volume fraction (V_f). The range of the V_f is from 0.15 to 3.5%. Ratio of aspect (l/d) is measurement of the fiber span (l) divided with the dimension (d) [5]. The non-circular cross section and fibers have a commensurate diameter for aspect ratio. Fibrous material has immense elasticity of modulus than mortar binder or concrete and may be utilized to import to the tensile strength of the material. The fibers which are too long create low workability. The recent research works indicate that in concrete, addition of fibers gives always low enact on its impact more resistance in concrete materials. Analysis is a scope for future construction since people thinking that the ductility increases when the concrete is with fibers [6]. The procedure analytical values mentioned that fibers in the size of micros are better for impact resistance either with long fibers.

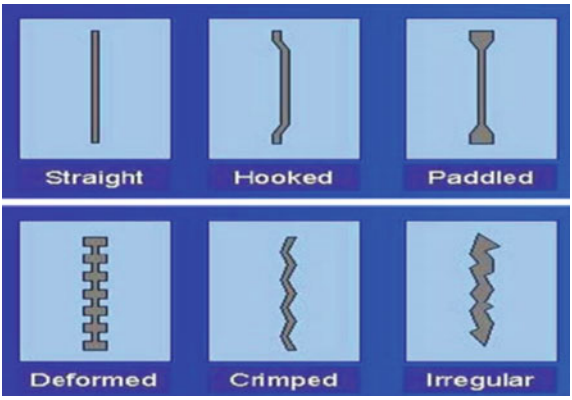


Fig. 1 Shape of steel used in construction

2.1 Types of Fibers

2.1.1 Studies Steel FRC
2.1.2 Polypropylene FRC
2.1.3 Glass FRC
2.1.4 Asbestos Fibers (AF)
2.1.5 Carbon Fibers (CF)
2.1.6 Organic Fibers (OF).

2.1.1 Steel FRC

The steel fibers are available in number as reinforcement. By cutting the round wire into short length will produce round steel fibers.The diameter lies between in the 0.25 and 0.75 mm range; in this size, rectangular c/s are made into sheets about 0.25 mm thickness. The fiber which is drawn from mild steel wire with 0.30–0.5 mm diameter is accepted by IS: 280-1976 in India. The typical c/s range 0.16 to 0.42 mm in thickness and width ranges from 0.26 to 0.92 mm of flat sheet produced from round steel fibers by cutting wires (Fig. 1).

2.1.2 Polypropylene Fiber Reinforced (PFR)

Polypropylene fibers resist the most chemical and cementatious material which could deteriorate under aggressive chemical attack. It is the cheapest and most available fiber. Its boiling mark is more than the working temperature that is 165 °C and 100 °C, respectively, which can be continued for precise periods without affecting the fiber characteristics; as the polypropylene fibers are hydrophobic, they are easy to mix and do not need much contact during mixing, but they should be dispersed evenly in the mix. The range of volume fractions 0.5–1.5% is commercial usage of polypropylene in the concrete (Fig. 2).

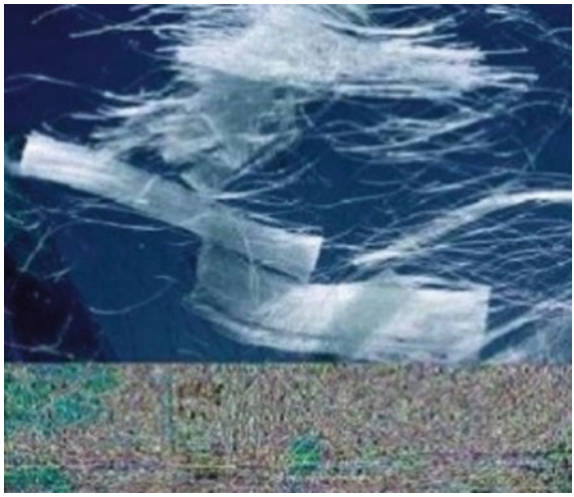


Fig. 2 Polypropylene fiber reinforced

2.1.3 Glass FRC

Glass fibrous is stands divided as different breadth and mixing to make a designable cloth mat or tape by mixing or adding glass fibers. This fiber is made by 200–400 entity tendrils that are bonded lightly to produce fixed stand. This fiber is limited to use more than 2% in the conventional type in volume and with 25 mm length. The extensive use is cement or mortar for thin-sheet products in reinforcing. Most regularly, the E-glass fiber is used. Molded and AR glass E-glass has deficient defiance that alkalis resistant character by AR glass in the port land cement in reinforcing. Physical property which is improved is moisture movement by adding fibrous material (Fig. 3).

2.1.4 Fibers like Asbestos

The asbestos fiber is added to cement paste to form special purpose as asbestos cement. Asbestos is naturally found and cheap mineral fiber and widely used nowadays. Fibers like asbestos have thermal mechanical and chemical resistance which is appropriate in layered pipes, coated and channeled roofing elements. In unreinforced matrix, asbestos cement board is approximately two or four times that. Therefore, the short length (10 mm) has relatively low impact strength (Fig. 4).

2.1.5 Fibers like Carbons

Fibers like Carbon have high modulus of flexural strength and elasticity. In recent times, it is the most addition range of fiber to add in commercial use. It is expansive,



Fig. 3 Glass-fiber-reinforced concrete

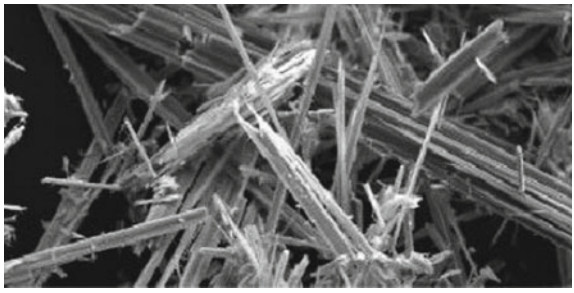


Fig. 4 Asbestos fiber

and the strength and stiffness of carbon are found to be more than steel but more vulnerable to damage than glass. Therefore, it is coated with a resin (Fig. 5).

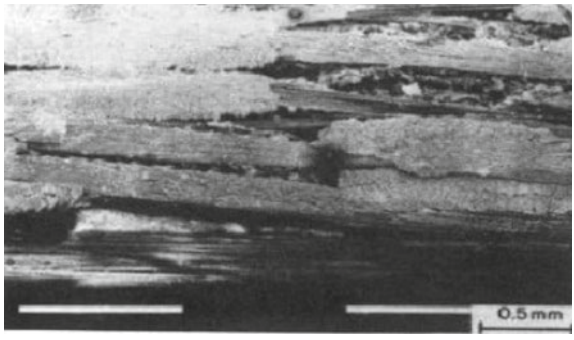


Fig. 5 Carbon fibers

2.1.6 Organic Fibers

Organic fiber is a natural and cheaper fiber. It is chemically inert than glass and steel fibers. It is made by using a high volume of vegetable fiber to produce a multiple cracking composite. Superplasticizers can be added to avoid even dispersion and mixing problems (Fig. 6).

2.2 Essential of FRC

- It improves the durability and strength properties.
- It decreases the air voids and the water voids to some variant.
- The glass and graphite are common fibers which have excellent resistivity to creep compared to other resins.
- The acclimatization of volume of fibers will influence the rebar's or tendons in creep performance.
- Reinforced cement concrete (RCC) of itself is a composite material, where the reinforcement is the strengthen fibrous and concrete has to cast. Accordingly, it is essential to analyze the behavior of thermal stresses under the composition of materials which have different deformations and reinforcement can be minimized [7].
- It is detected that addition of the small and closely evenly spread fibrous materials acts as the crack resistor in both dynamic and static properties.

2.3 Aspects that Are Affecting Characteristics of FRC

- As relative fiber cast firmness
- Amount of fibers

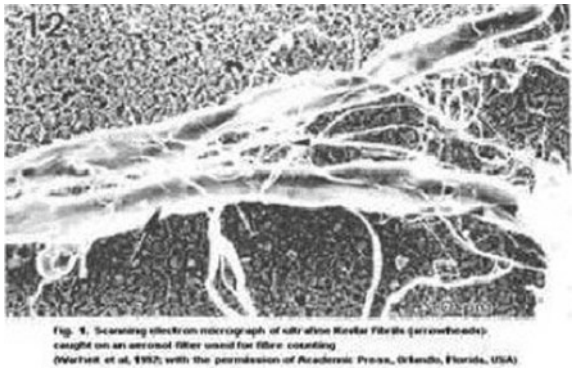


Fig. 6 Organic fiber

Table 1 Aspect ratio of the fiber

Concrete in time	Aspect ratio (AR)	Relative strength(RS)	Relative toughness (RT)
Convention concrete	0	1	1
Addition of fibers	26	1.6	2.2
Inconstantly	51	1.8	8.5
spread fibrous material	75	1.75	10.5

Table 2 Generic properties of fibers

Fibers	Diameter (μm)	Specific gravity	Modulus of elasticity (GPa)	Tensile strength (GPa)	Elongation to failure (%)
Polypropylene	20–200	0.91	5	0.5	20
Steel	5–500	7.84	200	1–3	3–4

- Aspect proportion
- Acclimatization of fibers
- Feasibleness and compacting of concrete
- Proportion of coarse
- Mixing.

3 Materials Properties and Charts

3.1 The Standard Properties of the Fiber Materials are Provided in Tables 1 and 2 [8]

3.1.1 Results of the Study

As the reference of the papers for the review, a example of test conducted is explained by considering them; we understand the improvement of properties in concrete with practical example [9]. The experimental values of the test conducted for 28 days in different amount proportions in cube specimens of fibers are given in Table 6. Table and graph show that addition of 1% HFRC increases the compressed strength of concrete. Compressive values of tested specimen are increased by 24.3, 24, 29.4, 21.9, 17.72 and 12.5% (Table 3, 4 and 5).

According to the compressive strength experimental values, the strength has been increased to 59.55 N/mm^2 in Table 6.

Table 3 Fibers used in project and their properties

Fiber	Format	Length (mm)	Equivalent Dia. (mm)	Tensile strength (MPa)	Density (kg/m^3)
Steel Fibers	Crimped	30	0.75	1100	7850
Polypropylene	Flat Fibrillated	12	0.6	550	910

Table 4 Compressive strength of trial mix

Sample ID	Compressive strength (MPa)
1	52.44
2	54.22
3	50.67

Table 5 Casting and testing of trial mix done for M40 grade

S. No.	Materials	Quantity (kg/m^3)	
		Mix 1	Mix 2
1	Cement	350	350
2	Water	140	140
3	Fine aggregate	896	896
4	Coarse aggregate	1140	1140
5	Chemical admixture	0	2.8
6	Water cement ratio	0.4	0.4

Table 6 Compressive strength

S. No.	Specimen	Compressive strength (N/mm^2)
1	Cubes for conventional concrete	48.88
2	Cube for HFRC (SP 1.0-0.0)	56.88
3	Cube for HFRC (SP 0.9-0.1)	57.77
4	Cube for HFRC (SP 0.8-0.2)	59.55
5	Cube for HFRC (SP 0.7-0.3)	58.22
6	Cube for HFRC (SP 0.6-0.4)	53.77
7	Cube for HFRC (SP 0.5-0.5)	52.00

4 Conclusions

- Based on the literature review, the hybrid fiber-reinforced concrete parameters are varied depending on combination of materials.
- The past research work can give scope for using the hybrid fiber-reinforced concrete in rehabilitation.
- The use of HFRC is improving engineering properties such as ultimate load, relative toughness, the first crack and strain capacity [10].
- Addition of more fibers into concrete makes more homogeneous and isotropic in nature.
- Type of orientation of selected fibers is key factor that controls application of HFC
- This enhances the ductility behavior of concrete under critical loads.
- So, we should know how to control when desired load carrying capacity is gained by addition of the hybrid fibers.

5 Future Scope

The investigation can be continued further by conducting tests on the hybrid fibers by choosing the combination of the individual to attain high strength and improved properties such as tensile test and cyclic loading on structural elements [6]. The scope of the paper is to decide the volume fractions in considerable quantities to make economical and use the fiber resources available.

References

1. Wilso A (2015) Study on hybrid fibre reinforced concrete property using silica fumes and steel l. Int J Innov Eng Technol IJIET 5(3)
2. Ganesan N (2017) HFRHPC interior beam column joints with slab under reverse cyclic loading. India Concr J
3. Anand M (2017) Comparative study on high strength hybrid fibre reinforced concrete with conventional concrete. Int J Eng Res Technol 6(04)
4. Thakur A (2017) A review study of strength properties of hybrid fiber reinforced concrete using PPC 04(08)
5. Kannan S (2016) Study on strength properties of hybrid fibre reinforced concrete 07(04)
6. Ganesan N (2014) Behaviour of hybrid fibre concrete beam-column joints under reverse cyclic loads. Mater Des 54
7. Narayanan SK (2019) Past investigations on mechanical and durability properties of hybrid fibre reinforced concrete. Int J Civil Eng Technol 10(03)
8. Kaithoju SV (2018) Behaviour of hybrid fibre reinforced concrete with partial replacement of cement by fly ash in flexure 07(05), May 2018, ISSN: (online) 2319-8753
9. Chakravarthy R (2016) Review on hybrid fiber reinforced high performance high volume fly ash concrete. Int J Struct Civil Eng Res 05
10. Vineetha V (2017) mechanical properties of hybrid fibre reinforced concrete using recycled aggregates. Int J Adv Sci Res Eng 03(05)

Design and Analysis of Hybrid Composite Leaf Spring for Automotive Applications: An Extensive Study



Smaranika Nayak, Isham Panigrahi, and Ramesh Kumar Nayak

Abstract The main objective of any automobile industry is to improve the behaviour of the vehicle which means improving vehicular stability (vibrational characteristics) during motion or in rest condition which in turn affects the safety of passengers. A good suspension system largely influences the behaviour of a vehicle. Leaf spring holds great importance in suspension system as it carries the vertical loads and absorbs vibrations produced. This review is basically done to emphasize on the different composite materials (natural/synthetic/hybrid) used while fabricating leaf spring as most of the automobile companies are looking for lightweight material apart from conventional steel. Other aspects like savings in weight, increase in strength and the overall cost incurred were taken into consideration. An in-depth focus is also provided to the design and analysis aspect.

Keywords Leaf spring · Composite · Synthetic fibres · Natural fibres · Hybrid composites

1 Introduction

Currently, there is a major challenge among different automobile sectors in reducing the weight of vehicles by conserving natural resources and economic use of energy. In order to achieve target, they are focusing on replacing the existing material with new, advanced and lightweight materials. In the present scenario, there is an inevitable demand for composite materials. It incorporates many significant applications apart from its extensive properties like high strength, stiffness, good wear, corrosion resistance, low density and high fracture toughness [1]. As suspension system is the only

S. Nayak (✉) · I. Panigrahi
School of Mechanical Engineering, KIIT Deemed to be University, Bhubaneswar, India
e-mail: smaranika.nayakfme@kiit.ac.in

R. K. Nayak
Department of Materials and Metallurgical Engineering, Maulana Azad National Institute of Technology (MANIT), Bhopal, India
e-mail: smaranika.nayakfme@kiit.ac.in

© Springer Nature Singapore Pte Ltd. 2020

A. Praveen Kumar et al. (eds.), *Advances in Lightweight Materials and Structures*,
Springer Proceedings in Materials 8, https://doi.org/10.1007/978-981-15-7827-4_12

component in the vehicle accounting for (10–20%) of the unsprung weight [2], it needs a replacement with a lighter one.

Leaf spring was originally known as carriage spring, laminated spring, semi-elliptical spring or cart spring. It came to use at around later 1700s in the carriages in England and is by far one of the oldest form of springing. The main purpose of a leaf spring is to provide a smoother ride and to provide support to the vehicle. The leaf spring helps in absorbing vertical vibrations as well as impacts which occur due to potholes and roughness in roads and sudden impact loads occurring due to travelling of wheel over the bumps. With the deflection of spring, the stored potential energy which is in the form of strain energy is thereafter gradually released. It carries braking torque, driving torque, lateral loads, etc. in addition to shock absorption. It also provides stability to the tires and controls the height of the vehicles. The leaves are arc-shaped, slender and long, stacked one upon the other. The length of the leaves gradually decreases as the number of leaves increases. The benefit of leaf spring over helical in addition to energy absorbing device is that along a definite path the spring ends may be guided. They are used in heavy commercial vehicles like trucks, sports utility vehicles, vans, electrical vehicles, etc. In farming vehicles like tractors, presence of leaf spring helps in hauling and transporting goods, ploughing fields, etc. In case of heavy transport vehicles and construction vehicles, leaf spring helps to support the over-bearing loads preventing it from breakdown. Sports cars such as the Chevrolet Corvette also use leaf spring in the rear axle. Several researchers have used different composite materials to substitute the existing leaf spring by reducing weight and overall cost without hampering the load bearing ability or strength of the material [3]. Many of them used various optimization techniques in arriving at the best suited replacement of the existing material.

Nowadays, extensive work is going on in replacing conventional leaf spring with the composite materials. Various authors focused on different fibre-reinforced composites looking at its widespread advantages over steel materials [4–6]. In the present research paper, a brief review on three different types of fibre-reinforced composites (synthetic, natural and hybrid) for leaf spring material was made. Most of the researchers and academia have followed the hand lay-up technique to fabricate the leaf spring.

2 Composite Materials as a Substitute for Steel Leaf Spring

2.1 Synthetic Fibre-Based Reinforced Composites

Many synthetic fibres such as carbon, graphite, glass and Kevlar with appropriate amount of resins are mostly used as composite materials because of superior properties like high strength-to-weight ratio and high modulus to density. Shankar and Vijayarangan [7] made a comparative study between steel and composite leaf spring by considering strength, weight and cost. A glass fibre-reinforced composite of varying

thickness and width was designed and fabricated by simple hand lay-up technique. Numerical simulation was carried out, and a good agreement was found with the experimental and analytical results. The geometrical dimensions of a leaf spring are given in Fig. 1.

Kumar and Teja [8] designed and used an E-glass/epoxy mono-composite leaf spring in place of a steel leaf spring. The weight was optimized and analysed with proper selection of design parameters. Then, with the help of Pro/E, it was modelled and using ANSYS software, the analysis was done by Rajesh et al. [9]. Bhanage and Padmanabhan [10] compared the fatigue features of a steel and glass/epoxy composite leaf spring. Various fatigue parameters, like fatigue life, damage, response, etc., were determined and plotted using simulation software ANSYS. This resulted in saving of weight and time. Generally, the irregularities at road have frequency of 12 Hz. So, in order to avoid the resonance condition it has to be designed taking road frequency into consideration and for passenger comfort, natural frequency should be adjusted accordingly. Hence, higher natural frequency is desired. The natural frequency of both the materials was tabulated. Pozhilarasu and Pillai [11] compared two different kinds of spring that is one steel spring and composite spring and finally fabricated a composite spring using hand lay-up technique. The steel leaf spring used for comparison is of the ambassador car and the material used is 55 Si 2 Mn 90 steel. Spring is modelled using Unigraphics NX Software and is analysed using ANSYS software. Deflection and bending stress were found to be less in comparison to steel leaf spring. Material saving of approximately 71.4% was observed. Melvin Savio et al. [12] also conducted performance analysis of composite (S2-glass/epoxy) leaf spring and steel using CAE and found a very good correlation between the normal steel and the composite material used. Here, savings in weight were approximated to be around 85%, and stresses were far below the range of steel. Mehul et al. [13] compared the load bearing ability and weight of carbon/epoxy-reinforced composite with the steel leaf spring. He too obtained reduction in weight of around 79.617% and a reduction of around 90.09% can be reached if single leaf spring is taken into consideration. Raghavedra et al. [14] also compared the steel spring of a Maruti 800 car with three kinds of composite materials that is E-glass/epoxy, S-glass/epoxy and carbon/epoxy. He found around 47% reduction in stresses, 25–65% increase in stiffness and 27–67% increase in frequency and savings in weight of around 73–80%. The stiffness of carbon/epoxy leaf spring is more as the deflection is less among the other leaf springs and hence load bearing capacity is higher among all these leaf springs. Similarly, the stresses are less in comparison to steel leaf spring which is

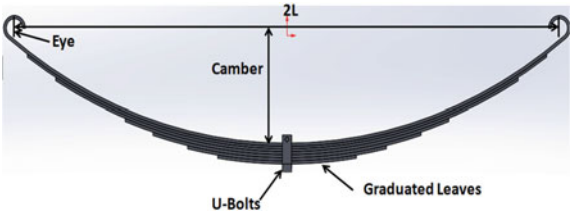


Fig. 1 Geometric drawing of a leaf spring

again an advantage over others. Suhas et al. [15] conducted different mechanical tests on E-glass/epoxy composites by varying the matrix and fibre in the ratio of 50:50, 60:40, 70:30. He concluded that the 60:40 ratio gave better results in comparison to others. About 44% reduction in weight of composite leaf spring was observed in comparison to steel leaf spring with further reduction in stress. Ravindra et al. [16] also compared the mono-steel leaf spring with the carbon/epoxy-reinforced composite leaf spring using ANSYS with respect to weight and strength. He found a reduction in weight of about 22.5%, and also the strength of the composite was high. The stresses were also found to be much lower than that of steel leaf spring.

2.2 Natural Fibre-Based Reinforced Composites

Looking at the cost perspective and conserving resources in the current scenario, many authors have tried to replace synthetic fibres with the natural for better results. They are biodegradable, renewable, recyclable, environment friendly and also cheaper in cost in comparison to synthetic fibres [17]. For automobile, sportings and other structural applications, various natural fibres, like jute, sisal, flax, coir, bamboo, etc., are used. Vinay [18] designed and fabricated five different hybrid combinations of laminates taking E-glass and silk in different proportion for the replacement of a steel leaf spring. He has also considered different proportion of epoxy, E-glass and silk in the design, analysis and fabrication of the natural fibre-reinforced composite. Different mechanical tests were conducted to test the specimens owing to its suitability. Five different hybrid combinations were fabricated by hand lay-up method along with the eye portion. Then, a comparison of weight was carried out to find the best suitable. Finally, it was concluded that the laminate with 40:45:15 yields better results in both tensile and flexural tests. Thus, hybridization may be considered as an important factor for determining the mechanical features. Ravi Kumar et al. [19] used natural (jute) fibre-reinforced composite leaf spring for weight savings and also to reduce the stress in comparison to steel and synthetic fibre that is glass/epoxy. Reduction in weight was around 60–70% and also the stress value was estimated to be much below the steel spring.

2.3 Hybrid (Synthetic/Natural) Composites

Fabrication and design of a hybrid composite (preferably glass/carbon reinforced) leaf spring for automobiles whose natural frequency was found to be high enough to evade resonance was done by Sureshkumar et al. [20]. The natural frequencies of mono steel leaf spring and hybrid composites were tabulated. Here, carbon fibres were placed at the outer layers for good load carrying capacity and glass at the inner layers for good damping factor. Analysis was done using ANSYS and it was found that the hybrid laminate can withstand maximum load and also the stresses

produced were lower. Keshavamurthy et al. [21] also designed and analysed hybrid glass/carbon-reinforced laminate using ANSYS and 70% reduction in weight was obtained. Singh and Brar [22] have successfully fabricated and tested two different types of composite specimens for replacing steel leaf spring in an automobile. One is Al (7075) reinforced with 25% boron carbide (B_4C) and the other is carbon/epoxy composite fabricated by stir casting technique and hand lay-up method. In order to determine the mechanical properties, hardness, tensile and flexural tests were carried out. Suprith et al. [23] carried out fatigue and static tests of hybrid composite springs and also steel and found a good agreement with the analytical and experimental results. Life data analysis was carried out using three approaches that is (a) Goodman/Gerber approach, (b) Soderberg approach and (c) mean stress theory. Out of the three methods, Soderberg results were found to be more effective in giving better results. Jancirani and Assarudeen [24] provided an overview on the various researches about the reduction in weight of leaf spring considering the selection of material processing methodology, modelling, analysis, etc. They also highlighted certain disadvantages as well as advantages of using composites against the standard material that is structural steel. Under certain road irregularities, chances of chipping action are possible where the possibility of fibre breakage in the bottom portion becomes prevalent. But, if we look at the merits 50% savings in weight, 20–30% reduction in stresses with an increase in the natural frequency was observed.

3 Conclusions

Fibre-reinforced composites are highly acknowledged by several researchers and academicians as a substitute for steel leaf spring. A greater reduction in weight has been observed when composites were used. This review paper primarily focused on the design and analysis of composite leaf springs. Ample focus was provided to use of different synthetic fibre-reinforced composites like glass, carbon, kevlar followed by natural fibre (jute/silk/bamboo/coir/basalt)-reinforced composite and hybrid composites. Different fabrication techniques were discussed and the composites were modelled and designed using Unigraphics NX/Pro-e/CATIA and ANSYS was used for their analysis. Apart from weight reduction, less deflection, high strength, low cost, etc., other major advantage includes the reduction in noise and vibration. Further development of hybrid nanocomposites may also be suggested as a substitute for automotive applications.

References

1. Nayak S, Nayak RK, Panigrahi I, Sahoo AK (2019) Tribo-mechanical responses of glass fiber reinforced polymer hybrid nanocomposites. Mater Today Proc 18:4042–4047

2. Tanabe K, Seino T, Kajio Y (1982) Characteristics of carbon/glass fiber reinforced plastic leaf spring. SAE Trans: 1628–1636
3. Ashwini K, Rao CM (2018) Design and analysis of leaf spring using various composites–an overview. Mater Today Proc 5(2):5716–5721
4. Raut LB, Jadhav SV, Jagadale VS, Swami V, Gavali SR, Gade SB (2020) Experimental investigation of basalt fiber/epoxy composite for automobile leaf spring. Techno-Societal 2018:777–787
5. Kuhn P, Loy C, Kuehnel M, Pinch W, Ebel C (2020) Innovative use of composites in suspension systems. In: 10th international Munich chassis symposium 2019, pp 249–261
6. Khatkar V, Behera BK, Manjunath RN (2020) Textile structural composites for automotive leaf spring application. Compos B Eng 182:107662
7. Shankar GSS, Vijayarangan S (2006) Mono composite leaf spring for light weight vehicle—design, end joint analysis and testing. Mater Sci 12(3):220–225
8. Kumar YS, Teja MV (2012) Design and analysis of composite leaf spring. Int J Mech Ind Eng IJMIE: 2231–6477
9. Rajesh S, Bhaskar GB, Venkatachalam J, Pazhanivel K, Sagadevan S (2016) Performance of leaf springs made of composite material subjected to low frequency impact loading. J Mech Sci Technol 30(9):4291–4298
10. Bhanage A, Padmanabhan K (2014) Design for fatigue and simulation of glass fibre/epoxy Composite automobile leaf spring. ARPN J Eng Appl Sci 9(3):196–203
11. Pozhilarasu V, Pillai TP (2013) Performance analysis of steel leaf spring with composite leaf spring and fabrication of composite leaf spring. Int J Eng Res Sci Technol 2(3):102–109
12. Melvin Savio S, Somasundaram D, Vijaya Rajan V (2015) Performance analysis of composite leaf spring using computer aided engineering. Appl Mech Mater 787:602–606
13. Mehul S, Shah DB, Bhojawala V (2012) Analysis of composite leaf spring using FEA for light vehicle mini truck. J Inf Knowl Res Mech Eng 2(2):424–428
14. Raghavedra M, Hussain SA, Pandurangadu V, PalaniKumar K (2012) Modeling and analy sis of laminated composite leaf spring under the static load condition by using FEA. Int J Mod Eng Res IJMER 2(4):1875–1879
15. Suhas JD, Hanumanthraya R, Vaishak NL, Mahesh BD (2014) Investigation on different compositions of E-glass/epoxy composite and its application in leaf spring. IOSR J Mech Civil Eng 1:74–80
16. Ravindra P, Raman M, Sanjay B (2014) Modeling and analysis of carbon fiber epoxy based leaf spring under the static load condition by using FEA. Int J Emerg Sci Eng Sci Eng IJESE: 2319–6378
17. Wambua P, Ivens J, Verpoest I (2003) Natural fibres: can they replace glass in fibre reinforced plastics? Compos Sci Technol 63(9):1259–1264
18. Vinay KM, Manujesh BJ (2014) Design and fabrication of hybrid composite springs. Int J Mech Eng Technol IJMET 5(9): 133–140
19. Ravikumar V, Narayana RL, Srinivas C (2013) Analysis of natural fiber composite leaf spring. Int J Latest Trends Eng Technol: 182–191
20. Sureshkumar M, Tamilselvam P, Kumaravelan R, Dharmalingam R (2014) Design, fabrication, and analysis of a hybrid FIBER composite monoleaf spring using carbon and E-glass fibers for automotive suspension applications. Mech Compos Mater 50(1):115–122
21. Keshavamurthy YC, Chetan HS, Dhanush C, Nithish Prabhu T (2013) Design and finite element analysis of hybrid composites mono leaf Spring. Int J Mech Prod Eng Res Dev: 2249–6890
22. Singh H, Brar GS (2018) Characterization and investigation of mechanical properties of composite materials used for leaf spring. Mater Today Proc 5(2):5857–5863
23. Suprith N, Annamalai K, Naiju CD, Mahadevan A (2013) Design and analysis of automo tive multi-leaf springs using composite materials. Appl Mech Mater 372:533–537
24. Jancirani J, Assarudeen H (2015) A review on structural analysis and experimental investigation of fiber reinforced composite leaf spring. J Reinf Plast Compos 34(2):95–100

Effect of Carbon Fiber-Reinforced Polymer Strips on Square Steel Tubular Sections Under Compression



S. Sivasankar, N. K. Amudhavalli, A. Praveen Kumar, and M. Shunmugasundaram

Abstract Strengthening of steel structural members with advanced lightweight composite materials is increased recent times since they have very high tensile strength and stiffness, high resistance against corrosion and earthquake. This research aims to predict the optimum width and influence of carbon fiber-reinforced polymer (CFRP) plies on hollow square steel (HSS) sections under compression. Totally, fourteen steel samples are used with length 600 mm and the width of CFRP sheets are 30 and 50 mm. Spacing between adjacent layer is kept constant as 40 mm for the two groups. All test samples were loaded till their failure, and the corresponding reading has been taken to identify the fracture criteria, stress–strain forms, and load improvement than the unwrapped sample. Test results showed that the HSS samples wrapped by CFRP strips produced the high load increment and deformation control compared to unwrapped samples. Among the two groups, sample reinforced with 50 mm ties of three plies displayed high load and deformation control.

Keywords CFRP strips · Compression · Buckling · Stiffness · Tubular section · Strengthening

1 Introduction

Advanced composites like fiber-reinforced polymer (FRP) tools are widely accepted for strengthening and restoration of concrete and steel structures in recent times. Since they had very good bonding property with concrete and steel, they act as

S. Sivasankar (✉)
Department of Civil Engineering, CMR Technical Campus, Hyderabad, Telangana 501401, India
e-mail: drssphd@gmail.com

N. K. Amudhavalli
Department of Civil Engineering, CMR College of Engineering & Technology, Hyderabad 501401, India

A. Praveen Kumar · M. Shunmugasundaram
Department of Mechanical Engineering, CMR Technical Campus, Hyderabad, Telangana 501401, India

© Springer Nature Singapore Pte Ltd. 2020

A. Praveen Kumar et al. (eds.), *Advances in Lightweight Materials and Structures*,
Springer Proceedings in Materials 8, https://doi.org/10.1007/978-981-15-7827-4_13

single unit. Though they provide better resistance in severe environmental conditions like corrosion and chemical action, several research works were carried out on concrete structures in the past decades both in strengthening and repair works. FRP jackets are effectively resisting the concentric and eccentric loading in concrete column [1, 2]. Slender reinforced concrete (RC) columns strengthened by CFRP sheets and performed significantly [3]. For various loading and impact resistance [4, 5], corrosion resistance [6, 7], seismic strengthening and repair of RC columns [8], shear and flexural resistance [9, 10] CFRP composites are performed significantly better for enhancing the load carrying and brought to service condition. These significant properties make these materials suitable to steel structural applications.

Various artificially degraded steel beams are repaired with carbon/glass composite system. The beams using the high modulus CFRP reached even higher ultimate loads and exhibited ductile response leading to very high deflections [11]. Circular steel tubular columns are braced by high modulus CFRP [12]. The parameters are bond length and number of layers. Test results showed that the CFRP fabrics are performed better in ultimate load through proper bonding. At the end, a numerical model was developed to compare the test results. A numerical derivation for plastic collapse load was achieved, and the predicted post-buckling was matched with the test results [13]. FRP materials for underwater applications were studied through an experimental work [14]. From the test results, it was observed that the CFRP fabrics are more preferable for submerged condition and normal environmental conditions. Design guidelines to steel columns with CFRP sheets provided the effective use of composite materials in external reinforcing and restoration [15]. Square steel sections reinforced with CFRP fabrics of width 30 mm, entire length, and varying spacing. Results obtained through experiment suggested the optimum usage of CFRP for HSS sections [16, 17]. This paper aims to predict the optimum width of carbon sheets for HSS sections.

2 Experimentation

2.1 Selection of Resources

2.1.1 Square Tubes (Steel)

Samples (steel) confirming IS (1161-19980 having dimensions (91.5 × 91.5) mm were used for research work. Thickness of the tube is 3.60 mm, and the yield strength is 480 Mpa.

Table 1 CFRP characteristics

Young's modulus	240×10^3 Mpa
Flexible strength	3800 Mpa
Total mass	230 g/m^2
Density	1.7 g/cm^2
Thickness	0.234 mm

Table 2 MBrace saturant characteristics

Proportion	100 (base):40 (hardener)
Density (kg/liter)	1.13 ± 0.03
Viscosity	4000 ± 500
Drying period	<3 h at 25 °C

2.1.2 Fabric

Unidirectional and low modulus carbon fiber sheets were used in this study. The characteristics of carbon fabric are summarized in Table1.

2.1.3 Resin

The MBrace saturant resin was selected for this research. Properties of epoxy are summarized in Table 2.

2.2 Specimen Preparation and Loading

Based on size requirement, CFRP strips were cut from the long rolled sheets. Before wrapping, the entire steel samples' surfaces were roughed by sand blasting and cleaned by acetone to remove the impurities. Figure 1 represented the image of specimens after sand blasting. Totally, fourteen samples were used in this study and each sample named is given in Table 3. Resin matrixes were prepared based on mix ratio prescribed by the manufacturer and applied on steel surface before laid the first layer. To reduce the risk of air foams, ribbed roller is moving along the CFRP orientation. Same procedure was repeated till the required numbers of layers were laid. Wrapping scheme (30 and 50 mm strips) is clearly mentioned in Fig. 2. CFRP strips were wrapped on steel tubes at the site as represented in Fig. 3. After the curing process, the samples are ready for compression test, and the instrumentation and the assembling are represented in Fig. 4.

Fig.1 Sand blasted samples

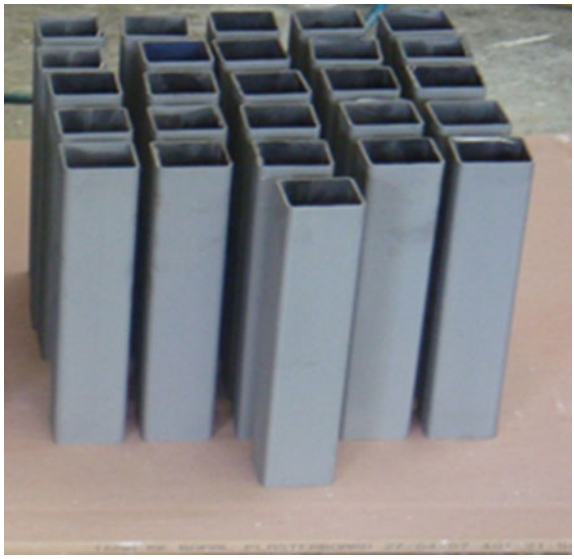


Table 3 Experimental results of tested samples

S. No.	Specimen	Failure at peak (kN)	Percentage	Deflection at failure in mm
1	CC2	565	–	8.89
2	HS-30-(T1)	589	4.24	8.12
3	HS-30-(T1)	585	3.539	8.15
4	HS-30-(T2)	609	7.787	8.04
5	HS-30-(T2)	610	7.964	7.98
6	HS-30-(T3)	627	10.973	7.75
7	HS-30-(T3)	625	10.619	7.79
8	HS-50-(T1)	676	19.646	7.56
9	HS-50-(T1)	677	19.823	7.50
10	HS-50-(T2)	685	21.23	7.39
11	HS-50-(T2)	689	21.946	7.38
12	HS-50-(T3)	705	24.778	7.28
13	HS-50-(T3)	703	24.424	7.31

3 Results and Summary

3.1 Failure Criteria

Failure criteria for control specimen CC2 are represented in Fig. 4, and the failure is pure buckling which occurred at the end portion of the samples. Figures 5, 6, and

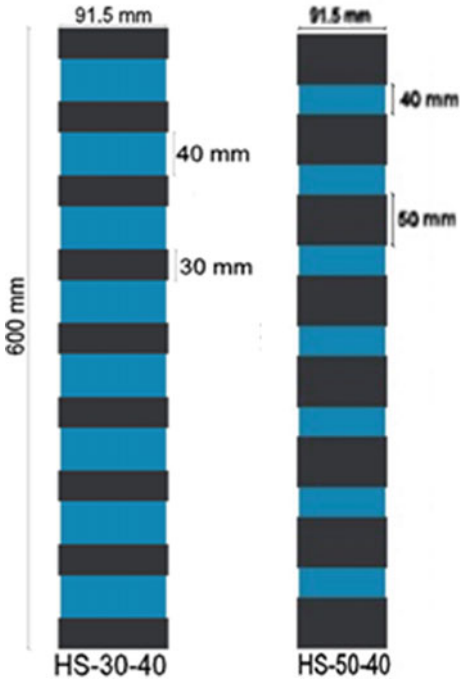


Fig. 2 Wrapping schemes—30 and 50 mm



Fig. 3 Samples after wrapping



Fig. 4 CC2-failure image



Fig. 5 HS-30-(T1)—failure image

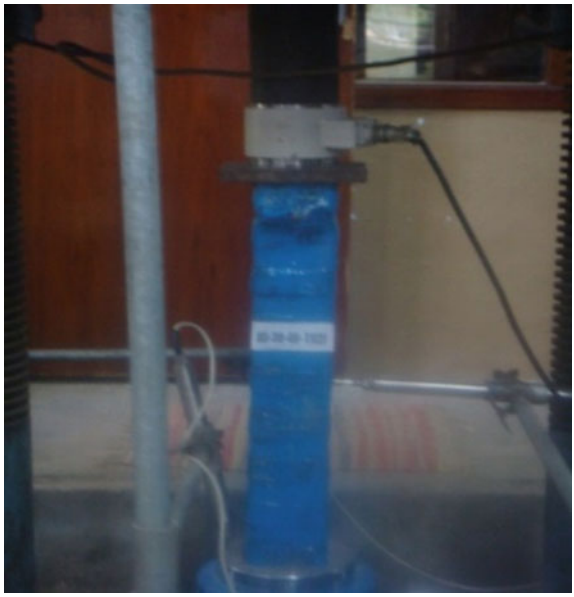


Fig. 6 HS-30-(T2)—failure image

7 represented the failure image of samples reinforced with 30 mm plies having one, two, and three layers of CFRP. Failure load of samples wrapped by 30 mm plies exhibited high load when compared to unwrapped control CC2 specimen. Sample enclosed by three coats exhibited high load compared to specimens with one and two coats, respectively. The same manner 50 mm wrapped samples displayed higher load



Fig. 7 HS-30-(T3)—failure image



Fig. 8 HS-50-(T1)—failure image

at failure associated with unwrapped sample. Current set, 50 mm wrapped samples with three coatings, exhibited high load compared to all columns. Reason for load increment was due to the width and better confinement produced by the CFRP strips (Figs. 8, 9 and 10).

3.2 Stress–strain Characteristics

Stress–strain characteristics of samples reinforced with 30 and 50 mm CFRP plies were presented in Figs. 11 and 12. Samples HS-30-(T1), HS-30-(T2), and HS-30-(T3) improved their vertical displacement resistance through 8.66%, 10.24%, and 12.82%, respectively, associated with control. Vertical displacement of the corresponding samples are 8.12, 7.98, and 7.75 mm. Axial stress–strain characteristics of samples HS-50-(T1), HS-50-(T2), and HS-50-(T3) compared to CC2 are presented graphically in Fig. 12. Percentage deformation control of corresponding samples is 15.64%, 16.98%, and 18.11%, respectively, more than the control sample CC2. Vertical displacement for sample HS-50-(T3) at peak load was found to be 7.22 mm.



Fig. 9 HS-50-(T2)—failure image

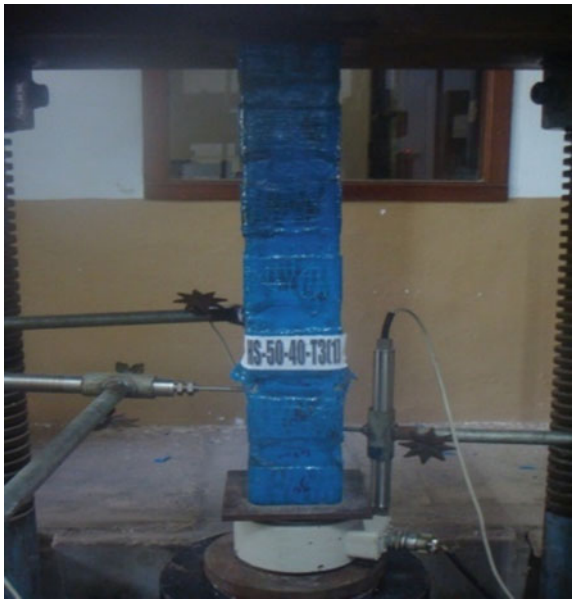


Fig. 10 HS-50-(T3)—failure image

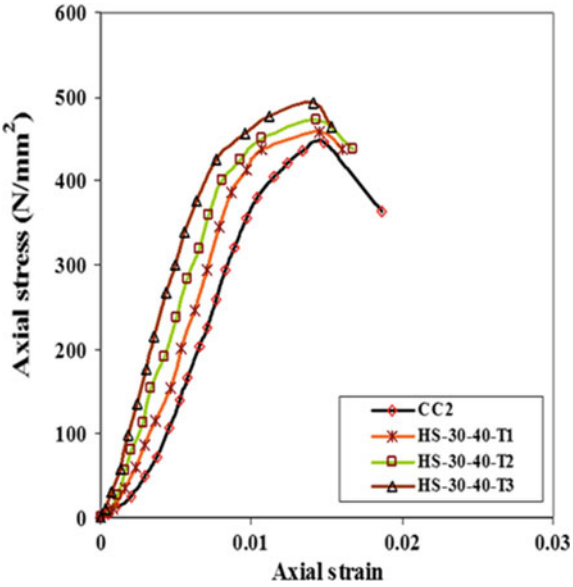


Fig. 11 Axial stress–strain—(30 mm)

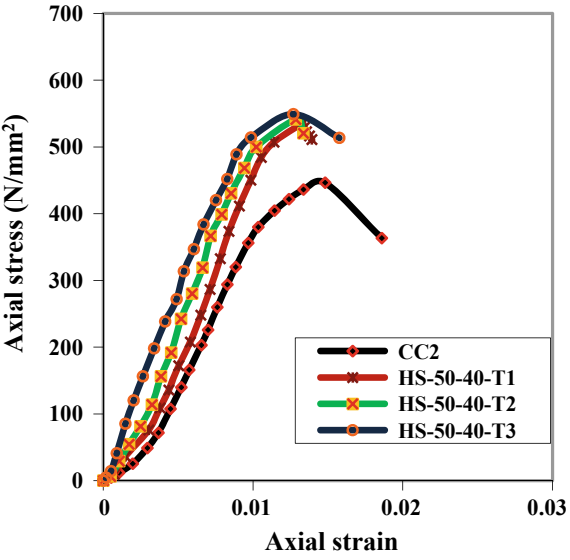


Fig. 12 Axial stress–strain— (50 mm)

3.3 Load Increment

Load increment of unwrapped sample and the samples wrapped by two sets of fiber fabrics (30 and 50 mm) was presented in Table 1 and Fig. 13. Percentage load increment of all samples wrapped with CFRP is provided in Table 3. Load increment

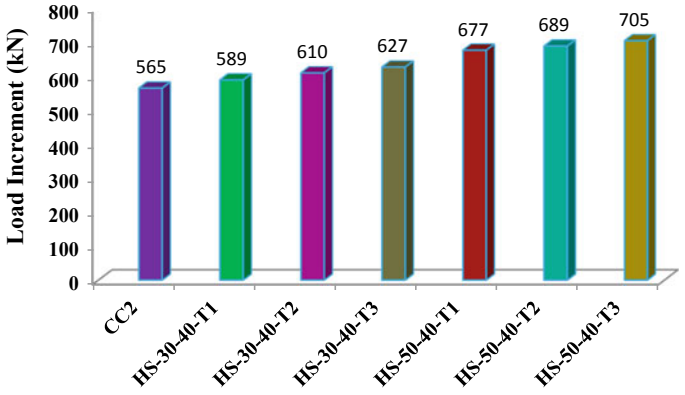


Fig. 13 Load increment

percentage of samples enfolded by thirty millimeter fabric related to unwrapped samples is 4.24%, 7.964%, and 10.973% for 1, 2, and 3 coatings, respectively. This category, three layers wrapped sample, performed better than the other samples. In the second group, the load increment percentage of 50 mm wrapped samples is 19.823, 21.946, and 24.778% high than the unwrapped sample. Similar to first group, samples wrapped by three layers displayed high percentage load increment. Overall the sample wrapped with fifty millimeters fabric with three layers HS-50-(T3) exhibited high percentage increment.

4 Conclusions

From the compression test performed on HSS tubular samples enforced with thirty millimeter and fifty millimeter plies and bare samples, the following conclusions were arrived. Failure criteria for the samples both wrapped by CFRP strips and unwrapped samples displayed local buckling. In both groups, CFRP wrapped samples showed higher compressive strength than unwrapped samples. vertical displacement decreased considerably while adding three layers. Compared to thirty millimeter (30 mm) plies, samples with fifty millimeter plies performed significantly better. Among the two groups, the sample confined by fifty millimeter plies with three CFRP fabrics performed considerably well. Load increment percentage of samples with thirty millimeter plies related to unwrapped samples are 4.24, 7.964, and 10.973% for 1, 2, and 3 layers correspondingly. Load increment percentages of 50 mm wrapped samples are 19.823, 21.946, and 24.778% high than the unwrapped sample.

References

1. Parvin A, Wang W (2001) Behavior of FRP jacketed concrete columns under eccentric loading. J Compos Constr 5:146–152
2. Song X, Gu X, Li Y, Chen T, Zhang W (2013) Mechanical behavior of FRP-strengthened concrete columns subjected to concentric and eccentric compression loading. J Compos Constr 17:336–346
3. Gajdosova K, Bilcik J (2013) Full-scale testing of CFRP-strengthened slender reinforced concrete columns. J Compos Constr 17:239–248
4. Praveen Kumar A, Ponraj Sankar L, Maneiah D, Raju B (2019) Crashworthiness characteristics of multi-cell tubular structures subjected to axial impact. Int J Recent Technol Eng 8(4):3911–3914
5. Praveen Kumar A, Ponraj Sankar L, Maneiah D, Upendra G (2019) Lateral crushing and energy absorption behavior of multicellular tube structures. Int J Innov Technol Explor Eng 9(1):2684–2687
6. Suh K, Mullins G, Sen R, Winters D (2010) Effective repair for corrosion control using FRP wraps. J Compos Constr 14:388–396
7. Gadve S, Mukherjee A, Malhotra SN (2011) Active protection of fiber-reinforced polymer-wrapped reinforced concrete structures against corrosion. Corrosion 67:1–11
8. ElSouri A, Harajli M (2011) Seismic repair and strengthening of lap splices in rc columns: carbon fiber-reinforced polymer versus steel confinement. J Compos Constr 15:721–731
9. Maalej M, Leongi KS (2005) Effect of beam size and FRP thickness on interfacial shear stress concentration and failure mode of FRP-strengthened beams. Compos Sci Technol 65(7–8):1148–1158
10. Sivasankar S, Praveen Kumar A (2019) Numerical modeling of square steel members wrapped by CFRP composites. Int J Innov Technol Explor Eng 8(10):3082–3087
11. Photiou NK, Hollaway LC, Chryssanthopoulos MK (2006) Strengthening of an artificially degraded steel beam utilising a carbon/glass composite system. Constr Build Mater 20:11–21
12. Fawzia S, Al-Mahaidi R, Zhao XL, Rizkalla S (2007) Strengthening of circular hollow steel tubular sections using high modulus CFRP sheets. Constr Build Mater 21:839–845
13. Praveen Kumar A, Sivasankar S (2019) Importance of anisotropic coefficients for material constitutive models in forming and crushing simulations. Int J Mech Prod Eng Res Dev 9(6):765–778
14. Seica MV, Packer JA (2007) FRP materials for the rehabilitation of tubular steel structures, for underwater applications. Compos Struct 80:440–450
15. Haedir J, Zhao X-L (2011) Design of short CFRP-reinforced steel tubular columns. J Constr Steel Res 67:497–509
16. Sundarraja MC, Sivasankar S (2012) Axial behaviour of HSS tubular sections strengthened by CFRP strips: an experimental investigation. Sci Eng Compos Mater 19:159–168
17. Sivasankar S, Vijaya Bhaskar Reddy S (2019) Axial behaviour of square HSS tubular members strengthening with CFRP sheets. Int J Eng Adv Technol 8(5):914–919

Design and Analysis of Cap Forward Armrest Component

Kishore Kumar Kandi, Nagaveni Thallapalli, Mayank Sunder, and Rahul Vuda

Abstract The aim of this paper is to design a mould cavity for a plastic component known as cap forward armrest component. Analysis was carried out in Moldex3D in which flow, pack, cooling and warp simulation are done for given component material and design parameters of process. Feed system designed is a submarine gate with geometrically balanced runners having diameter 6 mm to fill total injected plastic weight of 13.2 g. Fill time from fill and pack analysis is 0.473 s with no short shot (incomplete filling) and no weld lines created during moulding. With gate freezing completely, packing time calculated for the process is 5.5 s. Fill time in transient analysis is increased to 0.496 s. Form analysis injection pressure determined was 33 MPa, and the filling sprue pressure was found to be 27.71 MPa. The results obtained were satisfactory in producing good quality product within less time and with low cost.

Keywords Moldex3D · Filling and packing analysis · Transient analysis · Warpage · Filling time · Packing time

1 Introduction

Mould design is governed by the product design, and the design of mould should also accommodate any complex features on the part, such as undercuts or threads which require additional mechanisms devices to actuate and deliver [1, 2]. Most of these devices slide in and out of the cavity area during the cycle therefore known as slide core or lifters that also help in ejection of product. Thread feature of the mould design requires different types of devices to deliver the result.

Wong et al. [3] discussed the design of plastic injection mould for producing a plastic product in two different ways within the same mould. Pro/Engineer software

K. K. Kandi (✉) · R. Vuda
CVR College of Engineering, Hyderabad 501510, India
e-mail: kishorekumar01@gmail.com

N. Thallapalli · M. Sunder
Osmania University College of Engineering, Hyderabad 500007, India

© Springer Nature Singapore Pte Ltd. 2020

A. Praveen Kumar et al. (eds.), *Advances in Lightweight Materials and Structures*,
Springer Proceedings in Materials 8, https://doi.org/10.1007/978-981-15-7827-4_14

was used to develop the model of plastic part and pro-manufacturing to develop the machining programme. The plastic part was first simulated and analysed by using Moldflow part advisor software. Simulation was done for predicting visual defects, correct injection locations, material temperature, packing pressures and air traps. Hieber et al. [4] generalized Hele–Shaw flow model for an inelastic, non-Newtonian fluid under non-isothermal condition. The calculation algorithm uses finite element method for pressure and finite difference method for temperature. CAE software for plastic injection moulding is based upon Hele–Shaw flow model as conventional algorithm extracts mid-part to represent the 3D geometry. Li et al. [5] reports a configuration space (C-space) method to address this important issue of layout design of cooling system. Major problem in layout design phase is the interfering of mould component with the cooling channels. C-space method is generated using algorithm and considers feasibility greater than heuristic method. Further case study is done, and the proposed method was able to generate satisfactory layout. Jaruga et al. [6] studied the morphology and spherulite size of parts moulded in different cavities of injection mould with geometrically balanced runner system. The part material was polypropylene. The method of short shots was used so that the imbalance in filling of cavities can be examined. The method of optical microscopy was used. The samples were prepared from microtome slices from parts, and next, they were observed in polarized light. The skin-core morphology was analysed, and spherulitic structure was described by spherulites size measuring. The differences in morphology and spherulite size for parts from mould cavities were found. They are caused by different thermal conditions in each cavity. Chien et al. [7] discussed a new methodology to analyse the flow imbalance for runner system cavities when the runner is geometrically balanced. To demonstrate the results, both the original and modified, i.e. turn over runner designs, are experimentally compared. Firstly, hybrid mesh with mixed element is designed over the new geometry, and then, FVM technique of flow analyses of Moldex3D is used; the result shows how the melt properties of the shear rate, temperature and the viscosity produce the imbalance in the system.

Feed system design has major influence over the product quality. Unbalance filling of cavities occurs even though the runners are geometrically balanced, reason being thermal condition of the process. CAE software for mould flow analysis used Hele–Shaw flow model usually referred to as 2.5D analysis; now, it has advanced to a complete 3D simulation model. Warpage defect that occurs in plastic injection moulding is majorly affected by the design feature of the product, differential cooling effect of the process and volumetric shrinkage of cavities. The main objective of the work is mould cavity design and analysis for cap forward armrest component to a lower manufacturing cost while maintaining the component quality and dimension standards.

2 Problem Definition

Cap forward armrest shown in Fig. 1 is an automotive component used in front seats of the vehicles. For designing mould tool, a detail study of component is to be done to understand the functional requirement of component and matching surfaces. Dimensions are to be carefully studied to understand critical areas so that no problem occur during assembling. Material properties and specification of the cap forward armrest are given in Table 1. Polypropylene block copolymer grade has high fluidity, and it has medium impact and medium stiffness. It is suitable for automotive applications with intricate designs for thin-wall interior parts.

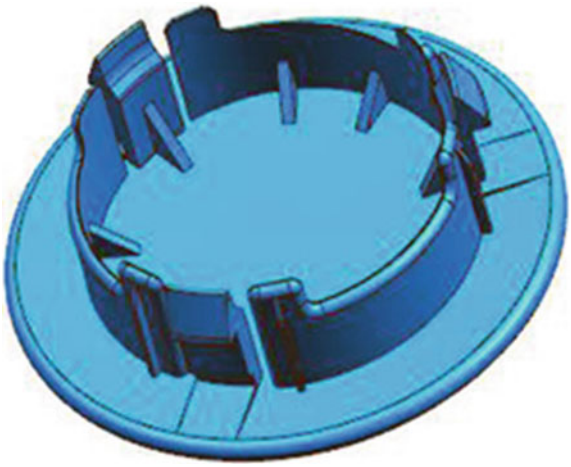


Fig. 1. 3D model of cap forward armrest

Table 1 Specifications and material properties of cap forward armrest

Component name	Cap forward armrest
Material	Polypropylene PP
Product size	45X45X16 mm
Weight	5.5 g
Tensile strength	21 MPa
Charpy impact strength (23 °C)	8 kJ/m^2
Mould shrinkage average	1.55%
Melt temperature	210–280 °C

3 Design Methodology

3.1 Preliminary Design Using Siemens NX

Preliminary design deals with the core and cavity extraction along with the layout of the cavity impression with feed system. NX, formerly known as "UG", is an advanced high-end CAD/CAM/CAE software [8]. Complete 3D designing of the mould tool was done in NX. 2D drawing was also generated through NX drafting module.

Design Concept. Component material shrinkage equal to 1.55% of 3D data was added for the shrinkage compensation. Slope analysis was used to determine the exact parting line over which cavity extraction occurred; for that, target faces of the component were selected with vector in direction as normal to grain area as shown in 2D drawing of component. Data range of −0.1 to +0.1 with three colour division was set.

Figure 2 shows the parting line over which moving and fixed half of the core will be formed. The green colour surfaces of the component represent zero slope and red colour stepped surfaces indicate the undercut. These undercuts require a side core or sliders for moulding without getting the component fouling during ejection. In total, three sliders are required per component.

Cavity Layout and Feed System. For two-impression cavity layout, the distance between the components considering cold runner feed system was 60 mm and sprue bush outer diameter was 14 mm.

$$\text{Runner diameter } (D) = \frac{\left(\sqrt{W} \times \sqrt[4]{L}\right)}{3.7} = \frac{\left(\sqrt{11} \times \sqrt[4]{60}\right)}{3.7} = 2.5\text{mm}$$

where W = Weight of the two components, L = Length of the runner.

Considering the narrow size of submarine gate, shrinkage and packing required to compensate, the runner diameter of 6 mm is considered. Sprue bush should have a

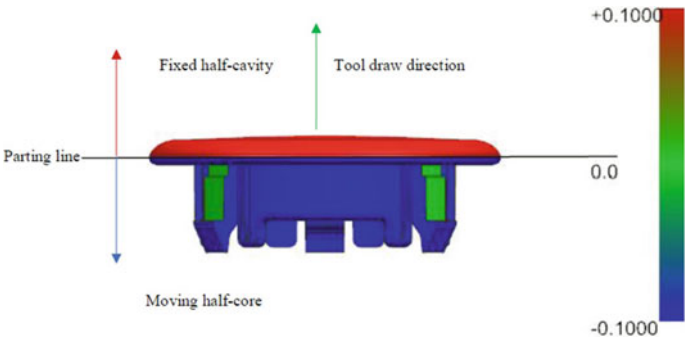


Fig. 2 Design concept

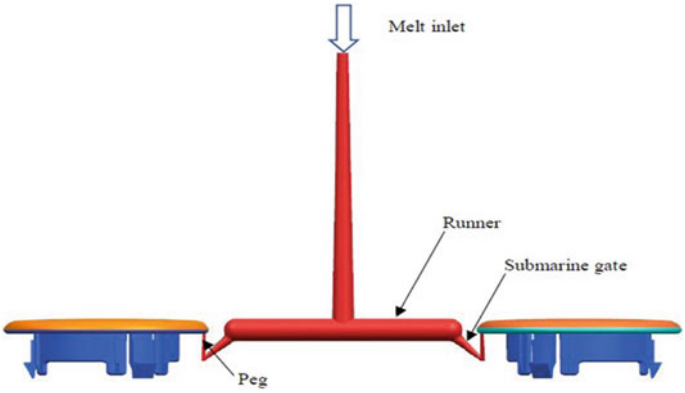


Fig. 3 Feed system

draft angle of 1 and 4 ° between the end opening diameters with maximum diameter at runner end and minimum diameter at machine nozzle orifice for pressure reduction and easy flow of material. Sprue diameter should be 0.5–1 mm larger than nozzle diameter. To feed into the inside surface of, a component a sub-surface gate also known as submarine gate was required. A submarine gate is used in two plate moulds, in which a tapered tunnel from end of runner feeds under the base of the component wall into one side of peg which is below the parting line as shown in Fig. 3.

3.2 Filling and Packing Analysis Using Moldex3D

Pre-processing in Moldex3D Designer. Moldex3D is a CAE tool which provides complete capability of pre-processing, analysis and post-processing [9, 10]. Imported the model file of part and runner geometry in dot step format and assigned injection moulding attributes of the imported geometry as cavity and cold runner. Data transfer from software to software and change in file type extension leads to loss in geometry surface feature. In next step solid mesh was generated using Boundary Layer Mesh (BML). BML is a mesh technology for CAE application of plastic injection technology. Elements in mesh are prism and tetrahedron elements with mesh size of 0.5 mm. Density of node over complex surface of cavity is high to achieve closeness to true shape by mesh. In the last step, the parting direction was set as $+Z$ and then exporting mesh file. Total element count of the complete model was 1,630,766.

Processing in Moldex3D Analysis. Process data for filling and packing analysis is given in Table 2. Packing pressure starts after 98% filling of cavities volume which is completed. 98% filling means injection machine changes from velocity control to pressure control. It is specified in terms of material's maximum injection pressure which is 140 MPa. The last 2% of the material volume is injected in high pressure

Table 2 Process data

Part weight of cavity #1	5.5 g
Part weight of cavity #2	5.5 g
Weight of cold runner #3	2.2 g
Total weight	13.2
Tensile strength	21 MPa
Mould temperature	30–55 ˚C
Packing time	4.73 s
VP Switch-over	98%
Injection pressure	33 MPa

to compensate for shrinkage and to prevent backflow of melt. Packing time covers till the gate freeze after which material does not flow any further.

4 Results and Discussions

4.1 Melt Front Time

Melt front advancement indicates the movement of melt material boundary at different time durations during filling process. Figure 4 shows melt front position in filling and packing analysis.

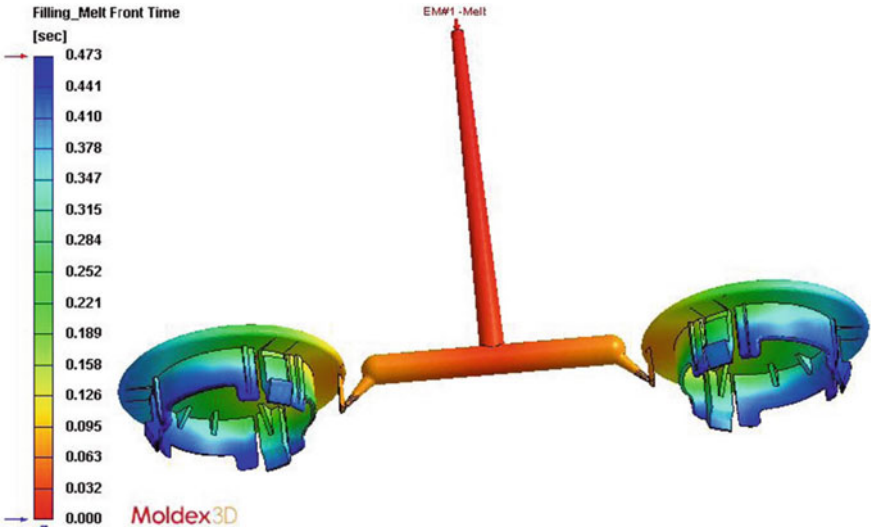


Fig. 4 Melt front position in filling and packing analysis

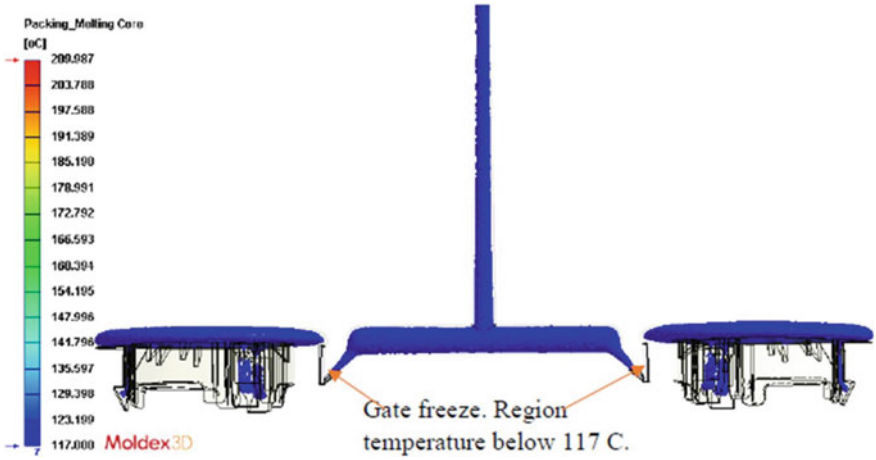


Fig. 5 Melting core gate freeze

For the given pressure and flow rate profile, the filling time is 0.473 s in filling and packing analysis and 0.496 s in transient analysis. From melt front advancement, there is no incomplete filling problem (no short shot). Gate flow is balanced as both impressions fill simultaneously, thus creating even filling and balance force over the mould. Filling pattern of moulding identifies no weld line as no melt flow front meet during advancement.

4.2 Packing Melting Core

Freeze temperature of plastic melt is 117 °C; below this, temperature plastic flow even under intense packing pressure is very low. Packing done for compensating shrinkage does not extend beyond freeze time. Figure 5 demonstrates the iso-surface of the freeze temperature of plastic melt at the current instant. Gate freeze is necessary to stop the backflow of material under back pressure. Sink mark indicator and displacement will not be accurate if gate does not freeze in CAE simulation.

4.3 Filling Pressure and Temperature

The initial pressure at the point of filling is 1 atm and as the flow front progresses through the flow length due to the configuration the flow path, pressure tends to increase. High pressure area is possible at the location where flash occur. The average pressure of runners and cavity is 5.8 MPa. Pressure drop over feed system can lead to backflow. Runner has higher pressure than cavities. Runner's major volume pressure

is at 11–14 MPa, whereas the highest of cavity pressure is at 6.6 MPa. Maximum pressure in the system is 19.3 MPa. Frictional flow of the plastic melt increases the temperature of plastic melt as it progresses through the flow length at high pressure. Result show that 73% of total injected plastic volume is in temperature range of 210–244 °C at end of filling, when inlet melt temperature setting is at 210 °C.

5 Conclusions

A two-impression cavity mould was designed with cold runner feed system with shot weight of 13.2 g per cycle and filling time of 0.496 s. The feed system designed is geometrically balanced with 50% gate contribution to each cavity impression. Packing time is 5.5 s from filling and packing analysis where gate freezes completely at 5.9 s. Packing time increases the density of the product and produces a defect-free product. Filling time has been increased from 0.473 to 0.496 s in transient analysis due to flow rate profiling, pressure profiling and addition of cooling in analysis. Filling temperature was in the range of 210–244 °C for 73% of the total injected plastic volume. Increase in temperature is due to the frictional flow of plastic and filling sprue pressure was found to be 27.71 MPa.

Warpage can be lowered by modifying part design, by adding talc to plastic material and using beryllium copper insert at cavity side to have higher heat conductivity. Cycle time can be reduced by with different coolants. Conformal cooling can be added to sub-insert to reduce differential cooling. Hot runner be used in place of cold runner to reduce wastage. Kinematic motion simulation can be performed to check full range of motion.

References

1. Mok CK, Chin KS, John K (2001) L H: An interactive knowledge-based CAD system for mould design in injection moulding processes. Int J Adv Manuf Technol 17:27–38
2. Lee RS, Chen YM, Lee CZ (1997) Development of a concurrent mold design system: a knowledge-based approach. Comput Integr Manuf Syst 10(4):287–307
3. Wong CT, Sulaiman S, Ismail N, Hamouda AMS (2004) Design and Simulation of Plastic Injection Moulding Process, Universiti Putra Malaysia. Pertanika J Sci Techno Suppl 12(2):85–99
4. Hieber CA, Shen SF (1980) A finite-element/finite-difference simulation of the injection-molding filling process. J Nonnewton Fluid Mech 7(1):1–32
5. Li CG, Li CL (2008) Plastic injection mould cooling system design by the configuration space method. Comput Aided Des 40(3):334–349
6. Jaruga T, Bociga E (2007) Structure of polypropylene parts from multicavity injection mould. Arch Mater Sci Eng 28(7):429–432
7. Chien CC, Chiang CC, Yang WH, Tsai V, Hsu DC True 3D CAE visualization of filling imbalance in geometry-balanced runners. CoreTech Systems Co., Ltd., HsinChu, Taiwan, ROC
8. Fadzly MK, Natasha A, Nordin F (2019) Experimental investigation of plastic part defect from plastic injection molding machine. AIP Conf Proc 2129:020149

9. Su TM, Liu YC, Huang CT, Hsu D (2012) Product Design optimization through seamless integration of CAD and CAE. Comput-Aided Des Appl 9(4):471–479
10. Zhou H, Shi S, Ma B (2009) A virtual injection molding system based on numerical simulation. Int J Adv Manuf Tech 40: 297–306

Design Optimization of Knuckle Stub Using Response Surface Optimization



A. Agarwal, O. B. Molwane, and R. Marumo

Abstract The knuckle stub is one of the vital components of steering assembly of ATV. The current research investigates the strength and safety factor of knuckle stub subjected to structural loads using techniques of finite element method. The CAD model is developed in ANSYS design modeler and analyzed in workbench. The design is then optimized using Taguchi response surface method using optimal space filling algorithm. The RSM optimization generated specific set values for optimization variables (major length and taper length) along with sensitivity plot and goodness of fit curve. The response surface plot for equivalent stress shows that maximum equivalent stress is observed for Mlength value ranging from 23 to 23.375 mm and Tlength value ranging from 28 to 31 mm. The optimized design of stub resulted in 2.72% mass reduction and 7.65% deformation reduction, while stress reduction of 13.54% is observed of stub.

Keywords FEA · Response surface · Stub · Structural analysis · Stress

1 Introduction

A major complication in the automobile industries is the existence of instability in the substantial properties and manufacturing processes. \query{Please check whether the sentence 'Knuckle joints are basically two or more rods superintend to tensile...' conveys the intended meaning.}Knuckle joints are basically two or more rods superintend to tensile and compressive forces are fastened together which allows a small angular moment of one to another. They are indeed rod couplings which are used to connect the members in trusses and other structures and cannot be used as a power transmitting component. Knuckle goes by different names steering knuckle,

A. Agarwal (✉) · R. Marumo
Department of Mechanical Engineering, FET, University of Botswana, Gaborone, Botswana
e-mail: agarwala@ub.ac.bw

O. B. Molwane
Department of Industrial Design and Technology, FET, University of Botswana, Gaborone, Botswana

© Springer Nature Singapore Pte Ltd. 2020

A. Praveen Kumar et al. (eds.), *Advances in Lightweight Materials and Structures*,
Springer Proceedings in Materials 8, https://doi.org/10.1007/978-981-15-7827-4_15

wheel carrier and upright. It is called the nexus of a vehicles front axle. They are designed mainly in two types: one with the hub and the other comes with the spindle; both have equal advantages and disadvantages factors. Knuckle has become one of the most important components in every mechanism starting from automobiles to human anatomy, in other words, biomechanics. Knuckle can be easily connected and disconnected. For an ATV, the steering system encompasses knuckle, stub and kingpin [1]. The knuckle converts linear motion of tie rod into rotational motion of stub. The knuckle design is determined by brake, vehicle type, steering subassembly [2]. The design of knuckle joint depends upon type of vehicle, type of suspension used. For an all-terrain vehicle (ATV), steering is connected to knuckle joint. The optimized design of stub used in knuckle joint enables to improve strength and reduces mass of knuckle joint. This optimization of could be achieved using advanced tools like response surface method. The competition in automobile industry demands for lighter and economical materials in manufacturing of components. The feasible methods included application of MMC composites in manufacturing of knuckle [4, 6]. Topological optimization of knuckle can be improved using integrated design and manufacturing approach with virtual manufacturing (VM) techniques [5]. The Taguchi design of experiments (DOE) is employed in optimizing billet dimensions of knuckle joint [7].

Service life of knuckle joint can be determined numerically using fatigue analysis. The ferrous material cast iron and ductile material forged steel and aluminum alloy were investigated. The results have shown that forged steel has better life as compared to other two materials [8, 11].

Anil et al. [9] have conducted shape optimization of knuckle using ANSYS FEA package and obtained 67% weight reduction with factor of safety ranging between 3 and 4.

One of the important parts of knuckle joint assembly is its stub located centrally and its design holds structural significance [5]. The current research investigates the strength of stub used for BAJA ATV vehicle using ANSYS FEA software. The design of stub is further optimized for mass minimization using response surface optimization technique.

2 Analysis and Strength of Stub Used for BAJA ATV

The static structural analysis is performed using ANSYS 18.1 software which is based on techniques of finite element analysis (FEA) [6]. The analysis comprises three stages, namely preprocessing, solution and post-processing [7]. The schematic of knuckle stub is shown in Fig. 1. Accordingly, the CAD model of stub is developed. The CAD model is meshed and applied with appropriate loads and boundary conditions.

The stub is meshed using tetrahedral elements as shown in Fig. 2. The tetrahedral element shape consists of four nodes and follows linear interpolation function [8] as shown in Fig. 3.

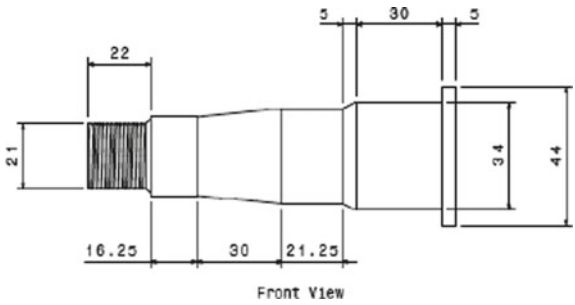


Fig. 1 Front view and side view of stub [3]

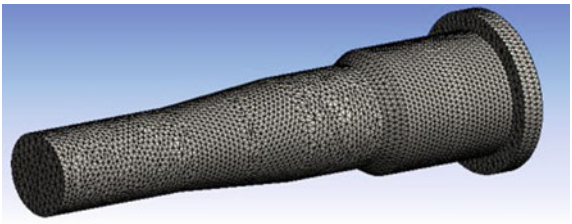


Fig. 2 Meshed model of stub

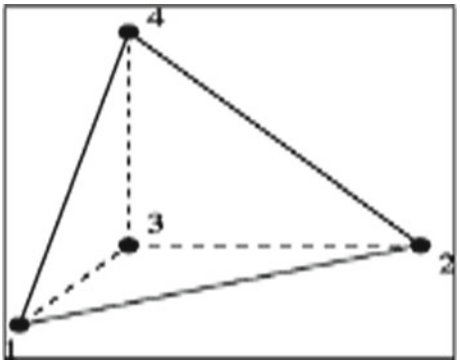


Fig. 3 Tetrahedral element shape

The loads and boundary conditions are assigned as shown in Fig. 4. The fixed support is applied in location A, and vertical force of 3210 N is applied on region B as shown by red color.

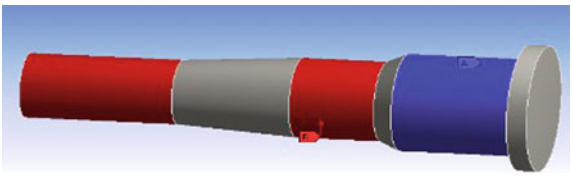


Fig. 4 Element shape of tetrahedral element

The loads and boundary conditions are taken from the literature [3]. The next stage involves algebraic formulation [9] of stiffness matrices to determine results at nodes.

3 Results and Discussion

The FEA structural analysis is conducted in stub to determine von Mises stress generated as shown in Fig. 5. \query{Please check the edits made in the sentence 'The FEA structural analysis is conducted in stub to determine...'.}The magnitude of maximum equivalent stress is 70.54 MPa near *v* shape shown by red-colored zone which reduces in regions away from it as shown in light blue and green color.

The maximum deformation obtained from FEA analysis is observed on left end of stub shown by dark red color with magnitude of 0.0612 mm in Fig. 6. FEA analysis results for stub are indicated in Table 1.

3.1 Response Surface Optimization of Stub

The optimization variables selected for response surface optimization [10] of stub are shown in Fig. 7. The first optimization variable is Tlength and second optimization

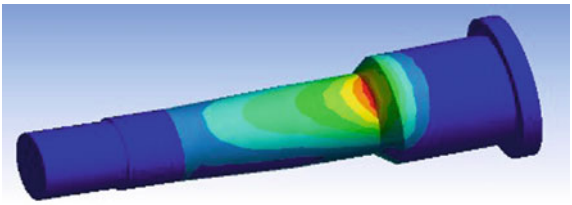


Fig. 5 Equivalent stress at different regions of stub

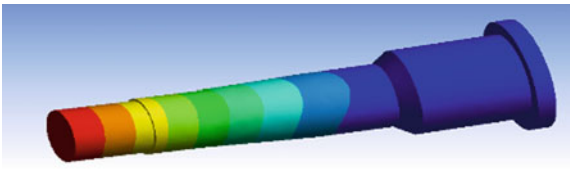


Fig. 6 Deformation at different regions of stub

Table 1 FEA analysis results for stub

Component name	Yield strength (MPa)	Deformation (mm)	Eq. stress (MPa)	Factor of safety
Stub	250	0.0612	70.54	3.54

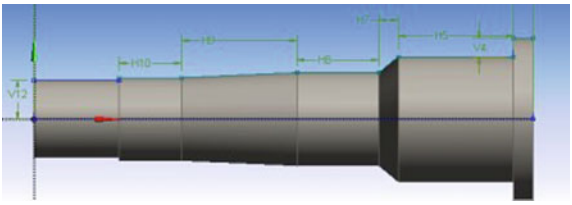


Fig. 7 Parameters selected for optimization

variable is Mlength. The variables are ticked in details tab of ANSYS design modeler.

The design points are generated using Taguchi design of experiments (DOE). The design points are generated using linear regression model. The relationship between the dependent variable and independent variables [11] can be represented as

$$y = f(X1, X2, X3, X4 \ldots Xn) + \in$$

where ε represents the noise or error observed in the response 'y'.

If we denote the expected response by

$$E(y) = f(X1, X2, X3, X4 \ldots Xn) = \eta$$

,then the surface represented by

$$f(X1, X2, X3, X4 \ldots Xn) = \eta$$

is called the response surface.

The DOE is conducted using ANSYS software and design points generated.

The equivalent stress vs design point is generated as shown in Fig. 8. The minimum equivalent stress is generated at design point number 4 with magnitude of 68.38 MPa, and maximum equivalent stress is generated at design point number 5 with magnitude of 79.135 Mpa. The solid mass vs design point generated is shown in Fig. 9. The maximum mass is observed for design point number 9 with magnitude of 0.610 kg, and minimum is observed for design point number 6 with magnitude of 0.593 kg.

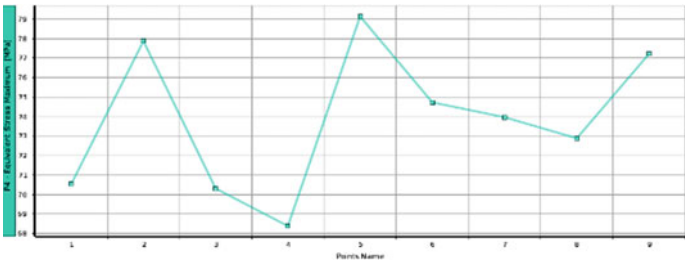


Fig. 8 Equivalent stress at different design points

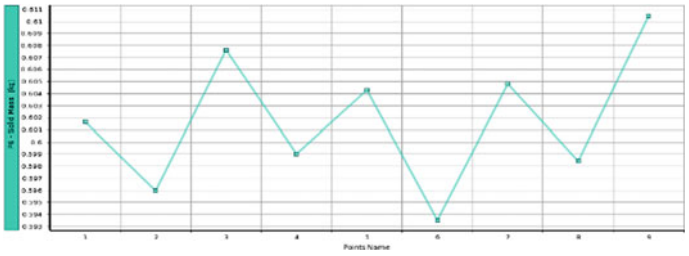


Fig. 9 Solid mass at different design points

The maximum and minimum values obtained from response surface optimization are shown in Table 2. The table shows maximum and minimum values of different parameters obtained from analysis.

The deformation value increases with increase in Tlength value linearly as shown in Fig. 10. The maximum value of deformation is observed for Tlength value of 33 mm, and minimum is observed for Tlength value of 27 mm.

The deformation value increases with increase in Mlength value linearly as shown in Fig. 11. The maximum value of deformation is observed for Mlength value of 23.375 mm, and minimum is observed for Mlength value of 21.25 mm.

The response surface plot for total deformation shows that maximum deformation is observed for Mlength value ranging from 20 to 23.375 mm and Tlength value ranging from 30 to 33 mm. The minimum value of deformation is observed for different values of Mlength and Tlength as shown by dark blue color region in Fig. 12.

Table 2 Maximum and minimum values of different parameters

	A	*B*	*C*
1	Name	Calculated min	Calculated max
2	P3—total deformation maximum (mm)	0.058609	0.063457
3	P4—equivalent stress maximum (MPa)	68.389	79.135
4	P6—solid mass (kg)	0.59352	0.61046

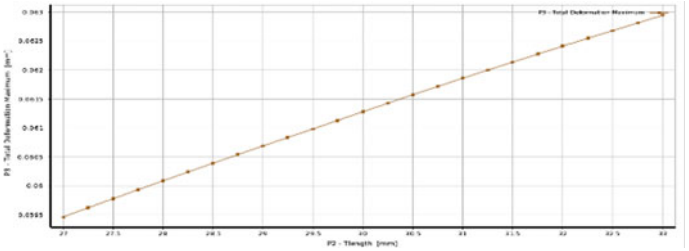


Fig. 10 Total deformation versus Tlength

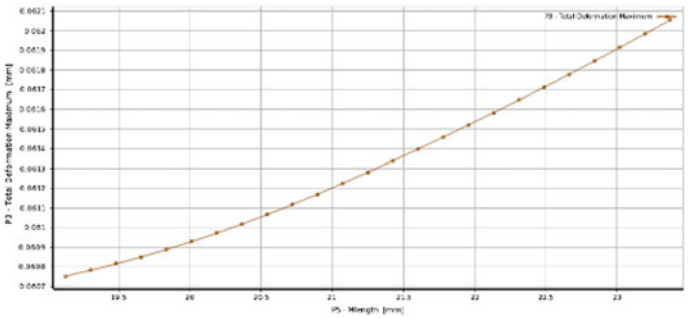


Fig. 11 Total deformation versus Mlength

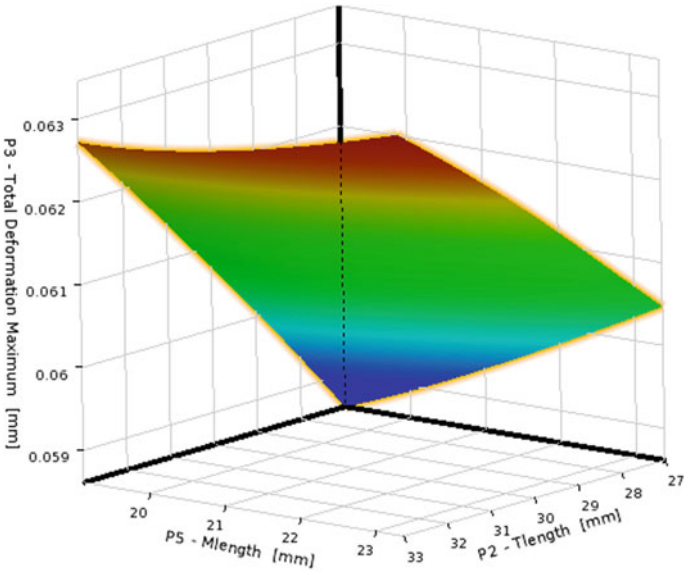


Fig. 12 Response surface plot of total deformation

The equivalent stress value decreases with increase in Tlength value linearly up to 30 mm. The maximum value of equivalent stress is observed for Tlength value of 27 mm, and minimum is observed for Tlength value of 31.25 mm. The equivalent stress value decreases with increase in Mlength value linearly up to 23.375 mm. The maximum value of equivalent stress is observed for Mlength value of 23.375 mm, and minimum is observed for Mlength value of 19.125 mm.

The response surface plot for equivalent stress shows that maximum equivalent stress is observed for Mlength value ranging from 23 to 23.375 mm and Tlength value ranging from 28 to 31 mm. The minimum value of deformation is observed

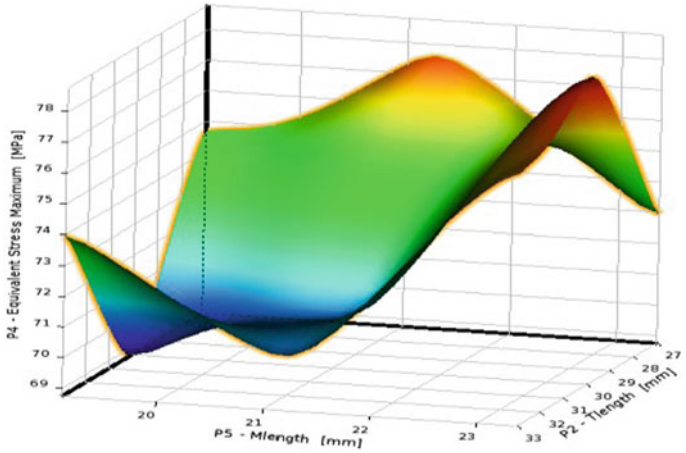


Fig. 13 Response surface plot of equivalent stress

for different values of Mlength and Tlength as shown by dark blue color region in Fig. 13.

The mass value decreases with increase in Tlength value linearly up to 33 mm. The maximum value of mass is observed for Tlength value of 33 mm and minimum is observed for Tlength value of 27 mm. The mass value increases with increase in Mlength value linearly up to 23.375 mm. The maximum value of mass is observed for Mlength value of 23.375 mm, and minimum is observed for Mlength value of 19.125 mm.

The response surface plot generated for solid mass shows the maximum value of solid mass for Mlength value ranging from 21 to 23.375 mm and Tlength value ranging from 30 to 33 mm as shown in Fig. 14.

The sensitivity plot generated in Fig. 15 shows effect of different variables on deformation, equivalent stress and mass. For total deformation, Tlength has positive sensitivity of 71.73 and Mlength also has positive sensitivity of 26.877.

Therefore, for total deformation, Tlength has higher effect as compared to Mlength. For equivalent stress, Tlength has negative sensitivity of 65.717 and Mlength also has positive sensitivity of 93.471. Therefore, for equivalent stress, Mlength has higher effect as compared to Mlength. For mass, Tlength has positive sensitivity of 68.881 and Mlength also has positive sensitivity of 31.107. Therefore, for mass, Tlength has higher effect as compared to Mlength.

4 Conclusion

The FEA analysis using ANSYS software is also a viable option against experimental testing which involves costly setup and is time consuming. From the FEA analysis

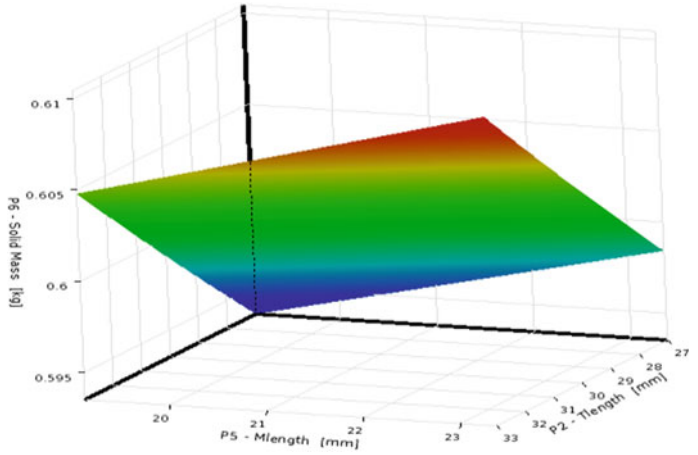


Fig. 14 Solid mass versus Mlength



Fig. 15 Sensitivity plot

conducted on stub, stress distribution and deformation plot are generated which led to identification of critical regions for design of knuckle joint assembly. Response surface optimization of stub is conducted to determine the effect of various parameters on stub design and knuckle design. The optimization has shown that 2.72% weight reduction and 13.54% stress reduction of stub are possible without much compromise in its strength.

Vast scope of research lies in optimizing material and other design parameters of knuckle stub like front spindle length, plate width. Application of composite materials like material matric composites (MMCs) in manufacturing of knuckle needs to be investigated.

References

1. Wong JY (2008) Theory of ground vehicles, 4th edn. Wiley
2. Milliken W (1995) Race car vehicle dynamics. Soc Autom Eng Int
3. Wala MB (2019) Design, analysis and optimization of ATV's front steering knuckle. Int Res J Eng Technol 6(11)
4. Vijayarangan S, Rajamanickam N, Sivananth V (2013) Evaluation of metal matrix composite to replace spheroidal graphite iron for a critical component steering knuckle. Mater Des 43:532–541
5. Chang KS, Tang PS (2001) Integration of design and manufacturing of structural shape optimization. Adv Eng Softw 32:555–567
6. Dumbre P, Mishra AK, Aher VS, Kulkarni SS (2014) Structural analysis of steering knuckle for weight reduction. Int J Adv Eng Res Stud: 86–86
7. Al-Arifi NS, Zamani AS, Khan J (2011) Billet optimization for steering knuckle using taguchi methodology. Int J Comput Theory Eng 3(4)
8. Zoroufi M, Fatemi A (2003) Fatigue life comparisons of competing manufacturing processes—a study of steering knuckle. SAE Int
9. Tagade PP, Sahu AR, Kutarmare HC (2015) Optimization and finite element analysis of steering knuckle. In: International conference on quality upgradation in engineering, science and technology
10. Patil MA, Chavan DS, Kavade MV, Ghorpade US (2013) FEA of tie rod of steering system of car. Int J Appl Innov Eng Manage 2(5)
11. Chandrakar SK, Soni DL, Gardia S (2013) FEA of a steering knuckle for life prediction. Int J Eng Res Technol 6(5)

Numerical Analysis of Rear Spoilers in Improving Vehicle Traction



R. Marumo, O. B. Molwane, and A. Agarwal

Abstract The vehicle aerodynamics is significantly influenced by its front shape covering hood, bumper, rounds and tapers. Similarly, vehicle rear geometry also influences its aerodynamics which includes trunks and spoilers. With high standards of road safety regulations, the use of aerodynamics can significantly improve vehicle stability especially at high speeds and at turning. The optimized design of spoilers inspired by aircraft wings can significantly increase negative lift and thus improve traction which gives stable and controllable drive at high speeds. The current research investigates the application of NACA inspired rear spoiler in passenger sedan cars using computational fluid dynamics. The CAD model of car is established in Creo project package and analyzed using ANSYS CFX 18.1 software package. The CFD analysis is conducted at four different air speeds (15.5, 25.5, 35.5 and 45.5 m/s) using standard k-epsilon turbulence model. The study shows that the application of spoilers significantly increased vehicle traction while minimal increase in drag force and power consumption. With increase in vehicle velocity the percentage increase in negative lift rises except at 35.5 m/s and with the increase in negative lift the traction rises and thus helps avoiding skidding of vehicles at high speeds or at sharp turns.

Keywords Spoiler · Vehicle aerodynamics · Velocity · Drag force

1 Introduction

Spoilers were first presented on automobiles in the late 1960s and used on sporting and racing cars in the 1970s [1]. Earlier, only the elite games vehicles and dashing autos used to introduce spoilers for having streamlined features benefits. In any case, they are entirely normal in traveler vehicles nowadays. A few people use it for just

R. Marumo · A. Agarwal
Department of Mechanical Engineering, FET, University of Botswana, Gaborone, Botswana

O. B. Molwane (✉)
Department of Industrial Design and Technology, FET, University of Botswana, Gaborone, Botswana
e-mail: molwaneob@ub.ac.bw

© Springer Nature Singapore Pte Ltd. 2020

A. Praveen Kumar et al. (eds.), *Advances in Lightweight Materials and Structures*,
Springer Proceedings in Materials 8, https://doi.org/10.1007/978-981-15-7827-4_16

aesthetic purposes, and those spoilers can even build the drag. Cars drifting at higher speeds have a trend to overturn at sharp radius of turning. The stream of air at the back side of the car tends to create a pressure force drop which it inductees the lift, a rear spoiler can be attached to the particular car to shrink this lift [1–3]. Without spoilers, the main thing keeping the tires worn out on a vehicle planted on the asphalt is the vehicle's own weight. In this manner, vehicle spoilers are introduced to guarantee that the hold of a vehicle out and about stays consistent, paying little mind to the heaviness of the vehicle. In a vehicle that does not have spoilers, the best way to improve the grasp of a vehicle without spoilers would be by altogether upgrading the heaviness of the vehicle or by changing the material or compound of which the tires are made.

Spoilers also produce essential down force and thus deliver stability dropping lift. Spoilers in the front portion are called dams and if installed in rear, in the form of wing [4]. The rear spoiler is designed with the gradual thickness toward the tail edge, and this seeks to disrupt the movement of the air particles. In addition, it adds stability to a motion car as it creates down force which is a vertical force that acts on the tires causing traction to the road.

The objective of current research is to analyze effect of rear spoiler used in passenger sedan car. The rear spoiler used in this research has design inspired from NACA series airfoil which has curved shape from front end. The CFD examination of passenger car with and without spoiler is conducted using ANSYS 18.1 software, and CAD model is developed using Creo design package. Standard k-epsilon turbulence model is used for CFD analysis. The increase in power requirement due to increase of drag by incorporation of rear spoiler is also analyzed.

2 Design and Analysis of Car Model

The method of computational fluid dynamics is centered on Navier's Stokes Equation in any control volume. Applying the step by step mass equation, momentum equation and energy management equation are described below.

2.1 Mass Conservation Equation

$$\frac{Dp}{Dt} + \frac{\rho \partial U}{\partial x} = 0 \tag{1}$$

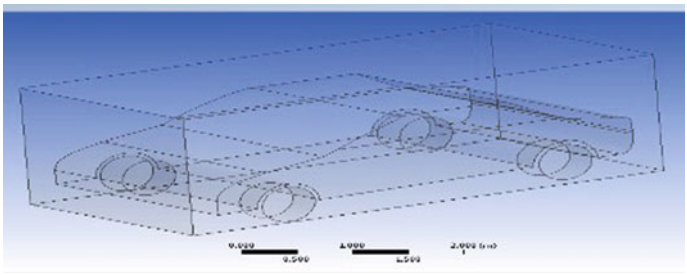


Fig. 1 Boolean operation in ANSYS

2.2 *Momentum and Energy Conservation Equations, Respectively*

$$\frac{\rho \partial U}{\partial x} + \frac{\partial U}{\partial x} = -\frac{\partial P}{\partial x} - \frac{\partial \tau}{\partial x} + \rho g \tag{2}$$

$$\frac{\rho c \partial T}{\partial t} + \frac{\rho c U \partial T}{\partial x} = -\frac{P \partial U}{\partial x} + \frac{\lambda \partial \tau}{\partial x 2} - \frac{\tau \partial U}{\partial x} \tag{3}$$

where, ρ is density of fluid, μ: viscosity of fluid, in differential terms, Ist is local energy change with time, IInd is convective term, IIIrd is pressure work, IVth is heat flux (diffusion), and Vth is irreversible transfer of mechanical energy into heat.

The first stage of analysis is preprocessing which encompasses CAD modeling, meshing and applying loads and boundary conditions. CAD stands for computer aided design. Initially, CAD model of car without spoiler and with spoilers is created in Creo parametric design software. The CAD model developed in Creo is converted in IGES format and then imported in ANSYS CFX module as shown in Fig. 1.

After developing CAD model, it is meshed into elements and nodes using CFX mesher. The meshing is done using combination of tetrahedral and hexahedral elements due to complexity of computational domain as shown in Fig. 2.

The mesh generated is formless as can be noticed in figure. The unstructured mesh is suitable for analysis of flows involving lower turbulence but not suitable for flows involving higher turbulence kinetic energy of vortices [5–7]. The equations motions are formulated for each discretized element of computational domain which forms a system of arithmetical equations. These algebraic equations are solved numerically [8, 9], and conditions are shown in Fig. 3.

The next stage involves defining borderline situations. The inlet, outlet boundary conditions are defined with constant inlet rates, i.e., 15.5, 25.5, 35.5, 45.5 m/s. The angle of attack of aircraft body is changed for different cases of analysis. The RMS residual values of mass, momentum and kinetic energy are generated from CFD simulation. The RMS residual values after 100 iterations were lower than 0.00001 which gives reasonably accurate solution. The aerodynamic resistance experienced by vehicle is given by

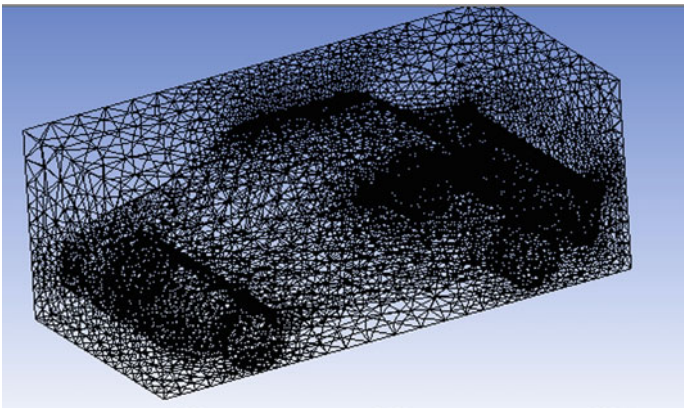


Fig. 2 Meshed model of computational domain

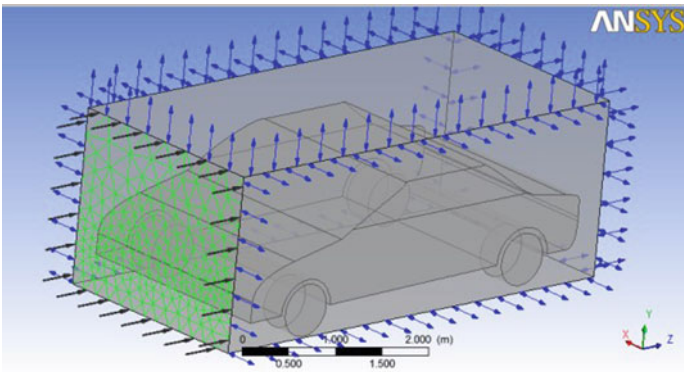


Fig. 3 Loads and boundary conditions

$$R_{\mathrm{A}} = C_{\mathrm{D}} \cdot \rho_{\mathrm{a}} \cdot S \cdot \frac{v^2}{2}[N] \tag{4}$$

where

C_{D} drag coefficient,
ρ_{a} air density (1.225 kg/m^3),
S projected section.

The aerodynamic lift experienced by vehicle is given by [1] where C_{L} is the lift coefficient.

$$L = C_{\mathrm{L}} \cdot \rho_{\mathrm{a}} \cdot S \cdot \frac{v^2}{2}[N] \tag{5}$$

3 Results and Discussion

From CFD analysis conducted on sedan car with and without spoilers, drag force and lift forces are determined. The velocity field above and below sedan car is shown in Fig. 4.

The velocity contour for car without spoiler shown in Fig. 4 shows low and constant flow field with slight variations due to rear bumper shape. The same can be seen from vector plot as shown in Fig. 5. The vector plot shows reduction in velocity vector as we move near to rear bonnet of car.

The velocity contour for car with spoiler shown in Fig. 6 shows obstruction to air flow due to spoiler edges. The zone below front end of spoiler has higher air speed as compared to zone above it as shown in velocity vector plot in Fig. 7. The air velocity reduces further as it moves toward end of spoiler both above and beneath spoiler.

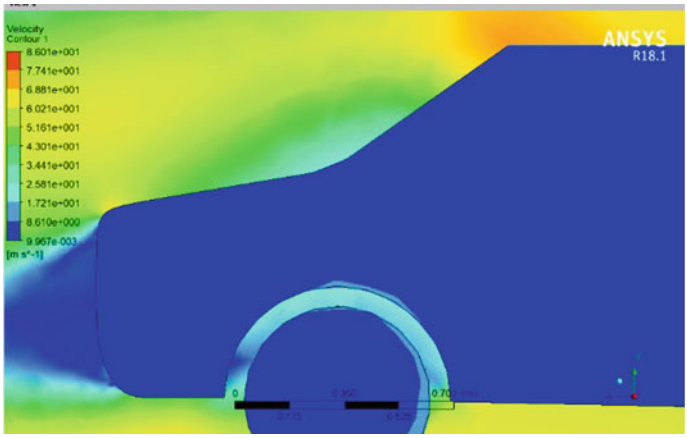


Fig. 4 Velocity field for car without spoiler

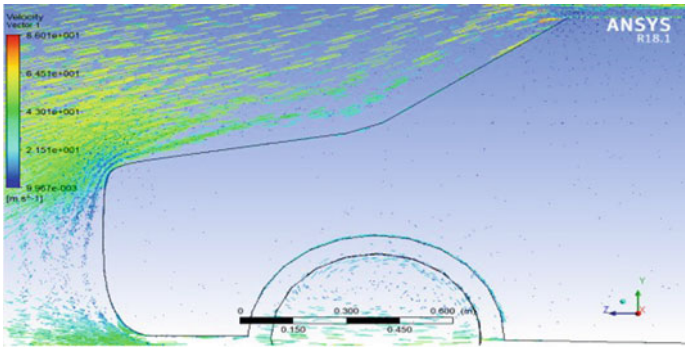


Fig. 5 Velocity vector for car near rear bonnet

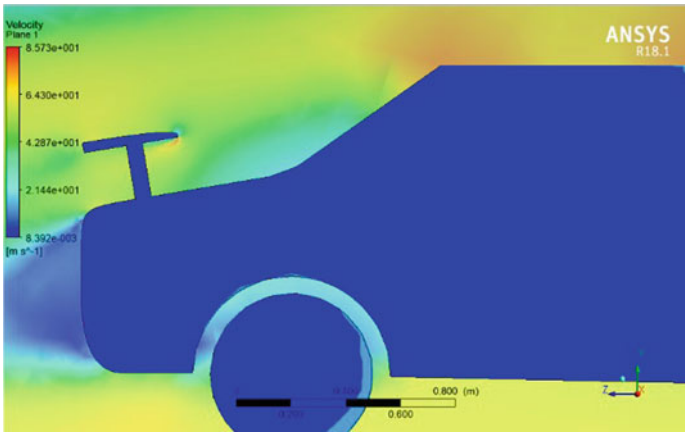


Fig. 6 Velocity field for car with spoiler

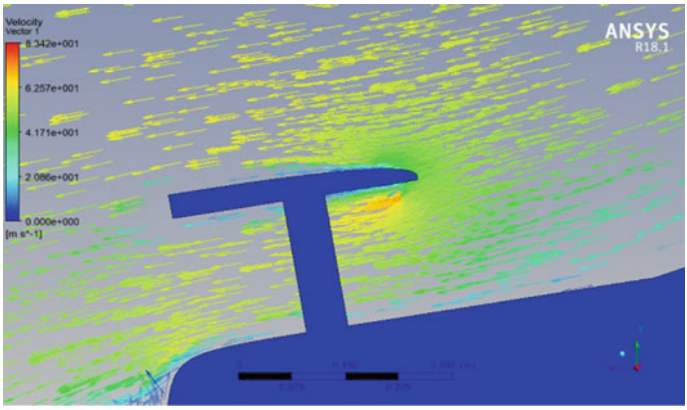


Fig. 7 Velocity vector for car with spoiler

Tables 1 and 2 are showing pressure, drag force, velocity with and without using spoilers, respectively.

The pressure developed below spoiler has higher magnitude (negative) as compared regions above spoiler as shown by light blue region in Fig. 8. This negative

Table 1 Pressure, drag force, velocity without using spoilers

Air velocity (m/s)	Drag force (n)	Lift force (n)
15.5	460.88	−33.89
25.5	1241.5	−88.37
35.5	2399.4	−167.46
45.5	3933.9	−270.82

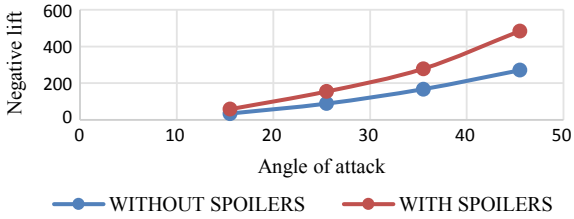
Table 2 Pressure, drag force, velocity with spoilers

Air velocity (m/s)	Drag force (n)	Lift force (n)
15.5	460.95	−57.17
25.5	1241.65	−152.79
35.5	2399.51	−270.01
45.5	3934.75	−483.94



Fig. 8 Pressure field near

Fig. 9 Negative lift comparison



pressure beneath spoiler results in generation of downward lift as shown in Fig. 9.

Using this equation, power is calculated for both designs, i.e., with spoiler and without spoiler.

The power calculation for any passenger vehicle due to external forces is given by

$$P_N = F_{\mathrm{T}}.v = (R_{\mathrm{T}} + R_{\mathrm{R}} + R_{\mathrm{A}}).v\,[\mathrm{W}] \tag{6}$$

Power calculation for design without spoilers

$$F_{T(15.5\,\mathrm{m/s})} = 0.85 + (1100 * 9.8 * 0.01) + 460.88 = 569.53\,\mathrm{N}$$
$$P_N = 569.53 * 15.5 = 8827.71\,\mathrm{W}$$
$$F_{T(25.5\,\mathrm{m/s})} = 0.85 + (1100 * 9.8 * 0.01) + 1241.5 = 1350.26\,\mathrm{N}$$
$$P_N = 1350.26 * 25.5 = 34431.63\,\mathrm{W}$$
$$F_{T(35.5\,\mathrm{m/s})} = 0.85 + (1100 * 9.8 * 0.01) + 2399.47 = 2508.12\,\mathrm{N}$$
$$P_N = 2508.12 * 35.5 = 89{,}038.26\,\mathrm{W}$$

Table 3 Percentage increase in negative lift

Velocity (m/s)	Percentage increase of negative lift (%)
15.5	71.64
25.5	75.1
35.5	66.61
45.5	79.06

$$F_{T(45.5\,\text{m/s})} = 0.85 + (1100 * 9.8 * 0.01) + 3933.98 = 4042.79\,\text{N}$$
$$P_N = 4042.79 * 45.5 = 183{,}946.945\,\text{W}$$

Power calculation for design with spoilers

$$F_{T(15.5\,\text{m/s})} = 0.85 + (1100 * 9.8 * 0.01) + 460.95 = 569.6\,\text{N}$$
$$P_N = 569.6 * 15.5 = 8828.8\,\text{W}$$
$$F_{T(25.5\,\text{m/s})} = 0.85 + (1100 * 9.8 * 0.01) + 1241.65 = 1350.3\,\text{N}$$
$$P_N = 1350.3 * 25.5 = 34432.65\,\text{W}$$
$$F_{T(35.5\,\text{m/s})} = 0.85 + (1100 * 9.8 * 0.01) + 2399.51 = 2508.16\,\text{N}$$
$$P_N = 2508.12 * 35.5 = 89{,}039\,\text{W}$$
$$F_{T(45.5\,\text{m/s})} = 0.85 + (1100 * 9.8 * 0.01) + 3934.75 = 4043.4\,\text{N}$$
$$P_N = 4042.79 * 45.5 = 183{,}974\,\text{W}$$

It has been observed that with increase in air velocity, the drag force and negative lift force increase with the following percentages as shown in Table 3.

4 Conclusion

The analysis is done using CFD simulation which has many advantages over the experiment in terms of cost, time, scale, safety and information. Drag, lift forces and pressure developed on traveler car body are studied. For both the designs with spoilers and without spoilers, the drag force almost remained constant. This is due to air flow above rear bonnet of car. With increase in vehicle velocity, the percentage increase in negative lift increases except at 35.5 m/s, and with the increase in negative lift, the traction increases and thus helps avoiding skidding of vehicles at high speeds or at sharp turns. As the power does not depend on negative lift, hence it remains almost same in both the designs, and hence, passenger car with spoiler is found to be improving vehicle performance as amount of negative lift generated without much increase in fuel consumption and adding weight to vehicle. The implementation of this work can be pursued by designing and building a prototype of the complex rear spoiler at the laboratory. However, further analysis and simulation can also be considered with other parameters to improve the vehicle performance.

References

1. Kyei SM (2014) Composite car rear spoiler. Degree Thesis, Plastics Technology
2. Hu X, Wong: ETT (2011) A numerical study on rear-spoiler of passenger vehicle. Int J Mech Mecha Eng 5(9)
3. Kumar N, Lalit Narayan K, Narasimha Rao LNV, Sri Ram Y (2015) Investigation of drag and lift forces over the profile of car with rear spoiler using CFD V. Int J Adv Sci Res 1(8)
4. Rear-spoiler-type. https://tagmotorsports.com/techart-991-2-rear-spoiler-type-ii. last accessed 18 Nov 2019
5. Liu Z (2015) Computational Fluid Dynamics Solver with preconditioned method for aerodynamic simulation of high-lift configuration. J Aircraft 53(4):1056–1064
6. Necci C (2009) Industrial computational fluid dynamics tool for evaluation of aerodynamic coefficients. J Aircraft 46(6):1973–1983
7. Hull DG (2007) Fundamentals of airplane flight mechanics. Springer, Berlin
8. Jamerson A (2017) Using computational fluid dynamics for aerodynamics—a critical assessment. Stanford University, California, United States of America, pp 5–8
9. Jamerson A (2006) Using computational fluid dynamics for aerodynamics. Stanford University, California, United States of America, pp 1–4

Automated Vision System to Measure Weld Length of Hand Brake

M. Palaninatharaja, S. Julius Fusic, S. Karthikeyan, and H. Ramesh

Abstract To measure the quality of welding joints, various inspection methods like laser triangulation, X-ray diffraction, ultrasonic detection, and band-pass filters are practiced. Automated quality check methods provide increased quality production. In this research paper, to check the quality of welded joint on a handbrake lever and to make decision based on the acquired data, the part image is captured by a camera and it undergoes image processing methods in MATLAB. To highlight each weld boundary, region of interest is used. The highlighted regions are then processed by techniques such as segmentation, thresholding, dilation, erosion, and morphological masking. The following facts are observed that there is lack of clarity in the acquired image, improper threshold value set while segmenting the image, erroneous mode of shape masking, thereby generating gaps between pixels. Finally, the method holds good for this particular material with weld in particular coordinates. The presence and length of the welds present in the material are successfully obtained. This inspection system is restricted only for the weld length and weld presence of the handbrake lever application.

Keywords Automated quality check · Image processing · Welding joints

1 Introduction

Various inspection methods like laser triangulation, X-ray diffraction, ultrasonic detection, and band-pass filters are used in weld inspection. Measurement is a mainstay for automated inspection and has provided the platform for ever faster, more efficient, and more accurate quality control. In addition, for preventing defective product reaching the customer, vision measurements can also be directly linked to improve product quality, reduce wastage, improve productivity, and streamline the process. Likewise in another research, Eriksson et al. [1] stated the methods for automatic inspection of weld geometry and various methods to find the geometry of

M. Palaninatharaja · S. Julius Fusic (✉) · S. Karthikeyan · H. Ramesh
Department of Mechatronics Engineering, Thiagarajar College of Engineering, Madurai, India
e-mail: sjf@tce.edu

© Springer Nature Singapore Pte Ltd. 2020

A. Praveen Kumar et al. (eds.), *Advances in Lightweight Materials and Structures*,
Springer Proceedings in Materials 8, https://doi.org/10.1007/978-981-15-7827-4_17

the weld as well as detect the defects in the weld piece using laser line projection and CMOS camera. It is possible to find defects like spatter, undercut, and sharp edges. Later the weld defect monitoring system researches were processed in various workpiece with various techniques. Based on that, the author Chu et al. [2] proposed a novel image processing method that can automatically extract the weld joint profile and feature points, measure the weld bead size, and detect defects. Subsequently, the three-dimensional (3D) profile of the weld surface can be reconstructed with the aim of monitoring the weld quality online. Tejwar Rao [3] elucidated about the welding inspection system which included laser sensor that illuminated the weld seam so that the CCD/CMOS camera used to get the image of the weld seam. Later, this image was transferred to MATLAB for image processing. After the image processing, the defected portion in welds were reduced. Yang et al. [4] anticipated specular reflections that created many difficulties in image processing and machine vision applications. Here, they proposed various methods based on color analysis and multi-baseline stereo that simultaneously eliminated specular reflections in weld material. Fleming et al. [5] dealt with the specular reflection based on perception of shapes. Xia et al. [6] discussed the automated precision measure of spot weld and accuracy of measure through online transmission. Yanqing et al. [7] proposed an algorithm for the light vision sensor setup to measure the weld bead in order to control the light conditions. Hart et al. [8] discussed the measure of quality defects on surface using structured light projection. The image processing system undergoes specular reflections by capturing the three-dimensional shape of the objects. They also proposed various approaches to overcome specular reflection of complex reflecting surfaces.

2 Selection of Vision Sensor and Software Tool

Welding plays a major part in manufacturing industry. Almost 90% of the manufacturing processes involve welding. Manual welding is still the best process for some gatherings. Automating this technique improves the dimensional accuracy as well as the time consumed in measuring them. Handbrake lever material made of steel pickle hot rolled coil (SPHC) is a material grade and designation defined in Japanese Industrial Standard—JIS G 3131. JIS G 3131 is a material standard for hot rolled steel.

Handbrake lever undergoes a process called pickling, to remove impurities such as stains, inorganic contaminants, rust, or scale from ferrous metals, copper, precious metals, and aluminum alloys and specifications are shown in Table 1.

Figure 1 shows the schematic flow of the work. The accuracy of the end result is hugely dependent on the quality of the captured image. It is thereby important to obtain a high-quality image. The selection of camera places a major role in the progress of this work. The pixel rate, maximum screen resolution, and the zoom rate are the preliminary considerations in choosing a camera. The specification of the camera used in this work is mentioned in Table 2.

Table 1 Workpiece material properties

Description	Specification
Type of material	Steel pickle hot rolled coil—phosphorous SPHC-P
Material standard	JIS-3131
Type of weld	Tungsten arc weld
Weld electrode	er70s6

Since multiple objects are to be tested, it is mandatory that the environment at which the image is captured is constant. The lighting and the camera properties may vary with environment and so it is mandatory that all images are from the same environment. The entire environment is made black to avoid further reflections of the light on the material. The external light source is the only light source for the material. This helps in segmenting the image better. Sufficient mountings are made to hold the material as well as the camera.

2.1 Image Capturing in LabVIEW

Visual programming environment in LabVIEW software using Vision and Motion Utilities have been utilized to grab the handbrake lever from a loop continually. LabVIEW function is programmed to capture the handbrake lever continuously from the acquiring video and process the MATLAB function to measure the weld length as shown in Fig. 2. And the Fig. 3 shows the circuit diagram for LabVIEW program.

3 MATLAB Image Segmentation

3.1 Edge Detection

Edge detection is done by three common tools in MATLAB, i.e., Canny, Prewitt, and Sobel. The weld must be subjected to edge detection initially to get proper boundaries. In both Canny and Sobel, the boundaries were not obtained clearly. The noise removal is poor in Canny, and the required boundary is added with multiple strands of boundaries. This makes it difficult to extract the needed edges. In case of Sobel, the edges were not obtained completely. Few edges of the images were not detected. Figure 4 is the output of the edge detection done in the weld.



Fig. 1 Schematic flow diagram

3.2 Thresholding Methods

Thresholding is done by using two methods—manual and adaptive [9]. In manual, the sensitivity is altered. After several iterations, the standard sensitivity value of the weld is around 100 (97 in most cases). After the sensitivity is fixed, the adaptive

Table 2 Vision sensor (camera) specifications

Description	Specification
Name of the camera	Honor 12MP f/2.2 PDAF and laser AF
Pixel rate	12 MP
Resolution (image)	3968 × 2976 p
Lens	8.00 × zoom
Dimension	157 × 78 × 7 mm
Weight	153 g



Fig. 2 LabVIEW front panel display grab image

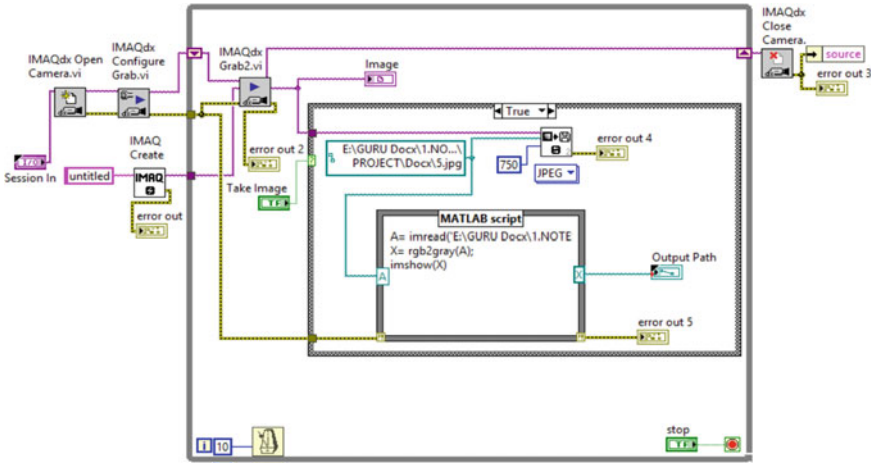


Fig. 3 LabVIEW block diagram of interfacing Camera

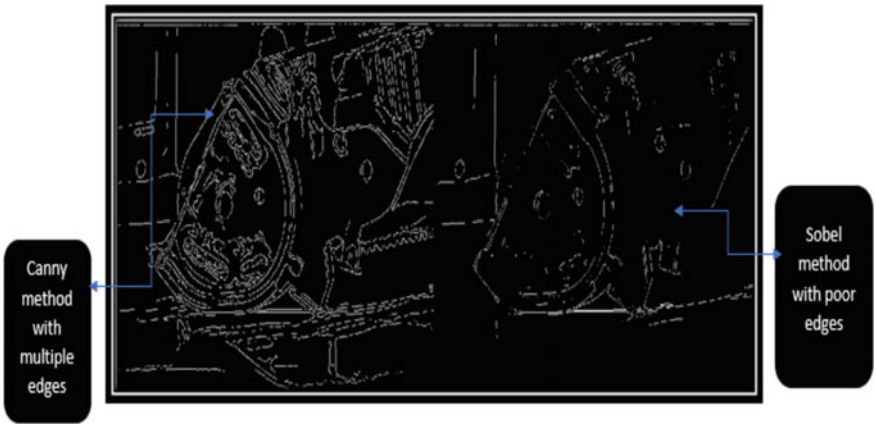


Fig. 4 Edge detection using Canny and Sobel method

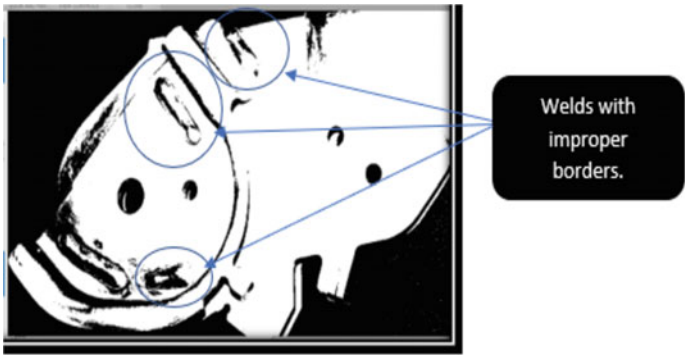


Fig. 5 Threshold resulted image

method is used to improve the contrast of the image. The value here is in the range of 60–70 for the weld. The threshold and sensitivity values are fixed based on the lighting and the environment at which the image is captured and it can be seen in Fig. 5 with improper welds shown.

3.3 Dilation and Erosion

Dilation and erosion are adding and removing pixels from the threshold image, which helps in enhancing the border of the image. The weld is initially dilated as the inner white pixels in the weld should be clearly visible. A dilation value of 0.8 is set with background being dark. Figure 6 shows using the dilation and erosion the borders could be visible better than before in Fig. 5.

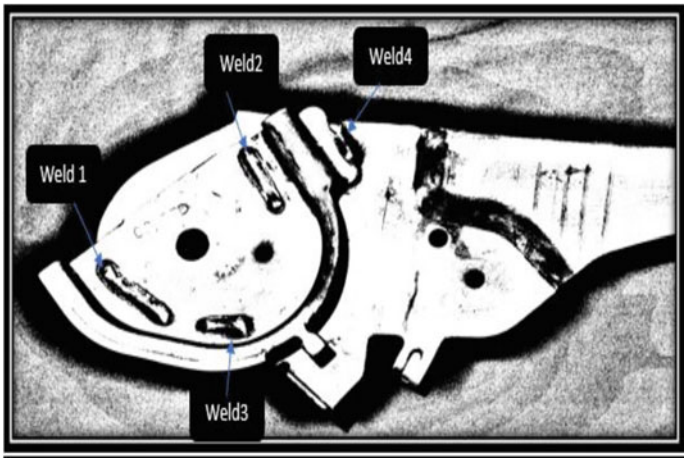


Fig. 6 Image generated after dilation and erosion

3.4 Morphological Masks

Open and close masks are used. The weld being considered as a rough ellipse is subjected to line- and circle-shaped masks. This is to fill the minute gaps in the borders. The circle is given a radius of 3 and the line length is 5 with an angle of 30°. Figure 7 shows the removal of backgrounds.

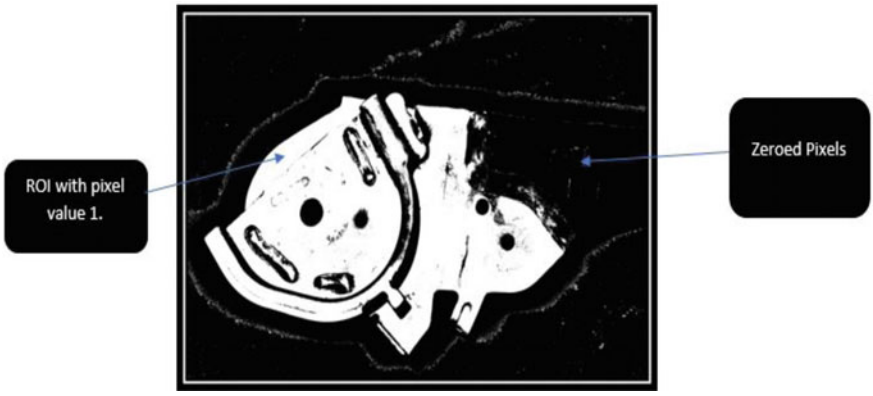


Fig. 7 Image generated after morphological mask

3.5 Skeletonization and Perimeter Generation

Skeletonization and perimeter are used to zero the unwanted pixels and make pixel value as 1 for the remaining pixel. When the weld is subjected to these methods, the weld bead is reduced down to a single line. This process was a failure in this image since the reduction was not so efficient and an improper image was generated as output.

3.6 Region Property Toolbox

The region property tool fits the improper shape into a proper bounding box. The property returns the area, centroid, major axis length, minor axis length, and filled area. The weld is subjected to a 4 connect region prop tool, wherein the shape of the weld is considered as an improper ellipse. This elliptical structure is fitted into a proper bounding box. Based on this, the weld indexes are extracted and then the length is calculated. Figure 8 shows the bounding box captured for the four weld spots.

The process of converting obtained pixel values as output from MATLAB to millimeters is as follows,

$$\text{horizontal dpi} = \frac{\text{pixel} * 1\text{inch}}{\text{width(mm)}} = \frac{200 \times 25.4}{110} = 46\,\text{dpi}$$

Step 1 Divide the pixel height which is noted down by the height in handbrake lever that is measured to get the handbrake lever's vertical dpi (dots per inch or pixel density per inch).

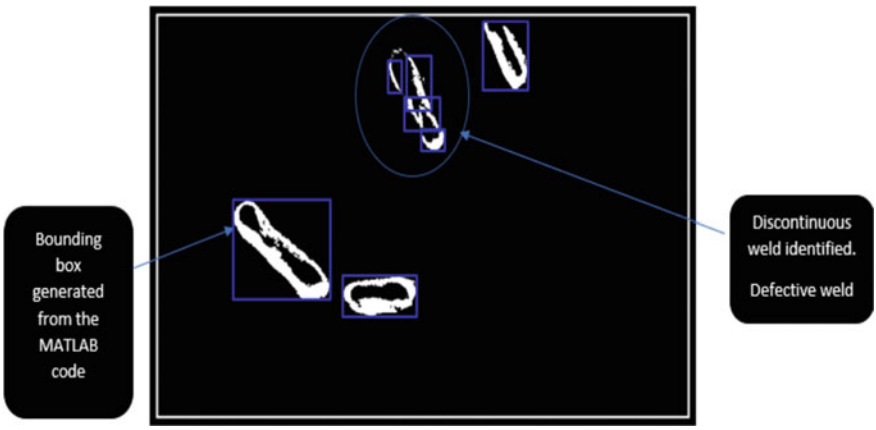


Fig. 8 Image bounding box generation

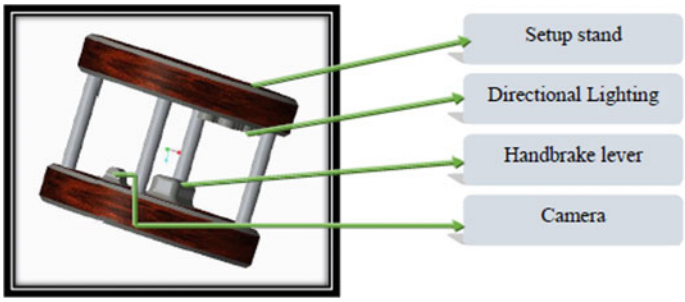


Fig. 9 3D CREO model of measuring jig

$$\text{vertical dpi} = \frac{\text{pixel*1inch}}{\text{width(mm)}} = \frac{200 \times 25.4}{110} = 46\,\text{dpi}$$

Step 2 Here, 46 dpi represents 46 pixels per inch. Therefore,

$$1pixel = \frac{1inch[25.4mm]}{46} = 0.55\text{mm}$$

Hence, the weld length of hand brake is calibrated [10].

4 Hardware Model of Measuring Jig

The 3D model for the experimental setup is carried out using the PTC CREO 3.0 software. PTC CREO is 3D modeling PARAMETRIC software, especially used in modeling the analysis and simulation part. Here, we modeled a measuring jig, which will be able to measure the weld length of handbrake lever. This is shown in Fig. 9.

5 Results and Discussion

The successful integration of LabVIEW and MATLAB creates a user-defined function in MATLAB and interfacing with LabVIEW. The length of the weld using the image is captured using suitable MATLAB algorithm and compared with bench mark data. Based on the length, the acceptance/rejection of the material is decided and the discontinuous weld is identified in the hand brake. The process is comparatively quick and precise than the conventional methods where in a vernier caliper is used. After segmenting the image, the code for region property to generate bounding box was performed. To make the result more accurate, individual welds were taken out from the single image using ROI-based grab techniques. This helps in the implementation of the bounding box creation which is simplified and more accurate.

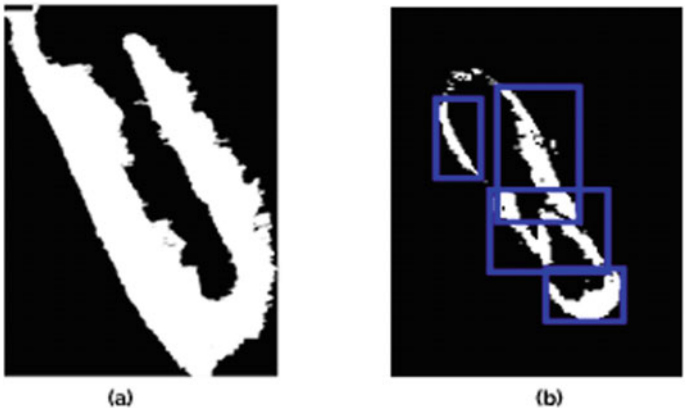


Fig. 10 **a** Individual weld, **b** improper bounding box

After extracting the individual welds, the corresponding filled area, major and minor axis lengths, and area are generated by the region prop tool. Using these pixel values and by suitable calibration methods, the weld length is generated. There are a few instances where multiple bounding boxes are generated for a single weld. This is because of improper weld borders, lack of clarity in the acquired image, improper threshold value set while segmenting the image, erroneous mode of shape masking, thereby generating gaps between pixels, and the improper selection of weld as shown in Fig. 10b. Using 1×4 box only considers 4 pixels surrounding a white pixel to generate a box. By doing so even a small pixel break is considered, thereby generating the result as improper weld.

6 Conclusion and Future Work

In an attempt to detect and measure the quality of weld spot on handbrake lever, the results are evident. Table 3 shows the obtained length of the weld and compared with the actual measurements. The lighting setup along with the hardware made the image acquisition better than in normal conditions, and this improved the image

Table 3 Actual length versus obtained length

Weld	Actual length in mm (+5 mm tolerance)	Obtained length in mm
Weld 1	27	30.1
Weld 2	11	14.7
Weld 3	22.5	25.8
Weld 4	16	19.5

acquisition. This algorithm holds good for this particular material as the specular reflection and lighting conditions were considered. This shows that light reflection on material and light conditions on subject becomes potential factor, and it may vary material to material. So, this inspection system is restricted only for the weld length and weld presence of the handbrake lever application.

6.1 Future Work

In future, this can be improved to inspect all the welded objects like the weld pores, cracks, incomplete fusion, and slag formation. Further, this inspection system can be modified to measure the dimensions and geometry of the weld which can be interfaced with hydraulic cylinders and piston for complete automation. Further, this inspection system is improved to train multiple welds by implementing machine learning techniques. In utilizing the machine learning techniques, the inspection system can be automated easily.

References

1. Eriksson I (2008) Methods for automatic inspection of weld geometry. Dissertation, Trollhättan
2. Chu HH, Wang ZY (2016) A vision-based system for post-welding quality measurement and defect detection. Int J Adv Manuf Technol 86: 3007
3. Tejeswar Rao K (2015) Welding inspection system under the supervision of Prof. B. B. V. L. Deepak published in National institute of technology, Rourkela
4. Yang Q, Tang J, Ahuja N (2015) Efficient and robust specular highlight removal. IEEE Trans Pattern Anal Mach Intell 37(6): 1304–1311
5. Roland W (2014) Fleming, Visual perception of materials and their properties. Vision Res 94:62–75
6. Xia W, Chen ECS, Pautler SE, Peters TM (2019) A global optimization method for specular highlight removal from a single image. IEEE Access 7:125976–125990
7. Han Y, Fan J, Yang X (2019) A structured light vision sensor for on-line weld bead measurement and weld quality inspection. Int J Adv Manuf Technol
8. Hartl R (2019) Automated surface inspection of friction stir welds by means of structured light projection. In: IOP conference series: materials science and engineering, vol 480
9. Shen J (2012) Application of image segmentation in inspection of welding: Practical research in MATLAB, Dissertation, University of Borås/School of Business and IT
10. Xia YJ, Su ZW, Lou M, Li YB, Carlson BE (2019) Online precision measurement of weld indentation in resistance spot welding using servo gun. IEEE Trans Instrument Measur 1–1

Behaviour of Multi-layered Hybrid Fibrous Ferrocement Panels

Srujan Varma Kaithoju, D. Vijay Venu Gopal, V. Aastritha Vatchala, and Uzair Ahmed

Abstract The present study shows the flexural behaviour of fibrous ferrocement panels reinforced with multiple layers of combined wire mesh (recycled wire mesh obtained from industry) and varying percentages of alkali-resistant glass fibres and polypropylene fibres (0.2, 0.4, 0.6, 0.8 and 1%). Fibrous mortar cubes with varying percentages of glass and polypropylene fibres (0.2, 0.4, 0.6, 0.8 and 1%) by weight of cement were cast, and compressive strength test is done to know the optimum dosage of fibres to be used. With the optimum dosage of fibres, fibrous ferrocement panels of size (600 mm × 200 mm × 30 mm) with varying layers of recycled wire mesh were cast, and flexural test is performed. From the test results, it was found that there was significant increase in flexural strength of ferrocement panels with increase in layers of wire mesh and increase in fibres up to 0.8%. This work can lay a path to development of lightweight roofing and supporting structures like thin shells, silos, etc.

Keywords Ferrocement · Fibrous ferrocement · Alkali-resistant glass fibres · Polypropylene fibres · Multi-layered wire mesh · Flexural strength

1 Introduction

Ferrocement is an eco-friendly lightweight material which can be effectively used in construction industry. Materials required for the construction of ferrocement are easily available. It is durable, cheap and versatile. Ferrocement is used for the first time in the construction of aircraft hangers, boats and buildings and a variety of other structures [1, 2]. Hybrid fibre refers to combination of two or more different fibres, hybridization process of fibres in cement matrix is achieved by combining polypropylene and glass fibres in cement matrix [3, 4].

S. V. Kaithoju (✉)
Civil Engineering, Kakatiya Institute of Technology & Science, Warangal, Telangana, India
e-mail: ksv.ce@kitsw.ac.in

D. Vijay Venu Gopal · V. Aastritha Vatchala · U. Ahmed
Kakatiya Institute of Technology & Science, Warangal, Telangana, India

© Springer Nature Singapore Pte Ltd. 2020

A. Praveen Kumar et al. (eds.), *Advances in Lightweight Materials and Structures*,
Springer Proceedings in Materials 8, https://doi.org/10.1007/978-981-15-7827-4_18

Table 1 Properties of cement (OPC 53 grade conforming to IS: 12269 (1987))

Brand	Specific gravity	Fineness	Initial setting time	Standard Consistency
RAMCO 53 grade	3.15	10%	42 min	30%

Ferrocement can be considered as a type of thin-walled reinforced concrete construction in which smaller diameter mesh is inserted throughout the cross section. Ferrocement is made with wire meshes with non-corrosive coating and varying diameters which is reinforced between cement mortars [5, 6]. Fibre reinforced mortar is a combination of cement and sand in required proportions containing fibrous material which increases its soundness. The advantages of using ferrocement in construction include reduced maintenance costs, lightweight and longer life time compared to steel structures. The desired shape may be built from a multi-layered construction of mesh, supported by grit, built with grit and tied with wire. A combination of two or more fibres and multiple layers of wire mesh is used to prepare the hybrid fibrous ferrocement panels [7, 8]. The load-carrying capacity of panels increases with the increase in number of mesh layers [9]. Multi-layered fibrous ferrocement can lay a path to the development of lightweight roofing elements [10], supporting structures, silos and thin shells, and it needs no advanced techniques during installation [11, 12].

The main objectives of this experimental work are to study the behaviour of multi-layered hybrid fibrous ferrocement under flexure. The different parameters considered are

1. To determine the optimum dosage of combination of fibres in hybrid fibrous ferrocement panels.
2. To determine the flexural strength of ferrocement panels by varying the layers of the recycled wire mesh with combination of polypropylene and glass fibres.

2 Experimental Investigation

2.1 Constituents of Ferrocement:

2.1.1 Cement

OPC of 53 grade, conforming to bureau of Indian standards is used for making the cement mortar and test sample. The properties of cement used are shown in Table 1.

2.1.2 Fine Aggregate

The fine aggregates used are procured from a local quarry. The fine aggregate confirming to IS 383-1971 of Zone II is used. The properties of fine aggregate are shown in Table 2.

Table 2 Properties of fine aggregate

Properties	Specific gravity	Fineness Modulus	Voids ratio	Porosity	Bulking
Value	2.65	2.87	0.66	35.70%	22.26%

2.1.3 Water

The water used for experimental investigations for mixing and curing is ordinary potable water which is free from impurities and suspended solids.

2.1.4 Glass fibres

Alkali-resistant glass fibres of size 12 mm as shown in Fig. 1 were used in this study. The properties of glass fibres are shown in Table 3.

Fig. 1 Glass fibres



Table 3 Properties of glass fibre

Property	Standard length (mm)	Filament diameter (μm)	Moisture content (%)	Density (g/cm^3)	Tensile strength (N/mm^2)	Modulus of elasticity (N/mm^2)
Value	12.0 ± 2.0	13.5 ± 2.0	1.5 ± 5.0	2.65	1500–3700	72,000

Fig. 2 Polypropylene fibres



Table 4 Properties of polypropylene fibre

Property	Diameter	Melting point	Flash point and ignition temperature	Relative density g/cm^3	Colour
Value	35–40 μm	162–167 °C	>329 °C and >450 °C	0.89–0.94	White

2.1.5 Polypropylene Fibre

Recron 3S polypropylene fibre of size 12 mm as shown in Fig. 2 was used in the present study (Table 4).

2.1.6 Wire Mesh

Hexagonal wire mesh (chicken mesh) and recycled wire mesh were used in the experimental investigation with the following physical properties. It is the reinforcing material which increases the stiffness and flexural strength of the specimen. The properties of hexagonal wire mesh are shown in Table 5.

Table 5 Properties of hexagonal wire mesh

Material	Mesh size (distance between faces of the hexagon)	Diameter of the wire mesh
Galvanized low carbon wire	10–12 mm	1 mm

2.2 Mix Proportions

According to Indian Standard Code IS 4031 (Part 6-1988) the cement—sand ratio (c/s) of 1:3 and water - cement ratio of 0.5 is adopted along with varying percentages of hybrid fibres (combination of glass fibre (0, 0.3, 0.6, 0.9, 1.2 and 1.5%)and polypropylene fibre (0, 0.2, 0.4, 0.6, 0.8 and 1.0%)) by weight of cement. The dry mix is thoroughly blended with hybrid fibrous matrix and required amount of water is added to attain proper consistency and workability of wet mortar.

2.3 Optimized Dosage of Hybrid Fibrous Matrix by Compressive Strength of Cement

To determine the optimum dosage of fibres, we compare the compressive strength of the hybrid fibrous cement mortar with varying percentages of glass and polypropylene fibres. The mortar cubes of standard size 70 mm * 70 mm * 70 mm were cast and cured for 28 days. After the curing is done, they are placed in the compressive testing machine of capacity 40 Tonnes, and a load rate of approximately 30 N/mm^2/min is applied axially on two parallel faces of the cubes. The compressive strength of the cubes is calculated by the maximum load applied to cross-sectional area of cube. From the obtained results, the optimized dosage of hybrid fibre (highest compressive strength) is determined. The results of compressive strength of hybrid fibrous mortar are shown in Table 6.

The maximum compressive strength of mortar cubes obtained was 59.22 N/mm^2 with a combination of 1.2% of glass fibres and 0.2% of polypropylene fibres (see Table 6).

Table 6 Compressive strength of hybrid fibrous mortar

Percentages of glass fibre	Compressive strength N/mm^2					
	Percentages of polypropylene fibre					
	0	0.2	0.4	0.6	0.8	1.0
0	49.31	52.55	45.69	40.42	58.41	52.21
0.3	50.12	49.31	48.55	47.87	51.92	38.42
0.6	48.21	50.39	50.32	40.24	55.81	41.83
0.9	55.68	53.66	51.74	38.12	57.68	47.69
1.2	43.32	59.22	56.93	47.69	41.83	45.71
1.5	43.56	50.99	43.45	37.25	44.61	50.22



Fig. 3 Hybrid fibrous ferrocement test samples

2.4 Sample Preparation

The test specimens for flexural strength test were cast using the wooden moulds of size 60 cm * 20 cm covered with impervious layer of plastic sheet on all the inner surfaces to avoid absorption of moisture from panels. The moulds were coated with grease for easy demoulding. Hexagonal wire mesh and recycled wire mesh with corrosion-resistant coating were cut into the size of panels and are reinforced in hybrid fibrous mortar in the moulds to achieve a thickness of 30 mm. The wire mesh is to be placed at equal spacing between the layers of fibrous mortar during the preparation of specimen. A set of three panels of standard size 60 cm * 20 cm * 3 cm were cast with one, two, three, four, five layers of wire mesh. The panels were demoulded after 24 h and transferred to curing tank for 28 days as sown in Fig. 3. The flexural strength test was performed according to IS: 516-1959.

3 Flexural Test

The specimens were tested under two-point loading in simply supported condition over an effective span of 500 mm. The test specimens were simply supported on rollers, and two-point loads were applied at equidistance from both the supports and in between them [3]. Through a hydraulic jack arrangement, loading was applied to cause downward deflection as shown in Fig. 4. A deflection dial gauge is arranged



Fig. 4 Flexural test setup for rectangular panel under two-point loading

at the centre of the panel to measure the downward deflection of panels. The loading was continued till the ultimate failure of the specimens.

The modulus of rupture in a flexure test is the ultimate strength determined. The modulus of rupture for each sample was evaluated using the following equation.

$$R = PL/bd^2$$

here

R Modulus of rupture,
P Ultimate load,
L Length of specimen,
b Width of specimen,
d Depth of specimen.

4 Experimental Results

Flexural Test: The flexural strength of hybrid fibrous ferrocement panels having multiple layers of wire mesh was done as per IS: 516-1959 on a universal testing machine (UTM) of capacity 100 Tonnes. The test results are as shown in Table 7. And the variation of test results is shown in Fig. 5 From the results obtained, it was observed that the flexural strength of hybrid fibrous ferrocement panels cast with glass and polypropylene fibre with five layers of wire mesh exhibited higher flexural strength (20.33 MPa).

Table 7 Flexural strength of hybrid fibrous ferrocement

Combination of glass fibre and polypropylene fibre	Number of layers	Flexural strength
1.2% + 0.2%	1	12.84
1.2% + 0.2%	2	14.76
1.2% + 0.2%	3	16.66
1.2% + 0.2%	4	18.13
1.2% + 0.2%	5	20.33

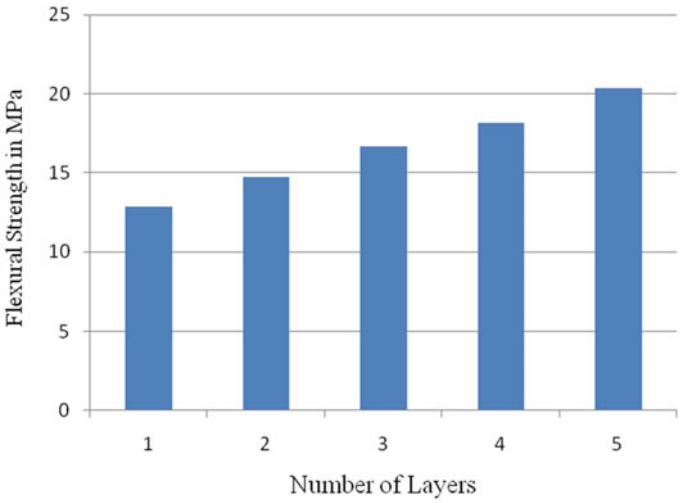


Fig. 5 Variation of flexural strength of fibrous ferrocement with increase in layers

5 Discussion on Test Results

It was observed that the flexural strength of hybrid fibrous ferrocement is increasing with increase in the number of reinforcing layers, as the experimental work was carried out limiting the number of layers up to five, there may be a chance to increase or decrease in flexural strength if the number of layers exceeds five.

The increase in flexural strength is purely due to the reinforced mesh which supports the fibrous mortar in tension and flexure, as the number of layers increased the stress distribution in the reinforcement is minimized and distributed which may be considered as one of the reasons behind increase in flexural strength of multi-layered fibrous ferrocement panels.

6 Conclusion

Based on the experimental investigations carried out on multi-layered hybrid fibrous ferrocement panels, the following conclusions can be made:

- It was observed that on a combination of 0.2% of polypropylene fibre and 1.2% of glass fibre resulted in the maximum increase in compressive strength (59.22 MPa), hence the combination (0.2% polypropylene + 1.2% glass fibres) is adopted as optimum dosage of fibres.
- Flexure strength increases as the number of layers of wire mesh increases. Here, for five layers of wire mesh, the flexure strength obtained is 20.33 Mpa. which is 58.33% higher than the flexural strength of single-layered hybrid fibrous ferrocement panels.
- The flexure strength of hybrid fibrous ferrocement panels increased with increase in layers of reinforced steel mesh.
- The overall result shows that the combination of 0.2% of polypropylene fibres and 1.2% of glass fibres along with the increase in the number of layers of wire mesh leads to the increase in the flexure strength.

7 Future Scope

- Development of multi-layered hybrid fibrous ferrocement can be a path to the development of lightweight supporting structures like lightweight roofing panels, thin shells, storage units like silos.
- Development of multi-layered hybrid ferrocement may help in developing portable lightweight structures like bunkers which can be used for armed forces and during natural calamities where providing shelters to hundreds of people is a challenge which can be addressed by this material.

References

1. Mughal UA, Azhar M, Abbas SS (2019) Comparative study of ferrocement panels reinforced with galvanized iron and polypropylene meshes. Constr Build Mater 210:40–47
2. Srujan Varma K, Ravali T (2017) Behavior of multilayered fibrous ferrocement panels. Int J Eng Res Technol 6: 818–822
3. Krishnaveni C (2015) Study on flexural behavior of hybrid ferrocement slabs. Int J Sci Technol
4. Abushwashi N et al (2014) Influence of mixture, wire mesh and thickness on the flexure performance on hybrid PVA fiber ferrocement panels. Int J Innov Res Sci Eng Technol
5. Ibrahim HM (2011) Experimental investigation of ultimate capacity of wire mesh-reinforced cementitious slabs. Constr Build Mater 25: 251–259
6. Saikiran et al T (2016) Comparision of compressive and flexural strength of glass fiber reinforcd concrete with conventional concrete. Int J Appl Eng Res

7. Phalke RJ et al (2014) Flexural Behaviour of ferrocement slab panels using welded square mesh by incorporating steel fibers Int J Res Eng Technol
8. Sakthivel PB, Jaganathan A (2012) Study on Flexural Behaviour of Ferrocement Slabs Reinforced with PVC-coated Weld Mesh. Int J Eng Res Dev 1(12):50–57
9. Reddy R, Vaijanath H (2015) Study on the ductile characteristics of hybrid ferrocement slab. Int J Innov Res Sci Technol 2(04)
10. IS 12269 (1987) Ordinary Portland Cement, 53 grade –specifications. Bureau of Indian Standards, New Delhi
11. IS 4031(part V) (1988) Indian Standard methods physical test for hydraulic cement", Bureau of Indian Standards, New Delhi.
12. IS 2386(part III) (1963) Methods of test for aggregates for concrete" Bureau of Indian Standards, New Delhi

Mechanical Behaviour of Composite Materials

Micromechanical Finite Element Elastic Properties Modeling of Plain Woven Composite

Agnes Listyo Rini, Tatacipta Dirgantara, Satrio Wicaksono, Khodijah Kholish Rumayshah, and Hermawan Judawisastra

Abstract This study performed a numerical micromechanics model of plain woven composite (PWC). A representative volume element (RVE) of carbon/epoxy PWC was modeled with a proper periodic boundary condition to represent the actual condition of the composite. Cosine equations were to define the waviness and the cross-sectional shape of the yarn. The result showed that the numerical model had a good agreement with the results of the experiment and numerical model by reference in estimating the longitudinal elastic modulus, Poisson's ratio, and longitudinal shear modulus. The effect of yarn volume fraction variation on the composite elastic properties is also analyzed.

Keywords Plain woven composite · Representative volume element · Periodic boundary condition · Elastic properties · FEM · Micromechanics

1 Introduction

Unidirectional (UD) laminate composite has excellent in-plane properties. However, it has poor out-of-plane properties, so it is vulnerable to delamination. Textile composite was developed to overcome those drawbacks by increasing the strength of laminate in all directions. Textile composite was also designed to have the ability to follow complex shapes. Furthermore, the fabrication of textile composites is cheaper and easier than the UD composite [1].

Several common types of textile composites are twill, 3D satin, and plain woven composite (PWC) [2, 3]. The characteristic of PWC that distinguishes it from the other textile composite is it has a warp and a fill intersect sequentially one above and one below to obtain a symmetrical shape. The advantage of PWC is that it has a high level of stability and acceptable porosity. Meanwhile, the drawback is PWC has low drape properties, namely the nature of textile composites to follow complex shapes while maintaining their properties [4].

A. L. Rini · T. Dirgantara · S. Wicaksono · K. K. Rumayshah · H. Judawisastra (✉)
Faculty of Mechanical and Aerospace Engineering, Institut Teknologi Bandung, Jl. Ganesha 10, Bandung 40132, Indonesia
e-mail: hermawan.judawisastra@material.itb.ac.id

© Springer Nature Singapore Pte Ltd. 2020

A. Praveen Kumar et al. (eds.), *Advances in Lightweight Materials and Structures*,
Springer Proceedings in Materials 8, https://doi.org/10.1007/978-981-15-7827-4_19

Tanov and Tabiei [5] developed a simplified semi-analytic model, and Aliabadi et al. [6] developed a numerical micromechanics model of PWC. Bacarreza et al. [1] showed that the mechanical properties of a PWC are influenced by so many factors, i.e., combination of yarn size, fiber orientation, fiber architecture, spacing between yarn, lamina stacking sequences, and fiber volume fraction. Therefore, a specific numerical model is needed for different type of fiber and matrix. Recently, Rumayshah et al. [7] performed micromechanics modeling of carbon/epoxy UD composite using periodical fiber idealization. It showed that the micromechanics model gives an excellent performance compared to the experiment and analytical model.

In this study, numerical micromechanics modeling of carbon/epoxy PWC is carried out by using a similar method as in the modeling of UD composite in [7]. The effect of fiber volume fraction on the composite elastic properties is analyzed. The obtained elastic properties are compared to the experiment [8], analytical [9], and numerical model [10].

2 Geometry Modeling

The type of PWC used in this analysis is EP121-C15-53 with HTA40 3 k carbon fiber and EP121 polymer matrix produced by Gurit Ltd. The warp and weft cross-sectional areas are assumed to have similar structure and properties, i.e., following a lenticular shape. The lenticular and waviness of the yarn are estimated using the cosine equation derived by Aliabadi et al. [6] and given in Eqs. 1 and 2, respectively.

$$y = 0.14 + 0.07\left(1 \pm \cos\left(\frac{\pi}{1.8}x\right)\right) \tag{1}$$

$$z = 0.07\left(1 - \cos\left(\frac{\pi x}{2}\right)\right) \tag{2}$$

Equations (1) and (2) are then modified into Eqs. (3) and (4) to fit the geometrical parameters B, C, and D as shown in Fig. 1.

$$y = D\cos\left(\frac{\pi x}{B}\right) \tag{3}$$

$$z = D\left(1 - \cos\left(\frac{\pi x}{C}\right)\right) \tag{4}$$

In performing the fiber volume fraction variation, the fiber fraction inside a yarn is assumed to be constant. Therefore, only the yarn fraction inside of the representative volume element (RVE) is taken into consideration. Equations (5)–(7) show the geometry formulation with the function of parameters B, C, and D. Figure 2 shows the resulted cross section of the RVE with three values of fiber volume fraction.

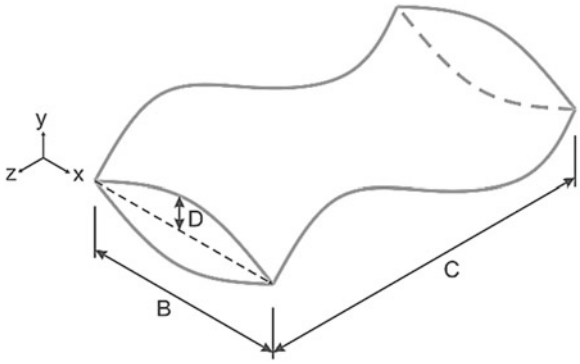


Fig. 1 Illustration of one yarn showing parameters *B*, *C*, and *D*

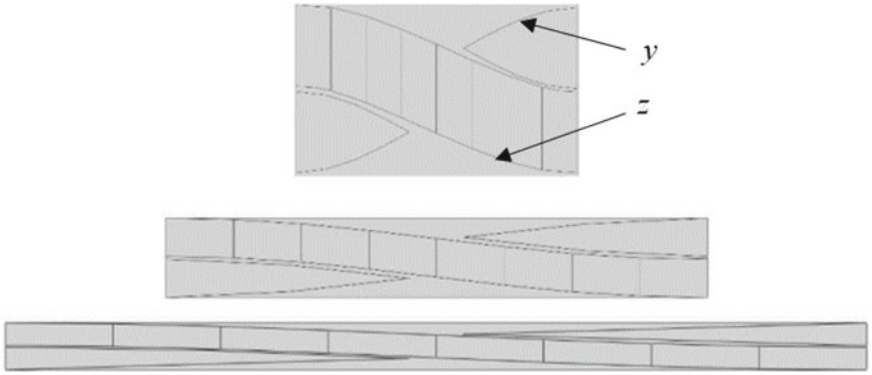


Fig. 2 Cross section of the RVE with the fiber volume fraction of 41, 43, and 45% (from top to bottom)

$$\phi_F = \frac{4V_y\phi_f}{V_{RVE}} \tag{5}$$

$$\phi_F = \frac{4\left(\frac{4DB}{\pi}\int_0^{2C}\sqrt{1+\left(\frac{D\pi}{C}\sin\frac{\pi x}{C}\right)^2}\mathrm{d}x\right)\phi_f}{4D(2C)^2} \tag{6}$$

$$\phi_F = \frac{B\phi_f\int_0^{2C}\sqrt{1+\left(\frac{D\pi}{C}\sin\frac{\pi x}{C}\right)^2}\mathrm{d}x}{\pi C^2} \tag{7}$$

Table 1 Material properties of the fiber and matrix [3]

Material	Property	Value	Unit
Carbon fiber HTA40 3k	E_{11}	161,640	MPa
	E_{22}	10,570	MPa
	G_{12}	5,520	MPa
	ν_{12}	0.27	–
	ν_{23}	0.33	–
Epoxy matrix EP121	E_m	3,110	MPa
	ν_m	0.36	–

3 Finite Element Modeling

The finite element modeling is carried out using Abaqus/CAE. Table 1 shows the material properties of the fiber and the matrix. A four-node linear tetrahedral element (C3D4) is used for the whole model. The application of periodic boundary condition and the calculation of the elastic properties are explained in detail by Rumayshah et al. [7]. The interface between matrix and yarn is assumed to be perfectly bonded.

4 Result and Analysis

4.1 The Stress Distribution

Figures 3a, 4a, 5a, and 6a show the von Mises stress distribution of the RVE due to normal longitudinal, normal transversal, shear longitudinal, and shear transversal, respectively. In the first three cases, there is a significant difference in the stress distribution between the yarn and the matrix because the fiber modulus is much higher than the matrix. Whereas in the latter case, i.e., transverse shear, the difference

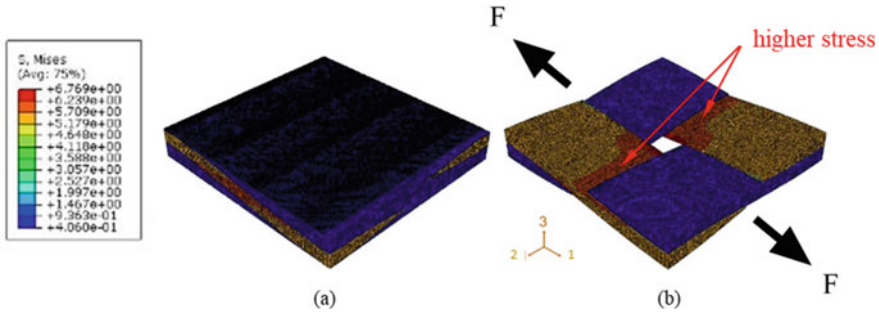


Fig. 3 Von Mises stress distribution in the **a** RVE and **b** only yarn due to normal longitudinal loading for the fiber volume fraction of 43%

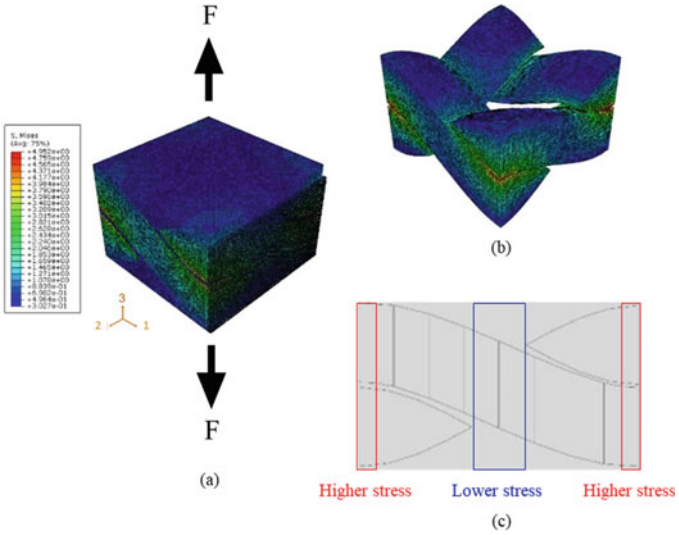


Fig. 4 Von Mises stress distribution in the **a** RVE and **b** only yarn due to normal transversal loading for the fiber volume fraction of 41%

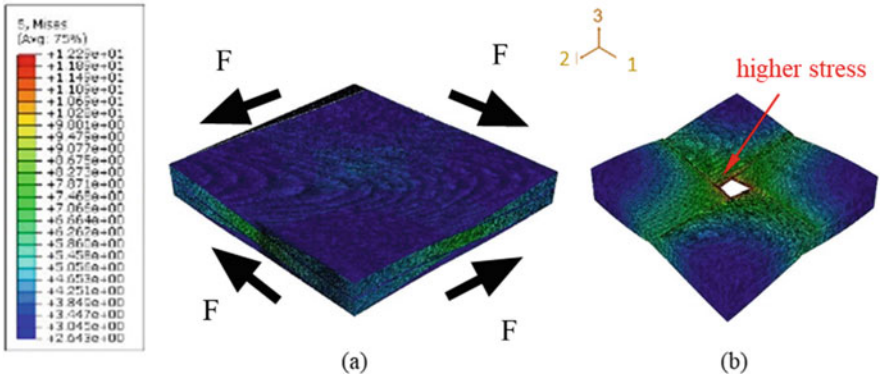


Fig. 5 Von Mises stress distribution in the **a** RVE and **b** only yarn due to longitudinal shear loading for the fiber volume fraction of 43%

in the stress distribution between yarn and matrix is not much different because both have almost similar shear modulus.

It is seen in Fig. 3 that the stress is only received by the yarn in the loading direction due to the transversely isotropic properties of the carbon yarn. There are several regions in the yarn that receive higher stress (indicated by red arrows in Fig. 3b) because there is a combination of tensile and shear load in those regions. Besides, the results of the fiber volume fraction variation prove that the slope of the

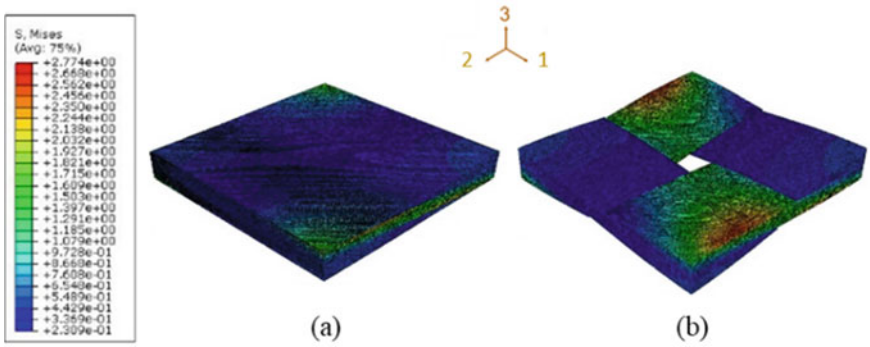


Fig. 6 Von Mises stress distribution in the **a** RVE and **b** only yarn due to shear transversal loading for the fiber volume fraction of 43%

crimp or the yarn waviness influences the stress distribution in normal longitudinal loading.

As seen in Fig. 4, the stress distribution difference between yarn and matrix due to normal transversal loading is not as significant as the normal longitudinal case. The highest stress occurs in the weft and warp stacking area because the highest value of local fiber volume fraction exists in that area. Meanwhile, Fig. 5 shows that stress is higher in the center of the RVE due to shear longitudinal loading. Both the normal transversal loading in Fig. 4 and shear longitudinal loading in Fig. 5 show that the weft and warp have similar stress distribution. Meanwhile, in shear transversal case, the stress is higher in the yarn aligned with the shear direction as shown in Fig. 6.

4.2 Comparison to the Other Model by Reference

The elastic properties resulted from the model developed in this research are compared to the experiment and the numerical model using the mesh-free Galerkin method [6]. The result is summarized in Table 2.

The E_{11} value obtained is lower than reference because there is a distance between yarn in the model so that it increases the volume of the matrix. The distance is added in purpose to make the geometry modeling easier. Also, the composite used in the experiment is a multiple-plies composite. Although the effect is not significant, Rahmani et al. showed that composite with more plies results in a higher tensile and flexural properties [11].

Table 2 Comparison of the elastic properties value for the fiber volume fraction of 43%

Properties	Experiment [6]	Numerical model [6]	Result		
			Value	Difference to experiment	Difference to numerical model (%)
$E_{11} = E_{22}$ [GPa]	50–55	53.68	48.51	−2.98%	−9.63
E_{33} [GPa]	–	9.09	7.32	–	−19.43
G_{12} [GPa]	–	3.56	3.19	–	−10.18
$G_{13} = G_{23}$ [GPa]	–	2.83	2.29	–	−19.05
ν_{12}	–	0.045	0.040	–	−11.55
$\nu_{13} = \nu_{23}$	–	0.409	0.453	–	10.72

4.3 The Effect of Fiber Volume Fraction

Figures 7, 8, and 9 show the effect of fiber volume fraction variation on the elastic properties of the RVE. The trend in elastic properties due to the change in fiber volume fraction is analyzed. The trend is compared to several references, i.e., the experiment result of twill composite by Karahan et al. [8], the analytical model of 3D satin composite by Liu et al. [9], and the numerical model of twill composite by Bostanabad et al. [10].

Figure 7 shows that the longitudinal elastic modulus increases logarithmically and the longitudinal Poisson's ratio decreases exponentially as the fiber volume fraction gets higher. These are because the fiber properties increasingly dominate the RVE

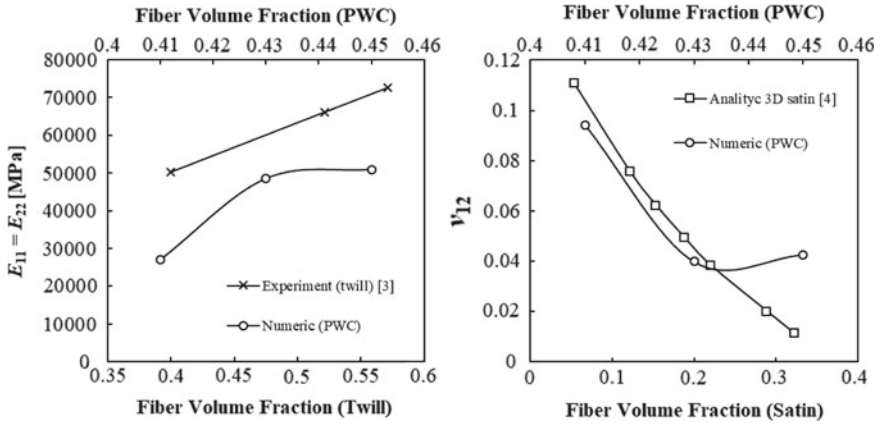


Fig. 7 Effect of fiber volume fraction to longitudinal elastic modulus (left) and longitudinal Poisson's ratio (right)

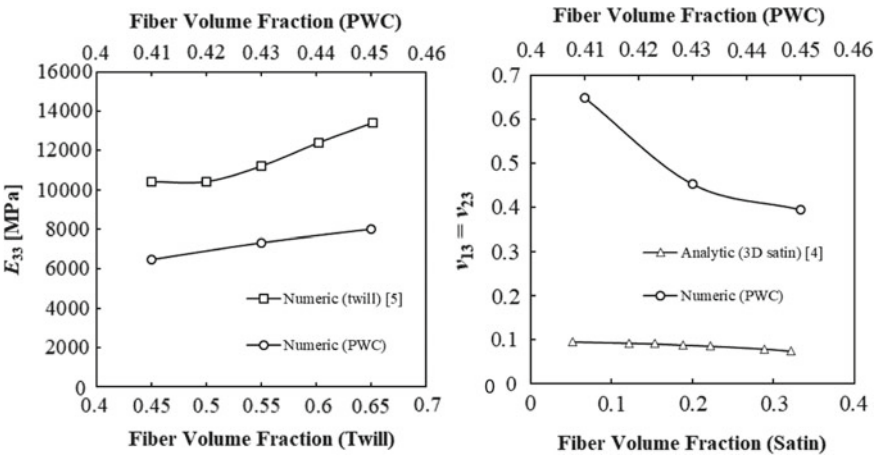


Fig. 8. Effect of fiber volume variation to transversal elastic modulus (left) and transversal Poisson's ratio (right)

as the fiber volume fraction gets higher. Fiber has a much higher longitudinal elastic modulus and lower longitudinal Poisson's ratio than matrix. Besides, the graphics in Fig. 7 shows a nonlinear relation between the elastic properties and the fiber volume fraction, which means that there is a crimp or waviness effect on the RVE stiffness in the longitudinal direction.

Figure 8 shows that higher fiber volume fraction results in higher transverse elastic modulus, although the increase is not as significant as the longitudinal direction. This is because the transverse elastic modulus of the fiber is only three times higher than the matrix. Meanwhile, the longitudinal elastic modulus of the fiber is 50 times higher than the matrix. Besides, Fig. 8 (left) shows a linear relation between fiber volume fraction variation and transverse elastic modulus. This shows that the crimp does not have a significant effect on the PWC stiffness in the transverse direction.

Figure 8 (left) shows that the increase of longitudinal shear modulus due to the increase of fiber volume fraction has a linear trend. This is in agreement with the numerical model result of the twill composite by reference. On the other side, Fig. 9 (right) shows that the value of transverse shear modulus tends to decrease linearly if the fiber volume fraction gets higher. This trend differs from the numerical model result of the twill composite by reference, where the modulus tends to increase. This shows that the geometry difference between plain woven and twill greatly influences the composite transverse shear modulus.

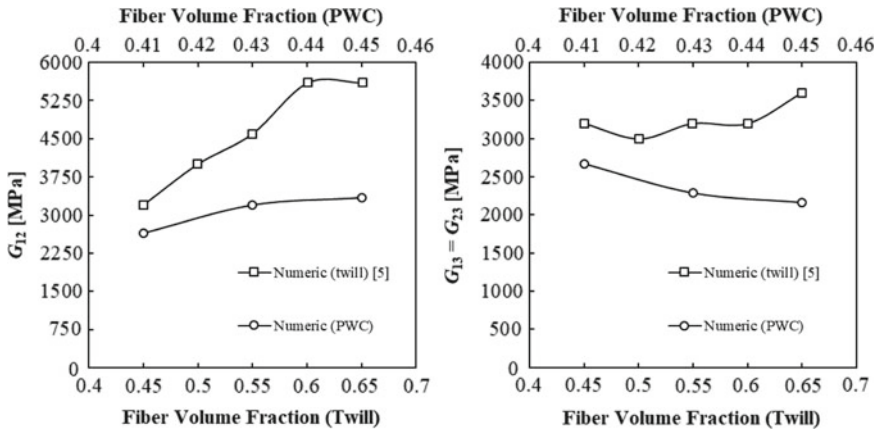


Fig. 9 Effect of fiber volume fraction to longitudinal shear modulus (left) and transversal shear modulus (right)

5 Conclusion

A numerical micromechanics modeling of carbon/epoxy plain woven composite is performed to estimate its elastic properties. Cosine equations were to define the waviness and the lenticular shape of the yarn cross section. The RVE model is loaded in four different cases, i.e., normal longitudinal, normal transversal, shear longitudinal, and shear transversal, to get the properties in all directions. The stress distribution between the yarn and matrix under all four loading conditions is analyzed. The result showed that the elastic properties are 2.98% different to the experiment result and less than 19.5% different to the mesh-free Galerkin numerical method. Besides, three RVEs with different fiber volume fraction are compared to analyze the effect of fiber fraction on the composite elastic properties. The trend is in a good agreement to experiment, analytical, and numerical model by reference using various types of textile composite other than plain woven composite.

Acknowledgements This research has been carried out by the partial support from Ministry of Research, Technology, and Higher Education of Republic Indonesia (Penelitian Dasar Unggulan Perguruan Tinggi, PDUPT 2021) and Institut Teknologi Bandung (Research and Community Service/P3MI 2021).

References

1. Bacarreza O, Wen P, Aliabadi MH (2015) Micromechanical Modelling of Textile Composite. Woven Composite. Imperial College Press, London, pp 1–74
2. Praveen Kumar A, Nalla Mohamed M (2018) A comparative analysis on tensile strength of dry and moisture absorbed hybrid kenaf/glass polymer composites. J Ind Textiles 47(8): 2050–2073

3. Praveen Kumar A, Jackson Irudhayam S, Naviin D (2012) a review on importance and recent applications of polymer composites in orthopaedics. Int J Eng Res Dev 5(2): 40–43
4. Praveen Kumar A, Nalla Mohamed M, Kurien Philips K, Ashwin J (2016) Development of novel natural composites with fly ash reinforcements and investigation of their tensile properties. Appl Mech Mater 852: 55–60
5. Tanov R, Tabiei A (2001) Computationally efficient micromechanical models for woven fabric composite elastic moduli. J Appl Mech Trans ASME 68(4):553–560
6. Aliabadi MH (2017) Multiscale analysis of damage and failure in advanced engineering materials: keynote lecture. In: Asian conference on experimental mechanics, pp 28–31, Aug 2017
7. Rumayshah KK, Dirgantara T, Judawisastra H, Wicaksono S (2020) Numerical micromechanics model of carbon fiber-reinforced composite using various periodical fiber arrangement
8. Karahan M (2015) The effect of fibre volume fraction on damage initiation and propagation of woven carbon-epoxy multi-layer composites. Text Res J 82(1):45–61
9. Liu F, Guan Z, Bian T, Sun W, Tan R (2017) A novel analytical curved beam model for predicting elastic properties of 3D eight-harness satin weave composites. Sci Eng Compos Mater
10. Bostanabad R, Liang B, Gao J, Kam W, Cao J (2018) Uncertainty quantification in multiscale simulation of woven fiber composites. Comput Method Appl Mech Eng 338:506–532
11. Rahmani H, Najafi SHM, Saffarzadeh-Matin S, Ashori A (2013) Mechanical properties of carbon fiber/epoxy composites: effects of number of plies, fiber contents, and angle-ply layers. Polym Eng Sci

Effect of Nano Fillers on the Mechanical Behavior of Mercerized Plain Weaved Flax Fabric Reinforced Polymer Composites



A. Praveen Kumar, M. Shunmugasundaram, S. Sivasankar, and N. K. Amudhavalli

Abstract The main reason of utilizing bio fibers and nano fillers as reinforcements in polymer composites is the enhanced toughness of the composite. The purpose of the current research study is to examine the influence of multi-walled carbon nanotubes (MW CNT) on the mechanical behavior of mercerized plain weaved flax fabric reinforced polymer composites prepared by using simple and economical hand layup method. The influence of MW CNT addition (1, 2 and 3 wt%) on the aforesaid characteristics was investigated experimentally. The results obtained showed that the 3 wt% of MW CNT fillers reinforced composites presented greater tensile and flexural strengths of 50.4 MPa and 64.8. MPa, respectively. The conclusions of this study exposed that the addition of nano fillers has a positive impact on the mechanical performance of flax fabric reinforced epoxy composites. These newly designed nano composites could be used as engineering structures for average load applications.

Keywords Tensile strength · Flax fabric · Nano fillers · Biodegradability · Lightweight

1 Introduction

Nano composite materials have been performing a significant role in lightweight structures for aerospace, automotive, defense, railway and marine applications. This is owing to their outstanding properties such as less weight, low cost, high stiffness and strength, corrosion resistance and resistance to thermal expansions for replacing

A. Praveen Kumar (✉) · M. Shunmugasundaram
Department of Mechanical Engineering, CMR Technical Campus, Hyderabad, Telangana 501401, India
e-mail: praveencmr18@gmail.com

S. Sivasankar
Department of Civil Engineering, CMR Technical Campus, Hyderabad, Telangana 501401, India

N. K. Amudhavalli
Department of Civil Engineering, CMR College of Engineering & Technology, Hyderabad 501401, India

© Springer Nature Singapore Pte Ltd. 2020

A. Praveen Kumar et al. (eds.), *Advances in Lightweight Materials and Structures*,
Springer Proceedings in Materials 8, https://doi.org/10.1007/978-981-15-7827-4_20

traditional metals [1–3]. Ecological and public concerns are encouraging the leading researchers and scientists to design and examine novel materials with enhanced properties for automotive structural applications. Such materials have an enhanced eco-friendly characteristics and an improved load-carrying capability [4, 5]. In this context, the nano filler reinforced bio fiber polymer composites are desired owing to their lightweight, recyclability and noticeable mechanical properties [6–8].

In this regard, the previous researchers have examined the mechanical performance of bio fiber polymer matrix composites reinforced with the various nano particles obtained from organic and inorganic sources [9, 10]. The particles like barium sulfate, kaolin, magnesium hydroxide, zinc oxide, etc., are inorganic nano fillers. Conversely, the cellulosic nano fillers such as coir, fly ash, nutshell powders, rice husk, carbon black derived naturally signify organic nano fillers. For instance, Hakamy et al. [11] examined the effect of calcined nanoclay fillers on the tensile properties of mercerized hemp fabric reinforced polymer composites. They reported that the tensile properties were enhanced by the addition of calcined nanoclay (CNC). Praveen Kumar et al. [12] examined the influence of nano fillers on the tensile strength of alkaline treated kenaf fabric reinforced epoxy composite and concluded that inclusion of nano fillers in polymer matrix can improve the tensile properties, but decreased the moisture resistance.

From the aforementioned literature studies, it was perceived that the inclusion of nano fillers in natural fabric composites had both merits as well as effects on enhancing the mechanical characteristics of the composite. As a result, it is significant to determine the selection of nano fillers and their proportion for its competent utilization to acquire the preferred characteristics. But, there were limited research studies available in the previous literature [13, 14] which investigated the influence of multi-walled carbon nanotubes on the tensile and flexural properties of bio fabric polymer composites. The present research study is concentrated on the fabrication of mercerized flax fabric with the inclusion of MW CNT particles blended polymer matrix to improve the preferred tensile and flexural characteristics of the bio composite.

2 Materials and Fabrication Method

A renowned cellulosic source woven flax fabric was utilized as primary reinforcement of the composite in this study. LY556 type epoxy resin along with the HY951type hardener was employed as materials for the matrix and mixed in the proportion of 10:1 as proposed by the supplier. To enhance the tensile and flexural properties, multi-walled carbon nanotubes was utilized as secondary reinforcement blended with the polymer matrix of various proportions. In the beginning, the woven flax fabrics were cut into the required size and chemically treated with an prepared alkaline solution of 6% sodium hydroxide (mercerization treatment) as suggested by the previous researcher [12] prior to fabrication of the proposed composite laminates.

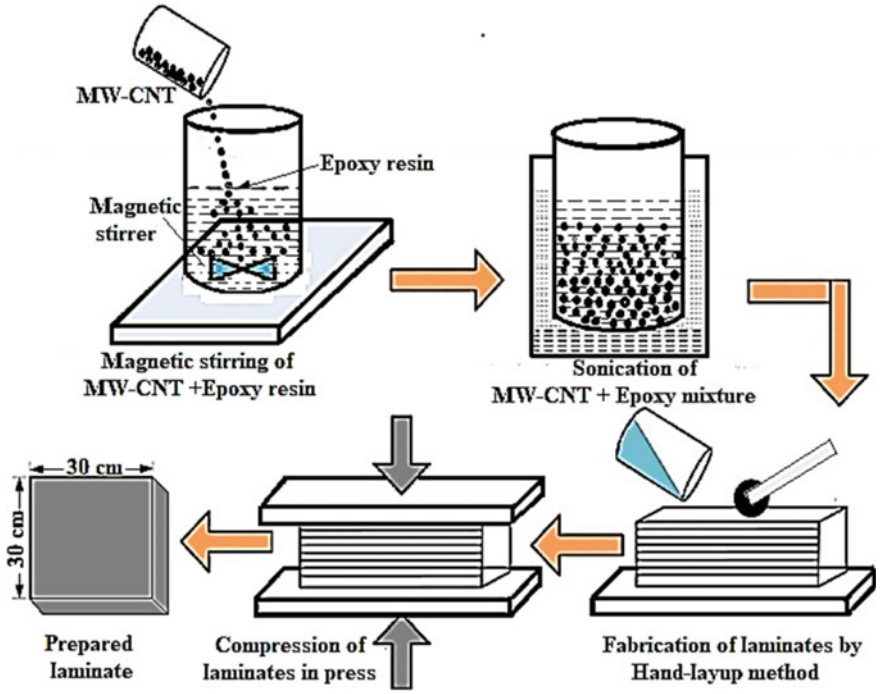
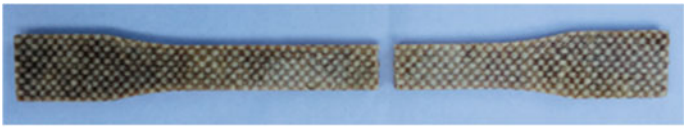


Fig. 1 Fabrication process of laminates

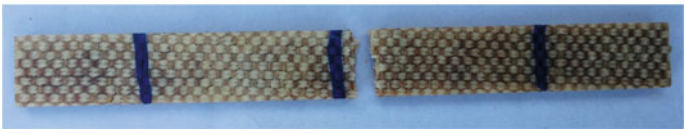
In the current research study, all the composite laminates were fabricated using the simple economic hand layup technique. In the beginning, the epoxy polymer resin was blended with multi-walled carbon nanotubes fillers at different weight proportions (1, 2, and 3%) for 3–5 min in a magnetic stirrer. Then, the hardener was dispersed in the 10:1 part (resin: hardener), and it was stirred again for 5 min to make a uniform mixture. Plywood mold of dimensions 0.31 m * 0.31 m * 0.05 m was utilized for the fabrication of the proposed composite plates. First layer was applied with the prepared resin mixture, and subsequently, the flax fabric was placed over it in the mold. The same steps have to be repeated for further layers. The overall fabrication process of the prepared composite plates is displayed in Fig. 1. The successfully fabricated composite plates were cured at room temperature of 25 0C by applying compression load for 24 h.

3 Results and Discussion

The effect of nano fillers on the mechanical behavior of mercerized plain weaved flax fabric reinforced polymer composites has been experimentally examined and discussed as follows. The tensile test is usually executed on universal testing machine



(a) Fractured tensile test sample



(b) Fractured flexural test sample

Fig. 2 Tested samples (4F configuration)

Table 1 Tensile and flexural test results

Composite samples designation	Tensile strength (MPa)	Flexural strength (MPa)
Epoxy	21.2	35
4F	37.428	48.72
4F + 1% N	42.818	52.29
4F + 2% N	46.159	58.31
4F + 3% N	50.405	64.81

(UTM) by the prepared dog-bone sample as shown in Fig. 2 based on the ASTM D638 standard, and the gauge length of the test sample used is 160 mm. Flexural test was also performed on UTM by the prepared rectangular sample in accordance with ASTM D790 standard. Samples of 127 mm length and 3 mm wide were pierced from the laminate and were loaded in three point bending as shown Figure in 2. The obtained tensile and flexural test results of the various percentages of MW CNT filler reinforced composite samples are shown in Table 1.

The comparative results on the tensile strength of MW CNT nano filler reinforced flax fabric polymer composites are presented in Fig. 3. The inclusion of MW CNT filler particles in the flax fabric composites showed better tensile properties than the traditional flax fabric composites.

From Table 1, it is witnessed that the tensile strength of neat epoxy resin is 21.2 MPa. When only laminates of flax fabric are reinforced with epoxy, it is found to be 37 MPa and 77% greater than the unreinforced epoxy matrix. It can be also noted that the flax fabric polymer composites with the addition of 1% MW CNT particles (4F + 1% N) composites showed better tensile strength of about 12% when related with the 4F composites. Furthermore, increasing the filler content to 2 and 3%, the tensile strength was improved to 10 and 11%, respectively. This is owing to the reason that the inclusion of nano MWCNT filler could confine movement of

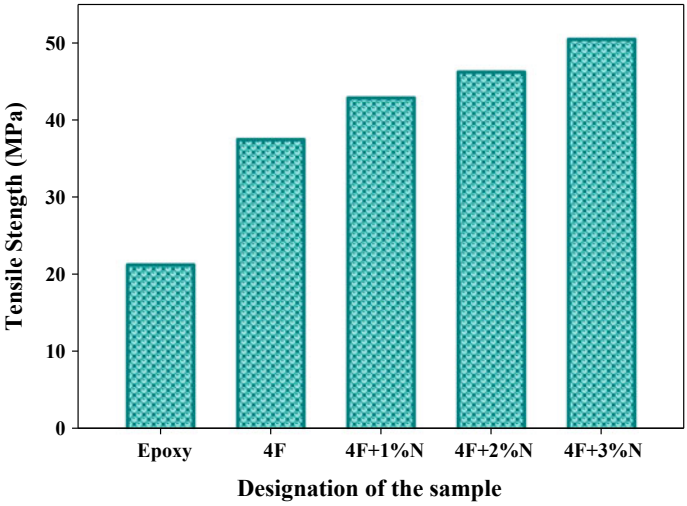


Fig. 3 Comparison of tensile strength of flax fabric composites with MW CNT fillers

the polymer matrix and shares stress to the nano MWCNT fillers, which absorb a portion of the applied force.

The comparative results on the flexural strength of MW CNT nano filler reinforced flax fabric polymer composites are illustrated in Fig. 4. Due to the reinforcement of flax fabric into the epoxy resin, the flexural properties of the composites increase to a great amount. The results showed that the inclusion of MW CNT filler particles

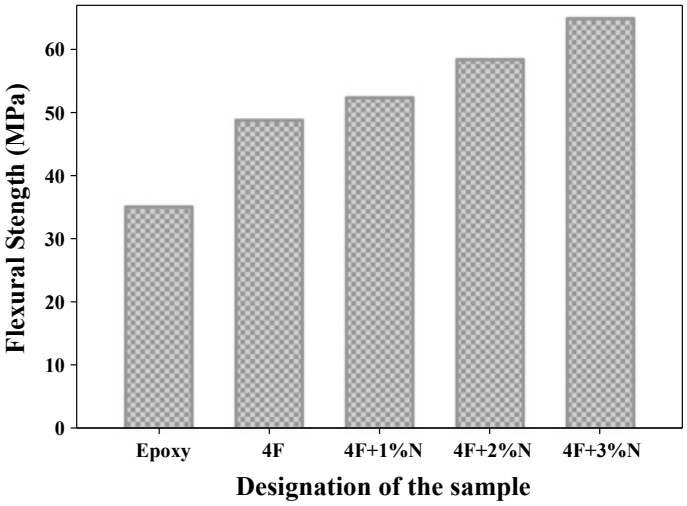


Fig. 4 Comparison of flexural strength of flax fabric composites with MW CNT fillers

(3 wt%) in the flax fabric composites showed better flexural strength by 33 percent compared to the flax fabric composites (4F). From the figure, it is also obvious that the rate of flexural strength improves with the percentage of reinforcement of MW CNT filler into the flax fabric composites.

4 Conclusions

The current research work was performed to examine the influence of nano filler addition with epoxy matrix on enhancing the tensile and flexural properties of flax fabric bio composite laminates. The main outcomes of the present study could be summarized as follows:

- The tensile strength of (4F + 3%N) composite laminate was 35% greater than the tensile strength of flax fabric composites without nano filler (4F) composite.
- The flexural strength of (4F + 3%N) composite was 33% better than the flexural strength of the traditional chemically treated flax fabric (4F) composites
- The overall outcomes of this study are encouraging to utilize the newly designed nano composites as body structures in automotive industries owing to their better tensile and flexural properties.

References

1. Rafiee MA, Rafiee J, Wang Z, Song H, Yu ZZ, Koratkar N (2009) Enhanced mechanical properties of nanocomposites at low graphene content. ACS Nano 3(12):3884–3890
2. Young RJ, Kinloch IA, Gong L, Novoselov KS (2012) The mechanics of graphene nanocomposites: a review. Compos Sci Technol 72(12):1459–1476
3. Praveen Kumar A, Jeyalal P, Barani Kumar D (2012) Hybridization of polymer composites. Int Adv Mater Sci 3: 173–182
4. Godovsky DY (2000) Device applications of polymer-nanocomposites. In: Biopolymers· PVA hydrogels, anionic polymerisation nanocomposites. Springer, Berlin, Heidelberg, pp 163–205
5. Praveen Kumar A, Jackson Irudhayam S, Naviin D (2012) A review on importance and recent applications of polymer composites in orthopaedics. Int J Eng Res Dev 5(2): 40–43
6. Wang H, Zeng C, Elkovitch M, Lee LJ, Koelling KW (2001) Processing and properties of polymeric nano-composites. Polym Eng Sci 41(11):2036–2046
7. Praveen Kumar A, Nalla Mohamed M, Kurien Philips K, Ashwin J (2016) Development of novel natural composites with fly ash reinforcements and investigation of their tensile properties. Appl Mech Mater 852: 55–60
8. Hassan SF, Gupta M (2005) Development of high performance magnesium nano-composites using nano-Al2O3 as reinforcement. Mater Sci Eng A 392(1–2):163–168
9. Wetzel B, Haupert F, Zhang MQ (2003) Epoxy nanocomposites with high mechanical and tribological performance. Compos Sci Technol 63(14):2055–2067
10. Miao C, Hamad WY (2013) Cellulose reinforced polymer composites and nanocomposites: a critical review. Cellulose 20(5):2221–2262

11. Hakamy A, Shaikh FUA, Low IM (2015) Effect of calcined nanoclay on microstructural and mechanical properties of chemically treated hemp fabric-reinforced cement nanocomposites. Constr Build Mater 95:882–891
12. Praveen Kumar A, Nalla Mohamed M (2018) A comparative analysis on tensile strength of dry and moisture absorbed hybrid kenaf/glass polymer composites. J Ind Text 47(8): 2050–2073
13. Saba N, Paridah MT, Abdan K, Ibrahim NA (2016) Effect of oil palm nano filler on mechanical and morphological properties of kenaf reinforced epoxy composites. Constr Build Mater 123:15–26
14. Hossen MF, Hamdan S, Rahman MR, Rahman MM, Liew FK, Lai JC (2015) Effect of fiber treatment and nanoclay on the tensile properties of jute fiber reinforced polyethylene/clay nanocomposites. Fibers Polym 16(2):479–485

Tensile and Bending Characteristics of Hybrid Basalt Fabric–Aluminium Laminates Reinforced with MW-CNT Fillers



A. Praveen Kumar, S. Lohith Reddy, D. Nageswararao, and L. Ponraj Sankar

Abstract The latest developments in the area of hybrid materials evidenced the advantages of fibre metal laminates (FMLs) over the conventional homogeneous materials in automotive structures. In the current research study, tensile strength and flexural strength of aluminium alloy basalt fabric laminate with and without multi-walled carbon nanotubes (MW-CNT) fillers were compared. The proposed laminate sheets were fabricated using the conventional hand layup method, and the test samples were pierced from the fabricated laminates according to ASTM standards. Subsequently, uni-axial tensile test and three-point bending test were performed on the Universal Testing Machine. The results revealed that the tensile and flexural properties of the proposed FMLs were enhanced considerably after the incorporation of MW-CNT nanofillers into the epoxy matrix. These types of newly designed FML could be used as body components in automotive applications.

Keywords Tensile strength · Basalt fabric · Nanofillers · Fibre metal laminate · Lightweight · Structures

1 Introduction

Fibre metal laminates are novel hybrid materials composed of thin metal alloy sheets and various layers of composite materials merging the merits of metals and composite systems. Metals are usually isotropic in nature and have a high tensile strength and bending resistance, while composite systems have high strength and outstanding energy absorption characteristics [1,2]. These materials can perform a significant role in lightweight structures for aerospace, automotive, and marine applications owing to their excellent properties such as less weight, low cost, high stiffness and strength, corrosion resistance, and resistance to thermal expansions for replacing traditional

A. Praveen Kumar (✉) · S. Lohith Reddy · D. Nageswararao
Department of Mechanical Engineering, CMR Technical Campus, Hyderabad 501401, India
e-mail: praveencmr18@gmail.com

L. Ponraj Sankar
Department of Civil Engineering, CMR Institute of Technology, Hyderabad 501401, India

© Springer Nature Singapore Pte Ltd. 2020

A. Praveen Kumar et al. (eds.), *Advances in Lightweight Materials and Structures*,
Springer Proceedings in Materials 8, https://doi.org/10.1007/978-981-15-7827-4_21

materials [3,4]. With outstanding mechanical properties, various nanofiller materials such as fly-ash, nanoclay, and carbon nanotubes are considered as best strengthening phases to the epoxy matrix to enhance its physical and mechanical properties [5].

In this regard, the previous researchers have examined the mechanical behaviour of fibre metal laminates reinforced with various organic and inorganic nanofillers [6, 7]. For instance, Jen et al. [8] examined that the addition of 1 wt.% SiO_2 nanofillers into the matrix gives rise to the increase in tensile strength and stiffness of carbon fabric-reinforced polymer, with slight enhancement in fatigue characteristics. Chan et al. [9] examined the interaction of nanoclay in the epoxy polymer matrix composites. They concluded that the inclusion of 5 wt.% nanoclay enhances tensile strength and Young's modulus by 25% and 34%, respectively. Chowdhury et al. [10] studied the influence of nanofillers on the bending characteristics of carbon fabric/epoxy composites. The results obtained revealed that incorporation of 2 wt.% nanoclay improves the bending strength of the composites by 14%. Nevertheless, rising the amount of nanoclay to 3 wt.% reduces bending properties because of nanoclay agglomeration.

From the above-mentioned studies, it was perceived that the addition of nanofillers in fibre metal laminates had positive effects on improving the mechanical properties. As a result, it is significant to determine the proportion of nanofillers to obtain the preferred characteristics. But, the influence of multi-walled carbon nanotubes on the tensile and flexural properties of the FML [2,11] has not been well explored in the literature. The current research work is focused on the fabrication of aluminium alloy-based basalt fabric laminates with the inclusion of MW-CNT particles blended polymer matrix to enhance the preferred tensile and bending characteristics.

2 Materials and Fabrication Method

In this study, Aluminium AA 6061 alloy was utilized as the outer skin of the FML. In the core composite, plain weaved basalt fabric of 210 GSM procured from the local supplier was utilized as reinforcement of the composite. LY556 type epoxy resin along with the HY951type hardener was employed as materials for the matrix and mixed in the proportion of 10:1 as proposed by the supplier. To enhance the mechanical properties, MW-CNTs were utilized as filler reinforcement blended with the polymer matrix of different proportions (1, 2, and 3 wt.%). Initially, the woven basalt fabrics were cut into the required size prior to fabrication of the proposed FML.

In the current research study, all the FMLs were fabricated using the simple hand layup method. In the beginning, the epoxy polymer resin was blended with multi-walled carbon nanotubes fillers at different weight proportions for 3–5 min in a magnetic stirrer. Then, the hardener was dispersed in the 10:1 part (resin: hardener), and it was stirred again for 5 min to make a uniform mixture. Plywood mould was utilized for the fabrication of the proposed composite plates. First, aluminium sheet was placed and the subsequent layer was applied with the prepared resin mixture,

and then, the basalt fabric was placed over it in the aluminium sheet. The same steps has to be repeated for further layers. Finally, the aluminium sheet was placed over the composite segment. The overall fabrication process of the prepared FML is displayed in Figs. 1 and 2. The successfully fabricated FMLs were cured at room temperature of 25 °C by applying compression load for 24 h.

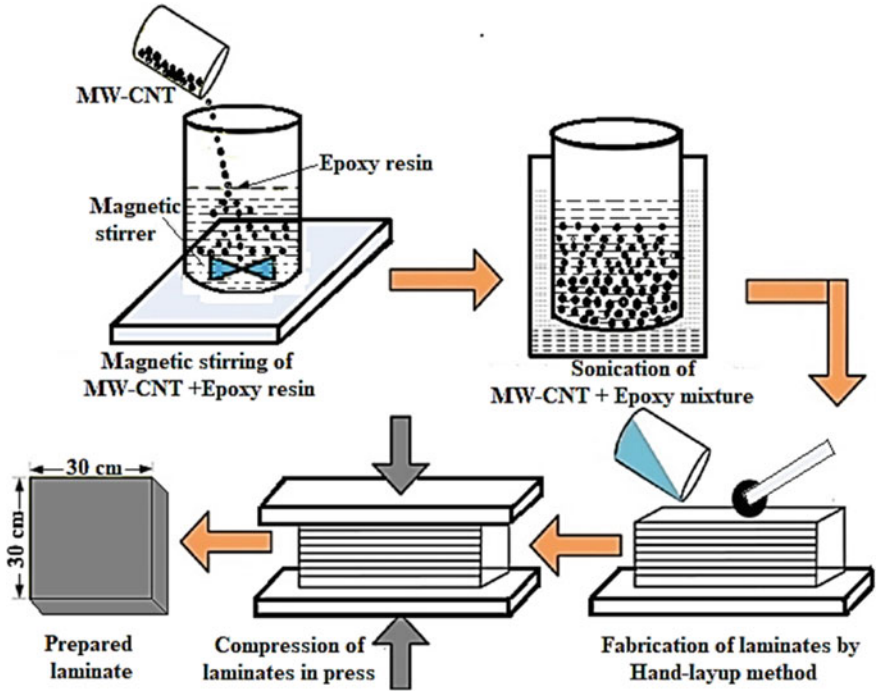


Fig. 1 Fabrication process of laminates

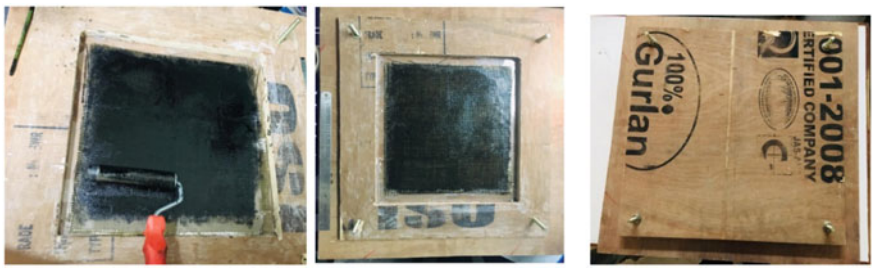
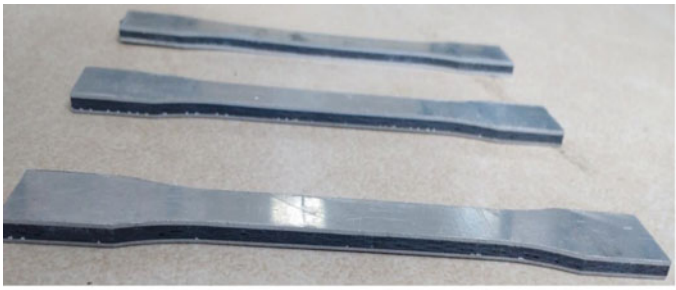


Fig. 2 Hand layup process

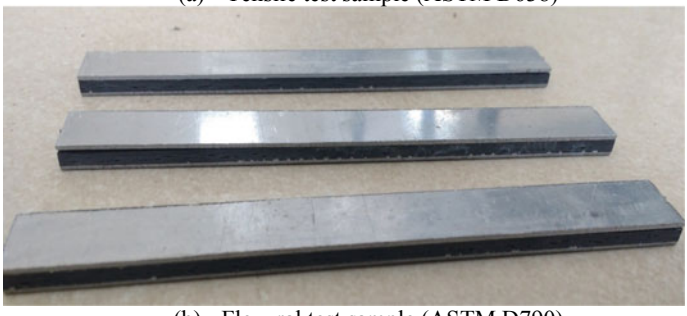
3 Results and Discussion

In the present study, the influence of MW-CNT nanofillers on the tensile and bending characteristics of aluminium alloy-based plain weaved basalt fabric-reinforced epoxy composite laminates has been investigated experimentally and discussed as follows. In order to determine the tensile strength, the uni-axial tensile test is performed on Universal Testing Machine (UTM) by the prepared dog-bone sample as shown in Fig. 3 in accordance with based on the ASTM D638 standard and the gauge length of the test sample used is 160 mm. In order to determine the flexural strength, three-point bending test was also did on UTM by the prepared test sample ASTM D790 standard. Samples of 127 mm length and 3 mm wide were pierced from the laminate and were loaded in three-point bending as shown in Fig. 3. The fractured test samples are presented in Fig. 4, and the obtained tensile and flexural test results of various percentages of MW-CNT filler-reinforced FML are shown in Table 1.

The outcomes on the tensile strength of aluminium alloy-based basalt fabric-reinforced epoxy composite laminates incorporated with various percentages of MW-CNT nanofillers are shown in Fig. 5. The addition of MW-CNT filler particles in the FML showed superior tensile strength than the traditional FML. From Table 1, it is witnessed that the tensile strength of laminates without nanofillers is found to be 188 MPa, but with the addition of 1% MW-CNT fillers (AB1N), it showed better



(a) Tensile test sample (ASTM D638)

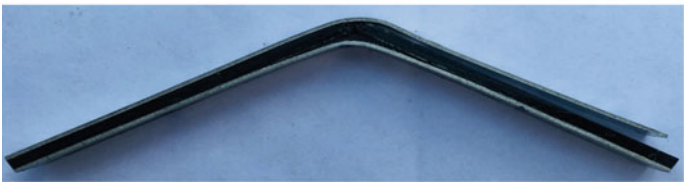


(b) Flexural test sample (ASTM D790)

Fig. 3 Prepared standard test samples



(a) Fractured tensile test sample



(b) Fractured flexural test sample

Fig. 4 Tested samples (AB2N configuration)

Table 1 Tensile and flexural test results

Laminate designation	Tensile strength (MPa)	Flexural strength (MPa)
AB	188	340
AB1N	200	368
AB2N	214.36	430
AB3N	203	375

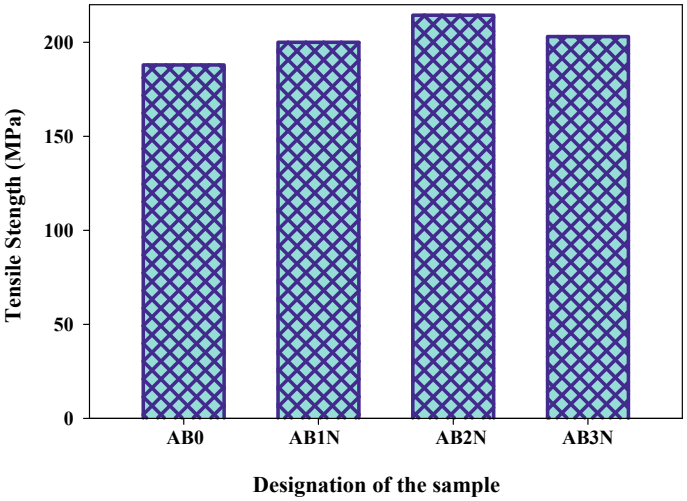


Fig. 5 Tensile strength results with various % of MW-CNT fillers

tensile strength of about 6% when related with the traditional (AB) laminates. Moreover, increasing the filler content to 2%, the tensile strength was improved to 13%. This is owing to the reason that the inclusion of nano-MW-CNT filler could confine movement of the polymer matrix and shares stress to the nano-MW-CNT fillers, which absorb a portion of the applied force. However, further increasing filler content to 3%, the tensile strength decreased by 5% due to the agglomeration of nanofillers which may lead to improper bonding between the composite and aluminium alloy.

The three-point bending test results on the determination of flexural strength of aluminium alloy-based basalt fabric-reinforced epoxy composite laminates incorporated with various percentages of MW-CNT nanofillers are illustrated in Fig. 6. Due to the reinforcement of flax fabric into the epoxy resin, the flexural properties of the composites increase to a great amount. It can be inferred from the plot that AB1N (1 wt. of nanofiller) laminates enhanced the flexural strength of about 8%. and further increasing the filler content to 2%, the flexural strength was increased to 26% when compared with the AB laminates. The MW-CNT nanofillers included in the epoxy matrix performed as proficient stress sharing agent in the AB2N laminates, prompting plastic distortion into the epoxy matrix, and enhances the flexural strength.

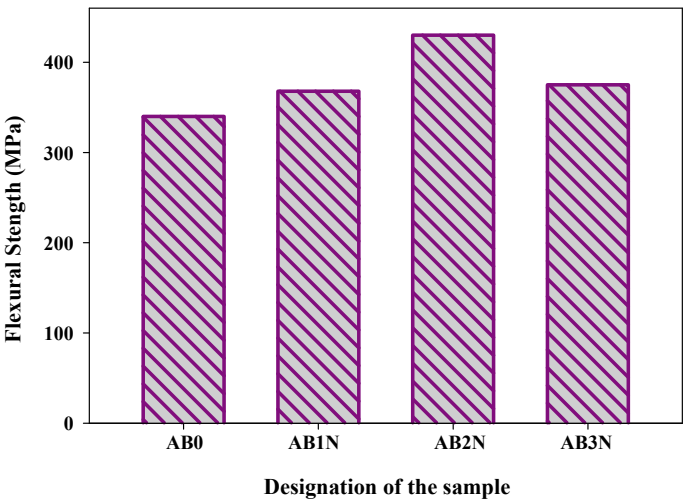


Fig. 6 Flexural strength results with various % of MW-CNT fillers

4 Conclusion

The present research study was performed to examine the influence of MW-CNT nanofiller addition with epoxy matrix on enhancing the tensile and flexural properties of the aluminium alloy-based basalt fabric-reinforced epoxy composite laminates. The main outcomes of this study could be summarized as follows: the tensile strength of (AB2N) laminate was 13% greater than the tensile strength of traditional (AB) laminates without nanofillers. The flexural strength of (AB2N) laminate was 26% better than the flexural strength of the traditional (AB) laminates without nanofillers. The overall outcomes of this study are promising to apply the newly designed aluminium alloy-based basalt fabric-reinforced epoxy composite laminates as body structures in aircraft manufacturing industries owing to their lightweight and better mechanical properties.

References

1. Botelho EC, Silva RA, Pardini LC, Rezende MC (2006) A review on the development and properties of continuous fiber/epoxy/aluminum hybrid composites for aircraft structures. Mater Res 9(3):247–256
2. Dhaliwal GS, Newaz GM (2016) Experimental and numerical investigation of flexural behavior of carbon fiber reinforced aluminum laminates. J Reinforced Plast Compos 35:945–956
3. Praveen Kumar A, Jeyalal P, Barani Kumar D (2012) Hybridization of polymer composites. Int J Adv Mater Sci 3:173–182
4. Gonzalez-Canche NG, Flores-Johnson EA, Carrillo JG (2017) Mechanical characterization of fiber metal laminate based on aramid fiber reinforced polypropylene. Compos Struct 172:259–266
5. Vermeeren CAJR (2003) An historic overview of the development of fiber metal laminates. Appl Compos Mater 10:189–205
6. Khan SU, Iqbal K, Arshad Munir, Kim JK (2011) Quasi-static and impact fracture behaviors of CFRPs with nanoclay-filled epoxy matrix. Compos Part A 42:253–264
7. Chai GB, Manikandan P (2014) Low velocity impact response of fiber-metal laminates—a review. Compos Struct 107:363–381
8. Jen RMH, Tseng YC, Wu CH (2005) Manufacturing and mechanical response of nano composite laminates. Compos Sci Technol 65:775–779
9. Chan ML, Lau KT, Wong TT, Ho MP, Hui D (2011) Mechanism of reinforcement in NCPs/polymer composite. Compos B 42:1708–1712
10. Chowdhury FH, Hosur MV, Jeelani S (2006) Studies on the flexural and thermo mechanical properties of woven carbon/NCPs-epoxy laminates. Mater Sci Eng A 421:298–306
11. Khosravi H, Eslami-Farsani R (2016) On the mechanical characterizations of unidirectional basalt fiber/epoxy laminated composites with 3-glycidoxy propyl trimethoxy silane functionalized multi-walled carbon nanotubes-enhanced matrix. J Reinforced Plast Compos 35(5):421–434

Effect of Silicon Carbide Particle Size on the Physical and Mechanical Properties of Hierarchical Layered Composite Material



Mulugundam Siva Surya and G. Prasanthi

Abstract Hierarchical layered composites are novel materials whose properties change gradually concerning their dimensions. These are light in weight and better in performance when compared to traditional composites. These have vast applications in the field of automobile and aerospace industries. In this research, to study the effect of silicon carbide particle size (37 and 60 μm) on physical and mechanical properties, two hierarchical composites with four and five layers were prepared through powder metallurgy. The microstructural characteristics of hierarchical layered composites are examined by scanning electron microscope (SEM); Rockwell and Charpy impact tests measure its mechanical properties hardness and toughness. Due to the presence of high silicon carbide content, the five-layered specimens exhibited better mechanical properties compared to four-layered specimens. The hierarchical composites' physical and mechanical properties are greatly influenced by silicon carbide's weight percentage and size.

Keywords Hierarchical layered composites · Al-SiC · Powder metallurgy · Microstructure and mechanical properties of composites

1 Introduction

Functionally graded materials (FGMs) find plenty of applications in engineering, especially in the fields of automobile, aerospace, electronics, defence industries and gas turbine engines [1, 2]. Owing to their stiffness, strength-to-weight ratio, corrosion and wear resistance, aluminium-based metal matrix composites are widely used [3]. In aluminium metal matrix composites, non-metallic and ceramic particles like SiC, Al_2O_3, B_4C and graphite are used as reinforcements, and among all, SiC and Al_2O_3 are widely used [4, 5]. Owing to its better mechanical properties, the absence of detrimental reactions at high temperatures and thermodynamic stability with aluminium

M. S. Surya (✉) · G. Prasanthi
Department of Mechanical Engineering, JNTUA, Ananthapuramu, India
e-mail: sivasurya.mtech@gmail.com

© Springer Nature Singapore Pte Ltd. 2020

A. Praveen Kumar et al. (eds.), *Advances in Lightweight Materials and Structures*,
Springer Proceedings in Materials 8, https://doi.org/10.1007/978-981-15-7827-4_22

as compared to other non-metallic and ceramic particles, SiC is a suitable reinforcement [6, 7]. Distribution of ceramic reinforcements in the matrix material is examined by the microstructural characterization [8–10]. In this work, hierarchical layered composites with different wt.% and particle size of SiC are manufactured and tested for their strength and microstructure behaviour to the applied loads.

2 Experimentation

The two different SiC particles 60 and 37 μm are used to prepare four- and five-layered test specimens by varying wt.% of SiC and aluminium powders in each layer.

SAMPLES 1 and 2: The four-layered two specimens are prepared with different wt.% of SiC. Samples 1 and 2 contain SiC particle size of 60 μm and 37 μm, respectively. The compositions are shown in Table 1.

SAMPLES 3 and 4: The five-layered two specimens are prepared with different wt.% of SiC. Samples 3 and 4 contain SiC particle size of 60 μm and 37 μm, respectively. The compositions are shown in Table 2.

Powder metallurgy route is selected to manufacture the hierarchical layered composite, as it is the most suitable method to obtain composition gradient and homogenous distribution. Four specimens were manufactured with varying SiC content from one layer to the other in each sample. The weight percentages of SiC in different samples are mentioned in Tables 1 and 2. Different mixtures of aluminium silicon carbide are prepared as per weight fractions in Table 1 and 2. Weight of

Table 1 Details of samples 1 and 2

Layers	% of SiC	% of Al	Weight of SiC (gm)	Weight of Al (gm)
1	0	100	0	2.94
2	3	97	0.09	2.85
3	7	93	0.21	2.73
4	10	90	0.3	2.64

Table 2 Details of samples 3 and 4

Layers	% of SiC	% of Al	Weight of SiC (gm)	Weight of Al (gm)
1	10	90	0.24	2.112
2	20	80	0.48	1.872
3	30	70	0.72	1.632
4	40	60	0.96	1.392
5	50	50	1.2	1.152

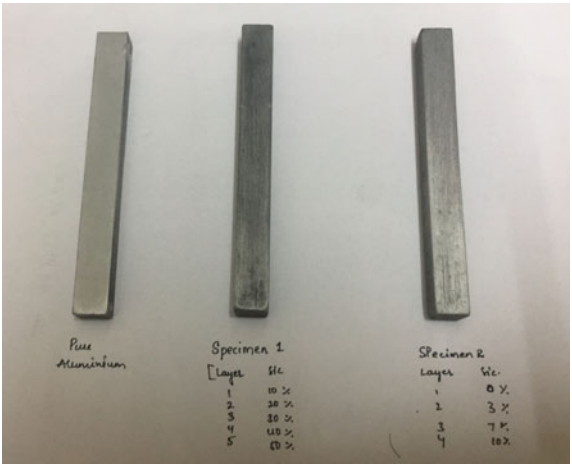


Fig. 1 Specimens after sintering

each sample was around 12 g. Composition of each sample was calculated, and the constituents were mixed using a ball milling machine with the ball-to-powder ratio 10:1 to obtain a uniform composition. 2% magnesium is added to the mixture as a binder. Ball-milled powders are filled in a layer by layer. Different mixtures are poured into die layer by layer with different sizes and wt.% of SiC; they are then cold-pressed by applying 100 KN force using Universal Testing Machine. Green samples are subjected to sintering process in inter-gas furnace. The sintering temp is raised 5 °C/min to attain temp of 510 °C and holding for 3 h. After furnace cooling, specimens are taken out as shown in Fig. 1. The samples are tested under a scanning electron microscope for studying their microstructure. The hardness and toughness values are obtained by Rockwell's hardness testing machine and Charpy impact testing machine.

3 Results and Discussions

3.1 Microstructure

Figure 2(a–d) shows the SEM microstructure images of four aluminium and silicon carbide hierarchical layered composites with 150× magnification. While examining, it is clearly evident that the number of voids is more, and uniform porosity was observed in Fig. 2a than in Fig. 2b, which will lead to the change of mechanical properties.

From the thorough examination, it has been observed in Fig. 2c, and d that 37 μm particle size represents good bonding nature images, less number of voids and very low agglomeration has been formed on Charpy impact test specimen at cutaway section. The porosity of the fourth specimen is less when compared with the

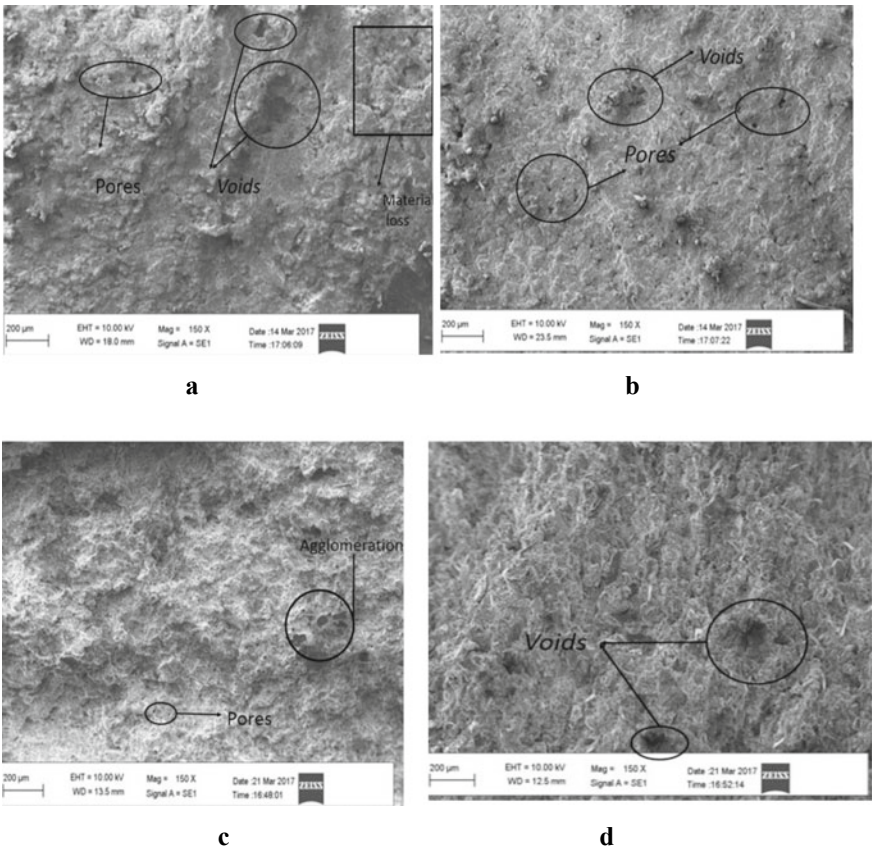


Fig. 2 (a–d) Microstructure of 60μm four-layered specimen, Microstructure of 60μm fivelayered specimen, Microstructure of 37μm four-layered specimen and Microstructure of 37μm five-layered specimen

remaining specimens through microstructure examination leading to better results. As the reinforcement particle size is small, it has been contributed more for better bonding with the aluminium matrix.

3.2 Hardness

The Rockwell's hardness test is conducted on each layer of samples with 100 kgf load for a dwell period of 15 s, and the values are recorded, as shown in Table 3. Figure 3 and Fig. 4 show the hardness values of four-layered and five-layered hierarchically composite with 37 μm and 60 μm, respectively. Figure 4 shows that the hardness values increase with an increase in SiC percentage. From Fig. 4, it is also clear that the

Table 3 Hardness values of all samples

No. of layer	%SiC for sample 1 and 2	Rockwell hardness number		%SiC for sample 3 and 4	Rockwell hardness number	
		Sample 1 60 μm	Sample 2 37 μm		Sample 3 60 μm	Sample 4 37 μm
1	0	41.3	43.3	10	40.6	53.6
2	3	42.6	47.3	20	43.8	55.6
3	7	45.1	49.5	30	45.1	57.6
4	10	46.3	50	40	46.6	60.5
5				50	47.3	61.3

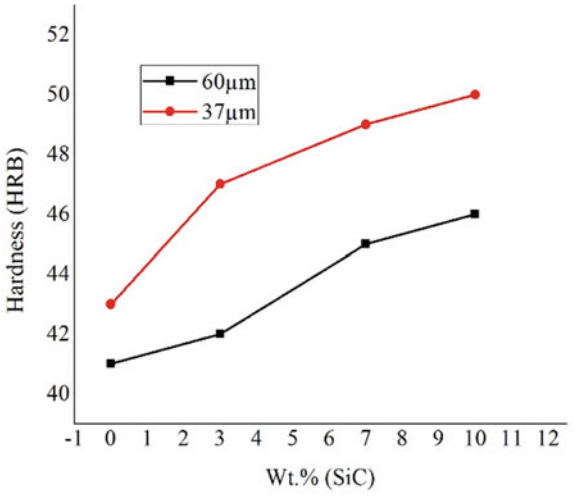


Fig. 3 Hardness values of four-layered specimens with 37 and 60 μm particle size

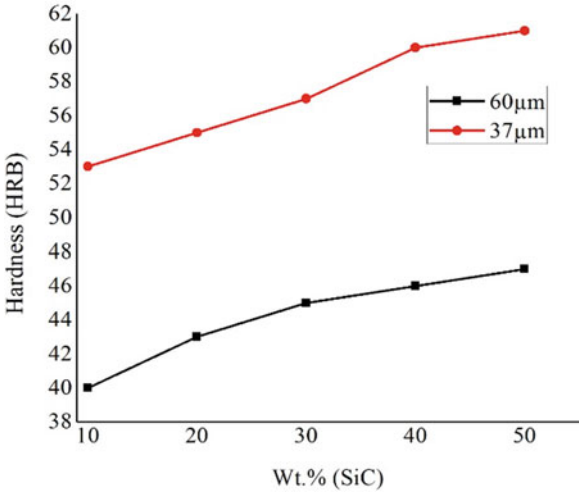


Fig. 4 Hardness values of five-layered specimens with 37 and 60 μm particle size

Table 4 Impact resistance values

S. No.	Specimen	Impact resistance (J)
1	Pure aluminium (S1)	2.6
2	37 μm four-layered (S2)	2.4
3	37 μm five-layered (S3)	3.6
4	60 μm four-layered (S4)	2.2
5	60 μm five-layered (S5)	3.0

hardness values of five-layered specimens are higher than four-layered specimens. In the five-layered specimens, the specimen with smaller particles size 37 μm has exhibited reasonably good hardness; as the SiC particle size decreases, there are more chances of uniform distribution and less chances of formation of voids and agglomerations.

3.3 Charpy Test

The Charpy impact test specimen standard dimensions are 55 mm × 10 mm × 10 mm with a V-notch of depth 2 mm which is hit through a sudden load, and its values are given as shown in the Table 4.

The mechanical properties of pure aluminium are less compared to hierarchical layered composites because the hierarchical composites have SiC reinforcement which will increase the properties. From Fig. 5, it is clearly evident that with 37 μm size reinforcement, hierarchical composite specimens are giving good results compared with 60 μm size. The hardness and Charpy results were comparatively high

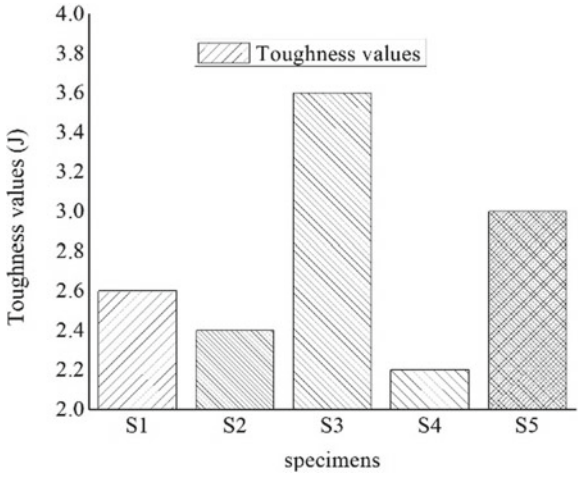


Fig. 5 Values of impact resistance of five specimens in joules

for five-layered 37 μm size specimens when compared with four-layered 37 μm size specimen.

4 Conclusions

The hierarchical layered composites are successfully produced by powder metallurgy route. The composite with five layers of SiC has exhibited better mechanical properties than four-layered composites. The silicon carbide composite with 37 μm particle size showed better results than 60 μm particle size composite. Smaller the size of silicon carbide particles, higher the chance of uniform distribution, lower the chance of agglomeration and formation of voids which leads to better mechanical properties. The hierarchical layered composites properties are influenced by reinforcement weight percentage and particle size.

References

1. Erdemir F, Canakci A (2015) Microstructural characterization and mechanical properties of functionally graded Al2024/SiC composites prepared by powder metallurgy techniques. Trans Nonferrous Met Soc China 25:3569–3577
2. Zhang N, Khan T et al (2019) Functionally graded materials: an overview of stability, buckling, and free vibration analysis. Adv Mater Sci Eng 2019:1–18
3. Habibur Rahman M, Mamun Al Rashed HM (2014) Characterization of silicon carbide reinforced aluminum matrix composites. Proc Eng 90:103–109
4. Surya MS, Prasanthi G (2019) Manufacturing and mechanical behavior of (Al/SiC) functionally graded material using powder metallurgy technique. Int J Innov Technol Expl Eng (IJITEE) 8(9):1835–1839
5. Surya MS, Prasanthi G (2018) Tribological behaviour of aluminum silicon carbide functionally graded material. Tribol Ind 40(2):247–253
6. Nuruzzaman DM, Kamaruzaman FB (2016) Processing and mechanical properties of aluminium-silicon carbide metal matrix composites. In: IOP conference series: materials science and engineering, vol 114
7. Sattari S, Jahani M (2017) Effect of volume fraction of reinforcement and milling time on physical and mechanical properties of Al7075–SiC composites. Powder Metall Met Ceram 56(5–6):283–292
8. Bhattacharyya M, Kumar AK (2008) Synthesis and characterization of Al/SiC and Ni/Al2O3functionally graded materials. Mater Sci Eng 524–535
9. Venkatesh B, Harish B (2015) mechanical properties of metal matrix composites (al/SiC) particles produced by powder metallurgy. Int J Eng Res General Sci 3(1):1277–1284
10. Praveen Kumar A, Meignanamoorthy M, Ravichandran M (2018) Influence of sintering temperature and the amount of reinforcement on the microstructure and properties of Al–TiO2 composites. Int J Mech Eng Technol 9(9):826–832

Mechanical Properties of Aluminum Wire-Reinforced GFRP Laminates



J. Jayapriya, D. Muruganandam, and C. Balasubramaniyan

Abstract Composite materials or composites in short are engineered materials in which a combination of two or more materials with different mechanical properties are mixed together to form a single structure with an identifiable interface and it remains separate within the finished structure. However when more than one material is combined together in such types of composites, we are unable to achieve the required mechanical property. In order to overcome this problem, we are inserting aluminum wire into GFRP laminates under two conditions, namely plain aluminum wire and twisted aluminum wire. This chapter mainly focuses on analyzing and studying about the characteristics of GFRP, GFRP with plain aluminum wire and GFRP with twisted aluminum wire. The mechanical properties which are examined and inferred are ultimate tensile strength, flexural strength and impact strength. The study of these properties is performed on 1/4th thick and 7 mm pitch laminates. Based on the results obtained, the properties are studied and the switch board is fabricated.

Keywords Aluminum wire embedded GFRP · Ultimate tensile strength · Impact strength · Flexural strength

1 Introduction

The inherent properties of natural fiber-reinforced composites are better, and thus, the mechanical properties are far better than synthetic reinforced polymer composites. There are several tests carried out to enhance mechanical properties like tensile strength, impact and flexural strength with different fiber volume and they were evaluated by Shaw et al. [1]. The results clearly show that there is drastic improvement in mechanical properties as stated by Angioni et al. [2]. The availability of fabricated composite plates of glass fiber in the form of flattened sheets is high. It has several

J. Jayapriya
Sathyabama Institute of Science and Technology Chennai, Chennai, India

D. Muruganandam (✉) · C. Balasubramaniyan
Sri Venkateswaraa College of Technology, Chennai, India
e-mail: murudurai@gmail.com

© Springer Nature Singapore Pte Ltd. 2020

A. Praveen Kumar et al. (eds.), *Advances in Lightweight Materials and Structures*,
Springer Proceedings in Materials 8, https://doi.org/10.1007/978-981-15-7827-4_23

advantages and holds good mechanical properties when compared to synthetic fibers. Several experiments were carried out to diagnose tensile, flexural properties of glass fiber in three variants. From the observation, it was found that both tensile and flexural strength of glass fiber increases as its thickness increases as suggested by Batra et al. [3]. It was also suggested that glass fibers had profound usage in moderate weight applications. The interfacial shear strength of glass fiber/epoxy bonding in composites modified with carbon nano-tubes was studied and found that interfacial shear strength increases when fiber sizing is modified along with carbon nano-tubes. The improvements in mechanical and thermomechanical properties of e-glass/epoxy composites using amino functionalized MWCNT's were characterized by dynamic mechanical analysis and found that there is an increase in trend in properties to a stronger level of mechanical and thermomechanical properties of the composites as suggested by Khondker et al. [4, 5]. Liao et al. [6] investigated on mechanical properties and behavior of glass fiber-reinforced silica aero gel nano-composites. Insights from all atom simulations found that by using molecular dynamics simulations, the tensile strength, elastic modulus and compressive behavior of silica aero gel were improved by adding glass fibers. Pickering et al. [7] experimented on mechanical properties and abrasion behavior of glass fiber-reinforced polymer composites and compared them with the experimental results of open literature. Sailesh et al. [8] carried out fabrication, testing and evaluation of mechanical properties of natural fiber composite material and found that there is an increase in properties of hybrid composites as it gets treated well to withstand the resistance offered by external resource.

Munoz et al. [9] reviewed on mechanical properties of natural flax fiber-reinforced polymer hybrid composite. Ricciardia et al. [10] investigated on mechanical properties of glass fiber composites based on nitrile rubber toughened modified epoxy resin and suggested that there is improvement in shear failure stress and shear failure strain. Praveen Kumar et al. [11] suggest that the latest composites produced by using treated kenaf fiber polymer composites in addition to fly ash as another reinforcement yields higher tensile strength. There is a considerable increase in the tensile strength of producing unique and newer composites than the conventional ones. Limited research has been carried out in the field of glass fiber-reinforced polymer with embedded aluminum wires. There is a need for studying the mechanical properties of such GFRPs in order to improve its application in the fiber based industries. In this work, we have fabricated Virgin glass fiber-reinforced polymer in two ways such as aluminum wire embedded GFRP and short fibers added aluminum wires embedded GFRP. The various mechanical properties like tensile strength, flexural strength and impact strength of these materials were analyzed. The properties of aluminum wires embedded GFRP are not widely reported, which forms a unique part of this work.

2 Materials and Fabrication

2.1 Materials

By hand lay-up method, synthesis of Virgin GFRP, aluminum wire embedded GFRP and short fibers added aluminum wires embedded GFRP were tested for properties like tensile strength and flexural strength. Using Instron machine, three point bend method was incorporated and checked the flexural and tensile strength. Impact properties of the laminates to be studied with an experimental setup were designed and the impact strength of the laminates was analyzed by drop weight method. GFRP, GFRP with plain aluminum wire and GFRP with twisted aluminum wire fiber laminates reinforced aluminum were fabricated. Aluminum wires and short fibers at quarter depth and second with ¾th depth with the thickness and as in the last replica of the specimens were tested reacted natural frequency effectively. The specimen with wire at ¾th depth showed greater strength when compared with the other specimens. On continuous observation, the frequency reacted to pitch distance of combined wire at ¾th depth only. The samples with aluminum wires were embedded at different pitch distances. The aluminum wires have been combined centrally and spaced at various pitch distances with the thickness in various directions. To observe the active functioning of the GFRP composites, the laminates were filled with plain aluminum wires and twisted aluminum wires and they were manufactured. Dynamic and static mechanical properties were checked for four layers of the laminated composites. It is recorded that addition of the aluminum wire reinforcement in the composites improved the mechanical properties of flexural, tensile and impact strength. Considerable improvement in mechanical properties was recorded with added in 7 mm pitch aluminum wire in composites.

2.2 Fabrication of Specimens

The reinforcement used here is both directional plain woven glass fiber and woven mat. Fabrication of the specimen of 3 laminae, 1×1 m^2 mat is taken and dimensioned to get three pieces of 300×300 mm. Considering the wastage and edge clearance, the dimensions of the layer size were fabricated by leaving a tolerance of 2 mm. The resin used in this case is epoxy LY556 with hardener HY 591. The manufacturing of the sample is weighed with the reinforcement. The required amount of resin is used such that the fiber to resin ratio is 1:1, if the weight of the reinforcement is 80 g. Some quantity of hardener is taken such that the resin to hardener ratio is 100:50. 40 g of hardener is mixed with the resin using stirrer. On application of the releasing agent to the thin sheet, the resin is not stuck to the lamination sheet. The lamination layer when applied over the epoxy resin keeps a bidirectional e-glass fiber woven cloth (Fig. 1).



Fig. 1 Aluminum wire-reinforced GFRP

Now using the roller, squeeze out the air pockets and the excess resin. Similarly keep all four mats one over the other and apply epoxy resin over it and remove the air pockets and excess resin using roller. Now place a coat on the lamination with releasing agent on top of the materials, the surface shining will be obtained. The laminate is cured with a load of 50 Kgs for 24 h at ambient temperature to procure the composite.

3 Mechanical Properties

3.1 Ultimate Tensile Strength Testing

The specimens used for recording the ultimate tensile strength were prepared as per the standard ASTM D3039. Three samples each were subjected to tensile load from laminates prepared with plain GFRP, GFRP with plain aluminum wire and GFRP with twisted aluminum wire. The stress–strain characteristics for the breaking load and extensions are studied for the composite laminates (Fig. 2).



Fig. 2 Tensile specimen GFRP

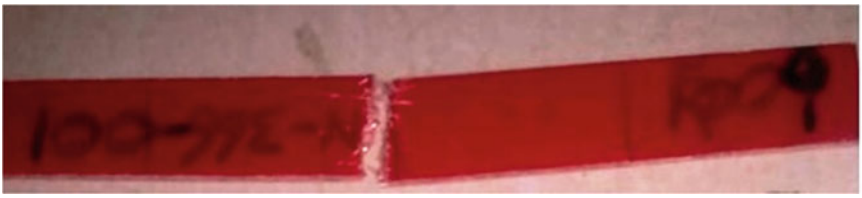


Fig. 3 Flexural test specimen GFRP

3.2 Flexural Testing

The flexural test is taken to evaluate the flexural strength and modulus of the laminates. A three point bending load was applied to the specimen that was prepared to the ASTM D790 standard. The deflection and breaking loads were measured and the flexural test was taken on the laminates using Instron flexural testing machine with cross head speed of 1 mm/min. The flexural strength of the composite laminate with 1/4th thickness and 7 mm pitch was having lesser flexural strength when compared with the specimen without aluminum wire (Fig. 3).

3.3 Impact Testing

The Izod impact strength test is used to study the impact in order to evaluate the energy stored in the laminates. A sudden load was applied and forced on to the specimen that was prepared to ASTM D256 standard. The high energy absorbed by the specimen before plastic deformation was observed.

4 Results and Discussion

4.1 Tensile Test Results

The tensile test was conducted on plain GFRP, GFRP with aluminum wire and GFRP with twisted aluminum wire laminates as per the ASTM D3039 standard and the ultimate tensile strength of the samples are documented as follows (Table 1 and Fig. 4).

From the tabulated results, we observe that GFRP with twisted aluminum wire has relatively higher tensile strength when compared with the other laminates.

Table 1 Ultimate tensile strength results

S. No.	Specimen	Ultimate tensile strength (MPa)
1	Plain GFRP	102
2	GFRP with plain aluminum wire	132
3	GFRP with twisted aluminum wire	163

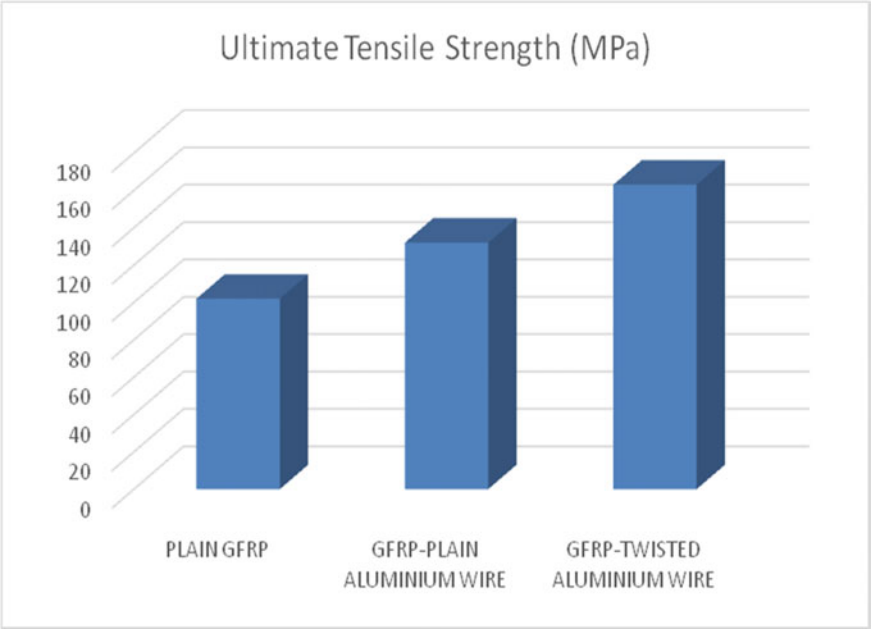


Fig. 4 Ultimate tensile strength comparison

4.2 Flexural Test Results

From the three point flexural test conducted on jute, aloevera and its hybrid composite specimens as per the ASTM D790 standard, the flexural strength of the samples are documented as follows (Table 2).

From the tabulated results, it is observed that plain GFRP laminates have relatively higher flexural strength as compared with GFRP with twisted aluminum wire. However, the GFRP with plain aluminum wire has a drop in the impact strength test which is a major point of concern (Fig. 5).

Table 2 Flexural strength results

S. No.	Specimen	Flexural strength (MPa)
1	Plain GFRP	125
2	GFRP with plain aluminum wire	112
3	GFRP with twisted aluminum wire	120

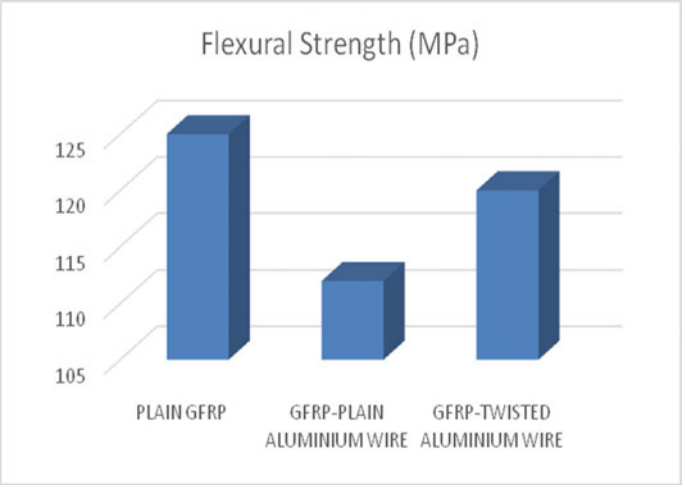


Fig. 5 Flexural strength comparison

4.3 Impact Test Results

The impact strength test performed on plain GFRP, GFRP with plain aluminum wire and GFRP with twisted aluminum wire as per the ASTM D256 standard and the impact strength of the samples are tabulated as follows (Table 3 and Fig. 6).

From the recorded results, it is documented that the impact strength of both GFRP with plain as well as twisted aluminum wire comes out to be same and it is greater than plain GFRP laminates.

Table 3 Impact test results

S. No.	Specimen	Impact strength results (MPa)
1	Plain GFRP	0.38
2	GFRP with plain aluminum wire	0.5
3	GFRP with twisted aluminum wire	0.51

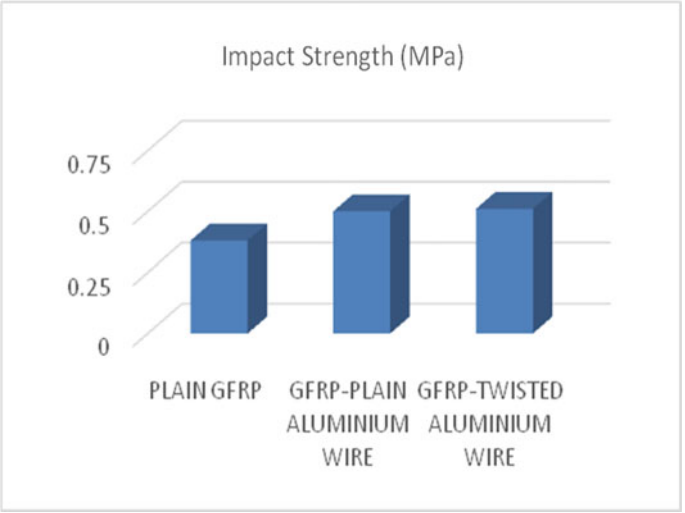


Fig. 6 Impact strength comparison

5 Conclusions

In order to increase the mechanical properties in this, hybrid laminates were made to know the effect of combination of various natural fibers. The mechanical tests performed on the composite specimens can be summarized as:

- Ultimate tensile test has been carried out as per ASTM D3039 standard and it shows that GFRP laminates with twisted aluminum wire shows an increase of 37.42% in comparison with plain GFRP laminates and 19.01% in comparison with GFRP having straight aluminum wire embedded. The increase in the tensile strength is a due to the inclusion of twisted aluminum wire which results in significant improvement in the tensile strength.
- Flexural strength of the GFRP laminates with twisted aluminum wire as well as plain aluminum wire is slightly lesser than that of plain GFRP Laminates. The role of aluminum wire added to the GFRP laminate is insignificant, and hence, the flexural strength is not improved in aluminum wire added GFRP.
- The Izod impact test has been conducted experimentally and results were analyzed in a graph for plain GFRP and aluminum wire embedded GFRP laminates. The inclusion of aluminum wire increases the energy stored. Impact strength increases by around 25.4% with twisted aluminum wire in comparison with plain GFRP laminates. However, the cases of plain aluminum wire and twisted aluminum wire do not differ much in terms of impact strength.
- The mechanical properties have improved significantly due to the addition of twisted aluminum wire in hybrid composites because the inclusion of aluminum wire increases the energy stored in the GFRP laminates.

References

1. Shaw A, Sriramula S, Peter D, Gosling Marios K, Chryssanthopoulos (2010) A critical reliability evaluation of fibre reinforced composite materials based on probabilistic micro and macro-mechanical analysis. Compos Part B 41:446–453
2. Angioni SL, Meo M, Foreman A (2011) impact damage resistance and damage suppression properties of shape memory alloys in hybrid composites, a review. Smart Mater Struct 20, 013001:24
3. Batra RC, Gopinath G, Zheng JQ (2012) Damage and failure in low energy impact of fibre-reinforced polymeric composite laminates. Compos Struct 94:540–547
4. Khondker OA, Hamada H et al (2006) A novel processing technique for thermo-plastic manufacturing of unidirectional composites reinforced with jute yarns. Compos Part A Appl Sci Manuf 37(12):2274–2284
5. Khondker OA et al (2006) Mechanical properties of textile-inserted PP/PP knitted composites using injection-compression molding. Compos Part A Appl Sci Manuf 37(12):2285–2299
6. Liao Y, Huijun Wu, Ding Y (2012) Engineering thermal and mechanical properties of flexible fiber-reinforced aerogel composites. J Sol-Gel Sci Technol 63:445–456
7. Pickering KL et al (2016) A review of recent developments in natural fibre composites and their mechanical performance. Compos Part A 83:98–112
8. Sailesh A et al (2018) Mechanical properties and wear properties of kenaf-aloe vera-jute fiber reinforced natural fiber composites. Mater Today Proc 5(2), Part 2:7184–7190
9. Munoz E et al (2018) Water absorption behaviour and its effect on the mechanical properties of flax fibre reinforced bio epoxy composites. Int JPolym Sci (2), Part 2:7184–7190
10. Ricciardia MR, Papa I, Langella A, Lopresto V, Antonuccia V (2018) Mechanical properties of glass fibre composites based on nitrile rubber toughened modified epoxy resin. Compos B Eng 139:259–267
11. Praveen Kumar A, Nalla Mohamed M, Kurien Philips K, Ashwin J (2016) Development of novel natural composites with fly ash reinforcements and investigation of their tensile properties. Appl Mech Mater 852:55–60

Investigations on the Tensile and Flexural Properties of Vacuum-Infused Areca Polymer Nanocomposites

M. Shunmugasundaram, A. Praveen Kumar, N. K. Amudhavalli, and S. Sivasankar

Abstract The main aim of this investigation effort is to examine the influence of nanofiller material in tensile and flexural characteristics of vacuum-infused natural fiber-based polymer matrix composites. In most of the research, only one nanomaterial is used for developing new composites. In this research, natural fiber and two nanofiller materials are used to develop new composites by vacuum infusion molding method. Areca fiber is chosen as reinforcement material, and epoxy LY556 resin is considered as a matrix material for developing this natural fiber materials-reinforced polymer matrix composites. The areca fiber polymer matrix composites and areca fiber nano-infused composites are prepared to check the tensile and flexural characteristics of areca fiber composite and the influence of nanofiller materials (graphene and multi-walled nanocarbon tubes). An average of 7.49 and 21.92% ultimate tensile strength and flexural strength of polymer matrix composite by adding nanofiller materials develop nano-infused natural fiber polymer matrix composites.

Keywords Areca fiber · Epoxy resin · Vacuum infusion molding; graphene · Multi-walled carbon nanotubes · Tensile strength · Flexural strength

1 Introduction

Environmental consciousness and regulation force the industry to search for alternative products that are more environmentally sustainable. Scientists and technologists have shown the interest of natural-based fiber materials such as coir, cotton, jute, sisal, and other natural fibers [1–3] and the need to identify natural fibers

M. Shunmugasundaram (✉) · A. Praveen Kumar
Department of Mechanical Engineering, CMR Technical Campus, Hyderabad 501401, India
e-mail: sundarprithiv@gmail.com

N. K. Amudhavalli
Department of Civil Engineering, CMR College of Engineering & Technology, Hyderabad 501401, India

S. Sivasankar
Department of Civil Engineering, CMR Technical Campus, Hyderabad 501401, India

© Springer Nature Singapore Pte Ltd. 2020

A. Praveen Kumar et al. (eds.), *Advances in Lightweight Materials and Structures*,
Springer Proceedings in Materials 8, https://doi.org/10.1007/978-981-15-7827-4_24

with outstanding manufacturing, mechanical, and physical properties to be used as replacements in polymer composites to satisfy the necessitate in the natural fiber-based composites industry [4, 5]. The natural fiber-based composites have been found to possess mechanical strength and other characteristics with greater conductivity, strong thermal, and acoustic thermal insulation properties [6–8]. The growing attention in reinforcing different natural-based materials has covered the way for expanded investigation activities in this natural fiber area. The plant-based fiber is having excellent mechanical characteristics, and these fibers are researched as suitable candidates for polymer matrix reinforcements [9]. In this analysis, the polyester resin utilized fibers extracted from the areca palm tree, widely known as areca palm or areca nut fruit, or Pinang, are selected as reinforcing material for developing composite materials. The common name areca derives from a term that was used historically on India's Malabar Coast [10]. Areca fiber is extremely hemicellulosic and somewhat broader than all other fibers. Using areca fibers as potential reinforcement in epoxy-Ly556 and the functional efficiency of epoxy-Ly556 resin may be significantly enhanced through adding such fibers, based on previous studies [11, 12].

While various studies have been performed on the mechanical behavior of natural fiber-based composites, there are very few researchers on areca fiber-based reinforced composites. Areca tends to be a popular commodity of all the natural fiber reinforcement.

Because it is less expensive, plentiful and also a very large potential perpetual seed. Several important constraints such as fiber width, modulus of elasticity of fiber, fiber weight, direction, and banding between fiber material and matrix material intensity depend on the mechanical properties of a natural fiber-reinforced composite. For the efficient transfer of load from the matrix material to the composite fiber material, a strong interfacial connection is needed [13–15].

In this research work, the areca is selected as reinforcement and the epoxy-LY556 resin is considered as a matrix for developing natural fiber-based reinforced polymer matrix composites. The graphene and carbon multi-walled nanotubes improve tensile and flexural strength of areca fiber-based reinforced polymer matrix composites.

2 Material Selection and Development Methods

2.1 Selection of Materials

2.1.1 Areca Fiber

Areca fiber is small and possessing a very low aspect ratio and the strength of the fiber-based on the length and diameter of the selected fiber. Areca fiber is extremely hemicellulosic, far wider than most other fibers. These fibers are strong in cellular form and exhibit resemblance to coir fibers. The composites were made using picked

areca fruit husks. About five days of dry areca husk was immersed in deionized mud. The soaking phase loosens the fibers and they are easy to remove. After that, the fibers were cleaned with deionized water again and then dehydrated for around 15 days at normal temperature. The dry fiber materials are classified as non-treated natural fibers. These areca fibers are bought from era composites, Chennai, Tamilnadu, India.

2.1.2 Nanomaterials

Nanofiller-infused polymer composites have tremendous promise in numerous biomedical applications. Also, biodegradation is a significant feature of these applications and can be regulated by integrating sufficient nanomaterials into the required polymer matrices. Due to the fillers, these excellent properties give these polymers a strong potential for usage in aeronautics, the automobile, telecommunications, medical devices, and consumer goods. The graphenes and multi-walled carbon nanotubes are chosen for developing this nano-infused polymer matrix composites. The graphene is selected because it is compact construction and the tight covalent bond between carbon atoms, 200 times stronger than steel, and extremely lightweight. The carbon nanotubes are often picked because of their lower thermal conductivity, lower electrical conductivity, very high tensile power, extremely resilient, and substantially bent without damage.

2.2 Fabrication of Composites

Vacuum infusion molding method is adopted for developing this polymer and nano-infused polymer matrix composites. This process is increasing adhesion between the matrix material and reinforcement material, and due to this bonding, tensile and flexural characteristics are improved in the developed polymer composite materials. The important parts of this setup are vacuum pump, vacuum chamber, and vacuum film (see Fig. 1.)

Four species of untreated areca are extracted with a size of 25 × 25 (cm) with a weight of 220 g. The Ly556 resin is taken in the ratio of 60% in weight of reinforcement, and hardener is chosen in the ratio of 10% in weight of the resin. The multi-walled carbon nanofiller and graphene are taken for developing nano-infused polymer matrix composites at 4% in the weight of the resin (Table 1).

2.3 Specimen Preparation

The developed polymer matrix and nano-infused polymer matrix composites are allowed to cure for 24 h in the vacuum infusion molding setup. The composite is removed from the setup, and it is displayed in Fig. 2. American society for testing

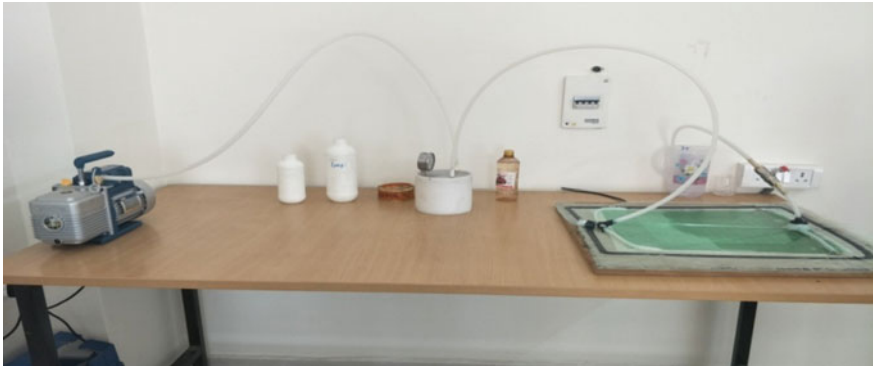


Fig. 1 Vacuum infusion molding setup

Table 1 Materials for kenaf-based composites

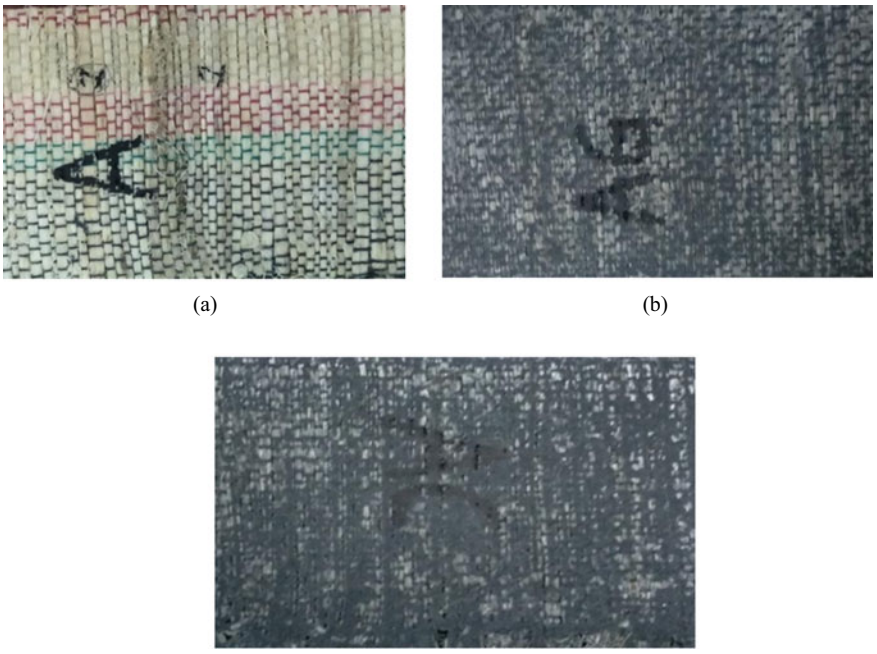
Materials	Weight
Areca fiber (25 × 25 (cm) × 4) LY-556 epoxy resin	220 g 132 g
Hardner HY-951	13.2 g
Resin: hardener Nanofiller	100:10 5.3 g

and materials standard is followed to extract the samples for checking the tensile and flexural strength of samples. The sample for the tensile test was extracted based on ASTM D3039 to find the tensile strength of the developed polymer matrix and nanofiller-infused composites, and the ASTM D790-10 is utilized to extract the samples for flexural strength exposed (see Fig. 3) to find the flexural strength of the developed polymer matrix and nanofiller-infused composites.

The prepared areca fiber-reinforced polymer and nano-filled polymer composites (graphene and carbon nanotubes) are displayed in Fig. 2. The most significant mechanical characteristics are tensile and flexural stress, and the samples are extracted with the size of 200 × 15 × 3 (mm) and of 127 × 13 × 3 (mm), respectively. The extracted samples for obtaining strength based on the tensile and flexural tests are shown in Figs. 4 and 5. The tensile property of the samples is measured by using a computerized universal tensile testing machine, and tested samples are shown in Fig. 6.

3 Result and Discussions

The tensile and flexural test results are shown in Table 3; the tensile strength of polymer composite is 126.34 MPa, and nano-infused polymer composite (graphene



(a) (b)

(c)

(a) Areca composite (b) Areca with graphene (c) Areca with carbon

Fig. 2 Developed polymer and nano-filled composites

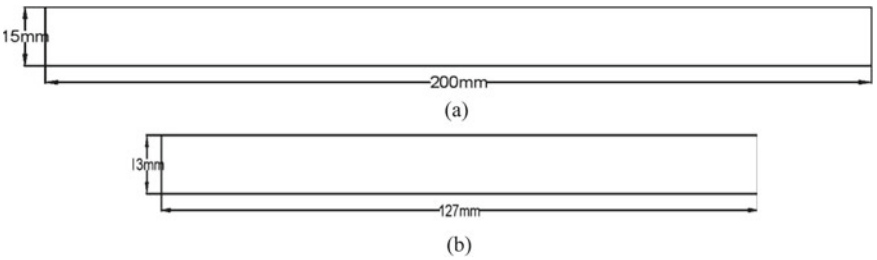


Fig. 3 ASTM standard test specimens for **a** tensile strength and **b** flexural strength

and multi-walled carbon nanotubes) is 138.22 MPa and 135.33 MPa correspondingly. The result clearly shows that the tensile strength of polymer matrix composite is increased by adding nano-infused material. The graphene has increased the polymer matrix composites by almost 12 MPa, but when multi-walled carbon nanotubes are increased by 9 Mpa, the flexural strength of polymer composite is registered as 42.91 MPa and nano-infused polymer matrix composite is shown as 56.24 MPa and 52.42 MPa, respectively. The tensile strength of areca natural fiber is almost equal to the areca fiber composite developed by another researcher (13).

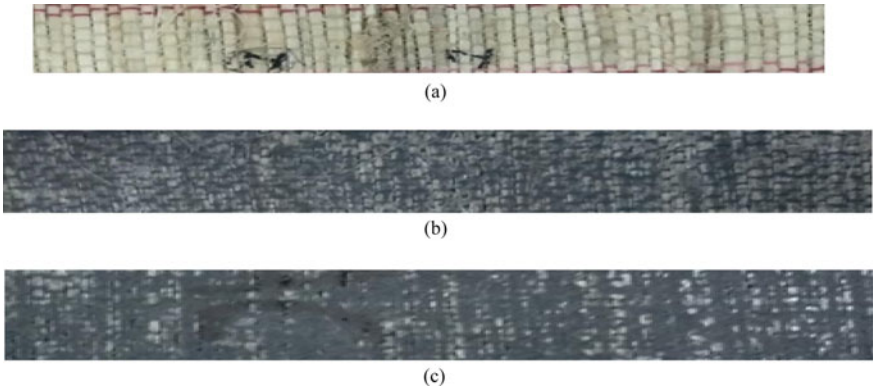


Fig. 4 Specimen extracted from polymer composites for tensile test

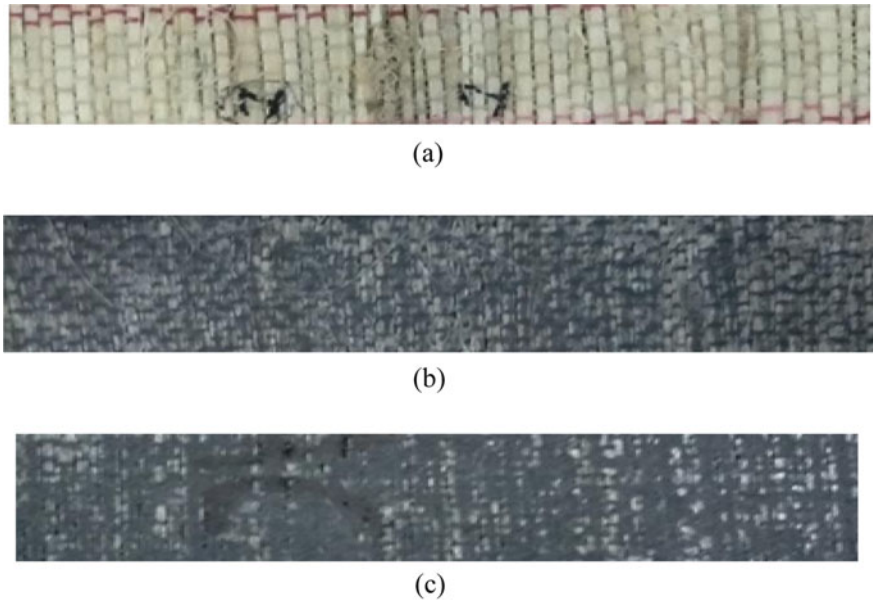


Fig. 5 Sample extracted from polymer composites for flexural test

The separate attachment setup is used in the computerized universal testing machine to check the flexural test of the developed natural and nanomaterial-infused composites. The natural polymer composite is registered as 42.91 MPa and is increased to 56.24 MPa by adding graphene, and it is increased to 52.42 MPa by infused carbon nanotubes. The polymer composite flexural strength is increased by

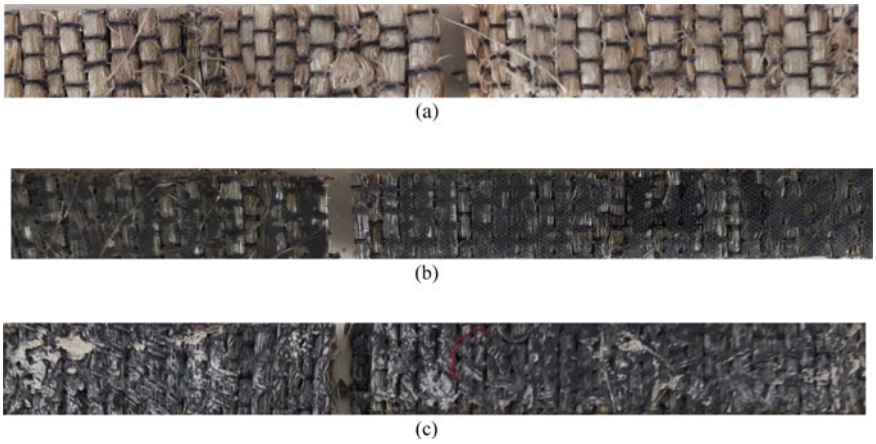


Fig. 6 Tested samples of tensile test

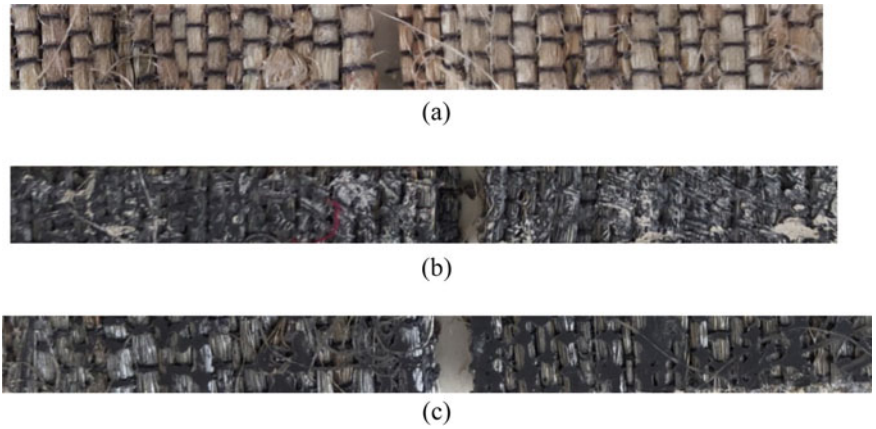


Fig. 7 Tested samples of flexural test

Table 3 Tensile test and flexural test result of areca-based composites

Sample no.	Composite	Tensile strength (MPa)	Flexural strength (MPa)
a	Polymer matrix	126.34	42.91
b	Graphene infused	138.22	56.24
c	Multi-walled carbon nanotubes infused	135.33	52.42

almost 14 MPa by adding graphene and is increased by 10 MPa by adding multi-walled nanotubes. The nano-infiller materials and vacuum infusion molding have enhanced the tensile strength and flexural strength of natural fiber composites.

4 Conclusions

The natural fiber composite is developed by using the vacuum infusion molding method, and the epoxy Ly556 resin is used as matrix and reinforcement is selected as areca fiber. The graphene and carbon multi-walled nanotubes are used as nano-infused materials for increasing the mechanical properties. The tensile and flexural characteristics are tested for checking the influence of nanofiller materials.

- The tensile strength of natural polymer matrix composite is 126.34 MPa, and the strength is increased by 8.59% by adding graphene and is increased by 6.39% by carbon tubes.
- The flexural strength of the areca composite is 42.91 MPa and 23.70% of flexural strength is increased by graphene and 18.14% of flexural strength in the natural polymer composite is improved by adding carbon-walled nanotubes in the areca fiber-based polymer matrix composites.
- The nano-infiller materials and vacuum infusion molding have enhanced the tensile characteristics and flexural strength of natural fiber composites.

In the future, chemically treated areca natural fiber can be used for developing natural fiber composites.

References

1. Hazarika SB, Choudhury SU, Panja SS, Dolui SK, Ray BC (2015) Natural fiber reinforced polyester based biocomposite: agro waste utilisation. J Sci Ind Res 74(5):589–594
2. Loganathan TM, Sultan MTH, Jawaid M, Shah AUM, Ahsan Q, Mariapan M, Majid MSBA (2020) Physical, thermal and mechanical properties of areca fibre reinforced polymer composites—an overview. J Bionic Eng 17(1):185–205
3. Praveen Kumar A, Kumarasamy GS, Nikhil N (2015) Analysis of carbon fiber reinforced polymer composite hip prosthesis based on static and dynamic loading.Int J Appl Eng Res 10(85):574–579
4. Basham MU, Krishnudu MD, Hussain P, Reddy MK, Karthikeyan N, Kumar AM (2015) Synthesis and characterization and properties comparison of epoxy filled filler millet (Ragi) filler and treated sacharun offinarum (sugar cane) fiber reinforced composites. Int Lett Chem Phys Astron 51(1):41–46
5. Jawaid M, Abdul Khalil HPS, Bakar AA, Khanam NP (2011) Chemical resistance, void content and tensile properties of oil palm/jute fibre reinforced polymer hybrid composites. Mater Design 32(2):1014–1019
6. Praveen Kumar A, Jeyalal P, Barani Kumar D (2012) Hybridization of polymer composites. Int J Adv Mater Sci 3:173–182

7. Padmaraj N, Keni LG, Chetan K, Shetty M (2018) Mechanical characterization of Areca husk-coir fiber reinforced hybrid composites. Mater Today Proc 5(1):1292–1297
8. Praveen Kumar A, Jackson Irudhayam S, Naviin D (2012) A review on importance and recent applications of polymer composites in orthopaedics. Int J Eng Res Devel 5(2):40–43
9. Dhanalakshmi S, Ramadevi P, Basavaraju B (2017) A study of the effect of chemical treatments on areca fiber reinforced polypropylene composite properties. Sci Eng Comp Mater 24(4):501–520
10. Qiu M, Sun ZT, Sang DK, Han XG, Zhang H, Niu CM (2017) Current progress in black phosphorus materials and their applications in electrochemical energy storage. Nanoscale 9(36):13384–13403
11. Arjmand M, Chizari K, Krause B, Potschke P, Sundararaj U (2016) Effect of synthesis catalyst on structure of nitrogen-doped carbon nanotubes and electrical conductivity and electromagnetic interference shielding of their polymeric nanocomposites. Carbon 98(1):358–372
12. Deep N, Mishra P (2018) Evaluation of mechanical properties of functionalized carbon nanotube reinforced PMMA polymer nanocomposite. Karbala Int J Modern Sci 4(1):207–215
13. Srinivasa CV, Arifulla A, Goutham N, Santhosh T, Santhosh HJ, Ravikumar RB, Anil SG, Santhosh Kumar DG, Ashish J (2011) Static bending and impact behaviour of areca fibers composites. Mater Des 32:2469–2475
14. Praveen Kumar A, Nalla Mohamed M, Kurien Philips K, Ashwin J(2016) Development of novel natural composites with fly ash reinforcements and investigation of their tensile properties. Appl Mech Mater 852:55–60
15. Yusriah L, Sapuan SM, Zainudin ES, Mariatti M (2014) Characterization of physical, mechanical, thermal and morphological properties of agro-waste betel nut (*Areca catechu*) husk fibre. J Clean Prod 72(1):174–180

Theoretical Research and Performance of Engineered Cementitious Composite

Lakshmi Meghana Srikakulam and Veerendrakumar C. Khed

Abstract This chapter explains overview on preceding research studies performed on properties of engineered cementitious composite (ECC) with addition of a variety of mineral admixtures and fibers. ECC is a mortar-based composite and can be easily molded with the help of short random fibers, usually of polymeric base. The ECC is tailored through micromechanics and fracture mechanics models to depict large tensile strain around 3–5%, when compared with normal concrete. Therefore, ECC does not have any exact material design. Effect of water–cement ratio, shape and length of fibers, mixing techniques, temperature, and use of fly ash in high volume on properties of ECC has been mentioned by a number of researchers. The quantity of fibers used in ECC is less than 2%. Literature survey on fresh and mechanical properties of different ECC mixtures evaluated by using supplementary materials has been done thoroughly.

Keywords Crumb rubber (CR) · Fine aggregates · Concrete · Polyvinyl alcohol fibers · ECC · Super-plasticizer (sp) · Micromechanics (MM) · Fly ash (FA)

1 Introduction

Concrete is broadly and popularly used building material with around 11.4 billion tons of the concrete used globally for construction [1]. Therefore, it is necessary to find an alternative to it by another material partially or completely. Traditionally, the raw materials are selected based on observations. But nowadays, composite materials are designed systematically, and engineered cementitious composite (ECC) is one such material. ECC is a new category of fiber-reinforced concrete mix with high performance, ultra-high ductility, developed to overcome the brittle nature of conventional concrete. This ECC shows a distinct strain hardening response when subjected to tensile load. This ECC finds its usage in cost saving constructions, exhibiting strain hardening behavior as shown in Fig. 1 [2], high ductile capacity, high tensile strain,

L. M. Srikakulam (✉) · V. C. Khed
Civil Engineering Department, Koneru Lakshmaiah Education Foundation, Green fields, Vaddeswaram, Guntur District, Andhra Pradesh 522502, India
e-mail: lakshmimeghana11@gmail.com

© Springer Nature Singapore Pte Ltd. 2020

A. Praveen Kumar et al. (eds.), *Advances in Lightweight Materials and Structures*,
Springer Proceedings in Materials 8, https://doi.org/10.1007/978-981-15-7827-4_25

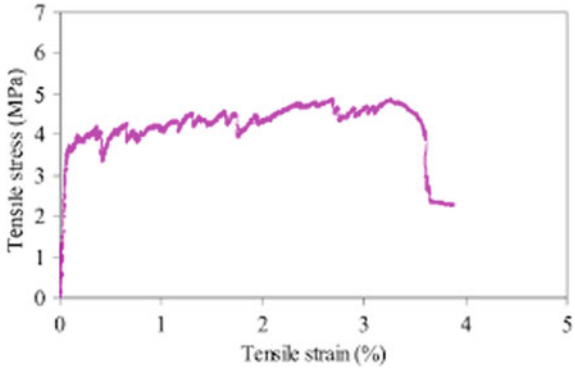


Fig. 1 Tensile stress–strain curve for ECC

and less microcrack width with minimum usage of fibers of about 2 percentage by volume [3, 4].

This ECC is tailored using a powerful tool called micromechanics. Micromechanics principle is analyzed at individual level; it involves manipulation at micromaterial structure to achieve specific behavior and expresses the interactivity between the fiber and mortar. ECC can be modified to achieve maximum output through the branch of micromechanics [5]. Fibers are in the scale of millimeter in length; with the use of these fibers, an increase in the penetration resistance, high tensile strength, and energy absorption capacity has been observed [6]. ECC matrix heterogeneities include defects, fine aggregate, binding composites, and mineral admixtures, having magnitude in the order of nano to mm level [7]. Preferably, the MM concept should be capable of capturing all the distortion movements at these levels. This material which is developed in recent times is safer, durable, more sustainable, and is environmentally friendly. These fibers used in ECC create microcracks less than 100 μm [8, 9] rather than very large cracks as in case of conventional concrete [10, 11]. This microcracking behavior leads to increased corrosion resistance, prevents percolation of water and other harmful substances [12], and also helps in self-healing [13, 14], self-consolidating [15] of the mix which helps in improving the performance of the structure. ECC had major advancement in materials and in its implementation.

ECC is not only limited for educational laboratory research purpose. It is managing implementation into precast plants, retrofitting and repairing jobs, and construction sites. It is to the anticipation of the author that, ECC technologies will improve continuously in the upcoming decade, improving society with improved safety, enhanced durability [16], construction productivity, and sustainable development of physical infrastructures [17].

1.1 Background

In the early 1980s, designing a fiber-reinforced concrete (FRC) with great tensile ductility was of great interest. But, in case of (FRC), the toughness was increased but the ductility remained same. With the increasing demand in industrial projects, especially in onsite constructions, the new classes of concrete have come out with strength in the order of 12 MPa and ductility in the range of 0.02–0.05%. The traditional concrete is exposed to high magnitudes of pressures before its failure, and a team guided by Prof. Victor Li had evolved a concrete that is flexible enough to bend under high pressures and has self-healing ability [18]. ECC was developed at University of Michigan, [19], and has a moderate tensile strength (4–6 MPa) and high ductility in the range of 3–5% [19]. Fibers added to concrete helped in restraining the brittleness of the matrix. The interaction between fibers and matrix provides a strong bond which results in high post-tensioning cracking strength of the matrix mix.

1.2 Ingredients of ECC Concrete

ECC is considered as group of materials with a wide variety of tensile strengths and ductilities which can be modified depending on the requirements of the project. This ECC mix consists of cement, fine aggregates FA, fibers, high-range water reducers (HRWR), and water. Coarse aggregate is generally avoided in the mix design to achieve low Young's modulus and high strain [17].

Cement:

Ordinary Portland cement is normally adopted and is distinguished by its physical properties. Few of these properties include setting time, fineness, and compressive strength. The fineness of the cement influences the hydration rate and in turn affects the strength. Finer cement is generally preferred than coarse, to prevent low strength and durability, that might have occurred due to leftover unhydrated portions. In general, OPC of 33 grade, 43 grade, 53 grade is widely adopted. Table 1 shows chemical composition of OPC. The setting time of cement is influenced by factors like water-to-cement ratio, fineness of cement, and admixtures. Normally two setting times are interpreted, initial and final set time. When the paste begins to stiffen, initial set time is estimated and final set time when cement has gained hardness and can bear some load without any impressions on the surface. Figure 2 shows image of cement.

Fine aggregates:

The amount of aggregate in the typical concrete mix plays a very important role. It not only acts as filler but also influences the strength and texture of the mixture. Widely used commercial sands are silica sand, and it is 98% pure. The sand used

Table 1 Chemical composition of fly ash and OPC [21]

Chemical composition in percentage	Fly ash	OPC
SiO_2	57.7	21.0
Al_2O_3	21.1	5.09
Fe_2O_3	6.39	2.99
CaO	4.26	61.6
MgO	1.80	2.07
Na_2O	1.06	0.21
K_2O	1.67	1.03
SO_3	0.52	2.41
LOI	3.91	2.66



Fig. 2 Figure showing cement and fly ash

by various researchers shall pass through 4.75 mm sieve and should be free from organic and earthy matter.

Fly ash:

FA is a fine residue obtained from combustion of powdered coal. This material is widely used in construction industry these days. The quality of FA is governed by IS3812-partII-2013 [20]. The spherical form of particles helps in improving workability and reduces water demand. Fly ash can be used as a replacement for cement, and its chemical composition is shown in Table 1. The primary function of FA is to settle in the voids which otherwise would have been occupied by water or cement.

Water:

Drinking water is generally regarded suitable for making of cementitious composite. Water free from all sorts of impurities carbonates, bicarbonates of sodium and potassium affect the setting time of cement. Water when reacted chemically with cement forms cement paste in the initial stages, where the aggregates are in suspension. Later, this water acts as a lubricator for the mixture.



Fig. 3 Polyvinyl alcohol fibers

Fibers:

In general, fibers used in ECC are polyvinyl alcohol (PVA) as shown in Fig. 3. These PVA fibers are no less than the reinforcement material. They are characterized by their high order of tensile strength, high modulus of elasticity, high durability, and its strong bonding with the cement matrix. PVA fibers have tensile strengths in the range of 880–1600 MPa. At the time of hydration, a layer of calcium hydroxide is formed which is useful for bond strength.

Super-plasticizer:

Super-plasticizer is used to influence material and fresh properties of concrete. Super-plasticizer distributes the cement uniformly in the mix thereby avoiding air entrainment. Super-plasticizer improves slump from 5 to 20 cm and also reduces water up to 15–20%. This in turn increases strength and various properties such as density, water tightness, and workability. In order to assess effectiveness in upgrading durability, melamine and polycarboxylate ether (PCE)-based super-plasticizers are generally preferred.

1.3 Unique Properties of ECC

The distinct properties of engineered cementitious composite as listed by Victor Li are given below [22]

- ECC is very ductile in nature and can be easily molded into mortar-based composite with short random fibers.
- It is up to 40% lighter.
- 500 times more improved crack resistance.
- Large strain is developed by sequential development of multiple cracks.

- It has high fracture toughness and controls crack width which improves serviceability and durability.
- High tensile properties when compared with other fiber-reinforced composites.
- Improved resistance to corrosion due to microcracking behavior.

The research aim of this paper is to investigate both fresh and hardened properties of engineered cementitious composite. The chapter helps us in guiding different alternative substances that can be adopted as a replacement for natural river sand and cement and the consequent effects on strength and durability parameters of ECC.

2 Review on Experimental Investigations on ECC

ECC is tailored mainly based on principal of micromechanics. The main idea of MM focuses on the connection between composite materials to the properties of constituent materials, i.e., the mechanical interactivity between the fibers, mortar matrix, and fiber-to-mortar bonding. This concept allows systematic tailoring of ECC at microstructure level [8] and also helps in material optimization. The fibers used in ECC are of very less volume with heights around 8–12 mm. The perfect mix proportions given in the literature regulates the proportions of varied elements in the mix. Various tests are performed on concrete to investigate on both fresh and hardened properties. Tests such as slump test and compaction factor test are used to regulate the fresh properties, whereas compressive strength test on cube specimens is used for evaluating hardened properties. The optimum mix proportions as suggested by authors [16] is as in Table 2.

2.1 Hardened Properties

En et al. [23] in the research engaged variables like FA of class F and C, w/b ratio, and quantity of super-plasticizer. An investigation on fresh and hardened properties was carried out on ECC. It was concluded that w/b ratio has more impact on plastic viscosity and this in turn has an effect on tensile properties. It is noticed that ultimate tensile strength increased with increase in plastic viscosity. Xiaoyan et al. [24] in this chapter made their first attempt by employing iron ore tailings and IOTs in amorphous form as a substitute to the cement to develop the environmentally safe ECC. This newly developed material consists of cement content of 117.2–350.2 kg/m^3 and has ductility in the range of 2.3–3.3%. The compressive strengths of 46–57 MPa can be

Table 2 Optimum mix proportions

	Cement	FA	Sand	water	Super-plasticizer	Fiber (vol %)
Ratio	1	1.2	0.8	0.54	0.03	0.02

achieved with ECC. It was observed that due to incorporation of IOTs there was a relative reduction in the energy consumption up to 10–32%, and emission of carbon dioxide was reduced up to 29–63%.

Li [25] from their research came out with two mix proportions for ECC with varied FA-to-PC ratios of 1.2 and 2.2, respectively. PVA fibers with tensile strength 1620 MPa and Young's modulus 42.8 GPa were used in mix preparation. It was remarked that the compressive strength at 7, 28, and 90 days of the first mix were 38.1 MPa, 50.2 MPa, and 55.4 MPa correspondingly, and to the second mix 21.6 MPa, 36.3 MPa, and 41.9 MPa. Mustafa et al. [26] from their perspective about ECC with and without fibers, it was observed that the 14 and 28 days strength for ECC due to incorporation of fibers were 39.2 MPa and 62.5 MPa, respectively, and parallel for the other mix the strength values were 36.1 MPa and 60.3 MPa, respectively. The tensile strength of the ECC mix with fibers was observed to be 5.1 MPa. Li et al. [27] in their study used polystyrene beads of 4 mm in ECC as coarse aggregate and the variation in strength was observed. Compressive strength of 47.5 MPa, 55.6 MPa, and 56.8 MPa for 7, 28, and 60 days, respectively. The tensile strength variation is as 5.56 MPa, 5.68 MPa, and 5.79 MPa for 7, 28, and 60 days, respectively.

Satishkumar et al. in their research worked on the influence of strength parameters due to incorporation of various fibers into ECC [10, 11]. Polyvinyl alcohol fibers, polyethylene, polypropylene, and polyester fibers have been used for research. It was observed that with the increase in fiber content from 1 to 2% depicted an improvement in the compressive, tensile, and flexure strength due to bridging effect, but for 2.5% of fiber content a slight decrease in strength for 7, 28, 56 days was noticed. Ked et al. in their research developed ECC with river sand of maximum size 30 μm and CR of 30 mesh and 1–3 mm. This ECC developed consists of 1.5% PVA fibers and 0.5% tire wires. The experiment involved design-by-design expert software and flow ability specifications from EFNARC guidelines. The CR can be used as a partial substitute for fine aggregate up to 60%. It was identified that with the use of CR there was a decrease in compressive strength due to its hydrophobic property that creates voids in the composite. It was concluded that with the use of fine CR there was a increase in compressive strength [28].

Khed et al. in research focused on the main objective to apply RSM optimization for modeling compressive strength, ultrasonic pulse velocity tests, and rebound hammer tests. In this research, the authors used nanosilica to improve the modulus of elasticity. Nanosilica and PVA fibers are varied (0%, 1%, 2%, 3%, 4%) and (0.5%, 1%, 1.5%, 2%), respectively. Rebound hammer and ultrasonic pulse velocity tests are performed to assess the compressive strength. The main aim of using nanosilica is to act as filler in the voids and in turn improving the compressive strength. It is observed that use of nanosilica up to 4% [29] showed a remarkable increase in compressive strength but, with percentage more that 4% the residue leftover caused less dense microstructure thereby leading to decreased compressive strength.

Based on the literature survey, the following that conclusions can be drawn, the w/b ratio plays an important role in the ECC mix. This ratio has an influence on the plastic viscosity which in turn affects the strength of the mix. With ECC, strengths in the range of 46–57 MPa can be easily achieved. After various studies, it can be

concluded that FA-to-Portland cement ratio can be chosen as 1.2 for better results. ECC with fibers showed better strength results than ECC without fibers, and this is due to the bridging effect produced due to fibers [30]. Fibers cross the cracks and thereby slow down the delamination growth. It is observed that maximum of 2% of fibers is preferable for achieving strength criteria. With the incorporation of IoTs into ECC, the carbon dioxide emission is reduced which shows a positive impact toward global warming and green house effect.

2.2 Workability

Yang et al. [23] in their investigation on fresh and hardened properties carried out on ECC concluded that w/b ratio has an impact on plastic viscosity. Dhawale et al. [31] in this chapter stated that melamine-based sp is chosen best for the research work on ECC. In their work, they have used melamine formaldehyde sulfonate to assess the effectiveness in improving the ductility. In the beginning, the required workability was not attained, volume of PVA fibers was changed to 1.2% and w/b ratio to 0.3048. And in the later mix, the sp dosage was brought down to 600 ml/bag and w/b ratio was taken as 0.33. For the fourth trial, mix water-to-binder ratio was changed to 0.3118. With the aim to increase the workability of the mix, the w/b ratio is finalized to 0.35 after subsequent trials. The mixing was done by hand mixing and fibers are added once a homogeneous mixture is obtained. Mustafa et al. [25] from their research came out with the following mix proportions for ECC mixes with FA to Portland cement (FA/PC) of 1.2 and 2.2. The experimental investigation was performed by taking water-to-cementitious material ratio of 0.27, and high-range water reducer (HRWR) was incorporated into the mix until required homogeneity is obtained.

Satishkumar et al. in their research worked on the influence of strength parameters due to incorporation of various fibers into ECC [9] Polyvinyl alcohol fibers, polyethylene, polypropylene, and polyester fibers have been used for research. It was observed that balling effect occurs when the fibers are added to dry mixes, and this effect is due to the insufficient fine aggregate content to overcoat the fibers. Due to this, there is a reduction in workability. It was observed that aspect ratio should be as low as possible to minimize workability. In order to maintain desired slump, water-reducing admixtures are added, and to maintain workability, super-plasticizers are added.

Workability of the concrete mix is described as the ability with which we can work with the mix easily. The workability of the concrete mix increases with the increase in the water content. With the incorporation of fibers the workability is reduced comparatively but the strength is improved [9]. PVA fibers of 1.2% is best suitable for both strength and workability criteria. Based on various researches, water-to-binder ratio of 0.35 is set as optimum for better strength. Melamine-based super-plasticizer is used to improve workability and also to enhance ductility.

2.3 Tensile Strain Capacity

Shuxin et al. [4] investigate on mechanical properties of ECC by incorporating FA. FA contents promote key micromechanical properties of ductility. Higher quantities of FA reduce the amount of polyvinyl alcohol fibers, increase matrix interface and toughness, and help in attaining high tensile strain capacity. Increase in FA content modifies the PVA content and helps in bridging effect. With further addition of FA, it is observed that matrix toughness decreases and tends to favor strain hardening. It is mentioned that a right mix proportions can achieve high performance even with the use of locally available low-quality cement replacements. Mustafa et al. [32] in the research worked on ECC using PVA fibers, and it was observed that 7-day tensile strength capacity of 3.48% was observed and for 28 days it was recorded as 3.16%. Li et al. [11] used polystyrene beads of 4 mm into ECC as coarse aggregate to control the preliminary defect size and its distribution to attain elevated tensile strength. The strain capacity of 3.52%, 3.47%, and 3.52% is obtained for 7, 28, and 60 days, respectively.

Shenzhen et al. in their research found out an alternative overlay material for pavements. This overlay material being brittle in nature responds weakly when subjected to high-pressure concentrations due to pre-existing joints in the substrate. In order to resolve this reflective cracking problem, PVA fiber-reinforced engineered cementitious composite is used for high ductility and damage tolerance. ECC overcomes this problem by developing a large number of microcracks. ECC has a tensile strain capacity which is 300 times that of normal concrete and provides excellent crack resistance behavior due to its reduced modulus of elasticity [33]. From different authors, the amount of FA helps in improving ductility properties of ECC. PVA fibers present in ECC help in increasing the tensile strain capacity by controlling the defect size.

2.4 Serviceability

Li et al. [34] reported that ECC constituted a different class of high-performance cementitious composite with increased tensile and durability characteristics. The paper reports that ultra-high volume of FA up to 85% by weight can be used as cement replacement and focuses on consequence of FA content on the microstructure and various properties of materials. From the paper, it was noticed that with the use of high volume FA in ECC, there was a decrease in the free drying shrinkage and crack width which in turn improve long-term durability. MM concept indicates that increase in fiber and matrix interface is responsible for tight crack widths. Li-Kan et al. [35] experimental report on self-curing characteristic of ECC shows that the specimens were subjected to wet–dry patterns immersing the specimens in water for 24 h at 20 °C. For preloading tensile strains of 0.3, 0.5, 1% at 90 days, the crack widths observed were 14, 13, 15 μm. Saharan et al. [24] from their experiment came

out with two ratios for different ECC mixes with varying FA to PC ratios of 1.2 and 2.2 correspondingly. For strain of 0.5, 1, and 1.5%, it is noticed that the average crack width of the first mix was 36, 44, and 50 μm and for the second mix 24, 30, and 28 μm.

Based on literature survey, it can be concluded that ECC produces strain hardening behavior which is due to the presence of fibers in it, and these fibers bridge the cracks and facilitate in self-healing behavior. The crack widths observed in ECC are less compared to that of usual concrete.

3 Conclusions

Cement is the material that has a vital use in construction industry. With rapid industrialization, requirement for cement and other materials has rapidly increased. With a rapid progress made in development of new classes of concrete from past few years, it may be expected that we will continue to discover more favorable characteristics of ECC. This ECC overcomes the brittle nature of the concrete thereby facilitating the use of high grade in construction. Due to its controlled crack width, it ensures that all the cracks are healed thoroughly, thereby achieving targeted structural performance levels. Association with this new material, a new generation infrastructure can be developed with minimum repair requirements, having self-adapting ability and also an eco-friendly in nature. Its usage in the actual world proves to be one of the best choices and environmental-friendly material for future constructions.

References

1. Baird G (2010) Sustainable buildings in practice: What the users think, Routledge
2. Pan Z et al (2015) Study on mechanical properties of cost-effective polyvinyl alcohol engineered cementitious composites (PVA-ECC). Constr Build Mater 78:397–404
3. John E et al (2018) Engineered cementitious composite (ECC) link slab for bridge deck. Int Res J Eng Technol (IRJET) 5
4. Wang S, Li VC (2007) Engineered cementitious composites with high-volume fly ash. ACI Mater J 104(3):233
5. Fukuyama H et al (2000) Ductile engineered cementitious composite elements for seismic structural applications. CD proceedings of the 12 WCEE, paper, 1672
6. Zhang L (2008) Impact resistance of high strength fiber reinforced concrete, University of British Columbia
7. Yang E-H et al (2008) Fiber-bridging constitutive law of engineered cementitious composites. J Adv Concrete Technol 6(1):181–193
8. Li VC (2003) On engineered cementitious composites (ECC). J Adv Concrete Technol 1(3):215–230
9. Li VC, Leung CK (1992) Steady-state and multiple cracking of short random fiber composites. J Eng Mech 118(11):2246–2264
10. Sathishkumar P et al (2016) Significance of various fibres on engineered cementitious concrete. Int J Sci Eng Technol 4(1):284–290

11. Wang S, Li VC (2006) High-early-strength engineered cementitious composites. ACI Mater J 103(2):97
12. Li VC (2007) Integrated structures and materials design. Mater Struct 40(4):387–396
13. Siad H et al (2018) Advanced engineered cementitious composites with combined self-sensing and self-healing functionalities. Constr Build Mater 176:313–322
14. Yang Y et al (2009a) Autogenous healing of engineered cementitious composites under wet–dry cycles. Cem Concr Res 39(5):382–390
15. Kong H-J, Bike SG, Li VC (2003) Constitutive rheological control to develop a self-consolidating engineered cementitious composite reinforced with hydrophilic poly (vinyl alcohol) fibers. Cement Concr Compos 25(3):333–341
16. Li M, Li VC (2006) Behavior of ECC/concrete layered repair system under drying shrinkage conditions
17. Şahmaran M, Li VC (2010) Engineered cementitious composites: can composites be accepted as crack-free concrete? Transp Res Rec 2164(1):1–8
18. Li VC (2008) Engineered cementitious composites (ECC) material, structural, and durability performance
19. Fischer G, Shuxin W (2003) Design of engineered cementitious composites (ECC) for processing and workability requirements. In: Brittle matrix composites, vol 7. Elsevier, pp 29–36
20. Marthong C, Agrawal T (2012) Effect of fly ash additive on concrete properties. Int J Eng Res Appl 2(4):1986–1991
21. Cho YK, Jung SH, Choi YC (2019) Effects of chemical composition of fly ash on compressive strength of fly ash cement mortar. Constr Build Mater 204:255–264
22. Armand M et al (2011) Ionic-liquid materials for the electrochemical challenges of the future. In: Materials for sustainable energy: a collection of peer-reviewed research and review articles from nature publishing group. World Scientific, pp 129–137
23. Yang E-H et al (2009b) Rheological control in production of engineered cementitious composites. ACI Mater J 106(4):357
24. Huang X, Ranade R, Li VC (2012) Feasibility study of developing green ECC using iron ore tailings powder as cement replacement. J Mater Civ Eng 25(7):923–931
25. Şahmaran M, Li VC (2009) Durability properties of micro-cracked ECC containing high volumes fly ash. Cem Concr Res 39(11):1033–1043
26. Şahmaran M, Lachemi M, Li V (2010) Assessing the durability of engineered cementitious composites under freezing and thawing cycles. In: Recent advancement in concrete freezing-thawing (FT) durability. ASTM International
27. Li M, Li VC (2011) High-early-strength engineered cementitious composites for fast, durable concrete repair-material properties. ACI Mater J 108(1):3
28. Khed VC, Mohammed BS, Nuruddin MF(2018) Effects of different crumb rubber sizes on the flowability and compressive strength of hybrid fibre reinforced ECC. In: IOP conference series: earth and environmental science. IOP Publishing
29. Mohammed BS et al (2017) Evaluation of nano-silica modified ECC based on ultrasonic pulse velocity and rebound hammer. Open Civil Eng J 11(1)
30. Khed VC et al (2018) Hybrid fibre rubberized ecc optimization for modulus of elasticity. Int J Civil Eng Technol (IJCIET) 9(7):976–1928
31. Dhawale A, Joshi V (2013) Engineered cementitious composites for structural applications. Int J Appl Innov Eng Manage 2:198–205
32. Sahmaran M, Li VC, Andrade C (2008) Corrosion resistance performance of steel-reinforced engineered cementitious composite beams. ACI Mater J 105(3):243
33. Lepech MD, Li VC (2010) Sustainable pavement overlays using engineered cementitious composites. Int J Pavement Res Technol 3(5):241–250

34. Yang E-H, Yang Y, Li VC (2007) Use of high volumes of fly ash to improve ECC mechanical properties and material greenness. ACI Mater J 104(6):620
35. Kan L-L et al (2010) Self-healing characterization of engineered cementitious composite materials. ACI Mater J 107(6)

Experimental Investigation on Tensile Property of Vacuum Infused Kenaf-Based Polymer Composite with the Presence of Nanofillers



M. Shunmugasundaram, P. Anand, Maughal Ahmed Ali Baig, and Yamini Kasu

Abstract The main objective of this research work is to investigate the influence of nanofiller material on the tensile property of polymer matrix composites. Kenaf fiber is selected as reinforcement material, and epoxy resin is chosen as a matrix for developing polymer matrix composites. The polymer matrix composites are prepared to compare a tensile property of graphene, and multi-walled nano carbon nanotubes are selected as nanofiller material for developing nano infilled polymer matrix. An average of 10.65% of ultimate tensile strength of polymer matrix composite is increased by adding 4% nanofiller material to develop polymer matrix composites.

Keywords Kenaf fiber · Glass fiber · Epoxy resin · Vacuum infusion molding · Graphene · Multi-walled carbon nanotubes · Tensile strength

1 Introduction

Last few decades, the development in the area of material engineering is growing worldwide because it is significant attainment in green technology during the development of natural fiber-reinforced polymer composites. Bio-composites are defined as at least one of the materials is selected from natural resources [1]. Generally, the bio-composites prepare the composite materials develop from the combination of petroleum-based polymers as matrix and natural fibers as reinforcement. Natural fibers polymer composites can sustain the capability of polymer with enhanced mechanical and thermal characteristics; however, biodegradable composite is accompanying the important place in the global market [2, 3]. Some of the natural fibers are used as reinforcement material for kenaf, jute, sisal, coir, flax, banana, wood starch, rice hulls, newsprint, pulp, and cellulose fibers. The increasing interest in

M. Shunmugasundaram (✉) · M. A. A. Baig · Y. Kasu
Department of Mechanical Engineering, CMR Technical Campus, Hyderabad 501401, India
e-mail: sundarprithiv@gmail.com

P. Anand
Department of Mechanical Engineering, Vel Tech Rangarajan Dr. Sagunthala R&D Institute of Science and Technology, Chennai 600062, India

© Springer Nature Singapore Pte Ltd. 2020

A. Praveen Kumar et al. (eds.), *Advances in Lightweight Materials and Structures*,
Springer Proceedings in Materials 8, https://doi.org/10.1007/978-981-15-7827-4_26

using natural fibers as reinforcement material and polymers are used as matrix material in the development of natural-based polymer composites [4, 5]. It is mainly used because of their benefits such as minimal cost, renewability, reasonable basic characteristics, lower density, simple preparation, lower energy requirements for manufacturing, biodegradability, wide availability and relative nonabrasive over conventional reinforcing fibers such as glass and carbon [6]. Typically utilized natural fibers are Jute, Sisal, Banan, Hemp [7, 8]. Reuse of natural fiber fabric reinforcement is a sustainable option for all the climate. The components of the polymer and reinforcement together with the correct and sufficient filler and improved characteristics and filler/matrix create a strong link between existing and modern technologies and approaches [9–11].

The easy-to-manufacture composite materials also encouraged the investigators to utilize non-expensive materials and equipment implemented locally to develop and study the properties of the natural fiber-reinforced composite. Effective reinforced polymer composite is easily produced for various applications by different applications [12]. The creation will enable the mechanically competent biodegradable substance to be obtained which might suit different applications [13, 14]. Also, the demand for materials derived from natural resources is expected to increase over the next 2–3 decades, primarily because of the materials and its environmental benefits. The products can offer different benefits in mechanical and thermal uses, varying from load systems to shipping, industrial and aero areas [15]. Kenaf fiber is one of the natural fibers used in the manufacturing of natural fiber-reinforced polymer matrix composites. Kenaf fiber is used in the automotive sector to replace the utilization of glass fiber or other synthetic fiber materials as bio-composite items such as vehicle dashboards, carpet padding and plywood medium [16, 17]. Kenaf fiber is often used in thermoplastics such as polyethylene and polypropylene, and thermosetting resins such as polyester and epoxy as insulation. Epoxy and vinyl are the two important polymers are used to develop the polymer matrix composite. Mostly, epoxy resin is used to develop natural fiber-reinforced polymer matrix composites [18, 19].

The properties of new polymer materials can show significant improvement when nanofillers are well embedded in kenaf-based polymer composites. Dispersion performs a crucial role in enhancing the performance of biodegradable nanocomposites, as homogeneously dispersed nanoscale particles can provide stronger interfacial interaction between the matrix and the particles. The mixing method is therefore important to make sure that the reinforcing characteristics of the natural fibers are fully utilized [20].

In this research, the kenaf fiber is adopted as reinforcement, and epoxy resin is used as a matrix to develop polymer matrix composites. To enhance the tensile property, graphene and muti-walled nanofillers are used as nanoparticles to develop nano infused polymer matrix composites.

2 Materials and Methods

2.1 Materials

2.1.1 Kenaf Fiber

Some of the natural fibers are used as support for kenaf, jute, sisal, coir, flax, banana, wood starch, rice hulls, newsprint, pulp and cellulose fibers. Among other natural fiber reinforcement content, kenaf is comparatively commercially available and economically inexpensive. Thanks to its great interest in the processing of industrial raw materials, kenaf normally denoted as industrial kenaf. Kenaf plant and its development were examined, and it was established that kenaf retains a mean height of 4–6 mm stem diameter and varies from 25 to 35 mm within 4–5 months. Recent developments in decoration equipment that distinguishes the heart from the bast fiber coupled with fiber scarcity have renewed interest in kenaf as a source of fiber. It has considerable potential to replace synthetic fiber such as glass fiber. The use of kenaf fiber can provide tensile strength, similar to that of low-density synthetic fiber than synthetic materials, resulting in lightweight and environmentally friendly polymer matrix composites.

2.1.2 Epoxy Resin

Epoxy is the matrix or resin substances which thermoset, containing at minimum one or several groups of epoxy in the molecule. Many of the marketable epoxy resins are diglycidyl ether oligomers of bisphenol A. Araldite LY 556 is chosen as the matrix to develop polymer matrix composites. Compared with other conventional thermoplastic or thermoset resins, epoxy resins provide distinct advantages are Max healing shrinkage, relatively cheaper and plentiful, mechanical, fatigue power enhanced and powerful adhesion for loads of substrates.

2.1.3 Nanomaterials

Nanoparticles, such as carbon nanotubes, nanoclays, and graphenes, are widely used to modify biological, mechanical, electrical, optical, and thermal properties of polymer nanocomposites. However, before the full potential of polymer nanocomposites can finally be recognized, a variety of key issues have to be tackled. Advancements in polymer matrix composite's mechanical, thermal and electrical properties by introducing nanofiller depend on several variables, such as manufacturing method, adsorption contact among nanofillers and used polymers and the condition of dispersion of nanofillers. In this research, graphenes and multi-walled carbon nanotubes are used to develop nano infilled polymer matrix composites.

2.2 Fabrication of Composites

The hand layup process has been utilized to prepare polymer matrix composites, but this method is not been useful for achieving good mechanical properties. So, in this research, vacuum infusion molding is adopted to develop the polymer matrix composite or nanofiller infused polymer matrix composites for improving the mechanical properties of the developed composites. The materials for kenaf composites are listed in Table 1.

The seven species of untreated kenaf are cut with a size of 20 × 20 (cm) and the weight of the kenaf is 102 g (See Fig. 1). The epoxy resin is taken in 100:60 percentage of the weight of reinforcement and hardener is taken as 100:10 of epoxy to develop polymer matrix composites. The nanofiller is added as 4% of epoxy resin to develop nanofiller infused polymer matrix composites. The graphene and carbon multi-walled nanocomposites are chosen as nanofiller material for preparing composites.

Table 1 Materials for kenaf-based composites

Materials	Weight
Kenaf fiber	170 g
Epoxy resin LY-556	102 g
Hardner HY-951	10.2 g
Resin: hardener	100:10
Nanofiller	4 g

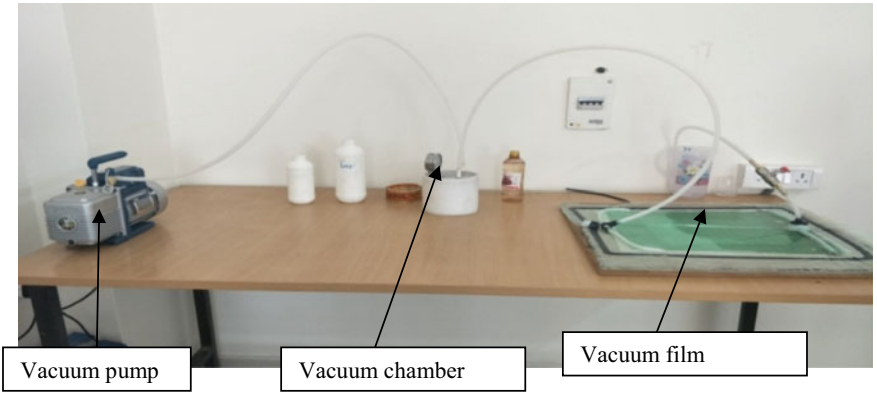


Fig. 1 Vacuum infusion molding setup

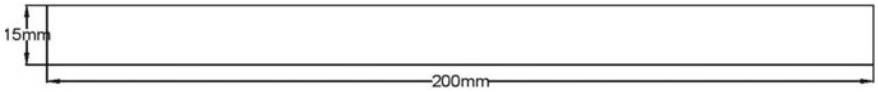


Fig. 2 ASTM standard test specimens for tensile test

2.3 Specimen Preparation

The polymer matrix composite is prepared and allowed for curing (24 h) and is taken from the vacuum infusion setup. American Society for Testing and Materials (ASTM) standard is followed to extract the tensile test specimens. The tensile test specimen was cut as per ASTM D3039 to find the tensile strength of the developed polymer matrix and nanofiller infused composites. The developed fabric reinforced composite and the extracted sample specimen for the tensile test are shown in Fig. 2.

The developed kenaf fiber-reinforced polymer matrix and nano infilled polymer matrix composite and extracted specimens are shown in Fig. 3. The proper utilization of the developed composite is always identified by different kinds of measurements by engineers and designers. The most important mechanical property is tensile strength, and as per ASTM standard, sample specimens are extracted for tensile test, and the specimens are shown in Fig. 3. The sample is extracted from each composite with a size of 200 × 15 × 3 (mm). The tensile strength of the specimens is measured by using a computerized universal testing machine, and tested samples are shown in Fig. 4.

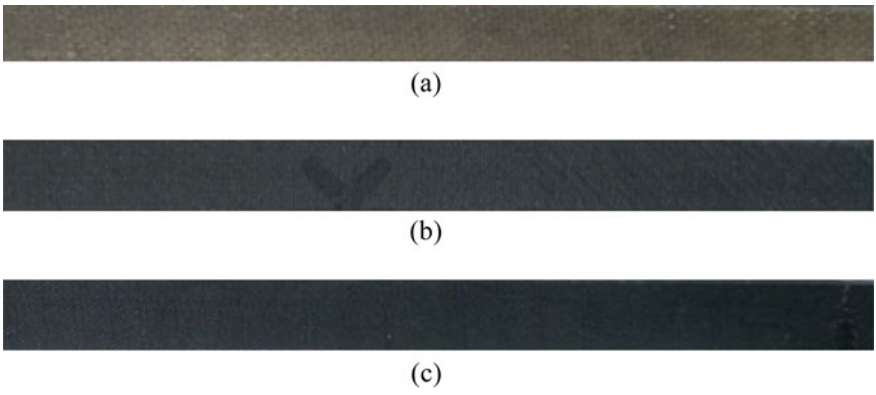


Fig. 3 Sample extracted from polymer composites

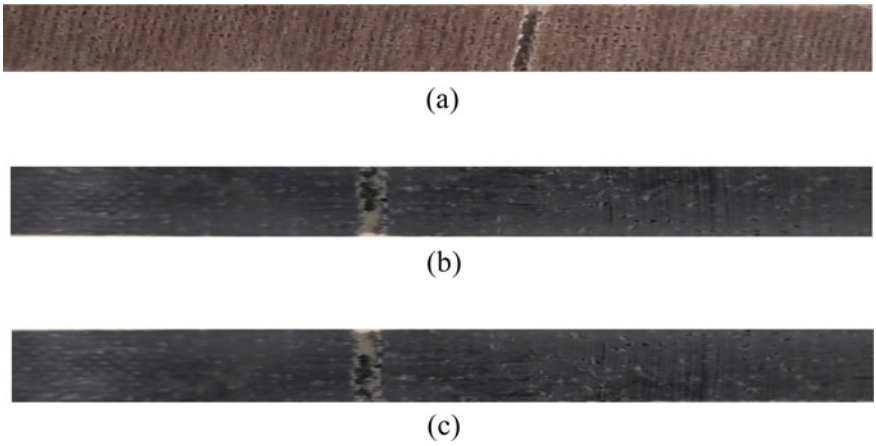


Fig. 4 Tested sample of polymer composites

3 Result and Discussions

Natural fiber-based polymer matrix composite and nano infused natural fiber-based composites are developed. The kenaf fiber is utilized to develop for checking the influence of kenaf fiber and nanofillers. The sample is extracted from each composite with a size of 200 × 15 × 3 (mm). The tensile strength of the specimens is measured by using a computerized universal testing machine, and tested samples are shown in Fig. 4. The results of the tensile test of the kenaf reinforced polymer matrix and nano infilled polymer matrix composite are shown in Table 2 and Fig. 5. The ultimate tensile strength of kenaf fiber-reinforced polymer matrix composite is 252.91 MPa, and nano infilled (graphene and multi-walled nanotubes) composite maximum tensile strength is 286.24 MPa and 279.42 MPa, respectively. The tensile strength of kenaf-based composite is almost equal to another researchers [15].The tensile strength of almost 44 MPa and 27 MPa is increased by adding graphene and carbon nanotubes. Almost 11.8% of ultimate tensile strength is increased by mixing the 4% of graphene nanofiller with resin for developing graphene infilled polymer matrix composites. Similarly, 4% of multi-walled carbon nanotubes have increased the tensile strength of polymer matrix composite by 9.5%. It clearly shows that the tensile strength is increased because of the adhesion between the fiber, resin and infillers. The vacuum

Table 2 Result of tensile test of kenaf-based composites

Sample No.	composite	Tensile strength (MPa)
a	Polymer matrix	252.91
b	Graphene infilled	286.24
c	Multi-walled carbon nanotubes infilled	279.42

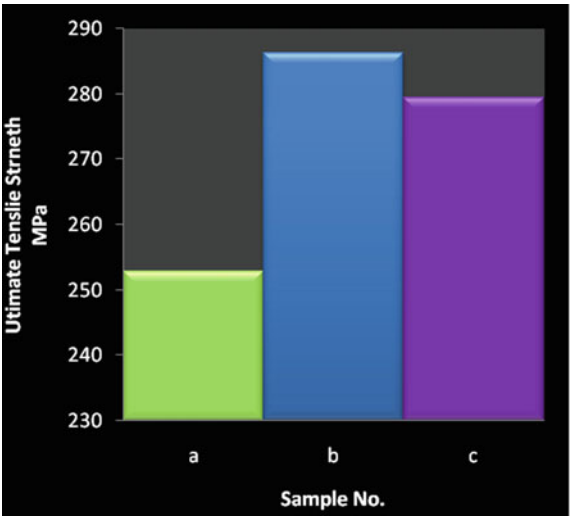


Fig. 5 Ultimate tensile strength of polymer composites

bagging method has developed the adhesion between the materials used in these natural fiber-based composites.

4 Conclusions

The kenaf fiber is chosen as reinforcement, and epoxy resin is selected as a matrix for developing polymer matrix composites, and nanofiller is added to increase the tensile strength of composites. The vacuum infusion molding method is adopted to develop polymer matrix composite and nano infilled polymer matrix composites. As per ASTM standard the specimens are extracted to find the ultimate tensile strength of the developed composites. The samples are tested by using a universal testing machine, and the result is displayed. The ultimate tensile strength is increased by using nanofiller materials for developing composites, and it is elevated the tensile strength by 10.65%. The result indicates that the graphene is influencing more than the multi-walled carbon tubes in the tensile strength. In the future, chemically treated kenaf natural fiber can be used for developing natural fiber composites.

References

1. Huang CT, Chen LJ, Chien TY (2019) Investigation of the viscoelastic behavior variation of glass mat thermoplastics (gmt) in compression molding. Polymers 11(2):335–346
2. Fan S, Yang C, He L, Du Y, Krenkel W, Greil P (2016) Progress of ceramic matrix composites brake materials for aircraft application. Rev Adv Mater Sci 44(4):313–325

3. Qiu M, Sun ZT, Sang DK, Han XG, Zhang H, Niu CM (2017) Current progress in black phosphorus materials and their applications in electrochemical energy storage. Nanoscale 9(36):13384–13403
4. Deep N, Mishra P (2018) Evaluation of mechanical properties of functionalized carbon nanotube reinforced PMMA polymer nanocomposite. Karbala Int J Modern Sci 4(1):207–215
5. Mashhadzadeh HA, Fereidoon A, Ghorbanzadeh Ahangari M (2017) Surface modification of carbon nanotubes using 3-aminopropyltriethoxysilane to improve mechanical properties of nanocomposite based polymer matrix: experimental and density functional theory study. Appl Surf Sci 420(1):167–179
6. Inagaki M, Toyoda M, Soneda Y, Morishita T (2018) Nitrogendoped carbon materials. Carbon 132(1):104–140
7. Praveen Kumar A, Kumarasamy GS, Nikhil N (2015) Analysis of carbon fiber reinforced polymer composite hip prosthesis based on static and dynamic loading.Int J Appl Eng Res 10(85):574–579
8. Rodríguez HA, Kriven WM, Casanova H (2019) Development of mechanical properties in dental resin composite: effect of filler size and filler aggregation state. Mater Sci Eng C 101(1):274–282
9. Singh SS, Parameswaran V, Kitey R (2019) Dynamic compression behavior of glass filled epoxy composites: Influence of filler shape and exposure to high temperature. Compos Part B Eng 164(1):103–115
10. Praveen Kumar A, Jackson Irudhayam S, Naviin D (2012) A review on importance and recent applications of polymer composites in orthopaedics. Int J Eng Res Devel 5(1):40–43
11. Akil H, Zamri MH, Osman MR (2015) The use of kenaf fibers as reinforcements in composites. Biofiber Reinforce Compos Mater 1(1):138–161
12. Akil HM, Omar MF, Mazuki AAM, Safiee S, Ishak ZAM, Abu Bakar A (2011) Kenaf fiber reinforced composites: a review. Mater Des 32(2):4107–4121
13. Ahmad R, Hamid R, Osman SA (2019) Effect of fibre treatment on the physical and mechanical properties of kenaf fibre reinforced blended cementitious composites. KSCE J Civil Eng 23(12):4022–4035
14. Hojo T, Zhilan XU, Yang Y, Hamada H (2014) Tensile properties of bamboo, jute and kenaf mat-reinforced composite. Energy Procedia 56(1):72–79
15. Praveen Kumar A, Jeyalal P, Barani Kumar D (2012) Hybridization of polymer composites. Int J Adv Mater Sci 3:173–182
16. Fiore V, Di Bella G, Valenza A (2015) The effect of alkaline treatment on mechanical properties of kenaf fibers and their epoxy composites. Compos Part B Eng 68:14–21
17. Liang K, Shi S, Wang G (2014) Effect of impregnated inorganic nanoparticles on the properties of the kenaf bast fibers. Fibers 2(3):242–254
18. Ramesh P, Durga Prasad B, Narayana KL (2020) Characterization of Kenaf/Aloevera fiber reinforced PLA-hybrid biocomposite. In: Voruganti H, Kumar K, Krishna P, Jin X (eds) Advances in applied mechanical engineering. Lecture Notes in mechanical engineering. Springer
19. Praveen Kumar A, Nalla Mohamed M, Kurien Philips K, Ashwin J (2016) Development of novel natural composites with fly ash reinforcements and investigation of their tensile properties.Appl Mech Mater 852:55–60
20. Ashok RB, Srinivasa CV, Basavaraju B (2019) Dynamic mechanical properties of natural fiber composites—a review. Adv Compos Hybrid Mater 2(2):586–607

Investigation on Mechanical Properties of Chemically Treated Banana and Areca Fiber Reinforced Polypropylene Composites

G. Sai Krishnan, Shanmugasundar, Raghuram Pradhan, and Ganesh Babu Loganathan

Abstract The intent of this work is to investigate the mechanical properties of chemically treated banana and areca fibers as reinforcement for various applications. Compression molding technique was used to prepare the composites. Fiber loading was varied by 5 and 10 volume weight percentages. Both areca and banana fiber were chemically treated with 5 wt.% sodium carbonate. Tensile, flexural and hardness Testes were carried out. On seeing the results, it was witnessed that the mechanical properties and thermal stability got increased with fiber loading and sodium carbonate treatment. Ten fibers reinforced composite provided the best set of mechanical and thermal properties, while banana fiber reinforced polypropylene composites had slightly better properties as compared to jute fiber reinforced polypropylene composites.

Keywords Banana fiber · Areca fiber fiber · Polypropylene composite · Mechanical properties

1 Introduction

Since the conclusion of World War II, in various engineering application, metallic and ceramic materials are being replaced by polymeric materials for its some outstanding properties like lightweight, corrosion resistant, low cost, easy processing and so on. Many of the modern technologies especially aerospace and transportation require the materials having the properties combination of metal, ceramics and polymer. Engineers of these field are searching high impact and tensile strength, abrasion and

G. Sai Krishnan (✉) · Shanmugasundar · G. B. Loganathan
Rajalakshmi Institute of Technology, Chennai 600124, India
e-mail: g.saikrishnan@gmail.com

Shanmugasundar · R. Pradhan · G. B. Loganathan
Sri Sairam Institute of Technology, Chennai, India

Shanmugasundar · G. B. Loganathan
Pace Institute of Technology and Sciences, Ongole, India

Tishk International University, Erbil, Iraq

© Springer Nature Singapore Pte Ltd. 2020

A. Praveen Kumar et al. (eds.), *Advances in Lightweight Materials and Structures*,
Springer Proceedings in Materials 8, https://doi.org/10.1007/978-981-15-7827-4_27

corrosion resistant lightweight materials. Composites materials are the best choice so far in that context [1]. Among various natural fibers, jute is the most widely used, easily available as natural resource and popular cash crop in southern Asia. On the other hand, banana comes as an interesting and attractive addition. In hot tropical country, banana is naturally grown and its trunk. Pseudo stem is thrown as agricultural waste to a great extent. The fiber obtained from banana fibers and other fibers has various superior applications and unique properties [2, 3]. Moreover, jute banana, areca, etc., fibers are lightweight, cheap, easily available and renewable [3–5].

In spite of having such outstanding properties, natural fiber provides very less reinforcement as compared to synthetic fiber. One way of increasing reinforcing effect is chemical treatment of natural fiber. This in turn increases adhesion between the matrix and the fiber and subsequently reinforcing capacity of natural fibers also gets increased [6]. The fibers were identified based on the locations in the geographical areas. In present research, attempts were taken to find out the better reinforcing material regarding its availability, bio degradability, cost, mechanical properties and extraction method. Jute and banana fiber reinforced polypropylene composites were prepared using a hot press machine. Both jute and banana fiber were chemically treated with Na_2CO_3 to increase the adhesion between polypropylene and fiber. Mechanical testing and thermal characterization of prepared composites were conducted. Finally, the effect of fiber type, fiber loading and chemical treatment on mechanical and thermal properties was evaluated [7].

1.1 Chemical Modification and Extraction of Fibers

The extracted fibers used in this process were subjected to retting. The banana and Areca fibers that were used were collected and extracted in the form of fibers jute fiber, banana fiber, commercial grade polypropylene and sodium carbonate were used in this study. All of them (except the banana fiber) were collected from the local market. The buckle of banana tree was cut and separated to appropriate size. Then, they were submerged in water about 10 days for fermentation. After retting, the husks of banana fiber were beaten with a hammer and cleaned with freshwater. Then, fibers were ripped off from the husks and separated from the comb. After drying, the fibers were combed with a cotton carding frame for several times further separate the fibers in to individual state. Polypropylene matrix was white in color, and the density was found to be 0.905 g/cm^3. Both Areca and banana fiber were treated with sodium carbonate for enhancing their compatibility with polypropylene. The fibers were put in a vessel containing solution of 5 wt.% sodium carbonate, and pressure was applied to ensure good impregnation of Na_2CO_3 solution for 1 day. The fibers were washed thoroughly with water to remove the excess of Na_2CO_3 from their surface. The fibers were finally air dried for 8 h. Four different composites were developed in the proportions such as 5 and 10%. They have given designation as BA5%, BA10% and AR5% and AR10%.

2 Formation and Characterization of Composites

The hand layup methods were used to develop the composites as shown in Figs. 1 and 2. The same procedure used by us in the previous work was followed to develop



Fig. 1 Development of chemically treated banana and Areca fiber composites



Fig. 2 Fabrication of composites

the composites. The developed composites were characterized for its tensile flexural and impact strength. The developed composites were tested as per ASTM standards. The test description carried out was made as per the same procedure in the literature provided [8–10].

3 Results and Discussions

The manufacturing of composites was done by using traditional hand layup method. Various mechanical properties were examined, and they mainly depend on three important factors such as interlocking of mechanical forces, Vander walls forces and interlock bonding. Strength and hardness depend on the crack present in the surface of the matrix and surface orientation of the matrix used in the composites.

3.1 Tensile Properties

The tensile strength of the developed composites got increased with the increase in the fiber content as shown in Figs. 3 and 4. The same trend is observed in the previous research also [11–13]. Both the areca and banana have higher tensile strength than polypropylene, incorporation of higher fiber into polypropylene increased tensile strength more. Banana fiber gave slightly better reinforcement in polypropylene matrix as compared to areca fiber. Banana fiber has more uniform cross section and greater aspect ratio as compared to areca fiber. Thus, banana fiber can distribute load from matrix in a better way. It also restricts crack growth and inhibits matrix failure better. As a result, banana fiber composites had higher tensile strength [12].The treatment of banana and areca fiber with 5 wt.% of sodium carbonate increased the tensile strength. The same trend was observed in the previous work.



Fig. 3 Tensile fractured tested specimen

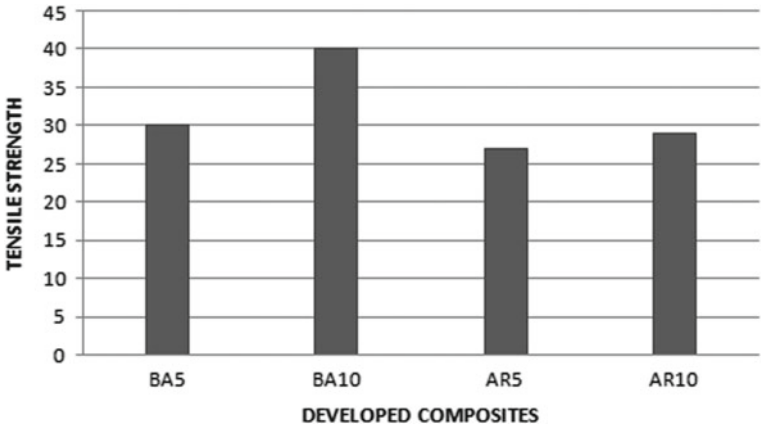


Fig. 4 Tensile strength of the composites

3.2 Flexural Properties

Flexural strength of the developed composites with 5 and 10 weight percentages of the alkali-treated sodium carbonate is carried out. Flexural strength varies with the similar fashion as tensile strength. Flexural strength of polypropylene and various prepared composites is shown in Fig. 5. The flexural strength increased with the increase in the percentage of fiber weight percentage. Out of the two composites, the chemically treated 10 wt.% of banana had good results. The favorable entanglement of the polymer chain with the filler may be the reason of improvement [14]. 0.5% Na_2Co_3 treatment increased flexural strength of both areca and banana fiber with 10 wt.% reinforced polypropylene composites as compared to 5 wt.% of areca and

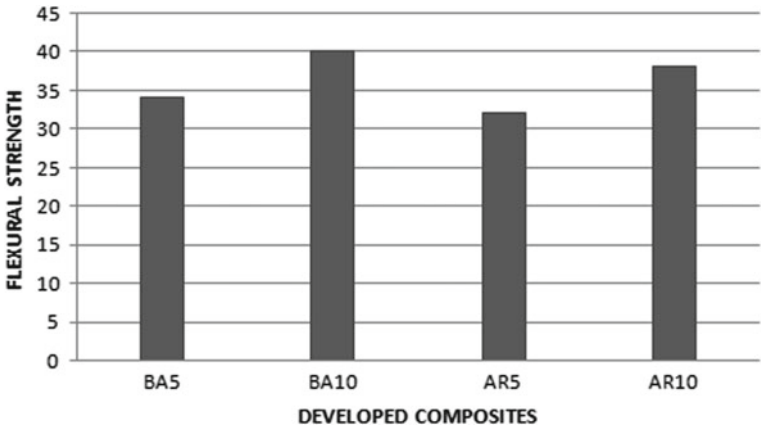


Fig. 5 Flexural strength of the composites

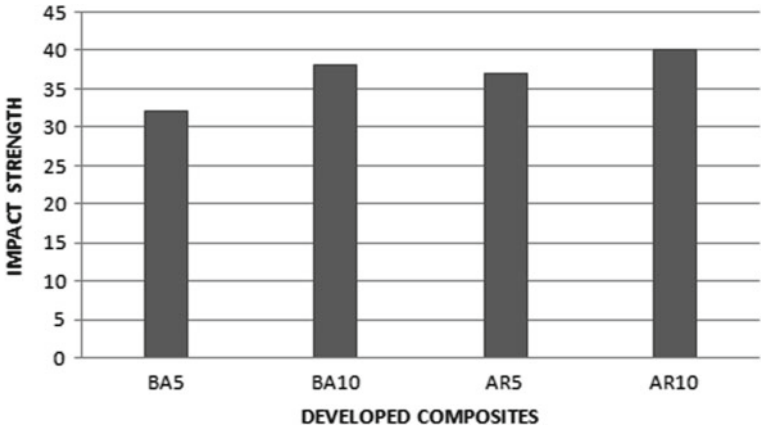


Fig. 6 Impact strength of composites

banana fiber reinforced polypropylene composites. Previous research confirmed this phenomenon due to surface modification of the fiber [15, 16, 18].

3.3 Impact Properties

Impact properties of the developed composites are identified and present in Fig. 6. Impact strength for the banana fibers was slightly higher than that of the areca fibers. This is mainly due to the fiber addition and alkali treatment of both the fibers. The addition of the natural fibers reduced the flexibility by reducing the molecular movement of the matrix material. Previous research confirmed this phenomenon due to surface modification of the fiber [17–19]. The 10 wt.% of the areca and banana had good properties. But there is not much difference in the impact strength of the developed composites. This is due to the poor bonding and improper adhesion.

4 Conclusion

In this present work, the areca and banana fibers were treated with sodium carbonate, and the composites were prepared.

- The results symbolize that the mechanical properties and thermal stability showed increasing trend on addition of fibers and sodium carbonate treatment.
- Both the areca and banana have higher tensile strength than polypropylene, incorporation of higher fiber into polypropylene increased tensile strength more. Banana fiber gave slightly better reinforcement property in polypropylene matrix

as compared to areca fiber. Banana fiber has more uniform cross section and greater aspect ratio as compared to areca fiber. Thus, banana fiber can distribute load from matrix in a better way.

- The flexural strength and impact strength also increased with the increase in the percentage of fiber weight percentage. Out of the two composites, the chemically treated 10 wt.% of banana had good results.
- Based on all the results, these fibers can be added as a reinforcement in various polymeric applications.

References

1. Sanjay MR, Siengchin S, Parameswaranpillai J, Jawaid M, Pruncu CI, Khan A (2019) A comprehensive review of techniques for natural fibers as reinforcement in composites: preparation, processing and characterization. Carbohydrate Polym 207:108–121
2. Liu Y, Fan Z, Ma H, Tan Y, Qiao J (2006) Application of nano powderedrubber in friction materials. Wear 261(2):225–229
3. Chang H (2013) Brake friction materials. In: Wang QJ, Chung Y-W (eds) Encyclopedia of tribology, Springer, Boston, MA, pp 263–273; Chang YH, Joo BS, Lee SM, Jang H (2018) Size effect of tire rubber particles on tribological properties of brake friction materials. Wear 394–395, 80–86
4. Praveen Kumar A, Jeyalal P, Barani Kumar D (2012) Hybridization of polymer composites. Int J Adv Mater Sci 3:173–182
5. Praveen Kumar A, Kumarasamy GS, Nikhil N(2015) Analysis of carbon fiber reinforced polymer composite hip prosthesis based on static and dynamic loading. Int J Appl Eng Res 10(85):574–579
6. Kumar D, Babu G, SaiKrishnan G (2019) Study on mechanical & thermal properties of PCL blended graphene bio composites, 29(2). ISSN 1678-5169. Published in Polímeros
7. Saikrishnan G, Jayakumari LS, Suresh G (2019) Investigation on the physical, mechanical and tribological properties of areca sheath fibers for brake pad applications. 2019/6/12 Published in Mater Res Express 6(8):085109
8. Saikrishnan G Influence of iron–aluminum alloy on the tribological performance of non-asbestos brake friction materials—a solution for copper replacement. Ind Lubric Tribol
9. Manoharan S, Sai Krishnan G, Ganesh Babu L, Vijay R, Lenin Singaravelu D Synergistic effect of red mud-iron sulfide particles on fade-recovery characteristics of non-asbestos organic brake friction composites. Mater Res Express 6(10)
10. Jafrey Daniel James D, Manoharan S, Saikrishnan G, Arjun S Influence of bagasse/sisal fibre stacking sequence on the mechanical characteristics of hybrid-epoxy composites. J Nat Fibers
11. Jafrey Daniel D, Sai Krishnan G and Velmurugan P Investigation on the characteristics of bamboo/jute reinforced hybrid epoxy polymer composites Mater Res Express 6:105346
12. Sai Krishnan G, Ganesh Babu L, Siva Shanmugam N (2019) Experimental investigation of wear behaviour of A356-Tib2 metal matrix composites. Int J Mech Prod Eng Res Develop (IJMPERD) 9(3):1353–1362. ISSN(P):2249-6890; ISSN(E): 2249-8001
13. Fidelis MEA, Pereira TVC, Gomes ODFM, Silva FDA, Filho RDT (2013) The effect of fiber morphology on the tensile strength of natural fibers. J Mater Res Technol 2(2):149–157
14. Ramnath BV, Manickavasagam V, Elanchezhian C, Krishna CV, Karthik S, Saravanan K (2014) Determination of mechanical properties of intra-layer abaca–jute–glass fiber reinforced composite. Mater Des 60:643–652
15. Reddy EVS, Rajulu AV, Reddy KH, Reddy GR (2010) Chemical resistance and tensile properties of glass and bamboo fibers reinforced polyester hybrid composites. J Reinf Plast Compos 29(14):2119–2123

16. Panthapulakkal S, Sain M (2006) Injection-molded short hemp fiber/glass fiber-reinforced polypropylene hybrid composites—mechanical, water absorption and thermal properties. J Appl Polym Sci 103(4):2432–2441
17. Praveen Kumar A, Nalla Mohamed M, Kurien Philips K, Ashwin J (2016) Development of novel natural composites with fly ash reinforcements and investigation of their tensile properties.Appl Mech Mater 852:55–60
18. Sai Krishnan Ganesh, Gunda Y, Mohan SRJ, Raghunathan V (2020) 2020 Influence of stacking sequence on the mechanical and water absorption characteristics of areca sheath-palm leaf sheath fibers reinforced epoxy composites 2020/7/9. J Nat Fibers
19. Krishnan GS (2020) Investigation of Caryota urens fibers on physical, chemical, mechanical and tribological properties for brake pad applications. Mater Res Express 015310

Tensile Loading Rate Effect on Open-Hole Tensile Strength and Failure Mechanism of Polymer Composites



Sunny, K. K. Singh, and Ruchir Shrivastava

Abstract Glass fiber reinforced polymer composite used in advanced engineering exercise as a frame in the aviation and automobile industries is often exposed to circular holes to connect different components through joints such as a bolt joint. In this article, the tensile strength of symmetric GFRP laminates with an open hole, and its failure mechanism under uniaxial varying tensile loading rate (1, 10, 50, and 100 mm/min) was investigated. The specimens were produced using the hand-lay-up process. Samples were prepared in compliance with the ASTM D5766 standard and tested with a 50 KN load cell on a universal Hounsfield H50KS testing machine. A numerical model was developed with shell model 3D deformable and meshed with the S4R element. Numerical results were compared with experimental results. Results suggest that the maximum tensile strength of composite specimens with open hole increased as the loading rate increased, and the debonding of fiber is a highly dominant failure mechanism as compared to other failures. The maximum tensile strength of specimens with a higher loading rate (100 mm/min) is maximum and is comparatively 15.04% greater than in slower loading rate of 1 mm/min. The experimental data reveal that rate-dependent constitutive relationships are helpful in modeling polymer composites and are used to estimate the effective failure response of composites.

Keywords GFRP · Hole · Tensile strength · Loading rate effect · Numerical simulation

1 Introduction

Composite materials play a crucial role in the development of high-performance, lightweight structures in recent years [1]. Along with corrosion resistance, these materials offer high stiffness and a high strength-to-weight ratio. Which make it relevant in the field of aircraft, vehicles shipbuilding and housing goods [2]. They are

Sunny · K. K. Singh · R. Shrivastava (✉)
IIT(ISM) Dhanbad, Dhanbad, India
e-mail: ruchirpanduka@gmail.com

© Springer Nature Singapore Pte Ltd. 2020

A. Praveen Kumar et al. (eds.), *Advances in Lightweight Materials and Structures*,
Springer Proceedings in Materials 8, https://doi.org/10.1007/978-981-15-7827-4_28

also found extremely useful in an orthopedic surgical substitute for bone implants [3].

Joints can be adhesive-bonded, mechanically bonded using bolts, and combination of both [4]. The bonded joints provide a lightweight and a tight grip on the frame, but for the sealed surface, they need other conditions. Relatively, mechanically fastened joints do not need location surface preparation to reduce complexity, therefore such composites are exposed to open holes to link with several other parts [5]. These holes will interfere with the force flow in the path of the fibers and produce large quantities of stress around the hole area. This stresses the level around the hole in the available space for the failure of the components. This causes weakening of elements of the structure leading to complete failure. The rise in the use of GFRP laminates in the development of structural components with significant mechanical efficiency demands comprehensible explanation of the tensile nature of these composites with holes [6]. The literature suggests need of further investigations of these composites, when it succumb to higher loading rates [7].

Shokrieh and Jamal-Omidi [8] examined the mechanical behavior of GFRP composites at different uniaxial strain rate (0.0017, 0.55, 5.6, 46, and $85s^{-1}$). The results of the experiment showed an increase of 51.52%, 11.83%, 8.98%, and 53.12% in tensile strength, elastic modulus, failure strain, and absorbed failure energy at $85s^{-1}$ strain rate, respectively, compared to lowest strain rate ($0.0017s^{-1}$). Gilat et al. [9] investigated material (carbon/epoxy laminate) response under tensile test at different strain rate (range is 0.4×10^3–0.6×10^3) and evaluated for different adhesives and laminate combinations at different strain levels. The results showed a significant impact on the material behavior of the strain speed. It was observed from the experiment result that the tests with [45°] and [$\pm 45^\circ$] specimens have a more dominant impact on the peak stress of the strain frequency. Lim et al. [10] analyzed the influence on deformation mechanisms and tensile yielding of the loading speed (0.0001–0.1/s) and temperature ($-45°$ to $70°$) of polymer (nylon 6-based nanocomposites) also contain rubber particles (poly oligo ethylene glycol methacrylate). The volumetric strains result suggested that nanocomposites decreased the delamination of the organoclay layer and increased shear deformation. Elanchezhian et al. [11] investigated the mechanical behavior of GFRP and CFRP by experiment with the specimen at different strain frequencies and temperatures. CFRP's tensile and flexural strength is comparatively larger compared to GFRP, and it has the highest load amount of 36.262 KN and 1.785 KN, respectively. Velmurugan [12] examined the strain-dependent nature of glass/epoxy laminate filled with nano clay and found that when strain rates increases both strength and stiffness increases. Li et al. [13] examined the impact of strain speeds under tensile as well as compressive loads over warp-knitted and flat woven CFRP laminate. The result identified that tensile strength increased when the strain frequency has grown in both types of composite material though marginal influences are found on compressive strength. Fereshteh–Saniee et al. [14] examined the material properties of GFRP composite at the low level of strain. As a consequence, the strength and rigidity increased by 24.70% and 4.20% accordingly, increasing the frequency of the strain from 10^{-4} to $11 \times 10^{-2}s^{-1}$. Amijima et al. [15] determined the influence of strain speed on the compressive

behavior of GFRP laminate. The strain speed ranged from 0.001 to 1.03 $\times$ $10^2 s^{-1}$, and increased compressive strength with higher strain rate was observed.

In the present work, an attempt has been made to investigate the tensile nature of circular hole GFRP laminate at various loading rates. In all tests, specimens with the same geometry are used. The loading rate effect on open-hole tensile strength was examined with emphasis on damage mechanism and later compared with numerical results.

2 Materials, Process, and Fabrication

The glass fabric [600 GSM (Gram per square meter)] used in this experimental study is bidirectionally woven and is purchased from S. S. Polymer, Bengaluru. Thermosetting epoxy (Bisphenol-A) and hardener (Amine) were also procured from same manufacturer used in these experimental sets.

Firstly, the matrix is prepared by mixing the thermosetting resin and curing agent (10:1 ratio), followed by mechanical stirring for 5–7 min. Based on the stacking sequence, the glass woven fabric plies are rinsed using a soft paintbrush, and a heavy steel roller forced out the excessive resin [16]. Subsequently, laminate was secured in a resealable plastic carrier and compressed using a compression molding machine under the constant pressure of 19.8 MPa. Besides, laminate was kept at ambient temperature for 12 h under constant pressure for curing. According to the ASTM D5766 standard [17], the specimens (150 mm $\times$ 36 mm $\times$ 2.8 mm) were cut from the laminate. A drilling machine drilled the specimens for creation of 6 mm diameter hole at the center of the specimen (Fig. 1).

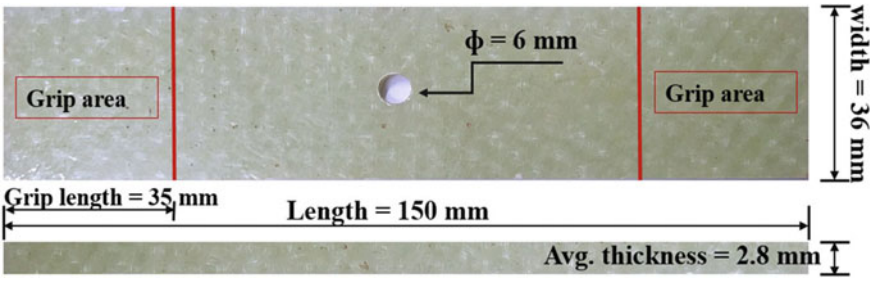


Fig. 1 Standard specimen dimensions

3 Experimental Setup

Testing was done on Hounsfield (H50KS), a computerized universal testing machine (UTM) with a peak load of 50 KN, as shown in Fig. 2. Tests were conducted at four separate loading speeds of 1 mm/min, 10 mm/min, 50 mm/min, and 100 mm/min. There were three specimens in each category of samples, and therefore, twelve specimens have been analyzed. The maximum tensile strength was determined from formula (1).

$$\sigma_{\max} = \frac{F_{\max}}{A} \tag{1}$$

where $F_{\max}$ is peak force sustained by experimental sample (N), A is gross cross-sectional area (excluding hole,mm^2), and $\sigma_{\max}$ is maximum tensile strength with an open hole (MPa).

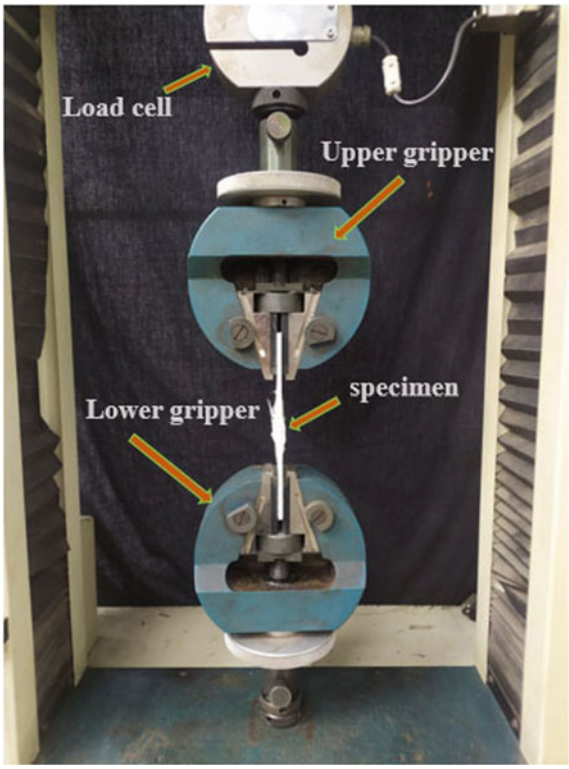


Fig. 2 Tensile testing experimental setup

4 Results and Discussion

The maximum load-carrying capacity of open-hole GFRP specimens increases, while deflection decreases when the loading rate is increased because of failing in a brittle way at a larger loading rate (Fig. 3). The load-carrying capacity increased by 5.6, 12.18, and 17.25% at loading rate of 10, 50, and 100 mm/min, respectively, compared with slower loading rate (1 mm/min), but deflection decreased by 5.83, 9.3, 12.22%.

Based on the results obtained from Eq. (1), the maximum tensile strength in composite specimens increased by increasing the loading rate, as shown in Fig. 4, due to non-homogeneous distortion in the sample and strain hardening after viscoelastic behavior of epoxy/hardener solution [18]. The ultimate tensile stress increased at a larger loading speed. The tensile strength increased by 7.02%, 8.72%, 15.04% at loading rate of 10, 50, and 100 mm/min, respectively. Lower the value of the CV in Table 1, so the result is precise in the experimental data from the same unit. Therefore, the result of specimens for a loading rate of 50 mm/min is more accurate as compared to other loading rates.

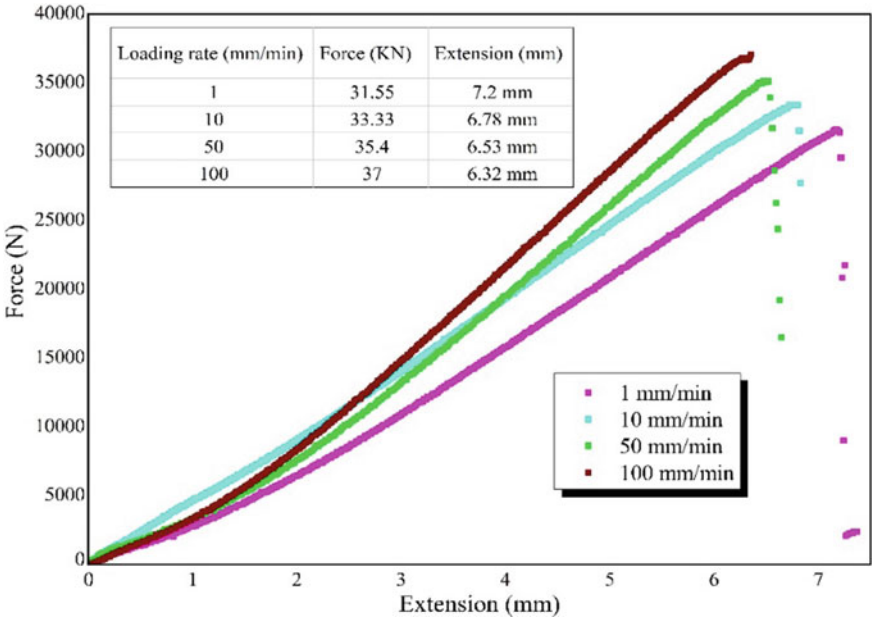


Fig. 3 Force versus extension curves of tested specimens at different loading rates

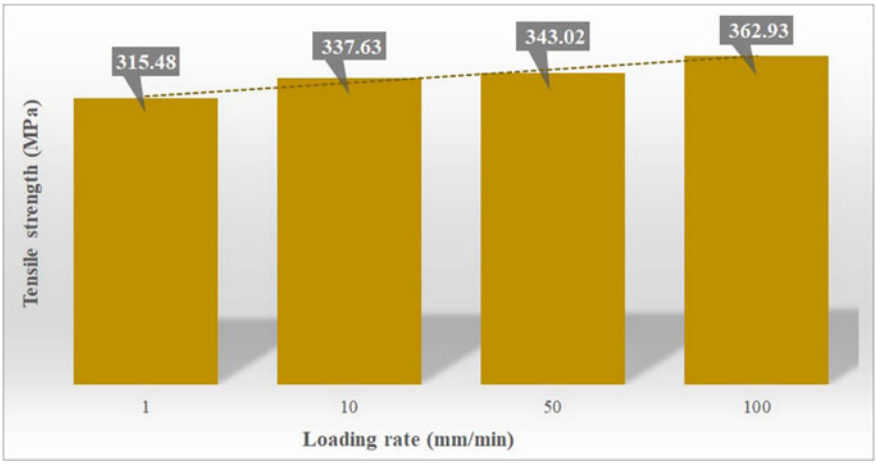


Fig. 4 Histogram of tensile strength at different loading rates

Table 1 Show precise results for each group specimen

Specimen group number	Loading rate (mm/min)	Tensile strength	
		SD	CV (%)
1	1	4.76	1.50
2	10	7.14	1.96
3	50	2.64	0.76
4	100	8.56	2.35

5 Fractographic Analysis

During the tensile test, the failure mechanism was observed through the digital microscope. The failure initiates with matrix cracking around the hole, whereas the crack surfaces around both upper and lower parts of the hole and exit to the edge side of the sample are shown in Fig. 5a.

Laminate fails at the hole in tension and displays several failure modes in various sub-laminates. The zero-degree plies failed laterally across the middle of the hole, and the angle plies failed through the lateral centerline of the hole in Fig. 5b.

Secondly, the delamination of ply, splitting of fiber, and fiber breakage have occurred simultaneously in the tensile test specimen, as shown in Fig. 6. However, the dominant mechanism of failure was observed to be splitting of fibers from the epoxy/hardener solution [19].

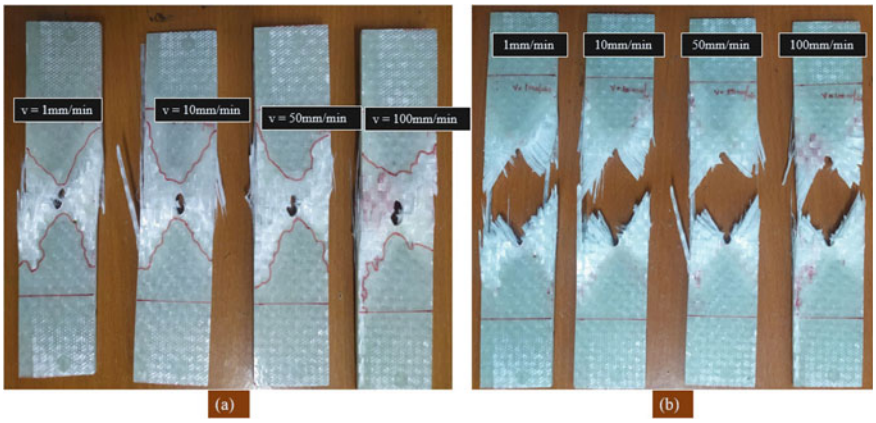


Fig. 5 Specimens after **a** failure, **b** fracture

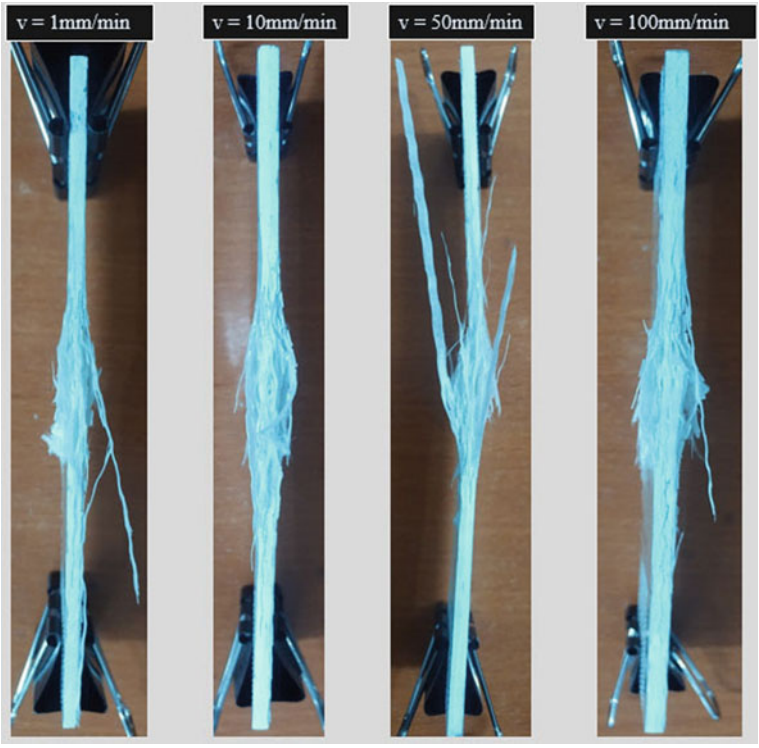


Fig. 6 Side view of samples after failure at different loading rates

6 Numerical Analysis

The numerical method is used to investigate the tensile failure pattern in the specimen at different time intervals during testing using Abaqus-6.14. The composite part with through-hole ($d = 6$) has been modeled as a deformable 3D shell. Nine engineering constants were defined for laminate, as shown in Table 2. Young modulus, shear modulus, and poison ratio of glass/epoxy lamina were chosen from Ref. [20]. GFRP laminate stacking sequence was created in the composite-layup option by taking each lamina thickness ($t = 0.35$ mm), material properties, and fiber angle. Create an instance in the assembly module and select dependent mesh. The step section specified analysis steps and forms of analysis. History output requests were also nominated in this module. Create constraint by coupling to hold the workpiece in the interaction module. The reference point (RP 2) was restricted as ENCASTRE in tension test simulation, while the reference point (RP 1) was moved by load. The meshed specimen is shown in Fig. 7.

The failure mechanism was observed from the simulation of the Abaqus model at different periods (52, 105, and 150 s) and loading rate (1, 10, 50, and 100 mm/min), as shown in Fig. 8. The area around the hole is more affected when the loading rate increases, and half of the hole is less moved than at a lower loading rate. The half portion of the hole is more shifted at a lower loading rate as it gives more time duration during testing and is at 45° sublamina in the laminate. During testing, the results in the failure mechanism are the same by both experimental and numerical methods,

Table 2 Engineering constants for simulation

Lamina	Physical properties (units of E and G = GPa)								
	E_{11}	E_{22}	E_{33}	G_{12}	G_{13}	G_{23}	ν_{12}	ν_{13}	ν_{23}
Glass/epoxy	36.9	10		3.3		3.6	0.32		0.44

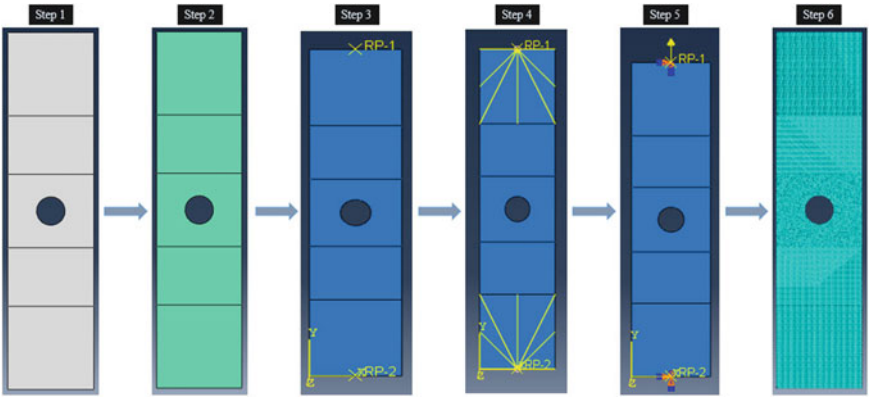


Fig.7 Process flow for preparing the model in Abaqus

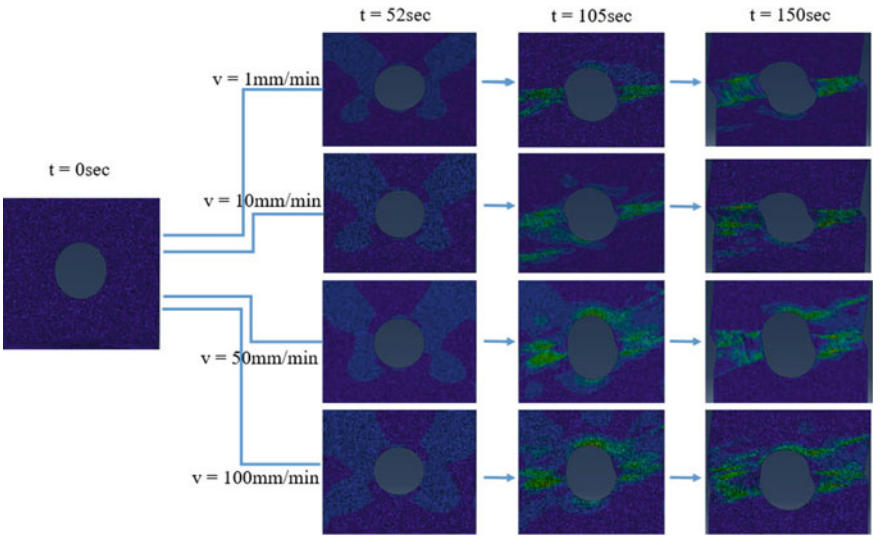


Fig. 8 Failure analysis through numerical simulation

as shown in Fig. 9. Thus, the simulation result is validated through a numerical approach.

7 Conclusion

The influence on maximum tensile strength and failure mechanisms of GFRP composites with an open hole of varying loading speed has been investigated. The work can be summarized as follows

- The load-carrying capacity of open-hole GFRP samples is increased, while the deflection decreases when the loading rate is increased. Compared with a slower loading rate (1 mm/min), the maximum load-carrying capacity increased by 17.25% at a loading rate of 100 mm/min, but maximum deflection decreased by 12.22% due to brittle fracture.
- As the loading rate increases, tensile strength increases. At the load speed of 100 mm/min, the maximum tensile strength increased by 15.04%.
- Fiber debonding is the highly dominant failure mechanism in open-hole tensile testing in comparison with matrix cracking, delamination, and fiber breakage.
- The area around the hole is more affected at a higher loading rate compared to a lower loading rate, and half portion of the hole moves more at the lowest loading rate.

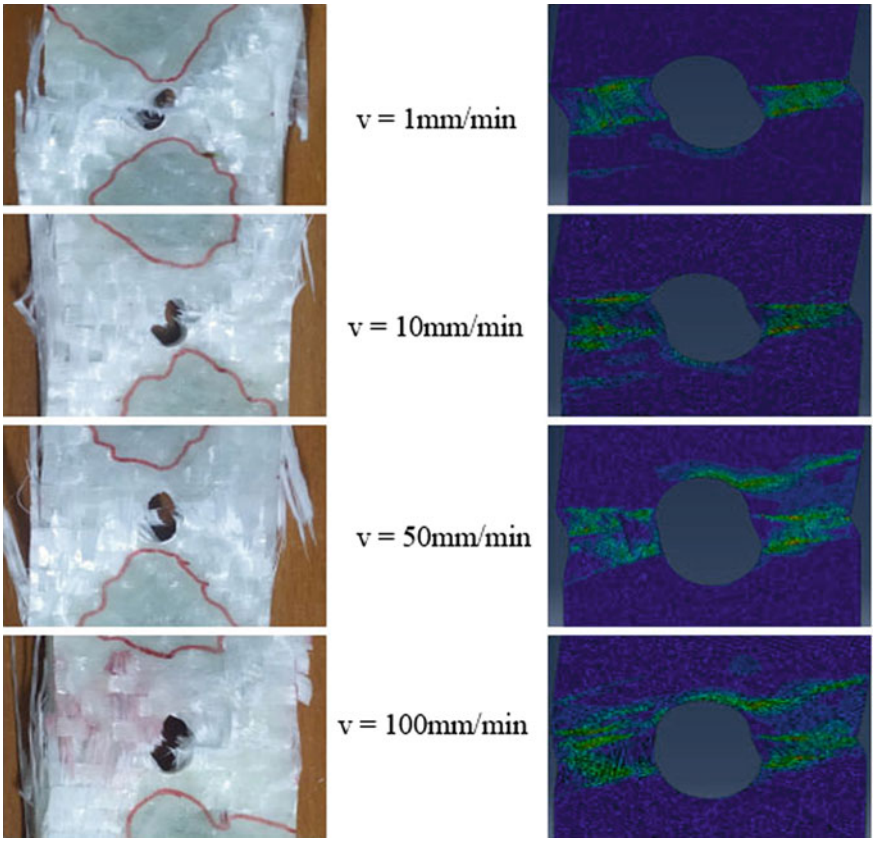


Fig. 9 Comparison between experimental and numerical approach through failure mechanism

- In the failure mechanism, the simulation outcomes had been in better covenant with the testing outcomes indicating the ability of the simulation methodology to estimate tensile failure behavior.

The experimental data reveal that rate-dependent constitutive relationships are helpful in modeling polymer composites and are used to estimate the effective failure response of composites. The information provided here is used to be useful for the creation of constitutive ideas.

References

1. Lambiase F, Durante M (2017) Mechanical behavior of punched holes produced on thin glass fiber reinforced plastic laminates. Compos Struct 173:25–34. https://doi.org/10.1016/j.compstruct.2017.04.003

2. Barkoula NM, Alcock B, Cabrera NO, Peijs T (2008) Flame-retardancy properties of intumescent ammonium poly(phosphate) and mineral filler magnesium hydroxide in combination with graphene. Polym Polym Compos 16:101–113. https://doi.org/10.1002/pc
3. Kumar PA, Irudhayam JS (2012) A review on importance and recent applications of polymer composites in orthopaedics. Int J Eng Res Dev 5:2278–2367
4. Mohan NS, Kulkarni SM, Ramachandra A (2007) Delamination analysis in drilling process of glass fiber reinforced plastic (GFRP) composite materials. J Mater Process Technol 186:265–271. https://doi.org/10.1016/j.jmatprotec.2006.12.043
5. Zhang Z, Yang Y, Hamada H (2015) The effects of open holes on the fracture behaviors and mechanical properties of glass fiber mat composites. Sci Eng Compos Mater 22:555–564. https://doi.org/10.1515/secm-2014-0069
6. Seidlitz H, Gerstenberger C, Osiecki T et al (2014) High-performance lightweight structures with fiber reinforced thermoplastics and structured metal thin sheets. J Mater Sci Res 4. https://doi.org/10.5539/jmsr.v4n1p28
7. Kroll L, Kostka P, Lepper M, Hufenbach W (2009) Extended proof of fibre-reinforced laminates with holes. J Achiev Mater Manuf Eng 33:41–46
8. Shokrieh MM, Omidi MJ (2009) Tension behavior of unidirectional glass/epoxy composites under different strain rates. Compos Struct 88:595–601. https://doi.org/10.1016/j.compstruct.2008.06.012
9. Gilat A, Goldberg RK, Roberts GD (2002) Experimental study of strain-rate-dependent behavior of carbon/epoxy composite. Compos Sci Technol 62:1469–1476. https://doi.org/10.1016/S0266-3538(02)00100-8
10. Lim SH, Yu ZZ, Mai YW (2010) Effects of loading rate and temperature on tensile yielding and deformation mechanisms of nylon 6-based nanocomposites. Compos Sci Technol 70:1994–2002. https://doi.org/10.1016/j.compscitech.2010.07.023
11. Elanchezhian C, Ramnath BV, Hemalatha J (2014) Mechanical behaviour of glass and carbon fibre reinforced composites at varying strain rates and temperatures. Proc Mater Sci 6:1405–1418. https://doi.org/10.1016/j.mspro.2014.07.120
12. Velmurugan R, Gurusideswar S (2014) Strain rate dependent behavior of glass/nano clay filled epoxy resin composite. Def Sci J 64:295–302. https://doi.org/10.14429/dsj.64.7331
13. Li X, Yan Y, Guo L, Xu C (2016) Effect of strain rate on the mechanical properties of carbon/epoxy composites under quasi-static and dynamic loadings. Polym Test 52:254–264. https://doi.org/10.1016/j.polymertesting.2016.05.002
14. Fereshteh-Saniee F, Majzoobi GH, Bahrami M (2005) An experimental study on the behavior of glass-epoxy composite at low strain rates. J Mater Process Technol 162–163:39–45. https://doi.org/10.1016/j.jmatprotec.2005.02.011
15. Rafique Rizvi M, Singh KK, Gaurav A, Kumar Singh R (2018) Effect of strain rate on flexure properties of GFRP laminates—an experimental and numerical investigation. IOP Conf Ser Mater Sci Eng 377. https://doi.org/10.1088/1757-899X/377/1/012085
16. Kumar AP, Jeyalal LP, Kumar DB (2012) Hybridization of polymer composites. Int J Adv Mater Sci 3:173–182
17. ASTM International (2014) ASTM D5766/D5766M-11 standard test method for open-hole tensile strength of polymer matrix composite. Annu B ASTM Stand 11:1–7. https://doi.org/10.1520/D5766
18. Ali A, Nasir MA, Khalid MY et al (2019) Experimental and numerical characterization of mechanical properties of carbon/jute fabric reinforced epoxy hybrid composites. J Mech Sci Technol 33:4217–4226. https://doi.org/10.1007/s12206-019-0817-9
19. Naresh K, Shankar K, Rao BS, Velmurugan R (2016) Effect of high strain rate on glass/carbon/hybrid fiber reinforced epoxy laminated composites. Compos Part B Eng 100:125–135. https://doi.org/10.1016/j.compositesb.2016.06.007
20. Koloor R, Khosravani MR, Hamzah RIR, Tamin MN (2018) FE model-based construction and progressive damage processes of FRP composite laminates with different manufacturing processes. Int J Mech Sci 141:223–235. https://doi.org/10.1016/j.ijmecsci.2018.03.028

Soil Stabilization with Nanomaterials and Extraction of Nanosilica: A Review



Karumanchi Meeravali, Nerella Ruben, and Mikkili Indira

Abstract The ability varied in the volume changes under moisture content in soft clays. The soil transformed into weak in the supporting of the structure leads to fail in various construction and geotechnical engineering failures. These type soils under these situations needed to stabilize with additives before making a substantial basement, embankment, and excellent foundations for any structures. This chapter approaches with analysis or review of some earlier works of literature done to develop the geotechnical properties of very soft clay by using nanomaterials such as terrasil and nanosilica. The properties of nanomaterials are excellent bonding with soils. The preparation and availability of nanomaterials are also needed to stabilize weak soils. The preparation of nanosilica from agricultural wastes using acid mixtures is mainly concentrated, and the microanalysis for stabilization with nanomaterials, and preparation of nanosilica by XRD, EDS, and FT-IR is done.

Keywords Soft-soil · Stabilization · Nanosilica · Terrasil · Microanalysis · Geotechnical properties

1 Introduction

Initially, improving soil properties used stabilizing agents such as cement, lime, and silica flume. These agents produced many environmental problems like CO_2 emission, increasing pollutants in the air. Stabilized soil used cement for many applications, but the problems are that it takes more curing period, more content of cement, and cost factor also. To overcome these problems, the nanomaterials as stabilizing materials are introduced—the nanomaterials, terrasil, nanosilica, and nanoclay. The act of nanomaterials increased in many applications like construction, geotechnical,

K. Meeravali (✉) · N. Ruben
Department of Civil Engineering, Vignan's Foundation for Science, Technology, and Research (Deemed To Be University), Vadlamudi, Guntur 522213, AP, India
e-mail: meeravali.k123@gmail.com

M. Indira
Department of Biotechnology, Vignan's Foundation for Science, Technology, and Research (Deemed To Be University), Vadlamudi, Guntur 522213, AP, India

© Springer Nature Singapore Pte Ltd. 2020

A. Praveen Kumar et al. (eds.), *Advances in Lightweight Materials and Structures*,
Springer Proceedings in Materials 8, https://doi.org/10.1007/978-981-15-7827-4_29

transportation engineering projects. The nanomaterials have proven with excellent results with any type of soils and treating the soil; the voids are filled in the nano-size of the soils with very low percentages. By adding the nanomaterials to weak soils, the structure is treated as water barrier against any type of load for a longer time [1–4]. The paper is divided into two sections, the primary sections the earlier works of literature about properties and preparation of nanomaterials and nanosilica. The second section explained the earlier works of literature about the improvement and stabilization of soft soils using nanomaterials such as terrasil, nanosilica, and nanoclay. The sections nanomaterials depend on the quality, properties, and qualities of the soils.

2 Nanomaterials: Properties and Preparation

The nanomaterials added to weak soil will complete in soil manipulation at the atomic level and influence improving all the properties of the soil. The nanomaterials treatment is very cheaper with using very low percentages. The properties of the terrasil are explained in Table 1, terrasil is in liquid form, and will mix smoothly with water. The property of the nanosilica is that powder form mixes directly with soils.

2.1 Terrasil

Terrasil is nanomaterials based on its chemical compound, procured by Zydex Industries Pvt Ltd. It's exhibiting proven results with all types of soils, and economical also. Table 1 indicated physical properties of terrasil, the preparation of terrasil is not possible with any type of polymers, so it is procured from industries [4].

2.2 Nanosilica

Among all nanomaterials, the preparation of nanosilica is not difficult and is easy compared to other nanomaterials. The preparation of the nanosilica is from agricultural waste such as straws, husks, and seedpods which are used as raw materials.

Table 1 Physical properties of terrasil [4]

Property	Description
Viscidity at 25 ℃	20–100 cP
Solubility	In liquid
Flash point	Less than 80 °C

Table 2 Residues from the incineration of agricultural wastes

Plant	Ash (%)	Silica (%)	Plant	Ash (%)	Silica (%)
Bagasse	14.71	73	Com	12.15	64.32
Bamboo	1.44	57.4	Lantana	11.24	23.38
Breadfruit tree	8.64	81.8	Rice husk	22.15	93
Wheat	10.48	90.56	Rice straw	14.65	82
Coffee	–	12	Sorghum	12.25	88.75

The properties of nanosilica are white powdered form with sizes varied from 10 to 80 nm, and the chemical compound is SiO_2 (nanoparticles of SiO_2 called nanosilica). The incineration of waste formed ash; it is converted to silica with acid mixtures [2]. Table 2 indicated the ash contents and silica contents in the percentages obtained from the agricultural wastes [2].

2.3 Preparation of Nanosilica

The preparation of the nanosilica is from agricultural waste such as straws, husks, and seedpods which are used as raw materials. The complete process explains prepared nanosilica in three ways with chemicals HCI, H_2SO_4, and NaOH [2]. Table 3 indicated the process of prepared nanosilica with acid solutions.

3 Soil Stabilization with Nanomaterials

The section explained the stabilizations of weak soil with nanomaterials applied to rectify many constructions, geotechnical, slope stability, and transportations failures. Table 4 consists of the stabilization of different types of soils with different materials with varying percentages.

Table 4 explained that in which percentages strengths devitations happened, that percentages recorded as optimal dosages based on the UCS, plasticity index, specific gravities, and compaction characteristics [16–18]. The index and engineering properties of weak soil improved all strengths with optimal dosages of nanomaterials [19, 20].

4 Microanalysis

Microanalysis carried out SEM (morphology), XRD (intensity of bonding), EDS (major oxides), and FT-IR (stimulates) on stabilizing the soil with nanomaterials

Table 3 Preparation of nanosilica from waste with acid solutions

Process	Mixed agents	Conclusions	References
Incineration process	HCI, H_2SO_4, and NaOH	SVSH washed, cleaned with distilled water. Added HCI, H_2SO_4, and NaOH with required proportions. The resultant nanosilica is the percentage of 98 Nanosilica is prepared from three processes, such as primary is to add acid mixtures with continuous stirring until the solution is transparent. The second process is the same as the primary, but HCI solution is added. The resultant filtered through paper burn it at 700 °C. The third process is to add NaOH and H_2SO_4 with the stirred process	[2]
Incineration with acid mixtures	H_2SO_4	The rice husk used as raw materials for the preparation of nanosilica, while the preparation process added H_2SO_4 at 800–900 °C	[3]

such as terrasil and nanosilica. Figure 1 indicated SEM images for 0–10% nanosilica added to sandy soil. These figures indicated that the void rations decreased with increased percentages of nanosilica. Figure 2 illustrated SEM micrographs, (a, c) dispersive soil, (b, d) treated dispersive soil with 1% nanosilica, and (e) treated dispersive soil with 2% nanosilica after seven days of curing. Figure 3 illustrated the images treated with nanosilica to weak soil.

XRD explained pozzolanic activity between particles and observed that the intensity of CSH gel compares to CH gel by adding or without adding nanosilica. Figures 4 and 5 illustrated more CSH gel on 4% of nanosilica compared to other percentages of nanosilica. EDS obtained major oxides with or without added nanomaterials; Fig. 5 indicated that more silica content compares to all indicated Ft-IR images, wavelengths of treated, and untreated nanomaterials.

5 Conclusion

Concluded from all earlier works of literature, the nanomaterials are used as stabilizing agents for improving geotechnical properties and controlled the properties such as permeability, settlement, seepage, and stability of the structures. Terrasil is

Table 4 Soil stabilization with different materials

Soils, admixtures	Percentages (By weight)	Optimal percentage	Conclusions	References
Sandy soil nanosilica, and cement	0, 4, 8, and 12%	8%	UCS, compaction characteristics improved with optimal dosages of nanosilica to sandy soil, microanalysis by SEM and AFM. CSH gel formed than CH gel	[5]
Soils, nanosilica	0.5–4%	1%	PI reduced 38%, UCS improved and analyzed SEM, FT-IR	[6]
Silty soil, nanosilica	1–12%	8%	Cohesion improved 117%, angle of inter friction improved 128.27% under normal stress 100 kpa	[7]
Iron slag, nanosilica	1–20, 0.1%	10%	Freeze–thaw durability improved on the addition of NS and slag	[8]
Residual soil, nanosilica	0.2–1%	0.4%	Strength, CEC, and ER improved CSH gel formed	[9]
Collapsible soils, nanosilica	2–5%	5%	Engineering properties improved	[10]
Weak soil, nano Ca	0.4–1.2%	1.2%	UCS, residual strength improved	[11]
BC soil, terrasil	0.03–0.09%	0.07%	UCS, permeability characteristics improved	[12]
Soil, terrasil	0.8- 1.2%	1%	Index and engineering properties improved with optimal dosage	[1]
Clay soil, terrasil	0.01–0.08%	0.041%	CBR strength improved from 6 to 13%	[13]
Soft clay, terrasil	0.05–1%	0.07%	6 times improved the characteristics of CBR as subgrade	[14]
Soft clay, fly ash	5–10%	7%	Settlements controlled	[15]

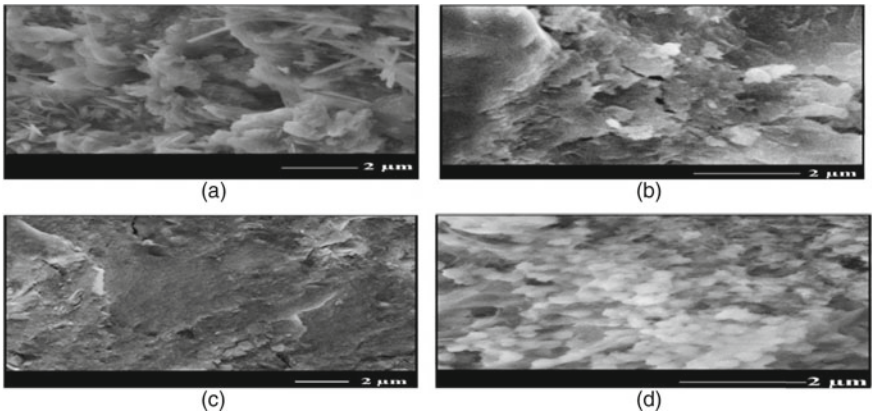


Fig. 1 SEM images **a** 0%, **b** 4%, **c** 8%, and **d** 12% of the nanosilica [5]

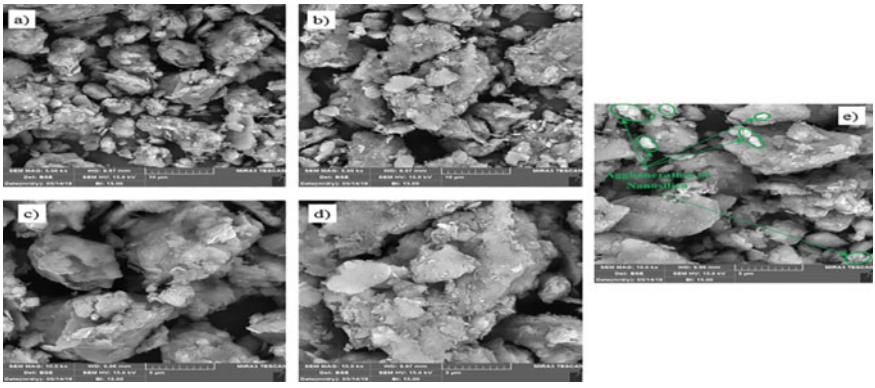


Fig. 2 SEM micrographs; **a**, **c** dispersive soil, **b**, **d** treated dispersive soil with 1% nanosilica, and **e** treated dispersive soil with 2% NS after seven days of curing [6]

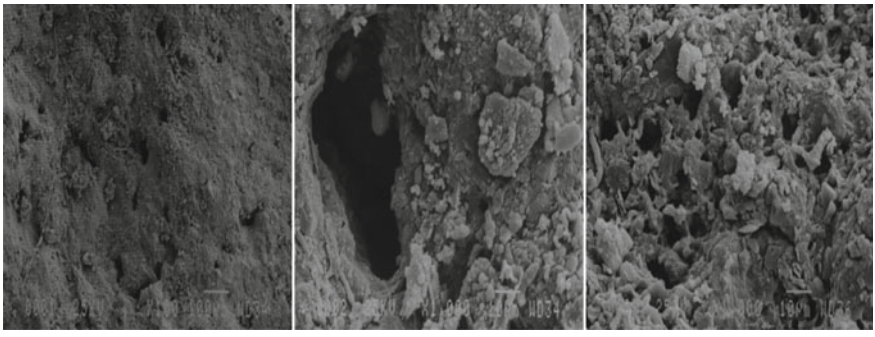


Fig. 3 SEM images for treated with nanosilica to weak soil [10]

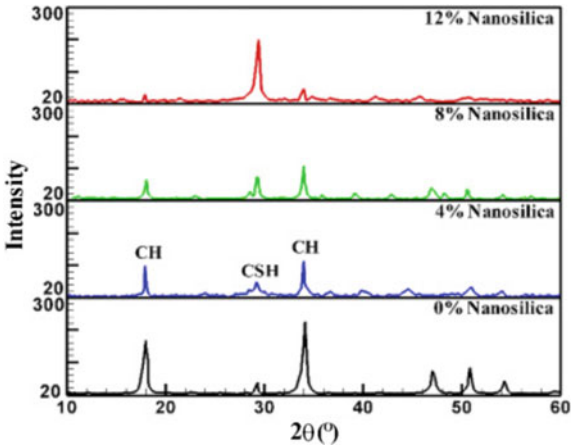


Fig. 4 Effect of nanosilica on sandy soil [5]

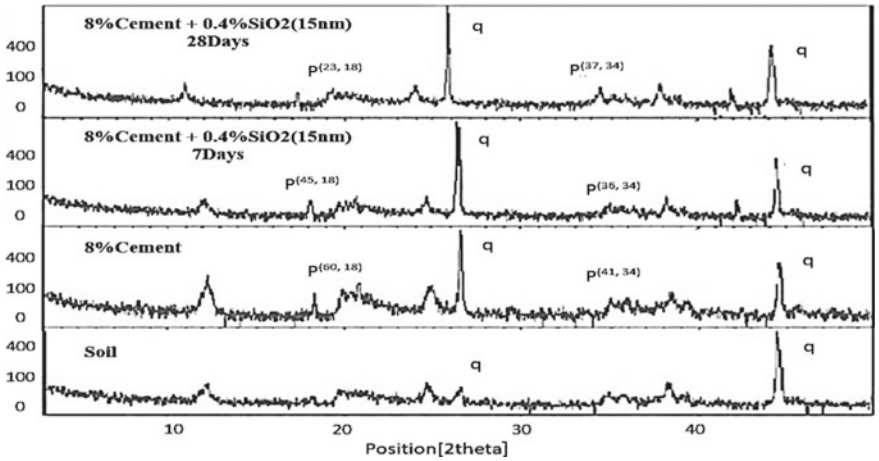


Fig. 5 XRD on nanosilica treated with soil [9]

procured from industries, and nanosilica is prepared from agricultural waste such as straws, husks, and seedpods which are used as raw materials. The specific gravities, UCS, CBR, and void ratios are improved with nanomaterials. The plasticity index, permeability characteristics, and settlements are controlled by increase in nanomaterials. The nanomaterials are used to improve all geotechnical properties and applied in all construction, geotechnical, and transportations engineering structures. In the future, other nanomaterials will be added to stabilize the weak soils.

References

1. Lekha BM et al (2013) Laboratory investigation of soil stabilized with nano chemical. In: Proceedings of Indian geotechnical conference, Dec 22–24
2. Balamurugan M et al (2012) Producing nanosilica from Sorghum Vulgare seed heads. Powder Technol 224:345–350
3. Carmonaa VB et al (2013) Nanosilica from rice husk: extraction and characterization. Ind Crops Prod 43:291–296
4. Selvaraj A et al (2018) Laboratory investigation of soil stabilization using terrasil. Int J Trendy Res Eng Technol (IJTRET) 2(3):6–13
5. Asskar et al (2017) Microstructure characteristics of cement-stabilized sandy soil using nanosilica. J Rock Mech Geotech Eng 9(5):981–988
6. Amir HV et al (2020) Contact erosional behavior of foundation of pavement embankment constructed with nanosilica-treated dispersive soils. In: Soil and foundations
7. Hongzhi C et al (2018) Effect of carbon fiber and nanosilica on shear properties of silty soil and mechanisms. Constr Build Mater 189:286–295
8. Hosam MS et al (2019) Influence of severe climatic variability on the structural, mechanical and chemical stability of cement kiln dust-slag-nanosilica composite used for waste solidification. Constr Build Mater 218:556–567
9. Sayed HB et al (2016) The effect of size and replacement content of nanosilica on strength development of cement-treated residual soil. Constr Build Mater 118:294–306
10. Arash H et al (2019) Feasibility of using electro kinetics and nanomaterials to stabilize and improve collapsible soils. J Rock Mech Geotech Eng 11(5):1055–1065
11. Asskar JC et al (2019) Mechanical properties soil stabilized with nano calcium carbonate and reinforced with carpet waste fibers. Constr Build Mater 211:1094–1104
12. Ajay Kumar P et al (2017) Experimental study on index properties of black cotton soil stabilized with terrasil. Int J Trendy Res Eng Technol 2(3):1337–1343
13. Nandan A et al (2015) Subgrade soil stabilization using chemical additives. Int Res J Eng Technol (IRJET) 02, 04. e-ISSN: 2395-0056
14. Johnson R, Rangaswamy K Improvement of soil properties as a road base material using nano chemical solution. In: 50th Indian geotechnical conference 17th–19th Dec 2015. Pune, Maharashtra
15. Mohamed A, El-sayed, El-Samni TM (2006) J King Saud Univ Eng Sci 19(1):21–30
16. Richard Alonge O et al (2017) Properties of hybrid cementitious composite with metakaoline, nanosilica and epoxy. Constr Build Mater 155:740–750
17. Ranasingle AP (1993) Use of rice straw as pozzolanic. Master thesis no. St-85-1, Asian Institute of Technology
18. Stober W, Fink A, Bohn E (1968) Controlled growth of mono-disperse silica spheres in micron size range. J Colloid Interf Sci 26:62–69
19. Mourhly A et al (2015) The synthesis and characterization of low cost mesoporous silica SiO_2 from local pumice rock. Nanomater Nanotechnol 2015:5–35
20. Najihah F et al (2020) Extraction and characterization of nano-cellulose from raw oil palm leaves. Arab J Sci Eng 45:175–186

Mechanical Properties of AA7050/Coconut Shell Ash Composites Manufactured via Stir Casting Technique



V. Mohanavel, M. Ravichandran, K. S. Ashraff Ali, and A. Praveen Kumar

Abstract Novel inventions and scientific needs in automobile and aircraft sectors ask for modified nonferrous alloy-based composites. The foremost reason of this present experimental work is to evaluate the mechanical characterization of composite materials that were synthesized by a stir casting technique. AA7050 is chosen as matrix material and coconut shell ash (CSA) particles as reinforcement. The base alloy and proposed composite samples were subjected to hardness and tensile test. Metallurgical characterization of parent material and synthesized material were inspected via scanning electron microscope (SEM). Mechanical properties like micro-hardness (HV) and ultimate tensile strength (UTS) of the developed composite materials were improved after the addition of reinforcement content.

Keywords Coconut shell ash · AA7050 alloy · Scanning electron microscope · Hardness · Tensile test

1 Introduction

In the last three decades, aluminium reveals the outstanding and never seen high-class properties like greater strength, good wear protection, nonflammable, low density, lightweight, and protection to corrosion [1]. Nonferrous alloy-based aluminium

V. Mohanavel (✉)
Department of Mechanical Engineering, Chennai Institute of Technology, Chennai, Tamil Nadu 600069, India
e-mail: mohanavel.phd@gmail.com

M. Ravichandran
Department of Mechanical Engineering, K. Ramakrishnan College of Engineering, Trichy, Tamil Nadu 621112, India

K. S. Ashraff Ali
Department of Mechanical Engineering, C. Abdul Hakeem College of Engineering & Technology, Vellore, Tamil Nadu 632509, India

A. Praveen Kumar
Department of Mechanical Engineering, CMR Technical Campus, Hyderabad, Telangana 501401, India

© Springer Nature Singapore Pte Ltd. 2020

A. Praveen Kumar et al. (eds.), *Advances in Lightweight Materials and Structures*,
Springer Proceedings in Materials 8, https://doi.org/10.1007/978-981-15-7827-4_30

composites (AMCs) have turn out to be greater capacity in engineering application like brake disk, piston, connecting rod, drive shaft, and cylinder liner and protection to excessive-temperature operations [2–4].

The utilizing of low-price reinforcement substances will slightly limit the general price of the developed composites and complements its utility. Otherwise, the powerful deployment of the thermal energy plant waste will protect the environment. The size, structure, and weight proportionate of the reinforcement substances work as a sound position in motivating the physical, mechanical, and tribological characteristics of the composites [5–12].

A very few experimental studies on preparation and characterization of composites made of aluminium alloys reinforced with low-priced ash particles were reported in the literatures [13–16]. Shankar et al. [13] have added several wt.% of sugarcane bagasse ash (SBA) to Al–Si10–Mg matrix and enhance in the mechanical characteristics of Al alloy by the inclusion of SBA filler material. They are discovered to enhance in tensile strength and hardness of the synthesized composites with enhance in the weight concentration of SBA reinforcement substances in the Al alloy material. Egg shell ash (ESA) filler material included with AA 6061 alloy matrix composite were produced by Chaithanyasi et al. [14] via liquid metallurgy technique, and they are detected as enriched in hardness and decreased in density of the AMCs with enhancing the mass concentration of ESA particle in the AA6061 alloy. Fly ash particulate incorporated with AA6061 alloy matrix composite were manufactured by Selvam et al. [15] through liquid metallurgy process, and the wear rate rises linearly with enhancing normal load following Archard's law. Alaneme et al. [16] have included 6 and 10 wt.% groundnut shell ash and silicon carbide particles to the Al alloy matrix composites prepared via liquid state method. They reported that the mechanical characteristics of the composites are improved for the addition of filler contents. In this, solid waste-based experimental work is mainly focusing the assessment of microstructure and mechanical characterization of the AA7050/CSA composites.

2 Materials and Methods

AA7050 was picked as a basic material, and the CSA particles of size 60–70 μm are employed as the filler material. AA7050 Al material has been liquefied in the Gr clay crucible inside an furnace, and filler content is included in various wt.% of CSA content. Firstly, eliminate the coconut shells, and then, they were washed, dried in sun light. After heating it in high flame, making into ash powder is by crushing it into fine powder. The measured quantity of filler materials was included to the molten Al. The temperature of the liquid Al melt was frequently maintained at 800 °C. The melt was frequently mixed at 500 rpm, and it was being prolonged for 10 min. Conclusively, the manufactured Al/CSA melt was poured into mold. Microstructure examines were carried out on metallographically polished and etched specimens of both basic alloy and manufactured composites. Figure 1 demonstrates the fabricated



Fig. 1 Fabricated sample

sample. The etched samples were noticed utilizing a scanning electron microscope. The hardness of the specimens is assessed utilizing micro-hardness machine with a force of 0.5 kgf and dwell period of 10 s. Tensile test analysis was conducted on the computer-integrated universal testing machine (CIUTM). The tensile specimens are prepared as per the ASTM E8 standard.

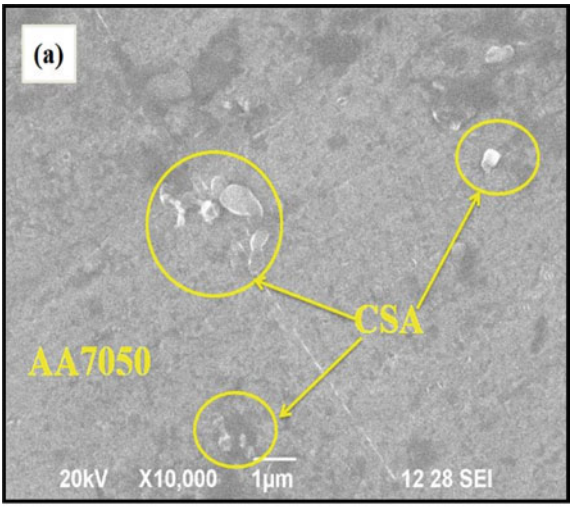
3 Experimental Results and Discussion

3.1 Evaluation of AA7050/CSA Microstructure

Figure 2 reveals the SEM micrograph of AA7050/CSA AMCs. The dissemination of the CSA contents is essentially ascribed to the appropriate mixing of the molten aluminium. The homogeneous dissemination is essentially useful to enhance the physical, mechanical, and tribological behavior of the AMCs [17–22]. The SEM micrograph discovered the occurrence of CSA particles in the fabricated composites with homogeneous dispersion of CSA particles in the aluminium alloy [12].

3.2 Hardness

Figure 3 demonstrates the micro-hardness of the fabricated composite and the basic metal. The hardness of the AMCs augments with acknowledge to addition of the weight concentration of CSA contents. The AA7050/8 wt.% CSA composites exposed superior hardness compare to the base alloy. The hardness has been



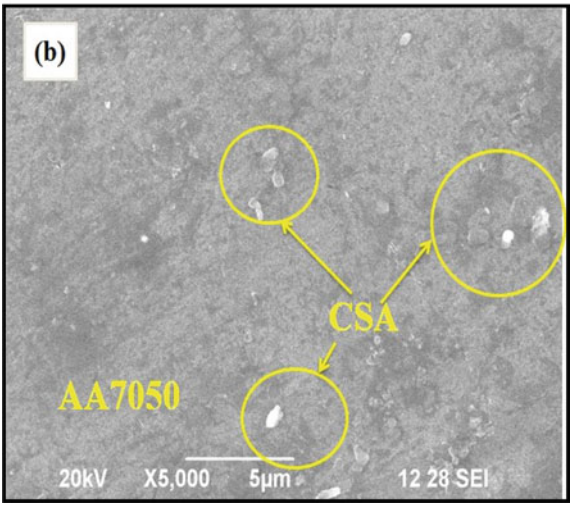


Fig. 2 SEM micrographs of **a** AA7050 + 4 wt.% CSA and **b** AA7050 + 8 wt.% CSA

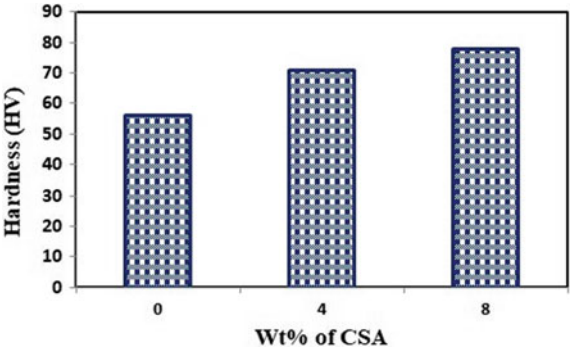


Fig. 3 Micro-hardness of Al and Al/CSA AMCs

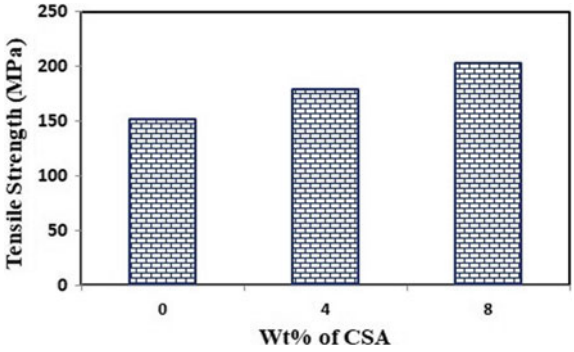


Fig. 4 Tensile properties (UTS) of Al and Al/CSA AMCs

observed to enhance with the increase in CSA contents, and it is noticeably higher to the hardness of the basic AA7050 alloy. This augmentation in hardness might be owing to existence of homogeneous dissemination of CSA particles in the Al alloy.

3.3 Ultimate Tensile Strength

Figure 4 reveals the UTS of the fabricated composite and the basic metal. The tensile test outcomes exhibit the tensile strength of the composite rises with increase in the mass concentration of CSA content, and this could be owing to strong mechanical bonding between the ductile Al metal and the brittle CSA particle. The tensile strength of the AMCs was originally enhanced with improved filler material. Including of CSA contents in to AA7050 melt during manufacturing provides favored sites for nonhomogeneous nucleation of Al matrix grains. Thus, AA7050 metal microstructure is refined by enhancing the mass concentration of CSA particles. The tensile results revealed that the AA7050/8 wt.% CSA AMCs has greater tensile characteristics when compared to the basic metal.

4 Conclusions

The AA7050/CSA composites were efficaciously made through melt stirring process with diverse mass concentration of CSA particle, and the microstructural and mechanical properties were inspected. From this research work, the following concluding remarks are drawn.

- The SEM micrographs exposed the existence of CSA contents in the synthesized composites with homogeneous spreading of contents in the aluminium alloy.
- The micro-hardness of the composite enhances with regard to inclusion of the weight concentration of CSA filler contents (i.e., from zero, four, and eight wt.%).

- The test results exhibited that the AA7050-8 wt.% CSA AMCs has higher mechanical behavior when compared to the base aluminium matrix.
- Finally, the produced composite materials are to be sound and effective candidates for marine, transportation, structural, and nonstructural applications.
Finally, the produced composite materials are to be sound and effective candidates for marine, transportation, structural, and nonstructural applications.

References

1. Sajjadi SA, Ezatpour HR, Beygi H (2011) Microstructure and mechanical properties of Al-Al_2O_3 micro and nano composites fabricated by stir casting. Mater Sci Eng A. 528:8765–8771
2. Akbari MK, Baharvandi HR, Mirzaee O (2014) Investigation of particle size and reinforcement content on mechanical properties and fracture behavior of A356-Al_2O_3 composite fabricated by vortex method. J Compos Mater 48(27):3315–3330
3. Doruk E, Pakdil M (2016) Effect of tempering conditions on the fatigue behavior of an AA6082 aluminum alloy. Mater Test 58(6):542–546
4. Mohanavel V, Rajan K, Suresh Kumar S, Chockalingam A, Roy A, Adithiyaa T (2018) Mechanical and tribological characterization of stir-cast Al-SiCp composites. Mater Today Proc 5:1740–1746
5. Praveen Kumar A, Jackson Irudhayam S, Naviin D (2012) A review on importance and recent applications of polymer composites in orthopaedics. Int J Eng Res Develop 5(2):40–43
6. Ravichandran M, Dineshkumar S (2016) Experimental investigations on Al-TiO_2-Gr hybrid composites fabricated through stir casting route. Mater Test 58(3):211–217
7. Mohanavel V, Ravichandran M (2019a) Influence of AlN particles on microstructure, mechanical and tribological behavior in AA6351 aluminum alloy. Mater Res Exp 6(10):106557
8. Mohanavel V, Naveen Kumar M, Magesh Kumar K, Jayasekar C, Dineshbabu N, Udishkumar S (2017) Mechanical behavior of in situ ZrB_2/AA2014 composite produced by the exothermic salt-metal reaction technique. Mater Today Proc 4(2PA):3215–3221
9. Nallusamy M, Sundaram S, Kalaiselvan K (2019) Fabrication, characterization and analysis of improvements in mechanical properties of AA7075/ZrB_2 in-situ composites. Measurement 136:356–366
10. Mohanavel V, Ravichandran M (2019b) Experimental investigation on mechanical properties of AA7075-AlN composites. Mater Test 61(6):554–558
11. Mohanavel V, Rajan K, Suresh Kumar S, Vijayan G, Vijayanand MS (2018) Study on mechanical properties of graphite particulates reinforced aluminium matrix composite fabricated by stir casting technique. Mater Today Proc 5(1):2945–2950
12. Praveen Kumar A, Nalla Mohamed M, Kurien Philips K, Ashwin J(2016) Development of novel natural composites with fly ash reinforcements and investigation of their tensile properties. Appl Mech Mater 852:55–60
13. Shankar S, Balaji A, Kawin N (2018) Investigations on mechanical and tribological properties of Al-Si10-Mg alloy/sugarcane bagasse ash particulate composites. Particul Sci Technol 36(6):762–770
14. Praveen Kumar A, Jeyalal P, Barani Kumar D (2012) Hybridization of polymer composites. Int J Adv Mater Sci 3:173–182
15. David Raja Selvam J, Robinson Smart DS, Dinaharan I (2016) Influence of fly ash particles on dry sliding wear behaviour of AA6061 aluminium alloy. Kovove Mater 54:175–183
16. Chaithanyasai A, Vakchore PR, Umasankar V (2014) The micro structural and mechanical property study of effects of Egg Shell particles on the aluminum 6061. Proc Eng 97:961–967

17. Mohanavel V, Suresh Kumar S, Sathish T, Adithiyaa T, Mariyappan K (2018) Microstructure and mechanical properties of hard ceramic particulate reinforced AA7075 alloy composites via liquid metallurgy route. Mater Today Proc 5:26860–26865
18. Praveen Kumar A, Dhilepan K, Nikhil N (2016) Influence of nano reinforced particles on the mechanical properties of aluminium hybrid metal matrix composite fabricated by ultrasonic assisted stir casting. ARPN J Eng Appl Sci 11(2):1204–1210
19. Jasper J, Praveen Kumar A, Bharanidaran R (2015) Synthesis, characterization and evaluation of properties of aluminium alloy based hybrid composite reinforced with nano SiC and nano grapheme. Int J Appl Eng Res 10(50):735–739
20. Mohanavel V, Rajan K, Ravichandran M (2016) Synthesis, characterization and properties of stir cast AA6351-aluminium nitride (AlN) composites. J Mater Res 31(2):3824–3831
21. Mohanavel V, Ravichandran M, Suresh Kumar S (2020) Tribological and mechanical properties of Zirconium Di-boride (ZrB_2) particles reinforced aluminium matrix composites. Mater Today Proc 21:862–864
22. Stalin B, Ravichandran M, Mohanavel V, Raj LP (2020) Investigations into microstructure and mechanical properties of Mg-5wt.% Cu-TiB_2 composites produced via powder metallurgy route. J Min Metall Sect B Metall 56(1):99–108

Improvement of Compressibility, Shear Strength Characteristics of Soft Soil with Quarry Dust and Vitrified Polish Waste



Satish Brahmalla, Habibunnisa Syed, and Banka Hadassa Joice

Abstract The structures are originated to rest ultimately on solid rock or soil. The materials taken are quarry dust (QD) and vitrified polish waste (VPW), and the soft soils contains a few minerals of clay as montmorillonite, lattice structure of illite, kaolinite's are appreciable in a quantity. Quarry dust and vitrified polish waste are used to improve soft soil in a good stabilization, and the compressibility and shear strength tests are conducted to improve soil techniques by adding QD and VPW in a different manner. The resulting beneficial effects of solid crushing wastes are obtained in laboratory studies to improve compressibility and shear strength characteristics of soft soil with quarry dust and vitrified polish waste.

Keywords Quarry dust · Vitrified polish waste · Compaction test · Unconfined compressive strength test · Atterberg limit test · Soft soil

1 Introduction

The depth of soil is minimum up to 1.5 m, but in this paper, we had picked up to 1.85 m for to know strata of soil and improve its conditions. The auger boring method is used to collect soil sample. The scope and objective is to improve and maintain homogenous conditions when soil is treated with different dust particles. Soil consistency is the strength with which soil materials are held together or the resistance of soils to deformation and rupture. The consistency of a soil sample changes with the amount of water present. Such changes in soil consistency may be accurately measured in

S. Brahmalla (✉)
Department of Civil Engineering, Jayamukhi Institute of Technological Sciences, Warangal, Telangana, India
e-mail: bl.satish665@gmail.com

H. Syed
Department of Civil Engineering Vignan's Foundation For Science, Technology& Research Vadlamudi, Guntur, Andhra Pradesh, India

B. Hadassa Joice
Department of Civil Engineering, Koneru Lakshmaiah Education Foundation, Guntur, Andhra Pradesh, India

© Springer Nature Singapore Pte Ltd. 2020

A. Praveen Kumar et al. (eds.), *Advances in Lightweight Materials and Structures*,
Springer Proceedings in Materials 8, https://doi.org/10.1007/978-981-15-7827-4_31

the laboratory following standard procedures which determine the Atterberg limits. These limits may then be used for judging the suitability of the soil. The Atterberg limit corresponds to the moisture content at which a soil sample changes from one consistency to another and particular interest for liquid limit and the plastic limit, which define the soil consistencies.

2 Materials and Experimentation

The soil and vitrified polish waste is collected from nearby Narsampet, Warangal, and quarry dust is collected from SSS sand suppliers in Warangal. The properties of soil include color, texture, structure, porosity, density, consistence, temperature, and air. Color of soils varies widely and indicates such important properties as organic matter, water, and redox conditions.

Quarry dust and vitrified polish waste were used in this investigation. The amount of soil is collected from the pits at depth in a rate manner of 1.8 m from the ground level, from the top soil, which contains matter of organic materials and other foreign materials.

2.1 Properties of the Soils Used

The plasticity index also gives a good indication of compressibility. Soil is collected and tested as per IS: 2720 part 1–17. The index properties of the soil such as Atterberg limits and moisture content are basic properties of the soils; therefore, it is possible to use these index properties to predict the compression index of the soil [1] (Table 1).

Table 1 Soil properties

S. No.	Property of soil	Value	Units
1	Plasticity index (P.I)	32.86	%
2	Differential free swell (D.F.S)	106	%
3	Optimum moisture content (OMC)	24.85	%
4	Maximum dry density (MDD)	1.42	gm/cc
5	Unconfined compressive strength (UCC)	138.38	Kn/m^2
6	Settlement	5.5	mm
7	Compression index (C_c)	0.505	
8	Degree of plasticity	High plastic	
9	Type of soil	Silty clay or clayey silt	

2.2 QD and VPW

2.2.1 QD

Quarry dust (QD), during stone crushing process, the dust is produced, and then, it used as quarry dust. The dust passes through 4.75 mm sieve in the sieve analysis process [2].

2.2.2 VPW

Vitrified polish waste (VPW), in manufacturing industries of vitrified tiles, these types of waste are produced. The present scenario of solid waste material producing every year are increased 20%, and 11–15 tones waste is generated in manufacturing industry. It also passes through 4.75 mm sieve [3].

2.3 Test Procedures

A. Standard Proctor Compaction Test
   The mold is placed on the base of solid and filled fully with soil in matured manner to about one-third height. A curve of compaction is plotted between water content of corresponding dry density and abscissa as the ordinate graph. Content of water corresponding to maximum density in dry condition is called as optimum moisture content (OMC).
B. Unconfined Compressive Strength Test
   The strength of compressive in unconfined is defined as the failure manner in ratio, load of X-sectional area of a sample soil, when it is not subjected to any lateral pressure. The initial length, diameter and weight measured of its specimen force applied, such as to produce load in axial at a rate of 0 0.6–2% per mint causing failure with 5.5–10%.

3 Optimum % of QD, VPW with Soil

Soft soils impose various foundation problems due to their sensitiveness to changes in moisture content. These soils pose problems on account of their low dry density, low shear strength and also depend upon compaction and compressive strength test. Quarry dust is widely being used to stabilize soft soil [4]. The main thing is that it directly depends upon the compaction (OMC), compressive strength (UCS), and Atterberg limit tests (AL), and the optimum percentage changes in soft soil by adding 0–20% of QD and 3–15% of VPW [5]

Table 2 Compaction

S. No.	Mix composition		MDD
1	Soil	0% quarry dust	1.51
2	Soil	5% quarry dust	1.52
3	Soil	10% quarry dust	1.55
4	Soil	15% quarry dust ust	1.59
5	Soil	20% quarry dust ust	1.62

Table 3 Compression index values of soil + QD%

S. No.	Mix composition		Cc value
1	Soil	0% quarry dust	0.5069
2	Soil	5% quarry dust	0.4644
3	Soil	10% quarry dust	0.4398
4	Soil	15% quarry dust	0.4055
5	Soil	20% quarry dust	0.3699

3.1 Soil + QD in Various %

Optimum percentage is added to soil with quarry dust in a good manner.

3.1.1 Compaction

Optimum values of soil is added with 0, 5, 10, 15, 20% quarry dust. The compaction also playsd a role to maintain relationship between the stress and strain [6].

It gives high MDD by adding 20% of quarry dust with soil samples, and it was given in Table 2. The compaction process is done as per IS 2720, part 1–17, by taking soft soil and adding 0–20% quarry dust.

The compressive strength (UCS) process is done as per IS 2720, part 1–17. Taking soft soil and adding 0–20% quarry dust has been show in Table 3 and Fig. 1.

3.1.2 Unconfined Compressive Strength (UCS)

Unconfined compressive strength of soft soils is stabilized with adding 0–20% QD. It improves and stabilizes soils which are widely used as an alternative in the test conducted in the laboratory [7]

Quarry dust gives stress value by adding 0–20% with the soil as been concluded in Table 4 and Fig. 2. The compressive strength (UCS) process is done as per IS 2720, part 1–17.

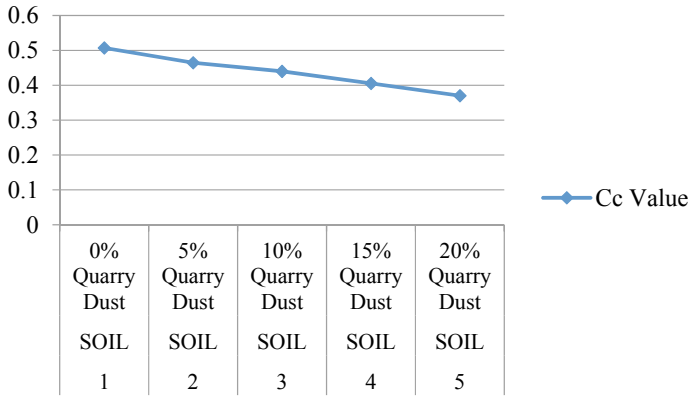


Fig. 1 Cc values of Soil + QD in various %

Table 4 Soil + QD% gives stress values

S. No.	Mix composition		Stress kn/m^2
1	Soil	0% QD	56.38
2	Soil	5% QD	79.56
3	Soil	10% QD	126.35
4	Soil	15% QD	154.23
5	Soil	20% QD	193.54

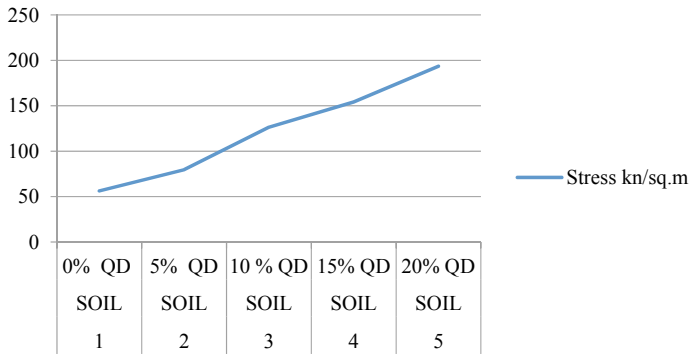


Fig. 2 Compressive strength of soil + QD%

Table 5 Soil + QD + VPW% gives liquid and plastic limit

S. No.	Mix composition			Liquid limit (W_L)	Plastic limit (W_P)
1	Soil	0% QD	3% VPW	52.5	23.56
2	Soil	5% QD	6% VPW	43.46	22.95
3	Soil	10% QD	9% VPW	38.85	22.56
4	Soil	15% QD	12% VPW	31.45	21.35
5	Soil	20% QD	15% VPW	25.9	20.35

3.2 Soil + QD + VPW in Various %

3.2.1 Atterberg Limit

It represents the moisture contents at which a specific soil's behavior changes from solid to plastic (plastic limit) and from plastic to liquid (liquid limit) [8].

The Atterberg limit process is done as per IS 2720, part 1–17, in Table 5. It has been shown by taking soft soil and adding 0–20% quarry dust.

3.2.2 Compaction

The optimum water content required for compaction decreases with an increase in the compaction effort. This effect of increase in compaction is significant only until the water content reaches its optimum level. After that level, the volume of air voids becomes almost constant, and the effect of increased compaction is not significant. It should be noted that the maximum dry density does not go on increasing with an increase in the compactive effort [9]. The compaction is done with a treatment of soil with 20% quarry dust and percentages in different of vitrified polish waste. The replacement of soil is done 3, 6, 9 12, and 15% of VPW, and then, it gives moisture content and dry density in the soft soil [10]

The compaction test is conducted process as per IS 2720, part 1–17, by taking soft soil and adding 20% of quarry dust which is constant, and gradually the VPW is included in a percentage manner to give good moisture content and dry density of soft soil in Table 6 [11].

3.2.3 Unconfined Compressive Strength (UCS)

The sample is prepared based on the OMC and MDD obtained from treated with a soil of 20% quarry dust, and percentage will be different of VPW, to produce strain and stress [12].

Table 7 and Fig. 3 indicate that uncompressive strength test conducted, process as done as per IS 2720, part 1–17, by taking soft soil, adding 20% of quarry dust and 15% of VPW gives linear shape which was shown in Fig. 3.

Table 6 Values of moisture content and dry density by adding percentage wise of soft soil + QD + VPW

S. No.	Moisture content	Dry density
1	12.05	1.24
2	14.33	1.38
3	19.44	1.356
4	25.16	1.43
5	30.56	1.45
6	35.89	1.13

Table 7 Values of compressive strength

S. No.	Mix composition			Strain (%)	Stress (kn/m^2)
1	Soil	0% QD	3% VPW	1.9	16.38
2	Soil	5% QD	6% VPW	3.1	28.56
3	Soil	10% QD	9% VPW	4.8	47.3
4	Soil	15% QD	12% VPW	6.3	68.2
5	Soil	20% QD	15% VPW	7.56	93.2

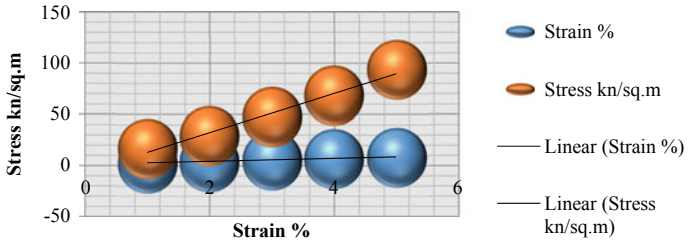


Fig. 3 Compressive strength of soil + QD + VPW%

3.2.4 Compression Index

The compression index is calculated for mix compaction of soil + QD + VPW adding in a different manner. It is observed that compression index value is less at 15% VPW mixed soil.

From Table 8 and Fig. 4, mix compaction of soil + 20%QD + 15%VPW shows that settlement of soil is 1.1 mm

Table 8 Variation of C_C values of soil + 0 to 20% quarry dust + 3 to 15% VPW

S. No.	Mix composition			Settlement (mm)	Compression index (Cc)
1	Soil	0% QD	3% VPW	4.53	0.2963
2	Soil	5% QD	6% VPW	3.8	0.2336
3	Soil	10% QD	9% VPW	2.5	0.2008
4	Soil	15% QD	12% VPW	1.5	0.1539
5	Soil	20% QD	15% VPW	1.1	0.1047

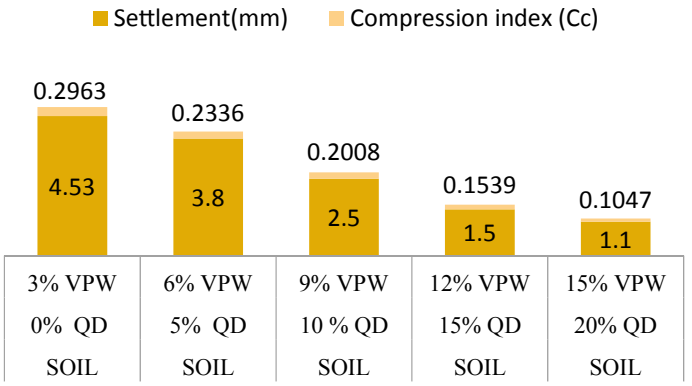


Fig. 4 Compression index of soil + QD% + VPW%

4 Conclusions

- Soft soil has high plasticity and cohesive nature.
- Soil preparation with various percentages of QD and VPW in a gradually increases and gives improvement, stabilization for soil in a good manner.
- Based on Atterberg limit test while adding QD and VPW, the liquid and plastic limit gradually decreases at 20% of QD and 15% of VPW.
- The dry density value of 1.13 gives a better performance while adding 20% of QD and 15% of VPW.
- Atterberg limit test shows that the degree of plasticity came through below the 7, then soft soil is changed to silt soil, and it becomes partly cohesive in nature.
- Unconfined compressive strength test result shows that stress and strain graph shows linear relation.
- The optimum content at dry density of soft soil was decreased in addition of 20% quarry dust and decreases with addition of 15% VPW compared with untreated expansive soil.
- Based on the test results, the shear strength parameters of soft soils are improved with the addition of QD and VPW.

5 Future Scope

The investigation can be continued further by conducting tests like permeability test, standard penetration test, bearing capacity test, to know the soil strata. Take 20% QD and 15% VPW as constant value for conducting remaining tests.

References

1. Jain VK (2015) Correlation of plasticity index and compression index of soil. Int J Innov Eng Technol (IJIET), 263 5(3). ISSN: 2319–1058
2. Kadir AA (2017) Physical and mechanical properties of quarry dust waste incorporated into fired clay brick, 020040-1, 1835, 020040
3. Srujan Kumar K (2019) Effect of vitrified polish waste in concrete as partial replacement to cement. Int J Sci Res Develop (IJSRD), 486 7(10). ISSN (online): 2321-0613
4. Agrawal V, Gupta M Expansive soil stabilization using marble dust. In: Ranjan G, Rao ASR (eds) Basic and applied soil mechanics
5. Sabat AK (2012) Stabilization of expansive soil using waste ceramic dust, EJGE, 3915 17
6. Gayatri A Geotechnical characterization of expansive soil and utilization of waste to control its swelling and shrinkage behaviour, 978-81-15-0990-2. Springer
7. Sabat AK (2012)A study on some geotechnical properties of lime stabilised expansive soil—quarry dust mixes. Int J Emerg Trends Eng Develop 1, 42(2). ISSN: 2249-6149[6]
7. Balamurugan G (2013) Use of quarry dust to replace sand in concrete—an experimental study. Int J Sci Res Publ 3(12). ISSN: 2250-3153
9. PrasadaRaju GVR, Srinivas M Field investigation of heave of chemically-stabilized expansive soil sub-grades
10. Agarwala VS, Khanna JS (1969) Construction techniques for foundations of buildings on black cotton soils
11. I.S: 2720, part 1 to 17 (1980) Determination of water content dry density relation using light compaction determination of liquid limit and plastic limit. Determination of unconfined compressive strength, bureau of Indian standards
12. Arora KR (2004) Soil mechanics and foundation engineering, Standard Publishers Distributors

Tensile and Fatigue Behavior of Glass Fiber Laminated Aluminum-Reinforced Epoxy Composite



Tripti Sonker, Ajaya Bharti, and Pranshu Malviya

Abstract Nowadays, there is a demand for structural elements especially in the aerospace industry having lightweight, high strength, wear-resistant, corrosion-resistant, fatigue resistant, etc. To fulfill these demands, researchers have made a lot of efforts to incorporate these all properties. In the series of development of various types of composite, Glass Laminate Aluminum-Reinforced Epoxy (GLARE) has been fabricated and employed in space vehicles. The chapter deals about how the random orientation of fibers will affect the tensile and fatigue characteristics of fiber laminated composites. The literature till now does not reveal the fatigue properties of GLARE containing randomly oriented glass fiber epoxy lamina.

Keywords GLARE · FML · Tensile test · Fatigue test

1 Introduction

In the current scenario, one of the important goals of aircraft industries is to develop lightweight, high-strength structural materials. The lightweight structures have encouraged toward the development of refined models for fiber–metal laminates (FMLs), increasing their demand in airplane sectors because of its high performance [1]. These fiber–metal laminate possesses the advantageous properties of both metal and fiber composites. Metals having isotropic nature and ductility permit easy repair and better tribological properties, while fiber composite has a higher specific strength and fatigue characteristics [2]. The multiple site damage and fatigue cracks will cause the catastrophic failures of the aircrafts which require the higher fatigue-resistant material. The concept of fiber–metal laminates was generated by sandwiching of one fiber laminate between two metal laminates.

T. Sonker (✉)
Civil Engineering Department, MNNIT Allahabad, Prayagraj, India
e-mail: rce1605@mnnit.ac.in

A. Bharti · P. Malviya
Department of Applied Mechanics, MNNIT Allahabad, Prayagraj, India

© Springer Nature Singapore Pte Ltd. 2020

A. Praveen Kumar et al. (eds.), *Advances in Lightweight Materials and Structures*,
Springer Proceedings in Materials 8, https://doi.org/10.1007/978-981-15-7827-4_32

The bonding of aluminum sheet with fiber epoxy laminate and making alteration of different layers of aluminum and fiber composites to form fiber–metal laminate [3]. The fiber–metal laminate can be comprised of glass fiber along with the aluminum metal known as GLARE [1, 4, 5], aramid fiber is also known as ARALL [6–8] or carbon fiber also known as CARALL [2, 9, 10]. Among all these fiber–metal laminates, GLARE is more advanced [11] and commercially used in aerospace industries [12] for structural application. GLARE is used in fuselage of the Airbus A380 airplane, cargo floors of Boeing 777, patch repairs of aircraft skin also seamless GLARE tubes [13]. The GLARE as a structural element serves the remarkable properties such as low weight density, corrosion resistance [12], impact resistance, high strength, improved fatigue life, resistance to crack growth [14]. However, all these properties are spatially dependent due to different orientation of fiber and plies of fiber possible. This induces directional dependent properties in GLARE. The research is available for the tensile and fatigue properties of unidirectional and bidirectional fiber orientation in GLARE [15].

This research involves the use of randomly oriented glass fiber to fabricate GLARE. The randomly oriented glass fiber induces isotropy in GLARE. The main focus of this research is to develop advanced fiber–metal laminate comprising of adhesively bonded glass fiber lamina and aluminum sheet and to reveal its strength and fatigue resistance properties in comparison to aluminum and glass fiber epoxy lamina. The numerical and experimental approach of the unidirectional orientation of fiber will be investigated via different sequence of stacking of fiber and metal laminate [16]. Thermotical, numerical and analytical approach will be applied to the fiber–metal laminates to investigate the delamination and fatigue analysis [17, 18].

2 Experimental Details

The following section highlights the materials used, fabrication and testing of composites. Fabrication of the fiber metal laminate composite (GLARE) through sandwiching of two halves of aluminum in between one layer of glass fiber composite. The main problem is the adhesion of the two dissimilar material one is metal and another is GFRP composite which is inorganic in nature. For interfacial bonding between two dissimilar material organo-silane compound is used. The brief discussion of material is discussed below:

2.1 Materials

The matrix material used for fabrication of the composites is epoxy resin (LY556), and corresponding hardener (HY951) is used. Chopped glass fiber is used as the reinforcing material, and for the fabrication of GLARE Aluminum Al 2024-T3 1-mm sheet is used.

2.2 Fabrication of Samples

Tensile and fatigue test specimen of aluminum is prepared by cutting and filing by hand saw and file, tensile and fatigue test specimen of glass fiber epoxy composite is prepared by hand layup method and finally preparing of sample by cutting it by saw blade manually.

For the preparation of GLARE sample aluminum surface is pre-treated by series of methods including surface cleaning by methyl ethyl ketone thereafter Hand abrasion with 320, 400, 600, and 800 grit silicon carbide paper after that alkaline and acid etching by NaOH solution and sulpho-chromic acid, respectively. Then by putting an Al sheet in a boiling water bath for 60 s pseudobohemite is produce, after that the aluminum surface is coated with an organo-silane adhesion promoter, y-glycidoxypropyltrimethoxy silane (y-GPS). Within 1 h of the aluminum surface preparation, bonding between the aluminum sheets and the GFRP composite was achieved using an autoclave through co-curing under a pressure of 25 psi at 120 °C. Fabrication of the fiber–metal laminate composite (GLARE) through sandwiching of two halves of aluminum in between one layer of glass fiber composite. GLARE 3/2 means three layers of Al 2024 and two layers of GFRP, the total thickness of the sample is 6 mm is prepared.

2.3 Tensile Test

For the tensile test of Aluminum Al 2024-T3, glass fiber epoxy lamina and GLARE sample are fabricated as per ASTM standards, and the test is carried out at a strain rate of 1 mm/min for three samples in each category. The sample of test and experimental setup depicted on Figs. 1, 2, and 3. Table 1 presents the specification of the samples.

2.4 Tension–Tension Fatigue Test

Fatigue life test is carried out for constant mean stress and by varying stress amplitude for five different stress amplitude ratios in each category of samples of aluminum Al 2024-T3, glass fiber epoxy lamina, and GLARE. Table 2 represent the specification of samples.

Tensile and fatigue test Aluminum Al 2024, glass fiber epoxy lamina and GLARE have been carried out on BISS Nano UTM in Machine Element Lab of Mechanical Engineering Department of Motilal Nehru National Institute of Technology, Allahabad Uttar Pradesh, India.



Fig. 1 Experimental setup of lab



Fig. 2 Tensile specimen

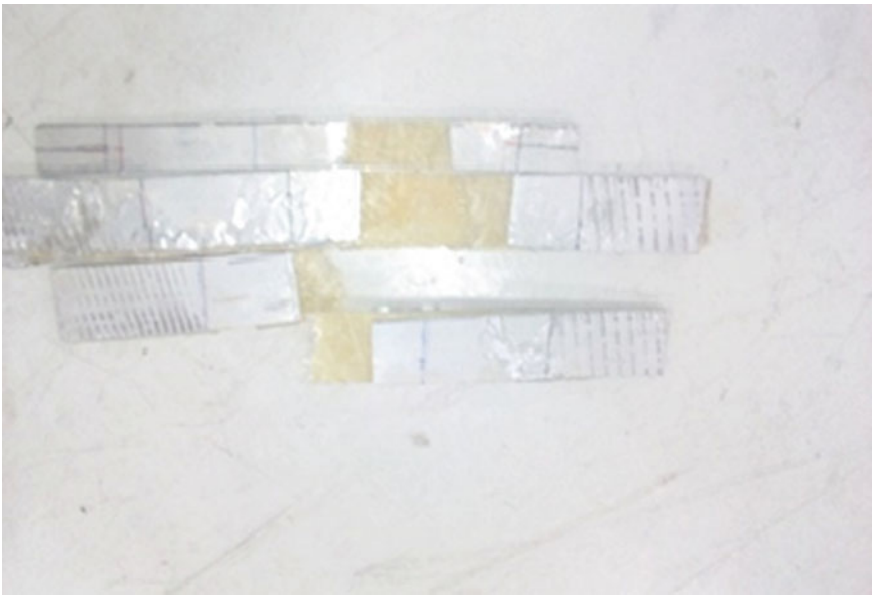


Fig. 3 Damaged samples after testing

Table 1 Tensile test sample specification

Specimen	ASTM standard	Specimen size		
		Gauge length (mm)	Width (mm)	Thickness (mm)
Aluminium Al 2024-T3	E8/E8M-15a	50	12.5	1
Glass fiber epoxy lamina	D3039/D3039M-14	50	25	3
GLARE	E8/E8M-15a	50	12	6

Table 2 Present the specification of samples

Specimen	ASTM standard	Specimen size	
		Width (mm)	Thickness (mm)
Aluminum Al 2024-T3	E466-15	20	1
Glass fiber epoxy lamina	D3479/D3479M-12	25	3
GLARE	E466-15	12	6

3 Results and Discussion

3.1 Tensile Test Result

Tensile test of Aluminum Al 2024, glass fiber epoxy lamina and GLARE have been carried out for three samples in each category. Thereafter, a stress–strain curve corresponding to minimum yield strength of three samples in each category is plotted on a common scale as shown in Fig. 4 and comparison in its tensile properties is shown in Table 3.

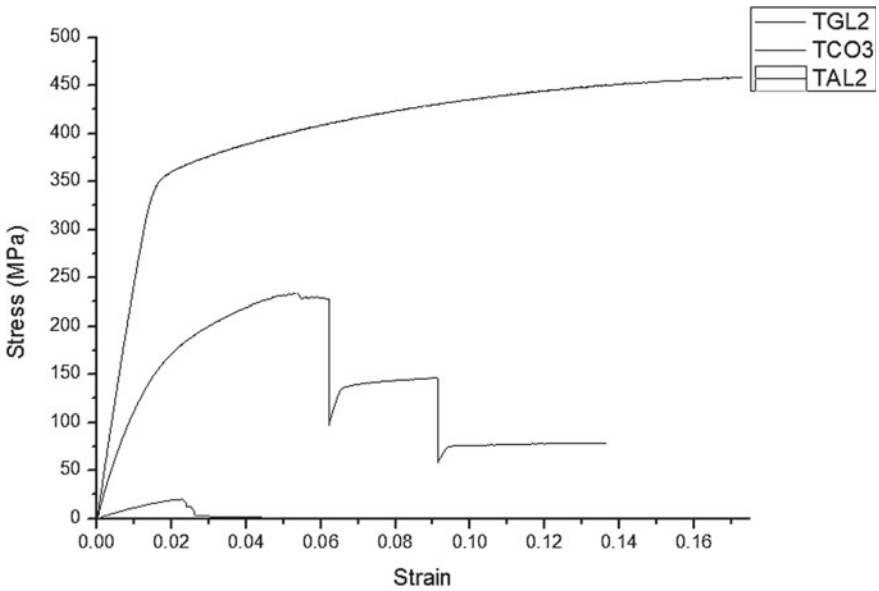


Fig. 4 Stress–strain comparison curve of Al 2024, glass fiber epoxy lamina and GLARE

Table 3 Tensile test result of Aluminium Al 2024, glass fiber epoxy lamina, and GLARE

Specification	Width (mm)	Thickness (mm)	Area (mm^2)	Gauge length (mm)	Peak stress (MPa)	Peak load (kN)	Yield load (kN)
Aluminum, TAL 2	12.5	1	12.5	50	460	5.755	4.294
Glass fiber epoxy lamina, TCO 3	25	3	75	50	20	1.511	1.125
GLARE TGL 2	12	6	72	50	234	16.826	10.80

Tensile test of all the samples reveals that the strength of Aluminum Al 2024-T3 is highest among all three. A result is found consistent with different samples of aluminum, while the glass fiber epoxy lamina has the lowest strength and the result is somewhat inconsistent for a different set of samples. This may be due to anisotropy induced during molding of the lamina. GLARE achieves strength which is in between the Aluminum Al 2024-T3 and glass fiber epoxy lamina, so it is definite advancement over the composite lamina because of ten times increase in peak stress value; however, peak stress sustained by GLARE is approximately half of peak stress value of Aluminum AL2024-T3. The stress–strain curve of GLARE has irregular shape. This is due to the failure of a different layer of aluminum at different intervals. This causes loss of strength and then strength regaining by sustaining load by other layers of aluminum and composite lamina. The lower strain was observed in the composite lamina. This causes the breakage of center aluminum layer first due to localized strain concentration. This localized strain concentration is due to adhesively bonded composite lamina on both sides of the aluminum layer which resists strain distribution throughout the length. Thereafter, the other two layers of aluminum fail one by one.

3.2 Fatigue Test Result

The fatigue life of Aluminum Al 2024, glass fiber epoxy lamina, and GLARE have been carried out on BISS Nano UTM to find the number of cycles to failure for constant mean stress and by varying the stress amplitude depicted in Fig. 5. The graph below presents the comparison of fatigue life of aluminum, glass fiber epoxy lamina, and GLARE.

The mean stress for all samples is kept constant by taking it as 0.6 times of yield stress value. The yield stress is found from the stress–strain curve by 0.2% line intercept method. Thereafter, loading of samples is done by varying the maximum and minimum stress values. The test results are similar to the tensile test result in a manner that the fatigue life of GLARE came out to be in between aluminum and composite lamina. From the test result, it has been found that fatigue strength of GLARE for 100,000 cycles increased by 85.26% in comparison to glass fiber-reinforced epoxy lamina, while it was found to decrease by 68.42% in comparison to the aluminum sheet.

4 Discussions on the Overall Results

Static tensile test and tension–tension fatigue test was carried out on Aluminum Al 2024-T3, glass fiber epoxy lamina, and GLARE, and comparison of tensile properties and fatigue life was made. The test results reveal the following details.

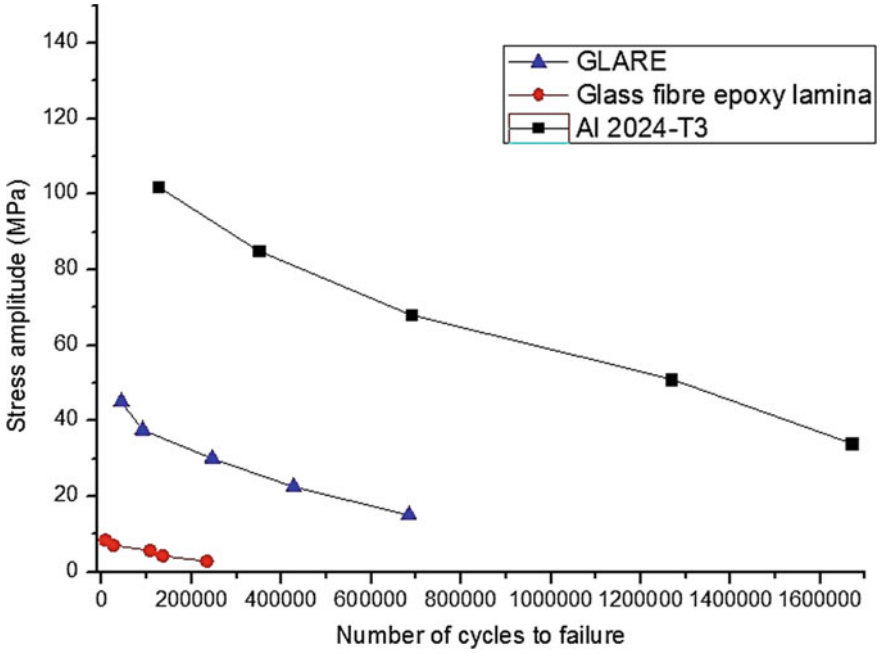


Fig. 5 S–N comparison curve of Al2024, glass fiber epoxy lamina, and GLARE

1. The strength achieved by GLARE is in between the Aluminum Al 2024-T3 and glass fiber epoxy lamina. Though the strength of GLARE is approximately ten times that of glass fiber epoxy lamina, while it is approximately half of the Aluminum Al 2024-T3.
2. The improvement in strength could be achieved by using unidirectional glass fiber epoxy lamina and loading the sample along the fiber direction.
3. GLARE fabricated in this research being of lower density could be used in the structural purpose where low weight is one of the important parameters for structural design.
4. Fatigue life achieved by GLARE is optimal and is in between the Aluminium Al 2024-T3 and glass fiber epoxy lamina.

5 Conclusion

In the present work, GLARE composite was fabricated in the laboratory in which the fiber-metal laminates (FML) consist of an alternation of 1-mm aluminum sheets and 1.5-mm glass fiber-reinforced epoxy lamina. In the laminated GLARE, there were three aluminum sheets and two sheets of randomly oriented glass fiber-reinforced epoxy lamina. To investigate the mechanical properties of GLARE laminated composite, samples were extracted as per the ASTM standards and mechanical

tests were performed. Also, to investigate the fatigue behavior, the samples prepared as per ASTM standards were subjected to cyclic loading. Through tensile tests, the GLARE laminated composite has shown 90% greater proof strength compared to randomly oriented glass fiber-reinforced epoxy lamina, whereas 29% lesser proof strength than the aluminum sheet. Through fatigue test, it was observed that the GLARE laminated composite can sustain 85.2% greater stress amplitude for 100,000 cycles, whereas GLARE can sustain 68.42% lesser stress amplitude for the same number of cycles compared to the Aluminum sheet.

The fiber metal laminates are widely used in the aircraft, but their fatigue characteristics will be monitored via theoretical and numerical approaches and experimentation to avoid the catastrophic failures. The continuous monitoring will also be required to the prevention against the delamination of layers and prediction of fatigue crack initiations.

References

1. Sinmazçelik T, Avcu E, Özgür M, Çoban O (2011) A review: fibre metal laminates, background, bonding types and applied test methods. Mater Des 32:3671–3685
2. Tamilarasan U, Karunamoorthy L, Palanikumar K (2015) Mechanical properties evaluation of the carbon fibre reinforced aluminium sandwich composites. Mater Res 18(5):1029–1037
3. Lawcock G, Ye L, Mai Y-W, Sun C-T (1997a) The effect of adhesive bonding between aluminum and composite prepreg on the mechanical properties of carbon-fiber-reinforced metal laminates. Compos Sci Technol 57(1):35–45
4. Tanwer AK (2014) Mechanical properties testing of uni-directional and bi-directional glass fibre reinforced epoxy based composites. Int J Res Advent Technol 2(11):2321–9637
5. Deogonda P, Chalwa VN (2013) Mechanical property of glass fiber reinforcement epoxy composites. Int J Sci Eng Res 1(4):6–9
6. Vogelesang LB, Vlot A (2000) Development of ® bre metal laminates for advanced aerospace structures. J Mater Process Technol 103:3–7
7. Abdala RWS, Bastian FL, Castrodeza EM (2006) Crack resistance curves of GLARE laminates by elastic compliance, vol.73, pp 2292–2303
8. Kotik HG, Ipiña JEP (2016) Short-beam shear fatigue behavior of fiber metal laminate (Glare). Int J Fatigue
9. Lawcock GD, Ye L, Mai YW, Sun C (1997b) Effects of fibre/matrix adhesion on carbon-fibre-reinforced metal laminates-II. Impact behaviour. Compos Sci Technol 57(97):1621–1628
10. Cortes P, Cantwell WJ (2004) The tensile and fatigue properties of carbon fiber-reinforced PEEKTitanium fiber-metal laminates. J Reinf Plast Compos 23(15):1615–1623
11. Zhong Y, Joshi SC (2015) Response of hygrothermally aged GLARE 4A laminates under static and cyclic loadings. JMADE 87:138–148
12. Tsamasphyros GJ, Bikakis GS (2013) Analytical modeling to predict the low velocity impact response of circular GLARE fiber—metal laminates. Aerosp Sci Technol 29(1):28–36
13. Bikakis GSE, Dimou CD, Sideridis EP (2017) Ballistic impact response of fiber-metal laminates and monolithic metal plates consisting of different aluminum alloys. Aerosp Sci Technol
14. Krishnakumar S (1994) Fiber metal laminates—the synthesis of metals and composites, vol 9, no 2
15. Alderliesten RC, Homan JJ (2006) Fatigue and damage tolerance issues of glare in aircraft structures. Int J Fatigue 28(10):1116–1123
16. Sharma AP, Khan SH, Parameswaran V (2017) Experimental and numerical investigation on the uni-axial tensile response and failure of fi ber metal laminates. Compos Part B 125:259–274

17. Wang W, Rans C, Benedictus R (2018) Theoretical analysis of fatigue failure in mechanically fastened fibre metal laminate joints containing multiple cracks. Eng Fail Anal 91:151–164
18. Wang W, Rans C, Benedictus R (2017) Analytical prediction model for non-symmetric fatigue crack growth in fibre metal laminates. Int J Fatigue 103:546–556

Comparative Study of Aluminium—Alumina Composite Prepared by Mechanical Mixing and Oxidation



Jayanta Kumar Mahato

Abstract The present investigation is aimed towards comparatively study the mechanical and corrosion resistance properties of aluminium-alumina metal matrix composites (AAMMCs) prepared by two different routes. In one route, different weight percent of commercially pure aluminium and alumina powders were mechanically blended and compacted at uniform pressure of 10 ton/inch^2 followed by sintering at different temperatures for specific time duration. In another route, commercially pure aluminium powders were oxidized at four different temperatures (500–800 °C) for three different time durations (15, 30 and 45 min) followed by blending of oxidized Al powder, compacting and sintering of composite samples. Scanning electron microscopy (SEM) images of blended powders were taken for confirming the uniform distribution of Al_2O_3 particle in Al matrix. Mechanical properties like hardness, wear resistance and chemical properties like corrosion resistance of AAMMCs were measured. It is observed that both mechanical properties and corrosion resistance of pure aluminium can be enhanced by preparing AAMMCs, whereas more enhancements can be achieved by oxidation route compared to mechanical mixing route of composites preparation. Therefore, the novelty of the present research work is to enhance the mechanical properties and corrosion resistance of aluminium by preparing AAMMCs without addition of Al_2O_3 in Al powder matrix material, i.e. following oxidation route of composite preparation. It is also observed that the mechanical properties and corrosion resistance of Al-Al_2O_3 composites increases with increase of weight percent alumina added, sintering temperature, oxidation temperature and oxidation time duration individually.

Keywords Aluminium-alumina metal matrix composite · Blending · Sintering temperature · Oxidation temperature and powder metallurgy

J. K. Mahato (✉)
Shobhit Institute of Engineering & Technology (Deemed To-Be University), Meerut 250110, Uttar Pradesh, India
e-mail: jayanta.mahato@gmail.com

© Springer Nature Singapore Pte Ltd. 2020

A. Praveen Kumar et al. (eds.), *Advances in Lightweight Materials and Structures*,
Springer Proceedings in Materials 8, https://doi.org/10.1007/978-981-15-7827-4_33

1 Introduction

In general, a composite material is composed of reinforcement material embedded in a matrix material. In this case, the matrix phase holds the reinforcement material to form the desire shape, while the reinforcement improves the overall properties of the matrix. Alumina (Al_2O_3) has received more attention as reinforcing phase as it is found to increase the stiffness, specific strength, hardness, wear resistance [1, 2] and corrosion resistance [3] of aluminium-alumina metal matrix composites (AAMMCs) which are used widely for a variety of engineering applications like aerospace applications, automobile components, etc. The powder metallurgy (PM) route is the commonly used procedure for fabrication of metal matrix composite (MMCs) which includes processes like blending, compacting and sintering. All these three steps for preparing composites have direct role on enhancement of mechanical properties and corrosion resistance of MMCs.

Several researchers [4–8] have studied by numerical modelling and experimental work on oxidation of aluminium (Al) particles. They have stated that aluminium oxide (Al_2O_3 or alumina) shell formed surrounding the Al metal particles by oxidation of micron-sized Al powder. They have also proposed that oxidation of Al particles occurs through a multi-stage mechanism, where particles effectively burn in the continuum regime with a boundary layer and a flame surrounding the particle. Rai et al. [4] have experimentally observed that by increasing oxidation temperature from 500 to 800 °C, the density of Al particles increases from 2.75 to 3.85 gm/cc (near the density of bulk Al_2O_3) which corresponds exactly to the conversion of Al to Al_2O_3. But further increase in temperature to 900 and 1000 °C results in a drop of density which they attributed from their TEM study to the presence of hollow particles. So, formation of Al_2O_3 by oxidation of Al powder depends on the oxidation temperature, beyond 800 °C the oxide shell gets thinning out and density of alumina present decreases. In this regard, it is important to study the mechanical, thermal and corrosion properties of aluminium-alumina composite prepared by oxidation of commercially pure aluminium powder at different temperatures for different time durations following powder metallurgy (PM) process of preparation. Such type of study is not available in open literature domain.

Several researchers have experimentally observed that the mechanical, thermal and corrosional properties of MMCs prepared by powder metallurgy routes strongly depend on various affecting factors like particle size [9, 10], reinforcement distribution [10, 11], weight percentage of reinforcement add [10, 12–14], sintering temperature, sintering time duration [14] and moreover nano-sized reinforced particles [15–17]. Tongsri et al. [10] have observed that both tensile strength and elongation decrease, whereas hardness increases by adding Al_2O_3 powder into the SS 316L matrix. They have also observed that the tensile strength increases by adding very fine size of Al_2O_3 particles. They have stated that very fine size of Al_2O_3 particles provide more uniform distribution in matrix material or less particle agglomeration, resulting smaller grain size and better resistance to plastic deformation [10]. Durai et al. [14] have experimentally observed that the density of aluminium composite increases,

whereas porosity of the composite decreases with the increase of sintering temperature, results to increase the hardness and improve wear resistance of the composite. In this regard, it is important to study the effect of weight percent alumina addition in aluminium matrix, sintering temperature and sintering time duration on mechanical properties, wear resistance and corrosion resistance of aluminium-alumina metal matrix composites prepared by powder metallurgy process of preparation because of unclear and less availability of information in open literature domain.

The objective of the present investigation is to comparatively study the mechanical properties, wear resistance and corrosion resistance of aluminium-alumina metal matrix composites prepared by two different routes; mechanical mixing of different weight percent alumina in aluminium matrix and oxidation of pure aluminium powder at different temperatures for different time durations followed by powder metallurgy route of composite preparation.

2 Experimental Procedure

Present investigation has been carried out on aluminium-alumina metal matrix composites (AAMMCs) prepared by two different routes followed by powder metallurgy process of composite preparation. In the first route of preparation, different weight percent (5, 10 and 15%) of commercially pure alumina (Al_2O_3) powders were mixed with commercially pure aluminium (Al) powders and mechanically blended by rotating the pestle into the mortar in both clockwise and anti-clockwise direction simultaneously over a period of 2 h. To make every AAMMC sample, 3 gm of blended Al–Al_2O_3 powders were poured into a die cavity of 14 mm diameter. Uniform pressure of 10 Ton/in.^{2} was applied on the blended powders for a few minutes with the help of hydraulic press by placing the die at just centre of applied load, shown in Fig. 1a. Composite samples were extracted very carefully from the die cavity and sintered in a tube furnace at three different temperatures (400, 500 and 600 °C) for 30 min. In the second route of preparation, commercially pure aluminium powders were oxidized at four different temperatures (500, 600, 700 and 800 °C) for three different time durations (15, 30 and 45 min.) to form aluminium oxide (Al_2O_3) on Al particles. The oxidized aluminium powders were then blended and compacted following the same procedures as mentioned earlier. Composite samples were then



Fig. 1 **a** Centre position of die in hydraulic press, **b** prepared AAMMC samples, **c** holder-on-disc-type friction and wear testing machine and **d** potentiodynamic scan test set-up

sintered in a tube furnace at 500 °C for 30 min. Composites prepared by the first route and second route of preparation are termed as 'Group-I' and 'Group-II' composites, respectively. Out of total 48 numbers of AAMMC samples, 24 numbers of samples were prepared in Group-I and 24 numbers of samples in Group-II category. The prepared AAMMC samples are shown in Fig. 1b.

SEM images of commercially pure aluminium, pure alumina and mixing of different weight percent Al_2O_3 in Al powders were taken in a scanning electron microscope (SEM), JEOL, JSM-6360 to observe the distribution of Al_2O_3 particle in Al matrix powder as well as morphology of the powder particles. SEM images of aluminium powder oxidized at 500, 600, 700 and 800 °C for 15 min were also taken to observe the formation of aluminium oxide (Al_2O_3). Scanning electron microscopy was performed under secondary electron imaging mode using an operative voltage of 15–20 kV.

Hardness values of AAMMCs were taken by both Vickers and Brinell hardness testers. Before starting the hardness test, one side of AAMMC samples was polished with very fine emery paper. Vickers hardness tests were done at applied load of 1 Kgf for dwell time of 15 s, whereas Brinell hardness tests were done at applied load of 15.625 Kgf for dwell time of 30 s. At least five hardness values from different positions of samples were taken by both hardness testers.

Wear resistance tests of AAMMCs were conducted by the holder-on-disc-type friction and wear monitor (DUCOM; TR-20LE-M2, Fig. 1c) against rotating hardened ground steel disc. All the variables like applied load, RPM of disc, sliding distance and sliding speed were kept constant for every test. The tests were performed at applied load of 1 Kgf on samples, attached at a sliding distance of 30 mm with a rotating disc of 320 RPM. The load was applied by dead weight through pulley string arrangement and tests were continued to 10 minutes for every test. Special cares were taken on the percentage area of contact with the rotating disc during testing. For most of the cases, around 80% of contact between samples and rotating disc were maintained throughout the entire test.

Before starting the electrochemical tests, one side of composite samples was metallographically polished using successively finer grades of silicon carbide base abrasive papers and finally polished with the cloth polisher. The open-circuit potential tests were carried out before potentiodynamic scan tests on every sample under 3% KCL test solution for few minutes to allow for attaining the steady state condition. Corrosion tests were carried out by using a conventional three electrode cells with a graphite rode and a saturated calomel electrode (SCE), Fig. 1d. In our experimental set-up, the polished sample worked as a working electrode, graphite as a counter electrode and SCE as a reference electrode. The potentiodynamic polarization curves were recorded at a constant scan rate of 1 mV/s.

3 Results and Discussion

Scanning Electron Microscopy (SEM) images of commercially pure Al, pure Al_2O_3, 5% Al_2O_3–Al and 15% Al_2O_3–Al powder materials are shown in Fig. 2a–d, respectively. Similarly, SEM images of aluminium powder oxidized at 500, 600, 700 and 800 °C are shown in Fig. 3a–d, respectively. Figure 2a–b represent the real morphology of commercially pure aluminium and pure alumina powder, respectively, whereas Fig. 2c–d represent the mixture of different weight percentage alumina and aluminium powder materials. It is observed from Fig. 2a–d that the morphology of pure alumina powder is different from that of pure aluminium powder. It is also observed from Fig. 2a–d that the morphology of pure aluminium powder slightly changes due to the blending effect and concentration of alumina in aluminium powder increases with increase of weight percent addition of alumina powder. It is also apparently observed that Al_2O_3 powder particles are homogeneously distributed in Al powder material.

It is observed by comparing Figs. 2a–d and 3 that oxide shells on aluminium particles were formed due to heating at higher temperature. It is also apparently observed that the amount of aluminium oxide formation increases with increase of oxidation temperature from 500 to 600 °C. But further increase in oxidation temperature to 700 and 800 °C results in thinning of oxide shell and forming of hollow particles. Similar observation has been reported by Rai et al. [4]. They have stated that with increase in oxidation temperature to 900 and 1000 °C, the density of Al drops down due to the formation of hollow particles. Therefore, it can be said that further increase in oxidation temperature to 700 and 800 °C results in drop of amount of aluminium oxide formation.

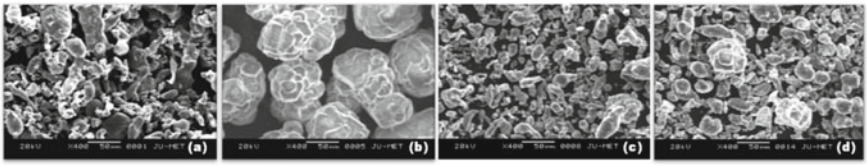


Fig. 2 SEM image of **a** pure Al, **b** pure Al_2O_3, **c** 5% Al_2O_3–Al and **d** 15% Al_2O_3–Al powder material

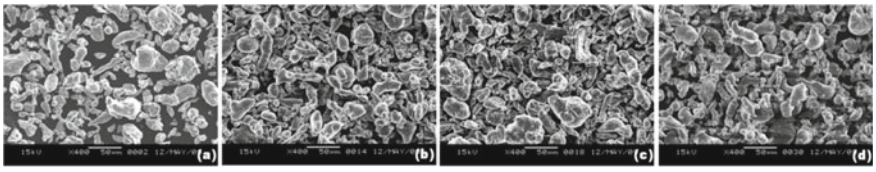


Fig. 3 SEM images of aluminium powder oxidized at **a** 500 °C, **b** 600 °C, **c** 700 °C and **d** 800 °C

Vickers and Brinell hardness values of Group-I and Group-II composites are shown in comparison bar diagram Fig. 4 and Fig. 5, respectively. It is clearly observed that the hardness values of Group-I and Group-II composites are more compared to pure aluminium irrespective of weight percent addition of alumina and oxidation temperature. This is attributed to the presence of much harder reinforcement material (hardness of alumina: 1500–1650 VHN) in aluminium matrix material. It is observed from Fig. 4a–b that both Vickers hardness and Brinell hardness of Group-I composites are increases with increase in wt.% addition of Al_2O_3 irrespective of sintering temperature. This is attributed to the increase of concentration of reinforcement material. It is also observed that both the Vickers and Brinell hardness of Group-I composites increase with increase in sintering temperature irrespective of weight percent addition of alumina. This is attributed to the fact that the density of AAMMCs increases, whereas porosity of the composite decreases with the increase in sintering temperature [14]. The lowest hardness values obtained in pure aluminium samples sintered at 400 °C are 26 VHN and 19 BHN, whereas maximum hardness values obtained in 15% Al_2O_3–Al composite sintered at 600 °C are 41 VHN and 35

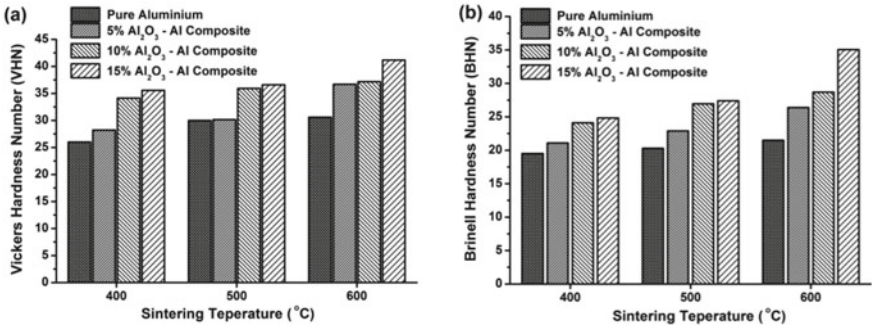


Fig. 4 Comparison bar diagram of hardness values of Group-I composites tested by **a** Vickers hardness tester and **b** Brinell hardness tester

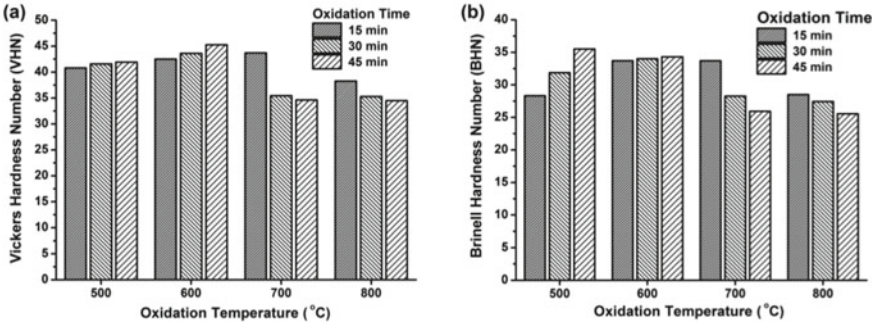


Fig. 5 Comparison bar diagram of hardness values of Group-II composites tested by **a** Vickers hardness tester and **b** Brinell hardness tester

BHN. Therefore, the hardness of pure aluminium can be increased up to double by making composite of 15 wt.% alumina in aluminium powder.

Interestingly, it is observed in case of Group-II composites that both the Vickers hardness and Brinell hardness increases with increase in oxidation temperature from 500 to 600 °C irrespective of oxidation time duration, but further increase in temperature to 700 and 800 °C both the Vickers hardness and Brinell hardness decrease. This is attributed to the fact of thinning of oxide shell and formation of hollow particles at higher temperature results in decrease of concentration of aluminium oxide. It is also interestingly observed that with increase in oxidation time, both the Vickers hardness and Brinell hardness increase for oxidation temperature of 500 and 600 °C. But in case of 700 and 800 °C oxidation temperature, both the Vickers hardness and Brinell hardness decrease with increase of oxidation time. This is also attributed to the increase of aluminium oxide concentration for longer oxidation time at 500 and 600 °C oxidation temperature. But in case of 700 and 800 °C oxidation temperature, the aluminium oxide concentration reduced due to thinning of oxide shell at higher temperature for long time duration. It is also observed from Group-I and Group-II composites that both the Vickers and Brinell hardness numbers are more in case of Group-II composites compared to Group-I composites. This is attributed to the more aluminium oxide concentration present in case of Group-II composites compared to Group-I composites.

Experimentally obtained amount of wear with respect to test time for both Group-I and Group-II composites are represented in Fig. 6a–b, respectively. It is observed from Group-I composites that initially the wear rate is more, and it decreases gradually with the test time and ultimately reaches a constant rate of wear irrespective of wt.% addition of alumina. In case of Group-II composites, wear tests occur initially vary rapidly followed by almost constant rate of wear irrespective of oxidation temperature. The cumulative wear and wear rate of both Group-I and Group-II composites were calculated from the wear tests raw data, Fig. 6a–b. The wear rate of both Group-I and Group-II composites are shown in comparison bar diagram, Fig. 7a–b, respectively. It is observed that the wear rate of Group-I composites decreases with

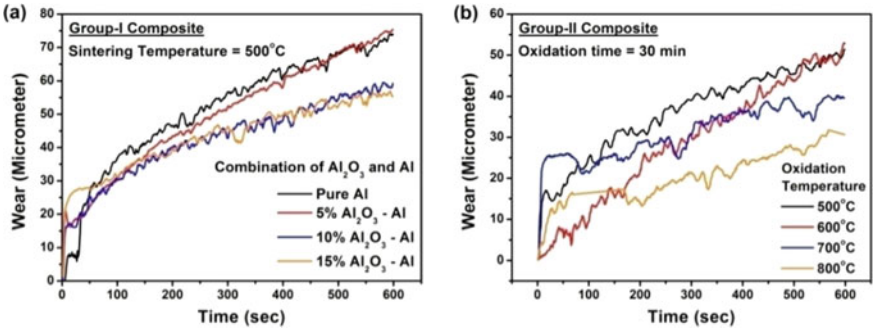


Fig. 6 Variation of wear with respect to test time for **a** group-I composites and **b** group-II composites

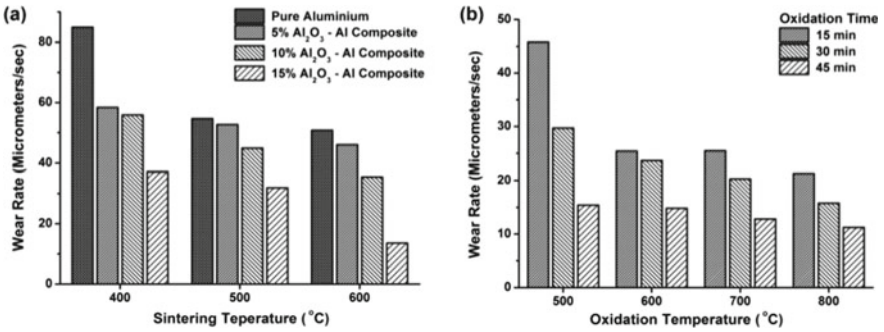


Fig. 7 Comparison bar diagram of variation of wear rate with respect to **a** wt.% addition of alumina and sintering temperature for Group-I composites, **b** oxidation temperature and time for Group-II composites

increase in both wt.% addition of Al_2O_3 and sintering temperature. Similar observation has been reported by several researchers [18, 19]. Such observation is attributed to the increase of concentration of more wear resisting reinforcement material by adding of Al_2O_3 powder in Al powder matrix material. The decrease of wear rate with increasing sintering temperature is attributed to the fact of increase of apparent density and decrease of porosity along with the increase of bonding strength between reinforcing material and matrix material.

It is observed from Fig. 7b that the wear rate of Group-II composites decreases with increase in oxidation temperature irrespective of oxidation time period. This is attributed to the fact that with increase in oxidation temperature, the density of pure aluminium increases up to the nearest value of 4 gm/cc which is the closer value of density of pure alumina [4]. Therefore, density of more wear resisting reinforcement material (aluminium oxide) increases with increase in oxidation temperature results in decrease of wear rate. It is also observed that the wear rate decreases with increase in oxidation time period irrespective of oxidation temperature. This is attributed to the general fact of increase of concentration of reinforcing material (Al_2O_3) for longer period of oxidation. Comparing Fig. 7a with b, it is found that the wear rate is more in case of Group-I composites compared to Group-II composites. Therefore, the wear resistance is more in case of AAMMCs prepared by oxidation route compared to mechanical mixing route of composite preparation.

The corrosion current density (i_{corr}) of pure Al sample, Group-I composites and Group-II composites were calculated from potentiodynamic polarization curves by Tafel extrapolation method. The variation of corrosion current density of Group-I and Group-II composites is shown in Fig. 8. It is clearly observed that the i_{corr} of pure Al sample is much more compared to Group-I and Group-II composites. The more corrosion resistance is observed in case of aluminium-alumina metal matrix composites compared to pure Al due to presence of higher corrosion resistive reinforcement material (Al_2O_3) in aluminium matrix. It is also observed that the i_{corr} of Group-I composites decreases with increase in weight percent addition of alumina.

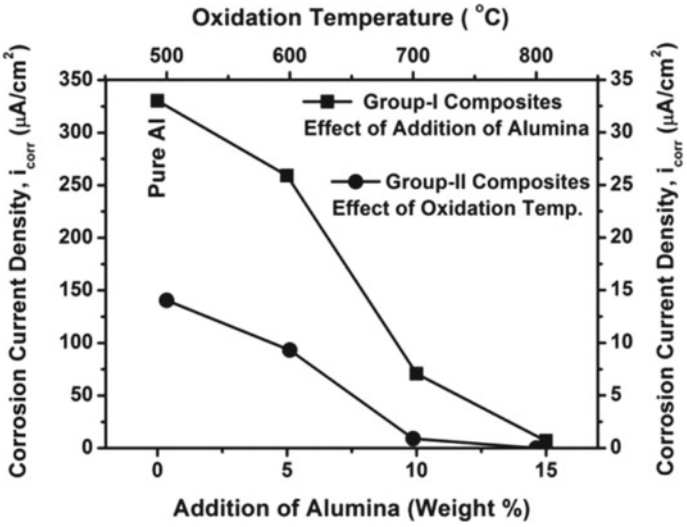


Fig. 8 Variation of corrosion current density of Group-I and Group-II composites

This is attributed to the general fact that the density of Al_2O_3 increases with increase of weight percent alumina addition. It is further observed that the i_{corr} of Group-II composites significantly decrease from 14 to 2.5 $\times$ 10^{-5} $\mu A/cm^2$ with increase in oxidation temperature from 500 to 800 °C. This is attributed to higher diffusivity due to the high ratio of surface to volume owing to the presence of very fine grains at higher oxidation temperature. This improves the formation of a corrosion protective layer. The corrosion resistance of Group-II composites is more compared to Group-I composites due to the formation of corrosion protective layer during oxidation of pure aluminium powder material at higher temperature.

4 Conclusions

From the present study, the following conclusions have been drawn:

- Mechanical properties, wear resistance and corrosion resistance of pure aluminium can be enhanced by preparing AAMMCs following both routes of composite preparation, whereas more enhancements can be achieved by oxidation route compared to mechanical mixing route of composites preparation.
- In case of Group-I composites, the mechanical properties like hardness and wear resistance increase with increase of both weight percent addition of pure alumina powder and sintering temperature. Corrosion resistance of pure aluminium also increases with increase of weight percent addition of pure alumina powder in aluminium powder matrix material.

- In case of Group-II composites, the hardness and wear resistance increase with increase of both oxidation temperature and oxidation time duration. Corrosion resistance of pure aluminium also increases with increase of oxidation temperature.

The future scope of the present research work is to prepare lightweight aluminium metal matrix composites (AMMCs) with nano-sized reinforced alumina particles and to improve high specific strength, higher corrosion resistance, better physical and mechanical properties of AMMCs.

Acknowledgements The author would like to gratefully acknowledge Prof. Akshay Kr. Pramanick and Jadavpur University for providing facilities to carry out the present research work.

References

1. Ravichandran MV, Krishna PR, Dwarakadasa ES (1992) Fracture toughness evaluation of aluminium 4% Mg-Al_2O_3 liquid-metallurgy particle composite. J Mater Sci Lett 11(8):452–456
2. Hoseini M, Meratian M (2005) Tensile properties of in-situ aluminium–alumina composites. Mater Lett 59(27):3414–3418
3. Alaneme K, Bodunrin M (2011) Corrosion behavior of alumina reinforced aluminium (6063) metal matrix composites. J Min Mater Chem Eng 10(12):1153
4. Rai A, Park K, Zhou L, Zachariah M (2006) Understanding the mechanism of aluminium nanoparticle oxidation. Combust Theor Model 10(5):843–859
5. Widener J, Beckstead M (1998) Aluminum combustion modeling in solid propellant combustion products. In: Joint propulsion conference and exhibit, p 3824
6. Liang Y, Beckstead M (1998) Numerical simulation of quasi-steady, single aluminum particle combustion in air. In: 36th aerospace sciences meeting & exhibits, p. 254
7. Liang Y, Beckstead M, Pudduppakkam K (1999) Numerical simulation of unsteady, single aluminum particle combustion. In: Proceedings of 36th JANNAF, pp 283–309
8. Trunov MA, Schoenitz M, Zhu X, Dreizin EL (2005) Effect of polymorphic phase transformations in Al2O3 film on oxidation kinetics of aluminum powders. Combust Flame 140(4):310–318
9. Kouzeli M, Mortensen A (2002) Size dependent strengthening in particle reinforced aluminium. Acta Mater 50(1):39–51
10. Tongsri R, Asavavisithchai S, Mateepithukdharm C, Piyarattanatrai T, Wangyao P (2017) Effect of powder mixture conditions on mechanical properties of sintered Al_2O_3-SS 316L composites under vacuum atmosphere. J Met Mat Min 17(1)
11. Olszówka-Myalska A, Szala J, Cwajna J (2001) Characterization of reinforcement distribution in Al/(Al2O3) p composites obtained from composite powder. Mater Charact 46(2–3):189–195
12. Kouzeli M, Weber L, San MC, Mortensen A (2001) Quantification of microdamage phenomena during tensile straining of high volume fraction particle reinforced aluminium. Acta Mater 49(3):497–505
13. Chiou J-M, Chung D (1991) Characterization of metal-matrix composites fabricated by vacuum infiltration of a liquid metal under an inert gas pressure. J Mater Sci 26(10):2583–2589
14. Durai T, Das K, Das S (2007) Synthesis and characterization of Al matrix composites reinforced by in situ alumina particulates. Mater Sci Eng A 445(100–105)
15. Kumar AP, Aadithya S, Dhilepan K, Nikhil N (2016) Influence of nano reinforced particles on the mechanical properties of aluminium hybrid metal matrix composite fabricated by ultrasonic assisted stir casting. J Eng Appl Sci 11(2):1204–1210

16. Jasper J, Kumar AP, Bharanidaran R (2015) Synthesis, characterization and evaluation of properties of aluminium alloy based hybrid composite reinforced with nano SiC and nano graphene. Int J Appl Eng Res 10(50):735–739
17. Afkham Y, Khosroshahi RA, Rahimpour S, Aavani C, Brabazon D, Mousavian RT (2018) Enhanced mechanical properties of in situ aluminium matrix composites reinforced by alumina nanoparticles. Arch Civil Mech Eng 18(1):215–226
18. Yalcin Y, Akbulut H (2006) Dry wear properties of A356-SiC particle reinforced MMCs produced by two melting routes. Mater Des 27(10):872–881
19. Naresh P, Acharya S (2004) Development of metal matrix composite using red mud an industrial waste for wear resistant applications. In: Proceedings of the international conference on industrial tribology. Mumbai, pp 164–170

Microstructure and Mechanical Characterization of AA7150/ZrO_2 Composites Manufactured by Stir Casting Route



V. Mohanavel, M. Ravichandran, S. Suresh Kumar, and A. Praveen Kumar

Abstract In this manuscript, it exhibits the fabrication of AA7150 aluminium alloy composites (AMC) which have been produced via stir casting route utilizing zirconium oxide (ZrO_2) as secondary content. The influence of secondary phase on the tensile strength and hardness of the composites was evaluated. The produced AMC and primary alloy were portrayed via scanning electron microscope (SEM). The examination outcomes reveal that the mechanical performance of the manufactured composites is enhanced via rising of the ZrO_2 content. SEM pictures expose the homogeneous spreading of ZrO_2 particles throughout the Al alloy.

Keywords Stir casting · Mechanical properties · Hardness · Zirconium oxide · AA7150

1 Introduction

Particulate reinforced aluminium composites (PRAMCs) are discovered to have tremendous tribological, physical, mechanical and friction properties. Thus, they are efficaciously employed in several product enhancements, such as air conditioner compressor piston, brake disc, cam material and piston [1–4]. Enormous quantum of investigators exhibited that hard ceramic filler materials incorporate PRAMCs have

V. Mohanavel (✉)
Department of Mechanical Engineering, Chennai Institute of Technology, Chennai, Tamilnadu 600069, India
e-mail: mohanavel.phd@gmail.com

M. Ravichandran
Department of Mechanical Engineering, K. Ramakrishnan College of Engineering, Trichy, Tamilnadu 621112, India

S. Suresh Kumar
Department of Mechanical Engineering, Panimalar Polytechnic College, Chennai, Tamilnadu 600029, India

A. Praveen Kumar
Department of Mechanical Engineering, CMR Technical Campus, Hyderabad, Telangana 501401, India

© Springer Nature Singapore Pte Ltd. 2020

A. Praveen Kumar et al. (eds.), *Advances in Lightweight Materials and Structures*,
Springer Proceedings in Materials 8, https://doi.org/10.1007/978-981-15-7827-4_34

outstanding mechanical and tribological properties than plain alloys [5–8]. The most extensively employed hard ceramic filler contents to incorporate the Al matrices are TiC, B_4C, SiC, TiB_2, WC, Al_2O_3 and Si_3N_4 [9–11]. Liquid state melt stirring route is highly adaptable, quite simple, well-situated and very low-priced method when compared to other manufacturing processes [12–15].

The mixture of the primary matrix and secondary filler contents reveals outstanding elastic modulus, excellent stiffness, superior hardness, low density, nominal thermal expansion coefficient, light in weight, good erosion and corrosion resistance which provides a conceivable candidate for several applications [16,17]. AA7xxx aluminium alloy series heat treated alloys discovered to be highly appropriate for these purpose owing to its strength to weight ration and natural ageing characteristics [18–21]. Amid the several 7xxx series of Al alloys, AA7150 achieves additional importance [22]. In the present research study, it targets to develop the AA7150/ZrO_2 composites with enhanced mechanical properties via stir casting process.

2 Experimental Procedure

AA7150 was taken as a primary plain alloy and the ZrO_2 powder was used as the secondary particle. Figure 1 displays the SEM morphology of ZrO_2. Plain AA7150 material has been liquefied in the Gr crucible inside a pit furnace (850 °C) and WC powders were merged in dissimilar mass percentages like AA7150 + 0% ZrO_2, AA7150 + 5% ZrO_2, AA7150 + 10% ZrO_2. The dissimilar mass percentages of ZrO_2p were united to the liquefied Al. The liquefied material was stirred repetitively at 300 rpm in 4 min. Finally, the liquefied material was discharged into mould. The micro-penetration (HV) was determined using micro-Vickers hardness tester at a load of 0.5 kgF pertained for a period of 5 s. Figure 2 displays the before hardness test specimen and after hardness test specimen. The tensile test was estimated employing computer integrated universal testing machine and average values were recorded. The tensile samples were made rendering to the standard ASTM E08. Figure 3 reveals the before and after tensile test sample.

3 Result and Discussions

3.1 Microstructural Inspection of AA7150/ZrO_2 PRAMCs

Figure 4 displays the SEM images of the PRAMCs. SEM images depict the unvarying distribution of ZrO_2 secondary material and also portray the solid interface between the primary material and the ZrO_2 material. It ought to amplify the load bearing

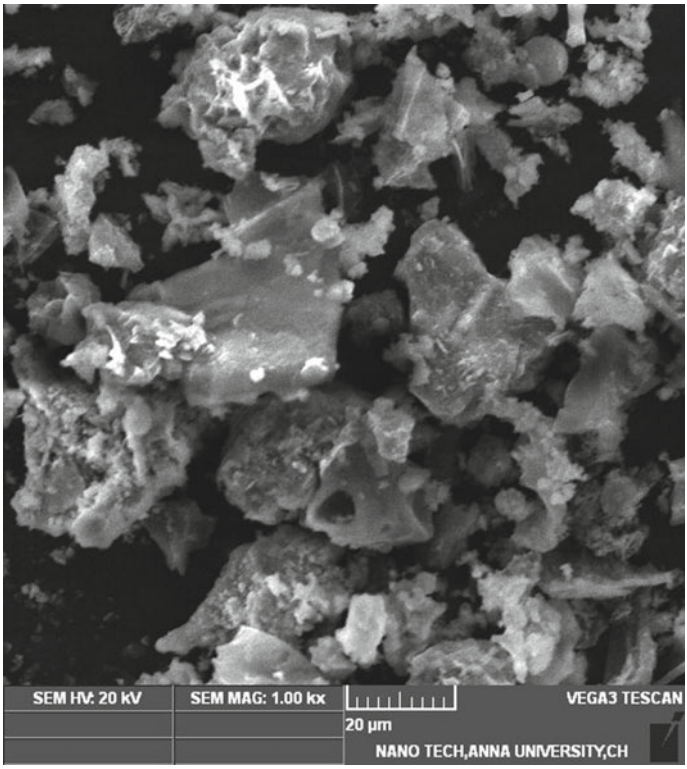


Fig. 1 SEM image of ZrO_2 particle



Fig. 2 Before and after hardness test specimen



Fig. 3 Before and after tensile test specimen

function of the expected PRAMCs. The enclosure of ZrO_2p in the primary alloy can somewhat evidently transform the micro-shapes and structures of the composites.

3.2 Hardness of the AA7150/ZrO_2 PRAMCs

Figure 5 expresses the performance of ZrO_2 particles on the Vickers micro-hardness (HV) of the primary metal and developed composites. The HV has been discovered to escalate with the increase in ZrO_2 secondary content and it is ominously higher than the HV of the primary material. It can be due to the ZrO_2 content operate as an obstruction to the penetration, which donates to enlightening the Vickers hardness of the PRAMCs [10, 19].

3.3 Ultimate Tensile Strength of the AA7150/ZrO_2 PRAMCs

Figure 6 expresses the ultimate tensile strength (UTS) of AA7150/ZrO_2 PRAMCs. The UTS of the PRAMCs upgrades progressively with the raise in ZrO_2 material. The manifestation of ZrO_2 secondary contents in the PRAMCs which operate as an obstruction to the movement of dislocation lead to supplementary augmentation in UTS [12, 14, 23, 24]. Likewise, the sound and solid intergap between the primary alloy and the ZrO_2 material extremely transfers the tension load from the

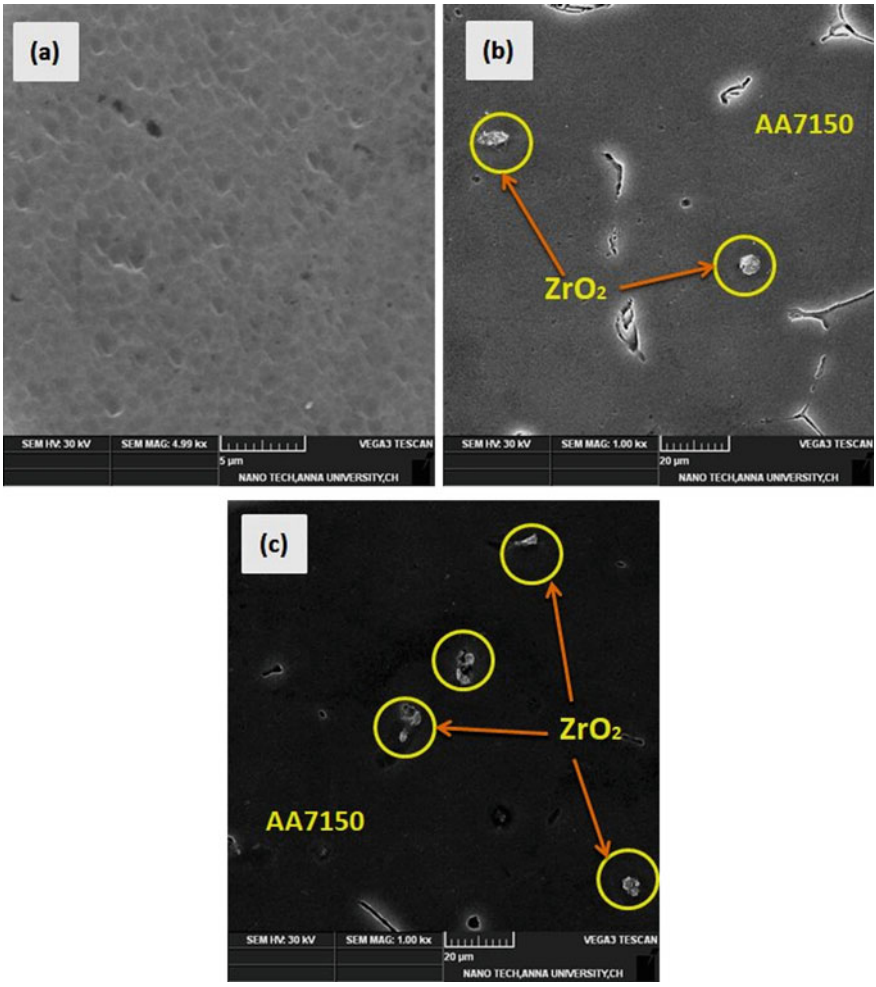


Fig. 4 SEM images of **a** AA7150 + 0% ZrO_2, **b** AA7150 + 5% ZrO_2 and **c** AA7150 + 10% ZrO_2

Al primary material to the secondary ZrO_2 material. Consequently, the UTS of the final composite is augmented.

4 Conclusions

AA7150-ZrO_2 composites were successfully manufactured using stir casting method. From this research study, the following concluding remarks are drawn.

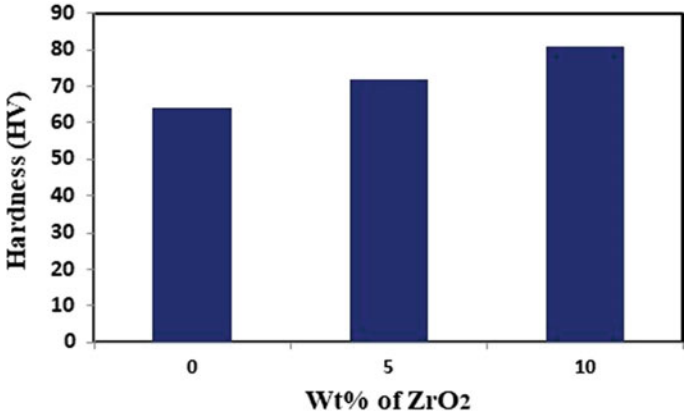


Fig. 5 Micro-hardness of the AA7150/ZrO_2 composite

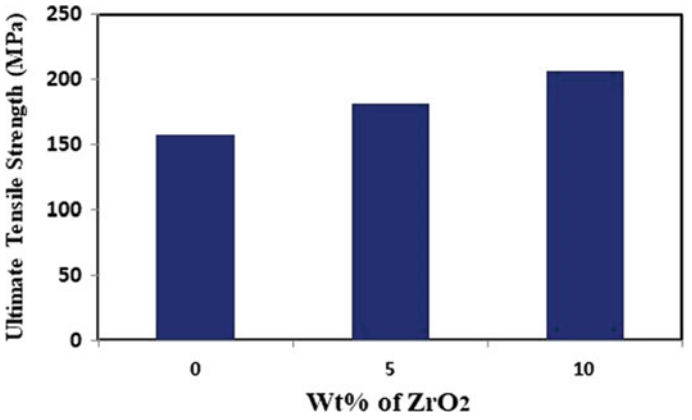


Fig. 6 Tensile strength of the AA7150/ZrO_2 composite

- The SEM image discovered the existence of ash filler contents in the prepared AMCs with reasonably homogeneous dissemination of ZrO_2 contents in the aluminium alloy.
- The micro-hardness and ultimate tensile strength of the composite augments with regard to inclusion of the weight fraction of ZrO_2 filler contents (i.e. from zero, five and ten wt.%).
- The AA7150/10 wt.% ZrO_2 composites revealed greater mechanical properties compare to plain alloy and the other composites.

References

1. Sajjadi SA, Ezatpour HR, Parizi MT (2012) Comparison of microstructure and mechanical properties of A356 aluminum alloy/Al_2O_3 composites fabricated by stir casting and compocasting processes. Mater Des 34:106–111
2. Mohanavel V, Rajan K, Suresh Kumar S, Vijayan G, Vijayanand MS (2018) Study on mechanical properties of graphite particulates reinforced aluminium matrix composite fabricated by stir casting technique. Mater Today Proc 5(1):2945–2950
3. Nas E, Gokkaya H (2016) Mechanical and physical properties of hybrid reinforced (Al/B4C/Ni(K)Gr) composite materials produced by hot pressing. Mater Test 57(6):524–530
4. Ravichandran M, Dineshkumar S (2016) Experimental investigations on Al-TiO_2-Gr hybrid composites fabricated through stir casting route. Mater Test 58(3):211–217
5. Ravichandran M, Sait AN, Anandakrishnan V (2014) Synthesis and forming behavior of aluminium-based hybrid powder metallurgic composites. Int J Miner Metall Mater 21(2):181–189
6. Mohanavel V, Naveen Kumar M, Magesh Kumar K, Jayasekar C, Dineshbabu N, Udishkumar S (2017) Mechanical behavior of in situ ZrB_2/AA2014 composite produced by the exothermic salt-metal reaction technique. Mater Today Proc 4 (2PA):3215–3221
7. Sajjadi SA, Ezatpour HR, Beygi H (2011) Microstructure and mechanical properties of Al-Al_2O_3 micro and nano composites fabricated by stir casting. Mater Sci Eng A 528:8765–8771
8. Doruk E, Pakdil M (2016) Effect of tempering conditions on the fatigue behavior of an AA6082 aluminum alloy. Mater Test 58(6):542–546
9. Mohanavel V, Rajan K, Suresh Kumar S, Chockalingam A, Roy A, Adithiyaa T (2018) Mechanical and tribological characterization of stir-cast Al-SiCp composites. Mater Today Proc 5:1740–1746
10. Mohanavel V, Ravichandran M, Suresh Kumar S (2020) Tribological and mechanical properties of Zirconium Di-boride (ZrB_2) particles reinforced aluminium matrix composites. Mater Today Proc 21:862–864
11. Stalin B, Ravichandran M, Mohanavel V, Raj LP (2020) Investigations into microstructure and mechanical properties of Mg-5wt.%Cu-TiB_2 composites produced via powder metallurgy route. J Min Metall Sect B Metall 56(1):99–108
12. Mohanavel V, Rajan K, Ravichandran M (2016) Synthesis, characterization and properties of stir cast AA6351-aluminium nitride (AlN) composites. J Mater Res 31(2):3824–3831
13. Shankar S, Balaji A, Kawin N (2018) Investigations on mechanical and tribological properties of Al-Si10-Mg alloy/sugarcane bagasse ash particulate composites. Particul Sci Technol 36(6):762–770
14. Kumar A, Kumar S, Mukhopadhyay NK (2018) Introduction to magnesium alloy processing technology and development of low-cost stir casting process for magnesium alloy and its composites. J Mag Alloys 6:245–254
15. Mohanavel V, Ravichandran M (2019a) Influence of AlN particles on microstructure, mechanical and tribological behavior in AA6351 aluminum alloy. Mater Res Exp 6(10):106557
16. Gao Q, Wu S, Lu S, Duan X, An P (2016) Preparation of in-situ 5 vol% TiB_2 particulate reinforced Al-4.5Cu alloy matrix composites assisted by improved mechanical stirring process. Mater Des 94:79–86
17. Praveen Kumar A, Dhilepan GE (2016) Influence of nano reinforced particles on the mechanical properties of aluminium hybrid metal matrix composite fabricated by ultrasonic assisted stir casting. ARPN J Eng Appl Sci 11(2):1204–1210
18. Jasper J, Praveen Kumar A, Bharanidaran R (2015) Synthesis, characterization and evaluation of properties of aluminium alloy based hybrid composite reinforced with nano SiC and nano grapheme. Int J Appl Eng Res 10(50):735–739
19. Suganuma K, Fujita T, Niihara K, Okamoto T, Koizumi M, Suzuki N (1989) Hot extrusion of AA7178 reinforced with alumina short fibre. Mater Sci Technol 5:249–254
20. Mohanavel V, Ravichandran M (2019b) Experimental investigation on mechanical properties of AA7075-AlN composites. Mater Test 61(6):554–558

21. Nallusamy M, Sundaram S, Kalaiselvan K (2019) Fabrication, characterization and analysis of improvements in mechanical properties of AA7075/ZrB_2 in-situ composites. Measurement 136:356–366
22. Madhukar P, Selvaraj N, Punugupati G, Veeresh Kumar GB, Rao CSP, Mishra SK (2019) Microstructure studies of AA7150-HBN nano composites fabricated by ultrasonic assisted stir casting, Mater Res Exp 6:116545
23. Mohanavel V, Suresh Kumar S, Sathish T, Adithiyaa T, Mariyappan K (2018) Microstructure and mechanical properties of hard ceramic particulate reinforced AA7075 alloy composites via liquid metallurgy route. Mater Today Proc 5:26860–26865
24. Rajan HBM, Ramabalan S, Dinaharan I, Vijay SJ (2013) Synthesis and characterization of in situ formed titanium diboride particulate reinforced AA7075 aluminum alloy cast composites. Mater Des 44:438–445

Tribological Characterization of Lightweight Hybrid Aluminium Composite Under Lubricated Sliding Condition



Pranav Dev Srivyas and M. S. Charoo

Abstract Lightweight advance composites are the new emerging class of the engineering materials that are rapidly replacing a large category of conventional material for various aerospace, automotive, structural industrial and marine applications because of excellent tribological as well as mechanical properties. The scope and objectives are to investigate tribological properties of the hybrid aluminium composite under lubricated sliding conditions. In this concern, lightweight aluminium hybrid composite is fabricated using non-conventional spark plasma sintering (SPS) route. The tribological behaviour of hybrid composite sample is examined using a ball-on-disc reciprocating universal tribometer configuration for 120 m sliding distance for variable load 10–80 N for 2 mm stroke and reciprocating frequency of 30 Hz. Wear test sliding distance is also performed for the (90–450 m) sliding distance. Two variable lubricants, i.e. Base PAO-4 lubricant and commercial SAE2W50 lubricant, are used in the present study. From the results, it is observed that the commercial SAE20W50 lubricant shows superior tribological properties with the fabricated sample and exhibit min coefficient of friction (COF) and wear rate. Abrasion and delamination are the main wear mechanisms that cause the removal of material while tribological testing. Reduction in the COF is attributed to the 2D graphene nanoplatelets (GNP) reinforcement in the composite samples that cause easy sliding due to weak van der Waals force and hence provide the exceptional lubrication mechanism for the composite sample.

Keywords Hybrid composite · Friction · Wear · Lubrication · Tribofilm

1 Introduction

Tribology is an interdisciplinary branch of engineering which includes three important mechanisms, i.e. friction, wear and lubrication [1–3]. Friction is the resistance to the motion of the bodies in the relative motion. Whenever two bodies are in relative

P. D. Srivyas (✉) · M. S. Charoo
Mechanical Engineering Department, NIT Srinagar, Jammu & Kashmir, India
e-mail: devpranav.srivyas_17@nitsri.ac.in

© Springer Nature Singapore Pte Ltd. 2020

A. Praveen Kumar et al. (eds.), *Advances in Lightweight Materials and Structures*,
Springer Proceedings in Materials 8, https://doi.org/10.1007/978-981-15-7827-4_35

motion, there is a resistance in the motion which is termed as friction mechanism [4]. Wear is the removal of material from one body or by the both bodies. Lubrication mechanism is used to reduce the friction and wear of the material [5]. Lubrication provides easy sliding of bodies in relative motion by forming a soft film between the body and the counter-body. Lubrication can be provided either by using liquid lubricants or by using solid lubricants [6, 7]. Hence, tribology can be defined as the science related to the rubbing.

Nowadays, various measures are opted by the engineer, scientist, material science experts to reduce the friction and wear of materials. Out of these, lightweight hybrid composites are the new class of materials which have the capability of reducing friction and wear of the materials. These materials find exceptional mechanical, tribological, chemical and physical properties which help to find applications in various automotive applications [8, 9]. Hybrid aluminium composites belong to the class of lightweight materials which find huge applications in automotive sector by replacing the currently used as well as conventional cast iron material [10]. Aluminium alloys are the lightweight materials, but in the past cannot be used because of the lack in the tribological properties.

Hybrid aluminium composites are the new class of materials which include aluminium alloy as the matrix material reinforced with ceramic and self-lubricating materials to provide exceptional outcome properties [11]. These materials have high strength-to-weight ratio, high hardness, high friction and wear resistance, superior lubrication. Use of high weight materials helps to reduce about 45% of the weight if used for the automotive applications. Due to its weight-reducing properties, it will also improve the fuel cost-effectiveness. The parameters that affect the outcome tribological properties of the composite include the selection of the matrix and reinforcement, their shape size, type volume concentration [12, 13].

In this concern, this study includes the tribological characterization of the Al–Si + Aluminium Oxide + Graphene Nanoplatelets (GNP) hybrid composite. Al-Si alloys are the most eligible aluminium alloy from the whole class of the aluminium alloys which exhibit superior wear and mechanical properties compared to other aluminium alloys. Aluminium oxide improves the wear resistance and hardness of the matrix alloy as the primary reinforcement. GNP as another reinforcement improves the exceptional lubricity and provides anti-friction and anti-wear properties to the hybrid composite. The scope and the objectives of the present study are to experimentally explore the lubrication behaviour of the GNP solid lubricant nanoparticles additives under wet sliding lubricating condition and to explore the tribological behaviour of the nanoaluminium oxide as the reinforcement in the Al-Si eutectic phase alloy. From the previous studies, it is clear that this novel advanced composite has not been studied in the past with PAO-4-based nanolubricant which opens up the new doors for this advanced composite with nanolubrication for various automotive applications especially cylinder bore and liners.

2 Material and Sample Fabrication

Micro-Al–Si alloy eutectic phase particles are used as the matrix material for the hybrid composite sample. The density of the matrix material is 2.66 g/cm^3 having 99.9999% purity. Nanoaluminium oxide is used as the secondary reinforcement having density 3.95 g/cm^3, and the GNP secondary reinforcement is having the density 2.3 g/cm^3. Raw powder material is purchased from the intelligent material Pvt. Ltd.

For the processing and fabrication of the hybrid composite, the raw powder is first blended and further fabricated using SPS fabrication route. For the blending of the raw powder, probe sonication as well as high-energy planetary ball milling (HEPBM) is used. Dispersion of the GNP as the reinforcement is an issue. By using the probe sonication, this issue can be resolved. The wet mixing of powder is done with ethanol used as the liquid medium. The 4 wt.% GNP is first sonicated in the ethanol for 2 h followed by the 6 wt.% aluminium oxide and balance Al–Si alloy. The whole sonication process is carried out for 4 h. Further, the suspension of the ethanol and powder milling is done at 240 rpm for 10 h for the uniform distribution of the reinforcement in the matrix material. The ball milling is done in the (silicon nitride) jar and ball (10 mm ball diameter). The ball-to-powder ratio is 10:1. After milling, wet suspension is dried using vacuum evaporator and oven to remove moisture from blended powder. Dried sample is ready for fabrication. For fabrication, SPS fabrication route is used. The powder sample is poured in the graphite die of 30 mm dia and then placed in the SPS chamber. The fabrication is done at 450 °C sintering temperature, 100 °C heating rate 10 min dwell time and 50 MPa load. The fabrication takes 14 min 30 s for complete processing the sample. Reduction in the fabrication time helps in improving the overall properties of the fabricated sample by limiting grain growth and unwanted phase formation. Fabricated sample is further prepared for the friction and wear (tribological) test. Samples are polished on the SiC emery paper followed by diamond paste and aerosol spray polishing on velvet cloth for high surface finish.

3 Tribological Testing Details

Further, the tribological test is performed on the polished sample using reciprocating ball-on-disc tribometer. Computer-controlled tribometer having data acquisition system (DAS) used to measure the friction force and COF for the tribo-pair. The counter-body used is the chrome steel ball plated with chromium. Load tests as well as sliding distance test are performed on the fabricated sample. For the load test variable, load is applied in the range 10–80 N with other parameters, i.e. stroke 2 mm, reciprocating frequency 30 Hz and sliding distance 120 m. For sliding distance 90–450 m, sliding distance is varied with load 20 N, and other parameters remain the same. After and before, the tribological testing the samples are cleaned with acetone

to completer removal the dust, contamination and wear debris from the sample. 3D surface profilometer is used to determine the wear volume of the wear scar generated. Further to determine the wear rate, Eq. 1 is used.

$$\text{SpecificWearRate} = \text{Wear Volume}/\text{Sliding Distance} \times \text{Load} \tag{1}$$

For the tribological test, PAO-4 base lubricant and SAE20W50 lubricating oil are used. For each test, one drop of the lubricating oil is poured on the sample before the tribological test to provide the lubrication effect.

4 Results and Discussion

4.1 Friction and Wear Analysis

For the friction and wear analysis, the tribological test is performed at variable load and sliding distance for the both lubricant oil on the fabricated sample. COF for the fabricated sample with variable load and lubricating oil is shown in Fig. 2. From the study, it is shown that there is a decrease in the COF observed for the SAE20W50 lubricating oil. Min COF of 0.0273 at 50 N load was observed for the PAO lubricant oil, whereas 0.026 COF at 80 N load is observed for the commercial SAE20W50 lubricating oil. The max COF of 0.0537 at 80 N load is observed for PAO-4 base lubricating oil, and 0.0396 COF for SAE20W50 lubricant oil is observed at 10 N load. COF for the variable sliding distance for the both lubricant oil is shown in Fig. 3. For PAO-4 base lubricant, the COF shows a maximum value of 0.049 for the initial sliding distance 90 m; afterwards, the continuous increase in the sliding distance leads to constant value for the COF. For the commercial lubricating oil, the COF fluctuates for the initial 270 m sliding distance, i.e. first increase up to 90 m sliding distance and then decrease further for 90 m and further increases, after that get constant for the further sling up to 450 m.

Wear volume and wear rate for the composite sample with both lubricating oils are shown in Figs. 4 and 5, respectively, for the variable load. Wear volume for the both lubricants increase with the increase in load. The maximum wear volume for the both lubricating oil is observed at the 80 N load and the minimum at the 10 N load. Increase in the load increases the wear volume of the composite sample. Wear rate continuously decrease for the lubricant sample. SAE20W50 commercial lubricating oil shows minimum wear volume and minimum wear rate compared to the PAO-base lubricating oil. Wear volume and wear rate with variable sliding distance (90–450 m) for the both lubricant samples are shown in Figs. 6 and 7. The results for the wear volume and wear rate show similar trends as of the load test. Results report that the wear volume and wear rate for the commercial lubricating oil show less wear compared to the base PAO-4 lubricating oil.

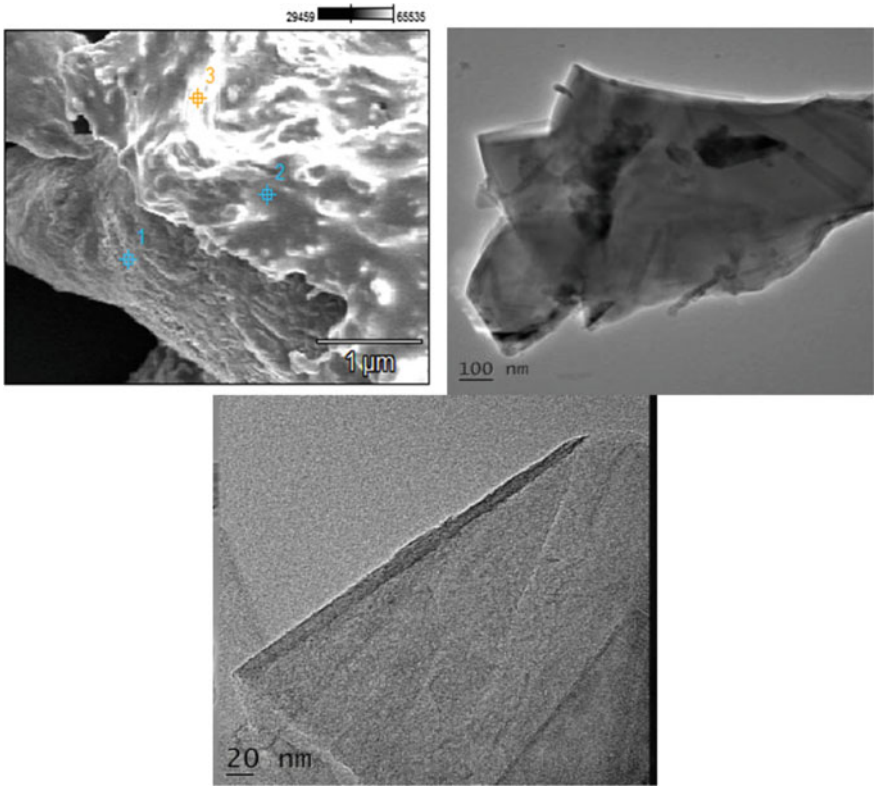


Fig. 1 SEM and TEM images of the raw powders used for sample fabrication **a** Al–Si eutectic alloy; **b** aluminium oxide; **c** graphene nanoplatelets

4.2 Wear Characterization Discussion

Scanning electron microscope (SEM) and optical micrographs shown in Figs. 8 and 9 reveal that for high loading and high sliding distance, the material gets protrude for the composite sample and gets adhere to the counter-body during the initial run-in-phase. After the initial run-in-phase, the GNP particles that get abrade from the composite surface act as the solid lubricant and get mixed with the lubricating oil, hence performed the exceptional lubrication mechanism. These GNP particles act as the solid lubricant which provides exceptional lubrication with the lubricating oil and helps in controlling and minimizing the friction mechanism. The GNP particle is having low shear stress and provides easy lubrication to the tribo-pair. Tribo layers of graphene oxide are formed on the sample surface between the sliding interfaces and ultimately reduce the COF as well as the wear of the composite. Energy dispersion spectroscopy (EDS) analysis as shown in Fig. 10 reveals that formation of graphene oxide layer as carbon and oxygen is present on the scar along with Al and Si. SEM

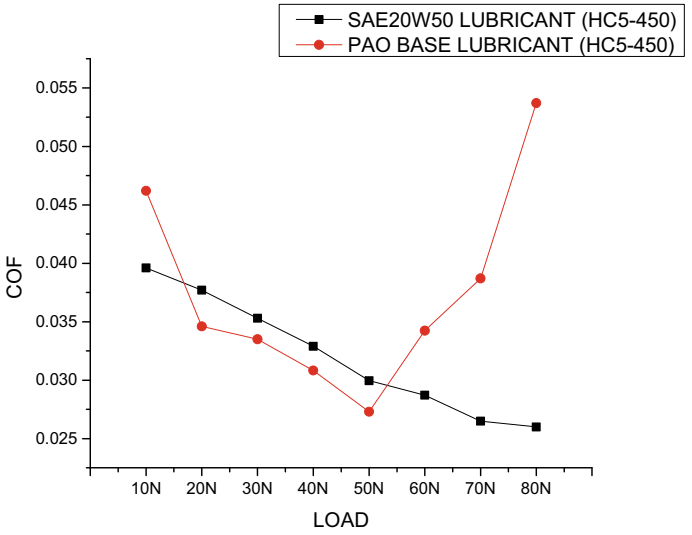


Fig. 2 COF versus load

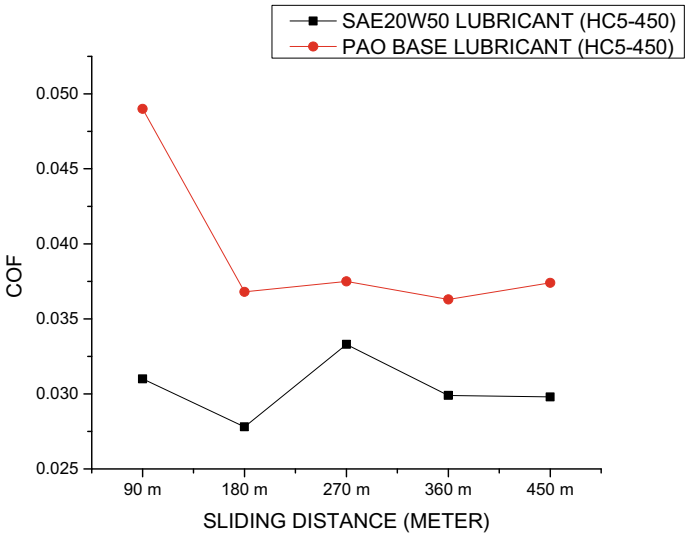


Fig. 3 COF versus sliding distance

analysis reveals that parallel grooves and the plastic deformation marks on the scar are evident of abrasion and plastic deformation on the scar zone. The reduction in the COF and wear rate with increasing load is attributed to the severity of contact pressure over the asperities.

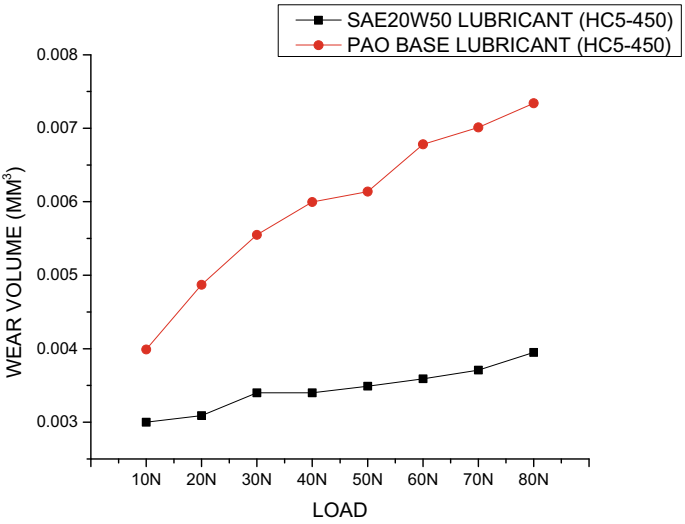


Fig. 4 Wear volume versus load

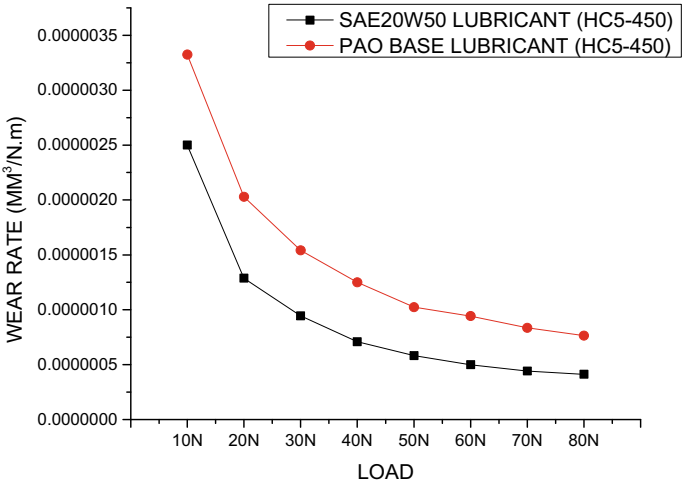


Fig. 5 Wear rate versus load

High applied load increases the sliding interface temperature reducing yield strength which in turns reduces the wear rate of the composite. Weak-layered GNP particles are attributed to the exceptional frictional and wear behaviour. The weak-layered GNP lamellar structure particles get easily dispersed and improve the friction and wear resistance. Better results for the commercial SAE20W50 lubricant are attributed to the anti-wear properties and additive that are already present in the

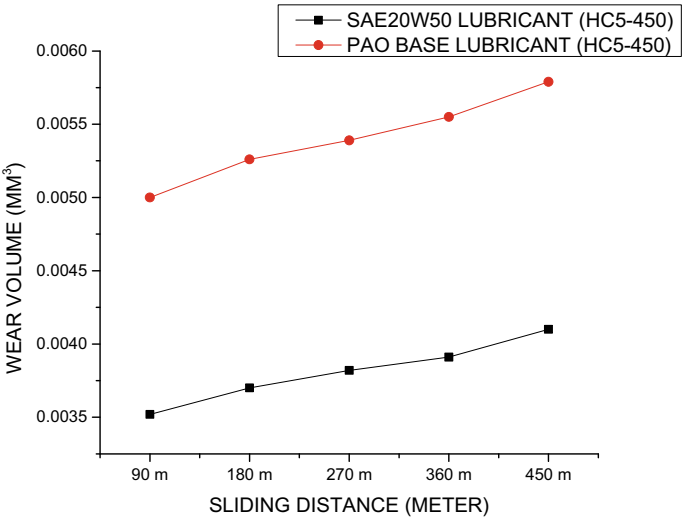


Fig. 6 Wear volume versus sliding distance

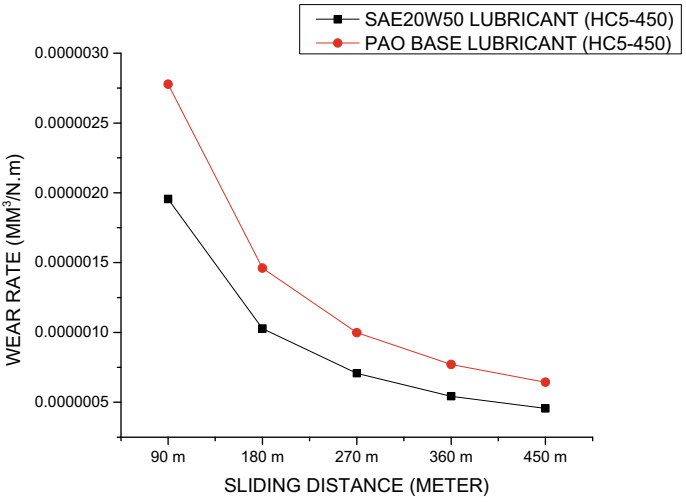


Fig. 7 Wear rate versus sliding distance

lubricating oil. The tribo layer protective film helps in easy sliding, and the GNP abrade particles attributed to show ball bearing mechanism with the lubricating oil changes the pure sliding mechanism to rolling mechanism and reduces the friction behaviour for the composite. 3D surface profilometer studies on the wear scar are shown in Fig. 11 which reveals that smooth scar surface is formed after the testing. High load as well as high sliding distance generally leads to high scar surface, but

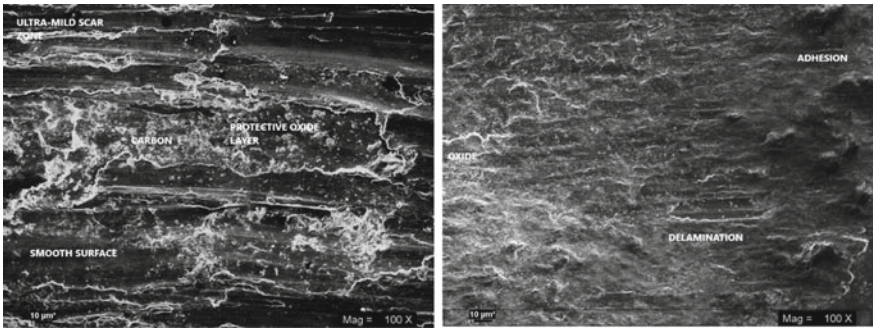


Fig. 8 SEM analysis of the wear scar

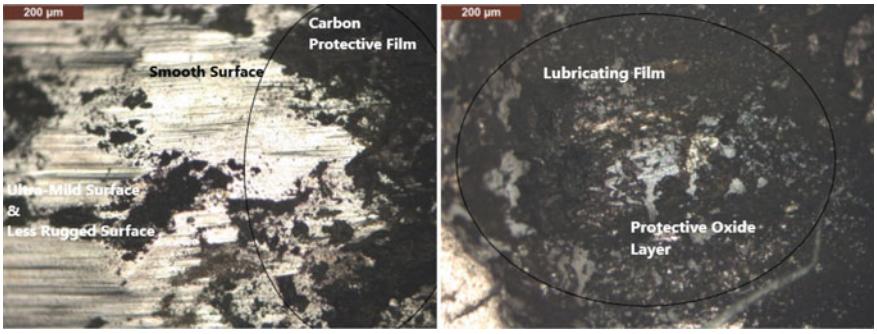


Fig. 9 Optical analysis of the wear scar

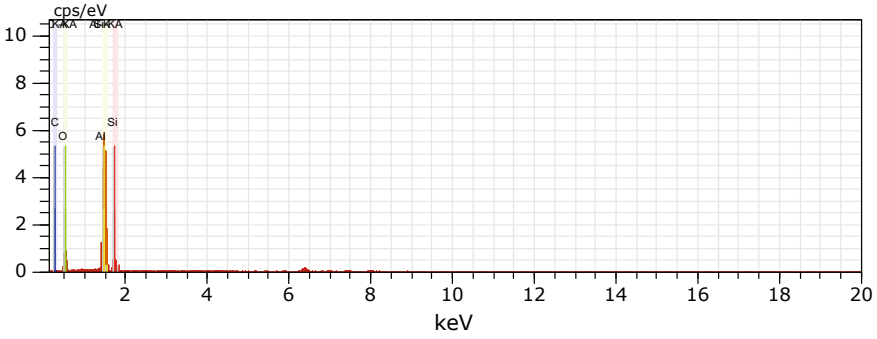


Fig. 10 EDS analysis of the wear scar

the formation of graphene oxide tribolayer smoothen the scar surface decreases the wear roughness.

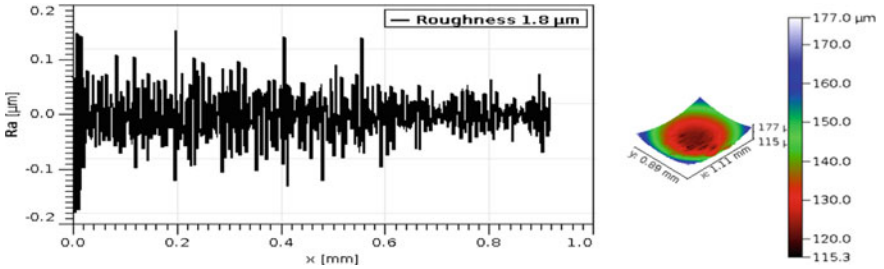


Fig. 11 Roughness analysis of the wear scar

5 Conclusion

In the particular study, the experimentation is conducted on the lightweight hybrid aluminium composite for variable load and sliding distance. Following are the conclusive points that are obtained after the experimentation:

- Lightweight hybrid composite exhibits exceptional tribological properties with both lubricating oil.
- Reduction in the COF and wear volume up to 55.4% is reported with the 4 wt.% of GNP as secondary reinforcement with SAE20W50 lubricating oil in comparison to the base PAO-4 lubricating oil.
- Reduction in the scar surface is achieved using GNP as the solid lubricating reinforcement within the hybrid composite sample.
- GNP inclusion as the secondary reinforcement enhances the lubrication mechanism of the fabricated composite sample and reduces the COF.
- Aluminium oxide as primary reinforcement improves the hardness of the matrix alloy, hence improves the wear resistance as the hardness is directly proportional to the wear resistance of the material.
- Plastic deformation and abrasion are the prominent wear mechanism observed after the experimental studies.
- GNP particles as the solid lubricant provide the exceptional lubrication with the lubricating oil. The abraded GNP particles get settle between the asperities reduce the direct asperities-asperities contact and also shows the ball bearing mechanism with the liquid lubricating oil.

Future Scope Overall enhancement in friction and wear (tribological) properties are observed for the hybrid lightweight composite which opens the door for its use in automotive sector, especially in the IC engine components. Further, this hybrid composite sample can be tribological and mechanically investigated with different other solid lubricants as the reinforcement either alone or in combination with the GNP with commercial lubricating oil to achieve the nanolubrication mechanism without using any additive in the lubricating oil.

References

1. Kim KS, Lee HJ, Lee C, Lee SK, Jang H, Ahn JH, Lee HJ (2011) Chemical vapor deposition-grown graphene: the thinnest solid lubricant. ACS Nano 5(6):5107–5114. https://doi.org/10.1021/nn2011865
2. Shin YJ, Stromberg R, Nay R, Huang H, Wee AT, Yang H, Bhatia CS (2011) Frictional characteristics of exfoliated and epitaxial graphene. Carbon 49(12):4070–4073. https://doi.org/10.1016/j.carbon.2011.05.046
3. Yan C, Kim KS, Lee SK, Bae SH, Hong BH, Kim JH, Ahn JH (2011) Mechanical and environmental stability of polymer thin-film-coated graphene. ACS Nano 6(3):2096–2103. https://doi.org/10.1021/nn203923n
4. Berman D, Erdemir A, Sumant AV (2013a) Few-layer graphene to reduce wear and friction on sliding steel surfaces. Carbon 54:454–459. https://doi.org/10.1016/j.carbon.2012.11.061
5. Berman D, Erdemir A, Sumant AV (2013b) Reduced wear and friction enabled by graphene layers on sliding steel surfaces in dry nitrogen. Carbon 59:167–175. https://doi.org/10.1016/j.carbon.2013.03.006
6. Tabandeh-Khorshid M, Omrani E, Menezes PL, Rohatgi PK (2016) Tribological performance of self-lubricating aluminum matrix nanocomposites: the role of graphene nanoplatelets. Eng Sci Technol Int J 19(1):463–469. https://doi.org/10.1016/j.jestch.2015.09.005
7. Senatore A, D'Agostino V, Petrone V, Ciambelli P, Sarno M (2013) Graphene oxide nanosheets as an effective friction modifier for oil lubricant: materials, methods, and tribological results. ISRN Tribol. https://doi.org/10.5402/2013/425809
8. Chen Z, Liu X, Liu Y, Gunsel S, Luo J (2015) Ultrathin MoS 2 nanosheets with superior extreme pressure property as boundary lubricants. Sci Rep 5:12869. https://doi.org/10.1038/srep12869
9. Azman SSN, Zulkifli NWM, Masjuki H, Gulzar M, Zahid R (2016) Study of tribological properties of lubricating oil blend added with graphene nanoplatelets. J Mater Res 31(13):1932–1938. https://doi.org/10.1557/jmr.2016.24
10. Meng Y, Su F, Chen Y (2016) Supercritical fluid synthesis and tribological applications of silver nanoparticle-decorated graphene in engine oil nanofluid. Sci Rep 6 https://doi.org/10.1038/srep31246
11. Rasheed AK, Khalid M, Javeed A, Rashmi W, Gupta TCSM, Chan A (2016) Heat transfer and tribological performance of graphene nano lubricant in an internal combustion engine. Tribol Int 103:504–515. https://doi.org/10.1016/j.triboint.2016.08.007
12. Zhang W, Zhou M, Zhu H, Tian Y, Wang K, Wei J, Wu D (2011) Tribological properties of oleic acid-modified graphene as lubricant oil additives. J Phys D Appl Phys 44(20):205303. https://doi.org/10.1088/0022-3727/44/20/205303
13. Eswaraiah V, Sankaranarayanan V, Ramaprabhu S (2011) Graphene-based engine oil nanofluids for tribological applications. ACS Appl Mater Interf 3(11):4221–4227. https://doi.org/10.1021/am200851z

Electrical Study of Lead Calcium Titanate Borosilicate Glass Ceramics

Sangeeta Das, S. S. Gautam, and C. R. Gautam

Abstract This chapter aimed at assessing electrical properties, viz. dielectric constant (ε_r) and dissipation factor (tanδ) of the melt quenched synthesized glass ceramic (GC) samples in $59(PbO_xCaO_{1-x}) \cdot TiO_2$–$40(2SiO_2 \cdot B_2O_3)$–$1Fe_2O_3$ composition with varying x values of 0.0, 0.1, 0.3, 0.5 and 0.7. The ε_r and tanδ of the GC samples were computed between the frequency ranges of 100 Hz−1 MHz by varying temperatures between 50 and 500 °C throughout the heating of the samples in air. The obtained result of ε_r and tanδ for the five different GC samples at 500 °C and at low frequency (100 Hz) lies in the range of 12,546−29,877 and 5.65−55.67, respectively. Capacitors are extensively used as an integral part of electrical circuits especially in electrical supply systems to make the voltage and power flow stable. A capacitor comprises of two electrodes that are separate out by dielectric, connecting leads and housing. The damage of one of these parts might be the reason of breakdown of the capacitors. High permittivity and breakdown voltage are the necessary qualities of the dielectric materials in order to maximize the charge carrying capacity of the capacitors. Hence, the synthesized GC with high ε_r can be suitably used for high density energy storage capacitors.

Keywords Glass ceramic · Dielectric constant · Dissipation factor · Capacitor · Electrical study

S. Das (✉) · S. S. Gautam
Department of Mechanical Engineering, North Eastern Regional Institute of Science and Technology, Nirjuli 791109, India
e-mail: sangeeta.das40@gmail.com

S. S. Gautam
e-mail: satyam.gautam@gmail.com

C. R. Gautam
Advanced Glass and Glass Ceramic Research Laboratory, Department of Physics, University of Lucknow, Lucknow 226007, India
e-mail: gautam_ceramic@yahoo.com

© Springer Nature Singapore Pte Ltd. 2020

A. Praveen Kumar et al. (eds.), *Advances in Lightweight Materials and Structures*,
Springer Proceedings in Materials 8, https://doi.org/10.1007/978-981-15-7827-4_36

1 Introduction

The evolving technologies require the development of novel materials bearing electrical and magnetic properties along with enhanced structural properties, for example, mechanical and thermal expansion [1]. The GC materials are immensely studied due to the possession of high dielectric constant that is suitable for electronic applications. Researchers investigated the electrical properties of different glass and GC systems [2–4]. Shankar and Deshpande [5] studied lead titanate based GC system having strontium oxide (SrO) to enhance their electrical properties. They observed that the assessed values of dielectric constant at normal room condition were present in between 100 and 200 which are applicable for capacitors with high energy storage. The electrical study of borosilicate GC containing strontium, titania and bismuth was studied by Thakur et al. [6]. They noted that the GC specimens with the major $TiO_2/SrTiO_3$ phase had large dielectric constant values with very little variation even at high temperatures and low dissipation factor. Abdel-Khalek et al. [7] studied the structural and dielectric properties of borate glasses and glass ceramics containing $BiFeO_3$ phase. They observed that the dielectric constant decreased with an increase in Fe_2O_3 and Bi_2O_3 content that depends on the distance between iron ions and the space charge polarization. Sahu et al. [8] studied the dielectric behavior of lead strontium titanate glass ceramics and observed that the curie temperature decreased with decreasing lead to strontium ratio in the parent glass. Lee et al. [9] studied the consequences of adding SiO_2 on the dielectric properties of barium titanate-based ceramics and found that a little addition of silica improves the dielectric properties.

The present analysis intends to assess the electrical properties, viz. dielectric constant (ε_r) and the dissipation factor ($\tan\delta$) of the fabricated glass ceramic samples in $59(PbO_xCaO_{1-x}) \cdot TiO_2$–$40(2SiO_2 \cdot B_2O_3)$–$1Fe_2O_3$ composition with varying x values between 0.0 and 0.7. It is the first dielectric study in the novel system $59(PbO_xCaO_{1-x}) \cdot TiO_2$–$40(2SiO_2 \cdot B_2O_3)$–$1Fe_2O_3$.

2 Experimentation

The GC samples were synthesized by weighing and blending different chemicals, viz. lead monoxide (PbO), quicklime (CaO), titania (TiO_2), silicon dioxide (SiO_2), boracic acid (H_3BO_3) and iron (III) oxide (Fe_2O_3), in a mortar-pestle. The mixture was then melt at 1400 °C in a programmable electric furnace (Fig. 1), followed by casting of rectangular samples (8 mm in length, 6 mm in breadth and 1 mm in thickness) at atmospheric air. The annealing of the samples was then carried out in a muffle furnace (Fig. 2) at a constant temperature of 400 °C for 3 h to make glasses after which they were reheated at 5 °C per minute to reach 800 °C where it was maintained for 4 h to crystallize the glasses to glass ceramics.

The dielectric experiments were performed in an LCR meter with the model HIOKI-LCR TESTER 3532-50 (Fig. 3). The GC samples for this experiment were



Fig. 1 Melting furnace



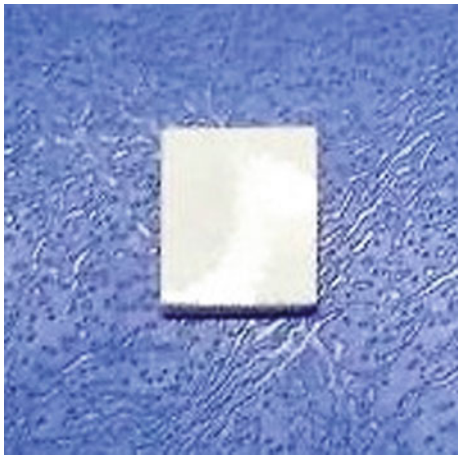
Fig. 2 Muffle furnace

finely polished rectangular shaped samples (Fig. 4). For the test, the samples were treated with highly pure conducting silver paste (SILTECH, Bangalore) and baked at 200 °C for 15 min in order to make the samples to behave as electrode. The ε_r and tanδ of the GC samples were computed between the frequency ranges of 100 Hz–1 MHz by varying temperatures between 50 and 500 °C when the samples are heated in atmospheric air.



Fig. 3 Hioki 3532-50 LCR hi-tester

Fig. 4 Dielectric sample



3 Analysis of Experimental Results

The variation of ε_r and tanδ of GC samples with definite values of $x = 0.0$, 0.1, 0.3, 0.5 and 0.7, with temperature and frequency is shown in Figs. 5, 6, 7, 8 and 9, respectively. The plots in Figs. 5a, 6a, 7a, 8a and 9a exhibit that ε_r remain nearly constant up to 150 °C and then rises with a rise in temperature at lower frequencies. Though, ε_r remains constant throughout the entire temperature at higher frequencies and reveals temperature independent behavior. The reason ascribed to this trend is that at low frequency; the dipole can follow the path of changing electric field. Whereas with increase in frequency, the dipole lags the electric field and finally ceases to follow the electric field leading to the attainment of constant ε_r at high frequency.

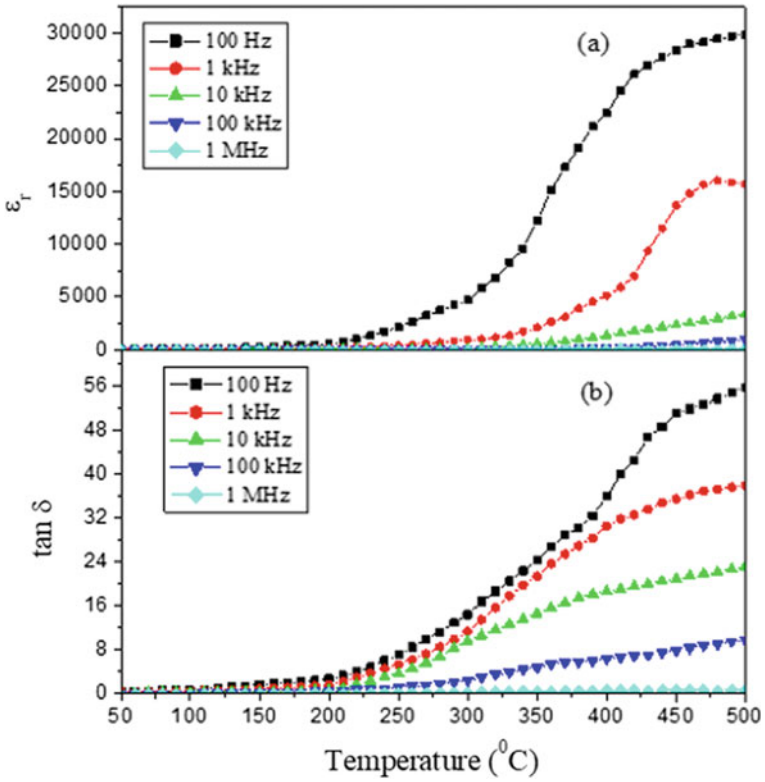


Fig. 5 Plot of **a** ε_r and **b** tanδ as a function of frequencies at varying temperatures for $x = 0.0$

The reason for constant ε_r up to 150 °C is the poor reaction of dipole to the employed external electric field resulting in small polarization of the samples. Beyond 150 °C, the dipole responds well to the employed electric field that increases the interfacial polarization leading to a rise in ε_r and tan δ of the samples [10]. Moreover, the high ε_r at low frequencies was due to combined influence of ionic and orientation sources to the total polarizability. Whereas the high ε_r at higher temperatures may be attributed to high involvement of electronic and ionic sources to the total polarizability [11]. The ε_r of the GC samples reduced with a rise in PbO content owing to decrease in the space charge polarization [7].The values of ε_r at 500 °C and at low frequency (100 Hz) are 29,877, 24,757, 22,987, 15,967 and 12,546 for GC samples with $x =$ 0.0, 0.1, 0.3, 0.5 and 0.7, respectively.

In Figs. 5b, 6b, 7b, 8b and 9b, it has been observed that the values of dissipation factor (tanδ) are higher at both low frequencies and high temperatures. Thus, tanδ follows similar trend as ε_r that indicates thermal actuation of the dielectric relaxation of the system [12]. The reason for the attainment of high tanδ at low frequencies was hopping of ions, conduction loss and loss due to electron polarization. Whereas low tanδ at higher frequencies was solely due to ion vibrations. The values of tanδ at low

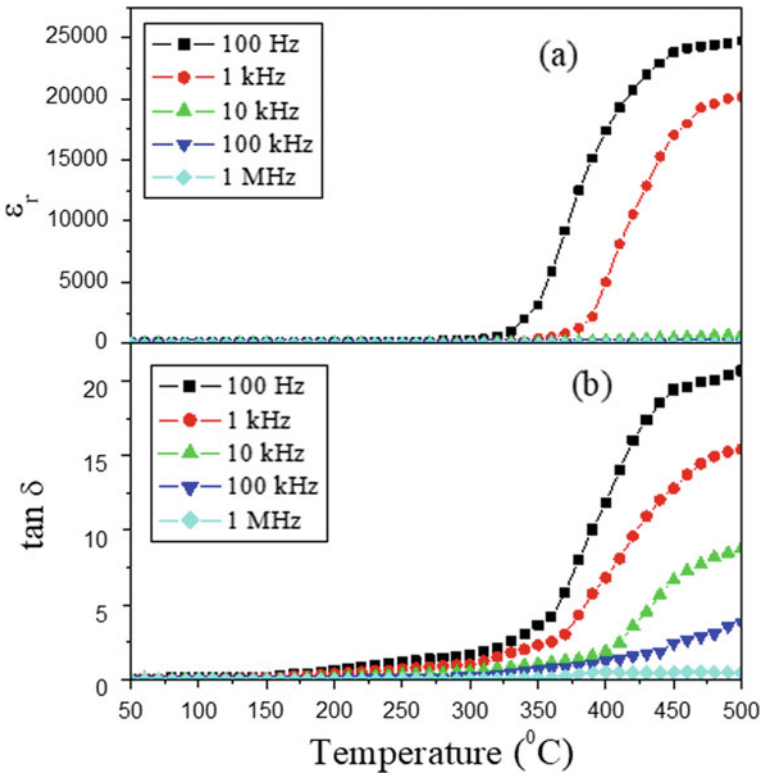


Fig. 6 Plot of **a** ε_r and **b** tanδ as a function of frequencies at varying temperatures for $x = 0.1$

temperature were mainly due to relaxation loss. But, with an increase in temperature, the conduction loss becomes dominant over relaxation loss. The tanδ decreased with an increase in PbO content due to the increase in density with increase in PbO content [11]. The values of tanδ at 500 °C and at low frequency (100 Hz) are 55.67, 20.67, 39.8, 15.67 and 5.65 for GC samples with $x = 0.0$, 0.1, 0.3, 0.5 and 0.7, respectively.

4 Conclusion

Different glass ceramic samples were fabricated in $59(PbO_xCaO_{1-x}) \cdot TiO_2$–$40(2SiO_2 \cdot B_2O_3)$–$1Fe_2O_3$ composition with varying x values of 0.0, 0.1, 0.3, 0.5 and 0.7 by melting and quenching method. The values of ε_r of all the samples increased with a rise in temperature at lower frequency values of 100 Hz and 1 kHz. Though, it almost continued constant with respect to temperatures at higher frequencies for the five GC samples. The ε_r remained constant up to 150 °C and increased with an increase in temperature from 150 to 500 °C. Moreover, the ε_r and tanδ decreased

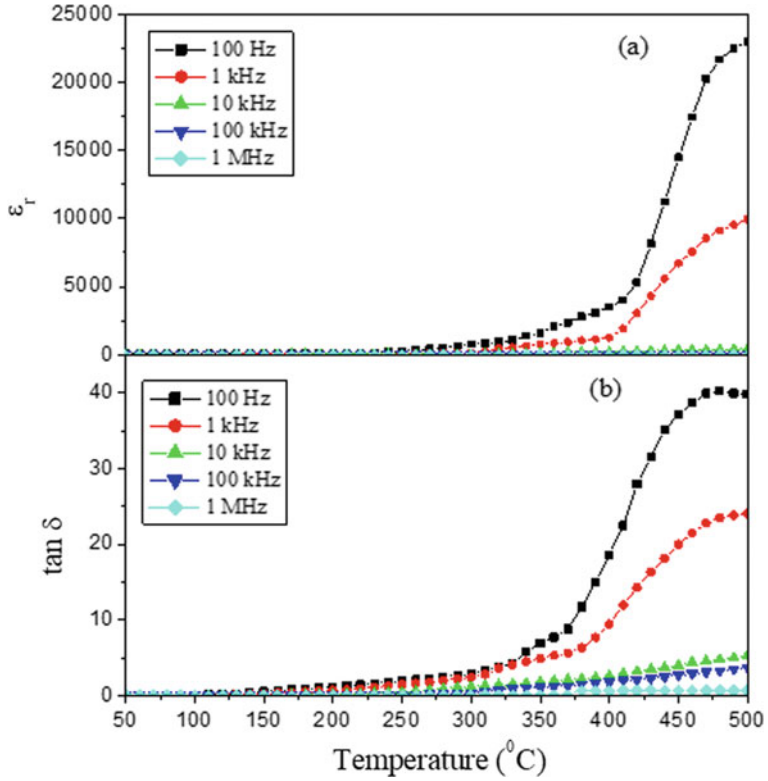


Fig. 7 Plot of **a** ε_r and **b** tanδ as a function of frequencies at varying temperatures for $x = 0.3$

with an increase in the amount of PbO between $x = 0.0$ and $x = 0.7$. The lead free sample, i.e., $x = 0.0$ (CT1F0.0800H) possess highest ε_r and tanδ of 29,877 and 55.67, respectively. The synthesized GC samples possess high dielectric constant that are suitable to be used as dielectric materials in capacitors. In future, these GCs can be further tested to evaluate its tribological properties in order to eliminate the failure of capacitors that are intended to operate in harsh environments.

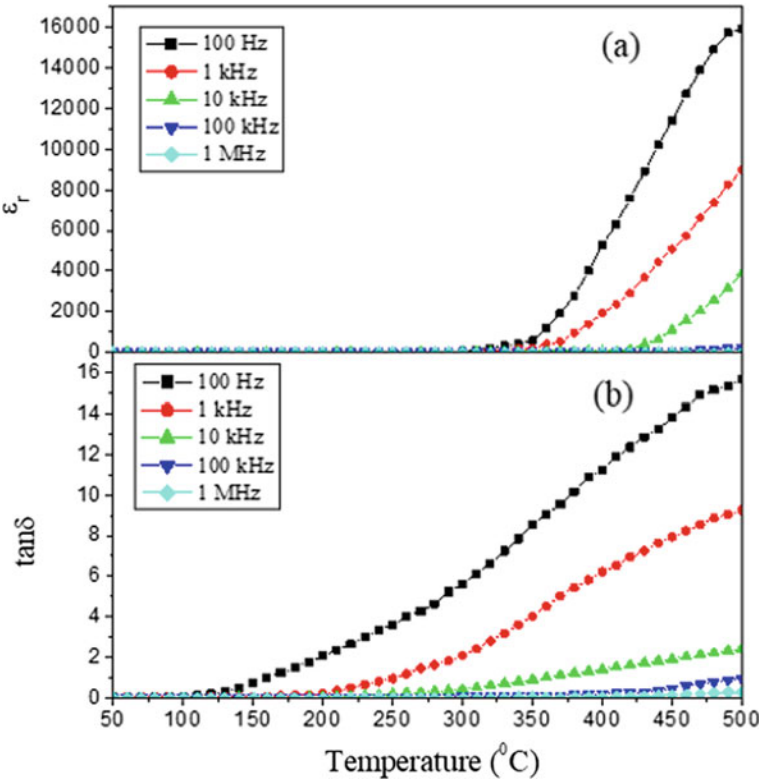


Fig. 8 Plot of **a** ε_r and **b** tanδ as a function of frequencies at varying temperatures for $x = 0.5$

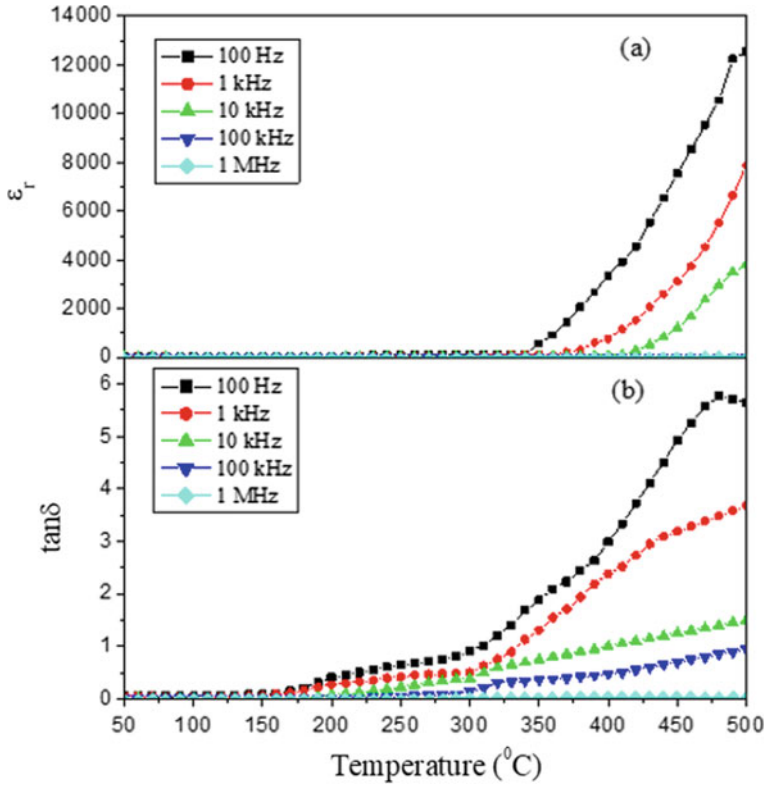


Fig. 9 Plot of **a** ε_r and **b** tanδ as a function of frequencies at varying temperatures for $x = 0.7$

References

1. Marković S, Jovalekić Ć, Veselinović L, Mentus S, Uskoković D (2010) Electrical properties of barium titanate stannate functionally graded materials. J Eur Ceramic Soc 30(6):1427–1435
2. Golezardi S, Marghussian VK, Beitollahi A, Mirkazemi SM (2010) Crystallization behaviour, microstructure and dielectric properties of lead titanate glass ceramics in the presence of Bi_2O_3 as a nucleating agent. J Eur Ceramic Soc 30(6):1453–1460
3. Rai R, Valente MA, Bdikin I, Kholkin AL, Sharma S (2014) Study of electrical and magnetic properties of Ba, La and Pb-doped $Bi_{1-x-y}Dy_xC_yFe_{1-y}Ti_yO_3$ perovskite ceramics. Solid State Commun 180:56–63
4. Gautam CR, Singh P, Thakur OP, Kumar D, Parkash O (2012) Synthesis, structure and impedance spectroscopic analysis of $[(Pb_xSr_{1-x})\cdot OTiO_2]$-$[(2SiO_2\cdot B_2O_3)]$-7[BaO]-3[$K_2O$] glass ceramic system doped with La_2O_3. J Mater Sci 47:6652–6664
5. Shankar J, Deshpande VK (2012) Study of PbO-SrO-TiO_2-B_2O_3 glass and glass ceramics. Phys B 407:2160–2163
6. Thakur OP, Kumar D, Prakash O, Pandey L (2003) Electrical characterization of strontium titanate borosilicate glass ceramics system with bismuth oxide addition using impedance spectroscopy. Mater Chem Phys 78:751–759

7. Abdel-Kalek EK, Mohamed EA, Salem SM, Kashif I (2018) Structural and dielectric properties of (100–x)B_2O_3-(x/2)Bi_2O_3–(x/2)Fe_2O_3 glasses and glass-ceramic containing $BiFeO_3$ phase. J Non-Cryst Solids 492:41–49
8. Sahu AK, Kumar D, Parkash O, Thakur OP, Prakash C (2006) Lead-strontium titanate glass ceramics: II-dielectric behavior. J Mater Sci 41:2087–2096
9. Lee YC, Lu WH, Wang SH, Lin CW (2009) Effect of SiO_2 addition on the dielectric properties and microstructure of $BaTiO_3$-based ceramics in reducing sintering. Int J Miner Metall Mater 16(1):124–127
10. Jakkula S, Deshpande V (2013) Effect of MgO addition on the properties of PbO–TiO_2–B_2O_3 glass and glass–ceramics. Ceram Int 39:S15–S18
11. Mohamed EA, Moustafa MG, Kashif I (2018) Microstructure, thermal, optical and dielectric properties of new glass nanocomposites of $SrTiO_3$ nanoparticles/clusters in tellurite glass matrix. J Non-Cryst Solids 482:223–229
12. Dutta A, Sinha TP (2006) Dielectric relaxation in perovskite $BaAl_{1/2}Nb_{1/2}O_3$. J Phys Chem Solids 67:1484–1491

Usage of Poly-Ether-Ether-Ketone Polymer for the Biomedical Application—A Critical Review



M. Ajay Kumar, M. S. Khan, and S. B. Mishra

Abstract Fast growing applications of 3D printing still lacked with a hurdle of printing high functional executing polymers. Poly-ether-ether-ketone (PEEK) produces excellent mechanical properties, chemical stability, biological stability and biocompatibility, especially employable for clinical applications. Previous literature is on fabrication of biomedical polymers by additive manufacturing (AM) such as poly-carpolactone, poly-lactic acid, poly-glycolic acid, poly-ethylene and polyurethanes. Only few studies are conducted on 3D printing of PEEK is due to its high melting point, non-availability of feed stock and poor properties of printed parts. This present review paper concentrates on printing of porous architecture which will be suitable for various medical applications with the use of the PEEK material.

Keywords Additive manufacturing (AM) · Fused deposition modeling (FDM) · Mechanical properties · Poly-ether-ether-ketone (PEEK) · Selective laser sintering (SLS)

1 Introduction

Poly-ether-ether-ketone (PEEK) is a semi-crystalline thermoplastic and belongs to the family of poly-aryl ether ketone (PAEK). PEEK is an exceptional industrial polymer and found applications in automotive, aircraft and space industries [1]. Remarkable outstanding properties of these materials such as biocompatibility and combined good strength, stiffness [2, 3] made them to be employable in medical field for surgical tools, dental equipments and bioimplants such as for the bone replacement. The material can undergo repeatable sterilization [4] due to its stable chemical structure, which is intend for the removal of bacteria or disinfection and an important requirement of surgical tools and dental equipments. One of the disadvantages

M. Ajay Kumar (✉) · M. S. Khan · S. B. Mishra
Kalinga Institute of Industrial Technology, Deemed To Be University, Bhubaneswar 751024, India
e-mail: ajay.madala4@gmail.com

M. Ajay Kumar
CMR Technical Campus, Kandlakoya, Medchal 501401, India

© Springer Nature Singapore Pte Ltd. 2020

A. Praveen Kumar et al. (eds.), *Advances in Lightweight Materials and Structures*,
Springer Proceedings in Materials 8, https://doi.org/10.1007/978-981-15-7827-4_37

of metal implants used for orthopedic application such as plates and screws for bone setting or joining is the stress protection or shield [5]. This due to its high stiffness [2, 3], a mechanical property resulted in diminished physiologic loading of the bone. PEEK has the nearer elastic module in comparison to bone; this resulted in decreased stress shield after implantation. Further advantage of PEEK in orthopedic implantation is its radiolucent property [6] that permits the image processing of human body with various techniques available such as X-ray, magnetic resonance imaging (MRI) and computer tomography (CT) [2, 7]. Biocompatible PEEK, PEEK-OPTIMA has been established by invi-bio [8] to reach with Food and Drug Administration (FDA) demanded qualities and has been employed in multiple clinical applications such as spinal cage fusion, total join replacement, and cranio-maxillofacial reconstruction [7, 9–11].

1.1 Manufacturing of Porous PEEK Parts

Orthopedic implants require pores for the transportation of cells and nutrients in to and out of the material of implant and vascular network for oxygen supply. Thus, the fabrication of porous structure for orthopedic applications constrained with the following requirements: (i) connection of pores forming network (ii) adequate pore diameter in the range of 100–600 μm and (iii) adequate structural coherence [12]. Thus, fabrication of orthopedic implants employing PEEK materials restricted in comparison to industrial applications. Existing industrial techniques are not employable directly with or without modification of process because of restrictions arise due to factors such as improper geometry and poison formation. However, small number of industrial process is suitable for modification to meet the medical applications. These are particulate leaching, heat and compression sintering, micromachining and additive manufacturing methods such as selective laser sintering (SLS) process, extrusion free forming or fused deposition modeling (FDM). Additive manufacturing (AM) is a layer-by-layer manufacturing method, fabricating specimens by fusing or depositing materials, such as metals, ceramics, plastics or even living cells [13]. AM is an attractive technique to print patient particular implants related to orthopedic surgery on the grounds of the cheaper cost, ability to print complex parts and the reduced fabrication time [14].

1.2 Particulate Leaching Method

Particulate leaching method involves the following steps (i) coatings of salt particles of desired porous size are coated on a mold made of required polymer solution, (ii) boiling of solution to remove solvent by evaporation and iii) removal of salt particle by leaching with water. Figure 1 depicts the common leaching process [15]. This method is easily adaptable and low cost of preparation in comparison to other process

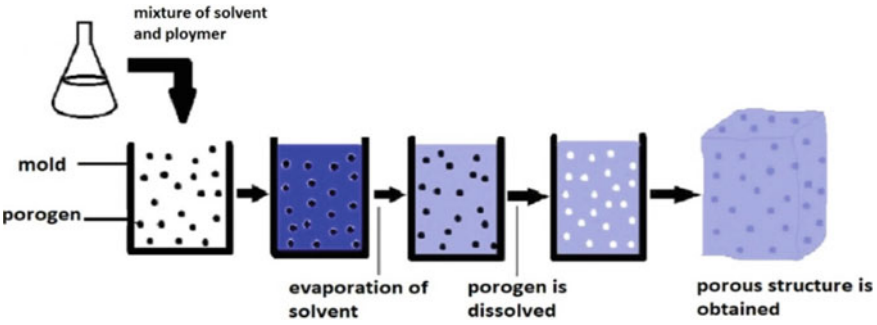


Fig. 1 Particulate leaching method for preparation of porous structure

mentioned. Disadvantages with this method are low control of porous structure, lack of consistency and often require manual intervention.

1.3 Integrated Compression Molding and Leaching Method

Compression molding and leaching process combined together to make PEEK porous structure and the schematic is shown in Fig. 2 [16]. During the compression process, salt particles are added as shown below. Fused salt beads leached out after the compression process using suitable solvent [16]. Siddiq et al. [16] adapted the above method to fabricate porous PEEK structures by employing PEEKOPTIMA ® powder and sodium chloride beads as leaching agent. They compared these structures with porous parts fabricated by dry mixing method. They observed almost uniform porous structures for both methods. They found that tapping method: integration of preexistent arrangement of salt beads in to fine PEEK powder, succeeded by compaction and sintering, resulted in porous architecture of uniform density and well-connected pores with consistent results and reduced processing time. The figure also shows the

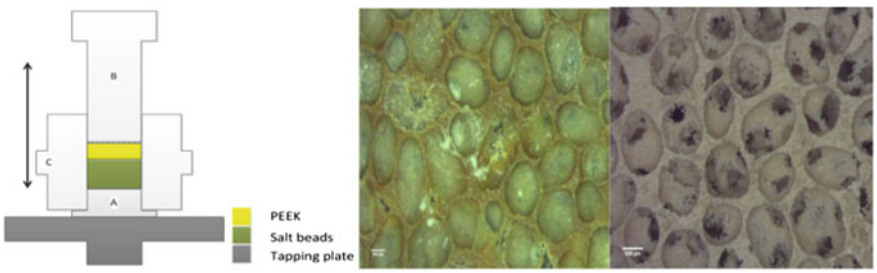


Fig. 2 Tapping instrument for integrated compression molding and leaching method. And optical micrographs of top surface of fabricated porous structures respectively

top surfaces images of fabricated parts by two methods obtained with optical micrograph method. They tested porous parts for mechanical strength and observed that tapping method resulted in compressive yield stress >1 MPa and stiffness >30 MPa for samples with 84% porosity.

2 Selective Laser Sintering (SLS)

SLS has been the favored AM process for manufacturing PEEK in the past decades [17, 18]. SLS, an additive manufacturing process, involves sintering of powder by laser beam projection in space based on 3D defined points. Powder is layered on part bed by the roller when the cartridges rise and subsequently sintered by laser. As the layer printed according to scanner system program and the part bed is lowered, the process is repeated to complete the fabrication of part. Figure 3 shows schematic process of SLS [19]. Tan et al. [20] fabricated scaffolds composed of different combinations of PEEK and hydroxyl apatite. They employed SLS to make the process free from solvent that is used to obtain porous structure. They printed scaffolds structure with an algorithm based on a scaffold library of cellular units. SLS system used for fabrication of PEEK scaffold employed by authors presented in Fig. 4. It consists of two powder cartridges, movable plat form, heater and laser. They prepared specimens for the testing by changing the weight percentage, 10–40 wt.% HA. They

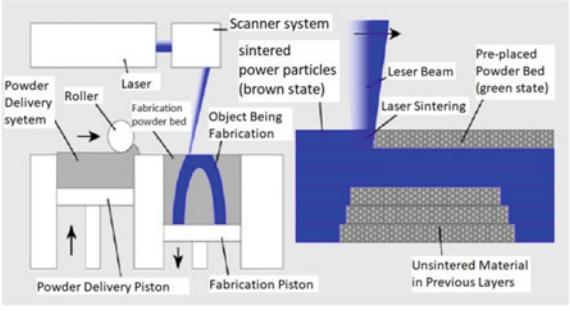


Fig. 3 SLS process of fabrication of structures



Fig. 4 SLS system for the fabrication of PEEK scaffold used by Tan et al. [20]. And developed **a** 3D printer for PEEK processing. **b** Printed specimens, respectively

carried material characterization of scaffolds. These tests are composed of porosity, microstructure and composition of the scaffolds, bioactivity and in vitro cell viability of the scaffolds. They concluded scaffolds could be fabricated by SLS with controlled microarchitecture and higher consistency. The figure also shows the developed 3D printer and directly printed PEEK specimens. Vaezi et al. [21] investigated feasibility of extrusion of PEEK material to produce porous architecture by employing powder and filament based FDM process. They found that critical parameters for printing are the design of hot extrusion head, extrusion temperature and ambient temperature. Proper settings of these parameters are required to print structures without manufacturing defects such as warpage, delamination and polymer degradation. They conducted mechanical tests such as compression and tensile to probe mechanical properties of printed PEEK structures. They found that mechanical properties are reduced due to the air gap between infill pattern and entrapped microbubbles inside it.

2.1 Extrusion Free Forming or Fused Deposition Modeling (FDM) Process

FDM process also belongs to AM technology and the filament or powder is extruded from the hot nozzle on build plate in layer by layer according to STL program built based on the CAD model of object. Schematic of equipment employed by Vaezi et al. [21] for producing PEEK porous parts is shown in Fig. 5. FDM become popular in recent days in comparison with SLS because of (i) economic cost, (ii) ease in usage

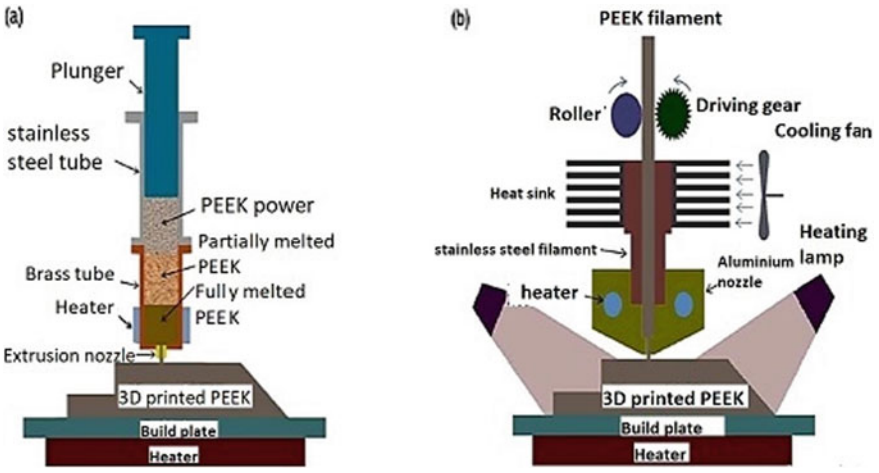


Fig. 5 Powder and filament-based extrusion equipment

(filament vs. powder), (iii) diminished hazard of material contamination or degradation and (iv) improving ability of FDM to print PEEK and its composites [22]. FDM is capable of pore architecture related to tissue engineering employing various materials such as ceramics, thermoplastics and cells with enormous control of micro/macro porous architecture [23]. In spite of the above advantages, it is relatively difficult in printing PEEK in comparison to poly-lactic acid (PLA) and acrylonitrile butadiene styrene (ABS) owing to its semi crystalline architecture and high melting temperature of PEEK. Valentan et al. [24] investigated modification of 3D printer to process PEEK for FDM. They developed new machine, which is capable of melting PEEK, and achieve required temperature for process. Their machine is able to fabricate the parts of up to 130 mm × 130 mm × 150 mm. They tested the fabricated parts for mechanical testing. Developed printer intended for prepare medical implants, specific maxillofacial prosthesis.

3 Application of PEEK in Medical Implantations

Figure 6a presents the various feasible implants such as dental, skull, osteo-synthesis plates and bone replacement material for nasal, maxillary or mandi-bular reconstructions. Cranio-maxillofacial imperfections are caused by tumors, traumas, infections

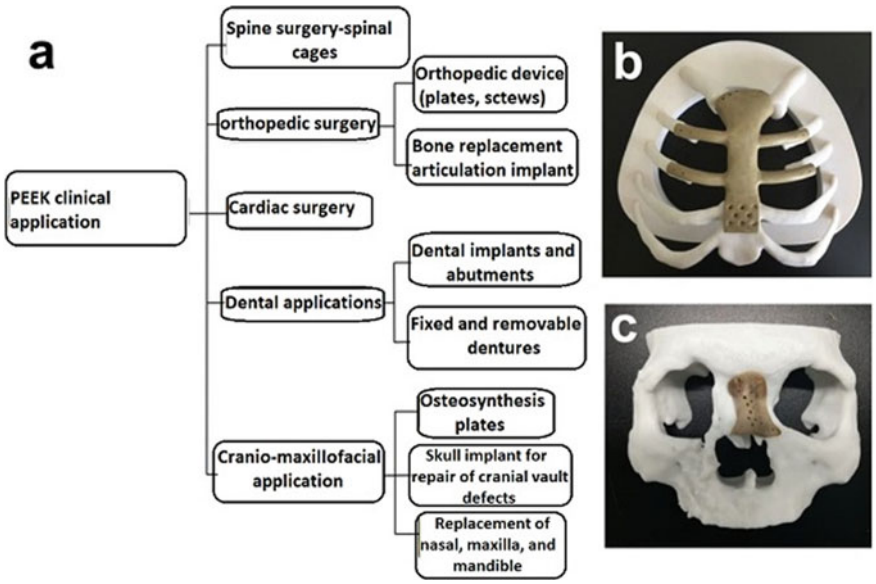


Fig. 6 **a** Clinical applications of PEEK; FDM-printed PEEK, **b** breastbone and **c** nasal reconstructions

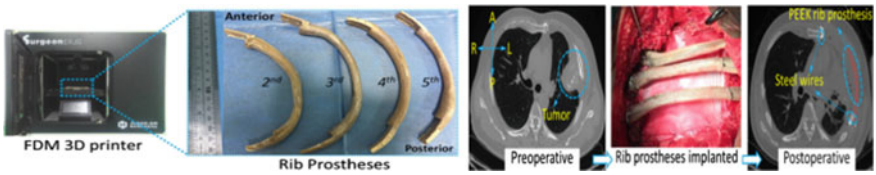


Fig. 7 FDM 3D printer and printed rib prostheses Images of pre- and post-operative PEEK rib prosthesis implantation due to tumor in chest, respectively

or congenital malformation. Reconstruction of these affected parts is tough task for oral and maxillofacial surgeons to reconstruct and presented in Fig. 6b, c.

4 FDM Printed Chest Rib Implant

Chest rib replacement is necessary in the cases of malicious tumors and inborn distortions in chest and removal of rib bones due to accident to keep usual respiration of patients. Rib prosthesis carried with different materials in the past printed the rib employing PEEK material by FDM process. They adapted a new method for designing rib for replacement that is based on centroidal trajectory of rib and adjusted the cross section according to strength requirement. They carried FEM analysis under similar mechanical loading of natural rib to ensure the mechanical strength of rib before printing. They found that new method offered design flexibility and good quality by FDM. Figure 7 presents the photograph of 3D printer and printed rib part by authors. They found the acceptable clinical functioning after the implantation and it also presents the images of pre and postoperative PEEK rib prosthesis implantation due to tumor in chest, respectively. Some designs suffer with the less optimal structures. These problems can be overcome with the help of lattice structures. AM capability of printing lattice structures offers an advantage for TO for the optimum design of object to be printed. This makes the researchers to investigate the employability of lattice structures for printing objects with applications in multifunction [23] and low weight design areas [24].

5 Conclusion

PEEK material is excellent candidate for medical application due to its mechanical strength that is nearer to bone mechanical properties. The printing of porous structure to meet scaffold architecture is not easy with traditional methods. FDM printed structures subjected thermal stress and inaccuracy in dimensions because of non-suitable printing conditions. Further, there is lack of standards in medical compatibility tests,

delayed its employability in medical field. Future research has to be carried to make availability of PEEK printed parts with reduced cost.

References

1. Skirbutis G, Dzingutė A, Masiliūnaitė V, Šulcaitė G, Žilinskas J (2017) A review of PEEK polymer's properties and its use in prosthodontics. Stomatologija 19(1):19–23
2. Kurtz SM, Devine JN (2007) PEEK biomaterials in trauma, orthopedic, and spinal implants. Biomaterials 28(32):4845–4869
3. Toth JM (2012) Biocompatibility of poly-arylether-ether-ketone polymers. In: PEEK biomaterials handbook. William Andrew Publishing, pp. 81–92
4. Godara A, Raabe D, Green S (2007) The influence of sterilization processes on the micromechanical properties of carbon fiber-reinforced PEEK composites for bone implant applications. Acta Bio-Mater 3(2):209–220
5. Sobieraj MC, Rimnac CM (2019) Fracture, fatigue, and notch behavior of PEEK In: PEEK biomaterials handbook. William Andrew Publishing, pp. 67–82
6. Kandarova H, Willoughby J, de Jong W, Bachelor M, Letasiova S, Breyfogle B, de la Fonteyne L, Coleman K (2015) Development, optimization and standardization of an in vitro skin irritation test for medical devices using the reconstructed human tissue model epiderm. Toxicologist 144(1):443
7. Kurtz SM (2012) Chemical and radiation stability of PEEK. In: PEEK biomaterials handbook. William Andrew Publishing, pp. 75–79
8. Toth JM, Wang M, Estes BT, Scifert JL, Seim HB III, Simon Turner A (2006) Poly-ether-ether-ketone as a biomaterial for spinal applications. Biomaterials 27(3):324–334
9. Lovald S, Kurtz SM (2012) Applications of poly-ether-ether-ketone in trauma, arthroscopy, and cranial defect repair. In: PEEK biomaterials handbook. William Andrew Publishing, pp. 243–260
10. Rao PJ, Pelletier MH, Walsh WR, Mobbs RJ (2014) Spine interbody implants: material selection and modification, functionalization and bioactivation of surfaces to improve osseointegration. Orthopaedic Surgery 6(2):81–89
11. Jarman-Smith M, Brady M, Kurtz SM, Cordaro NM, Walsh WR (2012) Porosity in poly-aryl-ether- ether-ketone. In: PEEK biomaterials handbook. William Andrew Publishing, pp. 181–199
12. Lee VC (2014) Medical applications for 3D printing: current and projected uses. Pharm Therap 39(10):704
13. Zhao F, Li D, Jin Z (2018) Preliminary investigation of poly-ether-ether-ketone based on fused deposition modeling for medical applications. Materials 11(2):288
14. Aishwarya V, Saranya D (2016) A review on scaffolds used in tissue engineering and various fabrication techniques. Int J Res Biosci 5:1–9
15. Siddiq AR, Kennedy AR (2015) Porous poly-ether ether ketone (PEEK) manufactured by a novel powder route using near-spherical salt bead porogens: characterisation and mechanical properties. Mater Sci Eng, C 47:180–188
16. Deng X, Zeng Z, Peng B, Yan S, Ke W (2018) Mechanical properties optimization of poly-ether-ether-ketone via fused deposition modeling. Materials 11(2):216
17. Zhao X, Xiong D, Liu Y (2018) Improving surface wettability and lubrication of poly-ether-ether-ketone (PEEK) by combining with polyvinyl alcohol (PVA) hydrogel. J Mechl Behav Biomed Mater 82:27–34
18. Singh S, Prakash C, Ramakrishna S (2019) 3D printing of poly-ether-ether-ketone for biomedical applications. Eur Polym J
19. Tan KH, Chua CK, Leong KF, Naing MW, Cheah CM (2005) Fabrication and characterization of three-dimensional poly (ether-ether-ketone)/-hydroxyapatite biocomposite scaffolds using laser sintering. Proc Inst Mech Eng Part H J Eng Med 219(3):183–194

20. Vaezi M, Yang S (2015) Extrusion-based additive manufacturing of PEEK for biomedical applications. Virtual Phys Prototyping 10(3):123–135
21. Punchak M, Chung LK, Lagman C, Bui TT, Lazareff J, Rezzadeh K, Jarrahy R, Yang I (2017) Outcomes following poly-etherether-ketone (PEEK) cranioplasty: systematic review and meta-analysis. J Clin Neurosci 41:30–35
22. Vaezi M, Yang S (2014) Freeform fabrication of nano-biomaterials using 3D printing. In: Rapid prototyping of biomaterials. Wood-head Publishing, pp 16–74
23. Valentan B, Kadivnik Ž, Brajlih T, Anderson A, Drstvenšek I (2013) Processing poly (ether etherketone) a 3D printer for thermoplastic modelling. Materiali in tehnologije 47(6):715–721
24. Najeeb S, Zafar MS, Khurshid Z, Siddiqui F (2016) Applications of poly-ether-ether-ketone (PEEK) in oral implantology and prosthodontics. J Prosthodontic Res 60(1):12–19

Effect of Silicon Carbide on Properties of Styrene-Butadiene Rubber



T. P. Anirudh Mohan, R. Harikrishnan, N. Rahulan, and Sundararaman Gopalan

Abstract In this research chapter, the effect of silicon carbide (SiC) on physical properties of styrene-butadiene rubber was studied. Styrene-butadiene rubber (SBR) is an important type of synthetic rubber used in tyre industries. Tensile strength, hardness, cure time, tear strength and rebound resilience were determined and compared for different compositions of silicon carbide on the rubber. The compositions of SiC were 2, 4, 6, 8 and 10% by weight. Samples were prepared and tested successfully according to ASTM standards. Required properties were determined from the test observations. The tensile strength, tear strength and rebound resilience of the rubber composite were found to be improved for all compositions. Hardness value showed slight increase with certain compositions of SiC.

Keywords Silicon carbide · SBR · Hardness · Tensile and tear strength · Rebound resilience

1 Introduction

Styrene-butadiene rubber (SBR) is an important type of synthetic rubber used in tyre industries. It is composed of butadiene and styrene copolymers. They are polymerized using emulsion or solution process. SBR is widely used in blends with other type rubbers. SBR has improved wear resistance and increased hardness with low specific gravity. SBR offers high abrasion resistance, good resilience and high tensile strength; hence, it finds more applications than natural rubber [1, 2].

T. P. Anirudh Mohan (✉) · R. Harikrishnan · N. Rahulan
Department of Mechanical Engineering, Amrita Vishwa Vidyapeetham, Amritapuri, India
e-mail: imtpmrk7@gmail.com

S. Gopalan
Department of Electronics and Communication Engineering, Amrita Vishwa Vidyapeetham, Amritapuri, India

© Springer Nature Singapore Pte Ltd. 2020

A. Praveen Kumar et al. (eds.), *Advances in Lightweight Materials and Structures*,
Springer Proceedings in Materials 8, https://doi.org/10.1007/978-981-15-7827-4_38

The mechanical properties of elastomeric networks are improved considerably by using fillers like silicon carbide (SiC). These properties depend on various parameters such as volume fraction, shape and size of particles, filler–matrix interactions. The incorporation of filler leads to increase of stiffness of material, alter the time-dependent behaviours like hysteresis and stress relaxation [3].

Composites of rubber with powdered materials are widely used due to their high performance and wide range of applications. Some of its applications include seals, tyre treads, hoses, gloves and soles [4].

Silicon carbides are produced by reactions between silica or silicon and carbon at 1400–1800 °C. This process involves gas–solid reactions and produces coarse particles that must be ground to required sizes [5, 6]. It is an important non-oxide ceramic with high melting point (2827 °C), high hardness, high wear resistance, low thermal expansion coefficient and good thermal and chemical resistance but is brittle in nature [7–10]. These properties make silicon carbide an attractive candidate material for many applications such as high-temperature structural materials and reinforcement in composites [8, 11–19].

The main properties under focus in our study are tensile strength, hardness, curing time, resilience and tear strength. Tensile strength is the maximum strength of the material when tension is applied, usually when the material fails completely. Hardness is a measure of a material's resistance to localized plastic deformation and is measured using durometer. Tear strength is the energy required to tear apart a cut specimen that has a standard geometry. The magnitude of tensile and tear strengths is related [1, 18]. The compound is subjected to vulcanization. Vulcanization changes the weak rubber compounds to a strong viscoelastic solid. The length of time taken for rubber to reach optimum modulus at a certain temperature is the curing time [20].

In this work, we conducted the mechanical characterization through tensile test, abrasion test, tear test, hardness test, curing time test and rebound resilience test on the rubber composite filled with 0, 2, 4, 6, 8 and 10% filler (SiC). The results have been presented and the relation between properties and filler percentage are plotted.

2 Materials and Methods

2.1 Materials for Research

A 1502 type of SBR was supplied by JJ Murphy Research Centre Pvt Ltd (Irapuram, Kerala). The SiC was manufactured and supplied by the PARSHWAMANI METALS Pvt Ltd (Mumbai) (Tables 1, 2 and Figs. 1, 2).

Table 1 Chemical analysis report of SiC

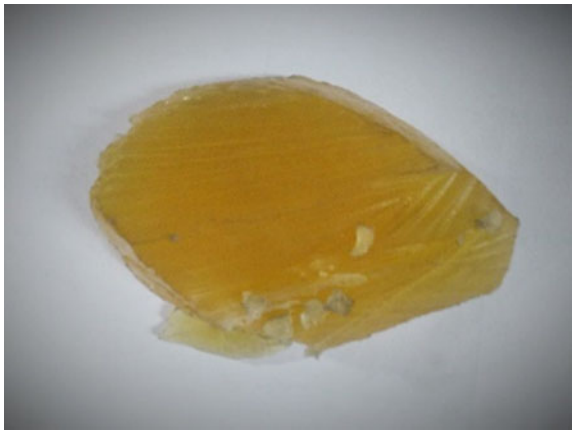
Formula	SiC
Density	3.21 g/cm^3
Molar mass	40.11 g/mol
Melting point	2730 °C
Purity	99.92%
Form	Powder
Particle size	325 mesh

Table 2 Elements used with SBR blend

Materials	Content (phr)
SBR	100
Zinc oxide (ZnO)	4
Stearic acid	2
Mercaptobenzothiazole (MBT)	1
Tetramethylthiuram disulfide (TMTD)	0.2
Silicon carbide (SiC)	0, 2, 4, 6, 8, 10
Sulphur	2.5

phr stands for parts per hundred (weight, in g) parts of rubber

Fig. 1 SBR



2.2 Sample Preparation

In this study, SiC of compositions of 2, 4, 6, 8 and 10% was added to SBR. The rubber sample was prepared in three steps. These are known as mastication, compounding and moulding. In the first process, the rubber was masticated on a two-roll mill (Kelachandra Machines Pvt Ltd) for 5 min. In next process, vulcanization chemicals were prepared and compounding was done for 25 min on a two-roll mill. Sulphur was

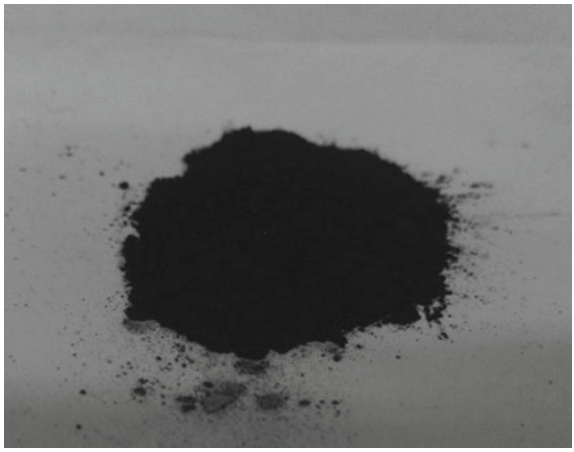


Fig. 2 SiC

added to the compound after 20 min. The compounds were kept at 25 °C and 50% relative humidity. The resultant rubber compounds were then compressed moulded using a hydraulic press (Minimetal Pvt Ltd) at 165 °C, and 100 bar was used to compress and mould the resultant rubber compounds.

3 Characterization

An oscillating die rheometer (ODR) by α technologies was used for measuring both torque and curing time. Test was carried out at 160 °C. According to ASTM D412 specifications, tensile properties of the rubber composites were tested. A hardness durometer (Shore A, Bariess Pvt Ltd Testing machine) was used to test specimen hardness. ASTM 02240 specifications were used. Five sets of measurements were taken, and the average value was noted. ISO 4662:1986 test method was used to conduct rebound resilience testing. It is defined as the ratio of the indenter energy after impact to its energy before impact. It is expressed as percentage. Test carried out on Wallace Dunlop Tripsometer.

4 Results and Discussion

4.1 Rheometric Characteristics

Table 3 shows the rheometric properties of the composites. The properties include optimum curing time, scorch time, minimum torque (ML), maximum torque (MH) and shore hardness with different compositions of SiC. The presence of the filler

Table 3 Curing and mechanical properties of SBR compounds with and without filler

Cure characteristics @ 160 °C and mechanical properties	The properties of SiC dispersion of					
	0%	2%	4%	6%	8%	10%
MH (dn-m)	49.87	50.99	49.88	47.94	53.51	50.52
ML (dn-m)	3.72	3.31	3.14	3.17	3.54	3.43
tan D @Min (s')	0.850	0.834	0.810	0.841	0.834	0.846
tan D @Max (s')	0.091	0.087	0.100	0.129	0.059	0.111
tan D @ 50% cure s'	0.081	0.080	0.080	0.093	0.079	0.090
tan D @ 90% cure s'	0.050	0.054	0.066	0.080	0.049	0.076
G' @ 90% cure s' (kpa)	587.96	600.13	583.42	566.13	622.65	595.97
Time @ 7.5 dn-m scorch s' (min)	1.60	1.56	1.69	1.62	1.87	188
Time @ 90% cure s' (min)	4.68	4.37	4.37	4.63	5.68	4.88
Hardness shore A	46.2	46	46	44.8	47	46.4

increases the maximum torque. Increase in torque reduces the intermolecular motion. The minimum torque (ML) is the measure of the stiffness of the vulcanized test specimen.

Figure 3 depicts a comparison of the hardness of SBR blends with filler material. It is clear from this figure that the property increments with blends in various percentages of SiC filler. Maximum shore A hardness is (47) produced at 8% filler and minimum value is (44.8) at 6% filler.

Figure 4 shows SiC filler (%) versus curing time characteristics. Maximum time at 90% cure s' is (5.68 min) at 8% filler, and minimum time is (4.37 min) at 2 and 4% filler.

The viscosity of the masticated rubber can be taken as the minimum torque in the rheograph. The viscosity will register a sharp decrease whenever there is an excessive mastication. Maximum torque is considered as the maximum viscosity of

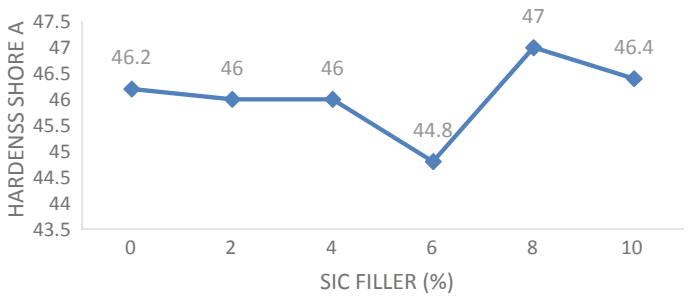


Fig. 3 Shore hardness versus SiC composition

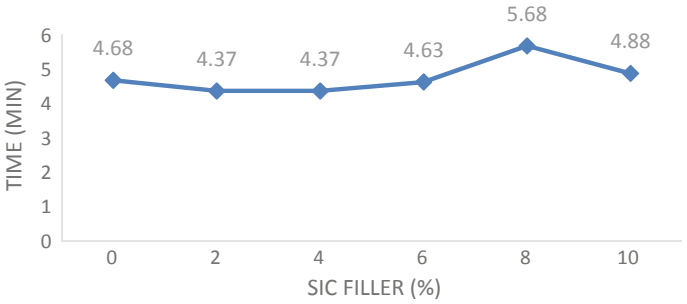


Fig. 4 Time at 90% cure versus SiC compositions

the compound. It is also a measure of the cross-link density of the sample. The cure characteristics are given in Table 3.

5 Tensile Properties

Tensile test specimens were prepared according to ASTM D412 specifications. Thickness, width and gauge length of test specimen were 2.02 mm, 6 mm and 7 mm, respectively.

Figure 5 shows the tensile stress of all specimens. Five specimens were tested from all compositions, and average values were taken. The tensile strength values

Table 4 Tensile test results

S. No.	Sample name	Max. tensile stress (kgf/cm^2)	%Elongation @BRC (%)	Modulus at 200% (kgf/cm^2)	Modulus at 100% (kgf/cm^2)	Max. load (N)	Modulus automatic (kgf/cm^2)
1	SBR neat	19.293	215.42	14.038	12.093	22.026	18.482
2	SBR + 2%SiC	20.063	202.022	19.932	12.963	23.048	20.320
3	SBR + 4%SiC	20.769	207.267	20.45	12.852	24.091	19.492
4	SBR + 6%SiC	22.061	222.363	20.492	13.219	25.357	19.918
5	SBR + 8%SiC	19.783	191.859	21.135	13.146	22.895	20.646
6	SBR + 10% SiC	21.447	227.126	19.603	12.966	24.519	19.773

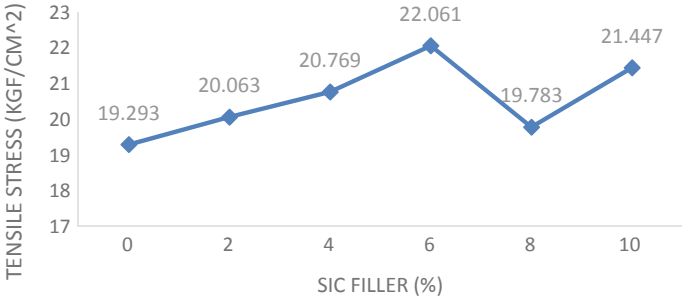


Fig. 5 Tensile strength versus SiC composition

show an increase up to 6% of filler addition. This can be due to the agglomeration of filler in the rubber blend. Maximum tensile stress is at 6% filler and is (22 kgf/cm^2).

6 Tear Properties

Figure 6 shows the effects of variation of weight fraction of SiC on the tear strength. Maximum tear strength is (132.6556 kgf/cm^2) at 4% filler, and minimum tear strength is (106.454 kgf/cm^2) at 0% filler (Table 5).

Table 5 Tear test results

S. No.	Sample name	Maximum tensile stress (kgf/cm^2)	% Elongation @ BRC (%)	Maximum load (N)	Modulus (Automatic) (kgf/cm^2)	Tensile stress @ Break (standard) (MPa)
1	SBR neat	106.454	72.2219	20.25	194.595	0.48889
2	SBR + 2% SiC	107.9956	73.4595	20.777	199.211	0.47653
3	SBR + 4% SiC	132.6556	98.2369	25.684	186.2547	0.39079
4	SBR + 6% SiC	111.7676	73.5407	21.256	201.842	0.34583
5	SBR + 8% SiC	107.313	64.3186	20.09	214.4436	0.58717
6	SBR + 10% SiC	121.457	92.8749	22.199	216.0402	0.5132

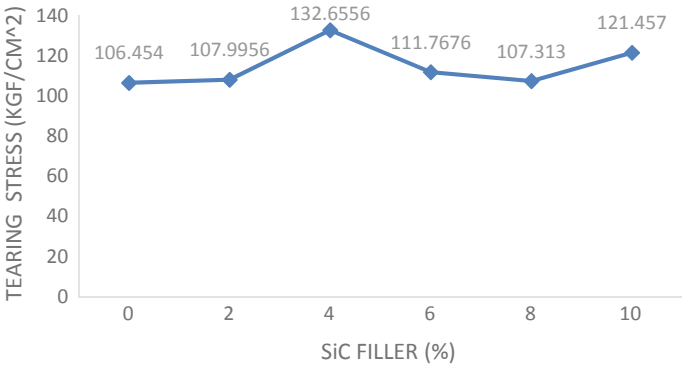


Fig. 6 Tear strength versus SiC composition

7 Rebound Resilience

Figure 7 shows the effects of variation of weight fraction of SiC on rebound resilience. Maximum rebound resilience is 70.92% at 4% filler, and minimum rebound resilience is 50.94% at 0% filler (Table 6).

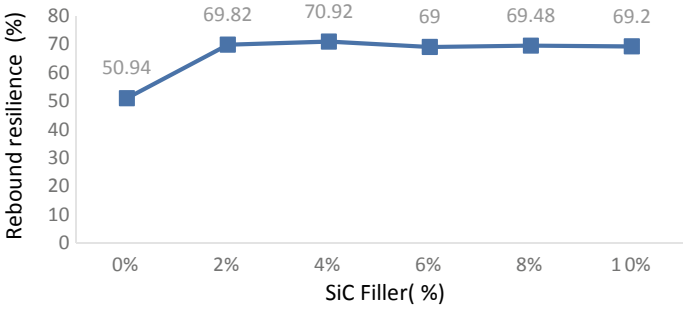


Fig. 7 Rebound resilience versus SiC composition

Table 6 Rebound resilience test results

S. No.	Sample name	Rebound resilience (%)	Average angle (°)
1	SBR neat	50.94	31.70
2	SBR + 2% SiC	69.82	37.33
3	SBR + 4% SiC	70.92	37.60
4	SBR + 6% SiC	69.00	37.07
5	SBR + 8% SiC	69.48	37.20
6	SBR + 10% SiC	69.20	37.13

8 Conclusion

- The tensile strength, tear strength and rebound resilience obtained for the rubber have improved in the composite form for all compositions of filler addition. Hardness value and curing time showed slight increase with few compositions of silicon carbide.
- SBR + 6% SiC shows.
- 15% increase in tensile strength.
- SBR + 4% SiC shows.
- 25% increase in tear strength.
- 36% increase in elongation.
- 19.98% increase in rebound resilience.
- From our observations.
- SBR + 4% SiC is recommended for better tear resistance and rebound resilience.
- SBR + 6% SiC is recommended for better tensile strength.
- Future applications for this improved rubber compound include making tyres that last longer and provide better mileage.

References

1. Arayapranee W (2011) Rubber abrasion resistance, Intechopen Publishing
2. Ashok N, Webert D, Suneesh PV, Balachandran M (2018) Mechanical and sorption behaviour of organo-modified montmorillonite nanocomposites based on EPDM—NBR blends. Mater Today Proc 5(8):16132–16140
3. Bergstrom JS, Boyce MC (1999) Mechanical behaviour of particle filled elastomers. Rubber Chem Technol 72:633–656
4. Tangudom P, Thongsang S, Sombatsompop N (2014) Cure and mechanical properties and abrasive wear behaviour of natural rubber, styrene–butadiene rubber and their blends reinforced with silica hybrid fillers. Mater Design 53:856–864
5. Konno H, Kinomura T, Habazaki H, Aramata M (2004) Synthesis of submicrometer-sized β-SiC particles from the precursors composed of exfoliated graphite and silicone. Carbon 42(4):737–744
6. Ren R, Yang Z, Shaw LL (2002) Synthesis of nanostructured silicon carbide through an integrated mechanical and thermal activation process. J Am Ceramic Soc 85:819–827
7. Sajith M, Jose B, Sambhudevan S, Sreekala CO, Shankar B (2019) Effect of matrix type and doping on polyaniline based natural rubber nanocomposites. AIP Conf Proc 2162(1)
8. Shi L, Zhao H, Yan Y, Li Z, Tang Ch (2006) Synthesis and characterization of submicron silicon carbide powders with silicon and phenolic resin. Powder Technol 169:71–76
9. Raman V, Bahl OP, Dhawan U (1995) Synthesis of silicon carbide through the sol-gel process from different precursors. J Mater Sci 30:2686–2693
10. Golestani-Fard NF, Rezaie HR, Ehsani N (2011) Synthesis and characterization of silicon carbide nano powder by sol gel processing. Iran J Mater Sci Eng 8(2), Springer publications
11. Lin Y-J, Chuang C-M (2007) The effects of transition metals on carbothermal synthesis of SiC powder. Ceram Int 32(8):899–904
12. Danforth SC, Symons W, Nilsen KJ, Riman RE, Binner JGP (1990) Advanced ceramic processing and technology. Noyes Publishing, New Jersey, pp 39–71
13. Chun Y, Kim Y (2005) Processing and mechanical properties of porous silica-bonded silicon carbide ceramics. Met Mater Int 11:351–355

14. Lee SH, Lee Y, Kim YW, Rong-Jun X, Mamoru M, Zhan GD (2005) Mechanical properties of hot-forged silicon carbide ceramics. Scripta Materialia 52(2):153–156
15. Negita K (1986) Effective sintering aids for silicon carbide ceramics: reactivities of silicon carbide with various additives. J Am Ceramic Soc 69(12):308-C-310
16. Braue W, Kleebe H-J, Wehling C (1993) Microstructure and densification of sintered (B C)-doped β-silicon carbide. In: MRS proceedings, vol 327. Cambridge University Press, p 269
17. She JH, Ueno K (1999) Densification behavior and mechanical properties of pressureless-sintered silicon carbide ceramics with alumina and yttria additions. Mater Chem Phys 59(2):139–142
18. Callister WD Jr, Rethwisch DG Materials science and engineering an introduction, Wiley Inc, New Jersey
19. Zhu S, Fahrenholtz WG, Hilmas GE (2007) Influence of silicon carbide particle size on the microstructure and mechanical properties of zirconium diboride–silicon carbide ceramics. J Eur Ceramic Soc 27(4)
20. Karaağaç B, İnal M, Deniz V (2012) Predicting optimum cure time of rubber compounds by means of ANFIS. Mater Des 35:833–838

Experimental Investigation of a Single Molecule Detection in Thermoplastics

V. V. Prathibha Bharathi

Abstract Nowadays, the research work has been more focused in developing the techniques on novel nanochannel fabrication. The techniques developed are either time consuming or expensive. One of the techniques in developing this type is by generating the sub-micrometer wide channels in thermoplastic chips. We can apply this technique in single molecule detection. For this, a mechanical rig was designed and subjected to strain to produce thermomechanical deformation in thermoplastic micro-channel cell. To optimize the initial and micro-channel dimensions, a rectangular micro-type of channels with different sizes and shapes was deformed. To reach sub-micrometer widths, the height and width of the channels designed should be with low aspect ratios with less initial dimensions. The manufacturing and assembly tolerances are affecting the nano-channels fabrication.

Keywords Micro-channels · Micrometer · Single molecule detection · Thermoplastic · Optimize

Abbreviations

SMD	Single Molecule Detection
PDMS	Polydimethylsiloxane
PSA	Plain Strain Analysis

1 Introduction

The detection of the individual molecules in a fluid is the most important means in the nano-fluids. One of the methods to investigate the individual molecule particularly

V. . V. Prathibha Bharathi (✉)
Anurag Group of Institutions, Hyderabad, Telangana, India
e-mail: prathibhaseenu@gmail.com

© Springer Nature Singapore Pte Ltd. 2020

A. Praveen Kumar et al. (eds.), *Advances in Lightweight Materials and Structures*,
Springer Proceedings in Materials 8, https://doi.org/10.1007/978-981-15-7827-4_39

is the single molecule detection (SMD) method. It detects the molecules collection individually from the set of molecules. For the purpose of the case study, the single molecule detection is well developed to make a group of separate things like electrophoresis, chromatography, mass spectrometry. For better studying the parameters for all the molecules, SMD ensembles in providing an arithmetic mean value. Qualitative and quantitative chemical analysis is highly taken up by SMD. It is advantageous in detecting the molecules with low concentration from the high concentration of normal molecules. The methods of grouping up of separate things are sensitive method [1] and are limited up to some extent only. To detect the molecules efficiently, it requires higher concentration for normal molecules. This method of detecting the molecules in cancer will be very difficult when the concentration of the tumor cell markers is very low. The method of conceptual design and method of fabrication for the nano-channel development in further explained in Sects. 2.1, 2.2 and 2.3. Their results are also discussed.

2 Nano Channel Fabrication Concept and Implementation

2.1 Conceptual Design

To calculate the reduction in micro-channel dimensions, based on the action of applied lateral and compressive strain, a finite element analytical mode is preferred. To perform PDMS mini channel for assessing the possibility in constructing the nano-channel and for corroboration of the concept, an investigational setup is used.

2.2 Fabrication Concept

The modus operandi of nano-channel fabrication presented and is a non-lithographic approach to fabricate local nano-channel constructions along micro-channels [2, 3] in thermoplastic micro-fluidic chips. This type of practical aspect, applying to each point in a micro-channel on a segment of the thermomechanical deformation, for forming a nano-scaled, aligned edifice. The polymers are thermoplastics [4] that can be shaped and can be reformed again and again in string of heating process.

This type of attribute became very attractive to the scientists and researchers who are working in the field of polymer micro and nano-fluids. The micro-channel networks can be made as a replica into thermoplastics [5] form single silicon template and reduce the manufacturer time and the cost.

The glass transition temperature is where the temperature of the thermoplastics becomes mechanically flexible. In elastic modulus, a sudden drop of temperature is observed by means of increase in temperatures causes the decrease of elasticity

modulus and makes them to bend perfunctorily [6]. This is the process of the nano-channel fabrication.

2.3 Model Approach

For better understanding the decrease in widths of the channel, an approach is made on changing the shape of micro-channel in PDMS. The decrease of the widths of the channels is made at the centre and bottom or top at a lower level in the practical use of the compressive strain. From 1 to 5 μm, the micro-channels height can be varied for making the width constant (8μm). To trim down the width of the final minimum channels from 0.625 to 0.3μm,, the augment of compressive strain should be made. This sort of performance is applied for the cases where the distinction of the height takes place from 0.5to 8μm by maintain the width 8μm as constant. For the width of 10μm, the change of shape of the micro-channel can be studied.

2.4 Model Result

In micrometers, the micro-channel is premeditated by using the dimensions as shown in Fig. 2. 'a' is the width of the channel centre, 'b' is the channel width at the top and bottom, 'c' is the centre height of the channel and 'd' is the height at the side walls. In Fig. 3, the ratio of the width at the top, bottom and in centre has to be abridged by increasing the height and width of the ratio, for the final stage of deformations [7] width of 0.625 μm at the centre of the channel.

The widths at the top and bottom will be above a micrometer if the centre of the channel reduces to the dimensions of the sub-micrometer for attaining the high range of channels, i.e., the height and width should be greater than 1. For attaining the micro-channels taller, after deformation, there should be an increase in the height at the centre of the channel where as for the same final deformation; for the micro-channels in shorter range, the width at the centre of the channel is 0.625 μm.

From Fig. 4, it was indicated that the rectangular cross section of micro-channel goes to deformation with some part of the area of the cross section in the region of sub-micrometer, when it is subjected to the motion of lateral compressive strain. On this analysis, the micro-channel deformation will be less that the height of the micrometer, where this process can be done by replacing small cross-sectional area of that curvature.

Based on the conditions of the combination of the fixed boundary, the width of the micrometers at the channel centre can be decreased to 1 from 5 μm, and the height of the micrometers at centre of the channel can be decreased to 0.32 from 5 μm. Similarly, during the deformation of the thermoperfunctory with the fixed boundary conditions, the nano-channel with one dimensional can be achieved by decreasing

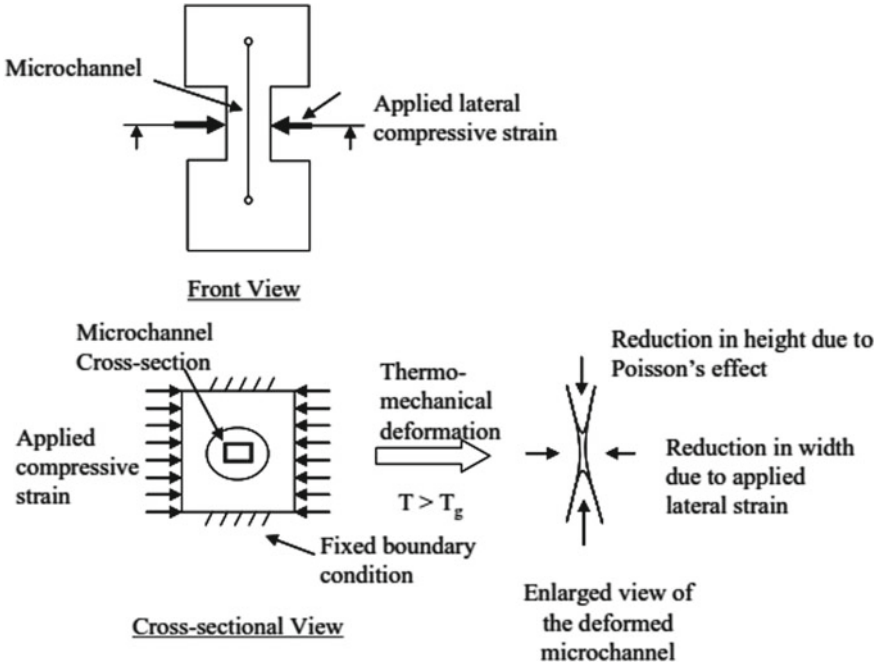


Fig. 1 Conceptual design layout of thermomechanical nano-channel

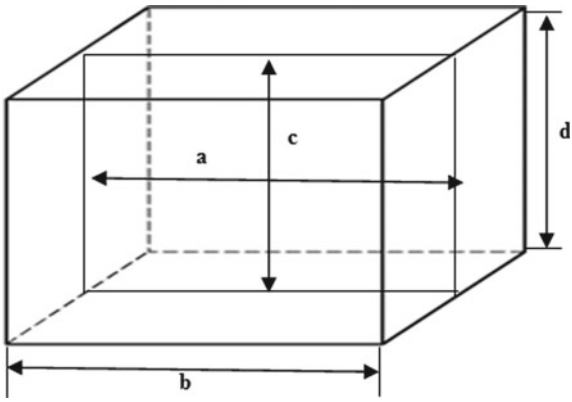


Fig. 2 Dimensioning of micro-channel cross section

[8] the width at the centre of the channel to 0.5 μm and by diminishing the height at the centre of the channel to 1.76 from 5 μm.

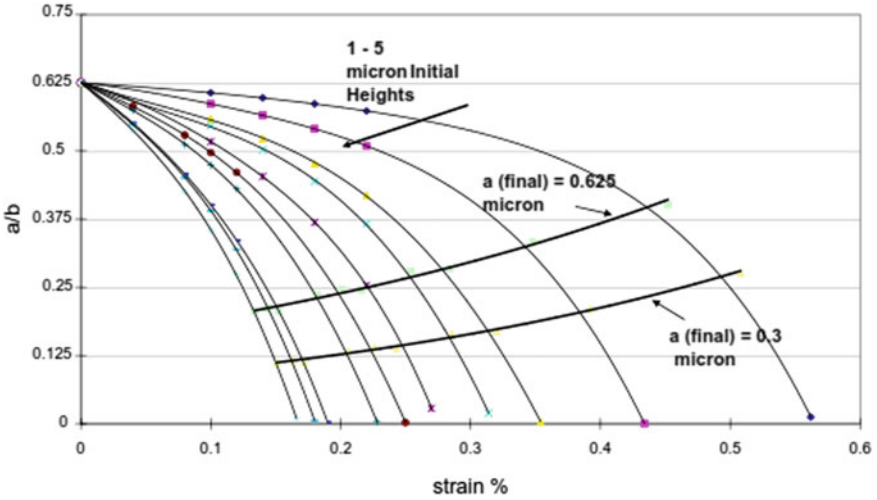


Fig. 3 Variation in the widths of micro-channel with applied strain

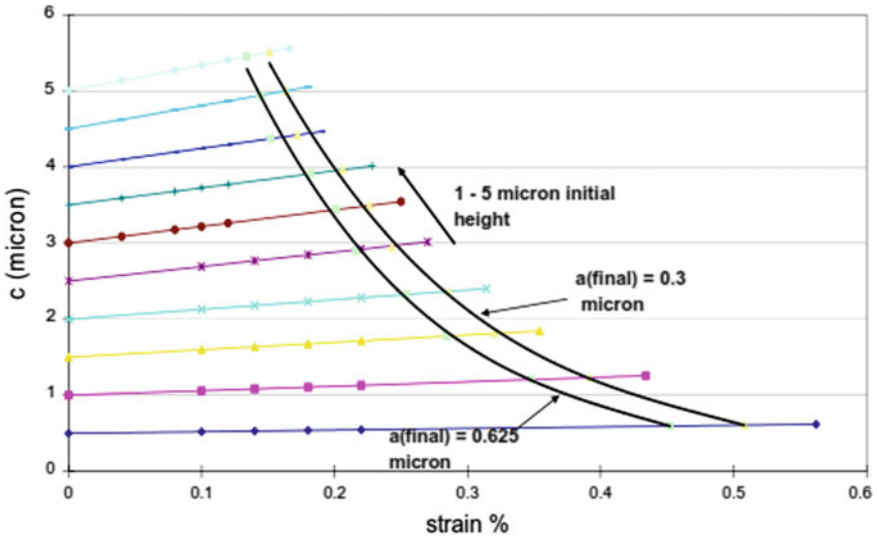


Fig. 4 Variation in the height of micro-channel with applied strain

3 Investigational Verification

The main aim of this experimental verification is to verify the channel deformation height and width where the strain was applied. In PDMS on a micro-channel type with 8 μm * 5 μm, compressive, lateral strain can be applied. For the formation of

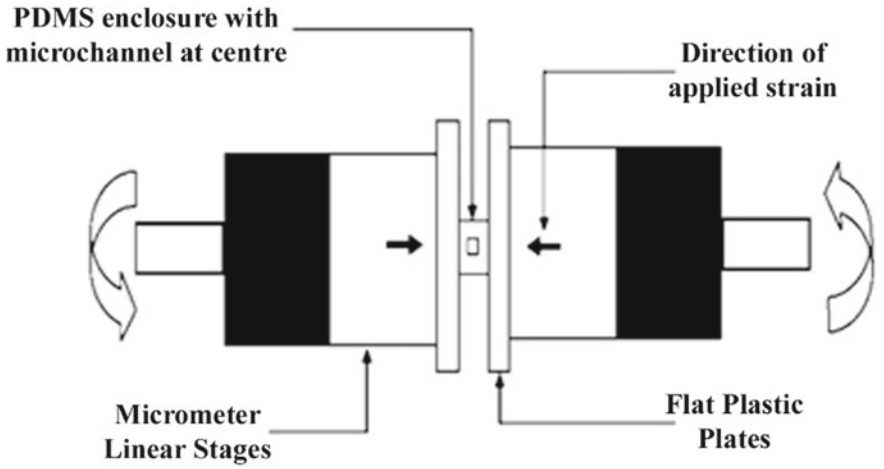


Fig. 5 Experimental setup of micro-channel deformation

smooth lithography, a sample silicon having a thin disk with neutral photoeffects was to be applied.

For the formation of thick layer of 0.5 mm, the PDMS should be poured on the object. To get the layer thickness of 0.5 mm accurately, PDMS volume can be made modify. Then the thick layer of the PDMS can be removed from the pattern with channel imprints and was covered with 0.5 mm layer thickness of PDMS for the formation of confined micro-channel [9]. By using a blade of 180 μm thick, the confined micro-channel of the PDMS was cut. By using an optical micro-scope, we can observe the deformation in the cross-sectional area.

4 Result and Discussion

Based on the application of strain, the change in the height and width in the micro-channel is observed. Along with the several experimental and manual limitations the differences between the experimental and model data can be attributed to the model assumptions shown in Figs. 6 and 7.

For the developed finite element model, the PSA was assumed. The strain which is in the direction normal to the deformation plane is negligible. This is the assumption underline for a plain strain analysis (PSA). Hence when compared to the strain acting in the deformation plane, the strain which is acting in the direction of the action is negligible.

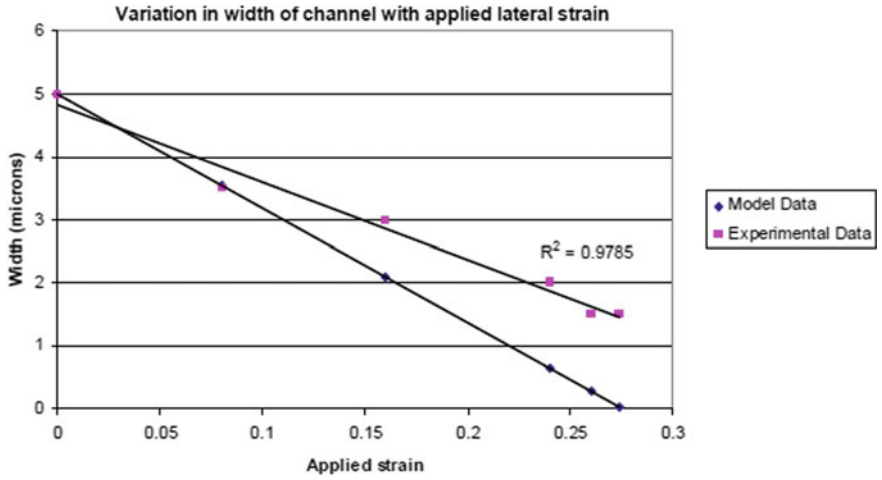


Fig. 6 Variation in width of micro channel with applied lateral, compressive strain

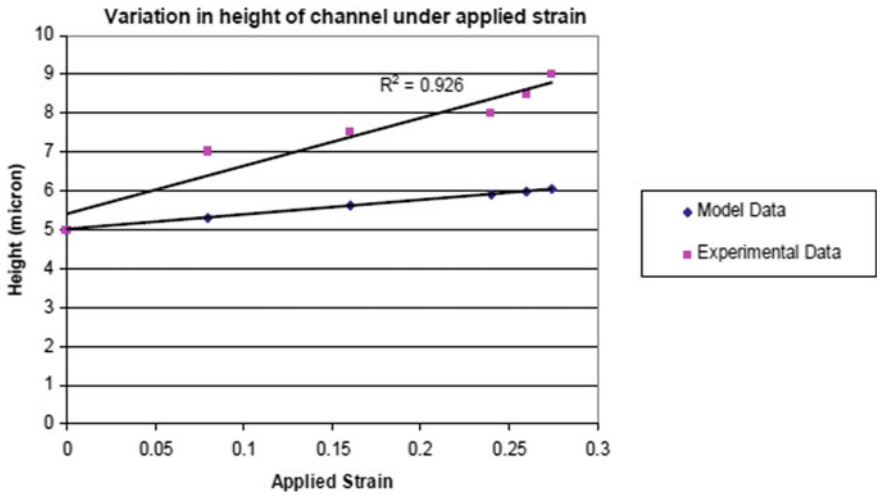


Fig. 7 Increase in height of the micro channel in PDMS

5 Conclusion

On conducting the experiment, the following conclusions are drawn.

- The strain normal to the plane of applied strain was plausibly high when observed in the cross section would be a free surface. Due to this, there is a disturbance among the model results of plane strain and the data obtained through the experiments.

- For getting the micro-channel exactly at the center position, there are some fabrication limitations in exact cutting of the enclosure of PDMS. Due to the effect of poisons ratio, applied lateral and compressive strain, the cross section of enclosure of PDMS results a bulge in the direction of variation observed [11].
- At the higher magnification of optical detection [10], overall micro-channel cross section is not at all a single plane of focus. This results in a blurred image in a channel which was deformed. Due to this, it becomes hard for the measurement of dimensions of deformed channel [12], which is applied for the higher strains and because of external effects such as vibrations, the measurements becomes less tolerable.

References

1. Ding Y, Choo J, deMello AJ (2017) From single-molecule detection to next-generation sequencing: microfluidic droplets for high-throughput nucleic acid analysis. Microfluid Nanofluid 21(3):2628. https://doi.org/10.1007/s10404-017-1889-4
2. Bilenberg B, Jacobsen S, Schmidt MS et al (2006) High resolution 100kV electron beam lithography in SU-8. Microelectron Eng 83(4–9):1609–1612. https://doi.org/10.1016/j.mee.2006.01.142
3. Guarini KW, Black CT, Milkove KR et al (2001) Nanoscale patterning using self-assembled polymers for semiconductor applications. J Vac Sci Technol B 19(6):2784. https://doi.org/10.1116/1.1421551
4. Huang C, Jevric M, Borges A et al (2017) Single-molecule detection of dihydroazulene photothermal reaction using break junction technique. Nat Commun 8:15436. https://doi.org/10.1038/ncomms15436
5. Temiz Y, Lovchik RD, Kaigala GV et al (2015) Lab-on-a-chip devices: how to close and plug the lab? Microelectron Eng 132:156–175. https://doi.org/10.1016/j.mee.2014.10.013
6. Szmigiel D, Hibert C, Bertsch A et al (2008) Fluorine-based plasma treatment of biocompatible silicone elastomer: the effect of temperature on etch rate and surface properties. Plasma Process Polym 5(3):246–255. https://doi.org/10.1002/ppap.200700130
7. Jackson JM, Witek MA, Hupert ML et al (2014) UV activation of polymeric high aspect ratio microstructures: ramifications in antibody surface loading for circulating tumor cell selection. Lab Chip 14(1):106–117. https://doi.org/10.1039/c3lc50618e
8. Ahn B, Lee K, Lee H et al (2011) Parallel synchronization of two trains of droplets using a railroad-like channel network. Lab Chip 11(23):3956–3962. https://doi.org/10.1039/c1lc20690g
9. Arjmandi-Tash H, Belyaeva LA, Schneider GF (2016) Single molecule detection with graphene and other two-dimensional materials: nanopores and beyond. Chem Soc Rev 45(3):476–493. https://doi.org/10.1039/c5cs00512d
10. Dharmasiri U, Balamurugan S, Adams AA et al (2009) Highly efficient capture and enumeration of low abundance prostate cancer cells using prostate-specific membrane antigen aptamers immobilized to a polymeric microfluidic device. Electrophoresis 30(18):3289–3300. https://doi.org/10.1002/elps.200900141
11. Trofymchuk K, Reisch A, Didier P et al (2017) Giant light-harvesting nanoantenna for single-molecule detection in ambient light. Nat Photon 11(10):657–663. https://doi.org/10.1038/s41566-017-0001-7
12. Chen W, Ahmed H (1993) Fabrication of 5–7 nm wide etched lines in silicon using 100 keV electron-beam lithography and polymethylmethacrylate resist. Appl Phys Lett 62(13):1499–1501. https://doi.org/10.1063/1.109609

Fabrication and Characterization of E-glass Fabric Composites Using Amine-Terminated Butadiene Acrylonitrile



Balu Maloth, N. V. Srinivasulu, and R. Rajendra

Abstract The main objective of this experimentation analysis is to improve the mechanical characteristics of E-glass fabric polymer matrix composites by utilizing amine-terminated butadiene acrylonitrile. In most of the research, only one matrix is used for developing new composites. In this research, two matrix materials are selected, namely epoxy-Ly556 resin and amine-terminated butadiene acrylonitrile, and glass fabrics (E-type) are acted as reinforcement material in the development of composites by vacuum bagging method. Samples are developed and experienced for testing the mechanical properties of the developed composites. The fractured samples are used to analyze the reason for the failures of the composite material during the test of mechanical properties by using scanning electron microscopy. The microscopic examination which is confirmed to the vacuum bagging approach has enhanced adhesion among the matrix material and reinforcement material, and this method has decreased the annullement in the composite materials. The glass fabric/epoxy-reinforced composite has an average tensile strength of 747.68 Kgf/cm^2 and a mean flexural strength of 42.99 Kgf/cm^2. This analysis shows that amine-terminated butadiene acrylonitrile created good bonding between the materials.

Keywords E-glass 8 mill fabrics · Amine-terminated butadiene acrylonitrile · Vacuum bagging method · E-glass fabric/epoxy composites · Mechanical properties

1 Introduction

Epoxy resins (EPs) are now used as matrixes for high-performance composites for aerospace, ship, and structural applications. Nevertheless, healed EPs show low

B. Maloth (✉) · R. Rajendra
Department of Mechanical Engineering, College of Engineering, Osmania University, O.U, Hyderabad, India
e-mail: balu.1703@gmail.com

N. V. Srinivasulu
Department of Mechanical Engineering, Chaitanya Bharathi Institute of Technology, Hyderabad, India

© Springer Nature Singapore Pte Ltd. 2020

A. Praveen Kumar et al. (eds.), *Advances in Lightweight Materials and Structures*,
Springer Proceedings in Materials 8, https://doi.org/10.1007/978-981-15-7827-4_40

impact strength (IS), weak crack propagation resistance, and low break elongation [1]. Over the last few decades, the development of mechanical and bonding properties without downgrading the thermal stability of epoxy resins has been of great importance [2]. The widely recognized methods of epoxy toughening include the use of synthetic particles, strong thermoplastics, responsive rubbers, and spill-linkable polymers to build unmanifested network structures of polymers. Several elastomeric materials such as acrylates and nitrile rubbers have been utilized as toughening agents for epoxy resins but their use is limited due to their limited resistance and strength characteristics [3, 4]. Through adding versatile molecular structure, The toughening cycle is used to remove the energy from cracks and improve the impact power of the polymer [5, 6].

The toughening method was designed to improve the effectiveness of polystyrene using elastomeric hardening agents in the form of a high impact product. This allowed several brittle thermoplastic materials to be transformed into solid, tough, and impact-resistant products that have several industrial applications [7, 8]. This thermoplastic toughening mechanism has been applied to heat-setting plastics to make them solid, impact-resistant, and suitable for coatings, adhesives, and matrix materials for advanced composites. However, in many advanced engineering applications, their inferior effect characteristics restrict their usage. Therefore, an improvement in the epoxy resin's impact behavior is necessary. Such studies indicate that in most cases, the thermoplastic alteration has led to greater resin strength [9, 10]. The modified epoxy has many uses, including FRP matrices and structural materials. Most of these FRPs give a strength ratio that is either greater than many traditional metal products or similar [8, 9].

Mechanical performance of the composites produced depends largely on matrix and reinforcement properties, and matrix–reinforcement interactions. These composite materials now also dominate architecture, sports, shipping, connectivity, and manufacturing chemicals [11, 12]. Particularly important is the localized fiber–matrix adhesion surrounded by the composite material while fracturing. The stabilization of the developed composite materials largely overlaps on its morphology. Glass fiber is a great performance boost for FRPs; the main strengths of glass-reinforced composites are high strength, lightweight, structural toughness, abrasion resistance, low cost (as compared to aramid and carbon), etc. [13, 14]. Glass fiber tightly supports both thermoplastics and thermosets. For materials scientists and engineers around the globe, the use of glass fiber as a framework for the manufacture of glass fabric-reinforced composites has been of great interest [15, 16].

The epoxy with styrene-co-acrylonitrile and polymer composites was researched by various researchers. The morphological and practical mechanical study of the current system has been dealt with more in-depth. The epoxy and styrene-co-acrylonitrile mix together explained good thermoelectric and visco-elastic characteristics while evaluated to other unify [17, 18]. Several experiments were executed in the past decades to identify a well-organized method to increase the adhesion between fabric with matrices and SAN. The main aim of the investigation is to examine the impact and the importance of the modification of thermoplastic epoxy

resin matrix on mechanical properties of the amalgamation of epoxy with amine-terminated butadiene acrylonitrile and E-glass fabric composite prepared using the epoxy resin (LY556) as the matrix with the bonding agent of amine-terminated butadiene acrylonitrile.

2 Material Selection and Fabrication Method

2.1 Material Selection

E-glass 8 Mill Fabrics

E-glass fabric is a lightweight material that is strong and robust. Although its strength and rigidity properties are somewhat weaker than carbon fiber, the material is usually much less fragile and the raw material is much cheaper. E-glass fiber fabrics have significant market variety and the strongest authority overall properties of glass fiber products of all types [19]. The lining of the 8 mill E-glasses is used as reinforcing. The cloth engineer suggested a great choice on regulated fabric properties that would meet the design needs of this research and its objectives.

Epoxy Resin

For this work, Araldite LY 556 is selected to utilize for as matrix. This LY 556 has exceptional adhesion to various materials with high strength and resilience to chemical attacks and humidity [20]. It has excellent electromechanical properties. It is odorless, tasteless, yet non-toxic. Hardener (Araldite) is used in the present work HY 951. This has a 10–20-poise viscosity at 25 °C.

Amine-terminated butadiene acrylonitrile (ATBN)

Hypro 1300X16 ATBN is an amine-finished butadiene acrylonitrile copolymer that is mainly used with epoxy resin and improves its composite performance when added to resin thermoset systems [21]. N-aminoethylpiperazine is the basis of the amine formation in hyper resin. This improves epoxy resin's durability and strength. This strengthens adhesion, decreases the attachment problems with additives, raises mechanical properties at low temperature, and boosts effect and tear tolerance as well.

2.2 Fabrication of Composites

The hand layup method is employed to prepare the E-glass fabric composites or natural fiber–matrix by most of the researchers. It is reducing the composites that have both functional and physical characteristics. So, within this investigation, one of the best methods, namely the vacuum bagging method, is utilized to prepare the

Table 1 Materials and their ratios in grams

Materials	Weight
E-glass 8 mill fabric LY-556 (epoxy resin) Resin: hardener	460 g 600 g 100:23
HY-951 (hardener)	135 g
ATBN	

E-glass fabric composites. This method (or laminating the vacuum bag) is a tightening process that utilizes atmospheric pressure to keep a lamination's adhesive or resin-coated materials in place until the adhesive cures. The laminate is prepared by using eight layers of E-glass fabric with a weight of 460 g, epoxy resin with the weight of 600 g, and is mixed with a hardener in the ratio of 100:23. In this process, the laminate is preparing by hand layup process. The vacuum bagging utilizes atmospheric pressure as a seal for bringing together laminate plies. The laminate being packed is sealed inside an airtight shell. Pressure on the outside and inside of this cover is equivalent to atmospheric pressure when the container is sealed to the laminates. As a vacuum pump evacuates gas from the inside of the shell, air pressure is lowered inside the cover when air pressure outside the covering stays at atmospheric pressure. Atmospheric pressure forces the sides of the cover together and everything inside the cover, placing equal and even pressure over the cover surface. The difference in pressure between the inside and outside of the cover determines how much clamping force the laminate has on. Theoretically, the maximum possible pressure can be applied on the laminate, if a complete vacuum could be reached and all the air from the cover or laminates eliminated. Table 1 demonstrates the background and structure of fabrics from epoxy resin, amine-terminated butadiene acrylonitrile, E-glass 8 mills, and hardener.

2.3 Specimen Preparation

The fabric-reinforced composite is developed by the vacuum bagging method, and composite is removed from the setup. American society for testing and materials standard is followed to extract the specimens for testing the mechanical properties (tensile and flexural). The sample for the tensile test was extracted based on ASTM D3039, and the ASTM D790-10 is utilized to extract the specimen for flexural strength exposed (see Fig. 1). The prepared fabric reinforced fabric composite material and take out the composite sample specimen for testing the mechanical properties that are displayed (see Fig. 2).

Mechanical properties are measured for the urbanized epoxy matrix fabric composites by using a universal testing machine. These two mechanical properties (tensile and flexural) are more important measurements for engineers and designers for the proper utilization of composites.

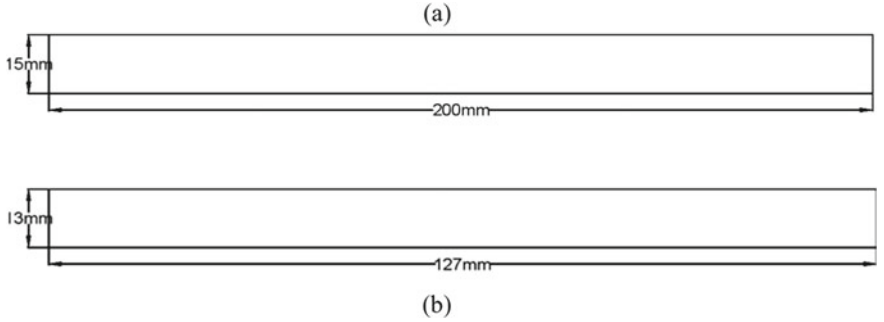
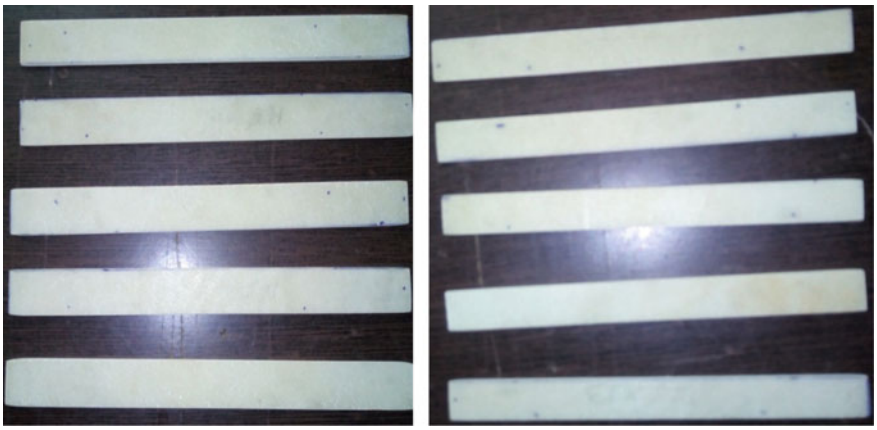


Fig. 1 American society for testing and materials standard composite specimens **a** tensile test and **b** flexural test

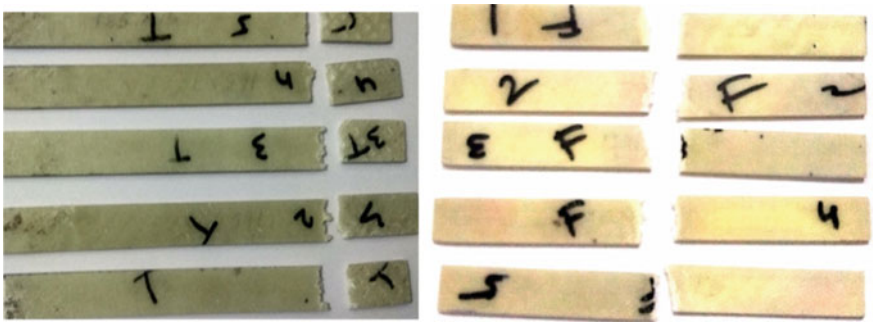


(a) sample for tensile test (b) Sample for flexural test

Fig. 2 Extracted fabric composites for testing the mechanical properties

Tensile loading can possess the ability of a material to withstand lossless friction loads. The five specimens are extracted from the developed polymer fabric matrix. The 30 tons capacity computerized universal tensile testing equipment is utilized to check the tensile strength of the extracted samples. Each experiment was conducted until a failure takes place at normal room temperature. The gauge length, width, and thickness of the specimen are 200 mm, 15 mm, and 3.5 mm, respectively. The sample used for testing is displayed in Fig. 2, and the examined samples are shown (see Fig. 3). The results of the test for flexural and tensile are displayed in Table 2.

A material's ultimate flexural strength is characterized as its capacity to withstand deformation under pressure. The flexural strength or flexural yield strength is defined as being the load at yield, usually estimated at 5% outer surface deformation, for specimens that bend considerably but do not crack. To measure the flexural strength of the specimens, the same computerized UTM with a capacity of 30 tons is used with



(a) Fracture sample of tensile test (b) Fracture sample of flexural test

Fig. 3 Tested specimens

Table 2 Result of mechanical for five samples

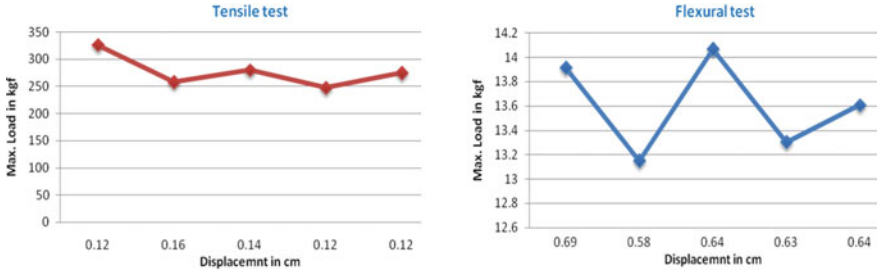
S. No.	Tensile test results (Kgf/cm^2)	Flexural test results (Kgf/cm^2)
1	881.137	45.144
2	696.222	42.664
3	732.701	43.063
4	653.955	41.671
5	774.408	42.447

flexural test attachment. Five tests were executed until a failure takes place at normal room temperature. Through knife edges, the only load is applied at the midpoint of the sample specimen. Exemplary material removed for testing of flexural is shown in Fig. 2, and tested specimens are displayed in Fig. 3.

3 Result and Discussions

3.1 Mechanical Properties

Tested results of five sample specimens for each test are shown in the Table 2. The experimentation result shows that the improvements in mechanical properties (flexural and tensile) of E-glass fabric polymer composite materials using amine-terminated butadiene acrylonitrile are influenced by those characteristics. The load against displacement graph for both test is shown in Fig. 4. The tensile graph shows with the purpose of the maximum load for the sample vary from 247.54 to 325.68 kgf for the displacement from 0.12 to 0.16 cm. Each sample is carrying the different load, but on an average of 277.02 kgf for the displacement of 0.132 cm. Because of the variation of load and displacement, the ultimate tensile strength of composites



(a) Tensile test (b) Flexural test

Fig. 4 Load versus displacement graph for mechanical properties

is also varied from 653.96 to 881.14 kgf/cm^2. The first sample has displayed high tensile strength of 881.14 kgf/cm^2, and it means that it withstands for high load. The fourth sample has registered a low tensile strength as 653.955 kgf/cm^2, and it shows that it is not able to withstand high load as the first sample (see Fig. 4a).

The flexural strength graph shows that the maximum load for the sample varies from 14.066 to 13.149 kgf for the displacement from 0.58 to 0.69 cm. Each sample is carrying a different load, but on an average of 13.61 kgf for the displacement of 0.636 cm. It proves that the first sample is having good bonding between the matrix, ATBN, and E-glass 8 mill fabric. It shows that the resin's addition is more or the adhesion between resin and fabric is not enough to withstand the load. The first sample has registered high flexural strength, and the fourth sample has exerted the low flexural strength. The fabric-reinforced composite has an average tensile strength of 747.68 Kgf/cm^2. It demonstrated that the tensile force mean is higher than the fabric's tensile strength (755 Kgf/cm^2). The flexural force varies from 41.67 Kgf/cm^2 to 45.14 Kgf/cm^2. The mean flexural power of E-glass 8 mill fabric is 42.99 Kgf/cm^2. This demonstrates that the typical flexural resistance is almost comparable to the fabric's flexural strength (43 Kgf/cm^2) (see Fig. 4b).

3.2 SEM Analysis

The tensile test is executed on the developed glass fabric composites, and the fractured specimens that have undergone the microscopic study are performed. The scanning electron microscopy has been used to perform the microscopic study on the fractured components, and SEM captured the images (see Fig. 5).

Vacuum bagging method is utilized to prepare the E-glass fabric reinforces composites, so the composites are having smooth and featureless fracture surface with very less fiber pullout (see Fig. 5a). It is also shown that there are no blow holes in the matrix. This scanning image is also exposed because of the brittle failure of the fabric (see Fig. 5b). It is shown that the non-appearance of enough fibers resists fiber's brittle fracture of the fabric composites. Adhesion of epoxy with ATBN

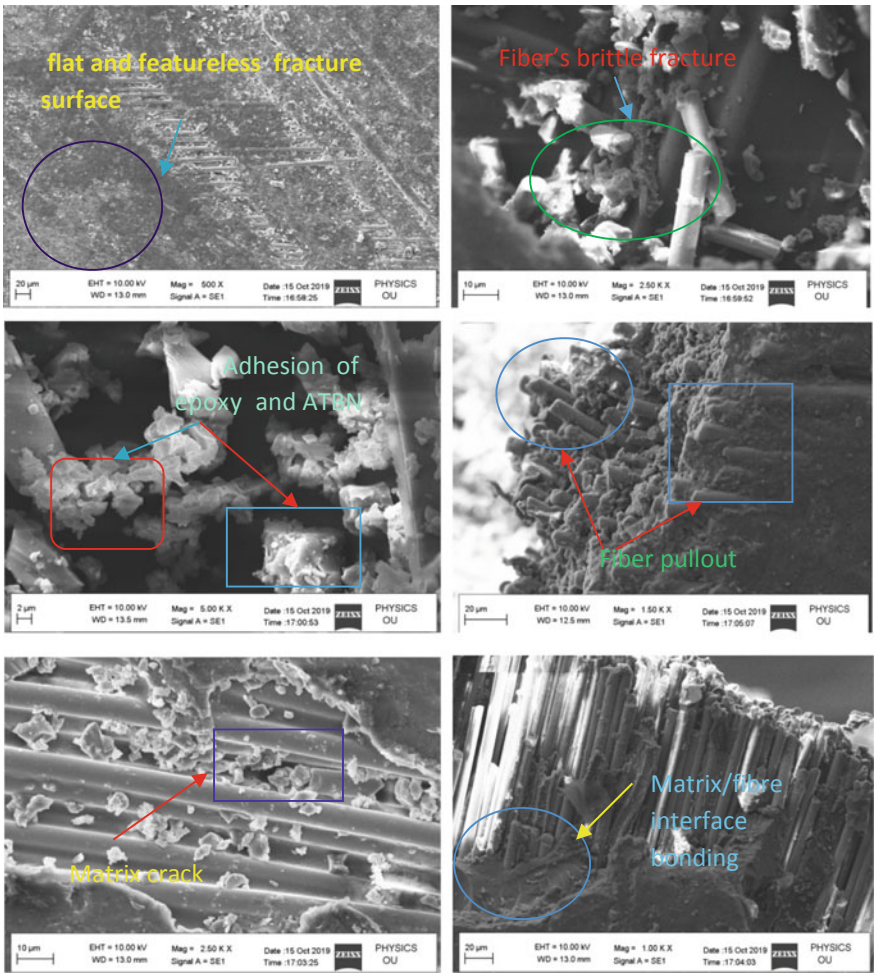


Fig. 5 Scanning electron microcopy's micrographs of ATBN-filled composite **a** flat and featureless fracture surface. **b** Fiber's brittle fracture. **c** Adhesion of epoxy and ATBN. **d** Fiber pullout. **e** Matrix crack. **f** Matrix–fiber interface bonding

and fabric is good in the prepared these composites (see Fig. 5c). This developing method and amine-terminated butadiene acrylonitrile are increasing the adhesion between the epoxy and reinforcement. More fiber pullout is shown in the tensile test specimen (see Fig. 5d) because of the absence of the ATBN in this particular specimen. The specimens exhibit the matrix crack (see Fig. 5e), and it shows the accumulation of resin and ATBN in the very few locations of composites. The interfacial bonding between the matrices and reinforcement (see Fig. 5f) displays that the vacuum bagging process is augmented adhesion strength of fabric composites. The scanning electron microscopy analysis confirms that there are no blowholes, the

good acquaintance strength among matrix and reinforcement, and increase in the mechanical characteristics (tensile and flexural strength) of composite materials.

4 Conclusions

This research was performed to conclude the influence of amine-terminated butadiene acrylonitrile on resin E-glass fabric-reinforced composite materials. The vacuum bagging process has been used to prepare five experiment samples for testing of flexural and tensile strength. The SEM is used to perform fractured specimen microscopic analysis.

- The experimentation result shows that the mean tensile strength of E-glass fabric composite material is almost equal to the mean tensile strength of the developed composites.
- The investigation result shows that the mean flexural strength of the developed composite is almost nearer to the mean flexural strength of the fiber.
- It proves that amine-terminated butadiene acrylonitrile has increased the bonding between resin and reinforcement.
- Improvements in mechanical characteristics of E-glass fabric polymer composites materials using amine-terminated butadiene acrylonitrile are influenced by those characteristics of the prepared fabric polymer composites materials.
- The bonding strength is increased between resin and ATBN, and E-glass fabric by vacuum bagging method is confirmed by using SEM analysis. This method is to reduce the voids and blow holes in the composites.
- In the future, with these two matrix materials and one reinforcement, the filler materials can be added to obtain high mechanical properties.

References

1. Toldy A, Szebényi G, Molnár K, Tóth LF, Magyar B, Hliva V, Czigány T, Szolnoki B (2019) The effect of multilevel carbon reinforcements on the fire performance, conductivity, and mechanical properties of epoxy composites. Polymers 11(2):303–315
2. Punetha VD, Rana S, Yoo HJ, Chaurasia A, McLeskeyJr JT, Ramasamy MS, Sahoo NJ, Cho JW (2017) Functionalization of carbon nanomaterials for advanced polymernanocomposites: a comparison study between CNT and graphene. Prog Polym Sci 67(1):1–47
3. Fombuena V, Petrucci R, Dominici F, Jordá-Vilaplana A, Montanes N, Torre L (2019) Maleinized linseed oil as epoxy resin hardener for composites with high bio content obtained from linen byproducts. Polymers 11:301–318
4. Praveen Kumar A, Nalla Mohamed M, Kurien Philips K, Ashwin J (2016) Development of novel natural composites with fly ash reinforcements and investigation of their tensile properties.Appl Mech Mater 852:55–60
5. Greiner L, Kukla P, Eibl S, Döring M (2019) Phosphorus containing polyacrylamides as flame retardants for epoxy-based composites in aviation. Polymers 11(2):284

6. Praveen Kumar A, Jeyalal P, Barani Kumar D (2012) Hybridization of polymer composites. Int J Adv Mater Sci 3(3):173–182
7. Dehkordi MT, Nosraty H, Shokrieh MM, Minak G, Ghelli D (2010) Low velocity impact properties of intraply hybrid composites based on basalt and nylon, woven fabrics. J Mater Decis 31(8):3835–3844
8. Gao C, Chen G (2016) Conducting polymer/carbon particle thermoelectric composites: emerging green energy materials. Compos Sci Technol 124(1):52–70
9. Praveen Kumar A (2019) Experimental analysis on the axial crushing and energy absorption characteristics of novel hybrid aluminium/composite-capped cylindrical tubular structures. Proc Inst Mech Eng Part L J Mater Design Appl 233(11):2234–2252
10. Asaro L, Villanueva S, Alvarez V, Manfredi LB, Rodríguez ES (2017) Fire performance of composites made from carbon/phenolic prepregs with nanoclays. J Compos Mater 51(25):1–10
11. Praveen Kumar A, Jackson Irudhayam S, Naviin D (2012) A review on importance and recent applications of polymer composites in orthopaedics. Int J Eng Res Devel 5(1):40–43
12. Triantou KI, Mergia K, Perez B (2017) Thermal shock performance of carbon-bonded carbon fiber composite and ceramic matrix composite joints for thermal protection re-entry applications. Compos Part B Eng (1):270–278
13. Kumar A, Ayyagari N, Fisher TS (2016) Effects of graphene nanopetal outgrowths on internal thermal interface resistance in composites. ACS Appl Mater Interf 8(10):6678–6684
14. Zhang M, Buekens A, Li X (2016) Brominated flame retardants and the formation of dioxins and furans in fires and combustion. J Hazard Mater 304(1):26–39
15. Zhang RL, Gao B, Du WT, Zhang J, Cui HZ, Liu L, Ma QH, Wang CG, Li FH (2016) Enhanced mechanical properties of multiscale carbon fiber/epoxy composites by fiber surface treatment with graphene oxide/polyhedral oligomeric silsesquioxane. Compos a Appl Sci Manuf 84(1):455–463
16. Zotti A, Borriello A, Ricciardi M, Antonucci V, Giordano M, Zarrelli M (2015) Effects of sepiolite clay on degradation and fire behaviour of a bisphenol A-based epoxy. Compos B Eng 73(1):139–148
17. Ying Z, Xianggao L, Bin C, Fei C, Jing F (2015) Highly exfoliated epoxy/clay nanocomposites: mechanism of exfoliation and thermal/mechanical properties. Compos Struct 132(1):44–49
18. Sabat L, Kundu CK (2020) Testing of mechanical properties of E-glass fiber and A-R glass fiber reinforced epoxy polymer composites. TEST Eng Manage 82(1):13266–13270
19. Keya KN, Kona NA, Razzak M, Khan RA (2020) Comparative studies of mechanical and interfacial properties between jute and E-glass fiber-reinforced unsaturated polyester resin based composites. Mater Eng Res 2(1):98–105
20. Praveen Kumar A, Kumarasamy GS, Nikhil N (2015) Analysis of carbon fiber reinforced polymer composite hip prosthesis based on static and dynamic loading. Int J Appl Eng Res 10(85):574–579
21. Chakraverty AP, Beura S, Mohanty UK, Mishra SC, Biswal BB (2020) Gamma-Irradiation of E-glass/epoxy composite: a study of its mechanical and thermal sustainability. Process Character Mater 978(1):296–303

Effect of Directional Grain Structure on Microstructure, Mechanical and Ballistic Properties of an AA-7017 Aluminium Alloy Plate



Pradipta Kumar Jena, K. Siva Kumar, R. K. Mandal, and A. K. Singh

Abstract The present work illustrates the correlation of microstructure along three directions namely, longitudinal (L), long-transverse (LT) and short-transverse (ST) on mechanical and ballistic properties of an AA-7017 aluminium alloy plate. The microstructure in L and LT direction exhibits high aspect ratio deformed grains, whereas low aspect ratio grains are observed in ST direction. The plate displays the highest strength value along LT, followed by ST and L directions. The L and ST direction samples show the highest and lowest impact energy values, respectively. Ballistic properties of the plate in three directions is evaluated by impacting with high hardness steel projectiles. It is noticed that the AA-7017 plate exhibits the best ballistic performance in ST direction.

Keywords Armour · Ballistic performance · AA-7017 alloy · Microstructure · Mechanical property

1 Introduction

Armour is employed to prevent damage to either individuals or vehicles against ballistic impact. In the battle field, armour protection increases survivability many folds. The main requirement of an effective armour material is that it should possess superior ballistic resistance in concurrence with optimized mechanical properties. Aluminium alloys are one of the prominently used materials for ballistic protection applications. These alloys are also utilized to minimize the weight of the protective structure. Therefore, it enhances mobility and reduces the fuel expenditure of vehicles used in battle field.

P. K. Jena (✉) · K. Siva Kumar · A. K. Singh
Defence Metallurgical Research Laboratory, Hyderabad 500058, India
e-mail: pradipta@dmrl.drdo.in

R. K. Mandal
Department of Metallurgical Engineering, IIT (BHU), Varanasi 221005, India

© Springer Nature Singapore Pte Ltd. 2020

A. Praveen Kumar et al. (eds.), *Advances in Lightweight Materials and Structures*,
Springer Proceedings in Materials 8, https://doi.org/10.1007/978-981-15-7827-4_41

In general, thick plates manufactured by a combination of different thermo-mechanical processes, e.g. forging, rolling and subsequent heat treatments are considered for ballistic protection applications. This introduces preferred direction of grains in the materials. As a result, these materials exhibit mechanical property anisotropy. It has been reported that aluminium alloys demonstrate anisotropy in properties due to preferred direction of grains developed during thermo-mechanical processing [1–3].

Three principal directions namely longitudinal (L), long-transverse (LT) and short-transverse (ST) are required to delineate a thick plate. The plate displays different microstructures along three directions. This results in different mechanical properties. In an earlier study, Lee et al. have shown from the split-Hopkinson pressure bar (SHPB) experiments that high strain rate properties of AA 6061-T6 alloy depend on the direction of grains [4]. It has been observed that the aluminium alloy 6061 in T6 condition exhibits maximum strength in samples parallel to transverse direction. In another study on aluminium 2024 alloy, it is observed that both the yield strength and elongation are higher along longitudinal and transverse directions than the through thickness direction [5]. Vignjevic et al. have established from the plate impact experiments that the longitudinal direction is stronger than the short-transverse direction in 7010-T6 aluminium alloy [6]. However, investigation of the ballistic behaviour of a material in three directions of a rolled plate product wherein microstructural variations are quite large is somewhat limited.

Aluminium-7017 is a commonly used material for ballistic resistance applications. Present work is concerned with understanding the ballistic performance of an AA-7017 plate of 70 mm thickness in L, LT and ST directions. The ballistic behaviour is correlated with the microstructure corresponding to the three directions of the AA-7017 plate.

2 Experimental Procedure

The AA-7017 alloy was purchased in peak aged (T6) condition from Alcan International (UK). The analysed composition of the as received AA-7017 material is given in Table 1. Typical metallographic techniques were applied for microstructural characterization. Keller's reagent was put to use as etchant to obtain the microstructure of the AA-7017 specimens.

The three principal directions of the AA-7017 plate are shown in Fig. 1. Tensile and impact samples were machined along three directions of the plate as illustrated in Fig. 1. For tensile testing, the cross section diameter and the gauge length of the samples were 4 mm and 20 mm, respectively. An extensometer was employed

Table 1 Chemical composition of the AA-7017 alloy

Material	Chemical composition (wt%)
AA-7017	4.5–5.1 Zn, 2.2–2.9 Mg, 0.37 Si, 0.38 Cr, 0.41 Fe, 0.18 Mn, balance Al

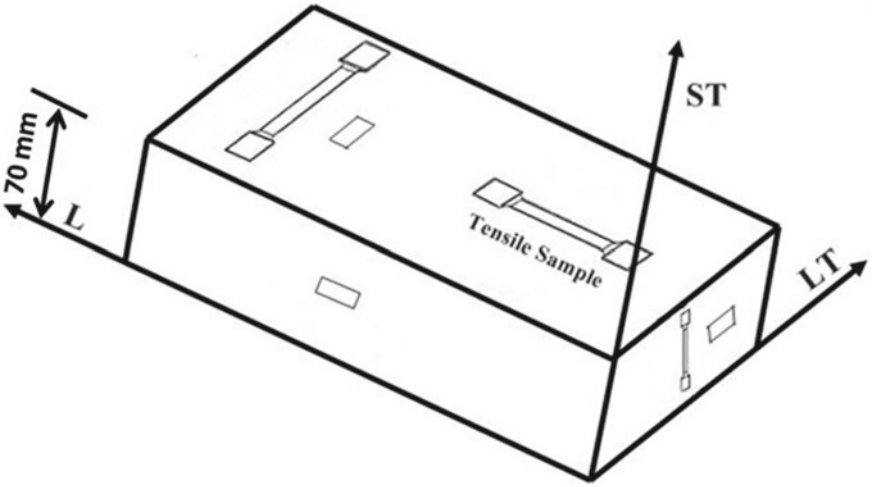


Fig. 1 Schematic of the three principal directions in the AA-7017 plate

to measure the elongation. Tensile testing of the AA-7017 alloy was performed following ASTM E8 standard at room temperature.

Charpy V-notch samples were machined, and impact tests were conducted in compliance with ASTM standard E23-02a. Three tensile and impact specimens were tested for each direction, and average value of the properties is illustrated in the current study. Fracture surface of a selected broken Charpy samples was studied employing a FEI scanning electron microscope.

For ballistic evaluation, plates of 200 × 70 × 70 mm were machined by using a water jet cutting machine (OMAX 55100) as shown in Fig. 2. Care was taken to keep the dimension of the ballistic testing samples equivalent in order to avoid any variation in ballistic performance due to difference in the target plate. Ballistic testing samples were prepared with at least one of the sides with a dimension of 200 × 70 mm parallel to a principal direction of the parent plate. Ballistic evaluation was conducted by impacting projectiles on these faces.

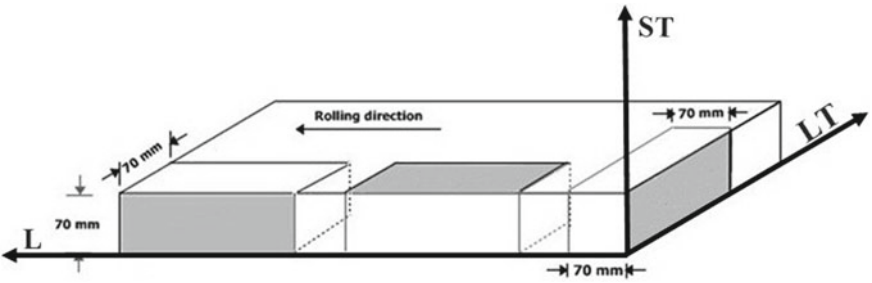


Fig. 2 Schematic sketch of cutting of samples for ballistic testing

Ballistic testing of the samples was performed in a testing range. The plates were tested at 0° angle of impact with steel projectiles of hardness about 700 HV. The projectile velocities were calculated by a projectile velocity measuring equipment. The measured impact velocities were between 830 ± 10 m/s. Following the ballistic tests, the penetration in the AA-7017 target plates was measured precisely. The ballistic testing procedure is described thoroughly elsewhere [7].

3 Results

The 3D optical microstructure representing three sample directions of the AA-7017 alloy plate is illustrated in Fig. 3a. The grain structure of the AA-7017 alloy plate varies significantly in the three directions. From the transmission electron microscope (TEM) studies, it is detected that the microstructure contains a large density of round-shaped precipitates, Fig. 3b.

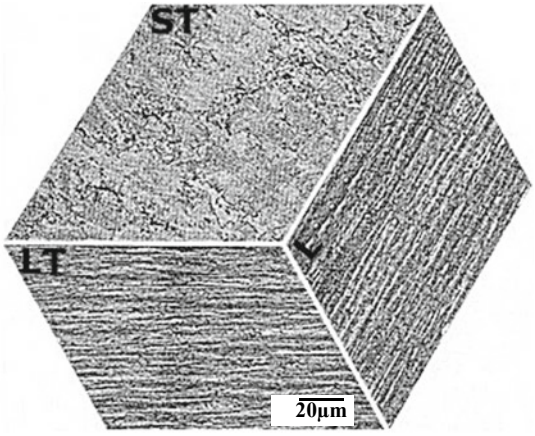
Figure 4 displays the mechanical properties of the AA-7017 plate in L, LT and ST directions. It can be seen that the maximum strength is noticed in LT direction. The L and ST direction samples show the highest and lowest elongation as well as impact energy values, respectively.

The anisotropy in fracture behaviour of the material can be seen from the SEM fractographs of the broken Charpy impact samples (Fig. 5). The fracture features of impact specimens along three directions display a notable change in the fracture behaviour. The fracture surfaces of L and LT samples exhibit dimples of different sizes in conjunction with secondary cracks at grain boundaries. Both the extent of secondary cracks and delamination are more severe in LT direction. In addition, voids are also observed to contain coarse intermetallic particles. The energy dispersive analysis of X-rays (EDAX) indicates that these are intermetallic particles of aluminium with Fe and Mn (Fig. 5b). The fracture surface of ST sample displays a slant type failure pattern with large number of intermetallic particles impinge on the voids.

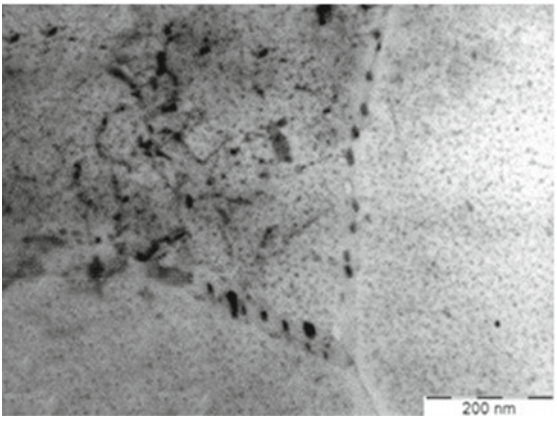
The depth of penetration (DOP) values of the ballistically evaluated specimens is depicted in Fig. 6. It is observed that ballistic resistance of ST direction samples is higher than those of the L and LT direction samples.

4 Discussion

It is evident from the optical microstructures that there is a considerable change in the grain size and structure in three directions of the AA-7017 plate. The plate exhibits equiaxed grains in ST direction, while elongated grains are observed in L and LT directions (Fig. 3). Similar type of difference in microstructure in three directions has also been observed in AA 7075 T651 alloy [8]. From the TEM micrograph, it is observed that the alloy contains precipitates along the grain boundaries. Three



(a)



(b)

Fig. 3 **a** 3D optical microstructure of the AA-7017 alloy and **b** intermetallic particles at the grain boundaries

types of particles have been reported in aluminium alloys. These are coarse "constitutive" particles, partially soluble "dispersoid" particles and the finer hardening phase particles known as "precipitates". Presence of Al_3Zr dispersoid particles and $MgZn_2$ precipitates in AA-7017 alloy has been reported by Rout et al. [9].

The difference in mechanical properties along three directions can be ascribed to the variation in microstructural constituents (grain size, morphology and distribution) present in the AA-7017 alloy plate. The plate displays the highest strength value along LT, followed by L and ST direction. Grain boundaries act as obstacles to the movement of dislocations and enhance the strength of the material. Hence, the lower strength observed in ST direction can be attributed to the lesser grain boundaries in comparison with L and LT directions. Similar observations in strength anisotropy have also been reported in AA-6061 alloy [4].

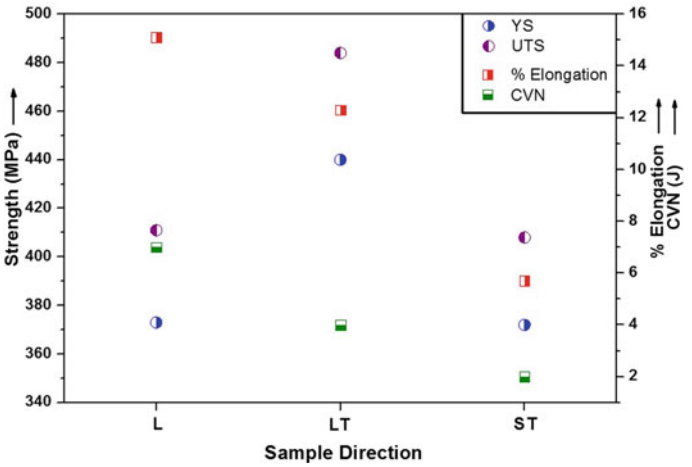


Fig. 4 Mechanical properties along three directions of the AA-7017 plate

The difference in impact toughness values can be explained from the anisotropy in fracture behaviour along three directions. In L and LT samples, dimples with transgranular cleavage facets dominate the fracture surface.

The fracture surface of ST samples exhibits an intergranular mode of fracture. It provides an easy path for crack growth and reduces the impact toughness of the material in ST direction. Presence of secondary cracks along the grain boundaries in case of L and LT samples and intergranular fracture in ST samples supports the presence of intermetallic particles along the grain boundaries.

The variation in ballistic behaviour of the material in different directions can be associated with the microstructural differences of the plate in three directions. It is observed that grain boundaries contain intermetallic particles. During ballistic impact, strain localization takes place easily around the intermetallic particles. This leads to a deterioration of the ballistic performance of the material. This explains the effectiveness of the surface with lesser grain boundaries against ballistic impact. For that reason, the plate demonstrates better ballistic performance in ST direction.

Usually, ballistic behaviour of any material is correlated with its mechanical properties like strength, hardness and Charpy impact toughness [10–16]. In this study, it is observed that the ability of the AA-7017 plate to resist the projectile penetration is maximum in ST direction. It is to be noted that, the material shows moderate strength, lowest ductility and Charpy impact toughness along ST direction. It clearly points out that the ballistic performance of a material does not depend solely on mechanical properties. The microstructure of the target material also plays a considerable role in the ballistic performance.

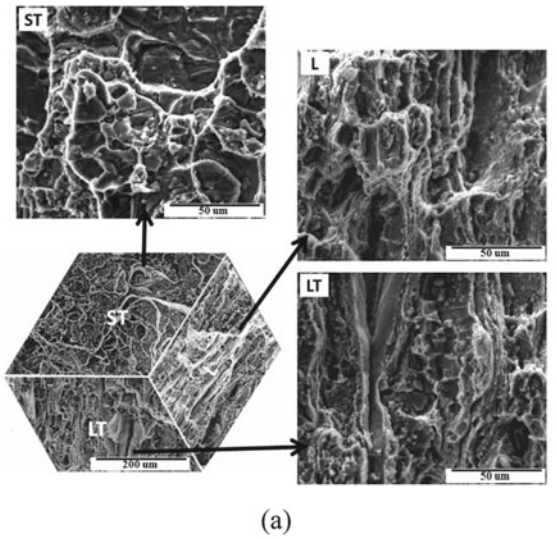


Fig. 5 **a** Fracture surfaces along three directions and **b** EDAX analysis of the particles present in the fracture surface

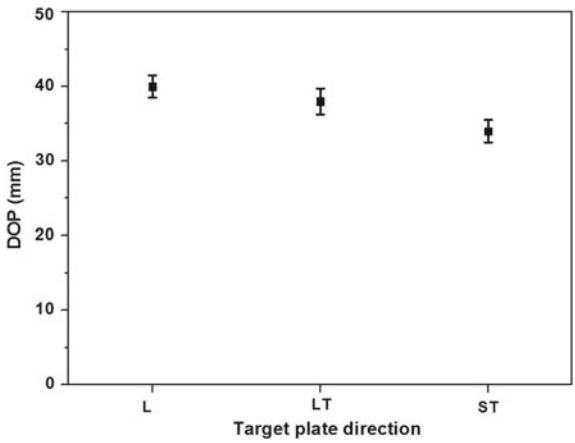


Fig. 6 Ballistic results in three directions of the AA-7017 plate

5 Conclusions

The following results can be contemplated from the present work.

(i) There is a variation in morphology and orientation of the grains along three directions of the AA-7017 plate. This has resulted in anisotropy in mechanical properties along the three directions.
(ii) Microstructural attributes appear to be a critical aspect in improving ballistic protection of materials. The best ballistic performance is observed along ST direction of the AA-7017 plate due to the presence of lesser grain boundaries.
(iii) The future investigations should emphasize on the performance of other metallic armour materials in three principal directions to analyse their ballistic behaviour.

Acknowledgements The authors would like to acknowledge Defence Research and Development Organization, India, for financial assistance to carry out this work.

References

1. Barlat F, Lege DJ, Brem JC (1991) A six-component yield function for anisotropic materials. Int J Plast 7(7):693–712
2. Seidt JD, Gilat A (2013) Plastic deformation of 2024–T351 aluminum plate under a wide range of loading conditions. Int J Solids Struct 50(10):1781–1790
3. Chen Y, Clausen AH, Hopperstad OS, Langseth M (2009) Stress-strain behavior of aluminium alloys at a wide range of strain rates. Int J Solids Struct 46(21):3825–3835
4. Lee WS, Liu MH (2014) Effect of directional grain structure and strain rate on impact properties and dislocation substructure of 6061–T6 Aluminum alloy. Key Eng Mat 626:50–56
5. Khan R (2013) Anisotropic deformation behavior of Al2024T351 Aluminum alloy. J Eng Res 10(1):80–87
6. Vignjevic R, Bourne NK, Millett JCF, De Vuyst T (2002) Effects of orientation on the strength of the aluminum alloy 7010–T6 during shock loading: Experiment and simulation. J Appl Phys 92:4342–4348
7. Jena PK, Mishra B, RameshBabu M, Aravindha B, Singh AK, SivaKumar K, Bhat TB (2010) Effect of heat treatment on mechanical and ballistic properties of a high strength armour steel. Int J Impact Eng 37:242–249
8. Jordon JB, Horstemeyer MF, Solanki K, Bernard JD, Berry JT, Williams TN (2009) Damage characterization and modeling of a 7075–T651 aluminum plate. Mater Sci Eng A 527:169–178
9. Rout PK, Ghosh KS (2012) Aging and electrochemical behavior of 7017 Al-Zn-Mg Alloy of various tempers. Mater Sci Forum 710:665–670
10. Dikshit SN, Kutumbarao VV, Sundararajan G (1995) The influence of plate hardness on the ballistic penetration of thick steel plates. Int J Impact Eng 16(2):293–320
11. Jung J, Cho YJ, Kim SH, Lee YS, Kim HJ, Lim CY, Park YH (2020) Microstructural and mechanical responses of various aluminum alloys to ballistic impacts by armor piercing projectile. Mater Charact 159:110033
12. Jena PK, Sivakumar K, Mandal RK, Singh AK (2019) An experimental study on the fracture behavior of different aluminium alloys subjected to ballistic impact. Procedia Struct Integr 17:957–964

13. Mondal C, Mishra B, Jena PK, Sivakumar K, Bhat TB (2011) Effect of heat treatment on the behavior of an AA7055 aluminium alloy during ballistic impact. Int J Impact Eng 38(8–9):745–754
14. Mishra B, Ramakrishna B, Jena PK, Sivakumar K, Gupta NK (2013) Experimental studies on the effect of size and shape of holes on damage and microstructure of high hardness armour steel plates under ballistic impact. Mat Des 43:17–24
15. Zhang P, Wang Z, Zhao P, Zhang L, Jin XC, Xu Y (2019) Experimental investigation on ballistic resistance of polyurea coated steel plates subjected to fragment impact. Thin-Walled Struct 144:106342
16. Ryan S, Li H, Edgerton M, Gallardy D, Cimpoeru SJ (2016) The ballistic performance of ultra-high hardness armour steel: An experimental investigation. Int J Impact Eng 94:60–73

Investigations on the Cutting Quality of Interleaved Flax Fiber with Fly Ash-Reinforced Hybrid Polymer Composite



K. Ramraji, K. Rajkumar, M. Rajesh, and K. M. Nambiraj

Abstract Fiber-reinforced polymer (FRP) composite has highly received performance characteristics of structural material. This work aims to investigate the mechanical properties and cutting quality on polymer composite designed with a multi-layer sequence of natural flax fiber interleaved with fine fly ash-reinforced vinyl ester composite by using abrasive water jet machining (AWJM). Composite laminates were made with multi-stacking of flax fiber with different fine fly ash particle filler loading (0–15 wt%) by an interleaving approach. Tensile and flexural strength of prepared laminates were measured for various fly ash filler loading conditions. Mechanical properties of laminates were limited by the agglomerated fine fly ash particles which are loading above 10 wt%. Further, enhancement of properties is attributed to the polymer chain termination by fly ash particles leading immobility of polymer link. SEM images of fracture surface revealed types of failure mode are fiber pullout, matrix cracking, and brittle failure of matrix and fiber. Analysis of surface cut quality done by varying the cutting parameters of AWJM by box Behnken design (BBD). The surface quality of the composite severely reduced with fly ash filler loading after a critical 10% loading. An increase in jet pressure intensity reduces the fiber edge pullout and damages.

Keywords Flax fiber · Fly ash · Erosion · Surface roughness · Box Behnken design

1 Introduction

Popularly aerospace and the automotive industry are the most widely employed fiber-reinforced polymer (FRP) composites for load-bearing structures since its superior static and dynamic properties [1–3]. In recent years, the natural fiber-reinforced composites created a great interest among researchers toward technological developments. Natural fiber-reinforced composite reduces environment concern, and also,

K. Ramraji · K. Rajkumar (✉) · M. Rajesh · K. M. Nambiraj
Department of Mechanical Engineering, SSN College of Engineering, Chennai, Tamil Nadu 603110, India
e-mail: rajkumark@ssn.edu.in

© Springer Nature Singapore Pte Ltd. 2020

A. Praveen Kumar et al. (eds.), *Advances in Lightweight Materials and Structures*,
Springer Proceedings in Materials 8, https://doi.org/10.1007/978-981-15-7827-4_42

it replaces the synthetic fiber usage. As one of the natural fibers, flax fiber offers a wide possibility in engineering applications due to its high order crystalline structure. More interestingly, the flax fiber-reinforced thermoset composites are elevated to structural applications due to their dynamical damping and good mechanical properties [4, 5]. In order to exploit their usage in such applications, secondary processing like machining is invoked.

Machining of FRP laminates is facing many challenges especially in trimming operation which produces various kinds of damage such as delamination of plies, fiber edge pullout and burr, and poor surface quality. These are however affecting mechanical performance. Moreover, excessive generation of dust during machining can be harmful to the environment [6, 7]. Shanmugam et al. [8] unveiled comprehensive reports on non-traditional machining operations that notified AWJM is the most suitable technique for FRP laminate machining. Quality of machining is mostly related to the AWJM process parameters like nozzle diameter, nozzle stands distance to work materials, depth of cut, travel cutting speed, and abrasive grain flow rate.

Several researchers studied the ability of machining by the AWJM process so far with different types of FRP laminates using a combination of process parameters and their levels. Hydraulic pressure is considered to be the most significant factor as compared to the other factors [9, 10]. The surface roughness of the glass, carbon, and kevlar fiber-reinforced plastic composites observed to decrease with hydraulic pressure that increased the kinetic energy of the abrasive particles [11, 12]. Hence, it enhances the cutting capability of water jet, and thus, fine machining was achieved. It is also proved that the delamination damage can be reduced by increasing kinetic energy of abrasive water jet stream, but it affected under a lower cutting speed [13]. Jani et al. [14] investigated the AWJ cutting performance on natural fiber with interleaved particle reinforced composite laminate. They reported that the interleaving particles reduce surface quality by seeing a fiber pullout or delamination. Haddad et al. [15] used the AWJM for the cutting process on carbon fiber-reinforced polymer composite. It is found that the surface quality of composite reduced by order when observing a reduction of compressive strength.

Thus, it is found that very few literatures are available which studies the machinability of fiber and particle reinforced vinyl ester composite. This study mainly focuses on the effect of fine fly ash particle filler interleaved flax fiber-reinforced polymer laminate by abrasive water jet cutting. The novelty of this work, the AWJ cutting is proposed to control the suitable input parameter for achieving an improved surface finish by BBD design experiment method. Further, investigation on mechanical properties of the fly ash interleaved flax multi-layered polymeric composite was done. The surface morphology of the flax/fly ash fiber-reinforced vinyl ester composite is evaluated through SEM images.

Table 1 Weight fractions of flax fiber, fly ash and vinyl ester of the composite laminates

Laminates	wt% flax fiber	wt% of fly ash	wt% of vinyl ester
UFFA0	20	0	80
TFFA0	20	0	80
TFFA5	20	5	75
TFFA10	20	10	70
TFFA15	20	15	65

2 Materials and Method

2.1 Fabrication

Flax fiber of 20 wt% and fine fly ash particle (5, 10, 15 wt%) were used in this study. For the preparation of composite laminates, initially, the wax was (releasing agent) applied inside of the mold. Accelerator, promotor, and catalyst were used as a curing agent for the vinyl ester resin, which is supplied by the Vasivibala Resin Pvt. Ltd., India. Aqua with a 5%NaOH chemical was used for surface treatment of flax fiber. It gives more resistance to fiber by reducing water intake ability. This provides more dimensional stability [5]. The ultrasonication was used to mix the fly ash with resin until it attains the proper mixing. After mixing, fly ash resin interleaved into five fiber layers for making a laminate. The laminate was removed after 24 h of curing. Four laminates namely untreated flax fly ash (UTFFA), treated flax fly ash (TFFA0), TFFA5, TFFA10, and TFFA15. The numeric numbers indicate the weight percentage of fly ash particles. Table 1 shows the weight fraction of flax fiber, fly ash, and vinyl ester of the prepared laminates.

2.2 Experimental Details

Tensile and flexural strength were measured by universal testing machine (UTM) according to the ASTM standards (D638 and D790) at cross head speed 5 mm/min [16, 17]. The S3015 model AWJ machine was used for conducting machining experiments. The 80-mesh garnet was used as the abrasives particles which flow out through the nozzle of 1 mm in diameter. According to BBD design technique, the optimization of machining variables over the surface roughness was done. Figure 1 shows the typical photocopy of AWJ cutting on the composite laminate. The roughness is one of the significant cutting performance indicators in AWJM. Roughness, as indicated in Ra, was measured by Surf test SJ-210 profilometer with a measuring range and speed of 350 μm and 0.25 mm/s. The roughness observation made at three different regions of the cut surface as follows smooth (top), transition (middle), and rough zone (bottom). In this work, R_a is measured along the traverse thickness direction of material being cut, and an average value was noted. Generally, a better machining

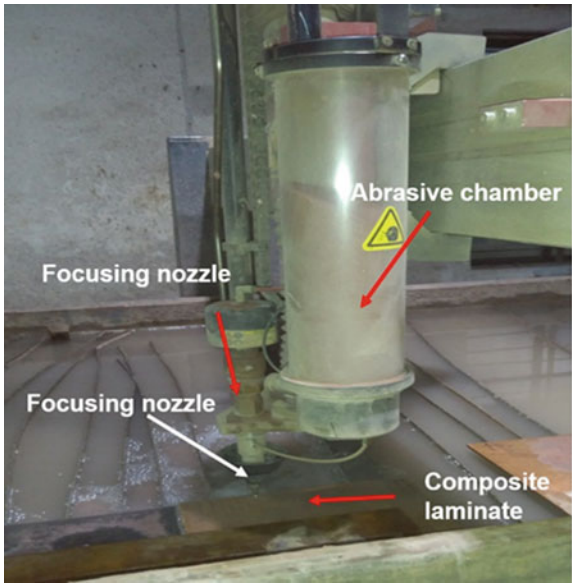


Fig. 1 Typical AWJ cutting of composite laminate

Table 2 Cutting parameters and their levels

Process parameters	Levels		
H_p-Hydraulic pressure (MPa)	125	175	225
SO_D Stand-off distance (mm)	1.5	2.5	3.5
Ts-Traverse speed (mm/min)	100	150	200

process is indicated by a smaller R_a value. Input cutting parameters and their levels are shown in Table 2, and corresponding optimization design and surface response are summarized in Table 3.

3 Results and Discussion

3.1 Tensile and Flexural Strength

The obtained tensile strength and modulus of the interleaved composite are shown in Fig. 2. This figure shows treated flax laminate (TFFA) giving a better tensile value than that of untreated laminate. Surface treatment normally improved adhesion between matrix and fiber. Hence, an increase in tensile strength and modulus of the laminate observed [3]. Further, fly ash filler loading up to 10 wt% increased tensile strength and modulus of the laminate. It is seen that at 15 wt%, the fly ash filler loading decreases the tensile value of the laminate (TFFA15). This could be due to

Table 3 Optimization design and corresponding R_a value

Run	H_P (MPa)	SO_D (mm)	Ts (mm/min)	TFFA laminate (fly ash wt%)	Surface roughness R_a (μm)
1	225	3.5	150	10	2.4685
2	125	2.5	100	5	2.9575
3	175	1.5	200	5	2.8778
4	175	1.5	200	0	3.3580
5	225	2.5	100	5	2.8769
6	175	3.5	100	0	3.3790
7	175	2.5	150	5	2.8975
8	225	2.5	200	5	2.8864
9	125	3.5	150	5	3.0209
10	225	1.5	150	5	2.7055
11	175	3.5	200	10	2.4905
12	125	1.5	150	10	2.4957
13	175	1.5	100	10	2.3877
14	125	2.5	100	0	3.4510
15	175	3.5	100	10	2.4817
16	125	1.5	150	0	3.3980
17	175	3.5	100	5	2.8958
18	225	2.5	200	0	3.3680
19	125	2.5	200	5	3.1289
20	125	3.5	150	10	2.5889
21	175	1.5	100	5	2.7861
22	175	3.5	200	0	3.3910
23	225	2.5	200	10	2.4736
24	175	2.5	150	10	2.4832
25	225	2.5	100	0	3.3570
26	225	3.5	150	0	3.3610
27	225	2.5	100	10	2.4655
28	225	1.5	150	0	3.1570
29	125	2.5	200	10	2.6815
30	225	1.5	150	10	2.3187
31	125	3.5	150	0	3.5250
32	175	3.5	200	5	2.9061
33	175	2.5	150	0	3.3810
34	175	1.5	200	10	2.4663
35	175	1.5	100	0	3.2510

(continued)

Table 3 (continued)

Run	H_P (MPa)	SO_D (mm)	Ts (mm/min)	TFFA laminate (fly ash wt%)	Surface roughness R_a (μm)
36	125	2.5	100	10	2.5346
37	225	3.5	150	5	2.8804
38	125	2.5	200	0	3.6510
39	125	1.5	150	5	2.9121

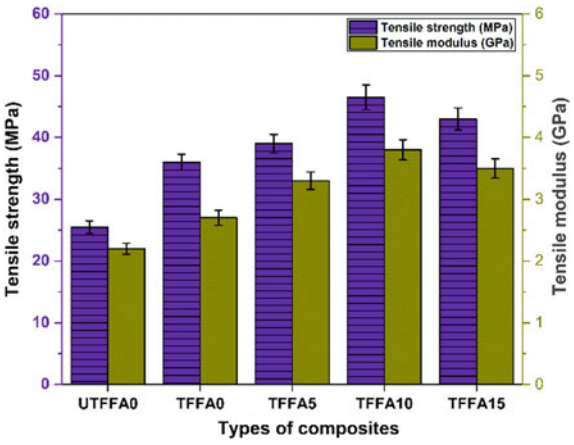


Fig. 2 Tensile strength of interleaved flax/fly ash composite

the agglomeration of the overloading of filler particles in the laminate. It is observed an increase of strength by 7.6% for TFFA5 and 26.5% for TFFA10 when compared to TFFA0 laminate. A similar report has been presented by Praveen et al. [18] with different amounts of fly ash particle loading in polymer laminates.

Flexural strength and modulus of fly ash interleaved flax multi-layered polymer composites are shown in Fig. 3. It is revealed that fly ash particles up to 10 wt% of particles enhanced the flexural strength and modulus of laminates. Flexural strength of TFFA10 laminate yields a higher value by 34.6% for UTFFA0 and 17.8% for TFFA0 laminates. This is due to the good dispersion of fine fly ash particles in the matrix. This is also reported by Ref. [18] where fine fly ash particle loading significantly improved the mechanical properties of the composite. Conversely, 15% of fly ash particle loaded laminate shows a downward trend because more particles present in a matrix create agglomerations resulting in weaker adhesion between them.

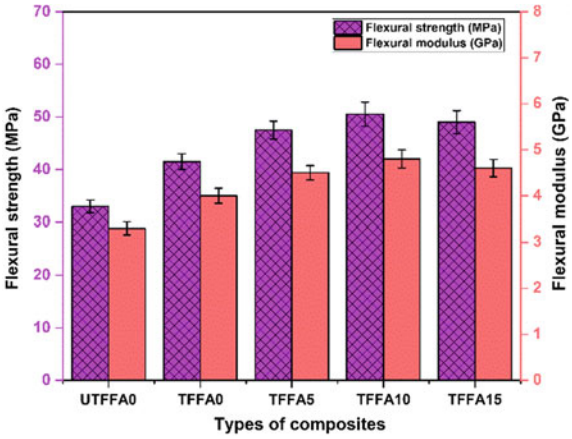


Fig. 3 Flexural strength of interleaved flax/fly ash laminate

3.2 SEM Micrographs of Fractured Surface

After tensile testing, the fractured surfaces of with and without fly ash interleaved composites were observed by scanning electron microscopy (SEM). SEM micrographs for with (TFFA10) and without fly ash (TFFA0) interleaved composites are shown in Fig. 4a, b. Micrographs revealing the causes and type of failure mode of the composites. Figure 4a reveals matrix crack, fiber de-bond, fiber pullout, and voids at the fracture surface without fly ash composite [5]. On the other hand, fly ash composite shows the better interfacial adhesion between fiber-matrix, and therefore, it reduced fiber-matrix debonding and fiber pullout, but there was a fiber splitting that occurred as shown in Fig. 4b.

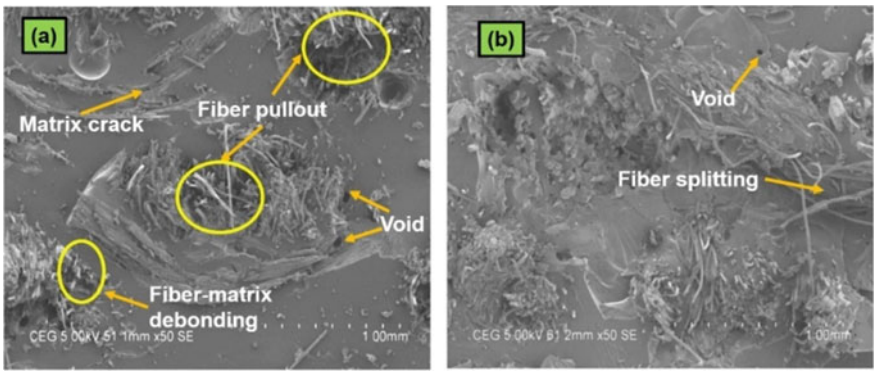


Fig. 4 Typical SEM micrographs of tensile fracture **a** TFFA0 and **b** TFFA10 composite

3.3 Impact of Cutting Parameters on Surface Quality

Figure 5a–d influence of input parameters on surface roughness is shown as a 3D view.

Effect of H_P on R_a

Table 4, ANOVA results show the relative significance of machining variables, as noted, H_P is strongly influenced surface roughness. Figure 5a reveals maximum R_a obtained with low H_P and high SO_D values. But R_a seems to be reducing with downing SO_D values and increasing H_P values. This is due to the increase in the kinetic energy of the water jet [11]. The high energy of the water beam removes the material steadily resulting in a smoother surface. Therefore, the measured R_a value was attained a minimum value. As seen, an increase of H_P from 125 to 225 MPa reduces R_a value by 14.53%.

Table 4 R_a analysis by ANOVA

Source	Sum of squares	Df	Mean square	F-value	p-value	
Model	5.64	17	0.3315	564.52	<0.0001	Significant
H_P	0.1711	1	0.1711	291.37	<0.0001	
SO_D	0.0677	1	0.0677	115.34	<0.0001	
T_S	0.0305	1	0.0305	51.89	<0.0001	
CL	5.27	2	2.63	4485.10	<0.0001	
H_P * SO_D	0.0033	1	0.0033	5.65	0.0270	
H_P * T_S	0.0200	1	0.0200	34.04	<0.0001	
H_P * CL	0.0027	2	0.0014	2.30	0.1250	
SO_D * T_S	0.0051	1	0.0051	8.60	0.0080	
SO_D * CL	0.0011	2	0.0005	0.9101	0.4178	
T_S * CL	0.0005	2	0.0002	0.4094	0.6692	
H_P^2	0.0107	1	0.0107	18.14	0.0004	
SO_D^2	0.0225	1	0.0225	38.38	<0.0001	
T_s^2	0.0046	1	0.0046	7.91	0.0104	
Residual	0.0123	21	0.0006			Not significant
Cor. total	5.65	38		R^2	0.9978	
				Adjusted R^2	0.9960	
				Predicted R^2	0.9923	
				Adequate precision	78.7271	

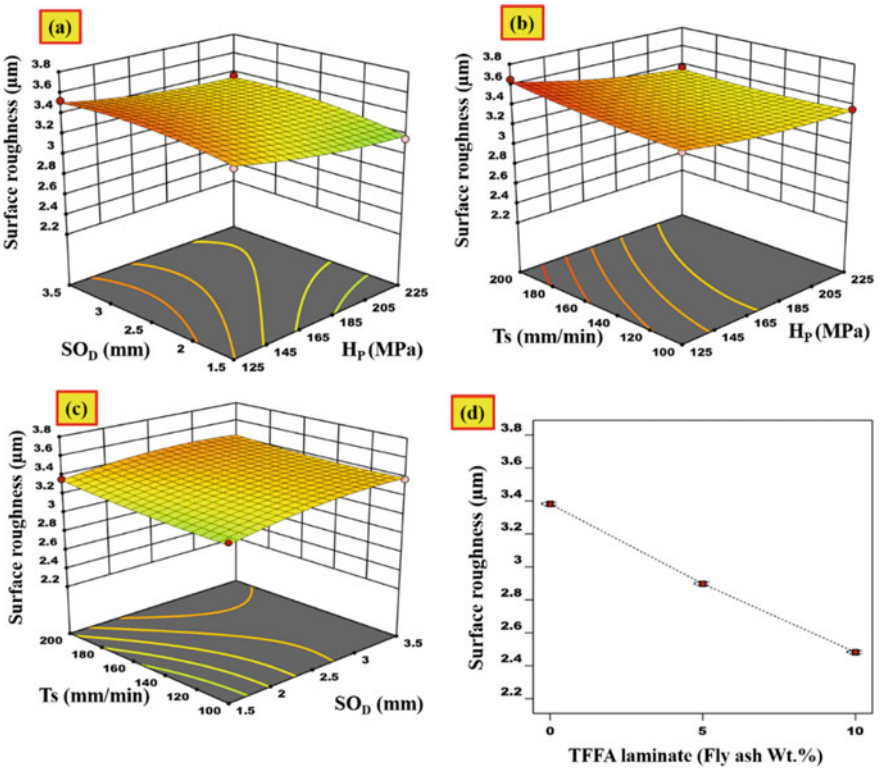


Fig. 5 Surface roughness versus parameter influences

Effect of SO_D on R_a

Next to H_p, the SO_D variable was much affecting R_a value. Figure 5a reveals a maximum R_a obtained at high SO_D. The large distance between nozzle and work increases the jet divergence affecting water beam energy. As a result, the energy transfer to the abrasive particle is attained low level [9]. This is reducing a material removal capability by abrasive particles, and hence, surface variation observed to be high during machining with a high SO_D value. It is a good practice to use optimum SO_D value, otherwise a low SO_D value reduces machining by deaccelerating water jet energy. It is observed an increase of SO_D from 1.55 to 3.5 mm increases R_a by 2.53%.

Effect of T_s on R_a

Table 4, ANOVA results indicate that T_s is not much affecting surface roughness, i.e., showing the least significance compared to other variables. Figure 5b, c reveals a low surface roughness (R_a) value at lower T_s but a condition of high H_P setting. Maximum R_a obtained at high T_s, at the same time, H_P value is kept as low. An increase in T_s increases the striation effect on the machining zone. The available abrasive particles are not completely involved in material removal because interaction time lagging

with advancing water jet. Hence, surface variation observed to be increased at higher T_s. Therefore, measured R_a increased with an increase in T_s. By increasing the T_s from 100 to 200 mm/min, the R_a increased by 5.53%. Accordingly, the machining quality of FRP composites is decided by jet pressure and SO_D [11, 14].

Effect of TFFA Laminate on R_a

From the ANOVA Table 4, CL is a weight percentage of fly ash filler loading in the laminate which is the most influenced factor on control the R_a of the machined surface of laminates. Figure 5d shows that an increase in weight percentage of fly ash reduced R_a. This is showed as fly ash at 0% displaying the highest R_a value when compared to the fly ash at 10%. This could be due to an increase of brittle nature of composite, by the way, increasing brittle–brittle interaction between abrasive and composite [14]. While machining with FA 10% laminate, it is observed a minimum R_a value as compared with fly ash 0 and 5%. The damages observed more in the TFFA0 and TFFA 5%. By increasing the fly ash content (0–10%), the measured R_a value is low by 23.56%. This shows a composite with fly ash particle yielded better surface finish with less R_a value than the without fly ash particle composite.

Figure 6a indicates actual values are very near to the forecast value, and Fig. 6b indicates the residuals against the run number. The residuals of the experiments are within upper and lower limits indicating consistency between run numbers. This evidence of an established model was acceptable for the present analysis.

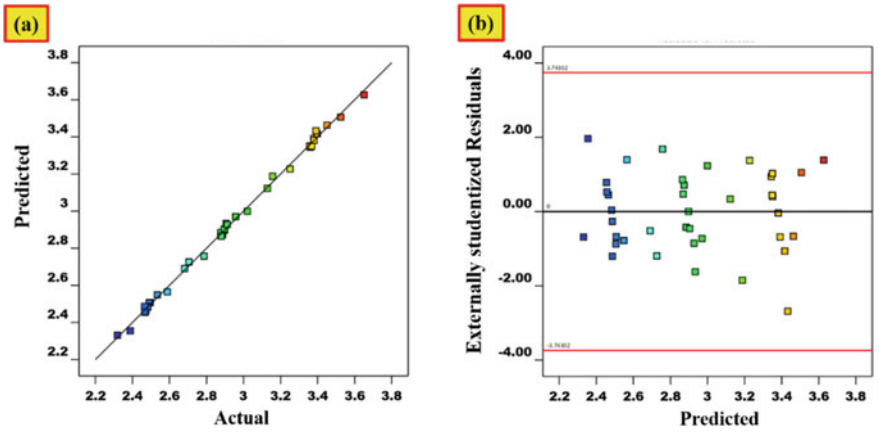


Fig. 6 Surface roughness **a** predicted versus actual, **b** residual versus predicted

4 Conclusions

The present study is to investigate the mechanical and AWJ cutting quality of fly ash filler interleaved flax multi-layered polymeric composite. From the investigation, the following important findings and conclusions are presented.

1. Fly ash fine particle significantly affected the mechanical properties of the interleaved composite. Moreover, fly ash interleaved (TFFA10) composite showed the maximum tensile and flexural strength at 10 wt%. Mechanical properties improved by the tensile strength of 26.5% and flexural strength of 17.8% than without fly ash composite (TFFA0).
2. Fly ash fine particle interleaved flax laminate has exhibited better surface quality without fiber pullouts and fiber splitting.
3. This study reveals attainment of surface quality by AWJ cutting of fiber FRP laminate is a challenging task. The factors considered for machining and its levels are limited by machine capacity, and hence, by controlling specific parameter, water pressure is more dynamic.
4. The surface quality of the laminate improved by increasing water pressure. The pressure is the most significant parameter for the incidence of surface quality.

References

1. Praveen Kumar A, Jeyalal P, Barani Kumar D (2012) Hybridization of polymer composites. Int J Adv Mat Sci 3: 173–182
2. Rajkumar K, Ramraji K, Manojkumar M, Gnanavelbabu A (2020) Validation of tensile strength of notched hybrid polymer composite using Whitney-Nusimer point stress model. Mater Today Proc.https://doi.org/10.1016/j.matpr.2020.01.263
3. Rajkumar K, Ramraji K, Hariprakash VP, Gnanavelbabu A (2019) Comparison study of mechanical and dynamic vibration properties of hole defect introduced in hybrid polymer composite. Mater Today Proc.https://doi.org/10.1016/j.matpr.2019.10.078
4. Praveen Kumar A, Nalla Mohamed M, Kurien Philips K, Ashwin J (2016) Development of novel natural composites with fly ash reinforcements and investigation of their tensile properties. Appl Mech Mater 852: 55–60
5. Ramraji K, Rajkumar K, Sabarinathan P (2019) Tailoring of tensile and dynamic thermo mechanical properties of interleaved chemical-treated fine almond shell particulate flax fiber stacked vinyl ester polymeric composites. Proc Inst Mech Eng Part L J Mater Des Appl 233(11): 2311–2322
6. A. Praveen Kumar, Kumarasamy, G. S. and Nikhil, N. “Analysis of carbon fiber reinforced polymer composite hip prosthesis based on static and dynamic loading.” International Journal of Applied Engineering Research; Vol. 10 No.85 (2015):574–579.
7. Haddad M, Zitoune R, Eyma F, Castanie B (2014) Study of the surface defects and dust generated during trimming of CFRP: influence of tool geometry, machining parameters and cutting speed range. Compos Appl Sci Manuf 66:142–154
8. Shanmugam DK, Chen FL, Siores E, Brandt M (2002) Comparative study of jetting machining technologies over laser machining technology for cutting composite materials. Compos Struct 57(1–4):289–296

9. Prabu VA, Kumaran ST, Uthayakumar M (2017) Performance evaluation of abrasive water jet machining on banana fiber reinforced polyester composite. J Nat Fibers 14(3):450–457
10. Azmir MA, Ahsan AK (2008) Investigation on glass/epoxy composite surfaces machined by abrasive water jet machining. J Mater Process Technol 198(1–3):122–128
11. Unde PD, Gayakwad MD, Patil NG, Pawade RS, Thakur DG, Brahmankar PK (2015) Experimental investigations into abrasive water jet machining of carbon fiber reinforced plastic. J Compos
12. Siddiqui TU, Shukla M, Tambe PB (2008) Optimisation of surface finish in abrasive water jet cutting of Kevlar composites using hybrid Taguchi and response surface method. Int J Mach Mach Mater 3(3–4):382–402
13. Mayuet PF, Girot F, Lamíkiz A, Fernandez-Vidal SR, Salguero J, Marcos M (2015) SOM/SEM based characterization of internal delaminations of CFRP samples machined by AWJM. Procedia Eng 132:693–700
14. Jani SP, Kumar AS, Khan MA, Kumar MU (2016) Machinablity of hybrid natural fiber composite with and without filler as reinforcement. Mater Manuf Processes 31(10):1393–1399
15. Haddad M, Zitoune R, Eyma F, Castanie B (2015) Influence of machining process and machining induced surface roughness on mechanical properties of continuous fiber composites. Exp Mech 55(3):519–528
16. D20 Committee, 2010. Test method for tensile properties of plastics. ASTM D638.
17. ASTM Standards (1958) Philadelphia: American Society for Testing Materials ASTM C
18. Praveen Kumar A, Nalla Mohamed M (2018) A comparative analysis on tensile strength of dry and moisture absorbed hybrid kenaf/glass polymer composites. J Ind Text 47(8): 2050–2073

Advanced Manufacturing Processes of Lightweight Materials

Impact Strength of Ramie/HDPE Composites Manufactured Using Hot Compression Molding

Andi Kuswoyo, Lies Banowati, Khodijah Kholish Rumayshah, and Bambang Kismono Hadi

Abstract In this paper, natural fiber composites made of treated ramie yarn and high-density polyethylene (HDPE) matrix in powder form were manufactured using hot compression molding. The fibers were arranged to make unidirectional ([0°] and [90°]) and bidirectional $[0°/90°]_s$ specimens. A Charpy impact test with a notch was performed to determine the impact strength of ramie/HDPE composites. Statistical analysis using two-parameter Weibull distribution with 50% reliability was used. The result showed that the unidirectional [0°] specimen has a higher impact strength than the bidirectional specimen. Meanwhile, the unidirectional [90°] specimen had the lowest impact strength. The morphology of the fracture surface was analyzed using scanning electron microscope (SEM). It revealed the dominant damage mode, i.e., fiber breakage and pull-out for the unidirectional [0°] specimen, matrix cracking for the unidirectional [90°] specimen, and the combination of matrix cracking and fiber pull-out for the bidirectional specimen.

Keywords Impact strength · Ramie · HDPE · Thermoplastic

1 Introduction

There has been increasing interest in the substitution of synthetic fiber with natural fiber in engineering applications. Several advantages that are offered by natural fiber composite over the synthetic ones are the recyclability, biodegradability, and abundance. In the automotive application, the use of natural fiber composite can reduce the weight up to 25%, thus saving up to 250 million barrels of crude oil [1]. Besides, the use of natural composite in the medical field can support the realization of affordable biomedical equipment [2].

A. Kuswoyo · K. K. Rumayshah · B. K. Hadi
Lightweight Structures Research Group, Faculty of Mechanical and Aerospace Engineering, Institut Teknologi Bandung, Jl. Ganesha 10, Bandung 40132, Indonesia

L. Banowati (✉)
Faculty of Engineering, Nurtanio University, Bandung, Indonesia
e-mail: liesbano@gmail.com

© Springer Nature Singapore Pte Ltd. 2020

A. Praveen Kumar et al. (eds.), *Advances in Lightweight Materials and Structures*, Springer Proceedings in Materials 8, https://doi.org/10.1007/978-981-15-7827-4_43

Indonesia has many natural resources to be used as the raw material for natural fiber because 50% of Indonesia's land is a forestry area [3]. Among the vast diversity of the plant species grown in Indonesia is the ramie plant (*Boehmeria nivea*). Ramie fiber is a strong, lustrous, soft, and fine bast fiber extracted from the inner bark of a ramie plant [4]. Ramie fiber has been used for fabric and clothing purposes since a long time ago. Further development to increase the economic value of ramie fiber led to the use of ramie fiber for a broader application, e.g., as an electrical insulator in industries [4], secondary parts in automotive [5], and medical equipment [2]. Among the countless list of natural fiber, the popularity of ramie fiber is increasing due to its competitive mechanical properties. Table 1 summarizes the mechanical and physical properties of ramie fiber compared to several natural fibers and the conventional glass, aramid, and carbon fiber [5].

Thermoset polymer is used extensively with natural fiber, e.g., ramie/epoxy [6], flax/epoxy [7, 8], natural fiber/vinyl-ester [9], and ramie/polyester [10]. Meanwhile, the use of thermoplastic polymer with natural fiber is focused only on polypropylene (PP) other than the other thermoplastic polymer [11, 12].

Recently, the tensile and flexural strength analysis of ramie fiber with thermoplastic high-density polyethylene (HDPE) matrix has been carried out for both unidirectional and bidirectional fiber in [13] and random fiber in [14]. The result showed that ramie/HDPE composite has moderate tensile and flexural strength.

In this research, a ramie/HDPE composite is manufactured using hot compression molding. The specimens are then prepared for the Charpy impact test with notch according to ASTM. The reliability of the ramie/HDPE composite in terms of its impact strength is analyzed using two-parameter Weibull distribution. In the end, the

Table 1 Physical and mechanical properties of several natural fibers compared to the commercial glass, aramid, and carbon fiber [5]

Fiber	Density [g/cm^3]	Tensile strength [ksi]	Tensile modulus [msi]	Elongation [%]
Ramie	1.50	60–135	8.9–18.6	3.6–3.8
Flax	1.50	75–215	4.0	2.7–3.2
Hemp	1.47	100	10.0	2.0–4.0
Kenaf	1.45	135	7.7	1.6
Jute	1.30	55–110	3.8	1.5–1.8
Sisal	1.50	75–90	1.4–3.2	2.0–2.5
Coir	1.20	85	0.6–0.9	~30.0
Cotton	1.55	60	0.8–1.8	3.0–10.0
E-glass	2.56	290–350	10.0	3.0
S-glass	2.57	665	12.5	2.8
Aramid	1.44	435–455	9.0–10.0	3.3–3.7
Carbon (PAN)	1.67	580	33.0–35.0	1.4–1.8

fracture surface will be analyzed under SEM to determine the damage mode under different fiber orientations.

2 Materials and Manufacturing Method

The mass of each HDPE powder and ramie fiber are measured to achieve the expected composite fiber volume fraction of 50%. The HDPE powder (Fig. 1a) is mixed with the NaOH-treated ramie yarn (Fig. 1b), and the mixture was then placed into a molding. In the first mold, fibers are arranged, so that the orientation is all uniform in one direction. While in the second mold, fibers are arranged, so that the fiber forms in two directions perpendicular to each other. The molds were then placed on a hot compression molding machine (Fig. 1c) with a temperature of 130 °C and pressure of 60 kg/cm^2 for 3 hours. The specimens are then cut to the size of 124.5–127.0 mm length, 12.7 mm width, and 6.35–7.00 mm thickness, and a notch is machined on one face according to the ASTM D6110-04 [15]. The resulted specimens are shown in Fig. 2.

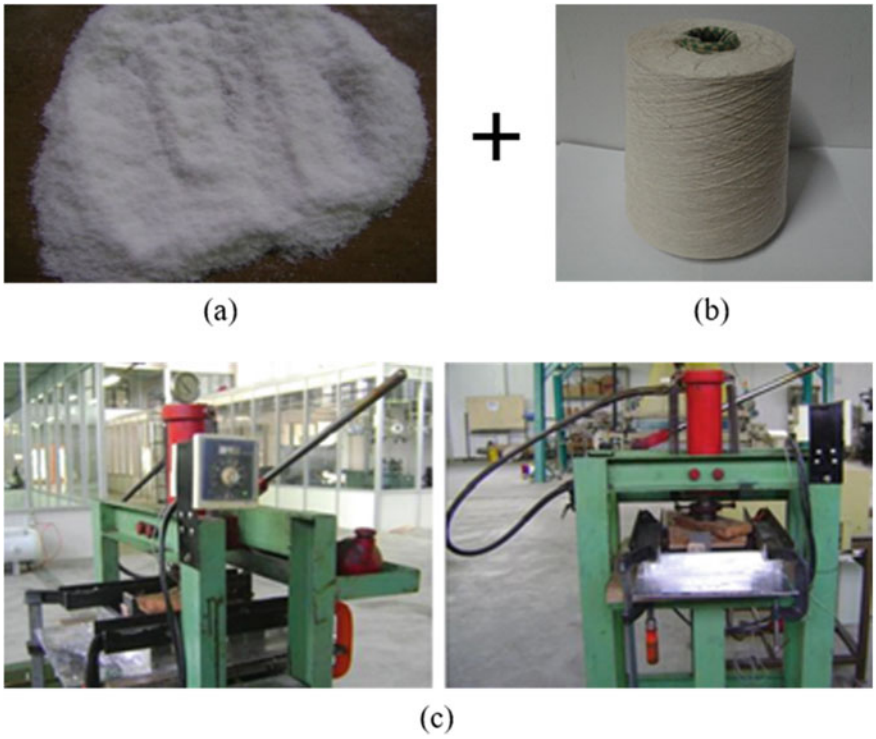


Fig. 1 **a** HDPE powder, **b** ramie fiber, and **c** hot compression molding machine

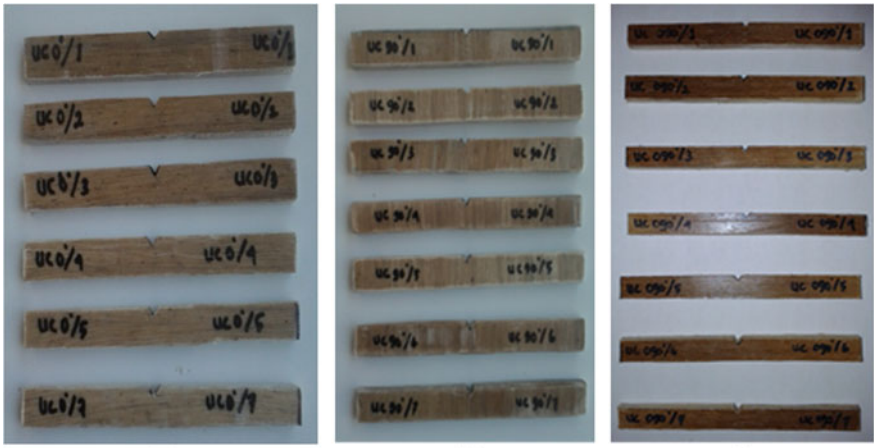


Fig. 2 **a** Resulted ramie/HDPE composite specimens with unidirectional fiber, i.e., **a** [0°] and **b** [90°], and bidirectional fiber, i.e., **c** $[0°/90°]_s$

3 Determination of Strength Using Reliability Analysis

Figure 3 shows the fractured specimen after the Charpy impact test. From the macroscopic observation, it can be seen that the damage mode differs between specimens that depend on the fiber orientation. The [0°] specimen fails from fiber breakage and pull-out, the [90°] specimen fails from matrix cracking, and the bidirectional specimen fails from the combination of matrix cracking and fiber pull-out.

The recorded impact energy from the charpy test is summarized in Table 2. The impact energy indicates the amount of energy absorbed by ramie/HDPE composite

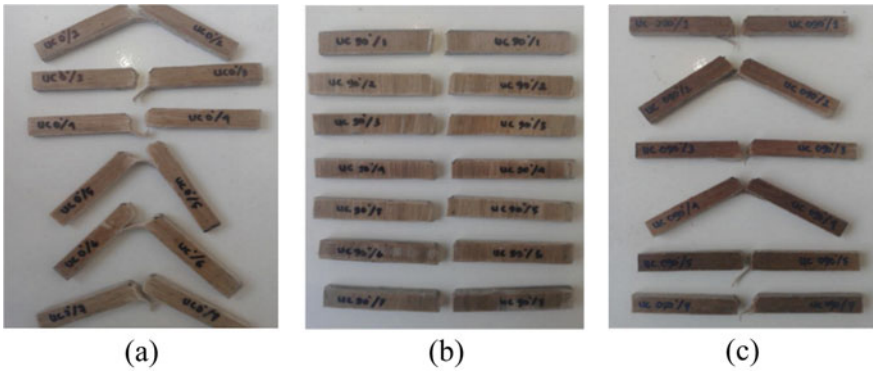


Fig. 3 Ramie/HDPE composite specimens after Charpy impact test with fiber orientation of **a** [0°], **b** [90°], and **c** $[0°/90°]_s$

Table 2 Charpy impact energy and strength of all specimens

Specimen number	Charpy impact energy [J]			Charpy impact strength [J/cm^2]		
	[0°]	[90°]	$[0°/90°]_s$	[0°]	[90°]	$[0°/90°]_s$
1	10.0	2.0	3.0	13.441	2.646	4.280
2	6.0	1.8	3.8	8.736	2.647	5.080
3	6.0	2.0	2.4	9.05	2.442	3.820
4	6.0	1.5	2.0	8.942	2.25	3.050
5	5.0	2.0	2.2	7.072	2.695	3.140
6	8.0	1.8	3.8	11.648	2.639	5.470
7	7.0	1.5	2.4	8.805	2.308	3.540
Average				9.671	2.518	4.059

during fracture. The impact strength is then calculated by dividing the impact energy with the cross-sectional area of the fracture plane. The maximum impact strength is further analyzed using two-parameter Weibull distribution. Figure 4 shows the reliability distribution for each configuration, and Table 3 summarizes the impact

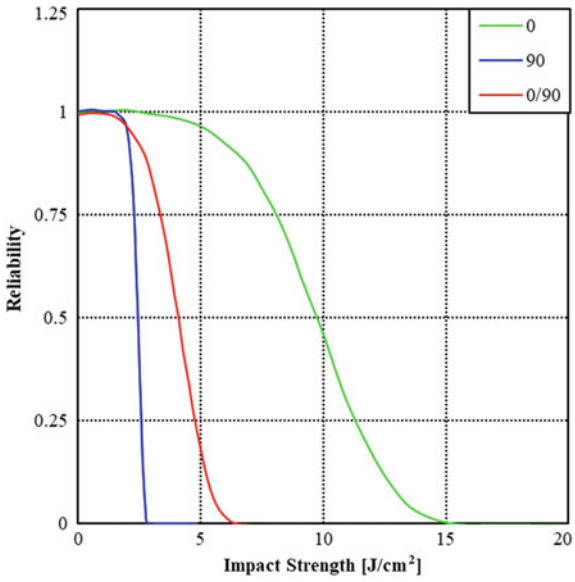


Fig. 4 Reliability curve of the impact strength using two-parameter Weibull distribution

Table 3 Charpy impact strength of the specimens with 50% reliability

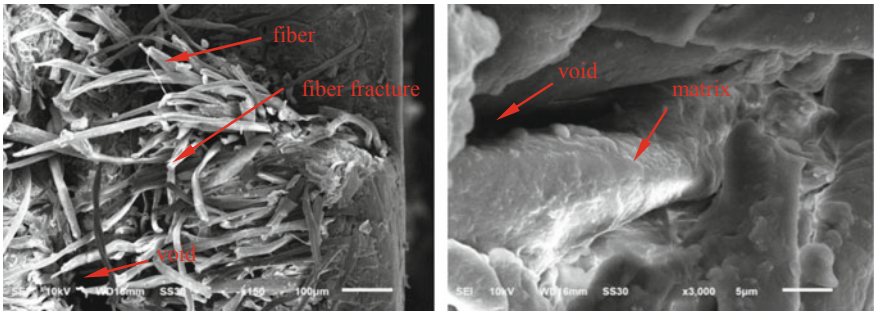
Specimen	Impact strength [J/cm^2]
[0°]	9.68
[90°]	2.52
$[0°/90°]_s$	4.06

strength of each specimen with a reliability of 50%.

In a Charpy impact test, the fracture will tend to propagate in a perpendicular direction to the impactor direction because of the notch presence. The [0°] specimen has the highest impact strength because the fracture is in a perpendicular direction to the alignment of the fiber. Meanwhile, the [90°] specimen has the lowest impact strength. The fracture will propagate in the matrix easily because no fiber is resisting the fracture (see Fig. 3). Therefore, the impact strength of the [90°] specimen will likely be similar to the impact strength of the HDPE matrix.

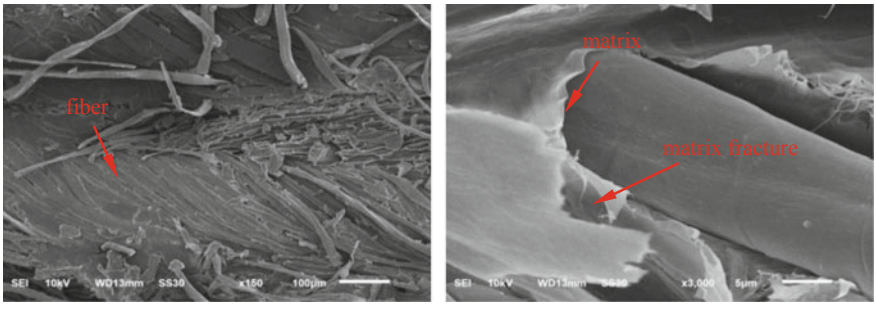
4 SEM Result

Figures 5, 6, and 7 show the scanning electron microscopy (SEM) result of the composite fracture surface after the Charpy impact test. It can be seen that the hot compression molding process results in a less neat fiber arrangement. Besides, as



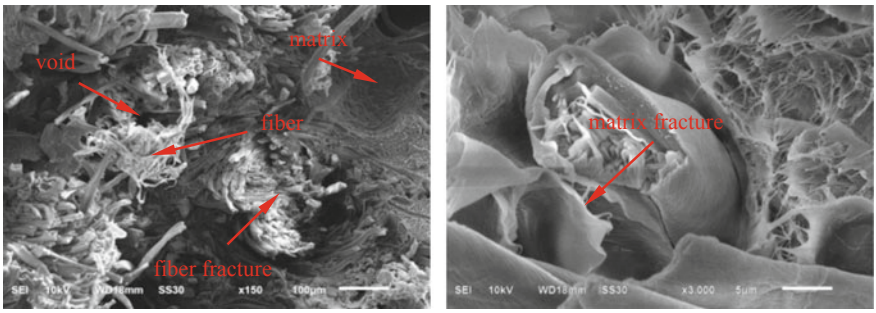
Magnification 150x Magnification 3000x

Fig. 5 SEM image showing the fracture morphology of [0°] specimen



Magnification 150x Magnification 3000x

Fig. 6 SEM image showing the fracture morphology of [90°] specimen



Magnification 150x Magnification 3000x

Fig. 7 SEM image showing the fracture morphology of $[0°/90°]_s$ specimen

seen in Fig. 5, voids are present between matrix and fiber. The presence of the voids makes the fiber-matrix interfacial bonding weaker.

Figure 5 proves that the dominant damage mode for the [0°] specimen is fiber fracture. The fibers appear to be uprooted from the matrix, indicating the low interfacial bonding strength. A further improvement to the fiber coating or the matrix mixture is suggested to increase the interfacial strength between ramie fiber and HDPE matrix. Figure 6 proves that matrix fracture is the dominant damage mode for [90°] specimen. Meanwhile, the dominant damage mode for $[0°/90°]_s$ is the combination of matrix cracking and fiber pull-out.

5 Conclusion

In this study, the impact strength of ramie/HDPE composite manufactured using hot compression molding is analyzed using a Charpy impact test with notch. The impact strength of three composites with different fiber orientations ([0°], [90°], and $[0°/90°]_s$) were compared. The result showed that the [0°] specimen gave the highest impact strength while [90°] is the lowest. The SEM result reveals that the damage mode is fiber breakage and pull out for [0°] specimen, matrix cracking for [90°] specimen, and combination of matrix cracking and fiber pull-out for $[0°/90°]_s$ specimen.

Acknowledgements This research has been carried out by the partial support from Ministry of Research, Technology, and Higher Education of Republic Indonesia (Penelitian Dasar Unggulan Perguruan Tinggi, PDUPT), and Institut Teknologi Bandung (Research and Community Service/P3MI) 2018.

References

1. Praveen Kumar A, Jeyalal P, Barani Kumar D (2012) Hybridization of polymer composites. Int J Adv Mater Sci 3: 173–182
2. Praveen Kumar A, Jackson Irudhayam S, Naviin D (2012) Review on importance and recent applications of polymer composites in orthopaedics. Int J Eng Res Dev 5(2): 40–43
3. Data and information on indonesian forestry thematic mapping. Indonesian Ministry of Forestry and Environment, 2018 (in Bahasa Indonesia)
4. Debnath S (2017) 3—Sustainable production of bast fibres. In: Sustainable fibres and textiles. Elsevier Ltd., pp 69–85
5. Praveen Kumar A, Nalla Mohamed M, Kurien Philips K, Ashwin J (2016) Development of novel natural composites with fly ash reinforcements and investigation of their tensile properties. Appl Mech Mater 852: 55–60
6. Kishi H, Fujita A (2008) Wood-based epoxy resins and the ramie fiber reinforced composites. Environ Eng. Manage J 7(5):517–523
7. Sparnins E (2009) Mechanical properties of flax fibers and their composites. Lulea University of Technology, Sweden
8. Bos H (2004) The potential of flax fibres as reinforcement for composite materials. TU Eindhoven
9. Alhuthali A, Low IM (2013) Mechanical properties of cellulose fibre reinforced vinyl-ester composites in wet conditions. J Mater Sci 48(12)
10. Wang HM, Sun YQ, Wang JB, Guan YT, Zheng SR, Sun ML Exploring of a new natural fiber composite Ramie Fabric/UP Composite
11. Taha I, El-Sabbagh A, Ziegmann G (2008) Modelling of strength and stiffness behaviour of natural fibre reinforced polypropylene composites. Polym Polym Compos 16(5): 295–302
12. Malkapuram R, Kumar V, Negi YS (2009) Recent development in natural fiber reinforced polypropylene composites. J Reinf Plast Compos 28(10):1169–1189
13. Banowati L, Hadi BK, Suratman R (2014) Tensile and flexural strengths of ramie/HDPE thermoplastic matrix composites. In: The 7th AUN/SEED-Net regional conference on mechanical and manufacturing engineering (RCMME), pp 99–103
14. Banowati L, Hadi BK, Suratman R (2016) Tensile strengths of random ramie yarn/HDPE thermoplastic matrix prepreg composites. In: International conference on computational modeling, simulation and applied mathematics (CMSAM 2016)
15. ASTM D6110-04 (2004) Standard test methods for determining the Charpy impact resistance of notched specimens of plastics. West Conshohocken, PA

A Review on Coolant Feeding System of CNC Machining Process

Araveeti C. Sekhara Reddy, D. V. Paleshwar, K. L. N. Murthy, and B. Sandeep

Abstract CNC manufacturing has been evolved into the modern multi-process and multi-axis machining operation. The advances in hardware design increased productivity. This development brought an advanced feature for CNC machines such as automatic lubrication systems, automatic tool length setters, and coolant-fed tooling systems. A large amount of heat can be liberated from CNC machining operation due to friction developed at the tool–work interface. To reduce friction at the cutting zone and to improve the cutting performance a coolant-fed tooling system is used. The coolant-fed tooling system greatly reduces the friction and temperature and improves the surface finish. The present paper focuses on various types of coolant supply systems, viz coolant-fed tooling system, through the spindle coolant system, etc. It was concluded that the coolant-fed cutting tools can best improve production efficiency due to the pressurized coolant.

Keywords CNC machine · Machine control unit · Coolant-fed system · Part program

1 Introduction

The computer numerical control (CNC) machine is a programmable unit capable of performing automatic machining operations. The term NC relates to automatic control of a cutter, and the concept of CNC came into existence for the replacement of integrated circuit (IC)-based controls with microprocessors and microcomputers. The cutting fluid can cool and lubricate the work–tool interface in the CNC machining process. It employs computerized controls for coolant supply, and the right coolant system can improve the tool life, surface finish, and accuracy.

A. C. S. Reddy (✉) · D. V. Paleshwar · K. L. N. Murthy · B. Sandeep
Department of Mechanical Engineering, Sreyas Institute of Engineering and Technology, GSI, Nagole, Hyderabad, India
e-mail: acsreddy64@gmail.com

© Springer Nature Singapore Pte Ltd. 2020

A. Praveen Kumar et al. (eds.), *Advances in Lightweight Materials and Structures*,
Springer Proceedings in Materials 8, https://doi.org/10.1007/978-981-15-7827-4_44

1.1 Constructional Feature of CNC Machines

The CNC machine is having different elements such as controllers, motors, and motion controls for performing different functions. However, CNC machines are more rigid and precise, compared to conventional machine tools. One of the most important elements in the CNC machine is the controller. It is brain of the machine which sends command signals required to run the program. The controller consists of an interface such as a Universal Serial Bus (USB) or a floppy disk to upload the part program into a central processing unit of the machine. It also has a mechanism to convert the low-voltage output of the computer into line voltage suitable to drive the motor. Either an open-loop or closed-loop controlled system can be used in a CNC machine, and Fig. 1 shows the closed-loop controlled system. The different types of motors viz stepper motor, servo

motor, linear motor, and the hydraulic motor is used. A stepper motor moves a small fraction called a "step" or " basic length unit" for every pulse of electricity. No feedback system builds using stepper motor in general and assumes that the required steps of rotation make accurate. The servo motor is sophisticated and runs significantly faster than the stepper motor with higher torque. The CNC machine can also be provided with different accessories such as bar feeders, tool changers, pallet, and coolant feeding tool.

2 Literature Review

Duda et al. [1] presented the architecture of the CNC machine program using the meta-knowledge obtained from the intermediate states of the work piece. It is the process plan used in CNC machining operation with the application of a computer.

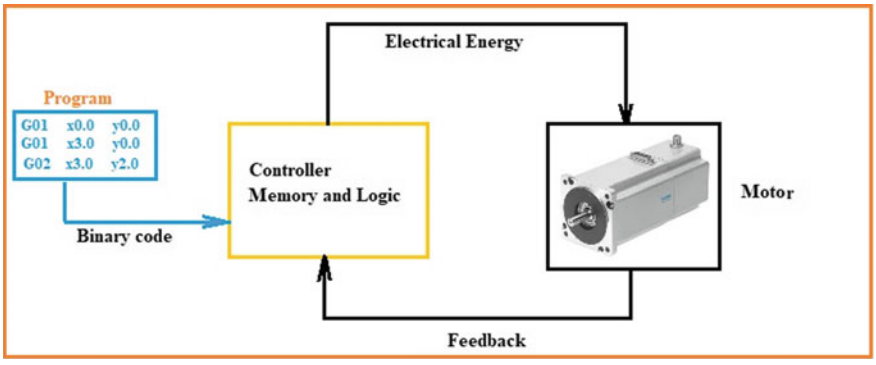


Fig. 1 Basic CNC schematic

Different types of algorithms were developed for CNC machining, and the manufacturing knowledge was presented in the sequence of hierarchical decision nets. Experimental analysis on the fluid power subsystems and relationships between specific energy demanded and the effect was studied by Weber et al.

Weber and Weber [2] while using the machining center and concluded that the control over the thermoelastic response from machine tools for the thermal deformations is necessary to develop systems to describe thermo–fluidal models. According to Wegener et al. [3], different fluids were used for lubrication, sealing, cleaning, and transmitting force/energy. It was found through their research that the fluid system remains an exciting field of research for finding out the interaction of tool elements with the lubricating system for the success of the CNC machine tool through the improvement of the performance and efficiency. They concluded that the success of CNC machine tools depends on the thorough understanding of fluid properties and their interaction with the elements of the machine tool. Tai et al. [4] summarized the challenges with the application of technology on the minimum quantity lubrication (MQL) concept. It is the process of applying a very little quantity of cutting fluid in the mist form at the cutting location instead of flooding of the cutting fluid over the workpiece. This saves significant energy. The authors also reviewed the present status and its limitations during machining, and also highlighted the possibilities of further research and development.

Tarek et al. [3]. experimented on Ti555–3 titanium alloy having wide applications in the aeronautical engineering industry. They performed a turning operation using high-pressure coolant (HPC) and compared the jet variable pressure with conventional machining operation under classical lubrication. It was proved that productivity was improved through machining under HPC conditions. The chip fragmentation was good and also increased tool life. It has to be kept in mind that the surface residual stresses were dropped to more negative with an increase of fluid pressure as shown in Fig. 2. This resulted in a reduction in the coefficient of friction and low temperature in the machining area and increased machinability of the Ti555–3 alloy material. Kundrak et al. [5] researched the effectiveness of coolant usage in large quantities on the environment. In the present days, environment protection has become a crucial factor, and the usage of a large quantity of coolant is injurious and polluting the atmosphere.

They concluded that the use of a huge quantity of coolant has to be replaced with dry machining through minimal coolant and lubrication.

Palanisamy et al. [6] performed an experimental analysis of titanium machining, to find out the influence of coolant pressure at a different pressure range of 7–70 bar. The use of highly pressured coolant improved the tool life of the cutting tool. The different factors of cutting while using the coolant under high pressure depend on cutting velocity, depth of cut, the position of the nozzle, and tool geometry. It was also observed from the experiment that the coolant nozzle outlet is an important consideration for having a good surface finish. The life and efficiency of the cutting tool depend upon the heat generated in the cutting zone, and low-pressure conventional methods of cooling are insufficient to penetrate to control thermal, frictional, and surface finish conditions. Kaminski et al. [7] explored the influence of a high

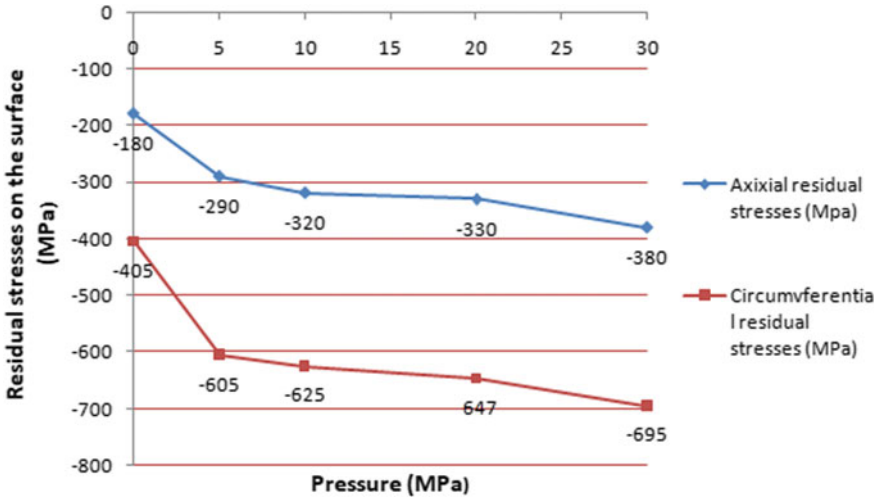


Fig. 2 Residual stresses variation w.r.t pressure ($Vc = 50$ m/min, ap $= 0.5$ mm, $f = 0.15$ mm/rev) [3]

and ultra high-pressure water jet coolant systems on cutting tool temperature, chip shapes, cutting forces, and roughness of the surface generated in regular turning operations. From the results, it was observed that 40–45% reduction of temperature at the tool edge with the coolant jet pressure range of 40–300 MPa.

3 Cooling Systems Used in CNC Machines

The cutting fluid performs cooling and lubrication for metal cutting operations. Most of the coolants are made from petroleum distillates, animal fats, plant oils, and water. The high-pressure coolant pumping system can be used to supply the coolant at a high pressure and speed without damage to the machine tool, the workpiece, and the tooling. The high-pressure cooling process outperforms the conventional flood cooling system and has the advantages viz 1. Increased life of the tool, 2. Good quality of machined surface, 3. Better evacuation of the chip generated, 4. Very smooth flow of the coolant, 5. Most economical way of coolant-fed tooling system, 6. less tool maintenance costs, 7. Any type of coolant can be effectively used, 8. Completely self-contained unit, 9. An automatically detection of overloading and protection, and 10. Dirty filter alarm arrangement facility.

According to the survey report from Simon et al. [8] and from Table 1, it was observed that the flood coolant is widely used in comparison to other coolants viz; high-pressure coolant, dry cutting, mist cooling, minimum quantity lubrication, etc.

According to Sarıkaya et al. [9], the use of MQL increases the surface finish. Sredanovic et al. [10] performed experimental tests for finding out the influence of

Table 1 Cooling systems used in a CNC machine tools

Cooling method	Companies using (%)
Flood coolant	56.7
High-pressure coolant	39.8
Dry	28.9
Mist	5.9
MQL	5.5
Other	10.5

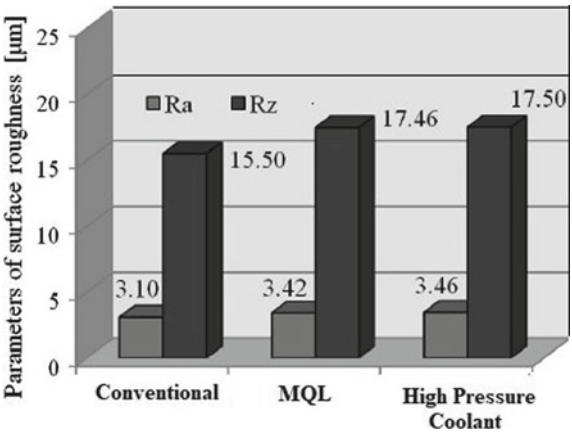


Fig. 3 Surface roughness parameters for different cooling and lubrication conditions [10]

different cooling and lubrication techniques using C45E carbon steel with 150 × 250 mm size. The machined surface with different cooling systems was shown in Fig. 3, and a high-pressure coolant system produced a better surface finish compared to conventional and MQL methods. A large amount of heat is liberated from CNC machining operations due to the friction developed at the cutting tool and work piece interface. Variety of coolants such as liquid (straight oil, synthetic oil, soluble oil, semisynthetic oil), straight oils (vegetable oil, fats, easters), synthetic fluid (organic and inorganic compounds), soluble oils, semisynthetic fluids, gels, aerosols, CO_2 can be used as a coolant. Air can be used for only very low cutting operations. During a heavy cutting environment, the tool has to be cooled continuously using liquid coolant for removing heat and to improve lubrication. The lubrication through coolant supplied can avoid a chip welding with the tool rake face. The coolant is pumped directly at high pressure, high volume on the tool–chip interface. With the advancement of technology, the principle of minimum quantity lubrication and cryogenic cooling methods have been developed. The major properties of coolant are effective cooling, lubrication, corrosion resistance, chemical, and physical stability. High-pressure coolant fed through holes in cutting tools has the advantages viz 1. It can improve the inner surface of the holes. 2. Lesser the chips, less likely have the impact and scar on the inside surface of the hole. 3. Highly pressured coolant improves

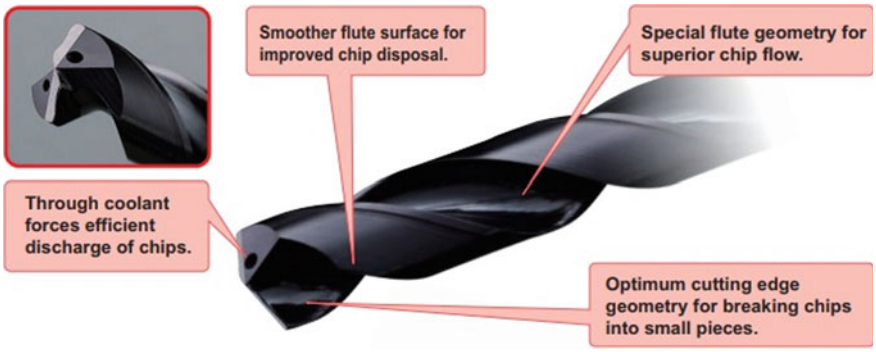


Fig. 4 Solid carbide drill with the coolant feeding holes

the hole straightness when drilling a deep hole of nine times the diameter of the hole. 4. The high pressure makes, no packing and clogging the flutes and subsequently, no pushing of drill around the hole make close tolerances in the hole generated. 5. The high-pressure coolant through holes increases feed rates and supports for quality chip formation. The high-speed cutting tools require cooling and lubrication to reduce tool wear and overheating which highly influences the life of the cutting tool. The Flood coolant system sprays onto the workpiece surface very near to the cutting and a having less influence in getting the fluid flow onto the edge of the cutting tool.

3.1 Coolant Fed Drilling Tools

Figure 4 shows the solid carbide drill having coolant feeding holes at the cutting point. Through coolant holes along the axis of the drilling extended up to the cutting tip makes the fluid to forcefully remove the chips from the drilled hole immediately after generation. It avoids the re-cutting of the chips and improves the surface finish.

Figure 5 shows the supply of the high-pressure coolant through the tooltip during the end milling operation. The high-pressure in the range of 1.5–7.0 MPa supplied to a tool cutting point can effectively remove the chips.

3.2 End Mills with Coolant Holes

Applying of high-pressure coolant through holes in tool shown in Fig. 6 can cool the cutting zone and aid chip evacuation. The cutting process with the provision of coolant holes in tools will avoid the welding of chips onto tool surfaces. In standard milling, the life of the cutting tool increased with the arrangement of coolant holes in the form of spiral shapes. Due to the increased demand from industries, there is a

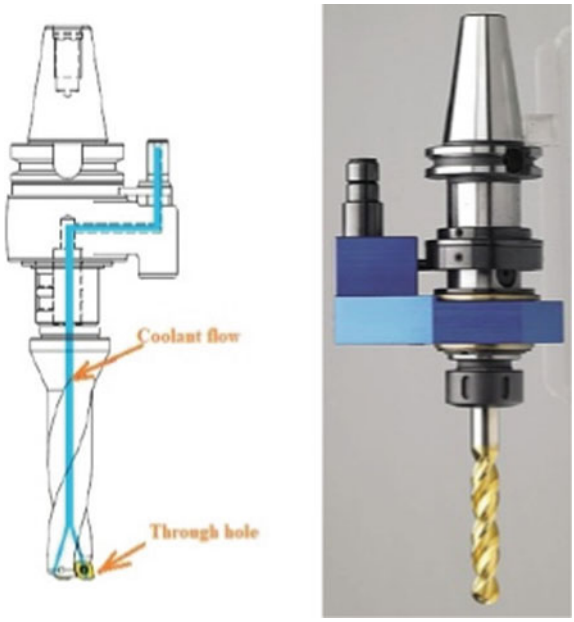


Fig. 5 Rotary coolant feeders

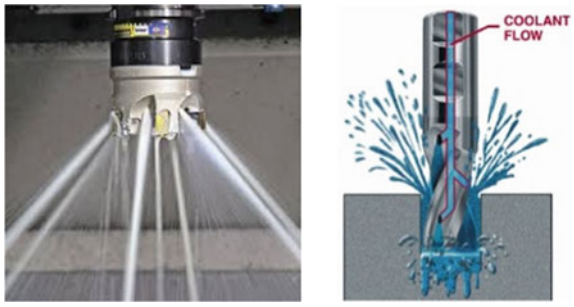


Fig. 6 Coolant-fed milling cutters

variety of face milling tools with multiple coolant holes for different applications. It is a much efficient tooling method than external coolant flow tooling and increases the tool life as well as the performance in different milling applications. A special coating for the tool surface reduces the cutting resistance and also increases the discharge of chips. This coating can also provide good resistance against heat and oxidation which allows low frictional coefficient and low wear of the tool. Various advantages of using coolant-fed tooling are 1. Improved surface finish, 2. Prolonged insert life, 3. Dynamically balanced holders, 4. Dramatically improved chip evacuation, and 5. Heavy-duty driving keys for transfer of high torque.

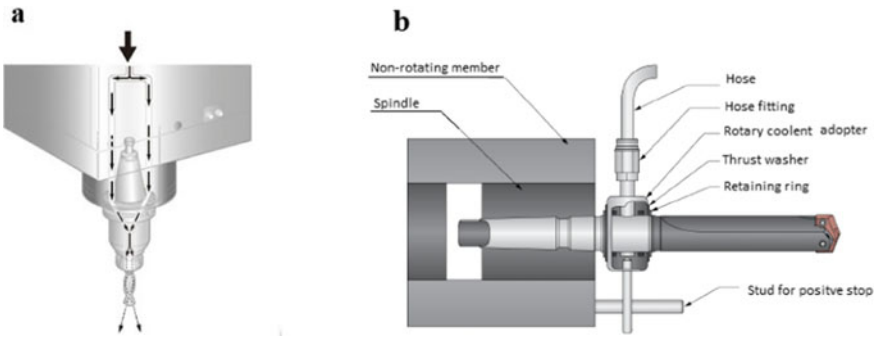


Fig. 7 Through-spindle coolant system **a** flow diagram and **b** sectional view

3.3 Through-Spindle Coolant (TSC) System

Through-spindle coolant (TSC) system is an alternative to flood coolant system.

Figure 7 shows the principle of the TSC system. The coolant flows through the tool and discharges at the cutting edge with high pressure, making easy removal of chips. The coolant from the rotating union flows into the spindle axially and makes better control on tool temperature rise. It offers low machining costs by means of control over the overheating of a tool along with higher productivity rates. A union can be used for delivering the coolant into the spindle. The special features of the coolant feeding system are 1. Ideal for indexable drills and solid carbide drills, 2. Increased surface finish, and 3. Reduced tool failure risk due to chip blockage.

4 Conclusion

The importance of the coolant system in the machining process has been discussed in this paper. Different types of coolant systems viz fed coolant systems and through-spindle coolant systems, were compared. It was concluded that the tool-fed cooling system is superior and having more tool life, increased surface finish, and less power consumption. Hence, the coolant-fed tooling system can be effectively used in a CNC machining operation, and it reduces the idle time and improves the machining quality by the use of an efficient coolant supply system.

References

1. Duda J, Pobozniak J (2017) The architecture of intelligent system for CNC machine tool programming. Procedia Manuf 11: 501–508

2. Weber J, Weber J (2014) Thermo-energetic analysis of the fluidic cooling systems in tooling machines. In: 9th international fluid power conference, Aachen
3. Braham-Bouchnak T, Germain G, Morel A, Furet B (2015) Influence of high-pressure coolant assistance on the machinability of the titanium alloy Ti555-–3. Mach Sci Technol 19(1):134–151
4. Tai BL, Stephenson DA, Furness RJ, Shih AJ (2014) Minimum quantity lubrication (MQL) in automotive powertrain machining. Procedia Cirp 14:523–528
5. Kundrak J, Mamalis AG, Gyani K, Markopoulos A (2006) Environmentally friendly precision machining. Mater Manuf Processes 21(1):29–37
6. Palanisamy S, Townsend D, Scherrer M, Andrews R, Dargusch MS (2009) High pressure coolant application in milling titanium. Mater Sci Forum Trans Tech Publ 618:89–92
7. Kaminski J, Alvelid B (2000) Temperature reduction in the cutting zone in water-jet assisted turning. J Mater Process Technol 106(1–3): 68–73
8. Simon AT, Lima CRC (2015) Computer numeric control machine tools utilisation by metalworking companies in Brazil. Int J Manuf Res 10(3): 267–285
9. Sarıkaya M, Güllü A (2014) Taguchi design and response surface methodology based analysis of machining parameters in CNC turning under MQL. J Clean Prod 65: 604–616
10. Sredanovic B, Globocki-Lakic G, Cica D, Kramar D (2013) Influence of different cooling and lubrication techniques on material machinability in machining. Strojnič̆ski Vestnik J Mech Eng 59(12):748–754

Experimental Execution Analysis of Wire Electric Discharge Machining



Manikyam Sandeep and P. Jamaleswara Kumar

Abstract Wire electrical discharge machining (WEDM) is electrowarm non-customary machining procedure utilize for machining electrically conductive equipment that are difficult machine. Material clearing in WEDM is by strategies for streak crumbling. WEDM is shown to be the choice for making complex parts with more significant level of dimensional precision and better surface culmination. Consistently, a lot of research was comprehensively completed to investigate the WEDM procedure capacity. This paper plans to investigate the examination work carried on parametric impact of WEDM process factors on different yield execution measures. The paper likewise features different demonstrating procedures to foresee ideal machining conditions and investigate the practicality of applying WEDM procedure to machine propelled materials. The last segment examines the advancement and conceivable research pattern in WEDM process.

Keywords Wire electrical release machining · Surface harshness · Material evacuation rate: surface roughness · Streamlining

1 Introduction

Wire electrical discharge matching (WEDM) is unique warm machining method that is ready to make undoubted machining parts with changing hardness or complex shapes, which have sharp edges that are difficult to machinate through standard machining structures. Investigated machining properties of Ti–6A1–4V as dielectric with lamp oil and purified water. The results show that MRR is progressively more noticeable when machining in purified water than in lamp oil and that relative anode wear range is low [1].Investigated Ebb and flow efforts to improve small-scale boring. The focus of this paper is to develop a novel approach to detect micro-scale gaps in micro-EDM capabilities with high aspect ratio. In the light of the fluidization building of ultrasonic degassing, a strategy for converting ultrasonic vibrations into

M. Sandeep (✉) · P. Jamaleswara Kumar
Department of Mechanical Engineering, Koneru Lakshamaiah Education Foundation (Deemed to be University, Guntur, Andhra Pradesh 522502, India
e-mail: sandeep.mech109@gmail.com

© Springer Nature Singapore Pte Ltd. 2020

A. Praveen Kumar et al. (eds.), *Advances in Lightweight Materials and Structures*,
Springer Proceedings in Materials 8, https://doi.org/10.1007/978-981-15-7827-4_45

micro-EDM forms is conceptualized and created [2]. The main ideas are that as the electrical filed between workpiece and tool has significant effect on the occurring sparks, reducing electrical field leads to descending sparks and as a logical result, influences EDM process factors, one of which is decreasing side overcut [3].

Ultrasonic vibration is brought into small-scale EDM and examines the effect of ultrasonic vibration on EDM method. A four-turn EDM machine device made to meet ultrasonic and low-level EDM [4]. Machining system that reinforces micro-electronic discharge machining (MEDM) and micro-ultrasonic machining (MUSM). They showed that diameter variation between entry and exit (DVEE) can be estimated at about 150 mm in width and about 2 mm in small-scale openings with depth of 500 mm. They received small-scale openings with roundness estimate of 2 mm [5]. Explained to make the execution in the microholes in conventional machines possible [6]. Investigates the mechanism by which flushing (flushing modes and flushing parameters) influences machining performance indices, i.e material removal rate and tool wear rate [7]. Explain that when width is less than 0.1 mm, parameters that affect machining process miniaturized scale openings are more than 20 times aspect ratio used by electro-diffraction penetration process [8]. Investigated the properties of small-scale EDM material ejection using single RC-beat discharges. They have point by point assessed breaking down capability of material departure at low-imperativeness [9,10].

2 Methods

2.1 Taguchi Method

Taguchi system remembers diminishing the assortment for a strategy through amazing structure of examinations. The general objective of the system is to make first rate thing expecting practically no push to the maker. Taguchi developed a system for arranging examinations to look at how different parameters impact the mean and change of a strategy execution trademark that portrays how well the method is functioning. The preliminary arrangement proposed by Taguchi incorporates using balanced groups to sift through the parameters affecting the strategy and the levels at which they should be contrasted, thusly saving time and resources.

3 Experimental Setup

For a rapid consistent evacuation of material, however, the control of flash conditions must be ideally controlled in the middle of activity of the material expulsion, contingent upon the state of release, and consequently one of the most significant issues are the strategy for controlling the sparkle hole and time of sparkle during

Table 1 Synthetic creation of the material

Material	C	Si	Mn	P	S	Cr	Mo	Cu	**V**
%	0.33	0.9	0.29	0.03	0.02	4.9	1.3	0.026	0.07

the material expulsion activity, is currently put it to the current procedure of sparkle disintegration machining. The synthetic creation of the material is shown in Table 1. This test study has been structured in regard to these conditions, and an item thereof is to give a sparkle control framework to kick the bucket sinking electrical release machining in which a bounce period and hop separation relating to state of release are naturally chosen by a servo control framework. The ideal sparkle hole and flash time are constrained by servo control dependent on the state of release.

4 Material Removal Rate (MRR)

Most extreme MRR is gotten at high pinnacle current 45 A and beat on time at 580 μs. This can be clarified based on increment in the pace of release vitality, as high centralization of release vitality in the sparkle hole prompts quick dissolving and vaporization of metal, which prompts ascends in the MRR. It was seen from the plots that MRR increments from 14 to 29.03 mm^3/m increment in top current and heartbeat on schedule. The material removal rate in EDM is shown in Fig. 1.

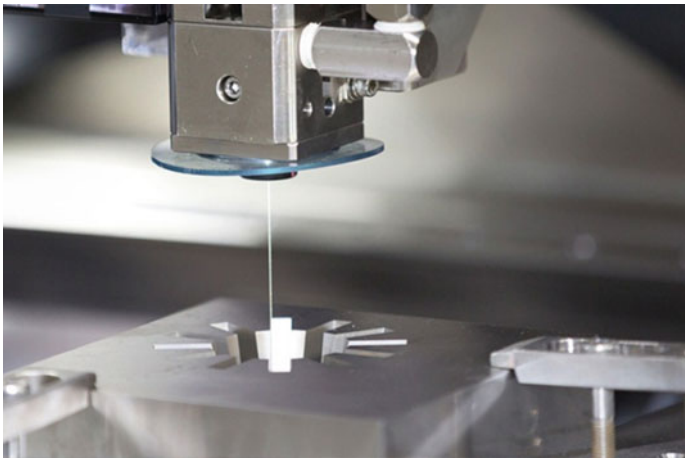


Fig. 1 Material removal rate in EDM

Table 2 Wire EDM parameters and their levels

S. No.	Parameter	Icon	Stage 1	Stage 2	Stage 3	Unit
1	Heartbeat under schedule	TON	5	10	–	μs
2	Heartbeat rotten moment	TOFF	23	36	52	s
3	Untie energy	OV	5	10	15	V
4	Supply velocity abrogate	FR	10	20	30	mm/min
5	Line supply	WF	5	10	15	mm/s
6	Servo energy	SV	35	55	75	V
7	Wire strain	WT	5	10	15	N
8	Flush force	WP	5	5	7	kg/cm^2

4.1 Surface Harshness Estimation

In view of ANOVA, the model estimation of 550.62 infers that the form important. There is only 0.01% probability that "model worth" colossal could occur in view racket. Inference of "Test >" under 0.0500 prove the "nonattendance of fit worth" of 0.8937 proposes that the nonappearance of fit is not imperative similar with the unadulterated goof. There is 89.37% plausibility that "nonappearance of fit worth" enormous can occur on account of upheaval. The "Pred." of 0.9921 reasonable simultaneousness with "Adj." of 0.9959. "Adel Precision" evaluates sign to uproar extent. An extent more noticeable than 4 is alluring. Wire EDM working parameter levels are shown in Tables 2 and 3.

4.2 Selection of Cutting Parameters

Force: It calls attention to the various degrees of intensity that can be provided by the generator of the EDM machine.

Heartbeat Frequency: Pulse frequency is depicted as number of cycles made at beginning second. Heart rate frequency (KHz) = 1000/Total Cycle Time (s) = 1000/Pulse On + Pulse Off (s).

Electrode Material: Generally, device materials are characterized into metallic, non-metallic, and mix of metallic and non-metallic materials.

Electrode Shape: The presentation qualities chiefly rely on the apparatus shape. Numerous shapes in cathode, for example, rectangular, square, cylindrical, hexagonal, and circular.

Kind of Dielectric: Dielectric medium goes about as a separator medium which does not immediate power and used to flush the deteriorated particles. Paraffin, white spirit,

Table 3 Working parameters of EDM

S. No.	Ton	Toff	OV	FR	WF	SV	WT	WP
1	5	22	5	15	7	40	5	5
2	5	22	15	15	25	45	15	7
3	5	22	10	20	15	65	20	5
4	5	37	5	25	20	65	20	3
5	5	37	15	25	10	70	7	3
6	5	37	10	25	7	30	15	5
7	5	37	5	30	5	70	15	5
8	5	52	15	30	15	30	10	5
9	5	52	10	25	10	50	5	5
10	10	22	5	20	25	40	15	3
11	10	22	10	15	5	40	10	3
12	10	22	10	10	15	55	3	3
13	10	37	2	15	10	55	10	5
14	10	37	3	25	5	50	5	7
15	10	37	10	15	15	50	15	7
16	10	52	3	10	15	35	5	7
17	10	52	10	15	10	30	7	3
18	10	52	15	25	5	65	10	3

kerosene, deionizer water, hydrocarbon fluids, and transformer oil are the distinctive EDM dielectric liquids.

5 Impact of Process Parameters on MRR

For the EDM process, the most part utilized in assembling of kick the bucket and shape segments, similar to sheet metal press bites the dust, expulsion passes, on and so on. Model and uncommon structure embeds producing, where surface harshness assumes a noteworthy job. Surface unpleasantness of the WEDM machined parts is basically subject to the procedure parameters. Examination because of procedure parameters on harshness of WEDM machined segments was completed by a few specialists. The impact of procedure parameters, for example, voltage and current on fluctuating thickness of various evaluations of steel material specifically 1040, cold work instrument steel, and plastic shape steel were done. It is watched for same procedure parameter blend, diverse unpleasantness esteems are gotten because of progress in the material property. The impact of procedure parameters, similar to beat length, beat off time, open circuit voltage, servo feed, servo voltage, dielectric

flushing pressure, wire feed, and wire strain on surface harshness of Ti6Al4V material, AISI 4140 steel material, and AISI D2 device steel material were considered. It was discovered that unpleasantness of Ti6Al4V was fundamentally influenced by servo voltage, wire feed, and wire strain while the effect of open circuit voltage was winning in machining AISI 1040 steel material. The effect of system parameters, for instance, beat on plan, beat off time, top stream, wire estimation, wire strain, wire feed, and dielectric flushing pressure on machining of Inconel 601 material was resolved.

6 Determination of Perfect Levels

An evaluation of the change (ANOVA) as shown in Table 4 shows centrality key segments toward the MRR. Reaction Table 5 shows generalizability every reaction trademark degree each factor. Tables land at places that depend on delta estimations, which are viewed as straightforward huge impacts. Delta estimation is less normal of each factor. Kills areas subject to Minitab delta undertakings. For the situation of the most significant delta from rank 1, the second generally significant from rank 2, etc. Positions show the general earnestness of each factor accordingly. Positions and

Table 4 Experimental outcomes for MRR and surface roughness request. MRR "most good"

S. No.	MRR mm/min	S/N	Surface μM	S/N
1	44.98	32.629	2.32	−3.367
2	53.22	33.154	3.23	−6.789
3	43.20	31.689	3.20	−8.778
4	42.60	31.319	3.34	−9.865
5	42.20	31.268	2.39	−5.757
6	38.20	30.617	3.90	−8.865
7	38.40	30.877	2.49	−4.56**3**
8	32.30	28.831	2.98	−8.986
9	32.50	28.386	1.53	−9.876
10	59.70	36.380	2.07	−5.875
11	56.70	36.134	3.98	−8.987
12	50.80	36.184	3.54	−9.985
13	53.80	37.179	4.65	−10.435
14	41.30	31.797	5.45	−8.546
15	49.10	31.648	2.88	−8.764
16	44.90	31.427	2.62	−6.874
17	46.60	32.263	1.23	−9.875
18	43.10	32.043	3.98	−10.876

Table 5 Analysis of variance of MRR

Level	Ton	Toff	Ov	Fr	Wf	Sv	Wt	Wp
1	31.02	34.3	34.9	33.9	34.06	33.98	32.52	33.32
2	33.89	32.0	34.9	34.9	33.8	34.9	33.36	33.4
3	3.92	32.8	32.8	33.8	33.4	32.8	33.05	32.9
Delta	1.89	2.55	0.97	12.0	0.44	0.9	0.83	0.35
Rank	4	1	3	4	5	9	3	5

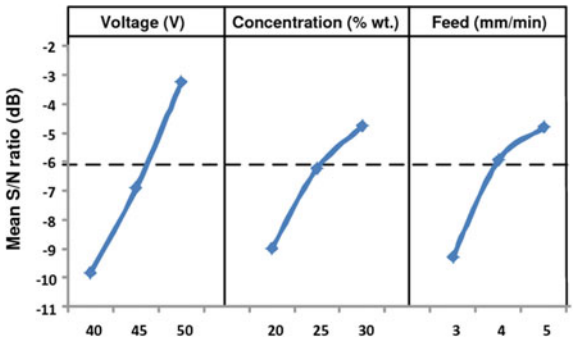


Fig. 2 Metal removal rate graph

delta signs show that pulse has the best effect on MRR and are lagging behind the beat on plan. Metal removal rate graph is displayed in Fig. 2.

First level of heart rate on type quality trademark, plan (2), heart rate of time (B1), first level open voltage (C1), second level feed rate override (D2), and third level wire feed (E3), third-degree servo voltage (F3), second-degree wire strain (G2), and second-degree flushing pressure (H2) gives check of MRR. The effect of control parameters on MRR is shown in Fig. 3.

Diagnostic Experiment

Verification in any structure of the investigation process is the final advance of the investigation. As seen in these Table 7, exploratory features are better with mild references, when trial results are contradicted, and trial honors are at 3.23% for MRR's S/N proportion and 9.76% for surface unusual S/N proportion. Therefore, utilizing the Taguchi method to improve preliminary outcome coordinating execution approves the improvement coordinating parameters (Table 6).

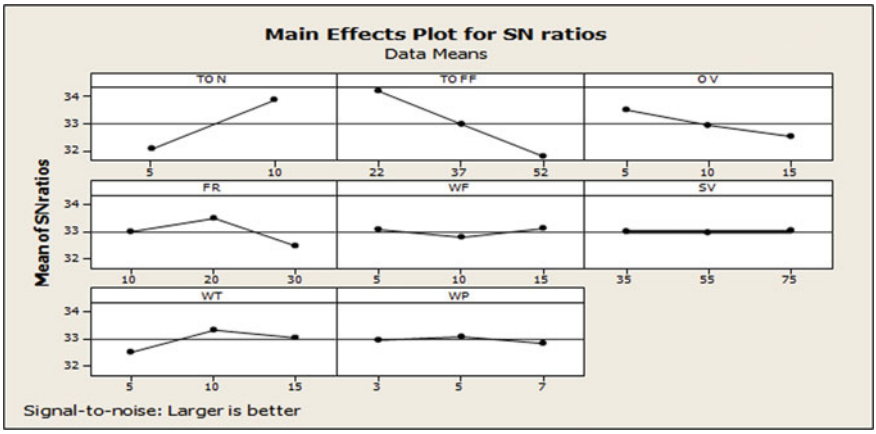


Fig. 3 Effect of control parameters on MRR

Table 6 Result of confirmatory experiment

	Predicted value	Experimental value	% Error
Optimal level	A1B1C1D3E1F3G2H1	A1B1C1D3E1F3G2H1	
Surface unpleasantness	1.27656	1.43	
S/N proportion unpleasantness	−3.34675	−3.45663	8.96

Table 7 Surface roughness

Source	DF	SeqSs	AdjSs	AdjMs	F	P
Ton	1	388.98	388.978	366.867	253.846	0.0002
Toff	2	460.708	460.708	230.387	209.31	0.0035
Ov	2	75.81	75.8181	36.983	35.769	0.0228
Fr	3	71.81	71.8281	3678.98	34.3635	0.0330
Wf	2	12.51	12.5191	7.675	5.72	0.1449
Sv	2	0.1418	0.1148	0.074	0.07	0.9537
Wt	2	58.1221	518.121	29.0361	26.41	0.0346
WP	2	14.6131	14.631	7.3316	6.65	0.1331
Blunder	2	2.2011	2.2101	1.1201		
Complete	17	1073.371				

7 Conclusions

From the above study, it might consequently be reasoned that due to high exactness and great nature of surface completion, WEDM is conceivably a significant procedure. It very well may be utilized for the creation of smaller scale parts, all the more productively and all the more viably on modern scale. Some work has been finished with cryogenic treatment on the various sorts of workpieces; this territory can assume a crucial job in the improvement of WEDM. Covered wires can perform better in the present situation where surface completion and apparatus life is generally liked. The zinc covered metal wires perform better when contrasted with basic metal wire as a result of its low wear rate and low breakage at expanded flows.

8 Future Scope

- The mathematical model can be developed with different workpiece and electrode materials for EDM and WEDM processes.
- Responses like Kerf width, roundness, circularity, cylindricity, machining cost, etc., are to be considered in further research.
- The standard optimization procedure can be developed and the optimal results are to be validated with different multi-criteria decision-making method.
- The weightage can be found with different techniques such as AHP and weighting approach.

References

1. Chen SL, Huang FY (1999) Influence of kerosene and distilled water as dielectric on the electric discharge machining characteristics of Ti-6Al-4V. J Mater Process Technol 87:107–111
2. Yan B, Huang F, Chow H, Tsai J (1999) Micro-hole machining of carbide by electric discharge machining. J Mater Process Technol 87(1–3): 139–145
3. Moghanizadeh A (2017) Reducing the overcut in EDM process by changing electric field between tool and workpiece. Int J Adv Manuf Technol 90: 1035–1042
4. Wansherg Z, Zhenlog W, Shichun D, Guanxin C, Hongyu W (2002) Ultrasonic and electric discharge machining to deep and small hole on titanium alloy. J Mater Process Technol 120: 101–106
5. Yan BH, Wang AC, Huang CY, Huang FY (2002) Study of precision microholes in borosilicate glass using micro EDM combined with micro ultrasonic vibration machining. Int J Mach Tools Manuf 42:1105–1112
6. Kaminski PC, Capuano MN (2003) Micro hole machining by conventional penetration electrical discharge machine. Int J Mach Tools Manuf 43:1143–1149
7. Wong Y, Lim L, Lee L (1995) Effects of flushing on electro-discharge machined surfaces. J Mater Process Technol 48:299–305
8. Sandeep M (2019) Enhancement and gray relational analysis of en 31 steel using parameters of wire cut electric discharge machine. ICMMSE, Mater Today proc. ISSN: 2214-7853

9. Sandeep M (2019) Experimental investigation and optimization of mrr, surface roughness and overcut of AISI 316 stainless steel in EDM using Taguchi method. Int J Adv Sci Technol IJAST 28(16). ISSN: 20054238
10. Ramakrishnan R, Karunamoorthy L (2008) Multi response optimization technique to predict and select the best cutting parameters of wire electro- discharge machining (WEDM) process. Mater Manuf Processes 24: 1312–1320

An Approach to Form Manual Power Generalized Experimental Model for Wood Chipping Process



V. M. Sonde, P. N. Warnekar, P. P. Ashtankar, and V. S. Ghutke

Abstract Motion is one the most sources of energy for gathering. This article plays a critical role in the construction of human energy which is a motivation research related to wood chipping process. A successful mathematical model has been developed for three parameters, i.e., power required speeding up the flywheel, blood pressure rise and time required to achieve flywheel speed, the five persons with different physical characteristic were used for pedaling the energy unit and accordingly the power required per person was calculated. The process form pedaling of bicycle to the clutch engagement can be the separate field of research which is done in this research work. The separate experimental plan was developed for measuring the human energy, and various variables were identified for detail study. The first time attempt has been made for calculation of human energy required for any machine operation. The novelty of this research is considered to be a prime importance because it is unique and applicable for any mathematical model formed.

Keywords Human energy · Blood pressure · Pulse rate · Flywheel · Time

1 Introduction

The human-energized flywheel motor basically includes two phenomena [1]. First is the process from pedaling of bicycle to the clutch engagement, and second is the process after engagement of clutch to the process unit. All previous researchers about human-powered concept have done the research work only after engagement of clutch to the process unit. Nobody has worked on the process from rider effort to the clutch the engagement in human-powered systems [2]. This is considered to be a research gap in this type of work area. The proper study based on the identified area is successfully incorporating the solution of human-operated mechanism. Here, the human energy required for pedaling the bicycling unit up to the required rpm is measured. The separate experimental plan was developed for measuring the

V. M. Sonde (✉) · P. N. Warnekar · P. P. Ashtankar · V. S. Ghutke
Priyadarshini College of Engineering, Nagpur, India
e-mail: mailtovivekms@gmail.com

© Springer Nature Singapore Pte Ltd. 2020

A. Praveen Kumar et al. (eds.), *Advances in Lightweight Materials and Structures*,
Springer Proceedings in Materials 8, https://doi.org/10.1007/978-981-15-7827-4_46



Fig. 1 Experimental setup of human-powered flywheel system with wood chipping unit

human energy. The energy is measured for all gear sets according to the developed experimental plan [3].

When rider begins pedaling of bicycle, the load of foot touch the pedal was measured with the assistance of load cell [4]. The load acting on both the pedal was recorded by using two separate load cells for both the pedals. The torque is then calculated by measuring the length of sprocket arm (load acting on pedal into length of sprocket arm). The calculated torque is then converted into the power required by dividing total time taken for flywheel rise [5]. The separate instrumentation system was designed in order to measure the load of the rider acting on the bicycle pedal.

As this research belongs to the human energy calculation, other parameters like blood pressure and pulse rate measurement must have been measured for detailed study [6]. The initial rises in lifeblood stress and pulse rate were measured for each person. Sixty observations were recorded for each second and for each rider [7].

2 Credentials of Variables

Various needy and autonomous variables are identified for measuring human energy required for wood chipper cutter as follows [8] (Fig. 1; Table 1).

3 Development of pi (π) Terms for All Needy and Autonomous Variables

The Buckingham's π Theorem is used for the dimensional analysis of proposed machine [5]. The power required to speed up the flywheel $P_{h,}$ blood pressure rise B_p, time required to speed up the flywheel t_f, and pulse rate rise P_r is function of gear proportion (G), hastening due to gravity (g), angular speed of flywheel (ω_f), weight of person (W_p), and height of person (H_p) [9].

Table 1 Variables related to human energy required for wood chipper cutter

S. No.	Variables	Unit	MLT	Nature (dependent/independent)
1	P_h = Power required for speed rise	N mm/s	ML^2T^{-1}	Needy
2	B_p = Blood pressure rise	N/mm	MT^{-2}	Needy
3	t_f = Time required to speed up the flywheel	s	T	Needy
4	P_r = Pulse rate rise	1/s	T^{-1}	Needy
5	G = Gear ratio	–	$M^0L^0T^0$	Autonomous
6	ω_f = Angular speed of flywheel	rad/s	T^{-1}	Autonomous
7	W_p = Weight of person	N	M	Autonomous
8	H_p = Height of person	mm	L	Autonomous
9	g = Acceleration due to Gravity	mm/s^2	LT^{-2}	Autonomous

Total number of variable = 9.
Number of needy variable = 4.
Number of autonomous variables, $n = 5$, therefore.

$$P_h/B_p/t_f/P_r = f(G, \omega_f, W_p, H_p, g) \text{ or } f(G, \omega_f, W_p, H_p, g) = 0.$$

g, W_p, H_p are consider as the recapping variables, therefore $m - 3$.
Total no. of autonomous variables—$n - 5$.
Number of Π terms $= n - m = 5 - 3 = 2$, therefore $\Pi_{D1} = f_1(\Pi_1, \Pi_2) = 0$.

4 Formation of Pi Terms for Needy Variables

4.1 First Π Term

$$\pi_1 = (g)^{a1}(W_p)^{b1}(H_p)^{c1}G.$$

$$(\text{Mass})^0(\text{Length})^0(\text{Time})^0 = \left(LT^{-2}\right)^{a1}(M)^{b1}L)^{c1}(M^0L^0T^0).$$

The values of a_1, b_1 and c_1 are compared by calculating the power of mass, length and time on equal sides as listed below.

'Mass'	'Length'	'Time'
$M - 0 = b_1$ $b_1 = 0$	$L - 0 = a_1 + c_1$ (From Eq. of T, subst. $a_1 = 0$) $0 = 0 + c_1$ Hence $c_1 = 0$	$T - 0 = -2a_1$ Hence $a_1 = 0$ Putting in equation of length to get significance of b_1

Putting the answer of a_1, b_1 and c_1 in the calculation of π_1 term, we get:

$$\pi_1 = (g)^{\circ}(D_s)^0(E_c)^0 G$$
$$\boldsymbol{\pi}_1 = \boldsymbol{G}.$$

4.2 Second Π Term

$$\pi_2 = (g)^{a2}(W_p)^{b2}(H_p)^{c2}\omega_f.$$
$$(\text{Mass})^0(\text{Length})^0(\text{Time})^0 = \left(LT^{-2}\right)^{a2}(M)^{b2}(L)^{c2}T^{-1}.$$

The values of a_2, b_2 and c_2 are compared by calculating the power of mass, length and time on equal sides as listed below:

'Mass'	'Length'	'Time'
$M - 0 = b_2$	$L - 0 = a_2 + c_2$ $0 = a_2 + c_2 - 0$ (From Eq. of T, subst. $a_2 = -1/2$) $0 = -1/2 + c_2 - 0$ Hence $c_2 = 1/2$	$T - 0 = -2a_2 - 1$ $0 = -2a_2 - 0 - 1$ Hence $a_2 = -1/2$ Putting in equation of length to get significance of c_2

Putting the answer of a_2, b_2 and c_2 in the calculation of π_2 terms, we get (Table 2):

$$\pi_2 = (g)^{-1/2}(W_p)^0(H_p)^{1/2}\omega_f,$$
$$\boldsymbol{\pi}_2 = \boldsymbol{\omega_f}\sqrt{\frac{\boldsymbol{H_p}}{\boldsymbol{g}}}.$$

Table 2 π terms for autonomous variables

π terms	π terms equations
π_1	$\pi_1 = G$
π_2	$\pi_2 = \omega_f\sqrt{\frac{H_p}{g}}$

5 Formation of Pi Terms for Needy Variables

5.1 First Needy Π Term

$$\Pi_{D1} = (g)^{a_{D1}}(W_p)^{b_{D1}}(H_p)^{c_{D1}}P_h.$$
$$(\text{Mass})^0(\text{Length})^0(\text{Time})^0 = \left(LT^{-2}\right)^{a_{D1}}(M)^{b_{D1}}L)^{c_{D1}}(ML^2T^{-1}).$$

The values of a_{D1}, b_{D1} and c_{D1} are compared by calculating the power of mass, length and time on equal sides as listed below:

'Mass'	'Length'	'Time'
$M - 0$ $b_{D1} + 1 = 0$ $b_{D1} = -1$	$L - 0 = a_{D1} + c_{D1} + 2$ (From equation of time, put $a_{D1} = -1/2$) $0 = -1/2 + c_{D1} + 2$ Hence $c_{D1} = -3/2$	$T - 0 = -2a_{D1} - 1$ Hence $a_{D1} = -1/2$ Putting in equation of length to get significance of c_{D1}

Putting the answer of a_{D1}, b_{D1} and c_{D1} in the calculation of π_{D1} term, we get:

$$\pi_{D1} = (g)^{-1/2}(D_s)^{-1}(E_c)^{-3/2}P_h$$
$$\boldsymbol{\pi_{D1}} = \frac{\boldsymbol{P_h}}{\boldsymbol{g}^{1/2}\boldsymbol{W_p}\boldsymbol{H_p}^{3/2}}.$$

5.2 Second Dependent Π Term

$$\Pi_{D2} = (g)^{a_{D2}}(W_p)^{b_{D2}}(H_p)^{c_{D2}}B_p.$$
$$(\text{Mass})^0(\text{Length})^0(\text{Time})^0 = \left(LT^{-2}\right)^{a_{D2}}(M)^{b_{D2}}L)^{c_{D2}}(MT^{-2}).$$

The values of a_{D2}, b_{D2} and c_{D2} are compared by calculating the power of mass, length and time on equal sides as listed below:

'Mass'	'Length'	'Time'
$M - 0$ $b_{D2} + 1 = 0$ $b_{D2} = -1$	$L - 0 = a_{D2} + c_{D2}$ (From Eq. of T, subst. $a_{D2} = -1$) $0 = -1 + c_{D2}$ Hence $c_{D2} = 1$	$T - 0 = -2a_{D2} - 2$ Hence $a_{D2} = -1$ Putting in equation of length to get significance of c_{D2}

Putting the answer of a_{D2}, b_{D2} and c_{D2} in the calculation of π_{D2} term, we get:

$$\pi_{D2} = (g)^{-I}(W_p)^{-I}(H_p)^1B_p$$

$$\boldsymbol{\pi_{D2}} = \frac{B_p H_p}{g W_p}.$$

5.3 Third Dependent Π Term

$$\pi_{D3} = (g)^{a_{D3}} (W_p)^{b_{D3}} (H_p)^{c_{D3}} t_f.$$
$$(\text{Mass})^0 (\text{Length})^0 (\text{Time})^0 = \left(LT^{-2}\right)^{a_{D3}} (M)^{b_{D3}} L)^{c_{D3}} (T).$$

The values of a_{D3}, b_{D3} and c_{D3} are compared by calculating the power of mass, length and time on equal sides as listed below:

'Mass'	'Length'	'Time'
$M - 0$ $b_{D3} = 0$	$L - 0 = a_{D3} + c_{D3}$ (From Eq. of T, subst. $a_{D3} = 1/2$) $0 = 1/2 + c_{D3}$ Hence $c_{D3} = -1/2$	$T - 0 = -2a_{D3} + 1$ Hence $a_{D3} = 1/2$ Putting in equation of length to get significance of c_{D3}

Putting the answer of a_{D3}, b_{D3} and c_{D3} in the calculation of π_{D3} term, we get:

$$\pi_{D3} = (g)^{I/2} (W_p)^0 (H_p)^{-I/2} t_f$$
$$\boldsymbol{\pi_{D3}} = \boldsymbol{t_f \sqrt{\frac{g}{H_p}}}.$$

5.4 Forth Dependent Π Term

$$\pi_{D4} = (g)^{a_{D4}} (W_p)^{b_{D4}} (H_p)^{c_{D4}} P_r.$$
$$(\text{Mass})^0 (\text{Length})^0 (\text{Time})^0 = \left(LT^{-2}\right)^{a_{D4}} (M)^{b_{D4}} L)^{c_{D4}} (T^{-I}).$$

The values of a_{D4}, b_{D4} and c_{D4} are compared by calculating the power of mass, length and time on equal sides as listed below:

'Mass'	'Length'	'Time'
$M - 0$ $b_{D4} = 0$	$L - 0 = a_{D4} + c_{D4}$ (From Eq. of T, subst. $a_{D4} = -1/2$) $0 = -1/2 + c_{D4}$ Hence $c_{D4} = 1/2$	$T - 0 = -2a_{D4} - 1$ Hence $a_{D4} = -1/2$ Putting in equation of length to get significance of c_{D4}

Putting the answer of a_{D4}, b_{D4} and c_{D4} in the calculation of π_{D4} term, we get (Table 3):

Table 3 π terms for needy variables

π terms	π terms equations
π_{D1}	$\frac{P_h}{g^{1/2} W_p H_p^{3/2}}$
π_{D2}	$\frac{B_p H_p}{g W_p}$
π_{D3}	$t_f \sqrt{\frac{g}{H_p}}$
π_{D4}	$P_r \sqrt{\frac{H_p}{g}}$

$$\pi_{D4} = (g)^{-I/2} (W_p)^0 (H_p)^{I/2} P_r$$

$$\boldsymbol{\pi_{D4}} = \boldsymbol{P_r} \sqrt{\frac{\boldsymbol{H_p}}{\boldsymbol{g}}}.$$

6 Formulation of Experimental Data Based Model

$$\frac{P_h}{g^{1/2} W_p H_p^{3/2}} = f_1 \left\{ (G) \left(\omega_f \sqrt{\frac{H_p}{g}} \right) \right\} \tag{6.1}$$

$$\frac{B_p H_p}{g W_p} = f_1 \left\{ (G) \left(\omega_f \sqrt{\frac{H_p}{g}} \right) \right\} \tag{6.2}$$

$$t_f \sqrt{\frac{g}{H_p}} = f_1 \left\{ (G) \left(\omega_f \sqrt{\frac{H_p}{g}} \right) \right\} \tag{6.3}$$

$$P_r \sqrt{\frac{H_p}{g}} = f_1 \left\{ (G) \left(\omega_f \sqrt{\frac{H_p}{g}} \right) \right\}. \tag{6.4}$$

7 Conclusion

Thus, the dimensional equations are recognized in condensed or compressed mode so as to form the entire investigation method minimum time taking having generation of optimal knowledge [10]. The experimental knowledge is going to be produced for construction of the mathematical model. The investigational setup will be planned which will contain the power required speeding up the flywheel, blood pressure rise and time required flywheel rise [11]. The catalogs of mathematical model are going

to be developed by multivariate examination. The investigation method enforced for the work can involve of sensitivity investigation, calculating of restrictive values, improvement, dependability and AI method which are found ANN model and to cut back error between investigational and measured knowledge. Supported the outcomes, decisions and hypothesis are going to be created.

References

1. McCartney N, Heigenhauser GF, Jones NL (1983) Power output and fatigue of human muscle in maximal cycling exercise. J Appl Physiol 55: 218–224
2. Sargeant AJ, Dolan P (1987) Effect of prior exercise on maximal short-term power output in humans. J Appl Physiol 63: 1475–1480
3. Kuntz K, Sainfort F, Butler M et al (2007) Decision and simulation modeling in systematic reviews. Methods research report. 2013 (Prepared by the University of Minnesota Evidence-based Practice Center under Contract No. 290-2007-10064-I.) AHRQ Publ 11(13): EHC037-EF.
4. Modak JP Human powered flywheel motor concept, design, dynamics and applications: 1–50
5. Rao SS (1984) Optimization theory and applications, 2nd edn. Wiley Eastern Ltd.
6. Costill DL, Thomason H, Roberts E (1973) Fractional utilization of aerobic capacity during distance running. Med Sci Sports 5:248–252
7. Philips Z, Ginnelly L, Sculpher M et al (2004) Review of guidelines for good practice in decision-analytic modelling in health technology assessment. Health Technol Assess 8(36):iii–158
8. Sakhale CN, Bapat PM, Singh MP (2011) Design of experimentation and application of methodology of engineering experimentation to investigation of processing torque, energy and time required in bamboo processing operations. Int J Bamboo Rattan JBR 9(1&2): 13–27
9. Brennan A, Chick SE, Davies R (2006) A taxonomy of model structures for economic evaluation of health technologies. Health Econ 15(12):1295–1310
10. Hooper D, Miller R, Layzer R, Giannini D, Milner-Brown HS, Koretsky A, Weiner M (1985) Correlation between high energy phosphates and fatigue in human muscle. Soc Mag Res Med 1:481
11. Margaria R, Aghemo P, Rovelli E (1966) Measurement of muscular power (anaerobic) in man. J Appl Physiol 21:1662–1664

Calculation of Reliability Approximation of Mathematical Model Formed for Manually Operated Wood Chipper

V. M. Sonde, P. N. Warnekar, P. P. Ashtankar, and V. S. Ghutke

Abstract A subject that therefore very important to several choices during this world might hardly escape measurement. The name "reliability" is given to the sector of study that makes a shot to assign numbers to the propensity of systems to fail. In a ton of restrictive sense, the term "reliability" is made public to be the likelihood that a system performs its mission with success. This paper presents an approach to reliability of mathematical model formed for manually operated wood chipper. The novelty of this research is considered to be a prime importance because it unique in applicable for any mathematical model formed. The mathematical model is formed for the three dependent π terms, i.e., processing time (tp), output weight of chips produced (Wo) and average resistive torque (Tr_avg) (Sonde in Int J Recent Trends Mech Eng IJRTME 2:17–25, 2013 1]. Error frequency distribution for developed models with graphical representation is done. These graphs were compared with likelihood density perform graphs of usually used life distributions. In applied mathematics analysis, distribution is most generalized case. Several applied mathematics distributions unit of measurement accustomed model varied responsibility parameters. Model dependableness approximation is dead by examination error frequency graphs of varied mathematical models with likelihood density perform graphs of usually used life distribution.

Keywords Wood chipper · Reliability · Mathematical model · Error frequency distribution and probability density function

V. M. Sonde (✉) · P. N. Warnekar · P. P. Ashtankar · V. S. Ghutke
Priyadarshini College of Engineering, Nagpur, India
e-mail: mailtovivekms@gmail.com

© Springer Nature Singapore Pte Ltd. 2020

A. Praveen Kumar et al. (eds.), *Advances in Lightweight Materials and Structures*,
Springer Proceedings in Materials 8, https://doi.org/10.1007/978-981-15-7827-4_47

1 Introduction

1.1 Concept and Working of Manually Operated Wood Chipper

The operator will pedal the mechanism while clutch is in disengaged position. The flywheel which operates manually act as an energy supply unit. The generated energy is then supplied to the chipper cutter through clutch and transmission. The regulator is accelerated and energized that stores some energy among it. Once the pedaling is stopped, clutch is engaged and keep energy within the regulator is transferred to the chipper unit input shaft by suggests that of clutch [1]. The process unit is wood chipper that contains of feeder, cutter disk, blade holder, cutting blades and foundation frame. Figure 1 depicts schematic arrangement of human powered wood chipper. Input shaft is then powered by transfer of energy flywheel and then clutch, the stalk or crop stem is fed and guided by the manually feeding process from front end, i.e., chipper cutting unit. Then, it comes in contact with the rotating disk on which the three cutting blades are mounted, the chips are then cut from stalk. The thickness of chip is depend upon the position of wood and cutting angle by changing the angle of cutting blades which can be move by means of studs fixed to the cutter frame. For continuous chip production, the constant supply of wood stem has to maintain this helps in adjusting any size of wood chips.

2 Concept and Introduction About Reliability

Life distribution is that the essential tool of reliability engineer; which can even be stated as failure distribution [2]. There will be either a combination of smaller distributions of assorted failure mechanisms or one distribution representing single failure mechanism [3]. Life distribution can have any form, but some traditional forms became usually used over the years [4]. Unremarkably used life distributions are: traditional, lognormal, exponential and Weibull. The conventional distribution is that the most generally celebrated and used of all distributions [5]. As a result of the conventional distribution approximates, several natural phenomena therefore well, it is developed into a typical of reference for several likelihood issues. It is additionally accustomed model dependableness [6]. The lognormal is applicable to maintenance tasks where the task time and frequency vary that is normally the case for advanced systems and merchandise [7]. In distinction to the mean of the standard distribution, the mean of the lognormal is not the fiftieth mark of the distribution and additionally the distribution is not symmetrical around the mean. Figure 2 shows the plot of the standard lognormal likelihood density performs for four values of σ.



Fig. 1 Human powered flywheel system with wood chipping unit

3 The Exponential Distribution

The exponential conveyance is wide acclimated model electronic data-based mishap inside the in activity area that will in general show a persevering disappointment rate [8]. To data exponentially implies the conveyance of disappointment times fits the exponential appropriation plot as appeared in probability thickness perform. Figure 3 speaks to probability densities perform for exponential circulation [9].

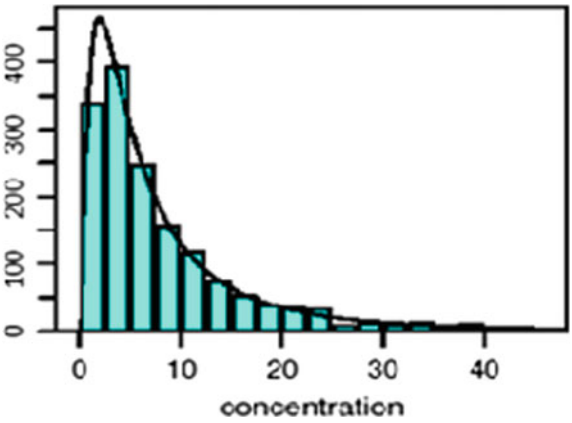


Fig. 2 Probability chart with lognormal distribution

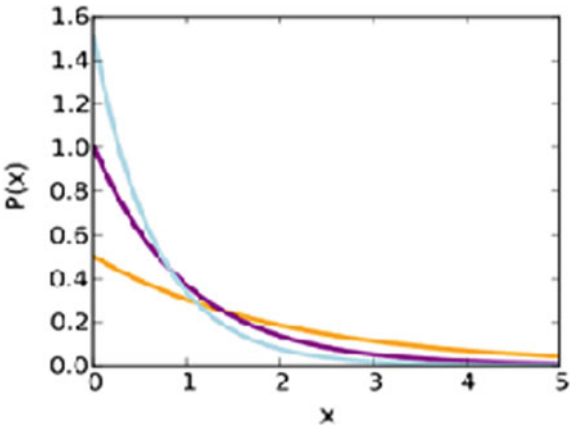


Fig. 3 Probability density function exponential distribution

4 The Weibull Distribution

The Weibull correlation gives the wide range of correlations as it is calculated on the basis of variety of values. It applies largely for probability distribution [10]. The source can be used to correlate a range of values and it flow that is shows the reliability distribution. Figure 4 shows the thickness and authenticated of density function.

5 Calculating Reliability

An output has to check for verification of the experimental procedure as well as to decide and check which data is impacting on output. The term reliability refers to the

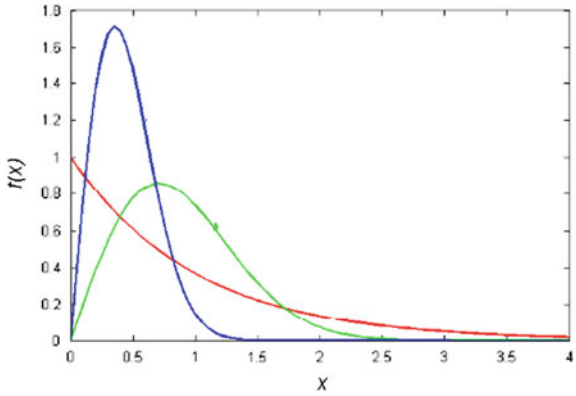


Fig. 4 Probability density functions Weibull distribution

accuracy and dependability of formed model that we can rely on. The main objective of verification is to eliminate the source of "error calculation" as far as possible [11].

The overcome the mistake, otherwise, calculate for standard deviation. In the event that we gauged the heaviness of one individual multiple times, we would wind up with estimations that are near the genuine weight and others that are further away. This spread of estimations has a specific anticipated variety and can be credited to arbitrary shot, some of the time alluded to as a standard deviation. Estimations that are outside of the standard deviation are viewed as because of an option that is other than arbitrary shot [12].

6 Error Frequency Distribution

In this experimentation, we have consider two sets of variables, i.e., output and system values of the indigent terms for all the three approaches, viz., are processing time, output weight of chips produced and resistive torque of wood chipper cutter operation by HPFM. The subtraction of output and system values gives the error. Repetitions of values of definite variance are estimated for three v of wood chipper cutter operation as representative sample [13]. Table 1 shows the error frequency distribution for mathematical model of the dependent terms Π_{01}, Π_{02} and Π_{03}, respectively. The error frequency distribution explains below (Figs. 5, 6 and 7; Table 2).

7 Establishment of Reliability of the Mathematical Model

The dependability is given by (1—mean failure) and mean failure is calculated as $\Sigma f_i * x_i / \Sigma f_i$ [14]. The calculations of dependability for all three dependent variables (pi) terms of wood chipper cutter by HPFM are shown in Table 1 [15].

Table 1 Error frequency distribution for mathematical model of the dependent terms Π_{01}, Π_{02} and Π_{03}

Π_{01} (i.e., Processing time)			Π_{02} (i.e., Output weight of chip)			Π_{03} (i.e., Resistive torque-avg		
% Error (f_i)	Frequency (x_i)	$f_i x x_i$	% Error (f_i)	Frequency (x_i)	$f_i x x_i$	% Error (f_i)	Frequency (x_i)	$f_i x x_i$
0	5	0	0	27	0	0	9	0
1	12	12	1	31	31	1	9	9
2	3	6	2	31	62	2	14	23
3	10	30	3	27	31	3	13	39
4	3	32	4	7	23	4	16	64
5	10	50	5	11	55	5	11	55
6	12	72	6	3	13	6	9	54
7	7	49	7	2	14	7	9	63
3	7	it	3	1	3	3	5	40
9	3	27	9	2	13		12	105
10	2	20	10	2	20	10	10	100
11	1	11	**55**	**144**	**335**	11	4	44
12	4	43				12	3	96
13	6	73				13	2	26
14	3	112				14	3	42
15	6	90				15	1	15
16	4	64				16	2	32
17	3	135				17	3	51
IS	2	36				13	3	54
19	4	76				20	1	20
20	4	30				**191**	**144**	**940**
21	3	63						
22	3	66						
23	2	46						
24	1	24						
29	2	53						
30	1	30						
31	1	31						
32	2	64						
39	2	73						
41	1	41						
502	**144**	**1586**						

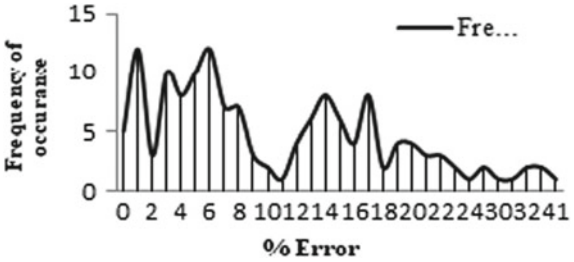


Fig. 5 Fault occurrence graph for processing time, tp (Π_{01}) [8]

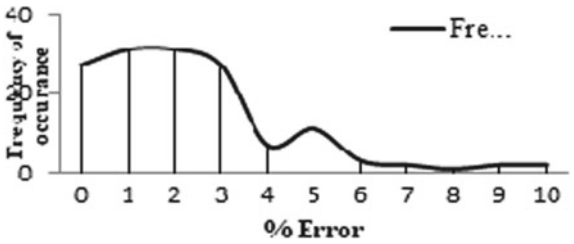


Fig. 6 Fault occurrence graph for output weight of chips produced, Wo (Π_{02}) [8]

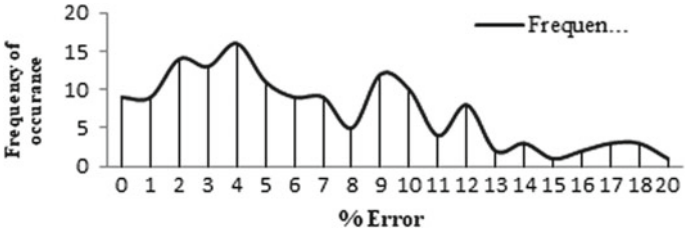


Fig. 7 Fault occurrence graph for resistive torque-average. Tr-avg (Π_{03}) [8]

Table 2 Reliability of all the dependent terms Π_{01}, Π_{02} and Π_{03}

Dependant terms of general model	Π_{01} (i.e., tp)	Π_{02} (i.e., Wo)	Π_{03} (i.e., Tr-avg)
$\Sigma fi * xi$	1586	335	940
Σxi	144	144	144
Mean error	11.01	2.32	6.52
Reliability	88.98%	97.67%	93.47%

Where f_i is the attempt of repetitions and x_i is the % of error. The total dependability of the all three dependent variables is given by the co-relation:

System Reliability, $R_s = 1 - \prod_{i=1}^{n}(R_i)$
And for the combined output, the reliability is calculated by co-relation:

$$R_p = 1 - \prod_{i=1}^{n}(1 - R_i)$$

Therefore, the dependability of the system for this research is given by:

$$R_p = 1 - \prod_{i=1}^{n}(1 - R_i) = 1 - \left\{\left(1 - R_{\mathrm{it}p}\right)(1 - R_{\mathrm{in}})(1 - R_{i\mathrm{Tr}})\right\}$$

where R_p is the total dependability of combined output $R_{\mathrm{it}p}$ is the dependability of processing time (Π_{01}), R_{in} is the dependability of output weight of chips produced (Π_{02}) and $R_{i\mathrm{Tr}}$ is the dependability of resistive torque (Π_{03})

Since, values were recorded frequently while demonstration.

Therefore, the total dependability [16] of models for wood chipper cutter is

$$= 1 - [(1 - 0.8898)(1 - 0.9767)(1 - 0.9347)] = 0.999832 = 99.9982\%$$

where value of $R_{i\mathrm{Tr}}$ is taken for resistive torque-average [17].

System Reliability = 99.9982%.

8 Conclusion

This paper has explained and method that approaches to reliability and co-efficient of determinant of numerical experimentation, from the reliability comparison (R_i) of all the models the reliability of processing time, output weight of chips produced and average resistive torque for all the models are found excellent [18]. Hence, we can say that the reliability of all response variables for mathematical models is perfectly fit with the data set. We can conclude that the mathematical model formed for manually operated wood chipper is reliable. This model can be practically applicable for any of the processing mechanism operated on the human powered. The reliability is defining the entire process which is completely responsible for good result. The above statement can be the future scope for the better performance. The reliability of the processing time model is 89.98%, for output weight is chips produced is 97.67%, and for average resistive torque 93.47%. The overall reliability is also calculated for the system of manually operated wood chipper is 99.9782%. So we can conclude that the development of wood chipper with manually operated system is very reliable and successful.

References

1. Sonde VM (2013) An experimental approach to formulate an approximate generalized experimental data based model for wood chipper cutter energized by HPFM. Int J Recent Trends Mech Eng IJRTME 2:17–25
2. Sqenck H Theory of engineering experimentation. McGraw-Hill, Inc. New York
3. Daniel S (2010) Reliability and optimization of structural systems. CRC Press, New York
4. Karki R, Billinton R, Verma AK (2014) Reliability modeling and analysis of smart power systems. Springer, Berlin
5. Gunasekaran M, Loganathan A (2019) Construction of reliability single sampling plans based on exponential distribution. J Test Eval 47(2)
6. Lu ZZ, Song J, Song SF et al (2010) Reliability sensitivity by method of moments. Appl Math Model 34(10):2860–2871
7. Rathod V et al (2011) Probabilistic modeling of fatigue damage accumulation for reliability prediction. Int J Qual Stat Reliab: 1–10
8. Bury K (1999) Statistical distributions in engineering. Cambridge University Press
9. Bergman B, Mare J, Svensson T, Loren S (2009) Robust design methodology for reliability: exploring the effects of variation and uncertainty. Wiley, New York
10. Figueiredo F, Ivette Gomes M (2013) The skew-normal distribution in SPC. REVSTAT Stat J 11(1): 83–104
11. Cui W (2002) A state-of-the-art review on fatigue life prediction methods for metal structures. J Mar Sci Technol 7(1):43–56
12. Mangey R (2019) Modeling and simulation based analysis in reliability engineering. CRC Press/Taylor and Francis Group, New York
13. Echard B, Gayton N, Bignonnet A (2014) A reliability analysis method for fatigue design. Int J Fatigue 59:292–300
14. Rahbi YA, Cowel A, Rizwan SM, Alkali BM, Taneja G (2017) Reliability analysis of a subsystem in aluminum industry plant. In: 2017 6th international conference on reliability, infocom technologies and optimization: trends and future directions, ICRITO 2017, pp 199–203
15. Adolfo C, Benoît IM (2007) A structured approach for the assessment of system availability and reliability using Monte Carlo simulation. J Qual Maintenance Eng 13(2):125–136
16. Gregory L, Wang C, Xing L (2019) Dynamic system reliability: modeling and analysis of dynamic and dependent behaviors. Wiley, New York
17. Kozachenko YV, Pogorilyak OO, Rozora IV, Tegza AM (2016) Simulation of stochastic processes with given accuracy and reliability. ISTE Press-Elsevier, New York
18. Gökdere G (2018) Time-dependent system reliability under stress-strength setup. Eksploatacja I Niezawodnosc Maintenance Reliab 20(3):420–424
19. Beck AT, Melchers RE (2005) Barrier failure dominance in time variant reliability analysis. Probab Eng Mech 20:79–85

Analysis of Machining Parameters on D2Tool Steel in Wire Cut EDM



Manikyam Sandeep and P. Jamaleswara Kumar

Abstract Non-regular machining procedure like electro release machining (ERM) and wire electrical release machining (WEDM) assumes significant job in accuracy assembling process. This small-scale machining procedure may help defeat the confinements and limitation looked during customary mechanical machining procedure. The choice of machining stricture in any machining procedure essentially influences creation rate, item value and generation rate completed one part. Line ERM procedure includes an enormous number of factors that influence its exhibition. In this research, an attempt is made to contemplate the force of different procedure parameter, for instance, strike on schedule, strike off moment in time and existing for elevated-carbon elevated-chromium bitter job instrument make stronger (D2). The trial has been finished with the assistance of design of analysis by Taguchi strategy is applied to make a symmetrical cluster of information factors utilizing the ANOVA. The relapse examination is utilized to upgrade the procedure parameter of surface unpleasantness. The test investigation demonstrated that the mix of heartbeat going on timetable, strike off moment moreover current be ideal toward accomplish minimization of surface harshness (Ra).

Keywords Wire EDM · Taguchi DOE · ANOVA · Regression analysis · D2 material · Surface harshness

1 Introduction

AISI D2 is one of the most prominent high-chromium and high-carbon steels of D arrangement and it is portrayed by its high compressive quality and wear obstruction, great through solidifying properties, high strength in solidifying and great protection from treating back. Cold work apparatus steels of Series D are high compound steels Fe–Cr–C-base. Inconel 718 was selected as work material to conduct experiments and brass wire of 0.25 mm diameter was used as tool electrode. Experiments were

M. Sandeep (✉) · P. Jamaleswara Kumar
Department of Mechanical Engineering, Koneru Lakshamaiah Education Foundation (Deemed to be University), Guntur, Andhra Pradesh 522502, India
e-mail: sandeep.mech109@gmail.com

© Springer Nature Singapore Pte Ltd. 2020

A. Praveen Kumar et al. (eds.), *Advances in Lightweight Materials and Structures*,
Springer Proceedings in Materials 8, https://doi.org/10.1007/978-981-15-7827-4_48

planned as per Taguchi L-9 orthogonal array. Experiments were performed under different cutting conditions of pulse on time, delay time, wire feed speed and ignition current.[1]. The performance of machining conductive ceramics (Al_2O_3 + 30 vol.% TiC) using electrical discharge machining (EDM). EDM processing parameters, such as the end point of the treatment, the upper current, the auxiliary current with a high voltage, the heartbeat range, the heap voltage and the reference servo voltage were considered [2]. Secondary dispersive X-ray spectroscopy and X-ray diffraction studies were additionally carried out on a composite lattice to confirm the closeness of the two distinguishable periods TiN and Al_2O_3 [3].

The previous researchers investigated an AEDM procedure tool, and polls explored. The last part of this article describes future AEDM patterns. Recently, the issue of expanding the production of processing in combination with targeted surface preparations has been studied [4]. Chakarborthy et al. investigated two schemes of tests, information on EDM procedures was broken using four improvement methods based on PCA. The literature shows improvements to these strategies contrast with the results achieved by past analysts, thinking that the overall proportion is expected to be (S/N) proportion as a measure of utility. Strategy (PQLR) provides the best implementation improvement [5]. Meena and Azad [6] investigated small-scale mechanical machining (miniature EDM) of Ti-6Al-V amalgam with a tungsten carbide cathode. Ti–6Al–4V, which is difficult to process using regular processing strategies, can be efficiently processed through EDM processing with careful selection of processing parameters to obtain ideal results. This study examines the effect of various informational current, voltage, repeatability and width parameters on the yield parameter, namely, metal ejection rate (MRR), device wear rate (TWR) and shear (OC). Dark social examination and study of the differences (ANOVA) were carried out to increase the degree of information parameters [7].

Sandeep reviewed test work performed on EDM EN31 (air-cured steel) using three distinctive materials for the device, such as copper, aluminum and EN31, and, in addition, problems, associated with the use of graphite and metal as a tool material. The treatment procedure was completed at three different levels of the current stock, the rate of material ejection, the wear rate of the device and its reduction [8]. The workpiece material selected in this experiment is AISI 316 stainless steel taking into account its wide usage in industrial applications. In today's world, 316 stainless steel contributes to almost half of the world's production and consumption for industrial purposes [9, 10]

2 Methodology

D2 equipment strengthen—elevated-carbon, elevated-chromium, freezing-job harden. The chief steels of wide application for since quite a while ago run passes on are steels in this gathering. Evaluation D2 containing 1.50% carbon is of moderate sturdiness and middle of the road wear opposition. From D2 strengthen every one gathering D steels have 1% Mo also be look solidified. Accordingly, apparatuses sort

Table 1 Chemical properties

Element	Content (%)
C	1.40–1.60
Mn	0.60
Si	0.60
Co	1.00
Cr	11.00–13.00
Mo	0.70–1.20
V	1.10
P	0.03
Ni	0.30
Cu	0.25

Table 2 Mechanical properties of reinforcing D2 steel

Properties	Metric	Imperial
Density	7.7 × 1000 kg/m	0.278 lb/in^3
Melting point	1421 °C	2590 °F

D2 steel will in general be fragile during solidifying. Strengthening the nature of D2 is the most common strengthening among collecting D steels. Amplifier D2 contains from 1.5 to 2.35% carbon and 12% chromium.

3 Element Composition

The following Table 1 shows the element composition of the D2 tool.

4 Material Properties

The material properties of the reinforcing tool D2 are shown in the following Table 2.

5 Mechanical Properties

Mechanical properties D2 steels are given in Table 3.

Table 3 Mechanical properties

Mechanical	Properties	Metric imperial
Hardness, knop (converted from Rockwel lC hardness)	769	769
Hardness, Rockwell C	62	62
Hardness, Vickers	748	748
Izod impact unnotched	77.0 J	56.8 ft lb
Poisson's ratio	0.27–0.30	0.27–0.30
Elastic modulus	190–210 GPa	27,557–30457 ksi

Table 4 Thermal properties

Properties	Conditions	
	T (°C)	Treatment
Thermal expansion	10.4×10^{-6} °C	20–100

6 Thermal Properties

The following Table 4 shows the thermal properties of D2 steels.

7 Experimental Analysis Method

The experimental analysis method on material is shown in Fig. 1. Strategies embraced for examination of preliminaries are Taguchi method and regression analysis intend of experiments (IOE) be incredible system employed signed for investigate original events, rising complete information of the current procedures with upgrading these

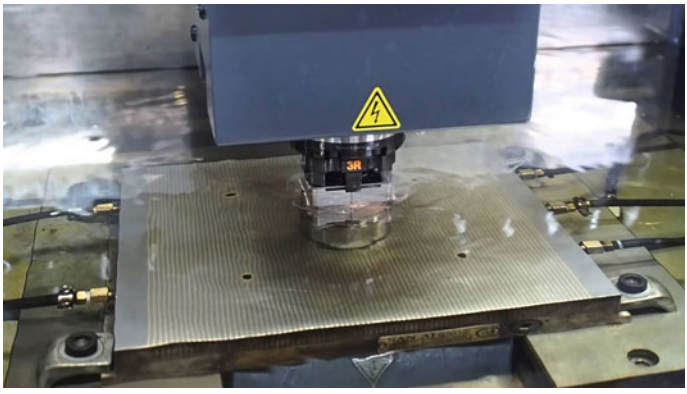


Fig. 1 Experimental analysis on material

measures used for accomplish human kind group implementation. Structure of experiments alludes near the technique just before arrange, setting up and contravention downward the test as a result legitimate with aim ends be capable of live trained sufficiently as well as productively. So as to reach measurably stable determinations from the analysis, it is important to coordinate straight forward and amazing factual techniques into the exploratory structure strategy. The accomplishment of any modernly structured test relies upon sound arranging, proper decision of plan, and measurable examination of information and collaboration abilities. The Taguchi make steps toward is IOE technique to have been broadly utilized in modern vigorous structure methodology. A few examinations have been made on plan of cutting procedures utilizing the Taguchi approach. Despite the fact that this methodology can distinguish the fundamental impacts of isolated structure factors, it is restricted in that associations among those components cannot be considered adequately.

The DOE strategy comprises of the accompanying four stages

(a) Planning: Meaning of the issue in addition to the goal, with improvement of an exploratory arrangement.
(b) Selection: Decrease of the quantity of factors with distinguishing the input factors to influence item value.
(c) Optimization: Assurance of the ideal qualities used for different test factors.
(d) Verification: Playing out a subsequent examination by the anticipated finest handling situation in the direction of affirm the improvement and outcome.

8 Stoop of Experiments by Taguchi Technique

Taguchi technique is a statistical method developed by Taguchi and Konishi. Taguchi policy be just as power tool designed for the structure of excellent frameworks. It present an incorporated method to be straightforward as well as creative in the direction of position the greatest capacity of plans designed for excellence, implementation and computational expenditure. In item or procedure structure of Taguchi strategy, there are three stages:

1. Framework plan: Determination of a framework for a given target work
2. Parameter structure: Choice of the ideal degrees of parameters
3. Resilience plan: Assurance of resistance around every parameter level.

Inside this investigation, limit configuration be attached in the direction of accomplish the ideal degrees of procedure parameter prompting least shrinkage during the assembling of plastic parts. During this examination, Taguchi limitation configuration be utilized designed for distinguishing the noteworthy handling parameter as well as streamlining base reduction. Significant devices utilized within limitation configuration be symmetrical exhibits with sign toward commotion (S/N) proportions (Fig. 2).

The collection of excellence methods includes three types of excellence personality within the Taguchi method, such as: the less input, the better, the higher, the better

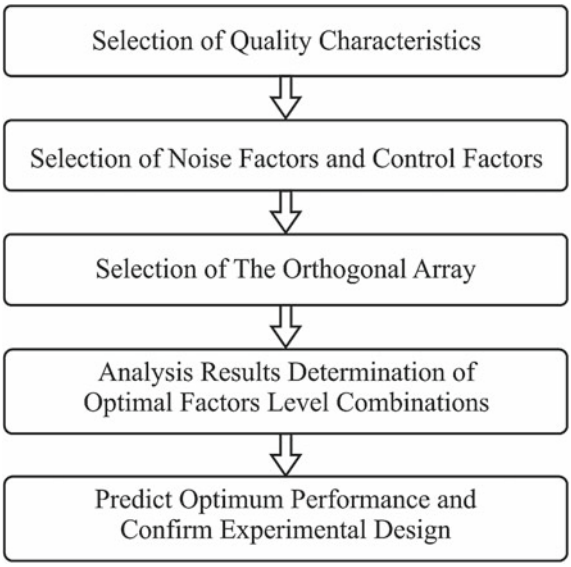


Fig. 2 Steps of designing Taguchi parameters

and nominally better. Signal to sound analysis is considered to calculate excellence. It is given by

$$\mathrm{S}\ /\ \mathrm{N}\ = -10\log 10\ (\mathrm{MSD})$$

where MSD = mean square division.

The smaller, the better the characteristic,

$$\mathrm{MSD} = (Y12 + Y22 + Y32 + \ldots)/n$$

Larger the better characteristic,

$$\mathrm{MSD} = (1/Y12 + 1/Y22 + 1/Y32 + \ldots)/n$$

Rated best performance

$$\mathrm{MSD} = \left[\left(Y1^{-m}\right)2 + \left(Y1^{-m}\right)2 + \left(Y1^{-m}\right)2 + \ldots\right]/n$$

where $Y1$, $Y2$, $Y3$ are the answers, and n is the number of tests in the test, and m is the target value of the result.

Table 5 Factors description and their levels

Notation	Factor description	Level 1	Level 2	Level 3
A	Current (A)	5	7	9
B	Pulse on time (μs)	16	32	48
C	Pulse off time (μs)	6	8	10

9 Selection of Parameters and Their Levels

Troubles are often a decent indication of the display of an automatic part, since external deviations can frame nucleation localizations designed for cleavage before use. Repulsive ability—the amount of the outer surface. This should be determined by the perpendicular deviation of the actual external from its best location. Troubles are regularly seen as the high-spitting short-wave part of an intentional surface. The limitation intended to use a volumetric element in favor of the overall external roughness is Ra. It measures the normal roughness for each individual vertex, as well as for the valley, using an indication column followed by averaging over the entire perimeter. External repulsive ability can be predicted using a surface stiffness analyzer.

The best three from the rundown of nine qualified variables were chosen for the examination. To keep the size of the analysis little and concentrate whatever number factors as could be expected under the circumstances, all elements were learned at two outrageous scopes of qualities (two levels).

These elements and their levels are appeared straightaway. Surface unpleasantness is administered by different control factors, for example.

(1) Existing, (2) beat resting on moment, (3) beat rotten moment, (4) beat breadth, (5) pulse interim, (6) speed, (7) applied voltage, (8) wire speed and (9) wire tension.

The best three from the rundown of nine qualified variables were chosen for the examination. To keep the size of the test little and concentrate whatever number factors as could be expected under the circumstances, all elements were learned at three levels. These components and their levels are appeared straightaway (Table 5).

10 Selection of Orthogonal Array

Because there are only three 3-level factors and no interaction is selected an L9 array is used to design the experiment as shown in Tables 6, 7 and 8 (Fig. 3).

Inside wake up machining of WPS D2 material on ERM, it very well may be noticed that current has the biggest impact superficially harshness. The beat off has the littlest impact superficially harshness. To accomplish better surface completion, surface harshness must be limited. From above principle impact plot, it can saw that for the three degrees of pinnacle flows the surface harshness is declining directly, and at current level, 9 amp the surface unpleasantness worth is the most minimal (- 16.34).

Table 6 Scheme for experimental design in accordance with the array L9 for material WPS D2

Exp. No.	A current (A)	B pulse on time (μs)	C pulse off time (μs)	Average	S/N ratio
1	5	16	6	3.30	−10.3703
2	5	32	8	3.58	−11.0777
3	5	48	10	3.90	−11.8213
4	7	16	8	5.00	−13.9794
5	7	32	10	4.90	−13.8039
6	7	48	6	5.15	−14.2361
7	9	16	10	6.60	−16.3909
8	9	32	6	6.30	−15.9868
9	9	48	8	6.80	−16.6502

Table 7 Response table for selected factors and levels

Notation	Factor description	Level 1	Level 2	Level 3
A	Current (A)	5	7	9
B	Pulse on time (μs)	16	32	48
C	Pulse off time (μs)	6	8	10

Table 8 Response table for signal to noise ratio on current and time

Level	Current	Pulse on time	Pulse off time
1	−11.09	−13.58	13.53
2	−14.01	−13.62	−13.90
3	−16.34	−14.24	−14.01
Delta	5.25	0.66	0.47
Rank	1	2	3

Essentially, the surface unpleasantness likewise lessens with expanded degrees of both, strike going on timetable, pulse off and pulse on. At pulse on schedule (48 μs), the SR worth watched was the least, for example—14.24 likewise for pulse off time (10 μs) and the littlest SR esteem (14.01) was checked. Consequently, the ideal condition for surface harshness watched were A3, B3 and C3, for example, current (9 amp.), pulse on (48 μs) and pulse off time (10 μs). Cooperation plot as shown in Fig. 2 which is the blend of every one of the three parameters cooperating with one another at various levels gives that present, strike lying on timetable in addition to pulse time had their impressive consequences for WPS D2 material surface unpleasantness while machining with EDM (Table 9).

Subsequent to machining of WPS D2 material on EDM, it tends to be noticed that current has the biggest impact superficially harshness. The beat off has the littlest impact superficially harshness. To accomplish better surface completion, surface unpleasantness must be limited. From above fundamental impact plot, it can saw

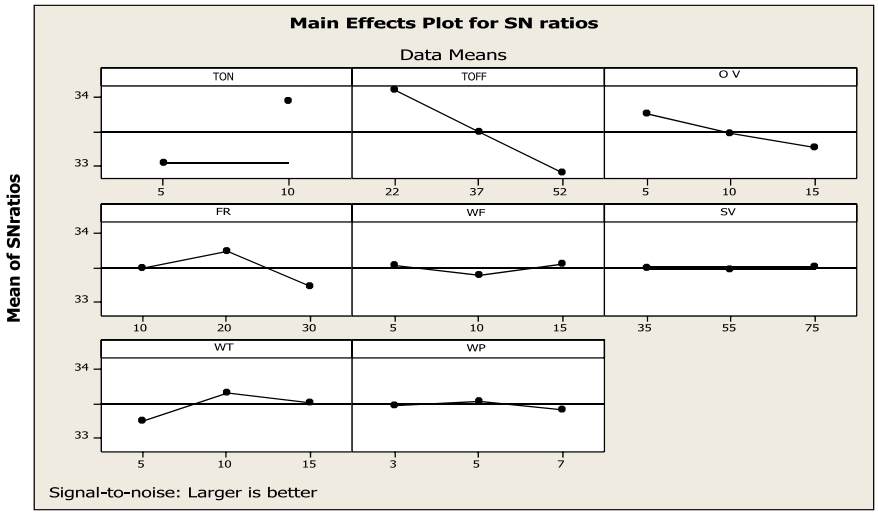


Fig. 3 Effect of control parameters on MRR

Table 9 Analysis of variance for signal to noise ratio of WPS D2 material $S = 0.308167$ R-sq = 99.56% R-Sq (adj.) = 98.23%

Source	DOF	Seq. SS	Adj. SS	Adj. MS	F	P
Current	2	41.5577	41.5577	20.7788	218.80	0.005
Pulse on time	2	0.8076	0.8076	0.4038	4.25	0.190
Pulse off time	2	0.3734	0.3734	0.1867	1.97	0.337
Residual error	2	0.1899	0.1899	0.0950		
Total	8	42.9286				

that for the three degrees of pinnacle flows, the surface unpleasantness is declining directly and at current level 9 amp, and the surface harshness worth is the most minimal (- 16.34). Additionally, surface harshness likewise reduces with expanded degrees of both, strike going on timetable and heart beat off time. At pulse on schedule (48 μs), the SR worth watched was the least, for example—14.24 likewise for pulse off time (10 μs) and the littlest SR esteem (14.01) was observed. Along these lines, the ideal conditions for the observed surface roughness were A3, B3 and C3, for example, current (9 amperes), pulse (48 μs) and pulse time (10 μs). Collaboration area as shown in Fig. 2, which is a combination of each of the three parameters interacting with each other at different levels and gives the fact that the current, pulse rate and pulse turn-off time had their impressive consequences for the surface hardness of the WPS D2 material when processed using EDM.

11 Conclusion

The outcome as of the Taguchi strategy picks an ideal arrangement as of blends variables on the off chance that it gives limited standardized joined S/N proportion of focused yields. The L9 OA was used to provide three control factors, and together with three levels for the research scheme, the process parameters were selected: current, pulse in time, pulse time for both materials, for example, WPS D2. The outcomes are abridged as pursues: (i) Among the three procedure parameters for cutting of WPS D2 material current has noteworthy impact on quality characteristic. (ii) For WPS D2 material, the amplification of current gives most extreme surface completion of part. (iii) The optimal degree of procedure parameter for WPS D2 material was seen as A3, B3 and C3, for example, current (9 amp.), pulse on (48 μs) and pulse off time (10 μs). (iv) The expectations made by Taguchi parameter plan system are in great concurrence with affirmation results. (v) The aftereffect of present examination is legitimate inside indicated scope of procedure parameters.

References

1. Ramakrishnan R, Karunamoorthy L (2008) Modeling and multi-response optimization of Inconel 718 on machining of CNC WEDM process. J Mater Process Technol 207:343–349
2. Lin Y-C, Chen Y-F, Wang D-A, Lee H-S (2009) Optimization of machining parameters in magnetic force assisted EDM based on Taguchi method. J Mater Process Technol 209:3374–3383
3. Bhaduri (2009) Precision shaping of small diameter wheels using micro electric discharge truing (MEDT) and hole-machining of Al2O3 material. Int J Mach Tools Manuf 40: 661–674
4. Kumar A, Maheshwari S, Beri N (2010) Research developments in additives mixed electrical discharge machining (AEDM): a state of art review. Mater Manuf Process 25:1166–1180
5. Chakraborty S, Dey V, Ghosh S (2015) A review on the use of dielectric fluids and their effects in electrical discharge machining characteristics. Precision Eng 40: 1–6
6. Meena and Azad (2012) Grey relational analysis of micro-EDM machining of Ti-6Al-4V Alloy. Mater Manuf Processes 27(9): 973–977
7. Arunkumar N, Shareef H, Rawoof A, Vivek R (2012) Investigation on the effect of process parameters for machining of EN31 (Air Hardened Steel) By EDM. Int J Eng Res Appl 2(4): 1111–112.1 ISSN: 2248-9622. https://www.ijera.com
8. Sandeep M Enhancement and gray relational analysis of En 31steel using parameters of wire cut electric discharge machine. ICMMSE, Mater Today Proc. ISSN: 2214-7853
9. Sandeep M Experimental investigation and optimization of mrr, surface roughness and overcut of AISI 316 stainless steel in EDM using Taguchi Method. Int J Adv Sci Technol
10. Yan BH, Wang AC, Huang CY, Huang FY (2002) Study of precision microholes in borosilicate glass using micro EDM combined with micro ultrasonic vibration machining. Int J Mach Tools Manuf 42:1105–1112

Dry Sliding Wear Performance Studies of WC–12Co Deposited on AISI 420 Steel Through Microwave Energy



Ajit M. Hebbale, J. S. Vishwanatha, M. S. Srinath, and Ravindra I. Badiger

Abstract The WC–12Co-based clad powder was deposited on the AISI 420 substrate using the microwave energy. The dry sliding action of the WC–12Co-based microwave coating on the substrate AISI 420 was studied using a pin-on-disk testing equipment. The dry sliding wear study was carried out as per Taguchi OA L9. Speed, sliding distance, and load parameters were considered at three various levels. The more wear rate was observed on the unclad surface than the clad surface. Enhanced sliding resistance of the microwave cladding is due to the uniform distribution of carbides. Unclad surface experiences the removal of binder and degradation of carbide grain, while clad surface suffers plastic deformation and undergoes microscale wear.

Keywords Microwave cladding · Sliding wear · Carbides · AISI-420 · Clad powder

1 Introduction

Surface depletion of components is a common issue faced by all industries worldwide. This degradation of the surface fails the whole part, which in turn is causing massive economic losses for emerging industries. Replacing the damaged part with a replacement part is not a value-effective solution. Furthermore, by using antiwear cladding/coatings, the surface that is likely to be damaged can be covered. Plasma

A. M. Hebbale (✉) · J. S. Vishwanatha
Department of Mechanical Engineering, N.M.A.M. Institute of Technology (Visvesvaraya Technological University, Belagavi) NITTE, Udupi District, Karnataka 574110, India
e-mail: ajit.hebbale@gmail.com

M. S. Srinath
Department of Industrial and Production Engineering, Malnad College of Engineering (Visvesvaraya Technological University, Belagavi) Hassan, Hassan District, Karnataka 573201, India

R. I. Badiger
Department of Mechanical Engineering, Yenepoya Institute of Technology (Visvesvaraya Technological University, Belagavi) Moodabidri, Mangalore, Karnataka 574225, India

© Springer Nature Singapore Pte Ltd. 2020

A. Praveen Kumar et al. (eds.), *Advances in Lightweight Materials and Structures*,
Springer Proceedings in Materials 8, https://doi.org/10.1007/978-981-15-7827-4_49

spraying, PVD, CVD, laser cladding, thermal spray process, etc., are the widely used methods of producing clad [1, 2]. Laser cladding is the most considerable technique, because of its unique features, like the development of metallurgical bonding among all other techniques. However, high installation and running costs are associated with laser cladding process [3, 4]. Besides, heat is applied to the material's surface during laser cladding, resulting in a large thermal gradient between the material's surface and core. Laser cladding also has some disadvantages owing to the elevated thermal gradient, such as the occurrence of porosity, high thermal, and residual stresses. Higher cooling rates often cause cracks on the produced clad surface in this process. Laser cladding is an expensive process, and the various physical characteristics of the layer and substrate often result in higher residual stress on the coated layer that is resistant to the need for target surface alteration techniques in industry [5, 6].

Due to cost savings and excellent wear resistance, thermal spraying is a general approach for producing usable surfaces. Typically, the technique is used to position a coat on a metal substrate. It uses gases like hydrogen or liquid fuel (kerosene) to be combusted and develops a really high velocity before particles impact the substrate, resulting in a high coating volume with minimum oxide content [7]. The superiority of sprayed WC–10Co–4Cr and WC–12Co coatings was investigated at high-temperature oxidation. Higher oxidation resistance of WC–10Co–4Cr coating may have resulted from dense chromium oxide layer structure. The carbide grain size effect on HVOF sprayed WC–12Co coatings was studied [8–10]. The porosity presence in the sprayed layer could have an effect on corrosion resistance in this technique [11, 12]. Microstructure of the developed layer is completely dependent on heat inputs. The intermetallic coatings show good corrosion and oxidation resistance. These techniques are easy but even more price-effective, since the price of the clad material is superior than that of the uncoated substrate. The limitations of several coating techniques are set out in Table 1.

Thus, the thermal sprayed deposits also exhibit poor flexural characteristics. The agglomeration of nanostructured materials also poses serious problems of treatment during spraying, which also affects structural homogeneity. The microwave heating technique provides significant potentials, such as increased processing speed and the advancement of uniform microstructures [14–16]. Microwave heating has been functionally very successful in heating and sintering ceramic-based materials over the last two decades. Microwave materials are unique from traditional thermal processing methods. Microwave energy heats the substance at the cellular stage, resulting in single-form bulk heating. Nevertheless, in modern system of heating, the material is warmed from the outside to the inside with a thermal gradient. Until 1998, microwave energy has been widely used in the development of ceramic and ceramic composite materials, and few studies on the heating of metallic materials by microwave radiation have been released [17–19].

In particular, the wear resistance and hardness of WC–12Co-based cermets improve with the reduction of a carbide particle size and the increase in the volume of the carbide fraction. The higher carbide volume fraction of carbide consists of a smaller exposure of the pretty soft matrix to the target surface material. As a result, there was an enormous deal of interest in wear-resistant nanostructured coatings

Table 1 Limitations of the general coating methods [13]

Method of coating	Limitations
HVOF	• Only the external surface can be coated • Due to the high amount of heat generated in the HVOF stream, excess heating of the substrate is experienced • Very difficult in masking of complex geometry components and also time-consuming • Capital cost seems to be high
Plasma spraying	• The spray gun usually requires frequent replacement to maintain proper coating uniformity • The process is very difficult for internal bore coating of small diameter and very limited access surfaces • The high temperature of the plasma jet may result in carbide decomposition and over-oxidation when spraying with air • The equipment does not suite for manual operations • The process produces high noise
Powder coating	• Difficulty in maintaining coating uniformity • Difficulty in coatings sharp-edged components • Thin films are very difficult to obtain.
Laser cladding	• Some technical difficulties are unexplored • Due to unreliable lasers, there is resistance from the industry. The cladding process induces large residual stresses on the developed surface • Highly skilled operators are required for experimentation

(WC–Co) [20]. Variants of cemented carbides based on WC are commonly used in various wear applications such as drilling, high-speed machining, mining due to their high strength, durability, compressive deformation resistance, and wear resistance [21]. WC–Co solidified carbide wear activity is primarily due to its chemical properties and microstructure. Based on the content of the cobalt, the volume of the carbide in the beginning powder may be changed [22, 23]. Tungsten carbide is a particular chemical compound that is about three times more rigid than steel. Tribo-mechanical characteristics like toughness, strength, and wear resistant are primarily determined by distribution and size of WC particles, thermo-mechanical and volume fraction characteristics of metal matrix and the composite hard metal coating [23, 24]. Martensitic stainless steel (AISI-420) is among the most prominent martensitic stainless steels used daily [25].

Remarkable mechanical properties such as high elastic modulus, strength and outstanding wear resistance, chemical, thermal resilience at high temperatures make WC–Co cermets economically desirable. The current work presents cladding of WC–12Co cermet that was performed on substrate (AISI-420) steel through a microwave hybrid heating (MHH) technique using a 2.45 GHz domestic microwave applicator. Dry sliding wear performance was carried out through a pin-on-disk tribometer as per ASTM standard. Finally, worn surface analysis through SEM was carried out.

2 Materials and Experimentation

WC-12Co-based clad powder was used to deposit on AISI-420 steel. The steel plate AISI-420 was machined to a desired size of 25 × 25 × 6 mm^3. Chemical composition (wt%) of the substrate AISI-420 is: C-0.36, Si-0.55, P-0.03, S-0.21, Mn-0.26, Ni-3, Si-1, Cr-28.67, Fe-Bal, and WC-12Co; clad powder: W-77.33, Co-12.45, C-10.22.

In the development of clads, It is essential to prepare substrate and clad powder. Raw WC–12Co powder was preheated at 120 °C for 8 h in a conventional furnace to remove any possible moisture content. The powder was then prepositioned manually on target sample by preserving an average thickness of 1 mm approximately. Initially, alumina casket was used during the experiment just to avoid exposure of metals directly with microwaves. The clad was finally developed with a microwave exposure of 10 min. Detailed discussion on clad development was discussed by Hebbale and Srinath [14, 16]. Primarily, several experimental studies were conducted to confirm microwave interaction time to the sound clad on the substrate.

2.1 Pin-On-Disk Wear Testing

A pin-on-disk tribometer was used to test the dry sliding efficiency of WC–12Co cladding against the EN-31 oil-hardened disk under different load conditions. The WC–12Co clad specimens of desired size were machined to fit as wear pins. Figure 1 shows the developed pins for wear test. The machined substrates were tested as per Taguchi L9 test parameters. Sliding speed, distance, and load are considered for the test at three various levels. The developed pins are polished with SiC abrasive #1500 grit papers to ensure consistent surface contact. The electronic weight balance with a precision of 70.1 mg has been used to calculate the pins pre- and post-actual test. Standard loading was applied to a clad substrate through dead weights by means of a lever, string, and pulley setup. Worn surface analysis was carried out concerning the

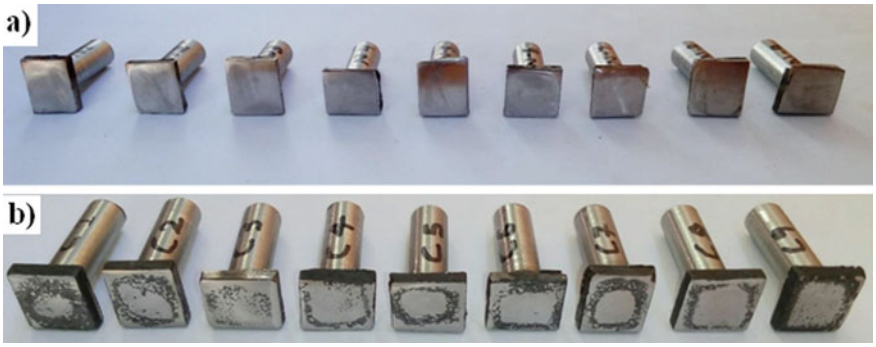


Fig. 1 **a** Unclad samples, **b** WC–12Co-based clad samples for pin-on-disk test.

level of wear and the total loss in the weight. Worn-out pins were finally analyzed through SEM for evaluation of wear mechanisms.

3 Result Analysis

Subsequently, the developed clads were tested through a pin-on-disk testing equipment as per Taguchi OA L9, and the findings are discussed in the following.

3.1 Wear Studies

The wear test of pin on disk was carried out with unclad and WC-12Co-based microwave clads as per Taguchi OA L9. Grain size is a significant factor that affects the wear quality of the WC–12Co clads. Wear rate of both clad and unclad samples is calculated and wear rates are tabulated in Table 2. As observed from Table 2, the initially WC–12Co-based microwave clad exhibits a higher rate of wear allocated to the run-in process of wear in which rough surface asperities are eliminated. Over and above 2000 m of sliding distance, the percentage of wear decreases smoothness of wear tracks. It is also noted that the normal load on the target surfaces plays an important role in the sliding form of tribocontact. These experiments were therefore carried out by changing the normal load to evaluate the tolerance of the microwave clads to the load. The characteristics of wear rate of unclad and clad samples are shown in Fig. 2. It is noticed from Fig. 2 that the wear rate is more on the unclad surface than clad surface. This shows the WC–12Co microwave clad has an impact on the target surface toward the improvement of the mechanical properties.

Table 2 Wear rate of clad and unclad samples

S. No.	Distance (M)	Speed (M)	Load (N)	Wear rate of unclad samples (gm)	Wear rate of clad samples (gm)
1	1000	2	20	0.0307	0.0063
2	1000	4	30	0.0687	0.0100
3	1000	6	40	0.0490	0.0094
4	2000	2	20	0.0979	0.0131
5	2000	4	40	0.1380	0.0158
6	2000	6	30	0.0809	0.0096
7	3000	2	20	0.1890	0.0290
8	3000	4	30	0.0353	0.0244
9	3000	6	40	0.2745	0.0330

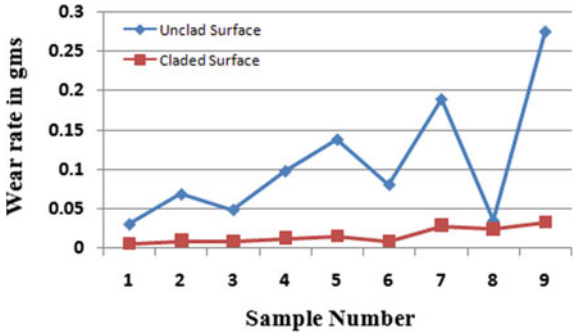


Fig. 2 Wear rate variations of unclad sample versus WC–12Co-based microwave clad samples

As a result, this region can be referred to as the constant wear zone. On the other hand, with a shift in normal load, the level of wear shows a growing trend due to the increase in the stress on the mating surfaces resulting in the removal of binders and the deterioration of carbide grains. Enhanced wear resistance of the WC–12Co cladding is due to decreased abrasion and improved crack distribution obstruction compared to unclad surface.

3.2 Microstructure Analysis of Worn Surface

To determine the functions of wear, worn-out structures of the WC–12Co-based microwave clad have been studied through SEM. Figure 3a, b demonstrates worn-out surfaces of unclad and WC–12Co-based microwave clad at 40 N loads. Slight wear is in the appearance of permeability, and abrasion could be experiential in the unclad surface at low loads.

Furthermore, pretty smooth wear trails and much less material degradation through mating surface were seen in the WC–12Co microwave cladding. Improved

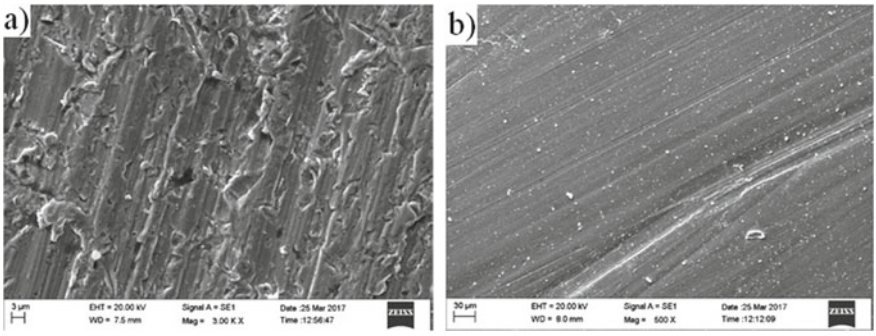


Fig. 3 Worn surface of the **a** unclad and **b** WC–12Co-based microwave clads

resistance to wear of the developed clad is due to increased obstruction and reduced abrasion to crack propagation. The occurrence of discontinuous plowing marks, moderate abrasion, and microcutting may also be observed. At elevated loads (40 N), the transformation of materials occurs between the counter surface and the clad surface. Figure 3a showed that the unclad surface experienced severe structural damage due to the plowing of the metal matrix. Under higher load, carbide grain fragmentation occurs, and fragmented grains behave as abrasive material, causing three-body abrasions. Extreme plowing of the unclad surface result is of intensive scratching of broken carbide grains and the development of large-scale debris. Para-bonded carbide particulates also induced microcutting. In Fig. 3b, the WC–12Co-coated wear grooves are found to be shallow. Material loss was caused by fatigue and plastic deformation due to the repetitive operation of the slider. Improved resistance to wear of the clad developed could also be due to occurrence of carbide bunch leading to higher toughness and improved clad durability.

4 Conclusions

The WC–12Co cladding was deposited on the AISI 420 substrate using the MHH technique. The dry sliding action of the substrate and developed clad was considered through a pin-on-disk tribometer. The appropriate inference may be drawn from the current investigation.

The WC–12Co microwave clad has a higher wear tolerance than unclad layer index. The mean weight loss for the developed microwave clad is reduced by more than the substrate.

- The improved sliding resistance of the microwave cladding is due to the uniform distribution of carbides and the improved microhardness of the cladding surface.
- During the sliding process, the unclad surface experiences the elimination of binder and the degradation of the carbide grain, while the clad surface suffers plastic deformation and undergoes microscale wear.

Scope of Future Enormous research opportunities are there in the area of microwave processing materials, and a lot of industrial challenges also need to be communicated in the coming future to make this process more industry familiarization.

References

1. Adachi S, Ueda N (2013) Surface hardness improvement of plasma-sprayed AISI 316L stainless steel coating by low-temperature plasma carburizing. Adv Powder Technol 24:818–823
2. Krishna NG, Thinaharan C, George RP, Parvathavarthini N, Kamachi Mudali U (2015) Surface modification of type 304 stainless steel with duplex coatings for corrosion resistance in sea water environments. Surf Eng 31:39–47

3. Hebbale A, Ms S, Doe J, Fellow L (2014) Evaluation of cobalt based microwave cladding on stainless steel S-355 13: 1–3
4. Babu A, Arora HS, Singh H, Grewal HS (2019) Microwave synthesized composite claddings with enhanced cavitation erosion resistance. Wear 422–423:242–251
5. Xu M, Li J, Jiang J, Li B (2015) Influence of powders and process parameters on bonding shear strength and micro hardness in laser cladding remanufacturing. Procedia CIRP 29:804–809
6. Shuja SZ, Yilbas BS, Ali H, Karatas C (2016) Laser pulse heating of steel mixing with WC particles in a irradiated region. Opt Laser Technol 86:126–135
7. Singh L, Chawla V, Grewal JS (2012) A review on detonation gun sprayed coatings. J Miner Mater Charact Eng 11:243–265
8. Jafari M, Enayati MH, Salehi M, Nahvi SM, Park CG (2013) Comparison between oxidation kinetics of HVOF sprayed WC–12Co and WC–10Co–4Cr coatings. Int J Refract Met Hard Mater 41:78–84
9. Yang Q, Senda T, Ohmori A (2003) Effect of carbide grain size on microstructure and sliding wear behavior of HVOF-sprayed WC–12% Co coatings. Wear 254:23–34
10. Chen H, Xu C, Zhou Q, Hutchings IM, Shipway PH, Liu J (2005) Micro-scale abrasive wear behaviour of HVOF sprayed and laser-remelted conventional and nanostructured WC–Co coatings. Wear 258:333–338
11. Chen J, Li XY, Bell T, Dong H (2008) Improving the wear properties of Stellite 21 alloy by plasma surface alloying with carbon and nitrogen. Wear 264:157–165
12. Wu P, Zhou CZ, Tang XN (2003) Microstructural characterization and wear behavior of laser cladded nickel-based and tungsten carbide composite coatings. Surf Coatings Technol 166:84–88
13. Gupta D, Bhovi PM, Sharma AK, Dutta S (2012) Development and characterization of microwave composite cladding. J Manuf Process 14:243–249
14. Hebbale AM, Srinath MS (2016) Microstructural investigation of Ni based cladding developed on austenitic SS-304 through microwave irradiation. J Mater Res Technol 5(4):293
15. Hebbale AM, Srinath MS (2017) Taguchi analysis on erosive wear behavior of cobalt based microwave cladding on stainless steel AISI-420. Meas J Int Meas Confed 99
16. Hebbale AM, Srinath MS (2018) Microstructural studies of cobalt based microwave clad developed on martensitic stainless steel (AISI-420). Trans Indian Inst Met 71:737–743
17. Prasad A, Gupta D (2013) Microwave cladding : emerging innovative cladding process. Proc Int Conf Emerg Trends Eng Technol
18. Nair R, Arora HS, Boyana AV, Saiteja P, Grewal HS (2019) Tribological behavior of microwave synthesized high entropy alloy claddings. Wear 436–437:203028
19. Singh S, Gupta D, Jain V, Sharma A (2014) Microwave processing of materials and applications in manufacturing industries: a review. Mater Manuf Process 6914:37–41
20. Al-Hamed A, Al-Fadhli HY, Al-Mutairi S, Yilbas BS, Hashmi MSJ, Stokes J (2013) Investigation of HVOF thermal sprayed nanostructured WC–12Co mixed with Inconel-625 coatings for oil/gas applications. In: WIT transactions on engineering sciences. WIT Press, pp 215–225
21. Yung DL, Antonov M, Veinthal R, Hussainova I (2016) Wear behaviour of doped WC-NI based hardmetals tested by four methods. Wear 352–353:171–179
22. Lee CW, Han JH, Yoon J, Shin MC, Kwun SI (2010) A study on powder mixing for high fracture toughness and wear resistance of WC–Co–Cr coatings sprayed by HVOF. Surf Coatings Technol 204:2223–2229
23. Marques AS, de Costa LDL, dos Santos GR, da Silva Rocha A (2019) Wear study of hot forging punches coated with WC–CoCr and Cr3C2–NiCr through high-velocity oxygen fuel (HVOF) process. Int J Adv Manuf Technol 100: 3–11
24. Gong T, Yao P, Zuo X, Zhang Z, Xiao Y, Zhao L, Zhou H, Deng M, Wang Q, Zhong A (2016) Influence of WC carbide particle size on the microstructure and abrasive wear behavior of WC–10Co–4Cr coatings for aircraft landing gear. Wear 362–363:135–145
25. Wu K, Liu GQ, Wang L, Xu BF (2010) Research on new rapid and deep plasma nitriding techniques of AISI 420 martensitic stainless steel. Vacuum 84:870–875

A Review on Influence of Cutting Fluid on Improving the Machinability of Inconel 718



Prajith Sivadasan, Gotimayum Sachidev Sharma, Ivan Sunit Rout, and P. Pal Pandian

Abstract Nickel-based superalloys are widely used in the production and manufacturing sectors that require processes or applications that endure or operate at very high superheating temperatures. With the properties of high tensile strength, high melting point, and lightweight structural arrangement of molecules within the alloy material composition makes it more suitable for industrial utilization in aerospace industries and marine applications. This review paper discusses the use of various coolant lubricants that improves the machinability of Inconel 718 based on parameters such as surface roughness and tool wear under the influence of cutting speed, feed rate, and depth of cut. The machine used for analysis is CNC milling machine which will be used for experimentation using ceramic inserts as end milling tool. Various cooling techniques such as hybrid cooling, flood emulsion cooling, minimum quantity lubrication, and cryogenic cooling are being summarized in this paper from various experimentations and conclusions of other authors. On the basis of review, the hybrid cooling technique is found to be better than other cooling techniques because of its ability to obtain long tool life and smoother surface finish on the workpiece. With the use of these reviewed data, further research for finding a more compatible and effective cooling lubricant has to be done by experimentation in order to obtain an improved machining process for Inconel 718 material.

Keywords Ceramic inserts · CNC milling machine · Inconel 718 · Flank surface · Rake surface

1 Introduction

Superalloy materials are predominantly used in manufacturing and engineering construction sectors involved in applications for energy supply. The most common type of superalloys used is nickel-based superalloys. Inconel 718 is a nickel-based superalloy that is most commonly used in aerospace and turbine industries. This

P. Sivadasan · G. S. Sharma · I. S. Rout (✉) · P. Pal Pandian
CHRIST (Deemed to be University), Bangalore, India
e-mail: ivan.rout@christuniversity.in

© Springer Nature Singapore Pte Ltd. 2020

A. Praveen Kumar et al. (eds.), *Advances in Lightweight Materials and Structures*,
Springer Proceedings in Materials 8, https://doi.org/10.1007/978-981-15-7827-4_50

alloy is mostly used in the blades of turbine engines and in the nose of aircraft body due to its high temperature resistance, high strength compared to weight, and high tensile strength. Due to it high melting point characteristic, it is used in superheating applications that require materials to withstand at high temperatures.

With the integration of the stated properties, these materials are hard to machine continuously for longer periods of time, and hence, require periodic changing of machining tool due to wear. This, in turn, creates a manufacturing downtime and costs in major industries and production factories due to constant machine breakdown or repair. In order to overcome this problem and achieve efficiency in machining process, research and study are being done on developing new tools and coated materials, and parameter optimization using various lubrication techniques such as cryogenic lubrication, flood lubrication, hybrid lubrication, and liquid nitrogen lubrication. [1].

According to Zhuang et al. [2], cutting fluids provide an effectual way in improving machining of hard-to-machine materials by reducing friction developed at the cutting contact area through effective lubrication that reduces the temperature at the machining zone due to cooling by convectional heat transfer, and hence, reduces tool wear which, in turn, provides improved surface finish [2].

According to Kaynak et al. [3], cutting fluids used in lubrication of machining process contain many harmful chemicals that are difficult to discard and recycle in the environment, also causing skin and lung disease to the operators. Due to strict environment laws, there is less flexibility in using cutting fluids, although various substituent formulants that does not include lead, sulfur, or chloride are made, and they are not yet achieved to be completely harmful. The total incurred costs regarding the usage of cutting fluids are approximated to be several billions per year [3].

Hence, there is a need for an effective and cost-efficient cutting fluid in the industrial market sector associated with environmental and economic impacts. This review is done to find out various suitable cutting fluids and techniques that meet required industrial environmental and economic standards, for effective machining of Inconel 718 material using ceramic inserts and CNC end milling machine as the basis for study, also to obtain longer tool life and smooth surface finish in accordance with various operating parameters.

2 Cooling Techniques

Studies have been done on various cooling techniques for improving the machining of Inconel 718. These techniques depend on economic and technical factors with respect to the machining process in various applications. Technical factors refer to the availability of particular cooling equipment during the machining process such as availability of a particular number of nozzles, nozzle diameter, pressure regulator, and so on. Industries and production units select the techniques for lubrication based on the manufacturing process and cost factors while fabricating or machining the components for the desired end product. Various cooling techniques based on recent research developments include hybrid cooling, cryogenic cooling, flood cooling,

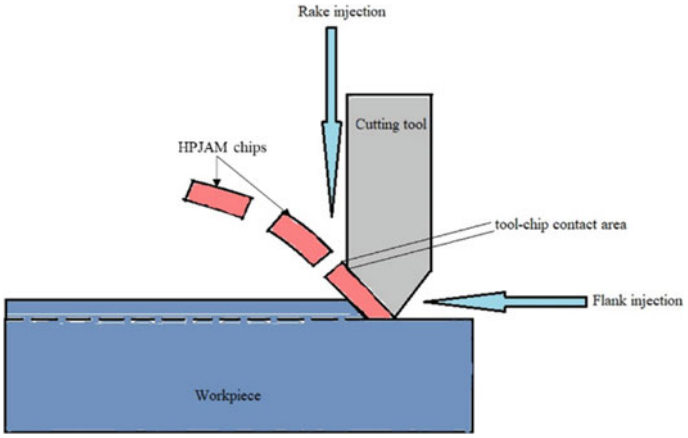


Fig. 1 Flank and rake injection of cooling lubricant in HPJAM

minimum quantity lubrication, and high-pressure jet assisted machining (HPJAM). According to Shokrani et al. [4], injection of pressurized fluid on the tool flank and rake surface provided less surface hardness with 10–15% decrease in overall machining force, and hence, obtained results with less surface defects in comparison with flood cooling [4], which provided less surface smoothness due to inability of the lubricant to reach the tool workpiece and chip interface creating a heat transfer barrier (Fig. 1).

Similarly, there exist other techniques that provide high production rate and optimum surface finish. In hybrid cooling, a cryogenic setup for spraying liquid nitrogen at the cut zone, in addition with simultaneously spraying pure rapeseed oil for coating the cold tool periodically was found to be effective in improving tool wear without much change in the surface roughness produced, regardless of the change in technique used. The tool life in hybrid cooling technique was found to be 50% greater than MQL, and 33% greater than cryogenic technique [5]. From experimentational studies, inclination of two jets in the direction of rake face and flank face of the machine tool was determined to be the most effective configuration in machining [6].

The experimentation conducted by Chopra et al. [7] determined flood cooling using emulsion-based oil provided better surface finish for shorter life when compared to cryogenic cooling using liquid nitrogen [7]. The cryogenic cooling technique provided best tool life and good surface finish after long machining duration, when compared to other techniques such as dry machining, flood emulsion, and blowing of cold air as a coolant as shown in Fig. 2.

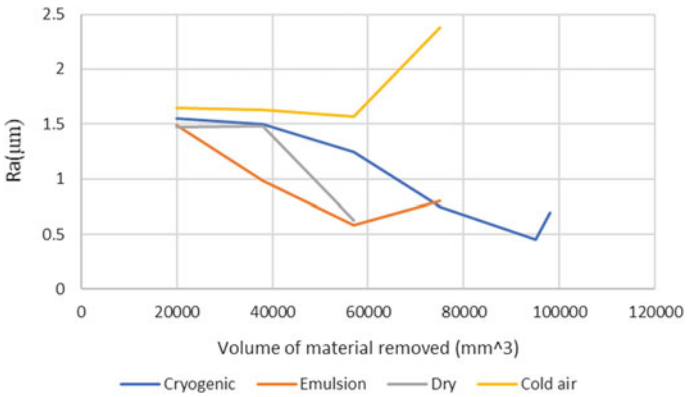


Fig. 2 Comparison of various lubrication methods on the basis of surface hardness and material removed

3 Parametric Observations

From Table 1, it can be observed that average cutting speeds used in most experimentations ranges from 30 to 140 m/min, with maximum feed rates up to 0.2 mm/rev. The maximum pressure ranges from 5 to 200 bars. Most of the tool inserts used were made up of coated carbide or ceramic material [8], and the lubricants used mostly included emulsifiers that mostly contain base oil as vegetable oils, along with intermittent use of liquid nitrogen in various experimentations. Higher cutting speeds were observed for ceramic tools and emulsifier lubricants (Figs. 3 and 4).

4 Analytical Study

Emulsified oils such as palm oil mixed with water had higher viscosity compared to synthetic esters. Hence, the lubrication during machining was improved as friction was reduced due to increase in viscosity. Oil–water ratio affects tool life under minimum quantity lubrication. Greater oil content in fluids leads to poor fluidness. Usage of emulsified oils, namely, palm oil and rapeseed oil improve the performance and deposition of lubrication film on the surface of tool or workpiece, due to the presence of greater amount of unsaturated fatty acids in the carbon chain [9]. Use of liquid nitrogen in cryogenic cooling or minimum quantity lubrication provides effective lubrication [10], but these lubricants are difficult to dispose in the environment because of the presence of harmful chemicals present in its chemical composition, and hence, contributes to global warming, skin and lung associated diseases to the operators present in the industrial environment after periodic exposure to nitrogen gas for long durations. Hence, these types of coolants provide less safe working conditions comparatively to other existing coolants. However, they can be used in

Table 1 List of studies on effective lubrication parameters

Authors	Cutting speed (m/min)	Feed rate	Flow rate	Surface roughness, Ra (μm)	Tool/tool life	Min pressure (bar)	Max pressure (bar)	Lubricant
Aziz Ul Hassan Mohsan et al.	140	–	10 L/min	Rz = 3, Rq = 0.4	Triple coated carbide	150	200	Eccoocool emulsifier, 10% conc
D.Fernańdez et al.	50	0.25 mm/rev	–	0.45	Precoated carbide tool/30.60 min	–	–	Liquid nitrogen
Yunn-Shiuan Liao et al.	60	0.1 mm/tooth	60 ml/hr	–	Coated carbide	5	5	BESOL 25
E. O Ezugwa et al.	250	0.2 mm/rev	5 L/min	–	Whisker reinforced ceramic	–	150	Emulsions of alkanolamine salts and di-cyclohexylamine
Alborz Shokrani et al.	140	–	15 kg/hr	0.4	Solid tungsten carbide	–	5	Liquid nitrogen and pure rapeseed oil
D. G Thakur et al.	40	0.08 mm/rev	10 ml/hr	–	Tungsten carbide	–	130	Water soluble cutting oil (20:1)
Erween Abd Rahim et al.	30	0.05 mm/rev	–	–	Coated carbide/90 s	–	–	Palm oil
Venkat Pradeep Allu et al.	70	–	0.6 kg/min	–	Multi-layered coated carbide	–	–	Oil and liquid nitrogen

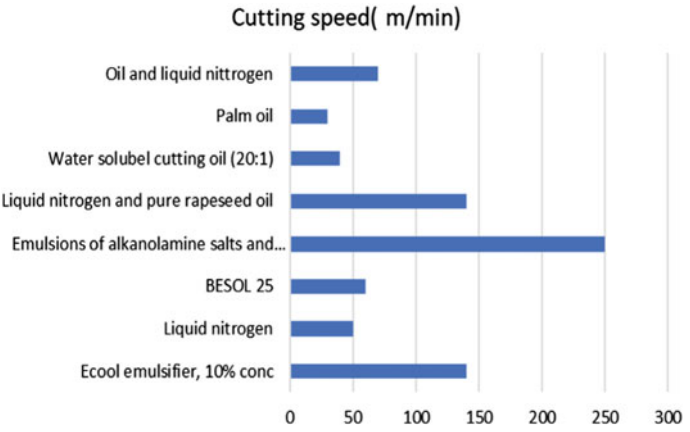


Fig. 3 Comparison of lubricants and cutting speed

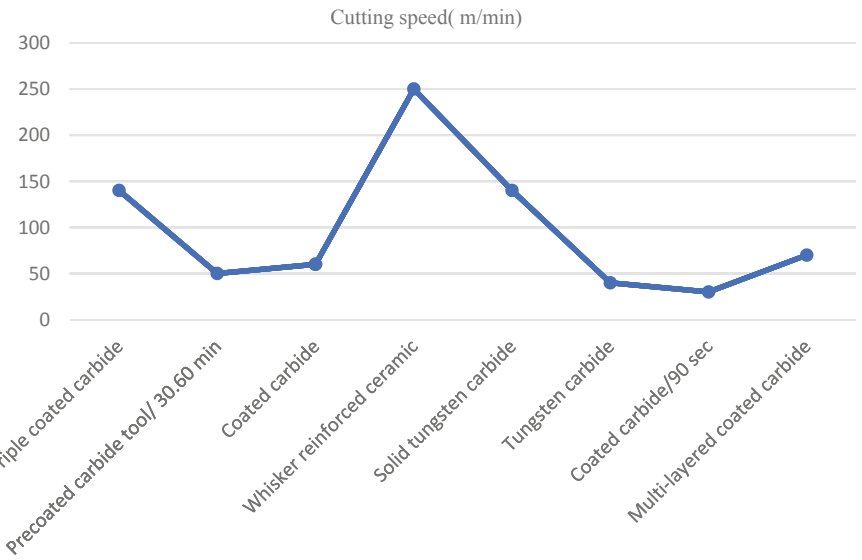


Fig. 4 Comparison of tool inserts and cutting speed

prescribed amounts as per industrial and environmental standards along with other coolants. According to Rout et al. [11], optimized cutting parameters for improving tool life under minimum quantity lubrication involve lower cutting speeds, less feed rates, and greater quantity of lubrication directed along an inclined axis [11]. As per experimentation conducted by Kaynak et al. [3], optimum and effective oil–water ratio and flow rate of fluid under minimum quantity lubrication are 60:40 and 60 ml/h, on the basis of observations from rake face wear of the tool.

5 Conclusion and Future Scope

Hybrid cooling and high-pressure jet assisted machining are the recent developments in cooling techniques that proved to be effective using combination of more than one property, or by varying external cooling environmental factors. These methods require an additional specifically designed equipment for operation. Among other already existing cooling techniques, cryogenic cooling was observed to provide longer tool life and smooth surface finish after long machining duration [7], whereas flood cooling provides better lubrication and smooth surface finish at lower cutting speeds. At higher cutting speeds, flood cooling provided optimum surface finish and shorter tool life, due to the developmental effect of heat exchange barrier of lubricant present between the workpiece material or cutting tool [12]. Emulsified oils exhibited comparable properties of lubrication to that of synthetic ester and gaseous fluids during machining operation. Emulsified oils tend to cause less harmful effects during machining process, and hence, it is considered to be a viable alternative.

With the use of these reviewed data, research has to be done for finding eco-friendly compatible coolants that improve the machinability of Inconel 718, and machining tool life by using the most appropriate methodology of lubrication.

References

1. Akhtar W, Sun J, Sun P, Chen W, Saleem Z (2014) Front Mech Engg 9: 106
2. Zhuang K, Zhang X, Zhu D, Ding H (2015) Employing preheating- and cooling-assisted technologies in machining of Inconel 718 with ceramic cutting tools: towards reducing tool wear and improving surface integrity. Int J Adv Manuf Technol 80:815–1822
3. Kaynak Y (2014) Evaluation of machining performance in cryogenic machining of Inconel 718 and comparison with dry and MQL machining. Int J Adv Manuf Technol 72:919–933
4. Shokrani A, Dhokia V, Newman ST (2017) Hybrid cooling and lubricating technology for CNC milling of Inconel 718 nickel alloy. In: 27th international conference on flexible automation and intelligent manufacturing, vol 11, pp 625–632
5. Shokrani A, Newman ST (2018) Hybrid cooling and lubricating technology for CNC milling of Inconel 718 nickel alloy. In: Procedia CIRP 77, 8th CIRP conference on high performance cutting (HPC 2018), pp 215–218
6. Pusave, F, Kramar D, Krajnik P, Kopac J (2010) Transitioning to sustainable production—part II: evaluation of sustainable machining technologies. J Cleaner Prod: 1–11
7. Chopra SA, Sargade VG (2015) Metallurgy behind the cryogenic treatment of cutting tools: an overview. In: 4th international conference on materials processing and characterization, vol 2, pp 1814–1824
8. Rout IS, Pandian PP (2018) Selection of cutting parameters for the machinability of Inconel using grey relational analysis. In: MATEC web of conferences, vol 172, p 04004
9. Abd Rahim E, Sasahara H (2017) Performance of palm oil as a biobased machining lubricant when drilling inconel 718. MATEC Web Conf 101:1–5
10. Nadig DS, Satisha GV (2012) Effect of cryotreatment on the wear performance of tungsten carbide tools. Ind J Cryogenics 137(1–4): 188–193

11. Rout IS, Pandian PP, Raj A, Lobo Ivan KC, Antony S (2020) Parametric investigation on the tool wear while performing face milling on Inconel 718 using round insert. Int J Mech Prod Eng Res Dev 10: 1–11
12. Rout IS, Pandian PP (2018) A Review on parametric study of hard machining of Inconel 718 using coated carbide tool. Adv Sci Eng Med 10: pp 234–239

Condition Monitoring of a Worm Gearbox Under Dynamic Loading Condition



Anupkumar Dube and M. D. Jaybhaye

Abstract Effective condition-based maintenance plays a vital role to extend the lifespan of the rotating equipment and helps in reducing the maintenance cycle intervals. The gearbox failure indication starts with the increased vibrations and abnormal increase in temperatures. Parameters like load, vibrations, temperature, etc., determine the overall life of the gearbox. By measuring and studying these parameters, we can predict the life of a new gearbox or the remaining life of a gearbox that is already in use. The present work deals with a foot-mounted worm reducer gearbox test rig. Different locations were selected for measuring temperature and vibration responses of the test rig. To study the test rig behavior and document the generated results, a test plan is designed. In the first phase reading, the test rig is operated for 70 min under normal conditions without any load applied. Readings are taken for every 10 min during the run. In the second phase reading, the operation time is kept the same 70 min, and the only change did is that the applied load is increased by 10 kg after every 10 min run operation. The temperature and vibration monitoring procedures were used to describe the behavior of the worm gear system as a function of load applied on the worm gear system. The temperature and vibration responses of the selected reading locations are compared for both phase readings. Commercial HP EP 90 gear oil is used in the gearbox for this experimentation.

Keywords CBM · Worm gear box · Temperature · Vibration · HP EP 90 · Load

1 Introduction

For the right operation and acquiescence of worm gear, thermal steadiness plays a vital role, and it largely depends on a lubricating oil and additive lubricating oils, and additives contribute an important role in the steady operations of the worm gears during its full working life. Oil viscosity directly shows its effects in the gear contact zones during the operational time, and hence, it is directly related to the temperature

A. Dube (✉) · M. D. Jaybhaye
College of Engineering Pune, Department of Production Engineering and Industrial Management, Pune,, Maharashtra, India
e-mail: anup.dube@gmail.com

© Springer Nature Singapore Pte Ltd. 2020

A. Praveen Kumar et al. (eds.), *Advances in Lightweight Materials and Structures*,
Springer Proceedings in Materials 8, https://doi.org/10.1007/978-981-15-7827-4_51

and vibrations. Ideal lubrication can be achieved only when the temperature of the lubricating oil is kept within the working range. Compared to the cylindrical and cone gear types, the worm gears have a high amount of sliding, and hence, the friction is more during worm gear operation which lowers the efficiency of the worm gears. The type of lubrication, the operational sliding speed, and the temperature play a vital role in the efficiency of the worm gear pair.[1]. As per the ANS for industrial enclosed gears, the working span of the gearbox be subject to the minimum working span of the gearbox parts. During designing of the gear pair, they are generally designed for higher working life depending upon the applications in which they are used. Researchers have observed that at around 43% of the sliding, rotating part's failures are related to the insufficient and improper lubrication, and the selection of incorrect lubricants [2]. The overheating phenomenon occurs if there is improper heat transfer to lubricants from the contacting zones of the gear pairs. Due to the overheating of the contacting parts, there is always a risk of contracting parts being failed during their operational life.

Trivedi and Bhatt [3] performed the friction and wear experiments using a pin-on-disc tribo tester. Their research has concluded that by comparing the constant and incremental load for various lubricants, increment load offers friction and wear. The authors in their research have observed by comparing the tribological properties of the selected lubricants, and it is cleared that SAE20W40 and SAE20W50 have better performance compared to SAE10W30. An investigation of the interrelation among vibration analysis and wear debris analysis is done by Penga et al. [4]. The researchers have achieved this by examining dissimilar working situations of an experimental rig, consisting of a worm gearbox driven by an electric motor. They have conducted a series of test conforming to the absence of proper lubrication, and with dissimilar contaminant particles added to the several lubricants. The results from their work have given more knowledge of the dependent and independent characters of vibration and wear debris analyses in predicting and diagnosing machine faults. Experimental analysis of the tribological behavior for aluminium alloy materials under the effect of sliding speed and for different loads using a pin on disk apparatus is presented by Nuraliza et al. [5]. Experiments were conducted under different parameters, different loads (10, 50, 100 N), and constant speeds of 3 m/s. Their study results show that load 100 N shows high coefficient of friction compared to 10 and 50 N. A variable speed gearbox (worm) having lubricated with oil with different viscosities for vibrational and temperature monitoring techniques to check the behavior of the worm gearbox is used by Ismon et al. [6] in their research work. The gearbox is rotated with three different predetermined speeds. The temperature and vibrations in the rotating gearbox is monitored regularly. The research works have shown that the higher the viscosity of the oil, the lower is the vibration produced for it, and the higher the temperature for it. The lower is the viscosity of the oil, the lower is the temperature.

A study of the condition monitoring of a gearbox (worm) to check the fault in the gear is done by Vahaoja et al. [7] by using vibrational analysis and oil analysis techniques. The research work has found out that a combination of ferrographic wear particle analysis and vibration analysis gives the best prediction of the worm

gears during its working cycle. The study work has suggested that the vibration measurement point should be as possible as near to the location where worm gears make contacts in the gearbox.

An integrated approach (vibrational and wear debris analysis) for diagnosing the machinery fault is used by Zhongxiao and Kessissoglou [8]. A fabricated test rig driven by an electric motor is used for this study. The study has observed that the mentioned two techniques individually can detect around 40% faults, but the prediction rate is more when the combination of these techniques is used. Focusing the type of gear faults, frequently used various condition indicators (CIs) for condition monitoring are described by Večeř et al. [9]. In the research work, vibrational signals are acquired for a manual helical gear transmission system for its durability testing. Based on the study results, they have shown that using the condition indicators, an early failure detection can be achieved. A decision tree-based algorithm for classifying the features collected from the vibration signals using wavelets is proposed by Srivastava et al. [10] for a helical worm hear box system. The researchers have observed that their proposed model can be effectively used in assessing the condition of equipment under monitoring.

The correlation among the sensor location and fault detection in the gearbox system is investigated by Alkhadafe et al. [11]. They have proposed a methodology locating the monitoring sensors on a gearbox system for getting high-quality vibration data. The study has concluded that the implemented approach is suitable for improving the reliability of the system. The worm gear faults using acoustic emission and vibration analysis are analyzed by Elforjani et al. [12]. In their study, a comparison of the results generated from the acoustic emission and vibration analysis is done. It has been observed that the results of acoustic emission have better capability to detect faults as compared with the vibration analysis. Kushwah and Sharma [13] have disclosed rigging wear because of unpredictability like time subordinate, framework reliant, and physical connection. This was finished by visual reviews and particles evaluated by weight estimation, after oil filtration for different burdens. They have reasoned that as the heap increases, the wear particle development will be quicker as a contrast with the past.

2 Test Rig Setup

A test rig with a worm gearbox is developed for conducting the experiment. A standard worm reducer gearbox of Gateej make is selected with a reduction ratio of 20 and with a half HP motor attached to it. The center distance between the input and out shaft is 45 mm. The input rod diameter is 30 mm, and the output shaft diameter is 25 mm. The input shaft is rotated with a constant speed of 1485 rpm. Figure 1a shows the test rig schematic diagram and b and c show the worm gears.

A hanger bearing is attached with the worm gearbox output rod, and a threaded rod with nut and plate is used for applying load on the output road of the gearbox. The tightening of the nut will increase the load applied to the output rod. For measuring

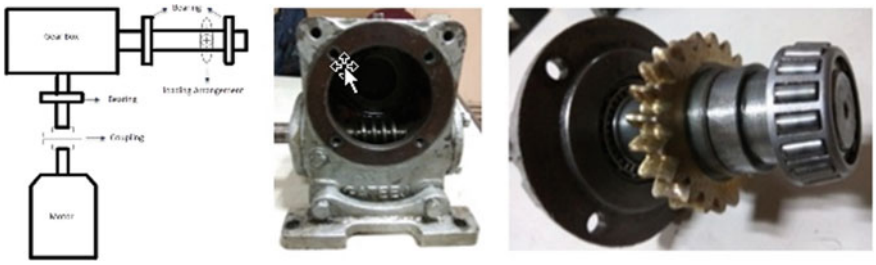
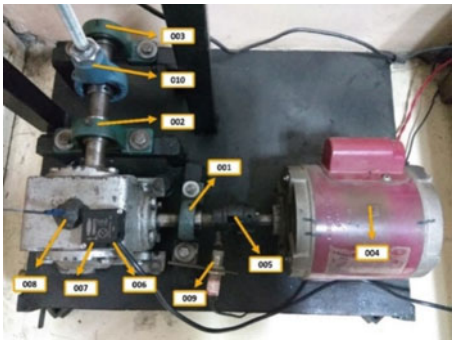


Fig. 1 **a** Schematic diagram of the test rig. **b** Right-handed worm shaft. **c** Worm gear taper roller bearing

the applied load in terms of kilograms unit, a load cell is attached in this mechanism between the hanger bearing and threaded rod. A commonly used weighing scale is used as a digital output display unit attached with the load cell which displays the applied load in the kilogram unit. The selected load cell is calibrated using a kilogram weight block, and speed of input shaft is measured by a non-contact type proximity sensor. A "*J*" type thermocouple with a probe is inserted in the gearbox by removing a top plug is used for measuring the gear oil temperature. The thermocouple is attached to a wire that is connected to a digital display which displays the temperature value. For measuring the gearbox temperature and vibration, Banner make (QM42VT2) plug and play type of handy sensor is selected. Through USB connector and sensor software, desired data can easily be recorded in the computer in text format. Digital temperature gun is used for measuring bearing, motor, and coupling temperatures. Figure 2 shows the location points in the designed test rig at which readings of various parameters are taken.



001 Input Rod Bearing Temperature
002 Output Rod Bearing Temperature
003 Output Rod Bearing Temperature
004 Motor Temperature
005 Coupling Temperature
006 Gear Box Temperature
007 Gear Box Vibration
008 Gear Box Oil Temperature
009 Motor RPM
010 Load Applied on Output Road

Fig. 2 Measurement locations on the Gear box test rig

3 Method of Experimentation

In all testing phases, the test rig is operated at a constant speed. A time gap of 10 min is selected to record the changes in vibration and temperature responses of the test rig and gearbox with and without increase in the applied load. In the first phase reading, the test rig is operated for 70 min under normal conditions without any load applied. The test rig is operated for 10 min, and after that, reading was taken. In the second phase as well the test rig is operated for 70 min, but in the second phase, with each ten-minute operation, a load of 10 kg is applied on the output road of the gearbox. In this phase as well, the readings were taken after each 10 min run. Two separate readings were taken in the second phase to confirm any discrepancies in the readings. The average of the collected two readings is considered as the final reading. For accurate data collection and maintenance, a detailed test plan was formulated. Different readings for the selected locations are documented in the formulated test plan. For measuring the gearbox oil temperature, a thermocouple with a probe is inserted in the gearbox from the top cap of the gearbox assembly, and later, it is properly sealed to avoid any oil leakage from this location. Commercially available HPEP90 oil is used for this experimentation. Reading were collected as per the developed test plan. Reading were collected as per the developed test plan. Table 1 shows the readings observed during the experimentation.

Figure 2 shows the location points in the test rig at which different readings are taken. Different instruments are used for collecting the readings from the test rig.

Table 1 Experimental observations of gearbox system

Reading	Run Time (Minutes)	Load Applied (Kg)	Temp. @brg-01 (°C)	Temp. @brg-02 (°C)	Temp. @brg-03 (°C)	Motor Temp. (°C)	Coupling Temp. (°C)	Gear oil Temp. (°C)	Gearbox Temp. (°C)	Motor RPM	RMS Velocity mm/s
Test-01 (No load applied run, Total Run Time 1 hr 10 mins)											
Test-01	Initial	0	27	27	27	27	27	27	27	0	0
	10 Min	0	39	31	31	40	51	31	30	1482	5.8
	20 Min	0	50	37	31	57	68	37	36	1482	4.4
	30 Min	0	54	40	31	65	75	41	40	1482	4.4
	40 Min	0	58	44	31	71	80	44	44	1481	4.3
	50 Min	0	59	45	34	74	82	46	46	1482	4.3
	60 Min	0	59	48	35	76	84	48	47	1485	4.4
	70 Min	0	62	48	36	77	85	49	49	1482	4.7
Test-02 (Load applied run, Total Run Time 1 hr 10 mins)											
Test 02	Initial	0	29	29	29	29	29	29	29	0	0
	10 Min	0	56	34	31	33	66	34	33	1482	5.5
	20 Min	10	65	38	32	54	71	40	38	1484	5
	30 Min	20	68	44	33	60	81	44	42	1485	5
	40 Min	30	72	47	35	65	85	47	45	1483	4.8
	50 Min	40	73	49	38	67	90	50	48	1484	4.7
	60 Min	50	73	52	39	71	92	52	50	1485	4.3
	70 Min	60	79	52	40	75	92	53	51	1484	4.5

4 Results and Discussions

It is important to understand the natural frequencies of complete assembly and correlate that with vibrations at various locations like gearbox, bearing 1, bearing 2, bearing 3, motor, structure base, etc. The test rig is not loaded to maximum due to limitations in the loading mechanism. Results are recorded as per the formulated test plan, and charts are plotted for the temperature and vibration responses with respect to the changing loading conditions. Figure 3a shows temperature changes at the selected locations with respect to time and for no loading condition. It is detected that temperature is higher at coupling location and lowest at the bearing 3 location which supports the out rod at its end location. Among three bearing locations, the temperature at bearing 1 location is highest, and the temperature at bearing 3 location is lowest. Figure 3b shows temperature changes with respect to time and for load-applied condition. It is detected that even for loading conditions as well the temperature is higher at coupling location and lowest at the bearing 3 location which supports the out rod at its end location. Even for loading condition as well, among three bearing locations, temperature at bearing 1 location is highest, and the temperature at bearing 3 location is lowest.

Figure 4a shows RMS velocity changes at gearbox top surface location locations with respect to time and for no-load condition. It has been observed that at the start, the velocity is high as there are system clearances and there is a sudden drop in it after the initial run cycle as the system clearances mentioned above settles after

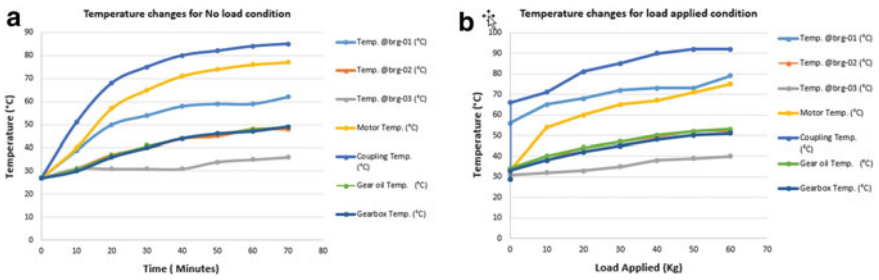


Fig. 3 **a** No-load condition temperature responses. **b** Load condition temperature responses

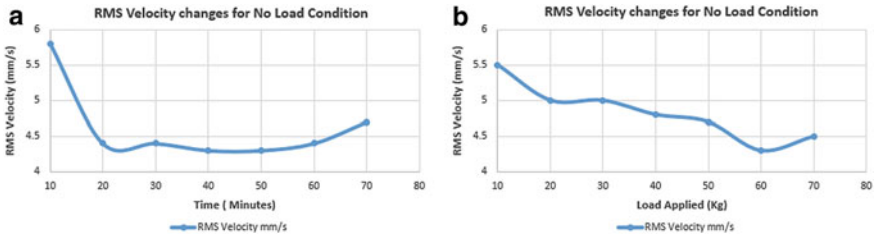


Fig. 4 **a** No-load condition RMS velocity responses. **b** Load condition RMS velocity responses

gearbox operation stabilizes. For no-load condition, the RMS velocity value is almost constant from 20 to 60 min run cycle, and after that, it starts increasing. Figure 4b shows RMS velocity changes at gearbox top surface location locations with respect to time and for load-applied conditions. It has been observed that at the start, the velocity is high, and it gets reduced with each load application cycle till the end. From 20 to 30 kg applied load, there is no change in the RMS velocity value. From the graph, it can be observed that there is a slight increase in the RMS velocity value from load value 60–70 kg, and in earlier 60 kg there was a constant drop in it with each increased load value.

5 Conclusions

The present study helped in determining the temperature and vibration variations for the selected locations in the designed test rig during its operating conditions with and without loading. From no-load test and constant load test, it is concluded that vibrations at no-load condition are higher than the loaded condition and as the load gradually increases the vibrations are reduced marginally. This can be termed as a minimum radial load for the system to run at lower vibrations, and after the minimum radial load is exceeded, the vibration levels start increasing. In the whole system, the coupling temperature is highest in both no-load condition and loading condition. The gear oil temperature and gearbox temperature in each individual reading are almost the same for both no-load condition and constant load condition.

In the future consideration, acoustics emission testing can be done on the same test rig with increased operating time and less increase in the applied load.

References

1. Szeri AZ (1998) Fluid film lubrication—theory and design. Cambridge University Press, New York
2. Harris TA (2007) Rolling bearing analysis. Wiley-Interscience Publication
3. Trivedi HK, Bhatt DV (2017) Effect of lubricating oil on tribological behavior in pin on disc test rig. Tribol Ind 39:90–99
4. Peng Z, Kessissoglou NJ, Cox M (2005) Study of the effect of contaminant particles in lubricants using wear debris and vibration condition monitoring techniques. Wear 258:1651–1662
5. Nuraliza N, Syahrullail S, Faizal MH (2016) Tribological properties of aluminium lubricated with palm olein at different load using pin-on-disk machine. J Tribol 9:45–59
6. Ismon M, Zaman I, Ghazali MI (2015) Condition monitoring of variable speed worm gearbox lubricated with different viscosity oil. Appl Mech Mater 773–774:178–182
7. Vahaoja P, Lahdelma S, Leinonen J (2006) On the condition monitoring of worm gear. In: Engineering asset management, proceedings of the 1st world congress on engineering asset management, pp 332–343
8. Peng Z, Kessissolou N (2003) An integrated approach to fault diagnosis of machinery using wear debris and vibration analysis. Wear 255:1221–1232

9. Večeř P, Kreidl M, Šmíd R (2005) Condition indicators for gearbox condition monitoring systems. Acta Polytechnica 45:35–42
10. Srivastava A, Singh A, Sugumaran V, Amarnath M (2016) Fault diagnosis of helical gear box using vibration signals through random tree and wavelet features. Indian J Sci Technol 9(33)
11. Alkhadafe H, Al-Habaibeh A, Daihzong S Lotfi A (2012) Optimising sensor location for an enhanced gearbox condition monitoring system. In: International congress on condition monitoring and diagnostic engineering, conference series 364
12. Elforjani M, Mba D, Muhammad A, Sirs A (2012) Condition monitoring of worm gear. Appl Acoustics 73(8):859–863
13. Kushwah AS, Sharma RB (2017) The wear condition of spur gearbox under variable loads using wear debris analysis technique—an investigation. Int J Automobile Eng Res Develop (IJAuERD) 7(2):1–8

A Review on Optimization of Process Parameters of EDM on Aluminum Metal Matrix Composites Using Various Optimization Techniques



S. Prashanth, M. Kannan, R. Karthikeyan, and K. Sunil Kumar Reddy

Abstract Electrical discharge machining (EDM) is the unconventional machining operation, it is appropriate for processing of hard and brittle metals like metal matrix composites. Aluminum-based metal matrix composites (AMMCs) are broadly utilized in aviation and defense parts in the view of their leading properties like greater strength to weight ratio and greater stiffness to weight ratio. The present paper reviews the optimization of EDM process parameters like discharge current, pulse-off-time, duty factor, open circuit voltage(gap voltage) and pulse-on-time on the material removal rate (MRR) and surface roughness of the composite responses by utilizing various methods like Taguchi method, response surface methodology (RSM), gray relational approach (GRA), TOPSIS and genetic algorithm.

Keywords AMMCs · EDM · TAGUCHI · RSM · TOPSIS · GRA · GA

1 Introduction

Composite material is the material produced by using two combining materials with significant various physical or chemical properties that when mixed to produce a material with quality different from an individual components. The aluminum metal matrix composites (AMMCs) are very difficult to machine by the traditional machining process. Because of abrasive particles are presents, due to this formation of impressive tool wear and recommended that the EDM process is the best choice for acquiring the exact removal of material from the metal matrix composites [1]. The different techniques are utilized for production of aluminum metal matrix composite like as the stir casting method, liquid infiltration, squeeze casting and powder metallurgy. The entire processes stir casting method is commonly used and easy to fabricate the aluminum metal matrix composite [2,3]. In EDM process, the

S. Prashanth (✉) · R. Karthikeyan · K. Sunil Kumar Reddy
GRIET, Hyderabad, India
e-mail: prashanthsriram551@gmail.com

M. Kannan
Annamalai University, Chidambaram, India

© Springer Nature Singapore Pte Ltd. 2020

A. Praveen Kumar et al. (eds.), *Advances in Lightweight Materials and Structures*,
Springer Proceedings in Materials 8, https://doi.org/10.1007/978-981-15-7827-4_52

operation is attained by achieving consistent discrete releases into the middle terminal of the wire tool electrode and workpiece and this is separated by dielectric fluid [4]. The processing method is suitable for achieves the effective metal removal rate and parameters assist to increase the tool life with the good surface finish and are also called as machinability with minimum expenses [5]. During the machining of materials by the electro-discharge machining process to obtain the good machinability and quality, copper was used as an electrode. A copper electrode tool is related to a brass electrode tool during the operation of AISI 329 stainless steel. A brass tool electrode has the low melting point, thermal conductivity and electrical resistivity occurs faster than the copper tool electrode [6]. These days aluminum, copper, magnesium and titanium, etc., are used as matrix materials and silicon carbide (Sic), boron carbide (B_4C), tungsten carbide (WC) and aluminum oxide (Al_2O_3) are used as reinforcements [7].

The EDM process works by spark erosion by the principle of spark generation and because of this remove the unwanted material from the workpiece. The erosion of the EDM spark is same as the electric spark which burns a short hole in a metal piece by which its contact. The spark developed through the operation produces the heat, which extract the material from the workpiece by erosion and evaporation. During the operation, both the anode and cathode tools are made from conductive materials, which is dipped in the dielectric fluid while the machining process. In EDM process, the input process parameters are pulse-on-time, pulse-off-time, duty factor, gap voltage and discharge current, etc. [15] (Fig. 1).

Taguchi strategy is a basic way to set up the plan of experiments to draft the orthogonal arrays. This strategy is a simple, precise and standard approach to optimization methods. A measurable examination of variance may be used in addition to S/N ratio, to show the effect of input machining parameters on the removal rate of material and surface roughness [8].

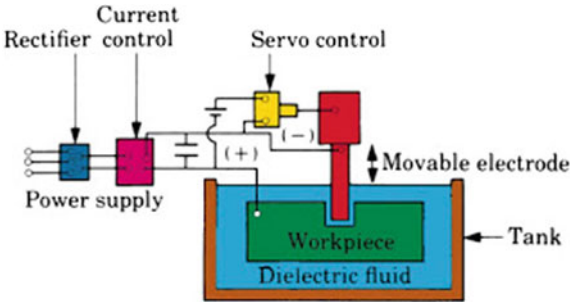


Fig. 1 EDM principle

2 Methods

2.1 Taguchi Technique

Kandpal et al. [9] explored the impact of input machining parameters like gap current, pulse-on-time and duty factor on the removal rate of material by utilizing the electrical discharge machining (EDM). AA6061-10% aluminum oxide (Al_2O_3) is a metal matrix composite (MMC) is manufactured by the stir casting method. After the manufacturing of the metal matrix composite, the SEM analysis is done after examining they disperse of reinforcement particles in the matrix material. In the present investigation, nine numbers of experiments are performed and consequently L9 orthogonal array (L9 OA) was choosing the Taguchi design of experiments. They concluded that MRR rises with rising the gap current and pulse-on-time. The optimum process parameters are at 14 Amps gap current, 200 μs pulse-on-time and 50% duty factor should be chosen to greater MRR. The duty factor increases, MRR will decreases. Pulse current is the most effective parameter on the removal rate of material. The Taguchi strategy is utilizing with the assistance of ANNOVA test and S/N proportion for optimization of machining parameters.

Choudary et al. [16] study the impact of input machining parameters like as tool electrode, gap current, open circuit voltage, pulse-on-time and duty factor on the electrode wear rate, surface roughness and removal rate of material by utilizing the EDM with various electrode tools (brass and copper tool electrodes of 10 mm diameter). In this investigation, 18 experiments are executed and consequently L18 orthogonal array was choosing the Taguchi design of experiments. AA6061-14% fly-ash is a metal matrix composite is manufactured though the stir casting process. A copper tool electrode has utilized to processing the AA6061-14% fly-ash with respect to input parameters. MRR of the composite rises with rise in gap current, pulse-on-time and duty factor. EWR of the composite rises with rise in gap current and pulse-on-time. While EWR reduces with rising the gap voltage. Surface roughness of the metal matrix composite rises with rise in pulse-on-time and duty cycle. The optimal values of EDM through brass electrode are maximum MRR is identified as 0.1996 g/min and EWR is identified as 0.0770 g/min at 150 μs pulse-on-time and 16A gap current.

2.2 Response Surface Methodology (RSM)

Kar et al. [10] accomplished the experimental investigation and mathematical modeling of aluminum metal matrix composites (AMMCs) on EDM according to the response surface methodology. Al-7075 is used the matrix material and 6% of red mud is utilized as reinforcement. This shows the effect of input machining parameters like as discharge current, open circuit voltage and pulse-on-time on output parameters like MRR, tool wear rate and radial over cut. The brass tool electrode

is utilized to machine this metal matrix material. Based on the central composite design of experiments, the levels of process parameters are chosen and experiments are completed in the wake of setting the levels of variables. More energy is available during, rise in a pulse-on-time and peak current leads to extract the unwanted metal from the workpiece by utilizing the electrode tool. They concluded that the pulse-on-time and discharge current increases with rise the MRR. Tool wear rate (TWR) is also similar to the removal rate of material. Radial over cut increases with increases the peak current, open circuit voltage and pulse-on-time. The peak current is the most influence on responses compared to other input machining parameters like open circuit voltage (gap voltage) and pulse-on-time.

Mohanty et al. [16] accomplished the experimental investigation and mathematical modeling of Al-12% Sic composite is processing through the electro-discharge machining with the use of copper electrode, according to the response surface methodology. This shows the effect of input machining parameters like as pulse-on-time, pulse-off-time and peak current on output responses are electrode wear rate, surface roughness and removal rate of material. Based on the central composite design (CCD) the experimental process is carried with different sequence of machining parameters. They concluded that the peak current rises with rise in removal rate of material and electrode wear rate. The surface roughness is directly proportional to the peak current.

2.3 Gray Relational Analyses (GRA)

Palanisamy et al. [11] explained the electrical discharge machining on LM6 aluminum oxide is manufactured through the stir casting method. LM6 aluminum alloy is used the matrix material and aluminum oxide 10% is reinforcement. An analyzing the influence of electrical discharge machining parameters like as discharge current, pulse-on-time and pulse-off-time on the removal rate of material and tool wear rate (TWR). A copper tool electrode is utilized to drill holes on the material with 12 mm diameter and 3 mm in depth. A dielectric fluid is used as kerosene oil. They concluded that increasing the discharge current, pulse-on-time and pulse-off-time increases the MRR and electrode wear rate. In these aluminum metal matrix composite, the MRR is considered as maximum as good and electrode wear rate is considered as a minimum as good. Increase in discharge current produces over heat during machining due to this overheat there is a chance of electrode wear. Design and optimization of machining parameters were done utilizing gray relation analysis. In electrical discharge, the machining of this composite surface roughness of the polished surface is treated as least as the best class. An increase of discharge current, pulse-off-time and pulse-on-time increases the roughness of the polished surface. The optimal values of input process parameters are discharge current 40amps, pulse-on-time 33 μs and pulse-off-time 9 μs for given responses with allotted weight values. The discharge current is the most precisely influences the roughness of the surface and then later on by pulse-on-time and pulse-off-time.

Shukla et al. [12] examined the effect of the EDM operation of input process parameters on the removal rate of material, tool wear rate, radial over cut and flatness in AMMCs. Aluminum alloy (Al-LM6) reinforced using silicon carbide (Sic) and boron carbide (B_4C) particles. The composition of sample one is 4wt% B_4C + 2wt% Sic and sample two is 2wt% B_4C + 4wt% Sic. Al-LM6/Sic/B_4C metal matrix composites are fabricated through the stir casting method. Gray relational analysis (GRA) is used for multi-response optimization. The gray relational coefficient is estimated to express the relation among the best and real normalized experimental results. A gray relational analysis applied to optimize the output parameters to maximize the MRR and minimize the tool wear rate. The optimum values of process parameters are pulse current 12A, pulse-on-time 150 μs and pulse-off-time 9 μs and these are obtained through the gray relational grade. A copper tool electrode was widely utilized in the EDM process.

2.4 Topsis

Satpathy et al. [13] investigate the machining parameters in die sinking type electrical discharge machining through multi-response utilizing TOPSIS. Copper tool electrode is used to processing Al-Sic (20% of Sic as reinforcement) metal matrix composites. Al-Sic composite is manufactured through the stir casting process. It was notified that MRR and an electrode wear rate. This electrical discharge machining (EDM) process is mostly affected through the different input machining parameters like peak current, pulse-on-time, duty cycle and gap voltage. In this investigation, 9 numbers of operations are to be performed and consequently L9 orthogonal array (L9 OA) was choosing the Taguchi design of experiments. They achieve that peak current, pulse-on-time and gap voltage are rises with a reduction in the electrode wear rate up to certain level and then it rises. The peak current increases with effect to increase the MRR, when pulse-on-time increases, decreases the MRR and it was noted that at primarily MRR rises with a rise in gap voltage up to certain level and then MRR decreases. Rise in gap voltage rises the peak current which removes the material from workpiece. The input current increases with rises the surface roughness. The pulse-on-time rises with decrease the surface roughness and then gap voltage rises, surface roughness remains constant up to certain level then it increases immediately. The PCA-TOPSIS approach is used to achieve the optimal values of input process parameters are input current 3A, pulse-on-time 75 μs, duty factor 80% and gap voltage 40 V. The SEM analysis is also carried out to examine the distribution of reinforcement particles in the Al-Sic metal matrix composite.

Bhuyan et al. [17] investigate the machining parameters on EDM through multi-response utilizing TOPSIS method is utilized to get a one numerical index. The analysis of variance (ANOVA) method is used to test the significance of the models and examine the effect of machining parameters. The statistical model is developed through the central composite design (CCD) approach for definite prediction of responses. Aluminum-24% Sic is used as the metal matrix composite. An analyzing

the influence of EDM parameters like as peak current, pulse-on-time and flushing pressure on the MRR, surface roughness (Ra) and electrode wear rate (EWR). The removal rate of material better to maintain least is the best, while tool wear rate and surface roughness are maintained to minimum is the best. The optimal values are MRR = 0.5, Ra = 0.3 and EWR = 0.2.

2.5 Genetic Algorithm (GA)

Aharwal et al. [14] estimated the input process parameters on material removal rate (MRR) of aluminum silicon carbide (Al-Sic) metal matrix composites by using electro-discharge machining (EDM). A copper tool electrode is utilized to processing the metal matrix composite. The input machining parameters are discharge current, discharge voltage, duty factor and pulse-on-time. 90% of aluminum and 10% of silicon carbide metal matrix composite is fabricated through the powder metallurgy technique. The investigation of MRR obtains an optimal values during discharge current is maximum and discharge voltage is minimum. The Taguchi method (L16 orthogonal array) is utilized to design of experiments and optimization for genetic algorithm (GA). Genetic algorithm technique is used to examine the optimal values of surface roughness (RS) and material removal rate (MRR). Roughness of the machined surface is good when discharge current and discharge voltage is low. Genetic algorithm utilizing MATLAB 12 and optimization values for higher material removal rate and lower surface roughness are achieved. The optimum process parameters are at input current 49.83A, pulse-on-time 124.02 μs, servo voltage 4.56 V and 1.30 duty factor should be choose to the maximum MRR. The optimum process parameters are at input current 1.07A, pulse-on-time 27.83 μs, servo voltage 1.74 V and 11.32 pulse duty factor to be choose to the least surface roughness.

3 Conclusion

In this paper, review was discussed related to machining of aluminum metal matrix composites through the EDM process. The different optimization methods are utilized by researchers to estimate the better combination of process parameters of electrical discharge machining process for operation of aluminum metal matrix composites like ANNOVA, response surface methodology, gray relational analysis, TOPSIS and genetic algorithm.

It is observed that the discharge current is the most prevailing factor which mostly influences the MRR, tool wear rate and surface roughness while machining of aluminum metal matrix composites through the electrical discharge machining process.

There is a scope of writing a review in the future by using all the methods are suitable for optimize the machining characteristics using the different machining process.

References

1. KaderEnden A, Arinc A, Kogmen F, Mater MJ (1995) Process. Manuf Sci 4:163–175
2. Taha MA (2003) Practicalization of cast metal matrix composites (MMCCs). Mater Des 22:431–441
3. YigezuBS, Jha PK, Mahapatra MM (2013) The key attributes of synthesizing ceramic particulate reinforced Al-based matrix composites through stir casting process: a review. J Mater Manuf Process 969–979
4. Crookall JR, Heuvelman CJ (1971) Electro-discharge machining the state of the art. Ann CIRP 20(2):113–120
5. Groover MP (1996) Fundamentals of modern manufacturing materials, process and systems. Prentice Hall International Editions
6. Sharma P, Singh S Mishra DR (2014) Electrical discharge machining of AISI329 stainless steel using copper and brass rotary tubular electrode. Procedia Mater Sci 5:1771–1780
7. Sakthivelu S, Sethusundaram PP, Meignanamoorthy M, Ravichandran M (2015) Mech Mech Eng 1:1–14
8. Muthuramalingam T, Mohan B (2015) Arch Civ Mech Eng 15(1):87–94
9. Kandpal BC, Kumar J, Singh H (2018) Optimization of process parameters Of EDM of fabricated AA6061/10% Aluminiumoxide (Al_2O_3) aluminum based metal matrix composite. Mater Today Proc 5:4413–4420
10. Kar C, Surekha B, Jena H, Choudhury SD (2018) Study of influence of process parameters in electrical discharge machining of aluminium-red mud metal matrix composite. Procedia Manuf 20:392–399
11. Palanisamy D, Devaraju A, Manikandan N, Balusubramanian K, Arulkirubakaran D (2019) Experimental investigation and optimization of process parameters in EDM of aluminium metal matrix composites. Mater Today Proc
12. Shukla M, Dhakad SK (2018) Optimization of electrical discharge machining of Al-LM6/SiC/B4C composite: a grey relational approach. Mater Today Proc 5:19147–19155
13. Satpathy A, Tripathy S, Senapati NP, Brahma MK (2017) Optimization of EDM process parameters for AlSiC-20% SiC reinforced metal matrix composite with multi response using TOPIS. Mater Today Proc 4:3043–3052
14. Aharwal KR, Sitaram, Krishna CM (2018) Optimization of material removal rate and surface roughness in EDM machining of metal matrix composite using genetic algorithm. Mater Today Proc 4:5391–5397
15. Image reference, https://mechanicalinventions.blogspot.com/2016/01/electrical-discharge-machining-edm.html
16. Choudary R, Singh G, Kumar K, Bharathi P, Kumar R, Kumar V (2018) Investigation of electrical discharge machining of Al6061/14%wt fly-ash composite with different tool electrodes. Mater Today Proc 5:19923–19932
17. Mohanty S, Routara BC, Bhuyan RK (2017) Experimental investigation of machining characteristics for Al-Sic 12% composite in Electro-discharge machining. Mater Today Proc 4:8778–8787
18. Bhuyan RK, Routara BC, Parida AK (2015) An approach for optimization the process parameter by using TOPSIS Method of Al-24% Sic metal matrix composites during EDM. Mater Today Proc 2: 3116–3124

Reliability Design for Bending Fatigue Strength of Carburized Gears of Low-Carbon Case Hardenable Steels 20CrMo, 20MnCr5, and SAE 8620

Rajeshkumar Ramasamy, Senthil Ram Nagapillai Durairaj, Thulasirajan Ganesan, and Praveen Chakrapani Rao

Abstract Bending fatigue test was performed on carburized gears made of different low-carbon hardenable steels such as 20CrMo, 20MnCr5, and SAE 8620. Hardness assessment and microstructure examination were conducted to confirm the homogeneity of phase presence and absence of network carbides and decarburization. Stress levels were chosen to find the fatigue limit of the different carburized gear materials. Fatigue life of the component can be predicted at various stress level with available test data by using Weibull distribution, which is suitable for random failure data. By fitting this failure data at various stress level, actual fatigue strength of the component can be calculated at different reliability. Reliable fatigue design for three different materials are predicted and compared, which disclosed SAE 8629 as superior.

Keywords Bending fatigue strength · Carburizing · Weibull distribution · Reliability

1 Introduction

Nowadays, various grades of carburizing grade materials are used to produce gears, and out of which, 20CrMO, 20MnCr5, and SAE 8620 are most extensively used due to their malleable properties and heat treatable composition. Carburizing is well-known and cost-effective process for hardening the gear material, which gives hard case and soft core in the gear component to meet the fatigue life design requirements. Though it is hardened, it can fail prematurely in service for variety of reasons including design, material, manufacturing, etc., However, common failure encountered during the service is fatigue. This will lead to the failure of the entire product. Bending fatigue life is important key characteristics for gear, which decides the component usage as a final product. Handschuh et al. investigated the low cycle bending fatigue behavior of AISI9310 steel spur gears with dithering-induced damage, and they revealed that

R. Ramasamy (✉) · S. R. N. Durairaj · T. Ganesan · P. C. Rao
Sona Comstar Automotive Technologies, Maraimalai Nagar, Chengalpattu 603204, India
e-mail: rrajesh@comstarauto.com

© Springer Nature Singapore Pte Ltd. 2020

A. Praveen Kumar et al. (eds.), *Advances in Lightweight Materials and Structures*,
Springer Proceedings in Materials 8, https://doi.org/10.1007/978-981-15-7827-4_53

induced damage does not affect the ending fatigue life [1]. Fernandes studied the various bending fatigue failures of gears made of different materials and reported the various causes for the failure in bending fatigue [2]. Ramasamy et al. studied the bending fatigue behavior of SAE 8620 and 20CrMO steel gears. It was reported that material with lower retained austenite will have higher bending [3]. Edoardo et al. compared the bending fatigue of carburized and nitrided steel gears by single-tooth bending fatigue on 20MnCr5. It is proven that carburized gear has higher bending fatigue endurance as compared to nitrided [4]. Lin et al. and Singh used strain life and fracture mechanics approaches to predict the bending fatigue life carburized materials [5,6]. The influence of surface defects, case depth, and residual stress on bending fatigue strength of carburized gears were studied [7,8]. The accumulated effect of the parameters on bending fatigue limit is variable, and it is quite difficult to calculate without reliability analysis [9]. Many statistical methods used to calculate the reliability design for bending fatigue strength of carburized such as normal, log normal, and two- and three-parameter Weibull distribution [10]

There are various papers, which reported about the bending fatigue life and its endurance limit of carburized gear materials, but very few papers disclosed about the reliable design of stress life curve for the specific materials. In this paper, the bending fatigue strength of three carburized grade materials were investigated and revealed the reliable design for bending fatigue life of carburized gears.

2 Experimental Work

The gears were made of steels 20CrMo, 20MnCr5, and SAE 8620, and its chemical composition is indicated in Table 1. Gears were treated for carburizing heat treatment to obtain the surface hardness of 61-64HRC and core hardness 32-44HRC. Carburizing treatment is optimized to control the retained austenite to less than 10% and to prevent the network carbides. Heat-treated samples were subjected to X-ray diffraction technique to quantify the retained austenite. Microstructure examination

Table 1 Chemical composition of 20CrMo, 20MnCr5, and SAE 8620

Elements in Wt%	20CrMo	20MnCr5	SAE 8620
Carbon	0.17–0.24	0.17–0.22	0.18–0.23
Manganese	0.40–0.70	0.70–0.90	0.70–0.90
Silicon	0.17–0.37	0.4 Max	0.20–0.35
Sulfur	0.04 Max	0.035 Max	0.04 Max
Phosphor	0.04 Max	0.025 Max	0.04 Max
Chromium	0.80–1.10	1–1.30	0.40–0.60
Nickel	0.3 Max	–	0.40–0.70
Molybdenum	0.15–0.25	–	0.15–0.25

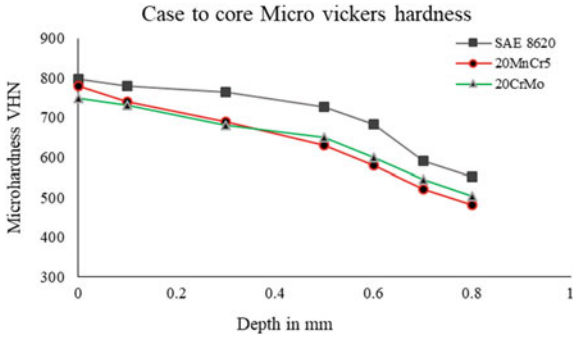


Fig. 1 Case to core microhardness profile for steel gears with 20CrMo, 20MnCr5, and SAE 8620

was carried out to confirm the component free from network carbides and decarburization which are deterioration to mechanical properties of the steel gears. The microstructure of the steel gear was tempered martensite as it is tempered after quenching. Core microstructure of the steel gear was low-carbon martensite. Hardness assessment was conducted to ensure the required hardness in both case and core of the steel gears. Figure 1 indicates that Vickers hardness measurement from the case to core.

Generally, gears are designed to meet the certain reliability requirements based on the product application. Each material has different requirements with respect to the operating stress. In this case, it is important to obtain the fatigue endurance of different reliability conditions, which has been carried out by analyzing and processing the samples from fatigue test of gear.

Fatigue life distribution will be varying in accordance to product variety. There are many statistical methods for gear bending fatigue test. Jing Zhang et al. described the stastical equation used for normal distribution and log normal distribution of gear bending fatigue test data. Weibull distribution is most oftenly used for modelling random failures of physical system [11].

3 Weibull Distribution

In this experiment, conventional group method was adopted to understand the correlation between the stress and bending fatigue life. In which, five group of test stress and five samples are tested for stress. The fatigue failure data were given in Tables 2, 3, and 4 for 20CrMo, 20MnCr5, and SAE 8620, respectively. Three-parameter Weibull distribution was used to analyze the test data from bending fatigue test which has special parameter such as η, β, and γ known to be scale, shape, and location parameter of failure, respectively.

Computer installed with Weibull+ + software was used to analyze and process the data. The mathematical expressions for probabilty density function $f(x)$ and reliability function are as follows.

Table 2 Test data for fatigue failure of 20CrMo

Fatigue life × 10^6 Cycles					
Stress (MPa)	620	580	530	490	460
1	0.20	0.36	1.8	2.6	4.3
2	0.15	0.28	1.76	2.62	4.21
3	0.31	0.66	2.18	3.12	6.25
4	0.45	0.78	2.58	3.96	8.24
5	0.24	0.56	3.12	4.12	8.56

Table 3 Test data for fatigue failure of 20MnCr5

Fatigue life × 10^6 Cycles					
Stress (MPa)	620	580	530	490	460
1	0.18	0.42	1.6	2.62	4.12
2	0.26	0.62	2.03	3.42	6.13
3	0.20	0.34	1.72	2.89	4.56
4	0.56	0.72	2.32	3.64	5.25
5	0.45	0.73	2.48	3.76	7.24

Table 4 Test data for fatigue failure of SAE 8620

Fatigue life × 10^6 Cycles					
Stress (MPa)	620	580	530	490	460
1	0.35	0.58	2.74	4.62	9.35
2	0.52	1.28	3.48	5.22	9.92
3	0.42	1.12	3.42	5.12	9.12
4	0.62	1.92	4.25	7.24	11.34
5	0.68	2.12	5.12	9.23	13.46

$$f(x) = \frac{\beta}{\eta}\left(\frac{x-\gamma}{\eta}\right)^{\beta-1} \exp\left[-\left(\frac{x-\gamma}{\eta}\right)^{\beta}\right], x \geq \gamma \tag{1}$$

$$F(x) = 1 - \exp\left[-\left(\frac{x-\gamma}{\eta}\right)^{\beta}\right], x \geq \gamma \tag{2}$$

η, β, and γ values are calculated by analyzing the fatigue test data composed of time to failure data for each individual steel gear materials using Weibull + + software. Higher fitting accuracy achieved with least square principal of regression analysis and obtained the higher correlation coefficient. Tables 5, 6, and 7 indicate the derived values of η, β, and γ for bending fatigue of carburized gear 20CrMo, 20MnCr5, and SAE 8620, respectively. Reliability data for the time to failure was calculated using

Table 5 Three-parameter Weibull distribution value for 20CrMo

Stress (MPa)	620	580	530	490	460
Beta β	1.547337	14.95432	1.547146	1.428779	3.313024
Eta η	173,798	2,473,258	853,910	1,030,053	6,047,759
Gamma γ	114,250	1,859,600	1,523,600	2,350,000	915,150

Table 6 Three-parameter Weibull distribution value for 20MnCr5

Stress (MPa)	620	580	530	490	460
Beta β	0.779057	1.622417	4.228596	2.780434	1.490498
Eta η	135,838	299,648	1,368,928	1,212,277	1,850,162
Gamma γ	175,600	295,950	790,000	2,191,150	3,790,100

Table 7 Three-parameter Weibull distribution value for SAE 8620

Stress (MPa)	620	580	530	490	460
Beta β	4.91125	4.58147	2.142048	0.910282	0.850773
Eta η	564,530	2,412,176	1,844,522	1,695,298	1,475,208
Gamma γ	1875	792,150	2,174,600	4,514,500	9,038,800

the formulas using (1) and (2). Reliability plots were obtained through Weibull++ software for the materials 20CrMo, 20MnCr5, and SAE 8620 which are shown in Figs. 2, 3, and 4, respectively.

From Figs. 2, 3, and 4, it is understood that SAE 8620 material has high reliability spread than 20CrMo and 20MnCr5 materials in all the manner. The reliability plot for different materials gives the clear idea on selection of material with respect to stress, life cycle, and reliability requirements. Among the three different steel gear materials, SAE 8620 gives higher bending fatigue reliability. Table 8 shows the extracted data from Fig. 5 for fatigue cycles of different reliability.

Bending fatigue limit and gear bending fatigue equation parameter was obtained through analyzing the obtained test data. Least square principal of regression analysis were adopted to calculate the logarithmic relationship between stress S and cycles to failure N. Logarithmic scale of stress vs life is shown in Fig. 0.7 for SAE 8620 which gives the values of fatigue endurance limit of SAE 8620 extracted from different probability survival limit. Failure probability and probability survival limit can be calculated from the given data by forming limit line parallel to mean line of probability data. These curves are known as probability S–N curve by using the curve reliability percentage for different fatigue strength which can be obtained [12,13].

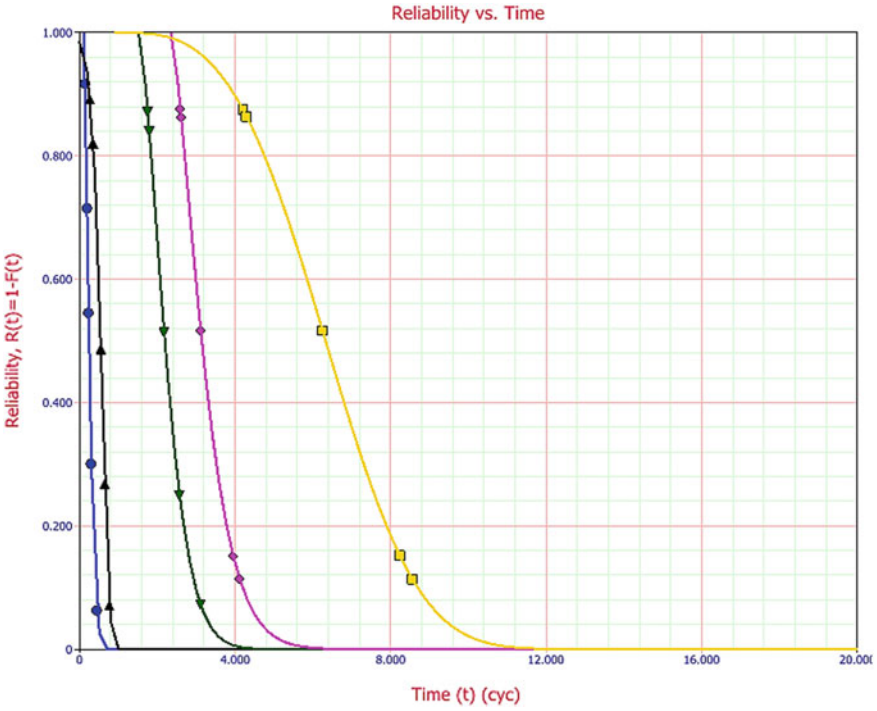


Fig. 2 Reliability plot for 20CrMo

4 Conclusion

The bending fatigue test for three carburized grade gear steels was conducted, and the test data was statistically analyzed using Weibull distribution to find the reliability of bending fatigue strength.

Here, five operating stress levels were chosen by using conventional group method, and each stress level had five set of samples. The three parameters of Weibull distribution beta β, eta η, and gamma γ were derived from Weibull++ software for 20CrMo, 20MnCr5, and SAE 8620 fatigue test data. The reliability plot for bending fatigue cycles of different stress was obtained, and the logarithmic relation between stress S and cycles to failure was found. The probability S–N curve for the bending fatigue strength of SAE 8620 was obtained and found to be superior in comparison with the other two materials. The bending fatigue limit of 99 and 5% reliability of SAE 8620 material is 438.23 and 490.34 MPa, respectively. Reliability design for bending fatigue strength of carburized gear at corrosive environment is future scope of this paper

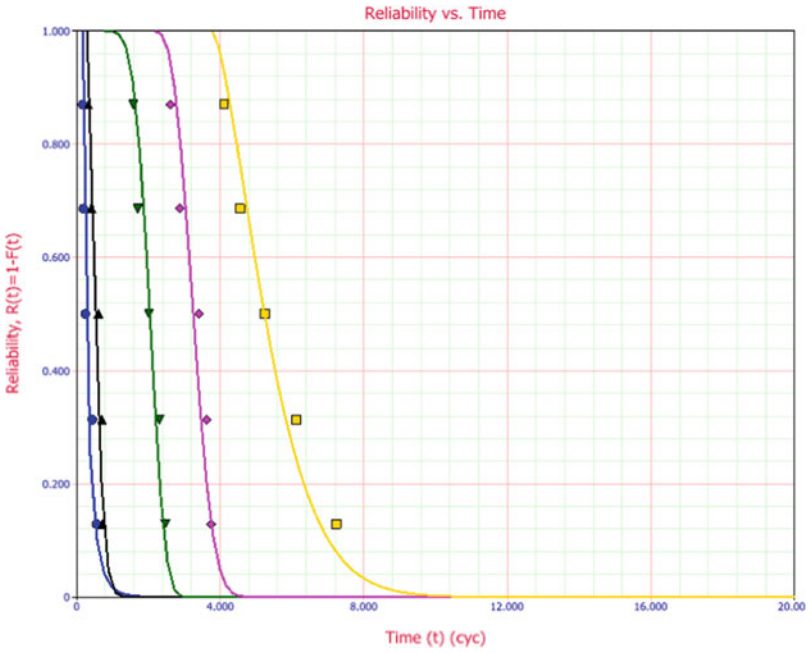


Fig. 3 Reliability plot for 20MnCr5

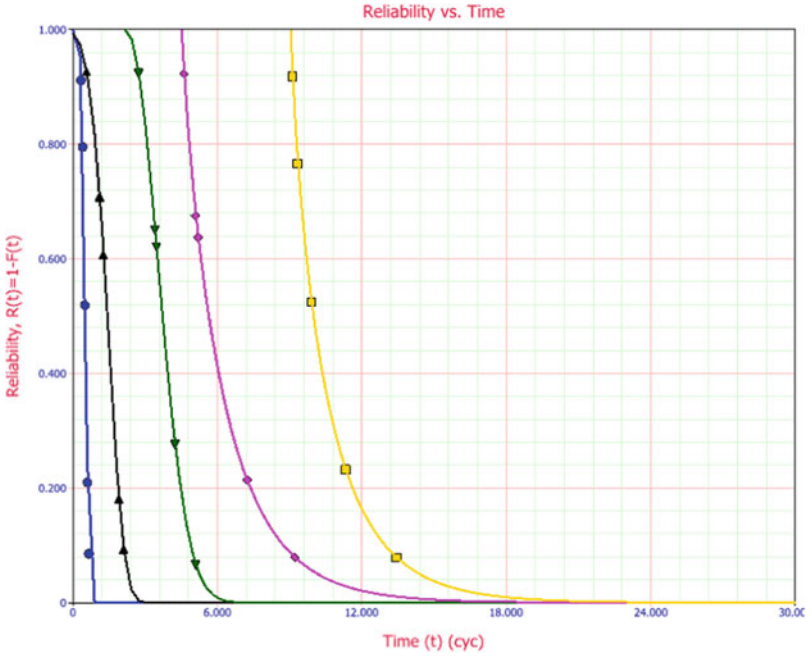


Fig. 4 Reliability plot for SAE 8620

Table 8 Fatigue cycles of different reliability for SAE 8620 material

% of Reliability of SAE 8620 gear for the stress level						
Stress/Cycles*10^6	R = 99%	R = 95%	R = 90%	R = 50%	R = 10%	R = 5%
460	9.14	9.08	9.14	9.97	12.97	14.39
490	4.98	5.22	5.38	6.24	8.26	11.23
530	2.28	2.53	2.64	3.47	4.41	5.78
580	0.18	0.26	0.28	0.42	0.65	0.91
620	0.13	0.19	0.22	0.36	0.59	0.82

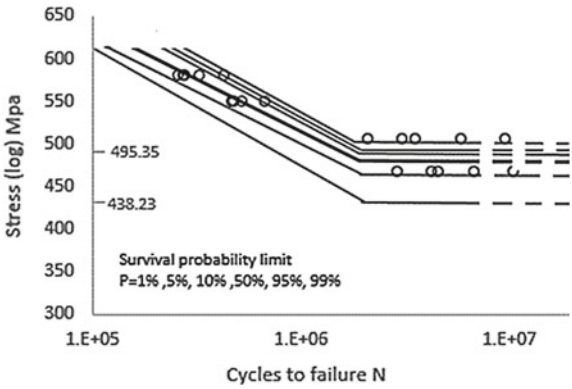


Fig. 5 Probability S–N curve for SAE 8620

Acknowledgements Authors would like to thank M/s Sona Comstar Automotive Technologies for giving opportunity and financial support to present the work in ICALMS 2K20-CMR technical campus.

References

1. Handschuh RF, Krantz TL, Lerch BA, Burke CS (2007) Investigations of low cycle bending fatigue of AISI 9310 steel spur gears. ASME PTD
2. Fernandes PJL (1996) Tooth Bending fatigue failures in gears. Eng Fail Anal 3(3):219–225
3. Ramasamy R, Sivathanu S, Neelakandan V, Ganesan T et al (2019) Influence of retained austenite on fatigue performance of carburized gears. SAE Technical Paper 2019–28–0102. https://doi.org/10.4271/2019-28-0102
4. Conrado E, Gorla C, Davoli P, Boniardi M (2017) A comparison of bending fatigue strength of carburized and nitrided gears for industrial applications. Eng Fail Anal 78:41–54
5. Lin H, Fett GA Binoniemi RR (2003) Bending fatigue life analysis of carburized components using strain life and fracture mechanics approaches. SAE World Congress Detroit, Michigan March 3–6, 2003
6. Singh A (2002) The nature of initiation and propagation S-N curves at and below the endurance limit. Fatigue Fract Eng Mater Struct 25(1):79–90

7. Masuyama T, Inoue K, Yamanaka M, Kitamura K, Saito T (2002) Evaluation of bending strength of carburized gears based on inferential identification of principal surface layer defects. JSME Int J Ser C 45:794–801
8. Tobie T, Oster P, Höhn B-R (2003) Systematic investigations on the influence of case depth on the pitting and bending strength of case carburized gears. In: ASME international design engineering technical conferences and computers and information in engineering conference. American Society of Mechanical Engineers, Chicago, Illinois, USA, pp 111–119
9. Yang Q (1996) Fatigue test and reliability design of gears. Int J Fatigue 18(3):171–177
10. Montgomery DC, Runger GC (2011) Applied statistics and probability for engineers. Wiley, pp 118–144
11. Zhang J, Zhang Q, Xu Z-Z, Gwi-Su-Shin, Lyu S (2013) A study on the evolution of bending fatigue strength of 20CrMoH gear. Int J Precis Eng Manuf 14(8):1339–1343
12. Devendran S, Ramasamy R, Neelakandan V et al (2019) Failure assessment using accelerated testing on IC engine's starter motor for reliability improvement. Life Cycle Reliab Saf Eng 8:175–181. https://doi.org/10.1007/s41872-019-00076-1
13. Bain LJ, Engelhard M (1991) Statistical analysis of reliability and life testing models: theory and methods, 2nd edn. Mercel Dekker, New York

Finish Hard Turning: A Review of Minimum Quantity Lubrication Using Paraffin-Based Nanofluids



Faraj Saeid Adrees Majeed, Nordin Bin Mohd Yusof, and Mohd Azlan Suhaimi

Abstract A wide range of cooling techniques for hard turning machining continues to be proposed and assessed. In this review, the overall characteristics of cutting tools and stainless steel materials were reviewed in terms of vibration, surface roughness, cutting force, and tool life while using minimum quantity lubrication (MQL) with paraffin-based nanofluids. Nanoparticles are particularly appealing in MQL due to its remarkable improvement in the cutting conditions. Under aggressive machining conditions, the lubricant media tends to evaporate or disintegrate when in contact with the cutting tool. With the addition of high thermal conductivity nanoparticle additives as cutting fluid, the performance of the MQL technique has improved remarkably. This review exposed that a few work has used MQL with nanofluid when machining martensitic stainless steel AISI 420 using TiAlN-coated carbide cutting tool. Furthermore, the application of MQL via paraffin oil, γ-Fe_2O_3, and xGnP nanofluid when machining hardened stainless steel using coated carbide cutting tools has not yet been examined.

Keywords Lubricant · Nanoparticles · Turning · Coated carbide

1 Introduction

The cutting process is carried out via conventional machines that remove materials from a different surface by producing chips [1]. Usually, low production with high costs challenging to cut materials due to difficulties in the formation of chips, which leads to a decrease in thermal conductivity generated by excessive heat and high strength and rigidity [2]. It is difficult for conventional machines to manufacture high hardness materials and to engineer complex parts geometries. The physical contact resulting from the continuous communication between the cutting tool and the workpiece in the machines that can be predicted by relative movement, which leads to wear performance and cause friction [3]. As per the definition typically

F. S. A. Majeed (✉) · N. B. M. Yusof · M. A. Suhaimi
Department of Manufacturing Engineering, School of Mechanical Engineering, University Technology Malaysia, 81310 Skudai, Johor, Malaysia
e-mail: safaraj@graduate.utm.my

© Springer Nature Singapore Pte Ltd. 2020

A. Praveen Kumar et al. (eds.), *Advances in Lightweight Materials and Structures*,
Springer Proceedings in Materials 8, https://doi.org/10.1007/978-981-15-7827-4_54

acknowledged in the material science network, nanoparticles ought to be objects having, in any event, one straight measurement $\leq$ 100 nm. Metalworking has many purposes, so nanoparticles have attracted a lot of attention due to their multiple functions. To give a better understanding of the working environment and the safety of production are evaluated several variables, including the surface roughness, the tool life of the cutting tool, and the cutting force to improve the surface quality of the product [4]. Nickel-based alloys were preferred because of their excellent properties such as corrosion resistance and high fatigue strength, especially in high-pressure disks of pneumatic actuators in the hottest section [5]. Pollution in the environment resulting from the working fluids used in metals during manufacturing leads to health risks for operators [6]. In terms of their sustainability, it is important for cutting operations are metal cutting operations. Although in the past decades, the focus was on lower production costs, the effects of a pleasant working environment led to an increase in productivity improvement [7]. The different operating processes, such as drilling, milling, and turning, have the same mechanical principles despite the various methods in engineering [8].

Metal cutting includes the shear disfigurement of the material part to produce chips utilizing cutting apparatuses. The corrosion that occurs during the process of metal cutting by the adhesion of the work material resulting from the cutting tool, therefore, begins to wear both at rake or flank face [9]. The cutting processes control three important variables, the rate of metal removal, surface finish, and tool life at different operating conditions at certain different parameters such as depth cut, depth, feed rate, and cutting speed [10].

2 Minimum Quantity Lubrication (MQL)

The technique is called minimum quantity lubrication (MQL), applying a small quantity of coolant directed to the tool-workpiece by utilizing air pressure [11]. Quality of products is required and achieved by obtaining a better surface by reducing risks and using the least amount of oil through an excellent alternative to dry cutting and flood cooling [12]. In (MQL) system, a little quantity of cutting fluid (10–500 ml/h) with compressed air is directed to the tool/chip interface. This constitutes lower than three or four times of magnitude compared with conventional cutting fluids. Oil mist has two functions, namely for the lubricating purpose, which is achieved by the compacted air used the cooling and oil. MQL is adequate to decrease the friction in the cutting zone area. It can be classified MQL technique into two categories inside delivery and external delivery to the cutting zone according to the mode of cutting fluid [13]. Researchers have focused in recent years on the technology of the minimum quantity of lubrication because of its excellent economic and environmental characteristics to meet the requirements of green machinery [14]. Although high temperatures on the inserts and at high cutting speed up to (122 m/min), MQL still produce positive results when turning Ti alloys. This improvement reaches 100%, which increases the life of the cutting tool with xGnP [15]. Quick paint damage has

been found due to EP additive in the MQCL method [16]. This outer explores MQL as alternate enrichment machinery and studies the restriction of this skill in the turning process of Ti alloys, and to continuous progress of tool and workpiece utilizing oil droplets directly due to surfaces of a cutting machine [15]. The use of minimum lubrication technology in steel manufacturing has not provided to increases efficiency by seven times the traditional system of cooling only, but it was found that it is very beneficial to the environment [17]. Moreover, it has been noticed in near-micro-milling the MQL can significantly decrease resistance among tool-workpiece and the tool–chip compared with dry machining [18]. Also, the final surface finishing quality is better under this technology equated to others [19].

3 Paraffin Oil Based Lubricant

Mineral oil became known after the discovery of crude oil, as it is derived from oil from many years ago. After being treated and refined raw materials consisting of a complex mixture of saturated hydrocarbons, thus mineral oils can be obtained and produced [20]. Mineral oil is known under a wide range of names. The explanation behind this is likely authentic as the item was made sometime before standard classification was executed. Equivalent words incorporate substantial mineral oil, petrolatum, liquid paraffin, paraffin liquid, and paraffin oil, etc. [21]. There are two types of hydrocarbon to compose the mineral oil (paraffinic and naphthenes). The paraffinic has a higher cloud point and viscosity than the naphthenic. The reason for using mineral oil rather than vegetable oil is that it has high production at a low cost. They are utilized in numerous applications such as mechanical, medicinal, industrial, foods, and cosmetics. From more than a hundred years ago, mineral oil has been used in beauty care products [22]. The mineral oil has no color, taste and it is transparent. This study dealt with paraffin oil and specifically to define nanoemulsion (oil-in-water) needs a system of chemical components of paraffin oil to reduce the oil content, protection of the environment [23]. A comparison was made of low-sulfur minerals paraffinic sulfur with a similar viscosity to soybean oil. The results showed that both extreme pressure EP additive work more effectively than soybean oil [24].

4 Cutting Fluids

In general, lubricant or cutting fluid is well-known plays an essential role in removing the chips in the cutting zone, and to reduce the temperature caused by friction between the workpiece and the cutting tool; lubricating oils are used for this purpose. Noordin [25] at a fixed depth of cut 0.4 mm and different cutting speeds, as well as various feeding rates without using any cooling fluids which turned on a martensitic stainless steel AISI 420 with a hardness of 47–48 HRC. Turned martensitic stainless steel AISI 420 (53 $\pm$ 2 HRC) with feed rate (f) and cutting speed (VC) [26]. Some parameters

Table 1 Summary of literature studies MQL turning using coated carbide and martensitic stainless steel AISI 420

Author	Cutting Tools	Cutting Conditions	Cutting parameters	Responses			
				Ra	T.L	C.F	V
Bruni [29]	Coated carbide	Wet, dry, MQL	C.S = 235 m/min DOC = 0.4 mm F.R = 0.08, 0.16 mm/rev	√	√	-	-
Kurniawan [28]	Coated carbide	Dry	C.S = 100, 130, 170 m/min DOC = 0.4 mm F.R = 0.125, 0.125 0.25 mm/rev	√	√	√	-
Elmunafi [30]	Coated carbide	Dry + MQL	C.S = 100, 130 and 170 m/min DOC = 0.2 mm F.R = 0.16, 0.0.20, 0.24 mm/rev	√	√	√	-
Elshwain [31]	Coated carbide	Dry, air oil mist, and nitrogen oil mist	C.S = 100, 135 and 170 m/min DOC = 0.2 mm F.R = 0.16, 0.0.20, 0.24 mm/rev	√	√	-	-

Where *Ra* surface roughness; *TL* tool life; *CF* cutting force; *V* vibration

in machining like nanofluids have useful characters depending on the concentration, size, and shape of nanoparticles [27]. Used AISI 420 stainless steel with 48 HRC and cutting tool PVD-TiAlN with 3.0–3.5 μm thickness [28]. Table 1 shows some previous studies MQL turning using coated carbide and martensitic stainless steel AISI 420.

5 Nanofluid

The concept of nanofluid was first coined owing to the improved heat transfer in mass transit, at Arjun National Laboratory has aroused much interest [32]. About 20% of the thermal conductivity has been achieved when using ethylene molecules, by conducting many experiments that have proven that nanoparticles enhance the inherent properties, which tends to improve thermal performance [33]. Nanometer-size by dispersing solid particles into essential liquids such as water, engine lubricant, and cutting liquids ethylene glycol this new class is called nanofluid [34]. The thermal conductivity has been increased to 150% when adding multi-walled carbon nanotubes [35]. Several characteristics such as higher flashpoints, viscosity, and thermal conductivity at nanofluids in comparison with base fluids [36].In thermal

engineering processes, a suitable application for the practical operation has been found which have an enhancement in heat transfer [37]. Compared to the base fluid of Al_2O_3 reported that the improvement up to 40% in heat transfer [38]. In the convective heat, nanofluids have been utilized extensively. Its value increase with particles' concentration and dependent thermal conductivity was much higher [39]. Thermal conduction, according to previous studies prepared by Chen and Ding, indicates the concentration of nanoparticles begins to increase in the thermal conductivity of food and carbon materials, as well as inorganic materials [40]. Moreover, it allows prolonging tool life for cutting with the best quality compared to base oils [41]. Maxing the xGnP with coconut oil it is observed in a reduction of cutting forces, surface roughness, and tool wear [42]. The experimental results on CNC turning operation using MQL system on the machinability characteristics of EN353 to a reduced temperature significantly and surface roughness as compared to vegetable oil [43]. Table 2 briefs of some previous machining works using nanoparticles.

Table 2 Summary of some previous machining works using nanoparticles

Author	Cutting Tools	Cutting Conditions	Cutting parameters	Responses			
				Ra	T.L	C.F	V
Vamsi [44]	Coated carbide	SAE-40, coconut oil nanoboric acid	C.S = 60, 80, 100 m/min DOC = 1.0 mm F.R = 0.14, 0.16, 0.2 mm/rev	-	-	√	-
Prasad [45]	Cemented carbide	Dry, soluble oil, nanographene	C.S = 105 m/min DOC = 1 mm F.R = 0.14 mm/rev	√	√	√	-
Sharma [40]	Coated carbide	MoS2 hybrid nano	C.S = 60, 90, 120 m/min DOC = 0.6, 0.9, 1.2 mm F.R = 0.08, 0.12, 0.16 mm/rev	√	-	√	-
Sharma [13]	Coated carbide	Dry, xGnP with Al-based nano	C.S = 60, 90, 120 m/min DOC = 0.6, 0.9, 1.2 mm F.R = 0.08, 0.12, 0.16 mm/rev	√	-	√	-

where *Ra* surface roughness; *TL* tool life; *CF* cutting force; *V* vibration

6 Chatter in Machining

The chatter vibration is one of the most prominent problems that occur in the manufacturing procedure vibrations in machining are complex phenomena. One of the main reasons that occur in manufacturing processes is the chatter that is produced by interactions, which are reflected in the work environment and the economic side [46]. In recent past years, through a wide range of manufacturing processes, the focus has been on several variables that have an impact on the industry environment, including dimensional accuracy and chip formation. The cutting time and the final surface obtained have been monitored, and also the focus has been on vibration [47]. Commonly, there are four types of raw signals, there are many techniques that are most significant in terms of converting the raw signal for processing, fast Fourier transforms (FFT) is the most famous and there are still other techniques such as Huang transforms (HHTs) and wavelet transforms (WT), via, in other words, including stable, nonlinear, non-stationary, and direct [48]. By using ultrasonic vibration in contrast to conventional turns, the serrated edge phenomenon and surface defects of the chip have significantly improved in the turning process [49]. Besides, increase characteristic peak ratio (CPR) and magnetic field intensity with decreased surface roughness because of the damping coefficient and vibration kinetic energy dissipation, which accurately predicted of a machined surface [50]. The determination of the prediction to measure the cutting forces requirement a significant for this proposal, several investigations were directed [51]. Mechanical stress is caused by a force to which its dependent workpiece responds by its deflection or by molecules compressing closer together. This explains the phenomenon of vibration is the transmission of this pressure across the workpiece as a whole. In cutting operations, the vibration caused by the repetition of the motion itself in various ways. Here are two kinds of vibrations happening throughout machining, self-excited vibration and forced. The force applied to the machine tool periodically is called forced vibration such as misalignment, pumps, machine tool components, and gear drives [52]. Noise in machinery is not desirable and is known as chatter, it creates self-turning and generating loud noises as namely chatter. Removal of the effect is the ideal solution for forced vibration. For the excess excitability to be removed in the machine to be verified, the product's cutting frequency should be near to that of the normal rate of the operation. Use of damping system is to reduce vibration or by increasing stiffness. Usually, independent motion and external is a force acting on the vibrating system [53].

7 Conclusion

The overall characteristics of cutting tools and stainless steel materials were reviewed. In terms of vibration, surface roughness, cutting force, and tool life, several types of stainless steel have been considered for different cutting conditions. Even though

there are many cooling technologies, but MQL is one of the best techniques of cooling systems because it reduces the cost of lubricants and improves the productivity of cutting operations. Besides, it has an impact on production efficiency. Moreover, previous studies examined different types of nanoparticles for various materials under the MQL system for machining processes, especially hard turning operations. Through past research, the determination of the effect of vibration behavior using nanographene and gamma iron oxide nanoparticles has not been experimented on AISI420 stainless using KC5010-coated carbide cutting tool has not been investigated. From the review, there exist crucial gaps in the performance enhancement of varying cutting conditions and cooling techniques using MQL. Although many researchers and the studies have been done of vibration/chatter this problem caused it performed on for more than a century. It was not possible to get rid of this phenomenon and because of its significant economic effects and also work to create a suitable work environment for the many manufacturing processes.

Acknowledgements We specially thank the reviewer(s) for their useful advice and comments. The author's wish to thank Research Management Center, UTM for their financial support to this work through the UTM Research University Grant (RUG) number Q.J130000.3551.07G23.

References

1. Liew PJ et al (2017) An overview of current status of cutting fluids and cooling techniques of turning hard steel. Int J Heat Mass Trans 114:380–394
2. Hegab H et al (2019) A model for machining with nano-additives based minimum quantity lubrication. Int J Adv Manuf Technol 1–16
3. Hanif M et al (2019) Optimization of process parameters using graphene-based dielectric in electric discharge machining of AISI D2 steel. Int J Adv Manuf Technol 1–15
4. Da Silva RB et al (2017) Surface integrity and tool life when turning of Ti-6Al-4V with coolant applied by different methods. Int J Adv Manuf Techno 93(5):1893–1902
5. Hafiz MSA et al (2017) A review on feasibility study of ultrasonic assisted machining on aircraft component manufacturing. IOP Conf Series Mater Sci Eng 270:012034
6. Ghosh S, Rao P (2019) Comparison between sustainable cryogenic techniques and nano-MQL cooling mode in turning of nickel-based alloy. J Cleaner Prod 231:1036–1049
7. Marini D, Cunningham D, Corney JR (2017) Near net shape manufacturing of metal: A review of approaches and their evolutions. Proc Instit Mech Eng Part B J Eng Manuf 232(4):650–669
8. Alkali AU et al (2013) Influence of cutting conditions on chip formation when turning ASSAB DF-3 Hardened tool steel. Int J Mater Mech Manuf 1:76–79
9. Sharma V, Pandey PM (2016) Recent advances in turning with textured cutting tools: a review. J Cleaner Prod 137:701–715
10. Rifat M, Rahman MH, Das D (2017) A review on application of nanofluid MQL in machining. In: AIP Conference Proceedings. AIP Publishing
11. Harshit Bhalachandra K et al (2017) A review on nanofluids for machining. Curr Nanosci 13(6):634–653
12. Sharif S et al (2017) A review of minimum quantity lubrication technique with nanofluids application in metal cutting operations. Int J Adv Sci Eng Info Technol 7(2):587–593
13. Kumar A, Pradhan SK (2018) Investigations into hard turning process using wiper tool inserts. Mater Today Proc 5(5, Part 2):12579–12587

14. Kumar Singh R et al (2018) Influence of graphene-based nanofluid with minimum quantity lubrication on surface roughness and cutting temperature in turning operation. Mater Today Proc 5(11)24578–24586
15. Nguyen D et al (2019) Wear performance evaluation of minimum quantity lubrication with exfoliated graphite nanoplatelets in turning titanium alloy. J Manuf Sci Eng 141(8)
16. Maruda RW et al (2019) The influence of the application of EP additive in the minimum quantity cooling lubrication method on the tool wear and surface roughness in the process of turning 316L steel. In: Advances in manufacturing engineering and materials. Springer International Publishing, Cham
17. Masoudi S et al (2018) Experimental investigation into the effects of nozzle position, workpiece hardness, and tool type in MQL turning of AISI 1045 steel. Mater Manuf Process 33(9):1011–1019
18. Singh RK et al (2017) Emerging application of nanoparticle-enriched cutting fluid in metal removal processes: a review. J Brazilian Soc Mech Sci Eng 39(11):4677–4717
19. Joshi KK, Behera RK, Anurag (2018) Effect of minimum quantity lubrication with Al_2O_3 Nanofluid on Surface Roughness and its prediction using hybrid fuzzy controller in turning operation of Inconel 600. Mater Today Proc 5(9, Part 3):20660–20668
20. Divijak JM (1970) Production of technical white mineral oil. Google Patents
21. Rawlings A, Lombard K (2012) A review on the extensive skin benefits of mineral oil. Int J Cosmet Sci 34(6):511–518
22. Darma I (2008) Dielectric properties of mixtures between mineral oil and natural ester from palm oil. World Scientific and Engineering Academy and Society (WSEAS). Trans Power Syst 3(2):37–46
23. Kumar D, Mishra DK (2018) Surfactant controlled lubricity of paraffin oil-based nano-emulsion. Tribol-Mater Surf Interf 12(3):130–136
24. Asadauskas SJ, Biresaw G, McClure TG (2010) Effects of chlorinated paraffin and ZDDP concentrations on boundary lubrication properties of mineral and soybean oils. Tribol Lett 37(2):111–121
25. Noordin M, Kurniawan D, Sharif S (2007) Hard turning of stainless steel using wiper coated carbide tool. Int J Precision Technol 1(1):75–84
26. Rosa GC, Souza AJ, Lorini FJ (2014) Comparative analysis on wiper and standard tools in dry finish turning of martensitic stainless steel AISI 420. In: Advanced Materials Research. Trans Tech Publications
27. Nune MMR, Chaganti PK (2017) Experimental investigation on turning of turbine blade material AISI 410 under minimum quantity cutting fluid. Mater Today Proc 4(2):1057–1064
28. Kurniawan D, Yusof NM, Sharif S (2010) Hard machining of stainless steel using wiper coated carbide: tool life and surface integrity. Mater Manuf Process 25(6):370–377
29. Bruni C et al (2006) Effect of the lubrication-cooling technique, insert technology and machine bed material on the workpart surface finish and tool wear in finish turning of AISI 420B. Int J Mach Tools Manuf 46(12–13):1547–1554
30. Elmunafi MHS, Kurniawan D, Noordin M (2015) Use of castor oil as cutting fluid in machining of hardened stainless steel with minimum quantity of lubricant. Procedia CIRP 26:408–411
31. Elshwain AE et al (2017) Machinability of stainless tool steel using nitrogen oil-mist coalant. Вестник Воронежского Государственного Университета Инженерных Технологий 79(3):143–147
32. Krishnamurthy S et al (2006) Enhanced mass transport in nanofluids. Nano Lett 6(3):419–423
33. Lee S et al (1999) Measuring thermal conductivity of fluids containing oxide nanoparticles. J Heat Transfer 121(2):280–289
34. Eastman JA et al (2001) Anomalously increased effective thermal conductivities of ethylene glycol-based nanofluids containing copper nanoparticles. Appl Phys Lett 78(6):718–720
35. Teng T-P, Yu C-C (2013) Heat dissipation performance of MWCNTs nano-coolant for vehicle. Exp Thermal Fluid Sci 49:22–30
36. Hwang Y et al (2006) Thermal conductivity and lubrication characteristics of nanofluids. Curr Appl Phys 6:e67–e71

37. Daungthongsuk W, Wongwises S (2007) A critical review of convective heat transfer of nanofluids. Renew Sustain Energy Rev 11(5):797–817
38. Albadr J, Tayal S, Alasadi M (2013) Heat transfer through heat exchanger using Al_2O_3 nanofluid at different concentrations. Case Stud Therm Eng 1(1):38–44
39. Saidur R, Leong K, Mohammad HA (2011) A review on applications and challenges of nanofluids. Renew Sustain Energy Rev 15(3):1646–1668
40. Sharma AK et al (2017) Novel uses of alumina-MoS2 hybrid nanoparticle enriched cutting fluid in hard turning of AISI 304 steel. J Manuf Process 30:467–482
41. Faraj Saeid Adrees Majeed et al (2020) Effect of paraffin oil with XGnP and Fe_2O_3 nanoparticles on tribological properties. Mater Today Proc 27(2):1685–1688
42. Padmini R et al (2019) Influence of green nanocutting fluids on machining performance using minimum quantity lubrication technique. Mater Today Proc 18:1435–1449
43. Sathishkumar S, Rajmohan T (2018) Multi-response optimization of machining parameters in CNC turning of AISI 316l stainless steel using MQL nano fluids. In: IOP conference series: materials science and engineering.. IOP Publishing
44. Krishna PV, Srikant R, Rao DN (2010) Experimental investigation on the performance of nanoboric acid suspensions in SAE-40 and coconut oil during turning of AISI 1040 steel. Int J Mach Tools Manuf 50(10):911–916
45. Prasad M, Srikant R (2013) Performance evaluation of nano graphite inclusions in cutting fluids with MQL technique in turning of AISI 1040 steel. Int J Res Eng Technol 2(11):381–393
46. Fallah M, Moetakef-Imani B (2019) Adaptive inverse control of chatter vibrations in internal turning operations. Mech Syst Signal Process 129:91–111
47. García Plaza E, Núñez López PJ, Beamud González EM (2019) Efficiency of vibration signal feature extraction for surface finish monitoring in CNC machining. J Manuf Process 44:145–157
48. Shrivastava Y, Singh B (2018) Possible way to diminish the effect of chatter in CNC turning based on EMD and ANN approaches. Arabian J Sci Eng 43(9):4571–4591
49. Xu Y et al (2019) Experimental study on chip shape in ultrasonic vibration–assisted turning of 304 austenitic stainless steel. Adv Mech Eng 11(8):1687814019870896
50. Yip WS, To S (2019) Reduction of tool tip vibration in single-point diamond turning using an eddy current damping effect. Int J Adv Manuf Technol 103(5):1799–1809
51. Zeqiri F et al (2018) Experimental research and mathematical modeling of parameters effecting on cutting force and surface roughness in CNC turning process. In IOP conference series: materials science and engineering. IOP Publishing
52. Altintas Y (2014) Adaptive control. In: CIRP Encyclopedia of production engineering, pp 17–19.
53. Hassan N (2014) Development of a dynamic model for vibration during turning operation and numerical studies. University of Liverpool

Neuro-Fuzzy Modeling and Wear Rate Predictions of Microwave Clads

Keerthana Chigateri, Ajit M. Hebbale, Baswanta S. Patil, and M. Anjani Prasad

Abstract SS-304 is extensively used in almost all industrial applications. Wear is one of the sever problems that reduce the life span of functional components. In the current work, an attempt is made to develop nickel-based clads though microwave energy at 900 W power. The developed clad shows excellent bonding with the target substrate without visible cracks. Microstructural and erosion analysis were carried out successfully. Taguchi L9 array was used with speed (*S*), impact angle (*A*) and various sizes of particles were considered for the erosion studies. The most reliable and popular neuro-fuzzy analytical technique was effectively used to forecast the wear behavior. Finally, the fuzzy predicted values were compared with experimentally obtained values. It was observed that the average percentage of error between fuzzy logic and experimental values is 10.34%.

Keywords Microwave cladding · Taguchi · Impact angle · Wear · Fuzzy logic · Neuro

1 Introduction

Hydroelectric power plants are always facing a problem of slurry erosion, especially during rainy seasons. Therefore, it leads to reduce life and performance of target

K. Chigateri
Department of Computer Science Engineering, N.M.A.M. Institute of Technology (Visvesvaraya Technological University, Belagavi) Nitte, Udupi Dist, Mangalore, Karnataka 574110, India

A. M. Hebbale (✉)
Depatment of Mechanical Engineering, N.M.A.M. Institute of Technology (Visvesvaraya Technological University, Belagavi) Nitte, Udupi Dist, Mangalore, Karnataka 574110, India
e-mail: ajit.hebbale@gmail.com

B. S. Patil
Centre for Material Characterization and Testing, International Advanced Research Centre for Powder Metallurgy and New Materials (ARCI), Hyderabad, India

M. A. Prasad
Department of Mechanical Engineering, JNTU College of Engineering, (JNTU Ananthapur), Pulivendula, India

© Springer Nature Singapore Pte Ltd. 2020

A. Praveen Kumar et al. (eds.), *Advances in Lightweight Materials and Structures*,
Springer Proceedings in Materials 8, https://doi.org/10.1007/978-981-15-7827-4_55

components, which raises functional charges and replacement of damaged components. As a result, wear is known to be major issues in hydraulic plants. Therefore, it is very crucial to comprehend the wear process to attain a solution that improves the life of the components and to reduce repair and replacement costs. Several authors have attempted to resolve the slurry erosive wear problems of metallic materials. Santa et al. [1] addressed the slurry erosion of different coatings, which were applied by wire arc spraying and oxy-fuel powder on AISI 304 steel, which is normally used for hydraulic turbine applications. The slurry consisted of quarts sand particles (212 and 300 μm) with distilled water, followed with 5.5 m/s of mean impact velocity, and erosion rate was determined by measure of loss of volume. The unclad surface shows lower wear resistance than the coated surfaces. The plastic deformation with brittle fracture was found in the microstructure [2]. The dry erosion rate was considerably more than slurry erosion. Cermets coatings with WC exhibited higher erosion wear rate and greater fracture toughness than the conventional cermet coatings [3]. Ni-Al_2O_3-based HVOF coatings performed two to three times greater erosion resistance than steel [4]. WC-12Co-based nano-sized powder besides 15% of nano-WC-12Co coating shows the enhancement of higher wear resistance than WC-10Co-4Cr-based coatings [5]. Dry erosion and slurry behavior of WC-CoCr-based cermet coatings were studied. Lip, crater, carbide fracturing, chipping and groove formation were observed through the morphology of the eroded surface [3]. Plasma-sprayed Cu-ceramic-based coatings were melted through laser energy was performed better to erosion than the coatings of plasma-sprayed, whereas plasma-sprayed coatings perform worst to erosion [6].

Sand slurry practices wear is the major problem that leads to the failure of many austenitic stainless steel components rather than a corrosion-related wear crisis. The presence of hard particles in the water medium helps to degrade the target surface of the interacted component [7]. When sand particles hit the exposed surface of target substances at a very high velocity, erosion of the target surface takes place. Slurry erosion is a very difficult phenomenon to understand because it is influenced by several factors that act simultaneously on the exposed surface. The factors include the properties of the target material, characteristics of the erodent particles, microstructure of material and impact angle are play a very important role in the mass-loss process [8–10]. The erosion rate of ductile material increases at lower angles (30° and 50°) and decreases at a higher impact angle (90°), while in the case of brittle material more erosion occurs at an angle of 90°. Impact angle effect on erosion mechanism of high chromium cast iron and 5117 steel was more [11–13]. Desale et al. [14] addressed that the erosion rate of two ductile materials (AA-6063, AISI-304L). The experiments were carried out to gauge the wear rate of the two materials. Three different natural erodent particles were used such as quartz, alumina to perform the loss of mass of the materials exposed surface at various impact angles. The river water mixed with sand particles affects severely on the performance of the hydraulic turbine. The erosion of the exposed surface considerably depends on the parameter levels (velocity, slurry concentration, particle size, shape and impact angles). The velocity and impact angle play a major part in the erosion mechanism [15, 16].

Wear is an inevitable phenomenon in several applications. Therefore, wear resistance and high strength are very important in such applications. SS-304 austenitic and martensitic SS-420 are extensively used in engineering materials due to their low cost and exceptional corrosion resistance nature. However, more mass loss of surface due to plastic deformation leads to avoiding the use of stainless steel in an aggressive interacting environment [17–19]. Furthermore, relevant literature highlights the properties of material play a very important role to influence the erosion rate and surface degradation in the tribological system. Several authors reported that the importance of target material properties such as ductility, hardness and toughness. Hardness was observed as the most influential factor in determining the erosion rate and a high hardened surface usually provides better erosion resistance [20–22]. Therefore, surface engineering is a solution to develop surface properties of material while maintaining its inherent properties.

In recent years, soft computing like fuzzy, ANN and some expert models emerged as the limitations of mathematical modeling. Fuzzy systems are used to control the wear system. "Fuzzy logic" is one among ANN methods that are capable of tackling the issue of complicated relationships between variables that cannot be solved by more conventional methods. It is a computational theory of incorrect thinking that enables the mechanism of human logic to be modeled in linguistic terms. It is commonly used for technological, economical, medical problems and special requirements in highly complex industrial systems. Fuzzy collection of theoretical modeling techniques is usually favored while the individual experience or estimation of both the process connoisseur plays a key role in identifying the subjective purpose and verdict variables. ANN and fuzzy-based simulation methods are efficient means of controlling intricate grinding processes.

The present job describes the erosive wear research of nickel-based clads developed by microwave energy. The Taguchi method L9 array structure was used to assess the rate of wear of the clads developed by microwave energy. Microstructural analysis of the worn surface was analyzed through SEM. Finally, Mamdani proposition technique was used for fuzzy inference interpretation. The triangular shape function was considered for optimizing the process variables of slurry erosion studies.

2 Experimental Process and Materials

2.1 Materials Detail

The microwave interaction with bulk metal is a greater challenge in the domestic microwave oven. Hence, many numbers of experiments were carried out to develop sound clad on the desired surface. Selections of materials for the manufacture of turbine components play a very important role in their performance at various operating conditions. As per the environment of the hydroelectric power plants, the component material must possess the qualities such as high hardness and tensile

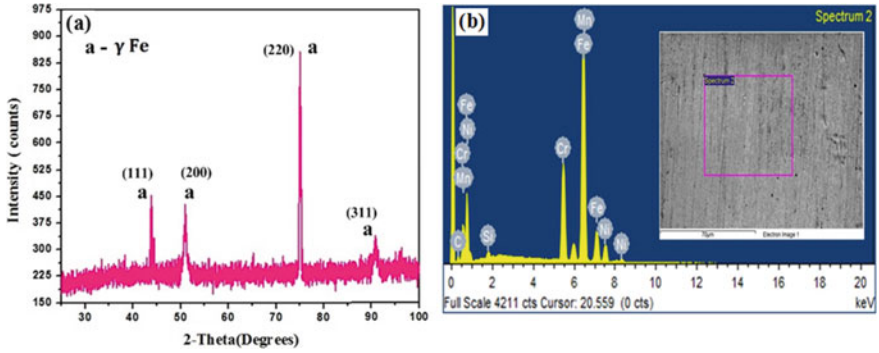


Fig. 1 **a** XRD spectrum of SS-304, **b** EDS spectrum of SS-304

strength, high resistance to corrosion. Different grades of stainless steel are considered as a best suitable material for the manufacture of turbine components, as it possesses the above-mentioned properties. Therefore, in the present work, SS-304 for nickel-based cladding through microwave hybrid heating. Austenitic grade steels are non-magnetic stainless steels that include a high level of chromium and nickel with the least amount of carbon. These grades are identified as good for formability and resistance to corrosion. XRD was carried out on the received substrate (SS-304) to confirm the presence of various phases. The obtained XRD spectrum of the as-received substrate (SS-304) is shown in Fig. 1a. It is observed from XRD analysis that the dominant presence of austenite phase γ Fe. Area analysis through EDS of the substrate was carried out and is shown in Fig. 1b. EDS study was analyzed to find out the composition of the substrate (SS-304).

Nickel-based coatings perform excellent against high-temperature wear and corrosion resistance. This type of coating is specially used in applications where wear resistance is pooled with oxidation or where hot corrosion resistance is necessary [23]. It finds more advantage especially in large-sized components like piston rods, earth working and hydroelectric turbines. Nickel-based hard facing alloys are also known for higher hardness at high temperature and pressure conditions. In the present work, nickel-based (EWAC 1005 EC) powder particle size 10–35 μm was used to develop clad on substrates SS-304 through a domestic microwave oven. Typical XRD and EDS spectrum of clad powder is shown in Fig. 2a and b.

2.2 Microwave Cladding Process

The nickel-based clad powder was placed manually on the SS304 substrate with an average thickness of one mm. Alumina (Al_2O_3) casket was used during an experiment to avoid exposure of metals directly to microwave. Finally, nickel-based microwave

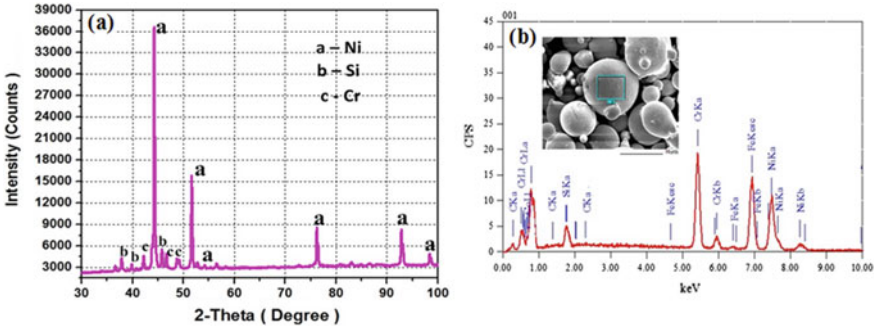


Fig. 2 **a** Typical XRD spectrum of nickel-based clad powder, **b** EDS spectrum of nickel-based clad powder

clads developed with microwave interaction of 10 min. The information in detail about the clad development was reported in our earlier work [24–27].

2.3 Slurry Erosive Wear Studies

Slurry constitutes of silica sand particles mixed with water was used for this study. The experimental setup consists of six spindles attached with a maximum speed of 1500 rpm. Experiments were carried out with various impact angles (15°,30°, 45°), sand particles (106 μm, 212 μm and 600 μm) and varying rotational speeds (1000 rpm, 1250 rpm, 1500 rpm). In this current work, the standard orthogonal array L9 was successfully used to experiment with the erosion rate of the developed clads.

2.4 Neuro-Fuzzy Predictions

Modeling of fuzzy logic is engaged through regulation-based structure. In imperative-based variables used in fuzzy systems are based on if-then conditions:

"IF (x_1 is A_1, x_2 is A_2 ,…, Xn is A_n) THEN (y_1 is B_1, y_2 is B_2, …, Y_n is B_n)".

Anywhere linguistic erratic $\times 1$, y_1 takes values of fuzzy sets A_1 and B_1, respectively. The popular defuzzification technique is centroid was used to bear out the projected work [28]. Mamdani FIS was executed in MATLAB 8.10. The parameters connected variables are shown in Fig. 3.

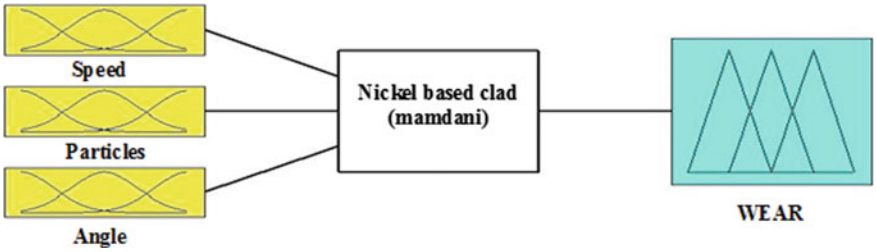


Fig. 3 Typical fuzzy interface system of Mamdani

3 Results Analysis

3.1 Microstructural Studies

Microstructure study refers to microscopic description of individual constituents of a material. The length scale is always well above the atomic levels (100–1 μm). Microstructure study of a material (such as metallic, polymeric, ceramic and composite) is the study of the crystal structure of a material, crystal size, composition, orientation, interaction and eventually their impact on the macroscopic actions in terms of physical properties. Microstructure analysis of clad material clearly shows the occurrence of diverse phases, porosities, cell boundaries and essentials of several elements. Hence, the study of microstructure was carried out for the developed clad structure. The SEM image of the developed clad is shown in Fig. 4a and b.

It is observed that the developed nickel-based clads are crack-free and visible porosity. The porosity count was measured through linear count method which is in the vary of 0.89%. Noticed porosity in the developed clad section is less than other coating processes such as thermal spray and laser cladding. The crack-free structure is the clear proof for the volumetric nature of heating which directly associated with the microwave heating process can be seen in Fig. 4a. The clad structure shows

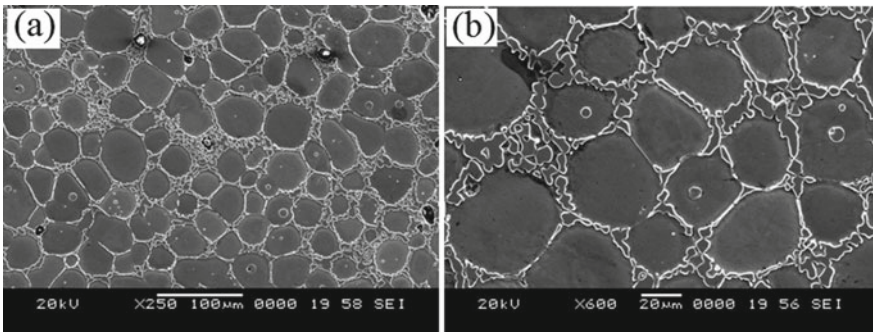


Fig. 4 **a** SEM image of the nickel-based clad, **b** enlarged view of the same clad

dendrite free with no transition of cellular. A good bonding with the target substrate is owing to the mutual diffusion of elements. Figure 4b representing an enlarged view of the developed clad structure, which shows very clear grains and grain boundaries.

3.2 *Erosive Wear*

The parameters considered and the obtained results are reported in Table 1. The wear studies results are analyzed through MINITAB 16 software tool, which presents experimental design techniques. The eroded samples of the nickel-based clads are as shown in Fig. 5.

Table 1 Experimental wear rate and fuzzy prediction of the developed clad samples

S. No.	S (rpm)	P (μm)	A (°)	Wear (mg)	Fuzzy prediction	% of error
01	1000	212	15	0.00184	0.011	11.818
02	1000	425	30	0.0005	0.0178	5.561
03	1000	600	45	0.00102	0.0102	15.686
04	1250	212	30	0.00048	0.0031	3.225
05	1250	425	45	0.0029	0.0175	22.857
06	1250	600	15	0.0041	0.0246	15.447
07	1500	212	45	0.00216	0.011	0.909
08	1500	425	15	0.00298	0.0146	6.849
09	1500	600	30	0.00574	0.028	10.714



Fig. 5 Eroded samples of the nickel-based clads

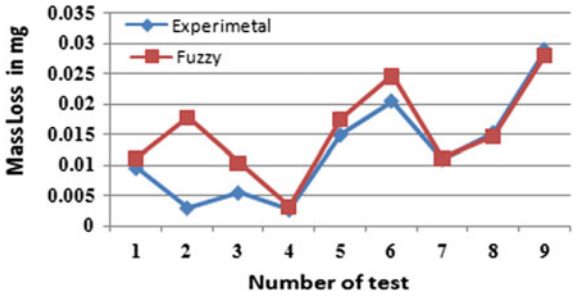


Fig. 6 Experimental versus fuzzy forecasted values of clad samples

3.3 Neuro-Fuzzy Prediction

In the fuzzy modeling process slurry, erosive wear parameters converted into fuzzy sets, which is greatly used in the inference levels. Finally, the fuzzy model was used by taking into account the important input parameters and one output parameter.

There are three input parameters such as speed (S) and striking particle sizes (P) and impact angle (A) as presented in Table 1; output was considered to be erosive wear rate in terms of weight loss. The erosive wear values of experimental with fuzzy prediction are reported in Table 1. Figure 6 displays the comparison between the experimental and the expected values of the clad samples. The average error rate between fuzzy logic and experimental value is 10.34%.

3.4 SEM Analysis of Worn Surfaces

Scanning electronic microscope was used to analyze the worn-out surface. The worn surface clearly shows the slurry particles, which impacts on the developed surface. When a high-velocity jet of mud particles hit the target surface that leads to damage to the surface and further cause to loss of mass is shown in Fig. 7.

4 Conclusion

- Nickel-based clads were developed on SS304 using a domestic microwave oven.
- The SEM images showed good metallurgical bonding with the substrate and crack-free clad structures were found.
- It was observed that the average percentage error among the investigational values and fuzzy predicted values were found to 10.34%.
- The worn surface of the developed clad reveals the minimal damage of the surface.

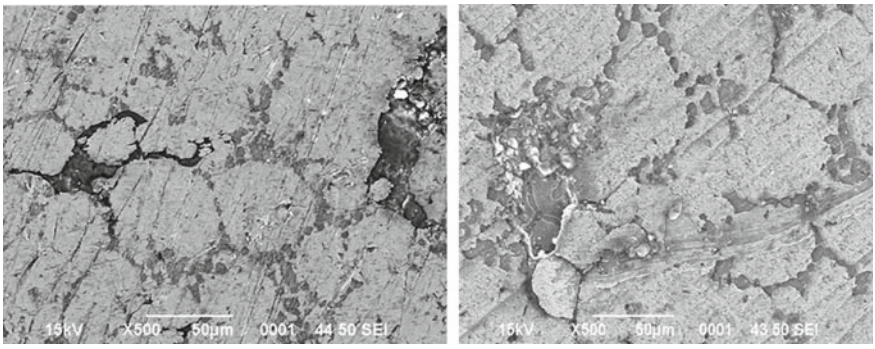


Fig. 7 Typical SEM images of the worn surfaces

Scope for Future Work

There is very limited literature available in the fuzzy prediction of wear studies of microwave clads. Hence, there is extensive scope to elaborate on it in the future for further investigation.

References

1. Santa JF, Baena JC, Toro A (2007) Slurry erosion of thermal spray coatings and stainless steels for hydraulic machinery. Wear 263:258–264
2. Shipway PH, Howell L (2005) Microscale abrasion—corrosion behaviour of WC-Co hardmetals and HVOF sprayed coatings. Wear 258:303–312
3. Thakur L, Arora N (2013) A comparative study on slurry and dry erosion behaviour of HVOF sprayed WC—CoCr coatings. Wear 303:405–411
4. Grewal HS, Agrawal A, Singh H, Shollock BA (2014) Slurry erosion performance of Ni-Al_2O_3 based thermal-sprayed coatings: effect of angle of impingement. J Therm Spray Technol 23:389–401
5. Liu SL, Zheng XP, Geng GQ (2010) Influence of nano-WC-12Co powder addition in WC-10Co-4Cr AC-HVAF sprayed coatings on wear and erosion behaviour. Wear 269:362–367
6. Dallaire S, Dube D, Fiset M (1990) Laser melting of plasma-sprayed copper–ceramic coatings for improved erosion resistance. 102–107
7. Sun Y, Bell T (2002) Dry sliding wear resistance of low temperature plasma carburised austenitic stainless steel. Wear 253:689–693
8. Anupam HSG, Singh AH (2013) Slurry erosion mechanism of hydroturbine steel : effect of operating parameters. 287–303
9. Burstein GT, Sasaki K (2000) Effect of impact angle on the slurry erosion—corrosion of 304L stainless steel. 240(1–2):80–94
10. Grewal HS, Singh H, Agrawal A (2013) Understanding Liquid Impingement erosion behaviour of nickel-alumina based thermal spray coatings. Wear 301:424–433
11. Emara KM, Ahmed SM (2014) Effect of impact angle on slurry erosion behavior and mechanisms of carburized AISI 5117 steel. 136:1–9
12. Emara KM, Ahmed SM (2012) Effect of impact angle on slurry erosion behaviour and mechanisms of carburized AISI 5117 steel (Received September 11 , 2012 Accepted October 8 , 2012). Abstract. 41:137–157

13. Abouel-Kasem A, Abd-elrhman YM, Emara KM, Ahmed SM (2010) Design and performance of slurry erosion tester. J Tribol 132:1–10
14. Desale GR, Gandhi BK, Jain SC (2006) Effect of erodent properties on erosion wear of ductile type materials. Wear 261:914–921
15. Desale GR, Gandhi BK, Jain SC (2008) Slurry erosion of ductile materials under normal impact condition. Wear 264:322–330
16. Grewal HS, Agrawal A, Singh H (2013) Tribology international slurry erosion performance of Ni–Al_2O_3 based composite coatings. Tribiol Int 66:296–306
17. Grewal HS, Agrawal A, Singh H, Grewal HS, Agrawal A, Singh H, Ropar T, Road N (2013) Design and development of high-velocity slurry erosion test rig using CFD. 22:152–161
18. Malka R, Nešić S, Gulino DA Erosion—corrosion and synergistic effects in disturbed liquid-particle flow. 262:791–799
19. Shimizu K, Xinba Y, Ishida M, Kato T (2011) High temperature erosion characteristics of surface treated SUS410 stainless steel. Wear 271:1349–1356
20. Islam MA, Alam T, Farhat ZN, Mohamed A, Alfantazi A (2015) Effect of microstructure on the erosion behavior of carbon steel. Wear 332–333:1080–1089
21. Smith JS, Swaminathan SV, Gandy MD (2010) High-temperature erosion testing standard and round robin testing. In: Sixth International Conference on Advances in Materials Technology for Fossil Power Plants; Santa Fe, NM. August 31st–Sept. 3rd, 0–17
22. Kosa E, Göksenli A (2015) Effect of impact angle on erosive abrasive wear of Ductile and Brittle materials. Int J Mech Aerospace Ind Mechatron Manuf Eng 9:1582–1586
23. Sidhu TS, Prakash S, Agrawal RD (2006) Hot corrosion and performance of nickel-based coatings. Curr Sci 90:41–47
24. Hebbale AM, Bekal A, Srinath MS (2019) Wear studies of composite microwave clad on martensitic stainless steel. SN Appl Sci 1(3):196
25. Hebbale AM, Srinath MS (2018) Microstructural studies of cobalt based microwave clad developed on martensitic stainless steel (AISI-420). Trans Indian Inst Met 71:737–743
26. Hebbale AM, Srinath MS (2017) Taguchi analysis on erosive wear behavior of cobalt based microwave cladding on stainless steel AISI-420. Meas J Int Meas Confed 99
27. Hebbale AM, Srinath MS (2016) Microstructural investigation of Ni based cladding developed on austenitic SS-304 through microwave irradiation. J Mater Res Technol 5(4):293–301
28. Srinath M, Hebbale AM (2017) Fuzzy prediction of slurry erosive behavior of cobalt based clad developed through microwave energy. Mater Today Proc 4(2):1804–1811

Microstructural Evaluation of Tungsten Carbide GT30 Machined by Abrasive Jet Machining



D. V. Sreekanth, P. Santosh Kumar Patra, and M. Sreenivasa Rao

Abstract Machining of small holes on tungsten carbide using the conventional machining processes is a difficult task due to its high hardness. This difficulty can be overcome by using an inexpensive unconventional machining process called abrasive jet machining (AJM). In this paper, the machining of tungsten carbide has been carried out using AJM, in which the material removal takes place due to mechanical erosion of the work piece under the action of high-velocity abrasive jet. In this paper, tungsten carbide work piece is used for the experimentation. The experimental investigation is performed by selecting the predefined optimal values for process parameter like pressure, stand-off distance (SOD), and nozzle diameter (ND). The present study focuses on the change in microstructures of WC GT30 before and after machining by SEM micrographs which can provide an understanding about the change in properties of hard metals during the abrasive jet machining process.

Keywords WC GT30 · AJM · Pressure · SOD · ND · SEM

1 Introduction

Many industry sectors like metal machining wear parts for mining and oil industries, cutting tips for saw blades, metal forming tools, etc., widely require the application of different grades of tungsten carbide. Recently, this material is even used in domestic applications like wedding rings, watch cases, ball for ball point pens, etc. Developed originally in Germany to meet the requirement for die materials that can withstand high wear found in the drawing of tungsten filaments for light bulbs, these hard

D. V. Sreekanth (✉)
Departmant of Mechanical Engineering, St. Martin's Engineering College, Hyderabad, Telangana, India
e-mail: dvsk75@gmail.com

P. S. K. Patra
St. Martin's Engineering College, Hyderabad, Telangana, India

M. S. Rao
Department of Mechanical Engineering, JNTU, Hyderabad, Telangana, India

© Springer Nature Singapore Pte Ltd. 2020

A. Praveen Kumar et al. (eds.), *Advances in Lightweight Materials and Structures*,
Springer Proceedings in Materials 8, https://doi.org/10.1007/978-981-15-7827-4_56

metals are produced through powder metallurgy process [1]. Tungsten carbide (WC) mainly consists of nearly equal quantities tungsten (W) and carbon (C) with cobalt (Co) as a binder. The hard particles of tungsten and carbide are embedded in a matrix of cobalt. The particular grade tungsten carbide used for this study is GT30 with chemical composition as of WC has 86% of WC with 14% of Co. Tungsten carbide GT30 exhibits the following mechanical properties: This grade usually has a hardness around 85.5 HRA (Rockwell hardness scale-A) [2]. This makes the machining of this material very difficult by the conventional machining process. This calls for the development of unconventional processes for machining this material.

Many industrial applications for tungsten carbide like manufacture of machine sleeves, oil sleeves, bushings, etc., require small holes to be made in this material. In this study, an unconventional low-cost machining process called abrasive jet machining is implemented to machine holes in tungsten carbide plate of dimensions 25 * 25 * 2 mm^3. The microstructures before and after machining has been studied to understand the change in the mechanical properties during machining.

Grating jet machining (AJM) is otherwise called rough miniaturized scale impacting, pencil impacting, small-scale rough impacting, and so forth. AJM is a mechanical vitality based non-conventional machining process. Right now, is evacuated by fine grating particles, generally about 0.001 in (0.025 mm) in width, driven by a high-speed liquid stream. Weights for the gas run from 25 to 130 psig (170–900 kPa or 4 bars) and speeds can be as high as 300 m/s. AJM uses the force impinged by the small abrasives to cause minute fractures on the metal surface. This result in good finishing, accurate machining, and less wear & tear of the material. This process has replaced many conventional methods of machining in the industry due to its various advantages. This method proved to be economical for hard and brittle materials like glass, silicon, tungsten, and ceramics [3]. This process is found to be suitable for machining holes and grooves. The entire work surface is exposed to the jet, and therefore, through proper shielding of the substrate surface, even patterns can be obtained through AJM.

The different hardware utilized in the development of the AJM setup are air compressor, air filter, dehumidifier, pressure check, mixing chamber, nozzle, arrangement to hold the work pieces. The below schematic shows the set of AJM process: Dry gas or air is first filtered through the filter and then passed through the compressor to feed compressed air to the mixing chamber where it gets mixed up with the abrasive particles. The feed rate of the abrasive particles to the mixing chamber can be controlled through the hopper [5]. The abrasive jet is then sent to the nozzle through the pressure regulator which regulates the pressure of the jet. From the nozzle, the jet is then impinged on to the work piece for machining [4].

2 Experimentation

The experiment was carried out in SMEC using the AJM test rig. The AJM setup used for this experimentation and machining of WC with AJM is shown in Figs. 1

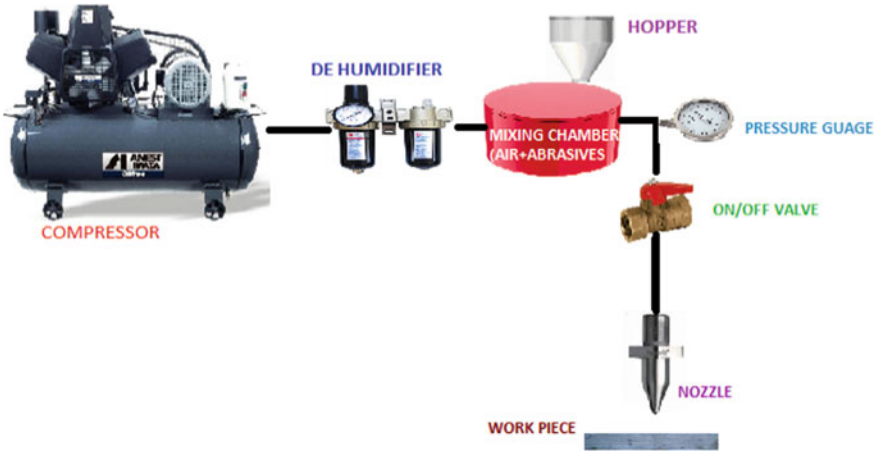


Fig. 1 Process of AJM

and 2: The mechanical properties are given in Table 1

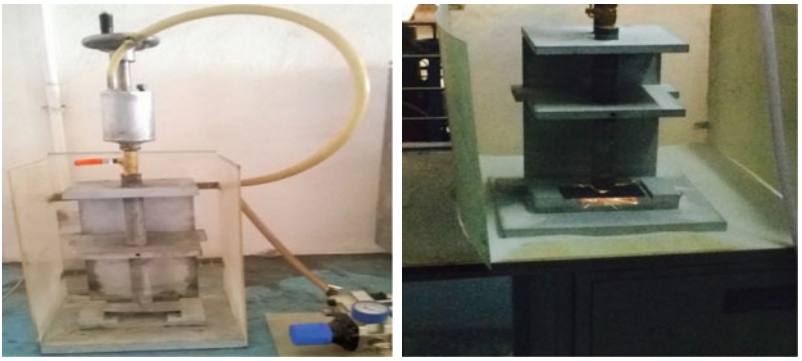


Fig. 2 **a** and **b** Abrasive jet machining setup established in SMEC and machining of WC by AJM

Table 1 Mechanical properties of tungsten carbide GT30

S. No.	Property	Values
1	Density	15.6 g/cm^3
2	Thermal conductivity	110 W/ (m–K)
3	Melting point	2785–28,300C
4	Boiling point	60,000C
5	Young's modulus	600–686 GPa

Table 2 Parameters in AJM with their factors

Parameter	Factors
Abrasive particles	Material, size, shape, and mass flow rate
Carrier gas	Composition, velocity, density, pressure, flow rate
Abrasive jet	Velocity, mixing ratio, stand-off distance, (SOD), impingement angle
Nozzle	Material, diameter, life

The main process criteria for AJM include material removal rate, geometry, and surface finish of the work surface, wear rate of the nozzle, etc. There different process parameters that govern the performance criteria for this AJM process are given in Table 2

The AJM test rig consists of the AJM apparatus and provision for securing the work piece during machining. A glass shield is arranged [6] to cover the apparatus from sides, so that the machining process remains uninfluenced from external environment and at the same time providing the operator to easily access the machine. The total setup is secured to the base to provide it more rigidity.

A variety of abrasive particles are available in the market like Al_2O_3, SiC, glass beads, crushed glass, sodium bicarbonate, etc., which are suitable for the AJM process. For this experimentation, the abrasive particles Al_2O_3 (aluminum oxide) and SiC (silicon carbide) are used (see Fig. 3).

The process parameters chosen for this study are pressure, stand-off distance, and nozzle diameter. The preferred ranges for these parameters are pressure: 2–10 bar, SOD: 0.5–15 mm, nozzle diameter: 1 mm to 4 mm, and abrasive grain size from 20 to 80 microns. From these ranges, the values of the parameters are selected (See Table 3).

It is discussed about various brittle and hard materials (glass, ceramics, composites etc.,) by AJM. In the present work, the main focus is on machining of tungsten carbide. By conventional processes, it is very difficult to drill WC but by using abrasive jet machining at high pressure, medium SOD, 3 mm nozzle diameter, and abrasive grain size of 40 microns. The abrasives selected for these experiments are silicon carbide due to its effectiveness of coarse attack on work surface. It is observed that the machining time is more for WC comparing with the other materials. By maintaining



Fig. 3 Abrasive particles of Sic, Al_2O_3

Table 3 Experimental values:

Parameters	Values
Pressure	8 kg/cm^2
SOD	8 mm
Nozzle diameter	3 mm
Abrasive grain size	40 microns

a suitable SOD, the kerf width will be decreased. Figure 4 shows the top surface of the work piece drilled by AJM, and Fig. 5 shows the top surface of the work piece drilled by AJM.

After machining, the responses of machining MRR and KERF are calculated. The pressure selected is maximum and AGS as 40 microns by maintaining the stand-off distance as 8 mm, and the type of nozzle used is sapphire-coated nozzle with 3 mm diameter. The abrasive flow rate selected for this machining is 4.5. All these values are identified as the optimal values in Taguchi. The two response values are given in Table 4.

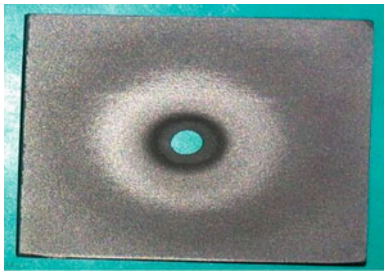


Fig. 4 WC specimen drilled by AJM (front portion)

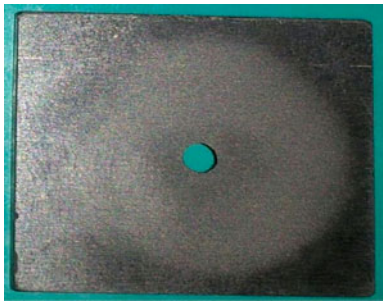


Fig. 5 WC specimen drilled by AJM (back portion)

Table 4 Input parameters and experimented output values of MRR and KERF

Parameters	Values	MRR (gm/s)	KERF (mm)
Pressure	8 kg/cm^2	0.0971	2.1
SOD	8 mm		
Nozzle diameter	3 mm		
Abrasive grain size	40 microns		

3 Results and Discussions

The experiments were carried out using the above parameters, and the microstructures were studied using the metascope metallurgical microscope through the ASTM B 390 procedure. The hexagonal structure can be envisioned as made up of a straightforward hexagonal cross section of metal atoms of layers lying legitimately more than each other, with carbon particles filling a large portion of the interstices giving both tungsten and carbon a customary trigonal kaleidoscopic. From the unit cell measurements, the accompanying bond lengths can be resolved; the separation between the tungsten molecules in a hexagonally stuffed layer is 291 pm, the most brief separation between tungsten particles in abutting layers is 284 pm, and the tungsten carbon bond length is 220 pm. The tungsten–carbon bond length is along these lines practically identical to the single bond in W (CH3)6 (218 pm) in which there is firmly contorted trigonal kaleidoscopic coordination of tungsten. For these examinations, WC of hexagonal structure is distinguished and machined [11].

Most of evaluations that we machine are made with standard size grains fluctuating somewhere in the range of 1 and 3 microns in size. Utilizing bigger grains of 2–6 microns will incredibly build the quality and sturdiness of the material in light of the fact that the bigger grains interlock better [10]. The exchange off is that bigger grain materials do not offer as a lot of protection from wear as better grain estimated materials. Submicron materials that shift somewhere in the range of 0.4 and 1.0 micron grain size are harder than standard grain materials with a similar cobalt content. The underlying hardness HRA is 85.5. In the wake of penetrating by AJM process, the miniaturized scale structure saw through metascope metallurgical magnifying lens of 500X amplification through the ASTM B 390 strategy that the grain shape changes from hexagonal to spiracle. The miniaturized scale photos reveal [7] an adjustment in grain size from 3.0 μm to 0.5–3.1 μm. The microstructure uncovers haphazardly conveyed tungsten carbide in the network. From Fig. 6, it is observed that area surrounding the drilled portion is effected with the heat and impact of abrasive particles. The microstructure after machining is also observed in the form of brown spotted grains of abrasives with long grain boundaries as shown in Fig. 7.

The scanning electron microscopy (SEM) and energy dispersive X-ray (EDX) was also employed in a view to characterize WC–Co material. ASTM E3 standards were followed for preparation [9]. The microstructure of material (with 6% cobalt) is depicted in Fig. 8a. The uniformly distribution of cobalt particles after machining can be observed throughout the matrix. Figure 8b depicts the surface topography of the



Fig. 6 Microstructure before machining (500X)



Fig. 7 Microstructure after machining (500X)

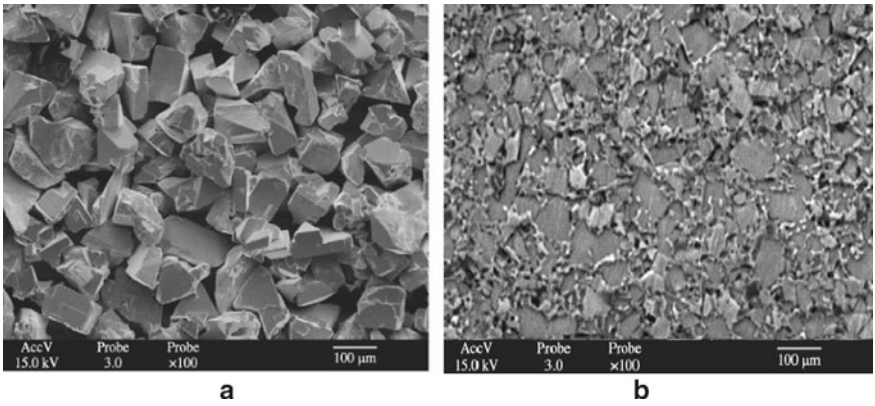


Fig. 8 **a** SEM microstructure of WC Gt30(100×); **b** SEM microstructure of work after machining (100×)

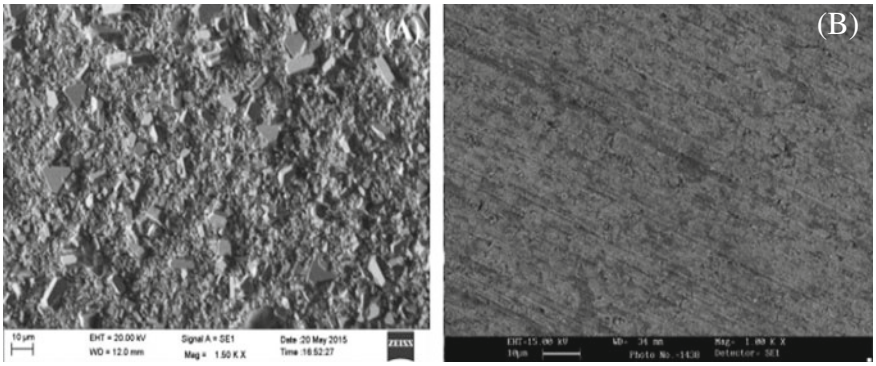


Fig. 9 (A) Microstructure of composite with 6%Co (1500×); (B) microstructure of composite with 24%Co obtained by SEM (1000×)

sample of composite with 24% cobalt. The uniform distribution of cobalt particles can be observed throughout the matrix (Fig. 9).

4 Conclusions

Machining of WC by AJM is effectively performed and broke down the miniaturized scale structure and checking electron microscopy additionally made and considered the adjustment in grain size.

- Breaking down the miniaturized scale basic attributes of WC assists with bettering to recognize the highlights that may associate to components, for example, quality and solidness of WC.
- To achieve this, more microstructure and SEM pictures will be required of more examples to help improve comprehension of any relationships between properties [8]. It would likewise be advantageous to have material science-based models to help decide how microstructure may influence preparing execution, for example, with crushing and cleaning. Improved information on tungsten carbide will keep on being required so as to see how to best utilize this noteworthy material.
- Parametric impact on machining of WC uncovers that the impact of pressure on MRR is more and impact of SOD on KERF width, it is likewise can be seen that the time take for machining is more for WC contrasting and different materials. This examination primarily featured the change in microstructure properties before machining and subsequent to machining

Future Scope

Parametric impact on machining of WC uncovers that the impact of pressure on MRR can be verified for more and impact of SOD on KERF width. The time

taken for machining for WC contrasting and different materials can be conducted at different parameters. The examination of the change in microstructure properties before machining and subsequent to machining can also be found at different magnifications.

References

1. Rajendra Prasad K, Ravindranath MLSD (2019) Parametric optimization in modified air abrasive jet machining. Multidis Model Mater Struct 15(3):617–629. https://doi.org/10.1108/MMMS-02-2018-0036
2. Alsoufi MS, Suker DK (2018) Experimental investigation of wire-EDM process parameters for surface roughness in the machining of carbon steel 1017 and aluminium alloy 6060. American J Mech Eng 6(3):132–147
3. Haldar B, Ghara T, Ansari R, Das S, Saha P (2018) Abrasive jet system and its various applications in abrasive jet machining, erosion testing, shot-peening, and fast cleaning. Mater Today Proc
4. Haldar B, Adak DK, Ghosh D, Karmakar A, Habtamu E, Ahmed M, Das S (2018) Present status and some critical issues of abrasive jet materials processing: a review. Proc Manuf 20:523–529
5. Mohammad Jafar RH, Spelt JK, Papini M (2013) Surface roughness and erosion rate of abrasive jet micro-machined channels: experiments and analytical model. Wear 303:138–145
6. Lai CP, Chan LC, Chow CL (2007) Effects of tooling temperatures on formability of titanium TWBs at elevated temperatures. J Mater Process Technol 191:157–160
7. Cheng CH, Chan LC, Chow LC, Lai CP (2006) Formability of Ti-TWBs at elevated temperatures. SAE Technical Paper, 2006–01–0353
8. Khan AA, Haque MM (2007) Performance of different abrasive materials during abrasive water jet machining of glass. J Mater Process Technol 191:404–407
9. Rahmah A (2005) Abrasive water jet machining of composite ballistic materials (Kevlar). Ph.D. Thesis, International Islamic University Malaysia, Kuala Lumpur
10. Alsoufi MS, Suker DK, Alsabban AS, Azam S (2016) Experimental study of surface roughness and micro-hardness obtained by cutting carbon steel with abrasive waterjet and laser beam technologies. American J Mech Eng 4(5):173–218
11. Jagadish, Gupta K Abrasive water jet machining of engineering materials. Springer Briefs in Applied Sciences and Technology. ISBN 978–3–030–36000–9, https://doi.org/10.1007/978-3-030-36001-6

A X-Ray Diffraction Study of Residual Stresses Due to Multipass Welding of INCONEL600

Harinadh Vemanaboina, R. Gopi Chandh, P. Sivakrishna, A. Kishore Kumar, K. Malli Karjuna, and Y. Sailinga Reddy

Abstract Gas tungsten arc welding process can be adaptable for all metals and can be used for all welding positions. It can be operated in both continues and pulsed mode current. The present study has been carried out with pulsed current gas tungsten arc welding of Inconel600 with three passes, and the filler wire of ERNiCrMo-3 has been considered. The single V-groove is employed for joining the plates with three passes welding. The residual stresses and tensile strength in weldments are studied. X-ray diffraction (XRD) technique is used to measure residual stresses. The measurement is carried out on the surface across the welding direction. The tensile residual stresses are observed at the fusion zone. The tensile strength of the weldment is higher than that of the base metal.

Keywords PCGTAW · Multipass welding · XRD · Tensile strength · Residual stresses

1 Introduction

Inconel materials are used to resist high temperature and corrosion applications required, i.e., aerospace, nuclear, and powerplants, etc. Arc welding process widely practices in the industries. Gas tungsten arc welding (GTAW) process is easy to establish and can be operated manually and automatic during the welding, and weld is protected by shielding gas and the defects are minimized. Welding made by depositing filler metal filler with two or more passes in succession is known as multipass welding. It is often employed with the submerged arc process. The gas metal arc welding (GMAW) process is the best choice for both manual and automatic root or first pass procedures. The effect of heat input in the weld causes distortion and residuals stresses in the finals butt weldments are experimentally studied and validated using finite element analysis [1, 2].

H. Vemanaboina (✉) · R. Gopi Chandh · P. Sivakrishna · A. Kishore Kumar · K. Malli Karjuna · Y. Sailinga Reddy
Department of Mechanical Engineering, Sri Venkateshwara College of Engineering and Technology (Autonomous), Chittoor, Andhra Pradesh, India
e-mail: harinadh.vh@gmail.com

© Springer Nature Singapore Pte Ltd. 2020

A. Praveen Kumar et al. (eds.), *Advances in Lightweight Materials and Structures*, Springer Proceedings in Materials 8, https://doi.org/10.1007/978-981-15-7827-4_57

The moving heat source model was developed for welding process to evaluate thermal and its effects on the residual stress in the weldments, and the experimental samples are measured with diffraction technique [3–6]. Tensile residual stresses are reported for high-strength alloys weldments at fusion zone. This phenomenon is due to increase in heat for all arc welding process with single and multipass welds. The heat input increases with thickness of the plate, type groove, groove angle, and filler wire diameter. With the increase in heat input, the heat-affected zones (HAZ) experience hot cracking and compressive stresses [7–12].

Haigh et al. [13] worked on SS304 pipe of 25 mm thickness, and the multipass was filled with two girths, first half of 11 passes with 5 layers and remaining 22 passes with 11 layers. The GTAW process was employed, and diffraction techniques are used to study the residual stress and were validated with finite element modeling. Vladimir Ivanovitch Monin [14] worked on residual stress measurement on duplex stainless steels for GTAW process using X-ray diffraction in longitudinal and transverse direction and observed that fusion zone was in ferrite and HAZ was in austenite phases. The study evaluates residual stress in titanium material, and its alloys were reported for plate and pipe structures. The stress measurement was done by X-ray diffraction measurement technique in transverse direction to the weld [15, 16]. Lucia Zauskova [17] had used triaxial method for measuring residual stress after machining the surface of the sample by high feed milling technology. The sample of 17 240 (X5CrNi18-10) is used for measuring on portable diffractometer, Proto iXRD, and the measurement is carried for axial and surface of component.

The demand of using high temperature and corrosion resistance materials is increased from a decade which has wide applications in nuclear, thermal plants and marine application. This study aims to evaluate the distribution of residual stresses in multipass weldment. The pulsed current gas tungsten arc welding process was used for welding of Inconel600. The residual stresses are measured on the surface of weldment in the transverse direction, i.e., perpendicular to weld direction.

2 Experimental Procedure

The pulsed current mode is used for welding of samples in multipass welding. The two different current modes are used during the process. The multipass welding process with three passes is shown in Fig. 1, and during the welding process, the material

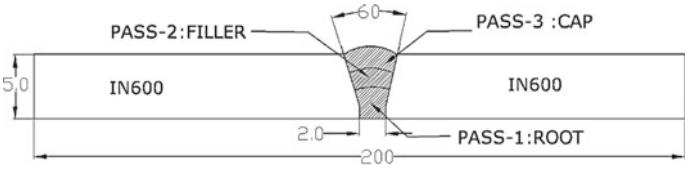


Fig. 1 Dissimilar welding of multipass PCGTAW process

Table 1 Base and filler material chemical composition

Element (% by mass)									
	Ni	C	Mn	S	Cu	Si	Cr	Fe	Others
Inconel600	72	0.2	1.0	0.02	1.0	1.0	14–17	10	–
ERNiCrMo-3	64	0.1	0.5	0.02	1.0	1.0	22.0–23.0	1.0	Al 0.40, Nb-3.6–4.5, Mo 0.015, Ti 0.40

was filled with ERNiCrMo-3 filler rod of 2.4 mm diameter. The plate dimensions are of 120 mm * 50 mm * 5 mm before welding. Standard single V-groove employed with an included angle of 60° is used with land of 1.6 mm. The butt joint is prepared with root gap of 2 mm between the plates. Table 1 shows the chemical composition of base material and filler wire employed for the current study. The welding process is carried out with pulsed mode current with gas tungsten arc welding process with base current as 130 Amps, background current as 60 Amps, and voltage of 20 V.

The weldment is free surface (hot cracking) and internal defects which were verified through X-Ray radiography. The final welded sample is shown in Fig. 2. Further, the sample goes through the electric discharge machine wire cut with standard gauge lengths for preparation of tensile strength specimen. The weldment is shear as per the standard gauge length of the weldment for tensile strength as shown in Fig. 3. The residual stresses are measured on the surface [10, 20] weldment across the welding. The measurement will cover all the zones of the weld surface. The residual stress is measured using the X-Ray diffraction.

The PROTO is in-site measurement system, and the measurement is carried out using the ASTM E975 standards. The X-ray method is employed for measuring in weldment, and the surface of the welded material by using Bragg's law as given in Eq. (1) and residual stresses using Eq. (2).



Fig. 2 Sample after welding



Fig. 3 Sample prepared for tensile sample

$$n\lambda = 2d \sin\theta \tag{1}$$

$$\sigma_\phi = \frac{m}{d_0}\left(\frac{E}{1+}\right) \tag{2}$$

whereas n = the order of reflection beam, d = interplanar lattice spacing θ = Bragg law, m is slope, d_o is lattice spacing, E is young's modulus, and ν is Poisson's ratio of the base material. The calculation of slope is carried out for all the positions on the surface of the weldment, based on the graphs drawn between $\sin^2$ psi (vs) D spacing as shown in Fig. 4. The yield stress (E) of the material is 310 MPa, and Poisson's ratio (ν) is 0.28 for the parent material. The measurement of the residual stresses is carried out using the Bragg's angle, and for measured Bragg angle is used 155.20°. The wavelength used for the measuring at 2.103 with a Gaussian distribution of about 80% is shown in Fig. 5.

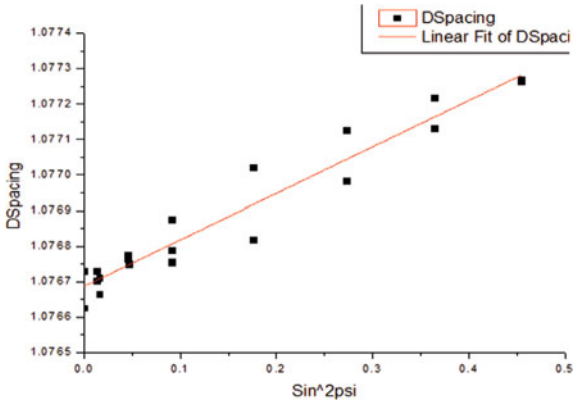


Fig. 4 Slopes at various positions on the surface of weldment

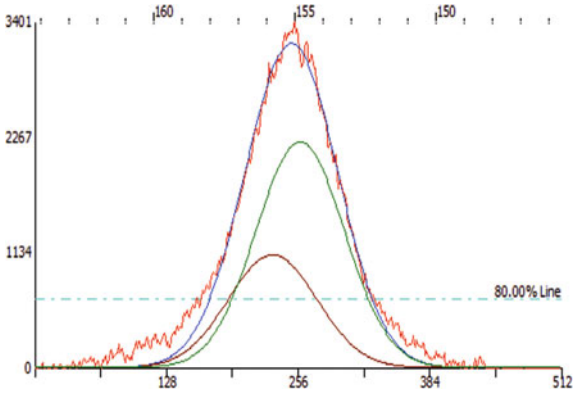


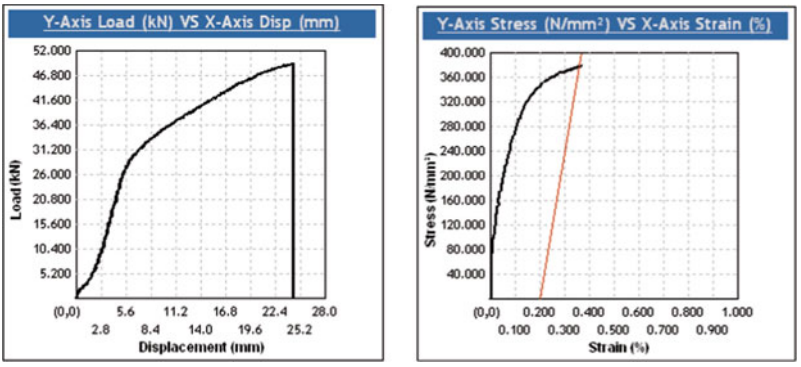
Fig. 5 Peaks of the weldment

3 Results and Discussion

The tensile strength is carried out for weldment with a strain rate of 2 mm/min. The weldment undergoes plastic deformation up to fracture with a standard of ASTM A 370–2013. Figure 6 shows the load versus displacement and stress–strain in the tensile specimen. The fracture of the weldment is taken place at fusion zone as shown in Fig. 7, the ductility in the material of 30%, with ultimate tensile strength of 719.68 MPa.

The stress distribution was calculated using Eq. (2) as explained in Sect. 2, where slope is calculated from Fig. 4 at various locations on the weldment. The residual stress distribution is measured in transverse direction, and the distribution of stresses on the surface of the weldment is shown in Fig. 8. The residual shows max peak at the fusion zone and future, and in HAZ, the lowest peak was observed because of the heat generated in the fusion zone; both sides of the plate experience compressive than fusion zone.

The maximum residual stresses in the final weld are about 140 MPa at the fusion zone and start decreasing moving further. In HAZ, it was observed that the stresses are 20 MPa and at the base plate the stress is in the increasing trend of about 40 MPa. The stresses are within the safe limits compared with yields strength of the base material



(a) (b)

Fig. 6 Graphs for tensile specimen **a** load versus displacement and **b** stress–strain curve of the weldment

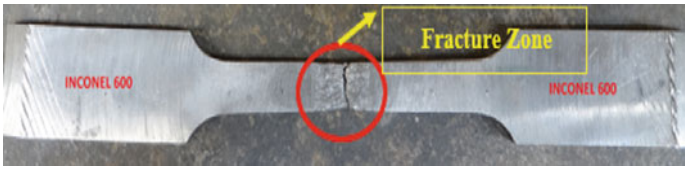


Fig. 7 Specimen after tensile test

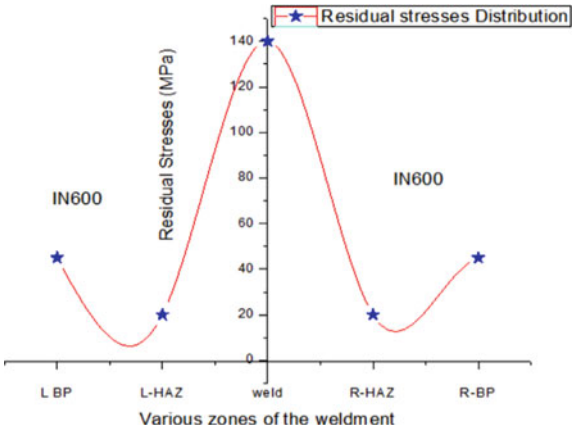


Fig. 8 Residual stress distribution on the weldment

and are not balanced at the measured point. This trend of stress distribution is due to influenced welding process parameters, thermal, cooling rate, and mechanical properties of the base materials.

4 Conclusions

(1) Successful, defect-free multipass weldment of Inconel600 could be obtained using PCGTA welding process employing ERNiCrMo-3.
(2) Hot cracking in the welds can be avoiding by using the interpass temperature between the passes.
(3) The tensile residual stress observed at fusion zone in the weldment, which is within the yield limits, shows a factor of safety of 2.21.
(4) Stresses were not self-balanced within the structure. It can be overcome by post-weld heat treatment.

References

1. Ravisankar A, Velaga SK, Rajput G, Venugopal S (2014) Influence of welding speed and power on residual stress during gas tungsten arc welding (GTAW) of thin sections with constant heat input: a study using numerical simulation and experimental validation. J Manuf Process 16(2):200–211
2. Deng D, Murakawa H (2008) Prediction of welding distortion and residual stress in a thin plate butt-welded joint. Comput Mater Sci 43(2):353–365
3. Deng D, Murakawa H (2006) Prediction of welding residual stress in multi-pass butt-welded modified 9Cr–1Mo steel pipe considering phase transformation Effects. Comput Mater Sci 37(3):209–219

4. Yaghi AH, Hyde TH, Becker AA, Sun W (2013) Finite element simulation of residual stresses induced by the dissimilar welding of a P92 steel pipe with weld metal IN625. Int J Press Vessels Pip 111–112:173–186
5. Muránsky O, Smith MC, Bendeich PJ, Holden TM, Luzin V, Martins RV, Edwards L (2012) Comprehensive numerical analysis of a three-pass bead-in-slot weld and its critical validation using neutron and synchrotron diffraction residual stress measurements. Int J Solids Struct 49(9):1045–1062
6. Bhatti AA, Barsoum Z, Khurshid M (2014) Development of a finite element simulation framework for the prediction of residual stresses in large welded structures. Comput Struct 133:1–11
7. Bhatti AA, Barsoum Z, Murakawa H, Barsoum I (2015) Influence of thermo-mechanical material properties of different steel grades on welding residual stresses and angular distortion. Mater Des 65:878–889
8. Harinadh V, Edison G, Akella S, Sanjeeva Reddy L, Buddu RK (2017) Multipass welding on inconel material with pulsed current gas tungsten arc welding. Mater Today Proc 4(2):1452–1458
9. Vemanaboina H, Akella S, Buddu RK (2014) Welding process simulation model for temperature and residual stress analysis. Procedia Mater Sci 6:1539–1546
10. Vemanaboina H, Edison G, Akella S, Buddu RK (2018), Effect of residual stresses of GTA welding for dissimilar materials. Mater Res 21(4)
11. Vemanaboina H, Edison G, Akella S, Buddu RK (2018) Simulation of hybrid laser-TIG welding process using FEA. J Eng Sci Technol 13(6):1782–1792
12. Xia J, Jin H (2016) Numerical study of welding simulation and residual stress on butt welding of dissimilar thickness of austenitic stainless steel. Int J Adv Manuf Technol 91(1–4):227–235
13. Haigh RD, Hutchings MT, James JA, Ganguly S, Mizuno R, Ogawa K, Okido S, Paradowska AM, Fitzpatrick ME (2013) Neutron diffraction residual stress measurements on girth-welded 304 stainless steel pipes with weld metal deposited up to half and full pipe wall thickness. Int J Press Vessels Pip 101:1–11
14. Monin VI, Lopes RT, Turibus SN, Payão Filho JC, de Assis JT (2014) X-ray diffraction technique applied to study of residual stresses after welding of duplex stainless-steel plates. Mater Res 17(Suppl-1):64–69
15. Moussaoui K, Segonds S, Rubio W, Mousseigne M (2016) Studying the measurement by X-ray diffraction of residual stresses in Ti6Al4V titanium alloy. Mater Sci Eng A 667:340–348
16. Holmberg J, Steuwer A, Stormvinter A (2016) Residual stress state in an induction hardened steel bar determined by synchrotron- and neutron diffraction compared to results from Lab-XRD. Mater Sci Eng A 667:199–207
17. Zauskova L, Czan A, Sajgalik M, Drbul M, Rysava Z (2017) Triaxial measurement of residual stress after high feed milling using X-ray diffraction. Procedia Eng 192:982–987

Evaluation of Surface Integrity of Multi-stacked Glass Interplyed with Flax Laminate by Abrasive Waterjet Machining



M. Rajesh, K. Rajkumar, K. M. Nambiraj, and K. Ramraji

Abstract This article presents an experimental investigation of surface integrity on glass/flax stacking layered composite machining using an abrasive waterjet energy process. Experimentation variables are SO_D-standoff distance, H_P-hydraulic pressure, and T_R-traverse rate. As to conduct experimentation, the central composite design module (CCD) was employed. The experimentation assessment is to make an effective process parameter selection for surface integrity. Surface unevenness was predicted by using the RSM-based mathematical model. Analysis of variance was done for measuring relative weightage of process variables which affect the surface roughness. From the experiment, pressure was found to be the highest influencing variable for surface roughness. It was found Ra was continuously decreasing with an increase in hydraulic pressure energy. It also reduced with decreasing SO_D and T_R. Scanning electron microscope (SEM) image reveals the roughness variations along the cutting surface of the stacked laminate.

Keywords Layered composite · Surface roughness · Water jet · Glass fiber · Flax fiber

1 Introduction

Fiber-reinforced polymer (FRP) composites are widely accepted for various engineering fields due to their excellent mechanical and structural properties [1–4]. Apart from that, they require a machining process to shape, size, and tolerance for multifarious applications. The machining of FRP done with conventional techniques was very difficult due to higher cutting force, tool wear, a failure by cutting temperature rise, and delamination of fiber plies. On the other hand, abrasive waterjet machining (AWJM) is one of the cutting methods that gives relief from different kind of defects occurring during cutting operations. It can be used especially for the machining of non-homogeneous materials [5, 6]. Material processing industries

M. Rajesh · K. Rajkumar (✉) · K. M. Nambiraj · K. Ramraji
Department of Mechanical Engineering, SSN College of Engineering, Chennai, Tamil Nadu, India
e-mail: rajkumark@ssn.edu.in

© Springer Nature Singapore Pte Ltd. 2020

A. Praveen Kumar et al. (eds.), *Advances in Lightweight Materials and Structures*,
Springer Proceedings in Materials 8, https://doi.org/10.1007/978-981-15-7827-4_58

have more relied on AWJ process, and it is more useful in the removal of material. It never produces heat on the work material [7].

Researcher shows that kerf taper proportion (K_{TP}), delamination, and surface roughness (R_a) are the major problems associated with the water jet-based cutting of composites [8]. Numerous parameters are influencing the machined surface integrity [9]. Surface integrity of machining zone is direct relationship with cutting variables like abrasive mass flow (A_{MF}), traverse rate (T_R), water pressure (W_P), standoff distance SO_D, etc. [10]. Arumuga prabu et al. [11] adopted AWJM on banana-based polymer composite. They concluded that the R_a and kerf angle are tremendously influenced by SO_D compared to the W_P and T_R. Selvam et al. [12] performed AWJM on hybrid composite and concluded that T_R was one of the major influencing factors to be controlled for reducing roughness variation. Gnanavelbabu et al. [13] investigated on machining of AA6061-B_4C-hBN using AWJM and reported that T_R and W_P were the most influencing process parameters on the kerf taper inclination and surface undulation. Kumar et al. [14] analyzed the R_a of Inconel 718 high-strength material. They concluded T_R is the most influencing parameter on R_a compared to the other parameters W_P, A_{MF}, and SO_D. Alberdi et al. [15] have evaluated the machinability of carbon-based polymer composite. They studied the effect of AWJM cutting variables to determine the quality of the machined surface. Azmir and Ahsan [16] used Taguchi's method to conduct the AWJM experiments on glass fiber–polymer composite to analyze the R_a. Kaliarasu et al. [17] evaluated AWJM characteristics on glass–coconut sheath hybrid composite. Interestingly, they found abrasive mesh size has highly affected the R_a and K_{TP}.

From the literature, many researches were focused on K_{TP} and surface quality of FRP machined by AWJM, and there was no report on AWJM of multi-stacked glass interlayered with flax fiber composites. The present work is conducted based on design of experiment approach and measured the machined surface's quality characteristic by AWJM on multi-stacked glass and flax layered composite. The acquired end results from the current study are cross-referenced with existing literature to asserting the influential parameters.

2 Materials and Methods

2.1 Materials

The interplay hybrid FRP composite was fabricated by woven fabrics of glass, flax, and using vinyl ester resin of grade VBR 4508 as a matrix. The regular promoter, accelerator, and catalyst were used for curing vinyl ester resin. The important physical properties of reinforcements are shown in Table 1.

Table 1 Glass–flax fiber properties [18]

Properties	Unit	Glass fiber	Flax fiber
Elongation at break	mm	3	3.15
Tensile module	GPa	73	87
Density	g/cm^3	2.55	2.80
Tensile strength	Pa	2400 * 10^6	4700 * 10^6

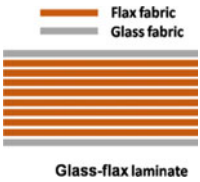


Fig. 1 Multi-stacked glass and flax layered composites

2.2 Fabrication of Composite Laminates

The flax fabric was treated with a 5% sodium hydroxide solution in one liter of water for a duration of 2.5 h at room temperature. The treated fibers were washed by ordinary water followed with distilled water. FRP composite was fabricated by a hand layup process with compression weight. The glass and flax fiber are stacked as a sequence for making a composite. The ratio of reinforcement weight fraction to the matrix weight fraction was maintained at 40:60. The size of the laminate was a square of 300 × 300 mm^2. The glass and flax multi-stacking laminate thickness is 4 mm, and its arrangement is shown in Fig. 1.

2.3 AWJM Process

AWJM on stacked glass–flax laminate is conducted based on the central composite design module (CCD) [19, 20]. All cutting experiments were done with a single pass. The AWJ cutting input parameters and their intermediate three variations are shown in Table 2.

Table 2 AWJM cutting parameters and their variations

Process parameters	Units	Levels		
		−1	0	1
Hydraulic pressure (H_P)	MPa	100	150	200
Traverse rate (T_R)	mm	150	200	250
Standoff distance (S_{OD})	mm/min	1	2	3

A two-axis OMAX-1530(CNC) waterjet cutting machine was used for machining experimentation. AWJM nozzle assembly consists of an orifice of 0.3 mm diameter with a sapphire jewel and carbide focusing tube having an internal diameter of 0.35 mm. The impinging angle of the water jet was perpendicular to work. The diameter of the mixing tube and abrasive particle size are 0.75 mm and 80 mesh. These standard sets of AWJ machine specifications are widely used in most industrial applications.

In this study, SURFTEST SJ-210 was used to measure R_a of the machined surface. The average of three values is used to record the R_a. Table 3 shows the R_a of the AWJ machined glass–flax stacked laminate.

Table 3 Experimentation results of surface roughness

Std	Run	H_P	T_R	SO_D	R_a
		MPa	mm/min	Mm	μm
10	1	1	0	0	2.628
5	2	−1	−1	1	3.237
18	3	0	0	0	2.814
13	4	0	0	−1	2.772
20	5	0	0	0	2.871
14	6	0	0	1	2.832
12	7	0	1	0	2.972
8	8	1	1	1	2.804
1	9	−1	−1	−1	3.123
19	10	0	0	0	2.814
2	11	1	−1	−1	2.534
16	12	0	0	0	2.814
4	13	1	1	−1	2.715
3	14	−1	1	−1	3.319
6	15	1	−1	1	2.591
7	16	−1	1	1	3.565
15	17	0	0	0	2.814
9	18	−1	0	0	3.285
17	19	0	0	0	2.814
11	20	0	−1	0	2.776

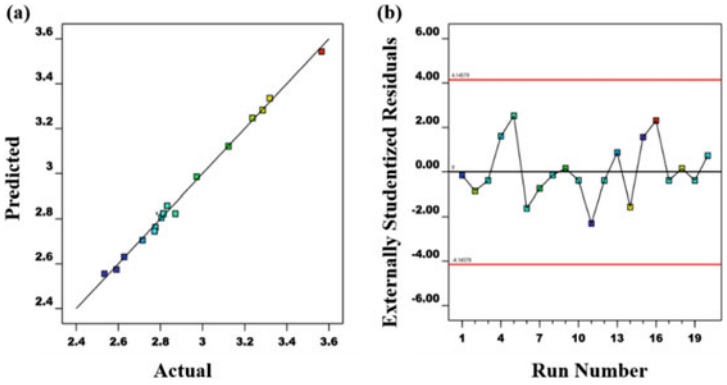


Fig. 2 Surface roughness **a** predicted versus actual **b** residual versus run number

3 Results and Discussion

Figure 2a indicates actual values that are very close to the forecast value, and Fig. 2b indicates the residuals against the run number; the residual experiment for corresponding run number is within upper and lower limits. This proves that the developed model was adequate for the current analysis. Table 4 shows ANOVA analysis of R_a for machined surface.

The obtained R^2 value 0.9954 is very closer to the one and adjacent R^2 value 0.9913 is well agreed with R^2. Then, the model is said to be suitable for further analysis of the interaction effects. A regression model of given experimentation for surface roughness (1) is given below,

$$\begin{aligned}\text{Surface roughness} = {} & +4.974500 - 020126H_P - 0.005726T_R + 0.140123SO_D \\ & - 6.50000E - 06H_P \times T_R - 0.000535H_P \times SO_D + 0.000410T_S \\ & \times SO_D + 0.000053H_p^2 + 0.000020T_R^2 - 0.021318SO_D^2 \end{aligned} \quad (1)$$

3.1 Machining Characteristics of Glass–flax Composites

4 Effect of Surface Roughness by Water Pressure

An influence of H_P on R_a was found to be very high by analyzing an ANOVA Table 4; the H_P contribution 77.94% on R_a was higher compared with T_R and SO_D. The effect of H_P on the R_a of glass–flax stacked laminate is shown in Fig. 3a. This figure shows that the R_a reduces with an increase in H_P. At high pressure, burr formation

Table 4 Ra analysis by ANOVA

Source	Sum of squares	df	Mean square	*F*-value	*p*-value	
Model	1.35	9	0.1499	241.9	< 0.0001	Significant
H_P	1.06	1	1.06	1712.3	< 0.0001	
T_R	0.1241	1	0.1241	200.32	< 0.0001	
SO_D	0.0320	1	0.0320	51.71	< 0.0001	
$H_P * T_R$	0.0021	1	0.0021	3.41	0.0946	
$H_P * SO_D$	0.0057	1	0.0057	9.24	0.0125	
$T_R * SO_D$	0.0034	1	0.0034	5.43	0.0421	
H_P^2	0.0488	1	0.0488	78.74	< 0.0001	
T_R^2	0.0071	1	0.0071	11.40	0.0070	
SO_D^2	0.0012	1	0.0012	2.02	0.1859	
Residual	0.0062	10	0.0007			
Cor total	1.36	19		R^2	0.9954	
				Adjusted R^2	0.9913	
				Predicted R^2	0.9630	
				Adequate precision	56.1031	

*Interaction (multiplication) of two variables

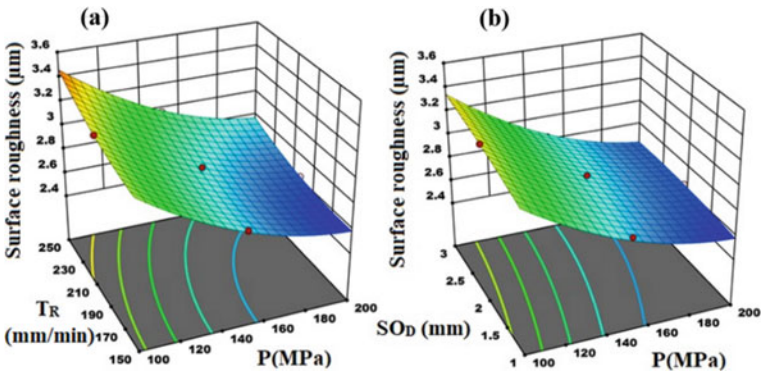


Fig. 3 Interaction between **a** pressure and traverse rate **b** pressure and SO_D (mm)

was minimum compared to the low-pressure waterjet beam, and this may be due to high pressure resulting in high waterjet energy that removed the material from

laminate, therefore an even material removal obtained [13]. The reduction of surface roughness by 19.42% at a pressure of 200 MPa is compared to 100 MPa.

Effect of Surface Roughness by Nozzle Traverse Rate

T_R was identified as a second influencing input process variable which affects the R_a. It contributes about 9.12% of the total effect of the parameters. Variation of the T_R effect on surface roughness of glass and flax multi-stacked composite is shown in Fig. 3a. Surface quality decreases with an increase in nozzle T_R on glass and flax layered composite [19]. This is attributed due to the uneven cutting with varied waterjet energy in the traverse direction. There was an increase in R_a of about 8.12% when increased the T_R from 150 to 250 mm/min.

Effect of Surface Roughness by Standoff Distance

The SO_D shows less influence on surface roughness by only 2.35%. The surface roughness of multi-stacked glass and flax fiber laminate is affected by the varying SO_D as shown in Fig. 3b. It is observed that R_a increases with every step increment of SO_D on glass and flax multilayered composite. This could be due to the waterjet energy varying with distance that possibly increases air drag, therefore loss of waterjet energy. So, the surface quality of the machined surface reduces with an increase in the standoff distance for glass and flax multilayered composite. In addition, the reduction in localized material erosion results in non-uniform cutting over the surface zone [20]. Surface roughness increases with 13.57% with an expansion of SO_D from 1 to 3 mm.

SEM Characterization

At high pressure, minimum burr was formed at the edge of the composite when compared to the low-pressure waterjet beam. This may be due to high waterjet energy which results in proper erosion; therefore, an even material removal occurred as shown in Fig. 4a. So, it is seen that the least surface roughness was observed at high pressure. At low pressure, the more burr formation was observed at the top and bottom fiber layers. This burr formation is due to the improper erosion arising from insufficient energy of water beam by the low pressure. As a result, it causes many uneven surfaces, and hence, high surface roughness was obtained at low pressure as indicated in Fig. 4b.

5 Conclusions

A study on AWJM of multi-stacked glass and flax layered composite has been presented in this article. Three AWJM input variable process parameters specifically H_P, T_R, and SO_D were considered. From the results, the following finding is observed.

1. Hydraulic pressure (H_P) was identified as the most significant parameter affecting the quality of the surface (77.94%).

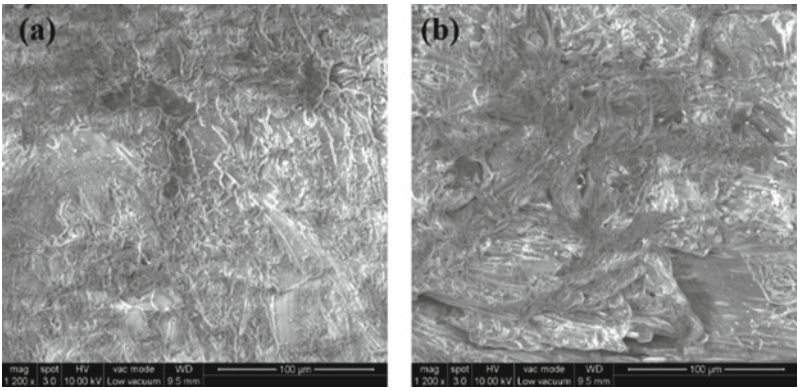


Fig. 4 SEM images showing machined surface **a** at high pressure **b** at low pressure

2. Surface roughness was found directly proportional to SO_D, traverse speed and indirectly proportional to water pressure.
3. Surface machined by AWJ with high pressure has produced superior quality than the surface machined by low pressure.
4. High-pressure fluid particles can easily machine the material due to its high kinetic energy which results in a smoother surface.
5. Authors planned to study the kerf dimension and material remover rate of this composite in future.

References

1. Ramraji K, Rajkumar K, Sabarinathan P (2018) Tailoring of tensile and dynamic thermo mechanical properties of interleaved chemical-treated fi-ne almond shell particulate flax fiber stacked vinyl ester polymeric composites. Proc Inst Mech Eng Part L J Mater Design Appl 233(11):2311–2322
2. Praveen Kumar A, Kumarasamy GS, Nikhil N (2015) Analysis of carbon fiber reinforced polymer composite hip prosthesis based on static and dynamic loading. Int J Appl Eng Res 10(85):574–579
3. Rajkumar K, Ramraji K, Hariprakash VP, Gnanavelbabu A (2019) Comparison study of mechanical and dynamic vibration properties of hole defect introduced in hybrid polymer composite. Mater Today Proc. https://doi.org/10.1016/j.matpr.2019.10.078
4. Praveen Kumar A, Nalla Mohamed M, Kurien Philips K, Ashwin J (2016) Development of novel natural composites with fly ash reinforcements and investigation of their tensile properties. Appl Mech Mater 852:55–60
5. Dhanawade A, Kumar S (2017) Experimental study of delamination and kerf geometry of carbon epoxy composite machined by abrasive water jet. J Compos Mater 51(24):3373–3390
6. Kumar D, Gururaja S (2019) Abrasive waterjet machining of Ti/CFRP/Ti laminate and multi-objective optimization of the process parameters using response surface methodology. J Comp Mater
7. Wang J, Kuriyagawa T, Huang CZ (2003) An experimental study to enhance the cutting performance in abrasive waterjet machining. Mach Sci Technol 7(2):191–207

8. Pahuja R, Ramulu M, Hashish M (2019) Surface quality and kerf width prediction in abrasive water jet machining of metal-composite stacks. Compos B Eng 175:107134
9. Hashish M (1991) Advances in composite machining with abrasive-waterjets. Process Manuf Com Mater 49(27):93–111
10. Babu MN, Muthukrishnan N (2014) Investigation on surface roughness in abrasive water-jet machining by the response surface method Mater Manuf Process 29:1422–1428
11. Prabu VA, Kumaran ST, Uthayakumar M (2017) Performance evaluation of abrasive water jet machining on banana fiber reinforced polyester composite. J Nat Fibers 14(3):450–457
12. Selvam R, Karunamoorthy L, Arunkumar N (2017) Investigation on perfor-mance of abrasive water jet in machining hybrid composites. Mater Manuf Process 32(6):700–706
13. Gnanavelbabu A, Rajkumar K, Saravanan P (2018) Investigation on the cutting quality characteristics of abrasive water jet machining of AA6061-B4C-hBN hybrid metal matrix composites. Mater Manuf Process 33(12):1313–1323
14. Kumar A, Singh H (2018) Kumar Study the parametric effect of abrasive wa-ter jet machining on surface roughness of Inconel 718 using RSM-BBD techniques. Mater Manuf Processes 33(13):1483–1490
15. Alberdi A, Suarez A, Artaza T (2013) Composite cutting with abrasive water jet. Proc Eng 63:421–429
16. Azmir MA, Ahsan AK (2008) Investigation on glass/epoxy composite sur-faces machined by abrasive water jet machining. J Mater Process Technol 198(1–3):122–128
17. Kalirasu S, Rajini N, Winowlin Jappes JT, Uthayakumar M, Rajesh S (2015) Mechanical and machining performance of glass and coconut sheath fibre polyester composites using AWJM. J Reinf Plast Compos 34(7):564–580
18. Singh J, Kumar M, Kumar S, Mohapatra SK (2017) Properties of glass-fiber hybrid composites: a review. Polym-Plast Technol Eng 56(5):455–469
19. Rao S, Sethi A, Das AK, Mandal N, Kiran P, Ghosh R, Dixit AR, Man-dal A (2017) Fiber laser cutting of CFRP composites and process optimization through response surface methodology. Mater Manuf Process 32(14):1612–1621
20. Dhanawade A, Kumar P, Kumar S (2020) Experimental study on abrasive water jet machining of carbon epoxy composite. Adv Mater Process Technol 6(1):40–53

Experimental Study on Machining of Aluminium Silicon Alloy (LM6) in Wire Electrical Discharge Machining



S. Ram Prakash, G. Selvakumar, and S. Vijayan

Abstract In this work, the machinability aspects of aluminium (LM6) alloy in wire electrical discharge machining were discussed. Owing to the poor machinability of LM6 alloy, WEDM is selected as the potential candidate to process it with utmost surface quality. The main intent of the work is to investigate the impact of the WEDM process parameters for the performance measures material removal rate and surface roughness. Further, resolidification layer of the WEDMed surface has been studied. Taguchi technique has been adopted to conduct the experiments. SEM micrographs revealed the surface integrity of the machined region. The pulse-on time and peak current were identified as the major parameter on deciding the material removal rate and surface roughness. LM6 has copious applications in marine, aircraft and automobile industries owing to its low cost, lightweight and excellent corrosion resistance.

Keywords LM6 aluminium alloy · Taguchi's methodology · Material removal rate · Surface roughness

1 Introduction

Aluminium silicon (LM6) alloys are the predominantly used cast alloys preferred in foundry owing to its high strength-to-weight ratio, superior castability, thermal conductivity, weldability and excellent wear resistance. Further, it is one of the outstanding materials possessing excellent ductility and corrosion resistance under any environmental conditions [1]. It paves the way to extend its use on marine and aerospace applications. It is the best suitable material to be used in marine decks, automobiles manifold, pipe fittings, motor housings, switches, doors and panels, and paint industry. Owing to its superior castability, it can be casted in any shapes based on the requirements [2]. Though it has been used in numerous applications, it has its own disadvantages like low elastic, low strength at high temperatures and difficulty in

S. Ram Prakash · G. Selvakumar (✉) · S. Vijayan
Department of Mechanical Engineering, Sri Sivasubramaniya Nadar College of Engineering, Chennai 603110, India
e-mail: selvakumaratju@gmail.com

© Springer Nature Singapore Pte Ltd. 2020

A. Praveen Kumar et al. (eds.), *Advances in Lightweight Materials and Structures*,
Springer Proceedings in Materials 8, https://doi.org/10.1007/978-981-15-7827-4_59

machining [3]. Wire electrical discharge machining (WEDM) is a renowned method for generating any sort of intricate shape in both 2D and 3D with utmost surface finish. Here, the material removal mechanism is a thermoelectric process where the metal melts and vapourize during sparking phenomenon. The metal erodes due to the occurrence of subsequent localized sparks between the sample and the wire under the influence of dielectric medium [4]. The microchips formed during the sparking were washed by the dielectric media which also acted as coolant during the machining process.

The unique characteristic of WEDM is that it can process any material regardless of its hardness but the limitation is that it should possess electrical resistivity less than 100 Ωcm. It is predominantly used for making intricate components in automobile, aerospace, tool and dye industries. It is indeed necessary to choose the optimal parameters during machining to cut down the production cost and downtime. The cutting rate and the roughness value decide the production efficiency of the process. The surface quality and the cutting rate rely on the workpiece material, and the WEDM process parameters opted during the machining process. Mouralova et al. [5] studied the surface and subsurface defects of the creusabro steel during WEDM machining. The process parameters of WEDM had a significant impact on the subsurface defects. The dimensional aspect of the cut profile majorly relies on the kerf width of the cut.

Mahapatra et al. [6] have discussed the significance of adopting suitable machining parameters in WEDM to evaluate the performances like material removal rate (MRR), surface roughness (Ra) and kerf width. The optimal parameter setting was identified for improving the MRR and minimizing the Ra and kerf width. Mathematical models were formulated by employing nonlinear regression technique. The crater form and its size during electrical discharges were investigated by Weingartner et al. [7]. An electrothermal model has been developed to inspect the crater variations. The experiment results were verified with the simulation result. Mohammadi et al. [8] explained the influence of WEDM parameters on machining cylindrical component. Using regression method, a mathematical model was computed to assess the roughness of the WEDMed component.

Chen et al. [9] developed a modified wire electrode by changing the wire surface microstructure to improve the WEDM performance. In comparison with brass and zinc-coated brass wire electrode, the modified wire shows better prospects in all dimensions like increased surface quality and machining rate. It further enhances the surface characteristics and curtails the formation of resolidification layer and surface crack. Zhang et al. [10] bid an attempt with the assistance of magnetic field and ultrasonic vibration to indeed improve the machining characteristics. The deployment of the hybrid technique detailed about the discharge and the surface topography of the cut surface. Further, the impact of process parameters is on the MRR, Ra and surface crack density. The present work investigates the WEDM machining of LM6 alloy for the responses material removal rate and surface roughness. The impact of WEDM parameters has been analysed using Taguchi method. The resolidification layer of the WEDMed surface has been examined using SEM micrographs.

2 Materials and Methods

LM6 aluminium alloy was selected as the workpiece, prepared by using stir casting process. The fabricated specimen was cut into proper form with the thickness of about 5 mm for investigating the effect of WEDM process parameters. The chemical composition of the LM6 used for this experimentation is tested and listed in Table 1. The experiment was performed in Ratnaparki CNC WEDM machine, model: smartcut 2530. Brass wire was used as the wire electrode material (diameter: 250 μm), and deionized water was chosen as dielectric medium. The experiments were carried out based on the Taguchi's L9 orthogonal array. Trail experiments were conducted to finalize the limits of the controllable process parameters considered for this experiment. Pulse-on time (Ton), pulse-off time (Toff), peak current (I) and wire feed (WF) were chosen as the variable parameters for this study.

The effect of process parameters to be studied and its levels were presented in Table 2. The kerf width of the cut region was measured by using imaging analysis. The image captured in optical microscope was imported to ImageJ software to measure the kerf width. The parameters which were considered as constant during the machining process were wire tension: 20 N, gap voltage: 32 V and water pressure: 9 bar.

MRR is computed by the below expression.

$$\text{MRR}\left(\text{mm}^3/\text{min}\right) = \text{cutting speed (mm/min)} \times \text{kerf} \times \text{width (mm)} \times \text{thickness (mm)} \quad (1)$$

Mitutoyo surftest, model: SJ 210 is employed to quantify the average surface roughness value of the cut region. The cut-off length was set as 0.08 mm. The roughness values have been taken at three different stages and its average value has been considered. During Taguchi's analysis, 'larger is better' is set as problem condition for evaluating MRR and 'smaller is better' is assigned as condition for estimating the

Table 1 Chemical composition of the selected aluminium alloy (LM6)

Elements	Si	Mn	Cu	Fe	Mg	Zn	Pb	Sn	Ni	Ti	Al
Percentage (%)	10.68	0.05	0.03	0.41	0.08	0.01	0.01	0.1	0.01	0.05	Remaining

Table 2 Chosen parameters and its levels

S. No.	Parameters/Levels	1	2	3	Units
1	Ton	0.1	0.2	0.3	(μs)
2	Toff	35	40	45	(μs)
3	I	1	3	5	(A)
4	WF	2	3	4	(m/min)

surface roughness. ANOVA tests were conducted to evaluate the impact of WEDM parameters for MRR and Ra.

3 Results and Discussion

The experiments were performed by following Taguchi's L9 orthogonal array, and its results were presented in Table 3. From Fig. 1 and Table 4, it is perceived that the MRR is dramatically influenced by the pulse-on time. Followed by pulse-on time, peak current is considered as the most influential factor that decides the MRR. The others factors have shown mere influence on the MRR on comparison with pulse-on time and peak current. Figure 1 represents that the MRR shows better results at Ton (0.3), Toff (35), I (5) and WF (3). In Fig. 1, similar trends were observed for both pulse-on time and current. The material removal in the WEDM is based on the occurrence of spark discharges. The spark discharge erodes the metal by melting and vapourization in both workpiece and wire. The discharge energy produced is maximum at the highest level of pulse-on time and peak current that in turn creates large craters, causing an enormous removal of material.

From Fig. 2 and Table 4, it is observed that the pulse-on time is indeed the predominant parameter on determining the surface quality of the machined region. Pulse current and pulse-off time are observed as the subsequent dominating parameter that defines the quality of the surface. The magnitude of spark discharge energy depends on the pulse duration. Further, the discharge energy plays a key role on the crater size formation. The surge in pulse duration and current produces craters at larger sizes and forms uneven surfaces. Therefore, maintaining at lower pulse-on time and peak current produces tremendous surface quality [11].

The surface quality of the cut region is based on the manifestation of the spark discharges, its frequency, dimension and morphology. Therefore, it is vital to investigate the surface morphology of the machined region to generate parts with required

Table 3 Experimental results

S. No.	Ton (μs)	Toff (μs)	I (A)	Wire feed (m/min)	MRR (mm^3/min)	Ra (μm)
1	0.1	35	1	2	0.9598	1.47
2	0.1	40	3	3	1.1569	1.56
3	0.1	45	5	4	1.0721	1.40
4	0.2	35	3	4	1.6756	1.64
5	0.2	40	5	2	1.5460	1.71
6	0.2	45	1	3	1.3831	1.32
7	0.3	35	5	3	2.6804	2.11
8	0.3	40	1	4	2.0261	1.56
9	0.3	45	3	2	2.1569	1.77

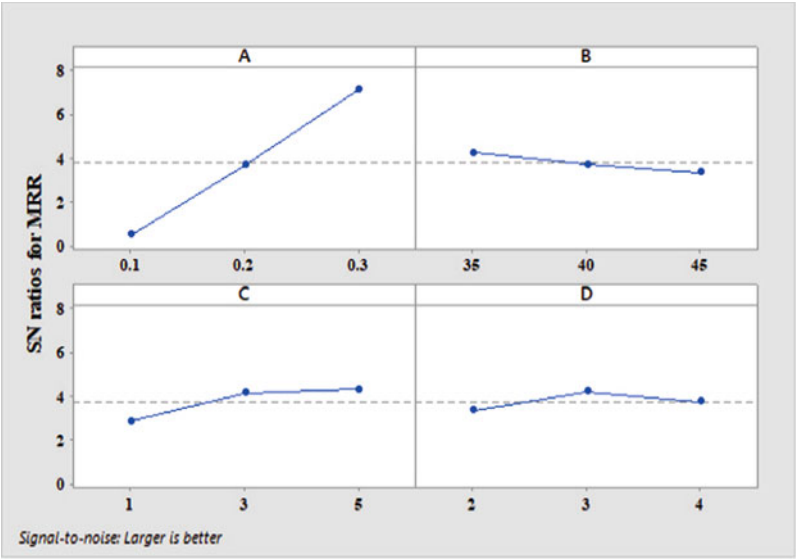


Fig. 1 WEDM parameter effects on MRR

Table 4 ANOVA result for the experiment values

Factor	Degress of freedom	MRR		Ra	
		Adj SS	Percentage of contribution	Adj SS	Percentage of contribution
Ton	1	2.2504	86.81	0.1676	38.08
Toff	1	0.08255	3.18	0.0889	20.19
I	1	0.1440	5.56	0.1289	29.28
W	1	0.00205	0.07	0.0196	4.45
Error	4	0.11314		0.0356	
Total	8	2.59221		0.4401	

surface quality. The surface morphology of the machined region was studied with the help of scanning electron microscope as shown in Fig. 3. From the figure, it is observed that some sites of the machined regions are encompassed with recast layer. It is evident that there are many molten droplets that are settled throughout the surface.

The material melts and vapourize during sparking were suddenly cooled by the dielectric media, and it accumulates on the surface of the machined zone. The foamy pattern formed on the surfaces is due to the entrapment of gas bubbles during machining. Deep holes, microcracks, resolidified molten globules and craters are clearly visible from the SEM micrographs. The strength and properties of the work-piece may diminish owing to the presence of these microcracks, recast layer and

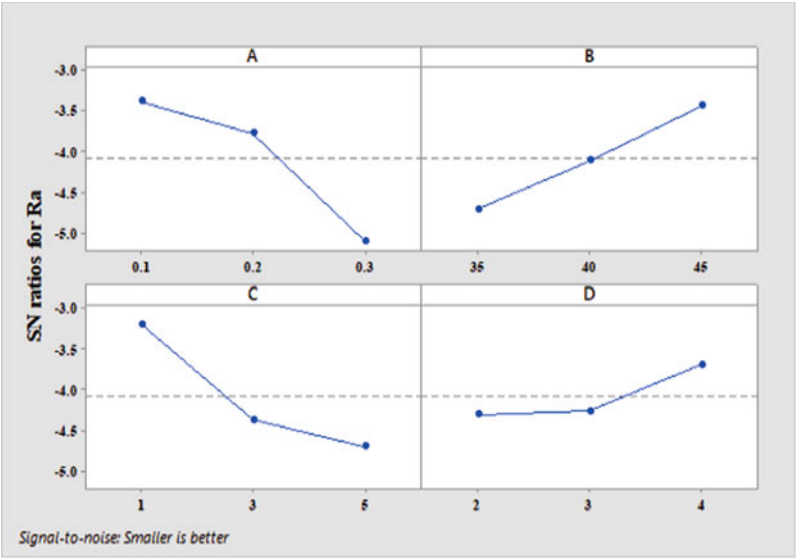


Fig. 2 WEDM parameter effects on Ra

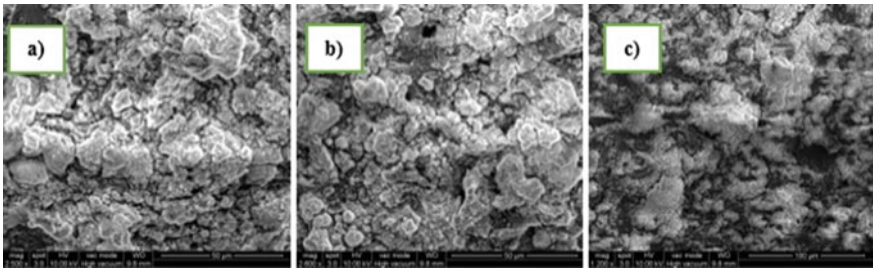


Fig. 3 Surface morphology of the WEDM machined region (**a**–**c**)

holes. Appropriate selection of process parameter and flushing will produce a better surface quality.

4 Conclusion

In this work, machining of LM6 in WEDM was successfully conducted. The impact of the WEDM process parameters for the performance measures, MRR and Ra on machining LM6 were discussed.

- Pulse-on time was observed as the prime factors on deciding both MRR and Ra.

- Besides, the peak current was the next dominant factor that greatly influences the discharge energy and controls the size of the craters.
- Pulse-off time and wire feed have moderate effect on the above said responses.
- The SEM micrographs of the machined detailed the presence of microcracks, recast layer and voids.
- In future, the effect of wire material and dielectric medium on the surface characteristics of the LM6 in WEDM will be investigated

Acknowledgements The authors would like to thank DST-SERB, India [Grant No: ECR/2016/001517] for their support extended for this project.

References

1. Jayaraman M, Sivasubramanian R, Balasubramanian V (2009) Effect of process parameters on tensile strength of friction stir welded cast LM6 aluminium alloy joints. J Mater Process Technol 25(5):655–664
2. Chelladurai SJS, Arthanari R, Nithyanandam N, Rajendran K, Radhakrishnan KK (2018) Investigation of mechanical properties and dry sliding wear behaviour of squeeze cast LM6 aluminium alloy reinforced with copper coated short steel fibers. Trans Indian Instit Metals 71(4):813–822
3. https://www.mrt-castings.co.uk/aluminium-diecasting-lm6.html
4. Singh MA, Das K, Sarma DK (2018) Thermal simulation of machining of alumina with wire electrical discharge machining process using assisting electrode. J Mech Sci Technol 32:333–343
5. Mouralova K, Prokes T, Benes L, Sliwkova P (2020) Analysis of subsurface defects occurrence in abrasion resistant Creusabro steel after WEDM including the study of morphology and surface topography. Mach Sci Technol 24:274–290
6. Mahapatra S, Patnaik A (2006) Parametric optimization of wire electrical discharge machining (WEDM) process using Taguchi method. J Brazilian Soc Mech Sci Eng 28:422–429
7. Weingartner E, Wegener K, Kuster F (2012) Wire electrical discharge machining applied to high-speed rotating workpieces. J Mater Process Technol 212:1298–1304
8. Aminollah M, Alireza FT, Ehsan E, Davoud K (2008) A new approach to surface roughness and roundness improvement in wire electrical discharge turning based on statistical analyses. Int J Adv Manuf Technol 39:64–73
9. Chen Z, Zhang Y, Zhang G, Li W (201) Investigation on a novel surface microstructure wire electrode for improving machining efficiency and surface quality in WEDM. Int J Adv Manuf Technol 102:2409–2421
10. Zhang Z, Hao H, Ming W, Zhong X, Yu H, Zhang G (2016) Study on machining characteristics of WEDM with ultrasonic vibration and magnetic field assisted techniques. J Mater Process Technol 234:342–352
11. Selvakumar G, Thiruppathi Kuttalingam KG, Ram Prakash S (2018) Investigation on machining and surface characteristics of AA5083 for cryogenic applications by adopting trim cut in WEDM. J Brazilian Soc Mech Sci Eng 40:267

Effect of Solid Lubricant in Dry Machining on Al-B_4C Composite

K. M. Nambiraj, K. Rajkumar, M. Rajesh, and A. Gnanavelbabu

Abstract Machining of metal matrix composites is extremely very hard because of its heterogeneity and hardness. However, it is possible through improving its inherent active lubrication. This is one way to reduce cutting forces and tool wear during machining. This work is to evaluate the effect of solid lubricant, hexagonal boron nitride (hBN), on dry machining of aluminum–boron carbide (B_4C) composite. Machining of fabricated composites is done with varying amounts of hBN particle from 5 to 15%. The machining performance is estimated by the measuring magnitude of cutting forces and tool wear with respect to different depth of cuts, feed rates, and cutting speeds. Mechanical property like hardness decreases with the increase in the amount of hBN particle. Polycrystalline diamond (PCD) insert was used to machine the work. Machining parameters like cutting speed reduce the cutting force and tool wear. The spatial presence of boron carbide and hBN particles in the microstructure is affecting machining performance. The presence of hBN particles in the composite spatial microstructure reduces tool flank wear. The reason contributed to the fact a shearing of hBN particles. These particles reduce shear stress between primary cutting zone and tool causing a low magnitude of surface roughness on the work.

Keywords hBN · Cutting force · Tool wear · Machining · Metal matrix

1 Introduction

Emerging industrial fields demanding engineering materials, particularly composite in the automobile, aerospace, marine, military, sports, and other structural applications, satisfy the design flexibility [1, 2]. One among aluminum alloys has workability, high functional provision, better wear resistance, high strength, and lightweight [3, 4]. Although Al composite materials are fabricated near net shape, they require a

K. M. Nambiraj · K. Rajkumar (✉) · M. Rajesh
Department of Mechanical Engineering, SSN College of Engineering, Chennai 603110, India
e-mail: rajkumark@ssn.edu.in

A. Gnanavelbabu
Department of Industrial Engineering, Anna University, Chennai 600025, India

© Springer Nature Singapore Pte Ltd. 2020

A. Praveen Kumar et al. (eds.), *Advances in Lightweight Materials and Structures*,
Springer Proceedings in Materials 8, https://doi.org/10.1007/978-981-15-7827-4_60

machining process to a specific geometry and surface finish. However, machining of composite is rather difficult due to the inclusion of hard particles in their microstructure. Composite machining with those characteristics produces rapid tool wear and poor surface finish [5, 6]. To avoid, a small amount of solid lubricant is recommended to include in the composite microstructure that produces an acceptable level of surface finish and ease of machining, and that admits economic benefits to the manufacturing industry [7, 8].

Generally, aluminum composites are produced with reinforcement in the form of particles, whiskers, and fibers which are reducing poor high-temperature properties [9]. Mostly, aluminum composites are synthesized by the addition of Al_2O_3, B_4C, SiC, and other ceramic particles to enhance their mechanical and tribological properties [10]. The presence of these particles in microstructure increases the friction characteristics of the particulate composite. It can be alleviated by the addition of hBN solid lubrication in particulate composite, therefore resulting in reduced cutting force and tool wear. This is due to the formation of tribo-layer in the machining zone. However, formation of tribo-layer is depending on the spatial distribution of hBN and volume fraction [11].

Through the addition of solid lubricant in microstructure, another factor tool property determines tool wear during machining. A selection of cutting tool material is to overcome the unusual damage and tool wear. High-speed steel (HSS) and carbide tools are not suitable for the machining of composite materials, due to pronounced high tool wear within a short period of machining. In fact, hard ceramic inclusion abrades on these cutting tools make them not useful in the composite machining industry. PCD and cubic boron nitride (cBN) are an alternate choice for machining of composite materials. These advanced cutting tools provide better surface finish, low cutting force, low tool wear, and increasing the tool life. Moreover, the PCD tool is showing relatively exceptional hardness and high thermal conductivity. Hence, PCD tool is preferred than the other cutting tools for machining of hard particulate composite [12, 13].

Machining of the composite is related to multiple factors of type of reinforcement, size, volume fraction, degree of distribution, cutting tool property, and machining parameters. Rajkumar et al. [12] investigated the machining experiment on aluminum alloy composite containing B_4C. It is reported that particle reinforcement increases cutting force when an increase in B_4C volume at all machining conditions. Moreover, the cutting force increases with an increase in depth of cut but reduces with an increase in cutting speed. Rajesh et al. [13] studied the effect of solid lubricant on metal matrix composite. They observed solid lubricant particles produce low shear strength layers between work and cutting tool surface which reducing cutting force.

Basavarajappa et al. [14] observed that the machining parameters are influencing on the machinability of metal matrix composites. It is concluded that surface roughness and feed force are mainly influenced by cutting speed and feed rate. Rajmohan et al. [15] investigated the effect of machining parameters on the drilling experiment of hybrid aluminum–matrix composites. It is seen that the surface roughness is greatly worsened at high tool feed rate due to pullout hard particles abrading the fresh cutting surface. Kilickap et al. [16] conducted a turning experiment on Al-5%SiCp

with coated and uncoated cutting tools. It is reported that cutting forces are majorly affected by cutting speed but surface roughness depends only on the feed rate. The solid lubricant containing coating tool decreases work–tool interface friction and temperature.

The above literature dealt with various machining parameters, tool condition, and composite characteristics in the machining of composites. There is a scope for changing material characteristics to the machining environment by selecting suitable boron family hard and soft particles such as B_4C and hBN. The designed composite system offers high strength and ease of machining. The purpose of this study is to obtain the effect of solid lubricant in aluminum–matrix composites on cutting force, surface finish, and tool wear while machining with PCD tool.

2 Materials and Methods

2.1 Composite Synthesis

The starting material for the preparation of a self-lubricating composite was Al6061 alloy as a base matrix, ceramic particle B_4C and solid lubricant hBN particles were reinforcement particles. The grain size of B_4C and hBN reinforcement particles were 20 and 10 μm, respectively. Three types of composites were made according to hBN concentration as given in Table 1. The fabrication of composite starts from aluminum melting in an electric furnace at a temperature of 750 °C for 90 min under the inert gas atmosphere. This step ensures that no oxygen evolved during melting, prior to feeding reinforcement particles. They were preheated to 300 °C in order to increase wettability between matrix and reinforcement. The B_4C and hBN particles were ball milled for 30 min in order to achieve a complete mixing. The planetary ball mill having tungsten carbide ball was rotated at 300 rpm with ball to powder ratio of 20:1.

Three steps addition process was used to mix the hBN and B_4C particles in molten liquid. In the first step, the total volume % of B_4C and hBN mixed particles were equally divided into three parts. Then, the first part of mixed particles was fed into the molten slurry followed by the stirring process. The same procedure was followed to the other two parts for mixing the reinforcement particles. This step improves the uniform distribution of particles and also eliminating agglomeration in the matrix.

Table 1 Concentration of Al-B_4C-hBN composite by volume %

Type	Al6061	B_4C	hBN
AMC1	90	5	5
AMC2	85	5	10
AMC3	80	5	15

2.2 Parameters and Machining of Composites

Aluminum–matrix composite was used to machine having a dimension of ϕ22*110 mm. Machining is done in a precision lathe—medium-duty machine under various cutting conditions. The aluminum composite was machined with SCLCR 1212 F09T3 tool holder having PCD insert with ISO designation CNMA 120,404. Machining experimentation was done with different cutting speeds of 20 and 80 m/min, depth of cut (DOC) of 0.2 and 0.6 mm, and tool feed rate of 0.1 and 0.4 mm/rev. All the machining experimentation was performed in dry conditions, and chip breakers were not employed. Prior to cutting force observation, three trail cuts were made with 0.1 mm DOC to remove the material from the top surface layer which contains cast defects to eliminate the errors. Lathe tool dynamometer was used to estimate the cutting force with a digital display unit. SEM image analyses were also done for assessing the tool wear mechanism.

3 Results and Discussion

3.1 Investigation on Composite

The mechanical strength measurement like hardness was made to correlate it with the effect of hexagonal BN particles inclusion in the matrix. Fabricated composites were tested by using a Brinell hardness tester machine with a steel ball indenter diameter of 10 mm. The surface was indented with a load of 500 kgf on the work material. Hardness was taken three times in different places, and an average hardness value is shown in Table 2. It clearly shows that the inclusion of hBN particle reduces the hardness.

The microstructural investigation on aluminum composites was made to confirm the uniform distribution of reinforcement particles using scanning electron microscope. Microstructure of fabricated composite is shown in Fig. 1. It is seen that there is no agglomeration of particles, voids, and microcracks found in the microstructure. This figure also witnesses the relative size of B_4C and solid lubricant hBN particles in the microstructure.

Table 2 Concentration of Al-B_4C-hBN composite by volume %

Composition	Brinell hardness (BHN)
AMC1	66.50
AMC2	64.89
AMC3	61.79

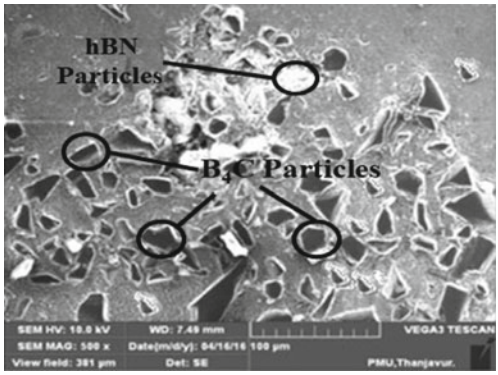


Fig. 1 Al- B_4C-hBN composite microstructure

3.2 Effect of Solid Lubricant on Cutting Force

A cutting force prediction of composite is quite difficult for understanding due to the reinforcement particle complexity by its distribution and size effect. The estimation of cutting force done through experimental method makes an understanding of the machining dynamics. This is simply done by varying the cutting parameters of speed, DOC, and feed rate, as to report an average by measuring cutting force three times for each condition. While measuring there is some fluctuation in cutting force which may be occurred due to hard abrasive particles interruption during aluminum composite machining. The cutting forces measured at various DOCs are shown in Fig. 2a, b. It is observed that with an increase in the hBN volume percentage cutting forces were reduced, as seen from Fig. 2a. The hard ceramic particles in the matrix increase the cutting force during machining. But a cutting tool when an encounter with soft hBN particle distribution in microstructure reduces the cutting force considerably. For all the machining conditions, cutting forces reduced by increasing the hBN volume fraction from 5 to 15%.

Cutting speed is the primary influencing factor for cutting force than other machining parameters. Cutting forces are reduced by increasing the cutting speed. This may be due to the increased machining temperature in the cutting zone. The generating heat is majorly taken away by the formed chip, and remaining heat may distribute to the work material. This results in thermal softening of the surface layer of work material. Another way helps in the easier formation of chip by reducing cutting forces. The magnitude of work material cutting force depends on feed rate and depth of cut also when machining of material. It is evident that an increase in feed rate at given cutting speed and depth of cut results in increased cutting force. This could be due to the high material removal rate within a short period of time. A similar trend was observed from Fig. 2b for the depth of cut of 0.6 mm. By comparing Fig. 2a and b, the effect of depth of cut on cutting force is determined. On increasing the depth of cut, the cutting forces are increased at all machining conditions. While increasing the depth of cut, the number of layers to be cut is very high, followed to increase very high cutting force.

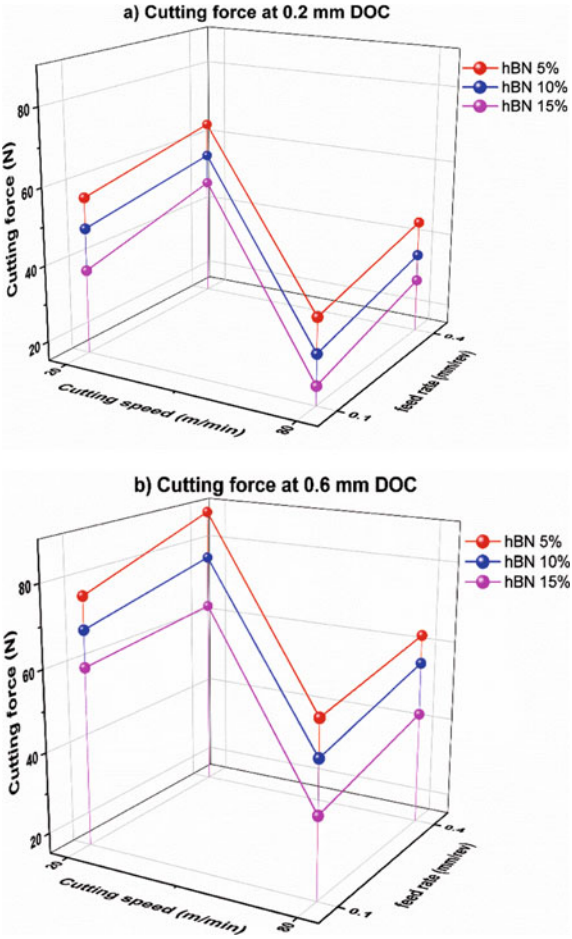


Fig. 2 Cutting forces hBN fraction **a** DOC, 0.2 mm and **b** DOC, 0.6 mm

3.3 Effect of Solid Lubricant on Surface Roughness

Surface roughness is one of the indicators for the quality of machining. This is related to the machining parameters such as speed, tool feed, and depth of cut. Surface roughness was estimated by using surface roughness tester Mitutoyo model SJ-210, after every cycle of machining. Figure 3a, b shows surface roughness value at a depth of cuts of 0.2 and 0.6 mm. Generally, the surface roughness of aluminum composite machining is mainly related to the microstructure. The mechanism behind the surface roughness is the combined effect of cutting tool material, geometry, shear forming, and plastic deformation.

It is seen that surface finish was reducing while there is an increase in the cutting speed from 20 to 80 m/min, as shown in Fig. 3a. As shown, surface roughness reduces

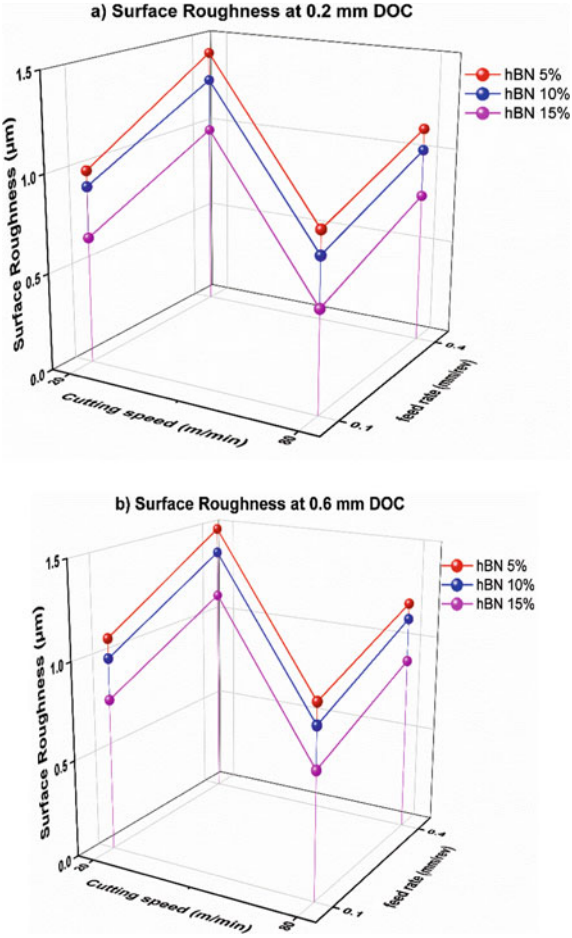


Fig. 3 Surface roughness measured at **a** 0.2 mm D.O.C. and **b** 0.6 m D.O.C

with an increase in hBN volume percentage from 5 to 15%. At low hBN concentration, inclusion in composite abrades the work–tool interface that was evident. It produces the worst surface finish. The random pullout of hard B_4C particle induces scratches and also damages the produced surface. However, the constant release of soft hBN particles from the machining surface eliminates the built-up edge formation, cracks, and adhesion over the tool and helps in improving the surface finish. Normally, dry machining within critical speed is recommended for composite machining which helps in reducing clogging of work with the tool.

It is also noted that poor surface finish may be occurred due to the high tool wear as a result of high cutting speed. Also, it may be with sticking property due to the ductility of work material at high temperatures. Surface roughness seems to increase with feed rate. Affirmatively, it leads to high tool wear by the chemical affinity of work with the tool at high temperature. Figure 3b shows a similar trend of surface

roughness for the 0.6 mm DOC. By comparing Fig. 3a and b, the effect of depth of cut on surface roughness is determined. A small increment in the depth of cut increased the surface roughness. The comparison shows that the depth of cut has minimum influence for obtaining a good surface finish than cutting speed and feed rate.

3.4 Tool Wear

Tool wear is one of the major issues in composite machining owing to hard particle inclusion in the microstructure. The tool subjected to high stress, continuous chip flow, high temperature, and microwelding is the major factor of tool wear involved during dry turning of composites. Tool wear is observed with scanning electron microscope (SEM). For every cutting condition, a fresh tool is taken for machining to observe the tool wear. Tool wear observed in the various depth of cuts is shown in Fig. 4a, b. Abrasive and adhesive mechanisms are involved in tool wear. Abrasive wear occurred on tool flank face because it has relative contact with the ceramic particles containing machining surface. Abrasive wear increases the cutting temperature due to the random hard particles pulled out from the work material that abrades over the tool during machining. Adhesive wear mechanism is involved in tool rake surface by transferring work material during plastic deformation. Generally, composite machining has diffusion mechanism too, but it was insignificant with the use of high hard PCD cutting tools.

From Fig. 4a, it is observed that the tool wear increased with increasing the cutting speed and feed rate at 0.2 mm depth of cut. The same trend was observed also in Fig. 4b at 0.6 mm depth of cut. An effect of depth of cut is studied by comparing Fig. 4a, b. It concluded that the depth of cut has a very low influence on cutting tool life. Generally, the hard B_4C particle makes major tool wear at flank and rake faces but it was minimized with the addition of soft hBN particles. The soft hBN particles flow freely between the work–tool interface and help in reducing the coefficient of friction, and lead to lesser cutting temperature. The cutting temperature reduction at machining zone benefits in improved tool life.

4 Conclusions

In this study, the hybrid aluminum composite was fabricated with the addition of 5% B_4C hard particles with a varying volume percentage of soft hBN particles from 5 to 15 vol% by stir casting technique. The aluminum fabricated composite was machined under the dry condition to reveal the effect of reinforcement and cutting conditions on cutting force, tool wear, and surface roughness. The machinability study produces the following outcomes.

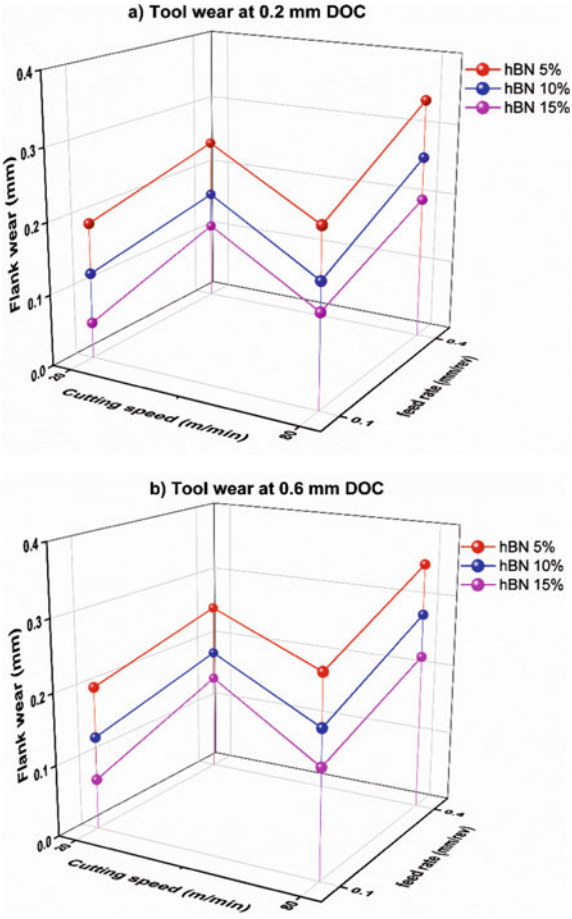


Fig. 4 Tool wear measured at **a** 0.2 mm D.O.C. and **b** 0.6 mm D.O.C

1. Cutting force measurements show some fluctuation due to hard particles present in the microstructure. The soft particles reduce the cutting force by free flow action between work and tool. Cutting forces are reduced by increasing the cutting speed and lowering feed rate and depth of cuts.
2. The presence of soft particles in the microstructure reduces surface roughness. It was further reduced by machining with higher cutting speed.
3. Tool wear was reduced by hBN particles due to the reduction of friction between sliding surfaces.
4. The soft hexagonal BN in microstructure reduced the hardness of aluminum composite and helps in reducing the cutting force, tool wear and improves surface finish.
5. Thus, the soft particles addition in microstructure may be used in future for beneficial reduction of cutting force, tool wear and for increasing the surface finish and tool life.

References

1. Rajkumar K, Gnanavelbabu A, Nambiraj KM (2019) Accelerated testing model prediction of fatigue life of AA5083-H111—AA6061-T6 Friction Stir Weldment. In: Advances in manufacturing processes. Springer, Singapore, pp 573–581
2. Praveen Kumar A, Aadithya S, Dhilepan K, Nikhil N (2016) Influence of nano reinforced particles on the mechanical properties of aluminium hybrid metal matrix composite fabricated by ultrasonic assisted stir casting. ARPN J Eng Appl Sci 11(2):1204–1210; Senapati AK (2018) Investigation on mechanical properties of Al-6061 alloy based MMC. IOP Conf Ser Mater Sci Eng 410(1):012016. IOP Publishing
3. Rajkumar K, Ramraji K, Nambiraj KM, Gnanavelbabu A (2009) A study on wear assessment of AA6061-B4C-Nanographite hybrid composite. Mater Today Proc
4. Jasper J, Praveen Kumar A, Bharanidaran R (2015) Synthesis, characterization and evaluation of properties of aluminium alloy based hybrid composite reinforced with nano SiC and nano graphene. Int J Appl Eng Res 10(50):735–738; Liu J, Cheng K, Ding H, Chen S, Zhao L (2018) Simulation study of the influence of cutting speed and tool–particle interaction location on surface formation mechanism in micromachining SiCp/Al composites. Proc Instit Mech Eng Part C J Mech Eng Sci 232(11):2044–2056
5. Singh PN, Raghukandan K, Rathinasabapathi M, Pai BC (2004) Electric discharge machining of Al–10% SiCP as-cast metal matrix composites. J Mater Process Technol 155:1653–1657
6. Muller F, Monaghan J (2000) Non-conventional machining of particle reinforced metal matrix composite. Int J Mach Tools Manuf 40(9):1351–1366
7. Arun Ramnath R, Thyla PR, Mahendra Kumar N, Aravind S (2018) Optimization of machining parameters of composites using multi-attribute decision-making techniques: a review. J Reinf Plast Compos 37(2):77–89
8. Vijayakumar S, Karunamoorthy L (2013) Wear characterization of aluminium metal matrix composites. Adv Compos Lett 22(4):096369351302200401
9. Tudela I, Cobley AJ, Zhang Y (2019) Tribological performance of novel nickel-based composite coatings with lubricant particles. Friction 7(2):169–180
10. Rajkumar K, Nambiraj KM, Gnanavelbabu A, Sabarinathan P (2018) Machining characteristics evaluation of aluminium composites based on cBN and PCD inserts. Mater Today Proc 5(2):8424–8430
11. Andrewes CJ, Feng HY, Lau WM (2000) Machining of an aluminum/SiC composite using diamond inserts. J Mater Process Technol 102(1–3):25–29
12. Rajkumar K, Charles JMA, Kumar KV, Praveen JJC, Padmanathan A (2013) Mechanical and machining characteristics of Al/B4C metal matrix composites. In: Proceedings of the national conference on emerging trends in mechanical engineering, NCETIME.
13. Rajesh M, Rajkumar K, Gnanavelbabu A, Nambiraj KM (2020) The role of HBN solid lubricant reducing cutting forces of dry machined Al-B_4C composite. In: Advances in unconventional machining and composites. Springer, Singapore, pp 697–705
14. Basavarajappa S, Chandramohan G, Davim JP (2008) Some studies on drilling of hybrid metal matrix composites based on Taguchi techniques. J Mater Process Technol 196(1–3):332–338
15. Rajmohan T, Palanikumar K, Davim JP (2012) Analysis of surface integrity in drilling metal matrix and hybrid metal matrix composites. J Mater Sci Technol 28(8):761–768
16. Kilickap E, Cakır O, Mustafa A, Inan A (2005) Study of tool wear and surface roughness in machining of homogenised SiC-p reinforced aluminium metal matrix composite. J Mater Process Technol 164:862–867

Lightweight Material Joining Techniques

Analysis of Synthetic Fiber-Reinforced LLDPE Based on Melt Flow Index for Rotational Molding



Nikita Gupta and PL. Ramkumar

Abstract Rotational molding is a plastic processing technique wherein a privilege of stress-free plastic product is obtained. LLDPE is widely preferred as it possesses favorable flow property as needed for rotational molding process. But when the criteria of strength are applicable, therein particle reinforcements into LLDPE deliver significant results. Glass fiber and confiber are the additives opted for particulate reinforcement in LLDPE for rotational molding process in the present study. Among the numerous analysis procedure, melt flow index (MFI) test is considered as the primary investigation to verify flowability of raw material. For rotational molding process, MFI value is considered in the range of 3–8 g/10 min. An attempt is made to confirm if the range is satisfied for LLDPE/glass fiber blend and LLDPE/confiber blend by mixing in different ratios. From the experimental results, 22% by weight of glass fiber/LLDPE and 34% by weight of confiber/LLDPE were found to be optimum blend which yields better processability.

Keywords Rotational molding · LLDPE · Melt flow index · Additives

1 Introduction

Polymers have taken over an abundant group of materials accessible till date. This is because of excellent properties of polymers like lightweight, least substance reactivity, effectively pigmented with color dye, and so forth. Among all the plastic-handling techniques, rotational molding process has been demonstrated to assume control over different procedures as it provides numerous advantageous results. Rotational molding is a plastic-handling technique that can deliver product from easy to complex geometries. The primary advantage of this process is that the mold needed is of low cost and negligible pressure is applied during processing of plastic which makes rotomolded product stress-free. It can likewise create complex shapes and can accord products with expansive scope of size and shape [1–3]. The use of this

N. Gupta · PL. Ramkumar (✉)
Mechanical Engineering Department, Institute of Infrastructure Technology Research and Management, Ahmedabad 380026, India
e-mail: plramkumarno1@gmail.com

© Springer Nature Singapore Pte Ltd. 2020

A. Praveen Kumar et al. (eds.), *Advances in Lightweight Materials and Structures*,
Springer Proceedings in Materials 8, https://doi.org/10.1007/978-981-15-7827-4_61

procedure covers a wide range of applications from a little kid's toy to enormous vessels. Henceforth, rotational molding process has picked up ubiquity over the most recent couple of decades, and thus a great deal of research is related with respect to rotational molding [4].

Generally, thermoplastics are favored as source material for rotational molding process. Around 80% of polyethylene from the group of thermoplastics is likely preferred [5, 6]. Among the different thermoplastics, there are a few criteria for which plastics need to fulfill for rotational molding procedure. The plastic should easily be melted and the fluidity must be maintained. Moreover, it should be viscous enough otherwise the chances of clumps may be prevalent. Thermal stability is an important parameter again so that there is less chance of degradation at high temperature range [7]. Considering these requirements, linear low-density polyethylene (LLDPE), from polyethylene, is more ideally utilized because of its unique melt flow properties and less shear affectability for rotational molding process. LLDPE coordinates all criteria yet lacks in the fundamental mechanical quality (strength being the major criteria) required in certain applications like armors, battle tanks, and so forth and subsequently, added substances or fillers can work in such case.

There have been several studies conducted to determine suitable material to reinforce with LLDPE for rotational molding process. Distinguished materials can be experimented for various ranges of additives that can be blended with LLDPE in order to achieve optimum processability as needed for rotational molding process and check uniform miscibility of additive with base resin. Fibers have an exceptional quality to improve strength of any end product. Natural and synthetic fibers can be utilized as additive. But natural fiber has comparatively less tendency to support the processability analysis as needed for rotational molding process. According to the study conducted by Nestere et al. [8], the mechanical and physical properties were investigated for LLDPE and natural fiber waste (cotton, flax, and hemp) composite, and it was observed that the tensile strength increases by up to thirty percent for hemp fibers which is a significant increase in flexure modulus and strength and decrease in deformability but extensive decrease of melt flow index was observed with increasing fiber content. Various other works have significantly denoted the similar analysis where an increase in strength was observed on adding natural fiber but an adverse effect on flowability has been observed [9–11]. On the basis of the above study, it can be deduced that natural fibers–LLDPE blends are less moldable making it less efficient for use in rotational molding process.

Synthetic fibers also make a viable option when the output is needed in terms of strength. The processability criteria are very well defined in favorable conditions when blended with LLDPE for rotational molding process analysis. In the examination led by Alqaflah et al. [12], polyethylene terephthalate (PET) and LLDPE were mixed and compounded with glass fiber (GF), reinforcement including 15–45% wt. of LLDPE and 5–3% wt. of GF, and it was seen that PET/LLDPE mix with GF brought about a composite with upgraded mechanical properties and thermal stability. As indicated by the examination did by Li et al. [13], when the non-isothermal conduct of LLDPE glass fiber composite was analyzed utilizing a differential scanning calorimeter (DSC), it was observed that LLDPE composites with 50% have

crystallization temperature peak (Tp) higher than that of unadulterated LLDPE at different cooling temperatures. They additionally saw that LLDPE/GF composite pursued modified Avrami and Mo techniques, and it was noticed that crystallization pace of LLDPE/GF composite was higher than that of pure LLDPE at a similar cooling rate. On contrary to literature available for glass fiber, confiber does not have much relevant literature accessible regarding rotational molding process. An attempt is made toward potentially utilizing confiber in mixing with LLDPE for experimentation of rotomolded product. Distinguished valuable literature has proven that the use of synthetic fiber as additive blend is found appropriate with LLDPE.

In the present work, glass fiber (GF) and confiber among synthetic fiber in powder form are selected for blending with LLDPE to verify flowability analysis as needed for rotational molding process. The prerequisite is checked on primary basis based on melt flow index. The range as needed for rotational molding processability according to the literature was validated for two separate blends with glass fiber blended with LLDPE in different percentage ratios from 14 to 38% and confiber blended with LLDPE in the ratios of 18–50% [14]. Melt flow index tests were carried out, and an optimum value from the various ratios is justified based on MFI value.

The outline of paper starts with the experimental details that include material procurement. After material availability, the experiments were performed. For experiments, in order to ascertain better processability, melt flow characteristic has been assessed. From the assessment, optimum percentage of glass fiber and confiber that needs to be mixed with LLDPE yielding better processability has been suggested.

2 Experimental Procedure

2.1 Materials

In this study, LLDPE has been used as base resin, whereas glass fiber and confiber are used as two different additives for preparing two distinguished blends. Pure LLDPE with rotomolded grade Ge3645 having MFI of 4.5 g/10 min with 0.936 g/cm^3 density was procured from Greenage Industries, Ahmedabad. E-glass fiber of density 2.55 g/cm^3 was acquired from HS Enterprise, Ahmedabad. Confiber with density 0.916 g/cm^3 and MFI 20 g/10 min was supplied from Mass India Inc., Ahmedabad. Seven different blends (LLDPE/GF) were prepared from 14 to 38% weight ratio with every 4% increase. Similarly, nine different blends (LLDPE/Confiber) from 18 to 50% were prepared with an increasing step of 4%.

2.2 Equipment Used

Melt Flow Index
In order to assess flow property, the melting characteristics of any material have to be calculated. For this, melt flow index (MFI) attribute is tested. This test is performed as per ASTM D1238. As per the standard, pressurized die is used through which the molten material flows. The pressurized material is measured in terms of flow rate in grams per 10 min. Usually, for rotational molding process, the favorable MFI value is in the range of 3–8 g/10 min [14]. MFI tests were performed for various percentage by weight ratios of glass fiber blended with LLDPE and confiber blended with LLDPE.

3 Results and Discussions

Assessment of Melt Flow Property
Melt flow index parameter depicts the flow property of material and also signifies the molecular structure of the material. MFI is inversely proportional to viscosity. Less MFI value shows that the material is having high viscosity and vice versa. MFI also gives significance of molecular weight distribution of material. Higher value shows shorter branch, which deteriorates the property of rotomolded product. Therefore, determining appropriate MFI value becomes essential for better processability of rotational molding process. For rotational molding process, the MFI range must be from 3 to 8 g/10 min [14]. The experiments were performed three times for each percentage ratio, and average value was obtained as mentioned in Tables 1 and 2 for glass fiber and confiber blended with LLDPE, respectively. The variation of MFI with respect to percentage change of glass fiber blended with LLDPE is shown in Fig. 1 and for confiber/LLDPE blend is shown in Fig. 2.

Melt flow index test analysis for LLDPE/glass fiber blend is depicted in Fig. 1. The trend value increases from 14 to 22%, after which the trend of graph follows a declination in the curve. The range of 14% to 38% is opted based on the preliminary tests experimented prior to MFI testing. From the range selected, MFI result shows that till 22%, value increases as LLDPE dominates but after the peak value obtained at 22%, there is a fall in graph which signifies the hindrance of flow due to an increasing amount of glass fiber into LLDPE, as low MFI signifies high viscosity which will make the flow of material prone to cluster formation. Glass fiber does not melt but acts as particulate reinforcement which may increase the strength of rotomolded product. This shows that below 22% GF/LLDPE, MFI value as needed for rotational molding processability is less than 3 g/10 min which makes the blend unsuitable for rotational molding flow analysis. In order to maintain the processability, optimum percentage of glass fiber that can be blended with LLDPE can be considered as 22% with value of MFI as 3.06 g/10 min for rotational molding process. Similar analysis is fetched from confiber/LLDPE blend.

Table 1 Melt flow index for various blend of glass fiber in LLDPE

Percentage of glass fiber (%)	Melt flow index (grams/10 min)	Average melt flow index (grams/10 min)
14	2.58	2.36
	2.38	
	2.78	
18	3.16	2.87
	3.25	
	3.07	
22	3.16	3.06
	2.76	
	2.96	
26	2.68	3.01
	2.83	
	2.98	
30	2.8	2.83
	2.75	
	2.8	
34	2.14	2.38
	2.4	
	2.6	
38	1.9	2.01
	2	
	1.95	

Figure 2 shows MFI data analysis for confiber/LLDPE blend. The graph depicts an increasing trend as the value of MFI for confiber is 20 g/10 min, so on increasing confiber percentage into LLDPE, the value of MFI will increase. The range of 14 to 50% is opted based on the preliminary tests carried out priory to MFI. 26 to 38% shows the value as needed for better processability in rotational molding. But 30% can be considered as optimum because at 26%, MFI value obtained is due to the presence of LLDPE as significance of confiber is minimal. And above 34%, confiber dominates wherein privilege to use LLDPE properties is hampered. Thus, it can be justified that based on melt flow index test analysis, 22% glass fiber/LLDPE and 34% confiber/LLDPE can be considered as an optimum blend that can yield better processability for rotational molding process.

Table 2 Melt flow index for various blends of confiber in LLDPE

Percentage of confiber (%)	Melt flow index (grams/10 min)	Average melt flow index (grams/10 min)
18	1.95	2.1
	2.38	
	2.05	
22	2.6	2.4
	2.25	
	2.5	
26	3.16	3.5
	2.76	
	2.96	
30	5.5	5.6
	5.4	
	5.5	
34	6.05	6.1
	6.25	
	5.95	
38	7.1	7.2
	7.3	
	7.2	
42	9.6	9.6
	9.3	
	9.4	
46	11.25	11.3
	11.6	
	11.2	
50	14.2	14.5
	14.6	
	14.4	

4 Conclusion

Rotational molding process is the process that is used for manufacturing seamless hollow tubes, and the product obtained is stress-free. For some critical applications, additives are added in LLDPE to achieve the necessary strength required.

Various experiments can be performed to attain an optimum blend of LLDPE/glass fiber that can accord better processability in rotational molding process. To get an appropriate value for better flow analysis, flow parameter was tested using melt flow index test. Glass fiber was added by weight fraction of 14–38% with an increase of

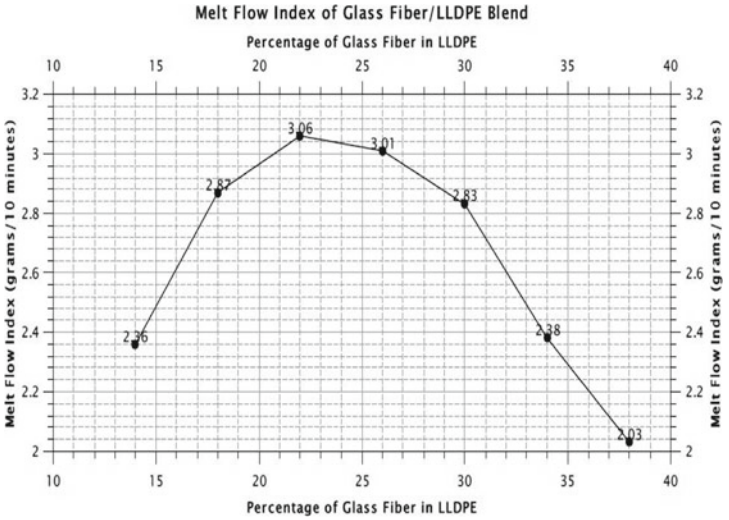


Fig. 1 Melt flow index value for LLDPE and glass fiber blend

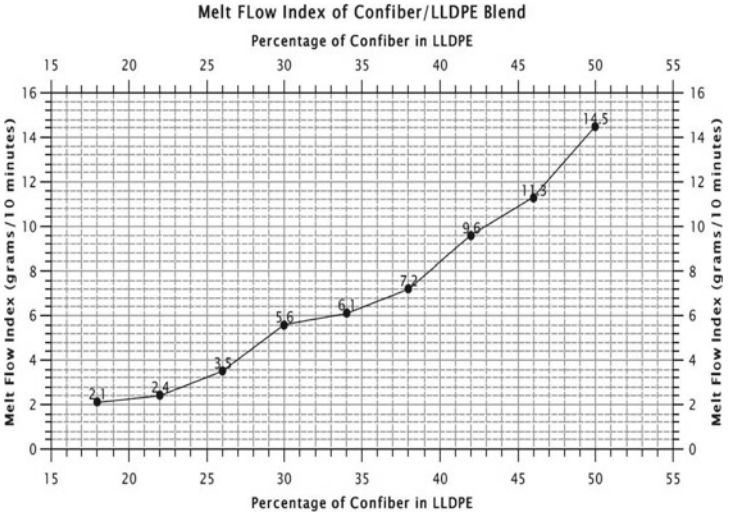


Fig. 2 Melt flow index value for LLDPE and confiber blend

4%. The result showed 22% as an optimum blend for which MFI was 3.06 g/10 min as required for rotational molding process.

Another blend was prepared with confiber blended with LLDPE in the ratio of 18–50% with a step value of 4%, for which the optimum value was obtained at 34% with MFI value as 6.1 g/10 min.

Experimental investigation revealed 22% by weight fraction of glass fiber blended with LLDPE and 34% by weight fraction of confiber blended with LLDPE can yield better processability for rotational molding process.

References

1. Crawford RJ (1996) Recent advances in the manufacture of plastic products by rotomolding. J Mater Process Technol 56:263–271
2. Crawford RJ (1998) Plastics engineering Elsevier
3. Kontopoulou M (1999) Polymer melt formation and densification. Rotation Mold Diss
4. Ramkumar PLK, Kulkarni DM (2016) Impact strength investigation of foamed linear low density polyethylene in rotational moulding process. Int J Mater Eng Inn 7(3–4):159–174
5. Ramkumar P, Kulkarni DM, Choudhary VV (2014) Parametric and mechanical characterization of linear low density polyethylene (LLDPE) using rotational moulding technology. Sadhana 39(3):625–635
6. Gupta VB, Mittal RK, Sharma PK, Mennig G, Wolters J (1989) Some studies on glass fiber-reinforced polypropylene. Part II: Mechanical properties and their dependence on fiber length, interfacial adhesion, and fiber dispersion. Polym Compos 10(1):16–27
7. AMCP A P (1966) Engineering design handbook. AMC, 706–189
8. Nestore O, Kajaks J, Vancovicha I, Reihmane S (2013) Physical and mechanical properties of composites based on a linear low-density polyethylene (LLDPE) and natural fiber waste. Mech Compos Mater 48(6):619–628
9. Ramkumar P, Waigaonkar SD, Kulkarni DM (2016) Effect of oven residence time on mechanical properties in rotomoulding of LLDPE. Sadhana 41(5):571–582
10. Ortega Z, Monzón MD, Benítez AN, Kearns M, McCourt M, Hornsby PR (2013) Banana and abaca fiber-reinforced plastic composites obtained by rotational molding process. Mater Manuf Process 28:879–883
11. Torres FG, Aragon CL (2006) Final product testing of rotational molded natural fibre reinforced polyethylene. Polym Testing 25:568–577
12. Alqaflah A (2017) Preparation and characterization of glass fiber–reinforced polyethylene terephthalate/linear low-density polyethylene (GF-PET/LLDPE) composites. Polymr Adv Technol 29(1)
13. Yuxin L, Yang Q, Guangxian L (2009) Nonisothermal crystallization behavior of LLDPE/glass fiber composite. Journal of Appl Polym Sci 109(2):782–788
14. Handbook on rotational molding technology. ISBN: 978–81–89765–25–5. (2012)

Experimental Investigation of Weld Charcteristics in Friction Stir Welded Joints Aa 6082-T6 Aluminum Alloy by X-Ray Radiography

K. Vijaya Krishna Varma, B. V. R. Ravi Kumar, and M. Venkata Ramana

Abstract Aluminum alloy 6082-T6 aluminum alloy (Aluminum–Silicon–Magnesium) has gathered wide acceptance in aerospace and automotive industries. In this novel, research work specially designed tool pin profiles were employed in order get defect-free sound weldments with good mechanical and microstructural properties. The aim of studying the present research work is to investigate the weld quality of AA 6082-T6 aluminum alloy weldments using friction stir welding (FSW) process with four different geometrical tool pin probes, namely MX-TRIVEX™, A-SKEW™, three flat threaded, and MX-TRIFLUTE™ concave shouldered tools with three different rotational speed's (1000, 1200, 1400 rpm's) at single traverse speed (25 mm/min). X—Ray radiography technique has been carried out to study the weld defects like lack of penetration, lack of fusion, worm hole, and cracks of weldments through MXR-451/26 make machine as per ASME Sec-IX 2017 QW 191. From this experimental study, it was found that influence of tool rotation speeds like 1000, 1200, and 1400 rpm on temperature and quality of aluminum alloy 6082-T6 weldments.

Keywords Friction stir welding · Temperature · Rotation speed · Traverse speed · Radiography

1 Introduction

Friction stir welding has gathered wide acceptance any homogeneous and hetrogeneous alloys with base material thickness in the range of 1–70 mm thick blocks

K. V. K. Varma (✉) · B. V. R. Ravi Kumar
Department of Mechanical Engineering, VNR Vignana Jyothi Institute of Engineering and Technology, Bachupally, Hyderabad 500090, India
e-mail: vijaykrishna705@gmail.com

B. V. R. Ravi Kumar
e-mail: rajaravikumar_bv@vnrvjiet.in

M. Venkata Ramana
Department of Automobile Engineering, VNR Vignana Jyothi Institute of Engineering and Technology, Bachupally, Hyderabad 500090, India
e-mail: venkataramana_m@vnrvjiet.in

© Springer Nature Singapore Pte Ltd. 2020

A. Praveen Kumar et al. (eds.), *Advances in Lightweight Materials and Structures*, Springer Proceedings in Materials 8, https://doi.org/10.1007/978-981-15-7827-4_62

[1]. As compared to other fusion base welding techniques routinely used for joining alloys, friction stir welding is an come up solid-state joining process in which the two adjacent sides of the weldments are joined by means of non-consumable rotating tool pin made to traverse along the weldline. Due to nonapperance of parent metal melting, the upcoming FSW process has observed several advantages on contray to fusion base welding [2]. Because of insufficient force, heat input excessive generation of heat during welding which reduces the soundness of weld joint thereby causes severe impact during manufacturing [3, 4]. Radiography technique is solely based on exposure of weldment to short wavelength by X-ray wavelength lesser than 0.001×10^{-8} cm to 40×10^{-8} cm from suitable source [5, 6]. Emamian et.al [7] performed friction welding on aluminum alloy 6061-T6 using four tool pin profiles, namely threaded cylinder, stepped cylindrical, conical, and square at tool rotational speeds 800, 1200, and 1600 rpm's and weld traverse speeds of 40, 70, and 100 mm/min obtained high tensile strength of 213 Mpa using cylindrical profile at 1600 rpm and 100 mm/min, and concluded that high welding speeds are prefered for sound tensile properties.

Madhusudhan reddy et.al [8] performed friction stir welding on 6061-T6 alloy using specially designed frustum-shaped cone at tool rotational speed 800 rpm and weld traverse speed of 15 mm/min obtained yield strength of 125 Mpa, ultimate tensile strength of 192 Mpa and elongation of 9%. Raghubabu et.al [9] performed friction stir welding on aluminum alloy 6082-T6 using cylindrical-tapered tool pin profile at 460, 630, 880, and 1230 rpm's at 115–170 mm/min and obtained defect-free weld at 1230 rpm and 115 mm/min and high hardness of 125 HV on the advancing side of the weldment. Soman et.al [10] performed friction stir welding on aluminum alloy 6082-O using taper screw threaded tool and triflute pin at 1200 rpm and 60, 70, 75, 85 mm/min traverse speeds and obtained 92.3% of ultimate tensile strength of base material using taper screw threaded pin. Ravi kumar et.al [11] performed friction stir welding on aluminum alloy 6061-T6 using taper threaded and half grooved tools at tool rotational speed 900 rpm, weld traverse speed 16 mm/min, and tool tilt angle of 2° and obatined defect-free weld by using half grooved tool with high tensile strength of 94 N/mm^2 and brinell's hardness of 69.5 BHN.

2 Materials Composition of Aluminum Alloy 6082-T6

Arificially aged and solution-hardened heat treatable is corrosion resistant and has best strength among 6000 aluminum alloys grades; the alloy finds wide applications in ship buiding and presure vessels applications. Friction stir welding is employed to join AA 6082-T6 6 mm thick plates. Plate dimensions of $200 \times 80 \times 6$ mm are procured for performing FSW [7]. The chemical composition was evaluated and summarized in Table 1.

Table 1 Chemical composition of aluminum alloy AA 6082-T6 (wt %)

Si	Fe	Cu	Mn	Mg	Ni	Zn	Ti	Sn	Zr	Al
1.02	0.2	0.01	0.5	0.7	0.006	0.02	0.01	0.0005	0.0013	97.23

3 Materials and Welding Procedure

Aluminum alloy 6082-T6 blank was cut on chap saw and milling operation was performed to acquire the requried dimensions 200 × 80 × 6 mm. BAYGILL KMC-1500 vertical 3-axis FANUC-controlled vertical milling machine was integrated to perform the fabrication the FSW joints as shown in Fig. 1. The weldments were produced with four different geometrical tool pin probes, namely as shown in Fig. 2

2. (a) A-SKEW™, 2 (b) MX-TRIVEX™, 2 (c) Three flat threaded and 2 (d) MX-TRIFLUTE™ concave shouldered and tools with three different rotational speed's (1000, 1200, 1400 rpm) at single traverse speed (25 mm/min). Measurement of temperature using infrared thermometer across the weldment during FSW is shown in Fig. 3. Finally, the images of the weldments fabricated by four different geometrical tool pin probes are shown in Fig. 4.



Fig. 1 BAYGILL KMC-1500 3-axis FANUC-controlled VMC

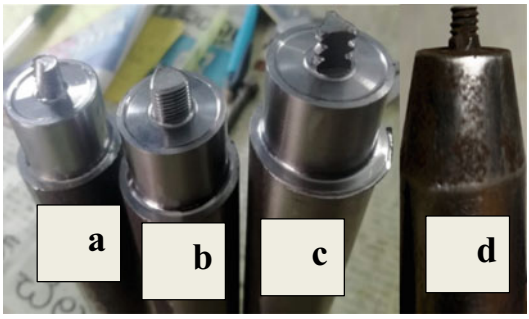


Fig. 2 Friction stir welding tools employed for fabricating the weldments

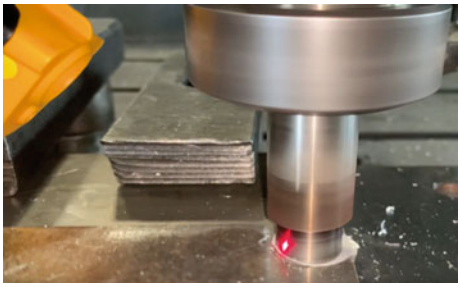


Fig. 3 Measurement of temperature along weld length using infrared thermometer



Fig. 4 Weldments fabricated using four different tool pin profiles

4 Radiography Method

X-ray radiography has been employed inorder to find out the defects, acceptance, and soundness of the **friction stir welded** weldments. Inspection has been carried out on COMET make MXR-451/26 model as shown in Fig. 5 according to radiography standards ASME Sec-IX 2017 QW 191. The intensity of radiographic exposure parameters are presented in Table 2.

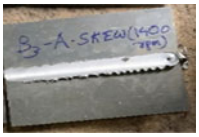
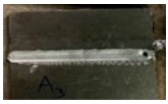


Fig. 5 COMET make MXR-451/26 model X-ray machine

Table 2 Intensities of radiographic exposure parameters

Voltage	170 kV
Activity/current	3.0 mA
Film	AGFA-D7
Exp. time	2.5 min
R.T technique	SWSI
Sensitivity	2%

Table 3 Illustrations of lateral flash in weldments

Tool pin profile			
MX-TRIVEX™	A-SKEW™	Three flat threaded	Concave-shouldered MX-TRIFLUTE™
 @ 1000 rpm	 @ 1200 rpm	 @ 1200 rpm	 @ 1200 rpm
 @ 1200 rpm	 @ 1400 rpm		
 @ 1400 rpm			 @ 1400 rpm

5 Results and Discussions

5.1 Visual Inspection of FSW Weldments

Visual inspection is prime way of scrutiny for surface defects like cracks, holes, and weld alignment along the weldment. Visual inspection was enacted on the weldments to condign the presence of irregularities on the weldments like surface tunnels, cracks, and lateral flash. The illustartions of lateral flash are shown in Table 3.

5.2 Radiographic Test Results of FSW Weldments

Radiographic test results of Aluminum alloy 6082-T6 FSW weldments produced with four different geometrical tool pin probes, namely MX-TRIVEX™ (A), A- SKEW™

(B), Three flat threaded, (C) and MX-TRIFLUTE™ Concave shouldered, and (D) tools with three different rotational speeds (1000, 1200, 1400 rpm) at 25 mm/min traverse speed was presented in Tables 4, 5, 6 and 7, respectively, comprising of code of tool pin, weldment photographs, radiographs, and the observations on each individual samples.

From the radiographs presented in Table 4 at 1000 rpm, 25 mm/min, identified that the weldments were prone to lack of fusion up to 90 mm, tunnel defects and kissing bonds merely occurred due to low rpm and insufficient plunging pressure, lack of fusion was identified up to 85 mm thereby indicates increasing rpm reduces defects like tunnel defects, kissing bonds and decrease in lack of fusion length on weldment, and lack of penetration was identified at 1400 rpm weldment up to 140 mm.

From the radiographs presented in Table 5 at 1000 rpm, 25 mm/min, identified that the weldments were prone to lack of fusion occurred up to 180, 135 mm zigzag line formation due to low rpm and less tool pin length. 1200 rpm weldment produced 135 mm Zigzag line where optimal weldment is obtained. 1400 rpm lack of fusion 45 mm and at 155 mm length, zigzag line was formed due high rpm, resulting in excessive generation of heat during welding. Results shows that, increase in rpm increases length of Zigzag line and decrease in length of lack of fusion.

From the radiographs presented in Table 6 at 1000 rpm, 25 mm/min, identified that the weldments were prone to lack of penetration occurred up to 99 mm, formed due to inappropriate generation of heat. At 1200 rpm, weldment lack of penetration was identified up to 115 mm. Similarly, at 1400 rpm, weldment lack of penetration was identified up to 200 mm. The weldments conclude that increase in rpm increases the length of occurrence of lack of penetration.

Table 4 Weldment images and radiographs (MX-TRIVEX™) at traverse speed 25 mm/min and different rpms

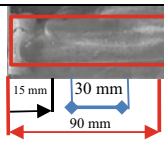
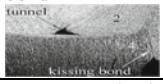
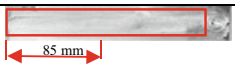
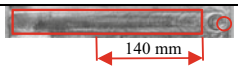
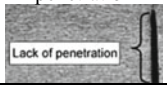
No.	Weld photo	Radiography	RPM	Observations
A_1		 Lack of fusion Tunnel defect Kissing bond	1000	90 mm Lack of fusion  15 mm tunnel defects 30mm kissing bond 
A_2		 Lack of fusion	1200	85 mm Lack of fusion
A_3		 Lack of penetration	1400	140 mm Lack of penetration 

Table 5 Weldment images and radiographs (A-SKEW™) at traverse speed 25 mm/min and different rpms

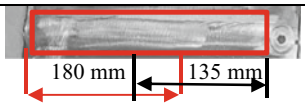
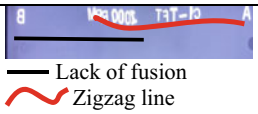
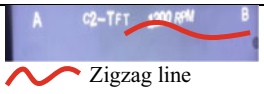
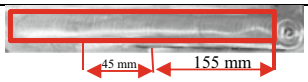
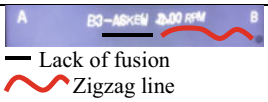
No	Weld photo	Radiography	RPM	Observations
B_1			1000	180 mm Lack of fusion 135 mm Zigzag line
B_2			1200	135 mm Zigzag line
B_3			1400	155 mm Zigzag line 45 mm Lack of fusion

Table 6 Weldment images and radiographs (Three flat threaded) at traverse speed 25 mm/min and different rpms

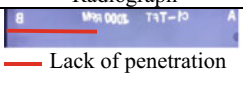
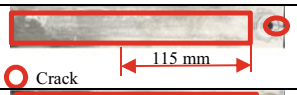
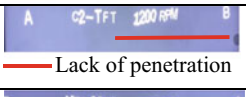
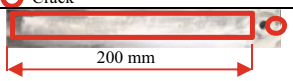
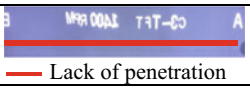
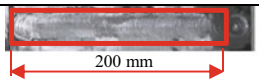
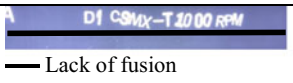
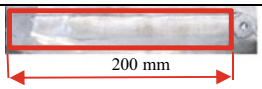
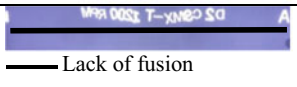
No.	Weld photo	Radiograph	RPM	Observations
C_1			1000	99 mm Lack of penetration
C_2			1200	115 mm Lack of penetration
C_3			1400	200 mm Lack of penetration

Table 7 Weldment images and radiographs (MX-TRIFLUTE™ concave shouldered) at traverse speed 25 mm/min & different rpms

No.	Weld photo	Radiogarphy	RPM	Observations
D_1			1000	200 mm Lack of fusion
D_2			1200	200 mm Lack of fusion
D_3			1400	200 mm Lack of fusion

From the radiographs presented in Table 7 at 1000 rpm, 25 mm/min, identified that the weldments were prone to lack of fusion occurred up to 200 mm, formed due to greater downward force, i.e., axial load. Similarly, at 1200 and 1400 rpm, weldments identified lack of fusion up to 200 mm due to greater downward force.

6 Conclusions

Non-destructive testing methods radiography and visual inspection tests were conducted on the weldments of aluminum alloy 6082-T6 weldments aluminum alloys at numerous weld parameter combinations. Hereby, x-ray radiographic testing technique merely detects the weldment defects and are said to be appropriate in this regard.

- In the major weldments, occurrence of lack of fusion is more due to geometry of tool pin profile, change in rpm, and abrupt change in axial load.
- Lack of penetration occurred mainly at low rpm's generally at 1000 and 1200 due to in appropriate generation of heat.
- Kissing bonds are formed at higher rpm and low traverse speed.
- Zigzag lines are formed mainly due to less tool pin length and more temperature reaction between precipitates and aluminum matrix.
- Sound weldment was produced by A-SKEW™ at 1200 rpm, 25 mm/min.
- Low temperature of 166^0 C was observed during welding of A-SKEW at 1000 rpm, 25 mm/min,
- High temperature of 277° C was observed by MX-TRIFLUTE™ concave shouldered at 1000 rpm, 25 mm/min.
- The reasons for change in test results are due to high weld traverse speed involving acute agglomeration of base material during welding.
- Friction stir welding can be performed by changing the tool pin geometry such as increasing tool rake angle in A-SKEW™ and also by increasing pitch of threads and flats the stirring action around the tool orbit can be improved.

Acknowledgements The authors are thankful to Dr. Gembali Srinivasa Gupta, Professor and HOD Mechanical engineering, VNR VJIET, Dr. Edupuganti Venkata Ramana P.G Coordinator, MED, VNR VJIET, Mr. Jaynath reddy M.D S.L Industries, G. Srinivasa rao Senior design engineer, S. Kiran CNC operator Vasudev industries Jeedimetla, and Mr. S. Rajasekhar M.D HEL Labs Balanagar, Hyderabad for assistance and guidance for carrying out the project research work.

References

1. Misra RS, Singh H (2017) Friction stir welding of 2xxx aluminum alloys including Al-Li alloys. Elsevier.

2. Elangovan K, Balasubramanian V, Valliappan M (2008) Effect of tool pin profile and tool rotational speed on mechanical properties of friction stir welded AA 6061 aluminium alloy. In: Materials and manufacturing processes, pp 251–260
3. Ilangovan M, Rajendra Boopathy S, Balasubramanian V (2015) Effect of tool pin profile on microstructure and tensile properties of friction stir welded dissimilar AA 6061-AA5086 aluminum alloy joints. Elsevier, pp 174–184
4. Edward Bohnart R (2014) Welding principles and practices, 3rd edn. McGraw-Hill
5. Patil C, Patil H, Patil P (2016) Investigation of weld defects in similar and dissimilar friction stir welded joints of aluminum alloys of AA7075 and AA6061 by X-ray radiography. SciEP, pp 11–15
6. Radhakrishnan VM (2002) Welding technology and design. 2nd edn. New Age International private Limited
7. Emamian S, Awang M, Hussai P, Meyghani B, Zafar A (2016) Influence of tool pin profile on the friction stir welding of AA 6061. APRN J Eng Appl Sci 12258–12261
8. Madhusudhan Reddy G, Mastanaiah P, Murthy CVS, Mohandas T, Viswanathan N (2006) Microstructure residual stress distribution and mechanical properties of friction-stir AA 6061 aluminium alloy weldments. ISNDTH, pp 1–14
9. Raghu Babu G, Murti KGK, Ranga Janardhana G (2008) An experimental study on the effect of welding parameters on mechanical and microstructural properties of AA 6082-T6 friction stir welded butt joints. APRN J Eng Appl Sci 68–74
10. Patil HS, Soman SN (2010) Experimental study on the effect of welding speed and tool pin profiles on AA 6082-O aluminium friction stir welded butt joints. IJEST 268–275
11. Srinivasa Rao MS, Ravi Kumar BVR, Manzoor Hussain M (2012) Experimental study of weld characteristics during friction stir welding of aluminium alloy (AA6061-T6). IJRET 469–473

Investigation on the 3D-Printed Vortex Tube as a Lightweight Cooling Device

Pushkar Kamble, Subodh Chavan, Gopal Gote, and K. P. Karunakaran

Abstract A *Vortex tube (VT)* is a very simple, compact, and light cooling device that separates the inlet stream of compressed air into two streams between which heat transfer occurs leading to one of them becoming hotter and the other colder. Its existing designs are too simple and hence inefficient due to (i) the lack of appropriate design tools and (ii) manufacturing constraints of that era. 3D printing/CNC technology can be utilized to realize the complex ducts, which could help make the VT more efficient in terms of air consumption and performance. These modern 3DP/CNC tools have hardly been exploited in the design of VT so far. To realize this, the authors ideated and recommended the design changes in the vortex generator and diverging nozzle, which are the main parts responsible for creating and sustaining the vortex. The authors fabricated the above parts by 3D printing and carried out post-processing. The experimental results obtained are discussed in this paper.

Keywords Ranque–Hilsch vortex tube · Energy separation phenomenon · Cooling device · 3D printing · FDM

1 Introduction

A vortex tube (VT) is a very simple, compact, and light cooling device that separates the inlet stream of compressed air into two streams between which heat transfer occurs leading to one of them becoming hotter and the other colder [1–3]. Such a phenomenon is known as temperature/energy (T/E) separation effect. Ranque discovered it in 1933. Later on, its performance was investigated by Hilsch. Hence, VT is also known as Ranque–Hilsch Vortex Tube (RHVT). Because of the absence of moving parts, it needs very little maintenance, thereby resulting in a long life. Its ability to produce instant cold and hot air simultaneously without any chemical input makes it very much useful in several applications such as cooling of plastic injection moulds and electronic control panels, chilling the suits of the operators working near

P. Kamble (✉) · S. Chavan · G. Gote · K. P. Karunakaran
Department of Mechanical Engineering, Indian Institute of Technology Bombay, Mumbai, India
e-mail: pushkarkamble@gmail.com

© Springer Nature Singapore Pte Ltd. 2020

A. Praveen Kumar et al. (eds.), *Advances in Lightweight Materials and Structures*,
Springer Proceedings in Materials 8, https://doi.org/10.1007/978-981-15-7827-4_63

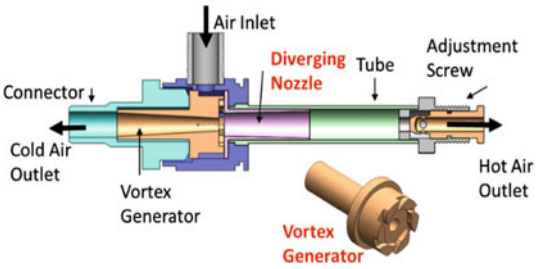


Fig. 1 Cross-section of a conventional vortex tube

furnaces in foundries and forging shops, underwater diving suits, cooling of ultrasonic welds and blow-moulded fuel tanks, liquefaction of gases, etc. Also, VT does not use any refrigerants like Freon, CFCs or HCFCs, and hence, it is environment-friendly. Even though it is simple in construction and usage, it involves a highly turbulent and complex nature of flow [4–6].

The compressed air enters the annular space of the tube from the tangential inlet (Fig. 1). The flow into the tube has high vorticity and turbulence. As the vortex progresses inside the tube, the density of the flow increases toward the walls of the tube due to inertia and the compressibility of the air [2]. Due to the centrifugal nature of the flow, a region of the low pressure is created at the injection port. The flow which tends to reach the periphery again turns back to the low-pressure region due to turbulence and the energy exchange takes place between return and forward vortices. Thus, the low-pressure central region of the tube becomes colder. The temperatures up to—40 °C can be achieved with this effect if the tube design is appropriate. Then, due to small vortices and backflow, the temperature of cold air tends to increase [7, 8]. The outer vortex that exits through peripheral outlet has a higher temperature. The flow can be adjusted from the hot outlet with the plug. The ratio of the flow coming out of the cold outlet to the inlet flow is called ‘cold mass fraction’.

Novel Design of the Vortex Tube

Two major limitations of the existing VT are (i) enormous air consumption and (ii) low-temperature separation between its two streams. Its existing designs are too simple and hence inefficient due to (i) the lack of appropriate design tools and (ii) manufacturing constraints of that era. 3DP/CNC technology can be utilized to realize the complex ducts which could help make the VT more efficient in terms of air consumption and performance.

The proposed design focuses on sustaining the vortex in the tube for a longer duration. It helps in the energy separation. As the vortex is more sustained and smooth flow is achieved, the centrifugal force can be exhibited by the flow very well. Due to the centrifugal action of the vortex, the low-pressure region can be sustained for a larger area which will further enhance the air utilization and with less air, more cooling can be achieved.

To realize this, the authors recommend the design changes in the vortex generator, which is the main part responsible for creating the vortex and the vortex diverging nozzle, where the energy separation effect actually takes place.

2 Geometric Changes

The geometric changes in the main components of the VT were done. The components are the vortex generator and diverging nozzle, which are responsible for the vortex action in the tube.

It can be seen from Fig. 2 that the vortex generator has channels cut on its surface, which let the air pass through the channels from the annual space to the tube.

The shape of the channels determines the flow characteristic of the vortex. It can be clearly seen that the vortex is created in a single plane by a vortex generator.

Channels are modified in such a way that the air inlet is titled at 5° angle in a longitudinal plane and the inlet opens in the tube tangential to the tube perimeter. The vortex can be directed and 'inserted better' this way into the divergent tube for creating a low-pressure region. It can sustain for a longer duration with geometrical changes in the divergent nozzle, as explained below, and can bring about the energy separation more efficiently. It is the hypothesis of this experiment.

Conventional CNC machines cannot easily manufacture these channels. But additive manufacturing can easily manufacture these channels enabling them to discover the possibility of studying the flow characteristics. Authors have used FDM technology to print the vortex generator with ABS plastic material.

Diverging nozzle made in brass has a smooth surface that sustains the vortex. The geometry of this part was so altered that the vortex gets sustained in part for a longer time. As explained in the previous sections, the air tends to be pushed at the periphery, i.e., near the walls due to centrifugal action of the vortex. To sustain the vortex, the grooves were made on the surface of the diverging nozzle, as shown in Figs. 2 and 3.

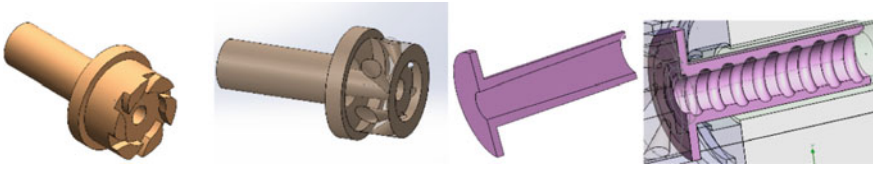


Fig. 2 From L–R; original vortex generator, modified generator, original DN, grooved DN



Fig. 3 L original vortex generator M original diverging nozzle R 3D-printed parts

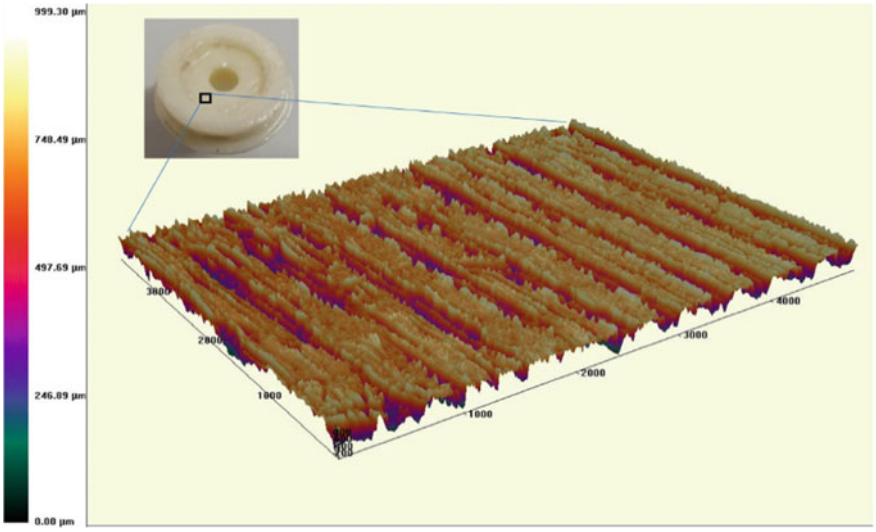


Fig. 4 3D map of surface roughness in planar surface of FDM parts before acetone treatment

3 Prototyping of the Parts Using FDM 3D Printer

The geometrical changes were incorporated in the CAD model and the parts were 3D printed using Stratasys FDM 3D printer as shown in Fig. 5. The surface quality of the 3D-printed parts was not good. Dimethyl ketone vapors were used for smoothing the surface of the FDM-printed parts [9, 10]. For post-treatment, the parts were dipped in the acetone for 10–15 s and then they were dried in the air. The surface finish was improved substantially due to the dissolution of the outermost layer in acetone. Surface finish was measured using the Zeta microscope (Figs. 4 and 5), the results are mentioned in Table 1 and compared in the graph as shown in Fig. 8.

4 Experimental Investigation of the Performance

Experimental verification of the 3D-printed parts was performed. The experimental set-up is as shown in Fig. 6. Vortex tube was held in place using a fixture, and thermocouple was used to monitor the temperature.

The thermocouple is a K-type thermocouple that has a range of—50 to +140 °C. The experimental parameters are mentioned in Tables 2 and 3.

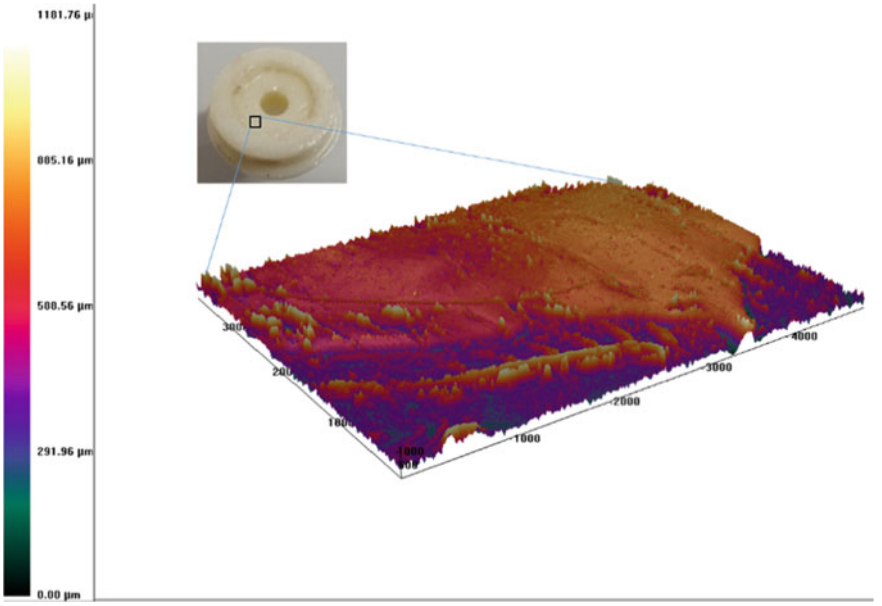


Fig. 5 3D map of surface roughness in planar surface of FDM parts after acetone treatment

Table 1 Experimental conditions

Sl. No.	Particular	Details
1	Pressure	6.3 Bar
2	Air inlet temperature	23.9 °C
3	Cold mass fraction	10% approximate
4	Divergent nozzle conditions Groves 3D-printed copy of original as a control	4 mm and 8 mm pitch
5	Vortex generator 3D-printed copy of the original as a control Modified as shown in figure	

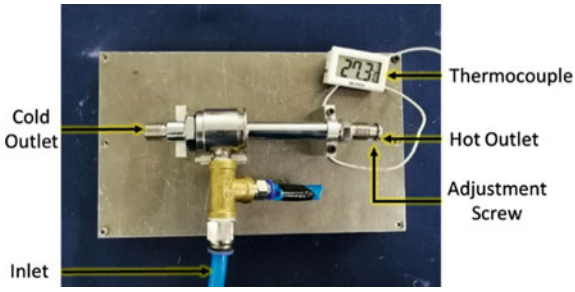


Fig. 6 Experimental set-up for vortex tube testing

Table 2 Part identification codes

S. No.	Part name	Description	Material	Identification code
1	Vortex generator	Original	Brass	VG1
2	Vortex generator	3D-printed copy of the original as c control	ABS plastic	VG2
3	Vortex generator	modified, 3D-printed	ABS plastic	VG3
4	Diverging nozzle	Original	Brass	DN1
5	Diverging nozzle	3D-printed copy of the original as a control	ABS plastic	DN2
6	Diverging nozzle	Helical grooves on internal surface 1 mm × 1 mm and 4 mm pitch	ABS plastic	DN31
7	Diverging nozzle	Helical grooves on internal surface 1 mm × 1 mm and 8 mm pitch	ABS plastic	DN32

Table 3 Observations from the experiments of the 3D-printed parts

Sl. No.	Vortex generator code	Diverging nozzle code	Minimum temp reached (°C)	Time for minimum temperature (s)
1	VG2	DN2	−2.5	132
2	VG2	DN31	4.1	126
3	VG2	DN32	4.2	81
4	VG3	DN2	−6.5	150
5	VG3	DN31	0.2	102
6	VG3	DN32	−0.8	93

4.1 Experimental Parameters

The results obtained from the experiments are given in Table 4. All the parts were tested for the lowest temperature. The various parts for identification were coded as follows:

Table 4 Observations from experiments on the original parts

S. No.	Vortex generator code	Diverging nozzle code	Minimum temp reached (°C)	Time for minimum temperature
1	VG1	DN1	−6.7	

4.2 Experimental Results

The minimum temperatures and time in which those minimum temperatures obtained were recorded for the 3D-printed geometry. At first, the divergent nozzles with different pitch were tested with the control vortex generator, VG2 (experiments 1, 2, and 3). Then, it was replaced with a modified vortex generator, VG3 (experiment 4, 5, and 6). The observations are as follows:

The original vortex generator and the divergent nozzle (DN) are made of brass. An experiment was carried out to measure the cold-side temperature with original brass parts (Table 5). The observations are as follows.

5 Conclusion

The experiments which were carried out confirm that the modified geometry influences the cold temperature of the VT (Table 4). As compared to the reference geometry, the modified geometry performs better in terms of temperature drop on the cold side. Following conclusions are significant for this study:

A 61.5% drop in the minimum temperature is observed with the modified geometry as against the 3D-printed prototype of the original geometry.
3D printing comes out as an important manufacturing process to manufacture the complex ducts which are required for realizing such turbulent flows.

Future Scope
It is evident that as the number of parts in the assembly increases, flow continuity gets hampered, and the losses set in. With the help of 3D printing, direct assembly of the vortex generator and diverging nozzle can be printed to reduce flow losses. Multiple such geometries can be investigated by varying the parameters using CFD, and the most successful design can be fabricated and tested. Extensive simulation of the flow with the help of CFD will help in the optimization of the design parameters.

References

1. Gutak AD (2015) Experimental investigation and industrial application of Ranque-Hilsch vortex tube. Int J Refrig 49:93–98
2. Kirmaci V, Kaya H, Cebeci I (2018) Analyse expérimentale et exergétique de la performance thermique d'un tube vortex de Ranque-Hilsch à contre- courant avec différents types de tuyères. Int J Refrig 85:240–254
3. Kaya H, Günver F, Kirmaci V (2018) Experimental investigation of thermal performance of parallel connected vortex tubes with various nozzle materials. Appl Therm Eng 136(March):287–292

4. Thakare HR, Monde A, Parekh AD (2015) Experimental, computational and optimization studies of temperature separation and flow physics of vortex tube: a review. Renew Sustain Energy Rev 52:1043–1071
5. Thakare HR, Parekh AD (2017) Experimental investigation & CFD analysis of Ranque-Hilsch vortex tube. Energy 133:284–298
6. Kirmaci V, Kaya H (2018) Effects of working fluid, nozzle number, nozzle material and connection type on thermal performance of a Ranque-Hilsch vortex tube: a review. Int J Refrig 91:254–266
7. Xue Y, Arjomandi M, Kelso R (2013) The working principle of a vortex tube. Int J Refrig 36(6):1730–1740
8. Agrawal N, Naik SS, Gawale YP (2014) Experimental investigation of vortex tube using natural substances. Int Commun Heat Mass Transf 52:51–55
9. Lalehpour A, Janeteas C, Barari A (2018) Surface roughness of FDM parts after post-processing with acetone vapour bath smoothing process. Int J Adv Manuf Technol 95(1–4):1505–1520
10. Colpani A, Fiorentino A, Ceretti E (2019) Characterization of chemical surface finishing with cold acetone vapours on ABS parts fabricated by FDM. Prod Eng 13(3):437–447

Strength and Hardness of 3D Printed Poly Lactic Acid and Carbon Fiber Poly Lactic Acid Thermoplastics



J. Durga Prasad Reddy, Debashis Mishra, and Nagaraj Chetty

Abstract The two different thermoplastic materials such as poly lactic acid (PLA) and carbon fiber poly lactic acid (CF-PLA) are selected for printed specimen preparation by the fused deposition modeling (FDM) technique. The FDM technique is also named as 3D printing technique. The experimental investigation is made to get the said materials specimen tensile and flexural strength and hardness properties to make a comparison between the two chosen printing materials with respect to the change in working limits of process parameters. The literature and trial experiments are performed to propose various and most effective process parameters of 3D printing technique like fill density (60, 80 and 100%), print speed (0.06, 0.08 and 0.1 m/s) and layer thickness (0.1, 0.2 and 0.3 microns). The influence of these process parameters is understood by analyzing the obtained testing results. The fill density and print speed are most accountable for getting maximum hardness, flexural and tensile strength of 3D printed PLA and carbon fiber material specimen. The most suitable material among CF-PLA, and PLA can be assessed and the working range of 3D printing process parameters can be assumed through this experimental investigation.

Keywords Carbon fiber poly lactic acid (CF-PLA) · Fused deposition modeling (3D printing) · Flexural strength · Hardness value · Tensile strength

1 Introduction

Manufacturing industries worldwide are facing different challenges to make products which will be economical and strong enough to produce the intended work. The rapid desire of bringing such manufacturing technique brought out additive manufacturing or 3D printing. The technique used rapid prototyping of complex parts by means of layer by layer deposition of materials from the feeder. The basic 3D printing factors are generally like raster angle, infill pattern, infill density, print speed, layer

J. Durga Prasad Reddy (✉) · D. Mishra · N. Chetty
CMR Technical Campus, Kandlakoya, Medchal, Hyderabad, Telangana, India
e-mail: reddy.durgaprasad@gmail.com

© Springer Nature Singapore Pte Ltd. 2020

A. Praveen Kumar et al. (eds.), *Advances in Lightweight Materials and Structures*,
Springer Proceedings in Materials 8, https://doi.org/10.1007/978-981-15-7827-4_64

thickness, etc. Many researchers are presented the research work in various aspects of additive manufacturing of different thermoplastic materials. The investigations mainly focused on getting the impacts of several machine or process factors on different physical, mechanical, chemical and microstructural properties.

One of the researchers reported the effect of process parameters on tensile and bending properties of 3D printed PLA specimen. It is reported as tensile properties changes with the simultaneous change in thickness of layers [1]. Continuous carbon fiber PLA is attempted to print by changing process parameters. The influence of chosen factors on temperature and pressure is studied. The results are shown as when fiber percentage increased to 27%, the flexural strength is obtained as maximum 335 MPa [2]. The carbon fiber of percentage 0, 3, 5, 7.5, 10 and 15 is added into ABS plastic to get better the properties (mechanical) printed specimens. The 5% carbon fiber addition produced better tensile, flexural strength and toughness [3]. The report is made to make a thorough analysis of production of composite parts using the additive manufacturing technique. The different case studies presented to eliminate the various susceptive deformations or defects in the production of complex parts for aerospace and automobile products. The volume of product can be increased by the additive manufacturing than other manufacturing processes. The traditional manufacturing process is more labor intensive and costlier for prototype building, whereas additive manufacturing process overcomes such limitations and proved to be low cost and more productive [4, 5].

The thermoplastic carbon fiber reinforced nylon composites specimens are printed by 3D printing technique, and its strength is experimentally evaluated and analyzed using existing literature. The printed specimens are made like 100% nylon with 10 layers and 2, 4 layers nylon and 6 layers of fiber. The 6 layers fiber with 2 layers of nylon produced better properties against others [6]. Reinforcement of short fiber with acrylonitrile–butadiene–styrene (ABS) composite which is 3D printed as a feedstock and the tensile specimens are prepared. The performance and mechanical properties are evaluated by performing tensile testing [7]. A mathematical model is developed using design of experiment tool to relate the measured tensile strength with preferred factors of 3D printing or additive manufacturing technique. The results included like minimum layer thickness and raster width, but increase in raster angle improves the strength of printed samples. The progress of additive manufacturing technique brought out the concept of simplicity in manufacturing of products are thoroughly studied following many researchers' ideas and findings [8–11].

The examination is carried to make a comparative investigation of impacts of various factors like layer height, infill density and layer orientation on mechanical properties of 3D printed ABS and PLA samples to suggest strongest material among the two. The results are presented like PLA produces more strength and rigidity than ABS [12–14]. The 3D printing factors like raster angle, infill speed and nozzle temperature and layer thickness have a major influence upon the strength of PLA sample [15]. PLA with and without the reinforcement of carbon fiber named as modified carbon fiber is prepared by the additive manufacturing technique. The tensile specimens are fabricated with the different percentage addition of carbon fiber. The outcome is presented as the higher percentage of carbon fiber produces higher

strength than plain carbon fiber PLA [16]. The researcher attempted to produce iron and copper filled ABS specimens by fused deposition modeling rapid prototyping process by changing its various factors. The substantial enhancement in mechanical properties of ABS sample is noted with the assimilation of metallic fillers.

When fiber content increased to 27% in carbon fiber reinforced PLA composite, the flexural strength is obtained maximum as 335 MPa and modulus 30 GPa. The performance and functions of prototype can be enhanced with reinforcement of short and long fiber in ABS and PLA composites for aerospace applications [2, 17, 18]. PLA filaments are produced for 3D printing, and the impacts of extrusion temperature, surface roughness on strength (tensile) are meticulously researched. The tensile strength is achieved as 51.7 MPa when the build layer 0.1 mm, temperature of extruder 220 °C and extruding speed 60 mm/s [19].

The literature is discussed to present a concept of the additive manufacturing technique and its process parameters. The researchers interest to produce an experimental output to suggest the factors and its working ranges for suited applications. The improper selection of factors will affect the mechanical, physical, chemical, thermal and microstructural properties. The present experimental work aimed to demonstrate a comparative investigation of the hardness value, tensile strength and flexural strength of 3D printed PLA and carbon fiber PLA material. The investigation will be helpful to get a thorough understanding of the productivity and behavior of 3D printed thermoplastic PLA and carbon fiber PLA materials to choose the suitable one for intended applications.

2 3D Printing of PLA and Carbon Fiber PLA Thermoplastics

The PLA and carbon fiber PLA material specimens are prepared by 3D printing technique. The specimens prepared considering 3D printing process parameters are print speed, fill density and thickness of printing material layers. The effect of selected factors and its working ranges on PLA and carbon fiber PLA are understood by the subsequent performance testing like tensile, flexural and hardness properties. The Fig. 1 is the illustration of 3D printing system arrangement used for the experimentation. Table 1 shows the chosen printing factors and its working conditions. The PLA and carbon fiber PLA tensile, flexural and hardness specimen and its CAD image are presented in Figs. 2, 3 and 4, respectively.

3 Result and Discussion

The various test results are discussed as hardness, compressive and flexural strength. Tables 2 and 3 present the obtained hardness value of PLA and carbon fiber PLA

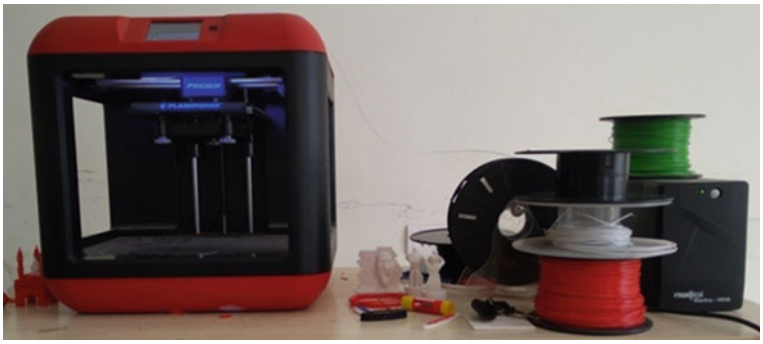


Fig. 1 Arrangement of 3D printing system used for experimentations

Table 1 Factors and its working range for PLA and carbon fiber PLA material

3D printing factors	Printing ranges for PLA and Carbon fiber PLA thermoplastics		
Fill density (%)	60	80	100
Printing speed (m/s)	0.06	0.08	0.1
Layer thickness (μ)	0.1	0.2	0.3

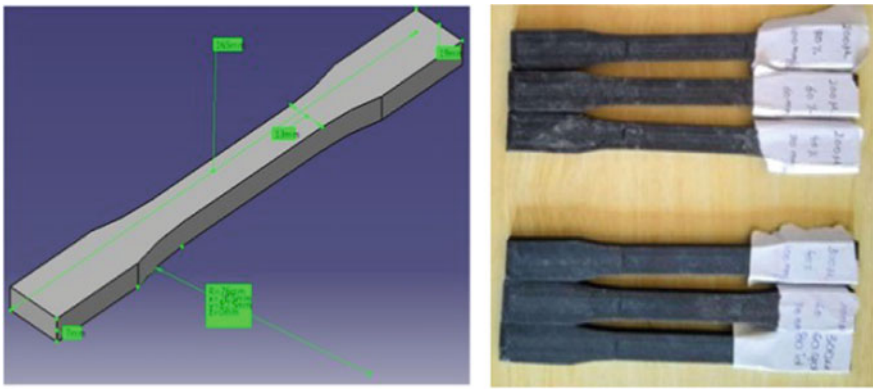


Fig. 2 CAD image and printed tensile specimen, respectively (ASTM D638)

material, respectively. The hardness value of PLA specimens, i.e., 78 and 80 BHN, is not affected with the change in process parameters. Whereas the carbon fiber PLA produced a variation in hardness value, i.e., 64, 76 and 74 BHN.

Tables 4 and 5 present the obtained tensile strength value of PLA and carbon fiber PLA material, respectively. The tensile strength of PLA and carbon fiber PLA is obtained as 41.42 and 39.55 MPa, respectively, when the process parameters are chosen as 60% fill density, printing speed 0.06 m/s and layer thickness 0.1μ. When the parameters are set at 80%, 0.08 m/s and 0.2 μ, the tensile strength of PLA and

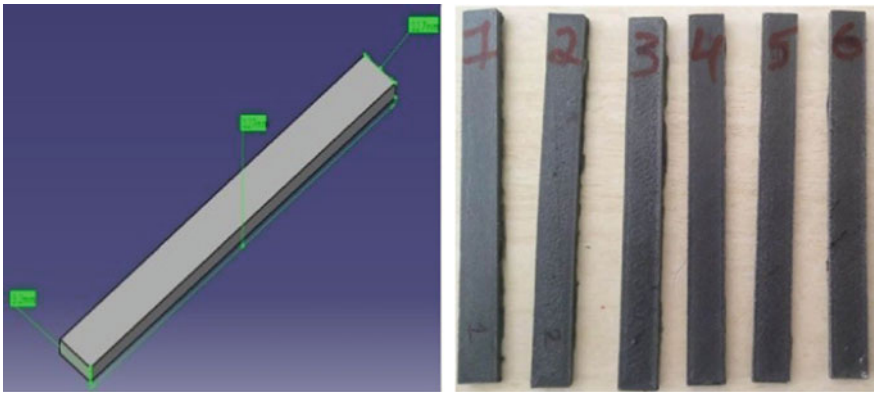


Fig. 3 CAD image and printed flexural specimen, respectively (ASTMD790)

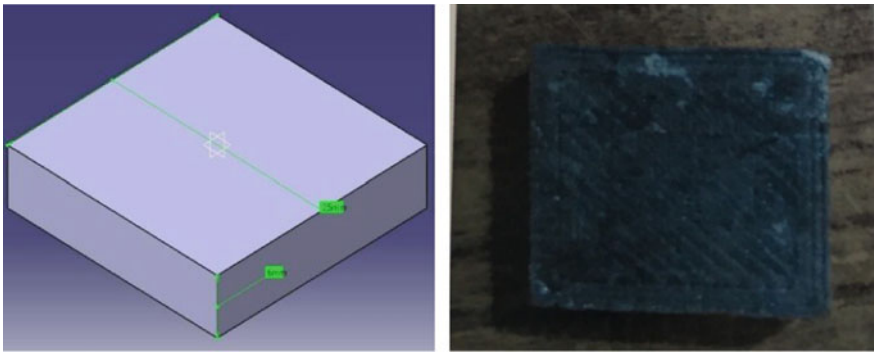


Fig. 4 CAD image and printed hardness specimen, respectively

Table 2 Hardness value of PLA thermoplastic materials

Test piece number	PLA hardness value (BHN)
1	80
2	78
3	78

Table 3 Hardness value of carbon fiber PLA thermoplastic materials

Test piece number	Carbon fiber PLA hardness value (BHN)
1	64
2	76
3	74

Table 4 Ultimate tensile strength PLA thermoplastic materials

Test piece number	Ultimate tensile load (kN)	PLA ultimate tensile strength value (MPa)
1	6.84	41.42
2	10.68	62.62
3	13.38	74.31

Table 5 Ultimate tensile strength of carbon fiber PLA

Test piece number	Ultimate tensile load (kN)	Carbon fiber PLA tensile strength value (MPa)
1	6.9	39.55
2	10.08	59.37
3	11.94	70.56

carbon fiber PLA is obtained as 62.62 and 59.37 MPa, respectively. Further change in process parameters to 100%, 0.1 m/s and 0.3μ, the tensile strength is reported as 74.31 and 70.56 MPa for PLA and carbon fiber PLA, respectively.

It is observed that PLA material has more strength than carbon fiber PLA. Tables 6 and 7 present the obtained flexural strength value of PLA and carbon fiber PLA material, respectively. The flexural strength is obtained as 123.53, 181.67 and 123.68 MPa for PLA material and 156.35, 171.05 and 128.01 MPa for carbon fiber PLA, respectively, with respect to the above said and chosen process parameters. The maximum flexural strength is reported as 181.67 MPa for PLA and 171.05 MPa for carbon fiber PLA when the process parameters are taken as 80% fill density, printing speed 0.08 m/s and layer thickness 0.2 μ.

Hardness, tensile and flexural strength are independent responses and affected by the change in range of the factors of 3D printing. The individual or simultaneous impact of factors may be responsible for the increase or decrease in hardness, tensile

Table 6 Flexural strength of PLA thermoplastic materials

Test piece number	Load (N)	PLA flexural strength value (MPa)
1	240	127.53
2	360	181.67
3	240	123.68

Table 7 Flexural strength of carbon fiber PLA thermoplastic materials

Test piece number	Load (N)	Carbon fiber PLA flexural strength value (MPa)
1	300	156.35
2	360	171.05
3	300	128.01

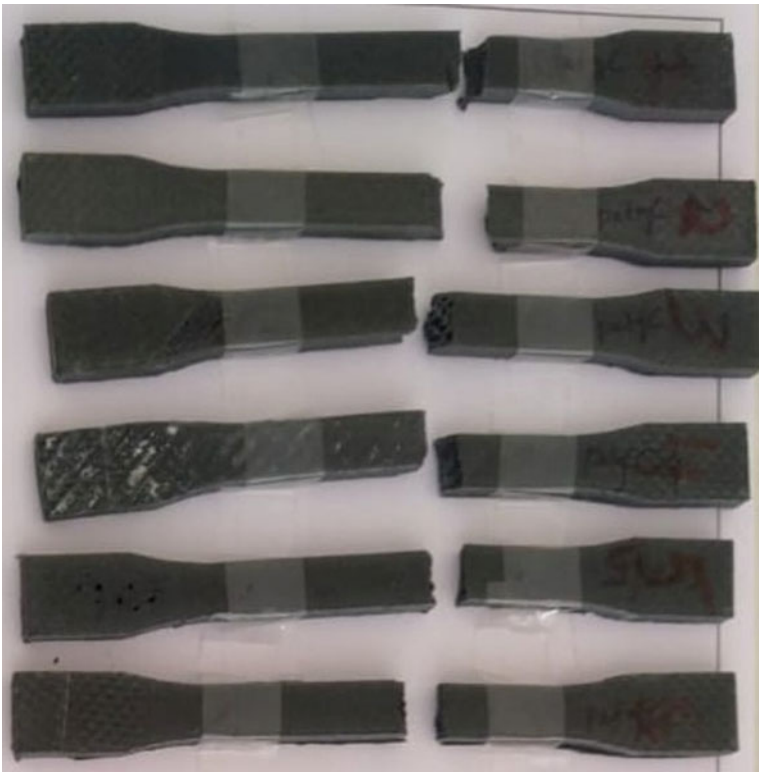


Fig. 5 Tensile specimen after testing

and flexural strength of PLA and carbon fiber PLA 3D printed specimens. The tensile and flexural specimen are shown in Figs. 5 and 6.

4 Conclusion

The PLA and carbon fiber PLA thermoplastic materials are fruitfully 3D printed by changing the factors like fill density, layer thickness and printing speed. The test specimens are printed as tensile, flexural and hardness. The test reports express that the maximum hardness is obtained as 80, 76(BHN), the ultimate tensile strength is as 74.31, 70.56(MPa), and flexural strength is gained as 181.67, 171.05(MPa) for PLA and carbon fiber PLA, respectively.

- The PLA produces more hardness, tensile and flexural strength than carbon fiber PLA material. The best combination of process parameter to obtain high hardness value for PLA is fill density 60%, printing speed 0.06 m/s and layer thickness 0.1 μ. For the carbon fiber PLA, the maximum hardness value is obtained with



Fig. 6 Flexural specimen after testing

the effective process parameters are fill density 80%, printing speed 0.08 m/s and layer thickness 0.2 μ.

- For PLA and carbon fiber PLA 3D printed material, the maximum tensile strength is obtained as 74.31 and 70.56 MPa, respectively. The process parameters are fill density 100%, printing speed 0.1 m/s and layer thickness 0.3μ.
- The maximum flexural strength is obtained as 181.67 and 171.05 MPa for PLA and carbon fiber PLA, respectively, when the process parameters are set at fill density 80%, printing speed 0.08 m/s and layer thickness 0.2 μ.
- Therefore, it is understood from this investigation that the hardness, tensile and flexural properties of 3D printed materials are independent. But these properties are tending to change with change in the input process parameters and experimental set conditions.
- Most influential 3D printing process parameters are fill density and printing speed.
- The comparative investigation will be helpful to get a thorough understanding of producibility of desired mechanical properties of 3D printed PLA and carbon fiber PLA thermoplastic material for various aerospace and automobile applications.

5 Future Scope of Work

The experiments can further carry in collections of the microstructures and SEM images of different 3D printed materials. The microstructures can be compared with the change in 3D printing process parameters and their effects can be studied. The other 3D printing materials can be further printed, and the various properties can be studied for the effective use in different applications. Finite element analysis can be produced for the better prediction of impacts of various factors. The process can be simulated to get an optimum and desired experimental condition. Other factors except

infill density, print speed and layer thickness can be used to study their effects on different properties of 3D printed materials. Different process optimization technique like response surface analysis, Taguchi analysis, linear model analysis and regression analysis can be followed to establish a statistical relationship between the process parameters and the measured responses.

References

1. Chacón JM, Caminero MA, García-Plaza E, Núnez PJ (2017) Additive manufacturing of PLA structures using fused deposition modelling: effect of process parameters on mechanical properties and their optimal selection. Mater Design
2. Tian X, Liu T, Yang C, Wang Q, Li D (2016) Interface and performance of 3D printed continuous carbon fiber reinforced PLA composites. Elsevier Compos Part A 88:198–205
3. Ning F, Cong W, Qiu J, Wei J, Wang S (2015) Additive manufacturing of carbon fiber reinforced thermoplastic composites using fused deposition modeling. Elsevier Compos Part B 80:369–378
4. Türk DA, Kussmaul R, Zogg M, Klahn C, Leutenecker-Twelsiek B, Meboldt, M (2017) Composites part production with additive manufacturing technologies. Procedia CIRP66:306–311
5. Black S (2015) A growing trend: 3D printing of aerospace tooling. Compos World
6. Van Der Klift F, Koga Y, Todoroki A, Ueda M, Hirano Y, Matsuzaki R (2016). 3D printing of continuous carbon fibre reinforced thermo-plastic (CFRTP) tensile test specimens. Open J Compos Mater 6(01):18
7. Tekinalp HL, Kunc V, Velez-Garcia GM, Duty CE, Love LJ, Naskar AK, Blue CA, Ozcan S (2014) Highly oriented carbon fiber–polymer composites via additive manufacturing. Compos Sci Technol 105:144–150
8. Chockalingam K, Jawahar N, Chandrasekhar U (2006) Influence of layer thickness on mechanical properties in stereo-lithography. Rapid Prototyp J 12(2):106–113
9. Tontowi AE, Ramdani L, Erdizon RV, Baroroh DK (2017) Optimization of 3D-Printer process parameters for improving quality of poly-lactic acid printed part. Int J Eng Technol 9
10. Kozior T, Kundera C (2017) Evaluation of the influence of parameters of FDM technology on the selected mechanical properties of models. Procedia Eng 192:463–468
11. Luca DV (2017) Design and Manufacture of optimized continuous composite fiber filament using additive manufacturing systems. Luca J Mater Sci Eng 6:4
12. Rodríguez-Panes A, Claver J, Camacho AM (2018) The influence of manufacturing parameters on the mechanical behaviour of PLA and ABS pieces manufactured by FDM: a comparative analysis. Materials11(8):1333
13. Vishwas M, Basavaraj CK (2017) Studies on optimizing process parameters of fused deposition modelling technology for ABS. Elsevier Mater Today Proc 4:10994–11003
14. Nagaraj C, Mishra D, Tirupati T (2019) Optimization of the FDM Process parameters to attain the desired strength of ABS specimens. Int J Recent Technol Eng (IJRTE)8(4)
15. Ning F, Cong W, Hu Y, Wang H (2017) Additive manufacturing of carbon fiber-reinforced plastic composites using fused deposition modeling: effects of process parameters on tensile properties. J Compos Mater51(4):451–462
16. Li N, Li Y, Liu S (2016) Rapid prototyping of continuous carbon fiber reinforced polylactic acid composites by 3D printing. J Mater Process Technol 238:218–225
17. Nikzad M, Masood SH, Sbarski I (2011) Thermo-mechanical properties of a highly filled polymeric composite for Fused deposition modelling. Elsevier Mater Design 32:3448–3456

18. Quan Z, Larimore Z, Wu A, Yu J, Qin X, Mirotznik M, Suhr J, Byun J-H, Oh Y, Chou T-W (2016) Microstructural design and additive manufacturing and characterization of 3D orthogonal short carbon fiber/acrylonitrile-butadiene-styrene preform and composite. Elsevier Compos Sci Technol 126:139–148
19. Liu W, Zhou J, Ma Y, Wang J, Xu J (2017) Fabrication of PLA filaments and its printable performance. IOP Conf Series Mater Sci Eng 275:012033
20. Dey A, Yodo N (2019) A systematic survey of FDM process parameter optimization and their influence on part characteristics. J Manuf Mater Process MDPI
21. Somi Reddy M, Singh CV, Czekanski A (2020) Mechanical behaviour of 3D printed composite parts with short carbon fiber reinforcements. Eng Failure Anal Elsevier 107
22. Srivastava A, Bhaskar J (2019) Experimental investigation of printing parameters of fused deposition modelling-based 3D printers for average surface roughness. Advances in Additive Manufacturing and Joining. Lecture Notes on Multidisciplinary Industrial Engineering. Springer
23. Luo H, Tan Y, Fan Z, Jun Z, Tu Y, Cui K (2019) Selectively enhanced 3D printing process and performance analysis of continuous carbon fiber composite material. Materials 12:3529
24. Jun Z, Zhou Z, Fan Z, Tang Y, Tu Y, Yang B (2020) Performance of 3D-printed continuous carbon fiber reinforced plastic with pressure. Materials 13:471

Open-Source Designing for Additive Manufacturing of Metallic Triply Periodic Minimal Surfaces



Hrushikesh Chavan, Ashish Kumar Mishra, and Arvind Kumar

Abstract Triply periodic minimal surfaces (TPMS) structures are non-self-intersecting mathematical isosurface of mean zero curvature. Such structures are being actively researched in-depth for potential application in impact energy absorption, heat exchangers and biomedical implants. However, designing and generating the required 3D CAD model of these structures have been a daunting task. In this study, open-source architecture has been described to generate and export the TPMS structures in CAD format. The developed architecture has been validated with the experimentally measured geometry of the manufactured TPMS lattice. While the geometrical compliance has been achieved satisfactorily, the printed TPMS wall thickness was larger than the as-designed values. Against the as-designed wall thickness of 0.2 mm, the built samples had an average wall thickness of 0.25851 mm, while the minimum and maximum wall thicknesses are 0.212 and 0.34655 mm, respectively. Distortions and deviations from the designed geometry are observed along the building direction. Nonetheless, a successful open-source designing architecture with excellent designing potential has been demonstrated in this paper, paving way for more such developments.

Keywords TPMS · Open-source designing · Lattice structures · Metal additive manufacturing

1 Introduction

Lattice structures are recently being actively researched for their potential applications in weight reduction and efficient material utilization in various industries like automotive, aerospace, packaging, biomedical, infrastructure and energy [1]. These structures, if optimally tuned, can show properties contrasting the parent material [2]. These structures basically are periodic repetition of single unit cell geometry which fills the space defined by the bounding surfaces of the desired component/design.

H. Chavan · A. K. Mishra · A. Kumar (✉)
Department of Mechanical Engineering, Indian Institute of Technology Kanpur, Kanpur 208016, India
e-mail: arvindkr@iitk.ac.in

© Springer Nature Singapore Pte Ltd. 2020

A. Praveen Kumar et al. (eds.), *Advances in Lightweight Materials and Structures*,
Springer Proceedings in Materials 8, https://doi.org/10.1007/978-981-15-7827-4_65

The lattice structures comprise two families broadly, one of which is based on the truss deformation mechanism and the other is based on bending deformation. These structures are hence called stretch-dominated and bending-dominated structures, respectively [3]. The bend-dominated structures comprise both strut-based as well as surface-based structures.

The triply periodic minimal surfaces (TPMS) are mathematical surfaces that have zero mean curvature, the smallest possible area for a given volume and are invariant under three-dimensional translation. Lattice structures based on these topologies have been explored for potential use in impact energy absorption [4], biomedical implants [5] and thermal applications [6]. Several examples of the TPMS structures are Schoen's Gyroid surface, Schwarz's P (Primitive) and D (Diamond) surfaces.

While the potential applications are explored, it has been a challenging task to manufacture such structures by conventional manufacturing routes. With the recent advancements made in additive manufacturing techniques though, the manufacturing has become possible. Additive manufacturing uses 3D CAD data to manufacture the parts in a layer by layer fashion. The uploaded 3D CAD data to the machine is sliced with constant thickness, and these slices are manufactured one by one [7].

Laser powder bed fusion (LPBF) is one such additive manufacturing technique used primarily for manufacturing metallic parts. As the name reveals, it uses a laser beam as an energy source to melt and consolidate the metal powder particles, spread in a powder bed form. Using a laser, ultra-high precision and accuracy can be achieved. This has prompted the manufacturing of TPMS-based metallic lattice structures through this technique. Yan et al. [8] have tested the manufacturability, quality and mechanical performance of LPBF manufactured 316L stainless steel TPMS lattice, based on the Gyroid unit cell. Kadkhodapour et al. [9] used LPBF to fabricate TPMS samples to study the deformation mechanics and mechanical property relationship. Ataee et al. [10] used LPBF process to manufacture very high strength TPMS scaffolds for biomedical implants. Han et al. [11] used this method to produce functionally graded TPMS bone implants.

Designing these structures is a challenging task and often impossible using conventional designing packages. Some customized platforms are available, but a strong urge is felt of having an open-source tool to design such structures. This said, only a few studies are available where such modeling tools are explored for TPMS designing [12–17]. The methods described in such works were largely based on using splines. While these methods are in no way less useful, development of an open-source tool able to generate solid wall structures directly from mathematical expressions of the surfaces will be more useful. This study aims the same, where we attempt to demonstrate a computational tool based on several Python™-based libraries and Lewiner marching cubes algorithm. The computational model is used in conjunction with the open-source tool Blender® to generate thickened solid CAD models for use in additive manufacturing. The open-source tool is then used to develop 3D CAD models of two TPMS structures—Schwarz P surface and Schwarz D surface. The samples are manufactured through LPBF process, and a comparison is presented between the as-designed and as-manufactured sample geometry and dimensions. Toward the end, the issues faced with the current developed tool

are listed to highlight the required future developments as an open problem to the interested researchers.

2 Open-Source Computational Tool Development

2.1 Python™ Libraries Used

Several Python™ libraries are used in the tool development. These libraries are.

1. NumPy 2. scikit-image 3. Stl 4. Matplotlib

NumPy is a general purpose array processing Python package. It provides a high performance multidimensional array object. It is also an efficient multidimensional container of generic data. It can also be used to seamlessly integrate a wide variety of arbitrary databases. The scikit-image is an image processing Python package that works with NumPy. It contains various algorithms for image segmentation and transformation, color analysis, filtering and feature detection. Stl is a library which reads and writes stl files. It is used in conjunction with the NumPy for generating both Binary and ASCII STL files. Matplotlib is a visualization library in Python for 2D plots of arrays. It provides a MATLAB-like interface and can be used in Python scripts and shells.

2.2 Computational Tool Development Details

To develop the computational tool, the libraries are imported to the program. After importing libraries, a function is declared which defines the mathematical formulation of TPMS surface to be generated. Following this, a 3D mesh grid is generated using the mgrid command of NumPy library. The declared TPMS function is used along with the Lewiner Marching Cubes algorithm to generate the 3D space data of the targeted TPMS structure. Lewiner Marching Cubes algorithm is used to extract a polygonal mesh of an ISO surface from a 3D volume. This algorithm works by iterating across the volume, looking for regions which cross the level of interest. If such regions are found, triangulations are generated and added to an output mesh. The final result is a set of vertices and a set of triangular faces. The numerical array containing the generated 3D model is then stored using NumPy commands. This data is then imported to the mesh module of Stl library, and a triangulated meshed surface in STL (stereo lithography) format is generated by applying the control loop, thereby supplying a zero thickness STL file (essentially surface) of the TPMS structure. Figure 1 presents a flowchart depicting various steps of the program.

The obtained STL file has zero wall thickness and hence cannot be used as such for manufacturing through LPBF process. An example of the zero thickness STL file is presented in Fig. 2, where a Schwarz D surface with zero thickness is shown. The

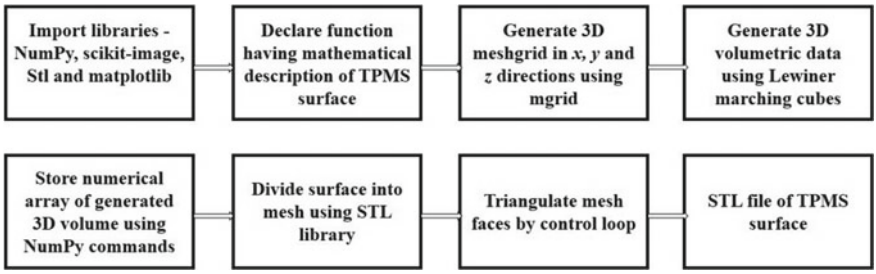


Fig. 1 Flowchart of the python program

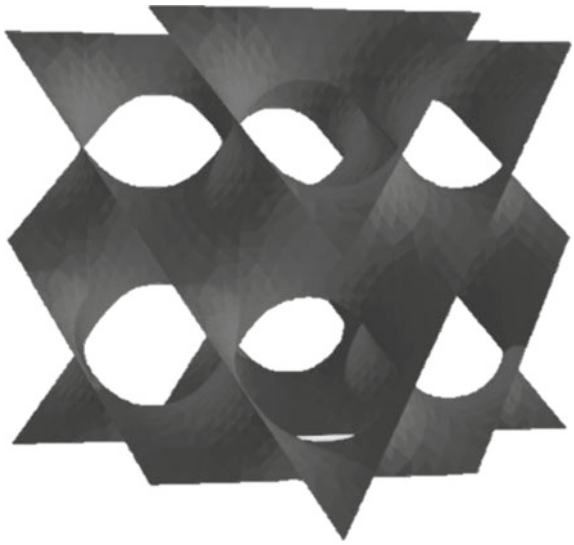


Fig. 2 Schwarz D surface with zero thickness as obtained using the developed designing tool

wall thickness is assigned to the wall by importing the STL file to Blender® software and using the object modifier command. The effect of thickening is shown in Fig. 3 where the Schwarz D surface of Fig. 2 is shown with a thickened wall.

3 TPMS Lattice Structure Generation

The developed program is used to generate two TPMS lattice structures, namely Schwarz P surface and Schwarz D surface. The mathematical formulation of these surfaces is provided below

$$U_D = \sin(k_x x)\sin(k_y y)\sin(k_z z) + \sin(k_x x)\cos(k_y y)\cos(k_z z) + \cos(k_x x)\sin(k_y y)\cos(k_z z) + \cos(k_x x)\cos(k_y y)\sin(k_z z) \quad (1)$$

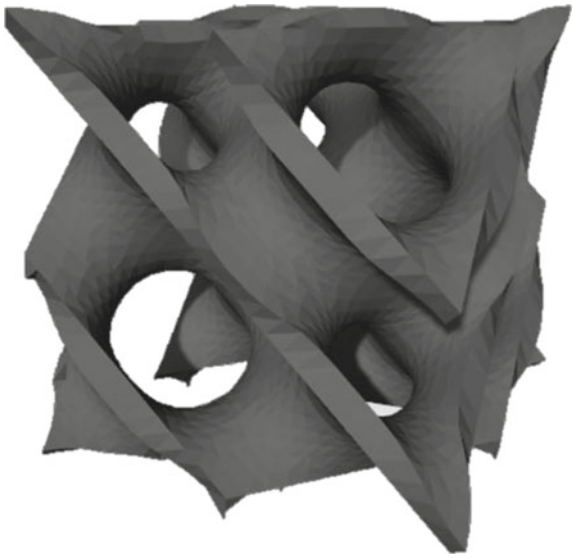


Fig. 3 Schwarz D surface after thickening

$$U_P = \cos(k_x x) + \cos(k_y y) + \cos(k_z z) \tag{2}$$

Diamond (D) and primitive (P) lattice structures with arbitrary numbers of cells can be generated by finding the $U = 0$ isosurface of these TPMS Eqs. (1) and (2).

In Eqs. (1) and (2), the k_i ($i = x, y, z$) are the periodicities and are defined as

$$k_i = (2\pi n_i / L_i) \tag{3}$$

where n_i are the numbers of cell repetitions in the directions x, y and z, and L_i are the absolute sizes of the structure in those directions.

4 Program Validation

To examine and validate the designing capability of the developed program, the designed TPMS lattices are manufactured through LPBF process. The as-designed and as-manufactured dimensions, thickness and geometry are compared to estimate the precision, accuracy and reliability of the program.

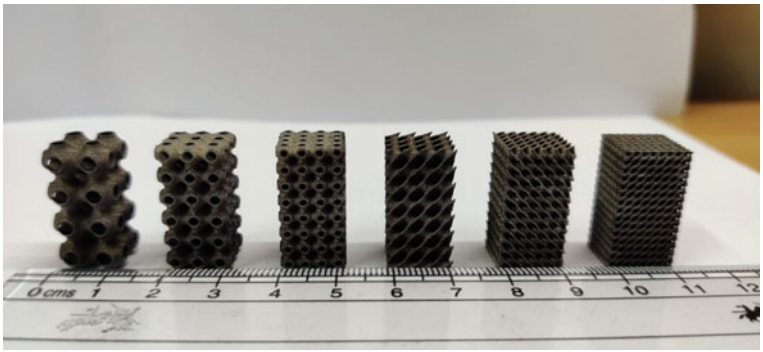


Fig. 4 As-manufactured TPMS lattice structures

4.1 Materials and Manufacturing

Three unit cell sizes of each surface (Schwarz P and D) are used to populate a cuboid volume of $12 \times 12 \times 24$ mm^3. The unit cell sizes are 3, 4 and 6 mm, respectively, resulting in a $4 \times 4 \times 8$, $3 \times 3 \times 6$ and $2 \times 2 \times 4$ repetition of unit cells. A constant thickness of 0.2 mm is assigned to all the TPMS lattices. The thickened STL files are used for LPBF additive manufacturing of the lattices. The TPMS lattices are manufactured using AlSi10Mg powder with a particle size distribution of 10–45 μm supplied by GE additive. The samples are manufactured under argon atmosphere in a commercial LPBF equipment Concept Laser MLab CusingR supplied by GE additive. The parts are manufactured at the in-built process parameters for best density. The printed samples are separated from the build platform through Wire electro discharge machining (EDM). The separated samples are ultrasonically cleaned using acetone to remove any adhered powder particle. The as-built samples are shown in Fig. 4.

4.2 Comparison of the As-Designed and As-Manufactured Samples

To make the comparison, the geometry and dimensions of the manufactured lattices are measured through optical imaging using an optical microscope (Nikon Eclipse LV100). While the geometrical compliance has been achieved satisfactorily, the as-manufactured TPMS wall thickness was larger than the as-designed values. As observed in optical microscopy images (Fig. 5), compared to the as-designed wall thickness of 0.2 mm, the as-built samples had an average wall thickness of 0.25851 mm. The maximum and minimum wall thicknesses are 0.212 and 0.34655 mm, respectively (Fig. 6). As we can see from images, the circular pores of Schwarz P surface are fabricated oval in shape. In the building direction, the designed

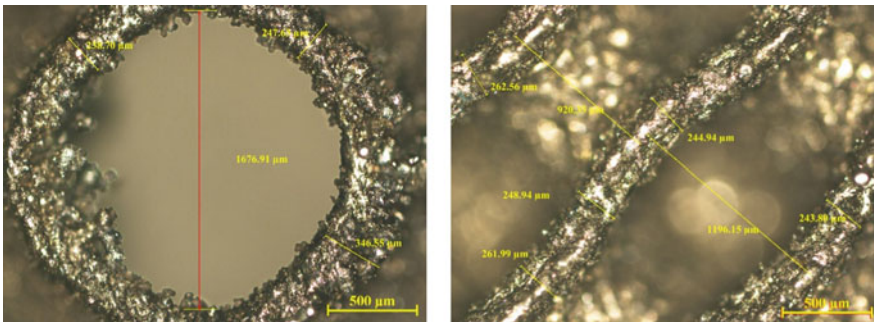


Fig. 5 Optical microscope images of as-manufactured TPMS lattice showing the dimensional variations

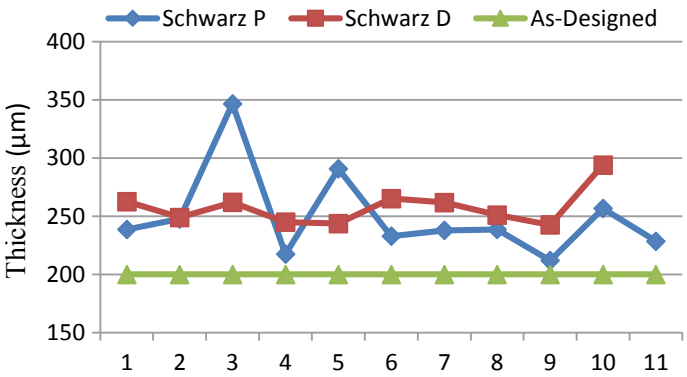


Fig. 6 Comparison of as-designed and as-manufactured wall thickness of TPMS lattice structures

geometry of Schwarz P surface is more distorted and deviated compared to transverse to building direction. It is observed that the distance between consecutive walls of Schwarz D surface is uneven. Also, walls of Schwarz D surface were not fabricated in linear fashion rather it seems slightly curvy.

Overall, the developed program has proved to be capable to design the TPMS-based lattice structures directly from the mathematical formulation of the surface to be manufactured. While the potential is huge, several issues are lying in open to be addressed in future.

4.3 Issues and Limitations

The developed program has been able to output STL files directly by receiving the mathematical formulation of the surface. However, the developed Python program is able to give only zero thickness STL surfaces of TPMS which cannot be directly sent

for manufacturing. The addition of the thickness to the file is done in software such as Blender®. In Blender®, controlling the direction of thickening is not uniform, i.e., controlling whether thickening is provided in one direction or in both directions is not possible as of now. This may lead to varied cell size of TPMS surface, and the distances between consecutive walls of surface are uneven. Also, the current program even after thickening is not able to output solid files that can be used in FEA analyses.

5 Conclusion

The article demonstrated a Python™-based open-source tool for designing and generating STL files of TPMS lattice structures that can be used for additive manufacturing through LPBF process. Numerous conclusions can be made from this work.

1. Direct generation of numerical arrays containing the surface data from the mathematical formulation of the surface being generated is possible. Using Python™ libraries, STL files are developed from these numerical arrays, without digging into the complex topics like splines, etc. The same approach is used and validated in this article.
2. The generated files can be LPBF manufactured after being properly thickened. This has been demonstrated successfully in this article.

6 Future Scope

The current tool has some issues which are needed to be addressed in detail. Generation of thickened file directly from the tool itself is essential. Also, generation of solid files that can be analyzed in FEA tools like ANSYS, etc., is desired but not possible through the current program. This indicates that further investigation is needed to generate solid part file in Python and to thicken surface in Python code itself to avoid uneven thickening as mentioned.

References

1. Maconachie T, Leary M, Lozanovski B, Zhang X, Qian M, Faruque O, Brandt M (2019) SLM lattice structures: Properties, performance, applications and challenges. Mater Des 183:108–137
2. Fang N, Xi D, Xu J et al (2006) Ultrasonic metamaterials with negative modulus. Nature Mater 5:452–456
3. Deshpande VS, Ashby MF, Fleck NA (2001) Foam topology: bending versus stretching dominated architectures. Acta Mater 49(6):1035–1040
4. Yan C, Hao L, Hussein A, Bubb SL, Young P, Raymont D (2014) Evaluation of light-weight AlSi10Mg periodic cellular lattice structures via direct metal laser sintering. J Mater Process Technol 214:856–864

5. Afshar M, Anaraki AP, Montazerian H, Kadkhodapour J (2016) Additive Manufacturing and mechanical characterization of graded porosity scaffolds designed based on triply periodic minimal surface architectures. J Mech Behav Biomed Mater 62:481–494
6. Fee C (2017) 3D-printed porous bed structures. Curr Opin Chem Eng 18:10–15
7. Gibson I, Rosen D, Stucker B (2015) Additive manufacturing technologies, 3D printing, rapid prototyping, and direct digital manufacturing. 2nd edon. Springer-Verlag, New York
8. Yan C, Hao L, Hussein A, Raymont D (2012) Evaluations of cellular lattice structures manufactured using selective laser melting. Int J Mach Tools Manuf 62:32–38
9. Kadkhodapour J, Montazerian H, Darabi ACh, Zargarian A (2017) The relationships between deformation mechanisms and mechanical properties of additively manufactured porous biomaterials. J Mech Behav Biomed Mater 70:28–42
10. Ataee A, Li Y, Brandt M, Wen C (2018) Ultrahigh-strength titanium gyroid scaffolds manufactured by selective laser melting (SLM) for bone implant applications. Acta Mater 158:354–368
11. Han C, Wang Q, Wen S, Wei Q, Yan C, Hao L, Liu J, Shi Y (2018) Continuous functionally graded porous titanium scaffolds manufactured by selective laser melting for bone implants. J Mech Behav Biomed Mater 80:119–127
12. Dinis JC, Morais TF, Amorim PHJ, Ruben RB, Almeida HA, Inforcati PN, Bartolo PJ, Silva JVL (2014) Open source software for the automatic design of scaffold structures for tissue engineering applications. Procedia Technology 16:1542–1547
13. Feng J, Fu J, Shang C, Lin Z, Li B (2018) Porous scaffold design by solid T-splines and triply periodic minimal surfaces. Comput Methods Appl Mech Engg 336:333–352
14. Yang L, Ferrucci M, Mertens R, Dewulf W, Yan C, Shi Y, Yang S (2020) An investigation into the effect of gradients on the manufacturing fidelity of triply periodic minimal surface structures with graded density fabricated by selective laser melting. J Mater Process Tech 275:116367
15. Yin H, Liu Z, Dai J, Wen G, Zhang C (2020) Crushing behavior and optimization of sheet-based 3D periodic cellular structures. Compos B 182:107565
16. Feng J, Fu J, Shang C, Lin Z, Li B (2019) Sandwich panel design and performance optimization based on triply periodic minimal surfaces. Comput Aided Des 115:307–322
17. Karcher H, Polthier K (1996) Construction of triply periodic minimal surfaces. Philos Trans Math Phys Eng Sci 354(1715):2077–2104

Production of Multi-functional and Lightweight Parts with the Use of Topology Optimization and Additive Manufacturing Technique—A Review

J. Durga Prasad Reddy, Debashis Mishra, and M. Ajay Kumar

Abstract Topology optimization (TO) be a technique employed to fill the design space with optimized amount of material based on the satisfaction of design variables. The design variables considered dependent on material properties, load conditions and geometric details. Optimized shape resulted from the TO process may cause manufacturing complexities. Additive manufacturing (AM) is capable of building complex parts. Combination of TO with AM makes an exploration to design areas to produce multi-functional and lightweight objects. AM offers the certain advantages with TO like printing of parts with lattice structures and multiple materials. AM also put constraints like support structure and mesh resolution. This paper briefly reviews the advantages and constrains of AM in combination with TO.

Keywords Additive manufacturing (AO) · Lattice structure · Layer-by-layer addition · Mesh resolution constraint · Topology optimization (TO)

1 Introduction

Topology optimization (TO) be a mathematical technique is intended for enhanced design with minimum design constraints [1]. TO can be applied to broad categories of design problems: solid mechanics [3, 4], fluid mechanics [5, 6] and thermodynamics [7]. Grégoire Allaire et al. suggested an algorithm to include overhang constraint, which imitates the layer-by-layer addition like AM process. They calculated shape derivative functions using Hadamard's concept. They numerically investigated this concept for the feasibility. The difficulty in formulation and implementation of algorithms attracted the researchers [2]. Additive manufacturing (AM) differs from subtractive machining as the parts are built in layer-by-layer addition of material. This makes additive manufacturing suitable for manufacturing parts with substantial complexity without effecting the cost. The ease of manufacturing makes the AM process as the most promising technique for designing the jobs with creativity.

J. Durga Prasad Reddy (✉) · D. Mishra · M. Ajay Kumar
CMR Technical Campus, Kandlakoya, Medchal Road, Hyderabad, Telangana 501401, India
e-mail: reddy.durgaprasad@gmail.com

© Springer Nature Singapore Pte Ltd. 2020

A. Praveen Kumar et al. (eds.), *Advances in Lightweight Materials and Structures*,
Springer Proceedings in Materials 8, https://doi.org/10.1007/978-981-15-7827-4_66

There is a tremendous growth in the field of AM research. The AM bridges the gap between complex and creative design created by TO with reduced difficulty of manufacturing. AM processes can be classified in to two broad categories, namely material extrusion and powder-based fusion. Most popular AM technologies are fused deposition modeling (FDM), stereo-lithography (SLA), poly-jet, selective laser sintering (SLS), and selective laser melting (SLM). FDM process involves deposition of material in layer-by-layer manner through a hot nozzle with extrusion of material from filament. The process is patented in 1992 by Crump [8]. SLA process includes the deposition of photopolymer liquid in sequential layer form and then dried by UV laser or identical. Patent on this process is done in 1986 by Hull [9]. Poly-jet slightly differs from SLA by formation of thin layers on the model by jetting process. SLS and SLM melt the powder deposited on the model in layer form. The major difference lies in the extension of material fully fused or not by laser. The process of replacement part production in 1998 is patented [10]. The process of SLS is patented in 1989. Figure 1 represents schematic sketch of SLS and FDM process [11].

Majorly, three different TO techniques are employed in AM; they are solid isotropic material with penalization (SIMP), bi-directional evolutionary structural optimization (BESO), and level-set method (LSM). Three methods differed in algorithm based on material distribution. SIMP is classified as a density-based approach. The design space is discretized in to finite elements. The optimizing variable is density of discrete element. Density gradient is calculated and sensitivity analysis performed iteratively. This approach does not require meshing to accommodate new boundary between material and void or between different elements. SIMP algorithm for a classic compliance optimization problem is shown below.

$$\min.C = U^T K U = \sum_{e=1}^{n} u^e k^e u^e = \sum_{e=1}^{n} \left(\rho^e\right)^p u^e k_0 u^e$$

$$\text{s.t. } V = \sum_{e=1}^{n} \rho^e \vartheta_0 \leq V_{\max}$$

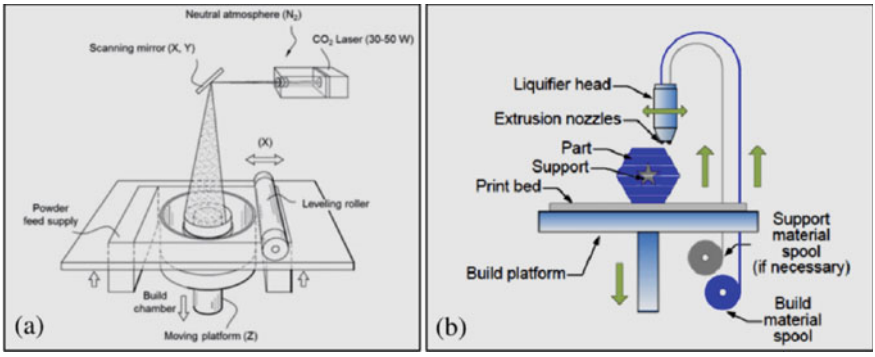


Fig. 1 3D printing system used in experiment

$$KU = F$$
$$0 < \rho_{\min} \leq \rho^e \leq 1 \tag{1}$$

where U and F are the global displacement vector and loading vector, respectively.

K is the global stiffness tensor.

u^e is the element displacement vector.

k^e is the element stiffness tensor after density interpolation.

k_0 and ϑ_0 are the stiffness tensor and material volume of a solid element, respectively.

ρ^e is the element density and ρmin is the lower bound.

$V_{\max}$ is the upper bound of the total volume of material.

BESO is classified as a hard-kill element approach, which involves removal or addition of material in an iterative manner. This method is also known as void–solid approach. The distribution of material based on heuristic criteria may or may not involve sensitivity calculation. LSM is classified as a boundary-based approach. This method intends to do the structural-based optimization and identifying smooth structure boundary during the process. Approximate Heaviside projection is employed to discrete the field into finite element. This method requires finite element method (FEM) analysis to carry the stress evaluation for efficient optimization. This present research paper objective is to review the TO implementation to fabricate the objects through AM. The paper focuses on constraint and advantages involved in the bridging of TO and AM process for making the additive manufacturing process simpler and user friendly.

2 Mesh Resolution Constraint

AM process can be employed for printing complex parts. This makes a constraint when it is combined with TO [12]. The number of finite elements in the design domain across the thickness of a part plays key role in optimization. More number leads to stable optimization but results in higher resolution. Jun Wu et al. suggested possible solution to print topologically optimized high-resolution model. The main problem for the high resolution models along with topology optimization is lies with the handling of millions of elements together and at a time. They obtained this by employing high-performance GPU solver that can handle million numbers of elements. They also included geometric shape constraints, symmetry and pattern repetition in the optimization algorithm. They printed parts of different interior structures to achieve high strength with low weight. The two of printed models by them are shown in Fig. 2. Arrow indicates the load, and the first part indicates interior material distribution. Neptune model is printed with a resolution of 621X488X1000 voxels and consists of 14.19 million finite elements. The hand part of Neptune model is filled with high density to ensure to carry the load. Time taken for TO is 12 min on the GPU solver. The hand is printed with 4.39 FEM elements with grid resolution of

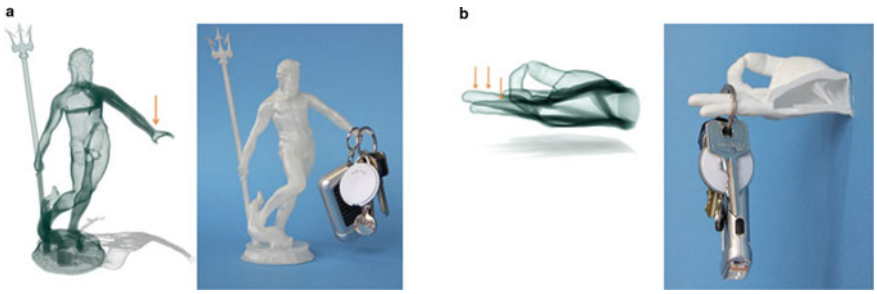


Fig. 2 **a** Neptune model **b** Hand model simultaneously

401X250X178. They ensured interior material distribution to support the load and minimized the material requirement [13].

3 Support Structure Constraint

One of the manufacturing constraints in AM is to build large overhanging parts. The structure is to be overhanging, when it exceeds the minimum inclination angle with horizontal. The buildability of these structures is difficult in material extrusion and powder bed fusion process. Material cannot be deposited on void in the case of the first one. Warpage problem due to residual thermal stresses enhances at overhang structure in the later one [14]. The added difficulty in the later one is falling of droplets of molten metal in the structure underneath the overhang parts and leads to the rough patches [15]. These problems are illustrated in Fig. 3 [16].

Nicolas Gardan et al. implemented topology optimization to optimize the volume of production material. They developed the concept to optimize material in interior part and conservation of material of the exterior skin. They tested the algorithm in different AM processes such as FDM, SLS, and SLA. They faced the difficulties

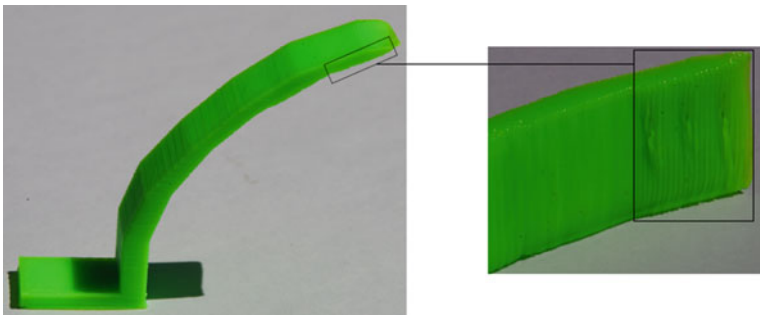


Fig. 3 Printed overhang structure and indicated warpage

in identifying support material zone in FDM and SLA process. There are different approaches to resolve overhang structure problems. One of the familiar methods is to use support structure without optimization in pre-design, and these supports will be removed in post-processing. The literature review on this approach is not discussed here, as this is not related with topology optimization. Another method involves making the structure as self-supporting by identifying the best build direction [16]. Christiansen et al. presented a method that can print a 3D model by 3D printer which can stand itself during process by automatic balancing.

They modeled the structure by tetrahedral mesh to ensure no deformation in exterior shape. They made automatic balancing of model by hollowing technique that can create cavities of lighter and heavier materials in interior. Further, parts are rotated around the base during printing. They optimized center of gravity of model. This is a function of density of tetrahedral elements and position of nodes. Their method can accommodate multiple materials to print infill patterns and support structures. They printed models by fused deposition method without requirement of support structures. They showed that fully void cavities in interior could control the shape of upper portion when bounder cavity exceeds overhang angle. A rare method is to penalize the overhang structure in topology optimization. Different methods are there to implement this idea. Most of the researchers carried investigation to implement the constraint based on the measurement of angle between the structural boundary and the build direction [17]. D. Brackett et al. proposed a topology optimization technique to find out optimum combination of overhang angle and horizontal distance. The suggested algorithm is based on BESO method to recognize boundaries instead of variable density approach. They have not included sensitivity analysis as their work of finding optimum combination algorithm in initial stage. They written algorithm for SLM process [18]. A. T. Gaynor et al. inserted least permissible self-support angle in topology optimization to investigate the printability of structures without employing support material. They eliminated supports by identifying underneath structures that are able to adequately support overhang parts. They evaluated this algorithm on standard problems related to minimum compliance topology optimization. They found the solutions that are satisfying different constraints and mainly that is for the minimum scale length, overhanging angle and volume of the 3D printed part [19].

M. Langelaar et al. investigated a density-based filter topology optimization to print structures using powder bed fusion process of AM. The objective of their research is to eliminate unprintable overhanging structure based on iterative optimization process which provides layer-by-layer printable design. This method imitates the typical AM process. They have not considered the other specifications associated with internal stresses, distortion, enclosed cavities, etc. They related the critical overhang angle and build orientations with the topology formulation. They printed structures for minimized compliance to assess this method. They claimed that computational cost of this method including sensitivity analysis is less in comparison with finite element analysis [20].

Mirzendehdel et al. proposed a topological sensitivity method to reduce the volume of support structure. They implemented this method to print overhang constrained structures such as classical 2D MBB and different brackets by FDM. The

method is preliminary and easy to implement as it does not consider the optimization of AM-related constraints [21]. Qian et al. proposed a density gradient topology optimization technique for minimization of support structure by constraining undercut and overhang angle. They employed density gradient based on Heaviside projection to make single constraint to control undercut and overhang angle. They added density grayness constraint to avoid problems related to intermediate density solutions on density gradient constraint.

They conducted numerical experiments related to MBB beams, cantilever beams, and 2D and 3D heat conduction problems to evaluate the effectiveness of this method [22].

4 Advantages of TO Over AM

SIMP method targets the modification of intermediate densities to result in solid–void structure. Some designs suffer with the less optimal structures. These problems can be overcome with the help of lattice structures. AM capability of printing lattice structures offers an advantage for TO for the optimum design of object to be printed. This makes the researchers to investigate the employability of lattice structures for printing objects with applications in multifunction [23] and low-weight design areas [24].

Wang et al. postulated a topology optimization method to manufacture structures from cellular lattice structures. The proposed method is to optimize load carrying capacity of the parts based on the global shape to be printed and unit cell. They intended to distribute the meso-structure cells globally based on strength requirement, i.e., varying the size spatially. They ensured inter-connections between meso-structure cells by shape metamorphosis technique. They conducted experimental tests to evaluate the stiffness of the optimized structures and compared with the fabricated structures from uniform cells. The TO process employed by them is shown in below Fig. 4. Figure 4a and b represents design domain and optimal structure. Figure 4c indicates the basic meso-structure-employed, (d) variation of relative density and (e) is the final object [25].

5 Concluding Remarks and Future Scope of Work

The topology optimization overcomes the complex design related to issues of material layout within a confined space for a given set of loads, boundary conditions and constraints to maximize the parts performance. With the help of this optimization technique, shape and size of the complex parts can be optimized for successful prototype building. Prototype making and complex parts manufacturing are quite difficult to produce in less cost and time with greater accuracy and having functional capabilities. The topology optimization technique makes the process simple and

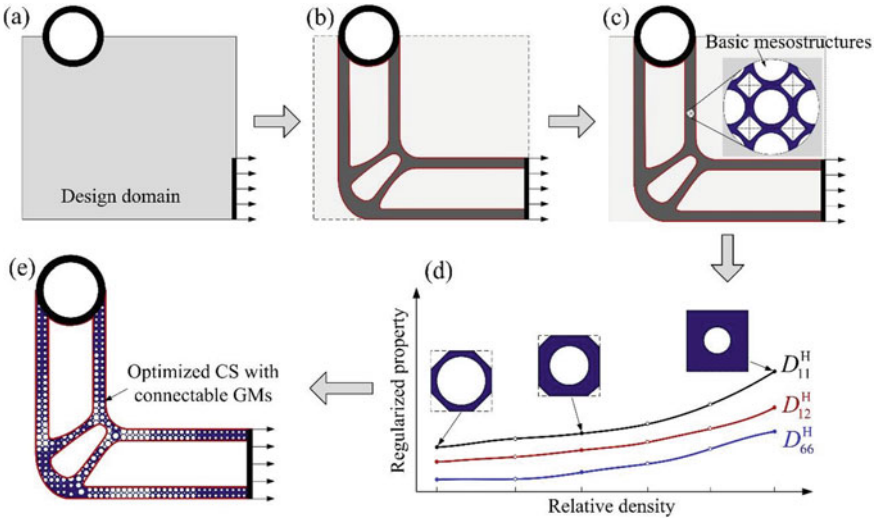


Fig. 4 Schematic presentation of process for optimizing object with graded lattice structure

removes the chance of getting failure in achieving the desired functions in complex parts and prototypes. Additive manufacturing overcomes machining activities, and the parts are manufactured by the addition of materials over and over. The topology optimization produces the platform to understand the design and its performance. The technique is widely accepted by the engineering and medical streams. Through this broad discussion, the readers can identify the researchers to make the process a useful and attained the desired results. The multi-functional and complex parts production difficulties can be analyzed by the use of this technique to make additive manufacturing more productive.

The survey will be helpful in prototyping and machine components manufacturing in aerospace, automotive and biomedical industries. The investigation can further proceed for printing various thermoplastic materials and tested for mechanical, physical, thermal and microstructural properties. The investigation can be planned following the design of experimental techniques to statistically correlate the chosen factors and measured responses. Various geometries and parts can be prepared to see their user ability for practical applications.

References

1. Zhou M, Raphael F, Sam P, Neil S, Dave M, Simon G (2011) Topology optimization-practical aspects for industrial applications. In: Proceeding in the 9th world congress on structural and multidisciplinary optimization. Shizuoka
2. Allaire G, François J, Anca-Maria T (2004) Structural optimization using sensitivity analysis and a level-set method. J Comput Phys 194(1):363–393

3. Bendsoe MP, Sigmund O (2003) Topology optimization–theory, methods and applications. Springer
4. Wang, Michael Y, Wang X, Guo D (2003) A level set method for structural topology optimization. Comput Meth Appl Mech Eng 192(1–2):227–246
5. Zhou S, Qing L (2008) A variational level set method for the topology optimization of steady-state Navier–Stokes flow. J Comput Phys 227(24):10178–10195
6. Ha S-H, Cho S (2005) Topological shape optimization of heat conduction problems using level set approach. Num Heat Trans Part B Fundament 48(1):67–88
7. Yamada T, Kazuhiro I, Shinji N (2011) A level set-based topology optimization method for maximizing thermal diffusivity in problems including design-dependent effects. J Mech Design 133(3):031011
8. Scott CS (1992) Apparatus and method for creating three-dimensional objects. US Patent 5,121,329
9. Hull, CW (1986) Apparatus for production of three-dimensional objects by stereo-lithography. US Patent 4,575,330
10. Meiners W, Wissenbach K, Gasser A (1998) Shaped body especially prototype or replacement part production. DE Patent 19
11. Deckard, CR. (1989) Method and apparatus for producing parts by selective sintering. US Patent 4,863,538
12. Wu J, Christian D, Rüdiger W (2015) A system for high-resolution topology optimization. IEEE Trans Visual Comput Graphics 22(3):1195–1208
13. Mumtaz K, Vora P, Hopkinson N (2011) A method to eliminate anchors/supports from directly laser melted metal powder bed processes. In: Proceedings of the solid freeform fabrication symposium. Austin, TX, USA, pp 8–10
14. Calignano F (2014) Design optimization of supports for overhanging structures in aluminum and titanium alloys by selective laser melting. Mater Des 64:203–213
15. Grégoire A, Dapogny C, Estevez R, Faure A, Michailidis G (2017) Structural optimization under overhang constraints imposed by additive manufacturing technologies. J Comput Phys 351:295–328
16. Gardan N, Alexandre S (2015) Topological optimization of internal patterns and support in additive manufacturing. J Manuf Syst 37:417–425
17. Christiansen AN, Andreas Bærentzen J, Nobel-Jørgensen M, Aage N, Sigmund O (2015) Combined shape and topology optimization of 3D structures. Comput Graphics 46:25–35
18. Brackett D, Ashcroft I, Hague R (2011) Topology optimization for additive manufacturing. In: Proceedings of the solid freeform fabrication symposium vol. 1. Austin, TX, pp 348–362
19. Gaynor AT, James KG (2016) Topology optimization considering overhang constraints: Eliminating sacrificial support material in additive manufacturing through design. Struct Multidis Optimiz 54(5):1157–1172
20. Langelaar MM (2017) An additive manufacturing filter for topology optimization of print-ready designs. Struct Multidisc Optimiz 55(3):871–883
21. Mirzendehdel AM, Krishnan S (2016) Support structure constrained topology optimization for additive manufacturing. Comput-Aided Design 81:1–13
22. Qian X (2017) Undercut and overhang angle control in topology optimization: a density gradient based integral approach. Int J Num Meth Eng 111(3):247–272
23. Valdevit L, Alan JJ, Julia RG, William BC (2011) Protocols for the optimal design of multi-functional cellular structures: from hypersonics to micro-architected materials. J American Ceramic Soc 94: s15–s34
24. Jian X, Mines R, Ghosh R, Vaziri A, Ma L, Ohrndorf A, Christ H-J, Wu L (2015) Advanced micro-lattice materials. Adv Eng Mater 17(9):1253–1264
25. Wang Y, Lei Z, Stephen D, Zhang H, Stefanie FM, Wang Y (2018) Design of graded lattice structure with optimized mesostructures for additive manufacturing. Mater Design 142:114–123

Design and Development of Digital Light Processing (DLP) 3D Printer

Yogesh Patil, Richa Patil, N. S. Chandrashekhar, and K. P. Karunakaran

Abstract Additive manufacturing (AM), also referred to as three-dimensional printing, produces three-dimensional parts by adding material of specific layer thickness layer by layer. It is well known for its capability to create intricate and complex geometric parts and minimize the wastage of material unalike conventional manufacturing. The digital light processing (DLP) is one of the AM technologies and uses photopolymer resin as a material in liquid form and ultraviolet (UV) light to convert liquid resin into solid geometry of size and shape as per 3D model. This technique comprises of two approaches, top-down and bottom-up. In this paper, the latter method has selected for further design and development. This paper explains the overall idea of designing and fabricating the DLP 3D printer through indigenization and innovation, starting from choosing an approach to conducting the experiments. The methodology behind the design and development of the indigenous DLP 3D printer and the various problems encountered during this development have been discussed. Further, it briefly explains in-depth study carried out for the selection of several components of the printer, viz. optical components such as the projector and its orientation, mechanical components such as build platform, vat, and electronic components like stepper motor and microcontroller and shield. Conclusions have been drawn based on the results obtained after several preliminary testing carried out during this study.

Keywords Digital light processing · Micro-stereolithography · Photopolymerization · Rapid prototyping · Additive manufacturing

Y. Patil (✉) · K. P. Karunakaran
Indian Institute of Technology Bombay, Mumbai 400076, India
e-mail: patil.yogesh0808@gmail.com

R. Patil
TATA Consultancy Services, Pune 411057, India

N. S. Chandrashekhar
K J Somaiya College of Engineering Vidyavihar, Mumbai 400077, India

© Springer Nature Singapore Pte Ltd. 2020

A. Praveen Kumar et al. (eds.), *Advances in Lightweight Materials and Structures*,
Springer Proceedings in Materials 8, https://doi.org/10.1007/978-981-15-7827-4_67

1 Introduction

Additive manufacturing (AM), including its various techniques known as "three-dimensional (3D) printing," is the youngest of all manufacturing principles. The key to the process is that it builds up parts gradually by the addition of material in layers under full digital control. That is in contrast to the "subtractive" conventional techniques, which involve taking material in the form of blocks, removing the material to get the right size and shape [1]. AM produces 3D parts from 2D layers built one over the other. The kin interest in AM technologies is not a surprise, as this layer-wise additive method is an advanced tool that creates complex 3D objects using a different material with no tools and fixtures [2]. AM is divided into several processes [3], viz. stereolithography (SLA), fused deposition modeling (FDM), digital light processing (DLP), selective laser sintering (SLS), etc. The DLP 3D printer consists of several components, viz. DLP projector (dynamic mask), photopolymer resin, resin container, and build platform shown in Fig. 1a.

The 3D model is modeled using computer-aided design (CAD) software and converted into the STL format. The STL file then sliced into several layers by using slicing or host software. Each layer, containing the geometric information, is transmitted to the 3D printer sequentially. An image then projected by the DLP projecting system on the transparent basin containing a photopolymer resin [4]. UV light falls on the resin containing photoinitiators, monomer, and blockers, then polymerization reaction takes place, and the layer gets cured. After curing a thin layer, the motor moves the build platform by a distance equal to the layer thickness in an upward or downward direction. A new image is projected, and this continues until a 3D part is ready [5]. In the photopolymerization process, a monomer and oligomer (liquid) converted into a polymer (solid) with the help of UV light of wavelength 360–420 nm. The objective of this study is to build a high-resolution DLP 3D printer by indigenization and innovation.

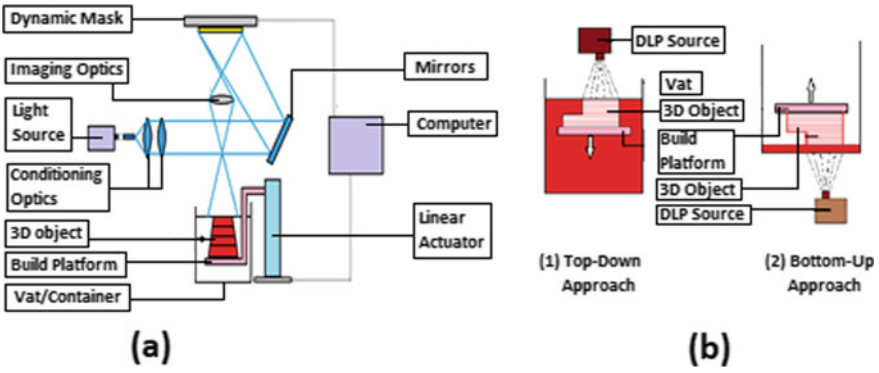


Fig. 1 **a** Schematic of the DLP 3D printer; **b** DLP 3D printing approach

2 Methodology

The methodology for this research paper has outlined as follows:

1. Literature survey: The literature survey for this research was done extensively by a detailed study of several research papers, journals, scientific projects, and similar existing machines.
2. Conceptualization: Understanding the working mechanism and identification of various components of the machine have been carried out.
3. Design: The design part includes a comparative study and selection of components for the designing of the machine.
4. Prototyping: The prototyping phase marks the beginning of the first tangible iteration of the design, which helps us to know the pitfalls in the method and how to overcome it in the subsequent iterations.
5. Preliminary testing: Preliminary testing conducted to create 3D objects under various conditions. Results were studied, and conclusions have been drawn to arrive at the optimal design of the machine to get better results.
6. Improvement: Modifications based on preliminary testing were carried out in the prototype to get the final machine.

3 Design and Fabrication of the DLP 3D Printer

The design and fabrication of the DLP 3D printer comprise optical, mechanical, and electronic components. The most critical consideration in the design of the DLP 3D printer is the orientation, how the system projects light on the build surface. There are two basic orientations, viz. top-down and bottom-up as shown in Fig. 1b.

The top-down approach is referred to as a free surface method, where the light source is mounted at the top of the system [4, 5], while the bottom-up approach is referred to as a fixed surface method. Considering the advantages and limitations of both approaches, it has decided to choose the bottom-up approach. Table 1 shows the design solutions implemented in the design of the DLP 3D printer.

Table 1 Solutions implemented in the design of the 3D printer [6, 7]

Sub-functions	Light source	Conditioning optics	Pattern light	Projector orientation	Imaging optics	Recoat method
Solutions	UV lamp	Collimation	DLP (DMD)	Bottom-up	Expansion	Gravity

3.1 Optical System

A UV light projector is required to project a sequence of images and to emit the UV light simultaneously. The minimum specifications required for a projector are 2500 lumens power and light wavelength in the range of 350–420 nm. The DLP projectors mentioned in Table 2 are considered for the projection.

The BenQ M525P was selected due to easy availability and mounted on the aluminum frame using a wooden base shown in Fig. 2a. Results of the preliminary tests performed found that the projector needs tweaking to get the desired power and the UV output. First, the color wheel needs to be removed, which prevents fast and reliable curing of the resin [8, 9]. But, removing the wheel will shut down the projector multiple times during the use. So, it was essential to remove the color wheel from the light path without shutting down the projector. Figure 2b shows the color wheel position in the projector. It was removed from the light path and kept inside the projector wherever enough space was available without cutting wires and then breaking the glass from the wheel motor.

Second, the UV filters may not be applied to all projector brands. In some projectors, the filters have been located within the projector's lamp assembly [10, 11]. Sometimes, one filter is located within the lamp and the other in front of it as shown in Fig. 2c. Both of them have been removed to reach the desired power output. But by removing them, the projector can be exposed to infrared (IR) radiation along with UV light, which eventually increases the heat and subsequently reduces the life of the projector, and hence installing an IR filter will avoid this, which allows only UV light to pass.

Final tweaking is the lens modifications, and the focus adjustment is not essential for short-throw lens projectors but can become critical for projectors that cannot

Table 2 Comparison between DLP projectors

Projector	Resolution	Contrast ratio	Brightness (lumens)	Lamp power (W)
Acer H6510BD	1920 * 1080	10,000:1	3000	210
Acer X1213P	1024 * 768	10,000:1	2700	210
BenQ M525P	1024 * 768	2600:1	2500 l	210



Fig. 2 **a** BenQ M525P mounting; **b** Color wheel; **c** UV filters; **d** lens stopper

focus when mounted very close to the build area [11]. As shown in Fig. 2d, a stop mechanism in the projectors does not allow the lens removal. The new turns for focus can be obtained by bending or removing this stopper, which can be a metallic piece or a screw. For the projector with a long throw, merely placing the projector farther away will not help since more significant the distance, higher the UV light loss, and thus resulting in low output. These are the necessary modifications required to attain a decent amount of power and UV output. But, if the projector's specifications do not comply with the absolute minimum requirements, these modifications will not be useful. After preliminary experiments, it was found that the time required for curing the 50 μm layer is five to ten times more than the time recommended by the respective resin manufacturer. So, we decided to buy a new DLP projector, Acer X1213P, for further study [5].

3.2 Build Material

Photopolymer resin in the liquid form is used as a material in the DLP 3D printer [9]. There are several resins available in the market; the Makerjuice G+ and Fun To Do resins are used for several preliminary tests.

3.3 Mechanical System

The mechanical system involves the design and fabrication of the mechanical components required for the DLP 3D printer which is shown in Fig. 1a. Aluminum profile extrusions of 30 mm * 30 mm cross section used for frame structure are shown in Fig. 2a because of the low weight and universal availability of fixtures and joints.

Resin bath or container is called vat in DLP 3D printing [12]. The selection of the vat depends upon the cost of the material and its transmissibility to the UV light. The build area calculation [13] is crucial to determine the size of the vat and is as follow:

Build area width = Projector width resolution in pixels * Desired *X* resolution.

Build area length = Projector width resolution in pixels * Desired *Y* resolution.

Hence, for the BenQ M525P projector with 50 μm *XY* resolution, the build area is 51 mm * 38 mm approximately. Since the vat size must be larger than the build area, initially, the borosilicate glass vat of size 200 mm * 200 mm * 40 mm was fabricated as shown in Fig. 3a. It has found that the vacuum force is directly proportional to the vat size. Hence, several design iterations were carried out and tested to decrease the vacuum force. So, the design in Fig. 3b was finalized due to its flexibility to use different anti-stick material with a size of 100 mm * 100 mm * 35 mm [14]. Also, acrylic was preferred over borosilicate glass as a vat base because of its availability and low brittleness. A silicone rubber gasket is also added to avoid any resin leakage.

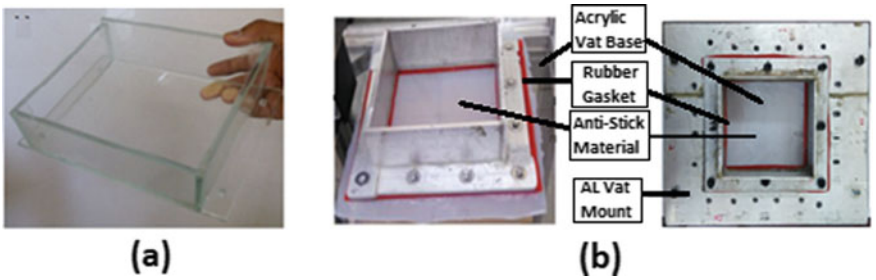


Fig. 3 **a** Vat design iterations; **b** final vat design

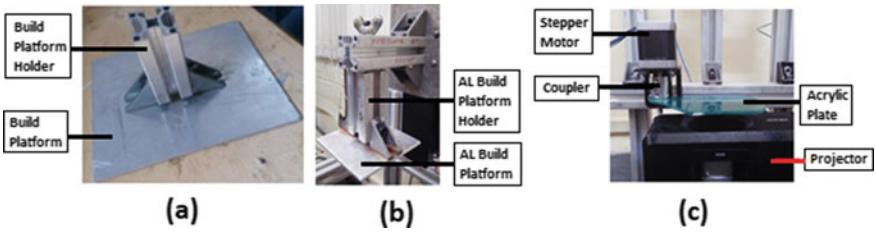


Fig. 4 **a** First build platform; **b** Final build platform; **c** Shutter mounting

The material for build platform is chosen such that the first layer sticks to its bottom surface, and the completed 3D object peeled off easily. Due to high corrosion resistance and rough at the microscopic scale, the anodized aluminum plate was used. Since platform size must be larger than the vat, initially, the platform of size 160 mm * 160 mm was fabricated, as shown in Fig. 4a. After several testings and iterations, it was found that the larger the platform size, the higher the vacuum force resulting in the first layer sticking to the vat surface instead of the platform. Hence, the platform size was reduced to 75 mm * 75 mm, as shown in Fig. 4b.

The DLP 3D printer features linear motion in the z-axis, achieved by the use of a linear guide—HIWIN KK50 with an anti-backlash nut. It has unique features of allowing high loading in all orientations. The alloy steel flexible coupler is selected to couple shafts of motor and ball screw shaft. In the preliminary testing, it has observed that when the projector is not projecting the sliced image, it projects a black image on the vat surface. The black image also contains a small amount of energy which tries to excess cure the resin to a small extent, results in degradation of resin; hence, a non-UV transparent shutter was introduced in front of the lens, as shown in Fig. 4c.

3.4 Electronic System

The electronic system involves microcontroller, power supply unit (PSU), motors, drivers, sensors, etc. The controller takes inputs from software and accordingly sends commands to the motors and sensors. It has decided to go with widely used microcontroller Arduino Mega 2560 along with Reprap Arduino Mega Polulu Shield (RAMPS 1.4) [15, 16]. To protect the system against current–voltage fluctuation, the ATX PSU has used. For the z-axis and the shutter movement, two NEMA 17 stepper motors were used [17]. Calculations performed to determine the minimum torque required. To specify the home/reference location, a three-wire mechanical end-stop has used.

3.5 Software and Firmware

A 3D CAD model is created using any 3D package [18]. A more reliable and open-source software named Creation Workshop (CW) is selected as host software [19] and also referred to as slicing software. It takes 3D files (.stl files) as input and slices into horizontal layers then converts into a series of paths. This information is then sent to the microcontroller via the firmware, which controls the movement of the printer. To write, edit, and upload the firmware into the Arduino board [16], the Arduino IDE software is used. Out of several open-source firmware available, Marlin firmware is considered for the study.

3.6 Fully Functional DLP 3D Printer

All the mechanical parts assembled, electric connections made, and a fully functional DLP 3D printer developed, as shown in Fig. 5, and Table 3 shows the brief specifications.

This 3D printer has several applications, such as making patterns for investment casting, functional testing prototypes, visual prototypes for market testing, molds for high precision industry, viz. dental, jewelry, art, and many more [20].

4 Conclusions

Following conclusions have been drawn from this research work:

1. The 3D printer based on DLP technology was successfully designed and fabricated by focusing on the critical aspects of it. The function of every possible component of the DLP was deeply studied to arrive at an optimal design.

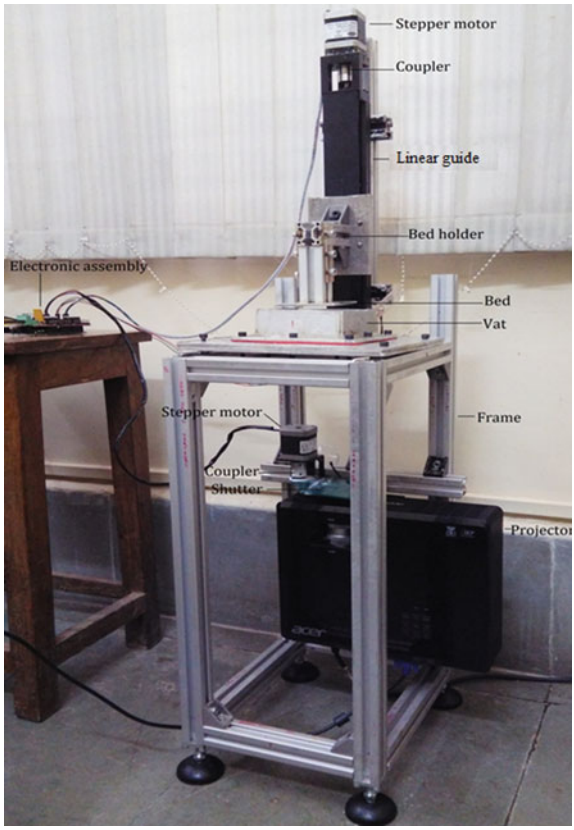


Fig. 5 Final 3D DLP 3D printer

Table 3 Final specifications of the DLP 3D printer

Layer thickness (μm)	*X*, *Y*, Resolution (μm)	Print speed (mm/hr)	Vat dimension (mm^3)	Actual build volume (mm^3)	Machine dimensions (mm^3)
5–50	50	4.0214	100 * 100 * 35	75 * 75 * 100	350 * 320 * 1065

2. A bottom-up approach has preferred over top-down, and further development is carried out. The prime focus has been given on the development of the machine, not on its aesthetic.
3. The design and development of the machine were categorized in different aspects, viz. mechanical, electronic, optical, build material, and software & firmware.
4. An in-depth study carried out shows that the vat, build platform, the projector are the essential aspects of the DLP 3D printer.

5. The leak-proof vat assembly is a must, and no air should be trapped. Experiments conducted show that the best solution to the vat sticking issue is the use of FEP film because of its low cost, wrinkle-free nature, better UV transmissivity, less deformation, etc.
6. Special care has been taken while designing the build platform such that the very first layer of resin should stick to its surface to get the final object.
7. The projector, BenQ M525P, after necessary tweaking, does not give the required amount of UV output, hence used Acer X1213P DLP projector.
8. The shutter is introduced to avoid any degradation of resin when it is not projecting the sliced image.
9. Stepper motor with DRV8825 gives better resolution compared to Polulu A4988 due to its higher micro-stepping format and better current management.
10. The use of the HIWIN KK0 linear guide provides the highest level of accuracy due to its anti-backlash property.

Further research can be carried out to improve peeling off the layer from the vat surface using various peeling mechanisms and anti-stick material. Also, the effect of focal distance on the UV light output, as well as the impact of the high-resolution projector on the mechanical properties of the object, can be studied.

References

1. Arnaud B, Philippe R (2016) Chapter 1.2 Microstereolithography. In: William Andrew Applied Science Publishers, Lausanne, Switzerland. https://doi.org/10.1016/B978-0-323-35321-2.00002-9
2. Gibson I, Rosen D (2015) Additive manufacturing technologies: 3D printing, rapid prototyping and direct digital manufacturing. Johnson Matthey Technol. Rev 59(3):193–198
3. Patil R, Patil Y (2016a) Microstereolithography: concepts and methods. Int J Modern Trends Eng Res (IJMTER) 3(4):1051–1057
4. Gibson I, Rosen DW, Stucker B (2010) Additive manufacturing technologies: rapid prototyping to direct digital manufacturing. Springer, New York, pp 61–82
5. Choi J-W, Kim H-C, Wicker R (2011) Multi-Material stereolithography. J Mater Process Technol 211(3):318–328. https://doi.org/10.1016/j.jmatpro-tec.2010.10.003
6. Mellor S, Hao L, Zhang D (2014) Additive manufacturing: a framework for implementation. Int J Prod Econ 149:194–201
7. Lambert PM, Williams CB, Long TB, Bickford LR (2014) Mask projection microstereolithography system for the characterization and processing of novel photopolymer resins
8. Galante AMS, Galante OL, Campos LL (2010) Study on application of PTFE, FEP and PFA Afluoropolymers on radiation dosimetry. Nucl Instrum Methods Phys Res A619:177–180
9. Chandrashekhar VA, Parag B, Prasanna G (2015) Effect of surfactant on dispersion of alumina in photopolymerizable monomers and their UV curing behavior for microstereolithography Ceram Int 41:5301–5308
10. Sun C, Fang N, Wu DM, Zhang X (2005) Projection microstereolithography using digital micro-mirror dynamic mask. Sens Actuat A121:113–120
11. Meier RE (1998) Digital light process for 3D printing. Texas Inst Technol J 15:64
12. Schwalm R (2012) Radiation curing polymer systems, 567–579
13. Patil Y, Patil R (2016b) Improving Stereolithography Resolution. Int J Modern Trends Eng Res (IJMTER) 3(4):1045–1050

14. Yogesh P, Richa P, Chandrashekhar NS, Karunakaran KP (2020) Layer separation mechanisms in DLP 3D Printing. In: Shunmugam M, Kanthababu M (eds) Advances in additive manufacturing and joining. Lecture notes on multidisciplinary industrial engineering. Springer, Singapore
15. Preserve Articles Chemistry glass type page, https://www.preservearticles.com/201012291928/glass-types.html. Last Accessed on 16 Oct 2019
16. Arduino Homepage, https://www.arduino.cc. Last Accessed on 5 April 2019
17. Jose Q (2010) High-resolution microstepping driver with the DRV8825/28/29/40. Texas Instruments. Application Report-SLVA443
18. Joseph MD, Alexander E, Nikita E, Edward TS (2014) WO2014126837 A2. Continuous Liquid Interphase Printing
19. Reprap Firmware page, https://reprap.org/wiki/List_of_Firmware. Last Accessed on 25 Jan 2019
20. Thnik3D 3d printing page, https://www.think3d.in/stereolithography-sla-3d-printing-service-india/. Last Accessed on 20 Mar 2019

A Review on the Challenges in Welding of Aluminium AA2219 Alloy



M. A. Trishul and Bijayani Panda

Abstract Al–Cu (2000 series) alloys are used for applications which require higher damage tolerance and fatigue resistance. Aluminium alloy AA2219 has superior weldability because of its low sensitivity to hot cracking. However, it suffers from poor strength at weld joint. The reduction in strength is because of melting and solidification of the alloy, which results in the dissolution of the strengthening precipitates and formation of large columnar grains. Also, due to the rapid melting and solidification process, the originally present precipitates may not dissolve completely. In such cases, the weld region may show small number of coarse precipitates, widely distributed. The segregation of Cu at grain and dendritic boundaries results in depletion of Cu at the grain interiors, resulting in a decrease in mechanical properties. The present paper reviews such kind of challenges faced during welding of aluminium alloy AA2219. Various methods like post-weld heat treatment (PWHT), weld pool agitation, pulsed current, magnetic arc oscillation, friction stir welding (FSW) and electron beam welding (EBW) are discussed.

Keywords AA2219 · Fusion welding · Hot cracking · HAZ · Precipitation

1 Introduction

Precipitation-hardened aluminium alloys are widely used in the aerospace sector as structural components for more than 80 years [1]. These precipitation-hardened aluminium alloys possess superior strength-to-weight ratio [2]. The most widely used alloys of aluminium are the 2XXX, 6XXX and 7XXX series, since these grades can be heat-treated.

The Al–Cu (2000 series) alloys are used for applications which require higher damage tolerance and fatigue resistance [1]. During fusion welding, aluminium

M. A. Trishul
Department of Mechanical Engineering, PES University, Bengaluru 560100, India

B. Panda (✉)
Department of Mechanical Engineering, CMR Institute of Technology, Bengaluru 560037, India
e-mail: bijayani.p@cmrit.ac.in

© Springer Nature Singapore Pte Ltd. 2020

A. Praveen Kumar et al. (eds.), *Advances in Lightweight Materials and Structures*,
Springer Proceedings in Materials 8, https://doi.org/10.1007/978-981-15-7827-4_68

alloys show loss of strength in the weld and HAZ region [3]. They are also susceptible to solidification cracking and hot cracking due to the high thermal expansion, wide solidification temperature range and large change in volume after solidification [4]. The aluminium alloy AA2219 exhibits very low sensitivity to high-temperature cracking [4, 5]. AA2219 is primarily an alloy of Al–Cu–Mn with small amounts of Zr, V, Ti and Fe. The low sensitivity to high-temperature cracking of the alloy is because of the amount of Cu (6.5%) which provides extra low melting eutectic (α-Al + $CuAl_2$, containing around 32% Cu) to heal the cracks [4–6]. Because of its low sensitivity to hot cracking, AA2219 has superior weldability. It also has superior fracture toughness, high specific strength and superior stress corrosion cracking resistance. AA2219 alloy is mainly used for fabrication of aircraft, space vehicle and missile [2, 3, 7, 8]. The superior fracture toughness of AA2219 in the range of + 250 to −250 °C makes it an ideal material for cryogenic applications such as storage tanks to store liquid nitrogen and oxygen [3, 4, 7, 9]. AA2219 alloy is generally used in T87 temper (solution heat-treated later cold worked to a reduced thickness of 10% and finally artificially aged). Although AA2219 has superior weldability, it possesses poor strength at the weld joint, like other heat treatable aluminium alloys [7, 8, 10].

2 Conventional Welding of AA2219

Generally, the preferred joining methods used for AA2219 alloy are gas tungsten arc welding (GTAW) and gas metal arc welding (GMAW) as they are economic and easy to apply [3, 7, 8]. GMAW possesses certain advantages like high in deposition rate, higher welding speed and also deep penetration [11]. However, the heat supplied is higher than in GTAW and it may result in distortion of the parts being welded, especially thin sheets or plates. The GMAW also result in coarse size in columnar grains at the weld zone Fig. 1a, b [5] and increased dissolution and redistribution of the copper-rich precipitates [5, 12]. Therefore, it results in hot cracking and poor mechanical properties in the as-welded joint. In such cases, GTAW method is preferable [4].

The reduction in strength of the weld can be as high as around 40% with respect to the base metal using conventional welding methods [13]. Due to rapid melting and solidification, the originally present precipitates may dissolve completely. In such cases, the weld region may show up minimum number of coarse size precipitates, widely distributed. In addition, the Cu segregation at grain and dendritic boundaries ends up in depletion of Cu at the grain interiors as shown in Fig. 2a, b [10], thereby resulting in decrease in mechanical properties [6]. The copper segregation at grain boundaries in the as-welded structure also results in poor response of the weld to natural ageing [10].

The HAZ region is exposed to a temperature of 490–548 °C which results in dissolution and re-precipitation of the strengthening precipitates in grain boundaries [12]. Also, the HAZ region shows overageing phenomena (formation of θ' and later

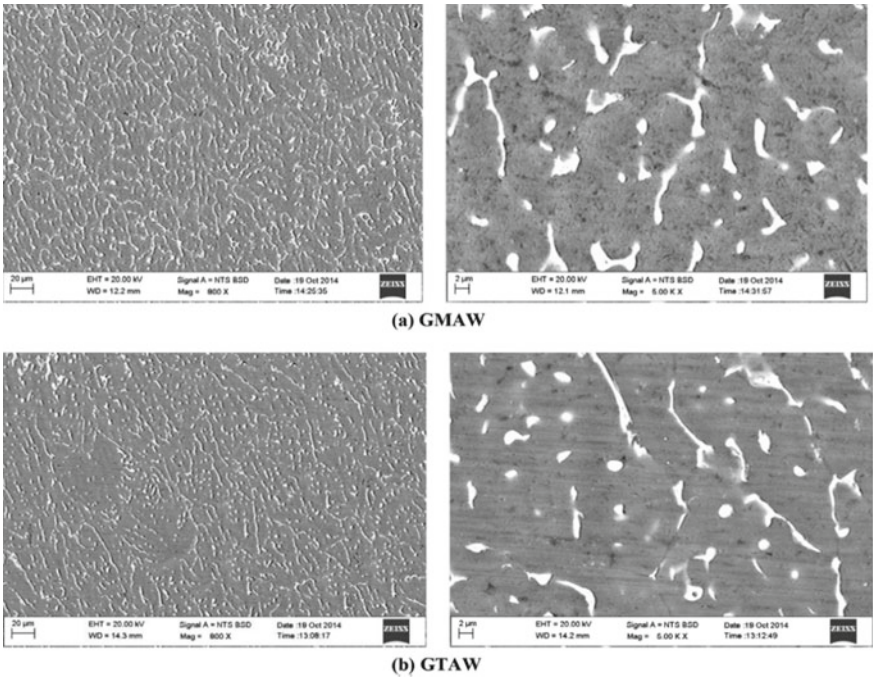


Fig. 1 **a**, **b** Minor variation in microstructure of GTAW compared with GMAW [5]

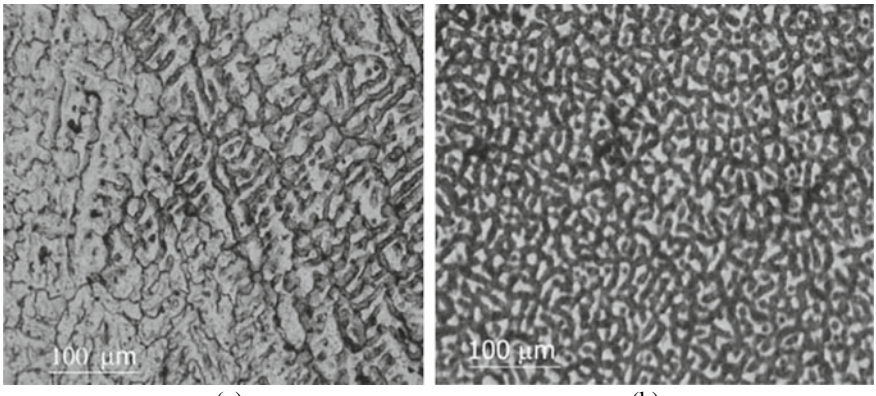


Fig. 2 Microstructure showing **a** Cu segregation at dendritic boundaries. **b** Cu segregation at the grain boundaries [10]

θ phase) due to the slow cooling rate, resulting in coarse grains and precipitates [14]. Overageing in the HAZ may result in poor mechanical properties in the HAZ region due to extended time of solidification in the HAZ region.

2.1 *Overcoming Problems Associated with Conventional Welding*

Post-weld heat treatment (PWHT) is preferred for aluminium alloys as it improves the size, shape as well as distribution of the strengthening precipitate, thereby results in improved weld strength [14, 15]. However, if the fabricated component is complicated or too large, it is practically not feasible to go for post-weld heat treatment after welding.

Apart from PWHT, weld pool agitation methods like pulse current techniques and magnetic arc oscillation have shown some improvement in the mechanical properties along with HAZ. These methods have been found to induce grain refinement due to stirring effect [10, 12, 14, 16]. The eutectics form discontinuous rounded particles, rather than connected network. Current pulsing with GTAW method helps in the refinement of the fusion zone microstructure [17]. Variable polarity tungsten inert gas (VPIG) process is also a novel method which enables cathode cleaning and reduces deterioration of the tungsten electrode [14]. This method was used by Ding et al. [14] to study the mechanical behaviour of welded AA2219 alloy. They found that PWHT significantly improved the mechanical properties of the welded samples. Similar work was carried out by Lin et al. [18] wherein they studied the cryogenic fracture toughness of AA2219 welded by VPTIG as shown in Fig. 3 [18].

They found that the opening of crack tip displacement values at 77 K was around 20% higher after PWHT. In another research work, the tensile strength increased by 44% while the corrosion resistance of AA2219 welds also improved on PWHT

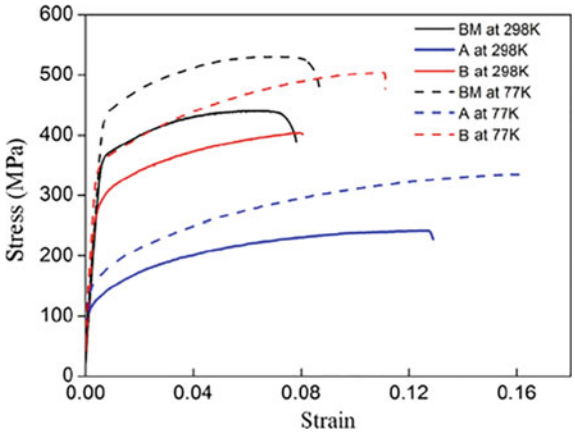


Fig. 3 Curves of micro-mechanical tensile tests. **a** The weld metal of as-welded joint, marked as sample A; **b** the weld metal of post-weld heat-treated joint, marked as sample B; **c** the base metal used for comparison, marked as BM [18]

after VPTIG welding. The improvement in properties was explained to be due to homogeneous microstructure obtained after PWHT [12].

3 Advanced Welding Methods

Other techniques like friction stir welding (FSW) and electron beam welding (EBW) results in faster cooling therefore incomplete dissolution of the $CuAl_2$ precipitates. These welding processes result in superior mechanical properties at the weld zone due to the uniform distribution of the $CuAl_2$ precipitates.

FSW is solid-state joining process where weld does not recast or melt [8]. FSW is feasible technique and also eco-friendly which could be preferred for joining high strength alloys of aluminium and other metallic materials which could be hard to weld by the conventional-type fusion welding processes [19]. During welding process, the heat generated followed with thermal cycle changes in the perpendicular path of welded region. The higher temperature in the FSW zone is caused due to action of stirring of the plasticized material, which results in altering the precipitate distribution in the base material. The temperature distribution in FSW results in change of strength and ductility of the joints [8, 20]. Further improvement in mechanical properties can be obtained by PWHT [21].

The size of the grain and effect on orientation of weld nugget are caused by the tool profile in case of FSW technique [22, 23]. The conical and triangular tool profiles are shown in Fig. 4 [23].

The high amount of heat generated using triangular profile causes strengthening precipitates dissolution in the nugget zone [23]. This leads to superior pitting corrosion resistance for triangular profile of tool in comparison with conical profile of

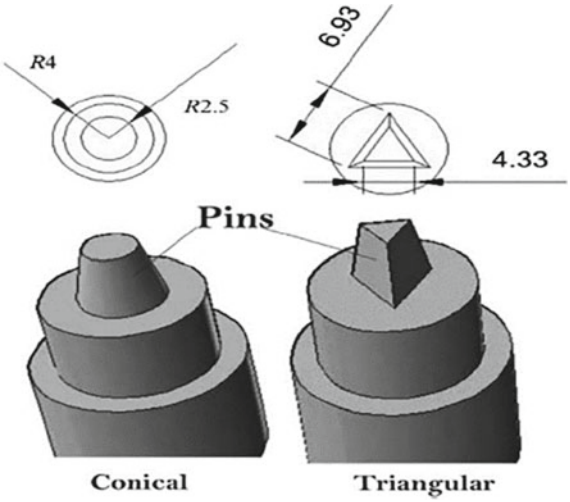


Fig. 4 Conical and triangular tool profile for friction stir welding (all the dimensions are in mm) [23]

tool. Proper selection of profile of tool is, therefore, critical in obtaining a combination, optimizing both corrosion and mechanical properties [22, 23]. If the corrosion properties are to be improved, the amount of $CuAl_2$ precipitates needs to be reduced but the mechanical properties will be adversely affected [23].

Electron beam welding (EBW) utilizes high power density and therefore allows for high-speed joining of much thicker sections than can be carried out using conventional arc welding methods [7]. PWHT has been found beneficial in improving the mechanical properties of welds obtained by EBW welding method [7, 13, 24]. EBW technique using pulsed current was shown to produce higher fusion zone strength and hardness because of grain refinement, low segregation of copper, increased number of dislocations, and also natural ageing [10]. In a study, the fatigue cracking of AA2219 alloy welded by EBW was studied after PWHT [13]. The fatigue cracking resistance was found to be superior after PWHT due to the uniformity in microstructure and removal of residual stresses. A comparison of the fatigue properties of AA2219 welded samples prepared by GTAW, EBW and FSW was done [25]. The results from Fig. 5 [25] indicate that FSW welded samples possessed superior fatigue properties compared to GTAW and EBW due to the formation of fine grains and fine precipitates at the weld zone.

However, the corrosion properties of the FSWs were much lower compared with other two welds prepared by GTAW and EBW methods [8]. The lowering of corrosion performance is explained as follows. In aluminium alloys, the second phase particles have different electrochemical potentials compared to the matrix. Mainly, in AA2219 alloys, the strengthening precipitate $CuAl_2$ is cathode with respect to the matrix (solution potential of -0.64 V of $CuAl_2$ compared to -0.73 V of the matrix) [20, 26]. Therefore, the noble $CuAl_2$ and the matrix form galvanic couple. With respect to the advanced welding methods, it has been brought into account that the corrosion properties of the weld joint are generally inferior due to more number of finely

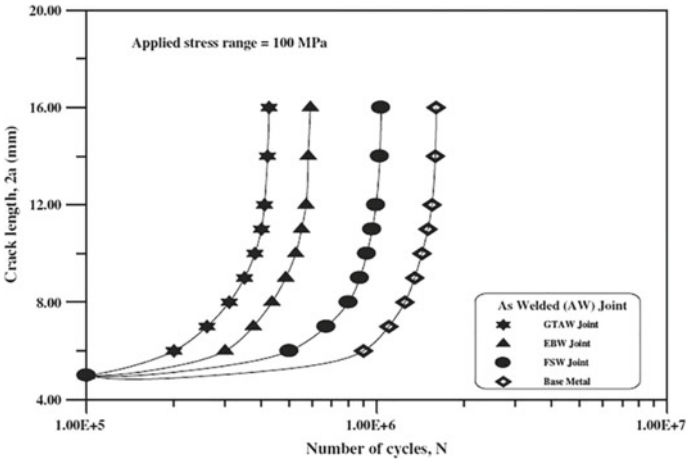


Fig. 5 Comparison of fatigue life for various joining process [25]

distributed $CuAl_2$ precipitates available in the welds, which results in more number of initiation sites for pitting corrosion [8, 20, 26].

In comparison, there are some reports which show that the corrosion property is also enhanced along with the improvement in mechanical properties. The pitting corrosion resistance property of AA2219-T87 alloy, as assessed by potentiodynamic polarization studies, was found to be superior for EBW welded alloy compared to GTAW welded alloy [27]. The tensile properties were also found to be superior. This has been explained by the presence of coarsened particles of $CuAl_2$ and also segregation of Cu at grain boundaries in case of GTAW weld leading to poor corrosion as well as tensile behaviour of the weld. Therefore, there are conflicting reports on the corrosion performance, although it has been widely accepted that the advanced welding techniques improve the mechanical properties of welded AA2219.

4 Conclusions

- Welding of AA2219 alloys poses several challenges during fusion welding due to coarse grains of strengthening precipitates, segregation of Cu at the grain boundaries and also because of grain coarsening.
- Stirring effect introduced in the conventional arc welding process, i.e. gas tungsten arc welding (GTAW) and gas metal arc welding (GMAW) and post-weld heat treatment (PWHT), generally produces a more uniform microstructure and improves the mechanical properties compared to any other type of welding process.
- Advanced welding methods like FSW and EBW are generally found to produce superior mechanical properties in AA2219 alloy.
- Interestingly, there are conflicting reports on the effect of these novel welding methods on corrosion behaviour of AA2219 alloy.
- By going through all the references, the authors suggest that future work needs to be carried out on the advanced methods of welding in order to optimize the corrosion as well as mechanical properties of AA2219 alloy.

References

1. Dursun T, Soutis C (2014) Recent developments in advanced aircraft aluminium alloys. Mater Des 56:862–871
2. Narasayya CVA, Rambabu P, Mohan MK, Mitra R, Eswara Prasad N (2014) Tensile deformation and fracture behaviour of an aerospace aluminium alloy AA2219 in different ageing conditions. Proc Mater Sci 6:322–330
3. KoteswaraRao SR, Madhusudhan Reddy G, SrinivasaRao K, SrinivasaRao P, Kamaraj M, Prasad Rao K (2004) Gas tungsten arc welded AA219 alloy using scandium containing fillers-mechanical and corrosion behavior. Trans Ind Inst Metals 57(5):451–459
4. Gupta RK, Narayan Murty SVS (2006) Analysis of crack in aluminium alloy AA2219 weldment. Eng Fail Anal 13:1370–1375

5. Arunkumar S, Rangarajan P, Devakumaran K, Sathiya P (2015) Comparative study on transverse shrinkage, mechanical and metallurgical properties of AA2219 aluminium weld joints prepared by gas tungsten arc and gas metal arc welding processes. Defence Technol 11:262–268
6. KoteswaraRao SR, Madhusudhan Reddy G, Prasad Rao K (2008) Effects of thermo-mechanical treatments on mechanical properties of AA2219 gas tungsten arc welds. J Mater Process Technol 202:283–289
7. Malarvizhi S, Raghukandan K, Viswanathan N (2008a) Effect of post weld ageing treatment on tensile properties of electron beam welded AA2219 aluminum alloy. Int J Adv Manuf Technol 37:294–301
8. Malarvizhi S, Balasubramanian V (2011a) Effect of welding processes on AA2219 aluminium alloy joint properties. Trans Nonferrous Metals Soc China 21:962–973
9. Narayana GV, Sharma VMJ, Diwakar V, Kumar KS (2004) Fracture behavior of aluminium alloy 2219–T87 welded plates. Sci Technol Weld Joining 2:121–130
10. Nair BS, Phanikumar G, Prasad Rao K, Sinha PP (2007) Improvement of mechanical properties of gas tungsten arc and electron beam welded AA2219 (Al–6 wt-%Cu) alloy. Sci Technol Weld Join 12(7):579–585
11. Manti R, Dwivedi DK, Agarwal A (2008) Pulse TIG welding of two Al−Mg−Si alloys. J Mater Eng Perform 17(5):667–673
12. Zhu ZY, Deng CY, Wang Y, Yang ZW, Ding JK, Wang DP (2015) Effect of post weld heat treatment on the microstructure and corrosion behaviour of AA2219 aluminum alloy joints welded by variable polarity tungsten inert gas welding. Mater Des 65:1075–1082
13. Malarvizhi S, Raghukandan K, Viswanathan N (2008b) Investigations on the influence of post weld heat treatment on fatigue crack growth behaviour of electron beam welded AA2219 alloy. Int J Fatigue 30:1543–1555
14. Ding J, Wang D, Wang Y, Du H (2014) Effect of post weld heat treatment on properties of variable polarity TIG welded AA2219 aluminium alloy joints. Trans Nonferrous Metals Soc China 24:1307–1316
15. Sharma C, Dwivedi DK, Kumar P (2013) Effect of post weld heat treatments on microstructure and mechanical properties of frictionstir welded joints of Al−Zn−Mg alloy AA7039. Mater Des 43(1):134–143
16. KoteswaraRao SR, Madhusudhana Reddy G, Kamaraj M, Prasad Rao K (2005) Grain h arc manipulation techniques in Al–Cu alloy GTA welds. Mater Sci Eng A 404:227–234
17. Matsuda F, Ushio M, Nakata K, Tsukamoto K, Miyanaga Y (1978) Trans Jpn Weld Res Inst 7(2):139–141
18. Tong Lin Y, ChaoWang M, Zhang Y, Zhang He Y, PoWang D (2017) Investigation of microstructure evolution after post-weld heat treatment and cryogenic fracture toughness of the weld metal of AA2219 VPTIG joints. Mater Design 113:54–59
19. Rambabu G, BalajiNaik D, VenkataRao CH, SrinivasaRao K, Madhusudan Reddy G (2015) Optimization of friction stir welding parameters for improved corrosion resistance of AA2219 aluminum alloy joints. Defence Technol 11:330–337
20. Surekha K, Murty BS, Prasad Rao K (2008) Microstructural characterization and corrosion behavior of multipass friction stir processed AA2219 aluminium alloy. Surf Coat Technol 202:4057–4068
21. Liu HJ, Chen YC, Feng JC (2006) Effect of heat treatment on tensile properties of friction stir welded joints of 2219–T6 aluminium alloy. Mater Sci Technol 22(2):237–241
22. VenkataRao C, Madhusudhan Reddy G, SrinivasaRao K (2015) Influence of tool pin profile on microstructure and corrosion behaviour of AA2219 Al-Cu alloy friction stir weld nuggets. Defence Technol 11:197–208
23. Rao CV, Madhusudhan Reddy G, SrinivasaRao K (2015) Microstructure and pitting corrosion resistance of AA2219 Al-Cu alloy friction stir welds—effect of tool profile. Defence Technol 11:123–131
24. Malarvizhi S, Raghukandan K, Viswanathan N (2008c) Fatigue behaviour of post weld heat treated electron beam welded AA2219 aluminium alloy joints. Mater Des 29(8):1562–1567

25. Malarvizhi S, Balasubramanian V (2011b) Fatigue crack growth resistance of gas tungsten arc, electron beam and friction stir welded joints of AA2219 aluminium alloy. Mater Des 32:1205–1214
26. Surekha K, Murty BS, Prasad Rao K (2009) Effect of processing parameters on the corrosion behaviour of friction stir processed ALUMINIUM ALLOY 2219 aluminum alloy. Solid State Sci 11:907–917
27. KoteswaraRao SR, Madhusudhan Reddy G, SrinivasaRao K, Kamara M, Prasad Rao K (2005) Reasons for superior mechanical and corrosion properties of 2219 aluminum alloy electron beam welds. Mater Charact 55:345–354.

Powder Feeding Mechanisms in Additive Manufacturing: A Review

Yogesh Patil, Ashik Kumar Patel, Amisha Goutam, Subodh Chavan, Milan Pandya, Mitesh Malaiya, and K. P. Karunakaran

Abstract Additive manufacturing (AM) is also known as 3D printing, a new way of manufacturing the three-dimensional objects layer by layer and well-known for its capability of manufacturing the objects with complex geometries, unlike a conventional manufacturing process. AM consists of the number of technologies, each comprised of materials in different forms, viz. liquid, powder, wire, etc. Each technology has its way of feeding or delivering the material to the working area. In the deposition or cladding and powder bed AM technologies, the powder feeding plays a vital role in the initiation and creation of powder beds, which in turn impacts the shape, dimensional accuracy, strength, etc., of an object. Also, because of its complex mechanical structure, powder feeding is a tedious job. In this chapter, different types of powder feeding mechanisms are reviewed based on the type of powder, location of powder supply container, feeding direction, and techniques used. This paper briefly discusses different types of powder feeder in AM available today, compares, and explains their advantages and limitations, which could be used as a common ground for choosing a proper mechanism.

Keywords Additive manufacturing (AM) · 3D printing · Powder feeding · Powder dispensing · Powder recoating

1 Introduction

Additive manufacturing (AM), also known as 3D printing, is a disruptive technology of this era owing to its unique geometric and matrix capabilities. AM comprises the number of technologies, viz. stereolithography (SLA), digital light processing (DLP), fused deposition modeling (FDM), selective laser sintering (SLS), and melting (SLM). Every AM process takes 3D CAD model in the standard format (.stl, .obj, .amf), slices it into the number of layers, and feeds the data (coordinates) of each layer to the machine which builds the complete object layer by layer.

Y. Patil (✉) · A. K. Patel · A. Goutam · S. Chavan · M. Pandya · M. Malaiya · K. P. Karunakaran
Indian Institute of Technology, Bombay, Mumbai 400076, India
e-mail: patil.yogesh0808@gmail.com

© Springer Nature Singapore Pte Ltd. 2020

A. Praveen Kumar et al. (eds.), *Advances in Lightweight Materials and Structures*,
Springer Proceedings in Materials 8, https://doi.org/10.1007/978-981-15-7827-4_69

In the powder bed AM technologies, the powder feeding plays a vital role in the initiation and creation of powder beds in the working area. The layer-by-layer feeding of powder results in the formation of powder beds. Hence, it is essential to know that the characteristics like compact density, layer thickness, flatness of the each two-dimensionally printed layer decide the overall attributes like strength, surface finish, dimensional accuracy of the printed object/s. Even small distortion in the thickness or density uniformity in a single layer could lead to progressive distortions in the final printed object/s [1]. And that is why the powder feeding mechanisms play an essential role in both deposition and powder bed AM technologies. In the nozzle type of powder feeding technique, the powder from the container delivered to the working area through the nozzle. The Aeromet Corporation [2] uses a nozzle for direct metal deposition and other laser welding applications. The 3D Systems Inc. [3], the EOS GmbH Electro Optical Systems [4–6], uses blades. The Technology Research Association for Future Additive Manufacturing (TRAFAM) uses one thick blade [7]. While 3D system Inc. [8] uses a roller, the ExOne company's [1] invention provides the versatile powder feeder.

The objective of this paper is to study different types of powder feeding mechanisms available in the AM and serve as a basis for choosing the right feeding mechanism based on the nature of the powder.

2 Powder Feeding Mechanism

In recent years, there has been tremendous research in powder bed AM technologies, especially in the powder feeding mechanisms. Each type of powder feeding mechanism has its advantages and limitations and can be used according to the application, feeding direction, and nature of the powder. The brief classification of powder feeding mechanisms for deposition/cladding and powder bed AM technologies is as shown in Fig. 1.

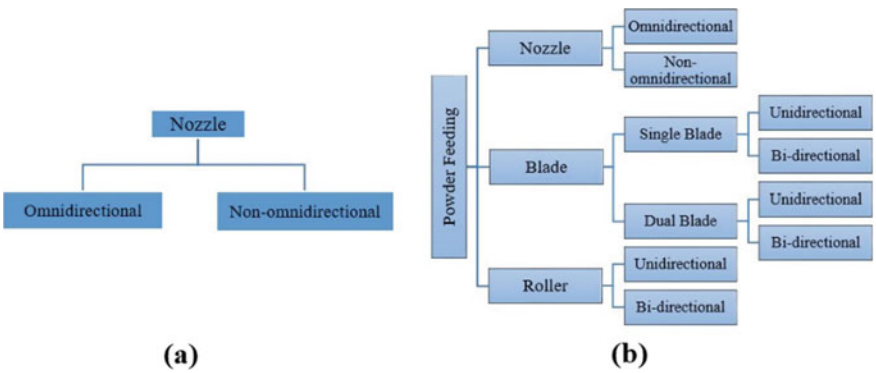


Fig. 1 Powder feeding classification: **a** deposition/cladding; **b** powder bed AM

2.1 Powder Feeding Using Nozzle

Powder feeding mechanism using nozzle delivers powder from hopper to working area. It can be either omnidirectional [9] or non-omnidirectional powder feeding. The Aeromat Corporation uses a nozzle to feed the powder for welding operation [2]. The nozzle-based powder feeding apparatus consists of a powder feeding path, initially larger in diameter, then converging to allow powder not to clog at corners and then a constant diameter powder discharge channel. So, this path acts as a delivery system for powder from a powder feed source to the working area. The nozzle positioned around the laser with respect to the crown position leading to three cases [2], viz. nozzle placed in front of the crown, the backside of the crown, or laterally oriented.

Thus, this is an omnidirectional powder feeding. While in the case of non-omnidirectional powder feeding, the nozzle position with respect to source remains constant. It can be either back feeding or front feeding or side feeding, but not all three together. The focus gas stream used to focus powder stream to the working field is not efficient, because even a small change in working conditions causes the powder to disperse anywhere. Eventually, problems like nozzle clogging, gas opening clogging due to powder debris and melting of the nozzle, and fresh powder arise due to rising temperatures.

2.2 Powder Feeding Using Blades

Blades used in the powder feeding have proven to be the most effective way of feeding the free-flowing powder. The simple movement of blades in a horizontal direction feeds the powder on the working platform easily and has the most straightforward mechanical arrangement among the other mechanisms. The bottom face of blade/s feeds the powder material to the working platform and has either a flat or sharp edge. The number of blades is either one or two, which could be uni- or bidirectional feeding.

In unidirectional powder feeding, one forward and backward motion generates one solid layer, and bidirectional powder feeding creates two solid layers. The single and dual blade powder feeding mechanisms explained below:

Single Blade Powder Feeding. The single blade powder feeding mechanism uses only one blade to feed and level the powder over the working platform and further divided into two types, either unidirectional or bidirectional.

Unidirectional Single Blade Powder Feeding. The unidirectional single blade powder feeding mechanism uses only one blade to feed and level the powder on the working platform and urther subdivided into the two types depending upon the location of powder storage container, viz. top-feeding and bottom-feeding have shown in Fig. 2.

The single blade unidirectional powder feeder consists of a single blade with only one powder storage container at one end [3]. Here, the powder is delivered in front

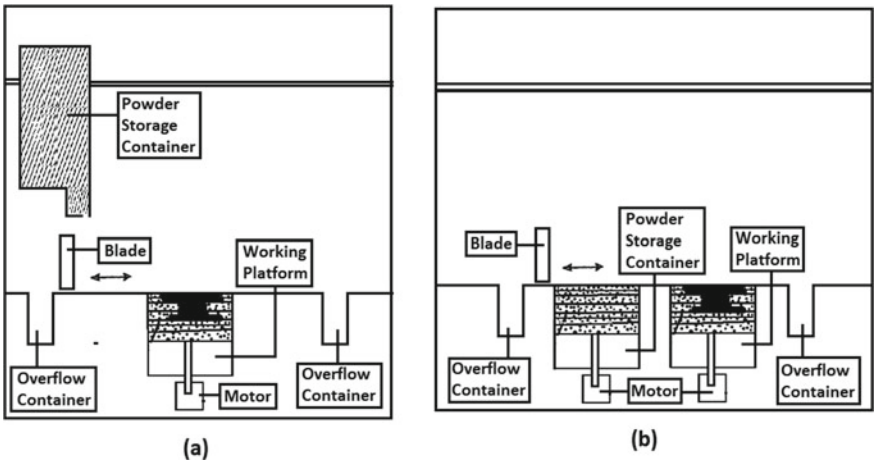


Fig. 2 Unidirectional single blade approach: **a** top-feeding; **b** bottom-feeding

of the blade then the blade moves forward by employing the drive provided. When it reaches the right side, it pushes the excess powder into the overflow container located at the right end and then comes back to its original position. While returning, pushes excess powder to overflow container, if any. Then the powder particles are bonded together by the source, thus forming one two-dimensional solid powder layer in one forward and backward motion. The EOS GmbH Electro Optical Systems [4] uses a similar powder feeding arrangement, where powder storage container placed above the working platform uses gravity assist in feeding the powder in front of the blade. If the powder storage container located below, that is the bottom-feeding mechanism. Here the piston pushes enough powder upwards in front of the blade.

Bidirectional Single Blade Powder Feeding. The bidirectional powder feeding mechanism uses two blades to feed and level the powder on the working platform. Like the unidirectional arrangement, bidirectional powder feeding is further subdivided into the two types, viz. top-feeding and bottom-feeding. The single blade bidirectional powder feeding mechanism shown in Fig. 3 consists of two powder supply containers located at both the end to hold and deliver powder to the blade at the right and left location [4].

This single blade powder feeder feeds powder in both directions, moving from left to right and right to left, and generates two powder layers. The 3D systems Inc. [3] uses a similar system for bidirectional powder feeding.

Dual Blade Powder Feeding. The dual blade powder feeding mechanism uses two blades to feed and level the powder on the working platform. In this case, top-feeding preferred over bottom-feeding because of the presence of a slit. A slit is a narrow gap between two blades used to hold powder. Pushing powder from the bottom into the slit is quite difficult compared to that from the top. The dual blade can be classified into two types depending upon the number of directions used for feeding powder, either unidirectional or bidirectional, shown in Fig. 4.

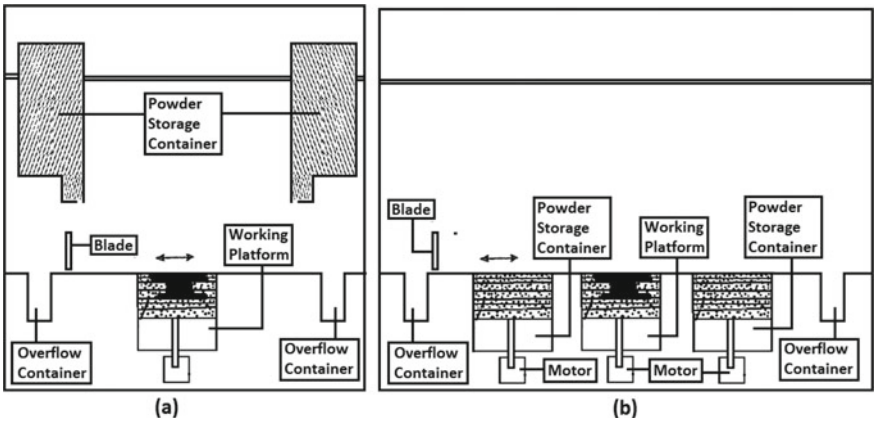


Fig. 3 Bidirectional single blade approach: **a** top-feeding; **b** bottom-feeding

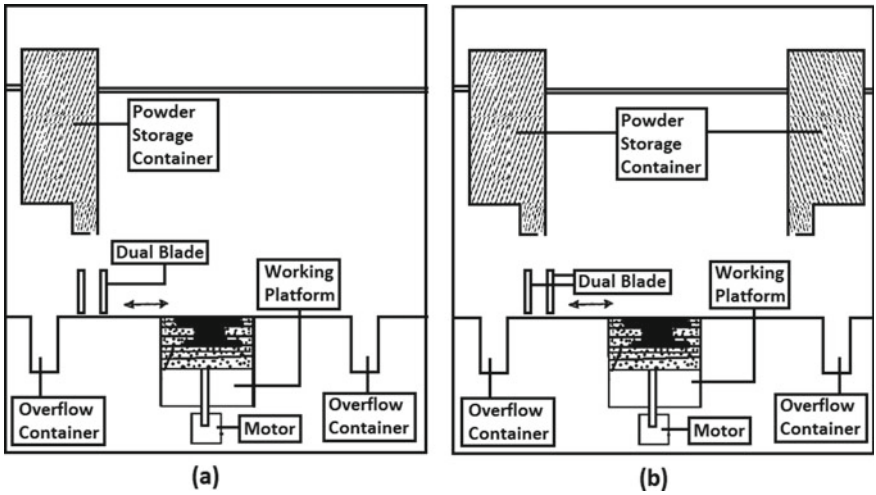


Fig. 4 Dual blade powder feeding approach: **a** unidirectional; **b** bidirectional

Unidirectional Dual Blade Powder Feeding. This type of powder feeder consists of the powder storage container to deliver powder into a slit, as shown in Fig. 4a. Here, feeding is done by the inner face of the rear blade when moving forward, while moving backward, both blades smoothen the already leveled powder layer using the smoothening element attached. The volume of the slit must be more than the quantity required for one layer of the powder. Thus, this arrangement generates only one layer in both forward and backward motion of blades. The EOS GmbH Electro Optical Systems [5, 6] uses a similar mechanism with additional means to deliver the required amount of powder into the slit, viz. conveyor pulley or spring arrangement.

Bidirectional Dual Blade Powder Feeding. This type of powder feeder consists of the powder storage container located at both ends or the addition of multiple mechanisms to deliver powder into a slit shown in Fig. 4b. This arrangement generates two layers: one in forward and another in backward motion of blades. The unidirectional mechanism by EOS GmbH Electro Optical Systems [5, 6] can be converted into a bidirectional feeding system in two ways: first, by using conveyor pulley or a spring arrangement at one end with delivering powder volume equal to two layers into the slit and second, by using conveyor pulley or spring arrangement along with powder storage container at each end with delivering powder volume equal to a single layer into the slit. Both ways it produces two layers, one in forward and other in a backward motion. Another powder feeding apparatus developed by Technology Research Association for Future Additive Manufacturing (TRAFAM) [7] uses one thick blade for feeding the powder on to the working platform. Study shows that blades are only suitable for free-flowing powder not for the moist powder as used in ExOne [10] and Voxeljet [11] 3D printers. Because wet powder particles bond together and result in the formation of the big size powder particles, these bigger powder particles are hard to feed by using blades and could result in uneven layers. Additional mechanisms must be employed that could crush big size powder particles into smaller ones.

2.3 Powder Feeding Using Roller

The roller-based powder feeding mechanism uses counter-rotating rollers to feed the powder to the working platform. The counter-rotating roller rotates in the opposite direction to the spreading direction because it has found that it is counter-rotating action picks up and redistributes powder in front of the roller instead of just pushing. It also provides compaction of the powder over powder bed [1] and further classified into unidirectional and bidirectional powder feeding mechanisms.

Unidirectional Roller Powder Feeding. The unidirectional roller feeding mechanism, as shown in Fig. 5, comprises a powder storage container on one side, which delivers powder in front of a roller [8]. One should note that the amount of powder delivered should be more than the volume of powder required for the single layer. Here, the roller moves forward by using a motor, and it rotates in the opposite direction that of feeding direction, counter-rotation. The counter-rotation of the roller pushes the powder over the underlying powder layer, and excess powder pushed into the overflow container. Then roller comes back to its original position without feeding. The powder delivery in front of the roller can be done in two ways, viz. top-feeding and bottom-feeding.

The 3D systems [8] use a similar top-feeding mechanism. In the bottom-feeding mechanism, powder pushed in front of the roller from a container located at the bottom.

Bidirectional Roller Powder Feeding. The bidirectional roller feeding mechanism, as shown in Fig. 6, forms two layers, one in forward and another in a backward motion [12]. The powder delivery in front of the roller can be done in two ways, viz.

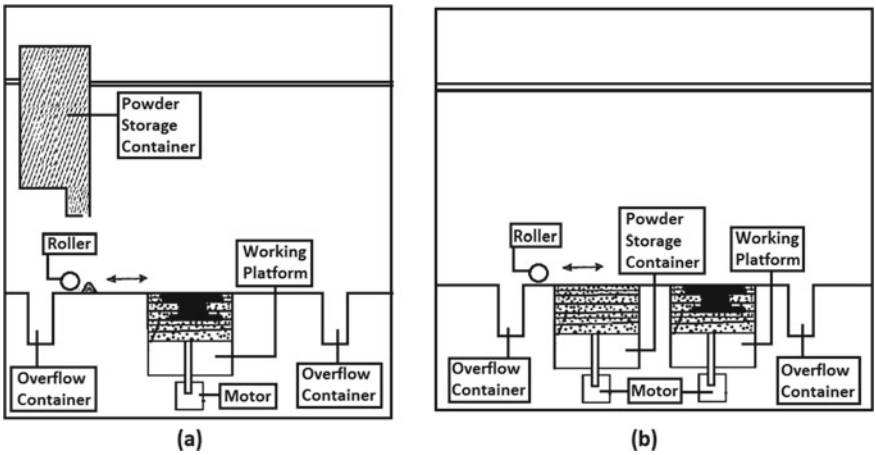


Fig. 5 Unidirectional contra-rotating roller: **a** top-feeding; **b** bottom-feeding

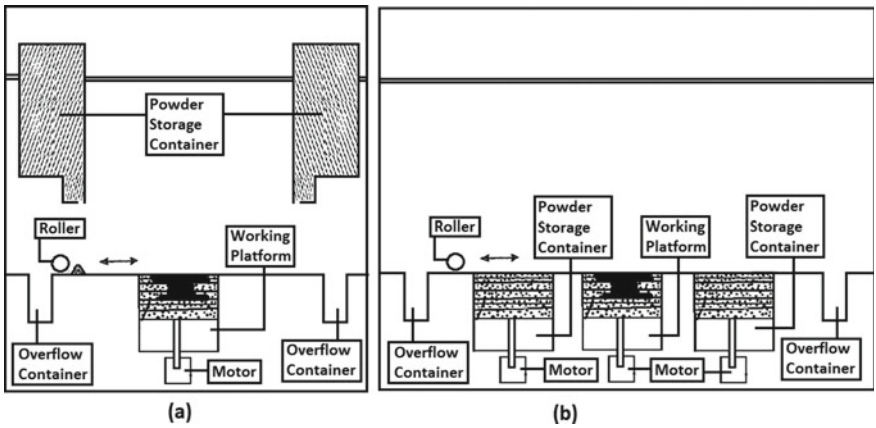


Fig. 6 Bidirectional contra-rotating roller: **a** top-feeding; **b** bottom-feeding

top-feeding and bottom-feeding have shown in Fig. 6a and b, respectively. The single side bidirectional roller feeding mechanism by 3D systems [8] is an example of the top-feeding mechanism. Here, roller, while feeding the first layer of the powder to the working platform, carries enough powder using powder carrying structure to the other end for feeding the next layer. Thus, it forms two layers: one in forward and another in a backward motion. Another bidirectional approach [12, 13] of using a roller for powder feeding by Aspect Inc. [12] is an example of a bottom-feeding mechanism. This apparatus uses a counter-rotating roller for bidirectional feeding of powder. At first, the roller parked at the left position of the first powder feeder compartment. The piston moves up and brings a sufficient amount of powder on the surface. Then the powder is feed to the working platform by moving roller from left

to right. For the next layer, the piston of the second powder compartment moves up and brings a sufficient amount of powder to the surface. Then it is feed to the working platform by moving roller form right to left. This process goes on repeating for subsequent layers until the object gets completed. The University of Texas System used a similar system for producing parts by sintering [14] using a counter-rotating roller [15].

Even though the counter-rotating roller provides reasonable control of powder, it has certain limitations. As roller diameter increases, the compaction force of the trailing side increases, and excess force damages the underlying printed layers. Hence, roller diameters are small. Even though short roller has proven to be effective, as they become longer to cover the bigger powder beds, they may get bend because of smaller diameter, which eventually compromises the flatness and uniformity of the powder bed. The versatile powder feeder developed by The Ex One Company [1] overcomes the disadvantages of counter-rotation roller powder feeders, and this powder feeder uses in-situ prepared moist powder as a material, which consists of a drive roller wrapped with a sleeve. The tension device, stiffening element, and nose used to adjust the parameters affecting the uniformity of layers. This feeder exhibits the same lifting and compaction actions. Still, it allows better control than the counter-rotating roller, which done by controlling three parameters, viz. lead angle, powder bed contact area, and trailing angle.

3 Conclusions

The study of three different types of powder feeder shows that,

1. The nozzle powder feeding mechanism delivers powder right to the required working area. But, it has certain limitations like intricate design involving the inert gas for focusing the powder stream and cooling fluid circulation for protecting nozzle from the rise in temperature. Also, laser reflections and powder debris lead to melting and clogging of gas and powder opening, which eventually leads to inaccurate powder feeding, thus decreases the efficiency.
2. The easiest way of powder feeding is by using blades, single or dual, unidirectional, or bidirectional. The design of such a feeding system is simple compared to that of the other two mechanisms, which is more effective for free-flowing dry powder material where gravity is enough for feeding the powder, but not for the moist one.
3. The bidirectional powder feeding found to be more effective than the unidirectional powder feeding since it cuts down the total build time.
4. Using roller for feeding is the most preferred mechanism for both dry and moist powder. It overcomes the limitations of using a blade and nozzle for feeding. For better results, rollers are supposed to have a small diameter.

5. Depending upon the nature of the powder, dry (angle of repose <30°) or moist (angle of repose >30°), the powder feeding mechanism changes as the angle of repose increases the complexity of the powder feeding system increases.

All powder feeding mechanisms discussed in this paper are contact type. They possess limitations, viz non-homogeneous density, non-uniformity in powder spreading, non-uniformity in layer thickness, breaking of the previously bonded layer, etc., all due to contact between the mechanical component of the feeder and already leveled powder. Future development in powder feeders can focus on overcoming these difficulties by developing non-contact powder feeding mechanisms.

References

1. Brunermer D (2013) Powder spreader, The ExOne Company (US), Patent no. US8568124B2
2. Pyritz CL, Arcella FG, House MA (2002) Powder feed nozzle for laser welding, Aeromet Corporation (US), Patent no. US6396025B1
3. Allanic A-L, Schaeffer P (2004) Fast three-dimensional modeling method & device, 3D Systems, Inc. (US), Patent no. US6764636B1
4. Perret H, Halder T, Philippi J, Keller P, Cantzler G, Göth M (2010) Device and method for applying layers of a powder material on to a surface, EOS GmbH electro optical systems (US), Patent no. US7820241B2
5. Perret H, Graf B-F, Sagmeister UC (2004) Device for supplying powder for a device for producing a three-dimensional object layer by layer, EOS GmbH electro optical systems (US), Patent no. US6672343B1
6. EOS 3D Printers Homepage, https://www.eos.info/en. Accessed on 15 July 2019
7. Hideaki M (2016) Powder recoater, technology research association for future additive manufacturing (TRAFAM), (JP), Patent no. EP3085517A1
8. Robert HW, Welch IV, Chung TM, Hanna CR (2005) Single side bi-directional feed for laser sintering, 3D Systems, Inc. (US), Patent no. US2005/0263933A1
9. Kapil S, Kulkarni P, Joshi P, Negi S, Karunakaran KP (2019) Retro fitment of a CNC machine for omni-directional tungsten inert gas cladding. Virt Phys Prototyping 14(3):293–306
10. ExOne 3D Printers Homepage, https://www.exone.com/. Accessed on 10 Aug 2019
11. Voxeljet 3D Printers Homepage, https://www.voxeljet.com/. Accessed on 12 Aug 2019
12. Hagiwara M (2007) Powder sinter layered manufacturing apparatus, Aspect Inc. (JP), Patent no. US2007/0026099A1
13. Bai Y, Williams CB (2016) An exploration of binder jetting of copper. Rapid Prototyping J 21(2):177–185. https://doi.org/10.1108/RPJ-12-2014-0180
14. Deckard CR (1997) Apparatus for producing parts by selective sintering, The University of Texas System, Austin (US), Patent no. US5597589
15. Selective Laser Sintering Brochure, https://www.3dsystems.com/3d-printers/prox-sls-6100/documents. Accessed on 15 June 2019

Influence of Friction Stir Welding Process Parameters on Mechanical Properties of AA6061-9 wt.% SiC Composites



B. N. Venkatesha and M. S. Bhagyashekar

Abstract Aluminum-based composites reinforced with ceramics particles are the most preferred materials for applications in the aerospace sector due to their superior properties. Friction stir welding is a novel potential joining process owing to its low distortion and environmentally friendly characteristics, and friction stir welding is widely used for joining aluminum matrix composites without any defects which as boosted the applications of composites. The present research work reports the results of experimental studies carried out on the effect of friction stir welding parameters on UTS and Vickers hardness of AA6061-9 wt.% SiC composite. The friction stir welding was carried out with tool rotation speed of 600–900 rpm in a step of 150, with the axial load 4–6 kN in a step of 1; the transverse speed adopted was 45 mm/min, with different tool pin profiles such as cylindrical, square, and taper. Results reveal that the welded joints produced at 750 rpm tool rotational speed, with the axial load of 5 kN using a square pin tool profile exhibits higher UTS of 124.3 MPa and Vickers hardness of 98.11; further, SEM microphotograph of FS Welded AA6061-9 wt.% SiC composite reveals the homogeneous distribution of SiC particles within the matrix.

Keywords AA6061-SiC composite · Friction stir welding · Ultimate tensile strength

1 Introduction

The process of joining the metals below its melting point is termed as friction stir welding and is a solid-state welding process in which welding temperature is 80% of the melting point of the base metal. FSW is extremely used to join the aluminum alloys and its composites. The FS welded joints have low-cost and high-quality joints. The

B. N. Venkatesha (✉)
JSS Academy of Technical Education, Bangalore, Karnataka, India
e-mail: raju79shetty@gmail.com

M. S. Bhagyashekar
HKBK College of Engineering, Bangalore, Karnataka, India

© Springer Nature Singapore Pte Ltd. 2020

A. Praveen Kumar et al. (eds.), *Advances in Lightweight Materials and Structures*,
Springer Proceedings in Materials 8, https://doi.org/10.1007/978-981-15-7827-4_70

FSW uses a non-consumable tool rotating at a suitable speed, and it consists of two parts such as tool shoulder and tool pin. During welding, the pin of the tool is inserted on the top surface of the welded joint and then moved horizontally in the direction of the FS welded joints. As the tool moves, it generates heat and mechanically sweeps the soften metal that forms the FS welded joint. FSW is environmentally friendly welding owing to low power consumption, no emission of gas and the absence of consumable materials and thus is a most preferred joining process. As the composites of aluminum alloys find immense application in aerospace and automobile industries, the present chapter discusses the experimental data on the influence of welding parameters of the composite.

The literature about FSW composite presents that welding speed shoulder diameter significantly affects UTS of welds and also welding severely affects the percentage of elongation [1]. Singarapu et al. in their work FSW of AZ31B magnesium alloy reported that the UTS and microhardness severely affected by tool rotational speed [2]. Rao et al. in their work FSW of AA2219 conclude that the hexagonal pin profiled tool exhibits superior mechanical properties [3] Kadaganchi et al. in their work FSW AA 2014-T6 reported that the smooth material flow is produced by using the hexagon tool pin profile tool [4]. Kalaiselva et al. in their work FSW of Al-B_4C composites concludes that 996–936 rpm, 1.329 mm/s, 9.306 kN were optimum FSW parameters [5]. Dinaharan et al. in their work FSW of aluminum matrix composites reported that the 5.8 kN, 51 mm/min, 1132 rpm and 10 wt.% of ZrB_2 were optimum welding parameters [6]. Panivel et al. in their work FSW of dissimilar aluminum alloy reported that the FS Welded joints fabricate by using a square profile tool exhibits the highest wear resistance [7]. Elatharasana et al. in their work optimization of AA6061-T6 FSW using RSM stated that the UTS and YS increase with an increase in axial force to a certain value and then decrease [8]. Kumar et al. in their study the optimization of FSW parameters of AA6061-T6/AlNp composite reported that the 55 mm/min, 1200 rpm, and 5 kN were optimum FSW parameters [9]. Salehi et al. in their work FSP of AA6061/SiC nanocomposites conclude that 40 mm/min and 1600 rpm were optimum welding parameters [10]. Shaha et al. in their work FSW of AlSiCp reported that the SiC wt. % contributes 39.77% and tool geometry 18.29% on ultimate tensile strength (UTS) [11]. Rajakumar et al. in their work FSW of AA 6061-T6 reported that the average grain size and UTS of FS welded joints were estimated by empirical relationship [12]. Selvamani et al. in their work FSW of AISI 1035 grade carbon steel rods conclude that the maximum UTS was attained at forging pressure/time of 24.41 rps [13]. Sevvel et al. in their work FSW of AZ31B Mg alloy stated that the FS welded joints fabricated at 0.5 mm/min and 1000 rpm, with a taper cylindrical tool profile, exhibits maximum UTS [14]. Elangovan et al. in their work prediction of UTS of FSW AA2219 reported that the FS welded joints fabricated at a 0.75 mm/s, 12 kN and, 1600 rpm by using a square pin tool profile exhibits higher UTS compared to other joints [15]. Feng et al. in their work, the FSW of AA2009-SiC composite reported that the UTS and YS of FS Welded composite were higher compared to extruded FS Welded composite both longitudinal and transverse directions [16]. Chena et al. reported in their work, FSW of AA6063-B_4C MMC's, that due to the stirring effect of the FSW process results

Table 1 The AA6061 chemical composition

Content	Zn	Cu	Fe	Mn	Mg	Si	Ti	Ni	Pb	Sn	Al
%	0.14	0.323	0.153	0.024	0.81	0.662	0.107	<0.045	0.024	0.01	Balance

in grain refinement of the weld zone [17]. X. G. Chena et al. reported in their work, FSW of AA6063-B_4C MMC's, that due to the stirring effect of the FSW process results in grain refinement of the weld zone [18].

2 Experimentation

2.1 Material Selection

In the present studies, AA6061 was used as a matrix material because of its good welding properties. Table 1 depicts the AA6061 chemical composition, and the silicon carbide of particle size 60 μm was used as reinforcement material for cast composites; 9 wt.% of SiC was used to prepare cast composites.

2.2 Preparation of Composites

The ingots of AA6061 were placed in the crucible of electric arc furnace (Make: Hi-Tech, No of coils 6, Voltage 440 V, Crucible material-Mild steel) and heated to a temperature around 800 °C till ingots melt and produce molten metal, to the molten metal a hexachloroethane degassing tablet is added. The degassing tablet absorbs the dissolved gases present in melt and forms a slag; the slag is removed by foundry tools. The melt is stirred at a stirring speed of 90 rpm and 9% by weight of silicon carbide particles is added as reinforcement to produce cast composites. The AA6061-9 wt.% SiC castings were machined to produce rectangular composite plates of dimensions 100 × 50 × 6 mm.

2.3 FSW of Composite Plates

In the present investigation, the AA6061-9 wt.% SiC composite plates are FS welded using friction stir welding equipment (Make: RV Machine Tools Coimbatore, Model: FSW 3T-300-NC, Tool rotational speed range: 450–1500 rpm, Power 7.5 KW, Welding speed range 30–100 mm/s, optional servo control, X-axis 300 mm) AA6061-9 wt.% SiC composites are FS Welded by using predominant welding parameters such as tool rotation speed of 600–900 rpm in a step of 150 rpm, tool pin profiles

Table 2 FSW parameters adopted during welding

S. No.	Parameters	Code	Unit	L1	L2	L3
1	Tool profile	TP		CY	SQ	TCY
2	Tool rotational speed	TR	rpm	600	750	900
3	Axial force	AF	kN	4	5	6



Fig. 1 Friction stir welded plates

selected was cylindrical, square and taper and axial load 4–6 kN in a step of 1 kN, Table 2 presents the FSW parameters adopted during welding, Fig. 1 represents the photograph of friction stir welded plates, and Fig. 2 details schematic diagram of tool profiles used for FSW.

2.4 Testing of FS Welded Specimens

The microstructure of AA6061-9 wt.% SiC composite before and after FSW was examined using a scanning electron microscope (SEM, TESCAN VEGA3). The specimens for the tensile test were cut from FS welded joints as per ASTM E8-16a. Figure 3 presents the tensile test specimens. The tensile test was carried out by using UTM (Make: Fuel instruments Pvt. Ltd) Capacity 20 ton, Length accuracy $\pm$0.1 mm, minimum graduation 0.2 kN. The microhardness test was performed by using Vickers hardness tester (Make: FIE Pvt Ltd) at load 10 Kgf, Max test height 230 mm).

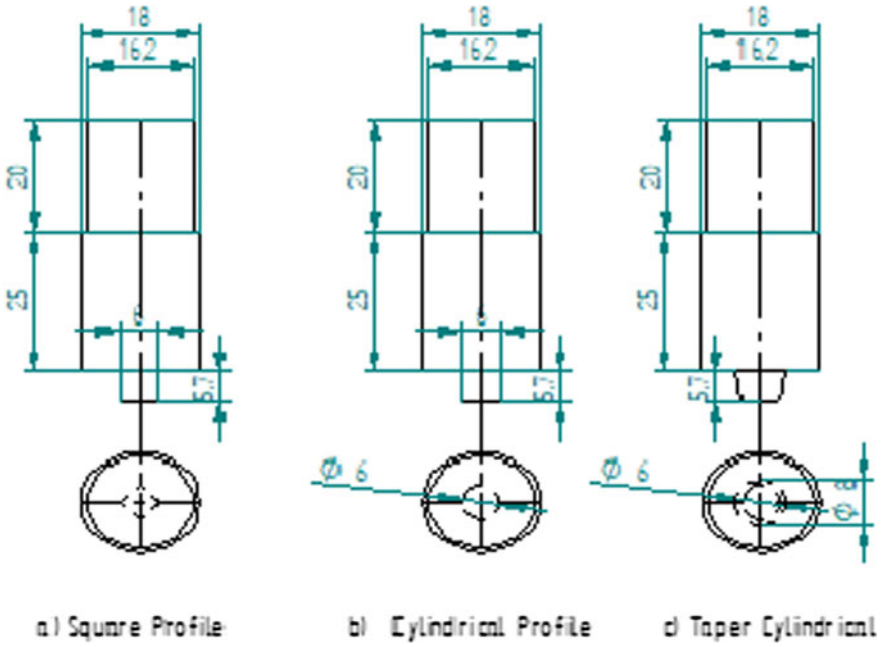


Fig. 2 Tool pin profiles used for friction stir welding

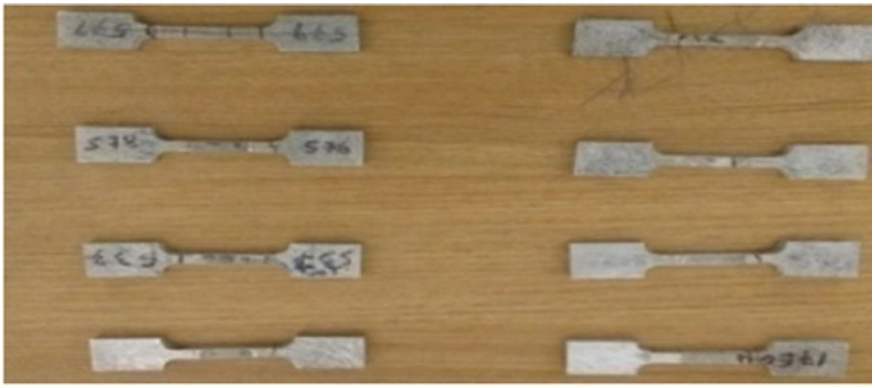


Fig. 3 Tensile test specimens

3 Results and Discussion

3.1 SEM Studies

Figure 4a depicts the SEM micrograph of cast AA6061; from figure, it is noticed

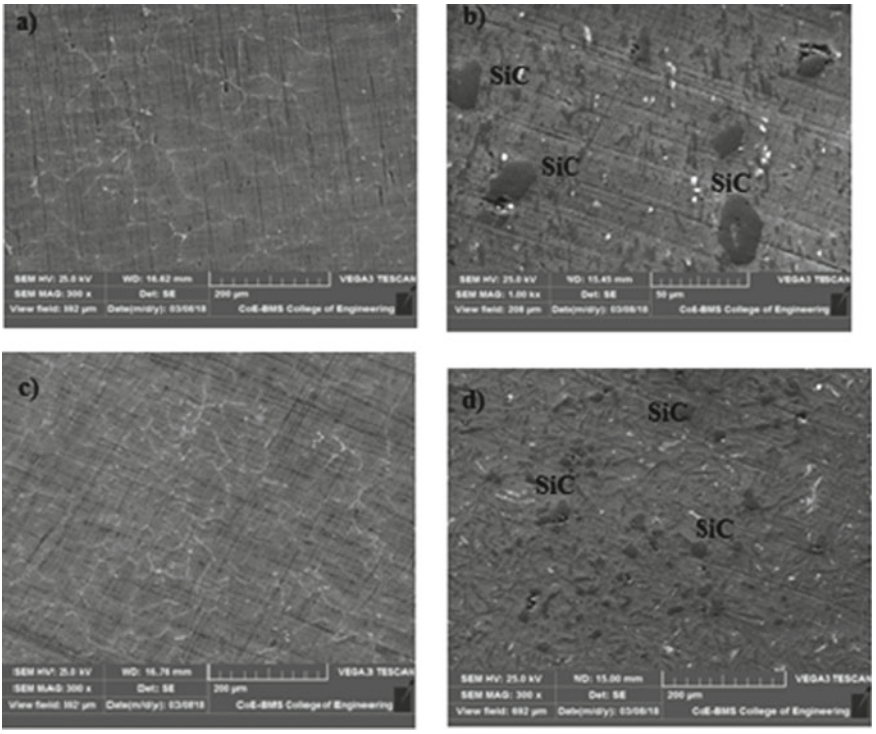


Fig. 4 SEM Micrograph of **a)** cast AA6061, **b)** AA 6061-9 wt.% SiC composite, **c)** FS welded cast AA6061, **d)** FS welded AA 6061-9 wt.%, SiC composite

that the presence of aluminum solid solution dendrites. Figure 4b presents the SEM micrograph of AA6061-9 wt.% SiC composite, and from figure, it is observed that the occurrence of coarse grains of the aluminum solid solution with a homogeneous distribution silicon carbide particles [5]; Fig. 4c reveals SEM micrograph of FS welded cast AA6061 at the weld zone, and from figure, it is noticed that the equiaxed recrystallized finer grains due to the fact that heavy plastic deformation during the FSW process [2]; Fig. 4d reveals SEM micrograph of FS welded AA6061-9 wt.% SiC composites at weld zone, and from figure, it is noticed that the homogeneous distribution of the SiC particles larger in a number smaller in size due to the tool pin stirring effect closed to the joint during FSW [5].

3.2 The Variation of Tool Rotational Speed Effect on UTS

Figure 5 depicts the variation of the tool rotational speed effect on UTS of FS Welded AA6061-9 wt.% SiC composite at an axial load 5 kN and welding speed 45 mm/min, from the Fig it is noticed that as the tool rotation speed increases from 600 to 750 rpm

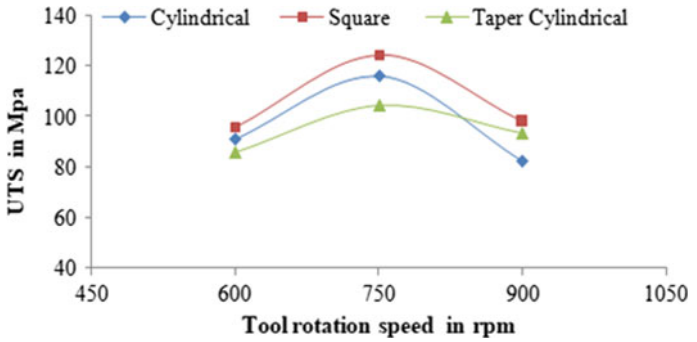


Fig. 5 Effect of tool rotational speed on UTS of FS Welded AA6061-9 wt.% SiC composite

the ultimate tensile strength increases and reaches a maximum value at 750 rpm, further increase in tool rotation speed results in a decrease in ultimate tensile strength, due to the fact that higher rotational speed above 750 rpm produces extra stir material on the top surface, this results in the formation of microvoids in the stir zone of welded joints and decreases UTS [5]. Higher tool rotation results in more heat input, avoid the nucleation of grains and decrease of UTS [9] higher tool rotation results in high heat input per unit length of joint and turbulence, which damage the regular flow behavior results in a decrease of UTS [15], therefore optimum tool rotation speed is 750 rpm for the joints produced by using cylindrical, square and taper cylindrical profile tools, further, the square profile tool exhibits a high UTS of 124.3 MPa.

3.3 The Variation of Axial Load Effect on UTS

Figure 6 depicts the variation of axial load effect on UTS of FS welded AA6061-9 wt.% SiC composite at a transverse speed of 45 mm/min and tool rotational speed 750 rpm. From figure, it is observed that as the axial load increases from 4 to 5 kN, the UTS increases and reaches a maximum at axial load 5 kN, and further, increase in axial load above 5 kN results in a decrease of UTS due to the fact that at higher axial load frictional force is more which in turn increases heat generation beneath the shoulder leads to a decrease in UTS [9]. At higher axial load, more shear lips on both advancing and retreating side of the welds result in a decrease in UTS [15]. The FS welded joints produced by the square profile tool at 5 kN exhibits a high ultimate tensile strength.

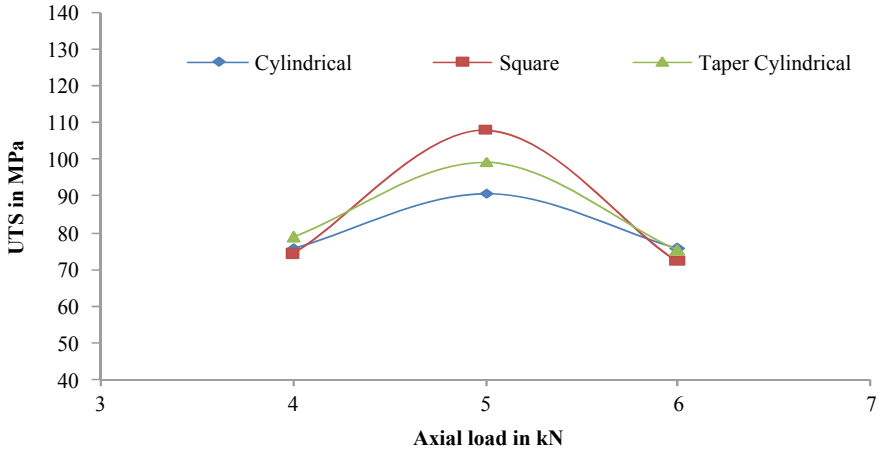


Fig. 6 Variation of axial load effect on the UTS of FS welded AA6061-9 wt.% SiC composite

3.4 The Tool Rotational Speed Variation Effect on Vickers Hardness

Figure 7 presents the tool rotational speed variation effect on Vickers hardness (VHN) of FS welded AA6061 composite containing 9 wt.% SiC at axial load 5 kN and welding speed 45 mm/min, and from figure, it is noticed that as tool rotational increases from 600 to 750 rpm the Vickers hardness increases and reaches a maximum at 750 rpm, and further increase in tool rotation speed decreases the Vickers hardness due to the fact that at high tool rotation speed; the heat generation rate is high, and this results in a material softening in the weld zone and decreases of Vickers hardness [2]. Higher tool rotational speed increases the axial force and causes grain coarsening in the weld zone of the joints, hence lower the hardness [3]. The optimum tool rotation is 750 rpm for the joints produced by cylindrical, square and taper cylindrical profile

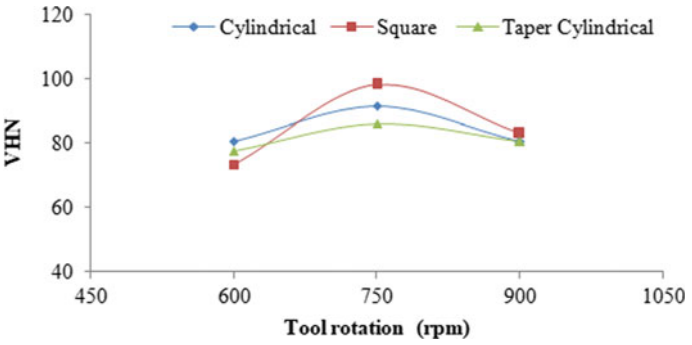


Fig. 7 Tool rotational speed variation effect on VHN of FS welded AA6061-9 wt.% SiC composite

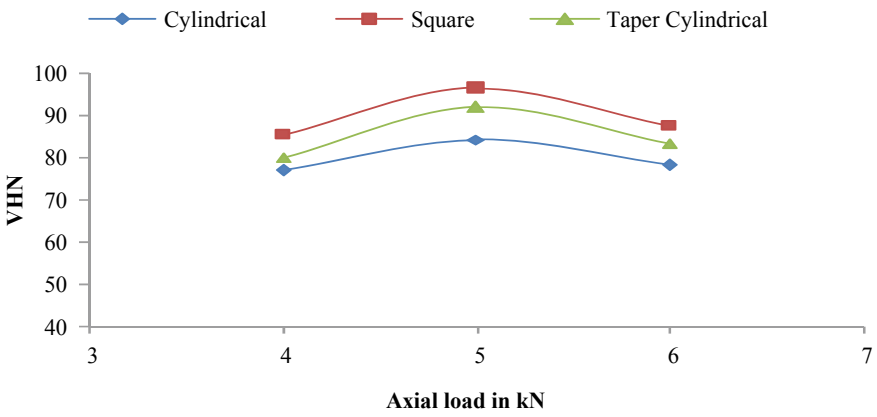


Fig. 8 Variation of axial load effect on VHN AA6061-9 wt.% SiC composite

tools. The FS welded joints fabricated by using a square profile tool at a tool rotation speed of 750 rpm exhibits a high Vickers hardness of 98.11 at the weld zone.

3.5 The Axial Load Variation Effect on Vickers Hardness

Figure 8 details the variation of axial load effect on Vickers hardness (VHN) of FS welded AA6061-9 wt.% SiC composite at a transverse speed 45 mm/min and tool rotation speed of 750 rpm. From figure, it is observed that as the axial load increases from 4 to 5 kN, the Vickers hardness increases and reaches a maximum at axial load 5 kN, and further increase in axial load decreases hardness because of the grain size of the stir zone is finer at higher axial load which results in a material strengthening and increases the hardness of the weld zone [2]; the joints produced by square profile tool at an axial load of 5 kN exhibit a high Vickers hardness.

4 Conclusion

The AA6061-9 wt.% SiC composite plates were produced by using the stir casting process; further, the effect of FSW parameters such as tool rotational speed, axial load, and tool profile on UTS and Vickers hardness of AA6061-9 wt.% SiC composite was evaluated. From this study, the following conclusions are derived.

1. SEM microphotograph of AA6061-9 wt.% SiC composite reveals the coarse grains of the aluminum solid solution with homogeneous distribution silicon carbide particles.

2. SEM microphotograph of FS welded AA6061-9 wt.% SiC composite reveals the homogeneous distribution SiC particles within the matrix, and the SiC particles appear in a smaller size but larger in number compared to the AA6061-9 wt.% SiC composite.
3. As the tool rotation speed increases from 600 to 750 rpm, the ultimate tensile strength increases and reaches a maximum value at 750 rpm, and a further increase in tool rotation speed results in a decrease in ultimate tensile strength. The joints produced at a tool rotation speed of 750 rpm, an axial load of 5 kN, and by using the square profile tool exhibits a high ultimate tensile strength of 124.3 MPa.
4. As the axial load increases from 4 to 5 kN, the Vickers hardness increases and reaches a maximum at axial load 5 kN, and further increase in axial load decreases hardness. The joints fabricated by using the square profile tool at an axial load 5 kN and a tool rotation speed 750 rpm exhibit a high Vickers hardness of 98.11.

References

1. Arora KS (2010) Effect of process parameters on friction stir welding of aluminum alloy 2219–T87. Int J Adv Manuf Technol 50:941–952
2. Singarapu U, Adepu K (2015) Influence of tool material and rotational speed on mechanical properties of friction stir welded AZ31B magnesium alloy. J Mag Alloys 3:335–344
3. Venkata Rao AG, Madhusudhan Reddy B (2015) Influence of tool pin profile on microstructure and corrosion behavior of AA2219 Al-Cu alloy friction stir weld nuggets. Defence Technol 11:197–208
4. Ramanjaneyulu Kadaganchi A, Reddy M (2015) Optimization of process parameters of aluminum alloy AA 2014-T6 friction stir welds by response surface methodology. Defence Technol 11:209–219
5. Murgan KN (2012) Optimization of FSW parameters for the welding of Al-B_4C composite plates using generalized reduced gradient method. Proc Eng 38:49–55
7. Dinaharan I, Murgan N (2012) Automation of friction stir welding process to join aluminum matrix composites by optimization. Proc Eng 38:105–110
7. Palanivel R, Koshy Mathews P, Murgan N, Dinaharan I (2012) Prediction and optimization of wear resistance of friction stir welded dissimilar aluminum alloy. Proc Eng 38:578–584
8. Elatharasana G, Senthil Kumar VS (2013) An experimental analysis and optimization of process parameter on friction stir welding of AA 6061-T6 aluminum alloy using RSM. Proc Eng 64:1227–1234
9. Kumar A (2014) Optimization of friction stir welding process parameters to maximize tensile strength of stir cast AA6061-T6/AlNp composite. Mater Design 57:383–393
10. Salehi M (2012) Optimization of process parameters for producing AA6061/SiC nanocomposites by friction stir processing. Trans Nonferrous Met Soc China 22:1055–1063
11. Shaha C (2015) Optimization of FSW process parameters for AlSiCp PRMMC using ANOVA. Mater Today Proc 2:2504–2511
12. Rajakumar S, Muralidharan C, Balasubramanian V (2010) Establishing empirical relationships to predict grain size and tensile strength of friction stir welded AA 6061–T6 aluminum alloy joints. Trans Nonferrous Met Soc China 20:1863–1872
13. Selvamani ST, PalanikumarK (2014) Optimizing the friction welding parameters to attain maximum tensile strength in AISI 1035 grade carbon steel rods. Measurement 53:10–21
14. Sevvel PA, Jaiganesh V (2014) Characterization of mechanical properties and microstructural analysis of friction stir welded AZ31B Mg alloy thorough optimized process parameters. Proc Eng 97:741–751

15. Elangovan K, Balasubramanian V, Babu S (2008) Developing an empirical relationship to predict tensile strength of friction stir welded AA2219 aluminum alloy. JMEPEG 17:820–830
16. Feng AH, Xiao BL, Ma ZY (2008) Effect of microstructural evolution on mechanical properties of FSW AA2009/SiC composite. Compos Sci Technol 68:2141–2148
17. Chena X-G, da Silva M, Gougeonb P, St-Georges L Microstructure and mechanical properties of friction stir welded AA6063–B4C metal matrix composites. Mater Sci Eng A 518 (1) 174–184 (2009).
18. Doude H, Schneider JB (2015) Optimizing weld quality of a friction stir welded aluminum alloy. J Mater Process Technol 222:88–196

Process Optimization of Segmented Object Manufacturing for Expendable Polystyrene Foam



Gopal Gote, Pushkar Kamble, Shishir Kori, and K. P. Karunakaran

Abstract Segmented object manufacturing (SOM) is a hybrid foam 3D printer for plastic foams especially Expandable Polystyrene (EPS), which uses a novel visible slicing route. SOM has three subsystems include machining, slicing, and gluing systems; among these, the machining system contributes more in process time and surface quality. SOM is not yet commercialized because of poor product surface quality and high process time. In this work, efforts are made to reduce the cycle time and to improve the surface quality by optimizing the machining system. Taguchi method is used to design the experiments and parametric analysis of cutting speed, linear feed, step-over, and step-down is performed to get a good surface finish. As a result, surface roughness reduced from 78.30 to 47.70 μm, at the same time tool path also modified to accommodate the optimized parameters by doing so, process time reduced from 42 to 18 min due to optimized tool path.

Keywords Segmented object manufacturing · Expandable polystyrene · Design of experiments · Surface roughness · Machining time

1 Introduction

3D Printing is an important area in the research community as well as in industries [1, 2]. The common materials for 3D printing are different grades of plastic, wood, metals, bonded sand, plastic foams, etc. [3]. Though it is a booming area still, because of high production cost and higher process time, it has limited applications in industries. Higher production cost is because of its proprietary raw materials. Foam 3D printing is the recent area of research and has many applications in large prototyping, sculptures, to create movie set, decoration, foam foundry, etc. [4, 5]. The researchers are trying to use the plastic foams such as expanded polystyrene (EPS), extruded polystyrene (XPS), polyurethane foam, polyethylene foam [5] which are the cheapest material available for the prototyping, cost-effectiveness, and its specific properties

G. Gote (✉) · P. Kamble · S. Kori · K. P. Karunakaran
Department of Mechanical Engineering, Indian Institute of Technology Bombay, Mumbai 400076, India
e-mail: gopalgote99@gmail.com

© Springer Nature Singapore Pte Ltd. 2020

A. Praveen Kumar et al. (eds.), *Advances in Lightweight Materials and Structures*,
Springer Proceedings in Materials 8, https://doi.org/10.1007/978-981-15-7827-4_71

play a big role for the selection of plastic foams to make prototypes. There are many companies which make the rapid prototyping machines for the plastic foams, and few names are CROMA, Wecutfoam, Megaplot [5], etc. Compared to other prototyping methods, foam prototyping is the fastest method because it can be easily machined by thermal cutting. Most of the foam prototyping machines are semiautomatic and are based on the hot wire cutting mechanism, which has certain limitations such as low product quality and high process time [5]. However, Karunakaran et al. [1] published the first article on segmented object manufacturing (SOM), in that they have proposed the first 3D printer for the expandable polystyrene (EPS) foam which was completely different from the available foam prototyping machines [1, 2, 4]. It uses a different slicing strategy called "visible slicing" which driven manufacturability and different from the uniform and adaptive slicing. It uses 3-axis kinematics for machining in conjunction with hot wire slicing and gluing; also, it can produce parts with internal features. Here gluing and slicing have less role in the process optimization as gluing glues the two segments which is thicker in size and slicing converts the block into segments using hot nichrome wire, but machining plays a vital role in the process optimization as it has a direct effect on surface quality. The previous finding has been done using milling and deburring cutters, and few authors reported that deburring cutters give a better surface finish than the milling cutters for EPS foam machining. Ranjeet et al. [2] performed the machining of EPS foam using milling as well as deburring cutters; in his finding, it has been observed that deburring cutters give better surface finish than the milling cutters. There is limited research available on the (expandable polystyrene) EPS machining.

Chen et al. [6] investigated the lost foam pattern making routes and found that machining is the best route for foam pattern making; they developed the foam milling cutters and concluded that foam mill with long cutting edges and higher flute volume will give a better surface finish. Similarly, Mallak et al. [7] investigated the machining behavior of polyurethane plastic foam, and they have selected different sizes of cutters with various rake angles and performed more than 100 experiments and concluded that surface finish is a primarily dependent depth of cut. The natural rubber also has similar to Young's modulus as that of plastic foam. Albert et al. [8] performed the number of end milling experiments on rubber and found that down cut woodworking milling tools give better surface finish than the up cut milling tools.

In short, there is a need to study the machining behavior of plastic foams especially EPS foam and also to optimize the segmented object manufacturing (SOM); in this paper, our objective is to reduce the processing time of SOM and also to improve the product surface quality.

2 Experimentation

SOM is a hybrid foam 3D printer that has subtractive as well as an additive route. For subtraction, machining and hot wire cutting are used, and additive hot melt gluing is used. This 3D printer has two indexable positions for the machining, and it can do

machining on top as well as the bottom table. Karunakaran et al. [2] explained the kinematics of SOM.

For this study, the expandable polystyrene foam (EPS) with 32 Kg/m^3 density foam has been chosen as it is very common in the industries. The multi-featured bracket used for the study as it has different features. Figure 3 shows the multi-featured bracket and has two visible slices glued together. For each visible slices, NC program has been generated using CAM software (Powermill 2019), and then it has been merged with the gluing NC code and slicing NC code; further by adding all necessary operations miscellaneous codes, it becomes a single NC file. Finally appended NC file has been transferred to the 0i Fanuc controller which drives the SOM machine.

The bracket making on making machine has some specific steps, and first foam block needs to mount on the top table using a double-sided adhesive tape followed by spindle points the cutter upward and mills all the surfaces visible to it on the top table. The further top table goes to the bottom table, and fist slicing takes place by hot wire which goes from one end to the other end. Further, top table retracts upward and spindle indexes to point the cutter downward to machines the top surfaces of the first v-slice on the bottom table. Further, spindle indexes to point the cutter upward and machine the bottom of the second v-slice on the top table. In continuation with that glue dispensing happens by the glue dispenser on the common part of both v-slice and the top table goes to the bottom table, the hot wire goes from one end to the other slicing the block. Further, top table retracts upward and spindle indexes to point the cutter downward and machine the top surfaces of second v-slice on the bottom table. Ranjeet et al. [3] explained the detailed working of SOM.

Primary studies have been done on bracket making, and it shows that machining time is contributing more to the processing time and also product surface quality. So here only the machining part needs to be optimized. Here two trials have been selected for the comparative study.

Here two trials have been used for the experimentation; Table 1 shows the process parameters during Trial-1 and Trial-2. In Trial-1, the work done by Ranjeet et al. [8]

Table 1 Tool and process parameters

Content	For trial-1	For trial-2
Tool type	Deburring tool	Deburring tool
Number of tools	01	03
Dimensions of tool	Single tool: 8 mm diameter and 40 mm cutting length, carbide, ball end	T-1: 25 mm diameter and 40 mm cutting length, carbide, flat end T-2: 25 mm diameter and 40 mm cutting length, carbide, ball end T-3: 15 mm diameter and 40 mm cutting length, carbide, flat end
Process parameters	Spindle speed:3000 rpm, linear feed: 2500 mm/min, step-over 2 mm, step-down: 2 mm	Optimized process parameters mentioned in Sect. 3.1

has been replicated which uses single tool and tool path has been generated in the same way as that of metal machining. In Trial 1, a single ball end deburring tool was selected; in Trial-2, appropriate tools have been selected, and for each tool, process parameters have been optimized and also optimized tool has been generated.

For both trials, the process parameters for the gluing and slicing were kept constant. For slicing, 1000 mm/s feed rate was used, and for gluing, 1500 mm/s feed rate was used as mentioned in the previous work. To optimize the process parameters in Trial 2, the Taguchi method [9] has been used as follows.

2.1 Design of Experiments

Three different deburring cutters have been selected as Tool 1 (Flat-end deburring cutter dia. 25 mm), Tool 2 (Ball end deburring cutter dia. 25 mm), and for Tool 3 (Flat end deburring cutter dia. 15 mm) for flat surface, curve surface, and holes, respectively, for bracket as shown in Fig. 3. For Tool 1, five control parameters with four levels have been selected as linear feed (3000, 3500, 4000, 4500 mm/min), plugging feed (2000, 2500, 3000, and 3500 mm/min), spindle speed (8000, 10,000, 12,000, and 14,000 rpm), step-over (5, 10, 15, and 20 mm), and step-down (5, 10, 15, and 20 mm). A flat surface of the bracket has been machined using Tool 1.

For Tool 2, four control parameters with four levels have been selected as linear feed (3000, 3500, 4000, 4500 mm/min), plugging feed (2000, 2500, 3000, and 3500 mm/min), spindle speed (8000, 10,000, 12,000, and 14,000 rpm), and step-over (2, 4, 6, and 8 mm). The curved surface of the bracket has been machined using Tool 2.

For Tool 3, five control parameters with four levels have been selected as linear feed (3000, 3500, 4000, 4500 mm/min), plugging feed (2000, 2500, 3000, and 3500 mm/min), spindle speed (8000, 10,000, 12,000, and 14,000 rpm), step-over (6, 8, 10, and 12 mm), and step-down (5, 10, 15, and 20 mm). Internal features of the bracket have been machined using Tool 3.

The selection of orthogonal array has been done using a standard mathematical expression [9] as shown below.

$$\text{No. of experiments} = 1 + \text{Number of parameters (Levels} - 1) \tag{1}$$

Here, for Tools 1 and 3, five control parameters with four levels have been identified, and for Tool 2, four control parameters with four levels have been identified. So according to Eq. 1, minimum number of experiments for Tool 1, Tool 2, and Tool 3 have been calculated as 16, 14, and 16, respectively. Here we have selected an L16 array for each tool as shown in Tables 2, 3, and 4. Each experiment has been performed thrice.

Table 2 Set of experiments (L16) for Tool 1

Serial No.	Linear feed (mm/min)	Plunging feed (mm/min)	Spindle speed (rpm)	Step-over (mm)	Step-down (mm)	Surface roughness (μm)
01	3000	2000	8000	5	5	48.50
02	3000	2500	10,000	10	10	62.86
03	3000	3000	12,000	15	15	68.11
04	3000	3500	14,000	20	20	72.34
05	3500	2000	10,000	15	20	74.02
06	3500	2500	8000	20	15	50.66
07	3500	3000	14,000	5	10	54.11
08	3500	3500	12,000	10	5	54.32
09	4000	2000	12,000	20	10	57.44
10	4000	2500	14,000	15	5	*41.48*
11	4000	3000	8000	10	20	55.66
12	4000	3500	10,000	5	15	46.15
13	4500	2000	14,000	10	15	52.86
14	4500	2500	12,000	5	20	48.55
15	4500	3000	10,000	20	5	72.23
16	4500	3500	8000	15	10	80.80

3 Results and Discussion

3.1 Surface Roughness

Average surface roughness (Ra) was calculated from the ZETA optical profilometer [9]. Three readings were taken, and the average of readings was listed in Tables 2, 3 and 4 for Tool 1, 2, and 3, respectively. Here average surface roughness was considered as output parameter which depends on the various process parameters such as linear feed, plunging feed, spindle speed, step-over, and step-down. The lower is better criteria that were selected for the optimization [10, 11]. From Table 2, Tool 1 shows the minimum surface roughness (Ra) value as 41.48 μm which shows quite similar to the minimum surface roughness value obtain using Tool 3 shown in Table 4; this may because of the similarity in the geometry of the tools, but in case of Tool 2, the minimum surface roughness shows comparatively higher value as 54.46 μm.

The mean effect plot was drawn using Minitab 18 software, and using lower is the better criteria, the optimized process parameter was found for Tool 1 as linear feed (4000 mm/min), plugging feed (2500 mm/min), spindle speed (14,000 rpm), step-over (5 mm), and step-down (5 mm). Also for Tool 2 as linear feed (4500 mm/min), plugging feed (2500 mm/min), spindle speed (8000 rpm), and step-over (2 mm).

Table 3 Set of experiments (L16) for Tool 2

Serial No.	Linear feed (mm/min)	Plunging feed (mm/min)	Spindle speed (rpm)	Step-over (mm)	Surface roughness (μm)
01	3000	2000	8000	2	*54.46*
02	3000	2500	10,000	4	90.23
03	3000	3000	12,000	6	122.83
04	3000	3500	14,000	8	98.33
05	3500	2000	10,000	6	144.11
06	3500	2500	8000	8	93.39
07	3500	3000	14,000	2	82.67
08	3500	3500	12,000	4	85.28
09	4000	2000	12,000	8	82.62
10	4000	2500	14,000	6	91.98
11	4000	3000	8000	4	88.62
12	4000	3500	10,000	2	110.88
13	4500	2000	14,000	4	91.73
14	4500	2500	12,000	2	78.86
15	4500	3000	10,000	8	83.31
16	4500	3500	8000	6	71.89

Similarly, for Tool 3 as linear feed (4500 mm/min), plugging feed (3500 mm/min), spindle speed (14,000 rpm), step-over (12 mm), and step-down (15 mm). These optimized process parameters were used in Trial 2.

Finally, the average surface roughness of multi-featured bracket for Trial 1 and Trial 2 was measured at different respective positions and was found as 78.30 μm in Trial 1 and 47.70 μm in Trial 2.

Spindle speed was the factor that influences the surface roughness the most. A similar result was obtained for all the cutters. From the mean effect plot, it was observed that with the increase in the spindle speed surface roughness tends to reduce, and a similar finding was observed in case of metal machining [12].

Figure 3 represents the brackets manufactured in each trial. It was observed that Trial 2 gave a better result than Trial 1. The surface profile for the multi-featured bracket for Trial 1 and Trial 2 is shown in Fig. 5 under the observations field of view 4900 μm × 3700 μm. Multi-featured bracket manufactured by Trial 2 shows the soother profile than the Trial 1.

Table 4 Set of experiments (L16) for Tool 3

Serial No.	Linear feed (mm/min)	Plunging feed (mm/min)	Spindle speed (rpm)	Step-over (mm)	Step-down (mm)	Surface roughness (μm)
01	3000	2000	8000	6	5	85.91
02	3000	2500	10,000	8	10	77.26
03	3000	3000	12,000	10	15	77.85
04	3000	3500	14,000	12	20	56.16
05	3500	2000	10,000	10	20	108.16
06	3500	2500	8000	12	15	71.78
07	3500	3000	14,000	6	10	58.61
08	3500	3500	12,000	8	5	67.94
09	4000	2000	12,000	12	10	59.62
10	4000	2500	14,000	10	5	71.21
11	4000	3000	8000	8	20	56.97
12	4000	3500	10,000	6	15	54.90
13	4500	2000	14,000	8	15	*46.58*
14	4500	2500	12,000	6	20	60.00
15	4500	3000	10,000	12	5	47.58
16	4500	3500	8000	10	10	58.59

3.2 Processing Time

Processing time of any part in SOM decides by the summation of machining time, slicing time, gluing time, and other time. All these times depend on the path, such as machining time depends on the milling tool path, slicing time depends on the hot wire travel path, and so on [13]. It was observed that machining time contributes more to the processing time. The tool path for each trial is shown in Fig. 2.

Each white line represents the path for the respective operation. The total length of the path has a direct relation with the time; as the tool path for the Trial 2 shows less white lines and quite simple compared to Trial 1, it requires less processing time than Trial 1.

In the case of Trial 1, the step-down and step-over were too small because of smaller tool diameter, also because of the same tool path strategy as that of metal machining, and Trial 1 was semiautomatic while Trial 2 was fully automatic as double-sided adhesive tape applied on the bottom table before starting the operation and covered with polythene sheet so that chips should not stick to the tape while top machining. Bracket making using Trial 1 took 42 min to complete. While for Trial 2 took 18 min, respectively. 57.14% reduction in processing time was achieved with Trial 2.

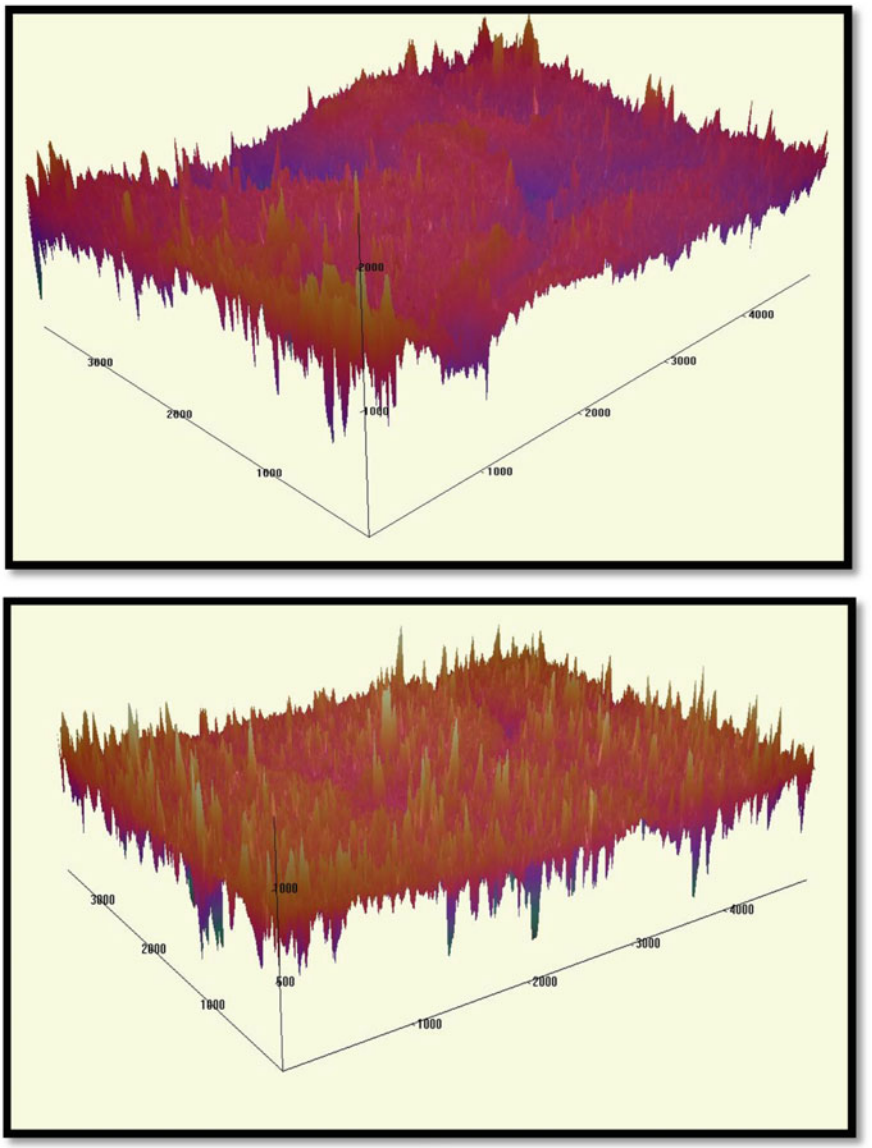


Fig. 1 Surface profile of the flat surface of the bracket in trial-1 and trial-2 using ZETA profilometer field of view was 4900 μm × 3700 μm

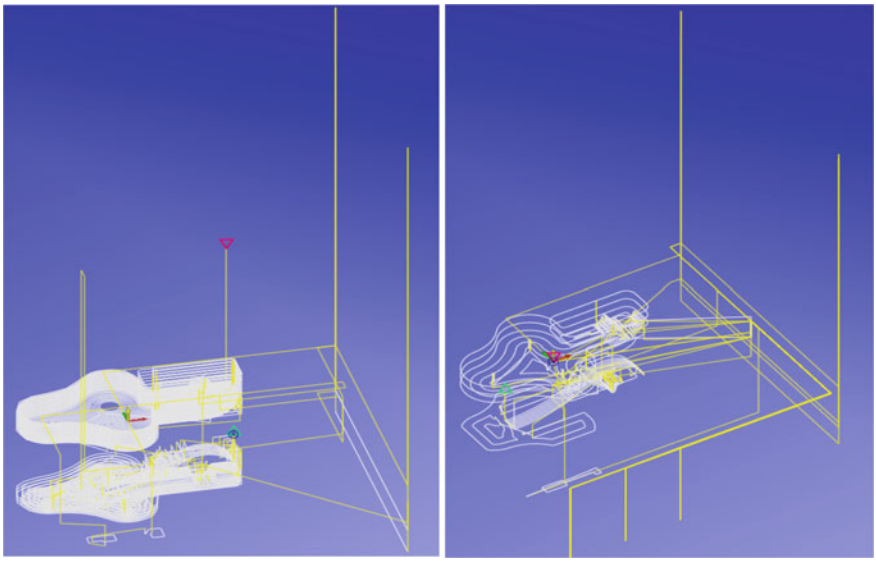


Fig. 2 A path for trial-1 and trial-2

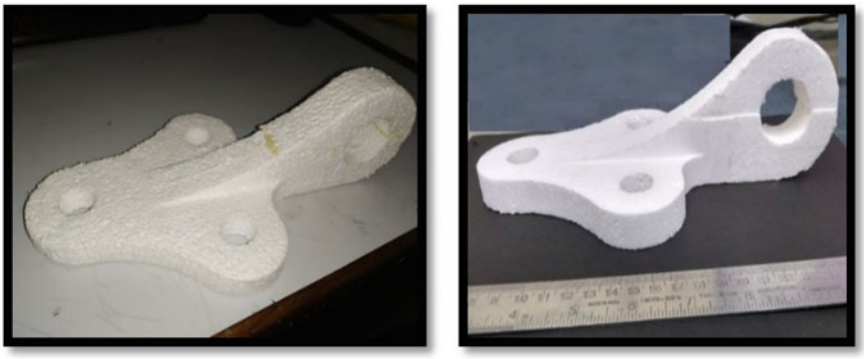


Fig. 3 Multi-featured bracket manufactured in trial 1 and trial 2

4 Conclusions

In this study, different trial has been performed on segmented object manufacturing to get a better surface finish as well as to reduce the cycle time. It has been observed that the machining system plays an important role in SOM which directly related to product surface quality and processing time.

In Trial 1, the only single tool has been used without considering the features of the bracket; also, process parameters and tool path for the same have been selected similar to the metal cutting from the available literature. At the same time in Trial 2,

three tools have been selected for different machine different features on the bracket; also, optimized process parameters and suitable tool path have been selected for the same.

It has been observed that average surface roughness (Ra) for multi-featured brackets has been reduced to 47.70 μm from 78.30 μm by adopting trial 2. Apart from this, tool path has been adjusted to accommodate the optimized process parameters, and process time for multi-featured bracket has been significantly reduced to 18 min from 42 min by adopting the trial 2, which shows 57.14% processing time reduction.

Further, research required in this area to understand the effect of tool geometry on the machinability of EPS foam. The processing time of SOM can be further reduced by optimizing the gluing and hot wire slicing operations. There is a need to develop special milling tools for plastic foams.

References

1. Karunakaran KP, Agrawal S, Vengurlekar PD, Sahasrabudhe OS, Pushpa V, Ely RH (2014) Segmented object manufacturing. IIE Trans 37(4):291–302
2. Bhagchandani RK, Kapil S, Kamble P (2018) Investigation of ablation studies of EPS pattern produce by rapid prototyping. Virtual Phys Prototyping 101–115
3. Kumar R, Kapil S, Negi S, Gehlot N, Gopalakrishna SH, Karunakaran KP (2017) Rapid prototyping of EPS pattern for complicated casting. Solid Freeform Fabric Additive Manuf 1877–1885
4. Karunakaran KP, Solanki PD, Sahasrabudhe OS, Pushpa V, Dwivedi R, Kovacevic R (2005) Simplified production of large prototypes using visible slicing, 16th solid free. Fabr Symp SFF 2005:406–417
5. Sun K, Li B, Fang L, Ye Q (2011) A novel rapid prototyping system for expandable polystyrene. Rapid Prototyping J 17(1):17–27
6. Brooks H, Davidson (2010) A review of state-of-the-art large-sized foam cutting rapid prototyping and manufacturing technologies. Rapid Prototyping J 16(5):318–327
7. Malak SFF, Anderson IA (2005) Orthogonal cutting of polyurethane foam. Int J Mech Sci (47):867–883
8. Shih AJ, Lewis MA, Strenkowski JS (2004) End milling of elastomers fixture design and tool effectiveness for material, removal. J Manuf Sci Eng 126:110–115
9. Balaraju J, Kulangara AJ, Rao CSP (2015) Application of Taguchi technique for identifying optimum surface roughness in CNC end milling process. Int J Eng Trends Technol 21(2):103–110
10. Mohammed IQ, Kadhum AH (2019) Optimizing the parameters of hot-wire CNC machine to enhance the cutting of plastic foam. Al-Khwarizmi Eng J 15(3):29–37
11. Anggoro PW, Bawono B, Andreyas W, Jamari J, Bayuseno AP (2016) Parameter optimization of strategies at CNC end milling machine Roland Modela MDX—40R Cam against surface roughness made insoles shoe orthotic EVA rubber foam. Int J Mech Mechatron Eng 16(4):96–102
12. Chen H, Shan Z (2018) Used by rapid prototype. Virtual Phys Prototyping (1):1–14
13. Chen H, Shan Z, Dong H (2013) Research of foam pattern processing for lost foam casting. Appl Mech Mater Online (331):600–603

Effect of Squeeze Casting on Microstructure and Wear Properties of Aluminium Al–Si Alloy



Reeturaj Tamuly, Amit Behl, and Hemant Borkar

Abstract Lightweight materials are of increasing interest to automotive and aerospace industries owing to their high specific strength and potential for reducing environmental impact due to lower CO_2 emissions. It has been found that many cast iron components are replaced by pure aluminium or aluminium alloy components which are manufactured by pressure-assisted casting operations. The application of pressure during solidification in squeeze casting improves mechanical properties, creates smoother surfaces and reduces porosities. In this work, the results highlight the effect of pressure-assisted casting (squeeze casting) process on microstructure, hardness and wear-resisting properties like fretting wear and dry sliding wear of Al–Si A356 alloy. It was observed that there was significant change in the microstructural characteristics like reduction in secondary dendrite arm spacings of α-Al phase/matrix, change in the eutectic Si morphology, reduction in microporosities. Effective precipitation of intermetallics was found to occur after heat treatment whereas mechanical properties like hardness and wear-resistant properties during fretting wear and dry sliding wear got improved on squeeze casting.

Keywords Microstructure · Al–Si alloy · Pressure-assisted casting · Squeeze casting · Fretting wear · Dry sliding wear

1 Introduction

Squeeze casting is a pressure-assisted casting process in which the molten metal is solidified under the application of pressure. Here, we obtain castings having mechanical properties similar to that of forged components. Chatterjee et.al. examined the effect of squeeze casting on Al–Si alloy of grade LM6 [1, 2]. They found that under the effect of pressure, the mechanical properties were improved. Heat treatable alloys

R. Tamuly (✉) · H. Borkar
Discipline of Metallurgy Engineering and Material Science, IIT Indore, Simrol 453552, India
e-mail: reeturajtamuly16@gmail.com

A. Behl
Hero MotoCorp Ltd., Neemrana 301705, India

© Springer Nature Singapore Pte Ltd. 2020

A. Praveen Kumar et al. (eds.), *Advances in Lightweight Materials and Structures*,
Springer Proceedings in Materials 8, https://doi.org/10.1007/978-981-15-7827-4_72

like LM24 and LM25/A357 were examined by Chadwick et.al. and concluded that squeeze casting process improves yield strength and ultimate tensile strengths of the material [3]. Maeng et al. found a significant refinement in grain microstructure for Al–Si alloy of grade B390 under a pressure up to 100 MPa [4]. Hence, from the literature survey, it can be concluded that squeeze casting process causes significant change in the microstructural characteristics of Al alloy which in turn improves the mechanical properties. Moreover, the heat treatment process plays a major role in improving the strength of the material.

Fretting wear is a major problem observed in most of the industrial applications. In fretting wear, when the oscillation of small-scale amplitude takes place between two different surfaces in contact under the influence of normal load, the resulting vibration causes damage in the surface quality, pit formation, high roughness of the surface, resulting in fatigue of the component. Fretting wear can be observed in a valve-seat assembly in internal combustion engines, gas turbine blade-root assembly and so on.

Dry sliding wear is another type of wear found in most industrial applications. In this type of wear, the contact surfaces are in continuous touch with each other under some applied load. Dry sliding wear experiments are typically conducted using pin/ball on disk tribometer [5–9].

Since most of the machinery parts are subjected to motion, there might be some loss in dimensional tolerances at the contact surfaces which in turn would damage the component. Hence, in order to safeguard the life span of such components, the study of various wear mechanisms has become a very important factor these days.

In this work, the effect of squeeze casting on microstructure, hardness, fretting wear and dry sliding wear is to be studied in Al–Si A356 alloy.

2 Experimental Procedure

2.1 Squeeze (Pressure-Assisted) Casting Process

The initial material for squeeze casting was obtained in the form of A356 alloy ingots from Hero MotoCorp Ltd. Laboratory-scale squeeze casting machine with stir casting assembly was used to cast Al alloy squeeze cast samples. The solidified cast product of 300 mm length and 50 mm diameter was obtained (Table 1).

2.2 Microstructure Study

The samples for microstructural examination were obtained from the pressure-assisted cast product (squeeze cast product). The samples were polished using a diamond paste and etched with Keller's reagent.

2.3 Heat Treatment Process

The squeeze cast samples were subjected to T6 type of heat treatment which involves solution treatment (520 °C for 4 h) followed by artificial aging (170 °C for 2 h).

2.4 Hardness

The hardness of the samples was tested using Rockwell hardness tester with 100 kgf load and (1/16)" diameter hardened steel ball. HRB limits were set as 20 HRB (minimum limit) and 100 HRB (maximum limit).

2.5 Wear Test

Fretting Wear

In fretting wear tribometer set-up, the upper specimen, made of Hardened steel of grade EN31, was loaded using a lever-dead weight assembly connected through a string. The upper specimen is in the form of steel pin with 6 mm diameter and a height of 15 mm. The frequency was set at 10 Hz, while the sliding amplitude was set at 250 μm at various loading conditions. The samples were tested at room temp and at an elevated temperature of 100 °C.

Dry Sliding Wear

The performance of the samples was also tested under dry sliding wear tests using a disc-shaped specimens of 5 mm thickness and 50 mm diameter. The test is done using a counter specimen, made of hardened steel ball of 8 mm diameter. One experiment was performed using sliding velocity of 0.15 m/s and 10 mm wear track diameter, while another experiment was carried out at sliding velocity of 0.25 m/s and 20 mm wear track diameter. The constant sliding distance of 300 mm and the constant load of 5 N were used in both the experiments.

3 Results and Discussions

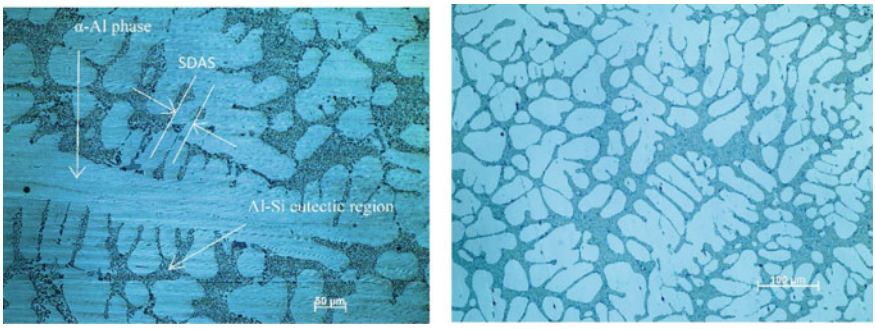
3.1 Microstructure

There was a significant change in microstructure on casting under pressure (squeeze casting) like change in the shape of α-Al matrix (from dendritic to globular), reduction

in secondary dendrite arm spacings (SDAS) to about 50% and uniform distribution of Al–Si eutectic regions (Fig. 1).

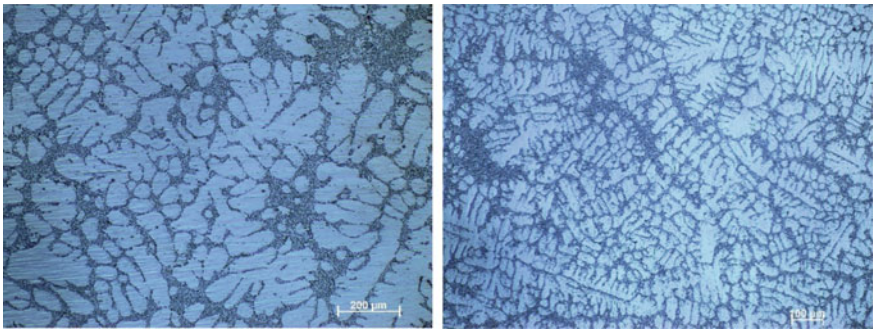
Effective precipitation was found in heat treated squeeze cast specimens than that of heat treated as-received A356 alloy (see Fig. 2).

Microporosity was found to be reduced after squeeze casting (see Fig. 3). The morphology of Si particles changed from needle/acicular to blocky shape on squeeze casting and on further heat treatment, its morphology was changed to spheroidal/globular shape (see Fig. 4a). After heat treatment, Mg-Si intermetallics (most probably, Mg2Si as detected in EDS analysis in Fig. 4b) got precipitated [12–15].



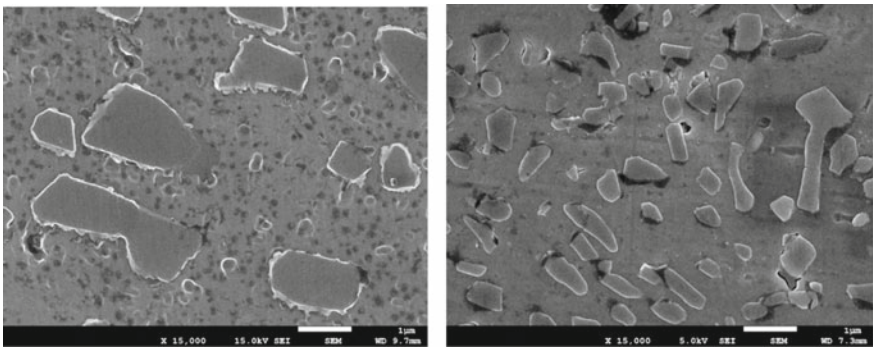
(a) (b)

Fig. 1 Optical microstructure of A356 alloy, **a** as received, and **b** squeeze cast



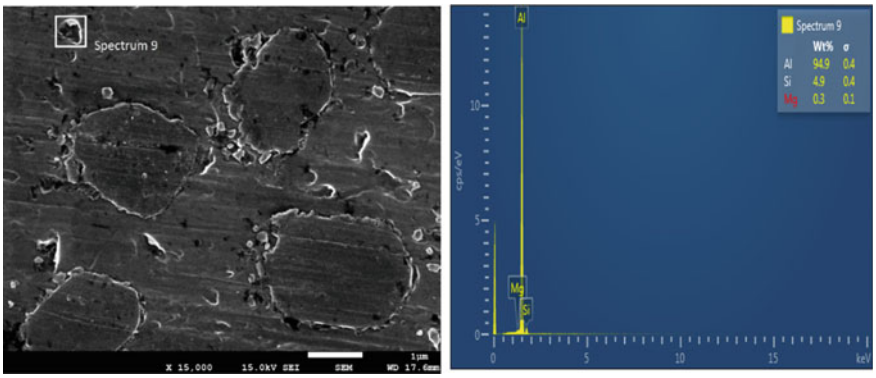
(a) (b)

Fig. 2 Optical microstructure of heat-treated A356 alloy **a** as-received, and **b** squeeze cast



(a) (b)

Fig. 3 SEM images of A356 alloy **a** as-received, and **b** squeeze cast alloy



(a) (b)

Fig. 4 Energy dispersive X-ray spectroscopy analysis of heat-treated squeeze cast A356 alloy

3.2 Hardness Test

The hardness was found to increase after squeeze casting while T6 heat treatment was shown to improve the hardness in both as-received as well as squeeze cast samples. The hardness value obtained for as-received A356 alloy is 71.94 (±5) HRB, squeeze cast A356 alloy is 86.3(±3) HRB, heat-treated as-received A356 alloy is 97 (±2) HRB and heat-treated squeeze cast A356 alloy is 98.2(±1) HRB.

3.3 Fretting Wear

SEM analysis on fretting wear tested sample (see Fig. 5) shows the presence of

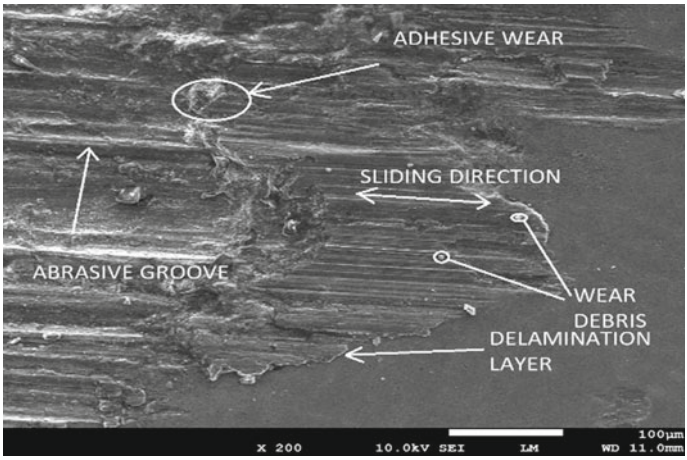


Fig. 5 SEM image of fretting wear tested squeeze cast A356 alloy sample

microstructural characteristics such as oxide debris, delamination layer, adhesive zone and abrasive wear grooves. A graph between friction coefficient and the number of fretting wear cycles was plotted for all the specimens at room temperature and elevated temperature.

With an increase in applied load, the average friction coefficient decreased as coefficient of friction is inversely proportional to applied normal load (see Table 2). The frictional coefficient values in all the cases were found to increase rapidly in the initial number of cycles (upto 1000–2000 cycles approx.) due to adhesive and abrasive action. The COF plot reaches a steady state in the later stages of fretting wear cycles due to formation of work-hardened layer by wear debris which restricts further wear.

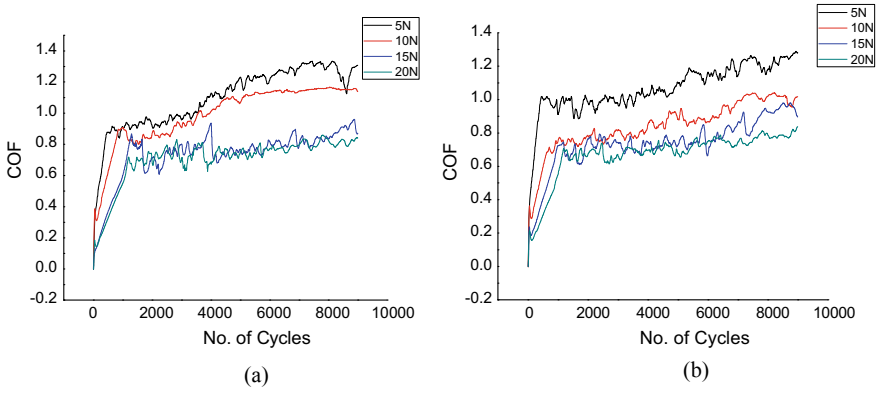


Fig. 6 Friction coefficient versus number of fretting cycles **a** as-received, and **b** squeeze cast

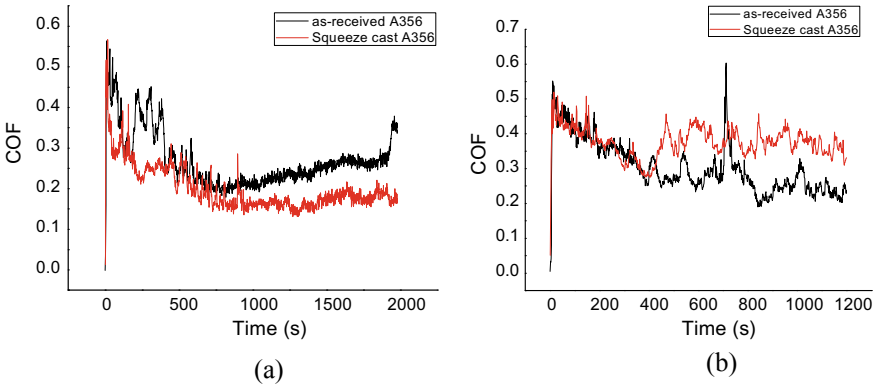


Fig. 7 Coefficient of friction versus wear time at sliding velocity of **a** 0.15 m/s, and **b** 0.25 m/s

Table 1 As received A356 alloy composition (wt.%)

Si	Ti	Mg	Sr	Fe	Others	Al
7.04	0.1346	0.3783	0.0154	0.09	0.0515	Balance

Table 2 Results of fretting wear tests (at room temperature)

Applied load	COF (as-received A356)	COF (squeeze cast A356)	COF (as-received heat-treated A356)	COF (squeeze cast heat-treated A356)
5	1.09	1.07	0.88	0.78
10	0.99	0.84	0.70	0.70
15	0.74	0.74	0.63	0.62
20	0.71	0.67	0.59	0.59

There were very minute changes in masses of the test specimen. Moreover, fluctuations in mass were observed which might be due to material transfer across the interface.

The coefficient of friction for squeeze cast A356 sample (heat-treated) was observed to be the lowest among all the specimens. Arun Prakash et al. for the first time observed (for dry sliding wear) that coefficient of friction and the hardness of the component are inversely proportional to each other [5]. Hence, similar predictions can be made for fretting wear conditions[10,11].

At an elevated temperature of 100 °C, the friction coefficient decreases because of the effect of softening of contact surfaces and reduction in adhesive joint strengths. But at the same time, the contact area increases at the interface. So, a greater number of adhesive joints get exposed and hence friction coefficient increases. Hence, the friction coefficient at elevated temperature is in intermediate range, i.e. neither too high nor too low (see Table 3). This was observed by Wan et al. under dry sliding

Table 3 Results of fretting wear tests (at 100 °C)

Load (N)	COF of as received A356	COF of squeeze cast A356	COF of heat-treated as received A356	COF of heat-treated squeeze cast A356
5	0.93	0.95	0.91	0.94
10	0.71	0.77	0.71	0.71

wear tests [6]. Similar predictions can be made for A356 alloy under fretting wear conditions.

3.4 Dry Sliding Wear

The average coefficient of friction for squeeze cast A356 alloy was observed to be lower than that of as received A356 alloy when the parameters used were 0.15 m/s and 10 mm as sliding velocity and wear track diameter, respectively. But the friction coefficient for the squeeze cast A356 alloy was observed to be higher than industrially cast A356 alloy when the parameters used were 0.25 m/s and 20 mm as sliding velocity and wear track diameter, respectively. Hence, we can predict that the friction coefficient may be affected by various factors like hardness, shear strength of weaker material, adhesive bonding between the asperities, etc. This observation was made by Moore et al. for any component which undergo sliding wear [7]. Similar predictions can be made for A356 alloy.

Moreover, lower the wear depth higher is the hardness of the specimen. Hence, from Table 4, one can predict that squeeze cast samples with lower wear depth have improved hardness properties.

Table 4 Results of dry sliding wear (ball on disk) test

Testing parameters	COF (as-received A356)	COF (squeeze cast A356)	as-received A356 wear depth (**μm**)	Squeeze cast A356 wear depth (**μm**)
WTD-10 mm, SV-0.15 m/s	0.269	0.199	156.317	80.494
WTD-20 mm, SV-0.25 m/s	0.303	0.375	246.569	119.158

4 Conclusions

Following conclusions can be obtained from the current work:

- Squeeze casting showed microstructural refinement with decreased SDAS, uniform distribution of eutectic and intermetallic phases and modified primary Al dendritic morphology. Effective precipitation was observed after T6 heat treatment process in case of the squeeze cast product.
- Increase in hardness values in case of squeeze cast samples were observed and the hardness was found to be the highest in case of squeeze cast samples further subjected to T6 heat treatment.
- Both fretting and dry sliding wear resisting properties were improved after squeeze casting process.

It may be concluded that Si being the hard phase, can provide high wear resistant properties in Si-based Al alloy. Hence in order to reduce the stress concentration created by the morphology of Si, further new modification techniques may be investigated.

Acknowledgements Corresponding author would like to thank Hero MotoCorp Ltd. for their assistance in experimental work and support in undergoing this research.

References

1. Chatterjee S, Das AA (1973) Some observations on the effect of pressure on the solidification of Al-Si eutectic alloys. Brit Foundryman 66
2. Chatterjee S, Das AA (1972) Effects of pressure on the solidification of some commercial aluminium base casting alloys. Brit Foundryman 65
3. Chadwick GA, Yue TM (1989) Principles and applications of squeeze casting. Metals Mater
4. Maeng DY, Lee JH, Won CW, Cho SS, Chun BS (2000) The effects of processing parameters on the microstructure and mechanical properties of modified B390 alloy in direct squeeze casting. J Mater Process Technol 105:196–203
5. Arun PN, Gnanamoorthy R, Kamaraj M (2012) Fretting wear behaviour of controlled ball impact treated aluminium alloy under dry sliding condition. Surf Coat Technol 207:450–460
6. Cai LWJ, Zhou J, Duszczyk J (2009) Characteristics of the friction between aluminium and steel at elevated temperatures during ball-on-disc tests. Tribol Lett 36:183–190
7. Moore AJW, Tegart WJM, Bowden FP (1952) Relation between friction and hardness. Proc R Soc Lond A 212(1111):452–458
8. Sarkar AD (1975) Wear of Al-Si alloys. Wear 31:331–343
9. Clarke J, Sarkar AD (1979) Wear characteristics of as-cast binary Al-Si alloy. Wear 54
10. Hurricks PL (1970) The mechanism of fretting—a review. Wear 15:389
11. Iwabuchi A (1991) The role of oxide particles in the fretting wear of mild steel. Wear 151:301
12. Han YS, Kim DH, Lee HI, Kim YG (1994) Effect of applied pressure during solidification on the microstructural refinement in an Al-Cu alloy. Scripta Metallurgica et Materialia 31(12):1623–1628
13. Gallerneault M, Durrant G, Cantor B (1995) Eutectic channelling in a squeeze cast Al-4.5wt%Cu alloy. Scripta Metallurgica et Materialia 32(10):1553–1557

14. Hong CP, Shen HF, Lee SM (1998) Prevention of macro defects in squeeze casting of an Al-7 wt pct Si alloy. Metall Mater Trans B 31B:297–305
15. Hong CP, Shen HF, Cho IS (1998) Prevention of macro segregation in squeeze casting of an Al-4.5 wt% Cu alloy. Metall Mater Trans A 29A

Numerical Analysis of Smart Materials

Double Diffusion Due to Centrally Heated Strip in Porous Material



N. Ameer Ahamad, Azeem, Maughal Ahmed Ali Baig, and A. Praveen Kumar

Abstract This work describes the analysis being carried out to find out the diffusion of heat and mass because of multiple sources of heat placed in the medium. A small heating strip is placed centrally apart from regular heating at the left surface. The height of the strip is varied to understand its effect on double diffusion in the medium. The mass diffusion occurs between the vertical surfaces of the cavity under the influence of concentration gradient as well as the thermal gradient. Finite element method (FEM) has been employed for solving the equations. Solution is obtained through an in-house code that works on FEM. The elements of the domain are selected such that they have triangular shape with three nodes. Solution of the equations is obtained following an iterative process, and the results are described using contour plots of concentration, isotherms, and streamlines.

Keywords Porous · Internal heating · Double diffusion

1 Introduction

Most of the engineering and scientific problems cannot be experimentally determined due to various restrictions imposed. Among those restrictions are the cost of experimentation as well as the time required to conduct such experiments. This is also true for the study of porous medium where many researchers have relied on the numerical investigation of different phenomenon such as natural convection [1–5], mixed convection [6–8], viscous dissipation [9, 10], and non-equilibrium [11, 12] to

N. Ameer Ahamad
Department of Mathematics and Computer Science, Taylor's University, No. 1 Jalan Taylo's Subang Jaya, 47500 Selangor Darul Ehsan, Malaysia

Azeem
Mathematics Department, Faculty of Science, University of Tabuk, P.O. BOX. 741, Tabuk 71491, Saudi Arabia

M. A. A. Baig (✉) · A. Praveen Kumar
Department of Mechanical Engineering, CMR Technical Campus, Hyderabad, Telangana, India
e-mail: mabaig13@gmail.com

© Springer Nature Singapore Pte Ltd. 2020

A. Praveen Kumar et al. (eds.), *Advances in Lightweight Materials and Structures*, Springer Proceedings in Materials 8, https://doi.org/10.1007/978-981-15-7827-4_73

name but a few. Among such phenomenon, the double diffusion is also an important case where the heat and mass diffusion take place simultaneously due to gradients created by applied heat and mass concentration at different surfaces in the domain. The diffusion of mass can depend on its own variables such as Lewis number and buoyancy ratio apart from the parameters which are common for the heat transfer [13–17]. The mass transfer behavior is studied extensively for the cases where the single heat source in regular form exists. However, the effect of multiple heat sources on the behavior of especially mass transfer is yet to be reported. The current article is a step in that direction to know the scenario when the heat source is present at two places, i.e., one at the outside surface of the domain and another at the internal section of the porous medium. The high concentration exists at left surface and low concentration at right surface.

2 Analysis

This work comprises the study of double diffusion due to multiple heat sources as shown in Fig. 1.

The related equations in porous domain can be derived from [18–22]

$$\frac{\partial u}{\partial x} + \frac{\partial \mathrm{v}}{\partial y} = 0 \tag{1}$$

$$\frac{\partial u}{\partial y} - \frac{\partial \mathrm{v}}{\partial x} = -\frac{gK}{\nu}\left(\beta_T \frac{\partial T}{\partial x} + \beta_c \frac{\partial C}{\partial x}\right) \tag{2}$$

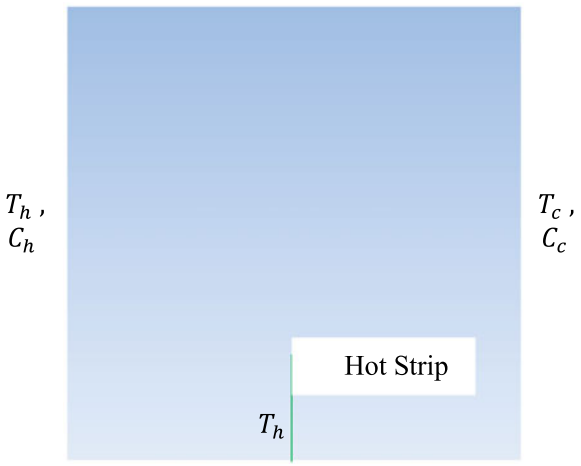


Fig. 1 Porous cavity

$$u\frac{\partial T}{\partial x} + \mathrm{v}\frac{\partial T}{\partial y} = \alpha\left(\frac{\partial^2 T}{\partial x^2} + \frac{\partial^2 T}{\partial y^2}\right) - \frac{1}{\rho C_p}\frac{\partial q_r}{\partial x} \tag{3}$$

$$u\frac{\partial C}{\partial x} + \mathrm{v}\frac{\partial C}{\partial y} = D\left(\frac{\partial^2 C}{\partial x^2} + \frac{\partial^2 C}{\partial y^2}\right) \tag{4}$$

$$q_r = -\frac{4\sigma}{3\beta_r}\frac{\partial T^4}{\partial x} \tag{5}$$

Expanding T^4 [23–28]

$$T^4 \approx 4TT_\infty^3 - 3T_\infty^4 \tag{6}$$

Boundary conditions are

$$x = 0, T = 1, C = 1, u = 0, \mathrm{v} = 0 \tag{7a}$$

$$x = L, T = T_c, C = 0, u = 0, \mathrm{v} = 0 \tag{7b}$$

$$y = 0, \partial T/\partial y = 0, u = 0, \mathrm{v} = 0 \tag{7c}$$

$$\partial T/\partial y = 0, \partial C/\partial y = 0, T = T_h, u = 0, \mathrm{v} = 0 \tag{7d}$$

At the strip

$$\partial C/\partial y = 0 \tag{7e}$$

Finite element method as employed in references [29–35] is used to solve the equations.

3 Results and Discussion

Figure 2 depicts heat and mass diffusion with the help of the contours of temperature, concentration, and stream functions at $\mathrm{R_d} = 0.5$, $\mathrm{Ra} = 100$, $\mathrm{Le} = 5$. $N = 0.1$, The left column shows the heating strip having the height 1/4th of cavity height and that of right column as ½ cavity height. The heat transfer should reduce from hot surface to the medium due to increase in the strip height which can be very much understood from the fact that the isotherm line with non-dimensional temperature of 0.95 has moved deep into the cavity. This ensures that the temperature gradient between two vertical surfaces and the cavity reduces, that in turn reduces the heat transfer. The mass transfer too is affected due to changing the strip height from 1/4th to ½ of cavity

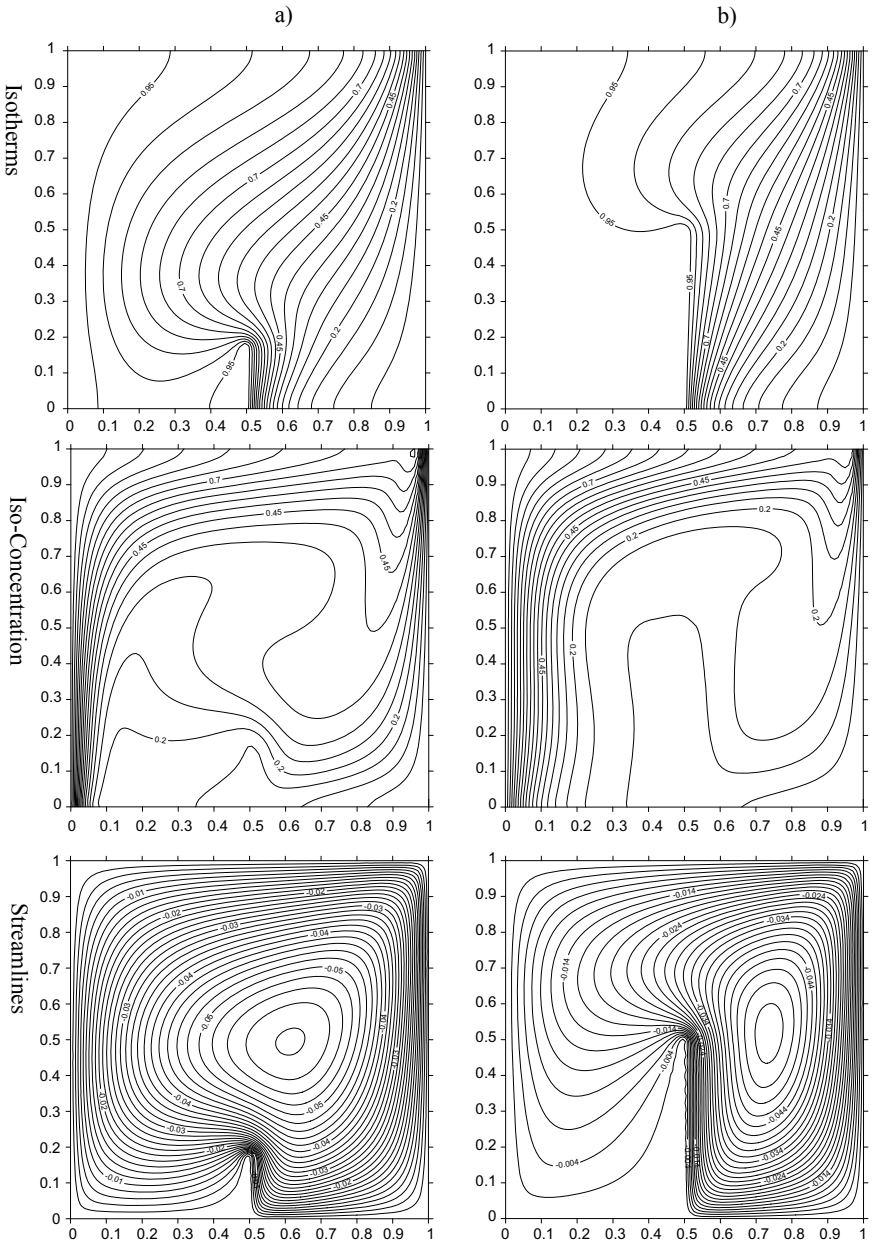


Fig. 2 Contours **a** St = 1/4, **b** St = ½

height. For the case of small strip height, the mass diffusion is more at the bottom of the cavity which can be observed through high concentration gradient at the lower part of the left surface and it decreases as the height of the left surface increases. This means that the mass transfer decreases from bottom of left surface until the top. However, the increase in the height of inside heater changes this scenario and the mass transfer across the left vertical surface remains almost constant which is indicated by almost straight concentration lines along that surface. There is large variation in concentration gradient in upper part of cavity due to increased strip height as compared to its smaller height. The streamlines mainly flow between the hot strip and the cold surface when strip height is more in comparison with lower height.

Figure 3 depicts buoyancy ratio (N) at $\mathrm{Ra} = 100$, $\mathrm{R_d} = 0.5$, $\mathrm{St} = 1/3$, $\mathrm{Le} = 5$, which is one of the important parameter to determine mass transfer. Heat transfer slightly decreases with increase in N which can be inferred from the isotherms. However, the concentration lines are seen to be aligned more closely to the left surface when the value of buoyancy ratio is increased as shown by the iso-concentration on right column of Fig. 3. The fluid movement changes the direction to more on left to right from being top to bottom surface when the buoyancy ratio is increased.

Figure 4 depicts another important parameter from mass transfer perspective, i.e., Lewis number (Le) at $\mathrm{Ra} = 100$, $\mathrm{R_d} = 0.5$, $N = 0.3$, $\mathrm{St} = 1/3$. The left column of figure corresponds to $\mathrm{Le} = 1$ and that of right column to $\mathrm{Le} = 10$. The isotherms are not much affected though it comes slightly closer to hot surface when Le is increased. However, there is drastic change in the shape of iso-concentration lines when Le is increased from 1 to 10. At $\mathrm{Le} = 1$, the concentration lines are highly spread out from each other that shows that the concentration gradient is smaller at $\mathrm{Le} = 1$. The concentration lines come very close to the left surface at increased Le ($\mathrm{Le} = 10$) which create high concentration gradient. This leads to substantially enhanced mass transfer as compared to the case of $\mathrm{Le} = 1$. The fluid flow pattern is also affected when Le is changed. At higher values of Le, the fluid cell flows from top to bottom, whereas its orientation is more toward left to right surface at $\mathrm{Le} = 1$.

4 Conclusion

This study aims to know multiple heating effects on double diffusion in a porous material. The study evaluates the effect of hot strip, the Lewis number, buoyancy ratio. It is noted that the

- Heat transfer decreased when height of the strip is increased.
- The mass transfer attains almost constant value all along the vertical surface when strip is elongated.
- Fluid orientation changes due to increased strip height.
- Mass transfer is highly sensitive to the Lewis number.

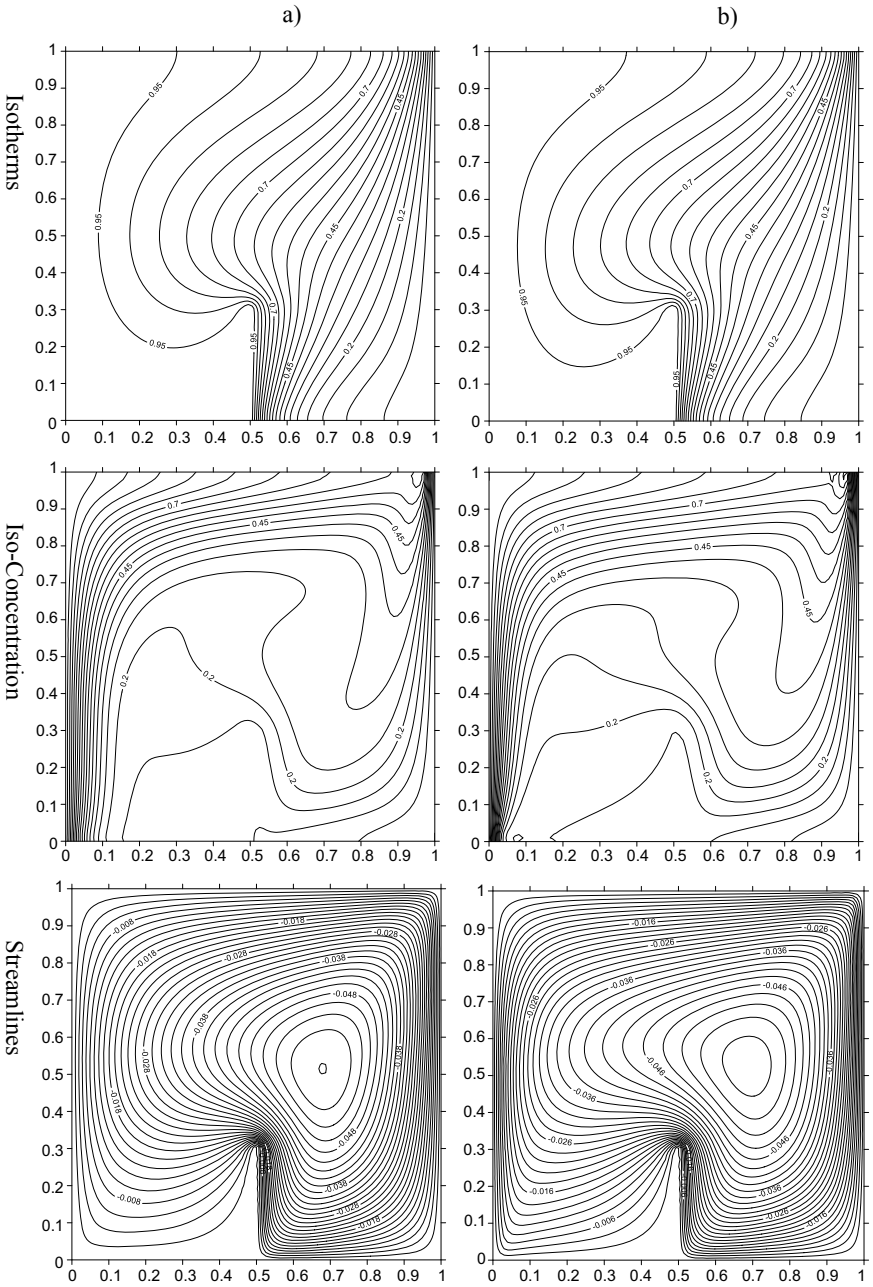


Fig. 3 Contours **a** $N = 0.1$, **b** $N = 0.5$

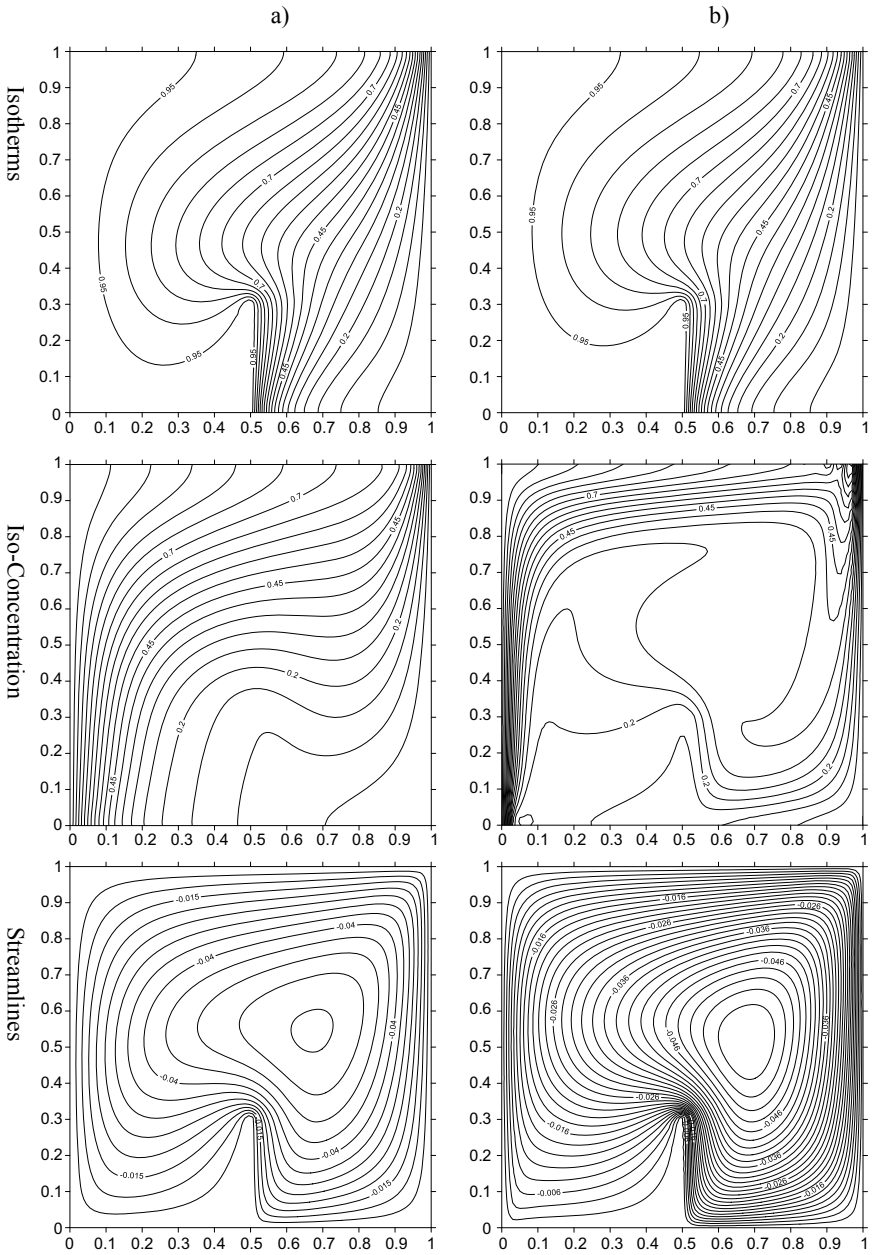


Fig. 4 Contours **a** Le = 1, **b** Le = 10

References

1. Badruddin IA, Zainal ZA, Narayana PAA, Seetharamu KN (2006) Heat transfer by radiation and natural convection through a vertical annulus embedded in porous medium. Int Commun Heat Mass Transf 33(4):500–507
2. Badruddin IA, Zainal ZA, Khan ZA, Mallick Z (2007) Effect of viscous dissipation and radiation on natural convection in a porous medium embedded within vertical annulus. Int J Therm Sci 46(3):221–227
3. Ahamad NA, Athani A, Badruddin IA (2018) Heat transfer prediction in a square porous medium using artificial neural network. AIP Conf Proc 1953:140017. https://doi.org/10.1063/1.5033192
4. Athani A, Ahamad NA, Badruddin IA (2018) Application of artificial neural network for heat transfer in porous cone. AIP Conf Proc 1953:140016. https://doi.org/10.1063/1.5033191
5. Badruddin IA, Al-Rashed AAAA, Ahmed NJS, Kamangar S, Jeevan K (2012) Natural convection in a square porous annulus. Int J Heat Mass Transf 55(23–24):7175–7187
6. Ahmed NJS, Badruddin IA, Kanesan J, Zainal ZA, Ahamed KSN (2011) Study of mixed convection in an annular vertical cylinder filled with saturated porous medium, using thermal non-equilibrium model. Int J Heat Mass Transf 54(17–18):3822–3825
7. Baig MAA, Salman Ahmed NJ, Ameer Ahamad N, Kamangar S, Reddy AR, Badruddin UA (2019) Discrete heating at bottom of annulus in case of mixed convection: aiding flow. AIP Conf Proc 2200:020051. https://doi.org/10.1063/1.5141221
8. Baig MAA, Salman Ahmed NJ, Ameer Ahamad N, Reddy AR, Badruddin IA, Mangesh L (2019) Discrete heating of opposing mixed convection heated at bottom of annulus. AIP Conf Proc 2200:020050. https://doi.org/10.1063/1.5141220
9. Khan TMY, Baig MAA, Azeem NA, Ahamad IA, Badruddin (2019) Heat and mass transfer with viscous dissipation in porous medium: FEM based methodology. AIP Conf Proc 2104(1):030058. https://doi.org/10.1063/1.5100485
10. Kamangar S, Baig MAA, Azeem NA, Ahamad IA Badruddin (2019) Finite element solution strategy for viscous dissipation in porous medium. AIP Conf Proc 2104(1):030057. https://doi.org/10.1063/1.5100484
11. Badruddin IA (2020) Thermal non-equilibrium in porous annulus: a new finite element solution technique. Arab J Sci Eng 45(2):1279–1292. https://doi.org/10.1007/s13369-019-04298-4
12. Badruddin IA (2019a) Numerical analysis of thermal non-equilibrium in porous medium subjected to internal heating. Mathematics 7(11):1085. https://doi.org/10.3390/math7111085
13. Baig MAA, Azeem NJ, Ahmed S, Kamangar S, Yunus Khan TM, Badruddin IA, Reddy AR, Khaleed HMT (2020) Finite element formulation of conjugate double diffusion in porous annulus. AIP Conf Proc 2204:040017. https://doi.org/10.1063/1.5141590
14. Badruddin IA, Ahmed NJS, Anqi AE, Kamangar S (2019) Conjugate heat and mass transfer in a vertical porous cylinder. J Thermophys Heat Transf 33(2):548–558. https://doi.org/10.2514/1.T5488
15. Badruddin IA, Ahmed NJS, Al-Rashed AAAA, Kanesan J, Kamangar S, Khaleed HMT (2012) Analysis of heat and mass transfer in a vertical annular porous cylinder using FEM. Transp Porous Media 91(2):697–715
16. Ahmed NJS, Badruddin IA, Zainal ZA, Khaleed HMT, Kanesan J (2009) Heat transfer in a conical cylinder with porous medium. Int J Heat Mass Transf 52(13–14):3070–3078
17. Badruddin IA, Azeem K, Idris MYI, Nik-Ghazali N, Ahmed NJS, Abdullah AAA, Al-Rashed (2017) Simplified finite element algorithm to solve conjugate heat and mass transfer in porous medium. Int J Numer Methods Heat Fluid Flow 27(11):481–2507
18. Azeem MEM, Soudagar NJS, Ahmed IA, Badruddin (2017) Fem formulation for heat and mass transfer in porous medium. In: IOP conference series: materials science and engineering 225:012022. https://doi.org/10.1088/1757-899X/225/1/012022
19. Azeem, Badruddin IA, Idris MYI, Nik-Ghazali N, Ahmed NJS, Al-Rashed A (2016) Conjugate heat and mass transfer in square porous cavity. Indian J Pure Appl Phys 54:777–786

20. Badruddin IA (2019b) Heat and mass transfer with soret/dufour effect in irregular porous cavity. J Thermophys Heat Transf 33(3):647–662. https://doi.org/10.2514/1.T5666
21. Badruddin IA, Abdullah AAAA, Ahmed NJS, Kamangar S (2012) Investigation of heat transfer in square porous-annulus. Int J Heat Mass Transf 55(7–8):2184–2192
22. Nik-Ghazali N, Badruddin IA, Badarudin A, Tabatabaeikia S (2014) Dufour and Soret effects on square porous annulus. Adv Mech Eng 6:209753
23. Ahamad NA, Kamangar S, Badruddin IA (2019) Heat transfer in a porous cavity in presence of square solid block. Int J Numer Meth Heat Fluid Flow 29(2):640–656. https://doi.org/10.1108/HFF-05-2017-0193
24. Badruddin IA, Khan IA (2017) Heat transfer in an l shaped porous medium using FEM. In: IOP conference series: materials science and engineering, vol 225, p 012012. https://doi.org/10.1088/1757-899X/225/1/012012
25. Badruddin IA (2019c) Investigation of heat transfer in irregular porous cavity subjected to various boundary conditions. Int J Numer Meth Heat Fluid Flow 29(1):418–447. https://doi.org/10.1108/HFF-04-2018-0132
26. Azeem MEM, Soudagar, Badruddin IA (2017) Investigation of heat transfer due to isothermal heater in irregular porous cavity: part I. AIP Conf Proc 1859:020044. https://doi.org/10.1063/1.4990197
27. Azeem IA, Badruddin N, Nik-Ghazali, Idris MYI, Anqi AE, Ahmed NJS, Kamangar S, Al-Rashed (2018) Effect of size and location of solid on conjugate heat transfer in porous cavity. Indian J Pure Appl Phys 56:792–801
28. Ahamad NA, Baig MAA, Ahmed NJS, Kamangar S, Khan TMY, Badruddin IA, Reddy AR, Khaleed HMT (2020) Finite element formulation of conjugate heat transfer in porous annulus. AIP Conf Proc 2204:040016. https://doi.org/10.1063/1.5141589
29. Yunus Khan TM, Badruddin IA, Quadir GA (2016) Heat transfer in a conical porous cylinder with partial heating. In: IOP conference series: materials science and engineering, vol 149, p 012211
30. Ahamad NA, Baig MAA, Kamangar S, Khan TMY, Badruddin IA (2019) Partial heating at upper section of annulus subjected to conjugate heat transfer in porous annulus. AIP Conf Proc 2105(1):020021. https://doi.org/10.1063/1.5100706
31. Ahamad NA, Baig MAA, Kamangar S, Khan TMY, Badruddin IA (2019) Conjugate heat transfer due to partial isothermal heating at center of annuls with two solids in porous annulus: part I. AIP Conf Proc 2105(1):020020. https://doi.org/10.1063/1.5100705
32. Azeem, Baig MAA, Khaleed HMT, Kamangar S, Badruddin IA (2019) Partial heating at lower section of annulus subjected to conjugate heat transfer in porous annulus. AIP Conf Proc 2105(1):020019. https://doi.org/10.1063/1.5100704
33. Ahmed NJS, Kamangar S, Badruddin IA, Al-Rashed AAAA, Quadir GA, Khaleed HMT, Khan TMY (2014) Conjugate heat transfer in porous annulus. J Porous Media 19(12):1109–1119
34. Badruddin IA, Ahmed NJS, Al-Rashed AAA, Nik-Ghazali N, Jameel M, Kamangar S, Khaleed HMT, Khan TMY (2015) Conjugate heat transfer in an annulus with porous medium fixed between solids. Transp Porous Media 109(3):589–608
35. Ahamad NA, Soudagar MEM, Kamangar S, Badruddin IA Fem formulation of coupled partial differential equations for heat transfer. In: IOP conference series: materials science and engineering 225:012023. https://doi.org/10.1088/1757-899X/225/1/012023.

Conjugate Heat and Mass Transfer Due to Solid Block in Porous Material

N. Ameer Ahamad, Azeem, Maughal Ahmed Ali Baig, and M. Shunmugasundaram

Abstract The impact of different variables, namely thermal conductivity ratio of solid to porous the radiation parameter and Rayleigh number, is investigated in a cavity being fixed with porous medium that contains a solid material. The solid material which is having square geometry is made to occupy the central position in the cavity. The conjugate heat transfer coupled with mass transfer is analyzed because of the presence of solid in the domain. The left surface of the cavity is forced to have the highest temperature as well as concentration as compared to the right surface that has the lowest temperature and concentration. The energy transport across the solid takes place due to conjugate effect, whereas convection also takes place in the porous domain. Finite element method based on simple triangular element with a node at each of three corners is employed to get the solution of equations across the medium.

Keywords Conjugate heat transfer · Porous material · Solid square block

1 Introduction

Heat transfer can be associated with variety of devices including almost all scientific and engineering disciplines. One of those important disciplines is the porous material or media [1–3] where the heat transfer can have substantial variation from that of its solid counterpart due to the presence of pores which facilitates the flow of liquid or gas which in turn helps to transfer the thermal energy. There are varieties of studies

N. Ameer Ahamad
Department of Mathematics and Computer Science, Taylor's University, No. 1 Jalan Taylor's, Subang Jaya 47500, Selangor Darul Ehsan, Malaysia

Azeem
Mathematics Department, Faculty of Science, University of Tabuk, Tabuk P.O. BOX. 741, 71491, Saudi Arabia

M. A. A. Baig (✉) · M. Shunmugasundaram
Department of Mechanical Engineering, CMR Technical Campus, Hyderabad, Telangana, India
e-mail: mabaig13@gmail.com

© Springer Nature Singapore Pte Ltd. 2020

A. Praveen Kumar et al. (eds.), *Advances in Lightweight Materials and Structures*,
Springer Proceedings in Materials 8, https://doi.org/10.1007/978-981-15-7827-4_74

being reported encompassing the phenomenon of heat transfer in porous material [4–7]. It is noted that the porous material heat transfer is a complex issue which needs to be modeled using multiple equations that are interconnected with each other by certain parameters [8–11] the number of equations to be solved to predict a heat transfer depends on the particular phenomenon being associated with the porous medium. For instance, there are two equations required for thermal equilibrium case [12–16] but three equations involved in thermal non-equilibrium condition [17, 18]. It requires three equations for double diffusion [19, 20] as well as conjugate heat transfer without mass transfer [21–28]. However, there would be 4 equations involved when double diffusion is coupled with conjugate heat transfer [29], thus making it a difficult phenomenon to simulate. It would be important to know the heat and mass transfer behavior and its influencing parameters. This study is particularly focused to evaluate the influence of thermal conductivity ratio, Rayleigh number, and radiation parameter on double diffusion when conjugate heat transfer is present because of solid.

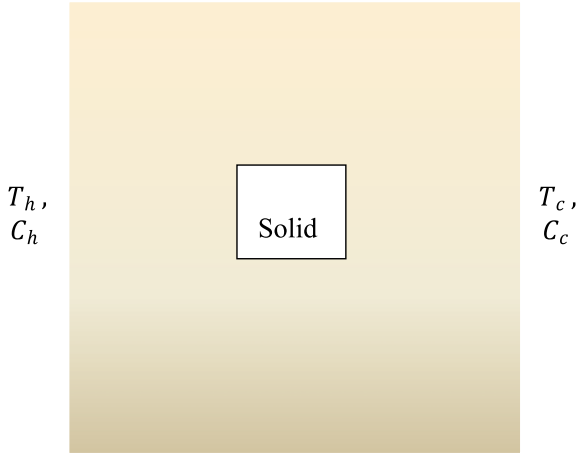
2 Analysis

The physical domain can be considered as in Fig. 1.

The related equations are

$$\frac{\partial^2 \overline{\psi}}{\partial \overline{x}^2} + \frac{\partial^2 \bar{\psi}}{\partial \overline{y^2}} = -Ra \frac{\partial \overline{T_p}}{\partial \overline{x}} \tag{1}$$

Fig. 1 Porous cavity



$$\left[\frac{\partial\overline{\psi}}{\partial\overline{y}}\frac{\partial\overline{T}}{\partial\overline{x}}-\frac{\partial\overline{\psi}}{\partial\overline{x}}\frac{\partial\overline{T}}{\partial\overline{y}}\right]=\left(\left(1+\frac{4R_{\mathrm{d}}}{3}\right)\frac{\partial^2\bar{T}}{\partial\bar{x}^2}+\frac{\partial^2\overline{T}}{\partial\overline{y}^2}\right) \tag{2}$$

$$\left(1+\frac{4R_{\mathrm{d}}}{3}\right)\frac{\partial^2\bar{T}}{\partial\bar{x}^2}+\frac{\partial^2\overline{T}}{\partial\overline{y}^2}=0 \tag{3}$$

$$\left[\frac{\partial\overline{\psi}}{\partial\overline{y}}\frac{\partial\overline{C}}{\partial\overline{x}}-\frac{\partial\overline{\psi}}{\partial\overline{x}}\frac{\partial\overline{C}}{\partial\overline{y}}\right]=\frac{1}{Le}\left(\frac{\partial^2\overline{C}}{\partial\bar{x}^2}+\frac{\partial^2\overline{C}}{\partial\overline{y}^2}\right) \tag{4}$$

where

$$R_{\mathrm{d}}=\frac{4\sigma T_c^3}{\beta_r k},\ Ra=\frac{g\beta\Delta T K L}{\nu\alpha},\ Le=\frac{\alpha}{D},\ N=\left(\frac{\beta_c\Delta C}{\beta_T\Delta T}\right)$$

$K_r\frac{\partial\bar{T}_s}{\partial\bar{x}}=\frac{\partial\bar{T}_p}{\partial\bar{x}}$ at the solid porous interface.

The Nusselt (Nu) and Sherwood (Sh) number are calculated as:

$$\mathrm{Nu}=-\left(\left(1+\frac{4}{3}R_{\mathrm{d}}\right)\frac{\partial\bar{T}}{\partial\bar{x}}\right)_{\bar{x}=0}\ \mathrm{Sh}=\left(-\frac{\partial\bar{C}}{\partial\bar{x}}\right)_{\bar{x}=0} \tag{5}$$

Using the procedure as described [30–36], FEM is used to solve the above-mentioned equations.

3 Results and Discussion

Figure 2 shows the outcome of thermal conductivity ratio between the solid block and the porous media with the constants as $B = 37.5\%$, $Le = 5$, $Ra = 100$, $R_{\mathrm{d}} = 0$, $N = 0.2$. Here B indicates the percent of solid size in comparison with that of cavity. The solid block allows more heat due to higher thermal conductivity ratio as compared to that of porous region and vice versa. Similar behavior is observed for the case of conjugate heat transfer. The increased thermal conductivity acts in favor of increasing the mass transfer as observed by iso-concentration of Fig. 2. However, it also leads concentration to be occupied at smaller area in cavity as compared to the case of lower thermal conductivity ratio.

Figure 3 predicts the role of Rayleigh number (Ra) at $B = 37.5\%$, $K_r = 2$, $Le = 5$, $R_{\mathrm{d}} = 1$, $N = 0.2$. Increased Rayleigh number along with radiation parameter leads to higher fluid velocity which hikes the thermal, concentration gradient at hot surface. The isothermal lines are almost parallel to the vertical surfaces when $Ra = 10$ which signifies that the heat transfer is dominantly taking place due to the conduction of thermal energy. However, the increase in Rayleigh number creates distortion of isothermal lines which is a result of higher fluid movement as shown

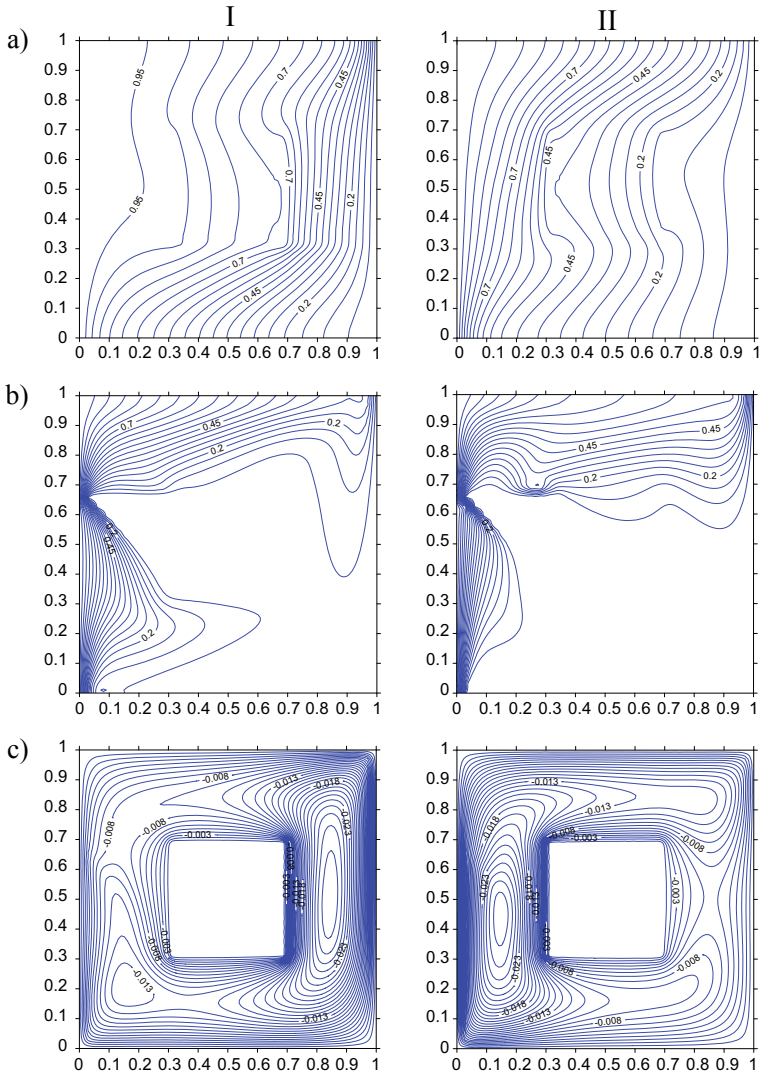


Fig. 2 (I) $K_r = 0.1$ (II) $K_r = 10$. Contours of **a** Isotherms, **b** Iso-concentration, **c** Streamlines

by the streamlines. The increased radiation parameter leads to higher fluid velocity which is shown by higher magnitude of streamlines in Fig. 4.

The heat transfer along with the mass diffusion is explained in Figs. 5, 6, 7, 8, 9, and 10. Figure 5 illustrates the Nusselt number for different values of K_r. The Nusselt number is higher for higher K_r due to low thermal resistance as shown in Fig. 5. The increased Rayleigh number also enhances the Nusselt number illustrated in Fig. 7, as a result of better fluid circulation, which is also indicated by Fig. 3. The increased radiation effect increases the Nusselt number expectedly (Fig. 9). The local Sh also

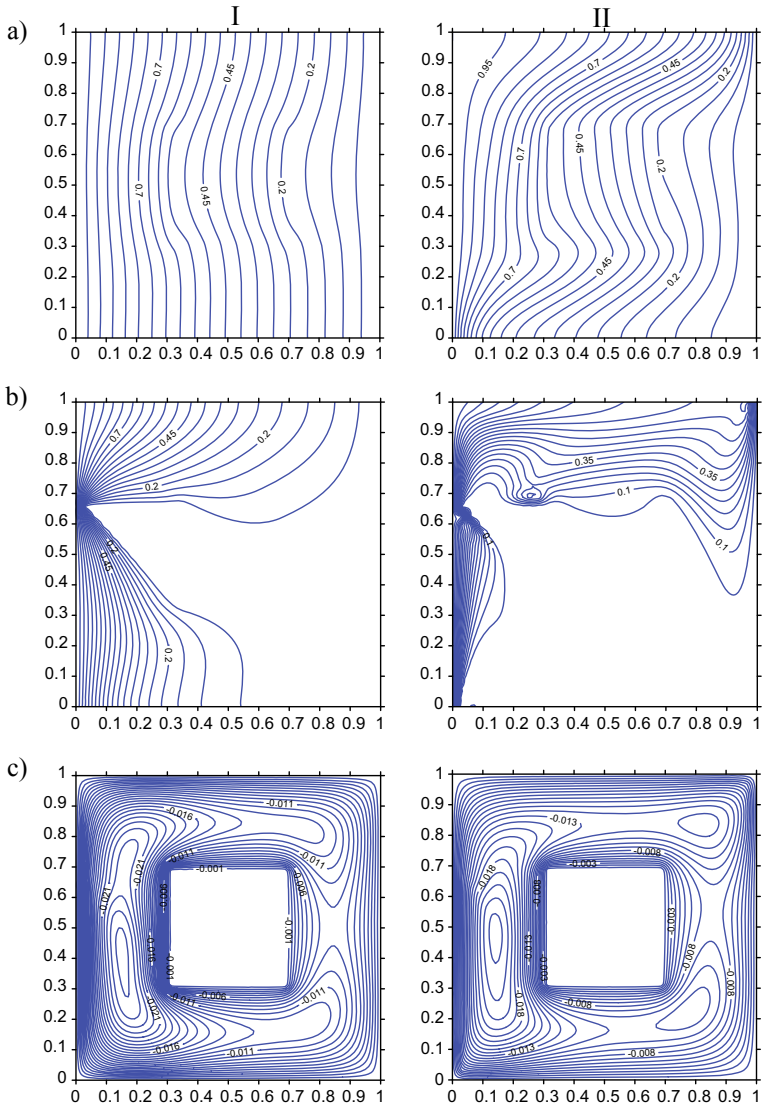


Fig. 3 (I) $Ra = 10$ (II) $Ra = 200$. Contours of **a** Isotherms, **b** Iso-concentration, **c** Streamlines

found to decrease with rise in cavity height. However, there is peculiar behavior of mass transfer for a specific value of solid width at which the Sh is found to have sharp rise and fall. This behavior is common for thermal conductivity ratio (Fig. 6), Rayleigh number (Fig. 8), and radiation parameter (Fig. 10). The mass transfer as seen in this case is unique which is not seen in any other case of conjugate heat transfer.

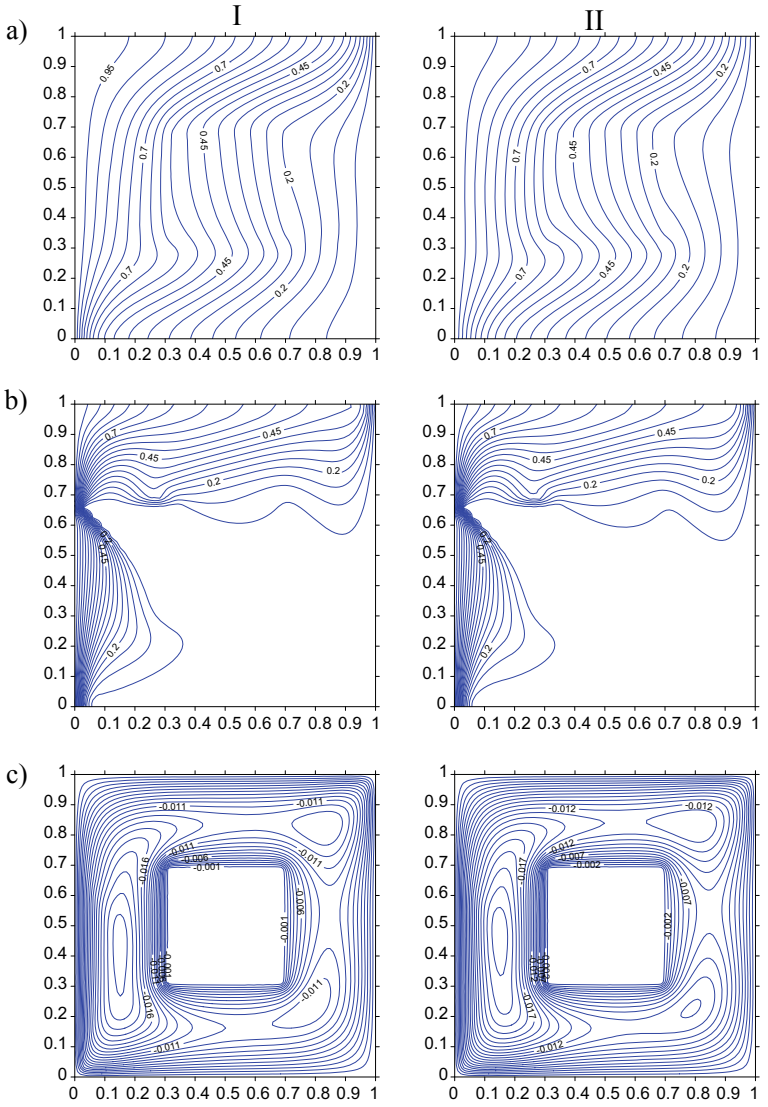


Fig. 4 (I) $R_d = 0.5$ (II) $R_d = 2$. Contours of **a** Isotherms, **b** Iso-concentration, **c** Streamlines

4 Conclusion

Numerical analysis of double diffusion along with conjugate heat transfer is studied for three parameters. The study found that the:

- Transfer of heat and mass in porous material is affected by the thermal conductivity of solid, radiation parameter, and Rayleigh number.

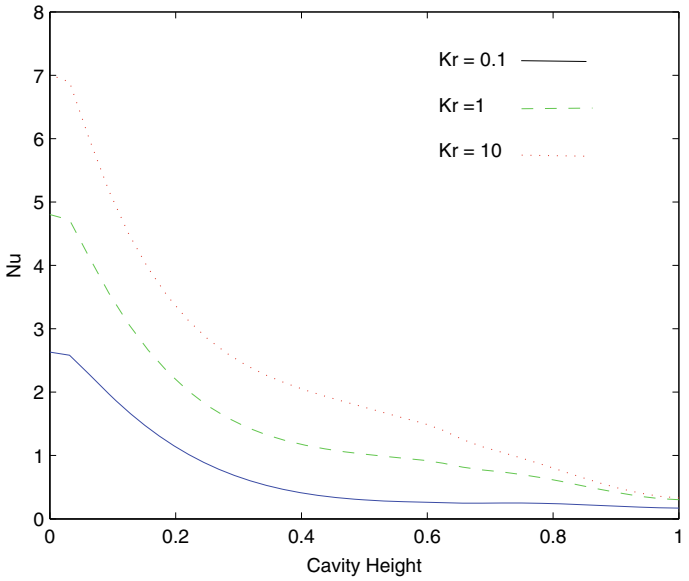


Fig. 5 Nu versus K_r at $N = 0.2$, $Le = 5$, $Ra = 100$, $B = 37.5\%$, $R_d = 0$

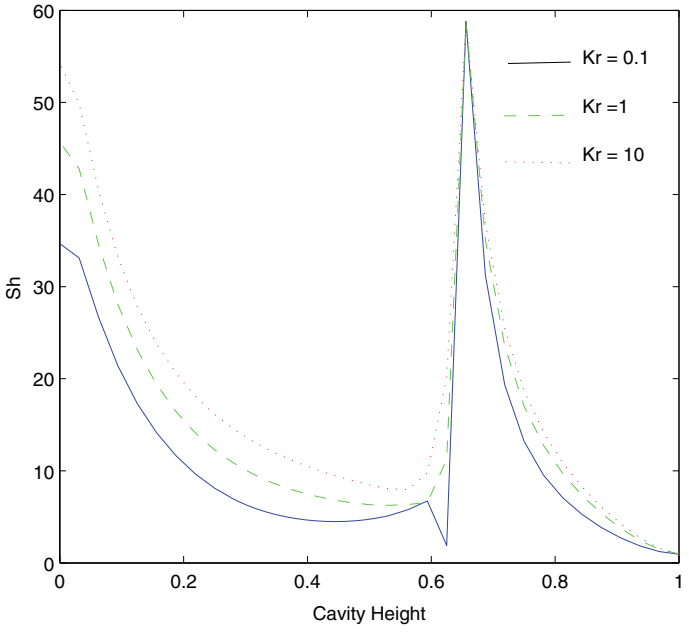


Fig. 6 Sh versus K_r at $N = 0.2$, $Le = 5$, $Ra = 100$, $B = 37.5\%$, $R_d = 0$

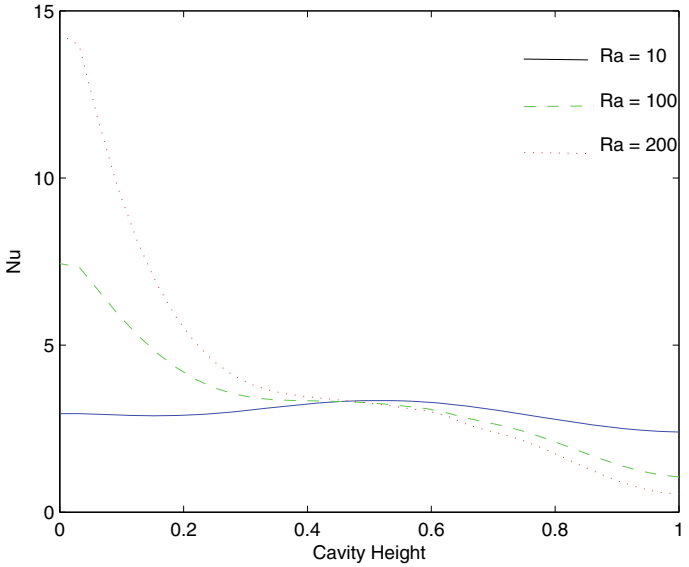


Fig. 7 Nu versus *Ra* at $N = 0.2$, $K_r = 2$, $Le = 5$, $B = 37.5\%$, $R_{\mathrm{d}} = 1$

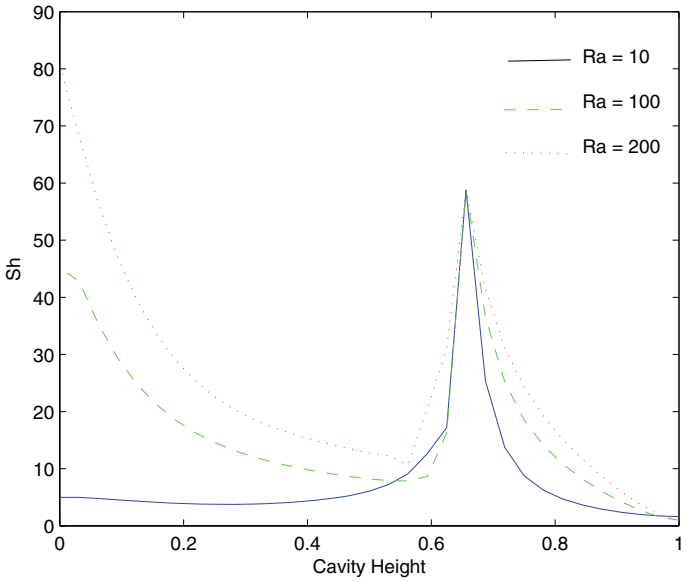


Fig. 8 Sh versus *Ra* parameter at $N = 0.2$, $K_r = 2$, $Le = 5$, $B = 37.5\%$, $R_d = 1$

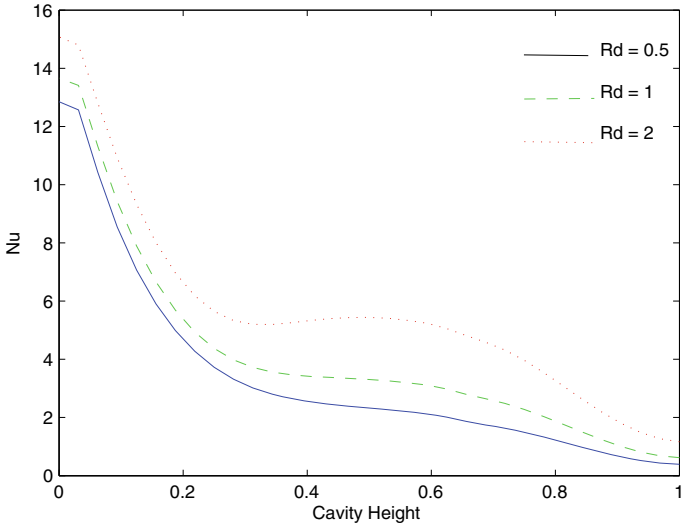


Fig. 9 Nu versus R_{d} at $N = 0.1$, $K_r = 2$, $Le = 2$, $B = 37.5\%$, $Ra = 200$

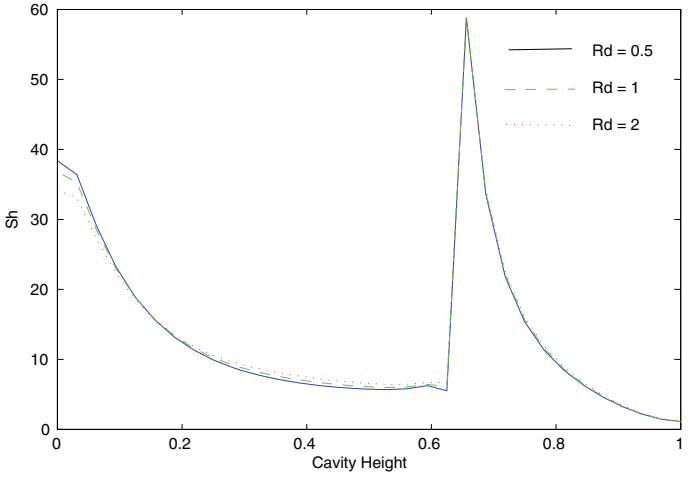


Fig. 10 Sh versus R_{d} at $N = 0.1$, $Le = 2$, $K_r = 2$, $B = 37.5\%$, $Ra = 200$

- The Nusselt number increases for higher values of Rayleigh number (Ra), Thermal conductivity ratio (K_r), along the cavity height
- The Sherwood number shows a sudden rise at a specific value of solid width
- Generally, the radiation parameter, thermal conductivity of solid, and Rayleigh number lead to increase in Nusselt number.

References

1. Ahamad NA, Athani A, Badruddin IA (2018) Heat transfer prediction in a square porous medium using artificial neural network. AIP Conf Proc 1953:140017. https://doi.org/10.1063/1.5033192
2. Athani A, Ahamad NA, Badruddin IA (2018) Application of artificial neural network for heat transfer in porous cone. AIP Conf Proc 1953:140016. https://doi.org/10.1063/1.5033191
3. Baig MAA, Salman Ahmed NJ, Ameer Ahamad N, Kamangar S, Reddy AR, Badruddin IA (2019) Discrete heating at bottom of annulus in case of mixed convection: Aiding flow. AIP Conf Proc 2200:020051. https://doi.org/10.1063/1.5141221
4. Ahmed NJS, Badruddin IA, Kanesan J, Zainal ZA, Ahamed KSN (2011) Study of mixed convection in an annular vertical cylinder filled with saturated porous medium, using thermal non-equilibrium model. Int J Heat Mass Transf 54(17–18): 3822–3825
5. Baig MAA, Salman Ahmed NJ, Ameer Ahamad N, Reddy AR, Badruddin IA, Mangesh L (2019) Discrete heating of opposing mixed convection heated at bottom of annulus. AIP Conf Proc 2200:020050. https://doi.org/10.1063/1.5141220
6. Ahmed NJS, Badruddin IA, Zainal ZA, Khaleed HMT, Kanesan J (2009) Heat transfer in a conical cylinder with porous medium. Int J Heat Mass Transf 52(13–14):3070–3078
7. Badruddin IA, Azeem K, Idris MYI, Nik-Ghazali N, Ahmed NJS, Al-Rashed AAAA (2017) Simplified finite element algorithm to solve conjugate heat and mass transfer in porous medium. Int J Numer Method Heat Fluid Flow 27(11):2481–2507
8. Azeem, Soudagar MEM, Ahmed NJS, Badruddin IA (2017) Fem formulation for heat and mass transfer in porous medium. IOP Conf Ser Mater Sci Eng 225:012022. https://doi.org/10.1088/1757-899x/225/1/012022
9. Badruddin IA, Ahmed NJS, Al-Rashed AAAA, Kanesan J, Kamangar S, Khaleed HMT (2012) Analysis of heat and mass transfer in a vertical annular porous cylinder using FEM. Transp Porous Media 91(2):697–715
10. Azeem, Badruddin IA, Idris MYI, Nik-Ghazali N, Ahmed NJS, Al-Rashed AAAA (2016) Conjugate heat and mass transfer in square porous cavity. Ind J Pure Appl Phys 54:777–786
11. Badruddin IA (2019) Heat and mass transfer with Soret/Dufour effect in irregular porous cavity. J Thermophys Heat Transfer 33(3):647–662. https://doi.org/10.2514/1.T5666
12. Badruddin IA, Abdullah AAAA, Ahmed NJS, Kamangar S (2012) Investigation of heat transfer in square porous-annulus. Int J Heat Mass Transf 55(7–8):2184–2192
13. Nik-Ghazali N, Badruddin IA, Badarudin A, Tabatabaeikia S (2014) Dufour and Soret effects on square porous annulus. Adv Mechan Eng 6:209753
14. Ahamad NA, Kamangar S, Badruddin IA (2019) Heat transfer in a porous cavity in presence of square solid block. Int J Numer Meth Heat Fluid Flow 29(2):640–656. https://doi.org/10.1108/HFF-05-2017-0193
15. Badruddin IA, Al-Rashed AAAA, Ahmed NJS, Kamangar S, Jeevan K (2012) Natural convection in a square porous annulus. Int J Heat Mass Transf 55(23–24):7175–7187
16. Badruddin IA, Zainal ZA, Narayana PAA, Seetharamu KN (2006) Heat transfer in porous cavity under the influence of radiation and viscous dissipation. Int Commun Heat Mass Transfer 33(4):491–499
17. Badruddin IA (2020) Thermal non-equilibrium in porous annulus: a new finite element solution technique. Arab J Sci Eng 45(2):1279–1292. https://doi.org/10.1007/s13369-019-04298-4
18. Badruddin IA (2019) Numerical analysis of thermal non-equilibrium in porous medium subjected to internal heating. Mathematics 7(11):1085. https://doi.org/10.3390/math7111085
19. Ahamad NA, Soudagar MEM, Badruddin IA (2017) Double diffusion in arbitrary porous cavity: Part I. AIP Conf Proc 1859:020050. https://doi.org/10.1063/1.4990203
20. Khan TMY, Baig MAA, Azeem, Ahamad NA, Badruddin IA (2019) Heat and mass transfer with viscous dissipation in porous medium: FEM based methodology. AIP Conf Proc 1:030058. https://doi.org/10.1063/1.5100485

21. Azeem, Badruddin IA, Nik-Ghazali N, Idris MYI, Anqi AE, Ahmed NJS, Kamangar S, Al-Rashed AAAA (2018) Effect of size and location of solid on conjugate heat transfer in porous cavity. Ind J Pure Appl Phys 56:792–801
22. Ahamad NA, Baig MAA, Kamangar S, Khan TMY, Badruddin IA (2019) Partial heating at upper section of annulus subjected to conjugate heat transfer in porous annulus. AIP Conf Proc 2105(1):020021. https://doi.org/10.1063/1.5100706
23. Ahamad NA, Baig MAA, Ahmed NJS, Kamangar S, Khan TMY, Badruddin IA, Reddy AR, Khaleed HMT (2020) Finite element formulation of conjugate heat transfer in porous annulus. AIP Conf Proc 2204:040016. https://doi.org/10.1063/1.5141589
24. Ahamad NA, Baig MAA, Kamangar S, Khan TMY, Badruddin IA (2019) Conjugate heat transfer due to partial isothermal heating at center of annuls with two solids in porous annulus: Part I. AIP Conf Proc 2105(1):020020. https://doi.org/10.1063/1.5100705
25. Azeem, Baig MAA, Khaleed HMT, Kamangar S, Badruddin IA (2019) Partial heating at lower section of annulus subjected to conjugate heat transfer in porous annulus. AIP Conf Proc 2105(1):020019 https://doi.org/10.1063/1.5100704
26. Ahmed NJS, Kamangar S, Badruddin IA, Al-Rashed AAAA, Quadir GA, Khaleed HMT, Khan TMY (2014) Conjugate heat transfer in porous annulus. J Porous Media 19(12): 1109–1119
27. Badruddin IA, Ahmed NJS, Al-Rashed AAA, Nik-Ghazali N, Jameel M, Kamangar S, Khaleed HMT, Khan TMY (2015) Conjugate heat transfer in an annulus with porous medium fixed between solids. Trans Porous Media 109(3):589–608
28. Badruddin IA, Ahmed NJS, Anqi AE, Kamangar S (2019) Conjugate heat and mass transfer in a vertical porous cylinder. J Thermophys Heat Transf 33(2):548–558. https://doi.org/10.2514/1.T5488
29. Baig MAA, Azeem, Salman Ahmed NJ, Kamangar S, Yunus Khan TM, Badruddin IA, Reddy AR, Khaleed HMT (2020) Finite element formulation of conjugate double diffusion in porous annulus. AIP Conf Proc 2204:040017. https://doi.org/10.1063/1.5141590
30. Kamangar S, Baig MAA, Azeem, Ahamad NA, Badruddin IA (2019) Finite element solution strategy for viscous dissipation in porous medium. AIP Conf Proc 2104(1):030057. https://doi.org/10.1063/1.5100484
31. Badruddin IA, Khan TMY (2017) Heat transfer in an L shaped porous medium using FEM. IOP Conf Ser Mater Sci Eng 225:012012. https://doi.org/10.1088/1757-899x/225/1/012012
32. Ahmed NJS, Zainal ZA, Badruddin IA, Hussain MTK (2008) Heat transfer analysis of porous medium in a conical cylinder with variable wall temperature. Int J Mechan Mater Eng 3(2):145–152
33. Badruddin IA (2019) Investigation of heat transfer in irregular porous cavity subjected to various boundary conditions. Int J Numer Meth Heat Fluid Flow 29(1):418–447. https://doi.org/10.1108/HFF-04-2018-0132
34. Azeem, Soudagar MEM, Badruddin IA (2017) Investigation of heat transfer due to isothermal heater in irregular porous cavity: Part I. AIP Conf Proc 1859:020044. https://doi.org/10.1063/1.4990197
35. Yunus Khan TM, Badruddin IA, Quadir GA (2016) Heat transfer in a conical porous cylinder with partial heating. IOP Conf Series Mater Sci Eng 149:012211
36. Ahamad NA, Soudagar MEM, Kamangar S, Badruddin IA (2017) Fem formulation of coupled partial differential equations for heat transfer. IOP Conf Ser Mater Sci Eng 225:012023. https://doi.org/10.1088/1757-899x/225/1/012023

Double Diffusion Caused by Hot Strip in Porous Material



N. Ameer Ahamad, Azeem, Maughal Ahmed Ali Baig, and D. Maneiah

Abstract This paper aims to analyze the diffusion of heat and mass in porous material, caused by thermal gradients created by two heating sources. The first heating source is a full surface of the cavity at left side. The second heating source is a small strip that is placed at $x = L/4$ with L indicating the length of cavity. The concentration gradient is maintained in the porous domain due to the high concentration at left surface and low concentration at right surface. The investigation is focused to evaluate the heat as well as mass diffusion due to strip height, Lewis number, Rayleigh number, buoyancy ratio, and radiation parameter. The solution is obtained by dividing the whole domain into smaller elements of triangular shape with each element having three nodes placed at the corner of triangle. Galerkin approach is utilized to get the finite element formulations of governing equations. The concentration distribution gets affected due to the heat source placed toward the left surface.

Keywords Porous · Heat source · Heat mass

1 Introduction

Porous media is an essential requirement in plenty of applications because of its special feature that is having small pores. Thus, it has found an important place among the researchers who have tried to investigate many aspects of such medium including the heat transfer [1–3]. Its study can be found in variety of ranges having different geometrical shapes such as square [4–6], cylindrical [5–11], or even irregular shapes

N. Ameer Ahamad
Mathematics Department, Faculty of Science, University of Tabuk, P.O. BOX. 741, Tabuk 71491, Saudi Arabia

Azeem
Department of Mathematics and Computer Science, Taylor's University, No. 1 Jalan Taylor's, 47500 Subang Jaya, Selangor Darul Ehsan, Malaysia

M. A. A. Baig (✉) · D. Maneiah
Department of Mechanical Engineering, CMR Technical Campus, Hyderabad, Telangana, India
e-mail: mabaig13@gmail.com

© Springer Nature Singapore Pte Ltd. 2020

A. Praveen Kumar et al. (eds.), *Advances in Lightweight Materials and Structures*,
Springer Proceedings in Materials 8, https://doi.org/10.1007/978-981-15-7827-4_75

[12–14] which do have some irregularities in the geometry or the prevailing boundary conditions. The complex boundary conditions are known to have additional difficulties in solving the problem through mathematical means [15–22] and this can be further complicated when many equations are involved that need to be solved at the same time [23, 24]. Heat and mass transfer is also one complex case that can occur simultaneously in may situations when the concentration of mass is present in the domain in such a way that there is gradient created because of lesser amount at one place and more quantity at the another location [25–29]. Thus, initiating the mass flow from high concentration to that of low concentration area. This is generally known as mass diffusion. There have been many studies which reported the heat and mass transfer having regular boundary conditions. However, not much work is available with regards to the double diffusion when additional heating elements are present in the domain that might affect the overall phenomenon of heat and mass diffusion due to multiple thermal gradients caused by more than one heating source. Thus, the current work is particularly interested to understand this case when a heating element is placed near the hot vertical surface.

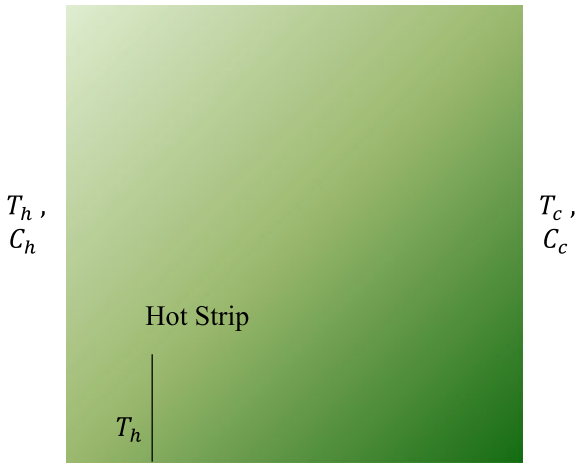
2 Analysis

Figure 1 depicts the physical domain along with the boundary conditions.

The equations are extracted from [29–34]

$$\frac{\partial u}{\partial x} + \frac{\partial \mathrm{v}}{\partial y} = 0 \tag{1}$$

Fig. 1 Porous cavity



$$\frac{\partial u}{\partial y} - \frac{\partial \mathrm{v}}{\partial x} = -\frac{gK}{\nu}\left(\beta_T \frac{\partial T}{\partial x} + \beta_c \frac{\partial C}{\partial x}\right) \tag{2}$$

$$u\frac{\partial T}{\partial x} + v\frac{\partial T}{\partial y} = \alpha\left(\frac{\partial^2 T}{\partial x^2} + \frac{\partial^2 T}{\partial y^2}\right) - \frac{1}{\rho C_p}\frac{\partial q_r}{\partial x} \tag{3}$$

$$u\frac{\partial C}{\partial x} + v\frac{\partial C}{\partial y} = D\left(\frac{\partial^2 C}{\partial x^2} + \frac{\partial^2 C}{\partial y^2}\right) \tag{4}$$

$$q_r = -\frac{4\sigma}{3\beta_r}\frac{\partial T^4}{\partial x} \tag{5}$$

Expanding T^4 [30, 31]

$$T^4 \approx 4TT_\infty^3 - 3T_\infty^4 \tag{6}$$

Boundary conditions are

$$x = 0,\ T = 1,\ C = 1,\ u = 0,\ v = 0, \tag{7a}$$

$$x = L,\ T = T_\mathrm{c},\ C = 0,\ u = 0,\ v = 0, \tag{7b}$$

$$y = 0,\ \partial T/\partial y = 0,\ \partial C/\partial y = 0,\ u = 0, v = 0, \tag{7c}$$

$$y = L,\ \partial T/\partial y = 0,\ \partial C/\partial y = 0,\ u = 0,\ v = 0 \tag{7d}$$

At the strip,

$$\partial C/\partial y = 0,\ T = T_h\ u = 0,\ v = 0 \tag{7e}$$

The solution of above questions can be obtained through finite element method as described [32–37].

2.1 Results and Discussion

Results are elaborated with respect to five different parameters which are the height of the strip (St) inside the domain, the radiation parameter (R_d), the Lewis number (Le), the Rayleigh number (Ra), and the buoyancy ratio (N). The results correspond to the contour plots of concentration, temperature and stream function that illustrates the behavior of mass transfer, thermal energy and the fluid flow, respectively, in the domain. Figure 2 shows the heat and mass diffusion in the domain which is extracted by taking the parameters as $Le = 5$, $Ra = 100$, $N = 0.1$, $R_\mathrm{d} = 0.5$. The variable in

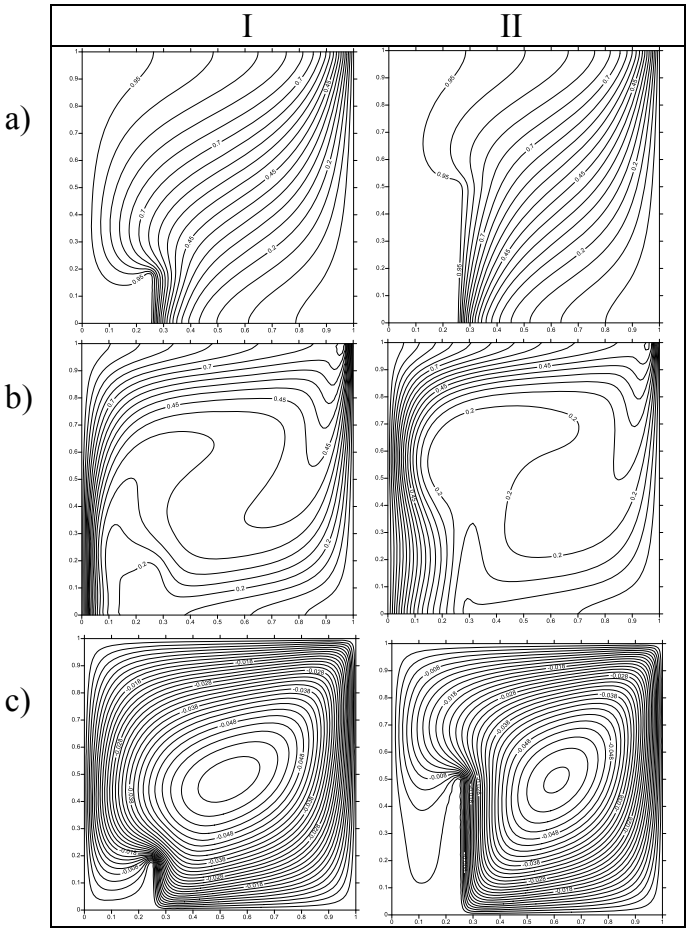


Fig. 2 (I) St = 1/4 (II) St = 1/2. Contours of **a** Isotherms, **b** Iso-concentration, **c** Streamlines

this figure is the non-dimensional height of the strip which is changed from 0.25 to 0.5. Left column of figure corresponds to St = 0.25 and right column to 0.5. The transfer of heat in this case differs as compared to case of no strip. As shown, the heat transfer rate is going to reduce because of the increase in the strip height which is obvious from the fact that the line belonging to 0.95 has pushed itself deep into porous medium when strip height is increased to 0.5. This is clear indication that the heat transfer decreased when strip height is increased. The impact of strip height on the mass transfer can be observed from the concentration lines of Fig. 2. The concentration lines too have moved deeper into the medium as because of increased strip height. This can be clearly seen from iso-concentration lines that have created some space between the two lines near the hot surface when St = 0.5 as compared to St = 0.25. The fluid cell concentrates within the inner heat source and cold surface

when strip height is elongated. This must be noted that the mass transfer when strip is placed at cavity center leading to almost constant value along the left surface. However, in the current case, the mass transfer seems to have increased at cavity height between 0.5 and 0.7, as illustrated by iso-concentration lines.

Figure 3 highlights the impact of buoyancy ratio N for the case under investigation at St = 0.37, $Le = 5$, $Ra = 100$, $R_d = 0.5$. Heat transfer is expected to be affected much due to change in N. However, the mass transfer shows the influence of N. The mass transfer seems to increase with increase in the N which is also the case being observed with other cases [34, 35]. The mass transfer in particular is high at cavity height 0.25–0.5. The orientation of fluid cell changes when N is enhanced.

Figure 4 highlights the effect of Lewis number (Le) being investigated at St = 0.37, $N = 0.2$, $Ra = 100$, $R_d = 0.5$ but $Le = 1$ and $Le = 10$. Expectedly, heat

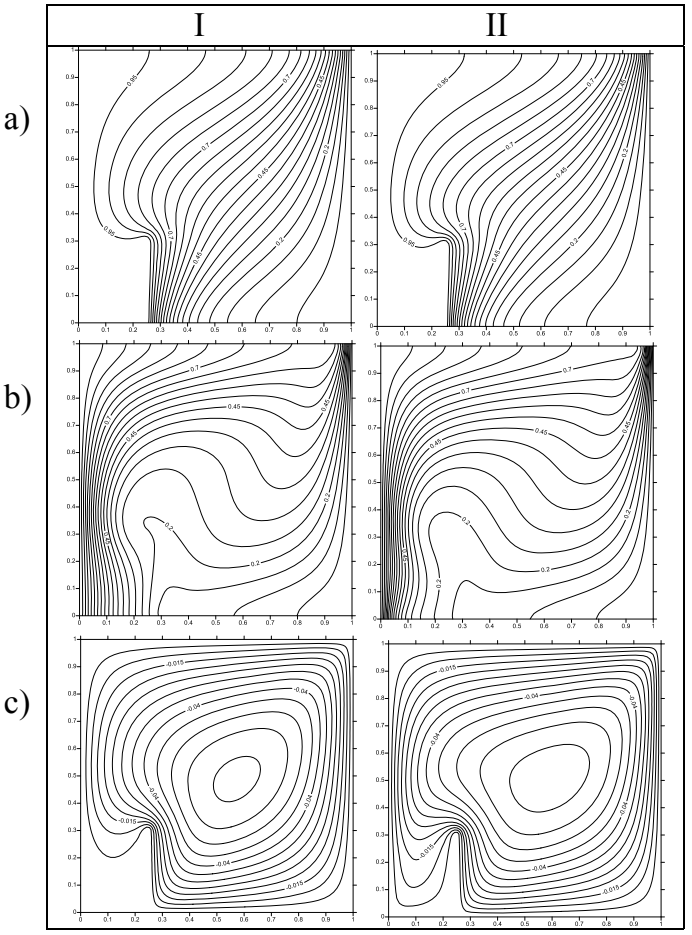


Fig. 3 (I) $N = 0.1$ (II) $N = 0.5$. Contours of **a** Isotherms, **b** Iso-concentration, **c** Streamlines

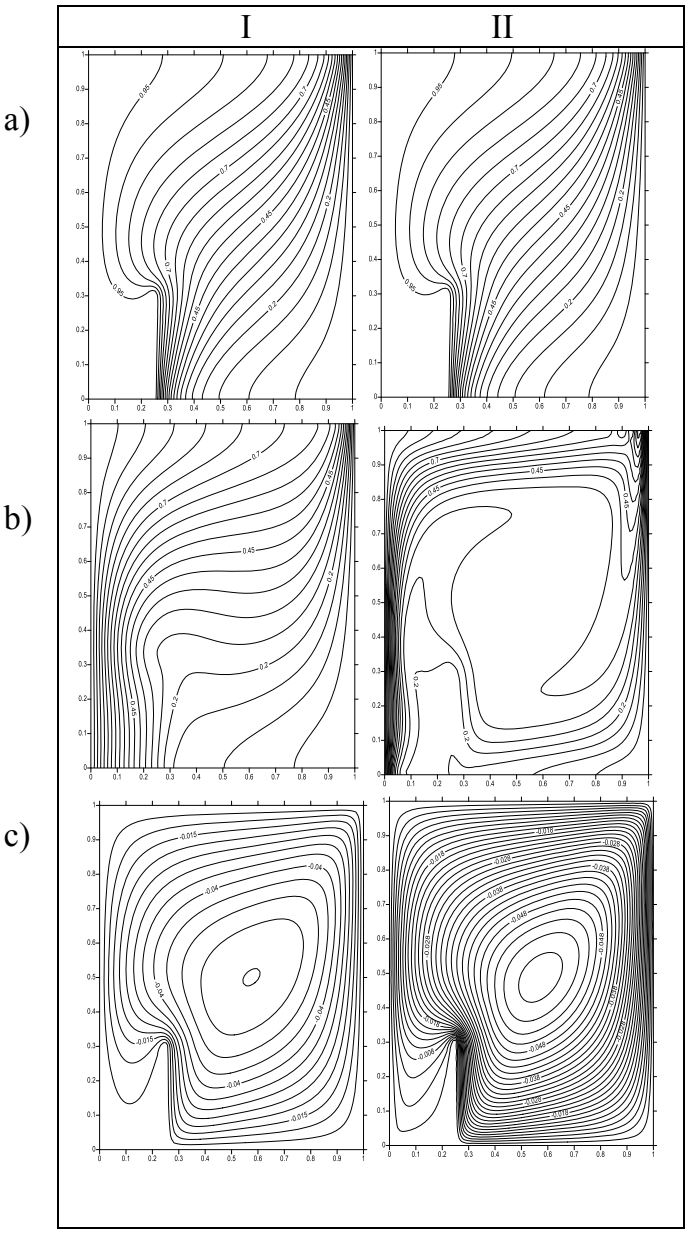


Fig. 4 (I) $Le = 1$ (II) $Le = 10$. Contours of **a** Isotherms, **b** Iso-concentration, **c** Streamlines

transfer is least affected but the mass transfer got influenced substantially as shown by concentration lines. The concentration gradient which is the function of the position of the concentration lines near hot surface increased substantially with increase in Le from 1 to 10. The presence of the hot strip close to the left surface makes sure that the concentration gradient is almost constant for most part of the left surface, which is not the case when the strip is at the centre of the cavity.

Figure 5 shows the impact of radiation parameter which belongs to the parameters St $= 0.37$, $Le = 5$, $Ra = 100$, $Le = 2$. The radiation paramour indicates to what extent radiation effect is present. The value $R_d = 0$ shows that there is no radiation. Expectedly, the isotherms have spread out when R_d is changed from 0 to 2. The impact of radiation is accounted in terms of conduction due to formulation of radiation term in governing equations. The effect of radiation parameter can be seen on iso-concentration by observing the line 0.2 which has dipped toward the bottom surface when R_d is increased. The role of Rayleigh number on diffusion of heat and mass is illustrated in Fig. 6 (St $= 0.37$, $Le = 5$, $N = 0.2$, $R_d = 0.5$). The lower Rayleigh number does not allow the fluid to have substantial energy to flow from one point to another which influences the heat and mass transfer. The increased Ra leads to more heat and mass transfer.

2.2 Conclusion

Investigation of heat and mas transfer because of heating strip toward the left hot surface is studied for various parameters. It is found that the heat and mass transfer gets affected for strip placed toward the hot surface. It is found that the mass transfer is higher at a particular region of left surface when strip height elongated. The strip height found to reduce the transfer of heat from hot surface. The mass transfer is affected when buoyancy ratio and Lewis number are increased. The impact of placing hot strip toward the left side is that the mass transfer behavior is different from the cases when no strip is placed. The strip is seen to influence the impact of Rayleigh number and radiation parameter as compared to the cases when no strip is present.

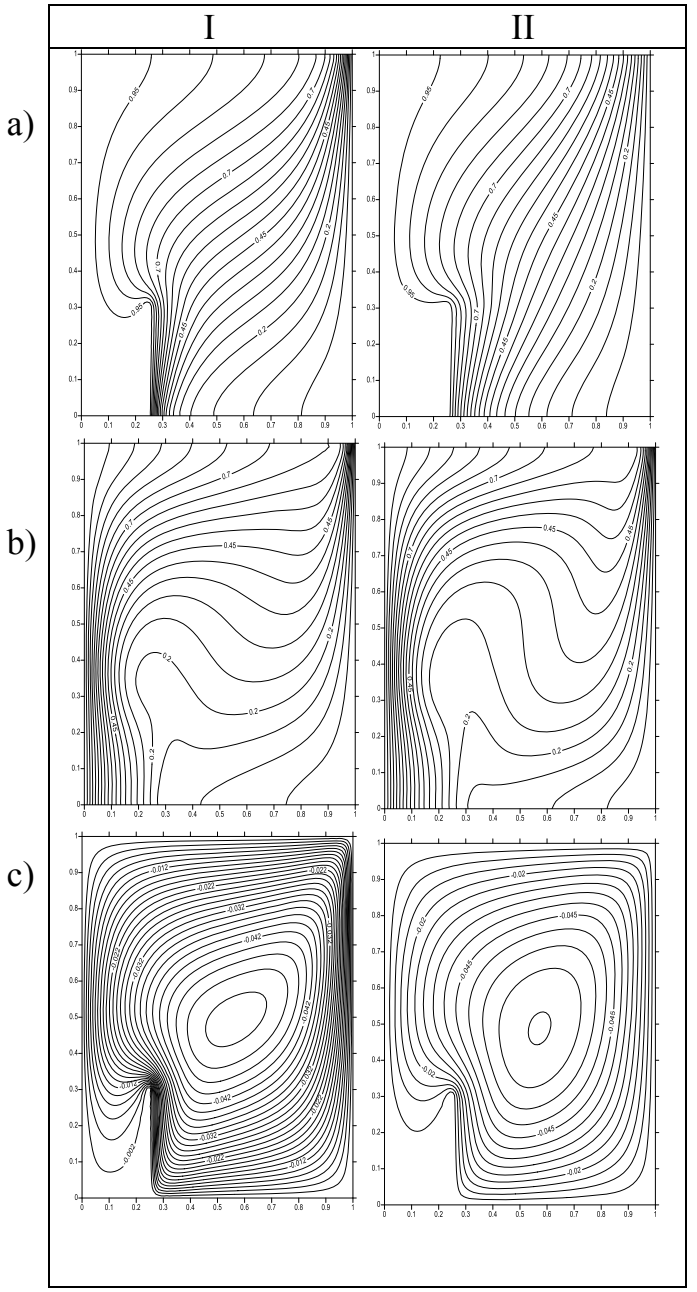


Fig. 5 (I) $R_{\mathrm{d}} = 0$ (II) $R_{\mathrm{d}} = 0$. Contours of **a** Isotherms, **b** Iso-concentration, **c** Streamlines

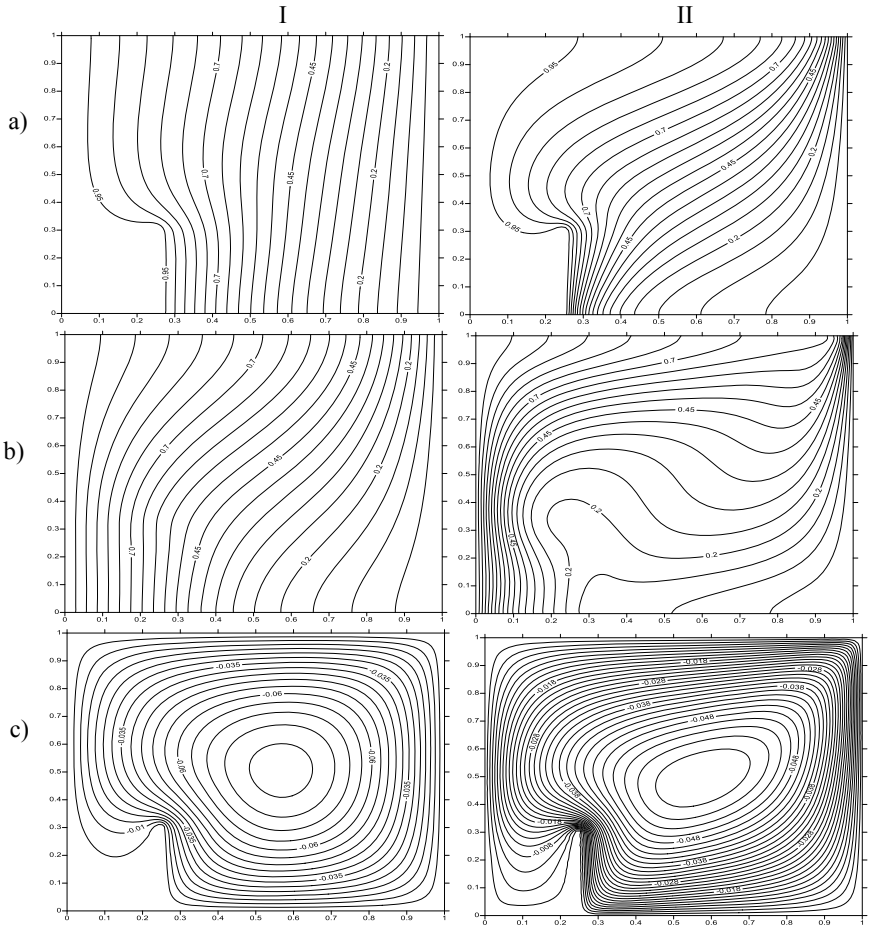


Fig. 6 (I) $Ra = 10$ (II) $Ra = 100$. Contours **a** Isotherms, **b** Iso-concentration, **c** Streamlines

References

1. Ahmed NJS, Badruddin IA, Kanesan J, Zainal ZA, Ahamed KSN (2011) Study of mixed convection in an annular vertical cylinder filled with saturated porous medium, using thermal non-equilibrium model. Int J Heat Mass Transf 54(17–18):3822–3825
2. Athani A, Ahamad NA, Badruddin IA (2018) Application of artificial neural network for heat transfer in porous cone. AIP Conf Proc 1953:140016. doi: https://doi.org/10.1063/1.5033191
3. Ahamad NA, Athani A, Badruddin IA (2018) Heat transfer prediction in a square porous medium using artificial neural network. AIP Conf Proc 1953:140017. https://doi.org/10.1063/1.5033192
4. Azeem, Badruddin IA, Idris MYI, Nik-Ghazali N, Ahmed NJS, Al-Rashed AAAA (2016) Conjugate heat and mass transfer in square porous cavity. Ind J Pure Appl Phys 54:777–786
5. Badruddin IA, Abdullah AAAA, Ahmed NJS, Kamangar S (2012) Investigation of heat transfer in square porous-annulus. Int J Heat Mass Transf 55(7–8):2184–2192

6. Badruddin IA, Al-Rashed AAAA, Ahmed NJS, Kamangar S, Jeevan K (2012) Natural convection in a square porous annulus. Int J Heat Mass Transf 55(23–24):7175–7187
7. Baig MAA, Salman Ahmed NJ, Ameer Ahamad N, Kamangar S, Reddy AR, Badruddin IA (2019) Discrete heating at bottom of annulus in case of mixed convection: Aiding flow. AIP Conf Proc 2200:020051. https://doi.org/10.1063/1.5141221
8. Badruddin IA, Ahmed NJS, Anqi AE, Kamangar S (2019) Conjugate heat and mass transfer in a vertical porous cylinder. J Thermophys Heat Transf 33(2):548–558. https://doi.org/10.2514/1.T5488.
9. Ahmed NJS, Badruddin IA, Zainal ZA, Khaleed HMT, Kanesan J (2009) Heat transfer in a conical cylinder with porous medium. Int J Heat Mass Transf 52(13–14):3070–3078
10. Ahmed NJS, Zainal ZA, Badruddin IA, Hussain MTK (2008) Heat transfer analysis of porous medium in a conical cylinder with variable wall temperature. Int J Mechan Mater Eng 3(2):145–152
11. Yunus Khan TM, Badruddin IA, Quadir GA (2016) Heat transfer in a conical porous cylinder with partial heating. IOP Conf Series Mater Sci Eng 149:012211
12. Badruddin IA (2019a) Investigation of heat transfer in irregular porous cavity subjected to various boundary conditions. Int J Numer Meth Heat Fluid Flow 29(1):418–447. https://doi.org/10.1108/HFF-04-2018-0132
13. Azeem, Soudagar MEM, Badruddin IA (2017) Investigation of heat transfer due to isothermal heater in irregular porous cavity: Part I. AIP Conf Proc 1859:020044. doi: https://doi.org/10.1063/1.4990197
14. Badruddin IA, Khan TMY (2017) Heat transfer in an L shaped porous medium using FEM. IOP Conf Ser Mater Sci Eng 225:012012. doi: https://doi.org/10.1088/1757-899X/225/1/012012
15. Ahamad NA, Baig MAA, Kamangar S, Khan TMY, Badruddin IA (2019) Partial heating at upper section of annulus subjected to conjugate heat transfer in porous annulus. AIP Conf Proc 2105(1):020021. https://doi.org/10.1063/1.5100706.
16. Ahamad NA, Baig MAA, Kamangar S, Khan TMY, Badruddin IA (2019) Conjugate heat transfer due to partial isothermal heating at center of annuls with two solids in porous annulus: Part I. AIP Conf Proc 2105(1):020020. https://doi.org/10.1063/1.5100705
17. Azeem, Baig MAA, Khaleed HMT, Kamangar S, Badruddin IA (2019) Partial heating at lower section of annulus subjected to conjugate heat transfer in porous annulus. AIP Conf Proc 2105(1):020019. https://doi.org/10.1063/1.5100704.
18. Ahmed NJS, Kamangar S, Badruddin IA, Al-Rashed AAAA, Quadir GA, Khaleed HMT, Khan TMY (2014) Conjugate heat transfer in porous annulus. J Porous Media 19(12): 1109–1119
19. Baig MAA, Salman Ahmed NJ, Ameer Ahamad N, Reddy AR, Badruddin IA, Mangesh L (2019) Discrete heating of opposing mixed convection heated at bottom of annulus. AIP Conf Proc 2200:020050. doi: https://doi.org/10.1063/1.5141220
20. Azeem, Badruddin IA, Nik-Ghazali N, Idris MYI, Anqi AE, Ahmed NJS, Kamangar S, Al-Rashed AAAA (2018) Effect of size and location of solid on conjugate heat transfer in porous cavity. Ind J Pure Appl Phys 56:792–801
21. Badruddin IA (2020) Thermal non-equilibrium in porous annulus: a new finite element solution technique. Arab J Sci Eng 45(2):1279–1292. https://doi.org/10.1007/s13369-019-04298-4
22. Badruddin IA, Ahmed NJS, Al-Rashed AAA, Nik-Ghazali N, Jameel M, Kamangar S, Khaleed HMT, Khan TMY (2015) Conjugate heat transfer in an annulus with porous medium fixed between solids. Trans Porous Media 109(3):589–608
23. Badruddin IA (2019b) Numerical analysis of thermal non-equilibrium in porous medium subjected to internal heating. Mathematics 7(11):1085. https://doi.org/10.3390/math7111085
24. Badruddin IA (2019c) Heat and mass transfer with Soret/Dufour effect in irregular porous cavity. J Thermophys Heat Transfer 33(3):647–662. https://doi.org/10.2514/1.T5666
25. Ahamad NA, Soudagar MEM, Badruddin IA (2017) Double diffusion in arbitrary porous cavity: Part I. AIP Conf Proc 1859:020050. https://doi.org/10.1063/1.4990203
26. Badruddin IA, Azeem K, Idris MYI, Nik-Ghazali N, Ahmed NJS, Al-Rashed AAAA (2017) Simplified finite element algorithm to solve conjugate heat and mass transfer in porous medium. Int J Numer Method Heat Fluid Flow 27(11):2481–2507

27. Badruddin IA, Ahmed NJS, Al-Rashed AAAA, Kanesan J, Kamangar S, Khaleed HMT (2012) Analysis of heat and mass transfer in a vertical annular porous cylinder using FEM. Transp Porous Media 91(2):697–715
28. Khan TMY, Baig MAA, Azeem, Ahamad NA, Badruddin IA (2019) Heat and mass transfer with viscous dissipation in porous medium: FEM based methodology. AIP Conf Proc 1:030058. https://doi.org/10.1063/1.5100485.
29. Nik-Ghazali N, Badruddin IA, Badarudin A, Tabatabaeikia S (2014) Dufour and Soret effects on square porous annulus. Adv Mechan Eng 6:209753
30. Ahamad NA, Kamangar S, Badruddin IA (2019) Heat transfer in a porous cavity in presence of square solid block. Int J Numer Meth Heat Fluid Flow 29(2):640–656. https://doi.org/10.1108/HFF-05-2017-0193
31. Badruddin IA, Zainal ZA, Narayana PAA, Seetharamu KN (2006) Heat transfer by radiation and natural convection through a vertical annulus embedded in porous medium. Int Commun Heat Mass Transfer 33(4):500–507
32. Baig MAA, Azeem, Salman Ahmed NJ, Kamangar S, Yunus Khan TM, Badruddin IA, Reddy AR, Khaleed HMT (2020) Finite element formulation of conjugate double diffusion in porous annulus. AIP Conf Proc 2204:040017. https://doi.org/10.1063/1.5141590
33. Ahamad NA, Baig MAA, Ahmed NJS, Kamangar S, Khan TMY, Badruddin IA, Reddy AR, Khaleed HMT (2020) Finite element formulation of conjugate heat transfer in porous annulus. AIP Conf Proc 2204:040016. https://doi.org/10.1063/1.5141589
34. Kamangar S, Baig MAA, Azeem, Ahamad NA, Badruddin IA (2019) Finite element solution strategy for viscous dissipation in porous medium. AIP Conf Proc 2104(1):030057. https://doi.org/10.1063/1.5100484.
35. Al-Rashed AAAA, Badruddin IA (2012) Heat transfer in a porous cavity. Int J Mechan Mater Eng 7(1):1–8
36. Azeem, Soudagar MEM, Ahmed NJS, Badruddin IA (2017) Fem formulation for heat and mass transfer in porous medium. IOP Conf Ser Mater Sci Eng 225:012022. doi:https://doi.org/10.1088/1757-899X/225/1/012022
37. Ahamad NA, Soudagar MEM, Kamangar S, Badruddin IA (2017) Fem formulation of coupled partial differential equations for heat transfer. IOP Conf Ser Mater Sci Eng 225:012023. doi:https://doi.org/10.1088/1757-899X/225/1/012023

Dynamic Characteristics of a Single Orifice Aerostatic Thrust Bearing with Nonlinear Spring Model of Air Film

K. S. Srinivasa Prasad, Sushil S. Athreya, Vaibhav Kamath, and Shyam Rajgopal

Abstract Aerostatic bearings are widely used in ultra-precision machining equipment and measurement equipment due to their extremely high accuracy. However, they are more susceptible to resonance problems than liquid film bearings. Utilization of static stiffness of the air film for the calculation of resonance frequency and response of the bearing system represents a simple method but fails to capture the nonlinearity present in the static characteristics. This paper aims at presenting the dynamic characteristics of the bearing system by modelling the air film as a nonlinear spring. This modelling has the advantage of a simple and an effective procedure, accurately representing the nonlinearity in the static characteristics of the bearing system. The dynamic characteristics are determined by both theoretical and experimental methods and the corresponding results are compared with each other.

Keywords Aerostatic thrust bearing · Single orifice · Dynamic characteristics

1 Introduction

Aerostatic bearings are used in many applications such as coordinate measuring machines (CMMs), semiconductor wafer processing machines, mass properties machines, and other high precision equipment, due to their advantages of lower friction, lower temperature rise, longer life, less contamination, etc. It is essentially important to consider dynamic performance of the aerostatic bearing during their design along with traditional static characteristics such as load carrying capacity and static stiffness due to the increasing requirements of high acceleration and smaller vibration. Further, aerostatic bearings are more susceptible to vibration instability, when compared to liquid film bearings.

Various researchers have already worked on the dynamic characteristics of aerostatic thrust bearing. Jin et al. [1] determined the dynamic stiffness and damping

K. S. Srinivasa Prasad (✉) · S. S. Athreya · V. Kamath · S. Rajgopal
Department of Mechanical Engineering, PES University, Electronic City Campus, Hosur Road, Bangalore 560100, India
e-mail: srinivasapks@pes.edu

© Springer Nature Singapore Pte Ltd. 2020

A. Praveen Kumar et al. (eds.), *Advances in Lightweight Materials and Structures*, Springer Proceedings in Materials 8, https://doi.org/10.1007/978-981-15-7827-4_76

characteristics of a circular pad aerostatic thrust bearing with dynamic grid technique in ANSYS. Kong et al. [2] utilized the single degree-of-freedom vibration model of an aerostatic bearing to analyse the pneumatic hammer stability of the bearing and the model was also used to check the influence of gas supply pressure and film thickness. Chen et al. [3] determined the transient response of an aerostatic bearing with groove by finite difference method and Euler's method. Ma et al. [4] utilized fourth-order Runge–Kutta method and FEM to quantitavely analyse the time dependant dynamic behavior of the bearing by graphical method. Khatait et al. [5], along with numerical analysis, utilized experimental approach to determine the static and dynamic characteristics of the aerostatic bearing.

Even though the above-mentioned literatures exhibit their importance in the dynamic analysis of aerostatic bearings, but, they are of less practical importance in the design stage of the bearing, due to the complexities involved in the analysis and formulation. A single degree-of-freedom model is usually utilized to make a quick estimate of the resonance frequency and the dynamic response of the bearing system, at the design stages [6]. The static stiffness of the bearing system is directly utilized to calculate the resonance frequency as in a linear single degree-of-freedom vibratory system. Even though this model is simple to use, it fails to completely capture the nonlinearity present in the static load-deflection characteristics of the bearing.

Therefore, the main objective of this study is to model the compressed air film as a nonlinear spring with cubic nonlinearity and to introduce it in the single degree-of-freedom model for the prediction of transient response of the aerostatic thrust bearing system. The dynamic characteristics so determined are also compared with the experimental results obtained from dynamic testing.

2 Methodology

The transient response of the single orifice aerostatic thrust bearing is determined using both theoretical approach as well as experimental approach. Theoretical approach involves dynamic analysis of the bearing system as an equivalent single degree-of-freedom system with the compressed air film represented by a nonlinear spring, whereas the experimental approach involves real-time time-vibration testing of the bearing system.

2.1 Theoretical Approach

The nonlinear spring model for the compressed air film of a single orifice aerostatic thrust bearing requires the determination of nonlinear static load-deflection characteristics initially. It is obtained with the help of the expression for load-carrying capacity of a single orifice aerostatic thrust bearing given by [7],

$$W = K_{\mathrm{g}}(P_o - P_{\mathrm{a}})\frac{\pi(b^2 - a^2)}{2\ln(b/a)} \tag{1}$$

where

W = Load carrying capacity; K_{g} = Gauge pressure ratio, a function of bearing slot factor G; P_o = Supply pressure; P_a = Ambient pressure; b = radius of bearing pad; a = radius of air pocket. The gauge pressure ratio is given by,

$$K_{\mathrm{g}} = \frac{2}{1 + \sqrt{1 + \frac{4}{G^2}}} \tag{2}$$

The bearing slot factor is given by,

$$G = \frac{P_a/P_o}{(1 - P_a/P_o)^{1/2}(1 + P_a/P_o)} \times \frac{24\mu(2RT)^{1/2}}{P_a} \times \frac{C_D d^2 \ln(b/a)}{8h^3} \tag{3}$$

where μ is dynamic viscosity of air; R is gas constant; T is temperature; C_{D} = coefficient of discharge of orifice; d = diameter of orifice; h = air film thickness. The known load capacity is used to calculate the gauge pressure ratio K_{g}, which in turn is used to calculate slot factor G, from which the corresponding air film thickness is calculated. The above-defined procedure is repeated for different load values and the corresponding air film thickness is calculated to obtain the nonlinear load-deflection characteristics of the bearing. The design data related to the bearing utilized for the calculation of load-deflection characteristics are shown in Table 1.

Values such as air pocket radius 'a' have been obtained from the standard design charts for the design of an aerostatic thrust bearing [7]. The load-deflection characteristics obtained using the above procedure are shown in Fig. 1.

To obtain the mathematical model of the nonlinear spring representing the compressed air film, the theoretical load-deflection characteristics data are subjected to curve fitting procedure using classical least squares method [8]. The mathematical model for the nonlinear spring is then obtained as,

$$f(x) = \alpha x + \beta x^3 \tag{4}$$

Table 1 Data of the single orifice aerostatic thrust bearing

S. No	Parameter	Value
1	Ultimate load carrying capacity	220 N
2	Outside diameter of the bearing	45 mm
3	Supply pressure	0.6 MPa (constant)
4	Coefficient of discharge of orifice	0.8
5	Diameter of orifice	0.8 mm

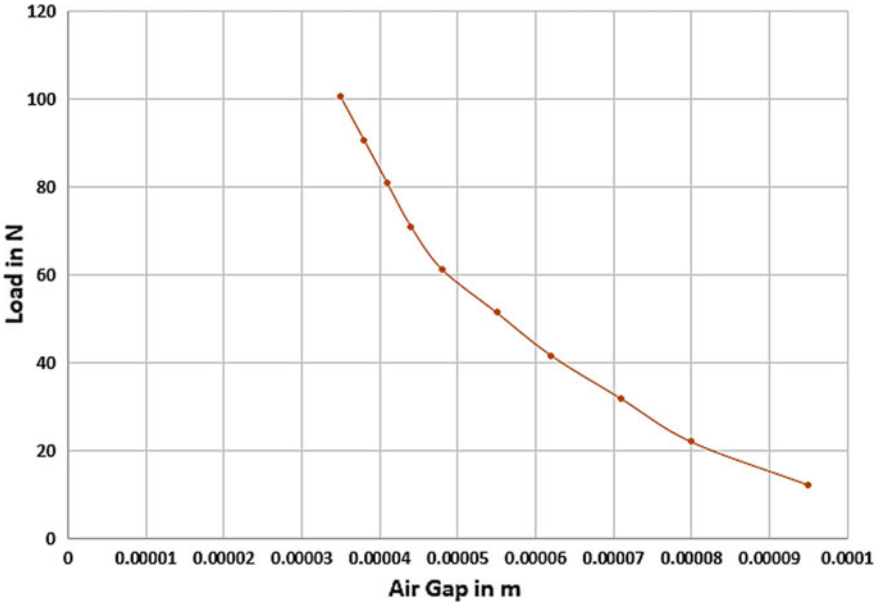


Fig. 1 Load deflection characteristics

where $\alpha = 1{,}959{,}206.465$ and $\beta = -2.3194 \times 10^{14}$. For the prediction of transient response of the bearing system subjected to harmonic base excitation, a single degree-of-freedom model is considered as shown in Fig. 2.

In the above shown single degree-of-freedom model, 'm' represents the total mass involving the mass of the bearing pad and the supported mass. The nonlinear spring represents the compressed air film whose mathematical model is given by Eq. 4. The

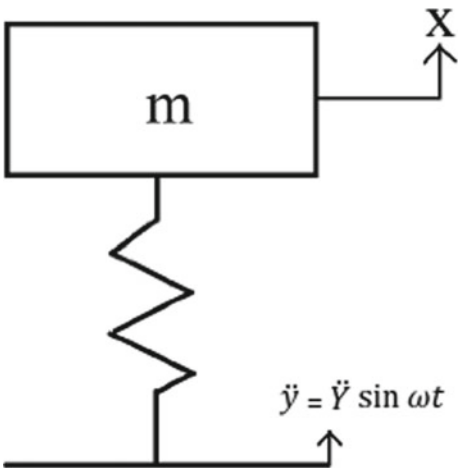


Fig. 2 Single degree-of-freedom model

system is subjected to a harmonic base excitation of the form $\ddot{y} = \ddot{Y} \sin \omega t$, where $\ddot{Y}$ represents the amplitude of base acceleration and ω represents the frequency of base excitation. The compressibility of an aerostatic bearing dominates dynamic performance and therefore the damping in the system has been assumed to be zero. The governing differential equation of the system is given by,

$$m\ddot{z} + \alpha z + \beta z^3 = -m\ddot{y} \tag{5}$$

where $z = x - y$ represents the relative displacement. The above equation is solved numerically in MATLAB software using ODE solver [9], which in turn employs Runge–Kutta method to obtain the transient response of the bearing system subjected to base harmonic excitation.

2.2 Experimental Approach

In order to validate the results obtained from theoretical approach described in the previous section, experimentation has been carried out using vibration testing employing a shaker and an accelerometer. The bearing pad was initially fabricated using stainless steel and then for the purpose of creating orifice, a hole of 0.8 mm was drilled in the centre of bearing pad using electro discharge hole drilling machine. Then, an air pocket of required diameter (as obtained from the design charts) was also made into the bearing pad. Additionally, the side of the bearing pad was milled to a flat surface and a hole of 8 mm diameter was drilled at the centre to create air channel and to create connection with ¼ inch connector, internal threads were created using tapping operation. This channel is responsible for the proper transportation of compressed air from the compressor to the bearing pad. The fabricated bearing pad is shown in Fig. 3.



Fig. 3 Bearing pad

In order to create an interface between bearing pad and the electrodynamic shaker, a circular base plate of the same diameter was also fabricated and a hole of suitable size to a suitable depth was drilled on the bottom of the base plate to mount the base plate on to the electrodynamic shaker. The components of the air bearing system are assembled in the form of a pneumatic system. The different components are connected using pneumatic pipes of diameter 10 mm. An air compressor compresses air to the required pressure and stores it in a cylinder. The cylinder is fitted with a valve that can be opened or closed to control the air flow. A hose clamp is used to hold the pneumatic pipes firmly in places. From the air compressor, the air then passes through a pneumatic filter that can filter particles of size greater than 40 μm. This is to ensure that no dust particles enter the bearing and cause damage. The filter has an inlet and outlet and is connected to the pipes with the use of ¼ inch connectors. From the filter, the pressure is measured with the help of a pressure gauge before entering the bearing pad. The compressed and filtered air then passes through the orifice leading to the junction between the bearing pad and the base plate creating lift. For the experimentation, the base plate was mounted on an electrodynamic shaker with the bearing pad placed on top of it. The air film was generated in between the base plate and the bearing pad. An ADXL 335 accelerometer was mounted on top of the bearing pad and was connected to an Arduino Uno circuit for the data acquisition. The PLX-DAQ plugin [10] for Microsoft Excel was used for the data acquisition. The electrodynamic shaker was adjusted to provide the required base harmonic acceleration at the required frequency. The excitation provided by the electrodynamic shaker was transferred to the base plate and eventually to the base of the bearing pad via the air film. The acceleration data acquired from the accelerometer was utilized to obtain the transient response of the bearing system (Fig. 4).

3 Results and Discussions

Theoretical and experimental approaches described in the previous section utilize a harmonic base acceleration of amplitude 2 g at a frequency of 23 Hz. The transient response of acceleration of the equivalent single degree of freedom is shown in Fig. 5.

The transient response of the acceleration of the bearing system obtained from experimental approach is shown in Fig. 6.

The maximum values of acceleration obtained from both the approaches are summarized in Table 2.

It can be seen from the above table that the maximum acceleration values obtained from both the approaches have less deviation between each other. The deviation present can be attributed to the factors like fluctuation in the pressure of compressed air film between bearing pad and base plate, minor effects of squeeze film damping which have been neglected in the analysis, etc. The latter assumption is due to a fact that the compressibility of gas film in the aerostatic bearing dominates its dynamic performance and it is possible to assume that damping coefficient equals to zero for the purpose of predicting resonance frequency and transient response. Further,

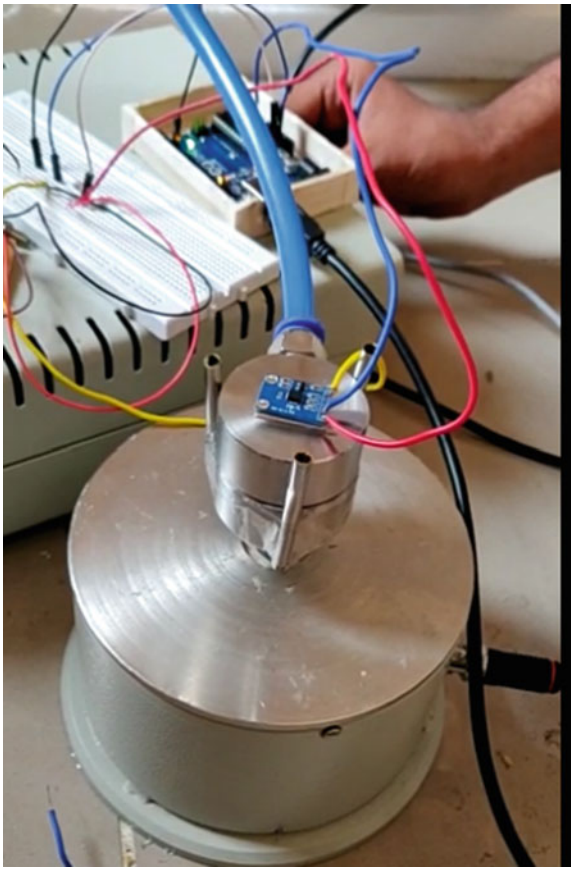


Fig. 4 Vibration testing setup

the value predicted by the theoretical approach is more than the value predicted by experimental approach, which paves the way for conservative design of the bearing system.

4 Conclusions

The present work mainly illustrates the significance of considering compressed air film as a nonlinear spring in the equivalent single degree-of-freedom model of the single orifice aerostatic thrust bearing system, in the early design stage of the bearing. The nonlinear mathematical model of the spring predicts more accurate dynamic response of the bearing system, which greatly helps the engineers to safely design the bearing system for its respective application. Further, the methodology utilized in

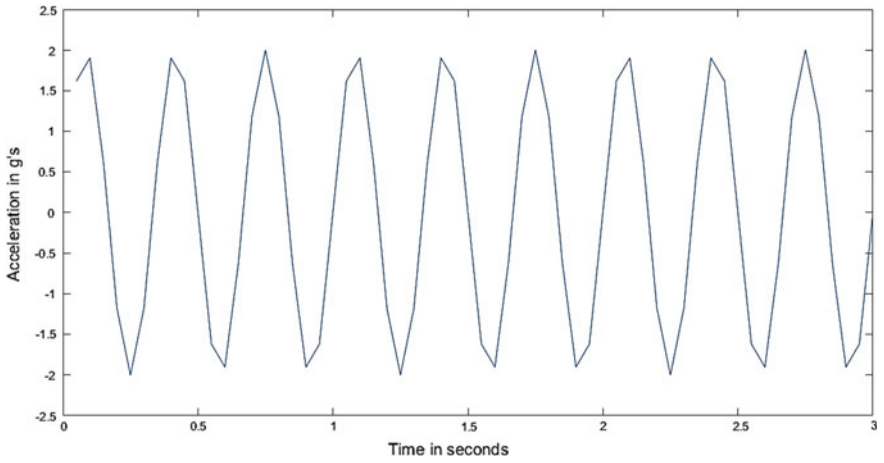


Fig. 5 Transient response of acceleration obtained from theoretical approach

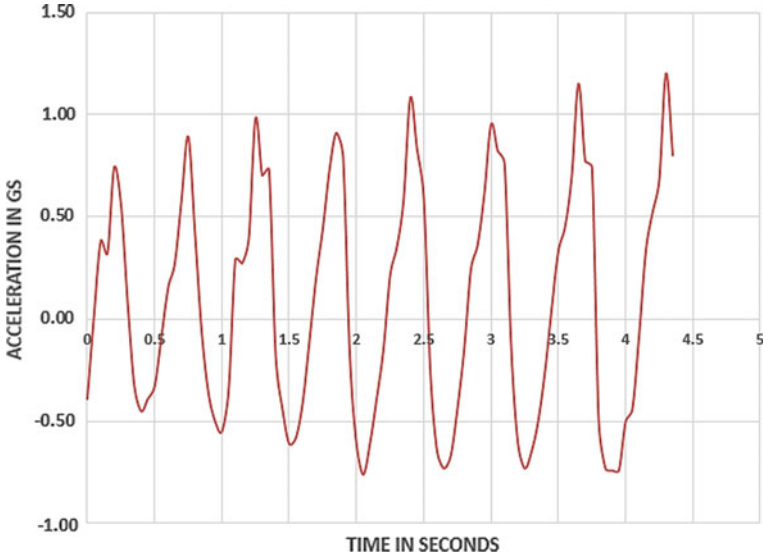


Fig. 6 Transient response of bearing system obtained from experimental approach

Table 2 Comparison of maximum value of acceleration obtained from both the approaches

S. No	Value obtained from theoretical approach	Value obtained from experimental approach
1	1.8 g	1.3 g

the work is highly simple from computational point of view and can be easily adopted in the design without much change from the conventional linear system. In the future work related to this topic, squeeze film damping can be considered to illustrate the presence of its effect for a particular bearing system. Also, a more detailed analysis can be done with multi-degree-of-freedom model, with deformation of pad taken into account.

References

1. Jin XDC, Zhu C, Chen H (2013) Dynamic characteristics of ultra precision aerostatic bearings. AdvManuf (Springer) 1:82–86
2. Kong ZK, Tao JZ (2013) Pneumatic hammer in aerostatic thrust bearings with single orifice compensation. Proc SPIE 8759
3. Chen MF, Lin YT (2002) Dynamic analysis of the X—shaped groove aerostatic bearings with disk-spring compensator. JSME Int J 45(2):492–501
4. Ma W, Cui J, Liu Y, Tan J (2016) Improving the pneumatic hammer stability of aerostatic thrust bearing with recess using damping orifices. Tribol Int 103:281–288
5. Khatait JP, Lin W-J, Lin W, Li H (2006) Modelling of an orifice-type aerostatic thrust bearing. In: Proceedings of ICARCV (Source: IEEE Xplore)
6. Brian Rowe W (2012) Hydrostatic, aerostatic and hybrid bearing design. Amsterdam: Elsevier
7. Powell JW (1970) The design of aerostatic bearings. The Machinery Publishing Co., Ltd., London
8. Chapra SC, Canale RP (2010) Numerical methods for engineers, 6th edn. Tata McGraw Hill, New York
9. Ordinary Differential Equations page. https://in.mathworks.com/help/matlab/ordinary-differential-equations.html?s_tid=CRUX_lftnav
10. Parallax Home Page. https://www.parallax.com/downloads/plx-daq

Industrial Computational Analysis of Aerodynamic Characteristics of Delta-Shaped Aircraft



O. B. Molwane, A. Agarwal, and R. Marumo

Abstract Supersonic fighter aircrafts are designed for high speed, good maneuverability, and high-altitude operations. These characteristics depend upon shape and design of aircraft wings which determine lift force and drag force generated. The current research investigates aerodynamic features of delta-shaped aircraft using computational fluid dynamics. The CAD prototypical of two different designs of aircraft (low taper ratio of 0.125 and high taper ratio of 0.4) is developed in Creo 2.0 software and CFD investigation is directed using ANSYS CFX software platform. The inlet velocity is kept constant for both designs and angle of attack is varied, i.e., 5°, 10°, 15°, 18°, and 20°. Lift coefficient and drag coefficient for each angle of attack are determined for both designs. The results have shown that taper ratio has significant effect on both the aerodynamic characteristics of an aircraft. The study of vortex produced also provide important information on flaws of delta-shaped aircraft design.

Keywords Aerodynamic characteristics · ANSYS CFX · Flow features · Wings · Pressure

1 Introduction

The aerodynamic characteristics of an aircraft are largely influenced by shape and design parameters of wing. Today's fighter aircrafts are designed for high speed and maneuverability which depends upon its wing shape and design. The wing design encompasses various design parameters which influences lift and drag force generated. These design parameters comprise wing part, wing width, taper ratio, aspect ratio, and root chord.

O. B. Molwane (✉)
Department of Industrial Design and Technology, FET, University of Botswana, Gaborone, Botswana
e-mail: molwaneob@mopipi.ub.bw

A. Agarwal · R. Marumo
Department of Mechanical Engineering, FET, University of Botswana, Gaborone, Botswana

© Springer Nature Singapore Pte Ltd. 2020

A. Praveen Kumar et al. (eds.), *Advances in Lightweight Materials and Structures*,
Springer Proceedings in Materials 8, https://doi.org/10.1007/978-981-15-7827-4_77

By altering the wing design parameters, the aerodynamic characteristics of an aircraft can be varied. Triet et al. [1] have conducted numerical analysis on NACA 2412 airfoil using ANSYS Fluent software. The aerodynamic characteristics which include coefficient of lift and coefficient of drag were determined along with pressure plot and velocity plot for inlet velocity range from 0 to 50 m/s. The numerical results were in close agreements with previously available experimental results.

Sureka and Satya Meher [2] have conducted static structural analysis on NACA 64,215 airfoil of A300 aircraft to determine its structural behavior using ANSYS FEA software. The material analyzed was aluminum alloy and aluminum 7068. The findings have shown that aluminum 7068 gives better strength as compared to aluminum alloy material.

Konayapalli and Sujatha [3] have conducted CFD analysis on NACA 4412 airfoil using ANSYS 14.5 software. The findings have shown decrease of dynamic pressure on leading edge with increased angle of attack and increase of static pressure. Kavya et al. [4] have conducted structural and modal analysis of modified wing comprising of spars and ribs using ANSYS software. The material analyzed was Kevlar 49, Boron, and S-Glass. The findings have shown reduction in stresses and deformation for wing with spars and ribs. Vinoth Kumar et al. [5] have conducted optimization of NACA 64A215 airfoil using MSC NASTRAN package for output parameters wing loading, take-off distance and lesser frequency modes of vibration and velocity of stall.

The objective of present research is to analyze effect of taper ratio on delta-shaped aircraft using computational fluid dynamics. Customary k-epsilon turbulence model is used for turbulence demonstrating to determine lift force and drag force at numerous angle of attack.

2 Modelling and Analysis Based on Different Boundary Conditions

The method of computational fluid dynamics is based on Navier's Stokes equation which is based on conservation of mass, momentum, and energy in any control volume. Applying the mass, momentum, and energy conservation, we can derive the continuity equation, momentum equation, and energy equation as follows. The equations of mass conservation, moment conservation, and energy conservation are described below.

2.1 Mass Conservation Equation

$$\frac{\mathrm{d}p}{\mathrm{d}t} + \frac{\rho \partial U}{\partial x} = 0 \tag{1}$$

2.2 Momentum Conservation Equations

$$\frac{\rho \partial U}{\partial x} + \frac{\partial U}{\partial x} = -\frac{\partial P}{\partial x} - \frac{\partial \tau}{\partial x} + \rho g \tag{2}$$

2.3 Energy Conservation Equations.

$$\frac{\rho c \partial T}{\partial t} + \frac{\rho c U \partial T}{\partial x} = -\frac{P \partial U}{\partial x} + \frac{\lambda \partial \tau}{\partial x 2} - \frac{\tau \partial U}{\partial x} \tag{3}$$

ρ is density of fluid, μ: viscosity of fluid, in differential terms Ist is local energy change with time, IInd is convective term, IIIrd is pressure work, IVth is heat flux (diffusion), and Vth is irreversible transfer of mechanical energy into heat.

The first stage of analysis is preprocessing which encompasses CAD modelling, meshing and applying loads, and boundary conditions. The CAD model of aircraft is developed using Creo 2.0 design software using blend and extrude tool. The parametric nature of this design software enables to easily modify the existing dimensions of model created as shown in Fig. 1

The CAD model developed is converted in.iges format to export it into ANSYS software. The iges is integrated graphics file format making model to easily open in any other design or analysis package. The computational domain is modeled in ANSYS design modeler. The first step is modeling cubical enclosure with dimensions and the next step involves subtracting enclosure with aircraft geometry which results in void zone where air flows.

The further stage of preprocessing is meshing of computational domain. The discretization of fluid flow domain is referred to as grid [6] is meshed using tetrahedral elements as shown in Fig. 2. Number of nodes generated is 127,638 and number of elements generated is 187,345. RMS residual values were lower than 0.0001.

Figure 2 shows sectional view of computational-meshed domain. The region of mesh represents volume from which fluid will flow. The unstructured mesh is suitable for analysis of flows involving lower turbulence but not suitable for flows involving higher turbulence kinetic energy of vortices [7–9]. The equations motions are formulated for each discretized elements of computational domain which forms a system of algebraic equations. These algebraic equations are solved numerically [10, 11].

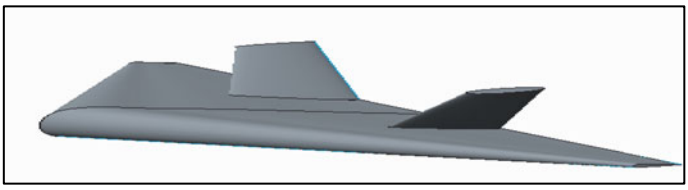


Fig. 1 CAD model of aircraft

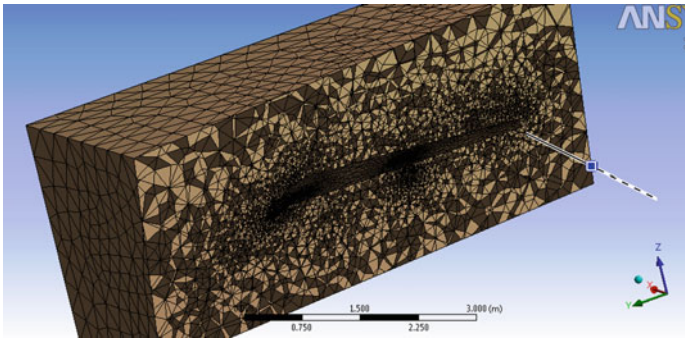


Fig. 2 Sectional View of meshes

The next stage involves defining boundary conditions as shown in Fig. 3. The inlet boundary and outlet boundary conditions are defined with constant inlet velocities. The angle of attack of aircraft body is changed for different cases of analysis. The criteria for which the simulation can be regarded as converged needs to be determined. RMS residual values are set to 1e-5 and max iterations to 100. The RMS residual values of mass, momentum, and kinetic energy are generated from CFD simulation. The RMS residual values after 100 iterations were lower than 0.00001 which gives reasonably accurate solution.

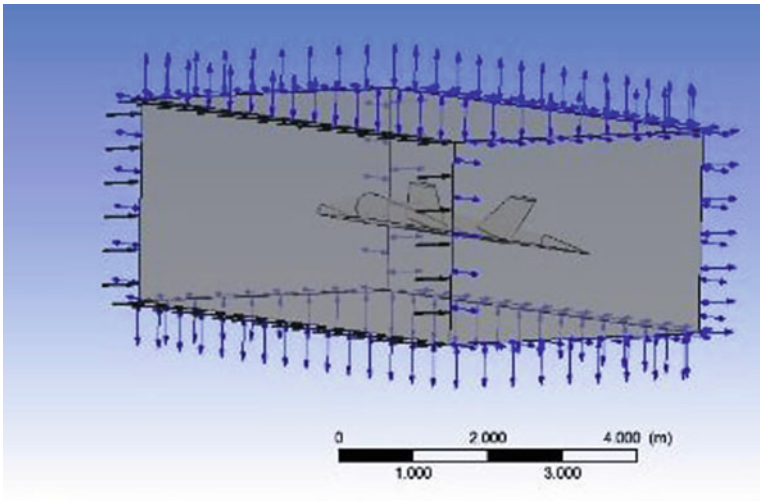


Fig. 3 Boundary conditions

3 Results and Discussion

The CFD analysis is conducted using ANSYS CFX software on two designs of aircraft wing. The first design analyzed has taper ratio of 0.125 and second design has taper ratio of 0.4.

The drag force and lift force generated for aircraft wing with taper ratio of 0.125 are shown in Figs. 4 and 5, respectively. The maximum drag force generated is 4.37 N and maximum lift force generated is 17.32 N for 5° angle of attack.

The drag force and lift force generated for aircraft wing with taper ratio of 0.4 are shown in Figs. 6 and 7, respectively. The maximum drag force generated is 4.97 N and maximum lift force generated is 23.47 N for 5° angle of attack. Table 1 shows value of C_L and C_D.

The curve in Fig. 8 shows linear increase in lift upto 18° angle of attack. The stalling of aircraft taken place after 18° angle of attack as lift generated decreases due flow separation.

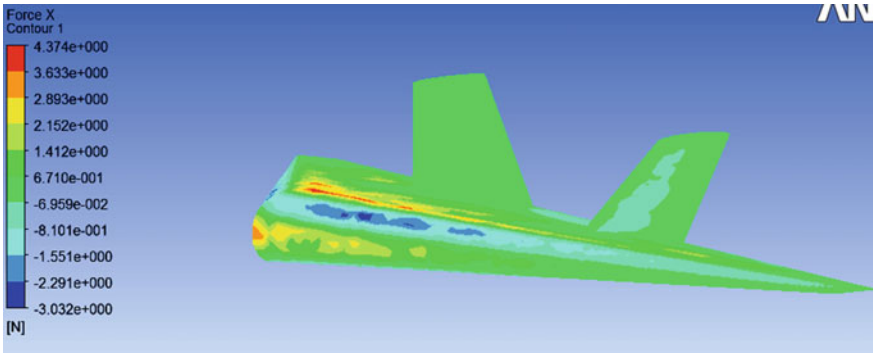


Fig. 4 Drag force at 5° for taper ratio of 0.125

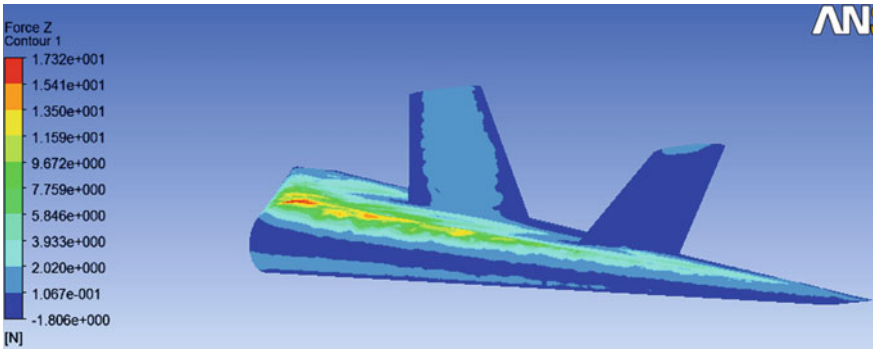


Fig. 5 Lift force at 5° for taper ratio 0.125

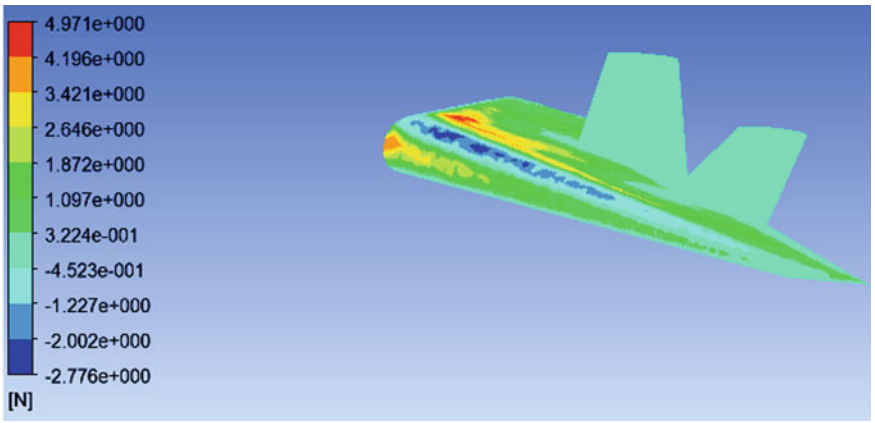


Fig. 6 Drag force at 5° for taper ratio 0.4

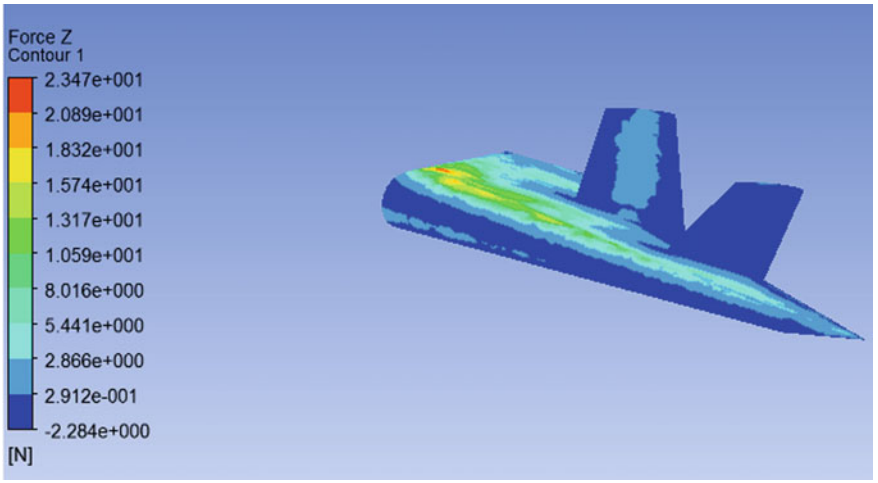


Fig. 7 Lift force at 5° for taper ratio 0.4

Table 1 C_L and C_D values for 0.125 taper ratio

Angle of attack	Pressure (Pa)	Drag force (N)	Lift force (N)	C_L	C_D
0°	1836	3.932	14.73	0.0006354	0.00016
5°	1843	4.37	17.32	0.0007471	0.00018
10°	1821	6.73	19.93	0.0008597	0.00029
15°	1876	10.47	23.12	0.0009974	0.00041
18°	1947	12.73	26.89	0.001160	0.00054
20°	1938	14.35	26.29	0.0011303	0.00061

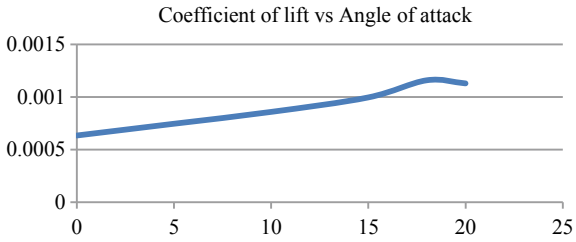


Fig. 8 C_L versus angle of attack for 0.125 taper ratio

The C_D versus angle of attack curve generated for aircraft wing with 0.125 aspect ratio is shown in Fig. 9. The drag force of C_D value increases constantly with increase in angle of attack. This can be attributed to increase in surface of aircraft wing exposed to incoming air flow.

The pressure field generated above and below aircraft wing is shown in Fig. 10. The low-pressure zone is developed above wing tip as shown in dark blue color region while high pressure zone is developed near bottom end tip as shown by dark red color plot. The zone above flat face of wing shows lower air pressure. The net result is higher air pressure beneath wing and lower pressure above wing tip thus resulting in lift force in upward direction. Table 2 shows value of C_L and C_D for 0.4 taper ratio.

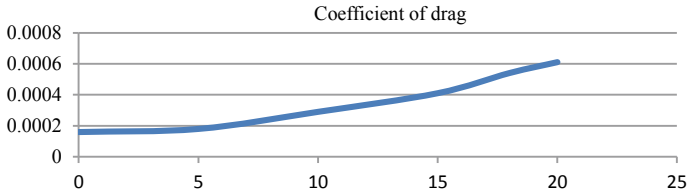


Fig. 9 CD versus angle of attack for 0.125 taper ratio

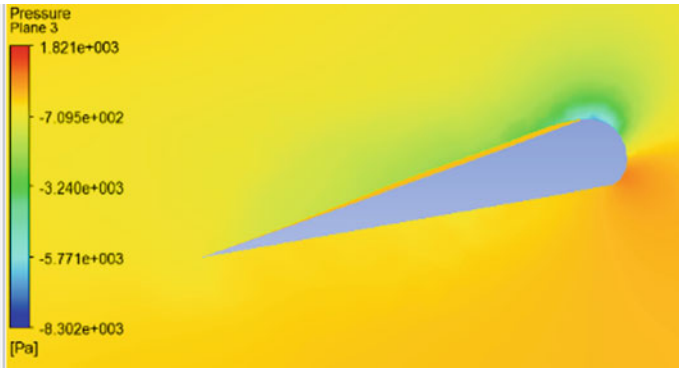


Fig. 10 Pressure field across aircraft wing

Table 2 C_L and C_D values for 0.4 taper ratio

Angle of attack	Pressure	Drag force	Lift force	C_L	C_D
0°	1849	4.77	19.18	0.000660	0.000164
5°	1889	4.97	23.47	0.000808	0.000171
10°	1896	6.94	20.31	0.000699	0.000239
15°	1919	10.19	28.75	0.000990	0.000351
18°	1966	12.90	26.56	0.000915	0.000444
20°	2071	15.89	31.17	0.001074	0.000547

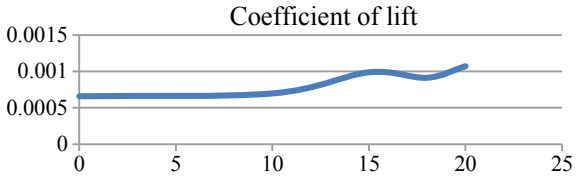


Fig. 11 C_L versus angle of attack for 0.4 taper ratio

The C_L curve generated from CFD analysis of aircraft wing having taper ratio of 0.4 is shown in Fig. 11. The curve shows increase in lift force with angle of attack. The lift increases 17° and then decreases.

The C_D versus angle of attack curve generated for aircraft wing with 0.125 aspect ratio is shown in Fig. 12. The drag force increases with increase in angle of attack which is due to increased surface area of aircraft wing to incoming area. When fluid flows about an axis line, vortex region is generated. The formation of vortexes leads loss of lift to the aircraft. In the present design of aircraft, vortex is formed in tail rudder and wing end. Wing tip vortexes are generated when there is interaction between airflows of upper and lower surfaces of a wing at the trailing edge and the tip as shown in Fig. 13.

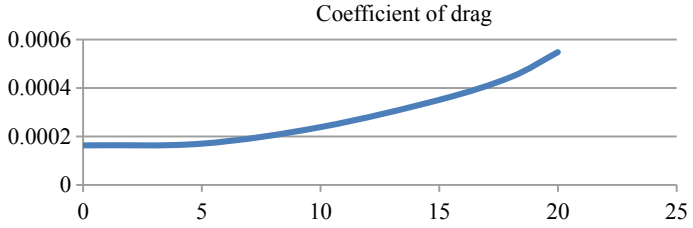


Fig. 12 C_D versus angle of attack for 0.4 taper ratio

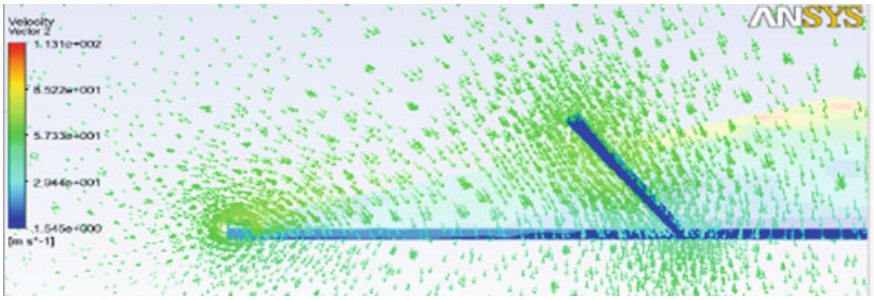


Fig. 13 Vortex generation at trail of rudder

4 Conclusion

The drag force is found to increase with angle of attack for both low taper ratio design and high taper ratio design. The lift force generated is higher for high taper ratio design of aircraft wing as against low taper ratio design of aircraft wing. The drag force generated is higher for high taper ratio design of aircraft wing as against low taper ratio design of aircraft wing. The pressure developed is lower in upper region of aircraft wing as shown by light green color and yellow color zone. The higher pressure is developed in lower region of aircraft wing as shown by dark red color. The high pressure in lower region and low pressure on upper region lead to upward lift force.

Stall angle with low taper ratio is found to be at 180 angle of attack and stall angle with high taper ratio is found to be at 150 angle of attack. Formation of vortex has been noticed on trail rudder which adversely affects the lift generated. The CFD analysis conducted on delta-shaped aircraft enabled to determine possible pressure field, velocity field around aircraft wing. Although increasing the taper ratio has advantage of getting higher lift but resulted in reduced stall angle. The new optimized design of airfoil possessed better lift-to-weight ratio and higher stall angle. Further research can be performed using other design parameters.

References

1. Triet NM, Viet NN, Thang PM (2015) Aerodynamic analysis of aircraft wing. VNU J Sci Math Phys 31(2):68–75
2. Sureka K, Satya Meher R (2015) Modeling and structural analysis on A300 flight wing by using ANSYS. Int J Mechan Eng Robot Res 4(2)
3. Konayapalli SR, Sujatha Y (2015) Design and analysis of aircraft wing. Int J Mag Eng Technol Manage Res 2(9)
4. Senthilkumar S, Velayudham A, Maniarasan P (2013) Dynamic structural response of an aircraft wing using ansys. Int J Eng Res Technol 2(6)
5. Vinoth Kumar TS, Waseem Basha A, Pavithra M, Srilekha V (2008) Static and dynamic analysis of a typical aircraft wing structure using MSC Nastran. Int J Res Aeronaut Mechan Eng 3(8)

6. Alobaid F (2013) Improvement, validation and application of CFD/DEM model to dense gas flow in a fluidized bed. Particuology 11(5):514–526
7. Liu Z (2015) Computational fluid dynamics solver with preconditioned method for aerodynamic simulation of high-lift configuration. J Aircraft 53(4):1056–1064
8. Necci C (2009) Industrial computational fluid dynamics tool for evaluation of aerodynamic coefficients. J Aircraft 46(6):1973–1983
9. Hull DG (2007) Fundamentals of airplane flight mechanics. Springer, Berlin
10. Jamerson A (2017) Using computational fluid dynamics for aerodynamics—a critical assessment. Stanford University, California, pp 5–8
11. Jamerson A (2006) Using computational fluid dynamics for aerodynamics. Stanford University, California, pp 1–4

Transient Thermal Analysis of Vehicle Air Conditioning System by Varying Air Vent Location

A. Agarwal, R. Marumo, O. B. Molwane, and I. Pitso

Abstract With increase in fuel prices, the customers demand for fuel efficient car. The air conditioning system employed in cars draws it power from vehicle engine and reduces its mileage. Air vent location has a significant impact on thermal comfort of cabin. In the current research, the location of air vents has been changed from all four in front dashboard (Design 1) to 2 front and two rear above passenger seat (Design 2). Transient thermal analysis is performed using ANSYS CFX 18.1. With the assistance of CFD, it is demonstrated that rear cooling air vents give a superior air comfort to passenger. The turbulence model used for CFD analysis is RNG k-epsilon which gives better prediction for swirl flows generated due to complex geometry. The transient thermal analysis has shown that cabin temperature reaches to 297.25 K from 308 K for design 1 (four vents on dashboard) during 50 counter seconds time. For front-seated passengers, design 1 offers more cooling as compared to design 2 due to more air flow due to location of all four air vents on front dashboard.

Keywords Air conditioning · Vent location · Cabin temperature · Blower speed · Comfort

1 Introduction

The tropical heat causes high temperature inside passenger car cabin. Although the vehicle air conditioners are efficient, it taken long time for cooling. The study conducted by National Renewable Energy Laboratory (NREL) shows that 27 billion liters gasoline is consumed annually in USA [1] alone.

The statistics has shown that with a minor 0.4-km/L increase of fuel economy in vehicles could enable $6 billion savings [2]. Various factors influence the load

A. Agarwal (✉) · R. Marumo · I. Pitso
Department of Mechanical Engineering, FET, University of Botswana, Gaborone, Botswana
e-mail: agarwala@ub.ac.bw

O. B. Molwane
Department of Industrial Design and Technology, FET, University of Botswana, Gaborone, Botswana

© Springer Nature Singapore Pte Ltd. 2020

A. Praveen Kumar et al. (eds.), *Advances in Lightweight Materials and Structures*,
Springer Proceedings in Materials 8, https://doi.org/10.1007/978-981-15-7827-4_78

on vehicle engine. First factor is outside environmental conditions encompassing humidity, temperature, sun radiation incident angle on glass, and outside air velocity.

The higher the difference of these parameters, higher will be load on engine. Second factor is vehicle internal cabin atmospheric conditions. Due to the differential air temperature distribution, the solar flux, and the radiation heat flux from the cabin surrounding interior-trim surfaces, non-uniformities exist. The non-uniformities cause non-uniform cooling. Third important factor is vehicle compressor speed which reduces during vehicle idling and thus reduces refrigerant mass flow and lesser cooling.

2 Design Configuration of AC Vents for Hatchback Car

The cooling efficiency of passenger car largely depends upon its compressor capacity and condenser designs. Apart from these factors, the location of AC duct inside car cabin also plays a vital role in achieving fast cooling. Without any rear vents, the more cooling time is required for rear-seated passengers. By the time, full cooling is achieved, and vehicle reaches its destination. Incorporation of additional blower puts an additional load on AC compressor; therefore, reducing fuel efficiency. The current research investigates the new design configuration of AC vents for hatchback car. The modified design used in the research has two front and two rear vents as compared to conventional four front vent designs. Heat transfer modes for car are shown in Fig. 1.

2.1 Modelling and Analysis

The CFD analysis is conducted on Indian hatchback car Maruti Alto 800. The schematic of car is shown in Fig. 2.

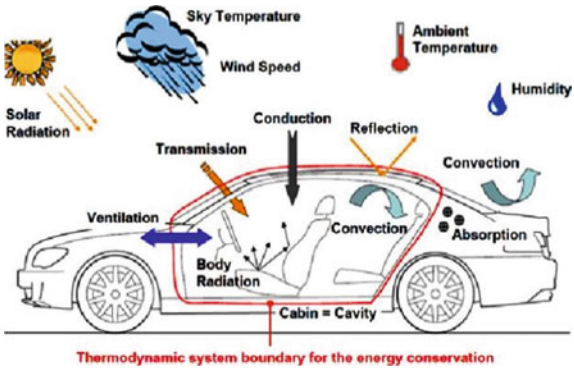


Fig. 1 Heat transfer modes for car [3]

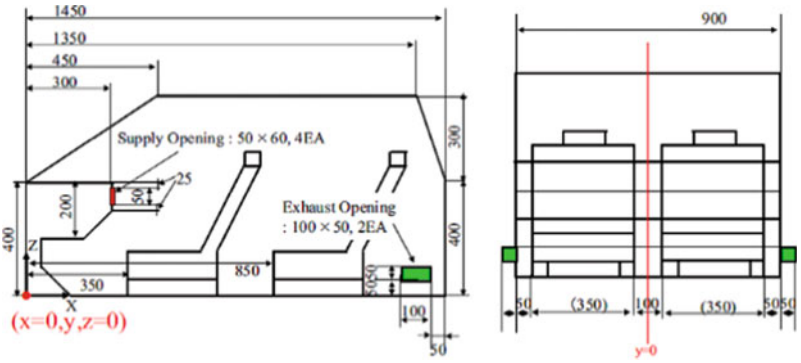
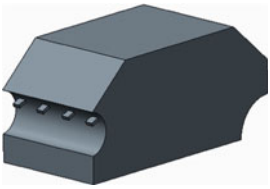


Fig. 2 Dimensions of car

Fig. 3 CAD model of Maruti 800 with vents



The CAD model of this hatchback car is developed using Creo Parametric design package. Two different CAD models are developed. The first CAD model has all four front air vents and second CAD model has two front and two rear air vents as shown in Fig. 3.

The CAD model developed is then meshed using tetrahedral elements and later applied with loads and boundary conditions described below.

2.1.1 Heat Load Calculation Procedure

The net heat gain by the cabin can be classified under different categories. The mathematical formulation of the heat load can thus be summarized as

$$Q_{\text{Total}} = Q_{\text{Metabolic}} + Q_{\text{Solar}} + Q_{\text{Equipment}} + Q_{\text{Fresh air}} \tag{1}$$

where metabolic load is given by

$$Q_{\text{Metabolic}} = M \times A \tag{2}$$

Solar load constitutes normal solar radiation, direct radiation, diffuse radiation, and is given by

$$Q_{\text{Solar}} = Q_1 + Q_2 + Q_3 \tag{3}$$

The equipment load in a car only equipment is the music system.

$$Q_{\text{equipment}} = 80W \tag{4}$$

The fresh air load is given by

$$\text{Fresh air flow } V = R_{\text{p}} \times P_{\text{z}} + R_{\text{a}} \times A_{\text{z}} \tag{5}$$

R_{p} Outdoor airflow rate required per person.

P_{z} Zone population, R_{a} Outdoor airflow rate required per unit area.

A_{z} Zone area $V = 0.708\,\text{m}^3/\text{min}$.

Mass of fresh air $m_{f_{\text{a}}} = 0.0129\,\text{kg/min}$.

Sensible load

$$\text{SH} = m_{f_{\text{a}}} C_{\text{pm}}(t_{\text{o}} - t_{\text{i}}) \tag{6}$$

$\text{SH} = 0.1977\,\text{KW}$.

$$\text{Total Load} = m_{f_{\text{a}}} C_{\text{pm}}(h_{\text{o}} - h_{\text{i}}) \tag{7}$$

$\text{TL} = 0.4347\,\text{KW}$.

$$\text{Latent Load} = \text{Total Load} - \text{Sensible Load}, \quad \text{LL} = 0.2370\,\text{KW}$$

Total load summary is given in Table 1.
Cooling load = 2.63/3.5.
Cooling load = 0.75TR.
Mass flow rate of refrigerant

Table 1 Total load summary

S. No	Source	Sensible load, W	Latent load, W
1	Occupant	605.34	287.28
2	Solar	1235.96	–
3	Equipment	80	–
4	Fresh air	197.7	237
5	Toal	2119	524.24
Total load		2643.24 W	

$$m_{\mathrm{a}} = \frac{\text{cooling load}}{h_{\mathrm{fg}}}$$

At 6 °C of coil ADP

$$h_{\mathrm{fg}} = 364.49\,\mathrm{kj/kg}$$
$$m_{\mathrm{a}} = 0.0072\,\mathrm{kg/s}$$

Volume flow rate of refrigerant

$$V = m_{\mathrm{a}} v_f$$
$$V = 0.00002451\,\mathrm{m}^3/\mathrm{s}$$

For turbulence modeling in CFD simulation, the RNG k-epsilon turbulence model is used which provides much better predictions for swirl flow. The equation is shown below.

$$\frac{\partial}{\partial t}(\rho k) + \frac{\partial}{\partial x_i}(\rho k u_i) = \frac{\partial}{\partial x_j}\left(\alpha k \mu_{\mathrm{eff}} \frac{\partial k}{\partial x_j}\right) + G_{\mathrm{k}} + G_{\mathrm{b}} - \rho\varepsilon - Y_{\mathrm{M}} + S_{\mathrm{k}} \quad (8)$$

The term G_{K}, G_{b} represents turbulence kinetic energies due to mean velocity and buoyancy, respectively.

3 Results and Discussion

The CAD analysis is conducted on cabin using ANSYS CFX. The temperature plot and curves are generated for both front- and rear-seated passengers. The blower speed is set to 0.67 m/s [4]. The duration of simulation was set to 50 counter sec and values are captured for every 10 counter seconds.

The temperature drop is achieved within 10 counter seconds of air flow inside cabin; the temperature difference is noticeable between 2 designs as shown in Fig. 4 and Fig. 5, respectively. Rear passengers receive significantly higher cooling in design 2 with temperature averaging to 298 K as compared to design 1 with temperature averaging 303 K. In 20 counter seconds, the cooling for rear passengers becomes almost stagnant showing similar temperature magnitude as in 10 counter seconds.

The temperature drops further in rear-passenger side in 30 counter seconds averaging of 297 K and for front seat passengers averaging 302.5 K as shown in Fig. 6 . In 40 counter seconds, temperature further drops for rear passenger domain averaging 296.8 K and front passenger temperature of 301 K as shown in Fig. 7. This variation shows that design 2 is better in providing more cooling thereby providing

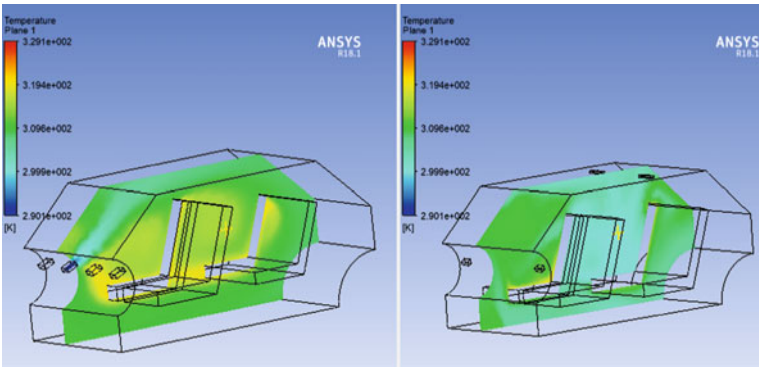


Fig. 4 Temperature at 10 s for design 1 and design 2 at 0.67 m/s

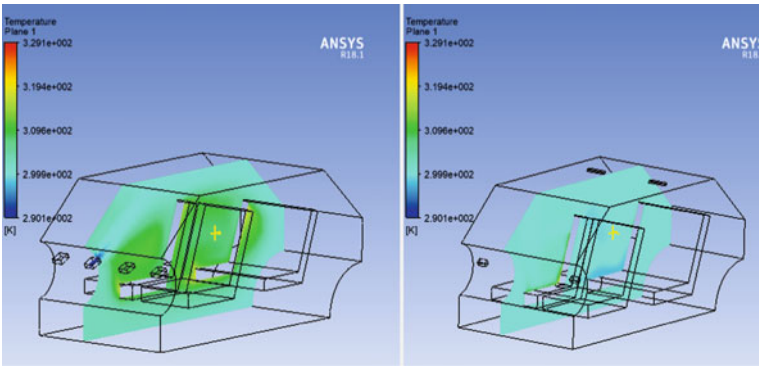


Fig. 5 Temperature at 20 s for design 1 and design 2 at 0.67 m/s

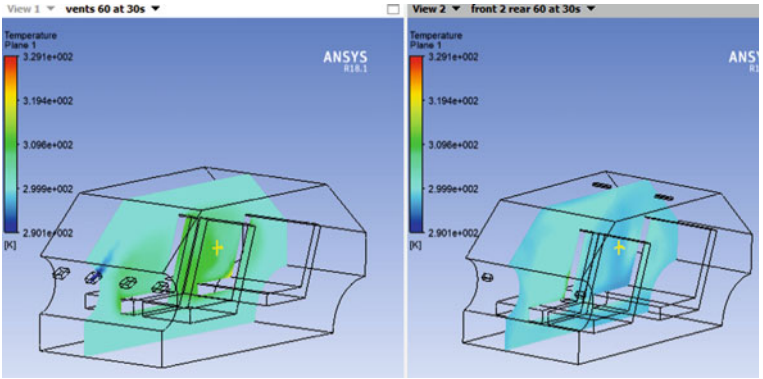


Fig. 6 Temperature at 30 s for design 1 and design 2 at 0.67 m/s

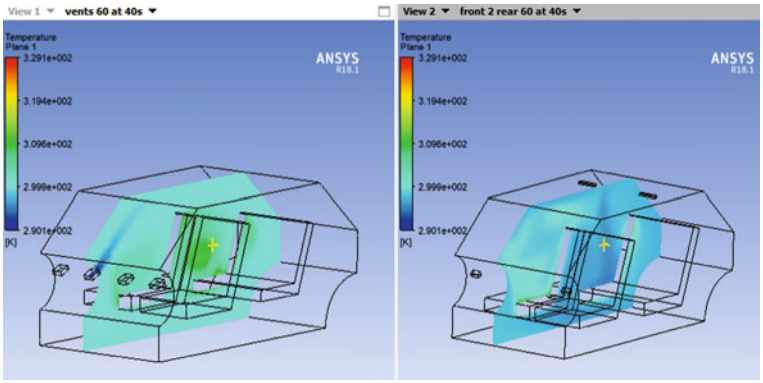


Fig. 7 Temperature at 40 s for design 1 and design 2 at 0.67 m/s

more thermal comfort. Thereafter, the cooling for rear passengers becomes almost stagnant showing similar temperature magnitude as in 10 counter seconds.

Figure 8 shows average temperature of car cabin at 0.67 m/s blower speed. Average temperature of cabin drops with increase in time counter for both design 1 and design 2, but for each time counters, design 2 shows lower temperature as compared to design 1. It must be noticed that the average temperature corresponds to volume average of whole cabin temperature as shown in Table 2.

Temperature versus time curve for front passengers as shown in Figs. 9 and 10 for both design 1 and design 2 shows temperature drop is consistently lower in design 2 as compared to design 1 for all counter seconds. The temperature drop in design 2 has reached to 296 K thereby maintaining constant level throughout. Similar trend can be seen in temperature drop curve for rear passengers where temperature drop is consistently lower in design 2 and reaching to an almost equilibrium point of 295 K. To determine time to subside, the cabin initial temperature for design 1 is set to

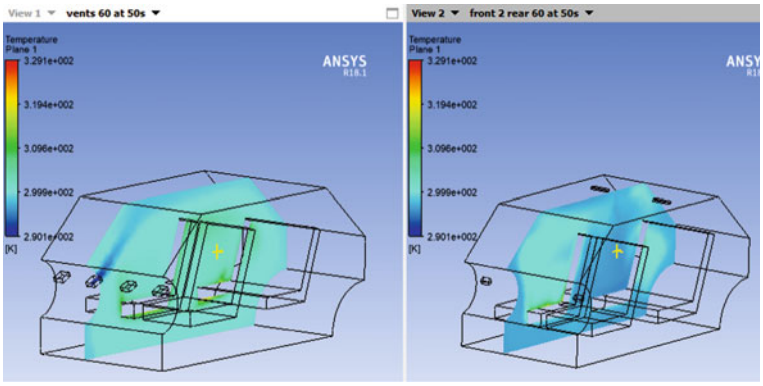


Fig. 8 Temperature at 50 s for design 1 and design 2 at 0.67 m/s

Table 2 Average temperature comparison at 0.67 m/s car blower speed

Time	Design 1 cabin temp (avg)	Design 2 cabin temp (avg)
10	308.56	305.93
20	302.79	299.18
30	299.14	296.74
40	297.94	296.10
50	297.25	295.55

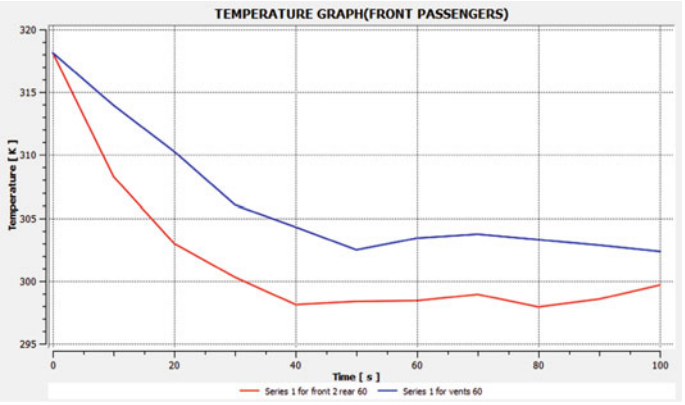


Fig. 9 Temperature graph for front passengers. Red for two front two rear vents and blue for four front vents

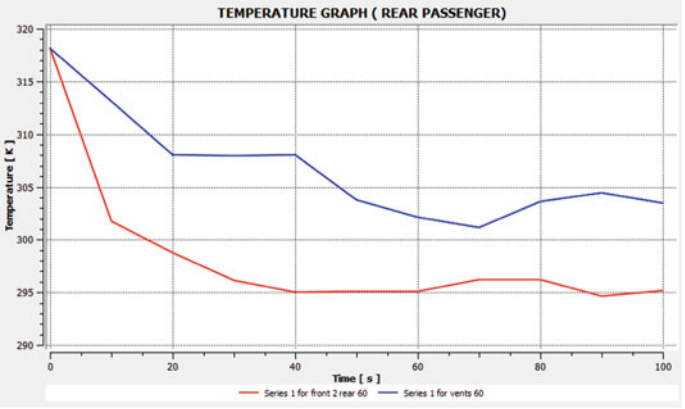


Fig. 10 Temperature graph for rear passengers. Red for two front two rear vents and blue for four front vents

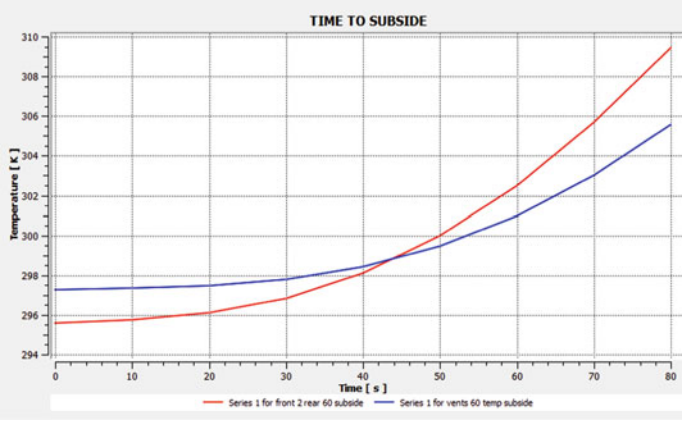


Fig. 11 Temperature versus time for subsiding red color for design 2, blue color for design 1

297.25 K and for design 2 cabin initial temperature is set to 295.55 K. Temperature versus time curve is plotted for both designs as shown in Fig. 11.

As it can be seen that within 80 counter seconds the temperature attained in design 2 is 309.45 K, while for design 1 is 305.75 K. The ambient temperature is 40 °C.

4 Conclusion

The CFD analysis is conducted on hatchback car under transient-state conditions. The heat from sun is applied as flux in windows while human load is kept same as on earlier analysis transient analysis is run. The analysis is conducted for 50 counter seconds. The results have shown that for every counter time, the average temperature of cabin with second design has lower temperature as compared to first design. The transient thermal analysis has shown that cabin temperature reaches to 297.25 K from 308 K for design 1(four vents on dashboard) during 50 counter seconds time. The transient thermal analysis shows that the cabin temperature reaches to 295.42 K from 308 K for design 2(two front and two rear) during 50 counter seconds time. For front-seated passengers, design 1 offers more cooling as compared to design 2 due to more air flow due to location of all four air vents on front dashboard. From the CFD simulation, the time to subside cabin temperature for design 2 is faster than design 1. The implementation of this work can be pursued by designing and building a prototype of the complex system at the laboratory. Further simulation and analysis can be conducted with different temperature range and parameters for human comfort.

References

1. Johnson VH (2002) Fuel used for vehicles air conditioning: a state by state thermal comfort approach, SAE Paper 2002–01-1957. SAE International, Detroit, MI
2. Farrington R, Rugh J (2000) Impact of vehicle air-conditioning on fuel economy, tailpipe emissions, and electric vehicle range. Department of Energy National Renewable Energy Laboratory, US
3. Rugh JP, Hendricks TJ (2001) Effects of solar reflective glazing on ford explorer climate control, fuel economy, and emissions. SAE Paper 200101–3077; SAE International, Detroit, MI
4. Limaye VM (2012) Design of dynamic air vents and airflow analysis in a passenger car cabin. SASTECH 11(1)

Energy Release Rate Evaluation of Bi-material Interface Cracks

M. Prajwal, K. B. Yogesha, Kalmeshwar Ullegaddi, and K. G. Basava Kumar

Abstract Fracture analysis of crack growth in between two material interfaces (different engineering materials) is one of the challenging tasks in the engineering field. In the present investigation, different properties of bi-material are considering to study the damage-tolerant design and analysis of fracture mechanics. A double cantilever beam (DCB) with a bi-material crack is considered for analysis. In FEM, specifically a post-processing command virtual crack closure technique (VCCT) is used for evaluation of mixed mode energy release rate of bi-material interface cracks. Validation of obtained results is done with a benchmark problem in the literature. Then parametric studies have been conducted on four different material combinations for a range of crack length and height of the beam. The results generated will be useful for assessing structural integrity.

Keywords Bi-material crack · Energy release rate · Interface crack · DCB · VCCT

1 Introduction

Fracture mechanics is a branch of science, which deals with propagation of crack and lead failure of the structure. Its assumptions are based on preexisting of the crack. The reason for the crack may be due to man-made or manufacturing defect. A critical crack may propagate during the service of the component which leads to catastrophic damage. Fracture mechanics deals with the question that existing crack likely to grow or not. Usually, fluctuating load tends to grow a crack, which then picks up speed. In subsequent stage, when the crack length is long enough to treat as a critical crack for catastrophic fracture failure. The analysis of fracture mechanics is done through different approaches, each having its own parameters. There are mainly

M. Prajwal (✉) · K. B. Yogesha · K. Ullegaddi
Department of Mechanical Engineering, JSS Academy of Technical Education, Bengaluru 560060, India
e-mail: prajwal.m.88@gmail.com

K. G. Basava Kumar
Department of Mechanical Engineering, RNS Institute of Technology, Bengaluru 560098, India

© Springer Nature Singapore Pte Ltd. 2020

A. Praveen Kumar et al. (eds.), *Advances in Lightweight Materials and Structures*,
Springer Proceedings in Materials 8, https://doi.org/10.1007/978-981-15-7827-4_79

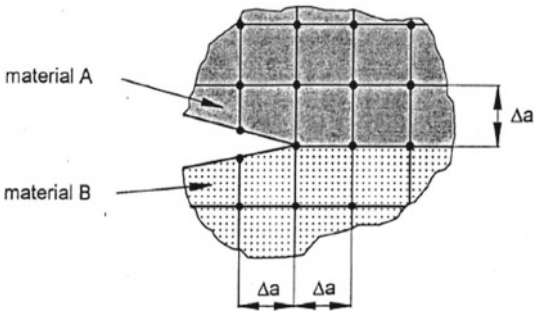


Fig. 1 Bi-material interface crack

four different parameters, such as stress intensity factor (K), J-integral (J) [1], energy release rate (G) [2], and crack tip opening displacement (COTD). The most known technique, i.e., VCCT, is used for measuring the energy release rates based on results from continuum (2D) and solid (3D) finite element analyses. This is used to supply the mode separation for mixed mode fracture criterion. This VCCT methodology can be utilized for simulations of crack initiation and propagation along with composite. The VCCT technology is based on the debond capability [3].

The crack exists along the interface of two different materials is named as bi-material interface crack. Crack propagation at the interface between two different materials with divergent properties is shown in Fig. 1. The fluctuation of stresses occurs at the immediate crack tip region. For larger values of Δa, the energy release rate components were found to be nearly constant, whereas for very small Δa the y are functions of element length. The total energy release rate G_T [4] is given by Eq. (1),

$$G_T = G_I + G_{II} + G_{III} \ldots\ldots\ldots\ldots \quad (1)$$

For the virtual crack closure technique, the energy release rates are defined as the virtual crack closure integral over a finite crack closure length. This crack closure length corresponds to the lengths of the elements adjacent to the crack front [5]. This element length, Δa, must be chosen small enough to ensure a converged finite element solution but large enough to avoid oscillating results.

2 Method and Methodology

Linear elastic fracture mechanics (LEFM) concepts are used in the VCCT for analysis of fracture mechanics of bi-materials interface crack. VCCT is based on the assumption that the strain energy released when a crack is propagated by a certain amount is the same quantity of energy required to close the crack [6–8]. It works based on computing

the energy release rates for normal and shear crack tip deformation modes and comparing energy release rates to inter-laminar fracture toughness [9].

2.1 Requirements of Virtual Crack Closure Technique

- Defining the contact pairs for potential crack surfaces.
- Bonded crack surfaces should be defined initially.
- Initiate crack propagation capability.
- The VCCT criterion has to be specified in an effective manner.

2.2 Elements Used for VCCT

In this study, plane strain elements are used for fracture analysis under VCCT technique. Preferably plane strain elements are used where homogeneous material analysis to be performed. For all plane strain elements, one must provide the element thickness. Otherwise, by default unit thickness is assumed. Each node exhibits two degrees of freedom. Since strain along the third direction is zero.

3 FE Model of a Double Cantilever Beam

The finite element node at the top and bottom surfaces which are in discontinue meshed model has identical coordinates. However, these nodes are not connected to each other, results in showing different faces. Independent deformation of the top surface elements from those of the bottom surface of the crack allows the crack to open rapidly as shown in Fig. 2.

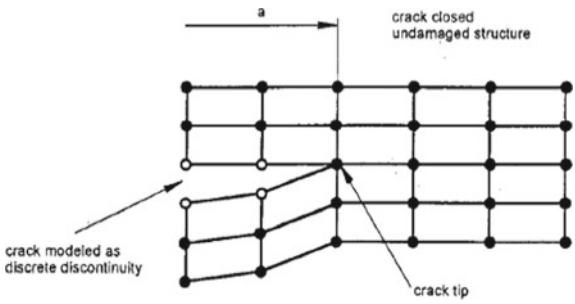


Fig. 2 Deformed finite element model

4 Validation of Fracture Analysis

The finite element model developed is validated using a benchmark [10]. A DCB is subjected to boundary and loading conditions [10]. A double cantilever beam (Fig. 3) with a crack is considered for the analysis. The dimensions and properties considered in the problem are listed in Table 1.

4.1 Target Solution

The results for the benchmark problem obtained from the literature [10] shown in Fig. 4 are taken as a target solution for validation of the finite element model. Stress intensity factor against the height is plotted for mode I failure.

4.2 Analysis of Benchmark Problem Using ABAQUS

FE model development: A typical FE model of DCB has been developed using 2D deformable continuum plane strain 4-noded elements (CPE4). While creating the crack, partition of the face is done to separate the crack tip area so that fine mesh is done at the crack front for converged results as shown in Fig. 5. Each node of the

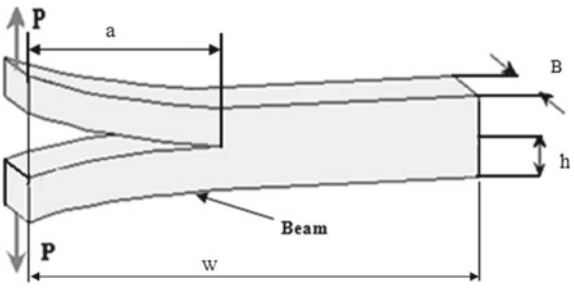


Fig. 3 Double cantilever beam

Table 1 DCB specifications [10]

Material	Steel
Young's modulus	$E = 2.1 \times 10^5$ N/m^2
Poisson's ratio	$\nu = 0.3$
Crack length	$a = 50$ mm
Thickness	$B = 30$ mm
Length	$W = 500$ mm
Load	$P = 15{,}405$ N

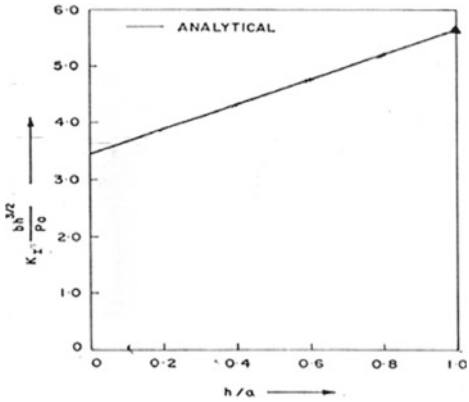


Fig. 4 Analytical solutions for a double cantilever beam

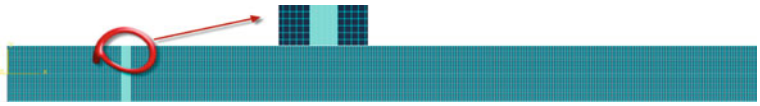


Fig. 5 FE model of DCB with fine mesh at the crack-front

element exhibit two degrees of freedom. Table 2 gives the specification of the finite element model.

Boundary and loading condition: Boundary and loading conditions are assigned to the DCB in the load module of ABAQUS [11]. Concentrated load is applied to stretch the crack along Y-direction at the corner point of DCB shown Fig. 6. The load along X-direction is set as zero, and a static load of 15,405 N [10] is applied in Y-direction.

Table 2 FE model specification

Component	DCB
Element type	Continuum plane strain 4-noded
Total number of element	18,000
Total number of nodes	19,232



Fig. 6 Double cantilever beam with loading and boundary condition

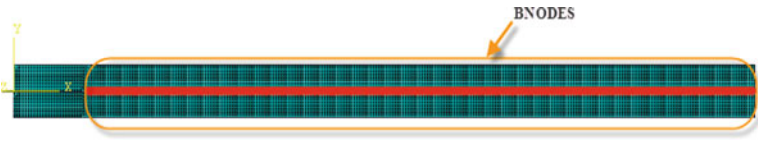


Fig. 7 Double cantilever beam with bonded nodes

Interaction: For assigning VCCT, it is required to create sets of nodes and surface of DCB model [12]. Since VCCT works in a predefined crack path, the nodes along with the interface except along crack length are bonded. Node set of BNODES is created as shown in Fig. 7. Since this study involves only energy release rate evaluation without crack propagation, the mode I and mode II critical energy release rate parameters are set to higher values, so that the preexisting crack does not propagate. Critical energy release rates at mode I and mode II are set as 8×10^{10} and mode III as zero, since there is no fracture in the third direction. A parameter called BK (Benzeggagh Kenane) parameter is to be specified for mixed mode behavior of fracture analysis.

Keyword interface: For VCCT to be activated in ABAQUS, it is not possible to provide all required input through the software itself. Some essential inputs need to be provided in the form of keyword at the background of the problem. Fracture criterion has to set after the debond commands.

ABAQUS prediction: The problem is analyzed using ABAQUS to obtain the energy release rate (G). A pre-defined crack length "a" of 50 mm with a height of the beam "h" ranging from 15 to 50 mm is considered for analysis. The G_I values are normalized with respect to G_0, calculated analytically using the Eq. (2). Figure 8 depicts a plot of G_I/G_0 against h/a for the benchmark problem [2],

$$G_I = \frac{1-\nu^2}{E} {K_I}^2 \ldots\ldots\ldots\ldots \quad (2)$$

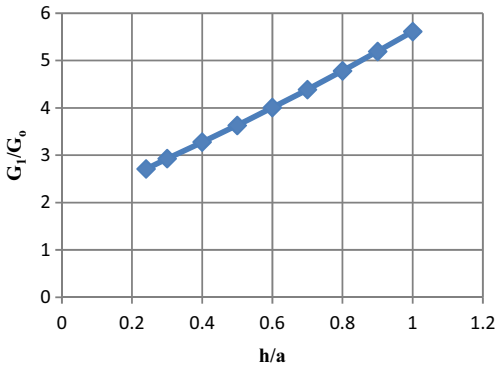


Fig. 8 Normalized energy release rate versus h/a ratio

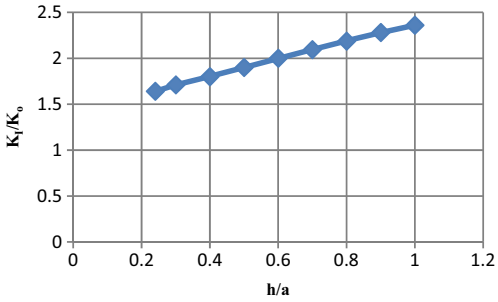


Fig. 9 Normalized energy release rate versus *h*/*a* ratio

The target solution [10] is in terms of stress intensity factor values, and the present result of G_I/G_0 is converted to normalized stress intensity factor values. Figure 9 shows a plot of normalized stress intensity factor against the height of the beam.

Comparison of target solution shown in Fig. 4 and the ABAQUS prediction shown in Fig. 9 concluded that obtained results are congruent with each other. Thus, the finite element model developed and procedure followed for the fracture analysis is successfully validated.

5 Case Study on Different Bi-materials

For the case study, the dimensions, interaction, loading and boundary conditions are considered to be same as that of the benchmark problem. The material at the bottom of the beam is taken to be steel, and different materials are considered for the top layer of the beam in all case studies [13]. Further, typical parametric studies are conducted by the varying height of the beam and crack length as parameters.

5.1 Material Properties

The DCB material is assumed to be homogenous, isotropic, and linearly elastic [14–17]. Table 3 shows the materials considered for the beam and their properties.

Case I In the first case, the crack length and thickness of double cantilever beam are considered (assumed) to be 50 and 30 mm, respectively. The height of each cantilever is varied from 15 to 50 mm for all material combination.

Case II In the second case, the height and thickness of the double cantilever beam are considered (assumed) to be 15 and 30 mm, respectively. The crack length is varied from 20 to 65 mm for all material combinations.

Table 3 Material properties

Material	Modulus of elasticity (E) in N/mm^2	Poisson's ratio (ν)
Steel	2.1×10^5	0.3
Cast iron	1.7×10^5	0.3
Titanium	1×10^5	0.3
Aluminum	0.7×10^5	0.3
Plastic	2.3×10^3	0.3

6 Results and Discussion

6.1 For Case I—Height as a Parameter

Cast iron and steel are considered as the first combination for the DCB analysis. The energy release rate values were noted down for the above condition case study. Variation of mode I energy release rate with height for steel–steel and cast iron–steel material combinations is shown in Fig. 10. Energy release rates for cast iron–steel material combination are slightly higher than the steel-steel combination. Titanium and steel are considered as the second material combination. The analysis is performed, and the energy release rate tabulated. The variation of G_I with h is shown in Fig. 11. It is observed that the energy release rate for titanium–steel combination is higher than

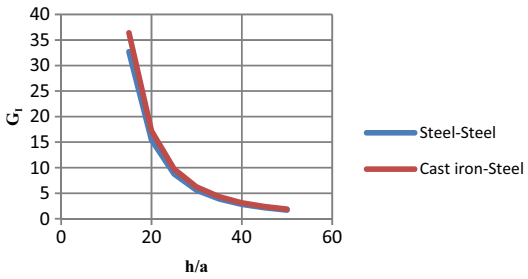


Fig. 10 Energy release rate against the height of DCB for steel-steel and cast iron–steel material combination

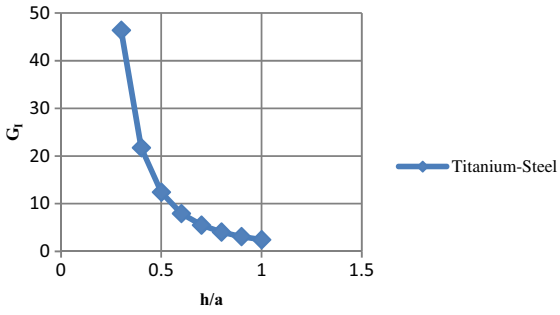


Fig. 11 G_I against the height of DCB for titanium and steel

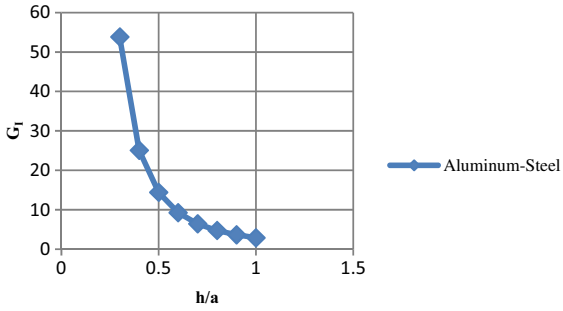


Fig. 12 Variation of energy release rate against the height of DCB for aluminum and steel

that of Cast iron–steel material combination. Aluminum and steel are considered as the third material combination. The analysis is performed, and the energy release rate obtained. The variation of G_I with h is shown in Fig. 12. It is obtained that the energy release rate for aluminum–steel combination is higher than that of titanium-steel material combination. Plastic and steel are considered as the fourth material combination. Since Young's modulus of plastic is too low, it is observed that mode I energy release rate increased to more significant values for different values of h.

6.2 For Case II-Crack Length as a Parameter

Cast iron and steel are considered as a first material combination. The fracture analysis is performed, and the energy release rate obtained for cast iron—steel combination is plotted as shown in Fig. 13. Titanium and steel are considered as the second material combination. The analysis is performed, and the energy release rate is obtained. The variation of G_I with h is shown in Fig. 14. It was observed that energy release rate for titanium—steel combination is higher than that of cast iron—steel material combination. Aluminum and steel are considered as the third material combination. Mode I ERR is obtained for aluminum–steel combination. The variation of G_I with h is shown in Fig. 15. It was observed that the energy release rate for aluminum–steel combination is higher than that of titanium-steel material combination. Plastic and

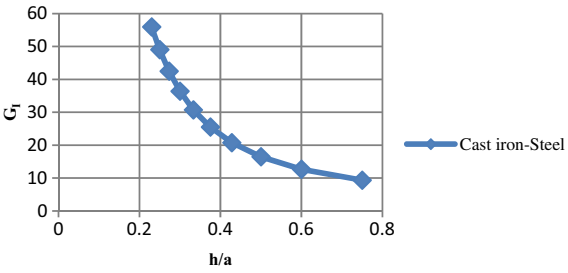


Fig. 13 Energy release rate against the crack length of DCB for cast iron and steel

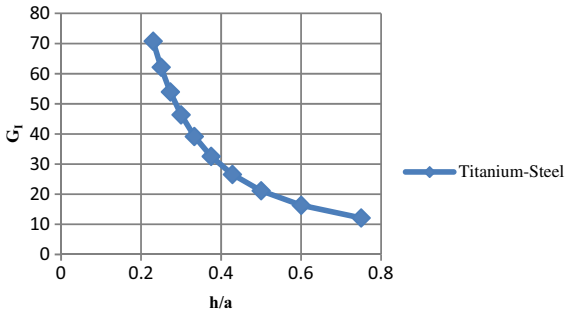


Fig. 14 Mode I energy release rate against the length of crack of DCB for titanium and steel

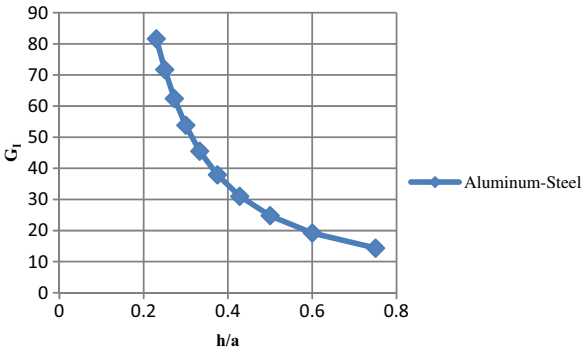


Fig. 15 Mode I energy release rate against the length of crack of DCB for aluminum and steel

steel are considered as the fourth material combination. The analysis is performed, and the energy release rate obtained is plotted as shown in Fig. 16. In the case of plastic and steel material combination, a considerable amount of energy release rate is obtained at mode II also and the graph is plotted considering both mode I and mode II fracture. Fracture analysis is performed on four material combinations, namely cast iron–steel, titanium–steel, aluminum–steel, and plastic–steel. The energy release rate is observed to be increasing with the reduction in stiffness from cast iron to the plastic material combination.

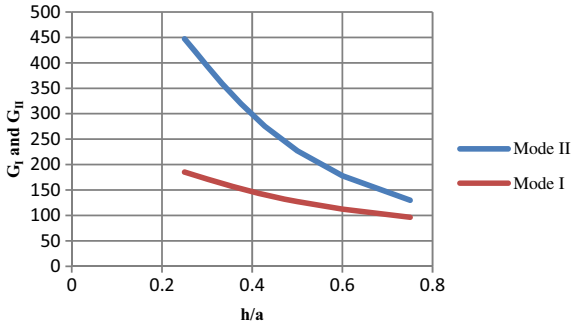


Fig. 16 Mode I and Mode II energy release rate against the length of crack of DCB for plastic and steel

7 Conclusion

Finite element modeling and solution procedures are followed to evaluate the energy release rate of bi-material interface crack using ABAQUS software. The finite element model for a double cantilever beam is developed, and the results of the energy release rate are compared with the target solution using a benchmark problem for validation. The case study involves evaluation of strain energy release rate for 4-different material combinations in a double cantilever beam with bi-material interface crack consideration. Further, parametric studies are conducted by varying the height and crack length of double cantilever beam.

From case I (height as a parameter) results, it is concluded that the energy required for a bi-material interface crack to grow is more for smaller height than the larger height of DCB, for all material combinations.

From case II (crack length as a parameter) results, it is concluded that the energy required for a bi-material interface crack to grow is more for a larger crack length than the smaller crack length of DCB.

On comparing the obtained results, it can be inferred that, energy release rate increases with increase in the difference between the stiffness values of the bi-material combination for a given set of loading and boundary conditions.

Future Scope

The present work is restricted only for mechanical loading in fracture analysis. This can be improved by applying both mechanical and thermal loading; hence, thermal–structural coupled field analysis can be performed keeping in mind an engineering application with a weld defect.

References

1. Shih CF, Moran B, Nakamura T (1986) Energy release rate along a three-dimensional crack front in a thermally stressed body. Int J Fract 30:79–102
2. Kumar P (2009) Elements of Fracture Mechanics. McGraw-Hill, New Delhi
3. Krueger R (2004) Virtual crack closure technique: History, approach, and applications. Appl Mechan Rev 57(2):109–143
4. Liu PF, Hou SJ, Chu JK, Liu YL, Zhou CL, Zeng JY, Yan L, Zhao A, Hu XY (2011) Finite element analysis of post-buckling and delamination of composite laminates using virtual crack closure technique. Compos Struct 93:1549–1560
5. Orifici AC, Krueger R (2010) Assessment of static delamination propagation capabilities in commercial finite element codes using benchmark analysis. NIA Report, NASA/CR-2010–216709, June-2010
6. Horst G (1985) Delorenzi, energy release rate calculations by the finite element method. Eng Fract Mech 21(1):129–143
7. Fan C, Jar B, Roger Cheng JJ (2007) Prediction of energy release rates for crack growth using FEM-based energy derivative technique. Eng Fract Mechan 74:1243–1254
8. Xie D, Biggers Jr SB (2006) Strain energy release rate calculation for a moving delamination front of arbitrary shape based on the virtual crack closure technique. Eng Fract Mechan 73:771–785

9. Krueger R, Goetze D (2006) Influence of finite element software on energy release rates computed using the virtual crack closure technique, NIA Report, NASA/CR-2006-214523, October 2006
10. Lakshminarayana HV, Bernard M, Bui-Quoc T (1992) A finite element study of interlaminar fracture in composite material. In: Proceedings of international conference on fracture mechanics
11. ABAQUS analysis, user's manual, vol 3, Version 6.10, Dassault Systemes Simulia Corp USA(2010)
12. Xie D, Biggers Jr SB (2006) Progressive crack growth analysis using interface element based on the virtual crack closure technique. Finite Elements Anal Des 42: 977–984
13. Leski A (2007) Implementation of the virtual crack closure technique in engineering FE calculations. Finite Elem Anal Des 43:261–268
14. Singh R, Goel S, Verma R, Jayaganthan R, Kumar A (2017) Mechanical behavior of 304 Austenitic stainless steel processed by room temperature rolling, materials science and engineering, vol 330. International conference on recent advances in materials, mechanical and civil engineering 1–2 June 2017, Hyderabad, India
15. Ambroziak A, Solarczyk M (2018) Application and mechanical properties of aluminium alloys. 10.1201/9781315166605-121
16. Chan R, Nakamura M (1969) Mechanical properties of plastic foams: the dependence of yield stress and modulus on the structural variables of closed-cell and open-cell foams. J Cell Plast 5(2):112–118
17. Sudhakar KV, Wood E (2016) Superplastic grade titanium alloy: comparative evaluation of mechanical properties, microstructure, and fracture behavior, vol 2016, Article ID 2309232, p 7

Vibration Analysis of Femur with Different Hyperelastic Materials



Sridhar Adibhatla, A. Satyadevi, and N. V. Swamy Naidu

Abstract Femur bone is one of the longest bones. It is also one of the strongest bones in the human skeletal system. It absorbs and transmits the forces to the lower extremity caused due to various physical activities. The understanding of vibrational characteristics of femur helps in diagnosing various deformities and/or diseases. In the present research, two different femurs with a porosity level of 75% were considered. The modal analysis is performed with four different hyperelastic materials, namely neo-Hookean, Blatz-Ko, Ogden (first order), and Yeoh (first order). The results indicate that the Ogden first-order model is superior in predicting the natural frequencies and mode shapes in comparison to the other material models considered. It is also observed that these results are very much sensitive to the geometry as well as the material model considered. These results would be helpful in predicting the dynamic behavior of femur with different porosity levels and help in diagnosing the existence and or possibility of fracture.

Keywords Femur · Vibration analysis · Hyperelastic · Porosity

1 Introduction

The femur is the most critical part which connects the upper extremity of the skeletal system to the lower extremity. It absorbs and transmits forces induced due to various activities, like walking, jogging, etc. It undergoes impact forces along with constant body weight. The understanding of vibrational characteristics of the femur provides a deep insight into various aspects related to fracture location, porosity, and various other deformities.

In the present study, two different femur bones with a neck-shaft angle (NSA) of 125° are considered. The published literature related to femur bone modal analysis

S. Adibhatla · A. Satyadevi
GITAM School of Technology, Hyderabad, India

N. V. Swamy Naidu (✉)
National Institute of Technology Raipur, Raipur 492010, Chhattisgarh, India
e-mail: nvsnaidu.mech@nitrr.ac.in

© Springer Nature Singapore Pte Ltd. 2020

A. Praveen Kumar et al. (eds.), *Advances in Lightweight Materials and Structures*,
Springer Proceedings in Materials 8, https://doi.org/10.1007/978-981-15-7827-4_80

is presented below. Rodrigues et al. [1] performed experimental modal analysis on a synthetic composite femur. In this study, the natural frequencies and mode shapes were extracted for femur with free-free modal analysis using isotropic material properties. These results were compared with the experimental results. Vijayakumar et al. [2] performed a pre-stressed modal analysis of femur with different material properties and with different body weights. Their study concluded that the neck and shaft are the most possible regions for fracture of the femur.

Chiu et al. [3] performed a modal analysis of femur with different types of internal fixations. This study was aimed at identifying fixated femur's status of healing. They have used different healing levels and different cut orientations to study their impact on the natural frequency. It is observed that 4 out of 5 cut orientations does not have any impact on the natural frequency. When the fixation type is intramedullary nail type, the cut orientation has a significant effect on the natural frequency of the femur. Kumar et al. [4] performed a modal analysis of femur bone with free-free and fixed-fixed boundary conditions to estimate the possible fracture locations. This study concluded that accident or continuous vibration as the major cause of femur fractures. The shaft and neck regions are more prone to fractures.

From the limited open literature, it was observed that most of the past research has considered isotropic material properties for the femur to evaluate the natural frequencies mode shapes. The present is aimed at evaluating the femur dynamic behavior using different hyperelastic material models and their impact on frequency behavior.

2 Constitutive Relationships

The following material models were used in this study to assess the impact of material properties on the frequency behavior [5–8].

$$\text{Neo-Hookean: } \bar{U} = \frac{\mu_1}{2}\left(\bar{I}_1 - 3\right) \tag{1}$$

$$\text{Blatz-Ko: } W = \frac{\mu}{2}\left(\frac{I_2}{I_3} + 2I_3^{1/2} - 5\right) \tag{2}$$

$$\text{Yeoh: } W = \sum_{i=1}^{3} C_i (I_1 - 3)^i \tag{3}$$

$$\text{Ogden: } W(\lambda_1, \lambda_2) = \sum_{p=1}^{N} \frac{\mu_p}{\alpha_p}\left(\lambda_1^{\alpha_p} + \lambda_2^{\alpha_p} + \lambda_1^{-\alpha_p}\lambda_2^{-\alpha_p} - 3\right) \tag{4}$$

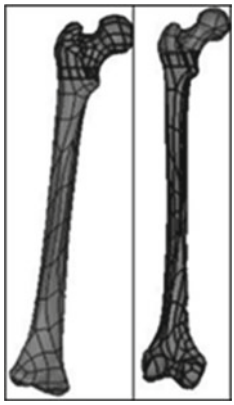


Fig. 1 Femur 1 and Femur 2 (left to right, respectively)

Table 1 Material properties

Constants/model	C_{10}/Mu_1 (MPa)	A_1 (MPa^{-1})
Yeoh	1389.457	–
NH	2778.914	–
BK	3375.236	–
Ogden	1495.348	0.003735

2.1 Materials and Methods

Figure 1 shows the different geometries for femur considered in this study.

The various material properties used in this study are shown in Table 1.

2.2 FE Modeling

The FE model was generated using SHELL 181 elements with an element size of 3 mm. In this study, a porosity level of 75% was considered for simulations. Modal analysis is performed under free-free boundary conditions, with the material properties mentioned in Table 1. The finite element mesh model and boundary conditions are shown in Fig. 2.

3 Results and Discussion

From the modal analysis performed on the femur bone with 75% porosity with different hyperelastic material models, the natural frequencies and corresponding mode shapes were obtained. The first bending mode, torsion mode, and longitudinal



Fig. 2 Femur model with load and boundary condition

extension modes were compared with the published results of Khalil et al. [10]. These were shown in Fig. 3. From left to right, respectively.

The results with Ogden first-order material model observed to be well in agreement with the published results [10], both in terms of the magnitude of natural frequencies and mode shapes, in comparison to the other material models used in this study.

The comparison of different material models to produce the considered modes was shown in Table 2.

Though material models other than Ogden first order closer to the published results [10] in terms of the magnitude of frequency, they were not able to produce the required mode shapes. The results of both Femur 1 and Femur 2 with different material models were presented in Table 3.

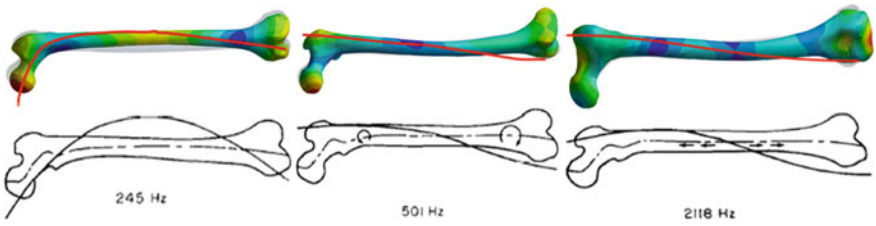


Fig. 3 First bending, torsion, and longitudinal modes (Present study versus Khalil et al. [10])

Table 2 Comparison of different material models

Mode No	Behavior	Frequency (Hz)				
		Ogden first order	Yeoh first order	Blatz-Ko	Neo-Hookean	Khalil et al. [10]
Mode 1	First bending mode	266.71	266.07	268.23	259.11	245
Mode 3	First torsion mode	475.35	474.2	505.1	469.31	501
Mode 9	First longitudinal extension mode	1896.6	1892	1839.6	1816.8	2118

4 Conclusion

From the modal analysis performed on the femur bone with different hyperelastic material models, it is concluded that the Ogden first-order model has produced approximately agreeable results both in terms of the magnitude of frequency and mode shape. This could be due to the fact that Ogden first-order model is highly nonlinear in comparison to the other material models used in this study. This resulted in capturing the mode shapes more accurately. The comparative results of both Femur 1 and Femur 2 reveal that the natural frequencies are sensitive to the geometry considered. These results will be useful in predicting the frequency in relation to the porosity level of the femur. Also, it is understood that the selection of a particular material model is of great importance while performing the modal analysis.

5 Future Scope

The future study should include more complex hyper elastic and anisotropic material models to predict the dynamic response of the femur bone under various loading conditions. It should also include physiologically correct boundary conditions in order to evaluate the natural frequencies of the femur bone in agreement with the in vivo conditions.

Table 3 Comparison of different femur models

Mode Number	Behavior	Frequency (Hz)								
		Ogden first order		Yeoh first order		Blatz-Ko		Neo-Hookean		Khalil et al. [10]
		Femur 1	Femur 2	Femur 1	Femur 2	Femur 1	Femur 2	Femur 1	Femur 2	
Mode 1	First bending mode	320.4	266.71	303.83	266.07	322.74	268.23	311.4	259.11	245
Mode 3	First torsion mode	578.46	475.35	562.25	474.2	608.54	505.1	569.29	469.31	501
Mode 9	First longitudinal extension mode	2014.8	1896.6	1864	1892	1960.1	1839.6	1930.2	1816.8	2118

References

1. Dias Rodrigues JF, Lopes H, Melo FQ, Simoes JA (2004) Experimental modal analysis of a synthetic composite femur. J Exp Mechan 44(No. 1):29–32
2. Vijayakumar R, Madheswaran M (2017) Modal analysis of femur bone using finite element method for healthcare system. In: Proceedings of IEEE conference on emerging devices and smart systems, 2017
3. Chiu WK, Ong WH, Russ M, Fitzgerald M (2017) Simulated vibrational analysis of internally fixated femur to monitor healing at various fracture angles, 6th Asia Pacific workshop on structural health monitoring. Proc Eng 188:408–414
4. Kumar A, Jaiswal H, Garg T, Patil PP (2014) 3rd international conference on materials processing and characterisation. Proc Mater Sci 6:1593–1599
5. Bower AF (2010) Applied mechanics of solids. CRC Press
6. Blatz PJ, Ko WL (1962) Application of finite elastic theory to the deformation of rubber materials. Trans Soc Rheol pp 223–251
7. Yeoh OH (1993) Some forms of the strain energy function for rubber. Rubber Chem Technol 66(5):754–771
8. Ogden RW (1997) Non-linear elastic deformations. Dover Publications, New York
9. Gaynor Evans F (1969) The mechanical properties of bone. J Artif Limbs 3(1):37–48
10. Khalil TB, Viano DC, Taber LA (1981) Vibrational characteristics of the embalmed human femur. J Sound Vibr 75(3):417–436

Analysis of Anterior Cruciate Ligament of the Human Knee Using a Mathematical Model

Ahmed Imran

Abstract Anterior cruciate ligament (ACL) of the knee is often injured particularly in sports and other strenuous activities. Approaches for replacement of the ligament surround controversies due to complexities and varied outcome. In the present study, mechanical behavior of the ligament is analyzed during knee motion considering changing geometric arrangements of the ligament fibers and their material properties during both unloaded and loaded states. An analytical model with sagittal plane representation of the knee was employed. The two cruciate ligaments were modeled as bundles of fibers that were nonlinearly elastic. Flexion motion in the unloaded state was guided by selected fibers. Effects of external loads were then superimposed to simulate activity. In a simulated Drawer test with 130 N external force applied during 0–120° flexion, the ACL stretched increasingly in early to mid-flexion. From mid to high flexion range, the stretching effect decreased continuously. Further, anterior bundle of fibers in the ligament resisted the external load at each flexion angle. The posterior bundle of fibers contributed to resistance in low and high flexion only. The model calculations compared reasonably with in vitro experimental measurements on human knees that are available in the literature. In conclusion, the analysis indicates that surgical replacement of the ACL requires careful attention to ligament insertion positions on bones. Also, rehabilitation of ACL-injured or replaced knee requires carefully designed exercises to be safe and effective. Future work will also focus on parametric analysis.

Keywords Knee ligaments · Anterior cruciate ligament replacement · ACL injuries · Rehabilitation of ACL · ACL properties

1 Introduction

Cruciate ligaments of the knee connect one bone to another and perform crucial role in providing a delicate balance between stability and mobility during a variety of

A. Imran (✉)
College of Engineering, Ajman University, Ajman, UAE
e-mail: a.imran@ajman.ac.ae; ai_imran@yahoo.com

© Springer Nature Singapore Pte Ltd. 2020

A. Praveen Kumar et al. (eds.), *Advances in Lightweight Materials and Structures*,
Springer Proceedings in Materials 8, https://doi.org/10.1007/978-981-15-7827-4_81

activities that may range from daily routine for the common population to strenuous activities for the sports persons [1–4]. The ligaments stretch while restricting the distraction of the connected bones. Certain postures or positions of the joints during specific activities can predispose involved ligaments to injuries [3, 4]. Anterior cruciate ligament or ACL at the knee is often damaged resulting in partial or complete tear of the constituent fibers, thus restricting activity and causing pain. ACL is more prone to damage during activities near extension or low flexion angles and with tibial rotation [1, 3]. As healing characteristics of the ligament are poor or nearly absent [5], restoration of the ligament function is achieved through surgical repair or replacement of the damaged structure with single or double bundle approach [6, 7]. However, such approaches for treatment vary in procedures and patient outcomes including restricted level of activity [5–7]. Also, understanding of the ligament behavior through experimentation is prone to uncertainties and errors as making reproducible experimental setup is many times difficult [8, 9]. Moreover, possible changes in the ligament behavior due to experimental configuration can also contribute to difficulties in interpretation of outcome as well as in comparison with other similar studies [8, 9].

Realistic computer-based models, therefore, can be useful tools to analyze the ligament behavior. This requires appropriate mathematical representation of the ligament-intact knee with anatomical parameters and physiological features that can guide simulation of the joint function. The present study is an attempt in this direction.

In this work, an analytical model of the human knee is used to study mechanical behavior of the ACL in different joint positions. Effects of external loads are superimposed in each joint position.

2 Methods

A mathematical model of the knee with intact cruciate ligaments was used in the sagittal plane similar to that reported in [3, 10, 11]. A brief description follows here.

The model knee joint is formed with two bones, namely femur and tibia, connected together with ligaments that comprised of bundles of fibers. Anterior cruciate ligament and posterior cruciate ligament (PCL) as well as collateral ligaments were modeled as bundles of nonlinear elastic fibers [3, 4, 9–12].

Figure 1 gives a graphical representation of the model knee at full flexion showing the bones connected through the cruciate and collateral ligaments. Effects of the collateral ligaments in the sagittal plane are shown to be relatively insignificant [9]. Accordingly, the model collateral ligaments had insignificant effect in the present analysis.

The model allows analysis of contributions of separate bundles of ligament fibers such as those located in the anterior part of the ACL that are reported in the literature as antero-medial bundle [3, 4, 9–11]. Similarly, fibers in the posterior part of the ACL were modeled that are reported in anatomical studies as postero-lateral bundle of the

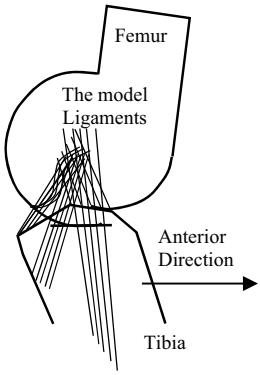


Fig. 1 Graphical representation showing outlines of the model knee and the ligaments represented as straight lines when taut or as curves when slack like those used in references [10, 16]

ligament [3, 4, 9–11]. The model articular surfaces were frictionless and impenetrable resisting compressive forces.

The knee motion was defined during 0–120° flexion such that in the absence of any external load or muscle action, one specific fiber in each cruciate ligament maintained constant length or isometricity throughout the range of motion. However, the isometric fibers changed their respective position and orientation relative to the bones [9]. The isometric fibers were located most anteriorly in the ACL and somewhat in the middle of the PCL [9]. The flexion motion of the joint guided by these isometric fibers defined what is considered as passive motion of the knee [10].

Effect of external load (or muscle action) during activity is to cause relative movement between the bones resulting in either stretching or slackening of the involved ligament fibers compared to their neutral lengths. To simulate this effect, the model required that as the distance between bony attachments of a ligament increased, its fibers were selectively stretched. Conversely, as the distance between the bony attachments decreased, the ligament fibers selectively became slack and buckled. The material properties of the ligaments and other model parameters were taken from anatomical studies conducted on human cadaver joints available in the literature [9–16].

To simulate application of external load, like in a Lachman test or Drawer test to assess joint instability in the sagittal plane, 130 N anterior directed load was applied on the lower bone, or tibia, along with an external flexing moment that provided a balancing effect and thus held the joint at a fixed flexion angle. This resulted in anterior translation of the tibia (AT) and stretched fibers of the ACL. The simulation was repeated at intervals of 30° throughout the defined flexion range. Results from the model calculations were compared with similar experimental observations reported in the literature from independent work conducted on cadaver knees [14]. This supported validation of the model calculations. Further, contributions from each of the anterior and posterior bundles of the ACL were calculated using the model and analyzed.

3 Results and Analysis

Figure 2 gives a graphical representation of the model knee during flexion shown for 0° and 60° positions of the joint. During simulated passive flexion, the femoral bone translated in the posterior direction on tibial bone as depicted by respective contact positions in (a) and (b) represented by a+ sign where the circular femur contacted flat tibial surface. This observation agrees well with previously reported posterior movement of femoral condyles on tibial surface available in the literature [15, 16].

(a) The model knee is shown at 0° flexion with fibers of the ACL just taut.
(b) The model knee at 60° angle compared with that at 0° flexion. Notice that the bones rotate and slide during flexion and the ligament fibers slacken progressively with increasing joint angle.

In Table 1, model calculations for 130 N simulated test are presented with experimental measurements by Lo et al. [14]. The model calculations and experimental observations are similar. Tibial translation first increased from 0–30° and then decreased in high flexion.

Table 2 gives a comparison of contributions from each of the two bundles of model ACL over 120° flexion in steps of 30°. In the simulation, these fibers resisted 130 N force that was applied on the model tibia. At each flexion position, the anterior fibers stretched and resisted the external force. In comparison, the posterior bundle

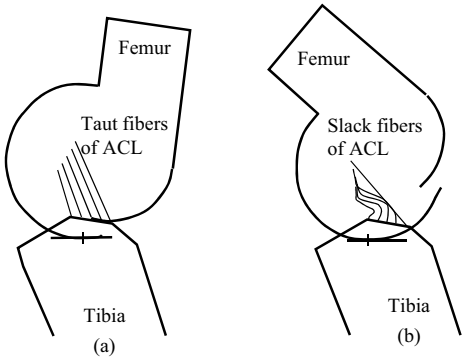


Fig. 2 Model knee at 0° and 60° flexion showing only ACL fibers. Other ligaments were removed from the graphics for clarity

Table 1 AT corresponding to 130 N simulated test—comparing the model calculations with in vitro measurements from Lo et al. [14]

Flexion angle	Model results AT (mm)	In vitro measurements [14] mean (Std. Dev.) (mm)
0	3.7	4.1 (0.6)
30°	6.4	7.5 (1.8)
60°	6.3	7.4 (2.2)
90°	5.8	6.2 (1.9)
120°	4.5	–

Table 2 Force in each of the anterior and posterior bundle of the ACL with respect to the total force developed in the ligament

Flexion Angle	% Posterior force in anterior bundle of the ACL	% Posterior force in posterior bundle of the ACL
0	45.4	54.6
30°	96.3	3.7
60°	100	0
90°	100	0
120°	88.6	11.4

developed resistance only in low and high flexion positions of the joint. In the mid-flexion range, anterior bundle fully resisted the external force.

Observations from the two tables suggest that as the external load is applied at different flexion positions, the tibia is pulled anterior to the femur stretching the anterior fibers much more than the posterior fibers of ACL. In fact, the posterior fibers did not stretch at 60 or 90° flexion. Since most activities involving the knee take place in early to mid-flexion range, these observations suggest possibly more critical role for the anterior part of the ACL during activity. Consistent with differential contributions of the ligament fiber bundles, several practitioners prefer double bundle replacement of the ACL against a single bundle approach. However, differences exist relating positioning and orientation of the bundles.

For the same reason that early to mid-flexion resulted in more tibial translation and involved the anterior fibers much more than the posterior fibers, rehabilitation exercises for ACL after reconstruction or injury must consider sufficient protection in these joint positions in order to avoid harm.

4 Conclusion and Clinical Relevance

Model calculations during a simulated 130 N anterior laxity test at the knee joint suggest that anterior fibers of the ACL stretch in all knee positions while the posterior fibers stretch mainly in extreme positions of the joint motion. This and more observations from the model agree with those from experiments in the literature. The current analysis shows that mathematical modeling of the human knee joint with appropriate representation for its structures can be useful for gaining understanding of the ligament characteristics. On the other hand, analysis of the ACL function with experimental techniques involves several limitations which make comparison between different studies difficult. Though the present study used a planar model, the results corroborated experimental observations and helped in gaining insight into the behavior of the knee ligaments. Future development of the model involves a parametric analysis of the ACL fibers to account for person-to-person variations in the ligament anatomy and material properties as well as effects of surgical positioning of

the ligament fiber bundles during reconstruction. This work has relevance to ligament reconstruction or rehabilitation.

References

1. Marieswaran M, Jain I, Garg B, Sharma V, Kalyanasundaram D (2018) A review on biomechanics of anterior cruciate ligament and materials for reconstruction. Appl Bionics Biomechan Article ID 4657824, 14 pages. https://doi.org/10.1155/2018/4657824. Last accessed 24 Mar 2020
2. Marieswaran M, Sikidar A, Goel A, Joshi D, Kalyanasundaram D (2018) An extended OpenSim knee model for analysis of strains of connective tissues. BioMed Eng OnLine 17(42):1–13
3. Imran A (2016) Analyzing anterior knee laxity with isolated fiber bundles of anterior cruciate ligament. Proceedings of the World Congress on Engineering, London, pp 869–872
4. Imran A (2012) Changes in the lengths of anterior cruciate ligament fibres during tibial translation at the knee. J Biomechan 45(S):373
5. Kiapour AM, Murray MM (2014) Basic science of anterior cruciate ligament injury and repair. Bone Joint Res 3(2):20–31
6. Leong NL, Petrigliano FA, McAllister DR (2014) Current tissue engineering strategies in anterior cruciate ligament reconstruction. J Biomed Mater Res, Part A 102(5):1614–1624
7. Chung EJ, Sugimoto MJ, Koh JL, Ameer GA (2017) A biodegradable tri-component graft for anterior cruciate ligament reconstruction. J Tissue Eng Regener Med 11(3):704–712
8. Pierre-Jean A, Damien S, Catherine M, Patrick C, Christian B (2005) Knee ligaments mechanics from experiments to FE simulations. Revue Européenne Des Éléments Finis, HERMÈS/LAVOISIER 14(4–5):577–600
9. Mommersteeg M, Blankevoort L, Huiskes R, Kooloos J, Kauer J (1996) Characterisation of the mechanical behavior of human knee ligaments: a numerical-experimental approach. J Biomechan 29(2):151–160
10. Imran A (2019) Computer graphics-based analysis of loading patterns in the anterior cruciate ligament of the human knee. In: Arai K, Bhatia R, Kapoor S (eds) Advances in intelligent systems and computing. Springer Nature, vol 998, no 2, pp 1175–1180
11. Imran A (2017) Relating knee laxity with strain in the anterior cruciate ligament. Lecture Notes in Engineering and Computer Science, pp 1037–1042
12. Kondo E, Merican A, Yasuda K, Amis A (2014) Biomechanical analysis of knee laxity with isolated anteromedial or posterolateral bundle deficient anterior cruciate ligament. J Arthroscop Relat Surg 30(3):335–343
13. Kawaguchi Y, Kondo E, Takeda R, Akita K, Yasuda K, Amis A (2015) The Role of fibers in the femoral attachment of the anterior cruciate ligament in resisting tibial displacement. J Arthroscop Relat Surg 31(3):435–444
14. Lo JH, Müller O, Dilger T, Wülker N, Wünschel M (2011) Translational and rotational knee joint stability in anterior and posterior cruciate-retaining knee arthroplasty. Knee 18(6):491–495
15. Goodfellow J, O'Connor J (1978) The mechanics of the knee and prosthesis design. J Bone Joint Surgery (Br) 60-B:358–369
16. O'Connor J, Imran A (2007) Bearing movement after Oxford unicmpartmental knee arthroplasty: a mathematical model. Orthopedics 30(5S):42–45

MATLAB-Based Educational Tool for Failure Analysis of Composite Laminates

J. S. Mohamed Ali and Iqtidar Mizuar

Abstract An educational software has been developed for stress analysis of laminated composites. The software can be used to study both micro- and macro-mechanics analysis of a lamina as well as a laminate. The software can also be used for the failure analysis of laminates, and hence can be useful for the design of composite laminates for given loading conditions. Apart from mechanical loading, the software can also handle hygrothermal loading. Four different failure theories have been used to predict the failure of any given laminate. Graphical user interface (GUI) based on MATLAB language was used to develop this software, thus, making it more user-friendly. Numerous case studies were carried out and validated against the existing literature.

Keywords Failure · Composite · Hygrothermal · Software · Education

1 Introduction

Composite materials exhibit impressive properties such as high strength and stiffness with low density that make them as a candidate material for the modern aerospace and automotive structures. Composites, as a new field, generate curiosity and interest in students everywhere around the world. Moreover, as the composite materials applications increase every day in the commercial sector, job opportunities in this field are also on the rise. Thus, many universities offer courses on composite structures for both undergraduate and post-graduate level.

Unlike the analysis of metallic structures, which are isotropic, the anisotropic nature of the composites with different properties in each directions makes the stress analysis complex and lengthy. As the macro-mechanical analysis of the laminate has repeated calculation of matrices, the procedure is lengthy and even a simple analysis of a laminate with more than three layers will be difficult to handle with the calculator and the repeated calculation involved will lead to boredom and makes the student

J. S. Mohamed Ali (✉) · I. Mizuar
Department of Mechanical Engineering, Kulliyah of Engineering, International Islamic University Malaysia (IIUM), Selangor, Malaysia
e-mail: jaffar@iium.edu.my

© Springer Nature Singapore Pte Ltd. 2020

A. Praveen Kumar et al. (eds.), *Advances in Lightweight Materials and Structures*,
Springer Proceedings in Materials 8, https://doi.org/10.1007/978-981-15-7827-4_82

lose interest in solving further problems. Moreover, with the failure analysis being a lengthy procedure and even a slightest slip in calculation made initially may lead to the student ending up with incorrect results after all the hard work, which can result in students loosing confidence in solving such problems. Therefore, a step by step results guiding the students throughout in solving the problem will make the students learn and solve more problems and hence build confidence in analysing composite structures. Lecturers can also frame numerous assignments and design projects using this software, moreover it can help them to prepare quick solutions for the course assessments. The advantages of developing an educational software for a complete course, such as mechanics of materials, can be well-understood through the work of Philpot [1].

Educational software for a course on aircraft structures has been developed by the author [2, 3] and effectively used in International Islamic University Malaysia (IIUM). Educational software for composite structural analysis is available [4, 5], but it is developed to suit their university requirement or bundled with a book with a price tag. Therefore, a software that is useful for the macro-mechanical analysis of composite laminates was developed by the author [6] to suit the IIUM course outline on composite structures. With the successful induction of this software in the class and based on the feedback from the students, it was found that students need a full-fledged software that is also capable of carrying out failure analysis, which can be useful for the design of laminates. In the present work, the module for failure analysis of composite laminates under mechanical and hygrothermal loads has been developed and added to the existing software in order to create a full package with the inclusion of design.

2 Macro-mechanical Analysis of Laminates

The following are the steps for analysing a laminated composite subjected to the applied forces and moments [7]:

1. Evaluate the reduced stiffness matrix $[Q]$ for each layer

$$\begin{bmatrix} \sigma_1 \\ \sigma_2 \\ \tau_{12} \end{bmatrix} = \begin{bmatrix} Q_{11} & Q_{12} & 0 \\ Q_{12} & Q_{22} & 0 \\ 0 & 0 & Q_{66} \end{bmatrix} \begin{bmatrix} \varepsilon_1 \\ \varepsilon_2 \\ \gamma_{12} \end{bmatrix} \tag{1}$$

$$\nu_{21} = \nu_{12} \frac{E_1}{E_2}$$

$$Q_{11} = \frac{E_1}{1 - \nu_{21}\nu_{12}}$$

$$Q_{12} = \frac{\nu_{12} E_2}{1 - \nu_{21}\nu_{12}}$$

$$Q_{22} = \frac{E_2}{1 - \nu_{21}\nu_{12}}$$
$$Q_{66} = G_{12}$$

where E_1, E_2, are the elastic moduli, ν_{12} the Poisson ratio, and G_{12} is the shear modulus.

2. Based on the ply-angle and $[Q]$, evaluate for each ply, the transformed reduced stiffness matrix.
3. Based on Fig. 1, find the z-coordinate of the top and bottom surface, h_i, $i = 1$, …, n, of every ply,
4. Evaluate the $[A]$, $[B]$, and $[D]$ matrices using

$$A_{ij} = \sum_{k=1}^{n} \left[\bar{Q}_{ij}\right]_k (h_k - h_{k-1}), \quad i = 1, 2, 6; \quad j = 1, 2, 6 \tag{2}$$

$$B_{ij} = \frac{1}{2} \sum_{k=1}^{n} \left[\bar{Q}_{ij}\right]_k \left(h_k^2 - h_{k-1}^2\right), \quad i = 1, 2, 6; \; j = 1, 2, 6 \tag{3}$$

$$D_{ij} = \frac{1}{3} \sum_{k=1}^{n} \left[\bar{Q}_{ij}\right]_k \left(h_k^3 - h_{k-1}^3\right), \quad i = 1, 2, 6; \quad j = 1, 2, 6 \tag{4}$$

5. Based on the loading conditions, apply the forces $\{N\}$ and moments $\{M\}$ in Eq. (5) to find the midplane strains $\{\varepsilon_o\}$ and curvatures $\{\kappa\}$.

$$\begin{bmatrix} N \\ \hline M \end{bmatrix} = \left[\begin{array}{c|c} A & B \\ \hline B & D \end{array}\right] \begin{bmatrix} \varepsilon_0 \\ \hline k \end{bmatrix} \tag{5}$$

6. Global strains may be evaluated in each ply as

$$\begin{bmatrix} \varepsilon_x \\ \varepsilon_y \\ \gamma_{xy} \end{bmatrix} = \begin{bmatrix} \varepsilon_x^0 \\ \varepsilon_y^0 \\ \gamma_{xy}^0 \end{bmatrix} + z \begin{bmatrix} \kappa_x \\ \kappa_y \\ \kappa_{xy} \end{bmatrix} \tag{6}$$

7. Using the stress–strain equation, evaluate the global stresses.
8. Using the transformation equation, evaluate the local strains.
9. Using local strains, find the local stresses.

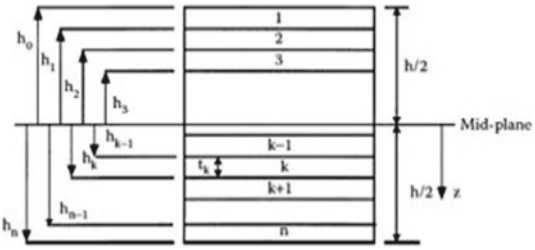


Fig. 1 Coordinate locations of plies in a laminate [7]

3 Hygrothermal Effects in Laminates

A laminate is generally a stack of plies which may have different fibre orientation and made of different materials. When such laminates are subjected to hygrothermal load, it will lead to residual stresses, as an individual ply is not free to expand. Hygrothermal loads are imposed on a structure, when it operates at a temperatures other than processing temperatures and when it is subjected to humid environments such as encountered by cruising aircrafts at high altitudes. When subjected to this hygrothermal loads, the deformation differences of adjacent plies lead to the stresses in the laminate. It should also be noted that the strains that are greater or lesser than the hygrothermal strains in the ply that is free to expand and produce the residual stresses.

Hygrothermal stresses in a lamina are given by [7]

$$\begin{bmatrix} \sigma_x^{\mathrm{TC}} \\ \sigma_y^{\mathrm{TC}} \\ \tau_{xy}^{\mathrm{TC}} \end{bmatrix} = \begin{bmatrix} \bar{Q}_{11} & \bar{Q}_{12} & \bar{Q}_{16} \\ \bar{Q}_{12} & \bar{Q}_{22} & \bar{Q}_{26} \\ \bar{Q}_{16} & \bar{Q}_{26} & \bar{Q}_{66} \end{bmatrix} \begin{bmatrix} \varepsilon_x^M \\ \varepsilon_y^M \\ \gamma_{xy}^M \end{bmatrix} \tag{7}$$

where TC stands for combined thermal and moisture effects.

The mechanical stresses are evaluated in the kth ply as

$$\begin{bmatrix} \sigma_x \\ \sigma_y \\ \tau_{xy} \end{bmatrix}_k = \begin{bmatrix} \bar{Q}_{11} & \bar{Q}_{12} & \bar{Q}_{16} \\ \bar{Q}_{12} & \bar{Q}_{22} & \bar{Q}_{26} \\ \bar{Q}_{16} & \bar{Q}_{26} & \bar{Q}_{66} \end{bmatrix} \begin{bmatrix} \varepsilon_x^M \\ \varepsilon_y^M \\ \gamma_{xy}^M \end{bmatrix}_k \tag{8}$$

where in the mechanical strains in that ply are given as

$$\begin{bmatrix} \varepsilon_x^M \\ \varepsilon_y^M \\ \gamma_{xy}^M \end{bmatrix}_k = \begin{bmatrix} \varepsilon_x \\ \varepsilon_y \\ \gamma_{xy} \end{bmatrix}_k - \begin{bmatrix} \varepsilon_x^T \\ \varepsilon_y^T \\ \gamma_{xy}^T \end{bmatrix}_k - \begin{bmatrix} \varepsilon_x^C \\ \varepsilon_y^C \\ \gamma_{xy}^C \end{bmatrix}_k \tag{9}$$

4 Failure Analysis

Failure theories of isotropic materials cannot be applied directly to laminated composites as they exhibit anisotropic behaviour. This led the researchers to focus on the area of failure criteria for fibre-reinforced laminated composite materials. Despite such an intense work on this field, none of the criterion was accepted universally for practical engineering design. In the present work, the following failure criteria (Macroscopic Ply-stress failure criteria) that are proven to be accurate for many problems of practical interest are used

(1) Tsai-Hill
(2) Tsai-Wu
(3) Maximum stress
(4) Maximum strain.

In the present study, the progressive failure analysis was carried out to predict the failure load for both first ply failure (FPF) and the last ply failure (LPF). In the progressive failure analysis, failed plies are still considered effective and new strength properties will be assigned for failed plies until the ultimate failure. Figure 2 gives the flowchart for failure analysis of laminate for FPF and LPF, respectively. In the present study, the failure loads for both FPF and LPF are predicted using all four different theories mentioned before and it is compared. The flowchart for the complete analysis, including all the components such as micro- and macro-mechanics of laminate along with the failure analysis of the software, is given in Fig. 3.

5 Results

The procedure displayed in Fig. 3 for both the first ply failure and last ply failure is transformed into a MATLAB-based code. As the failure analysis of fibre-reinforced composite laminates are dominated by matrix manipulation, MATLAB language was selected, as it is an extremely popular software for matrix manipulation. Graphical user interface (GUI) was used which enables the student interact easily with the software and hence it is very user-friendly as compared to the general command-line interface. To make the student comfortable in learning the software, a user manual as well as a step by step demonstrating video is incorporated. Typical input and output GUI's of the developed software are given in Fig. 4. The users are given an option to select the output results either in tabulated or in the graphical form.

In order to validate the software, the following example is taken from Kaw [7].

Case study (1): Given that the properties of a lamina as

$$E_1 = 181\text{GPa (in fibre direction)}, \quad E_2 = 10.30\ \text{GPa},$$
$$v_{12} = 0.280 \quad G_{12} = 7.17\ \text{GPa}$$

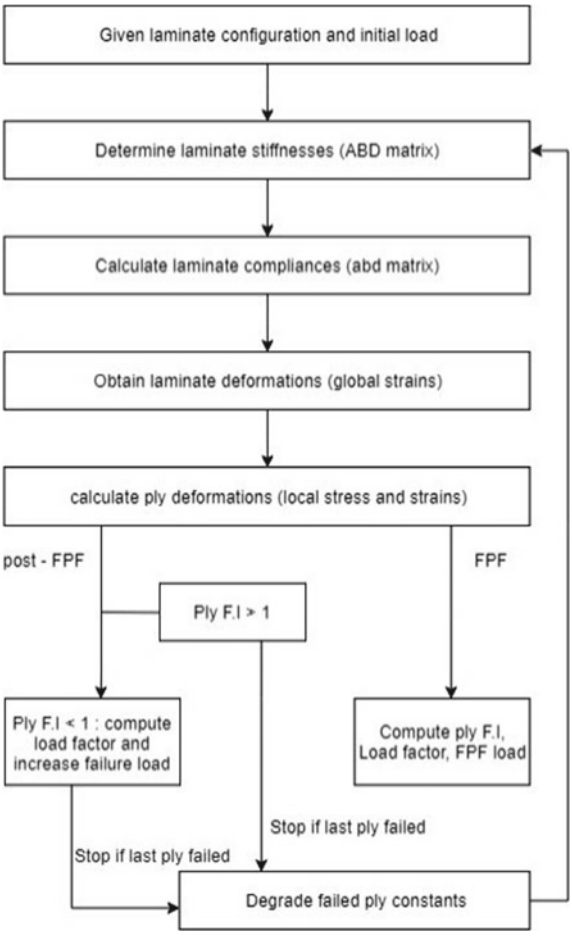


Fig. 2 First ply failure (FPF) and last ply failure (LPF) procedure [8]

and the ply thickness is taken to be 5 mm with laminate configuration of [0/90/0]. The applied load is taken to be only N_x.

Based on the procedure illustrated in Figs. 2, and 3, the final strength ratios for the first ply failure (FPF) and the last ply failure (LPF) are shown in Tables 1 and 2, respectively, wherein the strength ratio (SR)s defined as the ratio of the maximum load that can applied to the load applied [7]. If SR < 1, then the laminate is considered to be unsafe. The results attained agree well with the literature values.

Similarly, problems involving the failure analysis of laminates under hygrothermal loads from Kaw [7] and Datoo [8] have been solved through the software and the results seem to be conforming with the literature.

With the help of this software with laminate failure analysis, one can also design a laminate with various combinations of laminae (hybrid laminate) for a given loading as illustrated by the following example from Kaw [7].

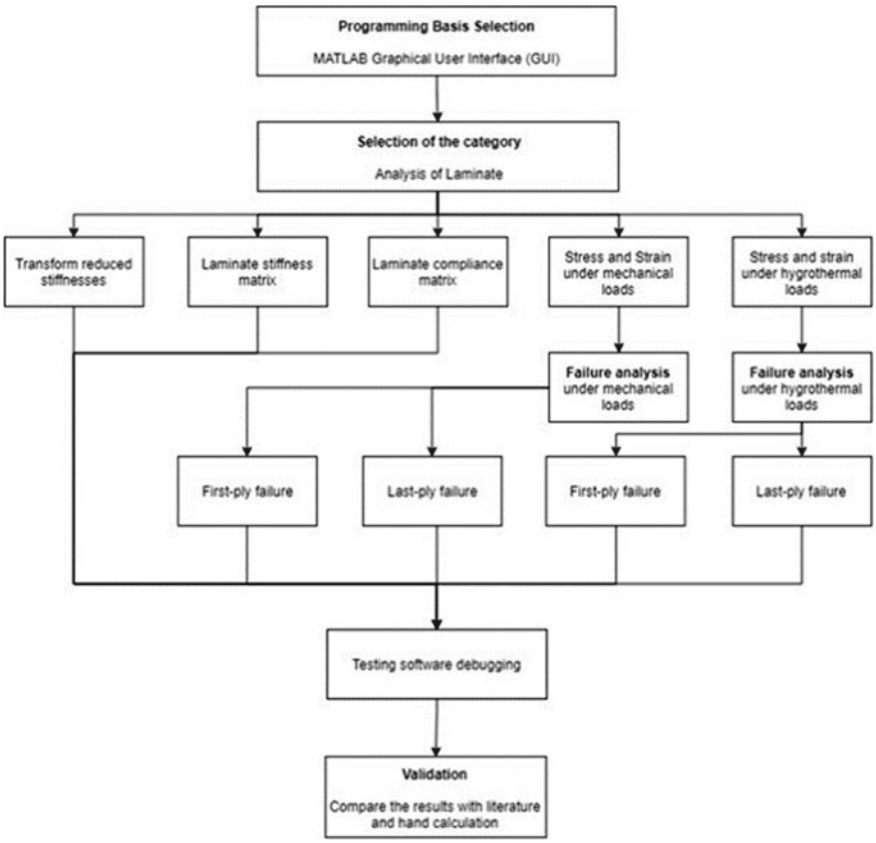


Fig. 3 Flowchart for overall software

Case study (2): Design a laminated composite plate that can replace a 4 × 4 in aluminium plate subjected to $M_x = 13000$ lb-in. It has to be designed such that the thickness is reduced to half of the aluminium plate. The thickness of the ply is taken to be 0.0049213 in. The designer can choose any combination of the following two unidirectional laminae with graphite/epoxy having a cost of 10 units and glass/epoxy having a cost of 4 units. Assume a factor of safety 2.

For this problem, the software was able to reproduce exactly the same results as reported by Kaw [7] for various combinations of glass/epoxy and graphite/epoxy. The final combination that resulted in minimum SR and minimum cost is 68 layers of glass/epoxy and 32 layers of graphite/epoxy leading to a value of SR of 1.014 and minimum cost of 592 units exactly similar to that obtained by Kaw [7].

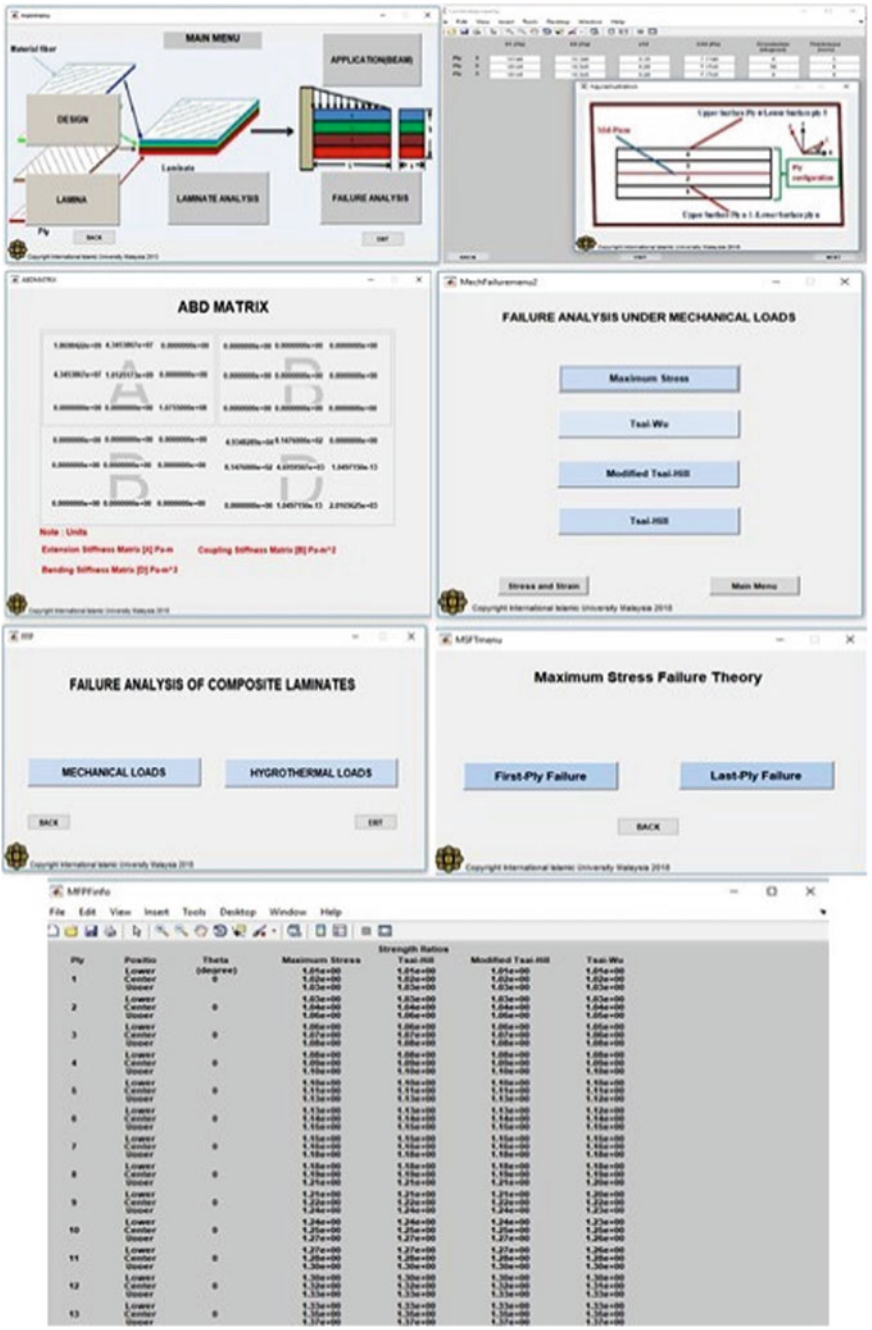


Fig. 4 Typical input and output GUIs of the software

Table 1 Validation of first ply failure (FPF) under mechanical loads

Ply number	Position	Maximum stress theory	Tsai-Wu theory
1 (0°)	Top	$1.54 \times 10^7 (1.548 \times 10^7)$	$1.34 \times 10^7 (1.339 \times 10^7)$
	Middle	$1.54 \times 10^7 (1.548 \times 10^7)$	$1.34 \times 10^7 (1.339 \times 10^7)$
	Bottom	$1.54 \times 10^7 (1.548 \times 10^7)$	$1.34 \times 10^7 (1.339 \times 10^7)$
2 (90°)	Top	$7.31 \times 10^6 (7.254 \times 10^6)$	$7.28 \times 10^6 (7.277 \times 10^6)$
	Middle	$7.31 \times 10^6 (7.254 \times 10^6)$	$7.28 \times 10^6 (7.277 \times 10^6)$
	Bottom	$7.31 \times 10^6 (7.254 \times 10^6)$	$7.28 \times 10^6 (7.277 \times 10^6)$
3 (0°)	Top	$1.54 \times 10^7 (1.548 \times 10^7)$	$1.34 \times 10^7 (1.339 \times 10^7)$
	Middle	$1.54 \times 10^7 (1.548 \times 10^7)$	$1.34 \times 10^7 (1.339 \times 10^7)$
	Bottom	$1.54 \times 10^7 (1.548 \times 10^7)$	$1.34 \times 10^7 (1.339 \times 10^7)$

Note The values in the bracket are as reported by Kaw [7]

Table 2 Validation of last ply failure (LPF) under mechanical loads

Ply number	Position	Maximum-stress theory	Tsai-Wu theory
1 (0°)	Top	1.5×10^7 (1.5×10^7)	1.5×10^7 (1.5×10^7)
	Middle	1.5×10^7 (1.5×10^7)	1.5×10^7 (1.5×10^7)
	Bottom	1.5×10^7 (1.5×10^7)	1.5×10^7 (1.5×10^7)
2 (90°)	Top	0	0
	Middle	0	0
	Bottom	0	0
3 (0°)	Top	1.5×10^7 (1.5×10^7)	1.5×10^7 (1.5×10^7)
	Middle	1.5×10^7 (1.5×10^7)	1.5×10^7 (1.5×10^7)
	Bottom	1.5×10^7 (1.5×10^7)	1.5×10^7 (1.5×10^7)

Note The values in the bracket are as reported by Kaw [7]

6 Conclusion

A stress analysis software which can evaluate stresses and strains on the fibre-reinforced laminated composite has been developed. The software can be used to analyse a lamina as well as laminates under both mechanical and hygrothermal loads. In addition to that, it can perform failure analysis of laminates made of any number of plies and made of different materials (hybrid laminate) to predict the failure load for both first ply failure and last ply failure. The software was developed with the help of MATLAB-GUI which makes the software very user-friendly. Case studies prove

that results from the software are found to be in good agreement with the existing literature. The software has been used by the students for the past two semesters at IIUM and a very positive feedback was received from them. The software can be further improved to handle thin-walled sections made of composite materials.

Acknowledgements This work is supported by the Research Management Centre, International Islamic University Malaysia.

References

1. Philpot TA (2000) MDSolid: software to bridge the gap between lectures and homework in mechanics of materials. Int J Eng Educ 16:401–407
2. Mohamed Ali JS, Fadhila HN, Aziz NAB (2013) Educational software for stress analysis of idealized thin walled open sections. Appl Mech Mater 315:339–343
3. Mohamed Ali JS, Ibrahim MOA, Mohammed RM (2019) Educational software for stress analysis of non-idealized closed thin-walled sections. Int J Eng Technol 7(6S):196–202
4. Kaw AK, Willenbring G (1997) A software tool for mechanics of composite materials. Int J Eng Educ 433–441
5. Voyiadjis GZ, Kattan PI (2005) Mechanics of composite materials with matllab. Springer, Berlin
6. Mohamed Ali JS, Abeid RA (2015) LEADME: an educational software for Composite laminate analysis and design. Adv Mater Res 1115:578–581
7. Kaw AK (2006) Mechanics of composite materials. CRC Press, Taylor and Francis Group, New York
8. Datoo MH (1991) Mechanics of fibrous composites. Elsevier Applied Science, London

A Discrete Artificial Immune System Algorithm for the Lot Streaming Flow Shop Scheduling Problem

R. Kamalakannan, M. Shunmugasundaram, R. Nagaraj, D. Aravindhan, and S. Mohammed Thouffic

Abstract This paper attempts to present the challenge of scheduling *n* jobs–*m* machines in the flow shop scheduling environment. In this scheduling, lot streaming is a method used to divide up multiple sublots to allow functions to intersect across multiple production systems. The purpose of this work is to reduce the time and save the manufacturing cost. In recent times, researchers have used bright heuristics to explain flow shop difficulties on a lot streaming problem. In this work, artificial immune system (AIS) algorithm is used to solve the lot streaming concept in the flow shop scheduling environment with the objective of minimizing the makespan time. In addition, a nature ability to change to suit different conditions for generating the neighborhood antibodies based on the inverse and pairwise mutation. The results obtained by this algorithm are compared with the standard benchmark instances. This proposed algorithm is capable and establishes to be a superior problem-solving technique for this flow shop scheduling with lot streaming.

Keywords Flow shop scheduling · Lot streaming · Sequencing · Makespan · Artificial immune system algorithm · Heuristics

1 Introduction

A timetable remains an adjustment of the activities to the period intermissions of the system and the goal is to discover a timetable which reduces the average conclusion period, named the makespan. In the flow shop arrangement, problematic n task is to be performed on dissimilar machineries. Through work is a set of tasks that must be completed on a given machine during a fixed-length uninterrupted time period. According to the restrictions that each flow has a given order of execution through the machines and that each device must execute at most one flow at a time, the overall

R. Kamalakannan (✉) · R. Nagaraj · D. Aravindhan · S. Mohammed Thouffic
Department of Mechanical Engineering, M. Kumarasamy College of Engineering, Karur, India
e-mail: kamalbritto@yahoo.co.in

M. Shunmugasundaram
Department of Mechanical Engineering, CMR Technical Campus, Hyderabad, India

© Springer Nature Singapore Pte Ltd. 2020

A. Praveen Kumar et al. (eds.), *Advances in Lightweight Materials and Structures*,
Springer Proceedings in Materials 8, https://doi.org/10.1007/978-981-15-7827-4_83

processing time required to process all flows. The records by Sule [1], Chao and Pinedo [2] and Baker [3] contain basic information on scheduling problems. Many investigators considered the difficulties of timing with spilling of plenty. Wassenhove and Potts [4] showed an inspection regarding these kinds of issues. Baker and Potts [5] researched the issue of streaming only invention lots in a flow store. Baker [6] recycled time-lagged arrangement templates and setup stages to evaluate multiple commodity lot spilling in a two-appliance flow shop with set up periods. They also addressed the applications of more than two computers to special cases. Glass et al. [7] suggested a network typical for examining three-mechanism flow shop problems with lot uploading, and then generalized their findings to three-apparatus exposed shop issues and two-mechanism task factory issues. In a two-mechanism flow yard with minimal barriers, Vick son [8] suggested a direct programming paradigm for batch spilling and arrangement of many products. Wagneur and Sriskandarajah [9] researched two-mechanism flow workshops in a no-wait environment, with both nonstop and numeral lot extents. Kumar et al. [10] found the problematic of outcome is the maximum sublots of numeral for an only product. In no-gap flow workshops problem, Hall et al. [11] advanced effective heuristic for arrangement and spilling of lots. Liu [12] suggested an experiential approach for distinct spilling of masses in a flow shop with variable sublots. The AIS algorithm is already used in a variety of applications including system and network security detection of faults and anomalies, configuration, data investigation and data withdrawal and flow plant arrangement wherever AIS has formed healthier results.

Several scholars tried to highlight the significance of heuristics and other evolutionary algorithms and their pitfalls. The use is added of the latest evolutionary thought viz. AIS is considered to explain the difficulties concerning flow shop scheduling. The study shows that one of the productive areas of research is flow shop scheduling with lot streaming. This paper presents about the problem of manufacture in timing and arrangement results below the lot of sizing setting from jobs–m-machineries flow shops. If portion sharing is allowed, the preparations of results become added as complicated. In a flow shop, the m-machines with ton spilling, there is room for powerful algorithms to schedule problems.

2 Problem Description

The arrangement of jobs considered in this paper is n job–m machine flow shop scheduling problem with uneven lot streaming. Each job j will be in sequence process on m-machines and it is similar on all the machines. Let P_{ij} be the time taken to process each sublot j in machine i, and the setup time is considered as S_{ij} for each sublot j in machine i. The time taken to complete job j on machine i is considered as C_{ij}. The objective of this work is to reduce the makespan time and let it be assumed as Z. The mathematical model can be written as.

2.1 Minimize

$$Z \geq C_{ij}, \forall i, j \tag{1}$$

Subjected to

$$A_{ij} + S_{ij} + P_{ij} \geq Z, \forall i, j \tag{2}$$

$$A_{ij} + S_{ij} + P_{ij} \geq A_{j(i+1)}, \ \forall i, j \tag{3}$$

$$S_{ij} \geq 0, \forall i, j \tag{4}$$

$$P_{ij} \geq 0, \forall i, j \tag{5}$$

$$C_{ij} \geq 0, \forall i, j \tag{6}$$

In the above mathematical model, Eq. (1) denotes the makespan time, Eq. (2) denotes a calculation of schedule that reduces the makespan, Eq. (3) denotes the calculation of arrival time of current job sequence to be processed is greater than the completion time of previous job sequence, Eq. (4) denotes the setup time of all jobs j on all machine i is greater than or equal to zero, Eq. (5) denotes the processing time of all job j on all machine i is greater than or equal to zero, and Eq. (6) denotes the completion time of job j on machine i is greater than or equal to zero.

3 Artificial Immune System Algorithm

From a theoretical point of view, the operating processes of the immune system are very effective [13]. The AIS remained based on the two ethics below for the protected structure is clonal collection process and affinity ripening process. Growing plan (antibody) takes a makespan rate which corresponds to the attraction rate of the antibody. Every plan's affinity rate remains to be determined using the affinity equation. Affinity's role is well defined by the way of affinity (p) = (1/makespan). An inferior makespan rate of this relation stretches an advanced rate of affinity. In fact, antibody cloning is done directly relative to the values of their biological activity. Therefore, there will be more clones of antibodies in the newly formed clone population which takes an inferior makespan standard than individuals with developed makespan standards. Popular [14], an immune-based approach has been suggested to raise the makespan on parallel processors. The schedules [15, 16] makespan values are used to describe an affinity function. We have also given a method of determining the number of clones that would proliferate [17, 18]. Affinity maturation theory is composed of binary operations, specifically alteration and deletion of receptors. At

adjustment process, a binary-phase alteration technique was employed aimed at the clones made [19] for the twins produced.

3.1 Inverse Mutation

Aimed at a classification *s* let *i* and *j* casually choose binary spots trendy the arrangements. Inverting the function arrangement between situations *I* and *j* will obtain a neighbor of *s*. If the mutated sequence's makespan value (after the reverse transformation) is lesser than that of the unique arrangement (a twin formed after an antibody), then the altered one is deposited in the original's residence. Additionally, the arrangement would be modified over by arbitrary pairwise swap transformation.

3.2 Pairwise Mutation

Provided an arrangement *s* allows for random selection of two locations in the sequence *s* for *i* and *j*. A national of *s* remains acquired in labor trade placed under fashionable situations *i* and *i*. If the makespan rate of the altered arrangement is less than that of the unique arrangement (after pair wise swap mutation), so, stock is transformed individual instead of the creative. In the event, the system could not invent a restored arrangement next the binary-mutation process, it will then supply the unique arrangements (produced twin).

4 Artificial Immune System Algorithm

From this result, the systems for an illustration problematic process (5 jobs–2 machineries) are specified in this segment. Given stand delivers the information measured in the illustration delinquent. In the overall process, the arrangement of *n*-jobs can be mathematically as follows: m-machineries flow yard lot spilling through equivalent sublots delinquent (Tables 1, 2 and 3):

$$\text{Cloning rate} = (\text{Affinity value} * \text{population size}) / \sum \text{Affinity value}$$

Table 1 2 machines 5 jobs data

Problem data	j				
	1	2	3	4	5
n_j	2	2	3	2	2
S_{1j}	2	3	4	2	3
P_{1j}	2	3	3	2	2
S_{2j}	2	3	2	3	4
P_{2j}	3	2	3	1	2

Table 2 Seed sequence randomly generated

Sequence	Seed sequence	Inverse mutation	Pairwise mutation	Make span	Affinity value	Rate of cloning
1	1-2-3-4-5	5-2-3-4-1	3-4-1-2-5	47	0.0212	0.972
2	2-3-4-5-1	2-4-3-5-1	4-5-2-3-1	48	0.0208	0.953
3	3-4-5-1-2	3-1-5-4-2	1-2-5-3-4	45	0.0222	1.017
4	4-5-1-2-3	5-4-1-2-3	2-3-1-4-5	46	0.0217	0.994
5	5-1-2-3-4	5-3-2-1-4	3-4-2-5-1	45	0.0222	1.017
6	5-4-3-2-1	4-5-3-2-1	5-2-1-4-3	46	0.0217	0.994
7	4-3-2-1-5	4-3-5-1-2	4-1-5-3-2	45	0.0222	1.017
8	3-2-1-5-4	3-2-4-5-1	3-5-4-2-1	47	0.0212	0.972
9	2-1-5-4-3	1-2-5-4-3	2-4-3-1-5	45	0.0222	1.017
10	1-5-4-3-2	1-4-5-3-2	4-3-1-5-2	44	0.0227	1.040

Table 3 Results evaluation of makespan and affinity of each sequence

Sequence	Seed sequence	Inverse mutation	Pairwise mutation	Make span	Affinity value	Rate of cloning
1	1-2-3-4-5	5-2-3-4-1	3-4-1-2-5	47	0.0212	0.972
2	2-3-4-5-1	2-4-3-5-1	4-5-2-3-1	48	0.0208	0.953
3	3-4-5-1-2	3-1-5-4-2	1-2-5-3-4	45	0.0222	1.017
4	4-5-1-2-3	5-4-1-2-3	2-3-1-4-5	46	0.0217	0.994
5	5-1-2-3-4	5-3-2-1-4	3-4-2-5-1	45	0.0222	1.017
6	5-4-3-2-1	4-5-3-2-1	5-2-1-4-3	46	0.0217	0.994
7	4-3-2-1-5	4-3-5-1-2	4-1-5-3-2	45	0.0222	1.017
8	3-2-1-5-4	3-2-4-5-1	3-5-4-2-1	47	0.0212	0.972
9	2-1-5-4-3	1-2-5-4-3	2-4-3-1-5	45	0.0222	1.017
10	1-5-4-3-2	1-4-5-3-2	4-3-1-5-2	44	0.0227	1.040

5 Genetic Algorithms (GA) and Artificial Immune System (AIS)

All AIS and GA are algorithms that focus on and are biologically informed by the human community. Around is no modification in the AIS among a GA gene and an antibody so they prepare contrast in the illustration of the machineries.GA similarly has health role, and also artificial immune system has an attraction role to decide the compatibility of respective person. Their evolutionary selection events however vary since one another. Now, highlight the alteration among our artificial immune system solution and a genetic algorithms approach. Initially, new generations have varied reproductions and preferences. Fusion and mutation are the main methods for developing new approaches within a standard GA; in artificial immune system (AIS), it is attained by replicating and transmuting anti-corps independent of their affinity role standards. For artificial immune system (AIS), transformations are directly verified aimed at approval before rejection, slightly than a segment in which a original group is chosen as in genetic algorithms (Tables 4, 5, 6 and 7).

Table 4 Cloning process in proposed AIS

Sequence	Cloned sequence	Seed sequence	Inverse mutation	Pairwise mutation	Make span	Affinity value
1	1	1-2-3-4-5	5-2-3-4-1	3-4-1-2-5	47	0.0212
2	1	2-3-4-5-1	2-4-3-5-1	4-5-2-3-1	48	0.0208
3	1	3-4-5-1-2	3-1-5-4-2	1-2-5-3-4	45	0.0222
	2	3-4-5-1-2	3-4-5-2-1	3-1-2-4-5	46	0.0217
4	1	4-5-1-2-3	5-4-1-2-3	2-3-1-4-5	46	0.0217
5	1	5-1-2-3-4	5-3-2-1-4	3-4-2-5-1	45	0.0222
	2	5-1-2-3-4	4-1-2-3-5	5-3-4-1-2	45	0.0222
6	1	5-4-3-2-1	4-5-3-2-1	5-2-1-4-3	46	0.0217
7	1	4-3-2-1-5	4-3-5-1-2	4-1-5-3-2	45	0.0222
	2	4-3-2-1-5	4-5-2-1-3	2-1-4-3-5	45	0.0222
8	1	3-2-1-5-4	3-2-4-5-1	3-5-4-2-1	47	0.0212
9	1	2-1-5-4-3	1-2-5-4-3	2-4-3-1-5	45	0.0222
	2	2-1-5-4-3	2-4-5-1-3	5-4-2-1-3	45	0.0222
10	1	1-5-4-3-2	1-4-5-3-2	4-3-1-5-2	44	0.0227
	2	1-5-4-3-2	5-1-4-3-2	3-2-4-1-5	44	0.0227

Table 5 Mutation process in proposed AIS

Sequence	Seed sequence	Inverse mutation	Pairwise mutation	Make span	Affinity value	Rate of cloning
1	1-5-4-3-2	1-4-5-3-2	4-3-1-5-2	44	0.0227	1.020
2	1-5-4-3-2	5-1-4-3-2	3-2-4-1-5	44	0.0227	1.020
3	2-1-5-4-3	1-2-5-4-3	2-4-3-1-5	45	0.0222	0.997
4	2-1-5-4-3	2-4-5-1-3	5-4-2-1-3	45	0.0222	0.997
5	4-3-2-1-5	4-3-5-1-2	4-1-5-3-2	45	0.0222	0.997
6	4-3-2-1-5	4-5-2-1-3	2-1-4-3-5	45	0.0222	0.997
7	5-1-2-3-4	5-3-2-1-4	3-4-2-5-1	45	0.0222	0.997
8	5-1-2-3-4	4-1-2-3-5	5-3-4-1-2	45	0.0222	0.997
9	3-4-5-1-2	3-1-5-4-2	1-2-5-3-4	45	0.0222	0.997
10	3-4-5-1-2	3-4-5-2-1	3-1-2-4-5	46	0.0217	0.975

Table 6 Receptor editing process in proposed AIS

Sequence	Seed sequence	Inverse mutation	Pairwise mutation	Make span	Affinity value	Rate of cloning
1	1-5-4-3-2	1-4-5-3-2	4-3-1-5-2	44	0.0227	1.020
2	1-5-4-3-2	5-1-4-3-2	3-2-4-1-5	44	0.0227	1.020
3	2-1-5-4-3	1-2-5-4-3	2-4-3-1-5	45	0.0222	0.997
4	2-1-5-4-3	2-4-5-1-3	5-4-2-1-3	45	0.0222	0.997
5	4-3-2-1-5	4-3-5-1-2	4-1-5-3-2	45	0.0222	0.997
6	4-3-2-1-5	4-5-2-1-3	2-1-4-3-5	45	0.0222	0.997
7	5-1-2-3-4	5-3-2-1-4	3-4-2-5-1	45	0.0222	0.997
8	5-1-2-3-4	4-1-2-3-5	5-3-4-1-2	45	0.0222	0.997
9	3-4-5-1-2	3-1-5-4-2	1-2-5-3-4	45	0.0222	0.997
10	3-4-5-1-2	3-4-5-2-1	3-1-2-4-5	46	0.0217	0.975

Table 7 Final result obtained after 500 iterations in proposed AIS

Sequence	Seed sequence	Inverse mutation	Pairwise mutation	Make span	Affinity value
1	1-5-4-3-2	1-4-5-3-2	4-3-1-5-2	44	0.0227
2	1-5-4-3-2	5-1-4-3-2	3-2-4-1-5	44	0.0227
3	2-1-5-4-3	1-2-5-4-3	2-4-3-1-5	45	0.0222
4	2-1-5-4-3	2-4-5-1-3	5-4-2-1-3	45	0.0222
5	4-3-2-1-5	4-3-5-1-2	4-1-5-3-2	45	0.0222
6	4-3-2-1-5	4-5-2-1-3	2-1-4-3-5	45	0.0222
7	5-1-2-3-4	5-3-2-1-4	3-4-2-5-1	45	0.0222
8	4-5-1-2-3	5-4-1-2-3	2-3-1-4-5	46	0.0217
9	1-2-3-4-5	5-2-3-4-1	3-4-1-2-5	47	0.0212
10	2-3-4-5-1	2-4-3-5-1	4-5-2-3-1	48	0.0208

6 AIS Algorithm Proposed for the Problem of Flow Shop Environment

In the process of flow diagram in Fig. 1 includes details of the artificial immune system (AIS) process used to explain the laboratory arrangement difficulties. Fashionable this job, potential plans are characterized by integer-evaluated sequences of the span

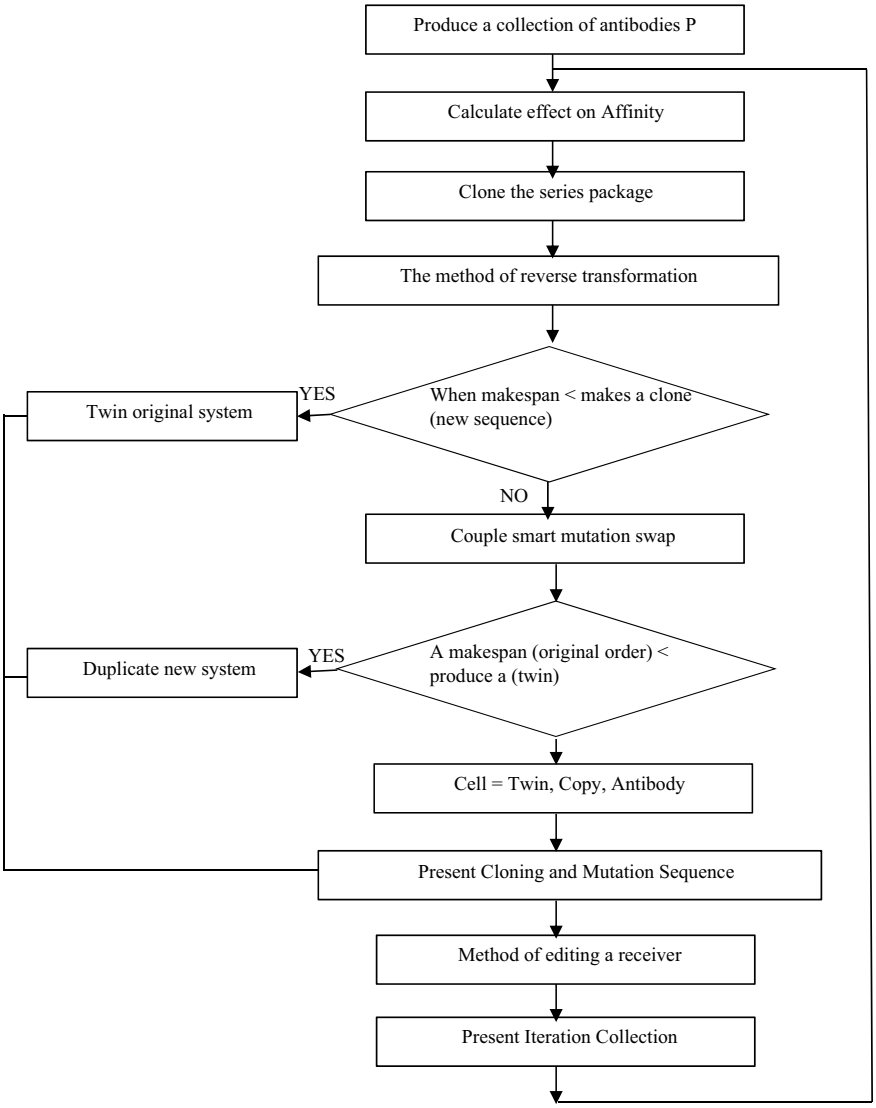


Fig. 1 Flowchart of AIS algorithm to plan flow shops

n (flows). The functions to be sequenced are the *n* array components. Thus, the filaments consist of transformations of the elements *n* (flows). These strings are taken as anti-corps artificial immune system (AIS). The system drives up to answer by the development of those antibodies. Creates P antibodies (flow orders) in population.

7 Result and Discussions

The recommended AIS algorithm has been tested with the benchmark problems from the literature, which includes Bakers algorithm and genetic algorithm. The results show that the proposed methodology is doing well for the small size, medium size problems, and showing the same performance for the large size problems. This AIS algorithm is coded in MATLAB 12.0 and executed in a Intel i5 processor, 4 GB RAM system. Since the algorithm considered for testing is the standard algorithm which already proved as a good algorithm for the makespan objective in two machine cases. The solution is attained with the particular number of iterations. AIS estimates fixed number of optimum solutions as antibodies in each iteration. The number of of generations performed by AIS is dealed with the number of jobs.

8 Conclusion

Artificial immune system (AIS) algorithm is proposed for reducing the makespan for n jobs-m-machines flow shop scheduling with lot streaming. This work assesses the performance of AIS algorithm in solving the flow shop scheduling problem with lot streaming. Evaluation with Baker and genetic algorithm shows that AIS is capable of giving good solutions. With reference to the computational time, AIS done well with other algorithms. The parameters of AIS are tested with several number of problems sets. They can be still fine-tuned and compared with the different problem size with high rigorous analysis. The directions for future research is this work can be further extended by including several objectives like flow time, tardiness, etc. In addition, the problem can be investigated with due data-related criteria [20] (Table 8).

Table 8 Comparisons of BA, GA, and AIS in two machine case for makespan

Job size	Problem in sequence	BA	Genetic algorithm	Artificial immune system		
		Makespan	Makespan	Makespan	%Difference with BA*	%Difference with GA*
15	1	429	429	429	0	0
	2	363	363	363	0	0
	3	249	249	234	15	15
	4	291	291	291	0	0
	5	305	305	305	0	0
Time	–	0.04	2.25	1.02	–	–
25	1	648	648	635	13	13
	2	581	581	581	0	0
	3	436	436	421	15	15
	4	489	489	489	0	0
	5	671	671	671	0	0
Time	–	0.05	9.28	4.09	–	–
35	1	914	914	910	4	4
	2	772	772	772	0	0
	3	709	709	681	28	28
	4	720	720	720	0	0
	5	892	892	892	0	0
	–	0.05	24.55	12.32	–	–
50	1	1258	1258	1211	47	47
	2	1153	1153	1154	1	1
	3	1013	1013	1013	0	0
	4	1035	1035	1021	14	14
	5	1250	1250	1250	0	0
Time	–	0.05	82.47	42.34	–	–

% Difference = % Variance through both GA versus BA system with AIS

References

1. Sule DR (1997) Industrial planning. PWS Publishing Company, USA
2. Pinedo M, Chao X (1997) Operational planning. Irwin McGraw-Hill, New York
3. Baker KR (1974) Introduction to sorting and planning. Wiley, New York
4. Potts CN, Wassenhove LN (1992) Compiling and integrating scheduling with lots of volume: a methodological and complex study. J Oper Res Soc 43(5):395–406
5. Potts CN, Baker KR (1989) Flow shop planning with lots of streaming. Oper Res Lett 8:297–303
6. Baker KR (1995) Lots of streaming in two machines ow ow store with setup times. An Opport Res 57:1–11
7. Glass CA, Gupta JNT, Potts CN (1994) Lots of streaming in a three-phase process. Eur J Oper Res 75:378–394

8. Kamalakannan R, Sudhakara Pandian R, Sivakumar P (2019) A simulated annealing for the cell formation problem with ratio level data. Int J Enterp Netw Manage 10(1):78–89
9. Sriskandarajah C, Wagner E (1999) Scheduling multiple products in the parking lot and two machine no-wait ow ow store. IIE Trans 31:695–707
10. Kamalakannan R, Sudhakara Pandian R, Sivakumar P (2018) A tabu search strategy for the cell formation problem using ratio level data. Int J Bus Intel Data Min 13(1–3):209–220
11. Hall NG, LaPorte G, Selvarajah E, Srikandarajah C (2003) Planning and streaming a lot in ow stores. J Plan 6(4):339–354
12. Liu SC (2003) A heuristic method for streaming unique lots with variable subplots in an ow ow store. Int J Adv Manuf Technol 22:662–668
13. Eng O, Doyen A (2004) A new approach to solving hybrid flow shop planning problems by artificial immune system. Future Gener Syst Syst 20:1083–1095
14. Zheng H, Zhang J, Nahawandi S (2004) Learning to detect textures by artificial immune approaches. Fut Gener Comput Syst 20:1197–1208
15. Vijay Chakravarthy G, Marimuthu S, Naveen Sait A (2012) Comparision of firefly algorithm and artificial immune system algorithm for lot streaming in m machine flow shop scheduling. Int J Comput Intel Syst 5(6):1184–1189
16. Chandrasekharan M, Asokan P, Kumanan S, Balamurugan T, Nickolas S (2006) Solving job scheduling problems using artificial immune system. Int J Adv Manuf Technol 31:580–593
17. Marimuthu S, Ponnambalam SG, Jawahar N (2008) Evolutionary algorithms for scheduling m-machine flow shop with lot streaming. Rob Comput Integr Manuf 24:125–139
18. Vijay Chakravarthy G, Marimuthu S, Ponnambalam SG, Kanagaraj G (2014) Improved sheep flock heredity algorithm and artificial bee colony algorithm for scheduling m-machine flow shops lot streaming with equal size sub-lot problems. Int J Prod Res 52(5):1509–1527
19. Marimuthu S, Ponnambalam SG, Jawahar N (2009) Threshold accepting and Ant-colony optimization algorithms for scheduling m-machine flow shops with lot streaming. J Mater Proces Technol 209:1026–1041
20. Khatami M, Salehipour A (2019) Hwang FJ, Makespan minimization for the m-machine ordered flow shop scheduling problem. Comput Oper Res 111:400–414